Macromolecules
PERSPECTIVE

Macromolecules **2011**, *44*, 417–428 **417**
DOI: 10.1021/ma1023457

Surface-Induced Polymer Crystallization and the Resultant Structures and Morphologies

Huihui Li and Shouke Yan*

State Key Laboratory of Chemical Resource Engineering, Beijing University of Chemical Technology, Beijing 100029, China

Received October 13, 2010; Revised Manuscript Received December 27, 2010

ABSTRACT: The dependence of properties on the structure and morphology of semicrystalline polymers offers an effective way to tailor the properties of these materials through crystal engineering. For purposeful control of the structure and morphology, and therefore the physical and mechanical properties, a full understanding of the crystallization habits of polymers under different environments and conditions is essential. This has stimulated a mass of research work on polymer crystallization. Considering that these materials are frequently in contact with some kinds of solid surfaces in a variety of applications, surface-induced crystallization of polymers has attracted considerable attention during the past decades. This Perspective provides the context as to how the solid surface influences the crystallization behavior of polymers and what kinds of unique crystal structure and morphology of the polymers can be fabricated. We hope that this will afford useful information for polymer processing in different application fields and promote the technical development of new methods of preparation of polymeric materials for advanced applications.

1. Introduction

Polymers offer many advantages for modern technologies, which lead to a permanent place of polymeric materials in many sophisticated applications. This has been generally correlated to their low cost, easy fabrication (e.g., there is no need for special clean-room and/or high-temperature processes), low density (which is one of the most important factors when choosing polymeric materials for a specific application), and so on. Of course, the effective utilization of polymeric materials is related not only to the above-mentioned factors but also to the most important fact that the properties of the polymeric materials can fulfill the requests of specific applications. Actually, polymeric materials offer a great potential to meet the requirements from the market better than other materials since their physical and chemical properties can be easily tailored by their structures at different scales. On the one hand, the chemical structure at molecular scale determines the essential property and/or functionality of a polymer. A subtle manipulation of the chemical compositions, functional groups, and chain architectures may give rise to completely new polymeric materials with dramatically different properties. On the other hand, the multiscale morphologies of the polymeric materials in the condensed state also exhibit pronounced influences on the mechanical and physical properties of the polymers. As examples, the stiffness and strength of highly oriented polymeric materials can exceed those of their isotropic counterparts by orders of magnitude,[1,2] while an increase of more than a factor of 100 has been reported for the electrical conductivity of doped and aligned conjugated macromolecules compared with their nonoriented counterparts.[3−5] Among many others, further examples of improved performance of oriented polymeric materials are the enhanced thermal conductivity, optical transparency, and piezoelectric properties.[6] For crystalline polymers, the crystalline structure and crystal orientation provide another most important key factor in regulating the property and/or even functionality of a polymer. For this aspect, poly(vinylidene fluoride) (PVDF) provides an excellent example. While its α-form crystals, composed of helical chains, can be used only as general thermoplastics, its β-form crystals, composed of planar zigzag chains, exhibit exceptional piezo- and pyroelectric properties.[7] It is examples such as these that result in the study on the crystallization of semicrystalline polymers under various conditions being an everlasting research topic.

The crystallization of polymers is generally divided into two stages, i.e., nucleation and crystal growth. The nucleation can take place homogeneously or heterogeneously when it is induced by the presence of heterogeneities. Surface-induced crystallization of polymers is a typical case of heterogeneous nucleation. It is also quite frequently encountered, since the polymers are deposited on various types of substrates in many scientific and technical applications.[8−11] In the fiber-reinforced polymer systems, induced crystallization of the matrix polymers at the fiber surfaces is also an unavoidable phenomenon. Therefore, the study of surface-induced polymer crystallization is of particular interest from both practical and scientific points of view. It is now well documented that the existence of a foreign surface can alter the crystallization kinetics, as well as the resultant crystal structure and morphology of a polymer, and therefore provides an efficient way for fabricating special structure with desired property or/and functionality of the polymeric materials.

The purpose of this Perspective is to provide context as to how the foreign surface may influence the crystallization process of polymers rather than to summarize all of the work to date on the issue of surface-induced polymer crystallization. After a brief introduction on the possible influences of foreign surfaces on the crystallization kinetics of the polymers, we will focus on the resultant unique crystal structure and morphology of polymers in contact with different surfaces. The advantages of surface-induced polymer crystallization to fabricate polymeric materials with improved property or enhanced efficiency will be described with some examples.

*To whom all correspondence should be addressed: e-mail skyan@mail.buct.edu.cn; Tel +86-10-6445 5928; Fax +86-10-6445 5928.

© 2011 American Chemical Society

Published on Web 01/10/2011



Huihui Li is currently Associate Professor in the College of Material Sciences and Engineering at Beijing University of Chemical Technology (BUCT). She earned her M.S. from Shandong University in 1998 and her Ph.D. in Polymer Science at the Institute of Chemistry, the Chinese Academy of Sciences (ICCAS), in 2004 under the guidance of Prof. S. Yan. After completing her graduate studies, she became an Assistant Professor at the ICCAS. She joined BUCT in 2009. Her current research focuses on the crystallization and multiscale structure manipulation of crystalline/crystalline polymer blends.



Shouke Yan is Professor in the College of Material Sciences and Engineering at Beijing University of Chemical Technology (BUCT) in Beijing. After receiving a B.S. from Qufu Normal University in 1985, he completed his M.S. in Polymer Science at the Changchun Institute of Applied Chemistry, The Chinese Academy of Sciences (CIAC-CAS), under the guidance of Prof. Enle Zhou. After completing his M.S. study, he joined the CIAC-CAS as an Assistant Professor and then earned his Ph.D. in Polymer Science at the CIAC-CAS under the joint guidance of Prof. Decai Yang and Prof. J. Petermann (Dortmund University, Germany) through a sandwich program between the CAS and the Max-Planck-Society. He then took a position on the research staff at Dortmund University under the direction of Prof. J. Petermann. In 2001, he returned to China through the Hundred Talents Program to become full Professor at the Institute of Chemistry, the Chinese Academy of Sciences (ICCAS). He has been recognized with several honors, including the Excellent Hundred Talents Award and an NSFC Outstanding Youth Fund. His current research involves surface-induced polymer crystallization, orientation-induced polymer crystallization, and phase transition of crystalline polymers.

2. Crystallization Kinetics

It is well-known that the specific interaction between the substrate and the polymer can strongly affect the physical properties of the polymers, including glass transition temperature[12−19] and molecular mobility,[20−23] which in turn influence the crystallization kinetics of the polymers.[24−26] Frank and co-workers have done systematic researches on the above-mentioned issues.[13,25−31] The influence of foreign surfaces on the crystallization kinetics is multifarious, depending on the polymer used, the film thickness, and the interaction between the substrate and the polymer melt. Generally, owing to the enhanced nucleation ability induced by the presence of heterogeneous surfaces, the overall crystallization rate will be increased remarkably, especially for those with difficulty in homogeneous nucleation. For example, isotactic poly(methyl methacrylate) (PMMA) is one of the polymers with extremely slow crystallization rate.[32−34] The temperature for its maximum crystallization rate has been reported to be 120 °C, at which temperature the bulk crystallization takes tens of days.[35] The crystallization of PMMA from the glassy state on oriented polyethylene (PE) surfaces is, however, much faster. It takes only tens of hours for a complete crystallization.[36] The enhanced nucleation and crystallization rates of polymers induced by a foreign surface can also be best revealed by the formation of transcrystalline layers in the fiber-reinforced polymer systems. On the other hand, in some cases, the situation for thin or ultrathin polymer films on a substrate with strong interaction may be quite different. It was reported that there is a substantial decrease in the lateral diffusion coefficient of polymer films thinner than 150 nm.[37] This will unambiguously reduce the crystal growth rate and therefore slow down the overall crystallization rate.[24,26,29] Actually, for some particular polymers in extreme cases, the work to cultivate crystallinity in thin or ultrathin films becomes impossible. As an example, the crystallization of poly(di-*n*-hexylsilane) is prohibited in ultrathin films less than 15 nm in thickness.[27] Another example is the inhibition of the crystallization in ultrathin films of poly(3-hydroxybutyrate) (PHB),[38] which provides a way to produce in-vivo-like amorphous PHB.[39]

The above is a brief description about the possible influences of foreign surfaces on the crystallization kinetics of polymeric materials, which can provide useful information for processing. The most important part of surface-induced polymer crystallization rests actually on the influence of foreign surface on the crystal structure and morphology of the polymers since they are the key factors in tailoring the property and even functionality of the polymeric materials. Therefore, we hereafter focus our attention on the surface-induced structure and morphology of polymers at different surfaces.

3. Flat-Surface-Induced Polymer Crystallization

Crystallization of polymer thin films on a flat surface can be encountered in many application fields, such as coating, electronics, and optoelectronics. The existence of the interface can affect both the crystal structure and the crystal orientation, depending on the film thickness, the crystallization temperature, and the interfacial interaction. Reiter and co-workers have performed excellent work on thin and ultrathin film crystallization of polymers.[40−47] Experimental results indicate that thin polymer films of tens to hundreds of nanometers crystallized at relatively lower supercoolings encourage a specific orientation of the typical thin lamellar crystals; in such thin films, the molecular chains lie normal to the substrate (i.e., the lamellae lie "flat-on" against the substrate.[48−64] Figure 1 presents AFM height and amplitude images showing regular flat-on single crystals of syndiotactic polypropylene (sPP). The inserted electron diffraction pattern demonstrates an upright chain orientation. On the contrary,

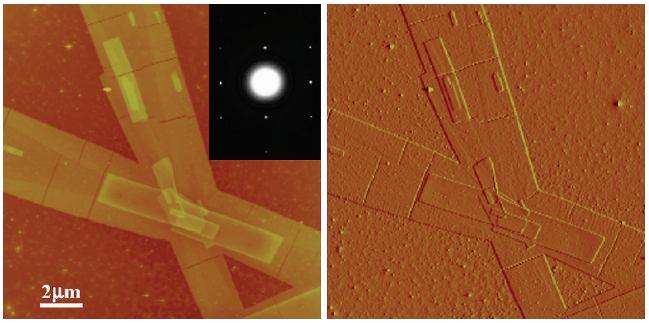


Figure 1. AFM height (left) and amplitude (right) images of sPP crystallized on a mica surface at 125 °C. The inset presents the electron diffraction pattern of the single crystal, which indicates an upright chain orientation. The single layer of the crystal is about 15 nm in thickness.

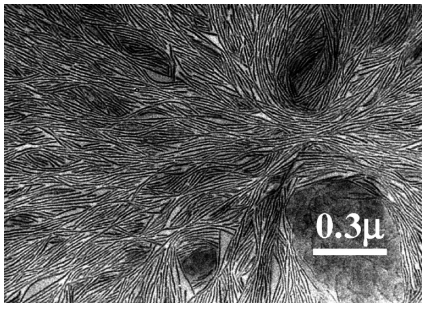


Figure 2. Transmission electron micrograph showing the edge-on lamellar structure of isotactic polystyrene crystallized on a carbon surface at 160 °C. The film thickness is about 50 nm.

when crystallizing a polymer thin film at higher supercoolings, spherulites made up of radially arranged edge-on lamellae (chain axes oriented parallel to the substrate) are generally observed,[65−69] This is seen in Figure 2, which shows the spherulitic structure of isotactic polystyrene composed of edge-on lamellae grown at 160 °C.[69] The different crystal orientation depends naturally also on the features of the substrate surface. Recent dynamic Monte Carlo simulation indicates that, at high temperatures, thin polymer films on a slippery wall exhibit dominantly edge-on lamellar crystals, while on a sticky wall they show mainly flat-on lamellar crystals.[40]

3.1. Crystallization of Polymers on Flat Crystalline Surface with Unique Interaction. The above describes only a general phenomenon of thin film crystallization of polymers on different surfaces at different temperatures. It does not reflect any kind of peculiar interaction between the substrate and the polymer, although such interactions actually exist between many substrate/polymer systems. For example, when crystallizing a polymer on a crystalline substrate, peculiar interactions at the molecular scale originating from the well-organized substrate molecules often exist. The existence of the unique interaction usually results in the crystallization of a polymer on the substrate in an unexpected manner and therefore leads to the formation of unique crystalline structure and morphology of the crystallizing polymer, a phenomenon known as epitaxy.

Epitaxy, meaning "on arrangement", is most generally defined as the crystals of one phase (guest crystal) growing on the surface of a crystal of another phase (host crystal) in one or more strictly defined crystallographic orientations.[70] The epitaxial crystallization phenomenon was first recognized by mineralogists in various natural minerals,[71] and the study on polymer epitaxy was started in the 1950s with the pioneer work of Willems and Fischer.[72,73] It has been well documented that polymer epitaxy could be realized on inorganic,[74−78]

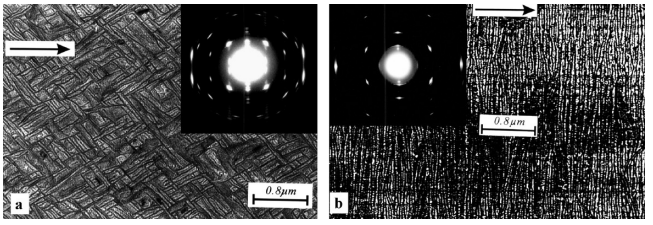


Figure 3. Bright-field (BF) electron micrographs and the corresponding electron diffraction patterns (insets of the BF images) of (a) PE/iPP and (b) PE/PTFE double-layered samples, which were heat-treated at 150 °C for 10 min and subsequently cooled to room temperature. The arrows show the chain directions of the corresponding substrate crystals.

organic,[79−88] and polymeric[89−115] substrates from solution, melt, and vapor phases. We will not summarize all of the work to date, as there are already several excellent reviews on these topics,[116−119] but rather provide a context as to how the surface-induced epitaxy influences the crystal structure and morphology of polymers as shown in recent new developments.

First of all, as described in the definition of epitaxy, the common features of the epitaxial systems are the fixed mutual orientation of the overgrowth materials with respect to the substrates. For polymer epitaxy, unlike the case without epitaxial ability, the epitaxial crystallization, if it takes place, leads always to an alignment of the polymer chains in the film plane, regardless of the film thickness and crystallization temperature. The chain orientation in the film can, however, be different, depending on the substrate. Two kinds of mutual chain orientations of the deposited polymers with respect to that of the substrates were manifested for polymer epitaxies. They are (i) the parallel chain alignment of epitaxial pairs[110,120−124] and (ii) the deposited polymer chains at fixed angles from the substrate molecular chains.[91,108,110,112,125] Parts a and b of Figure 3 present a most illustrative example of the different chain orientation of PE grown epitaxially on melt-drawn uniaxially oriented isotactic polypropylene (iPP) and friction transfer oriented poly(tetrafluoroethylene) (PTFE) substrates, respectively. While the epitaxy results in the molecular chains of PE ± 50° apart from the chain direction of iPP substrate crystals, producing a crosshatched lamellar structure of PE, a parallel chain alignment is identified for the PE/PTFE system, which induces a parallel aligned lamellar structure of PE. These strictly defined unique crystallographic orientations may be adopted within the field of macromolecular engineering. For the crosshatched lamellar structure, as schematically depicted in Figure 4, the mechanical soft amorphous interlamellar regions of one phase are bridged by the crystalline lamellae of the other phase, which leads to a significant improvement of the mechanical properties.[89,97] This can be utilized by stretching a blend of two components with this kind epitaxial relationship and then annealed at temperatures below the melting point of high melting component but above the melting point of the lower melting component. Moreover, for the composite materials, it is demonstrated that the adhesion between the polymer sheets with epitaxial crystallization can be enhanced remarkably. For example, by dipping the iPP sheets in a PE solution before thermal bonding, the adhesion between the laminae went up enormously.[126,127] The parallel chain epitaxies can also find applications for fabricating functional polymeric materials. For example, organic field-effect transistors (OFETs) based on soluble conjugated polymers have attracted considerable attention. Enormous effort has been devoted to improve the key

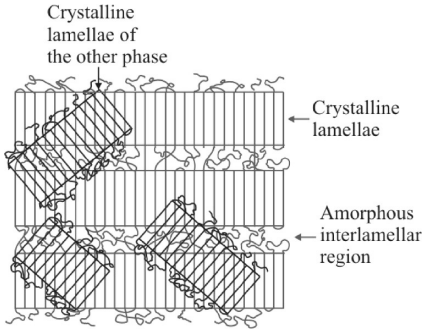


Figure 4. Schematic representation of epitaxially oriented lamellar crystals, in which the mechanically soft amorphous interlamellar regions of one phase are bridged by the crystalline lamellae of the other phase.

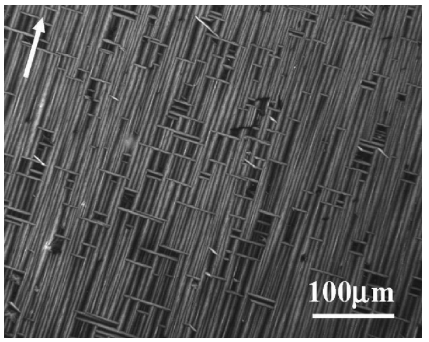


Figure 5. Optical micrograph shows the epitaxial morphology of PTH on highly oriented PE substrate. The arrow indicates the molecular chain direction of PE.[135]

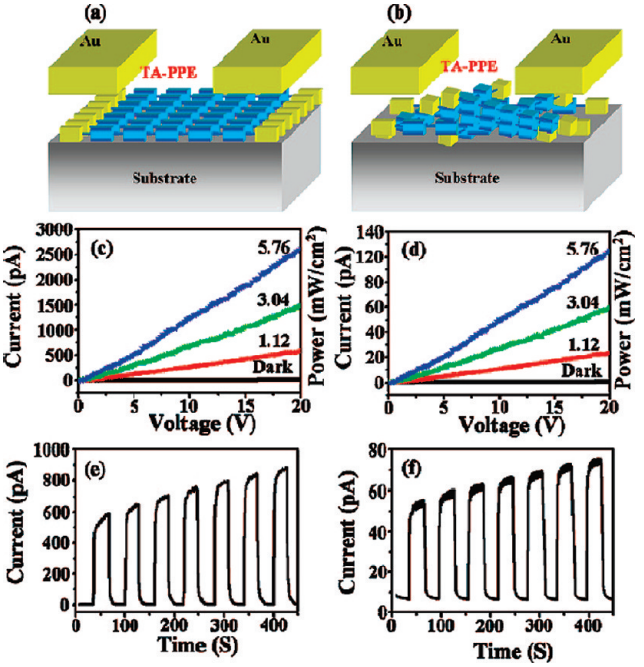


Figure 6. (a) Photoswitchers of aligned TA-PPE films, (b) photoswitchers of TA-PPE films without alignment, (c, e) photoresponse and photoswitch behavior of TA-PPE films with alignment, and (d, f) photoresponse and photoswitch behavior of TA-PPE films without alignment.[136]

performance parameters of OFETs, such as carrier mobility, on/off ratio, and threshold voltage. Now excellent properties have been achieved by individual wires with single crystal structure.[128,129] The performance of thin films is normally poor with respect to single crystal wires.[128] To improve the performance of thin films, epitaxial crystallization can be used to fabricate thin films of the semiconducting materials with unique crystal orientation. In this field, Brinkmann and co-workers have recently done beautiful work in fabricating P3HT through the epitaxial way.[130−134] Figure 5 shows an optical micrograph a large-area well-defined thin films with unique single crystal organization of a semiconducting material, which has been successfully produced by epitaxy on highly oriented PE thin film.[135] The fabricated films demonstrate indeed a significant property improvement, as illustrated in Figure 6.[136]

Second, except for the above-described crystal orientation control through surface-induced polymer epitaxy, a number of epitaxial systems have demonstrated the ability to regulate both the structure and orientation of the deposited polymers, another advantage of the surface-induced polymer epitaxy.[86,106,107,113,124,137−140] For example, poly(vinylidene fluoride) (PVDF) can be produced in its piezoelectric and pyroelectric β-form through epitaxial crystallization from the melt onto a potassium bromide surface at atmospheric pressure,[137] while iPP is successfully crystallized from the melt onto γ-quinacridone and dicyclohexylterephthalamide in a biaxially oriented metastable β-phase via epitaxy.[86] This is of great significance since even though the β-form iPP can be achieved by bulk crystallization with nucleation agents, oriented β-form iPP cannot be achieved by mechanical means due to the $\beta\alpha$ transition on stretching. The structure and orientation control was also found for the polymer−polymer epitaxial systems. As an example, Figure 7 shows a transmission electron micrograph and electron diffraction pattern with a sketch indicating the diffraction indexing of poly(butylene adipate) (PBA) epitaxially crystallized on highly oriented PE thin film.[124] The PBA, an aliphatic biodegradable polyester, has two different modifications designated as α and β,[141,142] which exhibit different degradation rates.[143] Experimental results indicate that the PBA normally crystallizes from melt in β-form at temperatures lower than 27 °C, while α-crystals are obtained at temperatures higher than 32 °C. Within temperature window of 27−32 °C, a mixture of α- and β-crystals of PBA was generally obtained. However, when crystallizing the PBA on an oriented PE substrate, oriented lamellae made up of β-PBA crystals are always observed, regardless of the crystallization temperature.[124] Similar crystallization behavior of PBA on oriented iPP substrates is also identified, but with a different crystal orientation.[113] In this case, unlike the case of parallel chain alignment with the PE substrate, a crosshatched lamellar structure of PBA with the molecular chain direction ±50° apart from the chain direction of iPP crystals is obtained, as in the case of PE-iPP epitaxy.

Third, for the mechanism, the epitaxial growth is generally based on the structural similarity between the substrate and overgrowth materials in the contact lattice planes. Therefore, epitaxy is often characterized in terms of some geometric matching. The matching may be accompanied by a match of crystallographic spacing such as a coincidence of unit-cell dimensions. The amount of mismatching is generally measured by the quantity $\Delta = 100(d_o - d_s)/d_s$, expressed sometimes also as disregistry or discrepancy in the form of a percentage, where d_o and d_s are the lattice periodicities of overgrowth and substrate crystals, respectively. A 10−15% disregistry was considered as the upper limit for the occurrence of the surface-induced epitaxial growth.[118] In reality, the structural similarity implies interactions at the molecular scale. The understanding of polymer epitaxy on such a level

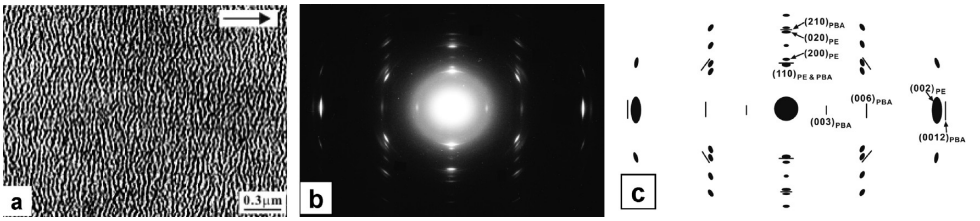


Figure 7. (a) Transmission electron micrograph, (b) the corresponding electron diffraction pattern, and (c) a sketch illustrating the mutual chain orientation of PBA crystallized from the melt onto a highly oriented PE substrate.[124]

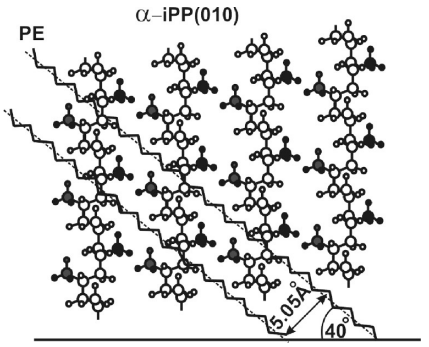


Figure 8. Schematic representation of PE/iPP epitaxial relationship. The contact planes are $(100)_{PE}$ and $(010)_{iPP}$.

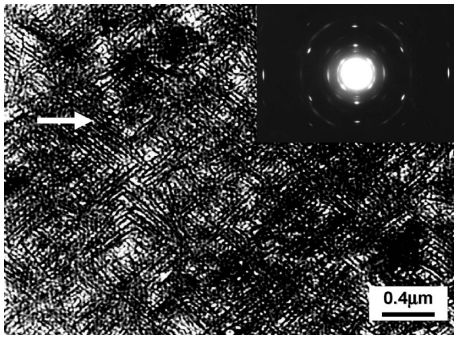


Figure 9. Electron micrograph and its corresponding diffraction pattern of iPP epitaxially crystallized from the melt on the uniaxially oriented PE substrate. The arrow represents the molecular chain direction of PE substrate film.

has indeed been reached by the elaborate work of Lotz et al.[86,88,92,144,145] For example, the epitaxial crystallization of PE on an iPP substrate has been explained in terms of a chain-row matching by parallel alignment of PE chains in the (100) lattice plane along the methyl group rows in the [101] direction of iPP with a mismatch of only about 2%[92] (see the sketch in Figure 8). The unique interaction between the polymer pairs infers the epitaxial crystallization a reversible process. As presented in Figure 9, when crystallizing the iPP on a uniaxially oriented PE substrate from the melt, the same mutual orientation but with iPP chains ±50° apart from the chain direction of the PE substrate is observed (compare Figure 9 with Figure 3a).[146]

On the basis of the specific molecular interactions, different contact planes and chain orientations of one polymer can be achieved by epitaxial crystallization on different substrates.[92,99,105,109] A good illustrative example is the epitaxial crystallization of PE on iPP and sPP, respectively. The $(100)_{PE}$ plane in contact with iPP produces an orientation of PE chains 50° from the iPP chain direction, while the $(110)_{PE}$ plane in contact with the sPP results in an orientation at 45° to the helix axis.[99,105]

Moreover, as epitaxyial crystallization is a surface-induced process, it starts unambiguously at the interacting interface. This may lead to different structures of the overgrowth polymer in the contact plane as compared to that at the top surface. Tracz et al. have indeed demonstrated the formation of highly ordered, unusually thick PE lamellae in contact with atomically flat solid surfaces.[147−149] Our recent experimental results on the epitaxial crystallization process of polycaprolactone (PCL) on an oriented PE substrate show that the PCL at the interface exhibits an ultrahigh melting temperature (close to the equilibrium melting point) compared with the PCL at top surface (see Figure 10).[150,151] This also indicates the formation of unusually thick PCL lamellae in contact with PE surface as confirmed by the AFM observation. As illustrated in Figure 10a, the increase and shift of the high-temperature melting peak, which associates to the PE-induced broad PCL lamellae, with time indicate an increment in amount and a further thickening of the PE substrate-induced PCL lamellae. For sufficient time, the appearance of only one melting peak at even higher temperature confirms the propagation of the induced PCL crystals from the interface toward the top surface.[150] Also an epitaxial chain orientation prior to the crystallization was recognized by infrared analysis.[151]

3.2. Crystallization of Polymers on Flat Amorphous Surface with Peculiar Interaction. The above describes the crystallization behavior of polymers on flat crystalline surfaces, which exhibit some kind of unique interaction. It was also well established that surface topography of an amorphous substrate can also influence the orientation of the overgrowing material, a process known as graphoepitaxy or artificial epitaxy.[152−158] It was generally believed that the occurrence of graphoepitaxy depends mainly on the topology of the surface relief with pattern symmetry. Of course, the interaction existing between the substrate and the polymer melt at the interface plays a very important role. This has been clearly demonstrated by the investigations on the melt−recrystallization behavior of oriented polymer thin films with vacuum-evaporated amorphous carbon layers.[159−165] Presented in Figure 11 are transmission electron micrographs with corresponding electron diffraction patterns of vacuum carbon-evaporated PE oriented thin films before and after subsequent melting followed by crystallization (melt−recrystallization). The same chain orientation of pristine and recrystallized PE films can be easily identified. With careful inspection, even an improved orientation of the recrystallized PE film can be recognized. As sketched in Figure 11 (the insets), while the pristine PE thin film exhibits only a uniaxial *c*-axis orientation, a biaxial orientation with both *b*- and *c*-axes in the film plane and highly oriented is obtained after melt−recrystallization. One may want to associate this simply to the occurrence of graphoepitaxy. This is not the case, since besides the preserved chain axis orientation, both the crystal structure and the morphology of the polymers are some times

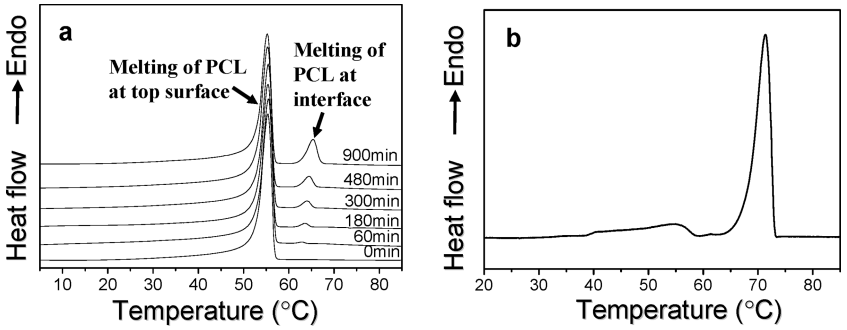


Figure 10. DSC heating scan of the PCL/PE samples: (a) heat-treated at 85 °C for 15 min, cooled to and kept at 60 °C for different times as indicated, and finally cooled to room temperature; (b) heat-treated at 85 °C for 15 min, cooled to and kept at 60 °C for 14 days, and finally cooled to room temperature. The heating rate is 10 °C/min. The high-temperature melting peak comes from the PE-induced thicker PCL lamellae.[150]

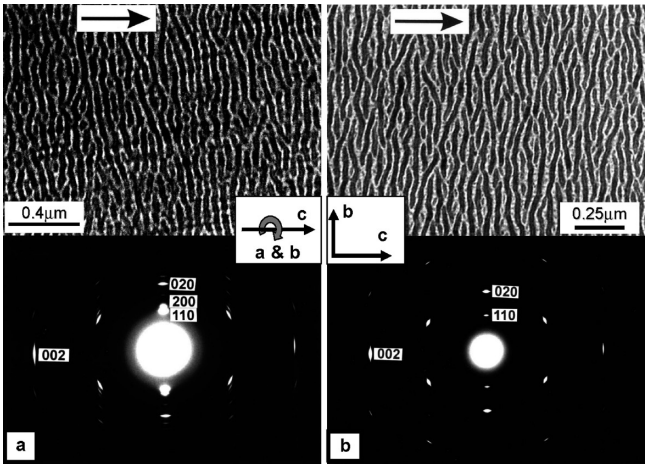


Figure 11. Electron micrographs and corresponding electron diffraction patterns of an oriented PE thin film with a vacuum-evaporated carbon layer before (a) and after (b) heat treatment. The heat treatment was performed by heating the sample to 150 °C for 15 min and subsequently crystallization isothermally at 120 °C for 2 h. The arrows in the picture represent the chain directions of the PE crystals.

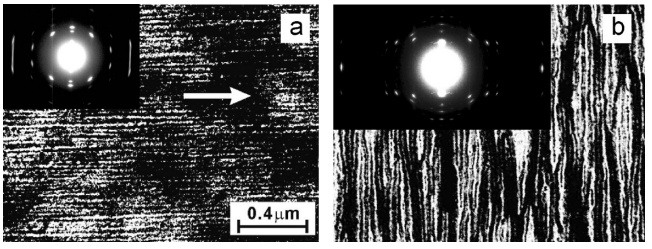


Figure 12. Electron micrographs and corresponding electron diffraction patterns (insets) of an oriented PB-1 thin film with a vacuum-evaporated carbon layer before (a) and after (b) heat treatment. The heat treatment was performed by heating the sample to 150 °C for 15 min and then cooling to room temperature. The arrow in the picture represents the chain direction of the PB-1 crystals.

altered after the melt−recrystallization. For examples, polybutene-1 changes from highly oriented extended-chain crystals in hexagonal form into oriented folded-chain crystals in tetragonal form (Figure 12),[162] whereas the PVDF transforms from oriented α-crystals into oriented β-crystals by melt−recrystallization, which normally promotes the β to α phase transition of PVDF (Figure 13).[161] Sophisticated experimental work demonstrates the existence of a strong fixing effect of the vacuum-evaporated carbon layer on the surface polymer chain segments via covalent bonding.[165] It is

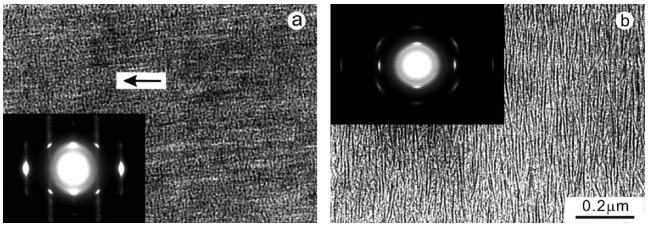


Figure 13. Electron micrographs and corresponding electron diffraction patterns (insets) of an oriented PVDF thin film with a vacuum-evaporated carbon layer before (a) and after (b) heat treatment. The heat treatment was performed by heating the sample to 200 °C for 10 min and then cooled with a rate of 2 °C/min to room temperature. The arrow represents the chain direction of the PVDF crystals.

a strong fixing effect that has retarded the relaxation of the polymer chains at the spot and, therefore, preserves the original orientation of the polymer stems at high temperature, which in turn derives the recrystallization of the polymer chains in an oriented structure.

The above-described oriented recrystallization behavior of polymers with controlled crystalline structures is also of great significance. Through this process, micropatterned polymer thin films with well-defined oriented and nonoriented structures, even in different crystalline modifications, can be simply prepared by selective carbon coating with the help of a mask and subsequent melt−recrystallization of the preoriented polymer films.[164] These patterned polymer thin films exhibit at least exceptional anisotropic optical properties and may potentially find applications such as in the field of nanometer- and/or micrometer-sized structures for optoelectronics and optical applications.[166,167] It should be pointed out that in the thus-prepared micropatterns only the orientation and the crystal structure of the carbon-decorated regions can be well manipulated. A fully crystal structure and orientation control at every corner of the polymer thin film can be realized by the combination of epitaxy and carbon decoration.[168]

4. Crystallization of Polymers at Fiber Surfaces

There are a number of interesting and technologically important features when fibers are used to induce crystallization. As illustrated in Figure 14, the well-known transcrystalline structure often emerges after polymer crystallization in fiber-reinforced polymer systems. In such cases oriented polymer layer close to the fiber surface is produced, with the polymer chains generally parallel to the fiber axis. The formation of this specific structure is a result of a high density of active nuclei at the fiber surface, which hinder the lateral development of spherulites and therefore

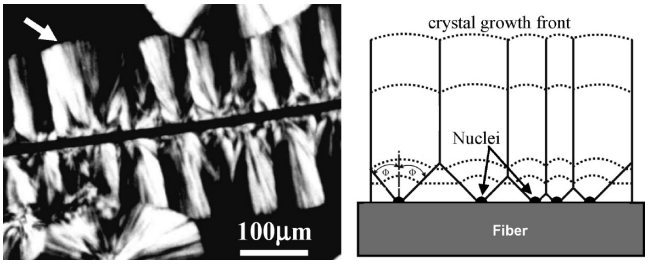


Figure 14. Optical micrograph (left) shows the growing transcrystalline zone (indicated by a white arrow) of iPP at the carbon fiber (center black part) surface, and a sketch (right) illustrates its nucleation and crystal growth processes.

force the crystal growth unidirectionally normal to the fiber axis. From Figure 14, it is clear that the transcrystallization is a nucleation-controlled process and that the enhanced nucleation at the fiber surface is the key factor for the formation of a transcrystalline morphology. The exact mechanism of the enhanced nucleation remains still not quite clear, despite extensive work since 1950s.

The situation for polymer transcrystallization around fibers is somewhat more complicated than the aforementioned flat surface-induced polymer crystallization. There are a number of factors that can control the occurrence of polymer transcrystallization.

(1) First of all, the intrinsic surface characteristics of the fibers play a very important role in generating polymer transcrystallization. For example, high-modulus carbon fibers are able to induce the transcrystallization of iPP, while their high-strength counterparts hardly exhibit an effect on the crystallization of iPP.[169] It was demonstrated that high-energy surfaces can increase the density of nuclei at surface and result in the formation of transcrystals in the interfacial region.[170,171] Also, the chemical composition of the fiber surface is important. Strong interactions between the fiber and polymer molecules were found to be in favor of transcrystallization.

(2) Second, the presence of interfacial stresses or a temperature gradient at the interface also encourages the formation of transcrystallization layer.[172,173]

(3) Third, it has been confirmed that the presence of a flow field, which is unavoidable during many processing procedures, is also an important factor affecting the nucleation of polymer at the fiber surface and the degree of polymer chain orientation near the fiber. It is noteworthy that the transcrystallization of polymers at fiber surfaces will always take place under shearing conditions, regardless of the fiber used. This has been best revealed by the crystallization of iPP in PP/fiber systems with the fibers being pulled along their long axes, a process developed by Varga et al.[174−178] For example, it has been demonstrated that Kevlar 49 fiber exhibits no nucleation ability toward iPP in a quiescent environment (see Figure 15a), resulting in the formation of iPP spherulites in its monoclinic α-form. However, oriented iPP column structures were always observed in the vicinity of the Kevlar 49 fiber whenever it was pulled along its axis (see Figure 15b,c), even though the induced column structures may be different, depending on the fiber pulling rate or/and pulling time. As illustrated in Figure 15b,c, when the Kevlar 49 fiber was pulled at a rate of 30 μm/s for 20 s, an oriented α-iPP column structure was obtained (see Figure 15b). On the contrary, if the Kevlar 49 fiber was pulled at a rate of 30 μm/s for 60 s, an oriented β-iPP column structure was observed (see Figure 15c). This has been unambiguously confirmed by the selective melting of the β-iPP crystals at 158 °C, as presented in Figure 15d.[179]

Moreover, if the fiber is in the crystalline state, as in the case of surface-induced polymer epitaxy, lattice matching between the

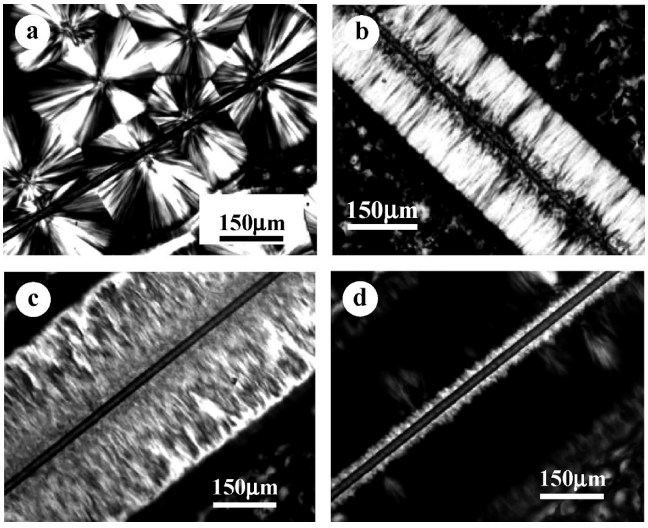


Figure 15. Optical micrographs show the interfacial morphologies of iPP/fiber (Kevlar 49) composites. The samples were heat-treated at 210 °C for 5 min and then quickly cooled to 137 °C for isothermal crystallization after fiber pulling. The fibers were pulled at a rate of 30 μm/s for (a) 0, (b) 20, and (c) 60 s. Part (d) displays the selective melting of (c) at 158 °C.[179]

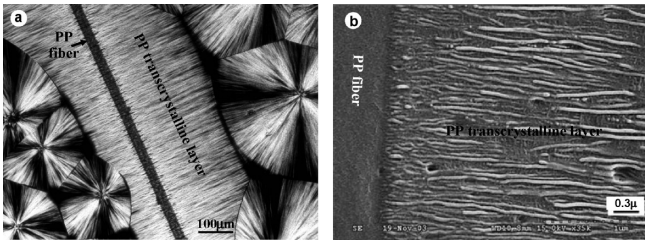


Figure 16. (a) Optical micrograph showing the growing transcrystalline layer of iPP on an iPP fiber surface and (b) a magnified scanning electron micrograph showing the interfacial structure on a lamellar scale. The samples were prepared by introducing the iPP fiber into the supercooled iPP matrix at 138 °C and then isothermally crystallizing for 6 h.

polymer and fiber crystals provides another favorable situation for transcrystallization. For example, the existence of excellent matching of nylons and iPP with high-modulus graphitic carbon fibers has led to the transcrystallization of nylons and iPP around the carbon fibers.[180] Taking this into account, the case in which both fiber and matrix are of the same polymer (single polymer matrix/fiber composites) is most conducive to surface-induced transcrystallization due to the identical chemical composition and perfect lattice matching.[181−186] As an example, Figure 16 presents the morphologies of iPP crystallized around iPP fibers.[182] Comparing Figure 16a with the left part of Figure 14, one can easily find the different nucleation densities of iPP formed on carbon and iPP fiber surfaces. While individual nucleation sites can be recognized at the carbon fiber surface with careful inspection, the nucleation and crystal growth of iPP at the iPP fiber surface seem to start simultaneously from every place on the fiber surface. As a result, the oriented transcrystallization layer of the former case is caused by the restricted crystal growth in the direction parallel to the fiber axis, whereas that of the latter case originates from the induced crystallization of each crystalline lamella by the presented fiber. The high-magnification scanning electron micrograph has confirmed the above conclusion.[183] As shown in Figure 16b, one can clearly see the growth of individual iPP lamellae from the iPP fiber surface, producing parallel aligned lamellae with their long axes perpendicular to the

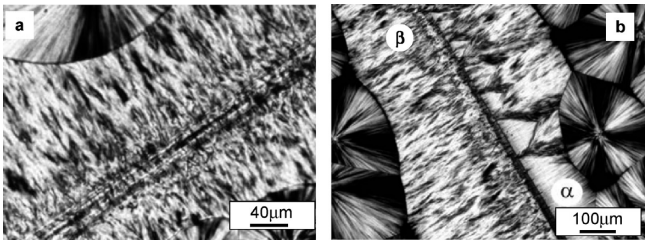


Figure 17. Optical micrographs show the interfacial transcrystalline layers of single polymer iPP composites, which have been prepared by introducing the iPP fibers into an iPP matrix melt at (a) 173 and (b) 168 °C and then crystallizing isothermally at 138 °C for 6 h. The α and β in (b) denote the α and β transcrystalline regions, respectively.

fiber axis. In this case, the crystal structure of the induced transcrystalline layers is generally the same as the solid fiber due to the epitaxial mechanism. The transcrystals of iPP shown in Figure 16 are attested indeed to be in the α-form. This is reasonable, since the iPP fibers exist only in the α-form, due to the $\beta\alpha$ transition on stretching.

For single polymer composites, if the fiber is partially surface molten, which may happen owing to the close melting points of both the fiber and matrix, the situation can be quite different. Our recent experimental results show that, in the single polymer iPP systems, oriented β-iPP lamellar structures are most frequently produced whenever the introduced iPP fibers are partially surface molten.[182−186] Figure 17a shows an optical micrograph of an iPP homogeneity matrix/fiber composite, which has been prepared by introducing the iPP fiber into its matrix melt at 173 °C and then crystallized isothermally at 138 °C for 6 h. In this case, the iPP fiber is clearly molten to some extent (compare Figure 17a with Figure 16a), and the induced transcrystalline zone was confirmed to be the β-iPP, indicating that melting of iPP fiber to a certain extent favors β-iPP crystallization. The molten fiber surface-induced β-iPP crystallization is more clearly illustrated by Figure 17b, where different supermolecular structures of iPP matrix are generated at different places of the same iPP fiber. At the top part, evident fiber surface melting results in the formation of β-iPP transcrystalline layers, while the solid fiber at the bottom part induces the crystallization of iPP principally in its α-form. This is in good agreement with the findings that oriented melt encourages the formation of β-iPP.

It should be noted that due to the amazing characteristics of nanofibers and nanotubes, such as extraordinary mechanical and electrical properties coupled with very large surface area to volume ratio, polymer-based composites with nanofibers and nanotubes have attracted great attention in recent years.[187−192] Taking the high aspect ratio into account, nanofiber- or nanotube-induced polymer crystallization could be totally different from traditional fiber-induced polymer crystallization. Therefore, the crystallization behavior of polymers around nanoscale fibers or tubes is another aspect deserving comment. In this field, the majority of work has been concerned with carbon nanotubes (CNT), as reviewed by Thostenson et al.,[192] while iPP was the most frequently used polymer matrix, owing to its wide applications. As an example, Figure 18a shows a micrograph of an iPP/CNT ultrathin composite film.[193] One can clearly see that while common crosshatched lamellar structure is observed in the intact area (see upper left corner of Figure 18a), the iPP grown at the CNT surface forms transcrystals, indicating the high efficiency of CNT in nucleating iPP. It should be pointed out that, unlike the carbon−fiber-induced iPP crystallization, where edge-on iPP lamellae propagated outward from the fiber surface with the molecular chain parallel to the long axis of the fiber were obtained (see Figure 16b), the iPP in the CNT-induced transcrystalline zone grows in flat-on form with molecular chains oriented

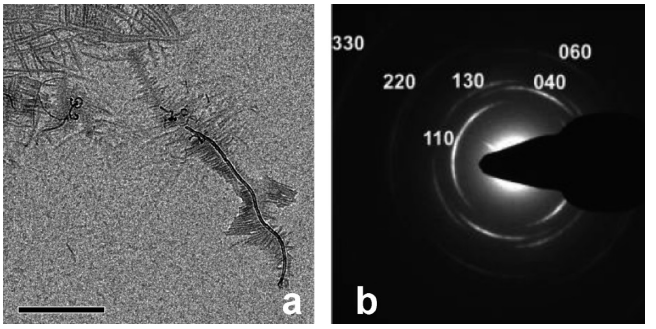


Figure 18. (a) Bright-field transmission electron micrograph of an iPP/CNT composite thin film nonisothermally crystallized from the melt during cooling at 5 °C/min; scale bar: 500 nm.[193] (b) Representative select area electron diffraction pattern of the transcrystalline grown iPP crystals around the CNTs in an ultrathin film.[194]

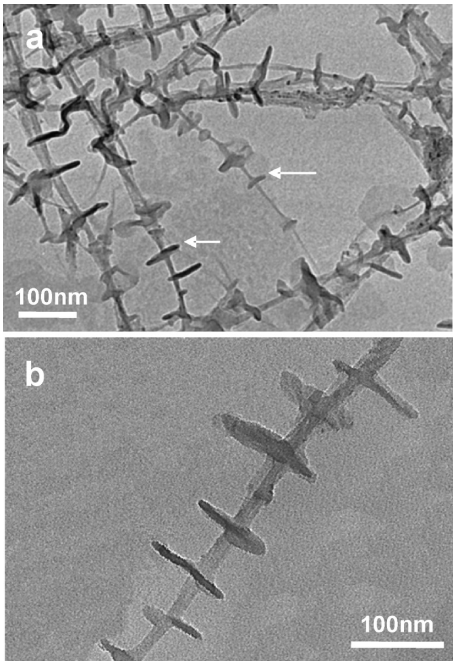


Figure 19. Bright-field transmission electron micrographs of SWNTs periodically patterned with PE lamellar crystals produced by crystallization of PE on SWNTs at 104 °C in *p*-xylene for 0.5 h. The PE and SWNT concentrations are (a) 0.01 and (b) 0.002 wt %, respectively. SWNT bundles can be seen in NHSK as shown in (b).[198]

perpendicular to the long axis of the CNT (see Figure 18b).[194] Moreover, it has once been reported that the CNT could induce the growth of the less-preferred β-form of iPP, even though it has not been confirmed by others.[195]

It has been confirmed that CNT exhibits high nucleation efficiency toward a number of polymers, promoting the formation of transcrystals of the semicrystalline polymers, even though with different orientation depending on the polymer used, as reviewed in ref 196. In this field, Li et al.[197−199] have done very nice work on the crystallization of polymers from solution at the surface of CNT. With controlled crystallization conditions, disk-like edge-on lamellar crystals surrounding the CNT have been successfully produced. Figure 19 shows two representative transmission electron micrographs of the PE crystallized from solution on the single wall CNTs.[198] Similar structures are also obtained when crystallizing polymers in supercritical CO_2 on the CNTs.[200−204] In those structures, lamellar single crystals of polymers were formed and periodically spaced along entire CNTs with an orthogonal orientation between polymer lamellar surface

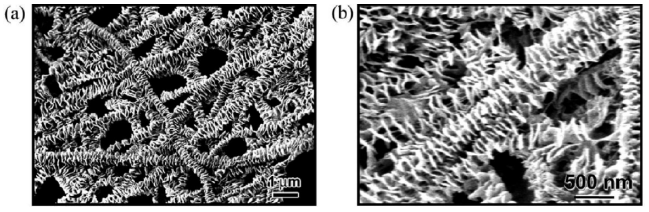


Figure 20. Electron micrographs of UHMWPE shish-kebabs by field-emission scanning electron microscopy (FE-SEM).[205]

and the long axis of CNTs. The periodicity of the polymer lamellar single crystals can be well controlled through regulating the crystallization conditions of the polymers, such as solution concentration, crystallization temperature, and solvent, etc. The mechanism of CNT-induced polymer crystallization rests most likely on the epitaxial growth of the polymer on the CNT surface, a situation like the traditional graphitic-carbon-fiber-induced polymer crystallization. On the other hand, taking the small diameter of CNT into account, it has also been suggested that the CNT itself serves as a macromolecule, leading to the preferred alignment of polymer chains along its long axis.[197] Whatever the mechanism is, the morphologies presented in Figure 19 closely resemble the shish-kebab structure of polymers formed in elongated or sheared melts (see Figure 20).[205−207] Actually, the formation of shish-kebab structures is also a kind of surface-induced polymer epitaxy, in which a stack of folded chain lamellae form around a prealigned long chain central part. This has been well explained through simulation work as performed by Hu et al.[208]

5. Outlook and Challenges

The straightforward dependence of properties on the crystal structure and morphology of semicrystalline polymers provides an opportunity to tailor the properties of these materials through crystal engineering. Therefore, a full understanding of the crystallization habits of polymers under different environments and conditions is essential for purposeful control of their structures and morphologies. This has stimulated a mass of research work on polymer crystallization since the 1920s. Considering that polymeric materials are directly in contact with some kinds of solid surfaces in a variety of applications (such as microelectronic devices and composites, etc.), surface-induced crystallization of polymers has attracted considerable attention during the past decades. It has been shown that solid surfaces most generally accelerate the crystallization of the polymers. Moreover, they can in some cases also promote the crystallization of polymers in unexpected manners and lead to the formation of unique crystal structure and morphology, e.g., the polymer epitaxy and transcrystallization as summarized in this Perspective. It should be pointed out that, to date, most of the work in this field focuses mainly on the mechanisms of the unusual crystallization behavior and the resultant special structure and morphology. Through sophisticated studies, understandings of some of these phenomena on a molecular level have been reached, for example the molecular epitaxies of polymers. On the other hand, although the positive effects of the resultant specific structures and morphologies on the mechanical and physical properties have clearly been demonstrated (e.g., the improved photoresponse characteristics[136] and the improved mechanical properties of fiber-reinforced polymer systems[170,172]), the use of these techniques to design and fabricate the polymeric materials with properties matching specific product requirement has not been well developed. Therefore, further challenges in this field are how to utilize the induced unusual crystallization behavior of polymers for preparing advanced polymeric materials.

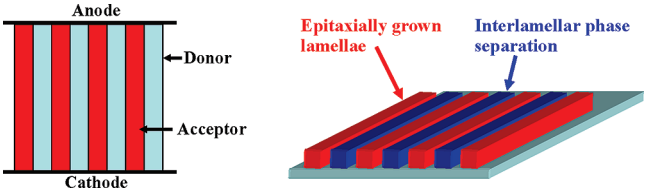


Figure 21. Sketch showing an ideal configuration of high-efficiency photovoltaic devices.

In the field of polymer thin film crystallization induced by flat surfaces, we take the polymer epitaxy as an example. As presented in the text, the strict mutual orientation between the polymer and the substrate results in the growth of the deposited polymers in unique crystalline modification and with unique crystal orientation, producing polymer thin films with anisotropic character. In addition, a significant improvement of the mechanical and physical properties has been demonstrated. All of these could undoubtedly widen the application of polymeric materials. Beyond the structural and morphological control of single polymer systems, technical development in the field of morphological manipulation of multiphase and multicomponent polymer systems can also be of importance for advanced applications. For example, polymeric solar cells, which allow fabrication onto flexible substrates using high throughput processing techniques, have emerged as attractive candidates for renewable energy sources. However, the best available polymer solar cells still lag behind that of conventional silicon devices in their efficiencies.[209] On the basis of the close relationship between microstructure of such polymeric devices and their final properties, the optimal design and implementation of the polymer structures in the devices may offer an effective approach for getting high-efficiency photovoltaic devices. It is reported that, for the devices with layered lamellar donor and acceptor materials sandwiched between two electrodes, a perpendicular orientation of the donor and acceptor layers, as depicted in the left part of Figure 21,[209] exhibits the highest efficacy. Of course, the length scale of separated donor and acceptor phases is another crucial factor influencing the photovoltaic efficiency. It is evident that only the excitons generated within a layer of ca. 10 nm from the donor−acceptor interface can contribute to the generation of charge carriers. It is highly possible to produce this kind of configuration by a parallel epitaxial crystallization of one component with controlled interlamellar phase separation of a blend,[210] as presented in the right part of Figure 21, in which the lamellar thicknesses are tailored to match the length scale requirement of a high-efficiency device. This kind of phase-separated structure has actually already been realized for block copolymer as reported by De Rosa, Lotz, and Thomas et al.[211]

For fiber/polymer systems there is still controversy about the influence of the interfacial structure on the mechanical properties of the composites. Some experimental results have demonstrated that the transcrystalline microstructures effectively improve the mechanical properties of the composites,[170,173] while some experiments did not show this effect.[212] Therefore, further studies for clarifying this issue are clearly warranted. Moreover, taking the excellent mechanical properties of highly oriented fibers into account, single polymer composites could become significant in the context easy recycling of strong materials. For example, single polymer composites with different crystalline modifications can be prepared by the partial melting of fibers of the same polymer. As in the case of iPP single polymer composites, by introducing the α-iPP fiber mat into its melt matrix under optimal condition, β-iPP sheet with α-iPP fiber backbones can be obtained through surface melting of the fibers. In this configuration, the mechanical

properties of the β-iPP sheet are expected to be improved remarkably by the nonmolten part of α-iPP fibers. This kind of β-iPP sheet is desirable for producing microporous battery separators.[213]

In summary, the existence of a solid surface can greatly influence the crystallization behavior of semicrystalline polymers. This behavior is manifested by accelerated crystallization kinetics as well as the resultant unique crystal structure and morphology. This clearly indicates that the surface-induced crystallization of polymers supplies an efficient pathway to regulate the crystal structure and morphology of polymeric materials. Because of the direct linkage of structure and properties of semicrystalline polymers, the induced special crystal structure and morphology means unparalleled physical and mechanical properties of the polymers compared with their bulk crystallized counterparts. Therefore, with an in-depth understanding of surface-induced crystallization of polymers, novel technological pathways for preparing polymeric materials for advanced applications can be expected.

Acknowledgment. A portion of this material is based on the research supported by the National Natural Science Foundation of China under Grants 50833006, 20974011, and 50973008.

References and Notes

(1) Ciferri, A.; Ward, I. M. In *Ultra-high Modulus Polymers*; Applied Science: London, 1979.
(2) Smith, P.; Lemstra, P. *J. Mater. Sci.* **1980**, *15*, 505.
(3) Oh, S. Y.; Akagi, K.; Shirakawa, H. *Synth. Met.* **1989**, *32*, 245.
(4) Gagnon, D. R.; Karasz, F. E.; Thomas, E. L.; Lenz, R. W. *Synth. Met.* **1987**, *20*, 245.
(5) Andreatta, A.; Tokito, S.; Smith, P.; Heeger, A. *J. Mol. Cryst. Liq. Cryst.* **1990**, *189*, 169.
(6) Lovinger, A. J. *Science* **1983**, *220*, 1115.
(7) Wada, Y. *Electronic Properties of Polymers*; J. Wiley & Sons: New York, 1982.
(8) Klein, J. *Science* **1990**, *250*, 640.
(9) Green, P. F.; Palmstrøm, C. J.; Mayer, J. W.; Kramer, E. J. *Macromolecules* **1985**, *18*, 501.
(10) Brown, H. R.; Char, K.; Deline, V. R.; Green, P. F. *Macromolecules* **1993**, *26*, 4155.
(11) Liu, F. P.; Gardner, D. J.; Wolcot, M. P. *Langmuir* **1995**, *11*, 2674.
(12) Keddie, J. L.; Jones, R. A. L.; Cory, R. A. *Europhys. Lett.* **1994**, *27*, 59.
(13) Frank, C. W.; Rao, V.; Despotopoulou, M. M.; Rease, R. F. W.; Hinsberg, W. D.; Miller, R. D.; Rabolt, J. F. *Science* **1996**, *273*, 912.
(14) Forrest, J. A.; Dalnoki-Veress, K.; Dutcher, J. R. *Phys. Rev. E* **1997**, *56*, 5705.
(15) DeMaggio, G. B.; Frieze, W. E.; Gidley, D. W.; Zhu, M.; Hristov, H. A.; Yee, A. F. *Phys. Rev. Lett.* **1997**, *78*, 1524.
(16) Forrest, J. A.; Mattson, J. *Phys. Rev. E* **2000**, *61*, R53.
(17) Fryer, D. S.; Nealey, P. F.; de Pablo, J. J. *Macromolecules* **2000**, *33*, 6439.
(18) Torres, J. A.; Nealey, P. F.; de Pablo, J. J. *Phys. Rev. Lett.* **2000**, *85*, 3221.
(19) Kim, J. H.; Jang, J.; Zin, W. C. *Langmuir* **2001**, *17*, 2703.
(20) Zheng, X.; Sauer, B. B.; van Alsten, J. G.; Schwarz, S. A.; Rafailovich, M. H.; Sokolov, J.; Rubinstein, M. *Phys. Rev. Lett.* **1995**, *74*, 407.
(21) Zheng, X.; Rafailovich, M. H.; Sokolov, J.; Strzhemechny, Y.; Schwarz, S. A.; Sauer, B. B.; Rubinstein, M. *Phys. Rev. Lett.* **1997**, *79*, 241.
(22) Russell, T. P.; Kumar, S. K. *Nature* **1997**, *386*, 771.
(23) Lin, E. K.; Kolb, R.; Satija, S. K.; Wu, W. L. *Macromolecules* **1999**, *32*, 3753.
(24) Reiter, G.; Sommer, J.-U. *Phys. Rev. Lett.* **1998**, *80*, 3771.
(25) Despotopoulou, M. M.; Frank, C. W.; Miller, R. D.; Rabolt, J. F. *Macromolecules* **1996**, *29*, 5797.
(26) Schönherr, H.; Frank, C. W. *Macromolecules* **2003**, *36*, 188.
(27) Despotopoulou, M. M.; Frank, C. W.; Miller, R. D.; Rabolt, J. F. *Macromolecules* **1995**, *28*, 6687.
(28) Schönherr, H.; Frank, C. W. *Macromolecules* **2003**, *36*, 1188.
(29) Schönherr, H.; Frank, C. W. *Macromolecules* **2003**, *36*, 1199.
(30) Schönherr, H.; Waymouth, R. M.; Frank, C. W. *Macromolecules* **2003**, *36*, 2412.
(31) Schönherr, H.; Wiyatno, W.; Pople, J.; Frank, C. W.; Fuller, G. G.; Gast, A. P.; Waymouth, R. M. *Macromolecules* **2002**, *35*, 2654.
(32) Brinkhuis, R. H. R.; Schouten, A. J. *Macromolecules* **1992**, *25*, 2717.
(33) De Boer, A.; Alberda van Ekenstein, G. O. R.; Challa, G. *Polymer* **1975**, *16*, 930.
(34) Zhao, D.; Li, L.; Che, B.; Cao, Q.; Lu, Y.; Xue, Q. *Macromolecules* **2004**, *37*, 4744.
(35) Schneider, B.; Štokr, J.; Spěváček, J.; Baldrian, J. *Macromol. Chem.* **1987**, *188*, 2705.
(36) Liu, J.; Wang, J.; Li, H.; Shen, D.; Zhang, J.; Ozaki, Y.; Yan, S. *J. Phys. Chem. B* **2006**, *110*, 738.
(37) Frank, B.; Gast, A. P.; Russell, T. P.; Brown, H. R.; Hawker, C. *Macromolecules* **1996**, *29*, 6531.
(38) Capitán, M. J.; Rueda, D. R.; Ezquerra, T. A. *Macromolecules* **2004**, *37*, 5653.
(39) Calvert, P. *Nature* **1992**, *360*, 535.
(40) Ma, Y.; Hu, W.; Reiter, G. *Macromolecules* **2006**, *39*, 5159.
(41) Reiter, G.; Sommer, J. U. *J. Chem. Phys.* **2000**, *112*, 4376.
(42) Sommer, J. U.; Reiter, G. *J. Chem. Phys.* **2000**, *112*, 4384.
(43) Vonau, F.; Aubel, D.; Bouteiller, L.; Reiter, G.; Simon, L. *Phys. Rev. Lett.* **2007**, *99*, 086103.
(44) Ma, Y.; Zha, L.; Hu, W.; Reiter, G.; Han, C. C. *Phys. Rev. E* **2008**, *77*, 061801.
(45) Grozeva, N.; Botizb, I.; Reiter, G. *Eur. Phys. J. E* **2008**, *27*, 63.
(46) Sommer, J. U.; Reiter, G. *Europhys. Lett.* **2001**, *56*, 755.
(47) Xu, J.; Ma, Y.; Hu, W.; Rehahn, M.; Reiter, G. *Nature Mater.* **2009**, *8*, 348.
(48) Keller, A.; O'Connor, A. *Nature* **1957**, *180*, 1289.
(49) Bassett, D. C.; Frank, F. C.; Keller, A. *Nature* **1959**, *184*, 810.
(50) Keller, A. *Polymer* **1962**, *3*, 393.
(51) Lovinger, A. J.; Keith, H. D. *Macromolecules* **1979**, *12*, 919.
(52) Kovacs, A. J.; Straupe, C. *Faraday Discuss.* **1979**, *68*, 225.
(53) Keith, H. D.; Padden, F. J.; Lotz, B.; Wittmann, J. C. *Macromolecules* **1989**, *22*, 2230.
(54) Bu, Z.; Yoon, Y.; Ho, R.-M.; Zhou, W.; Jangchud, I.; Eby, R. K.; Cheng, S. Z. D.; Hsieh, E. T.; Johnson, T. W.; Geerts, R. G.; Palackal, S. J.; Hawley, G. R.; Welch, M. B. *Macromolecules* **1996**, *29*, 6575.
(55) Sakai, Y.; Imai, M.; Kaji, K.; Tsuji, M. *Macromolecules* **1996**, *29*, 8830.
(56) Sutton, S. J.; Izumi, K.; Miyaji, H.; Miyamoto, Y.; Miyatashi, S. *J. Mater. Sci.* **1997**, *32*, 5621.
(57) Abe, H.; Kikkawa, Y.; Iwata, T.; Aoki, H.; Akehata, T.; Doi, Y. *Polymer* **2000**, *41*, 867.
(58) Taguchi, K.; Miyaji, H.; Izumi, K.; Hoshimo, A.; Miyamoto, Y.; Kokawa, R. *Polymer* **2001**, *42*, 7443.
(59) Zhang, B.; Yang, D.; De Rosa, C.; Yan, S.; Petermann, J. *Macromolecules* **2001**, *34*, 5221.
(60) Zhang, B.; Yang, D.; De Rosa, C.; Yan, S. *Macromolecules* **2002**, *35*, 4646.
(61) Hu, Z.-J.; Huang, H.-Y.; Zhang, F.-J.; Du, B.-Y.; He, T. B. *Langmuir* **2004**, *20*, 3271.
(62) Duan, Y.; Jiang, Y.; Jiang, S.; Li, L.; Yan, S.; Schultz, J. M. *Macromolecules* **2004**, *37*, 9283.
(63) Mareau, V. H.; Prud'homme, R. E. *Macromolecules* **2005**, *38*, 398.
(64) Jiang, S.; Li, H.; De Rosa, C.; Auriemma, F.; Yan, S. *Macromolecules* **2010**, *43*, 1449.
(65) Theodorou, D. N. *Macromolecules* **1989**, *22*, 4578.
(66) Mansfield, K. F.; Theodorou, D. N. *Macromolecules* **1990**, *23*, 4430.
(67) Mansfield, K. F.; Theodorou, D. N. *Macromolecules* **1991**, *24*, 4295.
(68) Harmandaris, V. A.; Kaoulas, K. C.; Mavrantzas, V. G. *Macromolecules* **2005**, *38*, 5796.
(69) Liu, T.; Yan, S.; Bonnet, M.; Lieberwirth, I.; Rogausch, K. D.; Petermann, J. *J. Mater. Sci.* **2000**, *35*, 5047.
(70) Bonev, I. *Acta Crystallogr., Sect. A* **1972**, *28*, 508.
(71) Seifert, H. In *Structure and Properties of Solid Surfaces*; Gomer, R., Smith, C. S., Eds.; University of Chicago: Chicago, 1953; p 318.
(72) Willems, J. *Discuss. Faraday Soc.* **1958**, *25*, 111.
(73) Fischer, E. W. *Discuss. Faraday Soc.* **1958**, *25*, 204.
(74) Koutsky, J. A.; Waiton, A. G.; Baer, E. *J. Polym. Sci., Part A2* **1966**, *4*, 611.

(75) Tuinstra, F.; Baer, E. *J. Polym. Sci., Polym. Lett. Ed.* **1970**, *8*, 861.
(76) Boucher, E. A. *J. Mater. Sci.* **1973**, *8*, 146.
(77) Ihn, K. J.; Tsuji, M.; Isoda, S.; Kawagushi, A.; Katayama, K.-I.; Tanaka, Y.; Sato, H. *Makromol. Chem.* **1989**, *190*, 837.
(78) Wittmann, J. C.; Lotz, B. *Polymer* **1989**, *30*, 27.
(79) Morossoff, N.; Lim, D.; Morawetz, H. *J. Am. Chem. Soc.* **1964**, *87*, 3167.
(80) Macchi, E. M.; Morossoff, N.; Morawetz, H. *J. Polym. Sci., Part A* **1968**, *6*, 2033.
(81) Smith, P.; Pennings, J. *Polymer* **1974**, *15*, 413.
(82) Wittmann, J. C.; John Manley, R. St. *J. Polym. Sci., Polym. Phys. Ed.* **1977**, *15*, 1089.
(83) Wittmann, J. C.; Lotz, B. *J. Polym. Sci., Polym. Phys. Ed.* **1981**, *19*, 1837.
(84) Wittmann, J. C.; Lotz, B. *J. Polym. Sci., Polym. Phys. Ed.* **1981**, *19*, 1853.
(85) Wittmann, J. C.; Hodge, A. M.; Lotz, B. *J. Polym. Sci., Polym. Phys. Ed.* **1983**, *21*, 2495.
(86) Stocker, W.; Schumacher, M.; Graff, S.; Thierry, A.; Wittmann, J. C.; Lotz, B. *Macromolecules* **1998**, *31*, 807.
(87) Zhang, J.; Yang, D.; Thierry, A.; Wittmann, J. C.; Lotz, B. *Macromolecules* **1998**, *34*, 6261.
(88) Mathieu, C.; Stocker, W.; Thiery, A.; Wittmann, J. C.; Lotz, B. *Polymer* **2001**, *42*, 7033.
(89) Gross, B.; Petermann, J. *J. Mater. Sci.* **1984**, *19*, 105.
(90) Lotz, B.; Wittmann, J. C. *Macromol. Chem.* **1984**, *185*, 2043.
(91) Wittmann, J. C.; Lotz, B. *J. Polym. Sci., Polym. Phys. Ed.* **1985**, *23*, 205.
(92) Lotz, B.; Wittmann, J. C. *J. Polym. Sci., Polym. Phys. Ed.* **1986**, *24*, 1559.
(93) Lotz, B.; Wittmann, J. C. *J. Polym. Sci., Polym. Phys. Ed.* **1987**, *25*, 1079.
(94) Kawaguchi, A.; Okihara, T.; Murakami, S.; Ohara, M.; Katayama, K.; Petermann, J. *J. Polym. Sci., Polym. Phys. Ed.* **1991**, *29*, 683.
(95) Broza, G.; Rieck, U.; Kawaguchi, A.; Petermann, J. *J. Polym. Sci., Polym. Phys. Ed.* **1985**, *23*, 2623.
(96) Petermann, J.; Broza, G.; Rieck, U.; Kawaguchi, A. *J. Mater. Sci.* **1987**, *22*, 1477.
(97) Jaballah, A.; Rieck, U.; Petermann, J. *J. Mater. Sci.* **1990**, *25*, 3105.
(98) Petermann, J.; Xu, Y.; Loos, J.; Yang, D. *Makromol. Chem.* **1992**, *193*, 611.
(99) Petermann, J.; Xu, Y.; Loos, J.; Yang, D. *Polym. Commun* **1992**, *33*, 1096.
(100) Petermann, J.; Broza, G.; Yang, D. *Polym. Bull.* **1993**, *31*, 465.
(101) Yan, S.; Lin, J.; Yang, D.; Petermann, J. *Macromol. Chem. Phys.* **1994**, *195*, 195.
(102) Yan, S.; Lin, J.; Yang, D.; Petermann, J. *J. Mater. Sci.* **1994**, *29*, 1773.
(103) Katzenberg, F.; Loos, J.; Petermann, J.; McMaster, T.; Miles, M. *Polym. Bull.* **1995**, *35*, 195.
(104) Lovinger, A. J.; Davis, D. D.; Lotz, B. *Macromolecules* **1991**, *24*, 552.
(105) Schumacher, M.; Lovinger, A. J.; Agarwa1, P.; Wittmann, J. C.; Lotz, B. *Macromolecules* **1994**, *27*, 6956.
(106) Park, Y. J.; Kang, S. J.; Lotz, B.; Brinkmann, M.; Thierry, A.; Kim, K. J.; Park, C. *Macromolecules* **2008**, *41*, 8648.
(107) Cao, Y.; Van Horn, R. M.; Tsai, C. C.; Graham, M. J.; Jeong, K. U.; Wang, B.; Auriemma, F.; De Rosa, C.; Lotz, B.; Cheng, S. Z. D. *Macromolecules* **2009**, *42*, 4758.
(108) Yan, S.; Yang, D.; Petermann, J. *Polymer* **1998**, *39*, 4569.
(109) Yan, S.; Katzenberg, F.; Petermann, J.; Yang, D.; Shen, Y.; Straupe, C.; Wittmann, J. C.; Lotz, B. *Polymer* **2000**, *41*, 2613.
(110) Yan, S.; Späth, T.; Petermann, J. *Polymer* **2000**, *41*, 4863.
(111) Yan, S.; Späth, T.; Petermann, J. *Polymer* **2000**, *41*, 6679.
(112) Yan, S.; Petermann, J. *J. Polym. Sci., Phys. Ed.* **2000**, *38*, 80.
(113) Sun, Y.; Li, H.; Huang, Y.; Chen, E.; Gan, Z.; Yan, S. *Polymer* **2006**, *47*, 2455.
(114) Cheng, S.; Hu, W.; Ma, Y.; Yan, S. *Polymer* **2007**, *48*, 4264.
(115) Zhang, J.; Duan, Y.; Yan, S.; Yang, C.; Takahashi, I.; Ozaki, Y. *Macromolecules* **2010**, *43*, 5315.
(116) Mauritz, K. A.; Baer, E.; Hopfinger, A. J. *J. Polym. Sci., Macromol. Rev.* **1978**, *13*, 1.
(117) Swei, G. S.; Lando, J. B.; Rickert, S. E.; Mauritz, K. A. *Encycl. Polym. Sci. Eng.* **1986**, *6*, 209.
(118) Wittmann, J. C.; Lotz, B. *Prog. Polym. Sci.* **1990**, *15*, 909.
(119) Petermann, J. Epitaxial growth on and with polypropylene. In *Polypropylene: Structure, Blends and Composites*; Karger-Kocsis, J., Ed.; Chapman & Hall: London, 1995; Vol. *1*, p 140.
(120) Liu, J.; Li, H.; Yan, S.; Xiao, Q.; Petermann, J. *Colloid Polym. Sci.* **2003**, *281*, 601.
(121) Takahashi, T.; Ogata, N. *J. Polym. Sci., Polym. Phys. Ed.* **1971**, *9*, 895.
(122) Takahashi, T.; Teraoka, F.; Tsujimoto, I. *J. Macromol. Sci., Phys.* **1976**, *B12*, 303.
(123) Fenwick, D.; Smith, P.; Wittmann, J. C. *J. Mater. Sci.* **1996**, *31*, 128.
(124) Sun, Y.; Li, H.; Huang, Y.; Chen, E.; Zhao, L.; Gan, Z.; Yan, S. *Macromolecules* **2005**, *38*, 2739.
(125) Petermann, J.; Xu, Y. *J. Mater. Sci.* **1991**, *26*, 1211.
(126) Lee, I. h.; Schultz, J. M. *Polymer* **1986**, *27*, 1219.
(127) Lee, I. h.; Schultz, J. M. *J. Mater. Sci.* **1988**, *23*, 4237.
(128) Sun, Y.; Tan, L.; Jiang, S.; Qian, H. L.; Wang, Z. H.; Yan, D. W.; Di, C. A.; Wang, Y.; Wu, W. P.; Yu, G.; Yan, S. K.; Wang, C. R.; Hu, W. P.; Liu, Y. Q.; Zhu, D. B. *J. Am. Chem. Soc.* **2007**, *129*, 1882.
(129) Dong, H.; Jiang, S.; Jiang, L.; Liu, Y.; Li, H.; Hu, W.; Wang, E.; Yan, S.; Wei, Z.; Xu, W.; Gong, X. *J. Am. Chem. Soc.* **2009**, *131*, 17315.
(130) Brinkmann, M.; Wittmann, J. C. *Adv. Mater.* **2006**, *18*, 860.
(131) Brinkmann, M.; Rannou, P. *Adv. Funct. Mater.* **2007**, *17*, 101.
(132) Brinkmann, M.; Rannou, P. *Macromolecules* **2009**, *42*, 1125.
(133) Brinkmann, M.; Contal, C.; Kayunkid, N.; Djuric, T.; Resel, R. *Macromolecules* **2010**, *43*, 7604.
(134) Kayunkid, N.; Uttiya, S.; Brinkmann, M. *Macromolecules* **2010**, *43*, 4961.
(135) Jiang, S.; Qian, H.; Liu, W.; Wang, C.; Wang, Z.; Yan, S.; Zhu, D. *Macromolecules* **2009**, *42*, 9321.
(136) Dong, H.; Li, H.; Wang, E.; Wei, Z.; Xu, W.; Hu, W.; Yan, S. *Langmuir* **2008**, *24*, 13241.
(137) Lovinger, A. J. *Polymer* **1981**, *22*, 412.
(138) Kopp, S.; Wittmann, J. C.; Lotz, B. *Polymer* **1994**, *35*, 908.
(139) Kopp, S.; Wittmann, J. C.; Lotz, B. *Polymer* **1994**, *35*, 916.
(140) Zhang, J.; Yang, D.; Thierry, A.; Wittmann, J. C.; Lotz, B. *Macromolecules* **2001**, *34*, 6261.
(141) Fuller, C. S.; Erickson, C. L. *J. Am. Chem. Soc.* **1937**, *59*, 344.
(142) Fuller, C. S.; Erickson, C. L. *J. Am. Chem. Soc.* **1939**, *61*, 2575.
(143) Gan, Z.; Kuwabara, K.; Abe, H.; Iwata, T.; Doi, Y. *Polym. Degrad. Stab.* **2005**, *87*, 191.
(144) Lotz, B.; Wittmann, J. C. *J. Polym. Sci., Part B: Polym. Phys.* **1986**, *24*, 1541.
(145) Stocker, W.; Magonov, S. N.; Cantow, H. J.; Wittmann, J. C.; Lotz, B. *Macromolecules* **1993**, *26*, 5915. Correction: 1994, 27, 6690.
(146) Yan, S.; Katzenberg, F.; Petermann, J. *J. Polym. Sci., Phys. Ed.* **1999**, *37*, 1893.
(147) Tracz, A.; Jeszka, J. K.; Kucińska, I.; Chapel, J. P.; Boiteux, G.; Kryszewski, M. *J. Appl. Polym. Sci.* **2002**, *86*, 1329.
(148) Tracz, A.; Kucińska, I.; Jeszka, J. K. *Macromolecules* **2003**, *36*, 10130.
(149) Takenaka, Y.; Miyaji, H.; Hoshino, A.; Tracz, A.; Jeszka, J. K.; Kucinska, I. *Macromolecules* **2004**, *37*, 9667.
(150) Chang, H.; Zhang, J.; Li, L.; Wang, Z.; Yang, C.; Takahashi, I.; Ozaki, Y.; Yan, S. *Macromolecules* **2010**, *43*, 362.
(151) Yan, C.; Li, H.; Zhang, J.; Ozaki, Y.; Shen, D.; Yan, D.; Shi, A. C.; Yan, S. *Macromolecules* **2006**, *39*, 8041.
(152) Darken, L. S.; Lowndes, D. H. *Appl. Phys. Lett.* **1982**, *40*, 1.
(153) Kasukabe, Y.; Osaka, T. *Thin Solid Films* **1987**, *146*, 175.
(154) Osaka, T.; Kasuhabe, Y. *J. Cryst. Growth* **1985**, *73*, 10.
(155) Klews, P. M.; Anton, R.; Harsdorff, M. *J. Cryst. Growth* **1985**, *71*, 491.
(156) Smith, H. I.; Geis, M. W.; Tompson, C. V.; Atwater, H. A. *J. Cryst. Growth* **1983**, *63*, 527.
(157) Wittmann, J. C.; Smith, P. *Nature* **1991**, *352*, 414.
(158) Givargizov, E. I. In *Oriented Crystallization on Amorphous Substrates*; Plenum Press: New York, 1991.
(159) Lü, K.; Yang, D. *Macromol. Rapid Commun.* **2005**, *26*, 1159.
(160) Taniguchi, N.; Kawaguchi, A. *Macromolecules* **2005**, *38*, 4761.
(161) Wang, J.; Li, H.; Liu, J.; Duan, Y.; Jiang, S.; Yan, S. *J. Am. Chem. Soc.* **2003**, *125*, 1496.
(162) Yan, S. *Macromolecules* **2003**, *36*, 339.
(163) Liu, J.; Li, H.; Duan, Y.; Jiang, S.; Miao, Z.; Wang, J.; Wang, D.; Yan, S. *Polymer* **2003**, *44*, 5423.
(164) Yan, S.; Lieberwirth, I.; Katzenberg, F.; Petermann, J. *J. Macromol. Sci., Part B: Phys.* **2003**, *B42*, 641.

(165) Chang, H.; Guo, Q.; Shen, D.; Li, L.; Qiu, Z.; Wang, F.; Yan, S. *J. Phys. Chem. B* **2010**, *114*, 13104.
(166) Tumala, R. R.; Pamaszewski, P. J. *Microelectronics Packaging Handbook*; Van Nostrand Reinhold: New York, 1989.
(167) Grebel, H.; Iskandar, B.; Pien, P.; Sheppard, K. *Appl. Phys. Lett.* **1990**, *57*, 2959.
(168) Wang, J.; Sun, Y.; Huang, Y.; Chen, E.; Li, H.; Yan, S. *Front. Chem. China* **2009**, *4*, 383.
(169) Thomason, J. L.; Van Rooyen, A. A. *J. Mater. Sci.* **1992**, *27*, 889.
(170) Schonhorn, H. *Macromolecules* **1991**, *24*, 3569.
(171) Cho, K.; Kim, D.; Yoon, S. *Macromolecules* **2003**, *36*, 7652.
(172) Thomason, J. L.; van Rooyen, A. A. In *Controlled Interphases in Composite Materials*; Ishida, H., Ed.; Elsevier Science: New York, 1990; p 423.
(173) Hsiao, B. S.; Chen, E. J. In *Controlled Interphases in Composite Materials*; Ishida, H., Ed.; Elsevier Science: New York, 1990; p 613.
(174) Varga, J. *J. Mater. Sci.* **1992**, *27*, 2557.
(175) Varga, J.; Fujiwara, Y.; Ille, A. *Period. Polytech. Chem. Eng.* **1990**, *34*, 255.
(176) Varga, J. In *Poly(propylene): Structure, Blends and Composites*; Karger-Kocsis, J., Ed.; Chapman & Hall: London, 1995; Vol. *1*, p 56.
(177) Varga, J. *J. Therm. Anal.* **1986**, *31*, 165.
(178) Varga, J.; Karger-Kocsis, J. *J. Polym. Sci., Part B: Polym. Phys. Ed.* **1996**, *34*, 657.
(179) Sun, X.; Li, H.; Wang, J.; Yan, S. *Macromolecules* **2006**, *39*, 8720.
(180) Hobbs, S. Y. *Nature* **1971**, *234*, 12.
(181) Ishida, H.; Bussi, P. *Macromolecules* **1991**, *24*, 3569.
(182) Li, H.; Jiang, S.; Wang, J.; Wang, D.; Yan, S. *Macromolecules* **2003**, *36*, 2802.
(183) Li, H.; Zhang, X.; Kuang, X.; Wang, D.; Li, L.; Yan, S. *Macromolecules* **2004**, *37*, 2847.
(184) Sun, X.; Li, H.; Zhang, X.; Wang, J.; Wang, D.; Yan, S. *Macromolecules* **2006**, *39*, 1087.
(185) Li, H.; Sun, X.; Yan, S.; Schultz, J. M. *Macromolecules* **2008**, *41*, 5062.
(186) Sun, X.; Li, H.; Zhang, X.; Wang, D.; Schultz, J. M.; Yan, S. *Macromolecules* **2010**, *43*, 561.
(187) Andrews, R.; Jacques, D.; Rao, A. M.; Rantell, T.; Derbyshire, F.; Chen, Y.; Chen, J.; Haddon, R. C. *Appl. Phys. Lett.* **1999**, *75*, 1329.
(188) Li., B.; Li, C. Y. *J. Am. Chem. Soc.* **2007**, *129*, 12.
(189) Lourie, O.; Cox, D. M.; Wagner, H. D. *Phys. Rev. Lett.* **1998**, *81*, 1638.
(190) Regev, O.; ElKati, P. N. B.; Loos, J.; Koning, C. E. *Adv. Mater.* **2004**, *16*, 248.
(191) Koganemaru, A.; Bin, Y. Z.; Agari, Y.; Matsuo, M. *Adv. Funct. Mater.* **2004**, *14*, 842.
(192) Thostenson, E. T.; Ren, Z. F.; Chou, T. W. *Compos. Sci. Technol.* **2001**, *61*, 1899.
(193) Miltner, H. E.; Grossiord, N.; Lu, K.; Loos, J.; Koning, C. E.; Van Mele, B. *Macromolecules* **2008**, *41*, 5753.
(194) Lu, K.; Grossiord, N.; Koning, C. E.; Miltner, H. E.; Van Mele, B.; Loos, J. *Macromolecules* **2008**, *41*, 8081.
(195) Grady, B. P.; Pompeo, F.; Shambaugh, R. L.; Resasco, D. E. *J. Phys. Chem. B* **2002**, *106*, 5852.
(196) Li, L.; Li, B.; Hood, M. A.; Li, C. Y. *Polymer* **2009**, *50*, 953.
(197) Li, C. Y.; Li, L. Y.; Cai, W. W.; Kodjie, S. L.; Tenneti, K. K. *Adv. Mater.* **2005**, *17*, 1198.
(198) Li, C. Y.; Li, L. Y.; Ni, C. Y. *J. Am. Chem. Soc.* **2006**, *128*, 1692.
(199) Li, C. Y.; Li, L. Y.; Ni, C. Y.; Rong, L. X.; Hsiao, B. *Polymer* **2007**, *48*, 3452.
(200) Yue, J.; Xu, Q.; Zhang, Z. W.; Chen, Z. M. *Macromolecules* **2007**, *40*, 8821.
(201) Zhang, Z. W.; Xu, Q.; Chen, Z. M.; Yue, J. *Macromolecules* **2008**, *41*, 2868.
(202) Zhang, F.; Zhang, H.; Zhang, Z. W.; Chen, Z. M.; Xu, Q. *Macromolecules* **2008**, *41*, 4519.
(203) Zheng, X.; Xu, Q. *J. Phys. Chem. B* **2010**, *114*, 9435.
(204) He, L.; Zheng, X.; Xu, Q. *J. Phys. Chem. B* **2010**, *114*, 5257.
(205) Somani, R. H.; Yang, L.; Zhu, L.; Hsiao, B. S. *Polymer* **2005**, *46*, 8587.
(206) Yang, L.; Somani, R. H.; Sics, I.; Hsiao, B. S.; Kolb, R.; Fruitwala, H.; Ong, C. *Macromolecules* **2004**, *37*, 4845.
(207) Hsiao, B. S.; Yang, L.; Somani, R. H.; Avila-Orta, C. A.; Zhu, L. *Phys. Rev. Lett.* **2005**, *94*, 117802.
(208) Hu, W.; Frenkel, D.; Mathot, V. B. F. *Macromolecules* **2002**, *35*, 7172.
(209) Shah, M.; Ganesan, V. *Macromolecules* **2010**, *43*, 543.
(210) Wang, H.; Gan, Z.; Schultz, J. M.; Yan, S. *Polymer* **2008**, *49*, 2342.
(211) De Rosa, C.; Park, C.; Lotz, B.; Wittmann, J. C.; Fetters, L. J.; Thomas, E. L. *Macromolecules* **2000**, *33*, 4871.
(212) Wu, C.; Chen, M.; Karger-Kocsis, J. *Polymer* **2001**, *42*, 129.
(213) Arora, P.; Zhang, Z. *Chem. Rev.* **2004**, *104*, 4419.

Macromolecules
COMMUNICATION TO THE EDITOR

Macromolecules **2011**, *44*, 429–431 **429**
DOI: 10.1021/ma102608a

Stimuli-Triggered Off/On Switchable Complexation between a Novel Type of Charge-Generation Polymer (CGP) and Gold Nanoparticles for the Sensitive Colorimetric Detection of Hydrogen Peroxide and Glucose

Changhua Li, Jinming Hu, Tao Liu, and Shiyong Liu*

CAS Key Laboratory of Soft Matter Chemistry, Department of Polymer Science and Engineering, Hefei National Laboratory for Physical Sciences at the Microscale, University of Science and Technology of China, Hefei, Anhui 230026, China

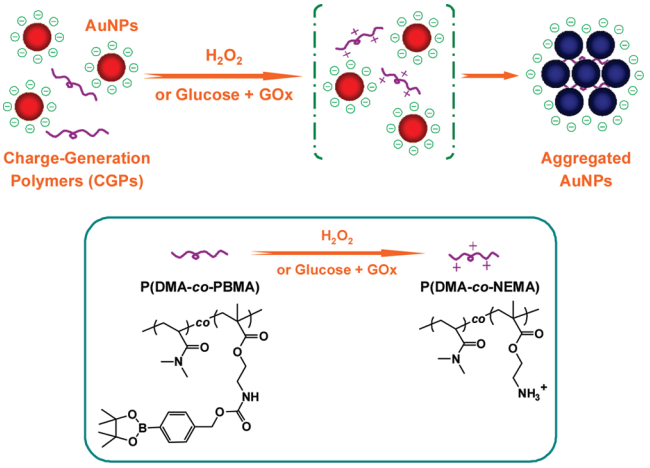
Received November 16, 2010
Revised Manuscript Received January 9, 2011

Hydrogen peroxide (H_2O_2) is a key oxygen metabolite which has been considered as a "necessary evil" owing to its "double-faced" physiological and pathological effects in living organisms.[1] Besides acting as a messenger in normal cellular signal transduction processes and a killing agent released by immune cells,[2] the abnormal production of H_2O_2 also leads to oxidative stress and damage events associated with aging and severe pathologies such as cancer and Parkinson's and Alzheimer's diseases.[3] Moreover, H_2O_2 is also involved in many environmental and industrial food processes.[4] Thus, the highly sensitive and selective detection of H_2O_2 is quite crucial. Although in recent years a variety of designing strategies based on chemiluminescence, fluorescence, and electrochemical techniques have been developed,[5] it is still a challenging task to explore a simple, reliable, cost-effective, and highly sensitive detection system for H_2O_2.

Colorimetric approaches based on gold nanoparticles (AuNPs) have been widely employed to probe various target species such as oligonucleotides,[6] protein,[7] small bioactive molecules,[8] explosives,[9] metal ions,[10] and other hazardous molecules[11] by taking advantage of their facile surface functionalization and unique distance-dependent surface plasmon absorption properties.[12] Target species mediated or triggered aggregation and disintegration of AuNPs typically leads to discernible colorimetric changes, which can be checked by the naked eye or more quantitatively by UV−vis spectroscopy. It is worthy of noting that nearly all the above colorimetric sensing systems are fabricated via small molecule or complementary oligonucleotide sequence-based molecular recognition. On the other hand, it has been well-established that charged inorganic nanoparticles are subjected to aggregation and assembly in the presence of oppositely charged (block) polyelectrolytes via the formation of electrostatic hybrid complexes.[13] However, to the best of our knowledge, polyelectrolyte-induced AuNP aggregation has not been utilized to design practicable sensing systems, mainly due to the lack of suitable analyte-triggerable polyelectrolyte/AuNP complexation systems.

The above two aspects have prompted us to design a special type of water-soluble synthetic polymers which can undergo stimuli-triggered transition from the initially uncharged state to the charged one, so that a colorimetric detection system for H_2O_2 and in a further step for glucose (in the presence of glucose oxidase, GOx) based on the triggered aggregation of AuNPs can be constructed. To differentiate from the recently emerged pH-induced charge-reversal polymers[14] and photoinduced charge-bearing polymers,[15] we have termed these novel types of polymers as stimuli-triggered charge-generation polymers (CGPs). Herein, we report a proof-of-concept example for the fabrication of colorimetric detection system for H_2O_2 and glucose by engineering negatively charged AuNPs and a water-soluble CGP exhibiting selective H_2O_2-triggered transformation into a cationic polyelectrolyte. Electrostatic complexation between AuNPs and the newly generated positively charged polymer can then lead to prominent colorimetric transitions due to the aggregation of AuNPs (Scheme 1).

Scheme 1. Schematic Illustration of the Construction of Colorimetric Sensing System for H_2O_2 and Glucose (in the Presence of GOx) via the Combination of Negatively Charged AuNPs with a Water-Soluble Charge-Generation Polymer (CGP) Exhibiting Selective H_2O_2-Triggered Transition from the Initially Uncharged State to a Cationic Polyelectrolyte



On the basis of the above proposed strategy (Scheme 1), we first designed and synthesized a new polymerizable monomer, PBMA, via the reaction of boronate ester-functionalized benzyl alcohol derivative with 2-isocyanatoethyl methacrylate (Scheme S1 and Figure S1 in the Supporting Information). It should be noted that in literature reports the aryl boronate motif has rendered the construction of a series of small molecule H_2O_2-selective fluorescent probes and in vivo imaging agents.[5b−d] As PBMA monomer lacks sufficient water solubility, we then opted to synthesize PBMA-containing water-soluble polymers via the free radical copolymerization of PBMA with *N*,*N*-dimethylacrylamide (DMA). The obtained P(DMA-*co*-PBMA) copolymer was subjected to further fractionation to afford relatively narrow-disperse samples. ^{1}H NMR (Figure S2a) and gel permeation chromatography (GPC, Figure S3) analysis revealed an overall degree of polymerization (DP) of 620, an M_w/M_n of 1.27, and a PBMA molar content of 11%. As expected, the initially uncharged $P(DMA_{0.89}$-*co*-$PBMA_{0.11})_{620}$ transforms into a positively charged polyelectrolyte in the presence of H_2O_2, as evidenced by ^{1}H NMR analysis from the complete disappearance of resonance signals characteristic of boronate ester moieties after treating with H_2O_2 (Scheme 1 and Figure S2). It is worthy of noting that pendent aliphatic amine moieties typically possess a pK_a of ∼9,[16] and under neutral pH conditions the newly generated amine residues triggered by H_2O_2 are in the protonated state, which can effectively eliminate any amine-involved side reactions such as the amidation of ester moieties.

Citrate-stabilized AuNPs with an average diameter of ∼13 nm were synthesized according to literature procedures (Figure S4).[17]

*To whom correspondence should be addressed. E-mail: sliu@ustc.edu.cn.

© 2011 American Chemical Society

Published on Web 01/12/2011

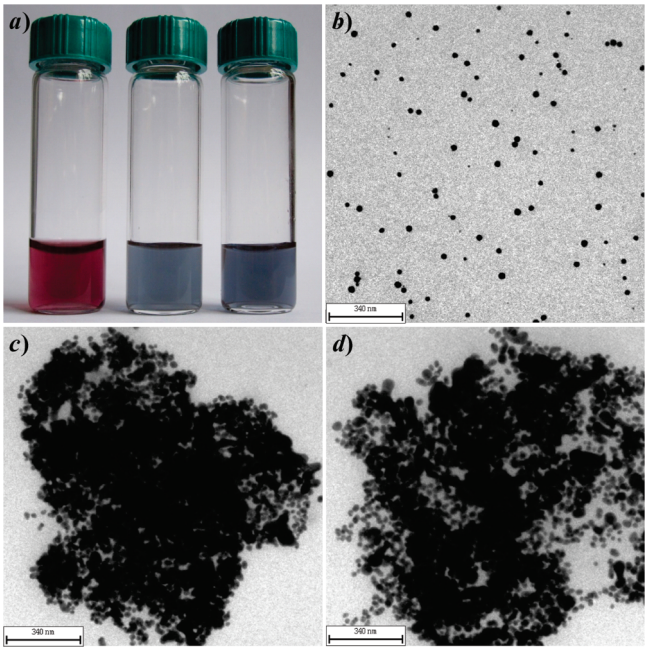


Figure 1. (a) Optical visualization of the colorimetric assay (4.5 nM of AuNPs and 1.8×10^{-3} g/L of CGP with [PBMA] = 1.5 μM) in the absence of H_2O_2 (left) and 1 h after the addition of the aqueous solution of (middle) H_2O_2 (120 equiv relative to PBMA moieties) or (right) the glucose oxidization mixture (300 equiv glucose and 0.2 g/L of GOx) at pH 7.4 and 25 °C. (b−d) The corresponding TEM images (scale bar is 340 nm) obtained by drying the three aqueous dispersions shown in (a).

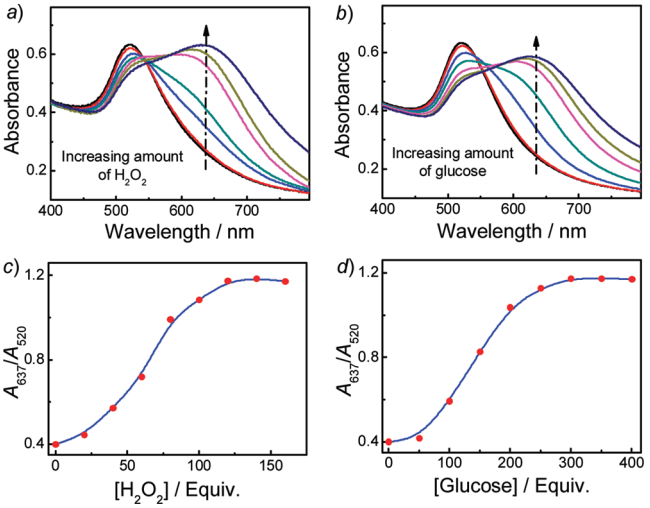


Figure 2. (a, b) UV−vis spectra and (c, d) absorbance intensity ratios, A_{637}/A_{520}, recorded for the aqueous colorimetric assay (4.5 nM of AuNPs and 1.8×10^{-3} g/L of CGP with [PBMA] = 1.5 μM) upon adding varying amount of (a, c) H_2O_2 (0−160 equiv relative to PBMA moieties) and (b, d) the glucose oxidization mixture (0−400 equiv glucose and 0.2 g/L of GOx were employed for the enzyme-catalyzed reaction) at pH 7.4 and 25 °C. All measurements were conducted 1 h after the addition of analytes.

The negatively charged wine red AuNP dispersion exhibits a characteristic surface plasmon resonance (SPR) band at ~520 nm, which is almost unchanged upon the sole addition of H_2O_2 (Figure S5), indicating that citrate-stabilized AuNPs do not react with H_2O_2. The aqueous colorimetric assay system for H_2O_2 was then optimized to consist of negatively charged AuNPs (4.5 nM) and the CGP, P(DMA$_{0.89}$-*co*-PBMA$_{0.11}$)$_{620}$ copolymer (1.8×10^{-3} g/L, [PBMA] = 1.5 μM) at pH 7.4. Initially, AuNPs remain well-dispersed in the aqueous solution of CGP, as revealed by the characteristic wine red color (Figure 1a), UV−vis absorption band at 520 nm (Figure 2a), and TEM analysis (Figure 1b). This is reasonable considering that there does not exist specific interactions between negatively charged AuNPs and the neutral P(DMA$_{0.89}$-*co*-PBMA$_{0.11}$)$_{620}$. For H_2O_2 detection, its aqueous solution with the volume being half of original aqueous assay mixture was used. Upon addition of the aqueous solution of H_2O_2 (120 equiv relative to PBMA residues), the dispersion gradually turns from wine red to purple blue within ~0.5 h. This apparently confirmed our design strategy as shown in Scheme 1. As expected, TEM analysis of the purple blue dispersion revealed the presence of aggregated AuNPs (Figure 1c). The presence of H_2O_2 can trigger the transformation of uncharged P(DMA$_{0.89}$-*co*-PBMA$_{0.11}$)$_{620}$ into a cationic polyelectrolyte (Figure S2). As ~68 positively charged amine moieties are present per newly generated polyelectrolyte chain if we assume 100% functional group transformation, it can act as an effective interparticle cross-linker for negatively charged AuNPs, and the dispersion containing aggregated AuNPs exhibits the characteristic colorimetric transitions.

H_2O_2-triggered aggregation of AuNPs can also be quantitatively determined by changes in the SPR bands. UV−vis spectroscopy analysis was then performed to evaluate the sensitivity of colorimetric H_2O_2 assay. The time duration needed for the colorimetric changes to reach the final stable state was determined at first (Figure S6). Upon addition of 120 equiv of H_2O_2 (relative to PBMA moieties), we can observe that the SPR band at 520 nm gradually decreases and exhibits a slight red shift with time and then stabilizes out after ~40 min, which is also accompanied by the appearance and the dramatic increase in intensity of a new absorption band at around ~637 nm originating from the interparticle coupled plasmon absorbance.[10d,12a,18] It is worthy of noting that the appearance of a new absorption band at ca. 640 nm has been typically observed for highly aggregated gold nanoparticles with diameters of ~13 nm.[10d,20b] To maintain the consistency of H_2O_2 assays, in subsequent experiments all aqueous mixtures were incubated for 1 h after the addition of H_2O_2. On the basis of the results shown in Figure 2a, we can tell that gradually increasing the amount of H_2O_2 led to more prominent red shift of the absorption spectrum, which can be qualitatively expressed as the absorbance intensity ratio, A_{637}/A_{520} (Figure 2c). An almost linear H_2O_2 concentration dependence of the absorbance intensity ratio was observed at $[H_2O_2] < \sim 120\ \mu$M, which matches quite well with the physiologically relevant concentration of H_2O_2 (~10−100 μM).[19] If we arbitrarily define the H_2O_2 detection limit as the concentration at which a 10% increase of A_{637}/A_{520} ratio can be achieved, the H_2O_2 detection limit was then determined to be ~20 μM (~0.68 mg/L) under the current setup conditions of H_2O_2 colorimetric assay, which is quite comparable with those of small molecule fluorescent probes based on aryl boronates.[5b−d] On the basis of the above results, we have established that highly sensitive colorimetric H_2O_2 detection system can be successfully constructed by combining negatively charged AuNPs with a novel type of CGP exhibiting H_2O_2-triggerable transformation from the uncharged state to a cationic polyelectrolyte. Moreover, it has been well-documented that H_2O_2 is quite selective over other reactive oxygen species (ROS) toward the deprotection of aryl boronate moieties.[5b,d] Thus, the reported H_2O_2 assay system possesses combined advantages such as high sensitivity, selectivity, and ease of fabrication. Apart from this, the current colorimetric assay can provide a facile and cost-effective readout of low concentrations of H_2O_2 even with the naked eye. This is excellent as compared to previously reported H_2O_2 assay protocols employing fluorometric or electrochemical and techniques.[5]

Since glucose oxidase (GOx) can specifically catalyze the oxidation of glucose to produce H_2O_2,[20] we then employed the above

H_2O_2 assay kit for the colorimetric detection of glucose. First, the mixture of glucose and GOx was incubated at 37 °C under an O_2 atmosphere for 10 min; then the oxidation product was analyzed by using the above H_2O_2 colorimetric assay at pH 7.4 and 25 °C. As shown in Figure 1a, upon addition of the glucose oxidation product, a gradual colorimetric transition of the assay mixture from wine red to purple blue can be observed (Figure 1a). This indicated that the H_2O_2 assay protocol established in the previous section can also be successfully employed for glucose detection, again via the aggregation of AuNPs induced by the CGP triggered by H_2O_2 (Figure 1d). In the control experiments, pure GOx or glucose was also separately added, none of them can induce the aggregation of AuNPs, and a colorimetric transition was not observed. Figure 2b,d further indicates that by increasing the amount of glucose used in GOx-catalyzed reaction, its oxidized product can induce more dramatic shift in the SPR band of AuNPs and concomitantly the more prominent changes in absorbance intensity ratios (A_{637}/A_{520}). On the basis of Figure 2d, we can determine that the glucose detection limit can be down to ~50 μM, which is quite comparable with those previously reported for the colorimetric assay based on ssDNA/AuNPs[20b] and fluorescent glucose probes based on aryl boronates.[20c] It has been well-known that the normal blood glucose concentration is in the range 3.5−6.1 mM, and abnormal glucose levels can reach as high as ~20 mM. Thus, the reported colorimetric H_2O_2 assay protocol based on AuNPs and the CGP can be facilely applied for the highly sensitive detection of glucose.

In summary, we presented an effective strategy for the quantitative and sensitive colorimetric detection of H_2O_2 and glucose by combining a novel concept of stimuli-triggered charge-generation polymer (termed as CGP) with AuNPs. The presence of H_2O_2 can trigger the transformation of the CGP from the initially uncharged state into a cationic polyelectrolyte via the deprotection of carbamate-based amine protecting moieties, which can then induce the aggregation of negatively charged AuNPs and result in a dramatic red shift of the SPR band and apparent colorimetric transitions. We expect that this proof-of-concept example can be further generalized to the design of a variety of other sensing systems by employing alternate trigger-specific charge-generation building moieties.[21]

Acknowledgment. The financial support from National Natural Scientific Foundation of China (NNSFC) Projects (20874092, 91027026, and 51033005), Fundamental Research Funds for the Central Universities, and Specialized Research Fund for the Doctoral Program of Higher Education (SRFDP) is gratefully acknowledged.

Supporting Information Available: Experimental details and spectroscopic/analytical data of ^{1}H NMR, GPC, TEM, and UV−vis measurements. This material is available free of charge via the Internet at http://pubs.acs.org.

References and Notes

(1) Rhee, S. G. *Science* **2006**, *312*, 1882–1883.
(2) (a) Veal, E. A.; Day, A. M.; Morgan, B. A. *Mol. Cell* **2007**, *26*, 1–14. (b) Miller, R. A.; Britigan, B. E. *Clin. Microbiol. Rev.* **1997**, *10*, 1–18.
(3) (a) Dickinson, B. C.; Chang, C. J. *J. Am. Chem. Soc.* **2008**, *130*, 9638–9639. (b) Lin, M. T.; Beal, M. F. *Nature* **2006**, *443*, 787–795. (c) Finkel, T.; Serrano, M.; Blasco, M. A. *Nature* **2007**, *448*, 767–774.
(4) Drabkova, M.; Admiraal, W.; Marsalek, B. *Environ. Sci. Technol.* **2007**, *41*, 309–314.
(5) (a) Lee, D.; Khaja, S.; Velasquez-Castano, J. C.; Dasari, M.; Sun, C.; Petros, J.; Taylor, W. R.; Murthy, N. *Nature Mater.* **2007**, *6*, 765–769. (b) Miller, E. W.; Tulyanthan, O.; Isacoff, E. Y.; Chang, C. J. *Nat. Chem. Biol.* **2007**, *3*, 263–267. (c) Lo, L. C.; Chu, C. Y. *Chem. Commun.* **2003**, 2728–2729. (d) Srikun, D.; Miller, E. W.; Dornaille, D. W.; Chang, C. J. *J. Am. Chem. Soc.* **2008**, *130*, 4596–4597. (e) Lyon, J. L.; Stevenson, K. J. *Anal. Chem.* **2006**, *78*, 8518–8525.
(6) (a) Elghanian, R.; Storhoff, J. J.; Mucic, R. C.; Letsinger, R. L.; Mirkin, C. A. *Science* **1997**, *277*, 1078–1081. (b) Xu, W.; Xue, X. J.; Li, T. H.; Zeng, H. Q.; Liu, X. G. *Angew. Chem., Int. Ed.* **2009**, *48*, 6849–6852. (c) Hong, M.; Zhou, X.; Lu, Z. Q.; Zhu, J. *Angew. Chem., Int. Ed.* **2009**, *48*, 9503–9506. (d) Su, X. D.; Kanjanawarut, R. *ACS Nano* **2009**, *3*, 2751–2759. (e) Song, G. T.; Chen, C.; Qu, X. G.; Miyoshi, D.; Ren, J. S.; Sugimoto, N. *Adv. Mater.* **2008**, *20*, 706–710. (f) Zhu, Z.; Wu, C. C.; Liu, H. P.; Zou, Y.; Zhang, X. L.; Kang, H. Z.; Yang, C. J.; Tan, W. H. *Angew. Chem., Int. Ed.* **2010**, *49*, 1052–1056.
(7) (a) Aili, D.; Selegard, R.; Baltzer, L.; Enander, K.; Liedberg, B. *Small* **2009**, *5*, 2445–2452. (b) Aili, D.; Enander, K.; Rydberg, J.; Nesterenko, I.; Bjorefors, F.; Baltzer, L.; Liedberg, B. *J. Am. Chem. Soc.* **2008**, *130*, 5780–5788.
(8) (a) Patel, G.; Menon, S. *Chem. Commun.* **2009**, 3563–3565. (b) Wang, J.; Wang, L. H.; Liu, X. F.; Liang, Z. Q.; Song, S. P.; Li, W. X.; Li, G. X.; Fan, C. H. *Adv. Mater.* **2007**, *19*, 3943–3946. (c) Lee, J. S.; Ulmann, P. A.; Han, M. S.; Mirkin, C. A. *Nano Lett.* **2008**, *8*, 529–533.
(9) Jiang, Y.; Zhao, H.; Zhu, N. N.; Lin, Y. Q.; Yu, P.; Mao, L. Q. *Angew. Chem., Int. Ed.* **2008**, *47*, 8601–8604.
(10) (a) Wang, Z. D.; Lee, J. H.; Lu, Y. *Adv. Mater.* **2008**, *20*, 3263–3267. (b) Liu, J. W.; Lu, Y. *J. Am. Chem. Soc.* **2004**, *126*, 12298–12305. (c) Xue, X. J.; Wang, F.; Liu, X. G. *J. Am. Chem. Soc.* **2008**, *130*, 3244–3245. (d) Li, D.; Wieckowska, A.; Willner, I. *Angew. Chem., Int. Ed.* **2008**, *47*, 3927–3931. (e) Liu, J.; Lu, Y. *J. Am. Chem. Soc.* **2005**, *127*, 12677–12683. (f) Zhou, Y.; Wang, S. X.; Zhang, K.; Jiang, X. Y. *Angew. Chem., Int. Ed.* **2008**, *47*, 7454–7456. (g) Kim, S.; Park, J. W.; Kim, D.; Kim, D.; Lee, I. H.; Jon, S. *Angew. Chem., Int. Ed.* **2009**, *48*, 4138–4141. (h) Li, X. K.; Wang, J. N.; Sun, L. L.; Wang, Z. X. *Chem. Commun.* **2010**, *46*, 988–990.
(11) (a) Ai, K. L.; Liu, Y. L.; Lu, L. H. *J. Am. Chem. Soc.* **2009**, *131*, 9496–9497. (b) Lee, J. H.; Wang, Z. D.; Liu, J. W.; Lu, Y. *J. Am. Chem. Soc.* **2008**, *130*, 14217–14226. (c) Zhang, J.; Wang, L. H.; Pan, D.; Song, S. P.; Boey, F. Y. C.; Zhang, H.; Fan, C. H. *Small* **2008**, *4*, 1196–1200. (d) Daniel, W. L.; Han, M. S.; Lee, J. S.; Mirkin, C. A. *J. Am. Chem. Soc.* **2009**, *131*, 6362–6363.
(12) (a) De, M.; Ghosh, P. S.; Rotello, V. M. *Adv. Mater.* **2008**, *20*, 4225–4241. (b) Daniel, M. C.; Astruc, D. *Chem. Rev.* **2004**, *104*, 293–346.
(13) (a) Mori, H.; Lanzendorfer, M. G.; Muller, A. H. E.; Klee, J. E. *Langmuir* **2004**, *20*, 1934–1944. (b) Berret, J. F.; Sehgal, A.; Morvan, M.; Sandre, O.; Vacher, A.; Airiau, M. *J. Colloid Interface Sci.* **2006**, *303*, 315–318. (c) Reinicke, S.; Dohler, S.; Tea, S.; Krekhova, M.; Messing, R.; Schmidt, A. M.; Schmalz, H. *Soft Matter* **2010**, *6*, 2760–2773. (d) Kim, J. W.; Kim, J. H.; Chung, S. J.; Chung, B. H. *Analyst* **2009**, *134*, 1291–1293.
(14) (a) Lee, Y.; Fukushima, S.; Bae, Y.; Hiki, S.; Ishii, T.; Kataoka, K. *J. Am. Chem. Soc.* **2007**, *129*, 5362–5363. (b) Lee, Y.; Ishii, T.; Kim, H. J.; Nishiyama, N.; Hayakawa, Y.; Itaka, K.; Kataoka, K. *Angew. Chem., Int. Ed.* **2010**, *49*, 2552–2555. (c) Xu, P. S.; Van Kirk, E. A.; Zhan, Y. H.; Murdoch, W. J.; Radosz, M.; Shen, Y. Q. *Angew. Chem., Int. Ed.* **2007**, *46*, 4999–5002. (d) Zhang, J. Y.; Zhou, Y. M.; Zhu, Z. Y.; Ge, Z. S.; Liu, S. Y. *Macromolecules* **2008**, *41*, 1444–1454.
(15) (a) Jiang, Y. G.; Wan, P. B.; Xu, H. P.; Wang, Z. Q.; Zhang, X.; Smet, M. *Langmuir* **2009**, *25*, 10134–10138. (b) Chen, S. L.; Jiang, Y. G.; Wang, Z. Q.; Zhang, X.; Dai, L. M.; Smet, M. *Langmuir* **2008**, *24*, 9233–9236.
(16) (a) Mutka, S.; Njegic-Dzakula, B.; Kovacevic, D. *Croat. Chem. Acta* **2008**, *81*, 593–597. (b) Petrov, A. I.; Antipov, A. A.; Sukhorukov, G. B. *Macromolecules* **2003**, *36*, 10079–10086.
(17) Grabar, K. C.; Freeman, R. G.; Hommer, M. B.; Natan, M. J. *Anal. Chem.* **1995**, *67*, 735–743.
(18) Su, K.-H.; Wei, Q.-H.; Zhang, X.; Mock, J. J.; Smith, D. R.; Schultz, S. *Nano Lett.* **2003**, *3*, 1087–1090.
(19) Finkel, T. *Curr. Opin. Cell Biol.* **2003**, *15*, 247–254.
(20) (a) Gordijo, C. R.; Shuhendler, A. J.; Wu, X. Y. *Adv. Funct. Mater.* **2010**, *20*, 1404–1412. (b) Jiang, Y.; Zhao, H.; Lin, Y. Q.; Zhu, N. N.; Ma, Y. R.; Mao, L. Q. *Angew. Chem., Int. Ed.* **2010**, *49*, 4800–4804. (c) He, F.; Feng, F. D.; Wang, S.; Li, Y. L.; Zhu, D. B. *J. Mater. Chem.* **2007**, *17*, 3702–3707.
(21) Hu, J. M.; Liu, S. Y. *Macromolecules* **2010**, *43*, 8315–8330.

DOI: 10.1021/ma102798j

Macromolecules
COMMUNICATION TO THE EDITOR

Fluorescent Viscosity Sensor Film of Molecular-Scale Porous Polymer with Intramolecular π-Stack Structure

Wang-Eun Lee,[†] Chang-Lyoul Lee,[‡] Toshikazu Sakaguchi,[§] Michiya Fujiki,[⊥] and Giseop Kwak*,[†]

[†]*Department of Polymer Science, Kyungpook National University, 1370 Sankyuk-dong, Buk-ku, Daegu 702-701, Korea,* [‡]*Advanced Photonics Research Institute, Gwangju Institute of Science and Technology, 1 Oryong-dong, Buk-gu, Gwangju 500-712, Korea,* [§]*Department of Materials Science and Engineering, Graduate School of Engineering, University of Fukui, Bunkyo, Fukui 910-8507, Japan, and* [⊥]*Graduate School of Materials Science, Nara Institute of Science and Technology, 8916-5 Takayama, Ikoma, Nara 630-0101, Japan*

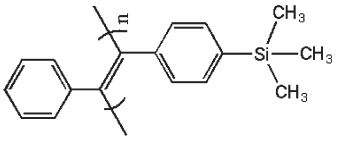
Received December 9, 2010
Revised Manuscript Received December 31, 2010

One of the hottest issues in petrochemical (refinery), biomedical, and automobile engineering is to accurately and conveniently determine the viscosity of organic solvents,[1−3] biofluids,[4−8] internal-combustion engine oils,[9,10] and other similar substances. Moreover, the viscosity measurement is also required for fuels, lubricants, adhesive agents, polymer solutions, and even soft drinks. The fluorescence (FL) intensity of molecular rotor dyes with twisted intramolecular charge transfer (TICT) characteristics significantly changes according to the media viscosity due to the torsional angle relaxation of the rotor molecules in the solution.[11−14] In recent times, several fluorescent molecular rotor dyes with the viscosity sensing function have been developed with many benefits such as easy applicability, high sensitivity, and high spatial/temporal resolution imaging to gain an advantage over conventional mechanical rheometers.[15−21] Especially in the biomedical field, these sensors have the potential to be used as diagnostic tools for disease detection.[4,5,8,22] Although these viscosity sensor systems well work with a high accuracy, their applications have been limited to only the dye-dissolving, polar media under wet conditions.[23] The sensing processes also have some disadvantages such as the needs of annoying calibration curves, potential reading errors due to fluctuations in the rotor concentration, and optical properties like the refractive index of the fluids.[6] Accordingly, a solid-state viscosity sensor would be a more desirable material because it can not only avoid contamination of the fluid but also make its application extend to a variety of viscous media such as nondissolving and/or nonpolar fluids. Ultimately, a solid-state viscosity sensor could provide a practical sensor device platform applicable in a wider viscosity range. Very recently, Haidekker et al. attempted to develop solid-state viscosity sensors based on dye-immobilized optical fibers and glass slides.[24,25] Although these solid sensors showed sufficient sensitivity compared to mechanical rheometers, the sensors have a much lower sensitivity relative to in-solution molecular rotors and still need higher reproducibility. The practical application of the sensor materials may also demand a chemically and physically better durability. However, the molecular rotor dyes are intrinsically polar at the excited state due to the TICT characteristics. Thus, they easily degrade as a result of not being able to endure even mild amounts of heat and light. Therefore, sensor materials with thermal, chemical, and mechanical stabilities in addition to high viscosity sensitivity would be more appealing for practical applications. The ultimate goal of this study is to develop a new class of high-quality solid-state viscosity sensors that satisfy the requirements above.

Fluorescent conjugated polymers can rapidly respond to a very subtle electronic perturbation due to their intrinsic conjugation cooperativity,[26−30] whereas such a cooperativity effect cannot be expected in the low molecular weight compounds of molecular rotors. Diphenylacetylene polymer derivatives are intensively fluorescent in a visible region due to the intramolecular excimer emission, which comes from the highly efficient exciton confinement between the bulky side phenyl rings.[31−36] Also, these polymer derivatives show rapid gas/liquid diffusion due to the intrinsic amorphous nature and the extremely large fractional free volumes (FFV). Recently, we found that poly[1-phenyl-2-(*p*-trimethylsilyl)phenylacetylene] (PTMSDPA in Chart 1), a representative of diphenylacetylene polymer derivatives, has an excellent FL response to external stimuli of various (bio)-chemicals.[37,38] The FFV of PTMSDPA film is about 0.26. When contacted to various organic solvents such as alcohol and hydrocarbon liquids, this polymer film shows a significant swelling-induced emission enhancement (SIEE). The SIEE phenomenon is now believed due to the fact that the solvent molecules diffuse into the PTMSDPA film through the many microvoids and then loosen the entangled polymer chains while simultaneously relaxing the intramolecular phenyl−phenyl stack structure, which results in the decrease in electronic $\pi^*-\pi$ transition energy (blue shift in FL band) and the increase in oscillator strength.[37,39] Notably, the larger the molecular size of the diffused molecules in the order of *n*-hexane < *n*-decane < paraffin oil, the higher the FL intensity ratio of I/I_0, where I_0 and I are FL maximum intensities of the PTMSDPA film before and after contacting the solvent chemicals, respectively. This indicated a feasibility of molecular size recognition using the PTMSDPA film while strongly suggesting there is a great potential for application using the PTMSDPA film as a solid-state viscosity sensor. In previous works, however, only the three hydrocarbon liquids (*n*-hexane, *n*-decane, and paraffin oil) and two alcohols (methanol and ethanol) were limitedly tested. Thus, the viscosity sensitivity of the PTMSDPA film has not been evaluated quantitatively.[37,39]

In order to discuss the viscosity sensitivity of PTMSDPA film in detail, we tested three types of organic fluid compounds while considering the difference in molecular affinity between the polymer film and the viscous media: (1) aliphatic hydrocarbon liquids with the carbon atom numbers of C5−C14 in a viscosity range of 0.24−2.32 cP at 20 °C, (2) alcohols with the numbers of C1−C7 in a viscosity range of 0.54−5.81 cP at 20 °C, and (3) silicon oils with different molecular weights in a viscosity range of 10−200 cP at 20 °C (Table S1 in Supporting Information). These compounds do not dissolve PTMSDPA. The hydrocarbons and silicon oils are hydrophobic fluids while the alcohols are hydrophilic ones.

Chart 1. Chemical Structure of PTMSDPA



*Corresponding author: Tel (+82) 53-950-7558; Fax (+82) 53-950-6623; e-mail gkwak@knu.ac.kr.

 Published on Web 01/07/2011 © 2011 American Chemical Society

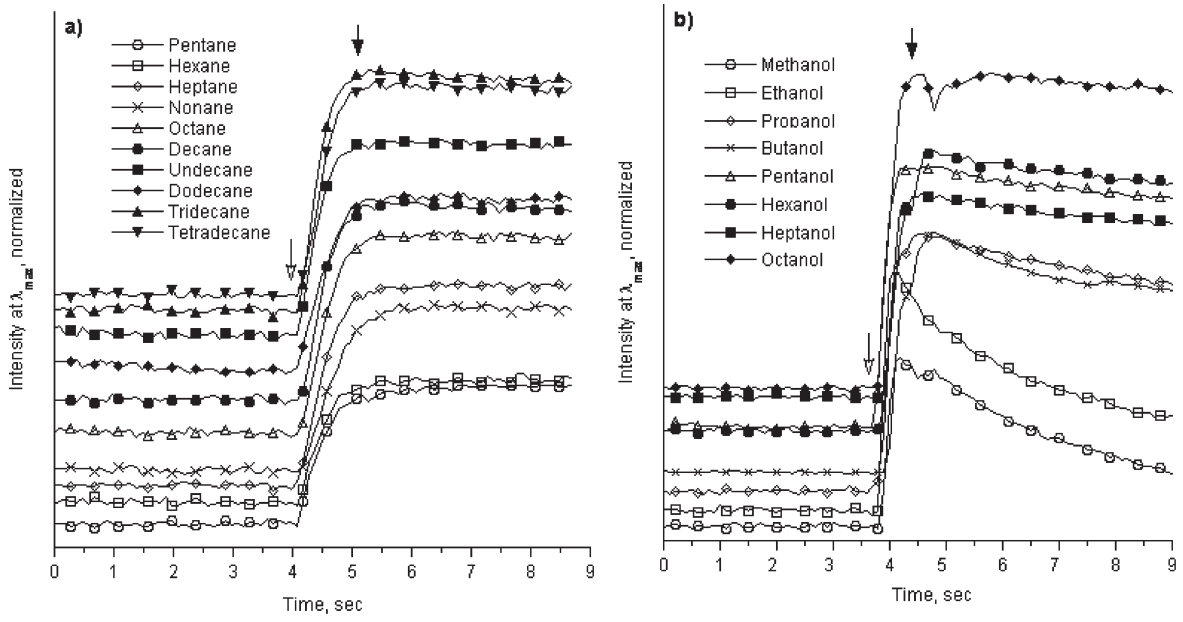


Figure 1. Plots of the changes in the integral FL intensity of PTMSDPA film in a wavelength range of 510−540 nm as a function of aging time when the polymer film was contacted to (a) hydrocarbons and (b) alcohols[61] (film thickness ≈100 nm; excited at 365 nm with an irradiation power of 1.73 mW/cm^2; scanning rate 10 dots/s). The blank and solid arrows indicate the fluid contact point and SIEE equilibrium point, respectively.

Newtonian fluids such as hydrocarbons and alcohols with relatively low viscosities rapidly diffused into the PTMSDPA film. We determined the FL response rate by the time-resolved FL spectroscopy in a millisecond time scale. Figure 1 plots the changes in the integral FL intensity of the PTMSDPA film at the emission maximum wavelength as a function of aging time when the polymer film came into contact with the fluids. The FL intensity instantly reaches the enhancing equilibrium in SIEE within ~1 s as soon as the film came into contact with hydrocarbons and alcohols. This result indicates the present polymer rapidly responds to the viscous media despite of the solid state. Thus, the effect of the FL response rate on the SIEE equilibrium was able to be ignored in the cases of the Newtonian fluids because every single FL spectra were measured when the time passed at least over 1 s after contacting to the media. On the other hand, silicon oils with much higher viscosities diffused slowly into the polymer film as compared to the Newtonian fluids. It took several to several tens of seconds for the silicon oils to thoroughly pass through the thin polymer films in the direction of the axial thickness (Figure S1 in Supporting Information). The aging time to reach the SIEE equilibrium became longer with increases in the viscosity of the silicon oils. Especially, the silicon oil with an extremely high viscosity of 200 cP showed quite a slow response rate of ~60 s to reach the enhancing equilibrium (Figure S2 in Supporting Information). Actually, the gradual increase in FL intensity according to the aging time was able to be recognized by the naked eye (movies S1 and S2 in Supporting Information). Thus, as for the silicon oils, we measured the FL spectra of the PTMSDPA film more carefully to confirm the SIEE equilibrium.

Parts a and b of Figure 2 show the FL spectra of PTMSDPA in thin films when they came into contact with the hydrocarbons and alcohols, respectively. The FL intensity of PTMSDPA increases significantly with increases in the viscosity of the media. Figure 2c,d plots the log FL intensity ratios as a function of the log viscosity of the fluids. The viscosity sensitivity of PTMSDPA film obeys the solvent free volume theory expressed by Förster−Hoffmann equation of $\log I = C + x \log \eta$.[40] The functional log−log equations of viscosity sensitivity of PTMSDPA for hydrocarbons and alcohols are also well expressed as a linear equation of $\log(I/I_0) = C + x \log \eta$, where η is the media viscosity, x is the probe-dependent constant, C is the proportional constant, and I_0 and I are FL intensities of PTMSDPA film at the FL maximum wavelength before and after contacting to the viscous media, respectively. Despite the solid-state sensor based on a thin solid polymer film, the present sensor system shows very high x values. The x values for hydrocarbons and alcohols are 0.50 and 0.28, respectively. This film type of polymer sensor needs neither to prepare the polymer solution nor to take the concentration into consideration, whereas in-solution molecular rotors necessarily need to compensate for concentration fluctuation. On the other hand, such film type sensors may need to take the film thickness dependency of FL variations into the consideration. Actually, the x values of PTMSDPA films were slightly dependent on film thickness when a thick film with thickness of several tens of micrometers was used (Figure S3 in Supporting Information). To completely avoid such potential errors, we thus used polymer films with the same thickness of 100 nm. Moreover, because all FL spectra were measured at the same temperature of 20 °C, we did not have to take the temperature dependency of the media viscosity into consideration.

The difference in the FL intensity of PTMSDPA films according to the viscous media was clearly recognized by the naked eye (Figure S4 in Supporting Information). To comprehensively understand the change in FL intensity according to the media viscosity, we performed a dynamic FL spectroscopy. Table 1 summarizes the FL lifetimes of PTMSDPA film in a swollen state in various hydrocarbons. The photoemission decay of PTMSDPA film obeys biexponential decay. As the media viscosity increases, the shorter-lived excited species (f_1) reduces, but the longer-lived one (f_2) increases. This means that the dominant shorter FL lifetime (τ_1) of PTMSDPA in less viscous media is due to a rapid energy migration into the energy trapping sites, while the polymer in more viscous media restrains generation of the shorter-lived excited species to be characterized by a longer lifetime (τ_2) as well as τ_1. As a result, the τ_{avr} increases with an increase in the media viscosity. The FL decay profiles also exhibited the viscosity sensitivity of PTMSDPA film well (Figure S5 in Supporting Information). The FL decayed slowly as the media viscosity increases, indicating significant exciton confinement in a more viscous media. This result corresponded

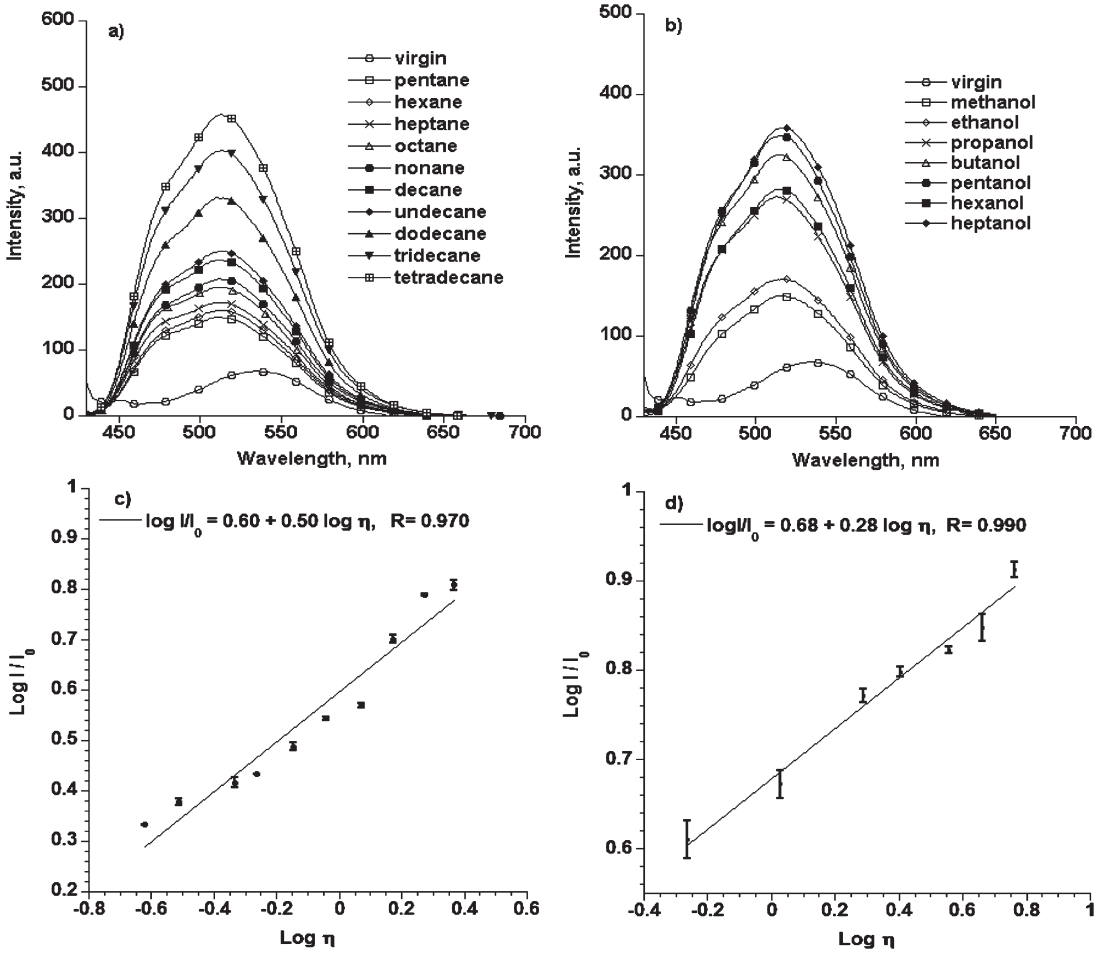


Figure 2. FL spectra of PTMSDPA thin films when contacted to (a) the hydrocarbons and (b) alcohols and plots of the log FL intensity ratios as a function of log viscosity of (c) the hydrocarbons and (d) alcohols (film thickness ≈100 nm; excited at 420 nm with an irradiation power of 2.23 μW/cm^2).

Table 1. Fluorescence Lifetimes of PTMSDPA in a Swollen State in Various Hydrocarbons[a]

viscous media	τ_1 (f_1), ns	τ_2 (f_2), ns	χ^2	τ_{avr}, ns
hexane	0.35 (0.78)	0.88 (0.22)	1.20	0.47
ocatane	0.42 (0.70)	1.00 (0.30)	1.06	0.60
decane	0.48 (0.62)	1.12 (0.38)	1.10	0.72
dodecane	0.53 (0.61)	1.21 (0.39)	1.08	0.79
tridecane	0.54 (0.59)	1.24 (0.41)	1.04	0.82
tetradecane	0.51 (0.56)	1.21 (0.44)	1.08	0.83

[a] Film thickness is 100 nm. Monitor wavelength is 520 nm. The τ_1 and τ_2 are lifetime (ns), f_1 and f_2 are fractional intensities, χ^2 is the reduced chi-square, and τ_{avr} is the average lifetime obtained from $f_1\tau_1 + f_2\tau_2$.

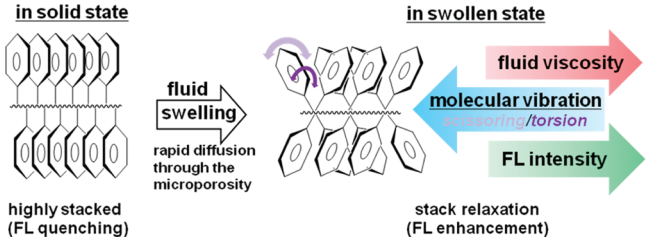


Figure 3. Schematic representation of the viscosity-sensing mechanism of PTMSDPA film. Trimethylsilyl groups are omitted for viewing clarity.

well with the results on the steady-state FL emission spectroscopy described above. The FL lifetimes of PTMSDPA film as a function of media viscosity were well expressed as a certain quadratic log−log equation (Figure S6 in Supporting Information).

The x values of PTMSDPA for hydrocarbons and alcohols are comparable to those of the conventional in-solution molecular rotors.[15−21] Herein we have two questions of concern. First, how does this polymer differentiate the viscosities of the fluids? According to previous studies, the FL emission of PTMSDPA originates from the intramolecular excimer due to the phenyl−phenyl stack structure of the side groups.[31−36] Such an aromatic stack structure is constructed on the basis of a weak force such as $\pi-\pi$ interaction and, thus, should be easily influenced by external obstructive compounds. Figure 3 shows the detailed schematic explanations of how the side phenyl stack structure changes through swelling and how the vibrational motion of the phenyl rings changes according to the media's viscosity. Because such a molecular conformation as intramolecular aromatic stack structure becomes loose in a swollen state, the FL emission should be enhanced while the emission band shifts simultaneously to a shorter wavelength. And then, because the stack structure should be variable in the swollen state, the molecular scissoring/torsional motions of the side phenyl rings should decrease with the increases in the media viscosity. Thus, nonradiative emission decay due to the molecular perturbation of the side phenyl rings should be effectively restrained in more viscous media. The next question is why this polymer has the high viscosity sensitivity and rapid responsivity even in a solid film. The PTMSDPA is a completely amorphous polymer with an extremely large FFV unlike the conventional π-conjugated polymers with planar geometries and strong intermolecular interactions that lead to a highly cofacial chain packing and crystallinity in the solid state.

The amorphous nature makes the viscous fluids rapidly diffuse into the polymer film, and then the many microvoids provide enough permanent porosity for the polymer chains to behave freely like solution-state isolated polymer chains with no interchain interaction. Moreover, this polymer has a discontinuously arranged phenyl−phenyl stack structure in a zigzag pattern, while the corresponding meta-substituted polymer, which has a trimethylsilyl group on the meta-position of the side phenyl ring, is continuously coiled in a helical manner.[41] This suggests that the motion freedom of the phenyl rings of the present polymer should be quite high in a swollen state. These facts should be responsible for the high viscosity sensitivity of PTMSDPA films. Accordingly, this type of polymer sensor system makes it feasible to exactly determine the viscosity of the fluids in real time simply by contacting the fluids to the polymer film.

It should be also noted that the x value for the hydrocarbons is greater than that for the alcohols. This is probably due to the difference in molecular affinity to PTMSDPA film between the hydrocarbons and alcohols. Because PTMSDPA is basically a hydrophobic polymer, this polymer should have a higher affinity to hydrocarbons than to alcohols. Both the hydrocarbons and alcohols, which can be considered as homogeneous media with bulk viscosity, are extremely small molecules. Also, such a polymer type fluorescent probe as PTMSDPA is much greater in molecular size as compared to the fluid molecules. Thus, in this case, the difference in the molecular affinity of the probe polymer between hydrocarbons and alcohols can be better explained by the solvent friction effect[42−44] rather than the cavity effect based on solvent free volume theory. Naturally, the friction energy transferred to the probe molecules is greater in more affinitive media. Thus, the hydrocarbon molecules more significantly influence the phenyl−phenyl stack structure of the polymer as compared to the alcohols. On the other hand, the conventional molecular rotors such as 9-(dicyanovinyl)julolidine (DCVJ) and 9-(2-carboxy-2-cyano)vinyljulolidine (CCVJ) hardly dissolve in nonpolar media due to the intrinsic high polarity with TICT characteristics, and thus, their viscosity sensitivity has been evaluated exclusively for polar media.[7] Therefore, the molecular affinity effect on viscosity sensitivity of the molecular rotor dye-based viscosity sensors has been ignored to date. In one exceptional example, Benniston et al. reported the viscosity sensitivity of a molecular rotor based on boron dipyrromethene (Bodipy) dye.[21] The FL intensity of the Bodipy dye was much greater in toluene than in methanol although the viscosities of toluene and methanol were almost the same. This fragmentary result hinted that factors other than the bulk viscosity should be taken into consideration in accurately evaluating viscosity sensitivity of the probe molecules. This idea is strongly supported by the present result that the x values for the hydrophobic and hydrophilic viscous media are significantly different from each other. In this respect, the present polymer film may be one of the most promising sensor material candidates, which make it possible to distinctively evaluate the viscosity of the various fluids.

The functional log−log equation of viscosity sensitivity of PTMSDPA film for silicon oils was also expressed as an equation of $\log(I/I_0) = C + x \log \eta$ with $x = 0.21$ (Figure S7 in Supporting Information). The x value of silicon oils is much smaller than that of the hydrocarbon fluids although the silicon oils are also hydrophobic fluids. The Debye−Stokes−Einstein (DSE) equation is valid for the rotational diffusion of spherical particles in a homogeneous medium with bulk viscosity.[45−47] However, it cannot be established when the molecular sizes of the fluids are much greater than the probe molecules. Silicon oils are non-Newtonian fluid compounds composed of polymeric siloxane linkage of Si−O−Si bonds. That is, they are viscoelastic oligomers or polymers with high molecular weights. Thus, silicon oils should have a great molecular cavity unlike the Newtonian fluids with bulk viscosity. Accordingly, it may be reasonable to think the non-Newtonian polymeric molecules of silicon oils restrain the molecular perturbation of the fluorescent probe moieties in PTMSDPA films by the media cavity effect rather than the molecular friction forces. This should be responsible for the lower x value for the silicon oils.

In summary, the present polymer, PTMSDPA, quickly responded to various kinds of fluids, such as hydrocarbons, alcohols, and silicon oils, simply by putting the fluids in contact with the films. The functional log−log equations of viscosity sensitivity of the PTMSDPA films were expressed well as a linear equation of $\log(I/I_0) = C + x \log \eta$. Especially, the probe-dependent constant (x) for hydrocarbons was as high as 0.50, which is comparable to that of the in-solution rotor dye of DCVJ that is known as the most viscosity-sensitive probe molecule. Also, the x values of the present sensor in hydrocarbons (0.50), alcohols (0.28), and silicon oils (0.21) significantly differed from each other due to the difference in the molecular affinities and sizes of the fluids. This result strongly suggests the molecular affinity between sensor and media should be considered to accurately evaluate the viscosity sensitivity of the sensor material. To our knowledge, this is the first study to evaluate the viscosity sensitivity of a fluorescent conjugated polymer for various types of fluids. The present polymer film is expected to be a universal, solid-state viscosity sensor material adaptable for various viscous fluids. Our molecular design concept for the high viscosity sensitivity and rapid responsivity of the probe polymer is based on the molecular-scale porosity and the intramolecular π-stack structure. This design rule is also expected to be extended to fluorescent conjugated microporous polymers (CMPs) with a permanently interconnected microporosity.[48−60]

Acknowledgment. The authors sincerely thank NOF Co., Ltd., Japan, for the donation of PTMSDPA. This work was supported by the Basic Science Research Program through the National Research Foundation of Korea (NRF) grants funded by the Korea government (MEST) (2010-0000569, 2010-0001883, 2010-0007255).

Supporting Information Available: Detailed experimental methods, FL response rate (Figures S1 and S2) for silicon oils, movies (movies S1 and S2), log−log plots (Figure S3), FL photographs (Figure S4), FL decay profiles (Figure S5), log−log plot of FL lifetime (Figure S6), log−log plot for silicon oils (Figure S7), and viscosities of the fluids (Table S1). This material is available free of charge via the Internet at http://pubs.acs.org.

References and Notes

(1) Vold, R. R.; Vold, R. L.; Szeverenyi, N. M. *J. Chem. Phys.* **1979**, *70*, 5213–5217.
(2) Woodle, R. A. U.S. Patent US 4137753 19790206.
(3) Appel, M.; Dria, D. E.; Elshahawi, H.; Epping, W. J. M.; Ostermeier, R. M.; Pearce, J. G.; l Prodan, I. D. PCT Int. Appl. 2009, 48 pp, WO2009070667 A1 20090604.
(4) Haidekker, M. A.; L'heureux, N.; Frangos, J. A. *Am. J. Physiol. Heart Circ. Physiol.* **2000**, *278*, H1401–1406.
(5) Haidekker, M. A.; Tsai, A. G.; Brady, T.; Stevens, H. Y.; Frangos, J. A.; Theodorakis, E.; Intaglietta, M. *Am. J. Physiol. Heart Circ. Physiol.* **2002**, *282*, H1609–1614.
(6) Haidekker, M. A.; Brady, T. P.; Chalian, S. H.; Akers, W.; Lichlyter, D.; Theodorakis, E. A. *Bioorg. Chem.* **2004**, *32*, 274–289.
(7) Haidekker, M. A.; Theodorakis, E. A. *Org. Biomol. Chem.* **2007**, *5*, 1669–1678.
(8) Nipper, M. E.; Majd, S.; Mayer, M.; Lee, J. C.-M.; Theodorakis, E. A.; Haidekker, M. A. *Biochim. Biophys. Acta* **2008**, *1778*, 1148–1153.
(9) Wang, S. S. *Sens. Actuators, B* **2001**, *73*, 106–111.
(10) Agoston, A.; Otsch, C.; Jakoby, B. *Sens. Actuators, A* **2005**, *121*, 327–332.

(11) Loutfy, R. O.; Law, K. Y. *J. Phys. Chem.* **1980**, *84*, 2803–2808.
(12) Loutfy, R. O.; Arnold, B. *J. Phys. Chem.* **1982**, *86*, 4205–4211.
(13) Allen, B. D.; Benniston, A. C.; Harriman, A.; Rostron, S.; Yu, C. *Phys. Chem. Chem. Phys.* **2005**, *7*, 3035–3040.
(14) Kottas, G. S.; Clarke, L. I.; Horinek, D.; Michl, J. *Chem. Rev.* **2005**, *105*, 1281–1376.
(15) Haidekker, M. A.; Brady, T. P.; Lichlyter, D.; Theodorakis, E. A. *J. Am. Chem. Soc.* **2006**, *128*, 398–399.
(16) Fischer, D.; Theodorakis, E. A.; Haidekker, M. A. *Nature Protoc.* **2007**, *2*, 227–236.
(17) Ghiggino, K. P.; Hutchison, J. A.; Langford, S. J.; Latter, M. J.; Lee, M. A. P.; Lowenstern, P. R.; Scholes, C.; Takezaki, M.; Wilman, B. E. *Adv. Funct. Mater.* **2007**, *17*, 805–813.
(18) Zhu, D.; Haidekker, M. A.; Lee, J.-S.; Won, Y.-Y.; Lee, J. C.-M. *Macromolecules* **2007**, *40*, 7730–7732.
(19) Stsiapura, V. I.; Maskevich, A. A.; Kuxmitsky, V. A.; Uversky, V. N.; Kuznetsova, I. M.; Turoverov, K. K. *J. Phys. Chem. B* **2008**, *112*, 15893–15902.
(20) Kuimova, M. K.; Yahioglu, G.; Levitt, J. A.; Suhling, K. *J. Am. Chem. Soc.* **2008**, *130*, 6672–6673.
(21) Alamiry, M. A. H.; Benniston, A. C.; Copley, G.; Elliott, H. J.; Harriman, A.; Stewart, B.; Zhi, Y.-G. *Chem. Mater.* **2008**, *20*, 4024–4032.
(22) Harkness, J. *Biorheology* **1971**, *8*, 171–193.
(23) Haidekker, M. A.; Brady, T. P.; Linchlyter, D.; Theodorakis, E. A. *Bioorg. Chem.* **2005**, *33*, 415–425.
(24) Haidekker, M. A.; Akers, W. J.; Fischer, D.; Theodorakis, E. A. *Opt. Lett.* **2006**, *31*, 2529–25331.
(25) Lichlyter, D. J.; Haidekker, M. A. *Sens. Actutators, B* **2009**, *139*, 648–656.
(26) Swager, T. M. *Acc. Chem. Res.* **1998**, *31*, 201–207.
(27) Yang, J.-S.; Swager, T. M. *J. Am. Chem. Soc.* **1998**, *120*, 11864.
(28) McQuade, D. T.; Pullen, A. E.; Swager, T. M. *Chem. Rev.* **2000**, *100*, 2537–2574.
(29) Kim, T.-H.; Swager, T. M. *Angew. Chem., Int. Ed.* **2003**, *42*, 4803–4806.
(30) Thomas, S. W., III; Joly, G. D.; Swager, T. M. *Chem. Rev.* **2007**, *107*, 1339–1386.
(31) Fujii, A.; Hidayat, R.; Sonoda, T.; Fujisawa, T.; Ozaki, M.; Vardeny, Z. V.; Teraguchi, M.; Masuda, T.; Yoshino, K. *Synth. Met.* **2001**, *116*, 95–99.
(32) Hidayat, R.; Fujii, A.; Ozaki, M.; Teraguchi, M.; Masuda, T.; Yoshino, K. *Synth. Met.* **2001**, *119*, 597–598.
(33) Shukla, A.; Ghosh, H.; Mazumdar, S. *Synth. Met.* **2001**, *116*, 87–90.
(34) Shukla, A. *Chem. Phys.* **2004**, *300*, 177–188.
(35) Yuan, W. Z.; Qin, A.; Lam, J. W. Y.; Sun, J. Z.; Dong, Y.; Haussler, M. J.; Liu, J.; Xu, H. P.; Zhen, Q.; Tang, B. Z. *Macromolecules* **2007**, *40*, 3159–3166.
(36) Qin, A.; Jim, C. K. W.; Tang, Y.; Lam, J. W. Y.; Liu, J.; Mahtab, F.; Gao, P.; Tang, B. Z. *J. Phys. Chem. B* **2008**, *112*, 9281–9288.
(37) Kwak, G.; Lee, W.-E.; Jeong, H.; Sakaguchi, T.; Fujiki, M. *Macromolecules* **2009**, *42*, 20–24.
(38) Kwak, G.; Lee, W.-E.; Kim, W.-H.; Lee, H. *Chem. Commun.* **2009**, 2112–2114.
(39) Lee, W.-E.; Kim, J.-W.; Oh, C.-J.; Sakaguchi, T.; Fujiki, M.; Kwak, G. *Angew. Chem., Int. Ed.* **2010**, *49*, 1406–1409.
(40) Förster, T.; Hoffmann, G. *Z. Phys. Chem.* (*Munich*) **1971**, *75*, 63–76.
(41) Lee, W.-E.; Oh, C.-J.; Park, G.-T.; Kim, J.-W.; Choi, H.-J.; Sakaguchi, T.; Fujiki, M.; Nakao, A.; Shinohara, K.; Kwak, G. *Chem. Commun.* **2010**, *46*, 6491–6493.
(42) Jin, H.; Liang, M.; Arzhantsev, S.; Li, X.; Maroncell, M. *J. Phys. Chem. B* **2010**, *114*, 7565–7578.
(43) Tan, X.; Gustafson, T. L. *J. Phys. Chem. A* **2000**, *104*, 4469–4474.
(44) Bessire, D. R.; Quitevis, E. L. *J. Phys. Chem.* **1994**, *98*, 13083–13092.
(45) Einstein, A. *Investigations on the Theory of Brownian Motion*; Dover: New York, 1956.
(46) Debye, P. *Polar Molecules*; Dover: New York, 1929; pp 72−85.
(47) Dote, J. L.; Kivelson, D.; Schwarz, R. N. *J. Phys. Chem.* **1981**, *85*, 2169.
(48) Cooper, A. I. *Adv. Mater.* **2009**, *21*, 1291–1295.
(49) Jiang, J.-X.; Su, F.; Trewin, A.; Wood, C. D.; Campbell, N. L.; Niu, H.; Dickinson, C.; Ganin, A. Y.; Rosseinsky, M. J.; Khimyak, Y. Z.; Cooper, A. I. *Angew. Chem., Int. Ed.* **2007**, *46*, 8574–8578.
(50) Kuhn, P.; Antonietti, M.; Thomas, A. *Angew. Chem., Int. Ed.* **2008**, *47*, 3450–3453.
(51) Schmidt, J.; Weber, J.; Epping, J. D.; Antonietti, M.; Thomas, A. *Adv. Mater.* **2009**, *21*, 702–705.
(52) Feng, X.; Liang, Y.; Zhi, L.; Thomas, A.; Wu, D.; Lieberwirth, I.; Kolb, U.; Mullen, K. *Adv. Funct. Mater.* **2009**, *19*, 2125–2129.
(53) Jiang, J.-X.; Su, F.; Trewin, A.; Wood, C. D.; Niu, H.; Jones, J. T. A.; Khimyak, Y. Z.; Cooper, A. I. *J. Am. Chem. Soc.* **2008**, *130*, 7710–7720.
(54) Kuhn, P.; Forget, A.; Su, D.; Thomas, A.; Antonietti, M. *J. Am. Chem. Soc.* **2008**, *130*, 13333–13337.
(55) Schwab, M. G.; Fassbender, B.; Spiess, H. W.; Thomas, A.; Feng, X.; Mullen, K. *J. Am. Chem. Soc.* **2009**, *131*, 7216–7217.
(56) Dawson, R.; Laybourn, A.; Clowes, R.; Khimyak, Y. Z.; Adams, D. J.; Cooper, A. I. *Macromolecules* **2009**, *42*, 8809–8816.
(57) Schmidt, J.; Werbner, M.; Thomas, A. *Macromolecules* **2009**, *42*, 4426–4429.
(58) Chen, L.; Yang, Y.; Jiang, D. *J. Am. Chem. Soc.* **2010**, *132*, 9138–9143.
(59) Chen, L.; Honsho, Y.; Seki, S.; Jiang, D. *J. Am. Chem. Soc.* **2010**, *132*, 6742–6748.
(60) Choi, J. H.; Choi, K. M.; Jeon, H. J.; Choi, Y. J.; Lee, Y.; Kang, J. K. *Macromolecules* **2010**, *43*, 5508–5511.
(61) Lee, W.-E.; Park, H.; Kwak, G. *Chem. Commun.* **2011**, *47*, 659–661. In this experiment, we used a very powerful irradiation light with a 1.73 mW/cm^2 to obtain a high spectral resolution and intensity ratios. The PTMSDPA film rapidly underwent photobleaching in polar solvents such as methanol (dielectric constant, $\varepsilon = 32.6$) and ethanol ($\varepsilon = 24.8$) when exposed to the intense UV light, which was condensed by an object lens in a fluorescence microscope system, from a super-high-pressure 100 W Hg lamp (OSRAM, HBO 103W/2). This is due to the formation of polymer$^{\delta+}$−solvent$^{\delta-}$ charge-transfer complex in a photooxidized form .

Macromolecules
COMMUNICATION TO THE EDITOR

Macromolecules **2011**, *44*, 437–439 **437**
DOI: 10.1021/ma102778d

Fast Photodegradable Block Copolymer Micelles for Burst Release

Dehui Han, Xia Tong, and Yue Zhao*

Département de chimie, Université de Sherbrooke, Sherbrooke, Québec, Canada J1K 2R1

Received December 6, 2010
Revised Manuscript Received January 5, 2011

There is increasing interest in designing block copolymer (BCP) micelles of which the assembly state in aqueous solution can be controlled or disrupted by light.[1−3] This is motivated by the potential application of such BCP micelles as nanocarrier for light-triggered release of guest molecules, which offers the remote-control possibility as well as the temporal and spatial selectivity. The main established approach allowing for photocontrolled dissociation of BCP micelles is to incorporate photochromic groups onto the hydrophobic block of a BCP, whose photoreaction can increase the polarity of the block and thus shift the hydrophilic−hydrophobic balance to render the micellar association of BCP chains thermodynamically unstable.[1−3] Upon micelle dissociation, loaded hydrophobic guest can be released to aqueous medium. Recently, several groups demonstrated a new approach that is based on using a photocleavable junction linking the hydrophilic and hydrophobic blocks.[4] After micelle formation, light can be applied to break BCP chains at the junction point. It is easy to imagine that, though interesting, this approach is not ideal for light-triggered release of guest molecules loaded in the micelle core because the chain aggregation state of the latter would not be loosened due to the removal of the hydrophilic corona.

Herein we demonstrate a novel BCP design strategy. Instead of using a single photolabile junction between the two blocks, photobreakable moieties are positioned repeatedly along the hydrophobic main chain. With this design, the resulting BCP micelle possesses a photodegradable core that, upon photoreaction, can be disintegrated very quickly. The sketch in Figure 1 illustrates the difference between having just one photobreakable junction and having many such units on the main chain of the hydrophobic block. We envision that fast disintegration of the micelle core should lead to a fast release of loaded guest molecules.

Scheme 1 shows the one-pot synthesis of an amphiphilic ABA triblock copolymer of which the end block A is water-soluble poly(ethylene oxide) (PEO) and the middle block B is a hydrophobic polyurethane containing nitrobenzyl groups (PEO-*b*-PUNB-*b*-PEO). The photodegradable PUNB block was first prepared by using condensation polymerization of 2-nitro-1,3-benzenedimethanol with tolylene 2,4-diisocyanate in slight excess. It was then terminated with monomethyl ether PEO to yield the triblock copolymer of PEO-*b*-PUNB-*b*-PEO. The size exclusion chromatograph (SEC) result in Figure 2 confirms the successful coupling between PUNB and PEO. As compared with monomethyl ether PEO, the BCP sample has a larger polydispersity index (increased from 1.06 to 1.38). This is likely caused by the PUNB block formed via condensation polymerization, with which a broader distribution of molecular weights is generally associated. The possibility of having some PEO-*b*-PUNB diblock could not be ruled out, but this does not affect the core−shell micelle formation. With this BCP, fast photoinduced micelle core disintegration could be expected by having an *o*-nitrobenzyl unit linked to two methyl ester groups in each repeating unit of the micelle core-forming PUNB block. Photoinduced degradation of the BCP in dissolved state in THF was first investigated, and the result obtained with SEC is also shown in Figure 2. After irradiation of a BCP solution (3 mL, 0.1 mg/mL) with UV light (300 nm, ∼ 60 mW/cm^2), the SEC trace shows dominant low molecular weight species while a remaining polymer peak matches the elution peak of PEO, indicating a complete separation of PEO chains from PUNB as well as the severe disintegration of the hydrophobic block into low-molecular-weight species. The continuous photodegradation at a high BCP concentration in THF (10 mg/mL) was also observed from SEC measurements (Figure S4 in Supporting Information). Moreover, the photoreaction of nitrobenzyl units could be monitored from UV−vis spectra that display an increased absorption over a wide range of wavelengths (300−500 nm) as the photoreaction progresses (Figure S5 in Supporting Information). From the BCP design, a variety of degraded nitro- and nitrosobenzyl species can be expected due to the randomly occurring photocleavage reaction on the main chain of PUNB.

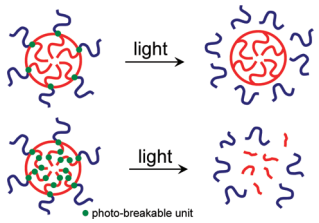


Figure 1. Schematic illustration of the difference between placing a photobreakable unit at only the block junction and repeatedly on the hydrophobic block.

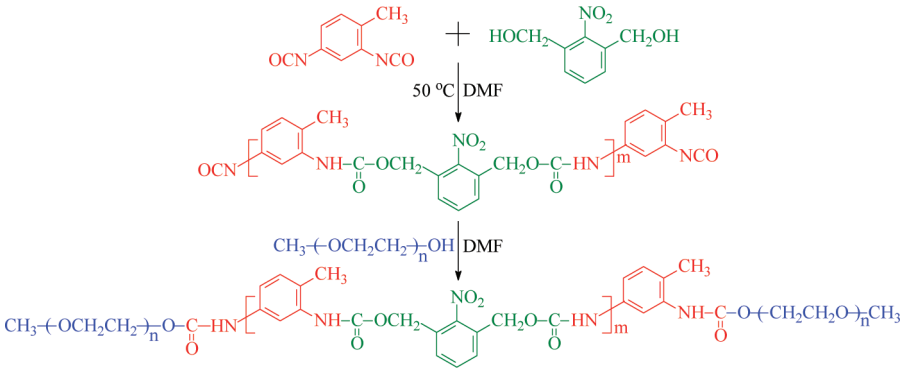
The fast photodegradation of the PUNB block indeed leads to fast disintegration of the BCP micelle in solution. We first carried out the experiment with BCP micelles in a mixed solvent of dioxane/water (1:1) where the photodegraded molecular species are soluble, which made it possible to monitor the micelle disintegration process through dynamic light scattering (DLS) measurements. In this experiment, micelles were prepared by dissolving the BCP in dioxane (0.2 mg/mL), followed first by slow addition of water (35% in volume with respect to dioxane) and then fast addition of water (dioxane/water, 1:1). Figure 3a shows the change in the scattering intensity of the micellar solution (1 mL) upon UV irradiation (300 nm, 250 mW/cm^2). The intensity of scattered light drops after only 10 s of UV exposure and changes little after 30 s of irradiation even though the photoreaction continues as revealed by the UV−vis spectra (Figure S6 in Supporting Information). This result suggests that the BCP micelles could be disrupted quickly as the PUNB block is broken into pieces upon cleavage of *o*-nitrobenzyl moieties. Figure 3b shows the change in the volume-averaged size distribution before and after 180 s UV irradiation of the solution. The BCP micelles (hydrodynamic diameter D_H ∼ 60 nm) are transformed into smaller species of various sizes after the short time irradiation. The situation after irradiation is understandable because, as mentioned above, the photodegradation of the PUNB block is expected to generate various species including PEO chains. The fast disintegration of BCP micelles is also observable on AFM.

*Corresponding author. E-mail: Yue.Zhao@Usherbrooke.ca.

© 2011 American Chemical Society

Published on Web 01/18/2011

Scheme 1. Synthetic Route to the Triblock Copolymer of PEO-*b*-PUNB-*b*-PEO



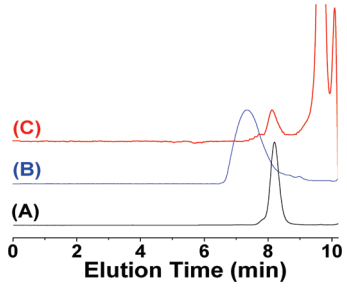


Figure 2. Size exclusion chromatograph (SEC) traces of (a) monomethyl ether PEO, (b) triblock copolymer of PEO-*b*-PUNB-*b*-PEO, and (c) PEO-*b*-PUNB-*b*-PEO triblock copolymer in THF after 1 h UV irradiation for photodegradation (3 mL, 0.1 mg/mL, 1 h exposure to 300 nm, 60 mW/cm^2).

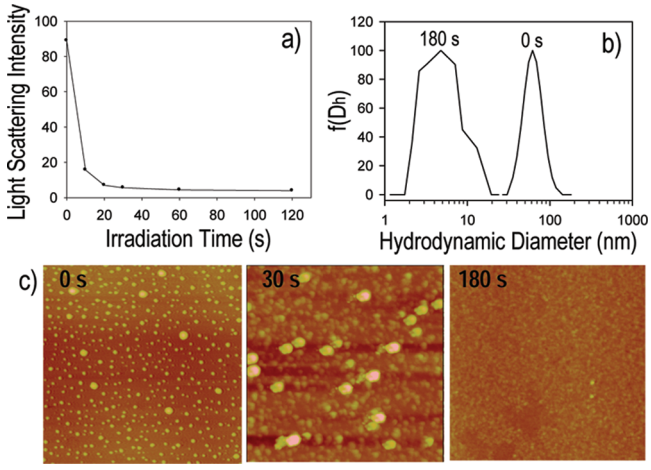


Figure 3. (a) Scattering intensity (measured at 90°) for BCP micelles in a mixed solvent (dioxane/water, 1/1) recorded after UV irradiation for various times (300 nm, 250 mW/cm^2, solution volume 1 mL). (b) Volume-averaged distribution of hydrodynamic diameters for the micelle solution before and after 180 s UV irradiation. (c) AFM height images of the micelle solution cast on mica before and after UV irradiation (30 and 180 s) (image area: 2 μm × 2 μm).

Figure 3c shows the height images of the sample cast from the solution before and after UV irradiation. The micelles ($D_H \sim 49$ nm from the cast sample) appear to be swollen and deformed after 30 s of irradiation. It is likely that at this short time of photoreaction BCP chains remain aggregated, but the degraded micelle core becomes more solvated prior to actual disintegration. After 3 min irradiation, clear micellar aggregates can no longer be observed.

We then investigated the release in aqueous solution of a model hydrophobic guest, Nile Red (NR), loaded in the BCP micelle upon photoinduced disintegration of the micelle core. Both NR and the BCP were dissolved in THF (0.5 mg/mL, NR to BCP ratio: 1:6); water was added to induce the micelle formation and the concomitant NR encapsulation by the micelle core; THF was removed by evaporation and nonsolubilized NR was filtered by microfiltration (0.2 μm pore filter). The final BCP concentration was adjusted to 0.2 mg/mL. Figure 4a shows the fluorescence emission spectra of NR loaded in the BCP micelle before and after short time UV irradiation (up to 60 s). Figure 4b shows the plots of normalized fluorescence vs time for the solution without UV irradiation and subjected to various times of irradiation. It is seen that the emission intensity remains constant over time in the absence of irradiation, indicating stable encapsulation of the dye in a hydrophobic environment. By contrast, the emission intensity drops by more than 70% after only 10 s of irradiation! AFM observation further confirmed the fast disintegration of NR-loaded micelles in aqueous solution. Figure 5 shows the height images recorded by casting the solution on mica before and after 60 s of irradiation. Prior to irradiation, the micelles had a uniform size of $D_H \sim 41$ nm (smaller than those in the mixed solvent), while after exposure to UV light, much larger aggregates of various sizes were observed, indicating the changing assembly state of the micelles caused by a short time of irradiation. The observed rate of fluorescence quenching is very fast, indicating burst release of loaded NR into an aqueous medium. Here we emphasize that the release of loaded NR means that NR molecules initially confined in a hydrophobic micelle core are brought into contact with water molecules. This can happen as a result of either photoinduced micelle core dissociation or swelling or, in the present case, disintegration. In the context of photocontrolled drug delivery applications, after being 'transported" to a target, hydrophobic drug molecules generally need to enter into an aqueous medium and have a chance to interact with biomolecules. We also carried out a control test by dissolving both NR and the BCP in THF or a THF/water mixture and found no fluorescence change after UV irradiation under the same condition, ensuring that the fast drop of NR fluorescence in Figure 4 is not caused by photodegraded PUNB block but by quenching by water molecules (Figure.S7 in Supporting Information). The results thus confirm the design hypothesis; that is, burst release could be achieved by fast disintegration of BCP micelle core. We mention that light-triggered burst release from polymer nanoparticles prepared by emulsification was reported recently by Fomina et al. using self-immolative monomers.[5] It would be interesting to apply the concept of self-immolative polymers[6] to prepare BCP micelles whose core degradation can be activated by removing a small number of trigger units and compare them with the fast photodegradable BCP micelles demonstrated in the present study.

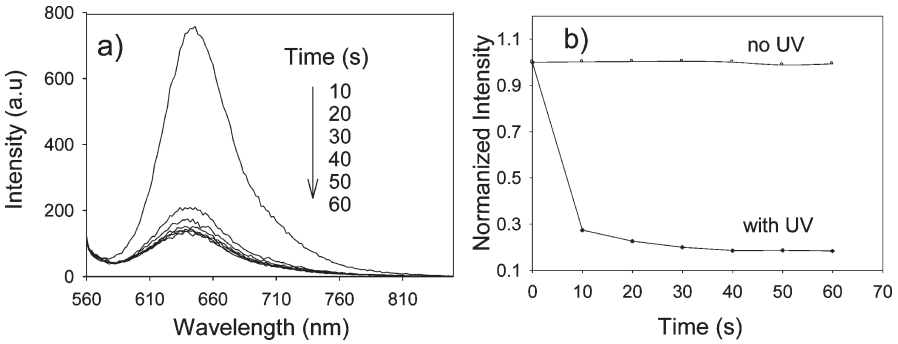


Figure 4. (a) Fluorescence emission spectra of Nile Red-loaded micelles in aqueous solution (λ_{ex} = 550 nm) recorded before and after UV irradiation for different times (300 nm, 250 mW/cm^2, solution volume 0.7 mL). (b) Normalized fluorescence emission intensity vs time for the Nile Red-loaded micelle solution with and without the UV irradiation.

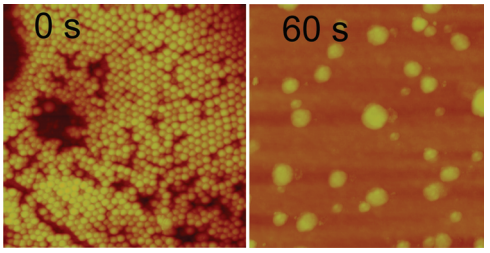


Figure 5. AFM height images of micelles obtained by casting an aqueous solution of Nile Red-loaded micelles on mica before and after 60 s UV irradiation (300 nm, 250 mW/cm^2, solution volume 0.7 mL). Image area: 1 μm × 1 μm.

In summary, we designed, synthesized, and investigated a novel photosensitive ABA triblock copolymer. The results demonstrated a new amphiphilic BCP design strategy for the preparation of fast light-breakable micelles. It consists in positioning a photocleavable unit repeatedly on the main chain of the hydrophobic block. This approach differs from those based on either light-changeable hydrophilic−hydrophobic balance or the use of a single photocleavable junction linking the constituting hydrophilic and hydrophobic blocks. We showed that with this type of BCP micelles undergoing fast photoinduced disintegration of micelle core, light-triggered burst release of loaded hydrophobic guest molecules in aqueous solution could be achieved. This progress is of fundamental interest because the approach is general and can easily be applied to design BCPs with photocleavable groups other than *o*-nitrobenzyl. Although UV light was utilized in this proof-of-principle study, light of longer wavelengths, which is more suitable for biomedical applications, could activate the same photoreaction and thus the same fast disintegration of BCP micelles through two-photon absorption of the photocleavable *o*-nitrobenzyl moieties on the main chain.[2d] By using coumarin-based photocleavable units, two-photon absorption allows the use of near-infrared light (NIR) at wavelengths ~800 nm.[2g]

Acknowledgment. We acknowledge financial support from the Natural Sciences and Engineering Research Council of Canada (NSERC) and le Fonds québécois de la recherche sur la nature et les technologies of Québec (FQRNT). Y.Z. is a member of the FQRNT-funded Center for Self-Assembled Chemical Structures.

Supporting Information Available: Details of block copolymer synthesis and more characterization results using ^{1}H NMR, UV−vis, fluorescence, and SEC. This material is available free of charge via the Internet at http://pubs.acs.org.

References and Notes

(1) (a) Zhao, Y. *J. Mater. Chem.* **2009**, *19*, 4887–4895. (b) Schumers, J.-M.; Fustin, C.-A.; Gohy, J.-F. *Macromol. Rapid Commun.* **2010**, *31*, 1588–1607. (c) Wang, B. Y.; Xu, H.; Zhang, X. *Adv. Mater.* **2009**, *21*, 2849–2864.

(2) (a) Wang, G.; Tong, X.; Zhao, Y. *Macromolecules* **2004**, *37*, 8911–8917. (b) Tong, X.; Wang, G.; Soldera, A.; Zhao, Y. *J. Phys. Chem. B* **2005**, *109*, 20281–20287. (c) Jiang, J.; Tong, X.; Zhao, Y. *J. Am. Chem. Soc.* **2005**, *127*, 8290–8291. (d) Jiang, J.; Tong, X.; Morris, D.; Zhao, Y. *Macromolecules* **2006**, *39*, 4633–4640. (e) Jiang, J.; Qi, B.; Lepage, M.; Zhao, Y. *Macromolecules* **2007**, *40*, 790–792. (f) Babin, J.; Lepage, M.; Zhao, Y. *Macromolecules* **2008**, *41*, 1246–1253. (g) Babin, J.; Pelletier, M.; Lepage, M.; Allard, J. F.; Morris, D.; Zhao, Y. *Angew. Chem., Int. Ed.* **2009**, *48*, 3329–3332.

(3) (a) Lee, H.; Wu, W.; Oh, J. K.; Mueller, L.; Sherwood, G.; Peteanu, L.; Kowalewski, T.; Matyjaszewski, K. *Angew. Chem., Int. Ed.* **2007**, *46*, 2453–2457. (b) Zou, J.; Guan, B.; Liao, X. J.; Jiang, M.; Tao, F. G. *Macromolecules* **2009**, *42*, 7465–7473. (c) Goodwin, A. P.; Mynar, J. L.; Ma, Y.; Fleming, G. R.; Fréchet, J. M. J. *J. Am. Chem. Soc.* **2005**, *127*, 9952–9953. (d) Wang, Y.; Han, P.; Xu, H.; Wang, Z.; Zhang, X.; Kabanove, A. *Langmuir* **2010**, *26*, 709–715. (e) Su, W.; Luo, Y. H.; Yan, Q.; Wu, S.; Han, K.; Zhang, Q. J.; Gong, Y. Q.; Li, Y. M. *Macromol. Rapid Commun.* **2007**, *28*, 1251–1256. (f) Barrio, J. D.; Oriol, L.; Sánchez, C.; Serrano, J. L.; Cicco, A. D.; Keller, P.; Li, M.-H. *J. Am. Chem. Soc.* **2010**, *132*, 3762–3769. (g) Feng, Z.; Lin, L.; Yan, Z.; Yu, Y. *Macromol. Rapid Commun.* **2010**, *31*, 640–644. (h) Jiang, X.; Lavender, C. A.; Woodcock, J. W.; Zhao, B. *Macromolecules* **2008**, *41*, 2632–2643. (i) Jochum, F. D.; Theato, P. *Chem. Commun.* **2010**, *46*, 6717–6719.

(4) (a) Kang, M.; Moon, B. *Macromolecules* **2009**, *42*, 455–458. (b) Schumers, J. M.; Gohy, J. F.; Fustin, C. A. *Polym. Chem.* **2010**, *1*, 161–163. (c) Katz, J. S.; Zhong, S.; Ricart, B. G.; Pochan, D.; J.; Hammer, D. A.; Burdick, J. A. *J. Am. Chem. Soc.* **2010**, *132*, 3654–3655.

(5) Fomina, N.; McFearin, C.; Sermsakdi, M.; Edigin, O.; Almutairi, A. *J. Am. Chem. Soc.* **2010**, *132*, 9540–9542.

(6) (a) Sagi, A.; Weinstain, R.; Karton, N.; Shabat, D. *J. Am. Chem. Soc.* **2008**, *130*, 5434–5435. (b) DeWit, M. A.; Gillies, E. R. *J. Am. Chem. Soc.* **2009**, *131*, 18327–18334. (c) Esser-Kahn, A. P.; Sottos, N. R.; White, S. R.; Moore, J. S. *J. Am. Chem. Soc.* **2010**, *132*, 10266–10268.

440 *Macromolecules* **2011**, *44*, 440–443
DOI: 10.1021/ma102322w

Macromolecules
COMMUNICATION TO THE EDITOR

Lower Critical Ordering Transition of Poly(ethylene oxide)-*block*-poly(2-vinylpyridine)

Chao-Lin Yeh,[†] Ting Hou,[†] Hsin-Lung Chen,*[,†] Lin-Ya Yeh,[‡] Fang-Chyou Chiu,[‡] Alejandro J. Müller,[§] and N. Hadjichristidis[⊥]

[†]*Department of Chemical Engineering, National Tsing Hua University, Hsin-Chu 30013, Taiwan,* [‡]*Department of Chemical and Materials Engineering, Chang Gung University, Kwei-Shan Tao-Yuan 33302, Taiwan,* [§]*Grupo de Polímeros USB, Departamento de Ciencia de los Materiales, Universidad Simón Bolívar, Apartado 89000, Caracas 1080-A, Venezuela, and* [⊥]*Department of Chemistry, University of Athens, 15771 Panepistimiopolis Zografou, Athens, Greece*

Received October 10, 2010
Revised Manuscript Received December 8, 2010

Microphase separation of block copolymers can yield a series of long-range ordered nanostructures governed by the degree of stretching of the block chains and the interfacial energy.[1,2] These factors are parametrized into the segregation strength (χN) and the volume fraction of constituent blocks for constructing the universal phase diagram[3] that predicts an order-to-disorder transition (ODT) with increasing temperature due to the reduction of the Flory−Huggins interaction parameter χ. Such an "upper critical ordering transition" (UCOT) has been predominately observed among a wide variety of block copolymer systems.

It is known that many blends of hompolymers exhibit an opposite "lower critical solution temperature" (LCST) phase diagram, where phase separation of an initially miscible mixture occurs upon heating. This behavior has been understood by the equation-of-state theories that consider the difference in thermal expansion coefficients of the constituents.[4−6] Such an effect leads to increasing difference in the pure component volumes with increasing temperature and hence a positive volume change on demixing.[7] A phase separation process then becomes entropically favorable at elevated temperature because the volume expansion increases the available configurations. The LCST type of phase behavior may also be operative in block copolymers (which is called "lower critical ordering transition" (LCOT) in this case); however, due to the significantly larger interfacial energy and the entropic loss from the stretching of block chains on microphase separation, the "disorder-to-order transition (DOT) temperature" (T_{DOT}) on heating of a block copolymer can be much higher than the phase separation temperature of the corresponding homopolymer blend.[8] As a result, LCOT is rarely observed among block copolymers.

The first block copolymer exhibiting LCOT behavior was reported by Russell et al.[9] It was found that a symmetric polystyrene-*block*-poly(*n*-butyl methacrylate) (PS-*b*-P*n*BMA) with a lower molecular weight (M_w = 68 000) exhibited solely LCOT, while the other sample with a higher molecular weight (M_w = 99 000) underwent a conventional ODT followed by a DOT on heating. Later, Ryu et al. also found similar LCOT behavior for polystyrene-*block*-poly(*n*-pentyl methacrylate) (PS-*b*-P*n*PMA).[10−12] However, this copolymer underwent an additional ODT following the DOT on heating, meaning that it displayed a closed-loop phase diagram.

Apart from the diblocks based on PS-*block*-poly(alkyl methacrylate)s, to our knowledge, no other system has been shown to display LCOT behavior because the T_{DOT} may easily exceed the thermal degradation temperature. In a previous study by Hashimoto et al., a PS-*block*-poly(vinyl methyl ether) was found to display a disordered state; however, the associated small-angle neutron scattering (SANS) intensity enhanced with increasing temperature, signaling an increased amplitude of concentration fluctuations.[13] It was thus suggested that this system should tend to microphase separate at higher temperature, although a true ordered state was not accessed.

In this study, we disclose a new diblock copolymer exhibiting the unconventional LCOT behavior. The system is composed of a poly(ethylene oxide) (PEO) and a poly(2-vinylpyridine) (P2VP) block. Here we probe the phase transition process of a symmetric and an asymmetric PEO-*b*-P2VP by temperature-dependent SAXS and compare their T_{DOT}s. This copolymer system is special considering that P2VP is susceptible to various functionalizations; in this case, the physical or chemical modification of P2VP block could fine-tune the interaction energy in the diblock and would thus allow for systematic investigation of the corresponding perturbation of the phase diagram. For instance, P2VP block may be selectively complexed with many metal ions and amphiphilic surfactants such as dodecylbenzenesulfonic acid.[14,15] The segregation strength between PEO and P2VP block may then be controlled by the degree of binding of metal ions or surfactants to P2VP. Moreover, the complexation with surfactant would introduce an additional self-organization mechanism associated with the microphase separation between the polar moiety of the headgroup-bound P2VP and the nonpolar tail of the surfactant.[16] The action of such a driving force is expected to result in richer self-assembled structures and more complex phase transition behavior of the system.

The PEO-*b*-P2VP samples studied here were synthesized by sequential anionic polymerization of 2-vinylpyridine and ethylene oxide.[17,18] The number-average molecular weights (M_n) of both blocks in the symmetric diblock were ca. 40 000, which prescribed the volume fraction of PEO (f_{PEO}) as 0.49. The M_n of PEO and P2VP blocks in the asymmetric diblock were 20 000 and 100 000, respectively, and the corresponding f_{PEO} was 0.16.

The thermally induced phase transition of PEO-*b*-P2VP was detected by the temperature-dependent SAXS measurement performed at station BL23A at the National Synchrotron Radiation Research Center (NSRRC) located at Hsin-Chu, Taiwan. The energy of X-ray source and sample-to-detector distance were 8 keV and 2259 mm, respectively. The scattering signals were collected by MarCCD detector of 512 × 512 pixel resolution. The scattering intensity profile was output as the plot of the scattering intensity (I) vs the scattering vector, $q = (4\pi/\lambda)\sin(\theta/2)$ (θ = scattering angle), after corrections for background, sample transmission, empty cell transmission, empty cell scattering, and the detector sensitivity. For the temperature-dependent study, the

*To whom correspondence should be addressed. E-mail: hlchen@che.nthu.edu.tw.

 Published on Web 01/12/2011 © 2011 American Chemical Society

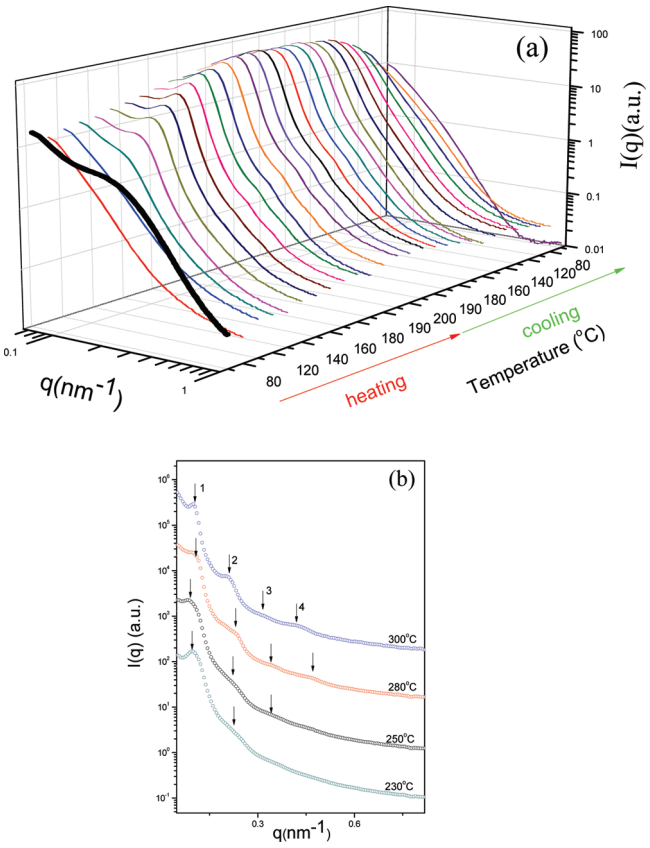


Figure 1. (a) Temperature-dependent SAXS profiles of the symmetric PEO-*b*-P2VP (f_{PEO} = 0.49) collected in a heating and subsequent cooling cycle. (b) SAXS profiles at temperatures from 230 to 300 °C obtained in the heating cycle to show the enhancement of structure order with increasing temperature.

sample was equilibrated at each prescribed temperature for 2 min followed by data collection for ca. 20 s.

Figure 1a shows the temperature-dependent SAXS profiles of the symmetric PEO-*b*-P2VP collected in a heating and subsequent cooling cycle. The copolymer displayed a broad peak at 0.23 nm^{-1} at the onset of heating (i.e., 30 °C). This peak was associated with the crystalline morphology formed by the crystallization of PEO blocks, as it vanished when the system was heated to 80 °C (> melting point of PEO). The fact that the SAXS profile was characterized by a monotonically decayed curve at 80 °C indicates that the copolymer was in the disordered melt state.

With further heating, a scattering peak at 0.14 nm^{-1} emerged at about 120 °C. The intensity of this peak grew with increasing temperature, and a second-order peak was discernible above 160 °C, signaling the formation of a microphase-separated lamellar morphology. The temperature dependence of SAXS profiles clearly showed the occurrence of a DOT process in the heating cycle. The formation of lamellar structure upon microphase separation was reasonable considering the symmetric copolymer composition.

The thermal reversibility of the phase transition was verified by the subsequent cooling experiment, with the corresponding SAXS profiles also being displayed in Figure 1a. It can be seen that the peak intensity reduced progressively with decreasing temperature, and the scattering peak became essentially unobservable below 120 °C. In addition to the change of intensity, the position of the peak was found to shift to lower q with increasing temperature (and vice versa), signaling a larger interdomain distance at higher temperature. This was consistent with the stronger "effective

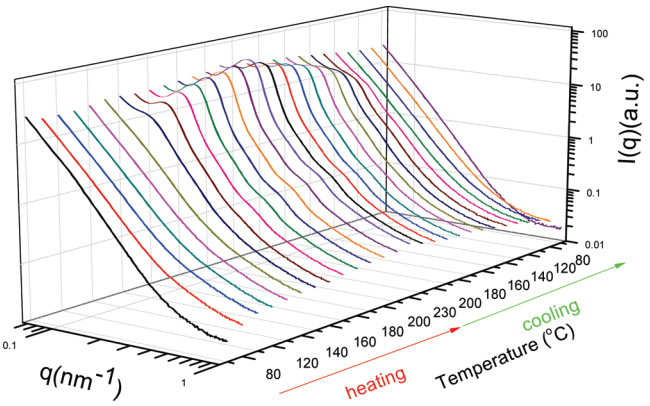


Figure 2. Temperature-dependent SAXS profiles of the asymmetric PEO-*b*-P2VP (f_{PEO} = 0.16) collected in a heating and subsequent cooling cycle.

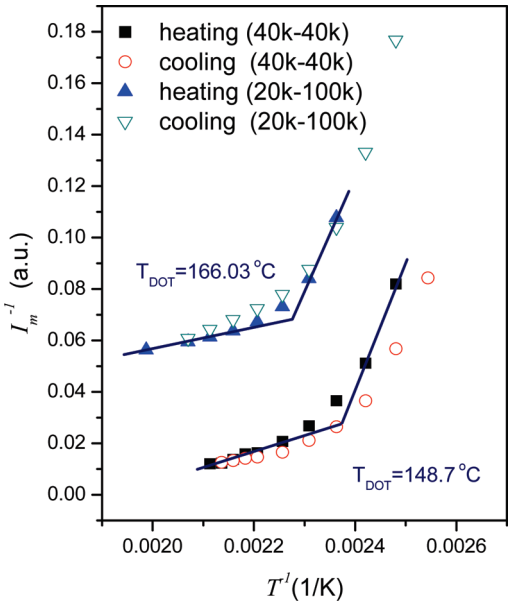


Figure 3. I_m^{-1} vs T^{-1} plots of the symmetric and asymmetric PEO-*b*-P2VP for determinations of T_{DOT}.

repulsion" between the two blocks at higher temperature that caused a greater stretching of the block chains to reduce the contacts or mixing of PEO and P2VP monomer units at the microdomain interface. Moreover, the SAXS profiles in Figure 1b, showing clearer higher-order lamellar peaks at higher temperature, demonstrate that the ordering of the nanostructure was enhanced by increasing temperature in spite of the intensification of thermal fluctuations. These results are in clear contrast to the system exhibiting the conventional UCOT behavior.

Figure 2 displays the temperature-dependent SAXS profiles of the asymmetric PEO-*b*-P2VP. It was obvious that this diblock also exhibited LCOT phase behavior, as a scattering peak emerged at ca. 150 °C and its intensity grew with increasing temperature. The higher-order or form factor peaks became discernible at 190 °C; however, the number of peaks was not enough to unambiguously assign the morphology formed by microphase separation.

Figure 3 plots the inverse of primary peak intensity (I_m^{-1}) against the inverse of absolute temperature (T^{-1}) for determination of T_{DOT}. The plots showed opposite trend to that associated with the UCOT behavior. The T_{DOT}s determined

from the intersection of the two straight lines at the higher and lower temperature side were 148.7 and 166.0 °C for the symmetric and asymmetric PEO-*b*-P2VP, respectively. The higher T_{DOT} of the asymmetric diblock is consistent with the prediction by the LCOT phase diagram.

The LCOT behavior of PEO-*b*-P2VP was verified by calculating the phase diagram of PEO/P2VP mixture using a theoretical model developed by Ruzette et al.[4,5] This simple free energy model took compressibility into account for weakly interacting polymer blends. In this case, the free energy of mixing per unit volume, Δg_{mix}, at atmospheric pressure is given by

$$\Delta g_{mix} = kT\left[\frac{\phi_A\tilde{\rho}_A}{N_A v_A}\ln\phi_A + \frac{\phi_B\tilde{\rho}_B}{N_B v_B}\ln\phi_B\right] + \phi_A\phi_B\tilde{\rho}_A\tilde{\rho}_B(\delta_{A,0}-\delta_{B,0})^2 + \phi_A\phi_B(\tilde{\rho}_A-\tilde{\rho}_B)(\delta_A{}^2-\delta_B{}^2) \quad (1)$$

where $\tilde{\rho}_i$ is the reduced density or, equivalently, one minus the "fractional free volume" in the compressible fluid, $\delta_i{}^2$ is the temperature- and pressure-dependent cohesive energy density, and $\delta_{i,0}{}^2$ is the hard-core cohesive energy density evaluated at 0 K and zero pressure. The reduced density $\tilde{\rho}_i$ is given by $\tilde{\rho}_i = \rho_i/\rho_i{}^*$, with ρ_i and $\rho_i{}^*$ being the temperature- and pressure-dependent mass density and the hard core density, respectively. Equation 1 contains three contributions, namely, the combinatorial entropy of mixing, the exchange interaction energy considered in the classical regular solution model, and the free energy change from compressibility. The third contribution is expressed as a function of pure component properties, which are obtainable from experimental $P-V-T$ data[19] or group contribution calculations.[20] Thus, this model allows one to predict the thermodynamic phase diagram of a given polymer mixture based on pure component properties of mass density, cohesive energy density (or solubility parameter), and thermal expansion coefficient. It is however not able to predict the phase diagram of block copolymers quantitatively because additional effects including the excess free energy from block chain stretching and interfacial free energy are not considered.

Table 1 lists the properties of PEO and P2VP homopolymers used to compute the phase diagrams of their blend. The values of $\delta_i(298)$ were calculated using group contribution methods[15] and were then extrapolated to absolute zero temperature to obtain the hard core cohesive energy density via the following manner:

$$\delta_{i,0}{}^2 \equiv \delta_i{}^2(0) = \delta_i{}^2(298)\frac{\tilde{\rho}_i(0)}{\tilde{\rho}_i(298)} = \frac{\delta_i{}^2(298)}{\tilde{\rho}_i(298)} \quad (2)$$

The phase diagram was then constructed by connecting the spinodal envelope obtained by[4]

$$g_{\phi\phi} = \left.\frac{\partial^2\Delta g_{mix}}{\partial\phi_A{}^2}\right|_{T,P} \approx \left.\frac{\partial^2\Delta g_{mix}}{\partial\phi_A{}^2}\right|_{T,P,\tilde{\rho}} = kT\left[\frac{\tilde{\rho}_A}{\phi_A N_A v_A}+\frac{\tilde{\rho}_B}{\phi_B N_B v_B}\right] + 2\tilde{\rho}_A\tilde{\rho}_B(\delta_{A,0}-\delta_{B,0})^2 - 2(\tilde{\rho}_A-\tilde{\rho}_B)(\delta_A{}^2-\delta_B{}^2) = 0 \quad (3)$$

The solid curves in Figure 4 represent the calculated phase diagrams of PEO/P2VP blends with the molecular weights

Table 1. Properties of PEO and P2VP Used To Calculate the Phase Diagrams of Their Blends

polymer	$\rho_1{}^*$ (g/cm^3)	α (10^{-4} K^{-1})	$\delta_i(298)$ (J$^{1/2}$/cm$^{3/2}$)	$\delta_{i,0}$ (J$^{1/2}$/cm$^{3/2}$)
PEO[a]	1.38	7.09	21.30	23.67
P2VP[b]	1.334	4.97	21.36	23

[a] Obtained from ref 4. [b] Determined from the group contribution calculations.[20]

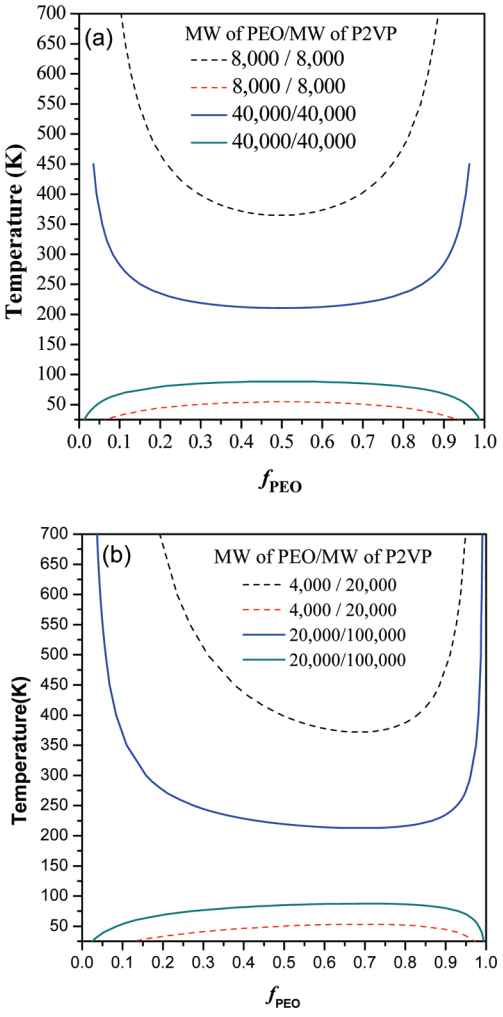


Figure 4. Calculated phase diagrams of the PEO/P2VP blends with (a) symmetric molecular weights and (b) asymmetric molecular weights of the constituents.

being identical to those of the corresponding block chains in the copolymers. It can be seen that both UCST and LCST envelops were predicted by the theory. As expected, the calculated spinodal temperatures at the compositions of $f_{PEO} = 0.49$ and 0.16 were significantly lower than the observed T_{DOT}s. According to the theoretical analysis of Yeung et al.,[8] the T_{DOT} of a diblock exhibiting LCOT behavior is approximately equivalent to the phase separation temperature of the corresponding blend with ca. 1/5 molecular weight for the homopolymer constituents. Therefore, we have also calculated the phase diagrams of PEO/P2VP blend with molecular weights of 8000/8000 and 4000/20 000, as shown by the dashed curves in Figure 4. The calculated phase separation temperatures were ca. 93 and 99 °C at $f_{PEO} = 0.49$ and 0.16, respectively, which were much closer to the observed T_{DOT}s of the corresponding diblocks. It is noted that in all cases the critical temperatures of the UCST envelops were found to

situate far below the T_g of the miscible mixture. As a result, the UCOT behavior was never identified in the diblocks under study. Below the melting point of PEO, the crystallization of PEO blocks from the disordered melt may dominate the morphological formation, and the resultant crystalline lamellar morphology gave rise to the broad scattering peak for the symmetric diblock (Figure 1a). However, crystallization of PEO in the asymmetric PEO-*b*-P2VP appeared to be completely hindered, presumably because the T_g of the miscible mixture of PEO and P2VP ($\cong$65 °C as estimated from the Fox equation[21]) was higher than the PEO melting point.

In summary, the LCOT behavior, which is uncommon among block copolymers, has been revealed for PEO-*b*-P2VP. The symmetric and asymmetric diblocks studied here displayed the disorder-to-order transition temperature at ca. 149 and 166 °C, respectively, on heating, as determined from I_m^{-1} vs T^{-1} plots. In contrast to the system showing the conventional UCOT behavior, the interdomain distance of PEO-*b*-P2VP was found to increase with increasing temperature due to the greater stretching of the block chains to reduce the contacts or mixing of the PEO and P2VP monomer units in the microdomain interface. The LCOT behavior was qualitatively consistent with the theoretical calculation of the phase diagram of PEO/P2VP blends using a thermodynamic theory considering the disparity in solubility parameter and thermal expansion coefficient. The calculated phase diagram also predicted a UCST envelop; however, the corresponding critical temperature situated well below the T_g of the miscible mixture, making the UCOT behavior unobservable for the diblocks studied.

Acknowledgment. We acknowledge the financial support of the National Science Council of the Republic of China under Grant No. NSC 97-2221-E-007-034.

References and Notes

(1) Hamley, I. W. *The Physics of Block Copolymers*; Oxford University Press: New York, 1998.
(2) Ruzzete, A. V.; Leibler, L. *Nature Mater*. **2005**, *4*, 19.
(3) Matsen, M. W.; Bates, F. S. *Macromolecules* **1996**, *29*, 1091.
(4) Ruzette, A.-V. G.; Mayes, A. M. *Macromolecules* **2001**, *34*, 1894.
(5) Ruzette, A.-V. G.; Mayes, A. M.; Russell, T. P. *J. Chem. Phys.* **2001**, *114*, 8205.
(6) Cowie, J. M. G.; Arrighi, V. *Polymers: Chemistry and Physics of Modern Materials*, 3rd ed.; CRC Press: New York, 2008.
(7) Pollard, M.; Russell, T. P.; Ruzette, A.-V. G.; Mayes, A. M.; Gallot, Y. *Macromolecules* **1998**, *31*, 6493.
(8) Yeung, C.; Desai, R. C.; Shi, A.-C.; Noolandi, J. *Phys. Rev. Lett.* **1994**, *72*, 1834.
(9) Russell, T. P.; Karis, T. E.; Gallot, Y.; Mayes, A. M. *Nature* **1994**, *368*, 729.
(10) Ryu, D. Y.; Jeong, U.; Kim, J. K.; Russell, T. P. *Nature Mater*. **2002**, *1*, 114.
(11) Ryu, D. Y.; Park, M. S.; Chae, S. H.; Jang, J.; Kim, J. K.; Russell, T. P. *Macromolecules* **2002**, *35*, 8676.
(12) Ryu, D. Y.; Jeong, U.; Lee., D. H.; Kim, J.; Youn, H. S.; Kim, J. K. *Macromolecules* **2003**, *36*, 2894.
(13) Hashimoto, T.; Hasegawa, H.; Hashimoto, T.; Katayama, H.; Kamigaito, M.; Sawamoto, M.; Imai, M. *Macromolecules* **1997**, *30*, 6819.
(14) Nandan, B.; Lee, C.-H.; Chen, H.-L.; Chen, W.-C. *Macromolecules* **2005**, *38*, 10117.
(15) Nandan, B.; Lee, C.-H.; Chen, H.-L.; Chen, W.-C. *Macromolecules* **2006**, *39*, 4460.
(16) Ruokolainen, J.; Mäkinen, R.; Torkkeli, M.; Mäkelä, T.; Serimaa, R.; ten Brinke, G.; Ikkala, O. *Science* **1998**, *280*, 557.
(17) Fragouli, P.; Iatrou, H.; Hadjichristidis, N. *Polymer* **2002**, *43*, 7141.
(18) Córdoba, M.; Lorenzo, A. T.; Müller, A. J.; Fragouli, P.; Iatrou, H.; Hadjichristidis, N. *Macromol. Symp*. **2010**, *282*, 101.
(19) Rodgers, P. A. *J. Appl. Polym. Sci.* **1993**, *48*, 1061.
(20) van Krevelen, D. W.; Hoftyzer, P. J. *Properties of Polymers. Correlation with Chemical Structure*; Elsevier: New York, 1972.
(21) Fox, T. G. *Bull. Am. Phys. Soc*. **1956**, *1*, 123.

444 *Macromolecules* **2011**, *44*, 444–452
DOI: 10.1021/ma102371d

Macromolecules
ARTICLE

General Avenue to Individually Dispersed Graphene Oxide-Based Two-Dimensional Molecular Brushes by Free Radical Polymerization

Lanyan Kan, Zhen Xu, and Chao Gao*

MOE Key Laboratory of Macromolecular Synthesis and Functionalization, Department of Polymer Science and Engineering, Zhejiang University, 38 Zheda Road, Hangzhou 310027, P. R. China

Received August 25, 2010; Revised Manuscript Received December 19, 2010

ABSTRACT: We present a general strategy for facile synthesis of 2D macromolecular brushes. The ultraflat one-atomic layer of graphene oxide with micrometer-scale sheet topology was employed as the macromolecular backbone; more than 10 types of polymer chains were covalently tethered to the nanosheets through free radical polymerization, producing various 2D molecular brushes with multifunctional arms covering from polar to apolar, water-soluble to oil-soluble, acidic to basic, and functional to common polymers. The resulting molecular brushes are well soluble in desired solvents in the forms of individually dispersed hairy nanosheets. The growing process of 2D molecular brushes was clearly visualized by AFM. The giant 2D brushes with arm density up to 1.59×10^4 arms per μm^2 of single side of graphene show high solubility (~15 mg/mL), low intrinsic viscosity (~100 mL/g), and fine electrical conductivity ($\sim 8.4 \times 10^{-3}$ S/cm), and they can possess numerous epoxy and other functional groups at their arms if necessary, promising a luciferous foreground in both scientific research and industrial applications. The polymer-grafted graphene oxide can be well dispersed in free polymer matrix and can be well soluble in solvents again, suggesting that nanocomposite of polymer-grafted graphene oxide and polymer can be readily produced by the solution-processing technique.

Introduction

Attaching high-density polymeric chains/arms with one end to a macromolecular backbone or a solid substrate affords a molecular polymer brush or a surface polymer brush. Interest in molecular brushes began more than 30 years ago for their unique structure and biomimetic applications such as water-based lubrication.[1−5] One-dimensional (1D) cylindrical molecular brushes have been widely addressed,[6,7] and cyclic brushes were also successfully synthesized in 2008 by Deffieux and co-workers.[8] Recently, surface brushes have been also prominently advanced with the utilization of controlled radical polymerization (CRP) techniques.[9−12] In this respect, 2D surface brushes are of particular interest because of their unusual stimuli-responsive properties and potential applications to stabilize colloids, reduce friction between surfaces, and provide lubrication in artificial joints.[13−16] However, the conventional 2D surface brushes are generally insoluble in solvents, posing a big barrier for their solution-based processing, and it is almost impossible to directly grow polymer brushes on a target surface in the practical applications. Hence, to construct 2D molecular brushes, annexing the features of good solubility of linear molecular brushes and flat-topology of 2D surface brushes becomes a dream for both scientists and engineers.

The synthesis of 2D molecular brushes seems to be a big challenge for chemists owing to the absence of both efficient methodology and active 2D molecular backbone even though the theoretical calculations of 2D molecular brushes had been reported.[17] Currently, the emergence of graphene[18−20] or graphene oxide[21−23] (GO) sheds a light on the accomplishment of such an object for its sheetlike structure. Although several groups had tried to graft polymer chains from/onto graphene/GO sheets via "grafting from", "grafting to", or *in situ* polycondensation approach,[24−29] no one approached the target of 2D molecular bushes intentionally. Three reasons are likely responsible for this situation. First, all of the reports focused their attention on the functionalization of graphene or GO for improving their solubility, whereas neglected that graphene or GO themselves are perfect candidates of 2D *macromolecular* backbone for 2D molecular brushes. As a consequence, polymer-grafted graphene or polymer-grafted GO hybrids are commonly applied as fillers to improve the mechanical properties of polymer composites due to their good compatibility and enhanced interfacial interactions, and they are never regarded as *macromolecules*, not to mention their molecular intrinsic characters such as viscosity. Second, the oxygen-contained functional groups of GO are mainly employed as grafting sites, usually leading to uneven and unstable grafting as well as strong aggregation because such groups are mostly located at the sheet edges and are easily decomposed during reaction.[30,31] Hence, individually dispersed sheet brushes demonstrated by distinct observations of AFM are rarely achieved. Notably, the aggregated compounds cannot be regarded as *molecular* brushes anymore but *nonmolecular* matter or the conventional surface/solid brushes from a strict point of view. Third, no general and facile methodology is presented. Although CRP techniques such as atom transfer radical polymerization (ATRP) had been used to graft specific polymer chains on graphene or GO surfaces, no one developed a general approach that is compatible to construct 2D molecular brushes with the three common classes of vinyl monomers of (meth)acrylates, styrenes, and acrylamides. Besides, it needs extra steps to introduce initiating groups on graphene or GO sheets before polymer grafting for CRP, so the procedure is relatively complex. More seriously, the multistep reactions raise the risk of their aggregation, which is adverse for the target of individually dispersible

*To whom correspondence should be addressed. E-mail: chaogao@zju.edu.cn.

 Published on Web 12/31/2010 © 2010 American Chemical Society

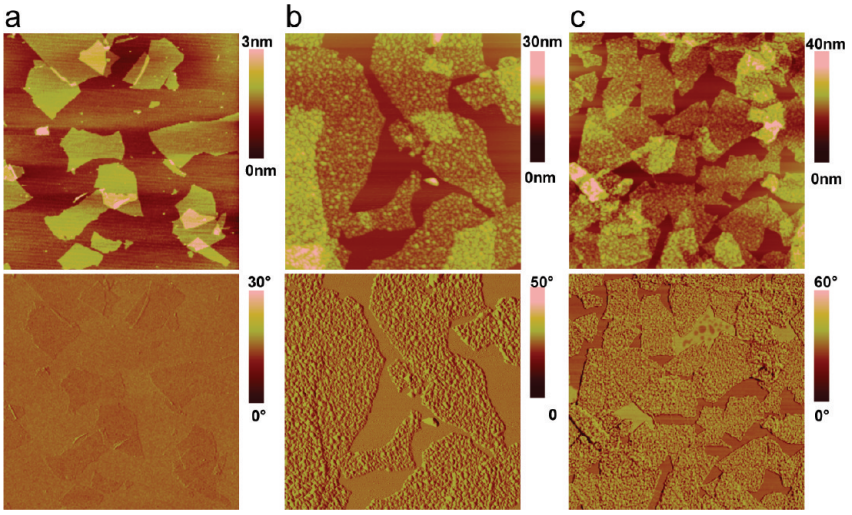


Figure 1. (a) Height (above) and phase (below) images of GO with size of 5 μm × 5 μm. (b, c) Height (above) and phase (below) images of the resultant GO-*g*-PGMA two-dimensional macromolecular brushes with molar feed ratios of monomer to initiator 50:1 (b) and 200:1 (c), with reaction time of 7.5 and 48 h and the sizes of 2.5 μm × 2.5 μm and 5 μm × 5 μm, respectively.

2D molecular brushes. Accordingly, effective synthesis of molecular-level soluble 2D brushes is still to be resolved.

Here, we present a general, facile approach to 2D molecular brushes by conventional free radical polymerization (FRP) using graphene and GO nanosheets as flat *macromolecular* backbones. The widely used FRP can not only be simply operated but also be workable for almost all of vinyl monomers. The growing process of 2D molecular brushes were clearly visualized by AFM, showing that GO sheets maintain isolated with each other after polymer grafting. The resultant 2D molecular brushes show unique attributes such as low intrinsic viscosity, high solubility, good solution processability, and fine electrical conductivity, foretelling extensive applications and opening the new mine of 2D molecular brushes.

Experimental Section

Materials. Glycidyl methacrylate (GMA, Aldrich) and other vinyl monomers (Aldrich except the specially stated) were further purified by basic alumina column chromatography to remove the inhibitor. Sodium *p*-styrenesulfonate (PSSNa, Aladdin 90%) was used as received. 2,2′-Azobis-(2-methylpropionitrile) (AIBN) and potassium persulfate ($K_2S_2O_8$) were employed after twice recrystallization. Graphite powder (40 μm) was purchased from Qingdao Henglide Graphite Co. Ltd.

Instrumentation. AFM characterization was carried out on Nanoscope IIIa (Figures 1 and 2, Figures S1−S7, S11−S17, and S19) and NSK SPI3800 (Figure S9) under tapping mode. The samples were prepared by spin-coating onto freshly peeled mica wafer at 800 rpm from sample solutions. Thermal gravimetric analysis (TGA) was carried out using a Perkin-Elmer Pyris 6 TGA instrument with a heating rate of 20 °C/min under a nitrogen flow (30 mL/min). ^{1}H NMR spectra were obtained through the equipment of NMK/300 MHz. Fourier-transform infrared (FTIR) measurements were performed on a Bruker Vector 22 spectrometer (KBr disk). Scanning electron microscopy (SEM) images were carried on a Hitachi S4800 field-emission SEM system. Transmission electron microscopy (TEM) images were obtained through a XDT-10 electron microscope operating at 120 kV accelerating voltage. The X-ray diffraction (XRD) measurements were taken on a Philips X'Pert PRO diffractometer equipped with Cu Kα radiation (40 kV, 40 mA).

Synthesis of Two-Dimensional Macromolecular Brushes. Well-dispersed graphene oxide (GO) is synthesized from natural graphite powder using a modified Hummers method.[29,32,33] A typical polymerization procedure is given as follows: 50 mg of GO dispersed in 40 mL of *N*,*N*-dimethylformamide (DMF) was added to 100 mL Schlenk and sonicated in a 40 kHz sonic bath for 1 h followed by introducing 50 mmol of GMA monomer. Under N_2 flow protection and vigorous stirring, 0.25 mmol of AIBN was added. The Schlenk was then immersed in a 65 °C oil bath. After reacting for certain time (normally 48 h), the resultant solution was precipitated in methanol. The precipitates were collected and redissolved in 200 mL of DMF. The solution was transferred into centrifuge tubes (6 × 50 mL) and then centrifugated at the speed of 15 000 rpm (23 300*g*) for 0.5−1 h to collect the bottom black solids. This centrifugation was repeated (at least four times) until the upper layer was colorless. Then 200 mL of acetone instead of DMF was used to disperse the precipitates, and a similar centrifugation process was used and repeated (at least three times) to collect the resulting solid product. The product was dried in a vacuum oven at 35 °C for 12 h.

Results and Discussion

Strategy Design and Synthesis Exploring. To achieve 2D molecular brushes, the most important two key factors are the macromolecular backbone and the construction method. The backbone should possess sheet topology and multiple reactive sites. In this paper, we choose the macromolecules of graphene oxide (GO) or chemically reduced graphene as backbones. The micrometer-scale dimension of graphene nanosheets would make direct visualization of the resulting sheet brushes readily accessible, providing a direct approach to evaluate the effect of polymer grafting. As to the synthesis method, we select the common FRP to construct the 2D molecular brushes due to its simplicity and generality.

Previously, FRP had been successfully used to covalently graft polymer chains on carbon nanotubes (CNTs) by macromolecular radical addition to the reactive carbon−carbon double bonds,[34−38] casting a positive light for the polymer grafting on graphene oxide or graphene surface. Our synthesis strategy is illustrated in Scheme 1. Both of highly soluble graphene oxide (GO) and less soluble graphene were tested as backbones in our experiments. To avoid the possible aggregation of the backbones, polymer chains are directly attached to the sp^2-hybridized or double bonds of GO, rather than their functional groups that were commonly used in the

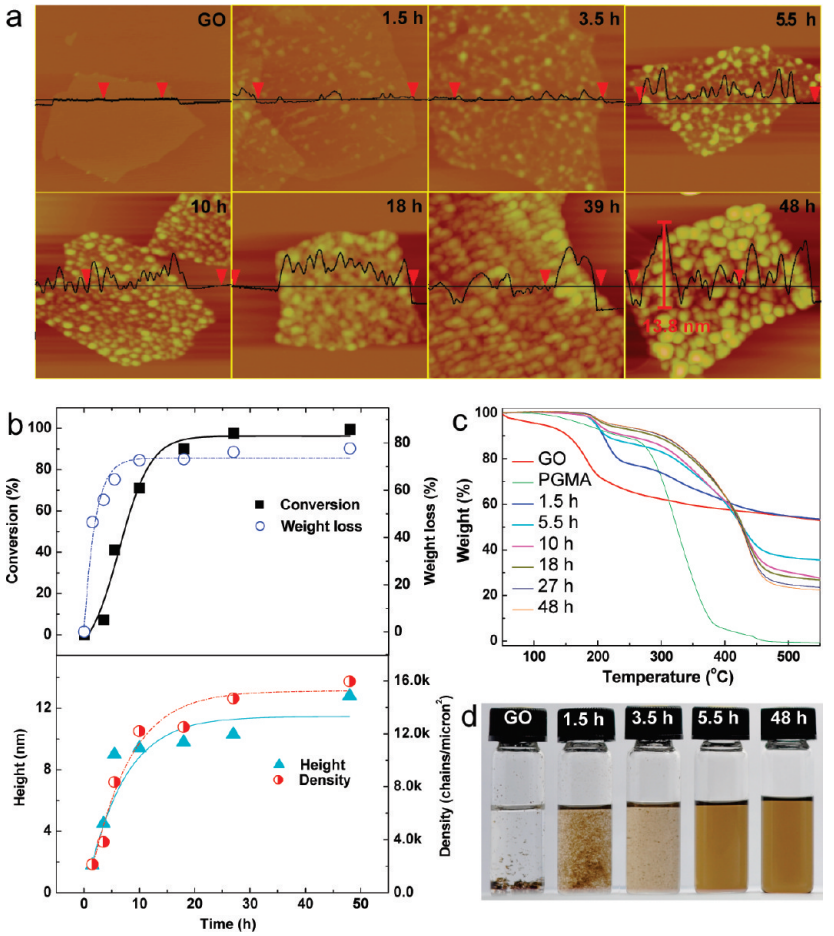


Figure 2. (a) AFM height images of GO and GO-*g*-PGMA 2D brushes at different reaction time (size for all images: 1 μm × 1 μm). (b) Conversion of monomer, TGA weight loss of brushes, the average height of polymeric arms on the 2D brushes, and the average density of polymeric arms as a function of reaction time. (c) TGA curves of GO, PGMA, and GO-*g*-PGMA brushes. (d) Photographs of GO and GO-*g*-PGMA brushes at different reaction time added into chloroform.

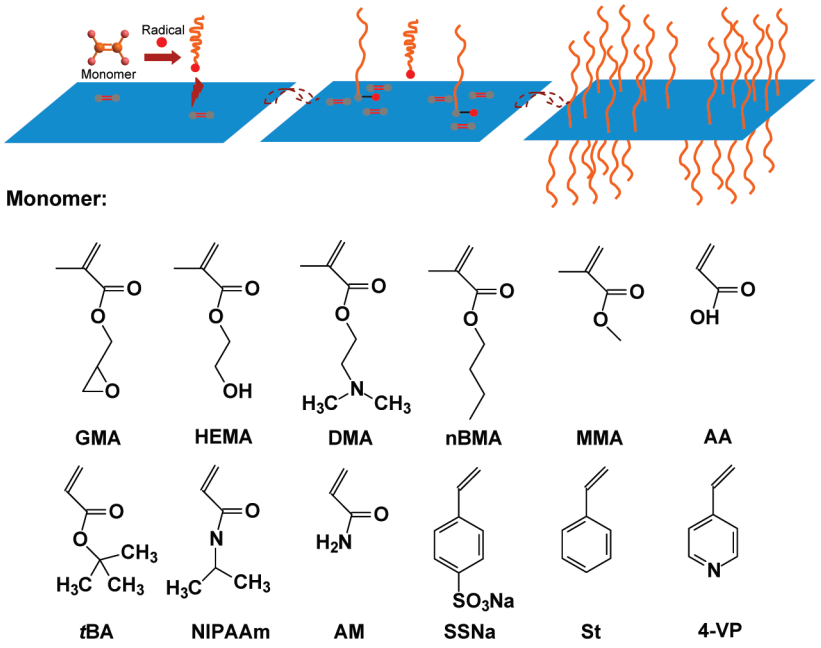
chemical modification.[31] After initiating of vinyl monomers by FRP, macromolecular radicals are formed immediately by chain propagation.[39] Part of the macromolecular radicals are added to double bonds of GO, producing graphene oxide-based brushes and simultaneously generating new radicals at its surface, which are then liable to further radical propagation, termination, or transfer. Notably, even though it is recognized that polymer chains can be directly grafted onto the graphitic surface by using such radical addition/coupling reaction between polymer radicals and the double bonds of surfaces, to provide the direct evidence for the detailed reaction mechanism is still an open question.

The macroradical coupling converts the sp^2 bonds into sp^3, which weakens the conjugacy of localized π-electron cloud and thus activates more sp^2 bonds nearby. It should be pointed out that many kinds of side reactions may happen during polymerization. For instance, V-shaped grafted polymers (when further chain propagation occurs on the same side of GO layer) and cyclic chains (when newly generated polymer radicals are subjected to coupling termination) would be formed. Resultantly, 2D molecular brushes with islands of arms would form.

To obtain molecular brushes with multifunctional reactive arms, we select GMA as the typical monomer to investigate the details. Figure 1 shows the AFM images of GO and poly(glycidyl methacrylate)-grafted GO (GO-*g*-PGMA). The original GO sheets spin-coated on a mica substrate are ultraflat indeed, with a thickness of 0.6−0.8 nm, indicating their single-layer atom structures.[40] For the two samples of GO-*g*-PGMA obtained at different polymerization conditions, various protuberances are observed on the sheet backbones with the average heights ($\bar{h}$) of 4.9 nm (Figure 1b) and 10.3 nm (Figure 1c), preliminarily demonstrating the success of polymer grafting. Significantly, the protuberances, tufts of polymeric hairs, are evenly distributed on the whole sheets, rather than just around their circumferences or edges that were usually figured as the highest reactive sites with the lowest steric hindrance, declaring the formation of 2D molecular brushes with relatively even arms. Lots of single hairy sheets are found in the view, implying the good dispersibility/solubility of the product and the reliability of the synthesis strategy. In addition, the sheet brushes showed the similar micrometer-scale dimension to the GO precursors, revealing the integrity of sheet backbones during the polymerization.

Brush Growth and Polymerization Kinetics. Besides the even grafting, another challenge is the controlled grafting on such a giant sheet, particularly upon the grafting density of arms. No one had ever tried to control the density of grafted polymers on both CNTs and GO yet, likely due to the difficulty of control over arm density through CRP. Herein, we attempt to resolve this problem by FRP kinetics, and thus we monitor the polymerization process by various techniques including AFM, nuclear magnetic resonance (NMR) spectroscopy, TGA, and gel permeation chromatography (GPC) characterizations.

Scheme 1. Synthesis of 2D Macromolecular Brushes by Free Radical Polymerization of Various Monomers with the Backbone of GO Sheets[a]



[a] The blue sheet represents GO, and the red dots and double bonds represent radicals and active grafting points, respectively.

Table 1. Selected Results of GO-*g*-PGMA 2D Macromolecular Brushes at Different Polymerization Time

reaction time (h)	average height (nm)[a]	weight loss (%)[b]	$\overline{d}_1$ (chains/10^4 carbon)[c]	$\overline{d}_2$ (chains/μm^2)[d]
1.5	1.8	46.5	1.1	2140
3.5	4.5	55.9	2.0	3830
5.5	9.0	64.6	4.4	8360
10	9.4	72.7	6.4	12200
18	9.8	73.2	6.6	12510
27	10.3	76.2	7.7	14670
48	12.8	77.7	8.4	15960

[a] Average height of polymer clusters on GO surfaces obtained from corresponding AFM images. [b] Weight loss in TGA curves below 550 °C. [c] Average density of the grafted polymer chains on GO with the unit of chains per 10^4 carbon atoms calculated from eq 2. For the samples above 3.5 h, W_P is the weight loss of brushes listed in the table because of the sharp increasing of grafted PGMA amount as well as partial reduction of GO backbone; for the samples at 1.5 and 3.5 h, W_P is equal to the total weight loss of brushes below 550 °C by subtracting the weight loss of unstable functional groups on GO backbone below 250 °C (i.e., 21.46 and 19.04 wt % for the two samples, respectively). [d] Average density of the grafted polymer chains on a single side of GO with the unit of chains per μm^2 calculated from eq 4.

AFM is found to be the most powerful tool for the visualization of graphene, GO sheets, and 2D molecular brushes. Figure 2a shows the kinetic AFM images of brushes traced at different polymerization time (see also Figures S1−S7). The pristine GO sheet is clean and smooth. After polymerization, bundles of hairy polymers are grafted on the sheet backbone. The cross-sectional view of kinetic AFM images indicates that the height and density of hairy polymers increased with the polymerization time. Obviously, at 1.5 h, sparsely isolated clusters of polymers are observed with the average height ($\overline{h}$) 1.8 nm; at 3.5 h, part of hairy islands are connected with $\overline{h}$ 4.5 nm; at 5.5 h, most of islands are merged into bigger ones with $\overline{h}$ 9.0 nm; at 10 h, the hairy clusters join together with $\overline{h}$ 9.4 nm and only a little of vacancy can be found on the sheet; after 18 h, continual hairy phase appear with the morphology of fused polymer clusters, and the $\overline{h}$ increases from 9.8 nm at 18 h to 11.3 nm at 39 h and 12.8 nm at 48 h (Table 1). From the AFM images, we can find that $\overline{h}$ increases with increasing the average grafting density ($\overline{d}$) of brushes. So the $\overline{d}$ and $\overline{h}$ of 2D molecular brushes can be tuned to some extent through the reaction time, which is favorable to the design, production, and application of the brushes-based devices, materials, and bio-nanoconjugates.

The kinetic samples were also characterized by ^{1}H NMR, GPC, and TGA measurements. ^{1}H NMR spectra (Figure S8) revealed that the polymerization in the presence of GO followed the typical kinetics rule of FRP:[39] the monomer conversion increased slowly at the initial 3.5 h with the conversion below 10%, rapidly within 18 h, and then very slowly after 25 h with the conversion above 90%, as shown in Figure 2b. In addition, the kinetics of GMA polymerization in the absence of GO was also investigated (Figure S9). It can be found that the polymerization of GMA in pure DMF solution was slightly quicker than that in GO dispersion. Nevertheless, the polymerization processes in two situations displayed a parallel trend. A similar phenomenon was also observed for other substrate-based polymerizations including CNT-based "grafting from" cases.[41] This is likely caused by the influence of the substrates on the monomer/initiators movements. The detailed reason is still an open question awaited for further investigations.

GPC results showed that the number-average molecular weight (M_n) of free polymers undulated around 5×10^4 g/mol after 5.5 h (see Table S1 and Figure S10), also being in agreement with the rule of molar mass variation for FRP.

Figure 2c shows the weight loss curves of GO and resulting brushes. There is an obvious weight loss stage (~36 wt %) for GO below 250 °C, which is assigned to the decomposition of oxygen-contained groups of GO.[42] For polymer-grafted GO

samples, two weight loss stages at 200−250 and 250−550 °C are observed. The first stage below 250 °C is resulted from the decompositions of unstable groups of GO as well as small part of grafted PGMA (see the neat PGMA curve for comparison); another stage above 250 °C belongs to the main decomposition of grafted PGMA. For the brushes obtained after 5.5 h of polymerization, the weight loss proportion below 250 °C is quite low, indicating that GO was partially reduced (see also XRD patterns for further evidence, Figure S11) and the labile groups in GO were degraded during the polymerization. Accordingly, all of the weight loss below 550 °C for the brushes after 5.5 h can be ascribed to the pyrolysis of grafted PGMA. We also clearly find that the amount of grafted polymers displays a similar rising tendency to the monomer conversion upon reaction time (Figure 2b). Notably, control experiments demonstrated that the ungrafted polymer can be efficiently removed by repeated washing (Figure S12). So, the measured polymer content by TGA is that of polymeric arms covalently grafted on GO backbone. Incidentally, the decomposition temperatures of grafted arms are increased by 30−55 °C (Figure 2c) and the glass transition temperatures enhanced about 7 °C[43] (Figure S13) as compared to the free polymers, revealing the role of free radical scavenger for GO and the confined chain movement for the anchored polymers.

The solubility of 2D brushes also increases with the reaction time: GO is totally insoluble and dispersible in chloroform, budding brushes at 1.5 h are dispersible as big conglomerates, part of brushes at 3.5 h are soluble accompanying with some small solid clusters, and all of brushes are well soluble after 5.5 h of polymerization (Figure 2d). These results demonstrate that the content and density of grafted polymer arms can be varied in a relatively wide range through polymerization time or monomer conversion.

Quantitatively, the $\bar{d}$ of 2D brushes (chains per 10^4 carbon atoms in GO, $\bar{d}_1$) can be calculated from the equation[44]

$$\bar{d}_1 = \frac{M_C}{M_P}\frac{W_P}{W_C} \times 10^4 \quad (1)$$

where M_C means the relative molar mass of carbon (M_C = 12), M_P the average molecular weight of grafted polymer (in this article, we assume that the grafted polymer has a comparable molecular weight to the free polymer, so $M_P = 5 \times 10^4$ is used for rough estimation of arm density), and W_C and W_P the weight fractions of graphene oxide backbone and grafted polymer, respectively. Since M_C and M_P are constants herein, eq 1 is simplified as

$$\bar{d}_1 = K_1\frac{W_P}{W_C} \quad (2)$$

where $K_1 = 2.4$.

Alternatively, the $\bar{d}$ of 2D brushes (chains per μm^2 GO backbone, $\bar{d}_2$) can be calculated from the equation

$$\bar{d}_2 = \frac{M_C}{M_P}\frac{W_P}{\frac{W_C}{2} \times 2 \times A_b \times 10^{-8}} = \frac{M_C \times 10^8}{M_P \times A_b}\frac{W_P}{W_C} \quad (3)$$

where A_b represents the area of a benzene ring in graphene (5.24 $Å^2$). So eq 3 can also be modified as

$$\bar{d}_2 = K_2\frac{W_P}{W_C} \quad (4)$$

Herein $K_2 = 4.58 \times 10^3$. Notably, the polymer arms are anchored on both sides of GO, so $\bar{d}_2$ means the average arm density on a single side.

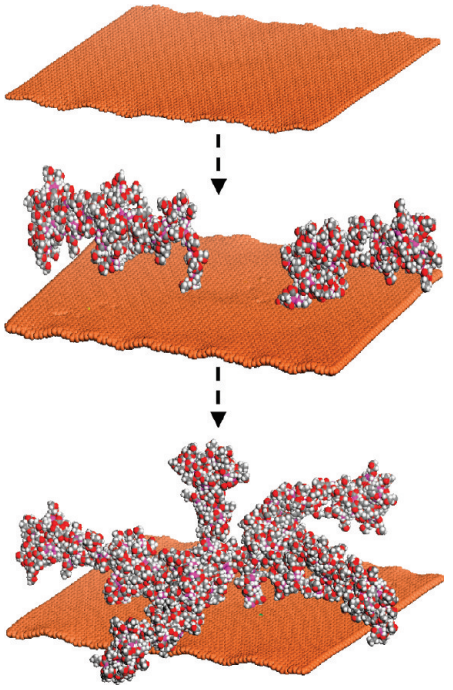


Figure 3. Cartoon pictures for the growing process of a cluster of PGMA chains (the degree of polymerization is 100) on a graphene sheet (made by Materials Studio software 4.0).

Consequently, to calculate the grafted arm density, W_C and W_P should be measured at first. Generally, W_C and W_P can be readily obtained from the TGA curves of brushes because the grafted polymer has a weight loss stage below 550 °C, and the residual weight fraction above 550 °C is assigned to W_C. The calculated $\bar{d}$ values are listed in Table 1 and plotted in Figure 2b. In order to evaluate the accuracy of the calculated density, we could deduce the specific surface area (S) of graphene as 2628.5 m^2/g from the final value of brush density ($S = (2W_pN_A)/(W_CM\bar{d}_2)$, where N_A represents the Avogadro constant, 6.02×10^{23}). Our deduced S is almost equal to the value reported in the literature (2630 m^2/g).[45]

As illustrated in Figure 2b, the $\bar{d}$ increases dramatically and almost linearly within the first 10 h, and relatively slowly after 18 h, and eventually reaches 15 960 chains per μm^2 of single side of GO at 48 h. Notably, from the AFM images, we can see that the $\bar{h}$ also increases from 1.7 to 12.8 nm with the reaction time, which is not resulted from the enlarging or growing of polymer arms since the propagation of a chain stopped rapidly after initiating but from the augmenting of grafting density. At a low density, the anchored arms could lie down or collapse on the sheet backbone for the van der Waals interactions; at a high density, the arms, especially those close to the center of polymer clusters, would stand up erectly due to the steric repulsion with each other, and the higher the density, the stronger the force, the longer the stretch of arms, the greater the height would be. From the increasing tendency of $\bar{d}$ and $\bar{h}$, we can speculate their relationship: $\bar{h} = k\bar{d}^{\alpha}$ for GO-*g*-PGMA brushes (herein $\alpha \approx 1$). The brush growing process can be depicted with cartoon pictures as shown in Figure 3.

Even though the fraction of grafted polymer (~80 wt %) is fairly high, the arm density on graphene oxide is obviously lower than that of CNTs-based polymer brushes or other surface brushes that were prepared by the "grafting from" approach.[41,46] This is mainly because our synthesis method basically belongs to a grafting to process. Another reason is

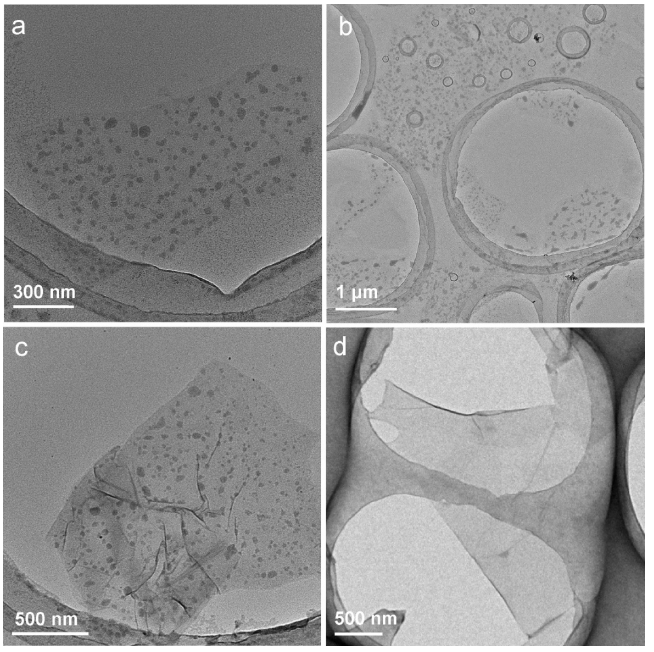


Figure 4. Representative TEM images of GO-*g*-PGMA (a, b), G-*g*-PGMA (c), and pristine GO (d).

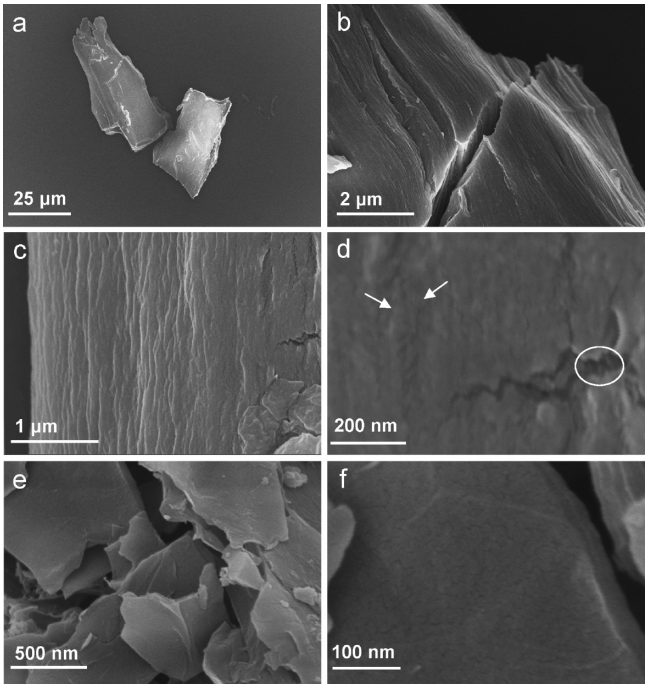


Figure 5. SEM images of bulk samples of GO-*g*-PGMA (a−d) and GO-*g*-PS (e, f) with the ratio of monomer to initiator 200:1 after centrifugal washing and vacuum drying, respectively.

that the molecular weight of grafted polymer arms is quite high. The strong steric hindrance associated with high molar mass of polymeric radicals is unfavorable to the high density grafting. Nevertheless, such a grafting density is comparable to that of previously reported "grafting to" cases on graphene (e.g., 1 chain of polystyrene with M_n 2500 g/mol per 980 carbon atoms).[47] In addition, the final $\overline{d}$ value is higher than the density of the elastic hairs or setae, including their end spatulae on a gecko foot by about at least 3 orders of magnitude, and also higher than the reported highest density of biomimic gecko foot, aligned carbon nanotubes array,[48] by about at least 2 orders of magnitude, indicating the possible biomimic applications of such soluble giant 2D molecular brushes.

Besides the window of time, we also tried to adjust the grafted arms by changing the feed ratio of monomer to initiator (R_{feed}) that may alter the molar mass of polymers to some extent. The results showed that the amount of arms could be slightly modulated (Figure 2 and Figure S13c), suggesting the flexibility of the synthesis strategy (Figures S14−S17). For instance, when R_{feed}s were changed to 50/1 and 1000/1 for cases of GO-*g*-PGMA, the grafted polymer contents approached 83.0 and 91.6 wt %, respectively, showing that the amount of arms increased with augmenting the R_{feed}. Moreover, we performed tens of experiments to repeat the experiments with different GO scales from tens of milligram to several grams, obtaining similar results to those mentioned above, revealing the good reproducibility of the presented synthesis strategy.

TEM and SEM Observations of 2D Molecular Brushes. The sheet structure and morphology of 2D molecular brushes of GO-*g*-PGMA were also observed and confirmed by TEM and SEM measurements. The representative TEM image (Figure 4a) shows a monolayer GO sheet attached with tufts of polymer protuberances that are evenly dispersed on the whole sheet. Under the low-magnitude image (Figure 4b), many individual sheets are observed, and each GO sheet has been evenly decorated with polymer clusters. As a comparison, no such kind of protuberances can be detected for the pristine GO sheets (Figure 4d). These results further indicate that the polymer chains have been successfully grafted on GO sheets through the *in situ* radical polymerization approach.

Figure 5 shows the typical surface morphology of the dried GO-*g*-polymer brushes. Well-packed layers are observed for the sample obtained by centrifugal washing at a low magnification (Figure 5a,b). From detailed observations, we can find that each layer is equipped with a shaggy surface (Figure 5c). The high-resolution SEM image shows that the flat surface is coated with a rough polymer layer (Figure 5d, marked by the arrows for a clear view). Furthermore, relatively blunt and coarse edges can be observed from the fracture (Figure 5d, marked by a circle).

Obviously, the observations of TEM and SEM are in agreement with the AFM visualizations, validating the successful synthesis of 2D molecular brushes.

Extension of the Synthesis Strategy. The above PGMA cases have sufficiently shown the feasibility, simplicity, and reproducibility of our synthesis strategy, paving the way for facile, large-scale production of individually dispersible 2D molecular brushes. To demonstrate the generality of our strategy, we conducted hundreds of experiments to extend it to all vinyl monomers available for us including acrylates (e.g., methyl acrylate (MA), hydroxyethyl acrylate (HEA), and acrylic acid (AA)), methacrylates (e.g., methyl methacrylate (MMA), butyl methacrylate (BMA), *tert*-butyl acrylate (*t*-BA), hydroxyethyl methacrylate (HEMA), 2-(dimethylamino)ethyl methacrylate (DMA), and methacrylic acid (MAA)), styrenics (styrene (St), and sodium *p*-styrenesulfonate (SSNa)), acrylamides (acrylamide (AM), and *N*-isopropylacrylamide (NIPAAm)), and 4-vinylpyridine (VP) (see Scheme 1). We got the unbelievable success for all cases, and obtained various 2D macromolecular brushes of polymer-grafted GO covering from polar to apolar, water-soluble to oil soluble, acidic to basic, and from functional to common polymers (Figures S18−S21 and Table S2).

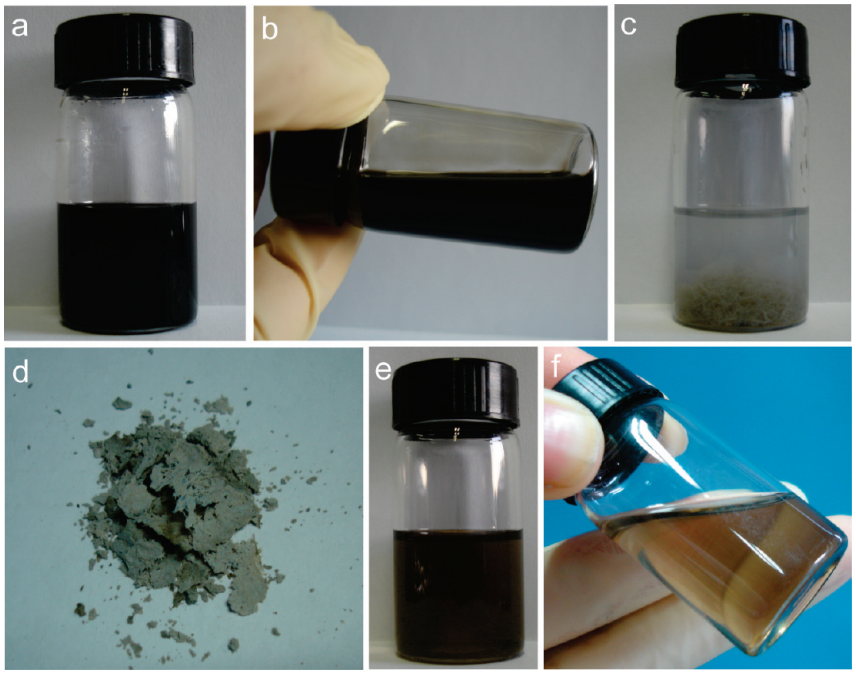


Figure 6. (a) Solution obtained after polymerization of GMA in the presence of GO for 48 h, and the vial was placed statically for around 2 months. (b) No sediment was observed at the bottom of the vial, indicating the "true solution" character for the dispersions. (c) The solution was precipitated by adding it into methanol. (d) Dried solid collected from (c). The solid in (d) was redissolved in DMF (e, f) with different background color, showing the superb solubility of the solid composite.

Additional typical SEM images of GO-*g*-PS are displayed in Figure 5e,f, clearly presenting sheet surfaces coated with dense brush clusters. The functional polymer-grafted GO brushes with pH, ion, salt, or temperature-stimuli responsive properties promise their great potentials in both academic and application fields, which will be reported later.

In addition, chemically reduced graphene sheets were also utilized as backbones to synthesize 2D brushes. TEM observations also show the similar structure to that of GO cases: hairy polymer clusters are evenly grafted on graphene backbones (Figure 4c). TGA curves and AFM images of polymer-grafted graphene are shown in Figure S22.

Properties of 2D Molecular Brushes and Their Composite. Notably, even through the amount of grafted polymer is relatively high, the fraction of grafted polymer compared to the free polymer is quite small (~2%). Regarding the potential application of the products and the high fraction of free polymers, we think that our approach can be used directly to produce nanocomposite of polymer-grafted GO and (free) polymer because of their good compatibility. As seen in Figure 6, the resulting solution after polymerization was homogenously black solution without any sediment after placing statically for 2 months (Figure 6a,b). After addition of methanol as precipitator to the solution, gray sediment appeared without any separately black granules (Figure 6c); after drying, we got pure gray solids (Figure 6d). This indicates that the GO-based brushes were well dispersed in polymer matrix. The dried solid can be well soluble in solvents again (Figure 6e,f). These results suggest that nanocomposite of polymer-grafted GO and (free) polymer can be readily prepared by the solution-processing technique. The application studies on such compatible composites are still in progress.

After efficient washing and centrifugation, neat polymer-grafted GO was obtained. A series of solvents were utilized to test the solubility of the resulting 2D molecular brushes, and parts of results are shown in Figure 7 as photographs. According to the nature of grafted arms, each kind of brush can be solubilized in selected solvents from the horizontal point of view; for a required solvent, corresponding soluble macromolecular brushes can be selected from the vertical point of view.

As mentioned above, after polymerization, the GO backbones were basically reduced (Figure S11). We further reduced the GO backbones by $N_2H_4 \cdot H_2O$[40] and found that the reduced 2D brushes of G-*g*-polymer preserved their morphology and solubility. This brings a significant progress to the process of such novel macromolecular brushes and GO/graphene-based polymer composites since pristine graphene and GO have very limited solubility in most of solvents.

It is noteworthy that GO-*g*-PGMA macromolecules show a very low intrinsic viscosity in DMF solution (~100 mL/g). This viscosity value is much lower than that of pristine GO dispersion (~780 mL/g) and close to the value of a common linear polymer such as polystyrene with 10^5 scale molar mass, indicating that the 2D molecular brushes have hardly intermolecular chain entanglements. This is similar to the globular macromolecules such as dendritic polymers.[49] This property probably enables the 2D brushes useful as nanofillers to improve the processability and performance of common polymers.

Because of their good solubility, the resulting 2D brushes can be readily coated homogeneously on solid substrates to form desired coating by direct painting (Figure 8a) as well as processed into self-standing films by solution casting (Figure 8b). Interestingly, the films of G-*g*-PGMA show the polymer content-dependent conductivity: 6×10^{-1} S/cm for reduced graphene, 6.5×10^{-2} S/cm for brushes at 24 h, and 8.4×10^{-3} S/cm at 48 h.[47,50,51] The highly processable 2D brushes could be used directly as building blocks to easily fabricate large-area surface brushes by solution casting or coating for biomimetic water-based lubrication, friction

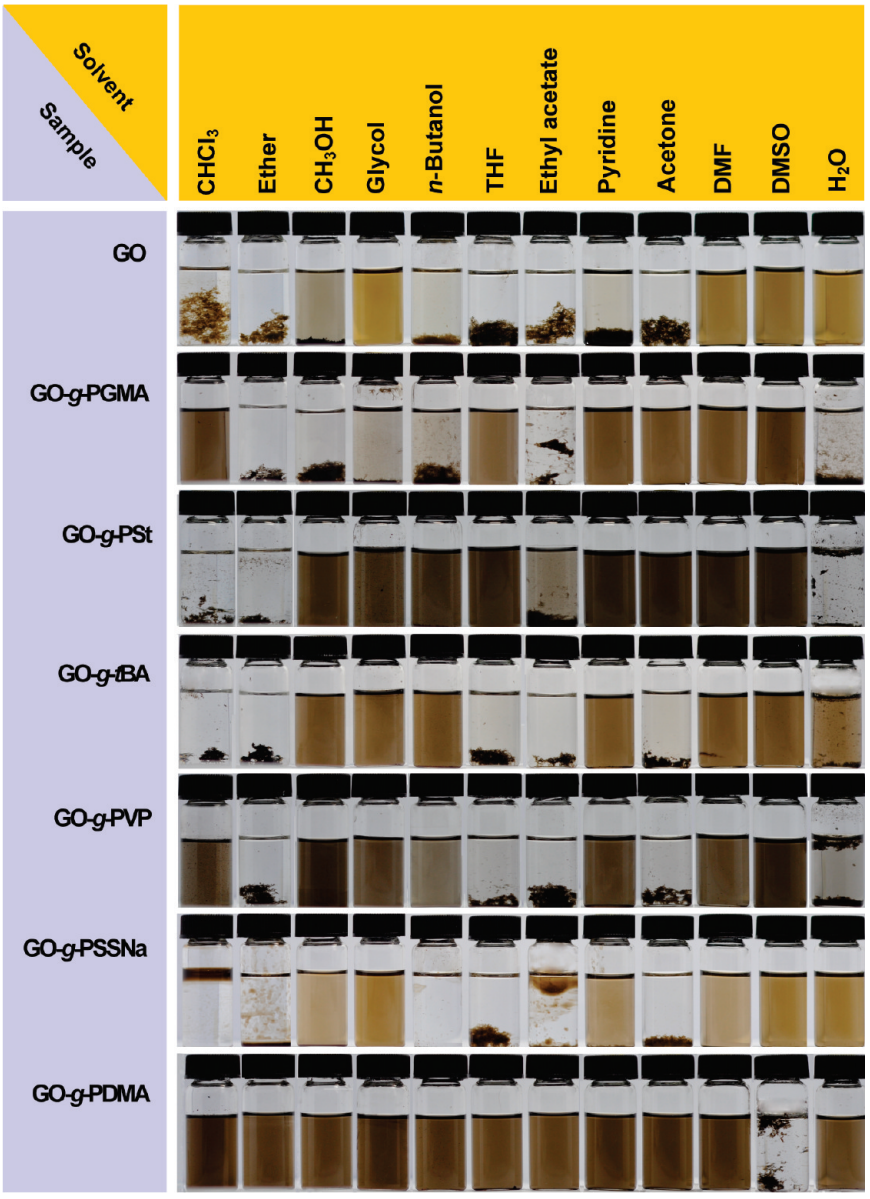


Figure 7. Photographs of GO and GO-*g*-polymer 2D macromolecular brushes placed in various solvents.

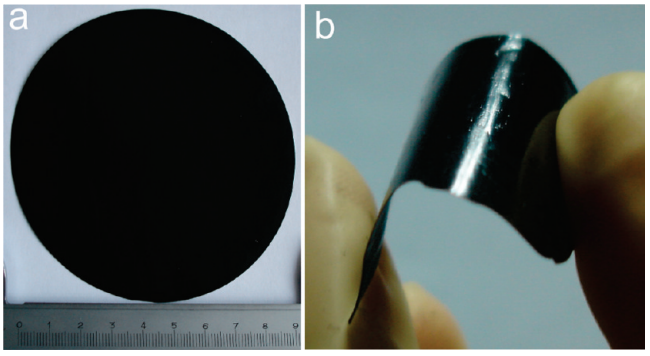


Figure 8. (a) Photograph of GO-*g*-PGMA coated on a nylon filter paper. (b) Self-standing film of pure GO-*g*-PGMA macromolecular brushes made by solution casting.

decreasing, and electrical conducting. Moreover, the numerous functional groups of brushes promise their use of molecular carriers to load guest matters and construct desired structures and composites.

Conclusions

In summary, we have developed a facile, powerful, reliable, and general strategy for scalable synthesis of GO/graphene-based 2D molecular brushes, a novel kind of giant molecules with sheet topology, laying the foundation for large-scale production of such giant macromolecules. The combination of high solubility, low viscosity, good processability, tunable electrical conductivity, and visible micrometer-scale sheet structures makes the 2D molecular brushes promising in a wide applications covering from biomimetic coatings to nanocomposites. Moreover, graphene or GO could be used as a novel kind of nanotable for the direct observation of molecular growth, polymerization kinetics, chemical reactions, and morphology of polymers and biomacromolecules, which would put a big forward for chemistry and biology. Other properties including rheology and viscoelastics of the 2D molecular brushes are currently investigated and explored.

Acknowledgment. This work was financially supported by the National Natural Science Foundation of China (No. 50773038 and No. 20974093), National Basic Research Program

of China (973 Program) (No. 2007CB936000), the Fundamental Research Funds for the Central Universities (2009QNA4040), Qianjiang Talent Foundation of Zhejiang Province (2010R10021), and the Foundation for the Author of National Excellent Doctoral Dissertation of China (No. 200527). The authors are grateful to Prof. Jinwen Qian for the help of viscosity measurements.

Supporting Information Available: Additional AFM images of 2D molecular brushes, ^{1}H NMR spectra, TGA curves, DSC curves, and XRD patterns. This material is available free of charge via the Internet at http://pubs.acs.org.

References and Notes

(1) Lee, S.; Spencer, N. D. *Science* **2008**, *319*, 575–576.
(2) Raviv, U.; Giasson, S.; Kampf, N.; Gohy, J.; JérÔme., R.; Klein, J. *Nature* **2003**, *425*, 163–165.
(3) Ryu, D. Y.; Shin, K.; Drockenmuller, E.; Hawker, C. J.; Russell, T. P. *Science* **2005**, *308*, 236–239.
(4) Klein, J. *Science* **2009**, *323*, 47–48.
(5) Klein, J.; Kumacheva, E.; Mahalu, D.; Perahia, D.; Fetters, L. J. *Nature* **1994**, *370*, 634–636.
(6) Zhang, M. F.; Müller, A. H. E. *J. Polym. Sci., Part A: Polym. Chem.* **2005**, *43*, 3461–3481.
(7) Sheiko, S. S.; Sumerlin, B. S.; Matyjaszewski, K. *Prog. Polym. Sci.* **2008**, *33*, 759–785.
(8) Schappacher, M.; Deffieux, A. *Science* **2008**, *319*, 1512–1515.
(9) Mansky, P.; Liu, Y.; Huang, E.; Russell, T. P.; Hawker, C. *Science* **1997**, *275*, 1458–1460.
(10) Milner, S. T. *Science* **1991**, *251*, 905–914.
(11) Edmondson, S.; Osborne, V. L.; Huck, W. T. S. *Chem. Soc. Rev.* **2004**, *33*, 14–22.
(12) Zhao, B.; Brittain, W. J. *Prog. Polym. Sci.* **2000**, *25*, 677–710.
(13) Klein, J.; Kumacheva, E.; Perahia, D.; Fetters, L. J. *Acta Polym.* **1998**, *49*, 617–625.
(14) Raviv, U.; Frey, J.; Sak, R.; Laurat, P.; Tadmor, R.; Klein, J. *Langmuir* **2002**, *18*, 7482–7495.
(15) Kobayashi, M.; Terayama, Y.; Hosaka, N.; Kaido, M.; Suzuki, A.; Yamada, N.; Torikai, N.; Ishihara, K.; Takahara, A. *Soft Matter* **2007**, *3*, 740–746.
(16) Drobek, T.; Spencer, D. *Langmuir* **2008**, *24*, 1484–1488.
(17) Subbotin, A.; Jong, J. D.; Brinke, G. T. *Eur. Phys. J. E* **2006**, *20*, 99–108.
(18) Geim, A. K.; Novoselov, K. S. *Nature Mater.* **2007**, *6*, 183–191.
(19) Geim, A. K. *Science* **2009**, *324*, 1530–1534.
(20) Ruoff, R. S. *Nature Nanotechnol.* **2008**, *3*, 10–11.
(21) Dikin, D. A.; Stankovich, S.; Zimney, E. J.; Piner, R. D.; Dommett, G. H. B.; Evmenenko, G.; Nguyen, S. T.; Ruoff, S. R. *Nature* **2007**, *448*, 457–460.
(22) Mkhoyan, K. A.; Contryman, A. W.; Silcox, J.; Stewart, D. A.; Eda, G.; Mattevi, C.; Miller, S.; Chhowalla, M. *Nano Lett.* **2009**, *9*, 1058–1063.
(23) Kudin, K. N.; Ozbas, B.; Schniepp, H. C.; Prud'homme, R. K.; Aksay, L. A. *Nano Lett.* **2008**, *8*, 36–41.
(24) (a) Fang, M.; Wang, K.; Lu, H.; Yang, Y.; Nutt, S. *J. Mater. Chem.* **2010**, *20*, 1982–1992. (b) Fang, M.; Wang, K. G.; Lu, H. B.; Yang, Y. L.; Nutt, S. *J. Mater. Chem.* **2009**, *19*, 7098–7105.
(25) (a) Stankovich, S.; Piner, R. D.; Chen, X. Q.; Wu, N. Q.; Nguyen, S. T.; Ruoff, R. S. *J. Mater. Chem.* **2006**, *16*, 155–158. (b) Lee, S. H.; Dreyer, D. R.; An, J.; Velamakanni, A.; Piner, R. D.; Park, S.; Zhu, Y.; Kim, S. O.; Bielawski, C. W.; Ruoff, R. S. *Macromol. Rapid Commun.* **2010**, *31*, 281–288.
(26) Shen, J. F.; Hu, Y. Z.; Li, C.; Qin, C.; Ye, M. X. *Small* **2009**, *5*, 82–85.
(27) Veca, L. M.; Lu, F. S.; Meziani, M. J.; Cao, L.; Zhang, P. Y.; Qi, G.; Qu, L. W.; Shrestha, M.; Sun, Y. P. *Chem. Commun.* **2009**, 2565–2567.
(28) (a) Kim, H.; Abdala, A. A.; Macosko, C. W. *Macromolecules* **2010**, *43*, 6515–6530. (b) He, H.; Gao, C. *ACS Appl. Mater. Interfaces* **2010**, *2*, 3201–3210. (c) Kou, L.; He, H.; Gao, C. *Nano-Micro Lett.* **2010**, *2*, 177–183. (d) Han, J.; Gao, C. *Nano-Micro Lett.* **2010**, *2*, 213–226.
(29) Xu, Z.; Gao, C. *Macromolecules* **2010**, *43*, 6716–6723.
(30) Dreyer, D. R.; Park, S.; Bielawski, C. W.; Ruoff, R. S. *Chem. Soc. Rev.* **2010**, *39*, 228–240.
(31) Li, D.; Müller, M. B.; Gilje, S.; Kaner, R. B.; Wallace, G. G. *Nature Nanotechnol.* **2008**, *3*, 101–105.
(32) Tung, V. C.; Allen, M. J.; Yang, Y.; Kaner, R. B. *Nature Nanotechnol.* **2009**, *4*, 25–29.
(33) Hummers, W. S.; Offeman, R. E. *J. Am. Chem. Soc.* **1958**, *80*, 1339–1339.
(34) Shaffer, M. S. P.; Koziol, K. *Chem. Commun.* **2002**, 2074–2075.
(35) Qin, S. H.; Qin, D. Q.; Ford, W. T.; Herrera, J. E.; Resasco, D. E.; Bachilo, S. M.; Weisman, R. B. *Macromolecules* **2004**, *37*, 3965–3967.
(36) Qin, S. H.; Qin, D. Q.; Ford, W. T.; Herrera, J. E.; Resasco, D. E. *Macromolecules* **2004**, *37*, 9963–9967.
(37) Samulski, E. T.; Desimone, J. M.; Jr, M. O. H.; Menceloglu, Y. Z.; Jarnagin, R. C.; York, G. A.; Labat, K. B.; Wang, H. *Chem. Mater.* **1992**, *4*, 1153–1157.
(38) Jeon, H. J.; Youk, J. H.; Yu, W. R. *Macromol. Res.* **2010**, *18*, 458–462.
(39) Flory, P. J. *Principles of Polymer Chemistry*; Cornell University Press: Ithaca, NY, 1953.
(40) Park, S.; Ruoff, R. S. *Nature Nanotechnol.* **2009**, *4*, 217–224.
(41) (a) Kong, H.; Gao, C.; Yan, D. Y. *J. Am. Chem. Soc.* **2004**, *126*, 412–413. (b) Kong, H.; Gao, C.; Yan, D. *Macromolecules* **2004**, *37*, 4022–4030. (c) Gao, C.; Muthukrishnan, S.; Li, W. W.; Yuan, J. Y.; Xu, Y. Y.; Muller, A. X. E. *Macromolecules* **2007**, *40*, 1803–1815.
(42) Gao, W.; Alemany, L. B.; Ci, L.; Ajayan, P. M. *Nature Chem.* **2009**, *1*, 403–408.
(43) Ramanathan, T.; Abdala, A. A.; Stankovich, S.; Dikin, D. A.; Herrera-Alonso, M.; Piner, R. D.; Adamson, D. H.; Schniepp, H. C.; Chen, X.; Ruoff, R. S. *Nature Nanotechnol.* **2008**, *3*, 327–331.
(44) Gao, C.; Vo, C. D.; Jin, Y. Z.; Li, W. W.; Armes, S. P. *Macromolecules* **2005**, *38*, 8634–8648.
(45) Stoller, M. D.; Park, S. J.; Zhu, Y. W.; An, J.; Ruoff, R. S. *Nano Lett.* **2008**, *8*, 3498–3502.
(46) (a) Ohno, K.; Kon, K.; Tsujii, Y.; Da, T. *Macromolecules* **2002**, *35*, 8989–8993. (b) Ohno, K.; Morinaga, T.; Kon, K.; Tsujii, Y.; Da, T. *Macromolecules* **2005**, *38*, 2137–2142.
(47) He, H. K.; Gao, C. *Chem. Mater.* **2010**, *22*, 5054–5064.
(48) Qu, L. T.; Dai, L. M.; Stone, M.; Xia, Z. H.; Wang, Z. L. *Science* **2008**, *322*, 238–242.
(49) Gao, C.; Yan, D. *Prog. Polym. Sci.* **2004**, *29*, 183–275.
(50) Stankovich, S.; Dikin, D. A.; Dommett, G. H. B.; Kohlhaas, K. M.; Zimney, E. J.; Stach, E. A.; Piner, R. D.; Nguyen, S. T.; Ruoff, R. S. *Nature* **2006**, *442*, 282–286.
(51) Rivadulla, F.; Mateo-Mateo, C.; Correa-Duarte, M. A. *J. Am. Chem. Soc.* **2010**, *132*, 3751–3755.

Macromolecules
ARTICLE

Macromolecules **2011**, *44*, 453–461 **453**
DOI: 10.1021/ma102847a

Single-Step Electrospinning to Bioactive Polymer Nanofibers

Rafael Gentsch,[†,‡] Falko Pippig,[§] Stephan Schmidt,[‡] Peter Cernoch,[‡,⊥] Julien Polleux,[∥] and Hans G. Börner*[,†]

[†]*Department of Chemistry, Laboratory of Organic Synthesis of Functional Systems, Humboldt-Universität zu Berlin, D-12489 Berlin, Germany,* [‡]*Max Planck Institute of Colloids and Interfaces, 14424 Potsdam, Germany,* [§]*Fraunhofer Institute for Applied Polymer Research, 14476 Potsdam, Germany,* [∥]*Max Planck Institute of Metals Research, Heisenbergstrasse 3, 70569 Stuttgart, Germany, and* [⊥]*Institute of Macromolecular Chemistry AS CR, v.v.i., Heyrovskeho nam. 2, 162 06 Praha 6, Czech Republic*

Received December 14, 2010

ABSTRACT: A single-step process to polymer nanofiber meshes that possess biofunctional peptide segments on their surfaces is described here, which requires a standard electrospinning setup only. Spinning a homogeneous mixture composed of a valuable polymer−peptide conjugate (poly(lactic acid)-*block*-CGGRGDS) and a biocompatible commodity poly(lactic-*co*-glycolic acid) (PLGA) leads to nonwovens where the bioactive peptide part is enriched up to 11 times on their fiber surface. This is determined by X-ray photoelectron spectroscopy (XPS). The surface accessibility of the peptide is proved on the macroscale by contact angle measurements comparing pure PLGA fibers with GRGDS-functionalized fiber meshes as well as on the nanoscale by probing electrostatic interaction between CGGRGDS surface functionalities and a colloidal silica probe via atomic force microscopy (AFM). Ultimately, bioavailability and bioactivity of the peptides on the fiber surfaces are demonstrated, showing that the meshes promote adhesion and migration of fibroblasts in comparison to pure PLGA meshes. The one-step production of hydrophilic PLGA-based fibers could be exploited to electrospin into living cell culture without indication of toxic adverse effects on cell proliferation. This might be useful for directly production of cell-loaded scaffolds or biohybrid materials.

Introduction

Functional nonwovens composed of polymeric nanofibers are of growing interest due to their broad applicability in diverse fields. Tailor-made nanofiber meshes have been successfully applied in biomedicine as well as fuel cell and sensor technologies.[1−3] Cell culture scaffolds, catalyst supports, affinity membranes, hierarchical filter materials, or protective clothing are only a few applications, where the large surface area and pore interconnectivity present in such nonwovens proved to be of advantage.[4−7] Different top-down and bottom-up approaches are currently available to produce meshes of nanofibers.[8,9] Because of its simplicity, diversity, and ability to upscale, electrospinning is one of the most successful methods to fabricate fibers from a broad range of materials such as synthetic polymers, biopolymers, composites, ceramics, and metals.[10−12] This technique is able to generate fibers with adjustable dimensions ranging from diameters of several micrometers down to a few nanometers.[11] In cell biology, it is well-known that cells spontaneously secrete and assemble fibrillar structures, the extracellular matrix (ECM), which shows similar morphological features as the ones accessible by electrospinning. Therefore, electrospun nonwovens became attractive scaffolds to synthetically mimic the microenvironment of biological systems.[13−15] Particularly, biodegradable electrospun meshes proved to be ideal candidates for tissue engineering, wound dressings, and drug delivery systems.[1,16,17] Additionally to the structural similarity, the chemical signaling functions of the ECM fibrils have to be mimicked to tailor cellular response.[8,18] Arginine−glycine−aspartate (RGD) is a conserved motif found in several matrix proteins like fibronectin, fibrinogen, vitronectin, von Willenbrand factor, and many other glycoproteins, which exhibit a high binding affinity to specific cell surface receptors.[19,20] These receptors are referred to as integrins, which physically connect the internal cell machinery to the ECM.[21−23] Grafting epitopes like GRGDS to cell culture substrates proved to support cell adhesion and growth.[24,25]

To address these surface chemistry requirements, different strategies aiming at functionalizing nanofibers were reported.[26−28] Commonly, the fiber surface of nonwovens is activated and modified with linker molecules in order to covalently graft functional biomolecules.[29,30] Although this modular post-treatment is advantageous because it decouples the electrospinning process from the functionalization step, multistep protocols and heterogeneous reactions usually hamper manufacturing processes (e.g., industrial upscaling). In addition, analytical characterization of the products is not trivial, e.g., the differentiation of physisorption and chemisorption of functional entities onto nanofibers. As an alternative, coaxial electrospinning was introduced to directly generate core−shell structures. However, the control of multiple feed rates of the coaxial nozzle makes the process complicated.[31]

To avoid the use of elaborate strategies, biomolecules, e.g. growth factors, recruitment factors, or ECM proteins, have often been blended with biocompatible commodity polymers like poly(ε-caprolactone) (PCL), poly(lactic-*co*-glycolic acid) (PLGA), or poly(ethylene oxide) (PEO).[32−35] Electrospinning of such blends is usually difficult, as compatibility problems and protein denaturation have to be considered. Moreover, strategies leading to the enrichment of biomolecules on the fiber surface are not commonly reported. Thus, biomolecules might be mostly entrapped into the fiber bulk, where they are inactive. This may not only corrupt the bulk properties of the fibers but is also of

*To whom correspondence should be addressed: e-mail h.boerner@hu-berlin.de; Ph +49 (0)30-2093 7348; Fax +49 (0)30 2093-7266.

© 2011 American Chemical Society
Published on Web 01/10/2011

disadvantage as bioactive compounds are rather expensive substances. Furthermore, the fraction of biomolecules that is located at the fiber surface might quickly undergo dissolution or only be partially accessible and therefore less active. In that respect, block copolymers combining a biofunctional segment and a synthetic polymer block are highly interesting.[36−38] While the synthetic polymer can be chosen to be compatible with a fiber-forming polymer, the biofunctional segment can be reduced to oligopeptide epitopes. Due to their limited length and complexity (i.e. 4−15 amino acids), oligopeptides do not suffer from denaturation issues and often exhibit reasonable compatibility with nonaqueous solvents. In a preliminary study a PEO−peptide conjugate was coelectrospun with high molecular weight PEO. A clear field-driven enrichment of the polar peptide on the PEO fiber surface was observed, leading to meshes made of a PEO core and a functional peptide shell.[39] Although the concept is interesting, the water solubility of this system and the biologically nonrelevant peptide sequence limits its applicability.

In other approaches block copolymers were spun to yield fibers with concentric lamellar substructures after annealing. Such higher ordered structures might be useful for incorporating functional systems like nanoparticles, drugs, or biomolecules. However, multistep protocols including often coaxial electrospinning were used to generate these systems, which might be a drawback.[40,41] In addition, emulsion-electrospinning was demonstrated to be a feasible method to encapsulate and spin diverse biomolecules or drugs.[42,43] Further evaluation of this approach has to show if the involved surfactants (e.g., SDS) might represent a risk to sensitive biological systems, whereas nonionic block copolymers as surfactants seem less problematic.

Here we report on a straightforward route using a standard electrospinning setup to directly generate bioactive polymer meshes, making additional activation or functionalization steps obsolete. The electrospinning of a homogeneous two-component solution blend composed of poly(L-lactic-*co*-glycolic acid) (PLGA) as commodity fiber-forming polymer and poly(L-lactic acid)-*b*-CGGRGDS (PLLA-*b*-CGGRGDS; cf. Scheme 1, V) as bioconjugate exhibiting the bioactive RGD epitope leads to nanofiber meshes with adjustable fiber diameters. Exploiting physicochemical means such as demixing and interface stabilization were used to enrich the GRGDS at the surface of the nanofibers.

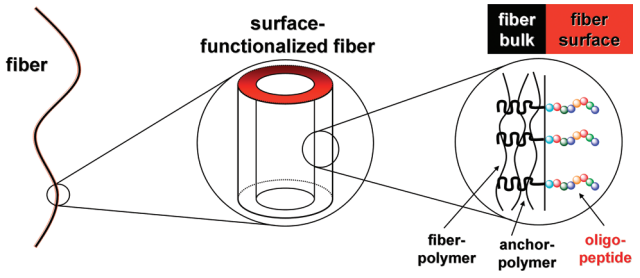


Figure 1. Idealized structure of peptide functionalized fiber surfaces, where the surface is enriched with the peptide fragment of the polymer−peptide conjugate, while the polymer part of the bioconjugate anchors the conjugate into the fiber bulk.

The polymer block of the bioconjugate compatibilizes the peptide with the fiber bulk forming PLGA and anchors the peptide into the fiber bulk, as shown schematically in Figure 1. Thus, direct spinning of a mixture of PLGA and PLLA-*b*-CGGRGDS leads to a core−shell like fiber morphology exhibiting biological activity.

Experimental Part

Materials. Poly(L-lactic-*co*-glycolic acid) (PLGA, 85/15 mol/mol, PUROSORB PLG8531, $M_{n,GPC}$ = 161 kg/mol, $M_w/M_{n,GPC}$) was friendly provided by Purac (Gorinchem, Netherlands). Methanol (Biosolve, 99+%) and chloroform ($CHCl_3$, 99+%, Merck, Darmstadt, Germany) were purchased. All chemicals were used as received.

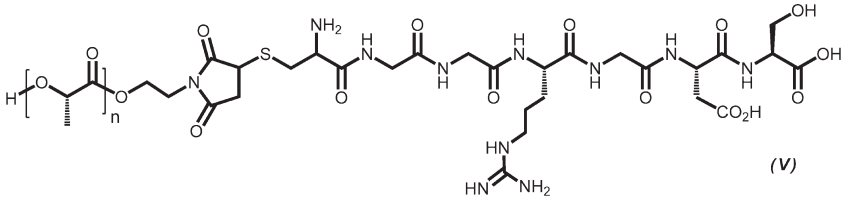
Synthesis. The maleimide functional PLLA (III) was synthesized according to literature protocols (cf. Supporting Information I−III; $M_{n,III,GPC,PS\text{-}standards} \sim 3000$ g/mol, $M_w/M_{n,GPC}$ = 1.48, $M_{n,III,NMR}$ = 2600 g/mol).[44] The peptide synthesis was performed by solid-phase supported peptide synthesis on a fully automated ABI 433a peptide synthesizer (Applied Biosystems, Darmstadt, Germany),[25] yielding a peptide with a sequence Cys-Gly-Gly-Arg-Gly-Asp-Ser (CGGRGDS) (cf. Supporting Information IV; $M_{IV,LC\text{-}ESI\text{-}MS}$ = 650 g/mol). The polymer−peptide conjugate was obtained by fragment coupling strategies, ligating a maleinimide-end-functionalized PLLA with the thiol functionality of the cysteine residue of the peptide segment by maleimide−thiol coupling to yield PLLA-*b*-CGGRGDS (cf. Scheme 1, V).[45] A detailed synthesis protocol including materials and analytics is provided in the Supporting Information.

Methods. Electrospinning was performed on a setup described elsewhere.[5] Shortly, the setup was composed of a high-voltage power supply (DC, HCP-serie 14−20000, FuG Electronik GmbH, Rosenheim, Germany) and a syringe pump (KD Scientific Inc., Holliston, MA). Plastic 1 mL syringes with disposable blunted tips (Howard Electronics, JG20-2, nominal inner diameter: 0.584 mm, El Dorado, KS) were positively charged, and an aluminum foil was used as a collector in a vertical setup. The polymer solution was fed at a rate between 0.2 and 1 mL/h by the syringe pump to the blunted needle tip, where a voltage of 5−11 kV was applied. The spinning distance between tip and ground collector was 7−10 cm.

The resulting fiber meshes were dried, cut into 0.5 × 0.5 cm^2 pieces, and sputtered with Pd/Au for SEM measurements (LEO 1550-GEMINI, Zeiss, Oberkochen, Germany) or further used for cell studies. To evaluate the fiber diameter the software ImageJ (1.38×, Wayne Rasband, National Institutes of Health, Bethesda, MD) was used.

For electrospinning or solution measurements freshly prepared polymer solutions were used by dissolving polymers overnight by shaking (shaker, ~200/min) or mixing with a rock and roll shaker. The different polymer solutions were characterized with a CDM83 conductivity meter (Radiometer, Copenhagen, Denmark) using a 0.05% NaCl/water (50 mg/100 mL) solution for calibration. Viscosity measurements of different polymer solutions were conducted at 25 °C on an automated microviscometer AMVn (Anton Paar, Graz, Austria), using glass capillary systems for different viscosity ranges (4 (3) mm diameter capillary/steel ball with 3 (2.5) mm in diameter). Viscosity (n) was determined by the falling time (t_1) of the steel ball according to the following equation: $n = K_1(d_K - d_P)t_1$, where K_1 is the

Scheme 1. Structure of the PLLA-*b*-CGGRGDS Polymer−Peptide Conjugate (V)



calibration constant, d_K the density of steel ball, and d_P the density of polymer solution.

Static contact angles were measured by using a contact angle measuring system G10 from A.KRÜSS Optronic GmbH (Hamburg, Germany). Contact angles were determined by placing a drop of water from a syringe onto the fiber mat and measuring the contact angle within < 10 s of application of the drop. Measurements were done at room temperature. Reported values are averages of at least three measurements taken at different points on the surface.

For X-ray photoelectron spectroscopy (XPS) measurements an Axis 165 instrument (Kratos Analytical, Manchester, UK) with monochromatic Al Kα radiation in hybrid mode, i.e., with electrostatic and with magnetic lenses, was used. The takeoff angle of the emitted electrons was set to 90° related to macroscopic sample surface. Because of the varying surface topography of the samples, the real takeoff angle will differ, and therefore the exact information depth will also change in the range from 1 to 10 nm. The size of the measured area (approximately 0.3×0.7 mm^2) led to an average information depth. The charging of the sample during the measurement was compensated with thermal electrons from a filament. A linear background correction was applied, and the high-resolution spectra were fitted with Gaussian functions. The data processing was done with Casa XPS software (Casa Software Ltd., version 2.1.13). Typically, different points within one sample and different samples were measured. The corresponding values were then averaged. In order to delete background (e.g., aluminum foil, glass, silicon wafer) and known impurities signal (silicon sealing grease), a correction according its chemical surface chemical composition was performed.

The colloidal probe atomic force measurements performed to probe electrostatic interactions were carried out on a Nanowizard I AFM (JPK Instruments AG, Berlin, Germany) in a closed liquid cell (Small Cell, JPK Instruments AG, Berlin, Germany) filled with 10^{-4} M hydrochloric acid at pH of 4. The AFM head was mounted on an optical microscope (IX51, Olympus, Japan). Using bright-field optics (objective 63×/1.25 Oil Ph3, Antiflex EC Plan-Neofluar, Carl Zeiss AG, Jena, Germany) single fibers could be resolved. The microscope stage allowed for micrometer-accurate positioning of the cantilever in order to map the fibers via so-called force mapping (also known as force−volume mode). The adhesion data were collected by conducting the force mapping at the apex of the fibers in a 100×100 nm^2 sized grid. To aim for the apex, the topography of the fiber was imaged by force mapping over its whole width in the first step. Then the colloidal probe was positioned using the AFM software, which can be done with nanoscopic precision. As force colloidal probe, silica particles (Microparticles GmbH, Berlin, Germany) were used with a diameter of 10 μm glued to the apex of the AFM cantilevers (with a nominal spring constant of 0.2 N/m; NSC 12 tipples, Mikromasch, Tallin, Estonia). Prior to the measurements, the cantilevers and colloidal probes were rinsed with analytical grade isopropanol and water followed by treatment in air plasma at a pressure of 1 mbar for 2 min while applying an intensity of 18 W (PDC-32G Plasma Cleaner, Harrick Plasma, Ithaca, NY).

Peptide−polymer conjugate solutions in chloroform and chloroform/methanol (3:1/v:v) were investigated by dynamic light scattering (DLS) using ALV-7004 Multiple tau digital correlator equipped with CGS-3 compact goniometer system, 22 mW He−Ne laser (wavelength $\lambda = 632.8$ nm), and a pair of avalanche photodiodes operated in a pseudo-cross-correlation mode (ALV-GmbH, Langen/Hessen, Germany). To remove dust, samples were filtrated with 0.45 μm PVDF or 1 μm glass filter. The density of the used filter was selected according to viscosity of the actual sample. Measurements were performed at room temperature at a scattering angle of 90°.

Cell Studies. Murine fluorescent kidney fibroblasts (kindly provided by R. Fässler, Department for Molecular Medicine, Max Planck Institute of Biochemistry, Martinsried, Germany) were cultivated by using Dulbecco's Modified Eagle Medium (DMEM) supplemented with 10% fetal bovine serum (FBS) (both from Gibco, Invitrogen, Darmstadt, Germany), 1% penicillin/streptomycin (PAA, Cölbe, Germany) in a culture incubator at 37 °C in an atmosphere containing 5% CO_2. After reaching 80% confluence, cells were first rinsed with sterile phosphate-buffered saline (PBS) and then released with a 1% trypsin−EDTA solution (Gibco, Invitrogen, Darmstadt, Germany) for about 3−5 min. Trypsinization was stopped by adding 10% FBS supplemented DMEM to the released cells, which were centrifuged at 1000 rpm for 3 min. The resulting cell pellet was resuspended in prewarmed growth medium, and the cells were seeded again in cell culture dishes. After trypsinization, approximately 1.2×10^5 cells in DMEM containing 0.2% FBS were seeded on electrospun fibers on glass slides. Cell spreading assays were conducted on the fibers for 24 h. Images were recorded with a Zeiss Axiovert 40 CFL microscope (Carl Zeiss, Jena, Germany). To prevent nonspecific protein adsorption and cell attachment on the piranha-cleaned glass slides, poly(L-lysine-*graft*-ethylene glycol) (PLL(20)-*g*-[3.5]-PEG(2)) (Standard PLL-*g*-PEG, SurfaceSolutions GmbH, Zurich, Switzerland) was used before the spinning step, as described elsewhere.[46] The PLL-*g*-PEG coating was performed by depositing a 200 μL drop of a 0.25 mg/mL PLL-*g*-PEG solution in 10 mM HEPES-buffer (pH 7.4) on parafilm. This drop was then flatten by the glass slide and incubated for 2 h. Subsequent washing with H_2O and drying with N_2 were performed.

Murine fibroblast L929 cell culture can be found in the Supporting Information.

Results and Discussion

While the poly(L-lactic-*co*-glycolic acid) (PLGA) is a commercially available, biocompatible polymer, the PLLA-*b*-CGGRGDS bioconjugate (V) was synthesized by fragment ligation strategy (cf. Supporting Information). First end-functionalized PLLA was synthesized via ring-opening anionic polymerization, started with a furan-protected maleimide of the 2-aminoethanol as initiator (4-(2-hydroxyethyl)-10-oxa-4-azatricyclo[5.2.1.02,6]dec-8-ene-3,5-dione).[44,47] Subsequently after polymerization the furan protective group was removed in a retro-Diels−Alder reaction leading to PLLA with a maleimide chain end functionality and a molecular weight of $M_{n,NMR} = 2600$ g/mol (III). The peptide with a amino acid sequence of CGGRGDS (IV) was obtained by automated solid-phase supported peptide synthesis.[48] Ligation of both the α-maleimide-PLLA and the thiol moiety of cysteine of the peptide took place by maleimide−thiol coupling chemistry and resulted in the PLLA-*b*-CGGRGDS bioconjugate (cf. Scheme 1, V).[45]

To obtain PLGA nanofibers with bioactive peptides as surface functionalities, electrospinning was investigated as a straightforward process technique.[11] The first strategy involved electrospinning of homogeneous mixtures of PLLA-*b*-CGGRGDS and PLGA in chloroform. It was hypothesized that the low dielectric constant of chloroform might facilitate field enrichment of the polarizable peptide segment to the fiber surface in analogy to previous reports, describing the electrospinning of a PEO/PEO−peptide system.[39,51] To establish appropriate conditions, electrospinning behavior of PLGA and PLLA-*b*-CGGRGDS in chloroform was investigated. Electrospinning of PLGA from a 5% w/v chloroform solution proved to be feasible, resulting in fiber meshes with an interesting bimodal fiber distribution as reported earlier.[5] The conjugate alone could not be spun properly due to the low molecular weight of the bioconjugate ($M_{n,PLLA\text{-}CGGRGDS} \sim 3000$ g/mol). A solution containing 10% w/v bioconjugate led to electrospraying and provided particles. A blended solution of 5% w/v PLGA with 9.1 wt % PLLA-*b*-CGGRGDS with respect to the solid composition could be

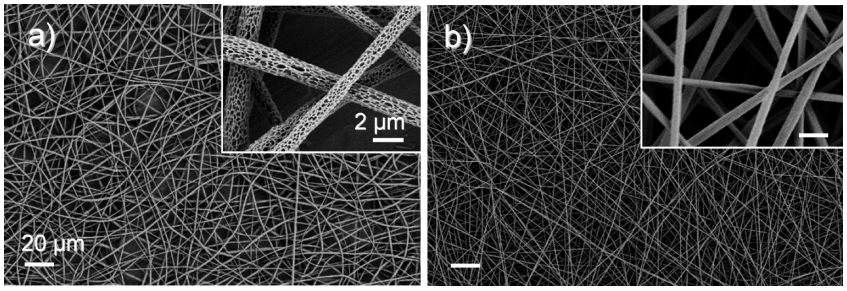


Figure 2. SEM images of PLGA/PLLA-*b*-CGGRGDS fibers, fabricated by electrospinning using (a) $CHCl_3$ and (b) $CHCl_3$/MeOH (3:1) solutions (5% w/v PLGA, solid composition, 9.1 wt % PLLA-*b*-CGGRGDS, conditions: (a) rate 0.2 mL/h, electric field 5.5 kV/7 cm, 72% relative humidity; (b) rate 0.7 mL/h, electric field 6.6 kV/10 cm, 27% relative humidity).

Table 1. Nitrogen Atom % (*N*) Derived from XPS Measurements of Fibers and Control References Processed from $CHCl_3$ and $CHCl_3$/MeOH Solutions To Evaluate Peptide Enrichment at the Fiber Surface

	c [% w/v]	shape	N_{corr}[c] [at. %]	N_{th}[d] [at. %]
		$CHCl_3$		
PLLA-*b*-CGGRGDS/PLGA[a]	5	fibers	1.1 ± 0.8	0.4
PLLA-*b*-CGGRGDS/PLGA[a]	5	film[b]	1.5 ± 0.0	0.4
PLLA-*b*-CGGRGDS/PLGA[a]	5	film^{DD}	3.0 ± 1.5	0.4
PLLA-*b*-CGGRGDS	10	particles	4.6	4.9
		$CHCl_3$/MeOH		
PLLA-*b*-CGGRGDS/PLGA[a]	5	fibers	4.5 ± 0.5	0.4
PLLA-*b*-CGGRGDS/PLGA[a]	5	film[b]	4.6 ± 0.4	0.4
PLLA-*b*-CGGRGDS	10	particles	5.0	4.9

[a] 9.1 wt % peptide−polymer conjugate with respect to the solid content of PLGA. [b] Spin-coating 1000−2000 rpm, fibers obtained by electrospinning, particles obtained by electrospraying. [c] Background corrected (cf. Supporting Information, Table S3/4). [d] Theoretical calculated values assuming homogeneous mixture and $M_{bioconjugate} = 3250$ g/mol.

electrospun, producing porous fibers[49] with diameters of 1.16 ± 0.47 μm (Figure 2a). Interestingly, the addition of the bioconjugate strongly enhanced the uniformity of the resulting fibers as compared to those spun from pure PLGA. The improved spinnability relatively nonpolar polymers by the addition of peptide−polymer conjugates could be rationalized by an increased conductivity, polarity, and viscosity of the mixture (Supporting Information Table S1/2). Phenomenologically, an earlier onset of the bending instability was visible, suggesting an increased stability of the electrospin process.

In order to quantify the chemical composition of the fiber surface, X-ray photoelectron spectroscopy (XPS) measurements were performed on thick fiber meshes. XPS determines the average atomic composition of such polymer fiber surfaces, penetrating a layer thickness of approximately 1−10 nm. The peptide can be clearly identified and quantitatively determined by measuring the nitrogen concentrations as neither PLGA nor PLLA contains nitrogen. Table 1 summarizes the XPS measurements. The peptide content on the fiber surface of meshes obtained from electrospinning of PLGA/PLLA-*b*-CGGRGDS chloroform solutions suggested a ~3 times enrichment of the peptide compared to calculated values assuming a homogeneous distribution of PLLA-*b*-CGGRGDS in the PLGA fiber bulk. Although the *N* values for the electrospun fibers were higher than the theoretical values, control measurements on films which were fabricated by drop-drying and spin-coating PLGA/PLLA-*b*-CGGRGDS chloroform solutions also exhibited higher values and thus slightly higher concentrations of the peptide at the film surface. This suggests that in the investigated bioconjugate/polymer/solvent system the surface enrichment was not dominated by a field-driven process under the used conditions. Apparently, phase separation and interface stabilization are likely to cause the peptide enrichment. In addition, reversing of the ground position did not affect dramatically the enrichment, indicating no field effect (cf. Supporting Information, Figure S1 and Table S3). Further evidence for surface enrichment by demixing is given by the fact that films produced from drop-drying PLGA/PLLA-*b*-CGGRGDS solutions resulted in the highest XPS (7.5-fold) nitrogen value (cf. Table 1). Drop-drying is a much slower process as compared to electrospinning or spin-coating, thus giving the peptide part more time to demix and enrich at the surface. However, none of the processes resulted in sufficient peptide enrichment at the surface as indicated by the reference experiment, where electrosprayed particles of pure peptide−polymer conjugates reached a nitrogen value that was even 1.5 times higher in comparison to the ones of the drop-dried films.

In order to investigate the surface segregation mechanism and to distinguish field enrichment versus phase separation, a different solvent system of methanol/chloroform with a ratio of 1:3 (v:v) was applied. Although methanol is a nonsolvent for PLLA and PLGA, it dissolves peptides well by providing possibilities of hydrogen bonding. The addition of MeOH improved the spinning behavior of the pure PLGA. Formation of unimodal fibers with fiber diameters of 910 ± 250 nm (cf. Supporting Information, Figure S2a) could be found, using the same concentration as for spinning PLGA/$CHCl_3$ solutions. Higher stability of the spin process might be attributed to the increased conductivity which overcame the decrease in overall viscosity by the addition of methanol (cf. Supporting Information, Table S1/2). The PLGA fibers prepared from this solution did not seem to possess a circular cross section, but rather wrinkled surfaces structures. This increased the active surface area, which might be interesting for bioapplications. Similar behavior had been already described in the literature and was attributed to a collapse of a not yet solidified core caused by the solvent mixture, where methanol is less volatile than chloroform.[50] Using a solution of pure polymer−peptide conjugates in

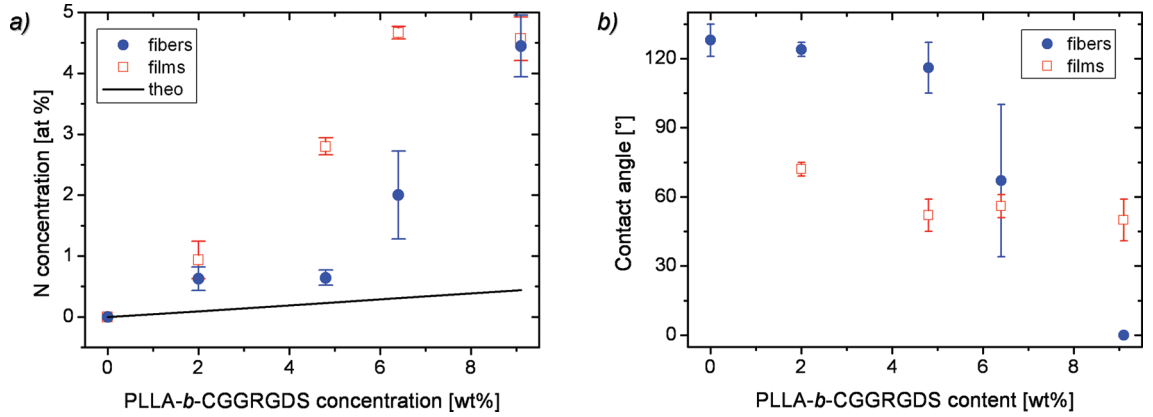


Figure 3. Nitrogen content derived from the XPS spectra shows a dramatic increase by increasing the peptide−polymer conjugate concentration (a), whereas the contact angle measurements confirm an enhanced hydrophilicity (b) for electrospun fibers and spin-coated films (corrected nitrogen values are used, raw data and conditions are shown in Supporting Information, Table S4 and Figure S3).

methanol/chloroform (1:3 (v:v)) resulted in particles as formed by electrospraying (cf. Supporting Information, Figure S2b).

The electrospinning of a PLGA/PLLA-*b*-CGGRGDS mixture from methanol/chloroform (1:3 (v:v)) solution was conducted keeping the polymer and bioconjugate concentrations comparable to the spin experiments with pure chloroform (5% w/v PLGA and 9.1 wt % PLLA-*b*-CGGRGDS with respect to the solid content). The addition of the peptide−polymer conjugate led to unimodal sized fibers with decreased fiber diameters of 640 ± 180 nm compared to meshes obtained by electrospinning of pure PLGA (cf. Figure 2b). Surface wrinkling was observed, but not to the same extent as in the case of pure PLGA fibers. The addition of the peptide−polymer conjugates increased the conductivity and the viscosity (cf. Supporting Information, Table S1/2) which was reflected by an increased stability of the electrospinning process, showing phenomenologically an early onset of bending instabilities.

Interestingly, the addition of MeOH to the solvent system has a dramatic effect on the peptide enrichment at the nanofibers' surface, which was produced by spinning polymer−peptide conjugate/PLGA blends from methanol/chloroform solutions. XPS measurements on those meshes showed an 11 times increased nitrogen surface concentration, compared to theoretically calculated values that assume a homogeneous distribution of the polymer−peptide conjugate and PLGA within the fiber bulk (cf. Table 1). Taking into account that the nitrogen surface contents of the blended fibers corresponds well to the nitrogen values measured and calculated for the pure polymer−peptide conjugate, it can be concluded that the mesh surface is mainly composed of peptide−polymer conjugates. A similarly increased nitrogen surface composition was found in control samples such as thin films of PLLA-*b*-CGGRGDS/PLGA blends produced by spin-coating and particles generated by electrospraying pure polymer−peptide conjugate. These references imply that the electric field plays a minor role, while changing the polarity of the solvent from a nonpolar solvent to a more polar mixture, seems to be primarily responsible for the enrichment of the peptide. In contrast to commonly reported surface enrichment of hydrophobic entities (e.g., fluorinated compounds)[52−54] in systems which are in equilibrium, the results demonstrate here a dynamic nonequilibrium surface segregation of the hydrophilic peptide part to the fiber surface.

In order to further study the effect of the bioconjugate on electrospinning and the peptide enrichment behavior, blends with different PLLA-*b*-CGGRGDS/PLGA ratios were electrospun from methanol/chloroform solutions (cf. Supporting Information, Figure S3). Decreasing the bioconjugate content resulted in an initial decrease and a subsequent increase in fiber diameter (9.1 wt % V → 640 ± 180 nm, 6.5 wt % V → 480 ± 190 nm, 4.8 wt % V → 550 ± 110 nm, 2 wt % V → 690 ± 190 nm). This behavior can be attributed to overlaying effects such as variations in viscosity, polarity, and conductivity, which lead to an initial decrease (viscosity dominated) and further increase (conductivity, polarity dominated) of the fiber diameter.

Quantification of fiber surface composition by XPS analysis revealed an increase of the nitrogen surface concentration with increasing peptide−polymer conjugate content (Figure 3a). The amount of nitrogen increased in a dramatic fashion for both films and fibers. All experimental values were higher than the calculated ones, suggesting a homogeneous mixing of PLLA-*b*-CGGRGDS and PLGA. The nitrogen contents for electrospun fibers increased initially rather slowly on increasing the PLLA-*b*-CGGRGDS content in the blend from 0 to ~4.8 wt %. Further increase in the PLLA-*b*-CGGRGDS/PLGA ratio up to 9.1 wt % peptide−polymer conjugate content resulted in a strong increase of the N surface content (up to 11-fold enrichment). In contrast to this, the nitrogen surface values of spin-coated films were found to increase more steadily on increasing the PLLA-*b*-CGGRGDS content from 2.0 to 6.4 wt %. Apparently, the nitrogen surface values level off upon increasing the bioconjugate content to 9.1 wt %.

XPS is sensitive for the first surface layers (approximately 1−10 nm analytical depth) and therefore provides an average value over a certain depth of the nanofibers. For biological application, it is of critical importance to determine the chemical fragments present on the nanofiber surface. To verify the peptide content at the fiber surface, the fiber mesh wetting was examined. The peptide part of PLLA-*b*-CGGRGDS should enhance the mats' hydrophilicity, if it is directly available on the fiber surface. This can be analyzed by using static contact angle measurements on electrospun mats (Figure 3b). Indeed, a clear increase in hydrophilicity was observed with increasing PLLA-*b*-CGGRGDS content of the electrospun fibers. Where a static contact angle of 124° was found with meshes containing 2 wt % PLLA-*b*-CGGRGDS (spun from chloroform/MeOH mixtures), the increase to 9.1 wt % PLLA-*b*-CGGRGDS leads to nonwovens, which are instantaneously wetted with a contact angle of 0°. Interestingly, the contact angle was found to decrease slowly until 116° (4.6 wt % of PLLA-*b*-CGGRGDS) and then dramatically reduce until H_2O droplet was soaked into the fiber mesh (contact angle of 0°). For microstructured surfaces such a behavior can be probably explained by the reduction of the surface energy or polarity to a critical value, which has to be undershot to enable capillary forces to soak the droplet into the fiber mesh.

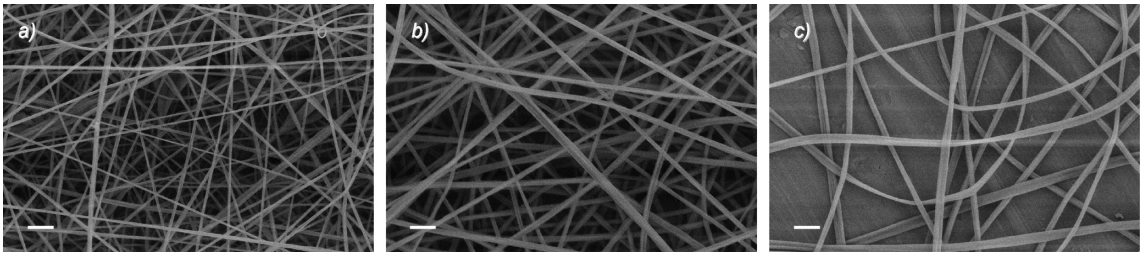


Figure 4. SEM images of fibers prepared at from 3% w/v solutions, indicating fiber mesh with different fiber diameters at variable PLLA-*b*-CGGRGDS concentration (a) 4.8, (b) 9.1, and (c) 18 wt % (solid ratio: PLLA-*b*-CGGRGDS-conjugate/total solid content, solution concentration: PLGA content/volume $CHCl_3$/MeOH (3:1); parameters: 1 mL/h, 7−10 cm, 7−8 kV, 28%; scale bars = 2 μm).

The contact angle measurements agreed well with the XPS measurements, indicating a similar change of contact angles and nitrogen contents as a function of PLLA-*b*-CGGRGDS concentration. In contrast, films produced by spin-coating presented only a slight decrease in contact angle from 72° to 50° when increasing the bioconjugate content from 2 to 9.1 wt %. This might be due to structural differences, e.g., surface roughness between the planar film and fibrous 3D mesh morphology. However, these findings together with the different evolution of the nitrogen surface content over peptide conjugate concentration for fibers and films suggests a different phase separation process. This distinction can be rationalized by a different confinement and faster solvent evaporation when comparing electrospinning to spin-coating. Therefore, the phase behavior commonly reported in spin-coated or casted films cannot be compared with the phase separation of block copolymers in electrospun fibers, which take place under non-equilibrium conditions.[55−57]

To imitate more closely the native microenvironment of cells, it is necessary to increase the mesh surface area by preparing thinner fibers.[58] In addition, thinner fibers lead to a decreased transport distance and therefore might enhance segregation of the polymer−peptide conjugate to the fiber surface. Reduction of the fiber diameter in electrospinning is typically achieved by a decrease in solution concentration. Reducing the PLGA concentration from 5 to 3% w/v, while keeping the relative amount of the bioconjugate constant at 2 wt %, decreases the electrospun fibers' diameter from 690 ± 190 to 270 ± 90 nm (3% w/v) (cf. Supporting Information, Figure S4). As the concentration was decreased, viscosity and resistance are lowered, which reduced the fiber diameter by increased fiber stretching. Electrospinning of 3% w/v solutions relative to PLGA but differing in the PLGA/peptide−polymer conjugate ratio (cf. Figure 4) resulted in fibers with an appropriate reduction in fiber diameter (Figure 4b vs Figure 2b). Using solid weight compositions of 4.8, 9.1, and 18 wt % bioconjugate led to the formation of meshes with fiber diameters between the 230 ± 40, 340 ± 50, and 360 ± 80 nm, respectively. The differences in fiber diameter can be explained by the viscosity increase overlaying the conductivity raise (cf. Supporting Information, Table S1/2).

The contact angle measurements displayed the hydrophilic surfaces of fiber mats made of 9.1 and 18 wt % bioconjugate and suggested the accessibility of the peptide at the upper layer of the fiber surfaces. However, the quantitative analysis of the enrichment of the peptide at the fiber surface by XPS measurements could not be performed with the required accuracy because thermal softening of the smaller fibers could not be avoided during analysis (occurrence was seen in SEM micrographs, data not shown).

Considering the aforementioned biological interactions between integrins and the RGD epitope, it is critical to determine the availability of adhesive sites on each fiber to ensure effective cell adhesion. To reveal the presence of polar chemical groups on the surface of single fibers, an attempt to directly probe the exposure of the peptide segment was performed. Electrostatic surface interactions between a single nanofiber and a colloidal silica probe were investigated, using colloidal-probe atomic force microscopy (AFM). Colloidal probe AFM reads the contact area of approximately 100 × 100 nm^2, which strongly overcame the lateral resolution compared to the 0.3 × 0.7 mm^2 resolution of the XPS measurements.

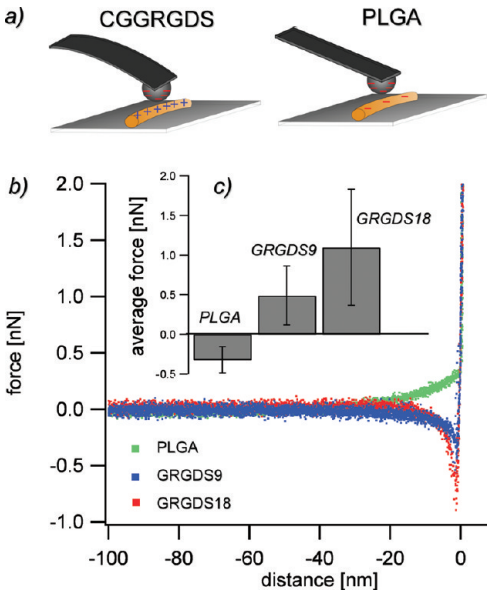


Figure 5. (a) Schematics describing the colloidal interaction probing for an GRGDS-functional and PLGA fiber. (b) Resulting force−displacement curves for a silica bead and GRGDS-functional fiber compared to PLGA fiber. (c) Adhesion force as a function of PLLA-*b*-CGGRGDS content are shown (0, 9, and 18 wt %).

The experiment takes place under water and involves the approach of a colloidal probe toward the fiber surface until contact is made. While the AFM tip approached the force was measured by deflection of the cantilever and the known cantilever spring constant. In this set of measurements single fibers made of PLGA and two different bioconjugate/PLGA blends (9.1 and 18 wt %) were probed with a silica bead of 10 μm in diameter in aqueous solution. To render attractive electrostatic probe−sample interactions possible, the pH was set to 4 and thereby charging the peptide segment positively due to the protonation of the side chains of arginine, aspartic acid, N-terminal amine of cysteine, and C-terminal carboxylic acid (net charge of +1.3 as calculated by Sednterp, V1.09). Because of the isoelectric point of silica of pH∼ 2, the silica probe is then negatively charged.[59] As schematically shown in Figure 5a, the peptide-functional fibers should attract the silica bead in contrast to the pure PLGA fibers, which are neutral or slightly negative. As predicted,

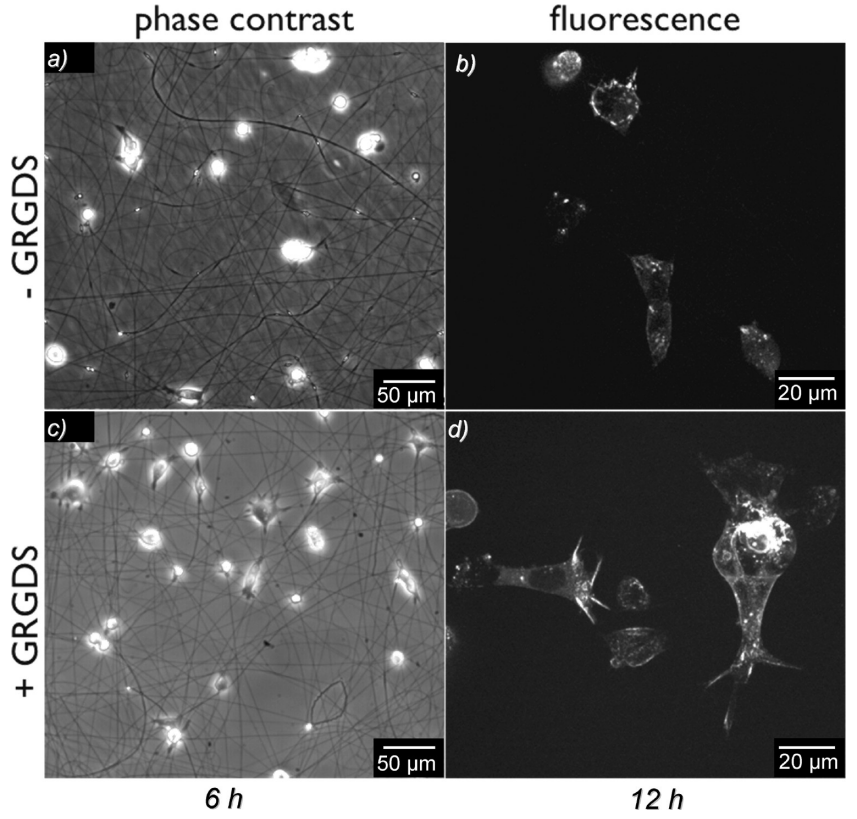


Figure 6. Phase contrast microscopy images of GFP-labeled ILK murine fibroblasts seeded in low serum-containing culture medium onto (a) pure and (c) GRGDS-functionalized PLGA fiber meshes after 6 h in culture. Confocal fluorescent microscopy images of the same cells grown for 12 h on (b) pure and (d) GRGDS-functionalized PLGA fibers.

the force− displacement curves from the interaction between the CGGRGDS-functionalized fibers and the 10 μm sized silica bead show clearly an attractive electrostatic interaction (Figure 5b). The force curves represent approach cycles, where the probe was driven from aqueous solution toward the fiber surface. Distinct attractive interactions emerged at a distance of ~10 nm by bending the cantilever actively toward the fiber surfaces. These attractive interactions are increased while raising the bioconjugate content in the fiber, reflecting the presence of more peptides on the fiber surface, which mediate an enhanced attraction between fiber and probe (Figure 5c). In contrast to this, repulsive interactions were observed for PLGA fibers. This can be attributed to a partially negatively charged PLGA surface due to carboxyl groups derived from degradation and polymer end groups (Figure 5b). Overall, small repulsive forces were observed for PLGA fibers whereas adhesion was monitored for GRGDS-functionalized fibers, where doubling peptide insertion resulted in an increase of the adhesive forces by more than 2 times. This clearly indicates the accessibility of the peptide on the fiber surface.

So far, three different characterization methods suggested the successful enrichment and availability of the PLLA-*b*-CGGRGDS bioconjugate at the PLGA fiber surface. To clarify the mechanism behind the peptide surface enrichment, the solutions used for electrospinning were investigated with dynamic light scattering (DLS) to determine the structure occurrence of the peptide−polymer conjugate. Solutions containing 3% w/v PLGA and 18 wt % peptide−polymer conjugate with respect to the PLGA (solid composition) were investigated. To elucidate the effect of the solvent, both chloroform/methanol solutions and pure chloroform solutions of the polymer blends were compared. It was anticipated that the peptide segment of the bioconjugate will aggregate in chloroform as assembly is driven due to ion and hydrogen bonding interactions. The PLLA block of the bioconjugate is well solubilized by the chloroform and probably will stabilize micelle formation. The addition of methanol—as a good solvent for peptides—should result in a more dynamic system. At the appropriate solvent ratio, the dissolution−aggregation equilibrium of the peptide−polymer conjugate might be shifted to a molecularly dissolved state (unimers). DLS roughly confirms this hypothesis by indicating different classes of aggregates depending on the solvent used (cf. Supporting Information, Figure S5). While both solvent systems include smaller species with comparable hydrodynamic radii (R_h) of 6 nm ($CHCl_3$) and 7 nm ($CHCl_3$/MeOH), the $CHCl_3$ system exhibited additionally larger species with R_h of 140 nm. Measuring pure PLGA in $CHCl_3$ resulted in no detectable signals (data not shown), implying a rather close dn/dc compared to $CHCl_3$ and suggesting that the measurable specie can be attributed to the bioconjugate. It is important to note that as the DLS measurements are size-weighted, therefore the number-dominating species are typically small species. However, the peak at R_h = 140 nm of the peptide−polymer conjugate/PLGA solution in chloroform might show the intrinsic characteristics of the system to form aggregates. While the $CHCl_3$/MeOH system suggests more unimers or smaller dynamic assemblies of the bioconjugate, the pure $CHCl_3$ solvent promotes aggregate formation.

For the electrospinning of PLGA/PLLA-*b*-CGGRGDS/PLGA solutions, the situation becomes more complex as solvent is gradually removed within the process. However, it appears to be straightforward to speculate that the tendency of the bioconjugate to aggregate in chloroform might lead to an overall slower diffusion constant, preventing the segregation to the surface and leaving it entrapped within the fiber bulk. In addition, even if the aggregates are surface segregated, the polar peptide part would not be available as it would be associated (i.e., inverse micelle).

In contrast, the bioconjugates in the chloroform/methanol mixture are better solvated, and it is believed to be dynamic enough to promote surface segregation.

In addition to characterize the enrichment and availability of the peptide segment at the nanofiber surface, it is essential to test the bioactivity of the fiber meshes by using a biological system. The tripeptide RGD is a conserved fragment present in many matrix proteins, which are responsible for integrin-mediated cell adhesion.[19,25] Therefore, cell adhesion and growth were investigated on peptide-functionalized fibers. Fluorescent murine kidney fibroblasts were seeded on nonwovens spun from an 18 wt % PLLA-*b*-CGGRGDS/PLGA blend. To specifically validate the bioavailability of GRGDS on the fiber surface, fibroblasts with green fluorescent protein (GFP)-labeled integrin-linked kinase (ILK)[60] were cultured onto the GRGDS-functionalized meshes. In order to avoid cross-contributions from the glass substrates that support the meshes, passivation of the glass surface with poly(L-lysine-*g*-ethylene oxide)[46] was utilized for both mesh types. Moreover, cell cultures with low serum-containing medium (0.5% FBS) should reduce unspecific protein adsorption at the fiber surfaces and favor cells to interact exclusively with the fibers. The cell adhesion behavior was monitored for 12 h after seeding GFP-labeled ILK fibroblasts on peptide-functionalized meshes and nonfunctional PLGA control meshes (cf. Figure 6 and movie in the Supporting Information). As shown in Figure 6, cell attachment occurs specifically on fibers where cells form dynamic small protrusion to initiate further spreading. Exclusively GRGDS-functionalized fibers offer the appropriate environment for the cells to spread and to migrate. In these experiments, the fibers confined the cell spreading area and play the role of migrating tracks. Interestingly, the cells can adapt the fiber distribution to their convenience by pulling on them in order to migrate faster. After 6 h, the cells can form up to eight filopods on different fibers to spread on GRGDS-functionalized meshes. In contrast to this, the pure PLGA control fibers exhibit poor affinities for integrins, preventing cells to spread and to migrate effectively. After 12 h, the trend was even more dominant, mainly showing nonadherent rounded cells on the PLGA fibers (Figure 6b) and elongated adhesive cells exclusively localized on the GRGDS-functionalized fibers (Figure 6d). The investigated cell line exhibits fluorescently labeled ILK, an essential intracellular protein that links integrins to the cytoskeleton. Fluorescent microscopy reveals that cells can form stable adhesive sites guided by GRGDS-functionalized fibers (arrows in Figure 6d), whereas they cannot on the PLGA fibers (cf. Figure 6b). This observation clearly supports the availability and the bioactivity of the peptide segment on the PLLA-*b*-CGGRGDS/PLGA blend fibers.

A notable side aspect of the single-step process toward bioactive nanofibers is the direct production of PLGA fiber mats with hydrophilic surfaces. Nonfunctionalized PLGA fibers exhibit hydrophobic surfaces and often require additional postprocessing steps such as plasma treatment to increase wettability with aqueous media e.g. for cell growth studies. As indicated by a contact angle study, GRGDS-functionalized fiber mats composed of an 9.1 wt % PLLA-*b*-CGGRGDS/PLGA blend show instantaneous wetting with Dulbecco's Modified Eagle Medium (DMEM), whereas pure PLGA fiber meshes did not wet (cf. Supporting Information, Figure S6a vs S6b).

The direct production of hydrophilic PLGA-fiber meshes appears to be promising for more advanced tissue engineering strategies like *in situ* step-by-step creation of fiber−cell−fiber sandwich or composite constructs. In order to investigate cell behavior in response to potential solvent remains or adverse effects of remaining charges, murine fibroblast L929 proliferation was examined. Cells were grown on tissue culture plates in advance, and fibers were directly electrospun into the cell culture (cf. Supporting Information, Figure S7a). No indication for a disturbed cell proliferation could be found on the cell culture after 1, 2, or 4 days (cf. Figure S7 and data not shown). The cells behaved similar to controls, where direct spinning took not place (cf. Figure S7b). In contrast to the nonwetted PLGA fibers, the fully wetted GRGDS-functionalized fiber meshes have a hydrogel-like topology, which appears to be of advantage for cell penetration. Taking advantage of this feature the creation of fiber−cell−fiber sandwich structures is currently ongoing.

Conclusion

In summary, a single step approach was demonstrated to produce bioactive fibers with a simple electrospinning setup, making post-treatment obsolete. Using a single-syringe setup and spinning a homogeneous solution of poly(lactic-*co*-glycolic acid) (PLGA) and a poly(L-lactic acid)-*block*-CGGRGDS peptide conjugate leads to an 11 times enrichment of the polar peptide segment on the fiber surface as compared to the homogeneous distribution of both components in the fiber bulk. This was confirmed by XPS, contact angle, and AFM measurements. Ultimately, GRGDS-functionalized fiber meshes showed a pronounced effect on cell adhesion as compared to pure PLGA fibers. This proved not only the availability of the peptide segment at the fiber surface but moreover showed its bioactivity. The resulting fiber meshes are promising cell culture substrates as they combine structural aspects with chemical functionality and potential mechanical properties that might be expected to lead to synergistic effects in a biological system. Furthermore, the instantaneous hydrophilicity offered by the fiber meshes makes the as-synthesized meshes attractive for cell infiltration and more sophisticated tissue engineering strategies.

Acknowledgment. The authors acknowledge M. Antonietti for his support. J. Brandt and K. Ostwald are thanked for the assistance with the polymer−peptide conjugate synthesis. A. Holländer is thanked for his support with the XPS measurements. A. Lankenau and Beate Morgenstern are thanked for their help with the L929 cell studies. The authors want to thank R. J. Spontak and X. Y. Sun for their initial study on field driven demixing. Purac (Gorinchem, Netherlands) is acknowledged for the generous gift of PLGA. R. Fässler and Korana Radovanac are thanked for providing GFP-labeled ILK murine fibroblasts. This work was granted by the joined program of Max Planck Society & Fraunhofer Society (MPG-FhG project on bioactive surfaces) and by the German Research Foundation (DFG, Emmy Noether Program BO 1762/2-3). J.P. acknowledges funding by the Marie Curie Action "Multi-PGNAs" under the European Community 7th Framework Programme FP7.

Supporting Information Available: Additional information about materials, synthesis, methods, and cell studies as well as SEM images, viscosity and conductivity measurements, and raw XPS composition. This material is available free of charge via the Internet at http://pubs.acs.org.

References and Notes

(1) Agarwal, S.; Wendorff, J. H.; Greiner, A. *Adv. Mater.* **2009**, *21*, 3343.
(2) von Graberg, T.; Thomas, A.; Greiner, A.; Antonietti, M.; Weber, J. *Macromol. Mater. Eng.* **2008**, *293*, 815.
(3) Liu, H.; Kameoka, J.; Czaplewski, D. A.; Craighead, H. G. *Nano Lett.* **2004**, *4*, 671.
(4) Ma, Z. W.; Kotaki, M.; Ramakrishna, S. *J. Membr. Sci.* **2005**, *265*, 115.
(5) Gentsch, R.; Boysen, B.; Lankenau, A.; Börner, H. G. *Macromol. Rapid Commun.* **2010**, *31*, 59.
(6) Garcia-Marquez, A.; Portehault, D.; Giordano, C. *J. Mater. Chem.* **2010**, DOI: 10.1039/C1030JM02612C.

(7) Lee, S.; Obendorf, S. K. *J. Appl. Polym. Sci.* **2006**, *102*, 3430.
(8) Gentsch, R.; Börner, H. G. *Adv. Polym. Sci.* **2010**, DOI: 10.1007/12_2010_80.
(9) Dalton, P. D.; Woodfield, T.; Hutmacher, D. W. *Biomaterials* **2009**, *30*, 2420.
(10) Ramakrishna, S.; Fujihara, K.; Teo, W.-E.; Lim, T.-C.; Ma, Z. *An Introduction to Electrospinning and Nanofibers*; World Scientific Publishing Co. Pvt. Ltd.: Singapore, 2005; p 275.
(11) Greiner, A.; Wendorff, J. H. *Angew. Chem., Int. Ed.* **2007**, *46*, 5670.
(12) Agarwal, S.; Greiner, A.; Wendorff, J. H. *Adv. Funct. Mater.* **2009**, *19*, 2863.
(13) Li, W.-J.; Laurencin, C. T.; Caterson, E. J.; Tuan, R. S.; Ko, F. K. *J. Biomed. Mater. Res.* **2002**, *60*, 613.
(14) Schindler, M.; Ahmed, I.; Kamal, J.; Nur-E-Kamal, A.; Grafe, T. H.; Chung, H. Y.; Meiners, S. *Biomaterials* **2005**, *26*, 5624.
(15) Mo, X. M.; Xu, C. Y.; Kotaki, M.; Ramakrishna, S. *Biomaterials* **2004**, *25*, 1883.
(16) Luu, Y. K.; Kim, K.; Hsiao, B. S.; Chu, B.; Hadjiargyrou, M. *J. Controlled Release* **2003**, *89*, 341.
(17) Khil, M. S.; Cha, D. I.; Kim, H. Y.; Kim, I. S.; Bhattarai, N. *J. Biomed. Mater. Res., Part B* **2003**, *67B*, 675.
(18) Patel, S.; Kurpinski, K.; Quigley, R.; Gao, H. F.; Hsiao, B. S.; Poo, M. M.; Li, S. *Nano Lett.* **2007**, *7*, 2122.
(19) Ruoslahti, E.; Pierschbacher, M. D. *Science* **1987**, *238*, 491.
(20) Hubbell, J. A. *Bio-Technology* **1995**, *13*, 565.
(21) Humphries, J. D.; Byron, A.; Humphries, M. J. *J. Cell Sci.* **2006**, *119*, 3901.
(22) Takagi, J. *Biochem. Soc. Trans.* **2004**, *32*, 403.
(23) Takahashi, S.; Leiss, M.; Moser, M.; Ohashi, T.; Kitao, T.; Heckmann, D.; Pfeifer, A.; Kessler, H.; Takagi, J.; Erickson, H. P.; Fassler, R. *J. Cell Biol.* **2007**, *178*, 167.
(24) Hersel, U.; Dahmen, C.; Kessler, H. *Biomaterials* **2003**, *24*, 4385.
(25) Hentschel, J.; Bleek, K.; Ernst, O.; Lutz, J. F.; Börner, H. G. *Macromolecules* **2008**, *41*, 1073.
(26) Liang, D.; Hsiao, B. S.; Chu, B. *Adv. Drug Delivery Rev.* **2007**, *59*, 1392.
(27) Agarwal, S.; Wendorff, J. H.; Greiner, A. *Macromol. Rapid Commun.* **2010**, *31*, 1317.
(28) Gentsch, R.; Pippig, F.; Nilles, K.; Theato, P.; Kikkeri, R.; Maglinao, M.; Lepenies, B.; Seeberger, P. H.; Börner, H. G. *Macromolecules* **2010**, *43*, 9239.
(29) Chua, K.-N.; Lim, W.-S.; Zhang, P.; Lu, H.; Wen, J.; Ramakrishna, S.; Leong, K. W.; Mao, H.-Q. *Biomaterials* **2005**, *26*, 2537.
(30) Grafahrend, D.; Heffels, K.-H.; Beer, M. V.; Gasteier, P.; Möller, M.; Boehm, G.; Dalton, P. D.; Groll, J. *Nat. Mater.* **2011**, *10*, 67–73.
(31) Sun, Z. C.; Zussman, E.; Yarin, A. L.; Wendorff, J. H.; Greiner, A. *Adv. Mater.* **2003**, *15*, 1929.
(32) Bhattarai, N.; Edmondson, D.; Veiseh, O.; Matsen, F. A.; Zhang, M. Q. *Biomaterials* **2005**, *26*, 6176.
(33) Ghasemi-Mobarakeh, L.; Prabhakaran, M. P.; Morshed, M.; Nasr-Esfahani, M.-H.; Ramakrishna, S. *Biomaterials* **2008**, *29*, 4532.
(34) Liu, S. J.; Kau, Y. C.; Chou, C. Y.; Chen, J. K.; Wu, R. C.; Yeh, W. L. *J. Membr. Sci.* **2010**, *355*, 53.
(35) Chew, S. Y.; Wen, J.; Yim, E. K. F.; Leong, K. W. *Biomacromolecules* **2005**, *6*, 2017.
(36) Lutz, J. F.; Börner, H. G. *Prog. Polym. Sci.* **2008**, *33*, 1.
(37) Börner, H. G.; Schlaad, H. *Soft Matter* **2007**, *3*, 394.
(38) Börner, H. G.; Kühnle, H.; Hentschel, J. *J. Polym. Sci., Part A: Polym. Chem.* **2010**, *48*, 1.
(39) Sun, X. Y.; Shankar, R.; Börner, H. G.; Ghosh, T. K.; Spontak, R. J. *Adv. Mater.* **2007**, *19*, 87.
(40) Ma, M. L.; Titievsky, K.; Thomas, E. L.; Rutledge, G. C. *Nano Lett.* **2009**, *9*, 1678.
(41) Kalra, V.; Lee, J.; Lee, J. H.; Lee, S. G.; Marquez, M.; Wiesner, U.; Joo, Y. L. *Small* **2008**, *4*, 2067.
(42) Xu, X. L.; Yang, L. X.; Xu, X. Y.; Wang, X.; Chen, X. S.; Liang, Q. Z.; Zeng, J.; Jing, X. B. *J. Controlled Release* **2005**, *108*, 33.
(43) Sy, J. C.; Klemm, A. S.; Shastri, V. P. *Adv. Mater.* **2009**, *21*, 1814.
(44) Pounder, R. J.; Stanford, M. J.; Brooks, P.; Richards, S. P.; Dove, A. P. *Chem. Commun.* **2008**, 5158.
(45) Ghosh, S. S.; Kao, P. M.; McCue, A. W.; Chappelle, H. L. *Bioconjugate Chem.* **1990**, *1*, 71.
(46) Kenausis, G. L.; Voros, J.; Elbert, D. L.; Huang, N. P.; Hofer, R.; Ruiz-Taylor, L.; Textor, M.; Hubbell, J. A.; Spencer, N. D. *J. Phys. Chem. B* **2000**, *104*, 3298.
(47) Mantovani, G.; Lecolley, F. o.; Tao, L.; Haddleton, D. M.; Clerx, J.; Cornelissen, J. J. L. M.; Velonia, K. *J. Am. Chem. Soc.* **2005**, *127*, 2966.
(48) Merrifield, R. B. *J. Am. Chem. Soc.* **1963**, *85*, 2149.
(49) Bognitzki, M.; Czado, W.; Frese, T.; Schaper, A.; Hellwig, M.; Steinhart, M.; Greiner, A.; Wendorff, J. H. *Adv. Mater.* **2001**, *13*, 70.
(50) Pai, C. L.; Boyce, M. C.; Rutledge, G. C. *Macromolecules* **2009**, *42*, 2102.
(51) Sun, X. Y.; Nobles, L. R.; Börner, H. G.; Spontak, R. J. *Macromol. Rapid Commun.* **2008**, *29*, 1455–1460.
(52) Thomas, R. R.; Anton, D. R.; Graham, W. F.; Darmon, M. J.; Sauer, B. B.; Stika, K. M.; Swartzfager, D. G. *Macromolecules* **1997**, *30*, 2883.
(53) Deitzel, J. M.; Kosik, W.; McKnight, S. H.; Tan, N. C. B.; DeSimone, J. M.; Crette, S. *Polymer* **2002**, *43*, 1025.
(54) Elman, J. F.; Johs, B. D.; Long, T. E.; Koberstein, J. T. *Macromolecules* **1994**, *27*, 5341.
(55) Cheng, G.; Böker, A.; Zhang, M.; Krausch, G.; Müller, A. H. E. *Macromolecules* **2001**, *34*, 6883.
(56) Goldacker, T.; Abetz, V.; Stadler, R.; Erukhimovich, I.; Leibler, L. *Nature* **1999**, *398*, 137.
(57) Thurn-Albrecht, T.; Steiner, R.; DeRouchey, J.; Stafford, C. M.; Huang, E.; Bal, M.; Tuominen, M.; Hawker, C. J.; Russell, T. *Adv. Mater.* **2000**, *12*, 787.
(58) Boudriot, U.; Dersch, R.; Greiner, A.; Wendorff, J. H. *Artif. Organs* **2006**, *30*, 785.
(59) Parks, G. A. *Chem. Rev.* **1965**, *65*, 177.
(60) Wickstrom, S. A.; Lange, A.; Montanez, E.; Fassler, R. *EMBO J.* **2010**, *29*, 281.

462 *Macromolecules* **2011**, *44*, 462–470
DOI: 10.1021/ma102569e

Macromolecules
ARTICLE

Nitroxide-Mediated Living/Controlled Radical Polymerization of *N*,*N*-Diethylacrylamide

Guillaume Delaittre,*,†,‡ Jutta Rieger,† and Bernadette Charleux*,§

†*UPMC Univ. Paris 6 and CNRS, Laboratoire de Chimie des Polymères, UMR 7610, 4, place Jussieu, Tour 44-54, 75252 Paris Cedex 05, France, and* §*Université de Lyon, Univ. Lyon 1, CPE Lyon, CNRS UMR 5265, Laboratoire de Chimie Catalyse Polymères et Procédés (C2P2), Equipe LCPP Bat 308F, 43 Bd du 11 novembre 1918, F-69616 Villeurbanne, France.* ‡ *Current address: Preparative Macromolecular Chemistry, Institut für Technische Chemie und Polymerchemie, Karlsruhe Institute of Technology (KIT), Engesserstr. 18, 76128 Karlsruhe, Germany*

Received November 10, 2010; Revised Manuscript Received December 12, 2010

ABSTRACT: Well-defined poly(*N*,*N*-diethylacrylamide)s were synthesized for the first time by nitroxide-mediated polymerization. The polymerizations were first performed in toluene solution, using BlocBuilder, a tertiary alkoxyamine based on the nitroxide SG1 (*N*-*tert*-butyl-*N*-[1-diethylphosphono-(2,2-dimethylpropyl)] nitroxide), as an initiator without initial free nitroxide. High monomer conversions were reached, up to completion and the number-average molar masses increased linearly with conversion. However the polydispersity indices (PDI) remained quite high, despite a constant diminution with increasing conversion until a value of 1.9 at high conversion. This could be corrected by the addition of free SG1 at the onset of the reaction, leading to PDI of 1.2 at 93% conversion in the best case. Various alkoxyamine concentrations were used to target different molar masses. The presence of SG1 functionality at the ω-end of the polymer chains was evidenced by size-exclusion chromatography coupled to electospray ionization mass spectrometry (SEC/ESI−MS) and the living character of the latter was proved by efficient chain extension with styrene or *N*,*N*-dimethylacrylamide.

Introduction

Among the range of monomers available to synthesize thermosensitive polymers, the acrylamide class is probably the most popular one, certainly because these monomers can be polymerized using a method as simple as radical polymerization. *N*-Isopropylacrylamide (NiPAAm) is the most studied monomer within this family. However a new trend seems to have recently emerged with the increasing use of *N*,*N*-diethylacrylamide (DEAAm). This can be explained by different features such as its liquid physical state at room temperature − which may be convenient in some applications − and its reactivity similar to that of *N*,*N*-dimethylacrylamide (DMAAm) in copolymerization,[1−3] the latter being undoubtedly a good candidate to replace acrylamide in the synthesis of neutral water-soluble polymers for toxicity reasons. Although only few studies show the biocompatibility[4,5] of poly(*N*,*N*-diethylacrylamide) (PDEAAm) and its lower toxicity compared to that of poly(*N*-isopropylacrylamide) (PNiPAAm),[6,7] it can be assumed that the degree of substitution of the acrylamide moiety is of first importance pertaining to this aspect. Regardless of the previous considerations, the temperature-dependent behavior of these two polyacrylamides can be a decisive factor when one aims at a specific application. Indeed, both exhibit a lower critical solution temperature (LCST) in aqueous solution around 32−33 °C, but the volume transition of PDEAAm is broader and more progressive.[8] This feature can be exploited when expansion of a gel or progressive release of an encapsulated compound is needed. In addition, a distinct difference in the structure of DEAAm with respect to NiPAAm is the absence of the N−H group as hydrogen bond donor. Hydrogen bonds between amide groups (N−H···O=C) may account for the nonreversibility of the temperature responsiveness in PNiPAAm.[9] DEAAm has already been employed to prepare hydrogels[10] and microgels.[11−14]

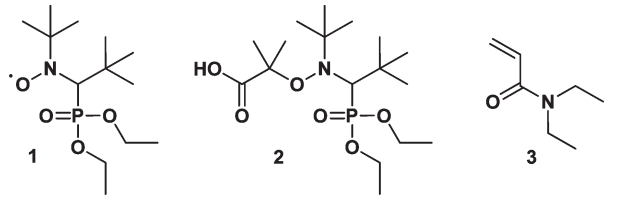
The field of controlled/living radical polymerization based on reversible deactivation of the propagating radicals[15] has shown an impressive growth during the last 15 years to constantly provide a better control over the composition, the structure, and the functionality of polymers.[16] Among all the techniques available, nitroxide-mediated polymerization (NMP) has the advantage of using a very simple system composed of few species: monomer, alkoxyamine playing the dual role of initiator and controlling agent, and solvent when needed. No metallic species are involved and purification of the monomers is not critical. Furthermore, the most commonly used nitroxides namely TEMPO (2,2,6,6-tetramethylpiperidine-1-oxyl), TIPNO (2,2,5-trimethyl-4-phenyl-3-azahexane-3-nitroxide), or SG1 *N*-*tert*-butyl-*N*-[1-diethylphosphono-(2,2-dimethylpropyl)] nitroxide, or alkoxyamines based on them are generally commercial or easy to synthesize.[17−25] Finally its main drawback, i.e., the need for high polymerization temperature, may be circumvented, in some circumstances, thanks to the recent development of photolabile alkoxyamines.[26,27] Recently the nitroxide SG1 has received most of the attention and several styrenic, (meth)acrylic and acrylamide monomers have already been (co)polymerized in a controlled fashion by SG1-mediated NMP.[28−41] The acrylamides have however been less studied despite the specific potential properties of their polymers like temperature-dependent water-solubility or high resistance to hydrolysis. The first attempt to control the polymerization of an acrylamide monomer via NMP was reported by Li and Brittain in 1998.[42] They used a bimolecular initiating system composed of

*Corresponding authors. (G.D.) Fax: +49(0)7216085740. Telephone: +49(0)7216083154. E-mail: guillaume.delaittre@kit.edu. (B.C.) Fax: +33(0)472431768. Telephone: +33(0)472431775. E-mail: bernadette.charleux@lcpp.cpe.fr.

 Published on Web 01/12/2011 © 2011 American Chemical Society

AIBN (2,2′-azobis(isobutyronitrile)) and TEMPO to polymerize DMAAm. When low molar mass polymers were targeted, high monomer conversion along with reasonable polydispersity indices could be reached. However it was possible neither to obtain high molar mass polymers with narrow distribution nor to reinitiate the polymerization with the addition of a second load of monomer. In 2000 and 2001, Fischer, Gnanou, and Hawker independently published successful results on the NMP of DMAAm in *N*,*N*-dimethylformamide (DMF) in presence of either SG1[43,44] or TIPNO.[45] In the same report Hawker also described the effective NMP of NiPAAm with TIPNO as well as did Studer with a highly sterically hindered TEMPO analogue.[46] Aldabbagh and co-workers reported the homopolymerization of *tert*-butylacrylamide (tBuAAm) at 120 °C in DMF with an AIBN/SG1 bimolecular initiating system and evidenced the occurrence of chain transfer to monomer, preventing the synthesis of living chains with number-average molar masses higher than 8000 g·mol^{-1}.[47] The same authors described the controlled copolymerization of tBuAAm and NiPAAm using not only the same initiating system, but also a polystyrene−SG1 macroalkoxyamine in the initial presence of free SG1 to obtain block copolymers.[48] In a high-throughput study aiming at designing a library of thermosensitive copolymers of hydroxypropyl acrylate with DMAAm or *N*-acryloylmorpholine (NAM), Hoogenboom and Schubert reported the successful homopolymerizations of DMAAm and NAM using the Arkema alkoxyamine BlocBuilder (Scheme 1) in conjunction with initial free SG1 at 110 °C in DMF.[49] Another important aspect of NMP is its relative tolerance to water. For example, Nicolay et al. managed to control the polymerization of sodium 4-styrenesulfonate (SSNa) in pure water thanks to a new water-soluble TIPNO analogue.[50] Shortly after, Grassl et al. reported a reasonable control over the aqueous polymerization of acrylamide using a bicomponent initiating system Vazo56 (2,2′-azobis(2-methylpropionamidine) dihydrochloride)/SG1,[51] and Phan and Bertin published results on the controlled polymerization of DMAAm, SSNa, and 2-(acryloyloxy)ethylbenzyldimethylammonium chloride in aqueous solution using BlocBuilder as the initiator.[52]

Scheme 1. Structures of the Nitroxide SG1 (1), the Alkoxyamine BlocBuilder (2), and the Monomer *N*,*N*-Diethylacrylamide (3)



This alkoxyamine, also called MAMA in diverse publications, bears a carboxylic acid function on the initiating fragment, allowing water-solubility[53] or facile α-end functionalization[54−57] (Scheme 1).

Using an SG1-capped poly(acrylic acid) macroalkoxyamine we have previously shown that the NMP of DEAAm could be successfully achieved in an aqueous dispersion polymerization process, toward the synthesis of temperature-sensitive nanogels.[13] However no kinetic study of the polymerization was performed. In this line, we focus here our attention on the nitroxide-mediated homopolymerization of DEAAm in solution in toluene using BlocBuilder as an alkoxyamine initiator. The aim of this work is to propose a better understanding of the NMP of DEAAm and to find the most appropriate conditions for the best control over molar mass, molar mass distribution and chain-end functionalization.

Experimental Part

Materials. *N*,*N*-Diethylacrylamide (DEAAm) was synthesized according to a previously reported procedure.[13,58] *N*,*N*-Dimethylacrylamide (DMAAm) and styrene were purchased from Sigma-Aldrich and distilled prior to use. The alkoxyamine BlocBuilder (99%) and the nitroxide SG1 (88.4%) were kindly supplied by Arkema. Toluene (Baker) was distilled over $CaCl_2$ and stored over molecular sieves (4 Å). *N*-Methylpyrrolidone (Sigma-Aldrich) and *N*,*N*-dimethylformamide (DMF, VWR Normapur) were HPLC-grade and filtered through a 200 nm filter prior to use.

Solution Polymerization of DEAAm. In a typical recipe (entry 4 in Table 1), DEAAm (2.4985 g, 19.7 mmol), BlocBuilder (151.4 mg, 397 μmol), and SG1 (11.5 mg, 34.6 μmol) were quickly dissolved in toluene (2.5205 g) in a beaker and introduced in a Schlenk tube. While being cooled in an ice bath, the medium was purged with argon for 30 min. It was then kept under argon atmosphere all along the reaction, which was started by introducing the tube in an oil bath preheated at 110 °C. Samples were withdrawn periodically. Aliquots of these samples were diluted in either deuterated chloroform or *N*-methylpyrrolidone for NMR or SEC characterizations, respectively.

PDEAAm Macroinitiator Synthesis. The method of preparation follows the same procedure as for the kinetic study with characteristics of entry 4 in Table 1 (vide supra). After 70 min, the polymerization solution was cooled down to room temperature and precipitated by dropwise addition in diethyl ether under vigorous stirring. After filtration, the polymer was recovered as a white solid and dried overnight under high vacuum: conversion = 0.54; theoretical number-average molar mass: $M_{n,th}$ = 3780 g·mol^{-1}; experimental

Table 1. Experimental Conditions and Kinetic Parameters for the Nitroxide-Mediated Homopolymerization of *N*,*N*-Diethylacrylamide in Toluene Solution (3.6 M) Initiated by the BlocBuilder Alkoxyamine

entry	symbol	T/°C	[BlocBuilder]/mM	$DP_{n,th}$	r^a/%	$k_p[P^\bullet]^b$/s^{-1}	$R^{2\,c}$	k_pK^d/s^{-1}
1	+	110	73.0	50	0	3.0×10^{-4}	0.9983	-
2	Δ	110	36.3	100	0	2.3×10^{-4}	0.9867	-
3	●	110	18.3	199	0	2.3×10^{-4}	0.9906	-
4	▲	110	72.8	50	8.7	1.5×10^{-4}	0.9976	1.3×10^{-5}
5	★	110	72.5	50	17.6	8.8×10^{-5}	0.9948	1.6×10^{-5}
6	×	110	36.5	99	4.9	2.4×10^{-4}	0.9964	1.1×10^{-5}
7	■	110	36.8	99	8.7	1.7×10^{-4}	0.9943	1.5×10^{-5}
8	○	110	36.2	100	17.7	9.0×10^{-5}	0.9924	1.6×10^{-5}
9	□	110	9.0	404	8.9	1.5×10^{-4}	0.9883	1.3×10^{-5}
10	♦	110	18.2	200	17.6	7.8×10^{-5}	0.9983	1.4×10^{-5}
11	⬡	110	9.0	403	17.7	1.1×10^{-4}	0.9899	2.0×10^{-5}
12	◊	105	72.4	50	0	1.4×10^{-4}	0.9977	-
13	⬢	95	71.7	51	0	5.2×10^{-5}	0.9939	-

[a] $r = [SG1]_0/[BlocBuilder]_0$. [b] $k_p[P^\bullet]$ is the slope of the $\ln(1/(1-x))$ vs time plot in the linear region. [c] R^2 is the coefficient of determination for the linear regression of the $\ln(1/(1-x))$ vs time plot in the linear region. [d] k_pK was calculated according to eq 2 from the slope of the $\ln(1/(1-x)$ vs time plots.

number-average molar mass (SEC/*N*-methylpyrrolidone, PS calibration): $M_{n,exp} = 2900\ g \cdot mol^{-1}$ and polydispersity index: PDI = 1.18.

Chain Extension with *N*,*N*-Dimethylacrylamide. DMAAm (1.0059 g, 10.1 mmol) and the PDEAAm macroinitiator (0.1514 g) were dissolved in toluene (1.1563 g). The mixture was introduced in a Schlenk tube and purged with argon for 30 min. The reaction was then performed under argon atmosphere and initiated by introducing the tube in an oil bath preheated at 110 °C. After 16 h, the reaction was stopped by cooling down the tube. An aliquot of the raw polymerization mixture was diluted in *N*-methylpyrrolidone for SEC characterization: $M_{n,exp} = 17300\ g \cdot mol^{-1}$ and PDI = 1.96.

Chain Extension with Styrene. The PDEAAm macroinitiator (0.1508 g) was dissolved in styrene (1.0020 g, 9.6 mmol). The mixture was introduced in a Schlenk tube and purged with argon for 30 min. The reaction was then performed under argon atmosphere and initiated by introducing the tube in an oil bath preheated at 120 °C. After 16 h, the reaction was stopped by cooling down the tube. An aliquot of the raw polymerization mixture was diluted in *N*-methylpyrrolidone for SEC characterization: $M_{n,exp} = 19050\ g \cdot mol^{-1}$ and PDI = 1.30.

Analytical Techniques. ^{1}H NMR spectroscopy was used to determine the conversion of monomer to polymer by relative integration of the vinylic protons compared to the protons at the α position of the nitrogen atom in both the monomer and the polymer repeat unit (see Figure S1 in the Supporting Information). The spectra were recorded on a Bruker DPX300 spectrometer at room temperature using $CDCl_3$ as a solvent. Chemical shifts are reported in ppm (δ) relative to tetramethylsilane as an internal standard. Size exclusion chromatography (SEC) was performed on two different apparatuses. The routine single-detection measurements were realized on a Shimadzu Prominence SEC system with a differential refractive index (RI) detector. *N*-Methylpyrrolidone was used as the eluent at 1 $mL \cdot min^{-1}$ and 60 °C through a guard column and a PL gel 5 mm mixed D column. Molar masses (M_n = the number-average molar mass; M_w = the weight-average molar mass and PDI = M_w/M_n, the polydispersity index) were determined using polystyrene standards. The triple-detection additional measurements were performed in DMF with added LiBr (1 $g \cdot L^{-1}$) at 60 °C and a flow rate of 0.8 $mL \cdot min^{-1}$. The steric exclusion was carried out on a PSS GRAM precolumn, two PSS GRAM 1000 Å columns (8 × 300 mm; separation limits, 1 to 1000 kg mol^{-1}) and one PSS GRAM 30 Å (8×300 mm; separation limits: 0.1 to 10 kg mol^{-1}). The detection was composed of two apparatuses: a Viscotek dual detector refractometer/viscometer Model 250 thermostated at 50 °C and a Wyatt Technologies MiniDAWN Static Light Scattering Detector operating at 3 different angles (45°/90°/135°) with a He−Ne laser (690 nm). The number-average molar masses, M_n, of the polymers were calculated from combined LS (light scattering), RI and viscometer signals (triple detection) with the OmniSEC 4.2 software, using an average refractive index increment (dn/dc) of 0.073 $mL \cdot g^{-1}$ previously determined using a PSS DnDc2010/620 differential refractometer.

The mass spectrum of the DEAAm oligomer (oligoDEAAm) was recorded on an LXQ mass spectrometer (ThermoFisher Scientific, San Jose, CA) equipped with an atmospheric pressure ionization source operating in the nebulizer assisted electrospray mode. The instrument was calibrated in the m/z range 195−1822 using a standard containing caffeine, Met-Arg-Phe-Ala acetate (MRFA) and a mixture of fluorinated phosphazenes (Ultramark 1621) (all from Aldrich). A constant spray voltage of 4.5 kV and a dimensionless sweep gas flow rate of 2 and a dimensionless sheath gas flow-rate of 12 were applied. The capillary voltage, the tube lens offset voltage and the capillary temperature were set to 60 V, 110 V and 275 °C respectively. The LXQ was coupled to a Series 1200 HPLC-system (Agilent, Santa Clara, CA) consisting of a solvent degasser (G1322A), a binary pump (G1312A), a high-performance autosampler (G1367B), followed by a thermostated column compartment (G1316A). Separation was performed on two mixed bed size exclusion chromatography columns (Polymer Laboratories, Mesopore 250 × 4.6 mm, particle diameter 3 mm) with precolumn (Mesopore 50 × 4.6 mm) operating at 30 °C. THF at a flow rate of 0.30 $mL \cdot min^{-1}$ was used as the eluent. The mass spectrometer was coupled to the column in parallel to an RI-detector (G1362A with SS420x A/D) in a setup described previously.[59] 0.27 $mL \cdot min^{-1}$ of the eluent were directed through the RI-detector and 30 $\mu L \cdot min^{-1}$ infused into the electrospray source after postcolumn addition of a 100 μM solution of sodium iodide in methanol at 20 $mL \cdot min^{-1}$ by a microflow HPLC syringe pump (Teledyne ISCO, Model 100DM). 20 μL of a polymer solution with a concentration of approximately 3 $mg \cdot mL^{-1}$ were injected into the HPLC system. Data treatment was performed, using a previously described procedure.[59]

Results and Discussion

Selection of Experimental Conditions. Polymerization of DEAAm in presence of the molecular alkoxyamine BlocBuilder was carried out in bulk first at 120 °C and then at 80 °C. The targeted M_n at full conversion was 15000 $g \cdot mol^{-1}$. For both temperatures, the reaction was highly exothermic, as demonstrated by the expulsion of the septum after 5 min in both cases. The conversion was found to be almost complete with M_n determined by triple-detection SEC close to the theoretical values (13200 and 12550 $g \cdot mol^{-1}$, respectively) but rather large PDIs (1.76 and 1.68, respectively). It can be found in the literature that acrylamide and acrylamide derivatives have rather high propagation rate constants, k_p.[60] For instance, k_p of acrylamide and NiPAAm determined by pulsed-laser polymerization coupled to SEC range from 10^4 to $9 \times 10^4\ L \cdot mol^{-1} \cdot s^{-1}$ depending on the temperature,[61−63] which is almost an order of magnitude larger than the values reported for the acrylates.[64] Interestingly Eggenhuisen et al. reported that DMAAm and NAM polymerized faster than 2-hydroxypropyl acrylate in SG1-mediated polymerization.[49] We then decided to conduct our study in solution to minimize this effect by reducing the monomer concentration. Toluene was chosen since it is a good solvent for the monomer−it is actually the solvent used for its synthesis−as well as the polymer, the alkoxyamine BlocBuilder, and the nitroxide SG1. It has also a convenient boiling point (111 °C at atmospheric pressure); i.e., it is sufficiently high to perform nitroxide-mediated polymerization, but not too high to allow easy evaporation. Furthermore, the use of a solvent facilitates the sampling, in the case of a polymer of a rather high T_g (for PDEAAm, T_g = 85.5 °C),[65] and thus the reaction monitoring. In this study the concentration of monomer was kept constant and equal to 3.6 $mol \cdot L^{-1}$, i.e., 50% w/w. Only the concentrations of free SG1 and alkoxyamine were varied. The polymerizations were mostly performed at 110 °C, which is in the typical temperature range for NMP. Details on the experimental conditions can be found in Table 1.

Effect of the Initial Concentration of Free SG1. As mentioned before, acrylamide derivatives are known to have high propagation rate constants and therefore, their NMP should be conducted in a similar manner to that of acrylates. In the latter case indeed it has been previously shown that the addition of a few percents of free nitroxide relative to the alkoxyamine at the onset of the reaction could help to obtain

a better control in SG1-mediated homopolymerization.[66] It is particularly the case when using an alkoxyamine in which the nitroxide is bound to the initiating fragment by a secondary radical.[30,31] In the present study we used the tertiary alkoxyamine BlocBuilder, which already proved to be able to control the polymerization of *n*-butyl acrylate in bulk without the need for added free SG1, owing to a higher dissociation rate constant.[21,67] In this case a large amount of SG1 is released in the very first instants of the polymerization and allows the rapid establishment of the persistent radical effect.[68]

A first attempt was thus made to control the polymerization of DEAAm without free SG1 (entry 2, Table 1) with a target number-average polymerization degree (DP_n) of 100. The polymerization was rather fast, reaching 90% of conversion in ca. 1.5 h following a first order kinetics (see Figure 1 and values of R^2 in Table 1) with a constant radical concentration throughout the reaction. The linear evolution of the number-average molar masses with monomer conversion (Figure 1) confirmed the controlled character of the polymerization. Nevertheless the polydispersity indices remained rather high, though decreasing in the course of the polymerization (1.88 at 92% conv.). To obtain a fully controlled character, we then introduced different amounts of free SG1 in the initial mixture. Molar ratios of free SG1 to BlocBuilder, *r*, were 0.05, 0.09, and 0.18. The polymerization rate was clearly decreased and again the curve representing $\ln(1/(1-x))$ (with *x* the fractional monomer conversion) as a function of time was linear (see Figure 1 and R^2 values in Table 1). The effect of the initial SG1 concentration is in agreement with its participation in the polymerization process, i.e., with the existence of an activation−deactivation equilibrium which controls the polymerization kinetics[69] (eq 1) (Scheme 2).

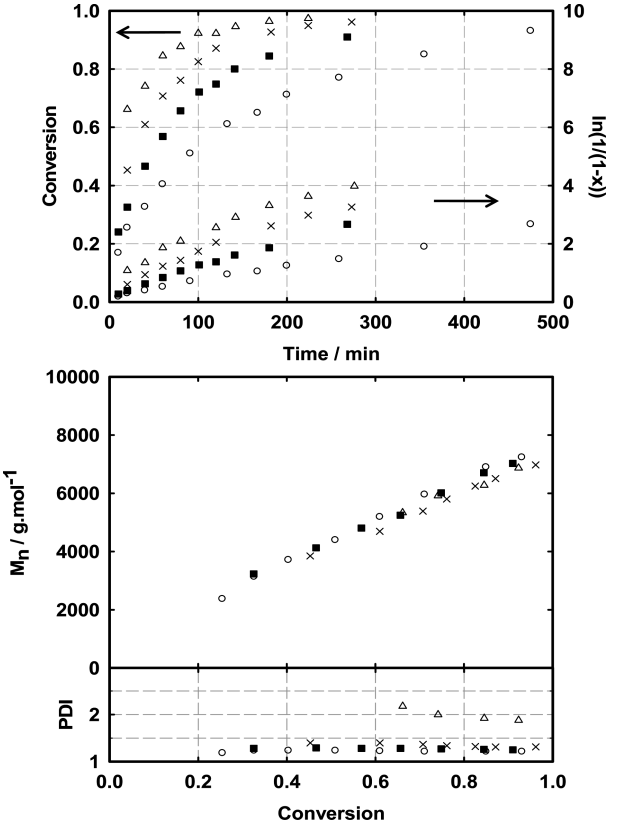


Figure 1. (Top) Conversion vs time and first-order kinetic plots for the NMP of DEAAm in toluene at 110 °C. Conditions: [DEAAm] = 3.6 M, [BlocBuilder] = $3.6 \times 10^{-2} - 3.7 \times 10^{-2}$ M with different initial concentrations in free SG1; (Δ) entry 2, $r = 0$; (×) entry 6, $r = 0.05$; (■) entry 7, $r = 0.09$; (○) entry 8, $r = 0.18$. (Bottom) Corresponding evolution of number-average molar masses and polydispersity indices (determined by SEC in *N*-methylpyrrolidine with a PS calibration) vs conversion.

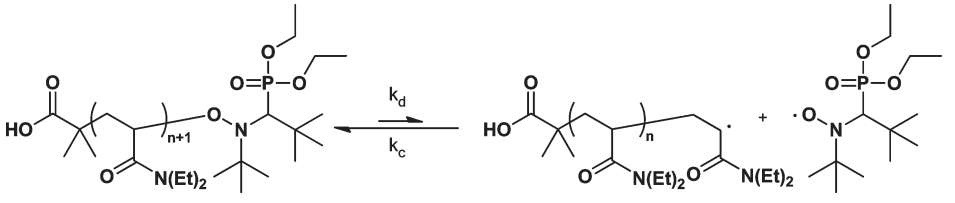
$$K = \frac{k_d}{k_c} = \frac{[P^\bullet][SG1]}{[P-SG1]} \quad (1)$$

In eq 1, *K* is the activation−deactivation equilibrium constant (Scheme 2), k_d is the rate constant of dissociation of the alkoxyamine, k_c is the rate constant of recombination between the propagating radicals and the nitroxide, [P•] is the concentration of propagating radicals, [SG1] is the concentration of free nitroxide, and [P−SG1] is the concentration of poly(*N*,*N*-diethylacrylamide)-based alkoxyamine.

As expected, no significant effect on the molar masses was observed. It shows that the polymerization takes place with fast initiation and a constant chain concentration, supposedly and ideally equal to the initial concentration of alkoxyamine ([P−SG1] = $[BlocBuilder]_0$). The effect of added SG1 was however noticeable on the quality of the molar mass distributions. The polydispersity indices were considerably decreased (Figure 1), remaining lower than 1.4 throughout the polymerization for all experiments and reaching 1.2 at 93% of conversion for the highest *r* value (entry 8). Figure 2 illustrates the constant increase in molar masses along with the monomer conversion with the shift of the chromatograms toward the lower elution volumes. The decrease of polydispersity indices induced by the addition of free SG1 is also evidenced by the progressive narrowing of the peaks from Figure 2a to Figure 2d. Consequently, even when a small amount ($r = 0.05$) of free SG1 was used, all the criteria for a controlled free-radical polymerization were met in the conditions used here. The advantage of a higher concentration of added free SG1 is that the polymerization is sufficiently slowed down, allowing one to stop it at a certain conversion, and thus to obtain the precise desired molar mass. We observed the same trends in a series of experiments where the concentration of alkoxyamine was doubled (See Supporting Information, Figure S2).

Effect of the Initial Alkoxyamine Concentration. Two sets of experiments were performed to determine the effect of the alkoxyamine concentration on the polymerization. The first one was carried out with $r = 0.09$ (Table 1, entries 4, 7, and 9) and the second one with $r = 0.18$ (Table 1, entries 5, 8, 10, and 11). Evolution of the kinetics and macromolecular characteristics are, respectively for these two series of experiments, depicted

Scheme 2. Activation−Deactivation Equilibrium in Nitroxide-Mediated Free-Radical Homopolymerization of DEAAm



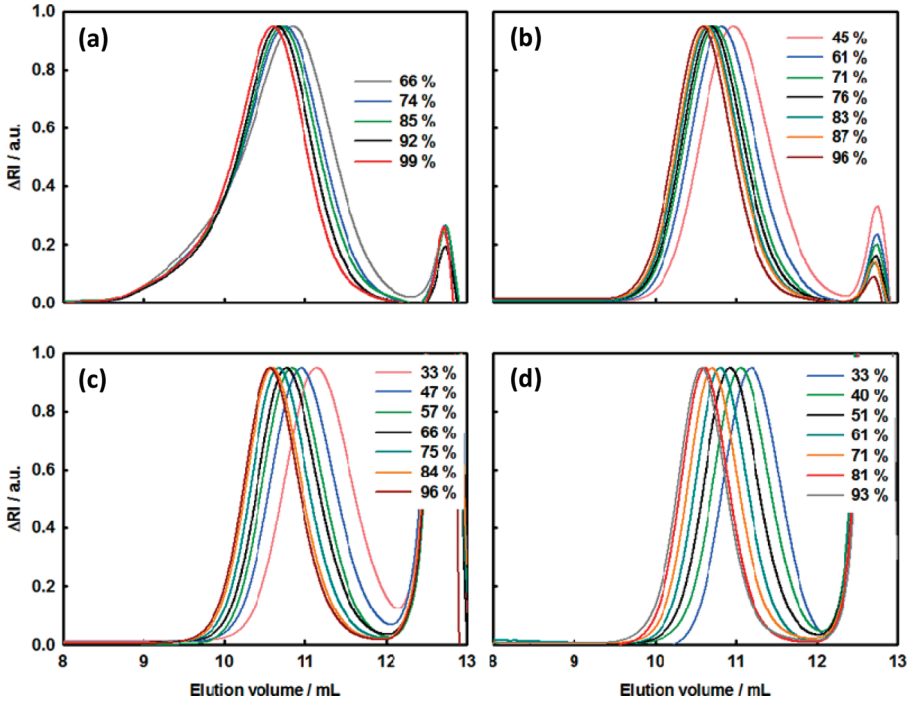


Figure 2. Size-exclusion chromatograms in *N*-methylpyrrolidone of PDEAAm obtained by NMP in toluene at 110 °C at different monomer conversions. Conditions: [DEAAm] = 3.6 M, [BlocBuilder] = 3.6×10^{-2} to 3.7×10^{-2} M with different initial concentrations in free SG1; (a) entry 2, $r = 0$; (b) entry 6, $r = 0.05$; (c) entry 7, $r = 0.09$; (d) entry 8, $r = 0.18$ (see Table 1).

on Figures 3 and 4. Both series revealed the same trends as experiments without added free SG1 (see Supporting Information, Figure S3). Whereas the variation in alkoxyamine concentration did not have a strong effect on the kinetics, its influence was much more noticeable on the macromolecular characteristics. Indeed, and as expected, at a given monomer conversion, the lower the initial alkoxyamine concentration, the higher the molar mass. Even for the lowest concentration of BlocBuilder, M_n increased linearly with monomer conversion. However the molar mass distributions were not as narrow as those obtained with the higher alkoxyamine initial concentrations. Indeed for [BlocBuilder] = 9 mM, the polydispersity indices remained higher than 1.4. On the contrary, when high concentrations of alkoxyamine were used, i.e., when a DP_n of 50 was targeted, PDI never exceeded 1.12 – at least between 28 and 87% of conversion. Such a trend is not the one normally expected from the theoretical description[70] but may be related to the existence of potential side reactions like transfer, although not clearly observed in this work. Figure 5 illustrates the controlled character of the polymerization through the constant and complete shift of the peaks, as well as the narrowing of the molar mass distributions with an increasing concentration of alkoxyamine.

Effect of the Polymerization Temperature. The alkoxyamine BlocBuilder decomposes very easily, with a half-life time of only 15 h at room temperature and a decomposition rate constant k_d equal to 0.3 s^{-1} at 120 °C.[21,67] We wanted then to see if it would be possible to carry out the polymerization at temperatures below 110 °C. We thus conducted a series of experiments with a targeted DP_n of 50 and without free SG1 at 110, 105, and 95 °C. While it is clear that the polymerization was slowed during the whole course on the reaction, it appeared that the rates of polymerization were still rather high since in the first instants of the polymerization the conversion was already very high (Figure 6). We could not see any effect of the temperature on the macromolecular characteristics of the formed PDEAAm. Other experiments

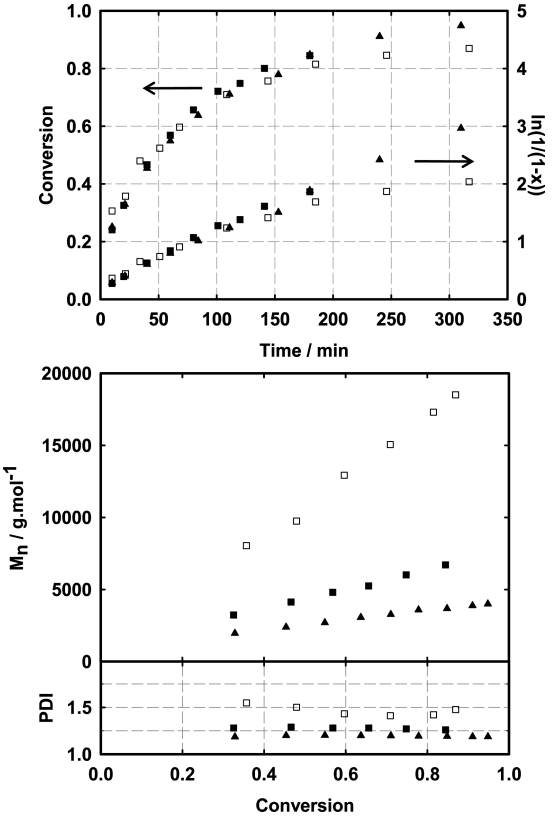


Figure 3. (Top) Conversion vs time and first-order kinetic plots for the NMP of DEAAm in toluene at 110 °C. Conditions: [DEAAm] = 3.6 M, $r = 0.09$ with different initial alkoxyamine concentrations; (▲) entry 4, [BlocBuilder] = 72.8 mM; (■) entry 7, [BlocBuilder] = 36.8 mM; (□) entry 9, [BlocBuilder] = 9.0 mM. (Bottom) Corresponding evolution of number-average molar masses and polydispersity indices (determined by SEC in *N*-methylpyrrolidone with a PS calibration) vs conversion.

could have been carried out at even lower temperatures but it would have been at the expense of reaction time. However it seems that the high lability of the alkoxyamine BlocBuilder combined with the high propagation rate constant of DEAAm makes the fully controlled SG1-mediated polymerization rather difficult to obtain without an initial amount of free SG1, even at low temperature.

Polymerization Kinetics. All polymerizations achieved large conversions, typically 85−99 mol % within 3 to 7 h. The slopes of $\ln(1/(1-x))$ vs time, giving $k_p[P^\bullet]$, were determined in the linear region (typically up to 80% conv.) and are reported in Table 1. For the experiments carried out with an initial amount of free SG1, the k_pK values can be roughly estimated (Table 1) from $k_p[P^\bullet]$ according to eq 2 (because the initial concentration of free SG1 was large, the amount of this nitroxide released owing to the persistent radical effect could be neglected, and thus [SG1]/[P−SG1] remains close to $r = [SG1]_0/[BlocBuilder]_0$).

$$k_pK = k_p\frac{[P^\bullet][SG1]}{[P-SG1]} \approx k_p[P^\bullet]r \qquad (2)$$

All k_pK were found to be in the same range, i.e., 1.1×10^{-5} to 2.0×10^{-5} s^{-1}. With k_p close to 10^5 $L \cdot mol^{-1}.s^{-1}$,[60−63] K

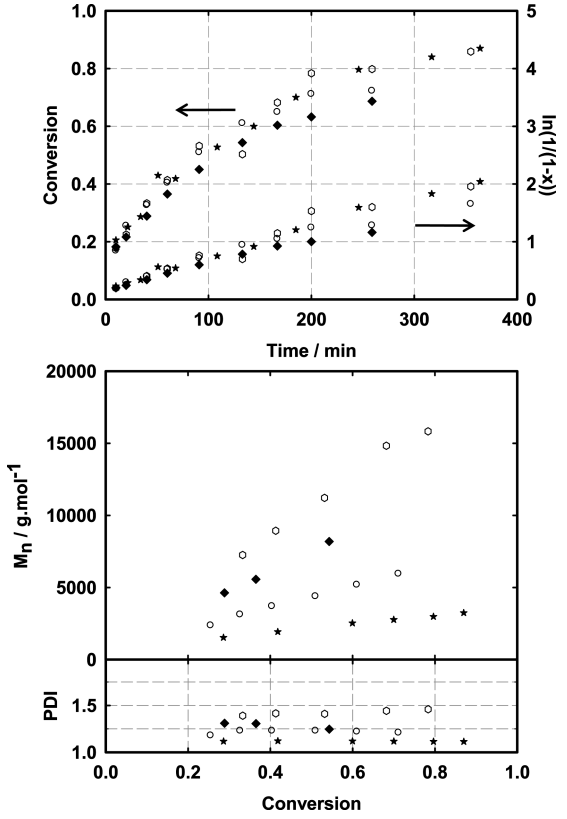


Figure 4. (Top) Conversion vs time and first-order kinetic plots for NMP of DEAAm in toluene at 110 °C. Conditions: [DEAAm] = 3.6 M, r = 0.18 with different initial alkoxyamine concentrations; (★) entry 5, [BlocBuilder] = 72.5 mM; (○) entry 8, [BlocBuilder] = 36.2 mM; (♦) entry 10, [BlocBuilder] = 18.2 mM; (⬡) entry 11, [BlocBuilder] = 9.0 mM. (Bottom) Corresponding evolution of molar masses and polydispersity indices (determined by SEC in *N*-methylpyrrolidone with a PS calibration) vs conversion.

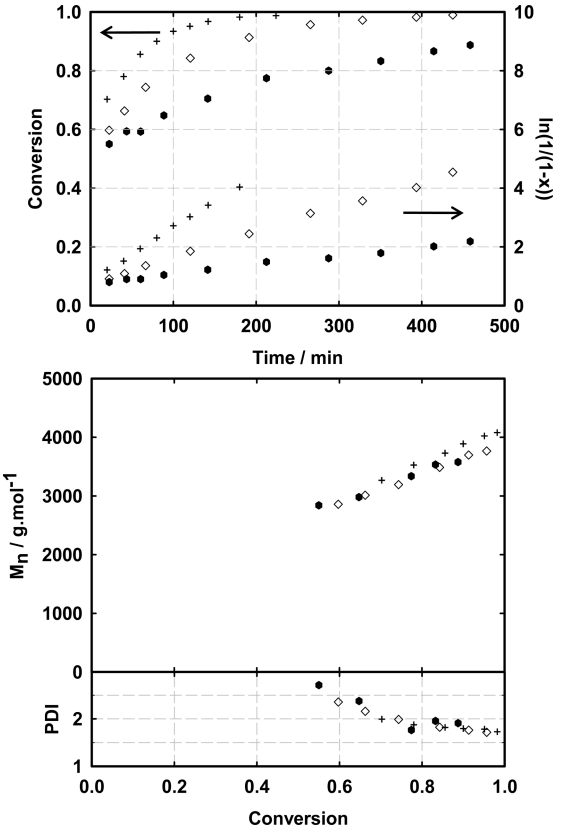


Figure 6. (Top) Conversion vs time and first-order kinetic plots for the NMP of DEAAm in toluene at different temperatures. Conditions: [DEAAm] = 3.6 M, [BlocBuilder] = $7.2 \times 10^{-2} - 7.3 \times 10^{-2}$ M, r = 0; (+) entry 1, 110 °C; (◊) entry 12, 105 °C; (⬢) entry 13, 95 °C. (Bottom) Corresponding evolution of number-average molar masses and polydispersity indices (determined by SEC in *N*-methylpyrrolidone with a PS calibration) vs conversion.

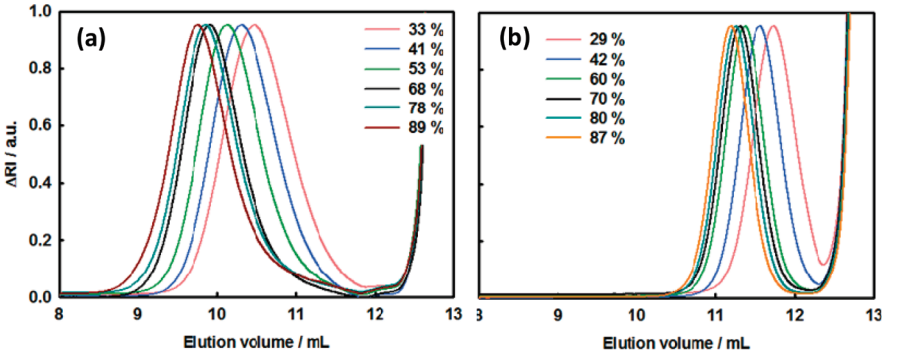


Figure 5. Size-exclusion chromatograms of PDEAAm obtained by NMP in toluene at 110 °C at different monomer conversions. Conditions: [DEAAm] = 3.6 M, r = 0.18 with different initial alkoxyamine concentrations; (a) entry 11, [BlocBuilder] = 9.0 mM; (b) entry 5, [BlocBuilder] = 72.5 mM.

should be around 10^{-10} mol L^{-1}. This is in the same range as for acrylic acid or *n*-butyl acrylate at temperatures between 112 and 120 °C,[29−31] and almost an order of magnitude lower than that of styrene. Thus, DEAAm exhibits a behavior in SG1-mediated CRP similar to that of acrylic acid or *n*-butyl acrylate (large k_p, low K). Although the alkoxyamine BlocBuilder proved to be very efficient to control the polymerization of styrenic monomers and, in general, acrylates without the need for an initial amount of free SG1, here this was necessary to obtain a proper control. This was already observed for the polymerization of acrylic acid,[31] oligo(ethylene glycol) acrylate,[34] NAM,[49] and DMAAm.[49]

Accurate Determination of Molar Masses. Although we always observed a linear evolution of the number-average molar masses with monomer conversion, the values determined by simple-detection SEC were significantly lower than the theoretical values. This is indeed due to the use of a conventional calibration with polystyrene standards which is not appropriate to determining the PDEAAm M_n values with accuracy. We therefore analyzed a series of polymer samples with an SEC apparatus equipped with a triple detection system giving access to the absolute molar masses. First, the determination of M_n by this technique showed us that the values previously determined by conventional calibration were underestimated. Second, the experimental absolute M_ns were found to be very close to the theoretical ones, proving the very effective control of the polymerization (Figure 7). This also corroborates the assumption that the concentration of growing polymer chains involved all along the reaction equals the initial concentration of molecular alkoxyamine initiator (vide supra). It can also be seen that it is possible to obtain high molar masses with reasonable PDI as shown in Figure 7 for entry 10 (at 86% conversion, M_n (triple SEC) = 45800 and PDI = 1.26).

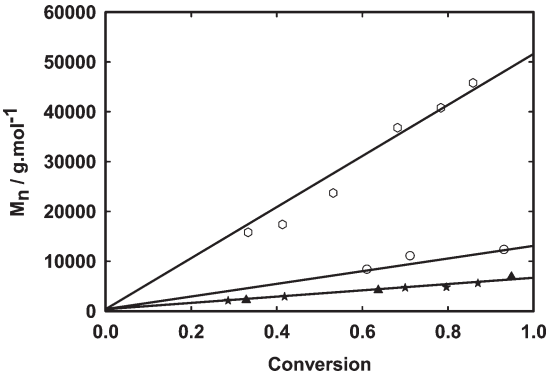


Figure 7. Number-average molar masses determined by triple-detection SEC of PDEAAm synthesized by SG1-mediated NMP in toluene: (⬡) entry 11; (○) entry 8; (▲) entry 4; (★) entry 5 (see Table 1).

Living Character: Chain-End Functionality and Chain Extension. The method of choice to determine the polymer chain-ends nature is mass spectrometry. Soft ionization techniques such as size-exclusion chromatography coupled to electospray ionization mass spectrometry (SEC/ESI−MS) proved to be mild enough to keep fragile polymer end groups away from degradation.[71] Here we prepared a rather short polymer in conditions identical to those of entry 4 so that single-charged species could be observed avoiding any ambiguity (absolute M_n = 2360 g·mol^{-1} as determined by SEC/ESI−MS using a previously described algorithm procedure[59]). We obtained a clear spectrum (Figure 8, left) displaying one single population of chains with 127 amu between the peaks, this value corresponding to the molar mass of one repeat unit. Each peak mass (m) is consistent with the expression $m = 380.22 + n \times 127.10 + 22.99$, where n is the degree of polymerization, 380.22 is the monoisotopic mass of BlocBuilder minus its acidic proton, 127.10 is the monoisotopic mass of the repeat unit, and 22.99 is the monoisotopic mass of the sodium counterion. For instance, for $n = 7$, we calculated a theoretical value of 1292.91 and observed a peak at 1293.50. A zoom on this region of the spectrum revealed a good match with the expected isotopic pattern.

After having proved the presence of the SG1 at the chain end of the polymer, we conducted some chain extension experiments. First, a purified macroalkoxyamine PDEAAm−SG1 was heated in the presence of *N,N*-dimethylacrylamide (DMAAm), which is a monomer structurally very close to DEAAm. The reaction was performed at 110 °C in toluene (50% w/w) and no free SG1 was added. A rather high degree of polymerization was targeted ([DMAAm]/[PDEAAm−SG1] = 250) and we chose to let the polymerization run for a long time to ensure a complete shift of the SEC peak and allow clear conclusion on the crossover efficiency. The polymerization of styrene was performed in typical conditions for its control in SG1-mediated NMP, i.e., in bulk at 120 °C, with a ratio [S]/[PDEAAm−SG1] = 240.

In both cases we obtained complete reinitiation since the two SEC peaks were symmetrical and no tailing toward the higher elution volumes was present (Figure 9). However the two chain extension reactions behaved differently. Indeed the PDEAAm-*b*-PDMAAm block copolymers exhibited a polydispersity index significantly higher than that of the PDEAAm-*b*-PS (1.96 versus 1.30). This is due to the difference in kinetic characteristics between DMAAm and styrene. In the case of DMAAm, the equilibrium constants, K_{DMAAm}

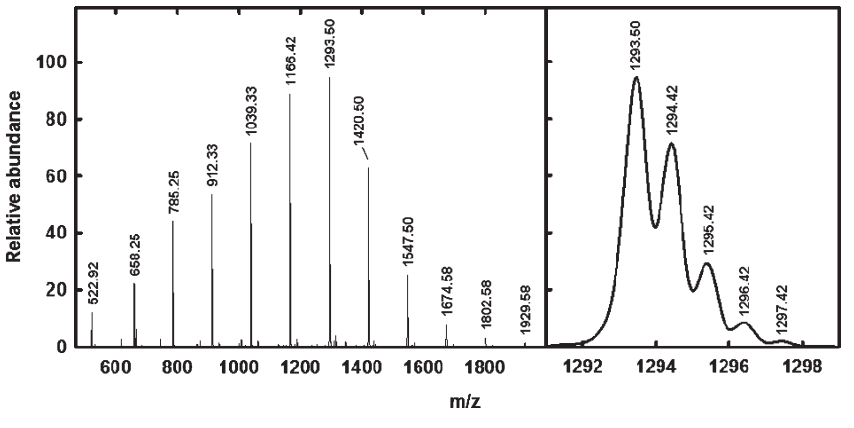


Figure 8. (Left) SEC/ESI−MS spectrum of an oligoDEAAm prepared by SG1-mediated polymerization in conditions similar to those of entry 4. (Right) Magnification of the m/z = 1291−1299 zone.

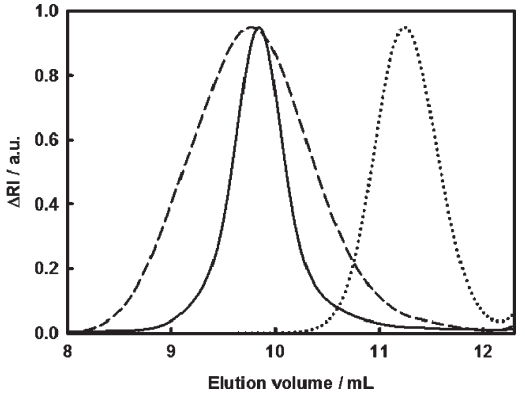


Figure 9. Size-exclusion chromatograms of the PDEAAm macroinitiator (dotted line) and of the block copolymers obtained after its chain extension with styrene (full line) and DMAAm (dashed line).

and K_{DEAAm}, are probably very similar since the two monomers possess very similar structure. Furthermore, since no free SG1 was used, the polymerization processed in the same fashion as we already observed for the polymerizations of DEAAm performed in the absence of free SG1 (entries 1−3, 12, 13). In the case of styrene, the complete reinitiation should normally not be favored when a PDEAAm macroalkoxyamine is used since the equilibrium constant K_S is higher than K_{DEAAm}. However the moderate value of the rate constant of propagation $k_{p,S}$ apparently implies that all the macroalkoxyamine PDEAAm−SG1 molecules had sufficient time to reinitiate before very long polystyrene blocks were formed.

Conclusion

The lack of information in the literature on the nitroxide-mediated homopolymerization of DEAAm in solution, along with the increasing use of this monomer in replacement of NiPAAm prompted us to present a complete study of its polymerization initiated by BlocBuilder, i.e., controlled by the nitroxide SG1. The best experimental conditions were defined in toluene as a solvent at a temperature of 110 °C or below, in the presence of free SG1. Very high monomer conversions were reached within short polymerization times, good control over molar mass, narrow molar mass distributions and high chain end-functionality. All those results represent a good basis for the design of well-defined (co)polymers based on DEAAm and featuring temperature sensitivity in water solution.

Acknowledgment. The authors gratefully acknowledge Arkema for the kind supply of the nitroxide SG1 and the alkoxyamine BlocBuilder. G.D. thanks Dr. T. Gründling for help on SEC/ESI−MS measurement.

Supporting Information Available: Typical ^{1}H NMR spectrum of a reaction mixture and conversion and kinetics of additional experiments with variable concentrations of nitroxide or alkoxyamine. This material is available free of charge via the Internet at http://pubs.acs.org.

References and Notes

(1) Liu, H. Y.; Zhu, X. X. *Polymer* **1999**, *40*, 6985–6990.
(2) Albarghouthi, M. A.; Buchholz, B. A.; Doherty, E. A. S.; Bogdan, F. M.; Zhou, H.; Barron, A. E. *Electrophoresis* **2001**, *22*, 737–747.
(3) Bian, F.; Xiang, M.; Yu,Y.; Liu, M. *e-Polym.* **2008**, no. 121.
(4) Li, Y.; Pan, S.; Zhang, W.; Du, Z. *Nanotechnology* **2009**, *20*, 065104.
(5) Ma, L.; Liu, M.; Liu, H.; Chen, J.; Cui, D. *Int. J. Pharm.* **2010**, *385*, 86–91.
(6) Panayiotou, M.; Freitag, R. *Polymer* **2005**, *46*, 6777–6785.
(7) Panayiotou, M.; Pöhner, C.; Vandevyver, C.; Wandrey, C.; Hilbrig, F.; Freitag, R. *React. Funct. Polym.* **2007**, *76*, 807–819.
(8) Maeda, Y.; Nakamura, T.; Ikeda, I. *Macromolecules* **2002**, *35*, 10172–10177.
(9) Maeda, Y.; Yamabe, M. *Polymer* **2009**, *50*, 519–523.
(10) Panayiotou, M.; Freitag, R. *Polymer* **2005**, *46*, 615–621.
(11) Saunders, J. M.; Alava, C.; Saunders, B. R. *Macromol. Symp.* **2007**, *251*, 63–73.
(12) Keerl, M.; Smirnovas, V.; Winter, R.; Richtering, W. *Macromolecules* **2008**, *41*, 6830–6836.
(13) Delaittre, G.; Save, M.; Charleux, B. *Macromol. Rapid Commun.* **2007**, *28*, 1528–1533.
(14) Rieger, J.; Grazon, C.; Charleux, B.; Alaimo, D.; Jerome, C. *J. Polym. Sci., Part A: Polym. Chem.* **2009**, *47*, 2373–2390.
(15) Jenkins, A. D.; Jones, R. G.; Moad, G. *Pure Appl. Chem.* **2010**, *82*, 483–491.
(16) Braunecker, W. A.; Matyjaszewski, K. *Prog. Polym. Sci.* **2007**, *32*, 93–146.
(17) Woodworth, B. E.; Zhang, X.; Metzner, Z.; Gaynor, S. G.; Matyjaszewski, K. *Macromolecules* **1998**, *31*, 5955–5957.
(18) Benoit, D.; Chaplinski, V.; Braslau, R.; Hawker, C. J. *J. Am. Chem. Soc.* **1999**, *121*, 3904–3920.
(19) Hawker, C. J.; Bosman, A. W.; Harth, E. *Chem. Rev.* **2001**, *101*, 3661–3688and references therein .
(20) Wetter, C.; Jantos, K.; Woithe, K.; Studer, A. *Org. Lett.* **2003**, *5*, 2899–2902.
(21) Chauvin, F.; Couturier, J. L.; Dufils, P. E.; Gerard, P.; Gigmes, D.; Guerret, O.; Guillaneuf, Y.; Marque, S. R. A.; Bertin, D.; Tordo, P. *ACS Symp. Ser.* **2006**, *944*, 326–341.
(22) Nesvadba, P. *Chimia* **2006**, *60*, 832–840.
(23) Braslau, R.; Tsimelzon, A.; Gewandter, J. *Org. Lett.* **2004**, *6*, 2233–2235.
(24) Guillaneuf, Y.; Couturier, J. L.; Gigmes, D.; Marque, S. R. A.; Tordo, P.; Bertin, D. *J. Org. Chem.* **2008**, *73*, 4728–4731.
(25) http://www.arkema-inc.com/index.cfm?pag=860
(26) Goto, A.; Scaiano, J. C.; Maretti, L. *Photochem. Photobiol. Sci.* **2007**, *6*, 833–835.
(27) Guillaneuf, Y.; Versace, D. L.; Bertin, D.; Gigmes, D.; Lalevee, J.; Fouassier, J. P. *Macromolecules* **2010**, *43*, 2204–2212.
(28) Grimaldi, S.; Finet, J. P.; Le Moigne, F.; Zeghdaoui, A.; Tordo, P.; Benoit, D.; Fontanille, M.; Gnanou, Y. *Macromolecules* **2000**, *33*, 1141–1147.
(29) Benoit, D.; Grimaldi, S.; Robin, S.; Finet, J. P.; Tordo, P.; Gnanou, Y. *J. Am. Chem. Soc.* **2000**, *122*, 5929–5939.
(30) Lacroix-Desmazes, P.; Lutz, J. F.; Chauvin, F.; Severac, R.; Boutevin, B. *Macromolecules* **2001**, *34*, 8866–8871.
(31) Couvreur, L.; Lefay, C.; Belleney, J.; Charleux, B.; Guerret, O.; Magnet, S. *Macromolecules* **2003**, *36*, 8260–8267.
(32) Bian, K.; Cunningham, M. *Macromolecules* **2005**, *38*, 695–701.
(33) Bian, K.; Cunningham, M. *J. Polym. Sci., Part A: Polym. Chem.* **2006**, *44*, 414–426.
(34) Lessard, B.; Marić, M. *Macromolecules* **2008**, *41*, 7870–7880.
(35) Charleux, B.; Nicolas, J.; Guerret, O. *Macromolecules* **2005**, *38*, 5485–5492.
(36) Dire, C.; Charleux, B.; Magnet, S.; Couvreur, L. *Macromolecules* **2007**, *40*, 1897–1903.
(37) Nicolas, J.; Couvreur, P.; Charleux, B. *Macromolecules* **2008**, *41*, 3758–3761.
(38) Lessard, B.; Marić, M. *J. Polym. Sci., Part A: Polym. Chem.* **2009**, *47*, 2574–2588.
(39) Ting, S. R. S.; Min, E. H.; Escale, P.; Save, M.; Billon, L.; Stenzel, M. H. *Macromolecules* **2009**, *42*, 9422–9434.
(40) Hoogenboom, R.; Popescu, D.; Steinhauer, W.; Keul, H.; Möller, M. *Macromol. Rapid Commun.* **2009**, *30*, 2042–2048.
(41) Nicolas, J.; Brusseau, S.; Charleux, B. *J. Polym. Sci., Part A: Polym. Chem.* **2010**, *48*, 34–47.
(42) Li, D.; Brittain, W. J. *Macromolecules* **1998**, *31*, 3852–3855.
(43) Schierholz, K.; Givehchi, M.; Fabre, P.; Nallet, F.; Papon, E.; Guerret, O.; Gnanou, Y. *Macromolecules* **2003**, *36*, 5995–5999.
(44) Diaz, T.; Fischer, A.; Jonquieres, A.; Brembilla, A.; Lochon, P. *Macromolecules* **2003**, *36*, 2235–2241.
(45) Harth, E.; Bosman, A.; Benoit, D.; Helms, B.; Frechet, J. M. J.; Hawker, C. J. *Macromol. Symp.* **2001**, *174*, 85–92.
(46) Schulte, T.; Siegenthaler, K. O.; Luftmann, H.; Letzel, M.; Studer, A. *Macromolecules* **2005**, *38*, 6833–6840.
(47) Gibbons, O.; Carroll, W. M.; Aldabbagh, F.; Yamada, B. *J. Polym. Sci., Part A: Polym. Chem.* **2006**, *44*, 6410–6418.

(48) Gibbons, O.; Carroll, W. M.; Aldabbagh, F.; Zetterlund, P. B.; Yamada, B. *Macromol. Chem. Phys.* **2008**, *209*, 2434–2444.
(49) Eggenhuisen, T. M.; Becer, C. R.; Fijten, M. W. M.; Eckardt, R.; Hoogenboom, R.; Schubert, U. S. *Macromolecules* **2008**, *41*, 5132–5140.
(50) Nicolay, R.; Marx, L.; Hemery, P.; Matyjaszewski, K. *Macromolecules* **2007**, *40*, 6067–6075.
(51) Grassl, B.; Clisson, G.; Koukh, A.; Billon, L. *Eur. Polym. J.* **2008**, *44*, 50–58.
(52) Phan, T. N. T.; Bertin, D. *Macromolecules* **2008**, *41*, 1886–1895.
(53) Charleux, B.; Nicolas, J. *Polymer* **2007**, *48*, 5813–5833.
(54) Vinas, J.; Chagneux, N.; Gigmes, D.; Trimaille, T.; Favier, A.; Bertin, D. *Polymer* **2008**, *49*, 3639–3647.
(55) Chevigny, C.; Gigmes, D.; Bertin, D.; Jestin, J.; Boué, F. *Soft Matter* **2009**, *5*, 3741–3753.
(56) Parvole, J.; Ahrens, L.; Blas, H.; Vinas, J.; Boissière, C.; Sanchez, C.; Save, M.; Charleux, B. *J. Polym. Sci., Part A: Polym. Chem.* **2010**, *48*, 173–185.
(57) Trimaille, T.; Mabrouk, K.; Monnier, V.; Charles, L.; Bertin, D.; Gigmes, D. *Macromolecules* **2010**, *43*, 4864–4870.
(58) André, X.; Zhang, M.; Müller, A. H. E. *Macromol. Rapid Commun.* **2005**, *26*, 558–563.
(59) Gründling, T.; Guilhaus, M.; Barner-Kowollik, C. *Anal. Chem.* **2008**, *80*, 6915–6927.
(60) Kamashi, M.; Yamada, B. In *Polymer Handbook*; Brandrup, J., Immergut, E. H., Grulke, E. A., Eds.; Wiley: New York, 1999.
(61) Ganachaud, F.; Balic, R.; Monteiro, M. J.; Gilbert, R. G. *Macromolecules* **2000**, *33*, 8589–8596.
(62) Ganachaud, F.; Monteiro, M. J.; Gilbert, R. G. *Macromol. Symp.* **2000**, *150*, 275–281.
(63) Seabrook, S. A.; Tonge, M. P.; Gilbert, R. G. *J. Polym. Sci., Part A: Polym. Chem.* **2005**, *43*, 1357–1368.
(64) Asua, J. M.; Beuermann, S.; Buback, M.; Castignolles, P.; Charleux, B.; Gilbert, R. G.; Hutchinson, R. A.; Leiza, J. R.; Nikitin, A. N.; Vairon, J.-P.; Herk, A. M. *Macromol. Chem. Phys.* **2004**, *205*, 2151–2160.
(65) André, X. Ph.D. Dissertation, Universität Bayreuth, 2005.
(66) Farcet, C.; Nicolas, J.; Charleux, B. *J. Polym. Sci., Part A: Polym. Chem.* **2002**, *40*, 4410–4420.
(67) Bertin, D.; Gigmes, D.; Marque, S. R. A.; Tordo, P. *Macromolecules* **2005**, *38*, 2638–2650.
(68) Nicolas, J.; Charleux, B.; Guerret, O.; Magnet, S. *Macromolecules* **2004**, *37*, 4453–4463.
(69) Fukuda, T.; Goto, A.; Ohno, K. *Macromol. Rapid Commun.* **2000**, *21*, 151–165.
(70) Fischer, H. *Chem. Rev.* **2001**, *101*, 3581–3610.
(71) Barner-Kowollik, C.; Davis, T. P.; Stenzel, M. H. *Polymer* **2004**, *45*, 7791–7805.

Macromolecules
ARTICLE

Macromolecules **2011**, *44*, 471–482 **471**
DOI: 10.1021/ma102134y

Synthesis, Characterization, and Electrospinning of Architecturally-Discrete Isotactic−Atactic−Isotactic Triblock Stereoblock Polypropene Elastomers

Carl Giller,[†] Giriprasath Gururajan,[†] Jia Wei,[‡] Wei Zhang,[‡] Wonseok Hwang,[‡] D. Bruce Chase,*[,†] John F. Rabolt,*[,†] and Lawrence R. Sita*[,‡]

[†]*Department of Material Science and Engineering, University of Delaware, Newark, Delaware 19716, United States, and* [‡]*Department of Chemistry and Biochemistry, University of Maryland, College Park, Maryland, 20742, United States*

Received September 15, 2010; Revised Manuscript Received December 7, 2010

ABSTRACT: Stereochemically homogeneous and architecturally discrete isotactic−atactic−isotactic triblock stereoblock PP (sbPP) thermoplastic elastomers in which the block lengths for each domain type can be varied in programmed fashion while keeping total molecular weight and molecular weight polydispersity the same has been achieved for the first time. Five sbPP materials were prepared: sbPP-1 (6*iso*-88*a*-6*iso*), total isotactic content, 12%; sbPP-2 (12*iso*-76*a*-12*iso*), 24%; sbPP-3 (18*iso*-64*a*-18*iso*), 36%; sbPP-4 (24*iso*-50*a*-26*iso*), 50%; and sbPP-5 (20*iso*-64*a*-33*iso*), 53%. All five sbPP materials were successfully processed by solution-based electrospinning to provide fiberous mats with feature sizes on the nanometer to micrometer length scale. Extensive characterization by analytical (SEM, AFM, tensile testing, DSC,), spectroscopic (FT-IR, FT-Raman), and synchrotron X-ray diffraction techniques of bulk samples, electrospun fibers and solvent cast films of the sbPP samples revealed well-defined trends in elastic properties, morphologies and crystallinity that are associated with a higher degree of crystallinity that emerges with higher isotactic contents. The results of these investigations serve to provide an important foundation that can be used to potentially identify the best combination of stereoerror level incorporation within the isotactic domains and total isotactic content for these architecturally discrete sb-PP materials for maximizing desirable elastomeric traits and solution-based (electrospinning) processing methodology with the goal of achieving the best possible structural forms for potential product applications.

Introduction

Thermoplastic polypropene (PP) elastomers have been the subject of intense academic and industrial interest ever since Guido Natta[1] first described such a material that was isolated through fractionation of bulk polypropene prepared with the stereoselective heterogeneous Ziegler−Natta catalyst, $TiCl_3$/$AlEt_3$.[2,3] The idealized solid-state structural model suggested by Natta to account for this elastomeric behavior is that of an isotactic−atactic stereoblock polypropene architecture in which long runs of several consecutive stereoregular enchainments of propene give rise to crystalline (hard) block domains possessing an isotactic microstructural configuration that are chemically linked through amorphous (soft) block domains associated with an atactic configuration generated from stereorandom sequences of propene insertions. As proposed for thermoplastic elastomers in general, the crystalline domains that are dispersed throughout the amorphous matrix serve as interchain physical cross-links that provide for elastic recovery after strain-induced deformation.[4] In addition to isotactic−atactic stereoblock PP, other stereochemical microstructural forms for PP that are claimed to impart elasticity have been reported, such as isotactic−hemiisotactic and syndiotactic−atactic stereoblocks.[5,6] From a commercial perspective, global annual production of PP-based materials stood at ∼44 million metric tons in 2009,[7] and accordingly, the potential of expanding the technological range and applications of PP with a variety of different grades of stereoblock thermoplastic elastomers through "simple" manipulation of stereochemical microstructure during transition-metal-mediated coordinative polymerization of commodity-volume propene monomer is exceedingly attractive.

Although a stereoblock microstructural form for PP is easy to conceptualize, in practice, it has been exceedingly difficult to prepare PP materials that meet the criteria for having discrete stereoblock architectures, and Busico[2] has recently presented a well-balanced and in-depth critical evaluation of reported claims that have appeared in the literature related to the production of stereoblock PP. In general, the specific challenge that renders stereoblock PP an extremely difficult target is the requirement that a mechanistic scheme must exist that incorporates a credible dynamic and reversible process that can "switch" the nature and degree of stereoselective transition-metal-centered chain-growth propagation from one well-defined state (e.g., highly stereoselective) to another state (e.g., aspecific). Unfortunately, observation of elastic behavior by itself cannot be used as definitive proof of a stereoblock microstructure,[8] and many of the reports of homogeneous "two-state" coordination polymerizations of propene actually produce elastomeric PP that is best described as having rather poorly defined stereochemical microstructures in which short runs of monomer insertions occur with a low degree of stereoselectivity within a generally much more stereoregular polymer backbone.[2,5,9,10] If irreversible chain-termination and chain-transfer is also occurring at rates that are competitive with propagation, then the final PP microstructure will also be, by

*Authors to whom correspondence should be addressed.

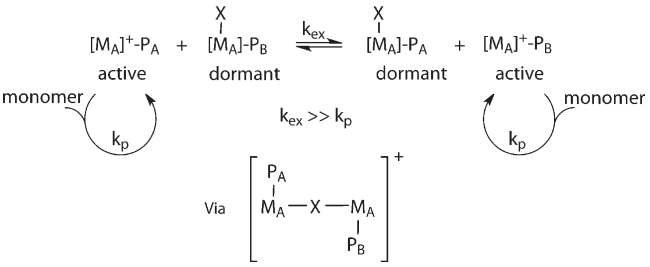
© 2011 American Chemical Society
Published on Web 01/10/2011

default, stereochemically heterogeneous, and, just as in the case of Natta's original sample, these materials almost invariably can be fractionated into components that possess either more, or less, stereoregularity.[11] Perhaps for this latter reason, the current body of literature regarding stereoblock PP is essentially silent on the topic of the postsynthesis processing of these materials into technologically interesting structural forms, such as films, fibers, blends, or composites. Thus, given the present state of the art, it is fair to say that the structural, morphological, thermal, and mechanical properties of well-defined and architecturally discrete stereoblock PP materials still remain enigmatic 60 years after having first been proposed by Natta.

Within the past decade, several groups have unequivocally demonstrated that certain classes of molecular transition-metal complexes can serve as initiators for the "living" coordination polymerization of ethene, propene, longer-chain α-olefins, and α,ω-nonconjugated dienes.[12] Our contribution to this effort was the introduction in 2000 of the class of group 4 metal dimethyl, monocyclopentadienyl, monoacetamidinate complexes of general structure, (η^5-C_5R_5)M(Me)$_2$[N(R^1)C(R^2)N(R^3)] (**I**), which in the case where M = Zr, R = R^2 = Me, R^1 = *t*-Bu, and R^3 = Et (**1**), could serve, after stoichiometric "activation" by the borate cocatalyst, [PhNHMe$_2$][B(C_6F_5)$_4$] (**2**), as a highly active initiator for the isospecific living coordination polymerization of 1-hexene.[13] On the basis of the degenerative group transfer polymerization mechanism involving rapid methyl group exchange between configurationally stable, cationic active propagating centers and configurationally unstable, neutral dormant sites that is depicted in Scheme 1,[14] we more recently reported the successful development of a highly versatile, living polymerization protocol by which temporal control over polyolefin stereochemical microstructure can be exerted simultaneously over all propagating centers in such a manner as to provide the first unequivocal examples of architecturally discrete isotactic−atactic stereoblock and stereogradient PP.[15−17] Given the strict living character of coordination polymerization that is achieved with **1**, this stereomodulation strategy can be employed to produce an endless variety of programmed linear isotactic−atactic stereoblock sequences in which the identity, length, and relative ordering of each stereoblock (atactic or isotactic) is known with certainty, and where the final PP materials are monodisperse with narrow molecular weight polydispersities and with polymer microstructures that are stereochemically homogeneous.

Our preliminary investigations of architecturally discrete stereoblock PP were limited to the synthesis and characterization of several *isomeric* isotactic−atactic multiblock materials in which the total isotactic content and the number-average molecular weight index, M_n, and molecular weight polydispersity, D (= M_w/M_n), were held approximately constant at 40%, 170 kDa, and 1.19, respectively, while the stereoblock architecture was varied according to an atactic−isotactic diblock, an atactic−isotactic−atactic triblock and an atactic−isotactic−atactic−isotactic tetrablock.[15] Gratifyingly, these results revealed a strong dependence of tensile strength and elasticity of melt-pressed samples on the material's specific stereoblock architecture (i.e., di- vs tri- vs tetrablock). However, not included in these initial studies was the synthesis of discrete stereoblock PP triblock materials possessing an *isotactic−atactic−isotactic* block sequence that might potentially exhibit the most favorable elastomeric properties due to the end-capping of a middle amorphous atactic domain with crystalline isotactic segments.[18] This omission was not due to oversight, but instead, it was deemed necessary at the time due to synthetic difficulties originally encountered with a limited solubility of the active polymeryl species when attempting to carry out the stereomodulated living coordination polymerization of propene at low temperature (~10 °C) in chlorobenzene in which the first block is both

Scheme 1



isotactic and of a significant degree of polymerization. Fortunately, further optimization of synthetic procedures have now circumvented this restriction, and herein, we report, for the first time, a family of the desired symmetric isotactic−atactic−isotactic stereoblock PP triblocks in which M_n and D are held constant while the total isotactic content is allowed to vary. Characterization and comparison of the mechanical properties of these new stereoblock PP materials with those reported previously[15] serve to expand the database of structure−property relationships for this intriguing new class of polyolefin elastomer.

Regarding postsynthesis processing, electrospinning is an electrostatically driven polymer processing technique that is useful for the production of polymeric fibers with diameters ranging from tens of nanometers to tens of micrometers.[19,20] In addition, the interconnected web-like porous morphology and the large surface area to volume ratio typically observed for electrospun mats make this fiber production process desirable for applications in biomedical engineering, filtration, and textile technologies. Although electrospinning has seen revitalization since 1995, most of the polymers studied to date have been processed at room temperature from common solvents and those polymers that cannot be processed under these conditions still present a special challenge. In this respect, Rabolt and co-workers[21−25] have begun to address this challenge and this group has now reported the electrospinning of a number of highly crystalline polyolefins, including polyethene,[21] syndiotactic PP,[22] isotactic poly(1-butene),[23] and isotactic poly(4-methyl-1-pentene),[24] as well as the structural and thermal characterization of the corresponding electrospun fibers. The successful electrospinning of these crystalline polyolefins at room temperature is significant, in part, due to the exhibited limited solubility of these materials in commercially available solvents. The now ready availability of a variety of monodisperse architecturally discrete isotactic−atactic stereoblock PP elastomers that are obtained through a living polymerization, coupled with successful demonstration of the electrospinning processing technique for polyolefins provides strong impetus for investigating the ability to prepare electrospun fibers of these novel stereoblock materials that might find use in applications such as medical stents, joint replacements and tissue engineering. Toward this end, further results are reported herein that now provide suitable conditions for the successful electrospinning of the targeted isotactic−atactic−isotactic stereoblock PP materials. Structural characterization of the morphology of the electrospun fibers as a function of isotactic content serve to enhance our understanding of the structure−processing−property relationships of these novel stereoblock PP elastomers.

Experimental Section

(a). General Considerations. All synthetic manipulations were performed under an inert atmosphere of dinitrogen using standard glovebox techniques. Dry, oxygen-free solvents were employed throughout with chlorobenzene (PhCl) being distilled from calcium hydride under an atmosphere of dinitrogen. Polymer grade propene was purchased from Matheson Trigas and further purified by passing through sequential packed columns of activated Q5 and 4 Å molecular sieves. The precatalyst,

Table 1. Block Compositions and Molecular Weight Indices for the Stereoblock PP Materials

sample	block composition	M_n (kDa)	M_w/M_n	total % isotactic
sbPP-1	6*iso*-88*a*-6*iso*	200	1.28	12
sbPP-2	12*iso*-76*a*-12*iso*	206	1.22	24
sbPP-3	18*iso*-64*a*-18*iso*	195	1.28	36
sbPP-4	24*iso*-50*a*-26*iso*	220	1.33	50
sbPP-5	20*iso*-47*a*-33*iso*	385	1.24	53

(η^5-C_5Me_5)$ZrMe_2$[N(Et)C(Me)N(*t*-Bu)] (**1**), and the methyl donator reagent for stereomodulation, (η^5-C_5Me_5)$ZrMe_2$[N(*t*-Bu)C(Me)N($CH_2C(CH_3)_3$)] (**3**), were prepared according to previously reported procedures,[13,15] while [$PhNHMe_2$][$B(C_6F_5)_4$] (**2**) was purchased from Boulder Scientific and used without further purification. Gel permeation chromatography (GPC) was performed using a Viscotek GPC system equipped with a column oven and differential refractometer, both maintained at 45 °C, and four columns also maintained at 45 °C. Tetrahydrofuran (THF) was used as the eluant at a flow rate of 1.0 mL/min. M_n, M_w and M_w/M_n values were obtained using the Viscotek OmniSEC software (conventional calibration) and 10 polystyrene standards (from Polymer Laboratories). $^{13}C\{^1H\}$ NMR spectra were recorded at 150 MHz using 1,1,2,2-tetrachloroethane-d_2 as the solvent at 90 °C.

(b). Polymer Synthesis of Isotactic−Atactic−Isotactic Stereoblock PP (General Procedure). To a solution of 39.8 mg (100 μmol) of **1** in 1.5 mL of PhCl, cooled to −10 °C in a 10 mL vial was added a solution of 84.1 mg (105 μmol) of **2** in 1.5 mL of PhCl all at once via pipet. The resulting yellow solution was then rapidly transferred by pipet to a 500 mL Schlenk flask that was previously charged with 200 mL of PhCl, cooled to −10 °C, and pressurized to 5 psi with propene. After the transfer of this catalyst mixture was complete, the Schlenk flask was pressurized once again to 5 psi and this pressure maintained for 1.5 h with continuous magnetic bar stirring of the polymerization mixture maintained at −10 °C. At this time, a solution of 24.5 mg (55 μmol) of **3** in 3 mL of PhCl was added all at once by pipet to the polymerization mixture by very briefly removing the septum. After repressurizing to 5 psi, the polymerization mixture was stirred at −10 °C for an additional 38 h, whereupon a 1 mL aliquot of the diblock solution was withdrawn and rapidly quenched with 1 mL of acidic methanol. At nearly the same time, a solution of 48.1 mg (60 μmol) of **2** in 4 mL of PhCl was added via pipet and the mixture stirred at −10 °C for a final 4.5 h, at which time the polymerization was quenched by addition of 1 mL of methanol. After purification through precipitation from a concentrated toluene solution into acidic methanol, 14 g of the stereoblock PP product was isolated as a white elastomeric material after drying in vacuo for 18 h. According to previously published procedures,[15] GPC and ^{13}C NMR stereochemical microstructural analyses of the intermediate diblock (M_w 217 kDa, PDI 1.18) and triblock (M_w 251 kDa, PDI 1.22) served to establish the desired stereoblock PP architecture and quantitatively determine the relative block lengths as being: 12% *isotactic*−76% *atactic*−12% *isotactic,* or hereafter more conveniently referred to as follows: 12*iso*-76*a*-12*iso*. In similar synthetic fashion, other isotactic−atactic−isotactic stereoblock PP materials were prepared and Table 1 provides a summary of isotactic−atactic block composition and final molecular weight indices that define the desired stereoblock PP products.

(c). Phase-Sensitive Tapping Mode Atomic Force Microscopy (ps-tm-AFM). Each of the stereoblock PP materials were dissolved into toluene to provide 1% (w/w) solutions that were then used to form ultrathin polymer films onto either a cleaned Si(111) substrate [pretreated by soaking in 70:30 conc. H_2SO_4: 30% H_2O_2 "pirahna" solution (CAUTION!), followed by rinsing with copious quantities of nanopure (< 18 ohm) water] or a mica substrate using a photoresist spin-caster running at 6000 rpm for 60 s. Film thickness for the polymer thin films was measured using an Gaertner ellipsometer for 3 different spots on each sample with the average film thickness value being recorded. Typically, the measured film thickness was ∼30 nm. For topological analysis of the thin films using ps-tm-AFM, a silicon etched tip (Nanosensors, spring constant k = 25−55 N/m, resonance frequency = 292−377 kHz) was used for tapping mode with a Nanoscope IIIa Multimode AFM equipped with the Extender Electronics package (Veeco Inc., CA). Both height and phase-shift data were recorded simultaneously. Scanning was performed in air under ambient humidity.[26,27]

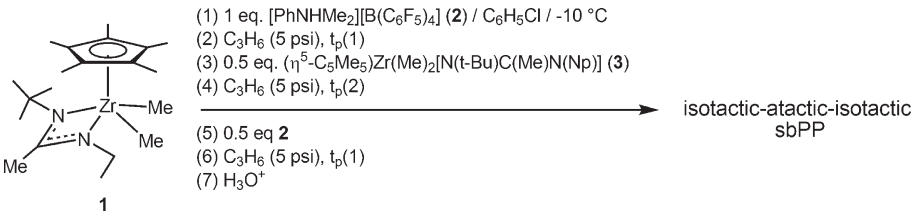
(d). Tensile Testing. Each of the stereoblock PP materials were compression-molded using 0.5 mm-thick sheet molds by first heating the sample to 150 °C for 30 min and then using 20K lbf pressure for 20 min before cooling to room temperature after the pressure was released. Dog-bone test strips were cut from the polymer sheets using the ASTM D638-5 die-cutter (sample dimension: length × width × thickness = 12.7 × 3.175 × 0.5 mm). Tensile testing was performed at room temperature (∼25 °C) on an Instron model 3345 tensile tester using pneumatic grips and an extension rate of 2 in/min. Recovery after break and recovery after 300% elongation were calculated as defined by the ASTM D412 protocol. For repetitive cycling tests, the specimens were stretched at 300% elongation and relaxed repeatedly 10 times with the hysteresis curves of each sample being recorded.

(e). Polymer Solutions and Electrospinning. The five stereoblock PP samples were each dissolved separately in a mixed solvent system comprising 80% (w/w) cyclohexane (Fisher Scientific) and 20% (w/w) acetone (Fisher Scientific) to provide 8 to 12% (w/w) polymer solutions. During preparation of the solutions, cycles of heating (40−45 °C) and cooling (20−25 °C) were carried out with 20 min durations for each cycle. The solutions were then cooled to room temperature and allowed to stir overnight. Electrospinning was carried out using an 18 gauge needle (Small Parts, Inc.) with an applied voltage of +12 kV and a working distance of 15 cm. The solutions were extruded to the tip of the needle with gravity. Solutions of the same composition were also solvent cast onto glass microscope slides and dried in a vacuum oven overnight.

(f). Morphological Characterization of Bulk Samples, Solvent Cast Films, and Electrospun Fibers. Images of the electrospun mats for all five samples were obtained with a JEOL JSM-7400 field emission scanning electron microscope using a 2 kV electron beam operating at 10 μA. Fiber diameters were measured with the associated software program. Fourier-transform infrared (FT-IR) spectra were acquired with a spectral resolution of 4 cm^{-1} using a Thermo Nicolet Nexus 670 FT-IR using a nine bounce Sensir Technologies DurasampleIR II with an attenuated total reflectance accessory employing a silicon crystal. FT-Raman spectra of the polymers were acquired with a Nicolet Raman 950 using a neodymium-doped yttrium aluminum garnet (Nd:YAG) laser operating at 1064 nm. For each sample, duplicate spectra were acquired with 16384 scans at a spectral resolution of 8 cm^{-1}. Differential scanning calorimetry (DSC) thermograms of bulk samples of the stereoblock PP samples were acquired on a TA Q1000, and for the solvent cast films and electrospun fibers a Perkin-Elmer Diamond Differential Scanning Calorimeter was employed using a heating rate of 10 °C/min and a cooling rate of 5 °C/min. Triplicate measurements were made for each sample. Heats of fusion for solvent cast films and electrospun fibers for all five polymers were analyzed using Pyris software by integration of the thermal transitions observed in the first heating cycle. The crystallinity values were calculated as reported in the literature using a standard heat of fusion of 148 J/g for 100% crystalline PP.[28] The average crystallinity values along with the standard deviations are reported.

X-ray diffraction (XRD) measurements were performed on the ID31 beamline at the European Synchrotron Radiation Facility (ESRF) in Grenoble, France, using radiation that had a wavelength of λ = 0.4999 Å. The reported d-spacings were calculated using the equation, $d = \lambda/[2 \times \sin((2\theta)/2)]$. The profiles

Scheme 2



consisted of six coadded scans, with each scan collected at the angular rate of 2°/minute, resulting in a scan time of 10 min and each sample taking 1 h to complete. The step size for each scan was 0.01°. Each of the reported profiles was collected at 293 K. Degrees of crystallinity for both electrospun fibers and solvent cast films for all five materials were calculated by smoothing the profile for electrospun sbPP-1 (the lowest crystalline material) to the point where the crystalline peaks disappeared. The resultant profile was assigned as the "amorphous halo". The amorphous halo was then scaled by an arbitrary factor and subtracted from each of the subsequent profiles for all of the remaining samples, with the resultant crystalline peaks then being integrated using the data processing and graphing suite of software, GRAMS AI (Thermo Scientific). Using the areas of the crystalline peaks, the amorphous halo of each of the profiles was then fit and the degree of crystallinity was calculated by dividing the area of the crystalline peaks by the total area.

Results and Discussion

(a). Synthesis and NMR Characterization. Synthesis of the isotactic−atactic−isotactic stereoblock PP materials followed the previously published procedures,[15] with the difference being that preparation of the first block through living coordination polymerization of propene was carried out by starting with a 1: 1 ratio of the precatalyst **1** to the borate cocatalyst **2** according to Scheme 2. It must be noted here that chain-growth propagation of propene by the initial in situ generated configurationally stable cationic active species proceeds under exclusive enantiomorphic site control with the degree of stereoselectivity for monomer enantioface complexation being 94%, and this translates to a *mmmm* pentad level of 71% as determined by stereochemical microstructure analysis employing high field ^{13}C NMR (150 MHz, 1,1,2,2-C_2Cl_4, 90 °C) spectra.[2,29] We believe that it is this somewhat lower degree of isotacticity that actually permits the living polymeryl species to remain in dilute chlorobenzene solution at −10 °C even at a relatively high number-average degree of polymerization that defines the first isotactic block length. As Scheme 2 further shows, after isotactic chain-growth of propene at ∼5 psi has occurred over a fixed period of time to set the first block length, a 0.5 mol equiv, relative to the initial amount of **1**, of the methyl donator complex, (η^5-C_5Me_5)$ZrMe_2$[N(*t*-Bu)C(Me)N($CH_2C(CH_3)_3$)] (**3**), was added to establish a 1:1 population of cationic active propagating species and configurationally unstable, neutral "dormant" species.[15] On the basis of the experimentally- supported mechanism of Scheme 1, rapid and reversible methyl group exchange between active and dormant species occurs at a rate that is substantially greater than that of propagation. Since metal-centered epimerization of the dormant sites also occurs at a rate that is significantly faster than propagation, further living coordination polymerization of propene now proceeds in an aspecific, atactic fashion for a second fixed period of time that serves to set the block length of the second atactic block.[14−17] By quenching a small aliquot of the living polymerization reaction mixture at this stage, ^{13}C NMR stereochemical analysis conducted at the pentad level of the isolated intermediate stereoblock diblock PP serves to establish the relative isotactic/atactic block composition. Inclusion of GPC molecular weight data for this diblock can then be used to fix the relative block lengths for the first (isotactic) and second (atactic) blocks.[15] To add the third (isotactic) block, as Scheme 2 reveals, addition of 0.5 mol equiv of **2** to the living polymerization mixture serves to remove all the exchangeable methyl groups from the system, and in doing so, no neutral dormant sites remain. Continuation of propene polymerization after this time will occur in isotactic fashion once again and ^{13}C NMR and GPC data for the final isolated isotactic−atactic−isotactic stereoblock triblock PP materials is used to establish the absolute block length of the third isotactic segment. Figure 1 presents the ^{13}C NMR spectra for the intermediate stereoblock diblock PP aliquots and of the final stereoblock triblock PP samples, sb-PP-1 to sb-PP-4. The ^{13}C NMR spectrum for sb-PP-5 is qualitatively quite similar to that of sb-PP-4 and is therefore not shown. Finally, Table 2 provides detailed results obtained from the quantitative ^{13}C NMR stereochemical pentad analyses of sb-PP-1 to sb-PP-5.

(b). Atomic Force Microscopy. Phase-sensitive, tapping mode atomic force microscopy (ps-tm- AFM) has previously proven to be a valuable analytical tool for simultaneously imaging both the topological (height) and the relative strength of the scanning probe tip−surface interactions (phase) of polymer film surface features with a resolution on the order of tens of nanometers.[27,28] Significantly, features that appear in the phase map tend to correlate with the relative "hardness" of material properties such that harder, crystalline domains can be easily distinguished from softer, amorphous areas. Relevant to the present investigation, ps-tm-AFM has been successfully used to image the crystalline morphology of highly isotactic PP that has crystallized in the α- or γ-modifications,[30] as well as stereochemically heterogeneous "stereoblock" PP elastomers,[31] and elastomeric PP of low isotactic content in which the stereoerrors are statistically distributed within the PP microstructure.[10]

Figure 2 presents phase maps obtained from ps-tm-AFM analyses of unannealed thin-films of the isotactic−atactic−isotactic PP samples, sbPP-1 to sbPP-4, that are supported on a Si(111) substrate. Thermally annealed samples (120 °C, 18 h) revealed nearly identical surface morphologies, and accordingly, these are not discussed further. Starting with sbPP-1 that has a 12% total isotactic content (Figure 2, parts a and b), crystalline lamellar structures that are embedded within an amorphous matrix are observed. For the remaining samples, an increase in the surface coverage density of these crystalline lamellae occurs with increasing total isotactic content of the stereoblock material [cf. Figures 2, parts a and b, for sbPP-2 (24%), parts c and d, for sbPP-3 (36%), and parts e and f, for sbPP-4 (50%)]. Significantly, the phase maps for the stereoblock PP materials materials all show the absence of microphase-separation that might have occurred on the nanometer length scale given their well-defined block structure.[27,28] These results are in keeping with an anticipated low Flory−Huggins interaction parameter χ, for the isotactic PP and atactic PP block domains and the

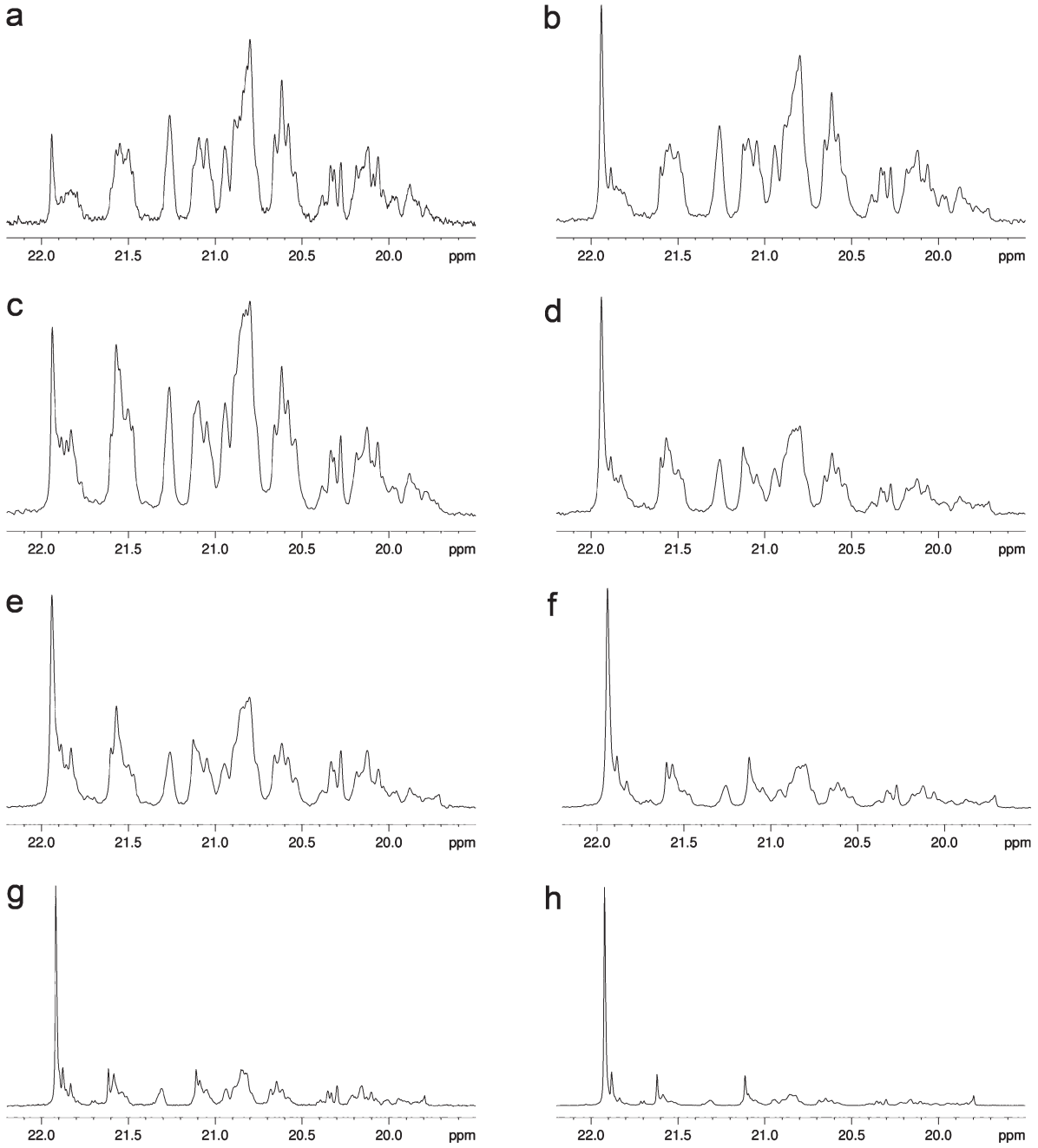


Figure 1. Comparisons of the ^{13}C NMR (150 MHz, 1,1,2,2-$C_2Cl_4D_2$, 90 °C) spectra for the intermediate isotactic−atactic diblock (left column) and isotactic−atactic−isotactic triblock (right column) PP materials obtained from the synthesis of (a and b) sbPP-1, (c and d) sbPP-2, (e and f) sbPP-3, and (g and h) sbPP-4.

Table 2. ^{13}C NMR Stereochemical Microstructure Pentad Distributions for Isotactic−Atactic Diblock and Isotactic−Atactic−Isotactic Triblock PP Materials Obtained from the Synthesis of the Stereoblock PP Samples

	sbPP-1		sbPP-2		sbPP-3		sbPP-4		sbPP-5	
	diblock	triblock	diblock	triblock	diblock	triblock	diblock	triblock	diblock	triblock
mmmm	0.068	0.114	0.125	0.191	0.184	0.278	0.258	0.417	0.233	0.434
mmmr	0.118	0.116	0.148	0.149	0.141	0.139	0.122	0.120	0.121	0.116
rmmr	0.064	0.061	0.056	0.053	0.045	0.038	0.041	0.029	0.042	0.026
mmrr	0.105	0.107	0.097	0.101	0.095	0.097	0.100	0.101	0.102	0.102
mmrm + *rmrr*	0.260	0.243	0.255	0.224	0.225	0.187	0.193	0.127	0.203	0.123
rmrm	0.153	0.141	0.127	0.111	0.105	0.082	0.097	0.062	0.104	0.060
rrrr	0.059	0.057	0.050	0.042	0.063	0.049	0.053	0.035	0.057	0.035
rrrm	0.115	0.120	0.091	0.082	0.094	0.085	0.097	0.064	0.093	0.061
mrrm	0.059	0.041	0.050	0.048	0.047	0.038	0.039	0.045	0.045	0.043

relatively modest total molecular weight values for the present sb-PP materials. Notably, microphase-separation has been observed in other classes of block-structured, semicrystalline thermoplastic elastomeric polyolefins with

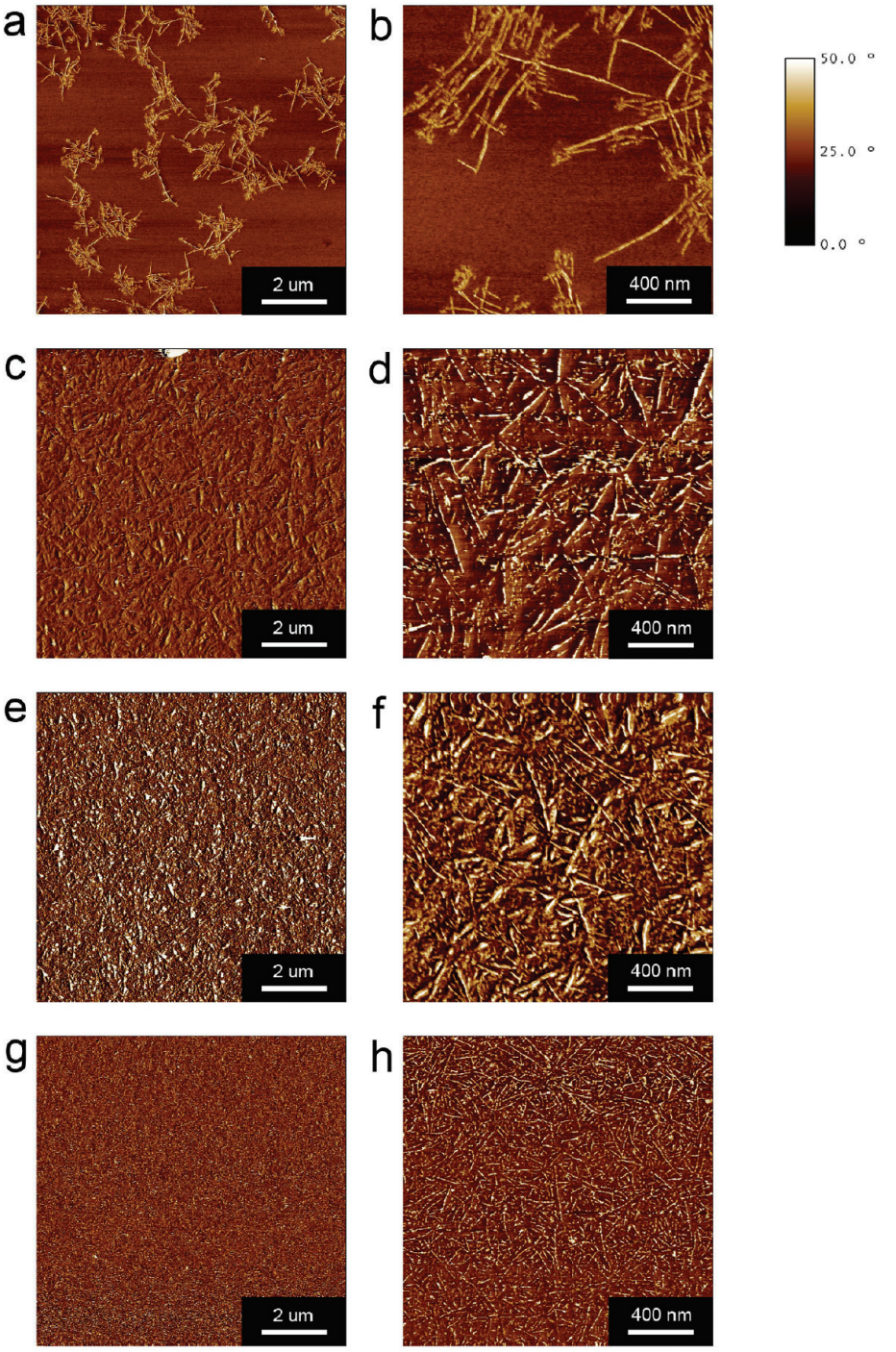


Figure 2. Phase maps obtained from ps-tm-AFM characterization of isotactic−atactic−isotactic triblock stereoblock PP materials as a function of increasing isotactic content: (a and b) sbPP-1 (total isotactic content: 12%), (c and d) sbPP-2 (24%), (e and f) sbPP-3 (36%), and (g and h) sbPP-4 (50%). Phase shift scale: 0−50°.

molecular weights of ~300 kDa., such as isotactic PP-*block*-regioirregular PP-*block*-isotactic PP and syndiotactic PP-*block*-poly(ethene-*co*-propene)-*block*-syndiotactic PP.[32,33] Since amorphous atactic PP has a lower T_g (~−10 °C) than the crystallization temperature of the isotactic PP domains, it is reasonable to assume that the crystalline lamellae were formed before the amorphous region vitrified.[34] The observed width of the crystalline lamellae is about 10 nm and this is also consistent with previous observations.[31c] Finally, De Rosa and co-workers[35] have reported that isotactic PP preferentially adopts an α-form crystalline structure over the γ-crystalline modification as the level of stereoerror incorporation within the polymer microstructure increases. On the basis that the isotactic domains within the isotactic−atactic−isotactic stereoblock PP materials presented here have a *mmmm* pentad level of 0.71 (*vide supra*), as well as observation of a cross-hatched crystalline lamellar morphology appearing in the AFM phase maps, it is reasonable to conclude that the observed crystalline lamellae exist in the α-modification. This conclusion is further supported by XRD characterization of these materials (*vide infra*). As a final note, no evidence for macrophase separation was obtained from ps-tm-AFM analyses of the stereoblock PP samples and this result is supportive of the highly homogeneous nature of

the material from a stereochemical microstructure point of view.

(c). Tensile Testing. As Figure 3 reveals, elastomeric behavior was observed for the architecturally discrete isotactic−atactic−isotactic triblock stereoblock PP materials where the total isotactic content was ≤36% and Table 3 compares data obtained from the mechanical testing of these materials at room temperature (~25 °C). Not surprisingly, sbPP-1, having the lowest total isotactic content of 12%, had a relatively poor recovery of only 94.6% after a break that occurred at 1963% strain, as well as the lowest ultimate tensile strength. With an increase in total isotactic content, however, the ultimate tensile strength sbPP-2 and sbPP-3 increased to a value of over 15 MPa for the latter (see Table 3). However, sbPP-4, with a total isotactic content of 50%, exhibited plastomeric behavior that might be expected on the basis of the much shorter amorphous atactic chains and larger crystalline domains. In our previous studies of the mechanical properties of architecturally discrete isotactic−atactic stereoblock PP,[15] the tensile strength of an atactic−isotactic−atactic triblock stereoblock PP material possessing a total isotactic content of 40% displayed a much lower ultimate tensile strength than that of sbPP-3 This observation can be explained in terms of differences in the specific stereoblock microstructure sequence by the fact that the crystalline domains which are dispersed in the material not only behave as physical cross-links, as in other thermoplastic elastomers, but also, as fillers.[36] In addition, the end-block crystalline PP segments serve to anchor the end-blocks within isotactic PP crystals to a much higher degree in an isotactic−atactic−isotactic architectural sequence relative to the isomeric atactic−isotactic−atactic microstructure, even though both possess similar levels of total isotactic content. Finally, in repetitive cyclic testing, stress-relaxation at 300% elongation curves were collected and these data reveal not only that tensile strength increases once again with increasing isotactic fraction but also that hysteresis diminishes (see Figure 3).

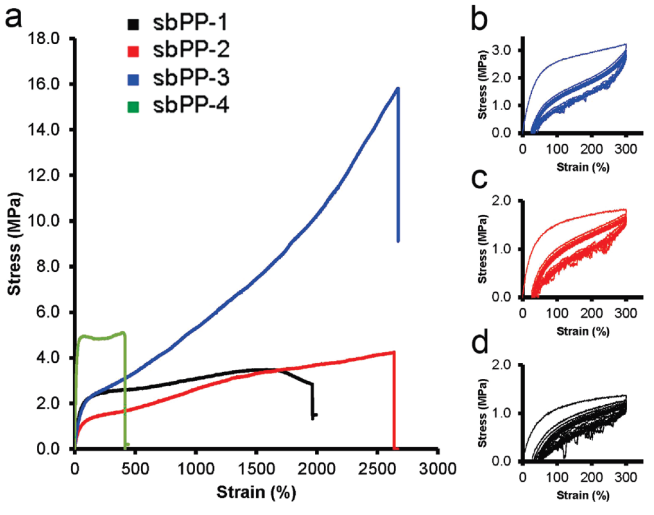


Figure 3. Stress−strain data for the isotactic−atactic−isotactic triblock stereoblock PP materials, sbPP-1 (black), sbPP-2 (red) sbPP-3 (blue), and sbPP-4 (green). Graph a presents elongation-to- break data for the stereoblock samples while graphs b−d present hysteresis curves for 10 repetitive cycles between 0 and 300% strain.

(d). Electrospinning. The stereoblock PP materials were soluble in chloroform, chlorobenzene, toluene, and cyclohexane. However, since dissolving these materials in any of these solvents results in solutions that are not conducive to electrospinning (i.e., low dielectric constant and/or high boiling point), a mixed solvent system was used for this study. The use of a mixed solvent system consisting of 80% (w/w) cyclohexane, 10% (w/w) acetone, and 10% (w/w) *N, N*-dimethylforamide for electrospinning polyolefins has been reported earlier.[22−25] In the current study, a binary solvent mixture of 80% (w/w) cyclohexane and 20% (w/w) acetone resulted in successful fiber formation during electrospinning of all five materials.

Figure 4 shows the field emission scanning electron microscopy (FE-SEM) images of electrospun fibers of sbPP-1 through sbPP-5. The FE-SEM images of sbPP-1 and sbPP-2 share similar morphological features - both appear to show fused and generally ill-defined fibers. Similar morphologies have been reported[37,38] for electrospun fibers formed from other elastomeric polymers. However, a relative comparison of the fibrous morphology of the lowest isotactic content polymer (Figure 4a) to the highest isotactic content polymer (Figure 4e) indicates that the morphologies of the fibers become less fused with better defined edges as the isotactic content increases.

Unlike the morphology of the stereoblock elastomeric PP fibers observed in this study, the morphology of electrospun fibers of highly crystalline polyolefins reported in the literature[22−25] appear with well-defined fiber geometry and with only sporadic fusion points between fibers. It is reasonable to conclude from this observation that, as the isotactic content of the stereoblock PP increases, the amount of crystallizable polymer increases along with a reduction in the compositional contribution of the low T_g atactic PP block domain. As a result, the electrospun sb-PP fibers adopt a more free-standing appearance with better defined geometries and a lower degree of fusion occurring between fibers as total isotactic content increases (*cf.* Figure 4).

The isotactic content of the stereoblock PP samples was characterized using FTIR spectroscopy with an attenuated total reflectance (ATR) attachment and Figure 5 shows the acquired FTIR-ATR spectra for bulk sbPP-1 through sbPP-5. The ratio of the absorbance band at 998 cm^{-1}, a CH_3 rocking mode found only in isotactic PP, to the absorbance band at 973 cm^{-1}, a CH_3 rocking and CC stretching combination mode found in both stereoregular and stereoirregular PP has been reported to be proportional to the isotactic content present in PP.[39] The ratio of these bands for the five materials is presented in Table 4, and as expected, sbPP-4 and sbPP-5 have the highest isotactic contents of ≈45%, followed by sbPP-3, sbPP-2, and sbPP-1. This correlation between the absorbance ratios and the isotactic content targeted by the synthetic strategy fit well for all five of the stereoblock PP samples.

The stereoregularity of the stereoblock PP samples was also probed using FT-Raman spectroscopy in order to determine whether any changes in microstructure had occurred with processing. The basis for this analysis is the

Table 3. Mechanical Testing Data for Stereoblock PP Samples

sample	elongation at break (%)	recovery at break (%)	ultimate tensile strength (MPa)	recovery at 300% elongation (%)
sbPP-1	1986	94.6	2.78	91.3
sbPP-2	2639	97.5	4.24	94.0
sbPP-3	2671	98.6	15.82	95.3
sbPP-4	405	67.7	4.86	

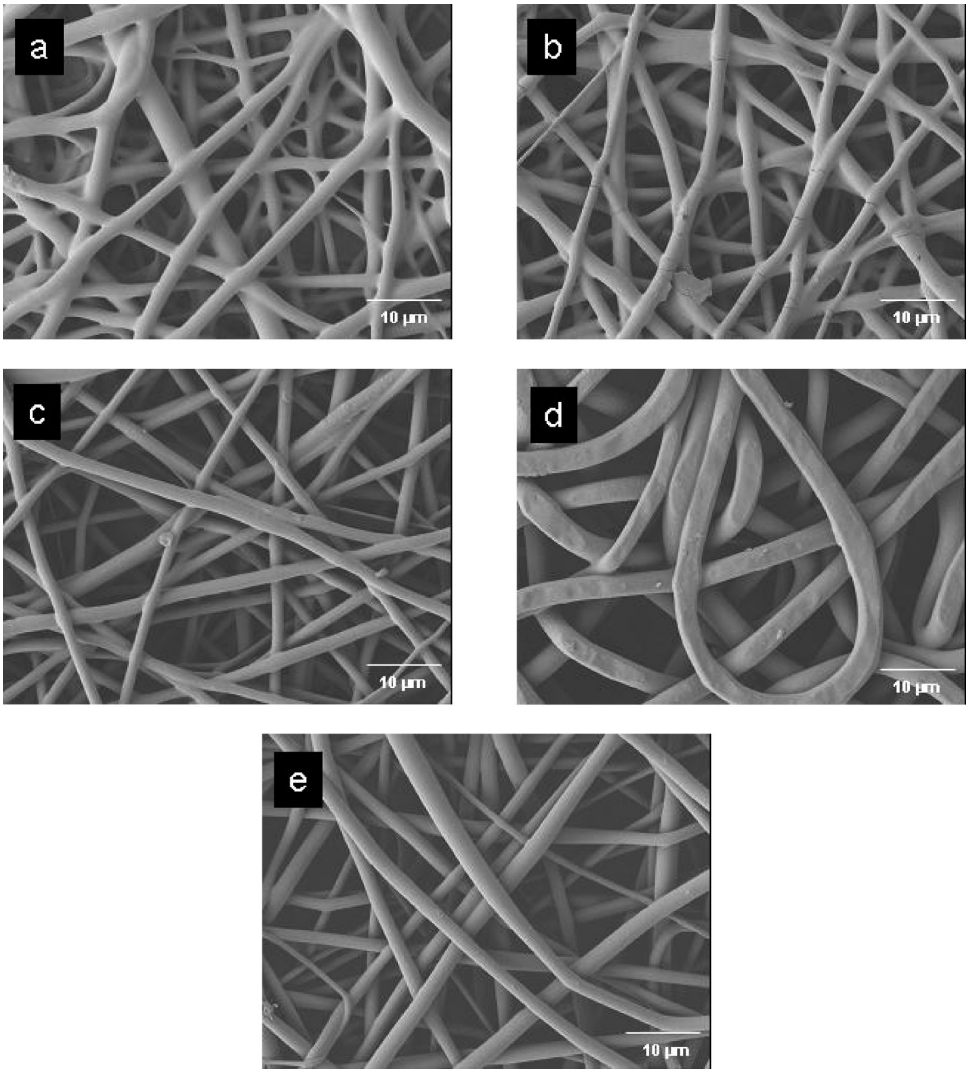


Figure 4. FE-SEM images of electrospun stereoblock PP materials as a function of increasing isotactic content: (a) sbPP-1 (12%), (b) sbPP-2 (24%), (c) sbPP-3 (36%), (d) sbPP-4 (50%), and (e) sbPP-5 (53%).

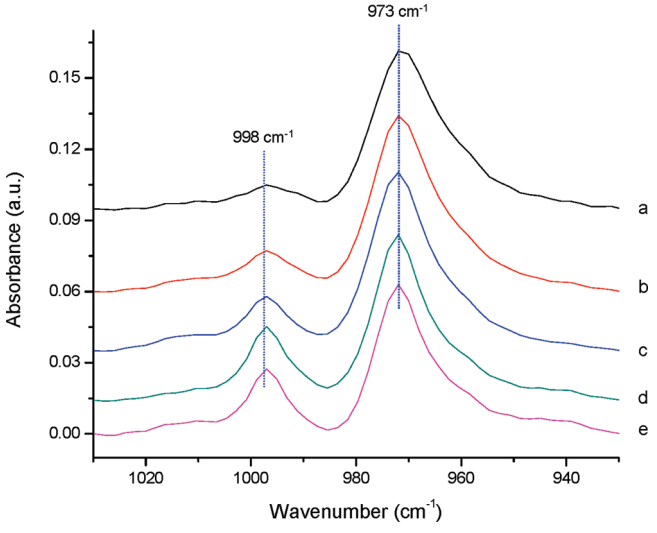


Figure 5. FTIR spectra of bulk stereoblock PP materials as a function of increasing isotactic content: (a) sbPP-1 (12%), (b) sbPP-2 (24%), (c) sbPP-3 (36%), (d) sbPP-4 (50%), and (e) sbPP-5 (53%).

correlation that has been established between isotactic helical content and crystallinity as reported in the literature,[28,40]

Table 4. Summary of the Ratios of the Bands at 997 and 972 cm^{-1}, Which Is Proportional to the Amount of Isotactic Content,[37] for All Five Bulk Stereoblock PP Materials Obtained by FTIR Spectroscopy

sample	A_{997}/A_{972}
sbPP-1	0.156 ± 0.010
sbPP-2	0.240 ± 0.008
sbPP-3	0.316 ± 0.010
sbPP-4	0.457 ± 0.014
sbPP-5	0.442 ± 0.010

and more specifically, between differences in helical backbone conformation and the degree of crystallinity of the polymers. For PP, the Raman bands of are at 809 cm^{-1}, 830 cm^{-1}, and 841 cm^{-1}, and as previously reported, upon cooling isotactic PP from the melt, a broad amorphous peak found in the melt at 830 cm^{-1} (due to nonhelical chains) resolves into two peaks—one centered at 809 cm^{-1} and the other centered at 841 cm^{-1}—that are attributed to an increase in isotactic helical chains within crystalline regions and those within amorphous regions (defects), respectively.[28] Accordingly, the intensity of the 809 cm^{-1} band, relative to the band at 841 cm^{-1}, which has further been recently established to originate with amorphous regions of PP, can be correlated to the number of isotactic PP chains in helical conformation within crystalline domains, and thus the degree of crystallinity of the polymer.[40]

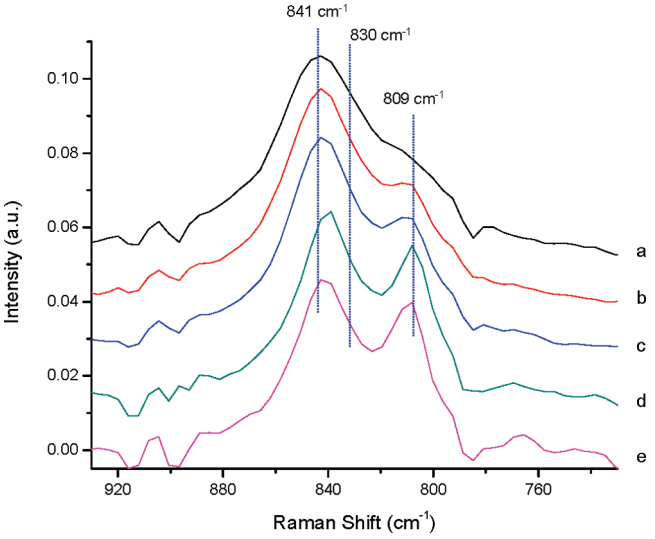


Figure 6. FT-Raman spectra of electrospun stereoblock PP materials as a function of increasing isotactic content: (a) sbPP-1 (12%), (b) sbPP-2 (24%), (c) sbPP-3 (36%), (d) sbPP-4 (50%), and (e) sbPP-5 (53%).

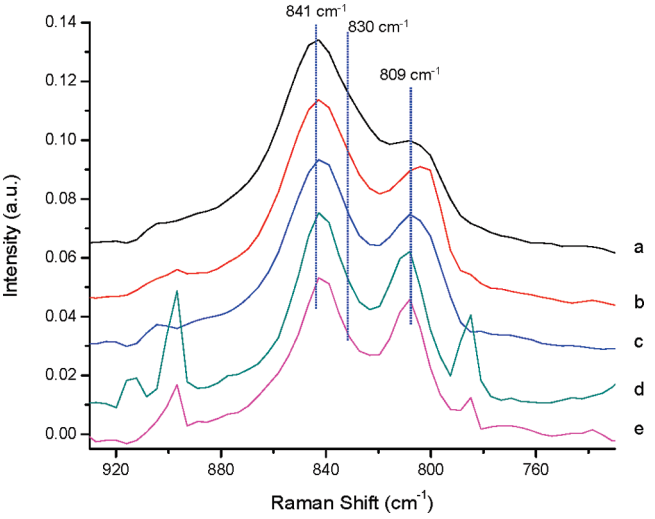


Figure 7. FT-Raman spectra of solvent cast films of stereoblock PP materials as a function of increasing isotactic content: (a) sbPP-1 (12%), (b) sbPP-2 (24%), (c) sbPP-3 (36%), (d) sbPP-4 (50%), and (e) sbPP-5 (53%).

Figures 6 and 7 show the acquired FT-Raman spectra for electrospun fiber mats and solvent cast films, respectively, of the stereoblock PP materials. Importantly, a visual comparison of the Raman spectra of sbPP-1 through sbPP-5 provided by these data clearly reveals an increase in the number of helical chains within crystalline domains as a function of increasing total isotactic, and hence, an increase in crystalline content as determined by an increase in the 809 cm^{-1} band relative to the 841 cm^{-1} band.[28,40] Another important comparison can be made from the data presented in Figures 6 and 7 that reveals that the apparent degree of crystallinity appears to be less in the case of the electrospun fibers relative to the solvent cast films as indicated once again by the relative intensities of the CH_2 rocking bands at 809 and 841 cm^{-1}. This observation suggests that there is an effect of the electrospinning process on the degree of crystallinity of the fibers formed, and in particular, it is likely that the suppression of crystallization of the electrospun fibers relative to that of solvent cast films may be due to very rapid evaporation of the solvent during the electrospinning process that restricts the amount of time required for the polymer chains to develop crystalline registration in the fibers.[41,42] More specifically, the higher degree of crystallinity in the solvent cast films is reasonably due to the slower solvent evaporation kinetics of this process as compared to electrospinning, giving the polymer chains more time to crystallize efficiently. In contrast, during the electrospinning process, the solvent evaporation kinetics are typically on the order of milliseconds, and it is likely therefore that the polymer is electrospun into a more highly disordered, noncrystalline state due to insufficient time to crystallize, thus resulting in a lower degree of crystallinity. In this regard, the electrospinning process can be generally compared to "quenching" process that freezes-in polymer chain disorder.

In order to quantify the effect of electrospinning on the polymer structure and morphology, the thermal properties of both electrospun fibers and solvent cast films of the stereoblock PP samples were investigated by differential scanning calorimetry (DSC). For this analysis, the first heating endotherm was used to study the effect of the process on the stereoblock PP samples, and in keeping with results obtained for other stereoblock PP materials reported in the literature, broad endotherms were typically observed in the present study.[11a,b,31a,31c,43,44] To a first approximation, these broad endotherms are consistent with a distribution of crystallite sizes, as well as crystallites with varying degrees of defects that are present within these materials. Table 5 presents the quantitative DSC results obtained for both the solvent cast films and electrospun fibers and from these data, it can be seen that there is an increasing trend in the width of the endotherm in going from sbPP-1, with low isotactic content, to sbPP-4 and sbPP-5 that have high isotactic content. It is of significant interest that the transition ranges observed for the endotherms of elastomeric PP materials reported in the literature were much broader compared to the materials reported in this study. This difference is most likely due to the fact that the stereoblock PP materials investigated here are architecturally well-defined with discrete block lengths, while, as previously mentioned, the other reported elastomeric PP materials have stereochemically heterogeneous microstructures, and in fact, these latter materials can be physically fractionated into ether soluble, heptane soluble, and heptane insoluble portions. Finally, from a comparison of the calculated degrees of crystallinity obtained from the DSC heat of fusion values presented in Table 5, it can be seen that the solvent cast films have a higher degree of crystallinity than the electrospun counterparts and this observation correlates well with the FT-Raman data for these samples discussed previously.

For a further understanding of the effect of electrospinning on the microstructure of the materials, all five of the stereoblock PP samples were analyzed by synchrotron based X-ray diffraction (XRD). It has been firmly established that isotactic PP can crystallize in three well-characterized structures: the α-form with a monoclinic[45] unit cell, and the β- and γ-forms with trigonal[46] and orthorhombic[47] unit cells, respectively. Isotactic PP generally crystallizes in the thermodynamically more stable α-form,[48] whereas the β-form is typically achieved via specific nucleating agents[30g,49] and the γ-form is attained under only very specific conditions.[50,51] In the present study, the XRD profiles of both the electrospun fibers and solvent cast films of the stereoblock PP samples were compared in order to determine what differences might exist with respect to the degree of crystallinity and the crystalline structure of the materials. As a frame of reference, the characteristic *d*-spacings unique to each of the crystal forms of isotactic PP are 0.477,[48] 0.535,[31b] and 0.441 nm[48] for the α-, β-, and γ-form, respectively.

Table 5. Summary of the Crystallinities and Melting Points Obtained from DSC Measurements of Electrospun Fibers and Solvent Cast Films of all Five Stereoblock PP Materials

material	processing	T_m onset (°C)	T_m peak (°C)	T_m end (°C)	crystallinity (%)
sbPP-1	electrospun	76	103	120	0.95 ± 0.14
	cast film	75	102	119	1.86 ± 0.20
sbPP-2	electrospun	84	104	121	2.90 ± 0.36
	cast film	78	100	120	4.02 ± 0.35
sbPP-3	electrospun	80	108	121	5.45 ± 1.22
	cast film	81	106	120	7.65 ± 1.91
sbPP-4	electrospun	81	116	137	16.9 ± 2.7
	cast film	82	118	138	24.2 ± 2.0
sbPP-5	electrospun	80	119	138	14.8 ± 1.8
	cast film	80	119	138	22.3 ± 1.4

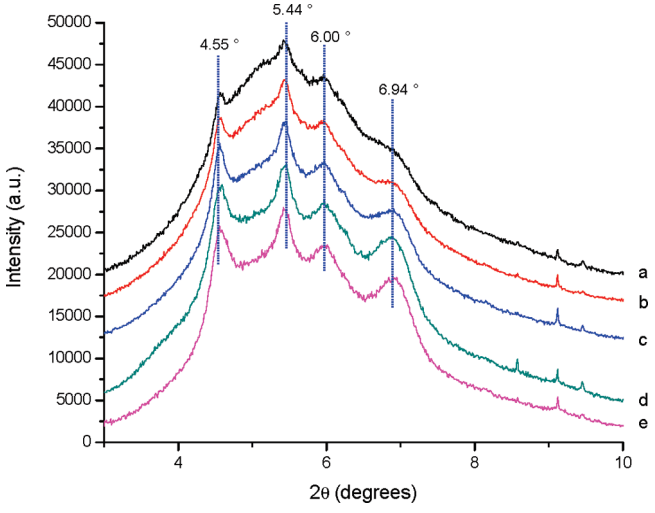


Figure 8. XRD profiles of electrospun stereoblock PP materials as a function of increasing isotactic content: (a) sbPP-1 (12%), (b) sbPP-2 (24%), (c) sbPP-3 (36%), (d) sbPP-4 (50%), and (e) sbPP-5 (53%).

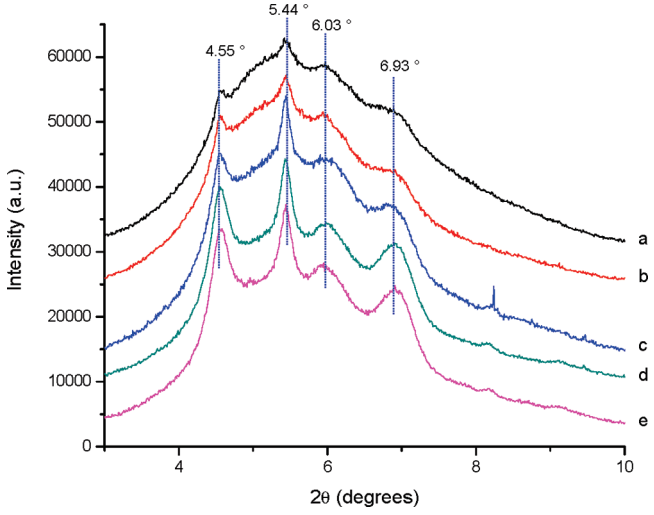


Figure 9. XRD profiles of solvent cast films of stereoblock PP materials as a function of increasing isotactic content: (a) sbPP-1 (12%), (b) sbPP-2 (24%), (c) sbPP-3 (36%), (d) sbPP-4 (50%), and (e) sbPP-5 (53%).

Figures 8 and 9 present the acquired XRD profiles of the electrospun fibers and the solvent cast films of the stereoblock PP materials, respectively. From these data, it can be clearly seen that there is an increase in the intensity of the peaks associated with crystalline phases relative to the amorphous halo with increasing isotactic content of the stereoblock PP sample—and this observation once again corroborates both the FT-Raman and DSC data. Another interesting observation is that all of the stereoblock PP materials, regardless of whether they were electrospun or solvent cast, appear to crystallize in the same form. This result suggests that the electrospinning process does not have an impact on the crystalline structure of the materials, with the thermodynamically stable α-form, as indicated by the peak at $2\theta \approx 6.0°$ (d = 0.476 nm),[48] being the only discernible form observed for both the electrospun fibers and solvent cast films of all five materials. Since each of the other peaks at $2\theta \approx 4.55°$ (d = 0.630 nm), $2\theta \approx 5.44°$ (d = 0.527 nm), and $2\theta \approx 6.94°$ (d = 0.413 nm) are not unique reflections for any of the other crystal forms of isotactic PP,[52] they could not be unambiguously assigned. Other reports in the literature concerning the crystalline structure of other classes of elastomeric PP materials examined under other conditions and during and after different processing treatments have indicated the presence of the α-form only,[31c,44] structures possessing characteristics of both the α- and γ-forms,[11a,53,54] as well as the α- and β-forms.[31b,43] A detailed examination of why only the α-form is observed in this set of well-defined stereoblock PP elastomers is presently beyond the scope of this current investigation.

The degrees of crystallinity of the electrospun fibers and solvent cast films for each of the five elastomers were also calculated and the results are shown in Table 6. Qualitatively, while the trends all remain the same, the XRD-determined degrees of crystallinity were observed to be consistently lower than that measured by DSC for both electrospun fibers and solvent cast films. Similar differences between XRD- and DSC-determined degrees of crystallinity have been reported for other elastomeric PP materials.[11a] In the present work, it is possible that the origin for this difference lies with contributions to the total degree of crystallinity from both well-ordered and more-disordered crystalline phases. More specifically, whereas the measured degree of crystallinity from DSC accounts for contributions from all crystalline phases, that calculated by XRD can be more biased toward contributions made from only the well-ordered crystallites within the sample, with the more disordered crystalline phases being included within the assigned amorphous halo that was determined for the lowest crystalline sample (electrospun sbPP-1). Nonetheless, similar to the FT-Raman and DSC results, both the electrospun fibers and the solvent cast films for the stereoblock PP samples demonstrate the same trend, namely, an increase in the crystallinity of the polymer correlates with an increase in isotactic content. In addition, in comparing the electrospun fibers and the solvent cast films, the higher isotactic content of sbPP-4 and sbPP-5 yield a higher degree of crystallinity for the solvent cast films relative to the electrospun fibers. However, for sbPP-1, sbPP-2, and sbPP-3, there was no discernible difference in crystallinities between the electrospun fibers and the solvent cast films. The fact that both solvent cast sbPP-4 and sbPP-5 have a higher degree of crystallinity than their electrospun counterparts can be attributed to the different

Table 6. Summary of the Crystallinities Obtained from XRD Measurements on Electrospun Fibers and Solvent Cast Films for All Five Stereoblock PP Materials

sample	processing	crystallinity (%)[a]
sbPP-1	electrospun	3
	cast film	3
sbPP-2	electrospun	4
	cast film	4
sbPP-3	electrospun	6
	cast film	6
sbPP-4	electrospun	7
	cast film	11
sbPP-5	electrospun	8
	cast film	11

[a] Due to time constraints, profiles for all of the samples could not be repeated. For samples that were reproduced, crystallinity calculations suggest an error on the order of 0.1%.

solvent evaporation kinetics between the two processes, with the rapid solvent evaporation kinetics of electrospinning[41,42] quenching a higher degree of disorder into the materials than their solvent cast analogues.

Conclusions

The results of the present study have served to document the ability to prepare, for the first time, stereochemically homogeneous and architecturally discrete isotactic−atactic−isotactic triblock stereoblock PP thermoplastic elastomers in which the block lengths for each domain type can be varied in programmed fashion while keeping the molecular weight indices, including polydispersity, the same. Part of the reason for the success in being able to synthesize these stereoblock PP materials may, in fact, rest with a greater solubility that arises due to the level of *mmmr, mmrr*, and *mrrm* stereoerror incorporation within the crystalline isotactic domains that have a % mmmm pentad content of 0.71. Although it remains to be seen what physical properties will emerge for similar stereoblock PP architectures in which the isotactic domains possess a higher or lower level of stereoerror incorporation, the solubility displayed by the current stereoblock materials has played an important role in the successful electrospinning processing of elastomeric fiber mats. Extensive investigation of the overall degree of crystallinity and of the isotactic PP crystal structure of these electrospun fiber mats reveal well-defined trends that are associated with the overall isotactic content—and most importantly, a less-fused, more well-defined morphology that emerges with higher isotactic contents. However, a clear trade-off exists with respect to achieving an excellent electrospun fiber morphology by increasing the total isotactic content of an isotactic−atactic−isotactic stereoblock PP, while at the same time, not losing desirable elastomeric properties, such as the case for the samples of sbPP-4 and sbPP-5. Fortunately, the methodology that has been developed by us for the programmed synthesis of architecturally discrete isotactic−atactic stereoblock PP also permits further modulation of the level of stereoerror incorporation for the isotactic domains.[14] Accordingly, additional studies are now in progress to identify the best combination of stereoerror level incorporation and total isotactic content for these well-defined stereoblock PP materials that can maximize desirable elastomeric traits and solution-based processing properties, while at the same achieving the best possible structural forms for potential product applications.

Acknowledgment. Funding for this work was provided by NSF CHE-0848293 (to L.R.S.) and NSF IGERT 0221651, NSF DMR 0704970, NSF DMR 0315461 (to J.F.R.) for which we are grateful. The authors would like to acknowledge Dr. Chris Snively for many pertinent discussions as well as Dr. Nikhil Sharma for his help with film processing. We also acknowledge Dr. Soenke Seifert and beamline 12-BM-B of the Advanced Photon Source at Argonne National Lab, Steve Bennett and beamline X10A of the National Synchrotron Light Source at Brookhaven National Lab, and Dr. Andrew Fitch and Dr. Irene Margiolaki and beamline ID31 of the ESRF in Grenoble, France for help with carrying out X-ray scattering experiments. We also thank Dr. Debra Norris and the Office of Graduate and Professional Education at the University of Delaware for additional travel funds.

References and Notes

(1) Natta, G. *J. Polym. Sci.* **1959**, *34*, 531–549.
(2) For a recent comprehensive review and in-depth evaluation of the literature related to stereoblock PP, see: Busico, V. In *Stereoselective Polymerization with Single-Site Catalysts*; Baugh, L. S., Canich, J. M., Eds.; CRC Press: New York, 2008; Chapter 8.
(3) For other leading reviews of stereoblock PP materials, see: (a) *Polypropylene Handbook*; Moore, E. P., Jr., Ed.; Hanser Publishers: New York, 1996. (b) Busico, V.; Cipullo, R. *Prog. Polym. Sci.* **2001**, *26*, 443–533. (c) Resconi, L.; Cavallo, L.; Fait, A.; Piemontesi, F. *Chem. Rev.* **2000**, *100*, 1253–1345. (d) Lin, S.; Waymouth, R. M. *Acc. Chem. Res.* **2002**, *35*, 765–773.
(4) (a) *Thermoplastic Elastomers*, 2nd ed.; Holden, G., Legge, N. R., Quirk, R. P., Schroeder, H. E., Eds.; Hanser Publishers: New York, 1996. (b) *Handbook of Thermoplastic Elastomers*, 2nd ed.; Walker, B. M., Rader, C. P., Eds.; Van Nostrand Reinhold: New York, 1998.
(5) (a) Miller, S. A.; Bercaw, J. E. *Organometallics* **2002**, *21*, 934–945. (b) Ewen, J. A.; Jones, R. L.; Elder, M. J.; Camurati, I.; Pritzkow, H. *Macromol. Chem. Phys.* **2004**, *205*, 302–307. (c) Miller, S. A. *Macromolecules* **2004**, *37*, 3983–3995.
(6) (a) Nishii, K.; Shiono, T.; Ikeda, T. *Macromol. Rapid Commun.* **2004**, *25*, 1029–1032. (b) Cai, Z.; Nakayama, Y.; Shiono, T. *Kinetics Catal.* **2006**, *47*, 274–277. (b) Cai, Z.; Nakayama, Y.; Shiono, T. *Macromolecules* **2008**, *41*, 6596–6598.
(7) National Petrochemical and Refiners Association Annual Report, **2007**
(8) Even fully amorphous atactic PP of sufficiently high molecular weight exhibits elastic properties; see, for instance: (a) Resconi, L.; Jones, R. J.; Rheingold, A. L.; Yap, G. P. A. *Organometallics* **1996**, *15*, 998–1005. (b) Balboni, D.; Moscardi, G.; Baruzzi, G.; Braga, V.; Camurati, I.; Piemontesi, F.; Resconi, L.; Nifant'ev, I. E.; Venditto, V.; Antinucci, S. *Macromol. Chem. Phys.* **2001**, *202*, 2010–2028.
(9) For reports of "two-state" coordination polymerization processes for producing elastomeric "stereoblock" PP, see: (a) Chien, J. C. W.; Llinas, G. H.; Rausch, M. D.; Lin, G. Y.; Winter, H. H.; Atwood, J. L.; Bott, S. G. *J. Am. Chem. Soc.* **1991**, *113*, 8569–8570. (b) Erker, G.; Aulbach, M.; Knickmeier, M.; Wingbermuehle, D.; Krueger, C.; Nolte, M.; Werner, S. *J. Am. Chem. Soc.* **1993**, *115*, 4590–4601. (c) Coates, G. W.; Waymouth, R. M. *Science* **1995**, *267*, 217–219. (d) Bravakis, A. M.; Bailey, L. E.; Pigeon, M.; Collins, S. *Macromolecules* **1998**, *31*, 1000–1009. (e) Dietrich, U.; Hackmann, M.; Rieger, B.; Klinga, M.; Leskelä, M. *J. Am. Chem. Soc.* **1999**, *121*, 4348–4355. (f) Volkis, V.; Nelkenbaum, E.; Lisovskii, A.; Hasson, G.; Semiat, R.; Kapon, M.; Botoshansky, M.; Eishen, Y.; Eisen, M. S. *J. Am. Chem. Soc.* **2003**, *125*, 2179–2194. (g) De Rosa, C.; Auriemma, F.; Circelli, T.; Longo, P.; Boccia, A. C. *Macromolecules* **2003**, *36*, 3465–3475. (h) Smolensky, E.; Kapon, M.; Woollins, J. D.; Eisen, M. S. *Organometallics* **2005**, *24*, 3255–3265.
(10) Thermoplastic elastomeric PP can also possess a microstructure with overall low isotacticity in which short runs of stereoregular insertions from small crystalline domains within an amorphous matrix, see: Hild, S.; Cobzaru, C.; Troll, C.; Rieger, B. in *Stereoselective Polymerization with Single-Site Catalysts*; Baugh, L. S., Canich, J. M., Eds.; CRC Press: New York, 2008; Chapter 9 and references cited therein.
(11) See for instance: (a) Hu, Y.; Krejchi, M. T.; Shah, C. D.; Myers, C. L.; Waymouth, R. M. *Macromolecules* **1998**, *31*, 6908–6916. (b) Carlson, E. D.; Krejchi, M. T.; Shah, C. D.; Terakawa, T.; Waymouth, R. M.; Fuller, G. G. *Macromolecules* **1998**, *31*, 5343–5351.
(12) For a recent comprehensive review of living coordination polymerization, see: Domski, G. J.; Rose, J. M.; Coates, G. W.; Bolig, A. D.; Brookhart, M. *Prog. Polym. Sci.* **2007**, *32*, 30–92.
(13) Jayaratne, K. C.; Sita, L. R. *J. Am. Chem. Soc.* **2000**, *122*, 958–959.
(14) Zhang, Y.; Keaton, R. J.; Sita, L. R. *J. Am. Chem. Soc.* **2003**, *125*, 9062–9069.

(15) Harney, M. B.; Zhang, Y.; Sita, L. R. *Angew. Chem., Int. Ed.* **2006**, *45*, 2400–2404.
(16) Harney, M. B.; Zhang, Y.; Sita, L. R. *Angew. Chem., Int. Ed.* **2006**, *45*, 6140–6144.
(17) Sita, L. R. *Angew. Chem., Int. Ed.* **2009**, *48*, 2464–2472.
(18) (a) Kennedy, J. P.; Price, J. L.; Koshimura, K. *Macromolecules* **1991**, *24*, 6567–6571. (b) Puskas, J. E.; Antony, P.; El-Fray, M.; Altstadt, V. *Eur. Polym. J.* **2003**, *39*, 2041–2049.
(19) Huang, Z. M.; Zhang, Y. Z.; Kotaki, M.; Ramakrisha, S. *Compos. Sci. Technol.* **2003**, *63*, 2223–2253.
(20) Greiner, A.; Wendorff, J. H. *Angew. Chem., Int. Ed.* **2007**, *26*, 5670–5703.
(21) Givens, S. R.; Gardner, K. H.; Rabolt, J. F.; Chase, D. B. *Macromolecules* **2007**, *40*, 608–610.
(22) Lee, K. H.; Ohsawa, O.; Watanabe, K.; Kim, I. S.; Givens, S. R.; Chase, B.; Rabolt, J. F. *Macromolecules* **2009**, *42*, 5215–5218.
(23) Lee, K. H.; Snively, C. M.; Givens, S.; Chase, D. B.; Rabolt, J. F. *Macromolecules* **2007**, *40*, 2590–2595.
(24) Lee, K. H.; Givens, S.; Chase, D. B.; Rabolt, J. F. *Polymer* **2006**, *47*, 8013–8018.
(25) Lee, K. H.; Givens, S. R.; Snively, C. M.; Chase, B.; Rabolt, J. F. *Macromolecules* **2008**, *41*, 3144–3148.
(26) (a) van Dijk, M. A.; van den Berg, R. *Macromolecules* **1995**, *28*, 6773–6778. (b) Stocker, W.; Beckmann, J.; Stadler, R.; Rabe, J. P. *Macromolecules* **1996**, *29*, 7502–7507. (c) Leclère, Ph.; Lazzaroni, R.; Brédas, J. L.; Yu, J. M.; Dubois, Ph.; Jérôme, R. *Langmuir* **1996**, *12*, 4317–4320.
(27) Jayaratne, K. C.; Keaton, R. J.; Henningsen, D. A.; Sita, L. R. *J. Am. Chem. Soc.* **2000**, *122*, 10490–10491.
(28) Nielsen, A. S.; Batchelder, D. N.; Pyrz, R. *Polymer* **2002**, *43*, 2671–2676.
(29) Busico, V.; Cipullo, R. *Prog. Polym. Sci.* **2001**, *26*, 443–533.
(30) (a) Vancso, G. J. In *Polypropylene: An A-Z Reference*; Karger-Kocsis, J., Ed.; Kluwer Academic Press: Dordrecht, The Netherlands, 1999. (b) Schönherr, H.; Snetivy, D.; Vancso, G. J. *Polym. Bull. (Berlin)* **1993**, *30*, 567–574. (c) Trifonava, D.; Varga, J.; Vancso, G. J. *Polym. Bull. (Berlin)* **1998**, *41*, 341–348. (d) Haeringen, D. T. V.; Varga, J.; Ehrenstein, G. W.; Vancso, G. J. *J. Polym. Sci., Part B: Polym. Phys.* **2000**, *38*, 672–681. (e) Stocker, W.; Magonov, S. N.; Cantow, H. J.; Wittmann, J. C.; Lotz, B. *Macromolecules* **1993**, *26*, 5915–5923. (f) Snétivy, D.; Guillet, J. E.; Vancso, G. J. *Polymer* **1993**, *34*, 429–431. (g) Stocker, W.; Schumacher, M.; Graff, S.; Thierry, A.; Wittmann, J. C.; Lotz, B. *Macromolecules* **1998**, *31*, 807–814.
(31) (a) Kravchenko, R. L.; Sauer, B. B.; McLean, R. S.; Keating, M. Y.; Cotts, P. M.; Kim, Y. H. *Macromolecules* **2000**, *33*, 11–13. (b) Wiyatno, W.; Pople, J.; Gast, A. P.; Waymouth, R. M.; Fuller, G. G. *Macromolecules* **2002**, *35*, 8488–8497. (c) Schöenherr, H.; Wiyatno, W.; Pople, J.; Frank, C. W.; Fuller, G. G.; Gast, A. P.; Waymouth, R. M. *Macromolecules* **2002**, *35*, 2654–2666. (d) Schöenherr, H.; Waymouth, R. M.; Frank, C. W. *Macromolecules* **2003**, *36*, 2412–2418.
(32) Makio, H.; Kashiwa, N.; Fujita, T. *Adv. Synth. Catal.* **2002**, *344*, 477–493.
(33) (a) Ruokolainen, J.; Mezzenga, R.; Fredrickson, G. H.; Kramer, E. J.; Hustad, P. D.; Coates, G. W. *Macromolecules* **2005**, *38*, 851–860. (b) Hotta, A.; Cochran, E.; Ruokolainen, J.; Khanna, V.; Fredrickson, G. H.; Kramer, E. J.; Shin, Y. W.; Shimizu, F.; Cherian, A. E.; Hustad, P. D.; Rose, J. M.; Coates, G. W. *Proc. Natl. Acad. Sci. U.S.A.* **2006**, *103*, 15327–15332. (c) Rose, J. M.; Deplace, F.; Lynd, N. A.; Wang, Z. G.; Hotta, A.; Lobkovsky, E. B.; Kramer, E. J.; Coates, G. W. *Macromolecules* **2008**, *41*, 9548–9555. (d) Deplace, F.; Wang, G. Z.; Lynd, N. A.; Hotta, A.; Rose, J. M.; Hustad, P. D.; Tian, J.; Ohtaki, H.; Coates, G. W.; Shimizu, F.; Hirokane, K.; Yamada, F.; Shin, Y. W.; Rong, L. X.; Zhu, J.; Toki, S.; Hsiao, B. S.; Fredrickson, G. H.; Kramer, E. J. *J. Polym. Sci., Part B: Polym. Phys.* **2010**, *48*, 1428–1437.
(34) (a) Rangarajan, R.; Register, R. A.; Fetters, L. J. *Macromolecules* **1993**, *26*, 4640–4645. (b) Zhu, L.; Chen, Y.; Zhang, A.; Calhoun, B. H.; Chun, M.; Quirk, R. P.; Cheng, S. Z. D.; Hsiao, B. S.; Yeh, F.; Hashimoto, T. *Phys. Rev. B* **1999**, *60*, 10022–10031.
(35) De Rosa, C.; Auriemma, F.; Di Capua, A.; Resconi, L.; Guidotti, S.; Camurati, I.; Nifant'ev, I. E.; Laishevtsev, I. P. *J. Am. Chem. Soc.* **2004**, *126*, 17040–17049.
(36) Mohajer, Y.; Wilkes, G. L.; Wang, I. C.; McGrath, J. E. *Polymer* **1982**, *23*, 1523–1535.
(37) Fang, J.; Lin, T.; Tian, W.; Sharma, A.; Wang, X. G. *J. Appl. Polym. Sci.* **2007**, *105*, 2321–2326.
(38) Stankus, J. J.; Guan, J. J.; Wagner, W. R. *J. Biomed. Mater. Res.* **2004**, *70A*, 603–614.
(39) Burfield, D. R.; Loi, P. S. T. *J. Appl. Polym. Sci.* **1988**, *36*, 279–293.
(40) Minogianni, C.; Gatos, K. G.; Galiotis, C. *Appl. Spectrosc.* **2005**, *59*, 1141–1147.
(41) Reneker, D. H.; Yarin, A. L.; Fong, H.; Koombhongse, S. *J. Appl. Phys.* **2000**, *87*, 4531–4547.
(42) Yarin, A. L.; Kataphinan, W.; Reneker, D. H. *J. Appl. Phys.* **2005**, *98*, 064501.
(43) Wiyatno, W.; Pople, J. A.; Gast, A. P.; Waymouth, R. M.; Fuller, G. G. *Macromolecules* **2002**, *35*, 8498–8508.
(44) Hu, Y. R.; Carlson, E. D.; Fuller, G. G.; Waymouth, R. M. *Macromolecules* **1999**, *32*, 3334–3340.
(45) Brückner, S.; Meille, S. V.; Petraccone, V.; Pirozzi, B. *Prog. Polym. Sci.* **1991**, *16*, 361–404.
(46) Meille, S. V.; Ferro, D. R.; Bruckner, S.; Lovinger, A. J.; Padden, F. J. *Macromolecules* **1994**, *27*, 2615–2622.
(47) Brückner, S.; Meille, S. V. *Nature* **1989**, *340*, 455–457.
(48) De Rosa, C.; Auriemma, F.; Circelli, T.; Waymouth, R. M. *Macromolecules* **2002**, *35*, 3622–3629.
(49) Dorset, D. L.; McCourt, M. P.; Kopp, S.; Schumacher, M.; Okihara, T.; Lotz, B. *Polymer* **1998**, *39*, 6331–6337.
(50) Thomann, R.; Wang, C.; Kressler, J.; Mülhaupt, R. *Macromolecules* **1996**, *29*, 8425–8434.
(51) Alamo, R. G.; Kim, M. H.; Galante, M. J.; Isasi, J. R.; Mandelkern, L. *Macromolecules* **1999**, *32*, 4050–4064.
(52) Auriemma, F.; De Rosa, C. *Macromolecules* **2006**, *39*, 7635–7647.
(53) De Rosa, C.; Auriemma, F.; Perretta, C. *Macromolecules* **2004**, *37*, 6843–6855.
(54) Auriemma, F.; De Rosa, C.; Corradi, M. *Adv. Mater.* **2007**, *19*, 871–874.

Macromolecules
ARTICLE

Macromolecules **2011**, *44*, 483–489 **483**
DOI: 10.1021/ma102373y

A Water-Soluble Organometallic Conjugated Polyelectrolyte for the Direct Colorimetric Detection of Silver Ion in Aqueous Media with High Selectivity and Sensitivity

Chuanjiang Qin,[†] Wai-Yeung Wong,*[,†] and Lixiang Wang*[,‡]

[†]*Department of Chemistry and Centre for Advanced Luminescence Materials, Hong Kong Baptist University, Waterloo Road, Kowloon Tong, Hong Kong, P. R. China, and* [‡]*State Key Laboratory of Polymer Physics and Chemistry, Changchun Institute of Applied Chemistry, Chinese Academy of Sciences, Changchun 130022, P. R. China*

Received October 18, 2010; Revised Manuscript Received December 10, 2010

ABSTRACT: A water-soluble organometallic conjugated polyelectrolyte **P1** and its corresponding model complex **M1** based on an aspartic acid-substituted fluorene spacer are reported, which possess good water solubility as well as intriguing fluorescent and phosphorescent dual-emissive properties in a completely organic-free aqueous medium at room temperature. A new colorimetric silver ion sensor based on **P1** is developed, which shows high selectivity and sensitivity for Ag^+ ions in buffered water solution because of the Ag^+-induced intersystem crossing from the singlet to triplet states. The obvious color change from colorless to yellow upon exposure to Ag^+ ion is visible to the naked eyes and can be quantified colorimetrically by the visible absorption spectroscopic method. On the basis of the fluorescence intensity of **P1** obtained in the fluorescence titration curves, a linear relationship is observed in the Stern−Volmer plot at low concentrations (1−5 μM), and the corresponding Stern−Volmer quenching constant (K_{SV}) of 1.9×10^5 M^{-1} for **P1** is comparable to that obtained from the fluorescence titration studies. As determined by the Benesi−Hildebrand plot obtained from the absorption spectra, a 1:1 complex formation is anticipated between the Pt compound and Ag^+ ion. The limit of detection is low at 0.5 μM, i.e., at concentrations in the ppb range. The present study represents an original approach using a water-soluble organometallic conjugated polyelectrolyte for the accurate and rapid detection of trace amounts of Ag^+ ion in pure water. It also establishes a new system featuring dual-emissive properties of platinum(II) acetylide-based conjugated polymers for chemosensing application.

1. Introduction

Silver ion is an environmental pollutant of great public concern and has adverse biological effects on human health.[1] Thus, there is an upsurge of interest in the development of rapid and selective detection method of Ag^+ ions in water or food resource within the scope of health science. Various methods, such as atomic absorption spectroscopy, inductively coupled plasma-mass spectroscopy, and electrochemical methods based on ion-selective electrodes, have been developed in such research endeavor.[2] However, most of these procedures are relatively time-consuming and not cost-effective in practice. On the other hand, fluorimetric methods are widely used for bioimaging and sensing applications owing to their high sensitivity, rapid response, and facile detection by purely optical means.[3] To date, there are a handful of literature reports on using molecular probes as fluorescent chemosensors for Ag^+ ion that are only applicable in organic or mixed aqueous−organic solutions,[4] and to our knowledge, only one example is presently known in exploiting conjugated organic polymers for Ag^+ ion sensing in nonaqueous medium.[4k] Recently, one successful example was reported by using a dye-labeled silver-specific oligonucleotide and graphene oxide in a buffer solution and river water.[5] Even that, there is no precedented report of using water-soluble conjugated polymers (either organic or organometallic in nature) for the accurate and rapid detection of trace amounts of Ag^+ ion in pure water, and this research frontier is certainly important for practical applications in environmental and biological assays in aqueous media.[6]

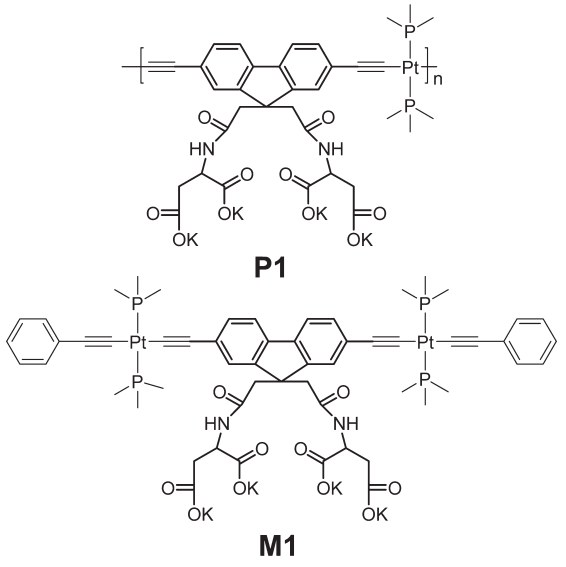
Conjugated polyelectrolytes (CPEs) have found wide applications in chemo- and biosensing technology because they combine the amplified quenching of fluorescent conjugated polymers with the good water solubility and processability and ionic nature of the polyelectrolytes.[7] However, most of the works in this field have proliferated largely in conjugated materials consisting of organic building blocks, and only a few examples of metal ion sensors (excluding those for Ag^+ ion, however) using water-soluble organometallic conjugated polyelectrolytes can be found in the literature.[8] In fact, platinum(II) acetylide-derived conjugated polymers have attracted much attention due to their rich room-temperature phosphorescence properties with potential applications in various research domains.[9] Although previous studies have demonstrated that triplet excitons are much less delocalized in the conjugated backbone as compared to singlet excitons, their long exciton lifetimes and inter- or intrachain triplet exciton migration can lead to the development of promising chemosensing materials with high sensitivity.[8b] We can also observe fluorescent and phosphorescent dual emissions simultaneously in a single conjugated polymer through the copolymerization of organic chromophores with platinum acetylide conjugated segments that would facilitate efficient intersystem crossing (ISC).[10] Interestingly, no published report involving the dual-emissive properties of platinum(II) acetylide-based conjugated polymers for chemosensing application is yet available, even though a dual-emissive-materials design concept has recently

*Corresponding authors. E-mail: rwywong@hkbu.edu.hk (W.-Y.W.); lixiang@ciac.jl.cn (L.W.).

© 2010 American Chemical Society

Published on Web 12/31/2010

Scheme 1. Chemical Structures of P1 and M1



been put forward by Fraser et al.[11] In fact, silver nitrate was shown to be a good candidate to function as a heavy-atom-induced room-temperature phosphorescent reagent.[12] This raises up a simple question here: Can we make use of the properties of both worlds (i.e., platinum acetylide-based conjugated polymer and Ag^+ ion) together to develop a new probe for Ag^+ ion sensing? In order to establish a selective and sensitive Ag^+ analyte sensor in an aqueous medium, the integration of water-soluble fluorene unit and platinum acetylide moiety appears to be a wise choice. It is also well-known that polyfluorene CPEs are promising class of materials.[13] Here, we report for the first time a novel water-soluble platinum acetylide-based CPE **P1** (Scheme 1) based on an aspartic acid-substituted fluorene spacer possessing high electron density and dendritic structure as the water solubilizer which can serve multiple functions: good water solubility coupled with strong fluorescence and phosphorescence as well as selective and colorimetric response to Ag^+ ion in water. The corresponding dinuclear model complex **M1** was also prepared for comparison studies.

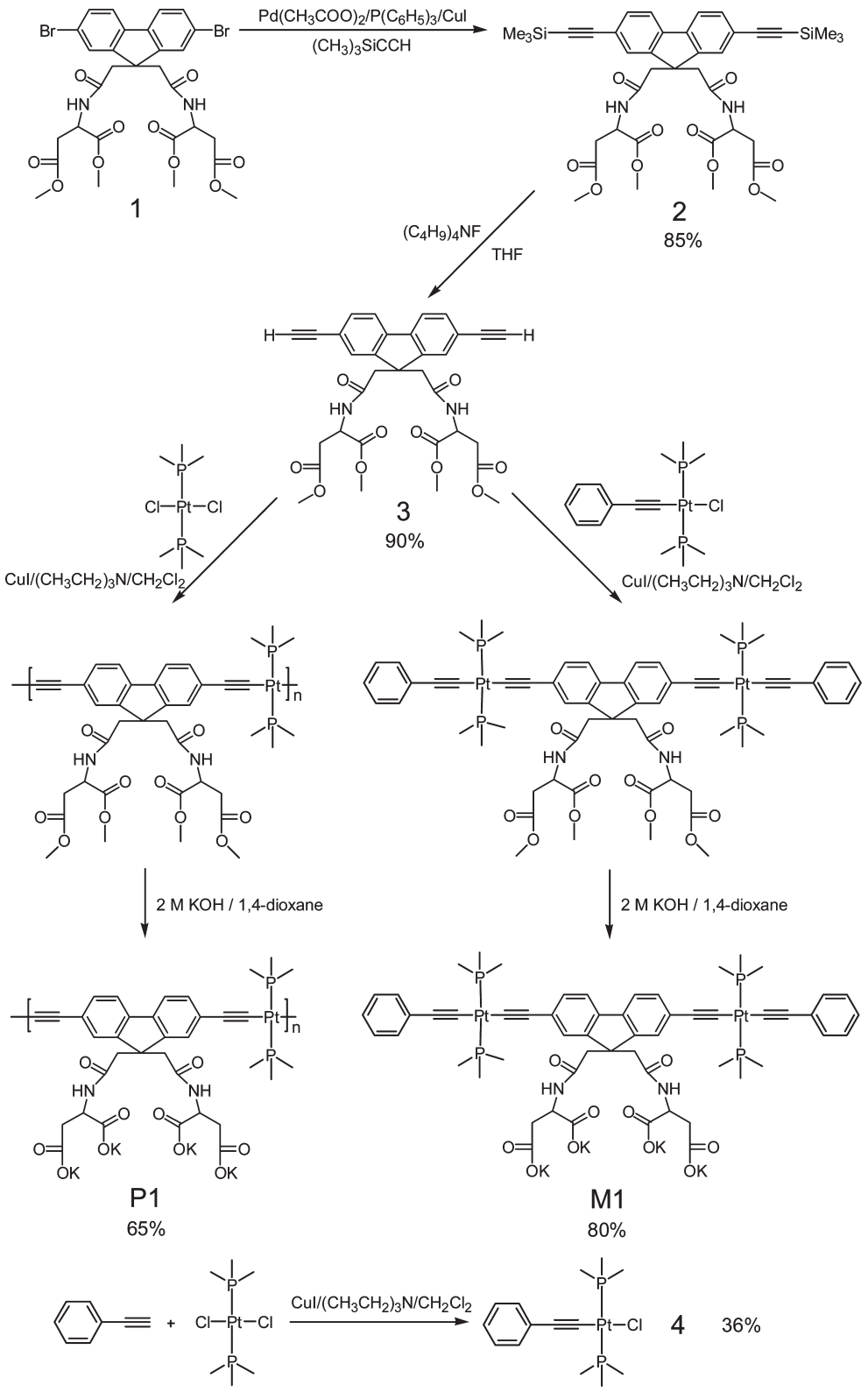
2. Results and Discussion

2.1. Synthesis and Characterization. The neutral diester precursor polymer of **P1** was obtained from the Sonogashira coupling reaction between $[Pt(PMe_3)_2Cl_2]$ and the diethynyl ligand (Scheme 2).[8−10] This precursor polymer is soluble in organic solvents such as $CHCl_3$ and THF, and its molecular weight was characterized by gel permeation chromatography (GPC) using polystyrene standards (M_n = 26 340 g mol^{-1} and M_w = 62 360 g mol^{-1} with polydispersity index PDI = 2.36). The anionic water-soluble CPE **P1** was obtained by hydrolysis of the ester using 2 M KOH solution as a base, and the desired polymer was purified by dialysis against Milli-Q water using an 8 kDa molecular weight cutoff dialysis membrane. The final polyelectrolyte **P1** containing ionic side groups was characterized via ^1H NMR, ^{31}P NMR, and IR spectroscopies.

2.2. Photophysical Characterization. As shown in Figure 1, **P1** exhibits an absorption peak at 390 nm due to the long-axis polarized π,π^* transition of platinum acetylide backbone in water. The emission from **P1** features two bands with λ_{max} at 405 and 540 nm in degassed water (Φ_{em} = 0.23%). The high-energy band belongs to the fluorescence from $^1\pi,\pi^*$ state (τ_F = 0.8 ns), whereas the low-energy one is due to the phosphorescence from $^3\pi,\pi^*$ manifold (τ_P = 11.3 μs). Both the absorption and emission spectra of **P1** are similar to those found for common organic-soluble fluorene-based platinum acetylide polymers in CH_2Cl_2.[9c] The observation of intense fluorescent and phosphorescent dual emissions (peak intensity ratio ~1:1) for **P1** at room temperature in water is a manifestation of the fact that it has a good water solubility, and the H_2O molecule could increase the ISC efficiency from the singlet to the triplet states.[14] Previous studies demonstrated that the absorption and PL spectra of CPEs are pH-dependent because the pH of water solution can influence the charge amount of these anionic CPEs.[7e,15] A series of absorption and PL spectra of our dendronized polymer were recorded in 5 mM phosphate buffer solutions at pH values ranging from 3 to 11 (at the pH interval of 2). As shown in Figure S1a of the Supporting Information, the absorption peak of **P1** is slightly red-shifted from 390 nm at pH = 11 to 393 nm at pH = 3. Simultaneously, its peak intensity is reduced by almost half. This is due to the protonation of the carboxylate groups which results in an aggregation of conjugated polymer chains.[15c] From the pH dependence of PL spectra of **P1** as shown in Figure S1b of the Supporting Information, when the pH value is 7, its fluorescent emission maximum can be kept quite stable, but the intensity of phosphorescent emission decreased to about 31% of its original intensity. When the pH value is 3, the fluorescent emission maximum slightly decreased with a red shift of 12 nm. However, the phosphorescent emission intensity was only about 4% of the original one when the pH value decreased from 11 to 3, and the peak position is only red-shifted by 3 nm. Such result would be expected since aggregation of the conjugated polymer chains typically exerts a stronger effect on the fluorescent peak position than that for the phosphorescence, but for the emission intensity, the observation is just the opposite. This phenomenon was also demonstrated in poly(*p*-phenyleneethynylene)-type Pt-acetylide-based CPE.[8a]

2.3. Silver Ion Sensing Studies. Our initial investigations were focused on the response of **P1** to different metal ions based on the absorption spectra. As illustrated in Figure 2, upon addition of an excess amount of each metal ion (10 μM), i.e., Ca^{2+}, Cd^{2+}, Cu^{2+}, Co^{2+}, Mg^{2+}, Ni^{2+}, Zn^{2+}, Pb^{2+}, Fe^{3+}, Li^+, and Cs^+, only a very slight decrease in intensity of the absorption peak (at 390 nm) was noted. When 10 μM Hg^{2+} was added into the solution of **P1**, the absorption intensity decreased dramatically with a hypsochromic shift of about 12 nm in absorption wavelength. In a sharp contrast, the addition of 10 μM Ag^+ resulted in a distinct intensity change and a large bathochromic shift of 25 nm. At the same time, we also examined the PL response of **P1** to different metal ions in degassed water (Figure S2 of the Supporting Information). For most cations, they quenched both fluorescence and phosphorescence of **P1** to some extent. While the addition of 10 μM Hg^{2+} induced a 6-fold fluorescence quenching, the intensity of phosphorescence increased slightly. All of the above metal ions mentioned could not induce a change of the emission peak position of **P1**, no matter for the fluorescence or the phosphorescence. However, akin to the absorption spectral changes of **P1**, both the fluorescent and phosphorescent peak positions experienced obvious red shifts (40 and 30 nm, respectively) on adding 10 μM Ag^+ into the polymer solution. The relative intensity of the two kinds of emission (I_F: I_P) changed from 1.4 to 0.5. Especially, when [Ag^+] is 1 μM, I_F decreased while I_P increased with a red shift in wavelength of 5 nm (Figure S3 of the Supporting Information), and τ_P changed from 11.3 μs in the absence of Ag^+ to 12.7 μs at [Ag^+] = 1 μM. Such an

Scheme 2. Synthetic Routes of P1 and M1



increase in τ_P upon Ag^+ binding was also observed previously in the phosphorescence signal from azurin.[16] These results indicate that Ag^+ could promote the ISC from the singlet to triplet states, and the ISC efficiency is high even at such a low concentration, presumably due to the coordinative interactions of Ag^+ ion with the conjugated backbone at a molecular level.[17] Meanwhile, τ_P decreased to 6.1 μs at $[Ag^+] > 5\ \mu M$. Thus, the effect of heavy Ag^+ ion on the lifetime of phosphorescence becomes rather complicated which depends on the solution concentration and viscosity and temperature.[16] Indeed, this represents the first literature study involving the possible utilization of dual-emissive properties of water-compatible platinum(II) acetylide-based conjugated polymers for chemosensing application. This can be further confirmed from the spectral and NMR titration studies for the model compound **M1** (Figure S4 of the

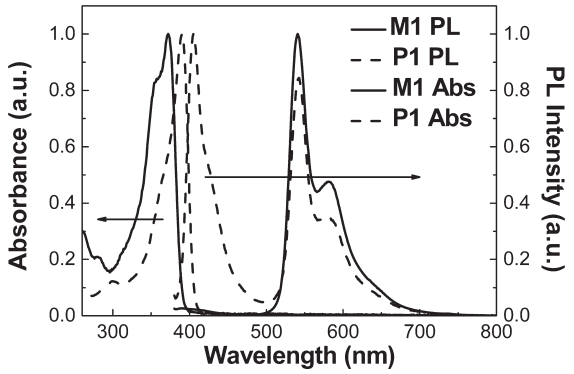


Figure 1. Absorption and PL spectra of **P1** and **M1** in degassed water (concentration = 5×10^{-6} M).

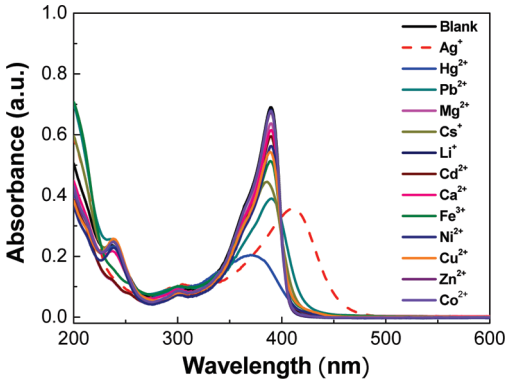


Figure 2. Absorption spectra of **P1** in the presence of various metal ions in degassed water. [**P1**] = 5×10^{-6} M. [Metal ion] = 1×10^{-5} M.

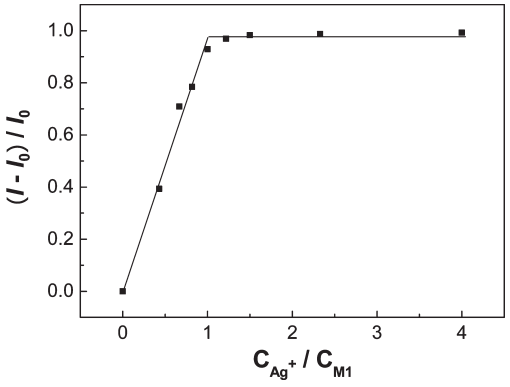


Figure 3. Benesi−Hildebrand plot of **M1** and Ag^+ in degassed water.

Supporting Information). Notably, the absorption maximum of **M1** gradually diminished in intensity and red-shifted in wavelength upon the addition of Ag^+ ion. To provide a possible explanation of why Ag^+ is the only metal that induces a change in color, the model complex **M1** was used for the study of its absorption spectral changes upon binding with Ag^+. Most likely, **M1** and Ag^+ formed a 1:1 complex as determined by the Benesi−Hildebrand plot obtained from the absorption spectra (see Figure 3). Such apparent absorption spectral changes indicate that the heavy Ag^+ ion binds with the electron-rich amino acid pendant of **M1** of each fluorene unit.[18] The idea of using amino acids stems from the fact that they are readily susceptible to chemical substances involving metal ions such as Ag^+ ion.[18e] It is known that

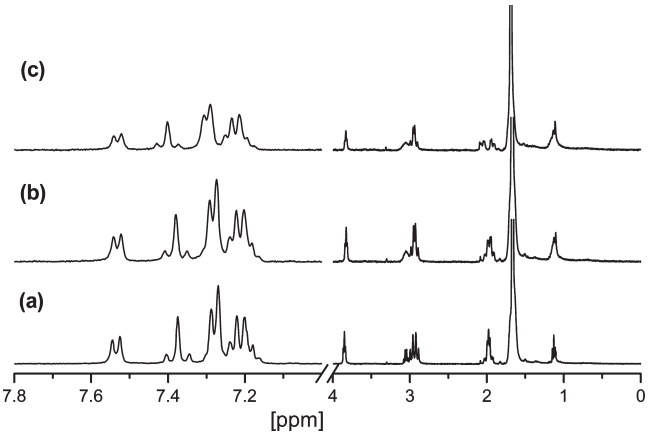


Figure 4. Partial ^{1}H NMR (400 MHz) spectral changes of **M1** (a) in D_2O and upon addition of (b) 0.5 equiv of $AgNO_3$ and (c) 1.0 equiv of $AgNO_3$ at 298 K.

silver−amine complexes form readily in aqueous solution because of their large formation constants and the preference of Ag^+ for linear coordination.[18a−c] The interaction between C═O group and Ag^+ ion is also possible.[18e] ^{1}H NMR spectra of **M1** in the presence of different concentrations of Ag^+ ion demonstrated that the signal at 1.9 ppm due to protons of the amino acid pendants was gradually splitted and broadened upon increasing the amount of Ag^+ ion (Figure 4). This further suggests the coordination of **M1** with Ag^+ and, hence, provides a good evidence for the interactions between **P1** and Ag^+. We found that the selectivity of **P1** for Ag^+ over other metal ions is high for both **P1** and **M1** systems. Remarkably, we can detect Ag^+ ion via a unique *absorption spectral change* which would not be interfered by the severe oxygen quenching problem commonly encountered using the phosphorimetric analytical methods and also makes the detection procedures simpler and quicker (e.g., no need for careful degassing of the solution before measurements). While **M1** shows a similar chemosensing function as **P1**, **P1** has a much broader detection range (0.5 μM−2 mM) than **M1** (1−35 μM). Simultaneously, **P1** shows a clear visual color change upon adding Ag^+; however, the color of **M1** solution displayed no virtual change under such condition. So, polymer **P1** appears to possess a better silver sensory property than model compound **M1**.

Next, cross-contamination experiments were performed to further gauge the selectivity for Ag^+ ion over other metal ions. By monitoring the wavelength change of absorption maximum ($\Delta\lambda$), Ag^+ can be distinguished apparently from other metal ions. From Figure 5a, other competitive metal ions such as Hg^{2+}, Pb^{2+}, and Cu^{2+} have very little impact on the $\Delta\lambda$ value of **P1** and Ag^+ solution mixture. These results clearly illustrate that **P1** shows an excellent selectivity for Ag^+ ion in the presence of other interfering metal ions.

More importantly, the color change of **P1** solution from colorless to yellow upon exposure to Ag^+ was readily visible to the naked eyes. From Figure 5b, the color of aqueous solution containing 5 μM **P1** did not show any change upon addition of an excess of each metal cation (10 μM), i.e., Ca^{2+}, Cd^{2+}, Cu^{2+}, Co^{2+}, Mg^{2+}, Ni^{2+}, Zn^{2+}, Pb^{2+}, Fe^{3+}, Hg^{2+}, Li^+, and Cs^+. However, the color of solution changed promptly to yellow as Ag^+ was added to it. Meanwhile, the yellow color gradually deepened with increasing [Ag^+]. Actually, the color of **P1** solution had significantly changed at [Ag^+] ≥ 3 μM. We also investigated the possible interference owing to the counteranion(s) used, and it was shown that different anions have almost no interaction with **P1** in water. These

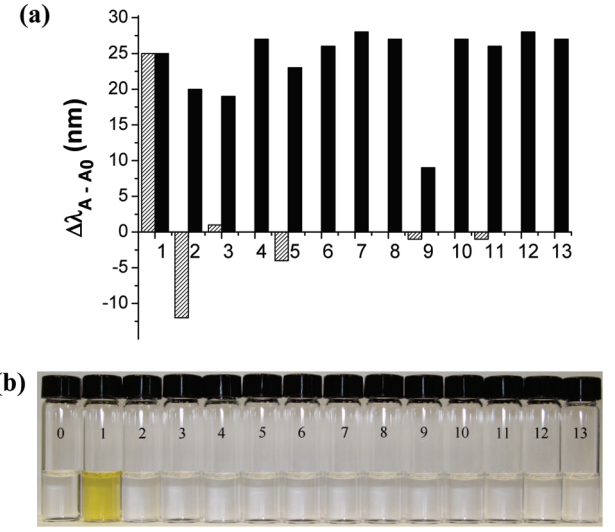


Figure 5. (a) Graph showing the wavelength change of the absorption maximum ($\Delta\lambda$) of **P1**. Gray bars represent the wavelength change in the presence of metal ions. Black bars represent the change in the presence of the indicated metal ions, followed by 1 equiv of Ag^+. (b) Color change of **P1** in the presence of various representative metal ions: 0, blank; 1, Ag^+; 2, Hg^{2+}; 3, Pb^{2+}; 4, Mg^{2+}; 5, Cs^+; 6, Li^+; 7, Cd^{2+}; 8, Ca^{2+}; 9, Fe^{3+}; 10, Ni^{2+}; 11, Cu^{2+}; 12, Zn^{2+}; 13, Co^{2+}. [**P1**] = 5×10^{-6} M. [Metal ion] = 1×10^{-5} M. Solvent: H_2O.

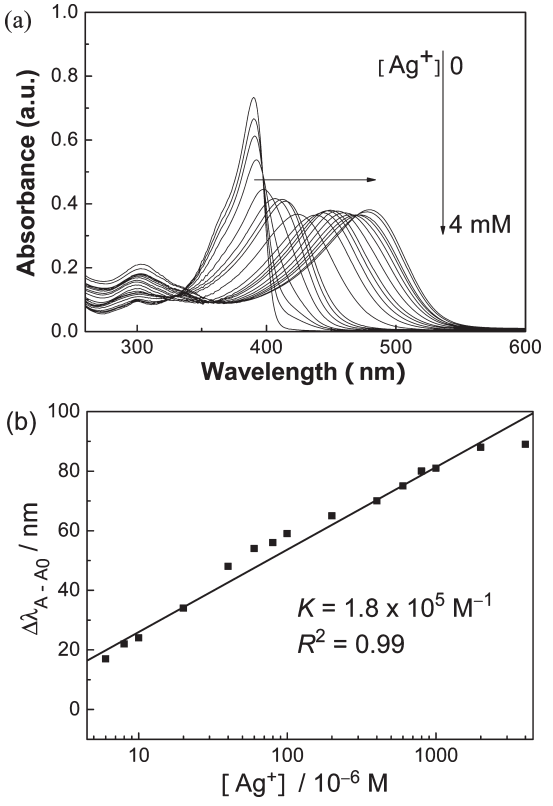


Figure 6. (a) Absorption spectral response of **P1** upon addition of Ag^+ ions in water and (b) the change of absorption maximum as a function of Ag^+ concentration. [**P1**] = 5×10^{-6} M. Solvent: H_2O.

results render **P1** a highly selective and sensitive chemosensory material for Ag^+ ion in a purely aqueous medium.

2.4. Titration Experiments. An absorption titration study of Ag^+ ion was conducted using a 5 μM solution of **P1** in water. As expected, the absorption maximum of **P1** decreased in intensity and was red-shifted upon the addition of Ag^+ ion (Figure 6a). The response range to [Ag^+] is very broad from 1 μM to 4 mM. Since the absorption maximum showed a gradual red shift upon adding Ag^+ ion at the concentration range of 1 μM to 4 mM, we can also study the relationship between [Ag^+] and $\Delta\lambda$ to quantify the response of **P1** to a given amount of Ag^+ ion. **P1** exhibited a linear relationship within the [Ag^+] range employed (1 μM to 2 mM, see Figure 6b). The limit of detection (LOD) is about 0.5 μM, i.e., at concentrations in the ppb range. These results reveal that there exists a wider linear response range to [Ag^+] via a change of the absorption wavelength in the present system.

Besides the colorimetric detection, **P1** allows for fluorescence detection of Ag^+. We also can quantify the response of **P1** to a given amount of Ag^+ by the Stern−Volmer (SV) equation[19] because the fluorescence signal also gradually decreased in intensity after adding a low concentration of Ag^+, and so Ag^+ ion could serve as a quencher. The Stern−Volmer equation becomes

$$I_0/I = 1 + K_{SV}[Q] \quad (1)$$

where I_0 and I are fluorescence intensities observed in the absence and presence of the quencher, respectively. [Q] is the quencher concentration, and K_{SV} is the SV quenching constant. On the basis of the fluorescence intensity of **P1** obtained in the fluorescent titration curves (Figure S3a), the SV plot could be obtained which displayed a linear relationship at low concentrations (1−5 μM) (Figure S3b). The corresponding K_{SV} value of **P1** was determined to be 1.9×10^5 M^{-1} (R^2 = 0.999 78). Therefore, both absorption and fluorescence detection limits of **P1** toward Ag^+ are as low as ppb range.

3. Conclusions

In summary, we describe a water-soluble fluorene-based platinum(II) acetylide conjugated polyelectrolyte, which shows attractive water solubility as well as fluorescent and phosphorescent dual-emissive properties in a completely organic-free aqueous medium at room temperature. This new system demonstrated remarkably high selectivity and sensitivity for Ag^+ ion because of the associated Ag^+-induced ISC from the singlet to triplet states. Saliently, a selective color modulation was observed in the presence of Ag^+ and the Ag^+-responsive coloration change from colorless to yellow is readily visible to the naked eyes and can be quantified using visible absorption spectroscopy. The present work definitely opens a new door to develop a sensitive and quick absorption spectrometric method for Ag^+ ion sensing in pure water, which is in complete contrast with the commonly used method relying on emission spectral changes. In addition, the detection of Ag^+ ion via such a unique absorption spectral change would be simpler and quicker than the typical phosphorimetric analytical methods because it would not be restricted by the undesirable oxygen quenching experienced for the phosphorescence emission. Work is still underway to better understand the detailed silver binding mechanism involved for the chemosensing phenomenon.

4. Experimental Section

General Information. All reactions were performed under nitrogen. Solvents were carefully dried and distilled from appropriate drying agents prior to use. The water used in all experiments was prepared in a Millipore Milli-Q plus purification system and displayed a resistivity of ≥18.2 MΩ cm^{-1}. Commercially available reagents were used without further purification unless otherwise stated. All reactions were monitored by thin-layer chromatography (TLC) with Merck precoated aluminum

plates. Flash column chromatography was carried out using silica gel obtained from Merck (230−400 mesh). Fast atom bombardment (FAB) mass spectra were recorded on a Finnigan MAT SSQ710 system. Proton NMR spectra were measured in $CDCl_3$ or D_2O on a Varian Inova 400 MHz FT-NMR spectrometer; chemical shifts were quoted relative to tetramethylsilane.

Physical Measurements. UV−vis spectra were obtained on a Cary-300 spectrophotometer. The photoluminescent properties and lifetimes of the compounds were probed on the Photon Technology International (PTI) Fluorescence Master Series QM1 system. Solutions of **M1** and **P1** were deoxygenated by bubbling with argon for 30 min prior to all measurements. The photoluminescent quantum yields were determined in degassed water at 293 K against quinine sulfate in 1 N sulfuric acid as a reference standard ($\Phi_{em} = 0.546$).[20]

Fluorescence Titration Procedure. A 10 × 10 mm quartz curet was used for recording the solution spectra, and the emission spectrum was collected at 90° relative to the excitation beam. The solutions of polymer **P1** and model compound **M1** were successively diluted to a concentration of 5×10^{-6} M in water (the concentration of polymer is based on the number of moles of the repeating unit). Solutions of perchlorate or nitrate salts of different metal ions with the concentration of typically 5×10^{-3} M were prepared by successive dilution in water. Fluorescence quenching experiment was carried out by sequentially adding small aliquots of stock solutions of metal salts to 3.00 mL of the polymer solutions by using a calibrated microliter pipet. The solutions were vibrated and bubbled with argon for 30 min prior to obtaining the fluorescence spectra. The pH-dependent experiment was carried out by adding 30 μL of **P1** or **M1** (5×10^{-4} M) to a 3 mL solution at different pH, and then the solutions were vibrated and bubbled with argon for 30 min prior to obtaining the fluorescence spectra.

Material Synthesis. All chemicals and reagents were used as received from commercial sources without further purification. Solvents for chemical synthesis were purified according to the standard procedures. All chemical reactions were carried out under an inert atmosphere. Compounds **1**[15c] and $[Pt(PMe_3)_2Cl_2]$[21] were synthesized as previously described.

Synthesis of Compound 2. To a degassed ice-cooled mixture of compound **1** (0.726 g, 1.0 mmol) in dry triethylamine (10 mL) and CH_2Cl_2 (10 mL) was added CuI (20 mg), triphenylphosphine (20 mg), and $Pd(OAc)_2$ (60 mg). After the solution was stirred for 30 min, trimethylsilylacetylene (0.57 mL, 4.0 mmol) was then added, and the suspension was stirred for 30 min in an ice bath before being warmed to room temperature. After reacting for 30 min at room temperature, the mixture was heated to 60 °C for 24 h under a nitrogen atmosphere. The solution was then allowed to cool to room temperature, and the solvent mixture was evaporated *in vacuo*. The crude product was purified by column chromatography on silica gel with a solvent combination of hexane/ethyl acetate (2:1, v/v) as eluent to provide **2** as a white solid (0.65 g, 85%). ^{1}H NMR (400 MHz, $CDCl_3$, δ_{ppm}): 7.61 (d, J = 8.0 Hz, 2H, Ar), 7.51 (s, 2H, Ar), 7.48 (dd, J = 1.3 and 8.0 Hz, 2H, Ar), 7.37 (d, J = 8.4 Hz, 2H, NH), 4.95 (m, 2H, CH), 3.75 (s, 6H, CH_3), 3.66 (s, 6H, CH_3), 3.26 (d, J = 13.6 Hz, 2H, CCH_2), 3.02 (dd, J = 4.4 and 16.8 Hz, 2H, $CHCH_2$), 2.81 (dd, J = 4.4 and 16.8 Hz, 2H, $CHCH_2$), 2.43 (d, J = 13.6 Hz, 2H, CCH_2), 0.25 (s, 18H, $SiMe_3$). ^{13}C NMR (100 MHz, $CDCl_3$, δ_{ppm}): 171.38, 171.08, 170.34 (C=O), 148.85, 138.85, 132.20, 127.89, 122.41, 120.33 (Ar), 105.30, 94.97 (C≡C), 52.89, 52.12 (alkyl), 50.46 (C9-fluorene), 48.39, 42.61, 36.07 (alkyl), 0.05 ($SiMe_3$). FAB-MS: m/z 761.3 (M^+). IR (KBr): ν(C≡C) 2135 cm^{-1}.

Synthesis of Compound 3. A solution of **2** (0.38 g, 0.5 mmol) in THF (10 mL) was stirred, and then 1.5 mL of 1 M n-Bu_4NF in THF was added at room temperature under nitrogen for 30 min. Solvent was removed under reduced pressure to leave a gray white residue. The residue was purified by column chromatography on silica gel using hexane/ethyl acetate (1:1, v/v) as eluent to afford a white solid of **3** (0.28 g, 90%). ^{1}H NMR (400 MHz, $CDCl_3$, δ_{ppm}): 7.66 (d, J = 8.0 Hz, 2H, Ar), 7.57 (s, 2H, Ar), 7.51 (dd, J = 1.3 and 8.0 Hz, 2H, Ar), 7.33 (d, J = 8.4 Hz, 2H, NH), 4.95 (m, 2H, CH), 3.75 (s, 6H, CH_3), 3.67 (s, 6H, CH_3), 3.22 (d, J = 13.6 Hz, 2H, CCH_2), 3.11 (s, 2H, C≡CH), 3.00 (dd, J = 4.8 and 17.2 Hz, 2H, $CHCH_2$), 2.82 (dd, J = 4.8 and 17.2 Hz, 2H, $CHCH_2$), 2.50 (d, J = 13.6 Hz, 2H, CCH_2). ^{13}C NMR (100 MHz, $CDCl_3$, δ_{ppm}): 171.27, 171.02, 170.24 (C=O), 148.96, 138.98, 132.27, 128.16, 121.37, 120.37 (Ar), 83.83, 77.91 (C≡C) 52.83, 52.07 (alkyl), 50.43 (C9-fluorene), 48.42, 42.48, 36.05 (alkyl). FAB-MS: m/z 617.1 (M^+). IR (KBr): ν(C≡C) 2124 cm^{-1}.

Synthesis of P1 Precursor. A solution of **3** (123.3 mg, 0.2 mmol), $[Pt(PMe_3)_2Cl_2]$ (83.6 mg, 0.2 mmol), and CuI (2 mg) in a mixture of CH_2Cl_2/Et_3N (10 mL, 1:1, v:v) was degassed with nitrogen for 10 min. The reaction mixture was stirred at room temperature for 24 h. The solvent was evaporated under vacuum, and the product was purified by silica gel chromatography using CH_2Cl_2 as the eluent. The product was obtained in 70% yield (136 mg). ^{1}H NMR (400 MHz, $CDCl_3$, δ_{ppm}): 8.43 (br, 2H, Ar), 7.60 (br, 2H, Ar), 7.18 (br, 2H, Ar), 4.62 (br, 2H, CH), 3.63 (d, J = 8.4 Hz, 12H, CH_3), 2.73−2.50 (br, 8H, alkyl), 1.72 (br, 18H, PCH_3). ^{31}P NMR (75 MHz, $CDCl_3$, δ_{ppm}): −20.24 (J_{Pt-P} = 2277 Hz). GPC (THF, polystyrene standards): M_n = 26 340, M_w = 62 360, PDI = 2.36.

Synthesis of P1. A solution of **P1** precursor (98 mg, 0.1 mmol), 1,4-dioxane (10 mL), and 2 M aqueous KOH (5 mL) was degassed for 30 min and stirred at 100 °C for 12 h. After cooling to room temperature, the solvent was evaporated under vacuum. The residue was redissolved in 20 mL of water and filtered through a 0.22 μm cellulose membrane. The filtrate was dialyzed against deionized water using a 8000 molecular weight cutoff cellulose for 3 days, and water was changed every 6 h. The polymer was isolated by freeze-drying of the water as a yellow solid in 65% yield (69 mg). ^{1}H NMR (400 MHz, D_2O, δ_{ppm}): 7.58 (br, 2H, Ar), 7.42 (br, 2H, Ar), 7.34 (br, 2H, Ar), 3.87 (br, 2H, CH), 3.54 (br, 1H, $CHCH_2$), 2.96 (br, 3H, $CHCH_2$), 2.00 (br, 4H, CCH_2), 1.73 (br, 18H, PCH_3). ^{31}P NMR (75 MHz, D_2O, δ_{ppm}): −20.37 (J_{Pt-P} = 2135 Hz).

Synthesis of Compound 4. A solution of $[Pt(PMe_3)_2Cl_2]$ (500 mg, 1.1 mmol) and 100 μL of phenylacetylene (1.1 mmol) in a mixture of CH_2Cl_2/Et_3N (12 mL, 3:1, v:v) was degassed with nitrogen for 10 min. The reaction mixture was stirred at room temperature for 3 h. The solvent was evaporated under vacuum, and the product was purified by silica gel chromatography using toluene/ethyl acetate mixture as an eluent. The product was obtained in 38% yield (180 mg). ^{1}H NMR (400 MHz, $CDCl_3$, δ_{ppm}): 7.31−7.15 (m, 5H, Ar), 1.70−1.61 (m, 18H, CH_3).

Synthesis of M1 Precursor. A solution of **3** (61.7 mg, 0.1 mmol), **4** (107 mg, 0.22 mmol), and CuI (5 mg) in a mixture of CH_2Cl_2/Et_3N (20 mL, 1:1, v:v) was degassed with nitrogen for 10 min. The reaction mixture was stirred at room temperature for 12 h. The solvent was evaporated under vacuum, and the product was purified by silica gel chromatography using toluene/ethyl acetate (10:1, v/v) as the eluent. The product was obtained in 70% yield (81 mg). ^{1}H NMR (400 MHz, $CDCl_3$, δ_{ppm}): 7.49−7.11 (m, 18H, Ar and NH), 4.89 (m, 2H, CH), 3.73 (s, 6H, CH_3), 3.65 (s, 6H, CH_3), 3.12 (d, J = 13.6 Hz, 2H, CCH_2), 2.98 (dd, J = 4.4 and 16.8 Hz, 2H, $CHCH_2$), 2.74 (dd, J = 4.4 and 16.8 Hz, 2H, $CHCH_2$), 2.55 (d, J = 13.6 Hz, 2H, CCH_2), 1.78 (m, 36H, PCH_3). ^{31}P NMR (75 MHz, $CDCl_3$, δ_{ppm}): −20.40 (J_{Pt-P} = 2298 Hz). FAB-MS: m/z 1511.7 (M^+).

Synthesis of M1. A solution of **M1** precursor (151 mg, 0.1 mmol), 1,4-dioxane (30 mL), and 2 M aqueous KOH (5 mL) was degassed for 30 min and stirred at 100 °C for 12 h. After cooling to room temperature, the solvent was evaporated under vacuum. The residue was redissolved in 20 mL of water and filtered through a 0.22 μm cellulose membrane. The filtrate was dialyzed against deionized water using a 500 molecular weight cutoff cellulose for 3 days, and water was changed every 6 h. The polymer was isolated by freeze-drying of the

water as a yellow solid in 80% yield (126 mg). ^{1}H NMR (400 MHz, D_2O, δ_{ppm}): 7.52−7.16 (m, 16H, Ar) 3.82 (t, J = 5.6 Hz, 2H, CH), 2.90 (m, 4H, CCH_2), 1.95 (m, 4H, $CHCH_2$), 1.64 (m, 36H, PCH_3). ^{31}P NMR (75 MHz, $CDCl_3$, δ_{ppm}): −20.41 (J_{Pt-P} = 2136 Hz).

Acknowledgment. This work was supported by the Hong Kong Baptist University (FRG2/08-09/111), the Hong Kong Research Grants Council (HKBU202709), and State Administration of Foreign Experts Affairs International Partnership Program for Creative Research Teams, Chinese Academy of Sciences. W.-Y. W. also thanks the Croucher Foundation for the Croucher Senior Research Fellowship.

Supporting Information Available: Photophysical properties and fluorescence quenching studies of **P1** and **M1**. This material is available free of charge via the Internet at http://pubs.acs.org.

References and Notes

(1) (a) Schildkraut, D.; Dao, P.; Twist, J.; Davis, A.; Robillard, K. *Environ. Toxicol. Chem.* **1998**, *17*, 642. (b) Wan, A. T.; Conyers, R. A.; Coombs, C. J.; Masterton, J. P. *Clin. Chem.* **1991**, *37*, 1683. (c) Ratte, H. T. *Environ. Toxicol. Chem.* **1999**, *18*, 89. (d) Kazuyuki, M.; Nobuo, H.; Takatoshi, K.; Yuriko, K.; Osamu, H.; Yashihisa, I.; Kiyoko, S. *Clin. Chem.* **2001**, *47*, 763.

(2) (a) Teixidor, F.; Flores, M. A.; Escriche, L.; Viñas, C.; Casabó, J. *Chem. Commun.* **1994**, 963. (b) Chung, S.; Kim, W.; Park, S. B.; Yoon, I.; Lee, S. S.; Sung, D. D. *Chem. Commun.* **1997**, 965. (c) Kimura, K.; Yajima, S.; Tatsumi, K.; Yokoyama, M.; Oue, M. *Anal. Chem.* **2000**, *72*, 5290. (d) Ceresa, A.; Radu, A.; Peper, S.; Bakker, E.; Pretsch, E. *Anal. Chem.* **2002**, *74*, 4027. (e) Javanbakht, M.; Ganjali, M. R.; Norouzi, P.; Badiei, A.; Hasheminasab, A. *Electroanal.* **2007**, *19*, 1307.

(3) (a) de Silva, A. P.; Gunaratne, H. Q. N.; Gunnlaugsson, T.; Huxley, A. J. M.; McCoy, C. P.; Rademacher, J. T.; Rice, T. E. *Chem. Rev.* **1997**, *97*, 1515. (b) Amendola, V.; Fabbrizzi, L.; Licchelli, M.; Mangano, C.; Pallavicini, P.; Parodi, L.; Poggi, A. *Coord. Chem. Rev.* **1999**, *190−192*, 649. (c) Prodi, L.; Bolletta, F.; Montalti, M.; Zaccheroni, N. *Coord. Chem. Rev.* **2000**, *205*, 59. (d) Zhao, Q.; Li, F. Y.; Huang, C. H. *Chem. Soc. Rev.* **2010**, *39*, 3007.

(4) (a) Paker, J.; Glass, T. E. *J. Org. Chem.* **2001**, *66*, 6505. (b) Ikeda, M.; Tanida, T.; Takeuchi, M.; Shinkai, S. *Org. Lett.* **2000**, *2*, 1803. (c) Park., C. S.; Lee, J. Y.; Kang, E.-J.; Lee, J.-E.; Lee, S. S. *Tetrahedron. Lett.* **2009**, *50*, 671. (d) Rurack, K.; Kollmannsberger, M.; Resch-Genger, U.; Daub, J. *J. Am. Chem. Soc.* **2000**, *122*, 968. (e) Yang, R.-H.; Chan, W.-H.; Lee, A. W. M.; Xia, P.-F.; Zhang, H.-K.; Li, K. *J. Am. Chem. Soc.* **2003**, *125*, 2884. (f) Akkaya, E. U.; Coskun, A. *J. Am. Chem. Soc.* **2005**, *127*, 10464. (g) Sessler, J. L.; Tomat, E.; Lynch, V. M. *J. Am. Chem. Soc.* **2006**, *128*, 4184. (h) Schmittel, M.; Lin, H. W. *Inorg. Chem.* **2007**, *46*, 9139. (i) Liu, L.; Zhang, D. Q.; Zhang, G. X.; Xiang, J. F.; Zhu, D. B. *Org. Lett.* **2008**, *10*, 2271. (j) Chatterjee, A.; Santra, M.; Won, N.; Kim, S.; Kim, K. J.; Kim, B. S.; Ahn, H. K. *J. Am. Chem. Soc.* **2009**, *131*, 2040. (k) Tong, H.; Wang, L. X.; Jing, X. B.; Wang, F. S. *Macromolecules* **2002**, *35*, 7169. (l) Wang, H. H.; Xue, L.; Qian, Y. Y.; Jiang, H. *Org. Lett.* **2010**, *12*, 292.

(5) Wen, Y. Q.; Xing, F. F.; He, S. J.; Song, S. P.; Wang, L. H.; Long, Y. T.; Li, D.; Fan, C. H. *Chem. Commun.* **2010**, *46*, 2596.

(6) Freeman, R.; Finder, T.; Willner, I. *Angew. Chem., Int. Ed.* **2009**, *48*, 7818.

(7) (a) Heeger, P. S.; Heeger, A. J. *Proc. Natl. Acad. Sci. U.S.A.* **1999**, *96*, 12219. (b) Thomas, S. W., III; Joly, G. D.; Swager, T. M. *Chem. Rev.* **2007**, *107*, 1339. (c) Jiang, H.; Taranekar, P.; Reynolds, J. R.; Schanze, K. S. *Angew. Chem., Int. Ed.* **2009**, *48*, 4300. (d) Nilsson, K. P. R.; Rydberg, J.; Baltzer, L.; Inganäs, O. *Proc. Natl. Acad. Sci. U.S.A.* **2003**, *100*, 10170. (e) Qin, C. J.; Cheng, Y. X.; Wang, L. X.; Jing, X. B.; Wang, F. S. *Macromolecules* **2008**, *41*, 7798. (f) Zhang, Y.; Liu, B.; Cao, Y. *Chem.—Asian J.* **2008**, *3*, 739. (g) Zhou, Q.; Swager, T. M. *J. Am. Chem. Soc.* **1995**, *117*, 7017. (h) Swager, T. M. *Acc. Chem. Res.* **1998**, *31*, 201. (i) Fan, C. H.; Wang, S.; Hong, J. W.; Bazan, G. C.; Plaxco, K. W.; Heeger, A. J. *Proc. Natl. Acad. Sci. U.S.A.* **2003**, *100*, 6297.

(8) (a) Haskin-Glusac, K.; Pinto, M. R.; Tan, C. Y.; Schanze, K. S. *J. Am. Chem. Soc.* **2004**, *126*, 14964. (b) Ogawa, K.; Guo, F. Q.; Schanze, K. S. *J. Photochem. Photobiol., A* **2009**, *207*, 79.

(9) (a) Wong, W.-Y.; Ho, C.-L. *Coord. Chem. Rev.* **2006**, *250*, 2627. (b) Khan, M. S.; Al-Mandhary, M. R. A.; Al-Suti, M. K.; Raithby, P. R.; Ahrens, B.; Mahon, M.; Male, L.; Boothby, C. E.; Köhler, A. *J. Chem. Soc., Dalton Trans.* **2003**, 74. (c) Wong, W.-Y.; Lu, G.-L.; Choi, K.-H.; Shi, J.-X. *Macromolecules* **2002**, *35*, 3506. (d) Wilson, J. S.; Dhoot, A. S.; Seeley, A. J. A. B.; Khan, M. S.; Kohler, A.; Friend, R. H. *Nature* **2001**, *413*, 828. (e) Wong, W.-Y.; Harvey, P. D. *Macromol. Rapid Commun.* **2010**, *31*, 671. (f) Haskins-Glusac, K.; Pinto, M. R.; Tan, C.; Schanze, K. S. *J. Am. Chem. Soc.* **2004**, *126*, 14964. (g) Hissler, M.; McGarrah, J. E.; Connick, W. B.; Geiger, D. K.; Cummings, S. D.; Eisenberg, R. *Coord. Chem. Rev.* **2000**, *208*, 115.

(10) (a) Wong, W.-Y. *Dalton Trans.* **2007**, 4495. (b) Bunten, K. A.; Kakkar, A. K. *Macromolecules* **1996**, *29*, 2885. (c) Silverman, E. E.; Cardolaccia, T.; Zhao, X.; Kim, K.-Y.; Haskins-Glusac, K.; Schanze, K. S. *Coord. Chem. Rev.* **2005**, *249*, 1491. (d) Long, N. J.; Williams, C. K. *Angew. Chem., Int. Ed.* **2003**, *42*, 2586. (e) Tao, C.-H.; Yam, V. W.-W. *J. Photochem. Photobiol., C* **2009**, *10*, 130. (f) Whittell, G. R.; Manners *Adv. Mater.* **2007**, *19*, 3439. (g) Nguyen, P.; Gomez-Elipe, P.; Manners, I. *Chem. Rev.* **1999**, *99*, 1515. (h) Abd-El-Aziz, A. S.; Shipman, P. O.; Boden, B. N.; McNeil, W. S. *Prog. Polym. Sci.* **2010**, *35*, 714.

(11) Zhang, G.; Palmer, G. M.; Dewhirst, M. W.; Fraser, C. L. *Nature Mater.* **2009**, *8*, 747.

(12) Segura Carretero, A.; Salinas Castillo, A.; Gutiérrez, A. F. *Crit. Rev. Anal. Chem.* **2005**, *35*, 3.

(13) (a) Liu, B.; Yu, W.; Lai, Y.; Huang, W. *Macromolecules* **2002**, *35*, 4975. (b) Liu, B.; Bazan, G. C. *Chem. Mater.* **2004**, *16*, 4467. (c) Brookins, R. N.; Schanze, K. S.; Reynolds, J. R. *Macromolecules* **2007**, *40*, 3524. (d) Gaylord, B. S.; Heeger, A. J.; Bazan, G. C. *J. Am. Chem. Soc.* **2003**, *125*, 896.

(14) Gradber, G.; Rechthaler, K.; Mayer, B.; Köhler, G.; Rotkiewicz, K. *J. Phys. Chem. A* **2000**, *104*, 1365.

(15) (a) Wang, F. K.; Bazan, G. C. *J. Am. Chem. Soc.* **2006**, *128*, 15786. (b) Gao, Y.; Wang, C. C.; Wang, L.; Wang, H. L. *Langmuir* **2007**, *23*, 7760. (c) Qin, C.-J.; Wu, X.-F.; Gao, B.-X.; Tong, H.; Wang, L.-X. *Macromolecules* **2009**, *42*, 5427.

(16) Strambini, G. B.; Gabellieri, E. *J. Phys. Chem.* **1991**, *95*, 4352.

(17) We also studied the effect of another heavy-atom-induced room-temperature phosphorescent reagent $TlNO_3$ on the absorption and emission spectra. There is no apparent change at the same concentration or even 10-fold higher in concentration. It means that there is only a low ISC efficiency induced by Tl^+ because Tl^+ cannot associate with the amino acid pendants and form notable molecular level interactions.

(18) (a) Maeda, M.; Nakegawa, G. *J. Phys. Chem.* **1983**, *87*, 121. (b) Hancock, R. D.; Nakani, B. S.; Marsicano, F. *Inorg. Chem.* **1983**, *22*, 2531. (c) Cotton, F. A.; Wilkinson, G.; Murillo, C. A.; Bochmann, M. *Advanced Inorganic Chemistry*, 6th ed.; Wiley-Interscience: New York, 1999; p 1089. (d) Kang, S. W.; Kim, J. H.; Won, J.; Char, K.; Kang, Y. S. *J. Membr. Sci.* **2005**, *248*, 201. (e) Garipcan, B.; Bereli, N.; Patur, S.; Arica, Y.; Denizli, A. *Macromol. Biosci.* **2001**, *1*, 332. (f) Kim, H.-J.; Lee, E.; Park, H.-S.; Lee, M. *J. Am. Chem. Soc.* **2007**, *129*, 10994.

(19) Lakowicz, J. R. *Principles of Fluorescence Spectroscopy*; Kluwer Academic/Plenum Publishers: New York, 1999.

(20) Demas, J. N.; Crosby, G. A. *J. Phys. Chem.* **1971**, *75*, 991.

(21) Evans, J. G.; Goggin, P. L.; Goodfell, R. J.; Smith, G. J. *J. Chem. Soc. A* **1968**, 464.

490 *Macromolecules* **2011**, *44*, 490–494
DOI: 10.1021/ma101296j

Macromolecules
ARTICLE

Relationship between Glass Transition Temperature and Polymerization Temperature for Cross-Linked Photopolymers

Sheng Ye,[†] Neil B. Cramer,[†] and Christopher N. Bowman*[,†,‡]

[†]*Department of Chemical & Biological Engineering, University of Colorado, UCB 424, Boulder, Colorado 80309, United States, and* [‡]*Department of Restorative Dentistry, University of Colorado School of Dentistry, Aurora, Colorado 80045, United States*

Received June 11, 2010; Revised Manuscript Received December 9, 2010

ABSTRACT: Monomeric resins are frequently polymerized at a temperature that is far below the desired glass transition temperature for the final polymer network. This work quantitatively investigates the relationship between the glass transition temperature (T_g), the cure temperature (T_{cure}), the maximum achievable glass transition temperature for a particular monomer formulation (T_{gmax}), and the network heterogeneity as indicated by the half-width of the glass transition region ($T_{g1/2width}$) for both chain growth and step growth polymerization systems. Various monomer resins were systematically photopolymerized at 25, 50, 75, and 100 °C to the maximum achievable double bond conversion with living radical photopolymerizations employed as necessary to eliminate issues associated with postcuring during heating of the samples for dynamic mechanical analysis. For polymer samples that have the potential for much higher glass transition temperatures than the curing temperature (i.e., where $T_{cure} < T_{gmax} - T_{g1/2width}$), mass transfer limitations and the network heterogeneity combine to control T_g such that $T_g \approx T_{cure} + T_{g1/2width}$. For systems polymerized at temperatures closer to their maximum glass transition temperature, i.e., where $T_{cure} \geq T_{gmax} - T_{g1/2width}$, the polymer structure becomes the dominant factor and $T_g \approx T_{gmax}$. These relationships were broadly and successfully applied to cross-linked networks formed from both chain growth and step growth polymerizations, incorporating networks of vastly different heterogeneity, with T_g's ranging from 35 to 205 °C with approximately 10% error found between predicted and experimental glass transition temperatures.

Introduction

The glass transition temperature (T_g) of a polymer network is oftentimes of singular importance in determining the performance and potential implementation of polymer networks. For applications requiring a high T_g, the polymerization temperature is often far below the final polymer T_g, even including the often significant polymerization-induced exotherm. Consequently, significant polymerization must occur after the transition to the glassy state if the T_g is to be sufficiently greater than the curing temperature. The decrease in free volume and the significant mobility restriction of polymer segments postvitrification typically reduce the reaction rate by orders of magnitude, making it difficult to achieve increased glass transition temperatures without significantly increasing the polymerization temperature.[1] For photopolymerization reactions in particular, where the initial reaction temperature is often ambient or near-ambient, these restrictions may be quite pronounced. Specifically, autodeceleration, reaction-diffusion-controlled termination, trapped radicals, and limited double bond conversion have all been found to be controlling factors in polymerization kinetics of polymer network forming systems.[2−5] These phenomena are strongly influenced by both the chemical structure of the monomers, the cross-link density of the resulting polymer, the heterogeneity of the material, the polymerization mechanism, and the curing conditions.[2,3,6,7] The understanding of these complex interrelationships that impact the ultimate glass transition temperature is thus an important factor for many practical applications such as coatings, dental restorative materials, and optical fiber coatings.

*Corresponding author. Phone: 303-492-3247. Fax: 303-492-4341. E-mail: christopher.bowman@colorado.edu.

Because of the complex nature and importance of the relationship between T_g, curing conditions, and network formation, extensive evaluation has been performed on the relationship between T_g and T_{cure}. Studies evaluating cross-linked epoxy-amines, cyanate esters, polyimides, and others have been performed.[8−13] Numerous studies focused on time−temperature−transition (TTT) diagrams for thermosetting systems, particularly those cured by step growth polymerizations.[8−11] Gillham and co-workers studied different epoxy systems and reported that the cure path did not affect the relationship between T_g and conversion.[12] Rozenburg reported that the reaction kinetics of epoxy systems were strongly affected by the network structure and properties in the glassy state rather than the rubbery state.[13] Oleinik reported that in epoxy-aromatic amine systems, $T_g \approx T_{cure} + 0.5\Delta T_g$ and further derived T_g was not above T_{cure} by more than 15−30 °C.[14] This work led to a long-established rule of thumb that the T_g cannot exceed T_{cure} by more than 25 °C.[8−11] Far less work has been conducted on the T_g vs T_{cure} relationship for polymers formed from chain growth photopolymerizations as these systems have several inherent complications. One primary difficulty is that the trapped radicals become mobile upon heating and result in significant postcure that made it traditionally difficult to evaluate the T_g of the as-cured polymer, which is necessary to determine the $T_g - T_{cure}$ relationship. Sample heating is necessary to determine T_g, and the resultant postcure affects (causes an increase in) the T_g during measurement of the same.[15,16] Additionally, chain growth polymerizations are also traditionally highly exothermic, leading to significant temperature rises during the reaction that alter the relationship between the cure and glass transition temperatures.

Here, two common polymerization mechanisms are evaluated, chain growth and step growth polymerizations.[17] Radical

 Published on Web 01/10/2011 © 2011 American Chemical Society

polymerizations that proceed via a chain growth mechanism result in networks that are very heterogeneous in nature.[18,19] Heterogeneous networks contain broad distributions of chain mobilities and relaxation times, resulting in a broad glass transition region,[20] as is often described by the half width of the tan delta curve at half its maximum value ($T_{g1/2width}$).[21] In contrast to chain growth polymerizations, step growth polymerizations are stepwise reactions between the functional groups of the monomers leading initially to the formation of dimers, trimers, tetramers, etc. and resulting in slow and uniform molecular weight and network development during the early stages of the reaction.[17] The step growth reaction mechanism results in the formation of ideal, homogeneous polymer networks.

Thiol−ene reactions are the examples of radical polymerizations that also exhibit a step growth polymerization mechanism.[22] The primary initiator radical abstracts a hydrogen from the thiol monomer to form a thiyl radical, which further reacts with an ene monomer to form a carbon-centered radical by an addition reaction. The thiyl radical is regenerated by a subsequent chain transfer step.[23,24] The alternating addition and chain transfer reactions result in step growth network development that ultimately leads to the formation of a homogeneous polymer network.[22,25]

Radical photopolymerizations are both rapid and strongly exothermic, making it difficult to maintain isothermal reaction conditions during polymerization, and the nonisothermal reaction conditions convolute the evaluation of the T_g vs T_{cure} relationship. Thus, it is critical to determine the maximum temperature achieved during the polymerization, which becomes the effective curing temperature, or to have the polymerization proceed slowly enough that heat transfer renders the polymer sample nearly isothermal.

To eliminate postcure effects associated with additional polymerization that occurs during the T_g measurement, living radical photopolymerizations initiated by *p*-xylyene bis(*N*,*N*-diethyl dithiocarbamate) (XDT)[26] have been employed and demonstrated to successfully eliminate the postcuring effect from trapped radicals.[27,28] XDT photocleaves upon absorption of ultraviolet light into a carbon-based initiating radical that will propagate with both a carbon−carbon double bond and thiol functional groups. The other cleavage product is a sulfur-based dithiocarbamate radical that acts to terminate propagating radicals. The living radical polymerization also results in a slower polymerization rate, thus decreasing the heat generated by the exothermic reaction.[29] The relationship presented here is similar in nature to the equation previously developed by Olienik.[14] In this work, the T_g ranges for the equation validity are defined and the equation is demonstrated to be valid for a wide range of polymerization mechanisms. Moreover, our relationship provides for a quantitative relationship describing the T_g range of the resulting polymer as it depends on both the polymerization mechanism and the polymer properties. This work proposes to develop a broadly applicable semiquantitative relationship between T_g and T_{cure} as a means for understanding the network evolution and as a means for controlling the polymer behavior.

To determine how different reaction mechanisms affect the T_g vs T_{cure} relationship, we evaluated radical-mediated chain growth polymerization systems (acrylates), step growth polymerization systems (thiol−enes), and mixed step-chain growth polymerization systems (thiol−acrylates) as well as analyzing previous data from step growth systems that are not radically mediated such as epoxy-amines systems. These polymerization systems represent a wide range of reaction mechanisms used throughout thermosetting systems and they result in significantly different network development and ultimate heterogeneity. Additionally, both aliphatic monomers with relatively flexible core structures and cyclic monomers with rigid core structures were utilized to ascertain the effect of monomer structure on these relationships.

Experimental Section

Materials. The monomers 1,6-hexanediol diacrylate (HDDA,), tricyclodecane dimethanol diacrylate (TCDDA), and triallyl-1,3,5-triazine-2,4,6-trione (TATATO) were purchased from Sigma-Aldrich Co. (Milwaukee, WI). Pentaerythritol tetra(3-mercaptopropionate) (PETMP) was donated by Evans Chemetics, and trimethylolpropane tri(norborn-2-ene-5-carboxylate) (TMPTN) was synthesized in our lab by a previously reported procedure.[30] 2,2-Dimethoxyphenyl acetophenone (Irgacure 651, DMPA, Ciba-Geigy Co., Hawthorne, NY) and *p*-xylyene bis(*N*,*N*-diethyl dithiocarbamate) (XDT, 3 M Corp., Minneapolis, MN) were used as photoinitiators.

FTIR. Fourier transform infrared spectroscopy (FTIR) was used to monitor conversion. Samples were cured inside a custom built FTIR chamber[31] (Magna 750, series II, Nicolet Instrument Corp., Madison, WI) with a UV-light source (Acticure, EFOS, Mississaugua, Ontario, Canada) with primary output at 365 nm. A horizontal-mounting unit, which redirects the IR light beam vertically, was used in combination with a temperature cell (0−120 °C) to allow for real-time kinetic characterization. The sample temperature was allowed to stabilize for 10 min prior to irradiation. Mid-IR was utilized to monitor the cure of monomer samples placed between NaCl crystals (~10 μm thickness) and initiated by 0.5 wt % DMPA. Thiol conversion was monitored by the S−H stretching peak at 2570 cm^{-1} while the acrylate, allyl ether, and norbornene conversions were monitored by the C=C vibration at 1636 cm^{-1}, C−H stretch at 1640 cm^{-1}, and C−H bending at 711 cm^{-1}, respectively. Near-IR was utilized to monitor the cure of monomer samples placed between glass slides (1 mm thickness) and initiated by 0.25% XDT. Conversion was monitored by the C=C vibration at 6020 cm^{-1}.

Mechanical Measurements. Dynamic mechanical analysis (DMA) was performed with a DMA Q800 dynamic mechanical analyzer (TA Instruments). The samples were rectangular films with dimensions of 1 mm × 5 mm × 10 mm. The multifrequency strain mode was used to measure moduli and loss tangent as a function of temperature by applying a sinusoidal stress of frequency 1 Hz over a temperature range of −40 to 100 °C with a ramping rate of 3 °C/min. The T_g was taken to be the maximum of the tan delta curve, which is the ratio of the loss modulus to the storage modulus. $T_{g1/2width}$ was taken to be the width of the tan delta curve at half the maximum value. Sample conversions were checked by FTIR after DMA testing to ensure that only a minimal amount of additional cure occurred during the heating. In no case was the increase in glass transition temperature observed from the first heating to the second heating cycle more than 10 °C.

Results and Discussion

Because of the complications associated with postcure effects, it is not feasible to determine the T_g versus T_{cure} relationship from a single experiment. Here, our method was to first cure samples at 100 °C initiated by XDT to various conversions. With the elimination of postcuring upon heating, it is then possible to accurately determine the glass transition temperature as a function of the conversion, verifying that a limited additional reaction occurs during the measurement. Critically, when cured to the same conversion, networks initiated by XDT have been demonstrated to exhibit similar network structures to those initiated by other traditional photoinitiators such as dimethoxy phenyl acetophenone (DMPA).[29] For the analysis, DMPA is then utilized as a traditional photoinitiator to determine how the conversion (and hence the glass transition temperature as determined from the XDT initiated samples) varies with the T_{cure}. Conversion versus

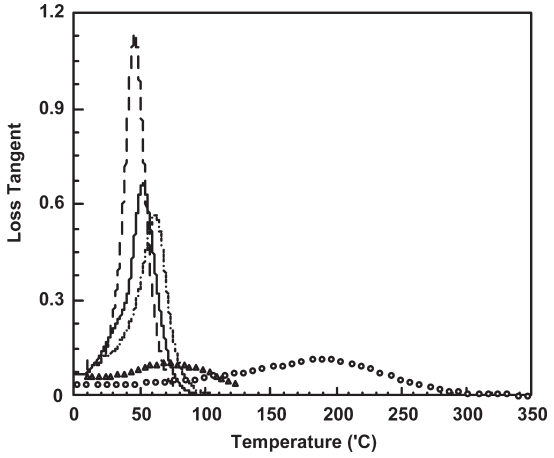


Figure 1. Loss tangent versus temperature for PETMP-TATATO (---), PETMP-TCDDA (—), PETMP-TMPTN (···), HDDA (▲), and TCDDA (○) cured to 85% (±1%) double bond conversion. Systems contain 0.25 wt % XDT and are irradiated at 15 mW/cm^2 and 100 °C until the sample achieves the desired conversion.

T_{cure} is determined from isothermally cured 10 μm thick samples initiated by DMPA to reach the maximum conversions at 25, 50, 75, and 100 °C, and the T_g vs T_{cure} relationship is then determined from the T_g values at the corresponding conversion.

Five model systems were studied in this work. HDDA and TCDDA are traditional chain growth acrylate systems that form heterogeneous polymer networks. TCDDA has a rigid monomer structure for comparison with the more flexible, aliphatic core structure of HDDA. PETMP/TATATO and PETMP/TMPTN are traditional radical-mediated step growth thiol−ene systems that lead to more homogeneous polymer networks while PETMP/TCDDA is a mixed mode step-chain growth thiol−acrylate system. These systems result in polymer networks with a wide range of glass transition temperatures and network heterogeneities as shown in the loss tangent curves in Figure 1 and the data in Table 1. The maximum achievable conversion and glass transition temperature achieved by reacting for long times at elevated temperatures are presented in Table 2.

To determine the T_g as a continuous function of conversion, the T_g vs conversion data were fit using free volume theory assuming that the free volume increases linearly with increasing temperature below or above the glass transition temperature, that at the glass transition temperature polymers have a universal free volume 0.025, and that the fractional free volumes of the monomer and polymer are added ideally.[32−34] Other methodologies result in similar interpolation of the relationship between glass transition temperature and conversion. The polymer volume fraction is calculated from monomer conversion[33] and the volumetric shrinkage factor[35] such that glass transition temperature (T_g) as a function of conversion (X) is obtained and is represented by eq 1:[29]

$$T_g = \frac{\alpha_m \nu_m T_{gm} + (\alpha_p \nu_p T_{gp} - \alpha_m \nu_m T_{gm})X}{\alpha_m \nu_m + (\alpha_p \nu_p - \alpha_m \nu_m)X} \quad (1)$$

in which α_m and α_p are expansion coefficients of the monomer and polymer (taken to be 0.0005 and 0.000 075 1/°C, respectively[34]); ν_m and ν_p are specific volumes of the monomer and polymer; T_{gm} is the glass transition temperature of the monomer taken to be the extrapolated glass transition temperature at $X = 0$; and T_{gp} is the extrapolated glass transition temperature of the polymer at 100% double bond conversion. For each system, the glass transition temperature was determined at a number of different conversions and the data were fit with eq 1 with the results presented in Figure 2.

Table 1. T_g and $T_{g1/2width}$ Values for Samples Cured to 85% (± 1%) Double Bond Conversion[a]

	T_g (°C)	$T_{g1/2width}$ (°C)
PETMP-TCDDA	52	20
PETMP-TATATO	46	17
PETMP-TMPTN	62	21
HDDA	69	50
TCDDA	189	103

[a] Systems contain 0.25 wt % XDT and are irradiated at 15 mW/cm^2 and 100 °C until the sample achieves the desired conversion.

Table 2. Conversion$_{max}$ and T_{gmax} for Samples Cured to Their Ultimate Conversion[a]

	conversion$_{max}$ (%)	T_{gmax} (°C)
PETMP-TCDDA	100 ± 0	94
PETMP-TATATO	100 ± 0	60
PETMP-TMPTN	98 ± 1	93
HDDA	93 ± 1	87
TCDDA	88 ± 2	n/a

[a] All samples were laminated between NaCl plates, cured at 100 °C with 0.5 wt % DMPA, and irradiated with 2.5 mW/cm^2 UV light to reach conversion$_{max}$. The T_{gmax} values at these conversions were calculated from the glass transition−conversion relationships presented in Figure 2.

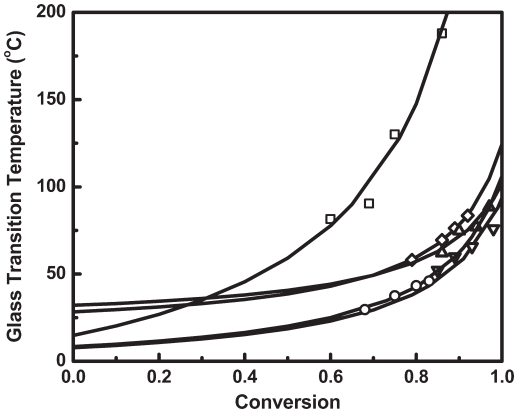


Figure 2. Glass transition temperature (T_g) as a function of double bond conversion for TCDDA (□), HDDA (◇), PETMP-TMPTN (Δ), PETMP-TCDDA (▽), and PETMP-TATATO (○). Curves were fit with the T_g vs conversion relationship as determined from eq 1. Systems contained 0.25 wt % XDT and were irradiated at 15 mW/cm^2 and 100 °C until they achieved the desired conversion.

To determine the conversion achieved at each cure temperature and obtain the conversion vs T_{cure} relationship, thin samples (10 μm) were cured at 25, 50, 75, and 100 °C. Since the samples are thin and heat transfer is extremely rapid to the salt crystals that act as effective heat sinks, the reactions are assumed to be isothermal. Heat transfer modeling[36] of similar systems predicts temperature changes of less than 0.3 °C during the reaction, verifying this assumption. Conversion versus T_{cure} data are shown in Table 3, and the T_g values are obtained from the T_g vs conversion relationships presented in Figure 2. Finally, the determined T_g vs T_{cure} data are shown in Figure 3.

Previous work on chain growth methacrylate systems indicated that the heterogeneity of polymer networks is an important factor in the T_g vs T_{cure} relationship, i.e., the more heterogeneous the sample, the larger the maximum difference between T_g and T_{cure}.[1] Another important factor in the T_g vs T_{cure} relationship is the maximum T_g (T_{gmax}). The data in Figure 3 help to illustrate this point by indicating that HDDA and PETMP/TMPTN have very similar T_g vs T_{cure} trends though they have different network

Table 3. Double Bond Conversion at Different Cure Temperatures for Various Monomer Systems[a]

T_{cure}	C=C Conversion					
(°C)	TCDDA	PETMP/TCDDA	PETMP/TMPTN	HDDA	PETMP/TATATO	
25	0.65	0.83	0.85	0.85	0.92	$T_{cure}<T_{gmax}-$
50	0.76	0.91	0.92	0.89	0.96	$T_{g1/2width}$
75	0.80	0.99	0.97	0.91	0.97	$T_{cure}\geq T_{gmax}-$
100	0.88	1.00	0.98	0.93	1.00	$T_{g1/2width}$

[a] The shaded values represent the samples cured under the condition where $T_{cure} < T_{gmax} - T_{g1/2width}$ and diffusion control dominates. The unshaded values represent the samples cured where $T_{cure} \geq T_{gmax} - T_{g1/2width}$ where topological control limits the polymerization. All samples were laminated between NaCl plates and cured at 25, 50, 75, or 100 °C with 0.5 wt % DMPA and were irradiated with 2.5 mW/cm^2 UV light.

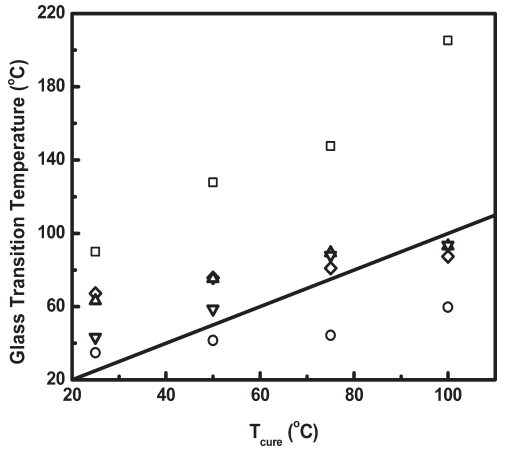


Figure 3. Glass transition temperature vs cure temperature for TCDDA (□), HDDA (◇), PETMP-TMPTN (△), PETMP-TCDDA (▽), PETMP-TATATO (○). For reference, $T_g = T_{cure}$ (—) is also plotted . All samples were laminated between NaCl plates and cured at 25, 50, 75, or 100 °C with 0.5 wt % DMPA and were irradiated with 2.5 mW/cm^2 UV light. The T_g values were obtained from the glass transition−conversion relationships presented in Figure 2.

heterogeneities associated with the different formation mechanisms. HDDA has a $T_{g1/2width}$ of 50 °C, and PETMP/TMPTN has a $T_{g1/2width}$ of 21 °C. The similarity in T_g vs T_{cure} behavior is primarily a result of these two systems exhibiting a similar maximum T_g (T_{gmax}). This result implies that both network heterogeneity and monomer structure, as evidenced by the maximum possible glass transition temperature, contribute to the T_g vs T_{cure} behavior. In summary, our hypothesis is that polymerizations continue as long as there are regions with sufficient mobility, independent of the specific type of polymerization reaction that is occurring. Mobility (and hence T_g) is a function of cure temperature, network heterogeneity, and molecular structure. These three factors can be further related to T_{cure}, $T_{g1/2width}$, and T_{gmax} (see Figure 1 and Tables 1 and 2). Therefore, the following relationship is proposed:

For polymerizing systems cured well below their maximum glass transition temperature, i.e., where

$$T_{cure} < T_{gmax} - T_{g1/2width} \tag{2}$$

we propose

$$T_g \approx T_{cure} + T_{g1/2width} \tag{3}$$

In contrast, for systems polymerized near or above their maximum possible glass transition temperature, i.e., for polymerizations where

$$T_{cure} \geq T_{gmax} - T_{g1/2width} \tag{4}$$

we propose

$$T_g \approx T_{gmax} \tag{5}$$

Thus, the relationship between the cure temperature and $T_{gmax} - T_{g1/2width}$ is utilized as a criterion to divide the polymerizing systems into two distinct regions, diffusion controlled and topologically controlled. For systems where $T_{gmax} - T_{g1/2width} > T_{cure}$, the samples are expected to be diffusion controlled, and for systems where $T_{gmax} - T_{g1/2width} < T_{cure}$, the samples are considered to be topologically controlled with limitations associated with the molecular structure and ultimate glass transition temperature of the material dominating.

In the diffusion controlled region, the cure temperature and network heterogeneity strongly affect the T_g vs T_{cure} behavior. As T_{cure} is increased, the free volume at a given conversion increases and diffusional limitations do not arise until later in the polymerization, ultimately resulting in the reaction proceeding to higher conversions. This result is evidenced in the shaded data of Table 3 where the conversions of the systems increase with increasing T_{cure}. For PETMP/TCDDA and PETMP/TMPTN systems, the conversions increase 8% and 7%, respectively, when increasing T_{cure} from 25 to 50 °C. In contrast, in the topologically controlled region, the conversions increase only 1% when T_{cure} is increased from 75 to 100 °C. Heterogeneity also strongly affects the T_g vs T_{cure} behavior. The more heterogeneous networks maintain regions of higher mobility, even when the overall glass transition temperature exceeds the cure temperature by a wide margin, resulting in greater differences between T_g and T_{cure}.[1]

In the topologically controlled region ($T_{cure} > T_{gmax} - T_{g1/2width}$), the unshaded data in Table 3, there is more free volume in the network which increases the mobility of the polymer segments and reduces diffusional limitations such that the polymers essentially achieve their maximum conversion. Thus, topological restrictions become the dominant factor controlling T_g. This phenomenon is illustrated in Figure 3 where the HDDA, PETMP/TMPTN, and PETMP/TCDDA systems achieve a maximum T_g that does not increase further with increasing cure temperature from 75 to 100 °C. For most of the systems that have been evaluated, there is minimal change in T_g when T_{cure} is increased from 75 to 100 °C. Therefore, T_{gmax} is taken to be the T_g when T_{cure} = 100 °C (see Table 2). TCDDA has a T_g of 205 °C at T_{cure} = 100 °C, which is significantly greater than the T_g at 75 °C. However, 205 °C is still approximated as the T_{gmax} for TCDDA.

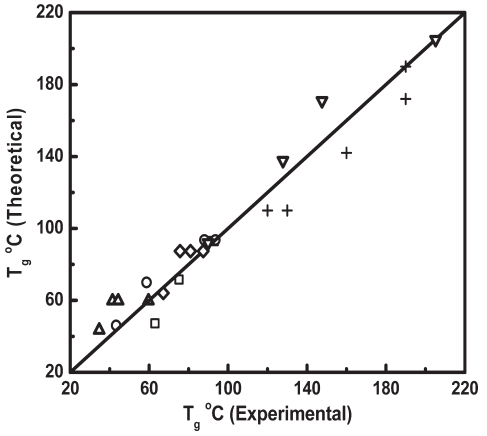


Figure 4. The predicted T_g (from eqs 3 and 5) as a function of the experimentally determined T_g for PETMP-TMPTN (□), PETMP-TCDDA (○), PETMP-TATATO (◇), HDDA (△), TCDDA (▽), and DGEBA-DDM (+), which were obtained from Figures 1 and 3 in Cook's paper.[21].

To demonstrate the validity of the proposed relationships, the experimental data and the predictions from eqs 3 and 5 are plotted in Figure 4. The same relationships are also applied to traditional step growth epoxy-amine thermoset systems studied by Cook et al.,[21] (diglycidyl ether of bisphenol A (DGEBA) and diaminodiphenyl methane (DDM)) and Gillham et al.,[10] (DGEBA and trimethylene glycol di-*p*-aminobenzoate (TGAB)). Figure 4 depicts the predicted T_g vs the experimental T_g for the step growth radical polymerization systems, the chain growth systems and the epoxy-amine polymerization systems with the average errors of 7, 7, and 13 °C, respectively. Given the simplistic nature of the proposed relationship, the broad range of glass transition temperatures and reaction mechanisms, and the very different heterogeneity and molecular structures of the polymer products, this relatively limited error represents significant agreement between the proposed relationships and the experimental data. Moreover, we analyzed the $T_{g1/2width}$ of Gillham's DGEBA-TGAB system.[10] Here, the $T_{g1/2width}$ for these thermosets ranges from 26 to 32 °C for the four T_g curves presented in the original work, which indicates that the originally proposed empirical rule of thumb that $T_g = T_{cure} + (15-30\ K)$[14] for these polymerizations is consistent with our proposed relationship for all systems that under these circumstances $T_g \approx T_{cure} + T_{g1/2width}$.

Conclusions

Here, the polymer T_g is determined to be a function of the cure temperature, network heterogeneity, and molecular structure. A quantitative relationship for glass transition temperature (T_g) as a function of T_{cure}, $T_{g1/2width}$, and T_{gmax} was successfully applied to a range of polymerization systems with minimal error found between experimental and predicted data for both condensation and radical-mediated step and chain growth polymerizations. For the polymerizations performed well below the maximum possible glass transition temperature, where $T_{cure} < T_{gmax} - T_{g1/2width}$, the reaction is diffusion controlled and the network heterogeneity dictates T_g such that $T_g \approx T_{cure} + T_{g1/2width}$. For other polymerizations where $T_{cure} \geq T_{gmax} - T_{g1/2width}$, the monomer structure becomes the dominant factor and $T_g \approx T_{gmax}$. The relationships between glass transition temperature and cure temperature describe well a range of polymerization systems covering chain growth, radical step growth, and condensation step growth systems.

Acknowledgment. The authors gratefully acknowledge the National Science Foundation Grant CBET 0626023 for funding this work.

References and Notes

(1) Lu, H.; Lovell, L. G.; Bowman, C. N. *Macromolecules* **2001**, *34*, 8021–8025.
(2) Kloosterboer, J. G. *Adv. Polym. Sci.* **1988**, *84*, 1–61.
(3) Anseth, K. S.; Newman, S. M.; Bowman, C. N. *Adv. Polym. Sci.* **1995**, *122*, 177–217.
(4) Anseth, K. S.; Wang, C. M.; Bowman, C. N. *Macromolecules* **1994**, *27*, 650–665.
(5) Anseth, K. S.; Wang, C. M.; Bowman, C. N. *Polymer* **1994**, *35*, 3243–3250.
(6) Bowman, C. N.; Kloxin, C. J. *AIChE J.* **2008**, *54*, 2775–2795.
(7) Cook, W. D.; Forsyth, J. S.; Irawati, N.; Scott, T. F.; Xia, W. Z. *J. Appl. Polym. Sci.* **2003**, *90*, 3753–3766.
(8) Gillham, J. K.; Enns, J. B. *J. Appl. Polym. Sci.* **1983**, *28*, 2567–2591.
(9) Gillham, J. K.; Aronhime, M. T. *Adv. Polym. Sci.* **1986**, *78*, 83–113.
(10) Wang, X.; Gillham, J. K. *J. Appl. Polym. Sci.* **1993**, *47*, 425–446.
(11) Venditti, R. A.; Gillham, J. K. *J. Appl. Polym. Sci.* **1997**, *64*, 3–14.
(12) Wang, X.; Gillham, J. K. *J. Appl. Polym. Sci.* **1992**, *45*, 2127–2143.
(13) Rozenburg, B. A. *Adv. Polym. Sci.* **1986**, *75*, 113–166.
(14) Oleinik, E. F. *Adv. Polym. Sci.* **1980**, *80*, 49–99.
(15) Cook, W. D.; Simon, G. P.; Bruchill, P. J.; Lau, M.; Fitch, T. J. *J. Appl. Polym. Sci.* **1997**, *64*, 769–781.
(16) Kloosterboer, J. G.; Lijten, G. F. C. M. *Polymer* **1990**, *31*, 95–101.
(17) Odian, G. In *Principles of Polymerization*, 4th ed.; John Wiley & Sons, Inc.: Hoboken, NJ, 2004; p 1.
(18) Funke, W.; Okay, O.; Joos-Muller, B. *Adv. Polym. Sci.* **1998**, *136*, 139–234.
(19) Chiu, Y. Y.; Lee, L. J. *J. Polym. Sci., Part A: Polym. Chem.* **1995**, *33*, 257–267.
(20) Sandler, S. R.; Karo, W.; Bonesteel, J.; Pearce, E. M. In *Polymer Synthesis and Characterization*; Academic Press: San Diego, CA, 1998; pp 198−206.
(21) Cook, W. D.; Scott, T. F.; Quay-Thevenon, S.; Forsythe, J. S. *J. Appl. Polym. Sci.* **2004**, *93*, 1348–1359.
(22) Hoyle, C. E.; Lee, T. Y.; Roper, T. *J. Polym. Sci., Part A: Polym. Chem.* **2004**, *42*, 5301–5338.
(23) Cramer, N.; Bowman, C. N. *J. Polym. Sci., Part A: Polym. Chem.* **2001**, *39*, 3311–3319.
(24) Hoyle, E. C.; Lowe, A. B.; Bowman, C. N. *Chem. Soc. Rev.* **2010**, *39*, 1355–1387.
(25) Hoyle, C. E.; Bowman, C. N. *Angew. Chem., Int. Ed.* **2010**, *49*, 1540–1573.
(26) Otsu, T.; Yoshida, M.; Tazaki, A. *Makromol. Chem. Rapid Commun.* **1982**, *3*, 133–140.
(27) Kannurpatti, A. R.; Lu, S.; Bunker, G. M.; Bowman, C. N. *Macromolecules* **1996**, *29*, 7310–7315.
(28) Lovell, L. G.; Lu, H.; Elliott, J. E.; Stansbury, J. W.; Bowman, C. N. *Dental Mater.* **2001**, *17*, 504–511.
(29) Kannurpatti, A. R.; Anderson, K. J.; Anseth, J. W.; Bowman, C. N. *J. Polym. Sci., Part B: Polym. Phys.* **1997**, *35*, 2297–2307.
(30) Carioscia, J. A.; Schneidewind, L.; O'Brien, C.; Ely, R.; Feeser, C.; Cramer, N. B.; Bowman, C. N. *J. Polym. Sci., Part A: Polym. Chem.* **2007**, *45*, 5686–5696.
(31) Lovell, L. G.; Berchtold, K. A.; Elliott, J. E.; Lu, H.; Bowman, C. N. *Polym. Adv. Technol.* **2001**, *12*, 335–345.
(32) Bueche, F. *Physical Properties of Polymers*; Interscience: London, 1962; p 112.
(33) Scheirs, J.; Priddy, D. *Modern Styrenic Polymers: Polystyrenes and Styrenic Copolymers*; John Wiley & Sons, Inc.: West Sussex, U.K., 2003; p 98.
(34) Anseth, K. S.; Bowman, C. N. *Polym. React. Eng.* **1992−1993**, *1*, 499–520.
(35) Lu, H.; Carioscia, J. A.; Stansbury, J. W.; Bowman, C. N. *Dental Mater.* **2005**, *21*, 1129–1136.
(36) O'Brien, A. K.; Bowman, N. B. *Macromolecules* **2003**, *36*, 7777–7782.

Macromolecules
ARTICLE

Macromolecules **2011**, *44*, 495–501 **495**
DOI: 10.1021/ma102149u

Solvent Composition Directing Click-Functionalization at the Surface or in the Bulk of Azide-Modified PEDOT

Johan U. Lind,[†] Thomas S. Hansen,[†] Anders E. Daugaard,[‡] Søren Hvilsted,[‡] Thomas L. Andresen,[†] and Niels B. Larsen*,[†]

[†]*Department of Micro- and Nanotechnology, Technical University of Denmark, DTU Nanotech, Ørsteds Plads 345ø, 2800 Kgs. Lyngby, Denmark, and* [‡]*Department of Chemical and Biochemical Engineering, Technical University of Denmark, Søltofts Plads, Building 227, 2800 Kgs. Lyngby, Denmark*

Received September 15, 2010; Revised Manuscript Received December 22, 2010

ABSTRACT: Thin films of the conducting polymer poly(3,4-(1-azidomethylethylene)dioxythiophene) tosylate (PEDOT−N_3) can be functionalized by reaction with alkynated reagents in aqueous solutions. Reaction in pure water resulted in surface specific modification of PEDOT−N_3 films, whereas both surface and bulk reaction was achieved in solvent mixtures of water and DMSO. These reaction patterns were confirmed by a combination of AFM and XPS measurements on the front- and back-side of the film. The phenomenon is attributed to a strong dependence of the swelling of PEDOT−N_3 on the solvent mixture used. Liquid AFM studies showed increasing film thickness with increasing DMSO content, with the measured thickness in pure DMSO being >250% of the thickness in pure water. A similar, but less pronounced, behavior was observed for unmodified poly(3,4-ethylenedioxythiophene) tosylate (PEDOT). High-density grafting of a number of alkynated compounds onto PEDOT−N_3 was achieved via controlled swelling of the polymer. In particular, grafting of alkynated poly(ethylene glycol) (PEG) was optimized to minimize protein adsorption to the conductive polymer surface. Intermediate swelling of PEDOT−N_3 during the reaction, using ∼50% DMSO, resulted in the formation of a dense PEG surface layer with low protein adhesiveness without adversely affecting the conductive properties of the film.

Introduction

The conductive polymer poly(3,4-ethylenedioxythiophene) (PEDOT) is employed for a wide range of applications, including solar cells,[1,2] organic light emitting electrodes,[3] photographic films,[4] biosensors,[5] fuel cells,[6,7] and actuators.[8,9] PEDOT is often chemically modified to facilitate a specific application. Various chemical entities have been incorporated, commonly through covalent bonding to the ethylene part of the PEDOT molecule, which is not part of the π-conjugated backbone,[10−18] but also noncovalently by adsorption or incorporation into the PEDOT matrix.[19−23] Such modifications can e.g. serve to change the electronic properties of the polymer,[10,14,20] or to add a biological functionality.[11,15,19] The "click"-type reaction between an azide group and a terminal alkyne, the copper(I)-catalyzed azide−alkyne Huisgen 1,3-dipolar cycloaddition (CuAAC) is a popular method for postpolymerization modification of polymers.[24−28] Recently, a number of studies have focused on the fabrication of PEDOT-type polymers containing alkyne and azide groups and functionalization of these using CuAAC.[29−32] We have previously developed a 3,4-(1-azidomethylethylene)-dioxythiophene (EDOT−N_3) monomer that can be chemically oxidized to yield PEDOT−N_3 films containing tosylate as counterions for the p-doped polymer. The films are stable, insoluble, highly conductive, and can be functionalized by a range of alkynated reagents.[30] We have also demonstrated localized functionalization under electrochemical control ("electro click") for individual modification of PEDOT−N_3 microelectrodes[33] or creation of complex chemical surface gradient patterns.[34]

*Corresponding author. E-mail: niels.b.larsen@nanotech.dtu.dk.

Here, we present a simple method for controlling the degree of reaction and the depth of modification of PEDOT−N_3 thin films by varying the solvent composition of aqueous solvents for a number of alkynated reagents (see Scheme 1). The methodology is based on our finding that the polymer undergoes significant, reversible and gradually increasing swelling in DMSO/water mixtures of increasing DMSO concentration. We further demonstrate the usefulness of the method to produce high-density poly(ethylene glycol) (PEG) coatings with low nonspecific protein adhesiveness on PEDOT−N_3 while retaining most of the thin film's electrical conductivity. This ability is central to many advanced biological uses, since the reduction of nonspecific interactions is a requirement for utilizing specific interactions between the substrate and, e.g., a living cell.[35,36] Formation of a high-density surface layer of PEG molecules by grafting from solution is difficult due to steric hindrance by initially bound PEG molecules.[37] We find that addition of DMSO to the aqueous solution results in a much denser PEG film and reduces its protein adhesiveness, probably due to the swelling of the PEDOT−N_3, which increases the number of accessible reactive azide groups. Such a dense PEG coverage can be achieved at intermediate DMSO concentrations without compromising the conductivity of the PEDOT−N_3, whereas the use of very high DMSO concentrations leads to a substantial bulk modification and concomitant reduction of the film conductivity.

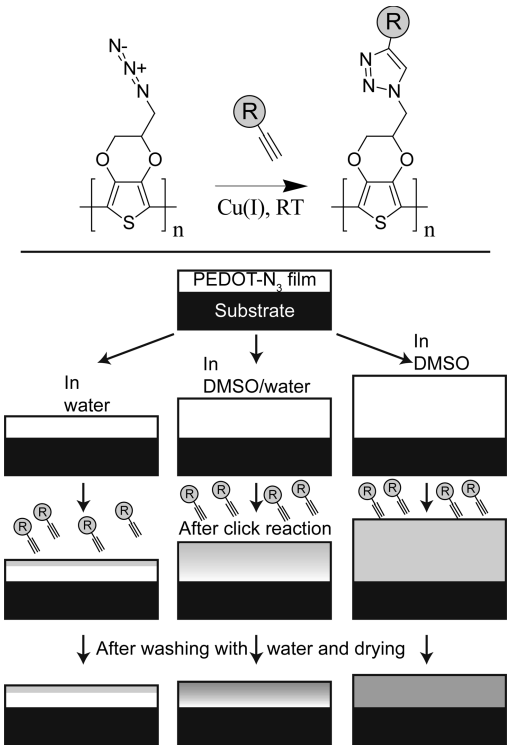
Experimental Section

Solvents. Ultrapure water of resistivity > 18.2 MΩ cm (Milli-Q water) was produced on a Millipore Quantum system (Millipore, MA). DMSO (>99% purity) was obtained from Merck (Darmstadt, Germany). DMSO concentrations in DMSO/water solutions are given in volume percent throughout the text.

© 2011 American Chemical Society

Published on Web 01/10/2011

Scheme 1. (Top) Cu(I)-Catalyzed Click Reaction between the Azide of PEDOT−N_3 and an Alkynated Reagent and (Bottom) Illustration of the Swelling of PEDOT−N_3 Thin Films (White) in Water, in Water/DMSO Mixtures, and in Pure DMSO, Respectively, and the Resulting Degrees of Reaction (Gray) at the Surface and in the Bulk of the Film in Its Swelled State after Reaction or after Washing with Water and Drying



Conducting Polymer Samples Fabrication. EDOT-N_3 was synthesized in accordance with our earlier reported procedure.[30] PEDOT:TsO and PEDOT−N_3:TsO thin films were fabricated by spin-coating and polymerizing on cyclic olefin copolymer (COC) supports as described previously[30,38] and as summarized in the Supporting Information. AFM studies used octadecyltrichlorosilane (OTS) treated glass microscope slides as substrates for PEDOT:TsO films or (3-aminopropyl)trimethoxysilane (APTMS) treated glass microscope slides as substrates for PEDOT:PSS film, instead of COC supports, to minimize the risk of film delamination. OTS treatment proceeded by immersion of the glass slides in a 0.5% solution of OTS (Sigma-Aldrich) in toluene for at least 15 min. After treatment the slides were rinsed in toluene, ethanol, and Milli-Q water. APTMS treatment was done by placing the microscope slide for 2 h in a 0.1 M solution of APTMS (Sigma-Aldrich) in 2-propanol containing 1.5 M water, and rinsing in 2-propanol, ethanol and Milli-Q water. PEDOT:PSS films for AFM investigation were made by spin-coating a 1.2−1.4% PEDOT:PSS aqueous solution (483095, Sigma-Aldrich) at 1000 rpm onto a glass microscope slide. Following spin-coating the film was annealed on a hot plate at 200 °C for 30 min.

Alkyne Reagents. The syntheses of the alkyne reagents are described in the Supporting Information. Propargyl alcohol and 4-pentynoic acid were purchased from Sigma-Aldrich.

Postpolymerization Click-Reactions on PEDOT−N_3 Substrates. All reactions were performed in a homemade reaction well system. The wells were defined by circular holes of 5−7 mm in diameter in a 2 mm thick silicone rubber film (Leewood Elastomer, Skogaas, Sweden) that was attached to the substrates via double-sided adhesive tape (ARcare 90106, Adhesive Research, Glen Rock, PA). Holes of 4−6 mm in diameter were punched in the adhesive tape and placed in registry with the holes of the silicone rubber film. This system allowed for the exchange of the well sidewalls in later protein adsorption studies, thus eliminating the influence of nonspecific protein adsorption to the sidewalls. In each reaction well, 70−75 μL of reaction solution was added. Unless otherwise noted, 10 mM alkyne reagent, 2 mM $CuSO_4$, and 40 mM sodium ascorbate were used. The reaction time and the DMSO content of the reaction solution were varied. During reaction each well was covered by a piece of PET foil to limit the access of air. After reaction the wells were rinsed in Milli-Q water.

AFM Measurements. AFM measurements were performed on a PSIA XE-150 (Park Systems, Suwon, Korea) operating in intermittent contact mode and using Tap300Al and Tap75Al cantilevers (Budget Sensors, Sofia, Bulgaria). Liquid measurements used a liquid probe hand (Park Systems) and a homemade sample chamber permitting complete immersion of the substrate. Film thicknesses were determined by measuring the step height of a step produced either by cutting a narrow line with a scalpel or through masked oxygen plasma etching of part of the film (Plasmatherm 740, Unaxis, St Petersburg, FL). The step heights of at least three points on each sample were measured. For measurement series using a sequence of solvent mixtures, the same measurement areas were probed in each step of the series. Exchange of DMSO/water mixtures proceeded by washing the sample chamber twice with the new mixture and a waiting period at least 30 min before analysis to allow the film to respond. The DMSO content was increased in each step of the measurement series, except for the final reimmersion in pure water.

XPS Investigations. XPS experiments were conducted using a Thermo Fisher Scientific K Alpha (East Grinstead, U.K.). A 400 μm spot on each sample was irradiated using monochromatized aluminum Kα radiation, and survey (pass energy 200 eV) and high resolution (pass energy 25 eV) spectra of relevant elements were acquired. Flood-gun charge compensation was used for all samples. Data analyses of the XPS spectra were performed using the Avantage software package supplied by the manufacturer. The elemental composition was obtained and a peak fit of the nitrogen high resolution data was conducted: The azide group gives rise to a nitrogen doublet peak with a peak area ratio of 1:2. The smaller peak at higher binding energy disappears upon click reaction as the azide reacts to form a triazole. For an unreacted surface a ratio of $^1/_2$ is expected, and smaller ratios correspond to increasing degrees of reaction. The back side of the PEDOT−N_3 films was made available for analysis by stripping the entire film off its OTS-coated glass substrate after reaction, using a piece of double-sided adhesive tape.

Conductivity Measurements. Conductivity measurements were done using a four-point probe (Jandel Engineering, Linsdale, U.K.) connected to a Keithly 2400 source-meter (Cleveland, OH). Two measurements in perpendicular orientations were performed on each sample. Measurements in water or DMSO were performed by immersing the contact pins of the four-point probe into a droplet of the solvent placed on top of the substrate. Control experiments were conducted on a nonconducting substrate with Milli-Q water and DMSO droplets, respectively. The control experiments verified that the conductivity of DMSO and of Milli-Q water did not significantly contribute to the values measured on the polymer films.

Protein Adsorption Studies. PEDOT−N_3 films reacted with alkyne-PEG were tested for their protein adhesiveness. The click reaction proceeded in a chemically reducing environment, and the samples were subsequently reoxidized by immersion in ~4% iron(III) tosylate in 10% 1-butanol/90% Milli-Q water for 10 min. The surface was then immersed in DMSO for 10 min and finally rinsed in Milli-Q. PBS (25 μL) was added to each well for 5 min, followed by addition of 25 μL of 7.5 μg/mL HRP-rabbit anti-goat IgG (611620 Invitrogen, Camarillo, CA) in PBS solution that was left to adsorb for 15 min. The protein solution was removed and the samples were washed twice with 0.1%

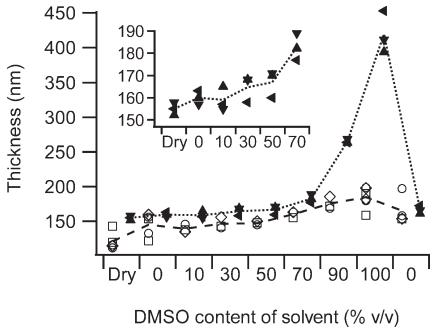


Figure 1. Thicknesses of PEDOT (open symbols) and PEDOT−N_3 (solid symbols) thin films were measured by AFM for gradually increasing DMSO content. The thickness was first measured under dry conditions and then in mixtures of water and DMSO, starting from pure water and increasing the DMSO content until reaching pure DMSO. The films were then reimmersed in pure water. For each film at least three different areas were measured with each symbol corresponding to one of the areas. The lines show average thickness of these points. Insert: The thickness of PEDOT−N_3 films at low DMSO contents shown at larger magnification.

Tween-20 in PBS for 5 min. As final procedure step, the samples were washed with Milli-Q water and blown dry in a stream of nitrogen. The wells were then removed and replaced with a new set of silicone wells. Quantification of the adsorbed HRP-containing protein was performed by adding 100 μL of 3,3′,5,5′-tetramethylbenzidine solution (TMB, Sigma-Aldrich) to each well and letting the enzymatic reaction run for 4 min on a rocking table. The solutions were then transferred to a 96-well plate and the light absorption at 450 nm was evaluated using a Wallac Victor 1420 plate reader (Perkin-Elmer).

Results and Discussion

Thin films of PEDOT−N_3 undergo substantial swelling in DMSO as compared to in water. The swelling of PEDOT−N_3 tosylate and of PEDOT tosylate films were investigated in a series of AFM measurements (see Figure 1). The changes in film thickness were measured in a series starting with pure water, followed by mixtures with gradually increasing amounts of DMSO in water, and ending with pure water to probe reversibility of the swelling process. The thickness of both PEDOT-type polymers increase with increasing DMSO content. For PEDOT−N_3 in mixtures with ≤50% DMSO in water, the effect is weak with an average relative increase of < 5% compared to the thickness in pure water. For > 50% DMSO in water, the thickness increases strongly with DMSO content up a maximum in pure DMSO of ∼260% of the film thickness found in water. Importantly, immersion in water of the maximally swelled film results in the thickness returning to its original value in water. The corresponding effect on PEDOT tosylate films is less pronounced with a measured thickness in pure DMSO of ∼150% of that in pure water. The thickness of PEDOT also decreases upon re-exposure to water, although is cannot be determined with certainty from these measurements if it returns to its original value in water.

PEDOT is usually employed in a p-doped state with counter-anions ensuring charge neutrality. Tosylate (TsO) or polymeric poly(styrenesulfonate) (PSS) counterions are commonly used (see Figure 2).[4] The investigated PEDOT and PEDOT−N_3 films contain tosylate counterions that lead to highly conducting films.[4,38] The generality of the observed swelling pattern was investigated by including PEDOT with polymeric PSS counterions (PEDOT:PSS) in the AFM and conductivity analysis series. Table 1 compares thickness and sheet resistance of PEDOT:PSS in the dry state, in water, and in DMSO, respectively, to the

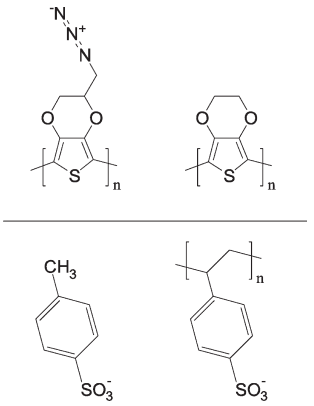


Figure 2. Structure of PEDOT-type polymers and counterions. Top left: PEDOT−N_3. Top right: PEDOT. Bottom left: Tosylate counterion. Bottom right: Poly(styrenesulfonate) counterion.

corresponding values found for PEDOT−N_3 tosylate (PEDOT−N_3:TsO) or PEDOT tosylate (PEDOT:TsO).

Our AFM studies revealed very large swelling of PEDOT:PSS with measured thicknesses in both DMSO and in water of > 700% of the dry state thickness. This finding is not surprising as it is well established that PEDOT:PSS is both hygroscopic and capable of absorbing large amounts of DMSO.[39,40] The interaction between DMSO and PEDOT:PSS has recently attracted considerable attention, as DMSO and a number of other polar organic solvents can be used to drastically increase PEDOT:PSS conductance.[40−42] Addition of these solvents to aqueous suspensions of PEDOT:PSS during or after spin-casting of films improves the conductance by orders of magnitude.[40,42,43] We similarly observe a ∼500 times lower sheet resistance of a preformed PEDOT:PSS film after immersion in DMSO followed by washing in water and drying (see Table 1, columns "dry" vs "dry after DMSO"). It is worth noting that even the heavily swelled state of PEDOT:PSS during DMSO treatment exhibit ∼200 times lower sheet resistance (columns "dry" vs "DMSO"). In contrast, PEDOT−N_3:TsO and PEDOT:TsO films show small increases in sheet resistance of ∼1.75 times and ∼1.1 times, respectively, upon DMSO treatment. In this comparison, it should be noted that the initial and final sheet resistance of the latter films are actually both close to the resistance for PEDOT:PSS after solvent treatment.

We also investigated if the swelling of PEDOT−N_3:TsO thin films and, to lesser extent, PEDOT:TsO thin films was associated with changes in light absorption or in changes of their surface morphology. Absorption spectroscopy revealed small variations in a broad absorption peak centered at 530 nm after exposure of PEDOT−N_3 films to different liquid environments (see Figure S4A), while no changes in visible and near-infrared absorption were found for PEDOT films exposed to the same treatments (see Figure S4B). AFM analysis of the film surface morphology after repeated exchange of the immersion liquids showed very little dependence on the degree of swelling, with mean and rms roughness values of less than 10 nm for all the conditions explored (see Figure S5 and Table S1).

We observe much stronger swelling of PEDOT:PSS than of PEDOT:TsO in both water and DMSO. The large volume fraction of hygroscopic PSS in PEDOT:PSS compared to the volume fraction of tosylate in PEDOT:TsO[44] likely accounts for most of this difference. We therefore considered if the larger swelling of PEDOT−N_3:TsO than of PEDOT:TsO in DMSO could reflect differences in the doping levels and tosylate content of the two polymers. However, estimation of the tosylate content from XPS analysis of the sulfur peak[44,45] does not indicate markedly different levels in PEDOT:TsO and in PEDOT−N_3:TsO. Another

Table 1. Thickness and Sheet Resistance of PEDOT−N_3 Tosylate, PEDOT Tosylate, and PEDOT:PSS Thin Films Prior to Immersion in Liquid, for Immersion in Liquid, and after Drying, Respectively

	film thickness in nm[a]			film sheet resistance in KΩ/square[b]					
	dry[c]	water[d]	DMSO[e]	dry[c]	water[d]	dry after water[f]	dry[c]	DMSO[e]	dry after DMSO[g]
PEDOT−N_3:TsO	155	160	420	0.71	1.15	1.00	0.77	1.33	1.34
PEDOT:TsO	121	145	185	0.08	0.11	0.11	0.09	0.10	0.10
PEDOT:PSS	266	2087	1879	267	h	241	218	1.10	0.45

[a] Average value of at least three different areas on each film measured by AFM after ≥30 min exposure. [b] Average of two four-point probe measurements of perpendicular orientations obtained after ≥10 min exposure. [c] Film in dry state before immersion in liquids. [d] Film immersed in water. [e] Film immersed in DMSO. [f] Film dried in a stream of nitrogen after immersion in water. [g] Film washed in water and dried in a stream of nitrogen after immersion in DMSO. [h] The PEDOT:PSS film immersed in water did not produce stable sheet resistance values.

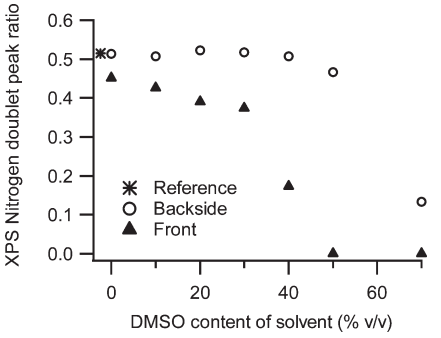


Figure 3. XPS analysis of the degree of reaction on PEDOT−N_3 films modified by PEG−alkyne as a function of DMSO concentration. All reactions used 10 mM PEG−alkyne, 2 mM $CuSO_4$, 40 mM sodium ascorbate, and a fixed reaction time of 4 h. A nitrogen peak intensity ratio of $^1/_2$ corresponds to zero degree of reaction, while full conversion of the azides yields a peak ratio of 0. Nitrogen peak analysis was performed both on the front side (facing the reaction solution; solid triangles) and on the back side (facing the substrate; open squares) of the film, with the reference (asterisk) being a freshly prepared PEDOT−N_3 film.

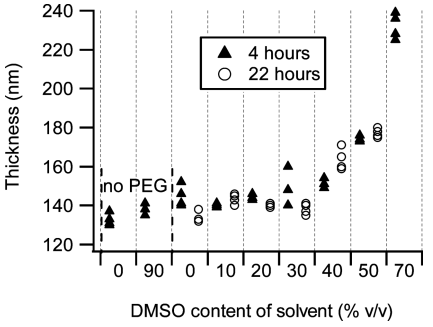


Figure 4. AFM analysis of the PEDOT−N_3 film thickness after reaction with PEG−alkyne at varying DMSO concentrations and reaction times (4 h, solid triangles; 22 h, open circles), followed by washing with water and drying the samples. All reactions used 10 mM PEG−alkyne, 2 mM $CuSO_4$, and 40 mM sodium ascorbate. The two controls to the left in the graph underwent all process steps except for the addition of PEG−alkyne.

explanation for their different swelling properties might be the presence or absence of the azide functionality. In a recent study by Sando et al. on the vibrational behavior of the inorganic azide ion in DMSO and water, no preferential solvation of the azide toward water or DMSO was reported.[46] We can therefore only suggest that the azide group in organic polymers may have a favorable interaction with DMSO, perhaps in synergy with other interactions such as those suggested by Ouyang.[41]

Our finding of a correlation of PEDOT−N_3 film swelling to the concentration of DMSO in water made us consider if the DMSO concentration in the click-reaction solution could be employed to control (a) the reaction depth into the PEDOT−N_3 film, and (b) the degree of reaction at its surface due to accessibility of a larger number of reactive groups in the swollen state. This was explored by functionalization of PEDOT−N_3 films with a PEG−alkyne (~815 Da). The DMSO concentration and the reaction time were varied in a series of experiments with fixed concentrations of PEG−alkyne, $CuSO_4$, and sodium ascorbate. XPS analysis was employed to quantify the degree of reaction via measurement of the nitrogen doublet peak characteristic of azide groups: The intensity ratio of the higher binding energy peak to the lower binding peak is 1:2 for azide groups. The higher binding energy peak disappears upon conversion of the azide to a triazole group, thus leading to a ratio of less than 1:2. Figure 3 presents the determined nitrogen peak intensity ratios for both the front side and the back side of the prepared films.

The analysis shows that some reaction occurs on the front side of the film in pure water after 4 h reaction time. However, the resulting PEG layer is of low density. Given a typical XPS mean-free-path-length in organic materials of ~2.5 nm,[47] the nitrogen peak ratio found for the reaction in pure water corresponds to a surface PEG layer thickness of <0.5 nm in the vacuum conditions of the XPS. Addition of DMSO to the aqueous solvent leads to gradually increasing degrees of reaction until no azides can be found on the front side within the XPS sampling depth. On the back side of the film, no reaction is seen for the pure water samples or for DMSO concentrations below 50%. For DMSO concentrations ≥50%, reaction occurs even on the back side of the film. Thus, the increased swelling at high DMSO concentrations does indeed allow reaction to occur deep into the film.

Figure 3 shows that smaller DMSO concentrations also have an effect, either by increasing the surface density of reacted groups or by permitting reaction deeper into the film. The degree of reaction in the film interior cannot easily be determined by XPS analysis, since the obvious option of performing XPS depth profiling may adversely affect the azide functionality. Stable coupling of PEG−alkyne to azides in the bulk of the film will result in a larger film volume, so measurement of the film thickness after reaction, washing with water, and drying the film is an indirect measure of the average degree of reaction. The PEDOT−N_3 film thickness in dry condition after reaction with PEG−alkyne was measured by AFM for a range of DMSO concentrations and reaction times of 4 and 22 h, respectively (see Figure 4). Some minor inhomogeneities in the film structure could be observed during the AFM measurements. Still, a correlation between the thickness of the film and the DMSO content of the reaction solvent is evident for both the 4 h and the 22 h series. For the 4 h reaction at 50% DMSO, the thickness was ~175 nm and at 70% DMSO it was 230 nm, equivalent to respectively 130% and 175% of the thickness of the reference areas without PEG. This clearly shows that bulk reaction does indeed take place for higher DMSO concentrations. We observed similar bulk reaction of a PEDOT−N_3 film in an earlier study on modifying PEDOT−N_3 with an alkynated fluorescein in dimethylformamide.[30] Notably for the low DMSO concentrations and for pure water, no significant thickness increase is

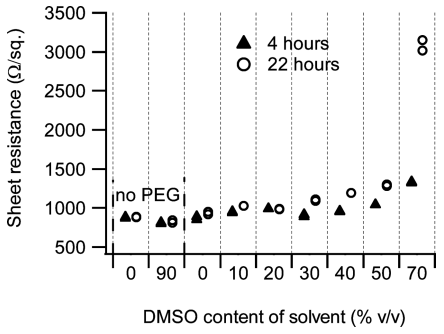


Figure 5. Sheet resistance of the PEDOT−N_3 film after reaction with PEG−alkyne at varying DMSO concentrations and reaction times (4 h, solid triangles; 22 h, open circles). All reactions used 10 mM PEG−alkyne, 2 mM $CuSO_4$, and 40 mM sodium ascorbate. Prior to the resistance measurement all films had been rinsed and reoxidized as described in the Experimental Section, since the click reactions are performed in a chemically reducing environment. The two controls to the left in the graph underwent all process steps except that no PEG−alkyne was added to the reaction solution.

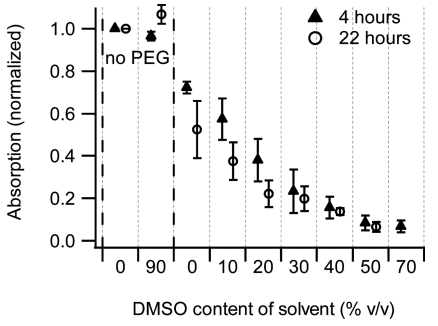


Figure 6. Protein adsorption to PEDOT−N_3 functionalized with PEG at varying DMSO concentration and reaction times (4 h, solid triangles; 22 h, open circles). The ability of the films to resist protein adsorption was tested using IgG-HRP. The relative adsorption of IgG-HRP was determined via the turnover of the HRP-substrate TMB and measured by light absorption at 450 nm. Four independent experiments were conducted. All results are normalized to the highest protein adsorption measured, i.e., for the reference point at 0% DMSO with no added PEG−alkyne. Error bars show the standard error of the mean (n = 4).

observed even for the 22 h reaction time, indicating the absence of bulk reaction. The importance of the reaction time for bulk reaction at high DMSO concentrations is stressed by the missing point at 70% DMSO for the 22 h series: This experiment was in fact performed, but the film was not sufficiently mechanically stable after the PEG−alkyne reaction to perform the height analysis procedure. In general the films often became unstable for reactions conducted in ≥70% DMSO. We take this as an indication that upon heavy PEG functionalization the material loses its cohesive strength and fractures during the rinsing steps. The swelling process itself is not responsible for the loss of mechanical stability, since the control sample of immersed in 90% DMSO without adding PEG−alkyne (see left side of Figure 4) remained perfectly stable after washing with water and drying.

Global and local volumetric expansion of the PEDOT−N_3 film upon covalent coupling of alkynes in the film interior may adversely affect its conductive properties in addition to its mechanical properties. The sheet resistance of the films after PEG modification is displayed in Figure 5. The conductivity is only weakly influenced by the reaction steps up to reaction conditions affecting the overall film stability (≥70% DMSO, cf. Figure 4). Interestingly, the AFM measurements in Figure 4 indicate incorporation of significant amounts of material in the

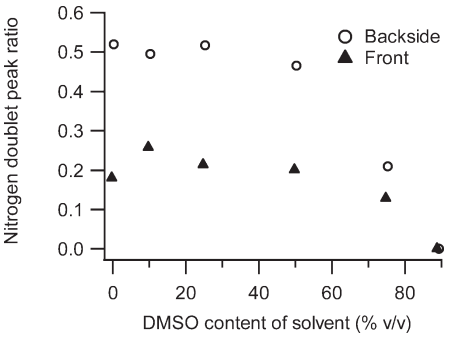


Figure 7. XPS analysis of the degree of reaction on PEDOT−N_3 films modified by pentynoic acid as a function of DMSO concentration. All reactions used 10 mM pentynoic acid, 2 mM $CuSO_4$, 40 mM sodium ascorbate, and a reaction time of 18 h. A nitrogen peak intensity ratio of 1/2 corresponds to zero degree of reaction, while full conversion of the azides yields a peak ratio of 0. Nitrogen peak analysis was performed both on the front side (solid triangles) and back side (open circles) of the film.

film using 40−50% DMSO in the reaction solution and yet only small increases in the sheet resistance are observed in Figure 5, in particular for the shorter reaction time of 4 h. These findings are in good agreement with earlier reports that large amounts of a second molecular (PEG) or polymeric (poly(methyl methacrylate)) material can be incorporated into PEDOT without compromising its conductivity.[48,49]

The XPS data (Figure 3) indicates that PEG−alkyne can be grafted at higher density in solvents with larger DMSO concentrations. Increased PEG coverage is expected to reduce the protein adhesiveness of the PEDOT−N_3 film surface[37] and thereby approach an ideal "non-fouling" surface. We tested this concept by means of adsorption of horseradish peroxidase conjugated to IgG (HRP-IgG) as test protein. The enzymatic HRP part allows for easy detection of the amount of adsorbed protein by following the formation of a colored product of the enzymatic process, similar to direct ELISA experiments. The results are displayed in Figure 6. Only a small reduction in protein adsorption was found for the PEDOT−N_3 film modified by PEG−alkyne in water, whereas increasing the DMSO content leads to decreasing protein adsorption. The minimum adsorption is found for film surfaces reacted in ≥50% DMSO. This is a very good agreement with the XPS analysis presented in Figure 3, which showed complete reaction of the azide groups within the XPS sampling depth for ≥50% DMSO in the reaction solution. An intermediate DMSO concentration of 40%-50% in the reaction solution may consequently be employed to form a dense PEG surface layer that strongly reduces protein adsorption without adversely affecting the conductive properties of the PEDOT−N_3 (cf. Figure 5).

The observed dependence on DMSO content might be particular to the PEG−alkyne, e.g. by influencing the solubility of the PEG-domain.[37] We tested the generality of our approach by reacting PEDOT−N_3 films with several other alkynated reagents. Figure 7 shows the results of reacting PEDOT−N_3 with pentynoic acid, a reagent being negatively charged and containing a short hydrophobic segment in contrast to the neutral hydrophilic domain of the PEG−alkyne. Reaction in solvent mixtures containing ≤50% DMSO results in intermediate reaction on the front side and no reaction on the back side of the film. Higher DMSO content leads to increasing degrees of reaction on the back side of the film, in full agreement with the results obtained for PEG−alkyne (cf. Figure 3). Three other alkynes spanning a range of molecular weights, propargyl alcohol (MW 42 Da), a Ni(II)-chelating nitrilotriacetic acid (NTA, MW 344 Da), and a PEG-modified undeca-peptide (MW 1727 Da), were reacted with

the PEDOT−N_3 using different DMSO concentrations, and evaluated using XPS analysis of the nitrogen doublet peak. These reagents all showed an increasing degree of reaction with increasing DMSO concentration (see Figures S6−S8, Supporting Information), confirming that the method is applicable to a wide range of reactants. The modification by the NTA and by the peptide was further independently probed by quantitative XPS analysis of heteroatoms specific to the two reagents (nickel and iodine, respectively; see Figures S7 and S8, Supporting Information). Reaction trends observed by the two analysis approaches were in agreement for both reagents tested.

An important final consideration is that DMSO could have a general accelerating effect on the click-reaction, independent of the type of alkyne. DMSO is often employed as solvent or cosolvent for click reactions, it is a good solvent for the catalytic Cu(I) ion,[24,50] and it has served to accelerate a number of reactions.[51] However, even when increasing the reaction time to 80 h for the smallest of the reactants (propargyl alcohol) we did not see any noticeable change in the degree of reaction for low DMSO concentrations, compared to a much shorter reaction time of 16 h (see Figure S6, Supporting Information). Thus, we maintain that film swelling is of key importance for the increased reaction depth observed upon adding DMSO, although changes in the reaction kinetics may play a secondary role.

We speculated earlier that the introduction of the azide functionality might be important to the observed swelling behavior of PEDOT−N_3 and the associated high accessibility of the azides for click reactions with alkynes. If so, other polymers containing azide groups should exhibit a similar behavior. As a simple test case, we performed preliminary tests of a click-reaction between an azide-modified polystyrene (PS−N_3, see Figure S9, Supporting Information) and PEG−alkyne at varying DMSO content in the reaction solution (see Figure S10, Supporting Information). The results show a strong dependence on the DMSO content with complete conversion of azides at the surface occurring for ≥40% DMSO and a 2-fold increase in the surface density of PEG chains over the reaction performed in pure water. Thus, our approach may be useful for achieving high grafting densities on a wider range of azide-modified polymers than only PEDOT−N_3.

Conclusion

We have observed a distinctive swelling behavior for the recently developed conducting polymer PEDOT−N_3. In water, the polymer film swelled only a few percent, whereas in DMSO the thickness increased to >250% of its thickness in water. PEDOT containing tosylate as counterions displayed a similar but less pronounced effect, while PEDOT with polymeric PSS counterions swelled to more than seven times its original thickness. We further showed how this swelling behavior could be exploited for directing a postpolymerization functionalization of PEDOT−N_3 thin films. In pure water and in water with low DMSO content, reaction only took place on the surface. Increasing DMSO content resulted in gradually larger swelling that lead to higher degree of bulk reaction. Such controlled reaction depth was demonstrated for a number of alkynated reactants. The modification with PEG−alkyne served to illustrate how such control of the degree of reaction via the swelling of the film can be employed to fabricate a conducting polymer film surface with minimal protein adhesiveness without adversely affecting the film conductivity.

Acknowledgment. The Danish Council for Technology and Innovation is acknowledged for financial support through the Innovation Consortium CEMIK, Grant 07-015463.

Supporting Information Available: XPS data for the reaction of additional alkynes on PEDOT−N_3 and PS−N_3 as well as details on the syntheses of the alkynated reactants, structures, optical data, AFM micrographs, and additional conductivity measurements. This material is available free of charge via the Internet at http://pubs.acs.org.

References and Notes

(1) Krebs, F. C.; Gevorgyan, S. A.; Alstrup, J. *J. Mater. Chem.* **2009**, *30*, 5442–5451.
(2) Sakurai, S.; Jiang, H.; Takahashi, M.; Kobayashi, K. *Electrochim. Acta* **2009**, *23*, 5463–5469.
(3) Armstrong, N. R.; Wang, W.; Alloway, D. M.; Placencia, D.; Ratcliff, E.; Brumbach, M. *Macromol. Rapid Commun.* **2009**, *9−10*, 717–731.
(4) Kirchmeyer, S.; Reuter, K. *J. Mater. Chem.* **2005**, *21*, 2077–2088.
(5) Park, J.; Kim, H. K.; Son, Y. *Sensor. Actuat. B—Chem.* **2008**, *1*, 244–250.
(6) Winther-Jensen, B.; Fraser, K.; Ong, C.; Forsyth, M.; MacFarlane, D. R. *Adv. Mater.* **2010**, *15*, 1727–1730.
(7) Winther-Jensen, B.; Winther-Jensen, O.; Forsyth, M.; MacFarlane, D. R. *Science* **2008**, *5889*, 671.
(8) Vidal, F.; Plesse, C.; Palaprat, G.; Kheddar, A.; Citerin, J.; Teyssié, D.; Chevrot, C. *Synth. Met.* **2006**, *21−24*, 1299–1304.
(9) Okuzaki, H.; Suzuki, H.; Ito, T. *Synth. Met.* **2009**, *21−22*, 2233–2236.
(10) Segura, J. L.; Gómez, R.; Blanco, R.; Reinold, E.; Bäuerle, P. *Chem. Mater.* **2006**, *12*, 2834–2847.
(11) Xie, H.; Luo, S. C.; Yu, H. *Small* **2009**, *22*, 2611–2617.
(12) Döbbelin, M.; Pozo-Gonzalo, C.; Marcilla, R.; Blanco, R.; Segura, J. L.; Pomposo, J. A.; Mecerreyes, D. *J. Polym. Sci., Part A: Polym. Chem.* **2009**, *12*, 3010–3021.
(13) Darmanin, T.; Nicolas, M.; Guittard, F. *Langmuir* **2008**, *17*, 9739–9746.
(14) Cutler, C. A.; Bouguettaya, M.; Kang, T. S.; Reynolds, J. R. *Macromolecules* **2005**, *8*, 3068–3074.
(15) Bazaco, R. B.; Gómez, R.; Seoane, C.; Bäuerle, P.; Segura, J. L. *Tetrahedron Lett.* **2009**, *28*, 4154–4157.
(16) Balog, M.; Rayah, H.; Derf, F. L.; Sallé, M. *New J. Chem.* **2008**, *7*, 1183–1188.
(17) Arias-Pardilla, J.; Otero, T. F.; Blanco, R.; Segura, J. L. *Electrochim. Acta* **2010**, *55*, 1535−1542.
(18) Xiao, Y.; Martin, D. C.; Cui, X.; Shenai, M. *Appl. Biochem. Biotechnol.* **2006**, *2*, 117–129.
(19) Menaker, A.; Syritski, V.; Reut, J.; Öpik, A.; Horváth, V.; Gyurcsányi, R. E. *Adv. Mater.* **2009**, *22*, 2271–2275.
(20) Jakobsson, F. L. E.; Crispin, X.; Lindell, L.; Kanciurzewska, A.; Fahlman, M.; Salaneck, W. R.; Berggren, M. *Chem. Phys. Lett.* **2006**, *1−3*, 110–114.
(21) Xiao, Y.; Li, C. M.; Wang, S.; Shi, J.; Ooi, C. P. *J. Biomed. Mater. Res. A.* **2010**, *2*, 766–772.
(22) Dai, T.; Qing, X.; Zhou, H.; Shen, C.; Wang, J.; Lu, Y. *Synth. Met.* **2010**, *160*, 791−796.
(23) Weng, C. H.; Yeh, W. M.; Ho, K. C.; Lee, G. B. *Sensor. Actuat. B—Chem.* **2007**, *2*, 576–582.
(24) Binder, W. H.; Sachsenhofer, R. *Macromol. Rapid Commun.* **2008**, *12−13*, 952–981.
(25) Fleischmann, S.; Hinrichs, K.; Oertel, U.; Reichelt, S.; Eichhorn, K. J.; Voit, B. *Macromol. Rapid Commun.* **2008**, *12−13*, 1177–1185.
(26) Chen, R. T.; Muir, B. W.; Such, G. K.; Postma, A.; Evans, R. A.; Pereira, S. M.; McLean, K. M.; Caruso, F. *Langmuir* **2010**, *5*, 3388–3393.
(27) Gauthier, M. A.; Gibson, M. I.; Klok, H. A. *Angew. Chem., Int. Ed.* **2009**, *1*, 48–58.
(28) Im, S. G.; Kim, B. S.; Tenhaeff, W. E.; Hammond, P. T.; Gleason, K. K. *Thin Solid Films* **2009**, *12*, 3606–3611.
(29) Sinha, J.; Sahoo, R.; Kumar, A. *Macromolecules* **2009**, *6*, 2015–2022.
(30) Daugaard, A. E.; Hvilsted, S.; Hansen, T. S.; Larsen, N. B. *Macromolecules* **2008**, *12*, 4321–4327.
(31) Bu, H. B.; Götz, G.; Reinold, E.; Vogt, A.; Schmid, S.; Blanco, R.; Segura, J. L.; Bäuerle, P. *Chem. Commun.* **2008**, *11*, 1320–1322.
(32) Xu, J.; Tian, Y.; Peng, R.; Xian, Y.; Ran, Q.; Jin, L. *Electrochem. Commun.* **2009**, *10*, 1972–1975.
(33) Hansen, T. S.; Daugaard, A. E.; Hvilsted, S.; Larsen, N. B. *Adv. Mater.* **2009**, *44*, 4483–4486.
(34) Hansen, T. S.; Lind, J. U.; Daugaard, A. E.; Hvilsted, S.; Andresen, T. L.; Larsen, N. B. *Langmuir* **2010**, *26*, 16171−16177.

(35) Goddard, J. M.; Hotchkiss, J. H. *Prog. Polym. Sci.* **2007**, *7*, 698–725.
(36) Heyes, C. D.; Groll, J.; Moller, M.; Nienhaus, G. U. *Mol. Biosyst* **2007**, *6*, 419–430.
(37) Kingshott, P.; Thissen, H.; Griesser, H. J. *Biomaterials* **2002**, *9*, 2043–2056.
(38) Winther-Jensen, B.; Breiby, D. W.; West, K. *Synth. Met.* **2005**, *1−3*, 1–4.
(39) Huang, J.; Miller, P. F.; De Mello, J. C.; De Mello, A. J.; Bradley, D. D. C. *Synth. Met.* **2003**, *3*, 569–572.
(40) Dimitriev, O. P.; Grinko, D. A.; Noskov, Y. V.; Ogurtsov, N. A.; Pud, A. A. *Synth. Met.* **2009**, *21−22*, 2237–2239.
(41) Ouyang, J.; Xu, Q.; Chu, C. W.; Yang, Y.; Li, G.; Shinar, J. *Polymer* **2004**, *25*, 8443–8450.
(42) Jönsson, S. K. M.; Birgerson, J.; Crispin, X.; Greczynski, G.; Osikowicz, W.; Denier van der Gon, A. W.; Salaneck, W. R.; Fahlman, M. *Synth. Met.* **2003**, *1*, 1–10.
(43) Kim, J. Y.; Jung, J. H.; Lee, D. E.; Joo, J. *Synth. Met.* **2002**, *2−3*, 311–316.
(44) Crispin, X.; Marciniak, S.; Osikowicz, W.; Zotti, G.; van der Gon, A. W. D.; Louwet, F.; Fahlman, M.; Groenendaal, L.; De Schryver, F.; Salaneck, W. R. *J. Polym. Sci., Polym. Phys.* **2003**, *21*, 2561–2583.
(45) Zotti, G.; Zecchin, S.; Schiavon, G.; Louwet, F.; Groenendaal, L.; Crispin, X.; Osikowicz, W.; Salaneck, W.; Fahlman, M. *Macromolecules* **2003**, *9*, 3337–3344.
(46) Sando, G. M.; Dahl, K.; Owrutsky, J. C. *J. Phys. Chem. B* **2007**, *18*, 4901–4909.
(47) Briggs, D. *Surface Analysis of Polymers by XPS and Static SIMS*; Cambridge University Press: Cambridge, U.K., 1998; .
(48) Winther-Jensen, B.; Chen, J.; West, K.; Wallace, G. *Polymer* **2005**, *13*, 4664–4669.
(49) Hansen, T. S.; West, K.; Hassager, O.; Larsen, N. B. *Synth. Met.* **2006**, *18−20*, 1203–1207.
(50) Meldal, M.; Tornoe, C. W. *Chem. Rev.* **2008**, *8*, 2952–3015.
(51) Habib, P. M.; Rama Raju, B.; Kavala, V.; Kuo, C. W.; Yao, C. F. *Tetrahedron* **2009**, *29−30*, 5799–5804.

DOI: 10.1021/ma102173a

Macromolecules
ARTICLE

Synthesis and Photovoltaic Performance of Low-Bandgap Polymers on the Basis of 9,9-Dialkyl-3,6-dialkyloxysilafluorene

Jae-Kyu Jin,[†] Jong-Kil Choi,[†] Bum-Joon Kim,[†] Hyun-Bum Kang,[†] Sung-Cheol Yoon,[‡] Hong You,[§] and Hee-Tae Jung*,[†]

[†]*Department of Chemical & Biomolecular Engineering, KAIST, 373-1 Guseong-dong, Yuseong-gu, Daejeon 305-701, Korea,* [‡]*Advanced Materials Division, KRICT, Sinseongno 19, Yuseong-gu, Daejeon 305-600, Korea, and* [§]*R&D Center, SK Energy, 140-1 Wonchon-dong, Yuseong-gu, Daejeon 305-712, Korea*

Received September 24, 2010; Revised Manuscript Received November 25, 2010

ABSTRACT: A new series of polysilafluorene-type low-bandgap polymers containing 3,6-dialkyloxy-9,9-dialkylsilafluorene and 4,7-di-2-thienyl-2,1,3-benzothiadiazole units has been synthesized. UV/vis absorption spectroscopy and grazing incident X-ray diffraction results showed that the alkoxy moiety on the silafluorene unit broadens the absorption band of the polymers because of its electron-donating property, enabling more efficient harvesting of photons from the solar spectrum. Furthermore, the silicon atoms of the polymers lead to a highly ordered structure, which is essential for high charge-carrier mobility. In addition, high molecular weight polymers can be prepared by using long octyloxy/hexyl solubilizing groups. The blend of new poly[2,7-(3,6-dioctyloxy-9,9-dihexylsilafluorene)-*alt*-5,5-(4′,7′-di-2-thienyl-2′,1′,3′-benzothiadiazole)] (**P4H**) and [6,6]-phenyl-C_{71}-butyric acid methyl ester ($PC_{71}BM$) exhibited a power-conversion efficiency of 4.05% with an open-circuit voltage of 0.67 V, a short-circuit current density of 11.1 mA cm^{-2}, and a fill factor of 54.3% under simulated 100 mW cm^{-2} air mass 1.5 global (AM1.5G) illumination.

Introduction

The organic photovoltaic (OPV) cell has emerged as a promising candidate renewable energy source because of its low processing cost, lightweight and portability.[1,2] The best known OPV devices consist of a mixture of conjugated polymers (donor) and fullerene derivatives (acceptor) between two electrodes as a single bulk-heterojunction (BHJ) active layer. On absorption of a photon, an electron in the highest occupied molecular orbital (HOMO) is excited to the lowest unoccupied molecular orbital (LUMO). This bound exciton migrates to an electron donor/electron acceptor interface and then dissociates into an electron−hole pair. After dissociation, each charge carrier moves to the anode and cathode to produce electricity. Thus, the conjugated polymers acting as the donor must have a low bandgap energy if they are to absorb a large portion of photons from the solar spectrum. Furthermore, the hole mobilities of the conjugated polymers must be high enough to extract holes to the anode from the interface of donor and acceptor before the hole and electron undergo recombination. In addition, a morphologically interpenetrating network with the electron acceptor is preferred to generate efficient exciton dissociation.[3−5]

Several low-bandgap polymers as BHJ donors have been developed to enhance the light-absorbing ability, charge-carrier mobility and charge dissociation. Although the blend system of poly(3-hexylthiophene) (P3HT) and [6,6]-phenyl-C_{61}-butyric acid methyl ester ($PC_{61}BM$) has dominated for the past several years,[3,4] there have been strong demands for the development of alternative donor materials to achieve high-performance BHJ devices. These include poly[2,7-(9,9-dioctyl-fluorene)-*alt*-5,5-(4′,7′-di-2-thienyl-2′,1′,3′-benzothiodiazole)] (PFODBT),[6−9] poly[*N*-9-heptadecanyl-2,7-carbazole-*alt*-5,5-(4′,7′-di-2-thienyl-2′,1′,3′-benzothiadiazole)] (PCDTBT),[10] poly[2,6-(4,4-bis(2-ethylhexyl)-4*H*-cyclopenta[2,1-*b*;3,4-*b*2]-dithiophene)-*alt*-4,7-(2,1,3-benzothiadiazole)] (PCPDTTBT),[11] poly[9,9-dioctyl-2,7-dibenzosilole-*alt*-5,5-(4′,7′-di-2-thienyl-2′,1′,3′-benzothiadiazole)] (PSiFDBT),[12,13] and poly[4,4′-bis(2-ethylhexyl)dithieno[3,2-*b*:2′,3′-d]silole]-2,6-diyl-*alt*-4,7-bis(2-thienyl)-2,1,3-benzothiadiazole)-5,5′-diyl] (PSBTBT).[14−18]

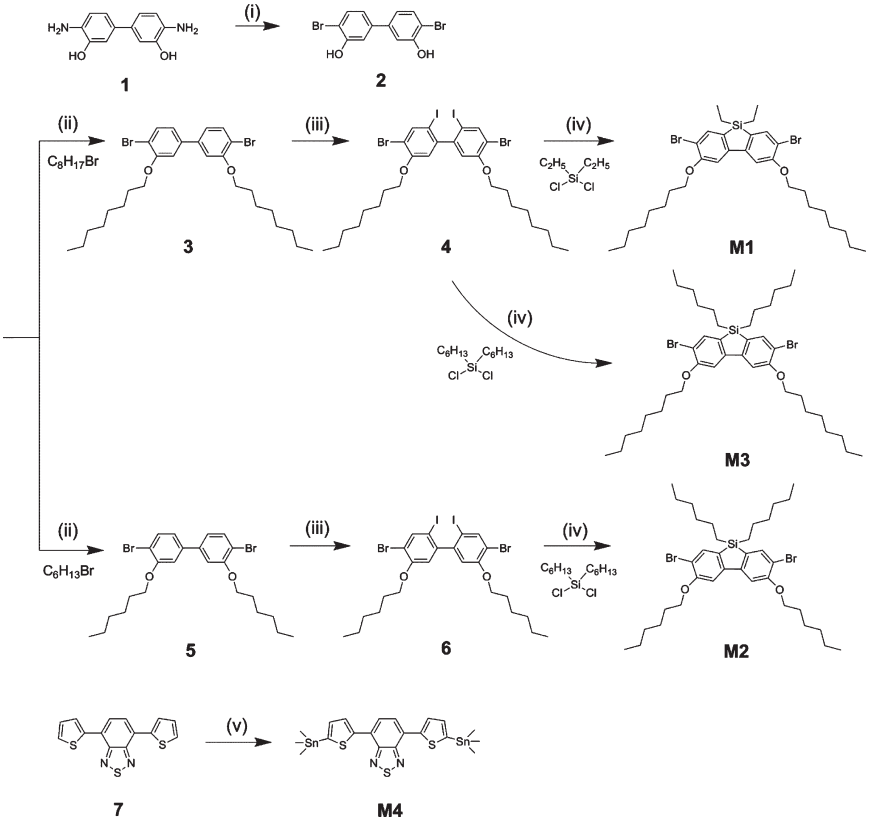
Among the conjugated polymers, silicon-containing conjugated polymers such as PSBTBT have attracted considerable attention in recent years because of their high charge-carrier mobilities. For example, it has been demonstrated that the substitution of a carbon atom at the 5-position of the conjugate PCPDTBT by a silicon atom greatly improved cell efficiency, which may be attributed to the unique electronic properties of the silicon atom, such as a low-lying σ^* orbital.[14,16,17] In addition, changes in the molecular architectures induce highly ordered structures because of the strong tendency of silicon-containing molecules to stack on each other, generating high charge-carrier mobility. To date, however, these silicon-containing polymers have suffered from poor solubility because of the strong intermolecular stacking, causing difficulties in obtaining high molecular weights (M_n > 25 kDa) and in preparing uniform thin films.[14] Indeed, it is well-known that a high molecular weight conjugated polymer is desirable for high power-conversion efficiency (PCE) because the absorption band and charge-carrier mobility are known to be strongly dependent on the molecular weight.[19−21] Also, a much broader absorption band of the silicon-containing conjugated polymers is required to collect more photons from the incoming solar light.[7,12,13]

In the present work, we synthesized a new series of silafluorene-based polymer donors having ethyl/octyloxy, hexyl/hexyloxy, and hexyl/octyloxy solubilizing groups. We show that the alkoxy groups on the silafluorene unit not only broaden the spectral absorption ranges but also significantly improve solubility. It was found that the length of the solubilizing alkoxy groups strongly affects the photovoltaic performance: A polymer donor (**P4H**) having hexyl/octyloxy groups exhibits good solubility, which enables preparation of a high molecular weight polymer

*Corresponding author. E-mail: heetae@kaist.ac.kr.

 Published on Web 01/06/2011 © 2011 American Chemical Society

Scheme 1. Molecular Structures and Synthetic Routes of the Monomers[a]



[a] Key: (i) HBr, acetonitrile, $NaNO_2$, reflux; (ii) NaOH, EtOH, reflux; (iii) I_2, KIO_3, H_2SO_4, acetic acid, 90 °C; (iv) 1.6 M *n*-BuLi, THF, −100 °C; (v) TMP, 1.6 M *n*-BuLi, $SnMe_3Cl$, THF, −78 °C.

(M_n, 63.9 kDa; M_w, 160 kDa), resulting in high photovoltaic performance. On the other hand, a polymer with short ethyl/octyloxy groups (**P2**) has relatively poor solubility with low molecular weight (M_n, 13.6 kDa; M_w, 17.9 kDa), leading to poor photovoltaic performance. As a result, a high PCE of 4.05% with open-circuit voltage (V_{oc}) = 0.67 V, short-circuit current density (J_{sc}) = 11.1 mA cm^{-2}, and fill factor (FF) = 54.3% under 100 mW cm^{-2} AM1.5G was achieved using the **P4H**:$PC_{71}BM$ system, which results from efficient light harvesting, high charge-carrier mobility and efficient charge dissociation because of the desirable phase separation between **P4H** and $PC_{71}BM$.

Results and Discussion

Synthesis. The chemical structures and synthetic routes of the monomers are depicted in Scheme 1. A series of silafluorene monomers (**M1**, **M2**, and **M3**) having ethyl/octyloxy, hexyl/hexyloxy, and hexyl/octyloxy groups was prepared using the Sandmeyer reaction, alkylation of the hydroxy substituents, iodination, selective lithiation of the 2,2′-iodo substituents and subsequent cyclization with a dialkyldihalosilane.[22] 4,4′-Dibromobiphenyl-3,3′-diol (**2**) was prepared from 4,4′-diaminobiphenyl-3,3′-diol (**1**) with a high yield of 87%. Then the hydroxyl groups of 4,4′-dibromobiphenyl-3,3′-diol (**2**) were alkylated with 1-bromohexane or 1-bromooctane in the presence of sodium hydroxide to afford 4,4′-dibromo-3,3′-bis(hexyloxy)biphenyl (**5**) or 4,4′-dibromo-3,3′-bis(octyloxy)-biphenyl (**3**), respectively. The iodination of 4,4′-dibromo-3,3′-bis(octyloxy)biphenyl (**3**) and 4,4′-dibromo-3,3′-bis(hexyloxy)-biphenyl (**5**) using I_2/KIO_3 gave 4,4′-dibromo-2,2′-diiodo-5,5′-bis(octyloxy)biphenyl (**4**), and 4,4′-dibromo-5,5′-bis-(hexyloxy)-2,2′-diiodobiphenyl (**6**), respectively. Then, the iodo groups on 4,4′-dibromo-2,2′-diiodo-5,5′-bis(octyloxy)biphenyl (**4**) were selectively lithiated by adding *n*-butyllithium dropwise at a reaction temperature of −100 °C and subsequently reacted with dichlorodiethylsilane and dichlorodihexylsilane to afford 2,7-dibromo-9,9-diethyl-3,6-bis(octyloxy)-9silafluorene (**M1**) and 2,7-dibromo-9,9-dihexyl-3,6-bis(octyloxy)-9-silafluorene (**M3**), respectively. 2,7-Dibromo-9,9-dihexyl-3,6-bis(hexyloxy)-9-silafluorene (**M2**) was prepared under the same reaction conditions using 4,4′-dibromo-5,5′-bis-(hexyloxy)-2,2′-diiodobiphenyl (**6**) and dichlorodihexylsilane. 4,7-Di(2′-trimethylstannylthiophen-5′-yl)-2,1,3-benzothiadiazole (**M4**) was prepared by reaction with 4,7-bis(thien-2-yl)-2,1,3-benzothiadiazole (**10**) and $SnMe_3Cl$.[23] The chemical structures of the compounds were identified by ^1H NMR, ^{13}C NMR, FD−TOF-MS and elemental analysis (see the Experimental Section).

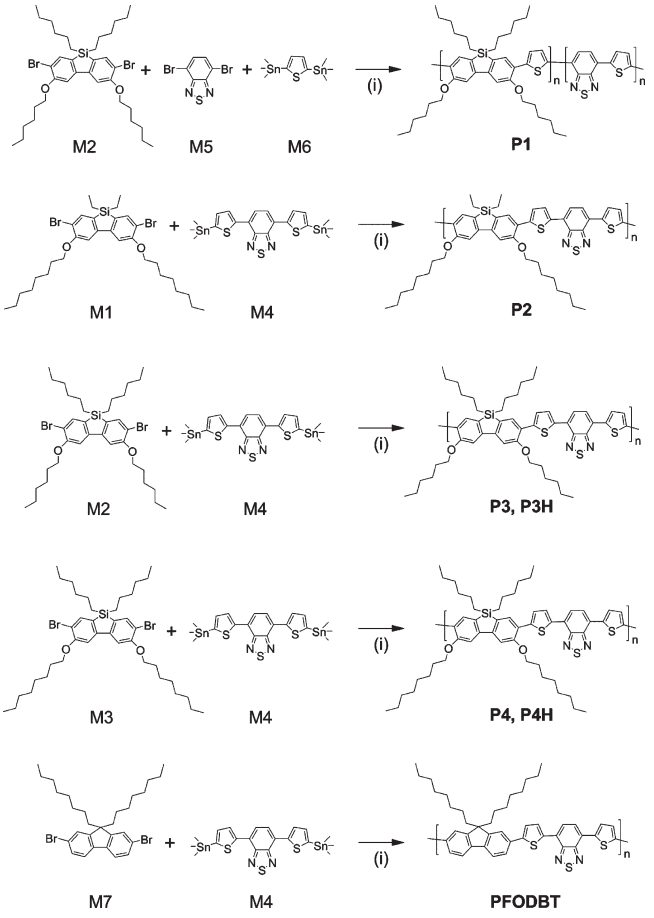
The Stille coupling reaction was used to prepare the polymers (Scheme 2). The Stille polymerization was carried out in toluene at 100 °C for 24 h using $Pd_2(dba)_3$ and P(*o*-tolyl)$_3$ as catalysts. As the polymerization proceeded, the color of the reaction solution changed from orange to dark brown and the viscosity gradually increased. The polymer was obtained by precipitation of the reaction solution in methanol, treatment with an aqueous solution of sodium diethyldithiocarbamate trihydrate and Soxhlet extraction with methanol, acetone and hexane. With the combinations of monomers of **M2/M5/M6** (**P1**), **M1/M4** (**P2**), **M2/M4** (**P3**), and **M3/M4** (**P4**), polymers having different solubilizing groups and molecular weights were prepared. **P1** and **P3** have hexyl groups as substituents at the silicon atom and hexyloxy groups on the silafluorene moiety. **P1** has the same building blocks as those of **P3**; however, in contrast to **P3**, it has an irregular backbone structure because **M5** and **M6** were used instead of **M4** (Scheme 2). **P2** has substituents of ethyl/octyloxy groups while **P4** has hexyl/octyloxy side groups.

Table 1. Molecular Weight and Optical and Electrochemical Properties of Polymers[a]

polymer	M_n (Da)	M_w (Da)	PDI	λ_{max} (nm)	E_g^{opt} (eV)	LUMO (eV)	HOMO (eV)	E_g^{ec} (eV)
P1	76 600	127 800	1.67	462, 601	1.69	−3.63	−5.48	1.85
P2	13 600	17 900	1.32	413, 576	1.82	−3.54	−5.29	1.75
P3	30 700	67 200	2.19	433, 642	1.75			
P3H	102 300	228 900	2.24	430, 649	1.75	−3.56	−5.26	1.70
P4	19 000	33 900	1.78	426, 638	1.75			
P4H	63 900	160 300	2.51	428, 644	1.75	−3.57	−5.28	1.71
PFODBT	31 200	93 900	3.01	394, 567	1.91	−3.59	−5.61	2.02

[a] E_g^{opt} was determined from the onset of the absorption edge and E_g^{ec} was determined by cyclic voltammetry measurements.

Scheme 2. Chemical Structures of the Polymers[a]



[a] Key: (i) $Pd_2(dba)_3$, P(*o*-tolyl)$_3$, toluene, 100 °C.

In addition, the well-known D−A-type polymer PFODBT was prepared to use as a reference. The molecular weights and polydispersity indexes (PDI) of the polymers are summarized in Table 1. **P2**, having ethyl/octyloxy solubilizing groups, showed a lack of solubility; thus, the molecular weight was reduced by adjusting the mole ratio of **M1**/**M4** to 1:0.95 and the resulting molecular weight (M_n) of the hot chlorobenzene-soluble part of polymer was 7.42 kDa with PDI of 1.30. On the other hand, **P1**, **P3** and **P4** have much higher solubilities because of the longer solubilizing groups than those of **P2** and the chlorobenzene-soluble part showed much higher molecular weights (M_n) of 76.6, 30.7, and 19.0 kDa, respectively. Furthermore, the molecular weight of **P3** and **P4** could be further increased by adjusting the reaction conditions (1.5 times larger amount of catalyst was used). The high molecular weight polymers **P3H** and **P4H** showed M_n values of 102.3 and 63.9 kDa, respectively (**P3H** and **P4H** have the same molecular structure as **P3** and **P4**, respectively).

UV/Vis Absorption Spectra. Figure 1 shows the normalized UV/vis absorption spectra of **P1**, **P2**, **P3**, **P3H**, **P4**, **P4H**, and PFODBT films. The films were spin-coated from *o*-DCB solutions and annealed at 140 °C (5 min) under N_2 atmosphere.

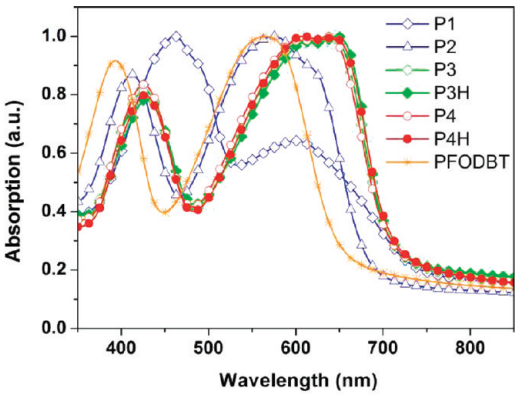


Figure 1. Normalized absorption spectra of **P1**, **P2**, **P3**, **P3H**, **P4**, **P4H**, and PFODBT films. The films were spin-coated from *o*-DCB solutions and annealed at 140 °C (5 min) under N_2 atmosphere.

The optical bandgaps of the polymers were calculated from the onset of absorption and are listed in Table 1. All of the polymer films except **P1** show absorption spectra typical of D−A alternating polymers; specifically, the spectra contain two distinct absorption peaks, one at short wavelength (λ_{max} ~384−433 nm) and another at long wavelength (λ_{max} ~567−649 nm). The absorption peak in the short wavelength can be identified with a delocalized excitonic $\pi-\pi^*$ transition and the long wavelength absorption band can be attributed to a localized transition between donor−acceptor charge transfer states.[24,25] However, **P1** shows a weak absorption peak at 601 nm and a strong absorption peak at 462 nm, which correspond to the randomly distributed DBT and silafluorene segments on the polymer backbone, respectively (Figure 1). The optical bandgap of PFODBT, used as a reference material, was ~1.90 eV, which is consistent with the reported value.[8] However, the λ_{max} of our PFODBT was slightly red-shifted with respect to the literature value, from 555 nm to ~567 nm, perhaps because of the high molecular weight of the PFODBT used in this study (M_n: 31.2 kDa) as compared with that in the previous report (M_n: 8.0 kDa).[8] **P2**, **P3**, **P3H**, **P4**, and **P4H** are significantly red-shifted compared with PFODBT (Figure 1b): **P2** (λ_{max} ~ 576 nm), **P3** (λ_{max} ~ 642 nm), **P3H** (λ_{max} ~ 649 nm), **P4** (λ_{max} ~ 638 nm), and **P4H** (λ_{max} ~ 644 nm). Therefore, the present findings clearly indicate that the electron-donating property of the alkoxy groups significantly reduces the bandgap energy of the polymers. Moreover, the steric hindrance effect of the alkoxy groups is not so strong as to greatly alter the planarity along the polymer backbone, considering that both PSiFDBT and PFODBT have λ_{max} values ranging from 560 to 565 nm.[12,13] Furthermore, the absorption peaks of **P3**, **P3H**, **P4**, and **P4H** are much broader than that of **P2**, suggesting stronger intermolecular interactions in **P3**, **P3H**, **P4**, and **P4H**.[17] In other words, such broad absorption spectrum of **P3**, **P3H**, **P4**, and **P4H** might be attributed to a favorable molecular conformation for chain packing or aggregation,

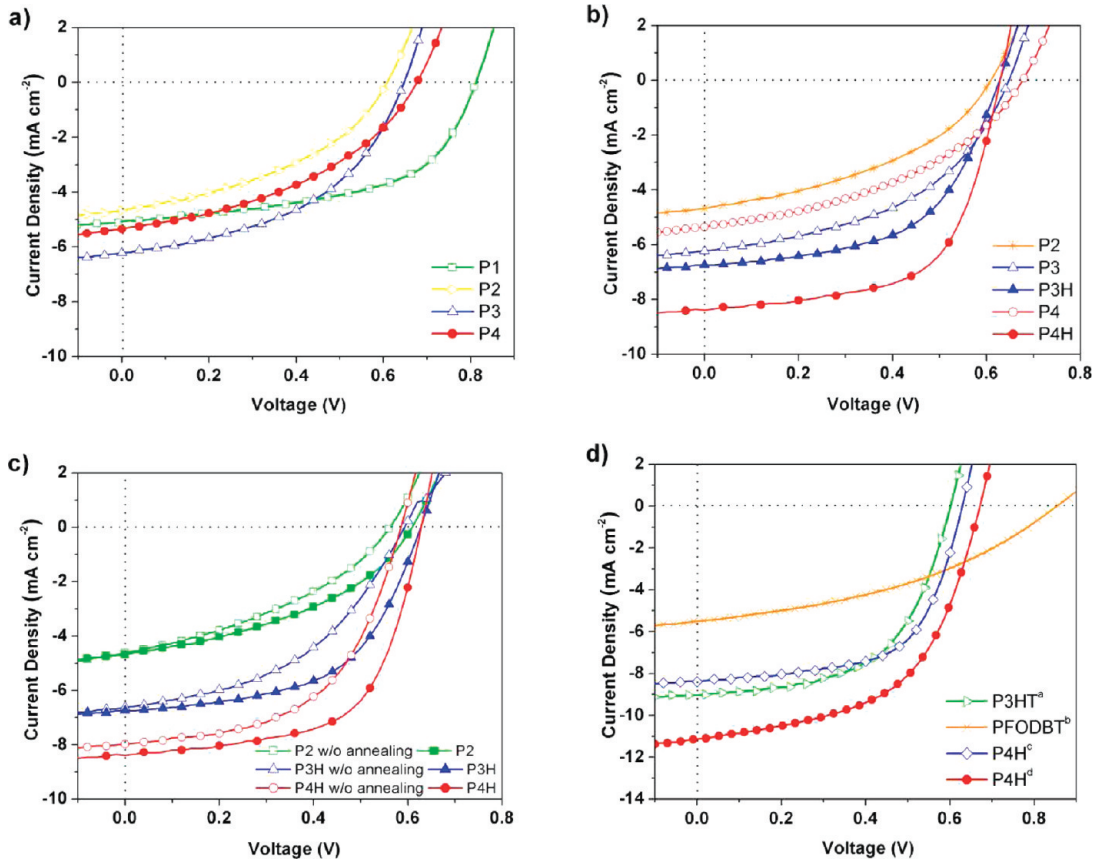


Figure 2. $J-V$ characteristics of photovoltaic devices under AM1.5G solar simulated light with an intensity of 100 mW cm^{-2}. The device structure is ITO/PEDOT:PSS/polymer:PCBM/Al. Key: (a) photovoltaic device performances of **P1**, **P2**, **P3**, and **P4**; (b) molecular weight effect on device performance of **P2** (M_n: 13.6 kDa), **P3** (M_n: 30.7 kDa), **P3H** (M_n: 102.3 kDa), **P4** (M_n: 19.0 kDa), **P4H** (M_n: 63.9 kDa); (c) effect of annealing on the $J-V$ characteristics of **P2**, **P3H**, and **P4H** devices; (d) comparison of the photovoltaic performances [[a] P3HT:$PC_{61}BM$ = 1:0.8 w/w; [b] PFODBT:$PC_{61}BM$ = 1:4 w/w; [c] **P4H**:$PC_{61}BM$ = 1:3 w/w; [d] **P4H**:$PC_{71}BM$ = 1:2.5 w/w].

Table 2. Performance of the photovoltaic devices

polymer	polymer/PCBM ratio (w/w)	J_{sc} (mA cm^{-2})	V_{oc} (V)	FF (%)	PCE (%)
P1	1:3 ($PC_{61}BM$)	5.04	0.81	55.2	2.26
P2	1:3 ($PC_{61}BM$)	4.68	0.61	41.2	1.17
P3	1:3 ($PC_{61}BM$)	6.23	0.65	46.8	1.89
P3H	1:3 ($PC_{61}BM$)	6.75	0.63	55.2	2.34
P4	1:3 ($PC_{61}BM$)	5.35	0.68	41.7	1.51
P4H	1:3 ($PC_{61}BM$)	8.39	0.63	61.0	3.22
P4H	1:3 ($PC_{71}BM$)	10.7	0.62	49.0	3.24
P4H	1:2.5 ($PC_{71}BM$)	11.1	0.67	54.3	4.05
P3HT[a]	1:0.8 ($PC_{61}BM$)	9.04	0.60	56.2	3.06
PFODBT	1:4 ($PC_{61}BM$)	5.49	0.85	39.6	1.86

[a] P3HT (grade: 4002-EE) was obtained from Rieke Metals, Inc.

compared to **P2**. In fact, **P2** may have a large torsion angle along the polymer chain because of the significantly unsymmetrical length of alkyl and alkoxy side chain or some other factors in molecular structure.[26] In addition, we cannot rule out any possibilities that the greater degree of conjugation as a result of their higher molecular weights of **P3**, **P3H**, **P4**, and **P4H**, affects the red-shifted absorption band.[6,8,12,13] Therefore, the light absorbing abilities of the hexyl/hexyloxy and hexyl/octyloxy side groups are much more desirable than those of the ethyl/octyloxy side groups.

Electrochemical Properties. To investigate the positions of the HOMO and LUMO levels of the polysilafluorene-type low-bandgap polymers, cyclic voltammetry (CV) measurements were carried out. CV results (Table 1) showed that the LUMO levels of **P1**, **P2**, **P3H**, **P4H**, and PFODBT are in the range −3.54 to −3.63 eV because they have the same electron-accepting segment (DBT). In contrast, the HOMO levels of **P1**, **P2**, **P3H**, and **P4H** are significantly increased compared with that of PFODBT (−5.61 eV) as a result of the alkoxy groups. The HOMO levels of **P2**, **P3H**, and **P4H** are −5.29, −5.26, and −5.28 eV, respectively, while **P1** shows a lower HOMO level of −5.48 eV, possibly due to the irregular backbone structure. As a result of the increased HOMO level, the bandgap energies become much smaller than that of PFODBT (2.02 eV), with values ranging from 1.69 to 1.82 eV. The V_{oc} values of devices fabricated from **P1**, **P2**, **P3H**, **P4H**, and PFODBT were estimated by using a semiempirical equation relating V_{oc} and the HOMO level of the donor.[27] The V_{oc} values of **P1** and PFODBT were calculated to be 0.88 and 1.01 V, respectively. **P2**, **P3H**, and **P4H** were estimated to have V_{oc} values of 0.69, 0.66, and 0.68 V, respectively, which are similar because of the similar HOMO levels of these polymers. These calculated V_{oc} results agree well with our findings on the performances of the photovoltaic devices (Figure 2).

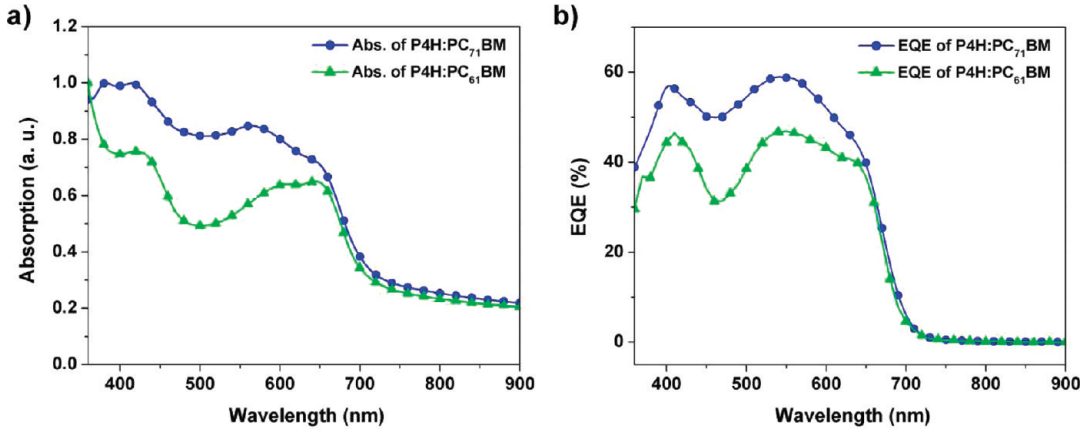


Figure 3. Absorption spectra and external quantum efficiency (EQE) and absorption spectrum of **P4H**:$PC_{71}BM$ and **P4H**:$PC_{61}BM$ (1:3 w/w).

Photovoltaic Properties. To investigate the photovoltaic characteristics of the polymers, photovoltaic devices with a structure of ITO/PEDOT:PSS (35 nm)/polymer:PCBM (100−130 nm)/Al (150 nm) were fabricated. The current density−voltage ($J-V$) curves of the devices measured under simulated illumination by AM1.5G (100 mW cm^{-2}) are shown in Figure 2, and their photovoltaic performances are summarized in Table 2. **P1**, **P2**, **P3**, and **P4** exhibit PCEs of 2.26%, 0.97%, 1.78%, and 1.51%, respectively. We found that the molecular weight of the polymers strongly affects the photovoltaic performance. Regardless of the length of the solubilizing alkoxy groups, the PCEs of **P2** (M_n: 13.6 kDa), **P3** (M_n: 30.7 kDa), and **P4** (M_n: 19.0 kDa) are strongly influenced by the polymer molecular weight. In addition, it is noteworthy that **P1** (M_n: 76.6 kDa) having irregular polymer backbone structure shows the highest PCE of 2.26% exhibiting J_{sc} comparable to those of the other polymers, which is due to the high V_{oc} of **P1**. This result clearly shows that the PCEs of D−A-type polymers are strongly affected by the molecular weight of the polymer donors, similar to previous results for P3HT/PCBM systems.[3,19,28]

To further confirm the molecular weight dependence, the photovoltaic performances of low molecular weight polymers (**P3** and **P4**) and high molecular weight polymers (**P3H** and **P4H**) were compared (Figure 2b). **P3H** (M_n: 102.3 kDa) and **P4H** (M_n: 63.9 kDa) have the same molecular structure as **P3** and **P4**, respectively, but have different molecular weights. Interestingly, **P4H** exhibits a much higher PCE of 3.22% than **P4** (PCE: 1.51%) and **P3H** exhibits a PCE of 2.34% while its low molecular weight counterpart **P3** exhibits a PCE of 1.89%, mainly because of the improved J_{sc} as well as FF. From these results it becomes evident that molecular weight control is very important for efficient photovoltaic performance. However, **P3H** shows a lower PCE of 2.34% than **P4H** in spite of its high molecular weight, indicating that too high a molecular weight could have an adverse effect on the PCE. On the basis of our results, to obtain a high PCE, the molecular weight of the polymer should be high enough but not too high, because too high a molecular weight polymer may not form nanoscale interpenetrating networks due to poor solubility.

In Figure 2d, the $J-V$ characteristics of devices fabricated from **P4H**, P3HT (4002-EE, Rieke Metals, Inc.) and PFODBT are plotted to compare their performances. PFODBT:$PC_{61}BM$ (1:4 w/w) and P3HT:$PC_{61}BM$ (1:0.8 w/w), which are used as references, show PCEs of 1.86% and 3.06%, respectively. Although **P4H**:$PC_{61}BM$ (1:3 w/w) has a lower V_{oc} (0.63 V) than PFODBT, **P4H**:$PC_{61}BM$ (1:3 w/w) exhibits a much higher PCE of 3.22% because of the significantly improved J_{sc} (8.39 mA cm^{-2}). In addition, when **P4H**:$PC_{71}BM$ (1:3 w/w) was used, the device showed an increased J_{sc} of 10.7 mA cm^{-2} because of the much stronger absorption of $PC_{71}BM$ (Figure 3a) and the PCE improved to 3.24%. As shown in Figure 3, **P4H**-based devices absorb a wide range of visible light. The absorption spectra and external quantum efficiencies (EQEs) of **P4H**:$PC_{71}BM$ and **P4H**:$PC_{61}BM$ (1:3 w/w) devices exhibit well-matched profiles. The EQEs of **P4H**:$PC_{61}BM$ and **P4H**:$PC_{71}BM$ start to increase steeply around 740 nm and reach 46.9% at 550 nm and 59.0% at 540 nm, respectively, and high EQEs are maintained over a wide range of wavelengths, 360 to 650 nm, showing average values of 52% and 40%, respectively. Furthermore, when the blending ratio of **P4H**:$PC_{71}BM$ was adjusted to 1:2.5 w/w and the annealing temperature of the spin-cast **P4H**:$PC_{71}BM$ was changed to 70 °C from 50 °C, J_{sc}, V_{oc}, and FF increased to 11.1 mA cm^{-2}, 0.67 V, and 54.3%, respectively, and as a result, the PCE was greatly improved to 4.05% (Table 2).

Morphology. By observing the morphologies of blend films, we found that the degree of phase separation between the conjugated polymers (electron donor) and PCBM (electron acceptor) plays a significant role in determining the device efficiency. The nanoscale morphologies of polymer:$PC_{61}BM$ films were investigated using noncontact atomic force microscopy (AFM). As shown in Figure 4, distinctly different morphologies of polymer:PCBM blend films were observed in their phase images, indicating that the active layer morphology is strongly affected by the solubility of the polymer. As mentioned, the nanoscale morphology of the active layer is a very important factor for efficient exciton dissociation because if the diffusion length of the photogenerated exciton (~10 nm) is too small, it is easy for recombination to occur before reaching the interface between the polymer and PCBM. PFODBT:$PC_{61}BM$ and **P1**:$PC_{61}BM$ contain a number of aggregates and the large grain size can be clearly observed in the phase images (Figure 4, parts a and d). In contrast, **P4H**:$PC_{61}BM$ has a well-connected percolated network for both the polymer and $PC_{61}BM$ phases with a significantly smaller phase domain (Figure 4c). The long polymer chain of **P4H**, with its high molecular weight, seems to favor the formation of well-percolated networks by bridging the neighboring crystalline domains, providing a connected pathway for charge carriers.[20] In addition, long side chains enable high solubility of polymer and lead to an increase in the interspacing between the polymer chains. Thus, it is expected that PCBM molecules easily diffuse between polymer chains giving large interfacial area while **P2** and PFODBT exhibit large aggregates

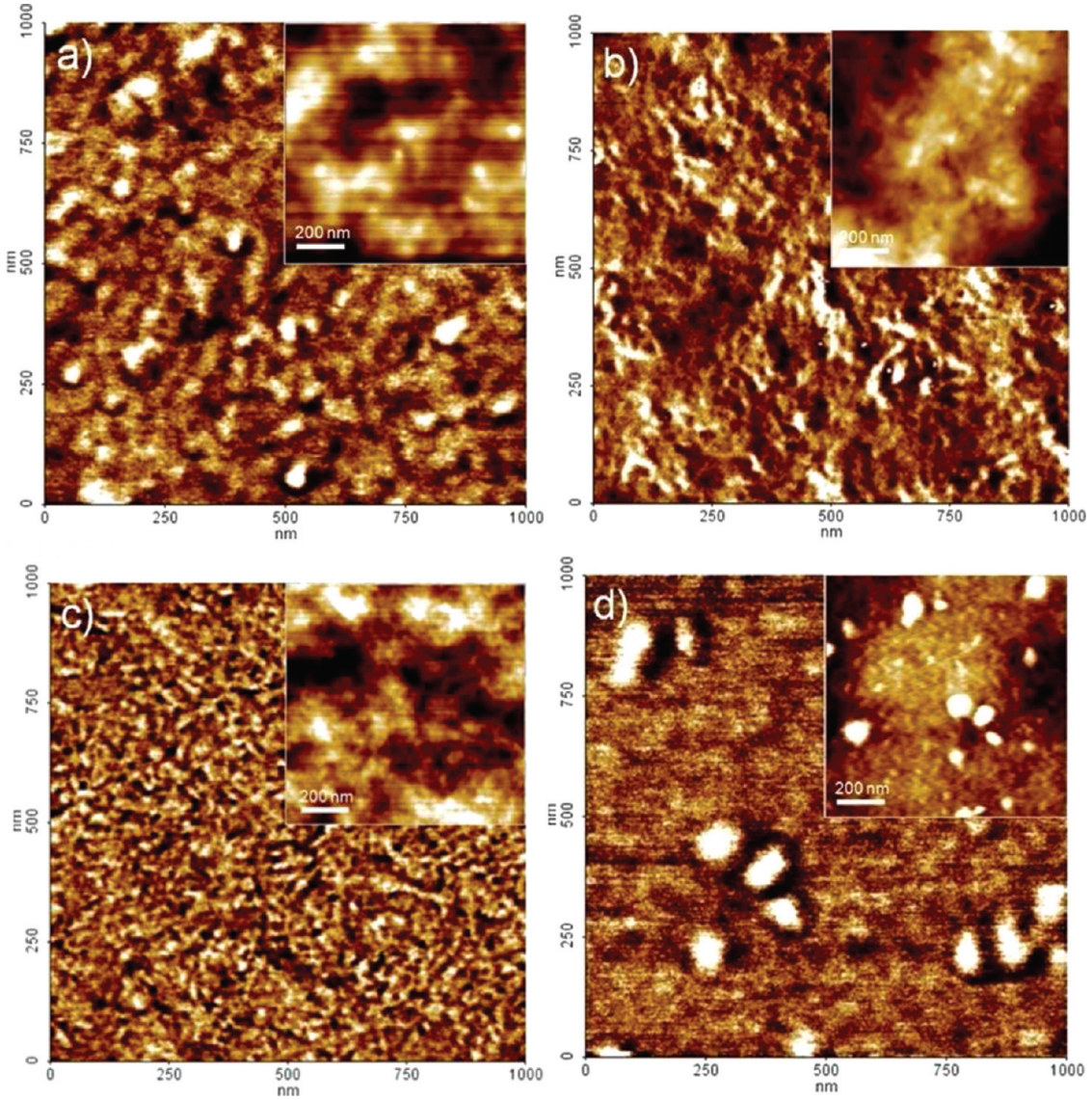


Figure 4. AFM phase images of polymer:PCBM films: (a) **P2**:$PC_{61}BM$ (1:3 w/w) film; (b) **P3H**:$PC_{61}BM$ (1:3 w/w) film; (c) **P4H**:$PC_{61}BM$ (1:3 w/w) film; (d) PFODBT:$PC_{61}BM$ (1:4 w/w) film. The insets show AFM topology images.

due to their unsatisfactory solubility in solvent. From these results, we conclude that the favorable morphology of the **P4H**-based device is the major reason for its high PCE.

Grazing Incident X-ray Diffraction. To study the effect of molecular structure on the crystallographic structure, one-dimensional plots of out-of-plane grazing incident X-ray diffraction (GIXRD) of as-spun and annealed polymer:PCBM films on PEDOT:PSS/ITO/glass substrates were examined (Figure 5). In the figure, the insets are the corresponding two-dimensional (2-D) images of annealed polymer:PCBM films. (In this study, we carried out GIXRD measurements of polymer:PCBM films without Al electrode. Indeed, there is a possibility that morphologies of the active layer of OPV devices are different between the devices in the presence and in the absence of Al electrode.[29]) **P1**:$PC_{61}BM$ and PFODBT:$PC_{61}BM$ exhibit a rather weak (100) peak at q_z equal to 0.2143 and 0.2057 $Å^{-1}$ (the corresponding d_{100} spacings are calculated to be 29.3 and 30.5 Å), respectively, and the peak intensities remain almost unchanged after annealing (Figure 5, parts a and f). On the other hand, **P2**:$PC_{61}BM$, **P3H**:$PC_{61}BM$, **P4H**:$PC_{61}BM$, and **P4H**:$PC_{71}BM$ films are shown to have a highly ordered molecular structure oriented normal to the substrate, showing strong (100) peaks at q_z equal to 0.3129 (d_{100} = 20.1 Å), 0.2868 (d_{100} = 21.9 Å), 0.2723 (d_{100} = 23.1 Å), and 0.2636 $Å^{-1}$ (d_{100} = 23.8 Å), respectively, (Figure 5b−e) and, after thermal annealing, the out-of-plane X-ray reflection intensities of **P3H**:$PC_{61}BM$, **P4H**:$PC_{61}BM$, and **P4H**:$PC_{71}BM$ increased significantly and the d_{100} spacings were slightly reduced to 21.3, 23.1, and 23.6 Å, respectively, indicating enhanced interchain packing. This result suggests that the changes in crystallographic structure of the polymer thin film after thermal annealing, such as enhanced interchain packing, seem to be one of the reasons for the improved PCE. (In addition, thermal annealing is known to increase PCE because of morphological changes and strengthened adhesion between the polymer:PCBM layer and Al.[30−32]) By thermal annealing at 140 °C for 5 min, the PCEs of **P2**:$PC_{61}BM$, **P3H**:$PC_{61}BM$, and **P4H**:$PC_{61}BM$ were improved from 0.97, 1.78, and 2.51% to 1.17, 2.34, and 3.22%, respectively, exhibiting significant increases in V_{oc}, FF, and J_{sc}.[17,33−35] (Figure 2c) The GIXRD results also clearly show that the d_{100} spacing is directly related to the length of the alkyl groups, and the silicon-containing polymers **P2**, **P3H**, and **P4H**, despite their long solubilizing groups, have long-range

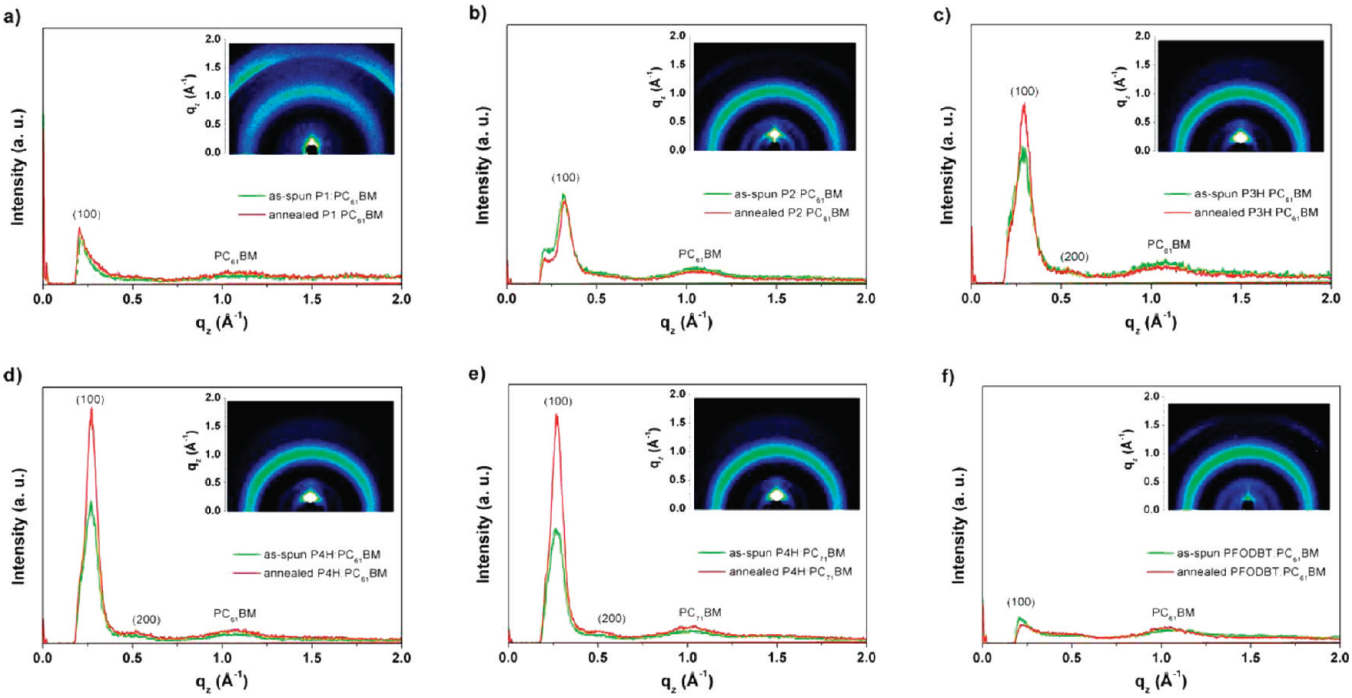


Figure 5. Out-of-plane GIXRD profiles of polymer films coated on PEDOT:PSS/ITO/glass. Insets are corresponding 2-D images of annealed polymer:PCBM films: (a) P1:$PC_{61}BM$ (1:3 w/w) film; (b) P2:$PC_{61}BM$ (1:3 w/w) film; (c) P3H:$PC_{61}BM$ (1:3 w/w) film; (d) P4H:$PC_{61}BM$ (1:3 w/w) film; (e) P4H:$PC_{71}BM$ (1:3 w/w) film; (f) PFODBT:$PC_{61}BM$ (1:4 w/w) film.

ordered structures even when mixed with PCBM, which is beneficial for high charge-carrier mobility. The d_{100} spacing is increased as the length of the solubilizing groups of the polymer is increased; **P2**:$PC_{61}BM$ (**P2** has ethyl/octyloxy groups) has d_{100} spacing of 19.5 Å, while **P4H**:$PC_{61}BM$, which has the longest solubilizing groups of hexyl/octyloxy substituents, exhibits d_{100} spacing of 23.1 Å. However, in spite of the long octyloxy solubilizing groups, **P4H**:$PC_{61}BM$ has a much smaller d_{100} spacing than PFODBT:$PC_{61}BM$, with a stronger peak intensity, indicating a more ordered structure and smaller interchain distance. These findings partially explain the much higher hole mobility of **P4H** compared to PFODBT. According to space-charge limited current (SCLC) hole mobility measurements, the hole mobility of PFODBT is 1.2×10^{-5} cm^2 V^{-1} s^{-1}. **P1** also exhibits a rather low hole mobility of 1.1×10^{-5} cm^2 V^{-1} s^{-1}, probably because of the irregular backbone structure, which might hinder the stacking of polymer backbones. On the other hand, **P2**, **P3H**, and **P4H** still have about 2 to 18 times higher hole mobilities than PFODBT, with values of 2.2×10^{-4}, 2.1×10^{-5}, and 4.5×10^{-5} cm^2 V^{-1} s^{-1}, respectively. In addition, upon blending with PCBM, the high molecular weight polymers **P3H** and **P4H** might be more efficient in charge transport because high molecular weight polymers can interconnect neighboring crystalline domains, enabling easy transport of the charge carrier through the connected pathway. Therefore, the OPVs based on **P3H** and **P4H** could be expected to have higher J_{sc} and FF as a result of a high hole-transporting ability and nanoscale interpenetrated network with PCBM.

Conclusion

We have prepared a series of new low-bandgap polymers containing 9,9-dialkyl-3,6-dialkyloxysilafluorene and 4,7-di-2-thienyl-2,1,3-benzothiadiazole units. These polymers showed a broadened absorption band compared with poly[2,7-(9,9-dioctylfluorene)-*alt*-5,5-(4′,7′-di-2-thienyl-2′,1′,3′-benzothiodiazole)] (PFODBT) because of the alkoxy groups; as a result, they show better overlap with the solar spectrum, enabling efficient photon harvesting. Interestingly, poly[2,7-(3,6-dioctyloxy-9,9-dihexylsilafluorene)-*alt*-5,5-(4′,7′-di-2-thienyl-2′,1′,3′-benzothiadiazole)] (**P4H**) exhibited good solubility in spite of its high molecular weight because of its sufficiently long solubilizing groups. As a consequence, **P4H**:PCBM exhibited high photovoltaic performance mainly because of the high J_{sc} and FF resulting from favorable **P4H**:PCBM blend morphology. **P4H** exhibited a high PCE of 3.22% when $PC_{61}BM$ was used as the electron acceptor. Furthermore, when $PC_{71}BM$ was used, the PCE greatly improved to 4.05% with a V_{oc} of 0.67 V, a J_{sc} of 11.1 mA cm^{-2} and an FF of 54.3% under 100 mW cm^{-2} AM1.5G. Therefore, we conclude that **P4H** is a promising polymer donor for light harvesting and that the PCE could be further improved by precise optimization of the fabrication procedures and device structure.

Experimental Section

Materials. 4,7-Dibromo-2,1,3-benzothiadiazole (**M5**) and 2,7-dibromo-9,9-dioctylfluorene (**M7**) were purchased from Aldrich and used after purification with column chromatography. All of the other chemicals were obtained from Aldrich and TCI and used without further purification. 2,5-Bis(trimethylstannyl)thiophene (**M6**) and 4,7-bis(5-(trimethylstannyl)thiophen-2-yl)-2,1,3-benzothiadiazole (**M4**) were prepared following the reported procedures with modification.[23]

Preparation of 4,4′-Dibromobiphenyl-3,3′-diol (2). 4,4′-Diaminobiphenyl-3,3′-diol (**1**) (15.00 g, 69.37 mmol) was added to a mixture of hydrobromic acid (40 M, 60 mL) and water (240 mL) and acetonitrile (240 mL), and dissolved by heating the reaction mixture to 90 °C. The reaction mixture was cooled to 0 °C in an ice bath, then sodium nitrite (12.21 g, 176.9 mmol) in water (20 mL) and cuprous bromide (22.10 g, 154 mmol) in hydrobromic acid (240 mL) were added successively with vigorous stirring. The reaction mixture was warmed to room temperature and refluxed. After 12 h of reaction, the reaction mixture was washed with deionized water and extracted with chloroform. The product was obtained as a white solid by column chromatography and recrystallized twice from a dichloromethane/*n*-hexane mixture.

The final product was obtained as a white solid (20.56 g, 60.14 mmol; yield: 87%). ^{1}H NMR (600 MHz, $CDCl_3$, δ ppm): 7.49 (d, 2H, ArH), 7.19 (s, 2H, ArH), 6.97 (d, 2H, ArH), 5.60 (s, 2H, OH). ^{13}C NMR (150 MHz, $CDCl_3$, δ ppm): 152.50, 141.15, 132.30, 120.38, 114.50, 109.77. FD−MS (m/z): calcd for $C_{12}H_8Br_2O_2$, 341.89; found, 341.97. Anal. Calcd for $C_{12}H_8Br_2O_2$: C, 41.90; H, 2.34; Br, 46.46; O, 9.30. Found: C, 41.3; H, 2.30.

Preparation of 4,4′-Dibromo-3,3′-bis(octyloxy)biphenyl (3). Sodium hydroxide (14.04 g, 351.0 mmol) was added to a solution of 4,4′-dibromobiphenyl-3,3′-diol (**2**) (20.00 g, 58.50 mmol) in ethanol (600 mL). The solution was heated to reflux and 1-bromooctane (67.41 g, 351.0 mmol) was added dropwise. After reaction for 24 h, the reaction mixture was cooled to room temperature, washed with deionized water several times and extracted with dichloromethane. Purification through column chromatography gave the product as a white solid (yield: 74%). ^{1}H NMR (600 MHz, $CDCl_3$, δ ppm): 7.56 (d, 2H, ArH), 7.01−6.96 (m, 4H, ArH), 4.06 (t, 4H, OCH_2), 1.89−1.82 (m, 4H, CH_2), 1.54−1.28 (m, 20H, CH_2), 0.90−0.86 (m, 6H, CH_3). ^{13}C NMR (150 MHz, $CDCl_3$, δ ppm): 155.76, 141.18, 133.45, 120.28, 111.97, 111.86, 69.35, 31.83, 29.79, 29.29, 29.28, 29.12, 25.00, 22.65, 14.09. FD−MS (m/z): calcd for $C_{28}H_{40}Br_2O_2$, 566.14; found, 566.25. Anal. Calcd for $C_{28}H_{40}Br_2O_2$: C, 59.16; H, 7.09; Br, 28.11; O, 5.63. Found: C, 59.3; H, 7.41.

Preparation of 4,4′-Dibromo-2,2′-diiodo-5,5′-bis(octyloxy)-biphenyl (4). 20% H_2SO_4 (30 mL), KIO_3 (1.66 g, 7.77 mmol), and I_2 (4.93 g, 19.4 mmol) were added to a solution of 4,4′-dibromo-3,3′-bis(octyloxy)biphenyl (**3**) (10.00 g, 17.66 mmol) in acetic acid (300 mL), and the mixture was heated to 90 °C and left for 12 h. The reaction mixture was cooled to room temperature, extracted with chloroform and washed with aqueous $Na_2S_2O_3$. After evaporation of chloroform, the product (13.2 g, 16.1 mmol) was obtained as a colorless solid by purification by column chromatography (yield: 91%). ^{1}H NMR (600 MHz, $CDCl_3$, δ ppm): 8.03 (s, 2H, ArH), 6.70 (s, 2H, ArH), 4.01−3.95 (m, 4H, OCH_2), 1.86−1.79 (m, 4H, CH_2), 1.50−1.28 (m, 20H, CH_2), 0.90−0.86 (m, CH_3). ^{13}C NMR (150 MHz, $CDCl_3$, δ ppm): 155.57, 148.01, 141.94, 114.31, 112.83, 87.19, 69.47, 31.76, 29.23, 29.17, 28.88, 25.88, 22.63, 14.09. FD−MS (m/z): calcd for $C_{28}H_{38}Br_2I_2O_2$, 817.93; found, 818.02. Anal. Calcd for $C_{28}H_{38}Br_2I_2O_2$: C, 41.00; H, 4.67; Br, 19.48; I, 30.94; O, 3.90. Found: C, 41.3; H, 4.70.

Preparation of 2,7-Dibromo-9,9-diethyl-3,6-bis(octyloxy)silafluorene (M1). 4,4′-Dibromo-2,2′-diiodo-5,5′-bis(octyloxy)biphenyl (**4**) (6.5 g, 7.95 mmol) was dissolved in 100 mL of THF and cooled to −100 °C. Then, 1.6 M *n*-butyllithium solution in hexane (9.98 mL, 16.0 mmol) was slowly added and the temperature was maintained below −100 °C for 1 h. Then dichlorodiethylsilane (1.31 g, 8.42 mmol) was added dropwise at −100 °C. After reaction for 1 h at this temperature, the reaction mixture was warmed to room temperature and stirred for 24 h. The organic layer was extracted with diethyl ether, washed with deionized water several times and dried over Na_2SO_4. After removal of solvent with a rotary evaporator, the product (2.62 g, 4.03 mmol) was obtained by column chromatography with *n*-hexane (yield: 51%). ^{1}H NMR (600 MHz, $CDCl_3$, δ ppm): 7.69 (s, 2H, ArH), 7.23 (s, 2H, ArH), 4.15 (t, 4H, OCH_2), 1.55−1.26 (m, 20H, CH_2), 0.97−0.85 (m, 16H, CH_2, CH_3). ^{13}C NMR (150 MHz, $CDCl_3$, δ ppm): 153.37, 144.70, 133.44, 126.51, 108.53, 102.09, 27.90, 25.41, 25.33, 25.28, 22.15, 18.76, 10.19, 3.54. FD−MS (m/z): calcd for $C_{32}H_{48}Br_2O_2Si$, 650.18; found, 650.31. Anal. Calcd for $C_{32}H_{48}Br_2O_2Si$: C, 58.89; H, 7.41; Br, 24.49; O, 4.90; Si, 4.30. Found: C, 58.9; H, 7.44.

Preparation of 4,4′-Dibromo-3,3′-bis(hexyloxy)biphenyl (5). Compound **5** was prepared following the same procedure as was used for compound **3**, using 1-bromohexane instead of 1-bromooctane. ^{1}H NMR (600 MHz, $CDCl_3$, δ ppm): 7.56 (d, 2H, ArH), 7.01−6.96 (m, 4H, ArH), 4.08 (t, 4H, OCH_2), 1.88−1.83 (m, 4H, CH_2), 1.54−1.51 (m, 4H, CH_2), 1.38−1.34 (m, 8H, CH_2), 0.92−0.90 (m, 6H, CH_3). ^{13}C NMR (150 MHz, $CDCl_3$, δ ppm): 155.79, 141.21, 133.48, 120.32, 112.00, 111.89, 69.38, 31.53, 29.11, 25.69, 22.60, 14.03. FD−MS (m/z): calcd for $C_{24}H_{32}Br_2O_2$, 510.08; found, 510.18. Anal. Calcd for $C_{24}H_{32}Br_2O_2$: C, 56.27; H, 6.30; Br, 31.19; O, 6.25. Found: C, 56.0; H, 6.25.

Preparation of 4,4′-Dibromo-5,5′-bis(hexyloxy)-2,2′-diiodobiphenyl (6). Compound **6** was prepared following the same procedure as for compound **4** but using compound **5** instead of compound **3**. ^{1}H NMR (600 MHz, $CDCl_3$, δ ppm): 8.03 (s, 2H, ArH), 6.71 (s, 2H, ArH), 3.99 (m, 4H, OCH_2), 1.84−1.81 (m, 4H, CH_2), 1.50−1.47 (m, 4H, CH_2), 1.35−1.32 (m, 8H, CH_2), 0.91−0.89 (m, 6H, CH_3). ^{13}C NMR (150 MHz, $CDCl_3$, δ ppm): 155.53, 147.98, 141.90, 114.29, 112.81, 87.21, 69.44, 31.43, 28.84, 25.54, 22.52, 13.99. FD−MS (m/z): calcd for $C_{24}H_{30}Br_2I_2O_2$, 761.87; found, 761.97. Anal. Calcd for $C_{24}H_{30}Br_2I_2O_2$: C, 37.72; H, 3.96; Br, 20.91; I, 33.22; O, 4.19. Found: C, 37.5; H, 3.93.

Preparation of 2,7-Dibromo-9,9-dihexyl-3,6-bis(hexyloxy)-silafluorene (M2). Compound **M2** was prepared following the same procedure as for compound **M1**, using dichlorodihexylsilane instead of dichlorodiethylsilane. ^{1}H NMR (600 MHz, $CDCl_3$, δ ppm): 7.68 (s, 2H, ArH), 7.22 (s, 2H, ArH), 4.15 (t, 4H, OCH_2), 1.91−1.86 (m, 4H, CH_2), 1.57−1.36 (m, 4H, CH_2), 1.30−1.17 (m, 24H, CH_2), 0.93−0.82 (m, 16H, CH_2, CH_3). ^{13}C NMR (150 MHz, $CDCl_3$, δ ppm): 157.21, 148.43, 137.38, 131.13, 112.46, 106.02, 69.26, 33.00, 31.54, 31.33, 29.16, 25.73, 23.79, 22.61, 22.55, 14.06, 14.03, 12.39. FD−MS (m/z): calcd for $C_{36}H_{56}Br_2O_2Si$, 706.24; found, 706.31. Anal. Calcd for $C_{36}H_{56}Br_2O_2Si$: C, 61.01; H, 7.96; Br, 22.55; O, 4.51; Si, 3.96. Found: C, 60.8; H, 7.97.

Preparation of 2,7-Dibromo-9,9-dihexyl-3,6-bis(octyloxy)-silafluorene (M3). Compound **M3** was prepared by the same procedure as described for compound **M1** using dichlorodihexylsilane. ^{1}H NMR (600 MHz, $CDCl_3$, δ ppm): 7.68 (s, 2H, ArH), 7.23 (s, 2H, ArH), 4.14 (t, 4H, OCH_2), 1.89−1.85 (m, 4H, CH_2), 1.56−1.53 (m, 4H, CH_2), 1.41−1.18 (m, 32H, CH_2), 0.90−0.82 (m, 16H, CH_2, CH_3). ^{13}C NMR (150 MHz, $CDCl_3$, δ ppm): 157.47, 148.55, 137.50, 131.41, 112.77, 106.42, 69.53, 32.96, 31.86, 31.38, 29.37, 29.34, 29.27, 26.15, 23.86, 23.82, 22.68, 22.55, 14.05, 13.99, 12.53. FD−MS (m/z): calcd for $C_{40}H_{64}Br_2O_2Si$, 762.3042; found, 762.42.

Preparation of 4,7-Di(2-trimethylstannylthiophen-5-yl)-2,1,3-benzothiadiazole (M4). 1.6 M *n*-butyllithium solution in hexane (13.27 mL, 21.24 mmol) was added to a solution of 2,2,6,6-tetramethylpiperidine (3.00 g, 21.2 mmol) in THF (60 mL), at a temperature of −78 °C. Next, the reaction mixture was kept at this temperature for 1 h and then warmed to room temperature. The reaction mixture was cooled to −78 °C again and a solution of compound **7** (2.45 g, 8.17 mmol) in THF (25 mL) was added dropwise. After reaction for 1 h at −78 °C, 1.0 M $SnMe_3Cl$ solution in hexane (21.67 mL, 21.24 mmol) was added. The reaction mixture was warmed to room temperature and stirred for 24 h. The organic layer was extracted with diethyl ether, washed with deionized water several times and dried over Na_2SO_4. After removal of solvent using a rotary evaporator, recrystallization from ether−ethanol gave the product (2.62 g, 4.03 mmol) as orange crystals (3.82 g, yield: 74%). ^{1}H NMR (600 MHz, $CDCl_3$, δ ppm): 8.17 (d, 2H, ArH), 7.85 (s, 2H, ArH), 7.29 (d, 2H, ArH), 0.43 (s, 18H, CH_3). ^{13}C NMR (150 MHz, $CDCl_3$, δ ppm): 152.65, 145.04, 140.21, 136.08, 128.38, 125.82, −8.02. FD−MS (m/z): calcd for $C_{20}H_{24}N_2S_3Sn_2$, 627.91; found, 628.04. Anal. Calcd for $C_{20}H_{24}N_2S_3Sn_2$: C, 38.37; H, 3.86; N, 4.47; S, 15.37; Sn, 37.92. Found: C, 38.1; H, 3.82; N, 4.97; S, 13.9.

Preparation of P1 Using M2, M5, and M6 in a Mole Ratio of 0.5:0.5:1 (P1). Compound **M2** (0.255 g, 0.364 mmol), compound **M5** (0.106 g, 0.364 mmol), and compound **M6** (0.300 g, 0.728 mmol) were dissolved in toluene (25 mL). The solution was purged with N_2 for 30 min, $Pd_2(dba)_3$ (0.033 g, 0.036 mmol) and P(*o*-tolyl)$_3$ (0.044 g, 0.146 mmol) were added, and then slowly heated to 100 °C. After 24 h, the reaction mixture was poured into methanol (400 mL) and the dark precipitate was collected

by filtration. The filtrate was dissolved in chlorobenzene (300 mL), an aqueous solution of sodium diethyldithiocarbamate trihydrate (6.0 g in 200 mL of deionized water) was added, and the mixture was stirred at 90 °C. After 12 h, the organic phase was washed with deionized water several times. The solution was concentrated, precipitated into methanol and collected by filtration. The filtrate was subjected to Soxhlet extraction with methanol, acetone, hexane, and chlorobenzene. The polymer solution in chlorobenzene was concentrated and slowly dropped into methanol. The polymer was obtained as a dark solid by filtration and drying under vacuum. GPC: M_n, 76 600; M_w, 127 800; PDI, 1.67. ^{1}H NMR (600 MHz, $CDCl_3$, δ ppm): 8.27−7.85 (m, 5H, ArH), 7.72−7.30 (m, 5H, ArH), 4.36−4.15 (m, 4H, OCH_2), 2.10−1.87 (m, 4H, CH_2), 1.73−1.20 (m, 28H, CH_2), 1.07−0.80 (m, 16H, CH_2, CH_3).

Preparation of Poly[2,7-(3,6-dioctyloxy-9,9-diethylsilafluorene)-*alt*-5,5-(4′,7′-di-2-thienyl-2′,1′,3′-benzothiadiazole)] using M1 and M4 in a mole ratio of 1:0.95 (P2). P2 was prepared following the same procedure as used in the preparation of **P1**. Compound **M1** (0.347 g, 0.533 mmol) and compound **M4** (0.318 g, 0.507 mmol) were used as monomers. GPC: M_n, 7420; M_w, 9670; PDI, 1.30. ^{1}H NMR (600 MHz, $CDCl_3$, δ ppm): 8.20−8.10 (m, 2H, ArH), 8.01−7.82 (m, 4H, ArH), 7.74−7.63 (m, 2H, ArH), 7.44−7.30 (m, 2H, ArH), 4.36−4.13 (m, 4H, OCH_2), 2.09−1.87 (m, 4H, CH_2), 1.72−1.24 (m, 20H, CH_2), 1.11−0.84 (m, 16H, CH_2, CH_3).

Preparation of Poly[2,7-(3,6-dihexyloxy-9,9-dihexylsilafluorene)-*alt*-5,5-(4′,7′-di-2-thienyl-2′,1′,3′-benzothiadiazole)] Using M2 and M4 in a mole ratio of 1:1 (P3, P3H). P3 was prepared following the same procedure as used in the preparation of **P1**. Compound **M2** (0.380 g, 0.538 mmol) and compound **M4** (0.338 g, 0.538 mmol) were used as monomers. GPC: M_n; 30,700, M_w; 67,200, PDI; 2.19. High molecular weight **P3H** was prepared using 1.5 times as much $Pd_2(dba)_3$ and P(*o*-tolyl)$_3$ as were used in the preparation of **P3**. GPC: M_n, 102 300; M_w, 228 900, PDI; 2.24. ^{1}H NMR (600 MHz, $CDCl_3$, δ ppm): 8.20−8.15 (m, 2H, ArH), 8.01−7.89 (m, 4H, ArH), 7.73−7.67 (m, 2H, ArH), 7.43−7.36 (m, 2H, ArH), 4.36−4.15 (m, 4H, OCH_2), 2.10−1.89 (m, 4H, CH_2), 1.74−1.22 (m, 28H, CH_2), 1.06−0.82 (m, 16H, CH_2, CH_3).

Preparation of Poly[2,7-(3,6-dioctyloxy-9,9-dihexylsilafluorene)-*alt*-5,5-(4′,7′-di-2-thienyl-2′,1′,3′-benzothiadiazole)] Using M3 and M4 in a Mole Ratio of 1:1 (P4, P4H). P4 was prepared following the same procedure as used in the preparation of **P1**. Compound **M3** (0.400 g, 0.525 mmol) and compound **M4** (0.323 g, 0.525 mmol) were used as monomers. GPC: M_n, 19 000; M_w, 33 900; PDI, 1.78. High molecular weight **P4H** was prepared using 1.5 times as much $Pd_2(dba)_3$ and P(*o*-tolyl)$_3$ as were used in the preparation of **P4**. GPC: M_n, 63 900; M_w, 160 300; PDI, 2.51. ^{1}H NMR (600 MHz, $CDCl_3$, δ ppm): 8.21−8.16 (m, 2H, ArH), 8.01−7.87 (m, 4H, ArH), 7.73−7.67 (m, 2H, ArH), 7.44−7.35 (m, 2H, ArH), 4.36−4.14 (m, 4H, OCH_2), 2.09−1.88 (m, 4H, CH_2), 1.72−1.21 (m, 36H, CH_2), 1.06−0.82 (m, 16H, CH_2, CH_3).

Preparation of Poly[2,7-(9,9-dioctylfluorene)-*alt*-5,5-(4′,7′-di-2-thienyl-2′,1′,3′-benzothiadiazole)] Using M7 and M4 in a Mole Ratio of 1:0.95 (PFODBT). PFODBT was prepared following the same procedure as used in the preparation of **P1**. Compound **M7** (0.134 g, 0.245 mmol) and compound **M4** (0.146 g, 0.233 mmol) were used as monomers. GPC: M_n, 31 200; M_w, 93 900; PDI, 3.01. ^{1}H NMR (600 MHz, $CDCl_3$, δ ppm): 8.16 (br, 2H, ArH), 7.92 (br, 2H, ArH), 7.74−7.58 (m, 6H, ArH), 7.47 (br, 2H, ArH), 2.13−1.97 (m, 4H, CH_2), 1.50−0.71 (m, 30H, CH_2, CH_3).

Characterization. NMR spectra were recorded on a Bruker Ultrashield Plus 600 spectrometer. Mass spectra were obtained using a Jeol JMS-T100 AccuTOF GC mass spectrometer. The number-average molecular weight (M_n) and weight-average molecular weight (M_w) were measured using a PL XT-20 Rapid high temperature GPC (Polymer Laboratories Ltd.). Polystyrene standards were used for calibration and TCB was used as an eluent. Elemental analysis was carried out using a FlashEA 1112 CHNS analyzer (Thermo Electron Corporation). Absorption spectra of polymer films were recorded on a Jasco V-530 UV−vis spectrometer and the optical bandgaps of the polymers were calculated from the onset of the absorption spectra. Cyclic voltammetry (CV) measurements were conducted on a CH Instruments 608B electrochemical analyzer at a scan rate of 50 mV s^{-1} with a 0.05 M solution of tetrabutylammonium hexafluorophosphate (Bu_4NPF_6) in acetonitrile. The oxidation and reduction potentials of polymer film coated on a Pt disk were measured using a Pt wire and a Ag wire as a counter electrode and a quasireference electrode, respectively. Under these conditions, the onset of oxidation and reduction potentials of the polymer thin films against the Ag quasireference electrode were measured and calibrated against the ferrocene/ferrocenium (Fc/Fc^+) redox couple. The HOMO and LUMO levels of the polymers were calculated by assuming the absolute energy level of Fc/Fc^+ as −4.80 eV to vacuum.[36]

Grazing incident X-ray diffraction (GIXRD) with a synchrotron X-ray beam (4CII beamline, Pohang Accelerator Laboratory) was used to investigate the crystallographic structure of polymer thin film coated on the PEDOT:PSS. The wavelength of the X-rays was 1.3807 Å, and the incident angle was fixed at 0.2°.

Device Fabrication and Measurement. The patterned ITO glass substrates were cleaned by ultrasonication in acetone, methanol and deionized water, after which they were dried by N_2 blowing and dry cleaned using UV−ozone for 10 min. The PEDOT:PSS (AI4083, H. C. Stack) was spin-coated on the cleaned ITO glass at a rate of 2,500 rpm and then the substrates were baked at 140 °C for 30 min in a N_2 glovebox. The polymer solutions (0.7−1.5 wt %) were prepared by dissolving in *o*-DCB with mild heating (70 °C) for 24 h, PCBM was added to afford polymer:PCBM blend solutions and mixed further for 12 h. The polymer:PCBM solutions were spin-coated at a rate in the range of 700 to 2,200 rpm and the spin-coated films were dried at 70 to 90 °C for 30 min in a N_2 glovebox. The thickness of the active layer was measured using an Alpha-Step IQ profilometer (KLA-Tencor). The spin-coated substrates were transferred to a vacuum evaporation chamber for cathode deposition. Al (150 nm) was deposited on the active layer by thermal evaporation at a pressure below 1.0×10^{-6} Torr and the resulting devices had an active area of 0.102 cm^2. Before measuring the photovoltaic performance, the devices were annealed at 140 °C for 5 min and the current−voltage behavior was recorded on a Keithley 236 Source Measurement unit under simulated 100 mW cm^{-2} light. A solar simulator (Newport) with a 300 W xenon lamp and AM1.5G air mass filter was used to evaluate the performance of the devices and the light intensity was carefully calibrated using a silicon photovoltaic reference cell (Bunkou Keiki Co., BS-520). EQE was measured using a Solar Cell Spectral Response IPCE Measurement System (PV Measurements, Inc.). For SCLC hole-mobility measurements of the polymers, the devices (ITO/PEDOT:PSS/Polymer/Al) were fabricated following the same method and their current−voltage behavior was recorded using a Keithley 236 Source Measurement unit.[36]

Acknowledgment. This research was supported by the EEWS (Energy, Environment, Water, and Sustainability) program of KAIST and the WCU (World Class University) program through the Korea Science and Engineering Foundation funded by the Ministry of Education, Science and Technology (*R*32-2008-000-10142-0).

References and Notes

(1) Mayer, A. C.; Scully, S. R.; Hardin, B. E.; Rowell, M. W.; McGehee, M. D. *Mater Today* **2007**, *10*, 28.
(2) Brabec, C. J.; Durrant, J. R. *MRS Bull.* **2008**, *33*, 670.
(3) Thompson, B. C.; Frechet, J. M. J. *Angew. Chem., Int. Ed.* **2008**, *47*, 58.
(4) Dennler, G.; Scharber, M. C.; Brabec, C. J. *Adv. Mater.* **2009**, *21*, 1323.

(5) Park, J. H.; Lee, T. W.; Chin, B. D.; Wang, D. H.; Park, O. O. *Macromol. Rapid Commun*. **2010**, DOI: 10.1002/marc.201000310.
(6) Svensson, M.; Zhang, F. L.; Veenstra, S. C.; Verhees, W. J. H.; Hummelen, J. C.; Kroon, J. M.; Inganas, O.; Andersson, M. R. *Adv. Mater*. **2003**, *15*, 988.
(7) Zhou, Q. M.; Hou, Q.; Zheng, L. P.; Deng, X. Y.; Yu, G.; Cao, Y. *Appl. Phys. Lett*. **2004**, *84*, 1653.
(8) Wang, E. G.; Wang, M.; Wang, L.; Duan, C. H.; Zhang, J.; Cai, W. Z.; He, C.; Wu, H. B.; Cao, Y. *Macromolecules* **2009**, *42*, 4410.
(9) Chen, M. H.; Hou, J.; Hong, Z.; Yang, G.; Sista, S.; Chen, L. M.; Yang, Y. *Adv. Mater*. **2009**, *21*, 4238.
(10) Blouin, N.; Michaud, A.; Leclerc, M. *Adv. Mater*. **2007**, *19*, 2295.
(11) Peet, J.; Kim, J. Y.; Coates, N. E.; Ma, W. L.; Moses, D.; Heeger, A. J.; Bazan, G. C. *Nat. Mater*. **2007**, *6*, 497.
(12) Boudreault, P. L. T.; Michaud, A.; Leclerc, M. *Macromol. Rapid Commun*. **2007**, *28*, 2176.
(13) Wang, E. G.; Wang, L.; Lan, L. F.; Luo, C.; Zhuang, W. L.; Peng, J. B.; Cao, Y. *Appl. Phys. Lett*. **2008**, *92*, 033307.
(14) Scharber, M. C.; Koppe, M.; Gao, J.; Cordella, F.; Loi, M. A.; Denk, P.; Morana, M.; Egelhaaf, H. J.; Forberich, K.; Dennler, G.; Gaudiana, R.; Waller, D.; Zhu, Z. G.; Shi, X. B.; Brabec, C. J. *Adv. Mater*. **2010**, *22*, 367.
(15) Huo, L. J.; Chen, H. Y.; Hou, J. H.; Chen, T. L.; Yang, Y. *Chem. Commun*. **2009**, 5570.
(16) Hou, J. H.; Chen, H. Y.; Zhang, S. Q.; Li, G.; Yang, Y. *J. Am. Chem. Soc*. **2008**, *130*, 16144.
(17) Chen, H. Y.; Hou, J. H.; Hayden, A. E.; Yang, H.; Houk, K. N.; Yang, Y. *Adv. Mater*. **2010**, *22*, 371.
(18) Liao, L.; Dai, L. M.; Smith, A.; Durstock, M.; Lu, J. P.; Ding, J. F.; Tao, Y. *Macromolecules* **2007**, *40*, 9406.
(19) Ma, W.; Kim, J. Y.; Lee, K.; Heeger, A. J. *Macromol. Rapid Commun*. **2007**, *28*, 1776.
(20) Kline, R. J.; McGehee, M. D. *Polym. Rev*. **2006**, *46*, 27.
(21) Cornil, J.; Beljonne, D.; Calbert, J. P.; Bredas, J. L. *Adv. Mater*. **2001**, *13*, 1053.
(22) Chen, R. F.; Fan, Q. L.; Zheng, C.; Huang, W. *Org. Lett*. **2006**, *8*, 203.
(23) van Mullekom, H. A. M.; Vekemans, J. A. J. M.; Meijer, E. W. *Chem.—Eur. J*. **1998**, *4*, 1235.
(24) Gadisa, A.; Mammo, W.; Andersson, L. M.; Admassie, S.; Zhang, F.; Andersson, M. R.; Inganas, O. *Adv. Funct. Mater*. **2007**, *17*, 3836.
(25) Jespersen, K. G.; Beenken, W. J. D.; Zaushitsyn, Y.; Yartsev, A.; Andersson, M.; Pullerits, T.; Sundstrom, V. *J. Chem. Phys*. **2004**, *121*, 12613.
(26) Andersson, M. R.; Thomas, O.; Mammo, W.; Svensson, M.; Theander, M.; Inganas, O. *J. Mater. Chem*. **1999**, *9*, 1933.
(27) Scharber, M. C.; Wuhlbacher, D.; Koppe, M.; Denk, P.; Waldauf, C.; Heeger, A. J.; Brabec, C. L. *Adv. Mater*. **2006**, *18*, 789.
(28) Koppe, M.; Brabec, C. J.; Heiml, S.; Schausberger, A.; Duffy, W.; Heeney, M.; McCulloch, I. *Macromolecules* **2009**, *42*, 4661.
(29) Kim, H. J.; Park, J. H.; Lee, H. H.; Lee, D. R.; Kim, J. J. *Org. Electron*. **2009**, *10*, 1505.
(30) Chen, L. M.; Hong, Z. R.; Li, G.; Yang, Y. *Adv. Mater*. **2009**, *21*, 1434.
(31) Li, G.; Shrotriya, V.; Huang, J. S.; Yao, Y.; Moriarty, T.; Emery, K.; Yang, Y. *Nat. Mater*. **2005**, *4*, 864.
(32) Ma, W. L.; Yang, C. Y.; Gong, X.; Lee, K.; Heeger, A. J. *Adv. Funct. Mater*. **2005**, *15*, 1617.
(33) Lee, T. W.; Park, O. O. *Adv. Mater*. **2000**, *12*, 801.
(34) Lee, T. W.; Park, O. O. *Appl. Phys. Lett*. **2000**, *77*, 3334.
(35) Park, S. H.; Roy, A.; Beaupre, S.; Cho, S.; Coates, N.; Moon, J. S.; Moses, D.; Leclerc, M.; Lee, K.; Heeger, A. J. *Nat. Photonics* **2009**, *3*, 297.
(36) Liang, Y. Y.; Feng, D. Q.; Wu, Y.; Tsai, S. T.; Li, G.; Ray, C.; Yu, L. P. *J. Am. Chem. Soc*. **2009**, *131*, 7792.

512 *Macromolecules* **2011**, *44*, 512–520
DOI: 10.1021/ma1024494

Macromolecules
ARTICLE

Steric Effects of the Initiator Substituent Position on the Externally Initiated Polymerization of 2-Bromo-5-iodo-3-hexylthiophene

Natalia Doubina,[†] Sergio A. Paniagua,[‡] Alexandra V. Soldatova,[†] Alex K. Y. Jen,[†,§] Seth R. Marder,[‡] and Christine K. Luscombe*[,§]

[†]*Department of Chemistry, University of Washington, Seattle, Washington 98195, United States,* [‡]*School of Chemistry and Biochemistry, Georgia Institute of Technology, Atlanta, Georgia 30332-0400, United States, and* [§]*Department of Material Science and Engineering, University of Washington, Seattle, Washington 98195-2120, United States*

Received October 27, 2010; Revised Manuscript Received December 17, 2010

ABSTRACT: Externally initiated polymerization of 2-bromo-3-hexyl-5-iodothiophene was attempted from four aryl and thiophene based small molecule initiators functionalized with a phosphonate moiety. Initiated poly(3-hexylthiophene) product was obtained in various yields depending on the nature of the initiating molecule. Reaction intermediates for the oxidative addition and the ligand exchange steps were analyzed utilizing both experimental and theoretical methods. It was observed that an *ortho* substituent plays a crucial role in the outcome of the polymerization mechanism and that aryl based initiators are generally more stable than thiophene based initiators. Density functional theory (DFT) calculations revealed the importance of the steric effects on the success of the externally initiated chain growth polymerization mechanism.

Introduction

Conjugated polymers, among these polythiophenes, are an important class of materials in current research field of organic electronics and photovoltaics. Poly(3-hexylthiophene) (P3HT) in particular has attracted much interest in photovoltaic applications due to its desirable electronic and physical properties such as high thermal and environmental stability, high charge-carrier mobility, low optical gap and high solubility.[1−12] Regiocontrolled synthesis of poly(3-alkylthiophenes) was first developed by McCullough[13−15] and Rieke.[16−18] Yokozawa[19,20] and McCullough[21] later pioneered the Kumada catalyst transfer polymerization (KCTP) and the Grignard metathesis (GRIM) technique respectively, which yields highly regioregular polymers with controlled molecular weights, narrow polydispersity index and uniform end groups. The catalytic cycle of the KCTP mechanism begins with the bithiophene initiator which is generated through the transmetalation reaction between two molecules of the grignard functionalized thiophene monomer and $Ni^{II}(dppp)Cl_2$ catalyst.[19,21] The polymerization control is thought to originate from either intramolecular transfer of the Ni catalyst or an associated pair formed by the growing polymer chain and the Ni catalyst. There has been substantial evidence for the propensity of the Ni catalyst to undergo selective intramolecular "ring walking" along conjugated and nonconjugated systems that leads to the desired "one-by-one" addition of monomers to a growing end of the polymer chain.[22−25] The KCTP technique has also been applied to the synthesis of other polymers such as polythiophene-containing block copolymers[26−33] as well as poly(*p*-phenylenes) and polypyrroles.[34−36] A few research groups including ours have succeeded in synthesizing poly(3-hexyl)thiophene (P3HT) directly from external aryl halide initiators both in solution and on the surface.[37−43] Senkovskyy et al. have successfully managed to externally initiate a P3HT polymerization from both small molecules and polymeric supports with the use of a $Ni(PPh_3)_4$ catalyst.[44] Our work, as well as by others mentioned above, indicates that oxidative addition of the aryl halide bond of the initiator to the Ni(0) catalyst (or catalyst precursor) is strongly dependent on the position and the type of functionality on the aryl group. In our previously published work, we observed that the presence of another substituent on the aryl halide initiator dramatically influenced the percent headgroup incorporation of the polymerization. The initiation decreases by at least 50% if such a substituent is an electron-withdrawing group and falls to almost 0% when the functionality is electron donating.[39] We hypothesized that this effect could be attributed to the *para* position of the substituent which renders the Ni initiator/catalyst complex less stable than its unsubstituted counterpart. Work published by Uchida et al.[45] indicated that in formation of aryl−Ni(II) complexes, *ortho*-substitution of the aromatic ligand resulted in a dramatic increase in the stability of the Ni complex. It is believed that the interactions of the *ortho*-substituent with the Ni atom increases the stability of the complex by lowering the energy of the highest occupied molecular orbital (HOMO) through bonding of the d_{xy}-orbitals of Ni with π-orbitals of the aromatic ring. We observed that while the initiation of *ortho*-chlorotoluene proceeds in almost quantitative manner, its *para*-substituted isomer fails to initiate at all, which provides support for this hypothesis.[40] Further experiments performed in our laboratory have indicated that the stabilization of the propagating Ni(II) catalyst−capped polymer by alkyl chains located *ortho* to the terminal Br is a factor in promoting chain-growth polymerization character.[46] Most of the studies on the external initiator performed by our group as well as others, have focused on the thermodynamic effect of the *ortho*-stabilization, however the investigation of the kinetic effects as a result of steric hindrance has not been well-documented. It has been shown that a methyl substituent *ortho* to the halide group on the aryl initiator stabilizes the complex, however the effect of other bulkier substituents in that same position has not been investigated. In fact, much about the intermediate Ni catalyst/initiator complex remains

*Corresponding author. E-mail: luscombe@u.washington.edu.

 Published on Web 01/12/2011 © 2011 American Chemical Society

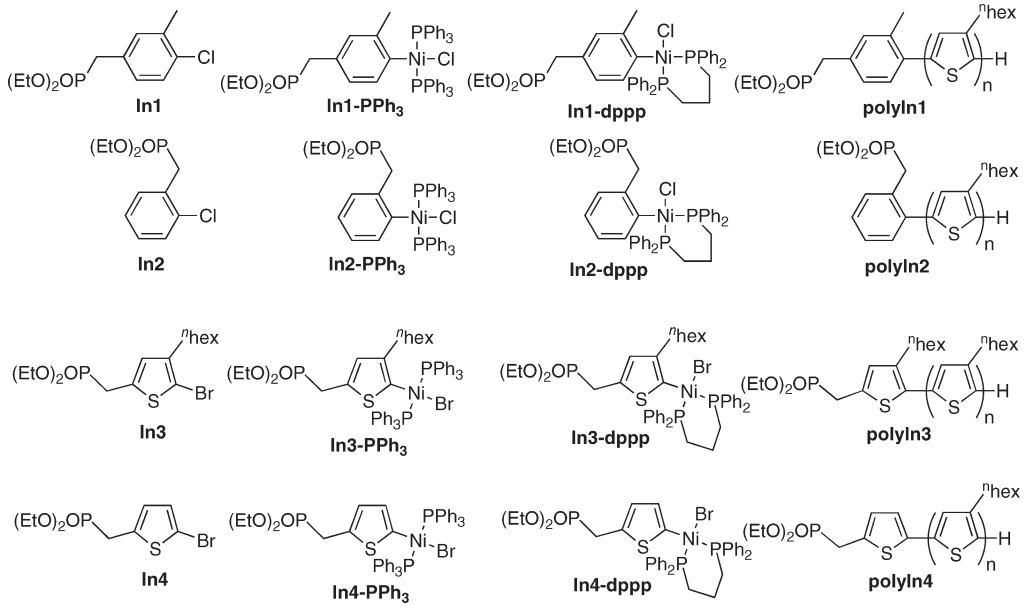
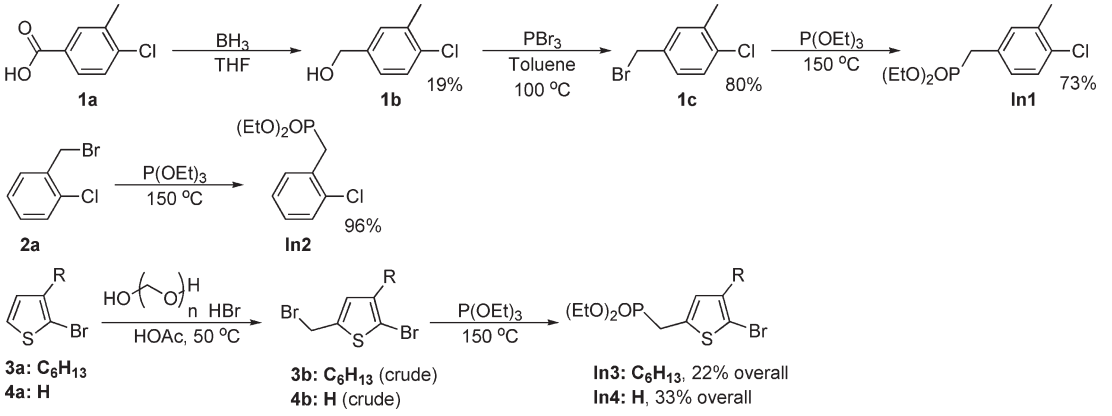


Figure 1. Molecular structures of the initiators, their Ni complexes with PPh_3 and dppp ligands, and the final polymer products.

Scheme 1. Synthesis of Phosphonate Initiators: Diethyl 4-Chloro-3-methylbenzylphosphonate, In1; Diethyl 2-Chlorobenzylphosphonate, In2; Diethyl (5-Bromo-4-hexylthiophen-2-yl)methylphosphonate, In3; and Diethyl (5-Bromothiophen-2-yl)methylphosphonate, In4



speculative as many have not been isolated and thoroughly studied due to their air-sensitive nature. We synthesized several initiators (Figure 1, Scheme 1) in order to study the electronic vs steric interactions and their effect on the chain-growth polymerization mechanism.

The phosphonate functionality on the initiator was chosen for its many potential applications such as the ability to be utilized in Horner−Wadsworth−Emmons reactions and the possibility of deprotection to the phosphonic acid moiety known to form robust monolayers on metal oxides which could possibly be utilized as an anchoring layer for polymer brush synthesis.[47] Therefore, we sought to verify whether we could incorporate such a functionality at the beginning of the polymer chain. It is worthwhile noting that when we have previously attempted P3HT synthesis from an aryl halide inititator with the phosphonate group *para* to the halide, we observed complete degradation of the Ni catalyst/initiator complex and it remained to be investigated whether or not the *ortho* substituent would provide sufficient stabilization to change the polymerization outcome. In order to fully understand which effects are significant in the formation of the nickel catalyst/initiator complex, it is important to know the geometry of this transiently formed complex. Since these materials are air-sensitive and thus difficult to structurally characterize experimentally, DFT modeling was utilized to get insight on the geometry of the intermediate complexes. Geometrical optimizations of the two starting initiators (Scheme 1), **In1** and **In2** and their corresponding nickel catalyst/initiator complexes were performed using Gaussian 09 program. Additionally, the relative energies of the starting initiator (**In1** and **In2**) to their oxidative addition product (**In1PPh$_3$** and **In2PPh$_3$**) were calculated. These theoretical studies combined with experimental results allowed us to elucidate main factors determining the initiator efficiency in the chain-growth polymerization reaction.

Experimental Section

Instrumentation and Materials. ^{1}H NMR spectra were obtained on Bruker AV300, Varian Mercuries Vx 300 and 400, and AV-500 spectrometers using $CDCl_3$ as a solvent (peak position $\delta^1H = 7.27$ ppm) and internal standard of ^{1}H NMR spectra was tetramethylsilane (0.00 ppm). ^{31}P NMR spectra were obtained on Bruker AV300, Varian Mercury Vx400, and AV499 spectrometers with phosphoric acid as the standard. MALDI spectra were recorded on Bruker Autoflex II spectrometer using terthiophene as the sample matrix. Samples were prepared by dissolving 0.5 mg in 100 μL of matrix solution in chloroform and approximately 1.5 μL of this solution was deposited on the plate. The MALDI experiments were performed in the reflecton mode. The % headgroup incorporation was calculated by analyzing

the MALDI−TOF and the NMR spectra. The area under the peaks on the MALDI spectra corresponding to the mass of the polymer with the attached initiator group were divided by the area under all the polymer peaks present and multiplied by 100 to obtain % headgroup incorporation. Molecular weights of polymers were determined using a Waters-1515 gel permeation chromatography (GPC) coupled with UV and RI detectors, in reference of polystyrene standards with THF as the eluent with a flow rate equal to 1 mL/min. GC-MS analyses were performed using a 60 m, 0.32 mm ID, 1.0 μm HP-1 column or a 30 m, 0.32 mm ID, 0.25 μm HP-5MS column, programmed at 70 °C for 2 min, to 300 or 340 at 15 °C/min holding for 20 min. All elemental analyses were done at Atlantic Microlab (Norcross, GA).

All chemicals were purchased from Aldrich, Alfa-Aesar, or TCI and used as received unless otherwise stated. Tetrahydrofuran (THF) and toluene were dried using a solvent drying system from Innovative Technologies. All polymerizations were performed under N_2.

Synthesis of Diethyl 4-Chloro-3-methylbenzylphosphonate (In1). The starting carboxylic acid was reduced to the alcohol by a procedure reported for a similar compound.[48] A mixture of 4-chloro-3-methylbenzoic acid in distilled THF was stirred at 0 °C under N_2 atmosphere. A solution of 1 M borane in THF (1.3 equiv) was added dropwise via an addition funnel and the mixture stirred for 4.5 h. The excess hydride was quenched by addition of water/THF (1:1) mixture, and basification with carbonate/bicarbonate followed. After extraction, **1b** was recovered as orange-colored crystals from toluene (19%). Conversion to **1c** was done by mixing **1b** in dry toluene with phosphorus tribromide under nitrogen at 40 °C, followed by heating to 100 °C for 10 min, then letting cool to room temperature (80% yield). After extraction, conversion to phosphonate proceeded through neat reaction of **1c** with triethyl phosphite at 150 °C under nitrogen (quantitative crude yield). Pure product was obtained in 73% yield after purification through silica plug with ethyl acetate as the eluent. ^{1}H NMR (300 MHz, $CDCl_3$) δ 7.21 (d, J = 8.2 Hz, 1H), 7.12 (dd, J = 2.4, 2.2 Hz, 1H), 7.01 (ddd, J = 8.2, 2.4, 2.2, 1H), 3.98 (dq, J_{H-P} = 8.4, J_{H-H} = 7.1 Hz, 4H), 3.03 (d, J_{H-P} = 21.6 Hz, 2H), 2.30 (s, 3H), 1.21 (t, J = 7.1 Hz, 6H). ^{13}C NMR (75 MHz, $CDCl_3$): δ 136.3, 133.2, 132.5, 130.3, 129.3, 128.6, 62.4, 33.2 (d, J_{C-P} = 138.6 Hz), 20.2, 16.6. ^{31}P NMR (162 MHz, $CDCl_3$): δ 26.6. HRMS: calculated, 276.0682; found, 276.0686. Anal. Calcd: C, 52.09; H, 6.56; Cl, 12.81. Found: C, 51.85; H, 6.67; Cl, 12.58.

Synthesis of Diethyl 2-Chlorobenzylphosphonate (In2). Neat reaction of bromide **2a** with triethyl phosphite (3 equiv) at 150 °C under nitrogen atmosphere overnight was followed by pump off at 60 °C under reduced pressure which resulted in **In2**, a colorless oil in 96% yield which did not require further purification.[49] ^{1}H NMR (300 MHz, $CDCl_3$) δ 7.46−7.38 (m, 1H), 7.37−7.32 (m, 1H), 7.24−7.12 (m, 2H), 4.02 (dq, J_{H-P} = 8.0, J_{H-H} = 7.1 Hz, 4H), 3.34 (d, J_{H-P} = 22.0 Hz, 2H), 1.25 (t, J = 7.1 Hz, 6H). ^{13}C NMR (75 MHz, $CDCl_3$): δ 134.4, 131.9, 130.1, 129.8, 128.5, 127.0, 62.4, 30.9 (d, J_{C-P} = 133 Hz), 16.6. ^{31}P NMR (162 MHz, $CDCl_3$): δ 26.3. HRMS: calculated, 262.0526; found, 262.0518. Anal. Calcd: C, 50.30; H, 6.14; Cl, 13.50. Found: C, 50.16; H, 6.41; Cl, 13.23.

Synthesis of (5-Bromo-4-hexylthiophen-2-yl)methylphosphonate (In3) and (5-Bromothiophen-2-yl)methylphosphonate (In4). The procedure was based on previous reports for the synthesis of **In4**.[50,51] Pure product of **In4** was obtained as lightly yellow colored oil. ^{1}H NMR (400 MHz, $CDCl_3$): δ 6.85 (d, J = 3.7 Hz, 1H), 6.69 (ddt, J = 3.7, 3.7, 0.9 Hz, 1H), 4.05 (dq, J = 7.1, 7.1 Hz, 4H), 3.23 (dd, J_{H-P} = 20.7, J_{H-H} = 0.8 Hz, 2H), 1.26 (t, J = 7.1 Hz, 6H).

Similar conditions were used to obtain **In3** (not previously reported in the literature). The crude phosphonate (a dark brown oil, 58% pure product by GC−MS) was subjected to silica column chromatography with 2% ethanol in DCM, followed by a subsequent column with 1:1 hexane:ethyl acetate as the eluent to afford **In3** as deep orange oil. ^{1}H NMR (300 MHz, $CDCl_3$) δ 6.63 (d, J = 3.6, 1H), 4.10−3.98 (m, 4H), 3.18 (dd, J_{H-P} = 21.7, J_{H-H} = 0.8 Hz, 2H), 2.45 (t, J = 7.6 Hz, 2H), 1.55−1.43 (m, 2H), 1.29−1.21 (m, 12H), 0.84 (t, J = 6.4 Hz, 3H). ^{13}C NMR (75 MHz, $CDCl_3$): δ 142.2, 132.3, 128.7, 122.4, 62.7, 30.8 (d, J_{C-P} = 150 Hz), 29.6, 29.5, 29.0, 27.7, 22.8, 16.6, 14.3. ^{31}P NMR (162 MHz, $CDCl_3$): δ 24.6. HRMS: calculated, 396.0524; found, 396.0507. Anal. Calcd: C, 45.35; H, 6.60; Br, 20.11; S, 8.07. Found: C, 45.52; H, 6.77; Br, 20.19; S, 8.33.

Synthesis of Nickel Catalyst/Initiator Complexes. Phosphonate initiators (15 equiv) were allowed to react with $Ni(PPh_3)_4$ (1 equiv) in 1 mL of toluene overnight in a glovebox environment to form **In1-PPh$_3$** (100%), **In2-PPh$_3$** (39%), **In3-PPh$_3$** (31%) (Figure 1). This step was followed by ligand exchange with dppp (1.5 equiv) for 2−3 h without purification to form **In1-dppp** (100%), **In2-dppp** (21%), **In3-dppp** (26%) also done in the glovebox environment. The complex yields were obtained by analyzing the ^{1}H NMR spectra of the crude reaction mixture. Upon reaction of **In4** with $Ni(PPh_3)_4$ and subsequent ligand exchange with dppp, the Ni/initiator complex underwent rapid decomposition, thus the reaction yields could not be obtained. After the reaction, the complex mixtures were transferred into sealed round-bottom flasks and taken out of the glovebox.

General Polymerization Protocol. The monomer, 2-bromo-3-hexyl-5-iodothiophene, was synthesized according to previously published procedures.[8] Addition of reagents into the reaction flask was carried out via a syringe under a stream of nitrogen. Polymerization was initiated by addition of the crude complex mixture to a solution of 2-bromo-5-chloromagnesio-3-hexylthiophene (30 equiv) which was prepared by the reaction of 2-bromo-3-hexyl-5-iodothiophene with 0.95 equiv of ^{i}PrMgCl at 0 °C in THF for 1 h. After the addition of the complexes, the reaction mixtures were allowed to polymerize for 1 h. After quenching, the solutions were precipitated into methanol and poly(3-hexyl)thiophene products, **polyIn1** (90%), **polyIn2** (78%), and **polyIn3** (69%) were collected via vacuum filtration and analyzed without further purification.

DFT Calculations. Density functional theory (DFT; B3LYP) calculations on the two chosen initiators, **In1** and **In2** as well as two initiator/catalyst complexes **In1-PPh$_3$** and **In2-PPh$_3$** were performed using the Gaussian 09 program.[52] The standard 6-31G* basis set was used for all the atoms except Cl, and Ni, for which 6-31G** and Ahlrichs' valence triple-ζ (VTZ) basis sets were chosen, respectively.[53] Geometry optimization was carried out using tight convergence criteria and an ultrafine integration grid. All calculations were performed assuming a singlet ground state. The optimized structures were verified to be true minima by frequency calculations. The nickel-catalyst binding energies to initiator complexes, $\Delta E_{\text{Ni-initiator}}$, were calculated via

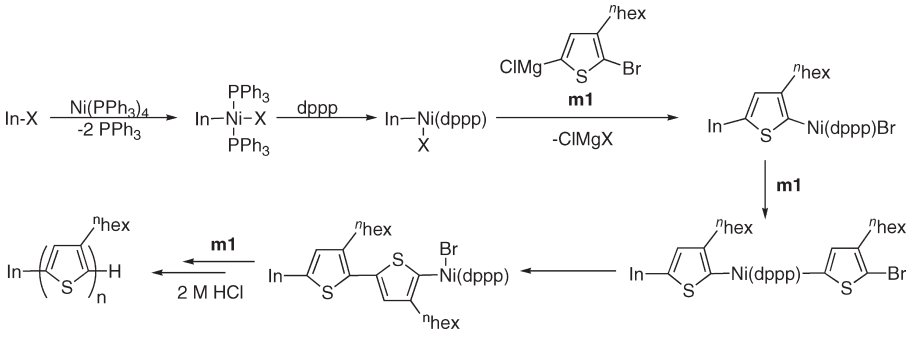
$$\Delta E_{\text{Ni-initiator}} = E_{\text{Ni-initiator complex}} - (E_{\text{initiator}} + E_{\text{Ni catalyst}})$$

where $E_{\text{Ni-initiator complex}}$ is the energy of the catalyst/initiator complex, $E_{\text{initiator}}$ is the energy of the initiator compound, and $E_{\text{Ni catalyst}}$ is the energy of Ni(II) diphosphine catalyst. To facilitate the calculations, the ethyl substituents on the phosphonate groups were replaced by methyl groups.

Results and Discussion

KCTP Reaction Pathway. If the reaction proceeds via a chain-growth polymerization mechanism, the P3HT product will have one set of terminal groups, a low PDI, a molecular weight that can easily be tuned by manipulating catalyst/monomer feed ratio and almost exclusively head to tail regioregularity (~98%).[54] During the "ideal" catalyst transfer polymerization, where one Ni catalyst molecule propagates through one polymer chain with addition of monomer one at a time, after the reaction is quenched with acid, only initiator/H end groups are observed (Scheme 2). However,

Scheme 2. Polymerization Reaction Pathway



undesired chain termination or chain-transfer reactions lead to a variety of end groups such as initiator/Br if the catalyst reductively eliminates from the polymer chain before complete conversion of the monomer is reached or H/Br, H/H, and Br/Br groups which result from the step-growth polymerization catalyzed by the various Ni species in the solution.[38] The externally initiated P3HT synthesis pathway begins with the oxidative addition of the aryl halide initiator to the $Ni(PPh_3)_4$ catalyst where the halide group is either chlorine or bromine. The oxidative addition step is followed by a ligand exchange with dppp: we have previously shown this ligand exchange procedure to yield fully regioregular P3HT from an externally added *o*-chlorotoluene initiator with controlled molecular weights and extremely narrow polydispersities (Scheme 2). The final step is the addition of the Grignard-functionalized 2-bromo-3-hexylthiophene monomer that initiates the polymerization.

^{31}P NMR Studies. The intermediates in the KCTP reaction of the four initiators were monitored via ^{31}P NMR spectroscopy. After the addition of $Ni(PPh_3)_4$, the ^{31}P NMR spectrum (Figure 2) shows a sharp peak at 19 ppm, consistent with *trans*-chloro-(3-methylbenzylphosphonate)bis(triphenylphosphine)nickel(II) complex (**In1-PPh$_3$**).[55] The peak at 24 ppm corresponds to the phosphonate group on the starting **In1** which was present in a 15 equivalent excess in the reaction mixture. The remaining peak at 26 ppm is attributed to the phosphonate group in **In1-PPh$_3$** complex. Addition of 1.5 equivalents of dppp resulted in rapid ligand subsitution to form the thermodynamically favored *cis*-chloro(3-methylbenzylphosphonate)(dppp)nickel(II)complex, (**In1-dppp**). The formation and the geometry of this complex were confirmed by the appearance of two sets of doublets at 18 ppm and −6 ppm (which is obscured by the peak of liberated PPh_3). A peak corresponding to $Ni(dppp)_2$ was also observed at 11 ppm. The ^{1}H NMR spectra of **In1-PPh$_3$** and **In1-dppp** show that the oxidative addition and ligand exchange reactions proceed to completion resulting in 100% yield of desired complexes.

The ^{31}P NMR spectrum of **In2-PPh$_3$** (Figure S2, Supporting Information), also confirms the successful formation of the *trans*-chloro(diethylbenzylphosphonate)nickel(II) complex via the presence of the PPh_3 peak which is slightly shifted possibly due to the coordination of the nickel with the nearby oxygen atom. The phosphonate groups of **In2-PPh$_3$** and of excess **In2** are present at 26 and 24 ppm respectively. After the addition of dppp, the two sets of doublets corresponding to the *cis* complex **In2-dppp** are observed at +19 and −7 ppm. The PPh_3 peak of **In2-PPh$_3$** is still present, which indicates that the ligand reaction did not reach completion in the allotted reaction time frame. The peak for $Ni(dppp)_2$ is also larger suggesting partial dissociation of the Ni catalyst from initiator/catalyst complex and its subsequent chelation by

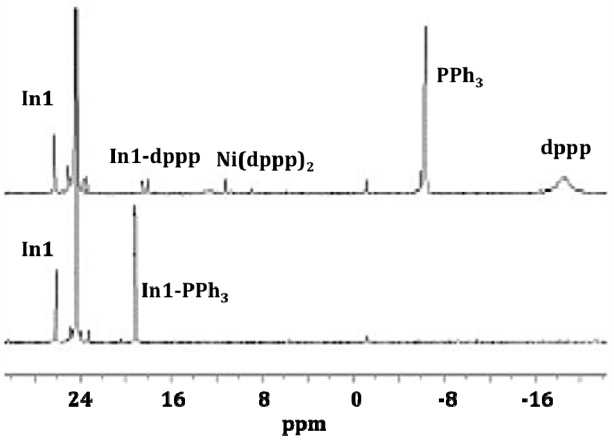
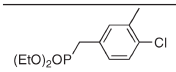
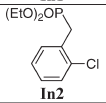
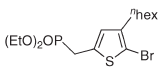


Figure 2. ^{31}P spectra of nickel(II) complexes in toluene: (top) **In1-dppp**; (bottom) **In1-PPh$_3$**.

dppp. Analysis of the ^{1}H NMR spectrum of **In2-PPh$_3$** reveals that the oxidative addition reaction did not proceed to completion as seen by two sets of peaks corresponding to the protons nearest to the reaction center. The yield of the oxidative addition adduct, which is obtained through integration of both peaks, is calculated to be 39%. After the addition of dppp, ^{1}H NMR data confirms only partial ligand exchange as evidenced by a set of three peaks. The analysis of the final mixture after oxidative addition and ligand exchange steps reveals the following species containing the initiator molecule: **In2** (58%), **In2-PPh$_3$** (21%), and **In2-dppp** (21%). $Ni(dppp)_2$ is present as well, however it is difficult to quantify with ^{1}H NMR. The ^{31}P NMR spectrum of **In3-PPh$_3$** (Figure S3, Supporting Information) indicates the presence of the *trans*-bromo(4-hexylthiophen-2-yl methyl phosphonate)nickel(II) complex. The phosphine peak of the complex appears in the region of 19 ppm while the phosphonate groups of **In3-PPh$_3$** and **In3** are present at 25 and 23 ppm respectively. An additional peak is observed at 21 ppm that could correlate to the phosphine peak where the thiophene ring is coordinating to the Ni complex. After the addition of dppp, the characteristic set of doublets can be seen at +16 and −5 ppm. Additional peaks are present between the phosphonate groups of **In3** and **In3-PPh$_3$** (22−24 ppm) that are attributed to the nickel species where the thiophene ring is coordinating to the metal center. ^{1}H NMR spectra reveals incomplete conversion of the original initiator into the desired oxidative adduct with the complex yield of **In3-PPh$_3$** determined to be 31%. However, the ligand exchange goes almost to completion evidenced by the lack of **In3-PPh$_3$** peak. The **In3-dppp** complex yield was calculated to be 26% over the two steps. **In4** has proved to be the least

Table 1. Overview of Results from the Polymerization Reactions of polyIn1, polyIn2, and polyIn3

Initiator	End Groups	M_n (Da)^{GPC} M_n (Da)^{NMR} (PDI) Yield	% Regioregularity	% Head-group incorporation
 **In1**	Initiator/H (75%) Initiator/^{i}Pr (9%) H/H (13%) Others (3%)	5200 4900 (1.2) 90%	94	84
 **In2**	Initiator/H (37%) Initiator/^{i}Pr (8%) H/H (47%) Others (8%)	3900 3600 (1.6) 78%	92	45
 **In3**	Initiator/H (18%) Initiator/Br (9%) H/Br (65%) H/H (8%)	2900 2000 (2.6) 69%	89	27

stable of the initiators. Upon addition of the $Ni(PPh_3)_4$ to the initiator, a white precipitate, likely being a mixture of Ni(II) halide salts and other decomposition products, was observed in the reaction mixture after a short period of time. The ^{31}P NMR analysis revealed the presence of only the starting material **In4** which was in excess. Since the desired **In4-PPh$_3$** and **In4-dppp** initiating complexes and consequently **polyIn4** are not formed with this thiophene molecule, this initiator was not included in further studies. The disproportionation reaction likely arises from the lack of a substituent in the *ortho* position. Since the aromatic stabilization of thiophene is already weak (less than half of benzene),[56] we speculate that in the absence of favorable interactions between the thiophene π system and the nickel d-orbitals the reacting species decompose rapidly.

Polymerization Results. The results of varying initiators on the polymer end groups and molecular weight are summarized in Table 1.

The use of **In1** has afforded a polymer with a good % headgroup incorporation, a molecular weight that is close to the calculated M_n and narrow PDI all of which indicate the predominance of a chain growth polymerization mechanism. Various end groups are observed such as initiator/H, initiator/^{i}Pr, and H/H. Other extremely small peaks in the MALDI−TOF spectrum could not be identified and are likely polymers with a fragmented initiator group. The initiator/^{i}Pr groups are likely to arise from a minor mismatch between the relative amounts of **m1** and ^{i}PrMgCl solution because of difficulties in precisely measuring very small volumes of ^{i}PrMgCl solution and its high sensitivity to the moisture and air. Despite a reaction time of only 1 h in order to avoid precipitation of P3HT at high conversion, the molecular weight determined by SEC (5200 Da) is very close to the calculated molecular weight (5224 Da) of the 30 unit 3-hexyl thiophene chain. The molecular weight calculated via NMR agrees quite well with the molecular weight determined by SEC showing a polymer with 30 monomer repeat units is indeed obtained in such a short reaction time. The PDI value of 1.2 is much lower than the PDI values for initiated P3HT using other ligands,[39] which shows the more controlled polymerization mechanism with the dppp ligand. As previously mentioned, ealier attempts of initiating a polymerization from a *para*-substituted benzylphosphonate molecule have failed and were attributed to the destabilization of the Ni catalyst by the phosphonate moiety. These polymerization results illustrate both the importance of the *ortho*-substituent and the possibility of introducing a phosphonate functionality with numerous potential applications onto the polymer chain. In agreement to the expected trend based on the ^{31}P NMR and ^1H NMR spectra as well as calculated complex

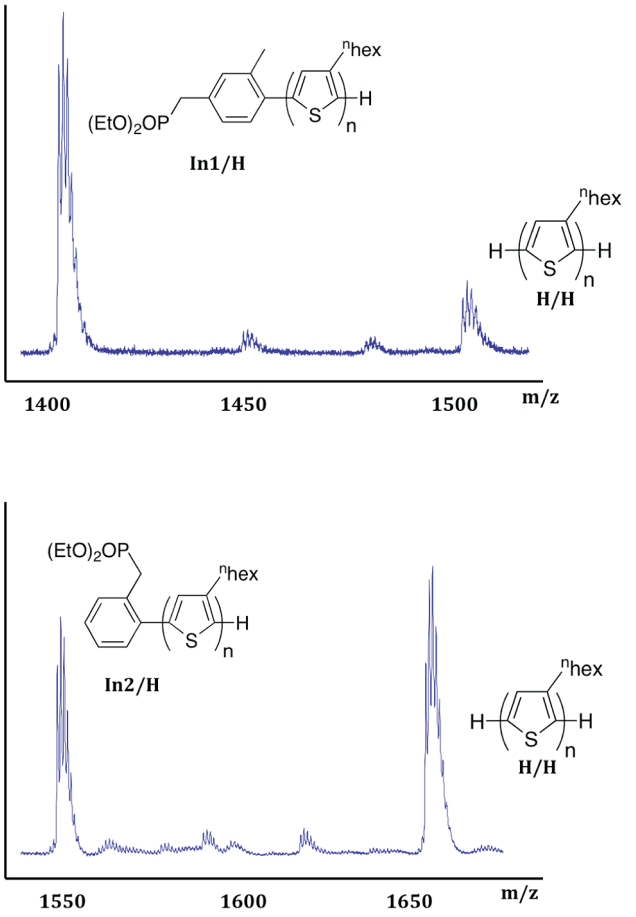


Figure 3. MALDI−TOF spectra of **polyIn1** (top) and **polyIn2** (bottom).

yields, **polyIn2** shows higher % headgroup incorporation than **polyIn3** (45% vs 27%). The end group distribution of **polyIn2** is similar to those for **polyIn1** albeit with a higher percentage of H/H (Figure 3). As previously mentioned, the final mixture composition before the monomer addition contained **In2**, **In2-PPh$_3$**, and **In2-dppp** with the total percentage of catalytically active species equal to 41%. Both **In2-PPh$_3$** and **In2-dppp** are able to initiate the polymerization, however the major difference between the two species is how long the Ni catalyst can propagate through the polymer chain. As evidenced in our previous work, Ni with PPh_3 ligand tends to reductively eliminate much faster than the catalyst with the dppp ligand.[38−40] Once the Ni catalyst leaves the polymer chain, it begins linking monomer units in a random step growth fashion, without the intramolecular reinsertion into the same polymer chain that is inherent to the KCTP mechanism, which results in the H/H terminated P3HT product. Thus, the % headgroup incorporation is very similar to the total amount of complexed initiator/catalyst species (45% vs 41%), however, the tendency of $Ni(PPh_3)_2$ species to quickly undergo reductive elimination results in a higher fraction of H/H polymer.

The major end groups of **polyIn3** such as H/Br and H/H indicate significant occurrence of chain-termination and chain-transfer processes that are common to a non-initiated step-growth polymerization mechanism. Lower molecular weights (3900 and 2900 Da) as well as higher PDIs (1.6 and 2.6) reflect the decreasing chain-growth character and increasing step-growth character of the polymerizations from **In2** and **In3**. The lowest % headgroup incorporation

from **In3** is supported by ^{1}H NMR data which reveals a low yield of the desired catalytic complex (26%). Thiophene is known to bond to metals in several different configurations in organometallic complexes.[57,58] It can bond through the aromatic π-system of the thiophene ring (η^5 configuration) or through the S atom as a weak Lewis base. Alternatively, the thiophene ring may pucker and the bonding can occur through the four carbon atoms (η^4 configuration) with the sulfur out of plane of the C_4 system. It was also previously demonstrated that thiophene initially coordinates to a platinium bisalkylphosphine fragment through the C−C double bond (η^2 configuration) through the π-backbonding from the metal d_{xy}-orbital to a thiophene C−C π*-orbital.[59] Other d^8 metals such as nickel and palladium are known to form thiophene metallocycle complexes which exist in equilibrium with thiophenic bridged dinuclear complexes and free thiophene.[60] In that case, the bonding interactions result from the donation of electron density from the HOMO of the Ni(dmpe) fragment into the LUMO of the thiophene fragment and back-donation from the HOMO of the thiophene into the LUMO of the metal fragment. Since donation of electron density from the metal to the thiophene ligand is the main factor in this coordination mechanism, it is reasonable to speculate that the strongly electron-withdrawing phosphonate group leaves the thiophene π-system electron deficient thus promoting the formation of the coordinated complex. We believe that the coordination of the nickel to the thiophene ring prevents the formation of **In3-PPh$_3$**, which decreases headgroup incorporation into the polymer chain.

Molecular Modeling and Binding Energies. In order to investigate the effects that may have played a role in the decrease in the initiation of **In2** as compared to **In1**, the geometries of both compounds as well as their corresponding oxidative adducts **In1-PPh$_3$** and **In2-PPh$_3$** were modeled with the Gaussian 09 program. Initially, the potential energies of the optimized structures of **In1-PPh$_3$** and **In2-PPh$_3$** were calculated and compared (for this purpose, a methyl substituent was added to the *para* position of **In2-PPh$_3$** in order to keep the equivalent number of atoms). It is interesting to note that changing the substituent at the *ortho* position of the initiator from a methyl group to the phosphonate group has no effect on the potential energy value of the molecule leading to the conclusion that both substituents offer similar degree of electronic stability to the nickel(II) complex. Therefore, it is likely that kinetic effects are responsible for the decrease in initiation. To test this hypothesis, the energies for the formation of **In1-PPh$_3$** and **In2-PPh$_3$** from the starting reaction components of **In1** and **In2** and Ni(PPh$_3$)$_2$ were calculated. If electronic effects played a determining role in the reaction mechanism, the binding energy of the complex with the more favorable substituent would be more exothermic. The energy of complexation of **In1** with Ni(PPh$_3$)$_2$, ΔE_1 was calculated to be −36.27 kcal/mol while the energy of the complexation of **In2** with the Ni catalyst, ΔE_2 afforded a very similar value with a negligible difference of less than 1 kcal. These values are similar to other reported values for the energy of formation for nickel complexes.[61] This shows that both reactions are equally spontaneous in agreement with the hypothesis that the effects on the decreased % headgroup incorporation are more likely due to kinetic effects rather than electronic effects. Optimized molecular structures of the starting compounds and the complexes are shown in Figures 4 and 5, respectively. Selected bond distances and angles are given in Tables 2 and 3. Compounds **In1** and **In2** have very similar C_1−Cl bond distances of *ca.* 1.763 Å. The bond angles are

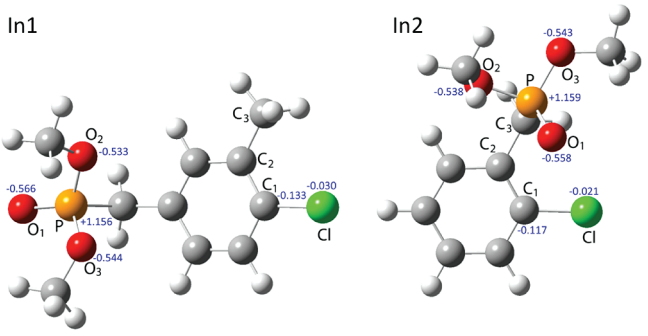


Figure 4. DFT-optimized structures and atom labeling for **In1** (left) and **In2** (right). Mulliken charges for the selected atoms are indicated in blue.

rather similar as well. Both catalyst-initiator complexes **In1-PPh$_3$** and **In2-PPh$_3$** have slightly distorted square planar geometries especially for **In2-PPh$_3$** where the angles slightly deviate from the expected 90°. In terms of bond length, the Ni(II) coordination site is also similar in both complexes. However, in **In2-PPh$_3$**, the oxygen atom of the *ortho*-phosphonate functionality on the aryl ligand comes to close proximity to the Ni(II) fifth coordination site. This structural feature might play a determining role in polymerization outcome, as outlined below.

There are at least two possible explanations how steric effects could inhibit the % headgroup incorporation for **In2-PPh$_3$**, one of which is the possible coordination of the oxygen atom of the phosphonate group to the Ni metal center, inhibiting reaction with an incoming ligand. There have been numerous reports of the P═O group coordinating to the metal center via the oxygen atom[62−75] particularly when the two are in close proximity to each other such as the case with **In2-PPh$_3$** where the Ni···O distance is 3.443 Å. Such binding would inhibit the dppp ligand exhange reaction as was observed in the ^{31}P NMR and ^{1}H NMR, where there was significant amount of **In2-PPh$_3$** remaining after the addition of 1.5 equiv of dppp. Since the dppp and PPh$_3$ ligand exchange occurs via an associative mechanism, as do a vast majority of ligand exchanges for the d^{10} metals,[76,77] a five-coordinate Ni complex would lack an available site that would facilitate the ligand exchange. Thus, a significant fraction of **In2-PPh$_3$** complex remains behind leading to a higher yield of step-growth polymer. It should be noted, however, that the DFT modeling of the **In2-PPh$_3$** complex showed that the phosphonate functionality can accept different orientations around the C_3−P_1 bond. The geometry optimization initiated with different starting geometries for the **In2-PPh$_3$** complex, led to stable structures with different phosphonate group orientations, where the oxygen atom was either in close proximity to the Ni center as shown in Figure 5, or turned away from the Ni. These structures were found to be less than 0.5 kcal/mol from each other. Thus, it is plausible that in solution, an average ensemble of these conformations exist allowing ligand exchange to take place, which was observed experimentally.

A second possible explanation is that a bulky phosphonate group *ortho* to the initiation site may affect the kinetics of the oxidative addition reaction. Kochi and others have shown that the mechanism of oxidative addition reaction of nickel(0) complexes with aromatic halides is quite complex and can involve multiple Ni(I) and Ni(II) species depending on the nature of the aryl halide and it was found that the mechanism involves several steps.[78,79] The first step is the equilibrium formation of the coordinatively unsaturated NiL$_3$ from NiL$_4$ (eq 1), with the ligand studied in this case being L = PEt$_3$.

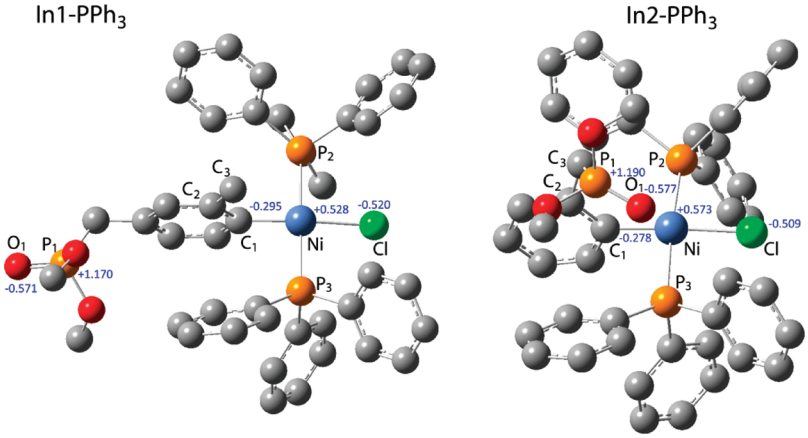


Figure 5. Top-view of the DFT-optimized structures of **In1-PPh$_3$** (left) and **In2-PPh$_3$** (right) showing Ni(II) coordination site (hydrogen atoms have been omitted for clarity). Mulliken charges for the selected atoms are indicated in blue.

Table 2. Selected Bond Lengths, Atom Distances, and Bond Angles for In1 and In2

	bond length/atom distance (Å)	
bond of interest	**In1**	**In2**
C_1-Cl	1.764	1.763
C_2-C_3	1.508	1.510
$P-O_1$	1.487	1.485
$C_3\cdots Cl$	3.094	3.139
$O_1\cdots Cl$	8.513	3.943
	bond angles (deg)	
angle of interest	**In1**	**In2**
$\angle ClC_1C_2$	119.8	120.7
$\angle C_1C_2C_3$	122.3	123.1

Table 3. Selected Bond Lengths, Atom Distances, and Bond Angles for the Ni(II) Complexes In1-PPh$_3$ and In2-PPh$_3$

	bond length/atom distance (Å)	
bond of interest	**In1-PPh$_3$**	**In2-PPh$_3$**
Ni−Cl	2.278	2.279
$Ni-C_1$	1.895	1.897
$Ni-P_2$	2.296	2.283
$Ni-P_3$	2.294	2.342
C_2-C_3	1.512	1.519
P_1-O_1	1.488	1.492
$C_3\cdots Ni$	3.295	3.395
$O_1\cdots Ni$	8.738	3.443
	bond angles (deg)	
angle of interest	**In1-PPh$_3$**	**In2-PPh$_3$**
$\angle C_1NiCl$	170.1	172.9
$\angle P_2NiP_3$	179.6	174.1
$\angle ClNiC_1C_2$	176.3	164.6

This step is followed by the slow rate-limiting electron transfer in eq 2 to afford an ion pair indicated in brackets. Cage collapse affords oxidative adduct in eq 3.

$$NiL_4 \leftrightarrows NiL_3 + L \quad (K_1) \tag{1}$$

$$Ni^0L_3 + ArX \rightarrow [Ni^IL_3ArX^-] \quad (k_2) \tag{2}$$

$$[Ni^IL_3ArX^-] \rightarrow ArNi^{II}XL_2 + L \tag{3}$$

They showed that the triphenylphosphine ligand is more highly dissociated and is less readily oxidized than the triethylphosphine ligand. Thus under comparable conditions, the reaction of aryl halides with $Ni(PPh_3)_3$ is significantly slower than that with $Ni(PEt_3)_3$.[80] Also, Kochi et al. have carried out a study of the steric effects from *ortho*-methyl substitution on the reaction of nickel(0) with bromobenzene in toluene solution and found that addional steric bulk from the substituents results in the decrease of the rate constant for the rate determining step (RDS).[79] Taking all of the above information into the account, it is reasonable to draw a conclusion that the phosphonate substituent in such close proximity to the reaction site, decreases the rate of the reaction. Since the two complexes are allowed to react for exactly the same time, the decreased rate constant for the **In2-PPh$_3$** reaction results in lower yield of the oxidative addition product as evidenced by ^{1}H NMR which would result in decreased % headgroup incorporation.

Conclusions

In this work, poly(3-hexylthiophene) was externally initiated from aryl and thiophene halide molecules with an attached phosphonate functional group with varying % headgroup incorporation. Attempts of polymerization from a *para*-phosphonate substituted aryl halide initiator were made in our previous work and proved unsuccessful.[39] These current findings further emphasize the importance of a stabilizing *ortho*-substituent on the success of the initiation of a KCTP reaction. Thiophene based initiator, **In4**, lacking a hexyl chain in the 3-position failed to form the desired oxidative adduct upon its reaction with the nickel catalyst, suggesting rapid decomposition of the reactant likely due to its weak aromatic stabilization and the lack of a stabilizing group. ^{31}P NMR studies of initiators **In1**−**In3** showed peaks attributed to desired products of oxidative addition and ligand exchange steps in addition to a few side product peaks. **In1** provided the best results, with the highest % headgroup incorporation of 84%, a molecular weight close to the calculated M_n and a narrow PDI which all pointed to a chain-growth mechanism and is considered the most promising initiator in this study. **In2** and **In3** resulted in a mixture of chain-growth and step-growth polymerization products. **In2** performed better than **In3** with % incorporation of 45% and 27% respectively. The poor yield of initiated polymer from the **In3** initiator was attributed to the nickel metal center coordinating to the thiophene ring and inhibiting its ability to undergo the crucial intermolecular transfer step. The difference in initiation efficiencies between **In1** and **In2** was suggested to originate primarily from the steric effects. The proximity of the phosphonate group to the oxidative addition site was speculated to promote oxygen atom coordination to the nickel preventing it from undergoing the dppp ligand exchange

and also to slow down kinetics of the reaction both contributing to decreased % headgroup incorporation.

Acknowledgment. This work was supported by the NSF (STC-MDITR DMR 0120967, MRSEC-GEMSEC DMR 0520567, CAREER Award DMR 0747489), and the Office of Science DOE Energy Frontier Research Center for Interface Science: Solar Electric Materials (DE-SC0001084).

Supporting Information Available: MALDI−TOF spectra of **polyIn1**, **polyIn2**, and **polyIn3**, ^{31}P NMR spectra of **In1-PPh$_3$**, **In2-PPh$_3$**, **In3-PPh$_3$**, **In1-dppp**, **In2-dppp**, and **In3-dppp**, and Cartesian coordinates of the DFT models. This material is available free of charge via the Internet at http://pubs.acs.org

References and Notes

(1) Bao, Z. N.; Lovinger, A. J. *Chem. Mater.* **1999**, *11*, 2607.
(2) Gunes, S.; Neugebauer, H.; Sariciftci, N. S. *Chem. Rev.* **2007**, *107*, 1324.
(3) Iovu, M. C.; Jeffries-El, M.; Sheina, E. E.; Cooper, J. R.; McCullough, R. D. *Polymer* **2005**, *46*, 8582.
(4) Loewe, R. S.; Khersonsky, S. M.; McCullough, R. D. *Adv. Mater.* **1999**, *11*, 250.
(5) Ma, W.; Yang, C.; Gong, X.; Lee, K.; Heeger, A. J. *Adv. Funct. Mater.* **2005**, *15*, 1617.
(6) McCullough, R. D. *Adv. Mater.* **1998**, *10*, 93.
(7) McCullough, R. D.; Lowe, R. D. *J. Chem. Soc., Chem. Commun.* **1992**, 70.
(8) Miyakoshi, R.; Yokoyama, A.; Yokozawa, T. *J. Am. Chem. Soc.* **2005**, *127*, 17542.
(9) Reyes-Reyes, M.; Kim, K.; Carroll, D. L. *Appl. Phys. Lett.* **2005**, 87.
(10) Sacco, A.; Mastrorilli, P. *J. Chem. Soc., Dalton Trans.* **1994**, 2761.
(11) Sirringhaus, H.; Brown, P. J.; Friend, R. H.; Nielsen, M. M.; Bechgaard, K.; Langeveld-Voss, B. M. W.; Spiering, A. J. H.; Janssen, R. A. J.; Meijer, E. W.; Herwig, P.; De Leeuw, D. M. *Nature* **1999**, *401*, 685.
(12) Sontag, S. K.; Marshall, N.; Locklin, J. *Chem. Commun.* **2009**, 3354.
(13) Loewe, R. S.; Ewbank, P. C.; Liu, J. S.; Zhai, L.; McCullough, R. D. *Macromolecules* **2001**, *34*, 4324.
(14) McCullough, R. D.; Lowe, R. D.; Jayaraman, M.; Anderson, D. L. *J. Org. Chem.* **1993**, *58*, 904.
(15) Sheina, E. E.; Liu, J. S.; Iovu, M. C.; Laird, D. W.; McCullough, R. D. *Macromolecules* **2004**, *37*, 3526.
(16) Chen, T. A.; Obrien, R. A.; Rieke, R. D. *Macromolecules* **1993**, *26*, 3462.
(17) Chen, T. A.; Rieke, R. D. *J. Am. Chem. Soc.* **1992**, *114*, 10087.
(18) Chen, T. A.; Wu, X. M.; Rieke, R. D. *J. Am. Chem. Soc.* **1995**, *117*, 233.
(19) Miyakoshi, R.; Yokoyama, A.; Yokozawa, T. *J. Polym. Sci., Part A* **2008**, *46*, 753.
(20) Yokoyama, A.; Miyakoshi, R.; Yokozawa, T. *Macromolecules* **2004**, *37*, 1169.
(21) Iovu, M. C.; Sheina, E. E.; Gil, R. R.; McCullough, R. D. *Macromolecules* **2005**, *38*, 8649.
(22) Beryozkina, T.; Senkovskyy, V.; Kaul, E.; Kiriy, A. *Macromolecules* **2008**, *41*, 7817.
(23) Zenkina, O. V.; Karton, A.; Freeman, D.; Shimon, L. J. W.; Martin, J. M. L.; van der Boom, M. E. *Inorg. Chem.* **2008**, *47*, 5114.
(24) Lanni, E. L.; McNeil, A. J. *J. Am. Chem. Soc.* **2009**, *131*, 16573.
(25) Lanni, E. L.; McNeil, A. J. *Macromolecules* **2010**, *43*, 8039.
(26) Iovu, M. C.; Craley, C. R.; Jeffries-El, M.; Krankowski, A. B.; Zhang, R.; Kowalewski, T.; McCullough, R. D. *Macromolecules* **2007**, *40*, 4733.
(27) Jeffries-El, M.; Sauve, G.; McCullough, R. D. *Adv. Mater.* **2004**, *16*, 1017.
(28) Ohshimizu, K.; Ueda, M. *Macromolecules* **2008**, *41*, 5289.
(29) Richard, F.; Brochon, C.; Leclerc, N.; Eckhardt, D.; Heiser, T.; Hadziioannou, G. *Macromol. Rapid Commun.* **2008**, *29*, 885.
(30) Urien, M.; Erothu, H.; Cloutet, E.; Hiorns, R. C.; Vignau, L.; Cramail, H. *Macromolecules* **2008**, *41*, 7033.
(31) Zhang, Y.; Tajima, K.; Hirota, K.; Hashimoto, K. *J. Am. Chem. Soc.* **2008**, *130*, 7812.
(32) Tu, G.; Li, H.; Forster, M.; Heiderhoff, R.; Balk, L. J.; Sigel, R.; Scherf, U. *Small* **2007**, *3*, 1001.
(33) Van den Bergh, K.; Huybrechts, J.; Verbiest, T.; Koeckelberghs, G. *Chem.—Eur. J.* **2008**, *14*, 9122.
(34) Adachi, I.; Miyakoshi, R.; Yokoyama, A.; Yokozawa, T. *Macromolecules* **2006**, *39*, 7793.
(35) Huang, L.; Wu, S. P.; Qu, Y.; Geng, Y. H.; Wang, F. S. *Macromolecules* **2008**, *41*, 8944.
(36) Stefan, M. C.; Javier, A. E.; Osaka, I.; McCullough, R. D. *Macromolecules* **2009**, *42*, 30.
(37) Beryozkina, T.; Boyko, K.; Khanduyeva, N.; Senkovskyy, V.; Horecha, M.; Oertel, U.; Simon, F.; Stamm, M.; Kiriy, A. *Angew. Chem., Int. Ed.* **2009**, *48*, 2695.
(38) Bronstein, H.; Luscombe, C. K. *J. Am. Chem. Soc.* **2009**, *131*, 12894.
(39) Doubina, N.; Ho, A.; Jen, A. K. Y.; Luscombe, C. K. *Macromolecules* **2009**, *42*, 7670.
(40) Doubina, N.; Stoddard, M.; Bronstein, H.; Jen, A. K. Y.; Luscombe, C. K. *Macromol. Chem. Phys.* **2009**, *210*, 1966.
(41) Khanduyeva, N.; Senkovskyy, V.; Beryozkina, T.; Bocharova, V.; Simon, F.; Nitschke, M.; Stamm, M.; Grotzschel, R.; Kiriy, A. *Macromolecules* **2008**, *41*, 7383.
(42) Khanduyeva, N.; Senkovskyy, V.; Beryozkina, T.; Horecha, M.; Stamm, M.; Uhrich, C.; Riede, M.; Leo, K.; Kiriy, A. *J. Am. Chem. Soc.* **2009**, *131*, 153.
(43) Smeets, A.; Van den Bergh, K.; De Winter, J.; Gerbaux, P.; Verbiest, T.; Koeckelberghs, G. *Macromolecules* **2009**, *42*, 7638.
(44) Senkovskyy, V.; Khanduyeva, N.; Komber, H.; Oertel, U.; Stamm, M.; Kuckling, D.; Kiriy, A. *J. Am. Chem. Soc.* **2007**, *129*, 6626.
(45) Hidai, M.; Kashiwag., T; Ikeuchi, T.; Uchida, Y. *J. Organomet. Chem.* **1971**, *30*, 279.
(46) Boyd, S.; Jen, A. K. Y.; Luscombe, C. K. *Macromolecules* **2009**, *42*, 9387.
(47) Paramonov, P. B.; Paniagua, S. A.; Hotchkiss, P. J.; Jones, S. C.; Armstrong, N. R.; Marder, S. R.; Bredas, J. L. *Chem. Mater.* **2008**, *20*, 5131.
(48) Kelley, J. L.; Linn, J. A.; Selway, J. W. T. *J. Med. Chem.* **1989**, *32*, 1757.
(49) Franke, A.; Frickel, F. F.; Schlecker, R.; Thieme, P. C. *Synthesis* **1979**, 712.
(50) Jiang, X.; Yang, X. C.; Zhao, C. Z.; Jin, K.; Sun, L. C. *J. Phys. Chem. C* **2007**, *111*, 9595.
(51) Mamane, V.; Ledoux-Rak, I.; Deveau, S.; Zyss, J.; Riant, O. *Synthesis* **2003**, 455.
(52) Frisch, M. J.; Trucks, G. W.; Schlegel, H. B.; Scuseria, G. E.; Robb, M. A.; Cheeseman, J. R.; Scalmani, G.; Barone, V.; Mennucci, B.; Petersson, G. A.; Nakatsuji, H.; Caricato, M.; Li, X.; Hratchian, H. P.; Izmaylov, A. F.; Bloino, J.; Zheng, G.; Sonnenberg, J. L.; Hada, M.; Ehara, M.; Toyota, K.; Fukuda, R.; Hasegawa, J.; Ishida, M.; Nakajima, T.; Honda, Y.; Kitao, O.; Nakai, H.; Vreven, T.; Montgomery, J., J., A.; Peralta, J. E.; Ogliaro, F.; Bearpark, M.; Heyd, J. J.; Brothers, E.; Kudin, K. N.; Staroverov, V. N.; Kobayashi, R.; Normand, J.; Raghavachari, K.; Rendell, A.; Burant, J. C.; Iyengar, S. S.; Tomasi, J.; Cossi, M.; Rega, N.; Millam, J. M.; Klene, M.; Knox, J. E.; Cross, J. B.; Bakken, V.; Adamo, C.; Jaramillo, J.; Gomperts, R.; Stratmann, R. E.; Yazyev, O.; Austin, A. J.; Cammi, R.; Pomelli, C.; Ochterski, J. W.; Martin, R. L.; Morokuma, K.; Zakrzewski, V. G.; Voth, G. A.; Salvador, P.; Dannenberg, J. J.; Dapprich, S.; Daniels, A. D.; Farkas, O.; Foresman, J. B.; Ortiz, J. V.; Cioslowski, J.; Fox, D. J. *Gaussian 09, Revision A.02*, Gaussian, Inc.: Wallingford, CT, 2009.
(53) Bauernschmitt, R.; Ahlrichs, R. *Chem. Phys. Lett.* **1996**, *256*, 454.
(54) Yokoyama, A.; Yokozawa, T. *Macromolecules* **2007**, *40*, 4093.
(55) Zeller, A.; Herdtweck, E.; Strassner, T. *Eur. J. Inorg. Chem.* **2003**, 1802.
(56) Huntley, D. R.; Mullins, D. R.; Wingeier, M. P. *J. Phys. Chem.* **1996**, *100*, 19620.
(57) Angelici, R. J. *Coordin. Chem. Rev.* **1990**, *105*, 61.
(58) Rauchfuss, T. B. *Prog. Inorg. Chem.* **1991**, *39*, 259.
(59) Atesin, T. A.; Jones, W. D. *Organometallics* **2008**, *27*, 53.
(60) Atesin, T. A.; Oster, S. S.; Skugrud, K.; Jones, W. D. *Inorg. Chim. Acta* **2006**, *359*, 2798.
(61) Craciun, R.; Vincent, A. J.; Shaughnessy, K. H.; Dixon, D. A. *Inorg. Chem.* **2010**, *49*, 5546.

(62) Chandrasekhar, V.; Azhakar, R.; Senapati, T.; Thilagar, P.; Ghosh, S.; Verma, S.; Boomishankar, R.; Steiner, A.; Kogerler, P. K. *Dalton Trans*. **2008**, 1150.
(63) Gahagan, M.; Mackie, R. K.; Colehamilton, D. J.; Cupertino, D. C.; Harman, M.; Hursthouse, M. B. *J. Chem. Soc., Dalton Trans*. **1990**, 2195.
(64) Grushin, V. V. *Chem. Rev*. **2004**, *104*, 1629.
(65) Heinicke, J.; Musina, E.; Peulecke, N.; Karasik, A. A.; Kindermann, M. K.; Dobrynin, A. B.; Litvinov, I. A. *Z. Anorg. Allg. Chem*. **2007**, *633*, 1995.
(66) Konar, S.; Clearfield, A. *Inorg. Chem*. **2008**, *47*, 5573.
(67) Kong, D. Y.; Medvedev, D. G.; Clearfield, A. *Inorg. Chem*. **2004**, *43*, 7308.
(68) Morise, X.; Braunstein, P.; Welter, R. *CR. Chim*. **2003**, *6*, 91.
(69) Morise, X.; Braunstein, P.; Welter, R. *Inorg. Chem*. **2003**, *42*, 7752.
(70) Oberbeckmann-Winter, N.; Morise, X.; Braunstein, P.; Welter, R. *Inorg. Chem*. **2005**, *44*, 1391.
(71) Popa, A.; Davidescu, C. M.; Negrea, P.; Ilia, G.; Katsaros, A.; Demadis, K. D. *Ind. Eng. Chem*. **2008**, *47*, 2010.
(72) Reisinger, C. M.; Nowack, R. J.; Volkmer, D.; Rieger, B. *Dalton Trans*. **2007**, 272.
(73) Sgarbossa, P.; Pizzo, E.; Scarso, A.; Sbovata, S. M.; Michelin, R. A.; Mozzon, M.; Strukul, G.; Benetollo, F. *J. Organomet. Chem*. **2006**, *691*, 3659.
(74) Weis, K.; Rombach, M.; Vahrenkamp, H. *Inorg. Chem*. **1998**, *37*, 2470.
(75) Cadierno, V.; Diez, J.; Garcia-Alvarez, J.; Gimeno, J.; Rubio-Garcia, J. *Dalton Trans*. **2008**, 5737.
(76) Crabtree, R. H. *The organometallic chemistry of the transition metals*; Wiley-Interscience: NJ, 2005.
(77) Kalek, M.; Stawinski, J. *Organometallics* **2008**, *27*, 5876.
(78) Stille, J. K.; Lau, K. S. Y. *Acc. Chem. Res*. **1977**, *10*, 434.
(79) Tsou, T. T.; Kochi, J. K. *J. Am. Chem. Soc*. **1979**, *101*, 6319.
(80) Parshall, G. W. *J. Am. Chem. Soc*. **1974**, *96*, 2360.

Macromolecules
ARTICLE

Macromolecules **2011**, *44*, 521–529 **521**
DOI: 10.1021/ma102354k

Facile Construction of Multifunctional Nanocarriers Using Sequential Click Chemistry for Applications in Biology

Anjali Sharma,[†] Kevin Neibert,[‡] Rishi Sharma,[†] Rami Hourani,[†] Dusica Maysinger,*[,‡] and Ashok Kakkar*[,†]

[†]*Department of Chemistry, McGill University, 801 Sherbrooke St. West, Montreal, Quebec, H3A 2K6, Canada, and* [‡]*Department of Pharmacology and Therapeutics, McGill University, 3655 Promenade Sir-William-Osler, Montreal, Quebec, H3G 1Y6, Canada*

Received October 14, 2010; Revised Manuscript Received December 14, 2010

ABSTRACT: Bi- and trifunctional dendrimer and miktoarm nanocarriers, containing a combination of covalently linked model drug (α-lipoic acid), fluorescent dye (BODIPY), and poly(ethylene glycol) (PEG), are synthesized using a core with orthogonal functional groups, on which Huisgen alkyne−azide "click" reactions are performed in sequence. These carriers are internalized into the cells where they reduce H_2O_2 induced reactive oxygen species formation. In addition, miktoarm nanocarriers conjugated with α-lipoic acid enhance intracellular glutathione (GSH) concentrations.

Introduction

Designing well-defined multifunctional nanocarriers, into which a combination of the desired drug, an imaging dye, and a solubilizing agent can be covalently introduced, continues to be a focus of current research in theranostics.[1−3] Dendrimers[4] constitute an intriguing class of macromolecules that are increasingly being evaluated for applications in biology.[1−4] Dendrimers are hyperbranched and monodisperse in nature, and numerous synthetic methodologies have been developed to expand the scope of these complex yet highly elegant nanomaterials.[5] Many dendrimers are now available in which the core, backbone or peripheral groups have been modified to contain a single functionality. Introduction of multiple covalent functionalities into a single dendrimer has faced synthetic challenges, and the effort has been largely limited to bifunctional dendrimers.[6] However, there are few reports of dendrimers with more than two functionalities,[7] and there remains a need for a simple and versatile synthetic methodology which can be used to incorporate desired functionalities in a controlled manner. We report here a versatile synthetic route to bi- and trifunctional nanocarriers, using "click" chemistry which involves Cu^I-catalyzed coupling of an alkyne with an azide,[5d,8] in sequence, on building blocks with orthogonal reactive moieties.[9] This simple methodology allows facile, high yield synthesis of multifunctional dendrimers in which any desired combination of functionalities such as therapeutic (α-lipoic acid), solubilizing (PEG) and imaging (BODIPY dye) agents can be incorporated with relative ease.

α-Lipoic acid is a multimodal antioxidant tested in a number of preclinical and clinical trials involving subjects with neurodegenerative, cardiovascular and liver disease as well as diabetes and diabetic neuropathy.[10−12] It is a naturally occurring, amphipathic compound with a low redox potential (−0.29 V) and contains a thiol group which allows α-lipoic acid to function as a metabolic antioxidant, cystein precursor and heavy metal chelator.[13,14] Administration of thiol-containing antioxidant compounds such as α-lipoic acid leads to the enhancement and regeneration of several intracellular antioxidant molecules including glutathione, thioredoxins and vitamin E which protect against oxidative stress.[15] Glutathione (GSH) is the most abundant of the endogenous thiol containing antioxidants and plays a key role in the maintenance of cellular homeostasis.

Through the use of an appropriate delivery vehicle, the stability and efficacy of a therapeutic agent can be significantly improved. Dendrimers and miktoarms are an emerging class of polymeric nanocarriers for controlled intracellular delivery of drugs owing to the tailored density of reactive functional groups, carrying capacity, well-defined structure and monodispersity.[16] Several recent findings have reported the unique benefits of introducing antioxidant moieties into dendrimer scaffoldings,[17] and GSH-inducing antioxidant drugs such as *N*-acetyl-L-cysteine (NAC) have been previously coupled to the dendrimers.[18] We demonstrate that the conjugated dendrimer and miktoarm carriers reported here are noncytotoxic within micromolar concentrations, and are effective in reducing reactive oxygen species in pheochromocytoma (PC12) cells. Interestingly, the miktoarm carrier also enhances glutathione concentrations in these cells. Trifunctional and bifunctional carriers containing the imaging probe BODIPY are internalized into these cells and tend to accumulate in the cytoplasmic lipid droplets.

Results and Discussion

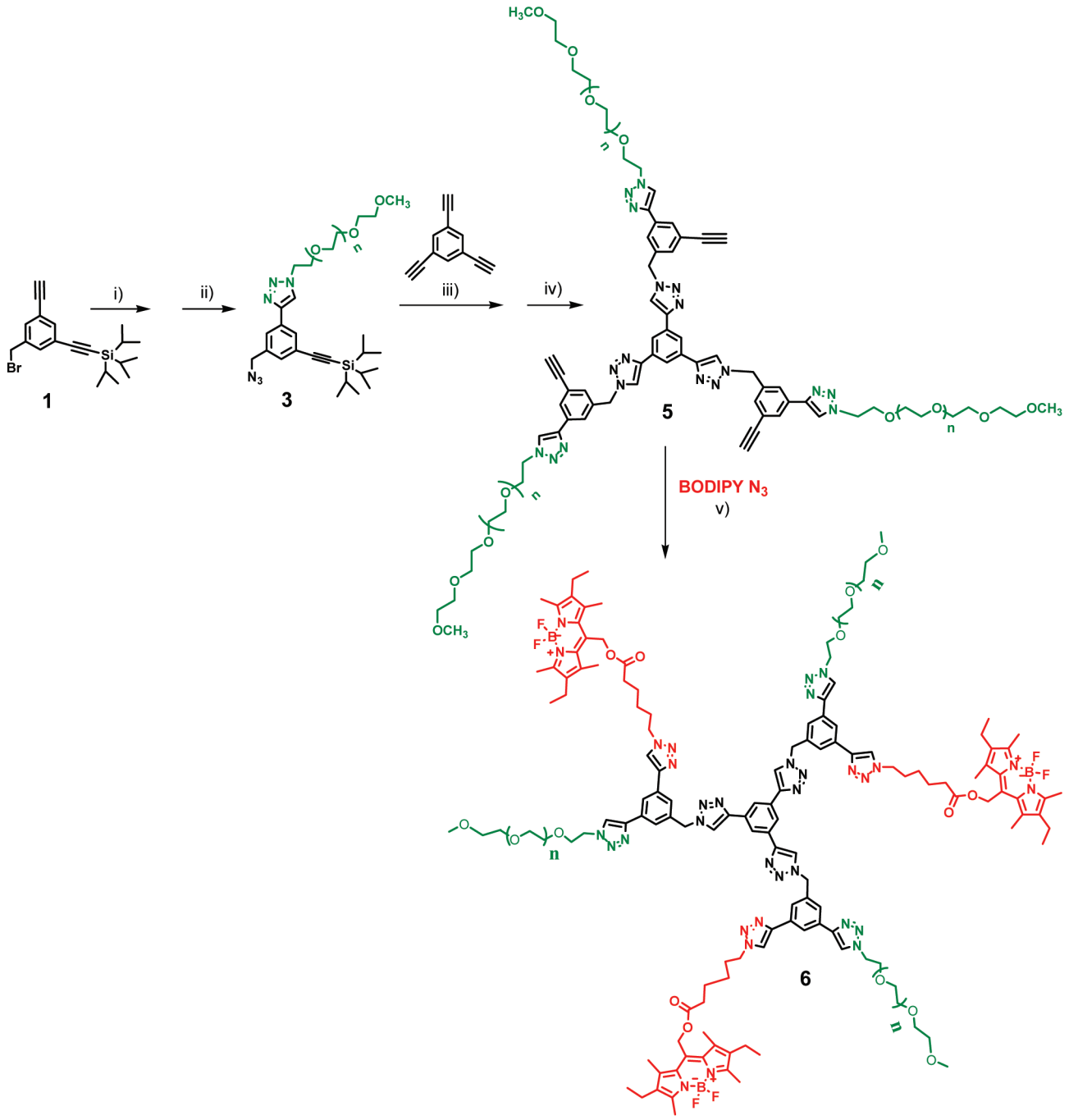
The synthesis of multifunctional nanocarriers is carried out on building blocks that allow covalent linking of different functionalities using Cu(I) catalyzed alkyne−azide "click" chemistry, in sequence. The construction of the bifunctional dendrimer **6** containing three PEG_{750} chains and three BODIPY dye molecules was carried out using the core compound **1** (Scheme 1). The latter molecule with free and protected acetylene centers was synthesized using a procedure developed earlier in our group.[6e] The free acetylene arm of **1** was first used to covalently bind a PEG chain using "click" reaction with PEG_{750}-azide in the presence of copper sulfate pentahydrate and sodium ascorbate. This is a clean and straightforward reaction with a high yield. The bromo focal point of the resulting compound was then converted to azide via an azidation reaction with sodium azide to give compound **3** in a good yield. The latter was then clicked on the triethynylbenzene core, followed by deprotection of triisopropylsilyl−acetylene groups. The corresponding free acetylene centers were subsequently

*Corresponding authors. E-mail: (D.M.) dusica.maysinger@mcgill.ca; (A.K.) ashok.kakkar@mcgill.ca.

© 2011 American Chemical Society

Published on Web 01/12/2011

Scheme 1. Synthesis of Bifunctional Dendrimer 6 Containing BODIPY Dye and PEG_{750} Chains[a]

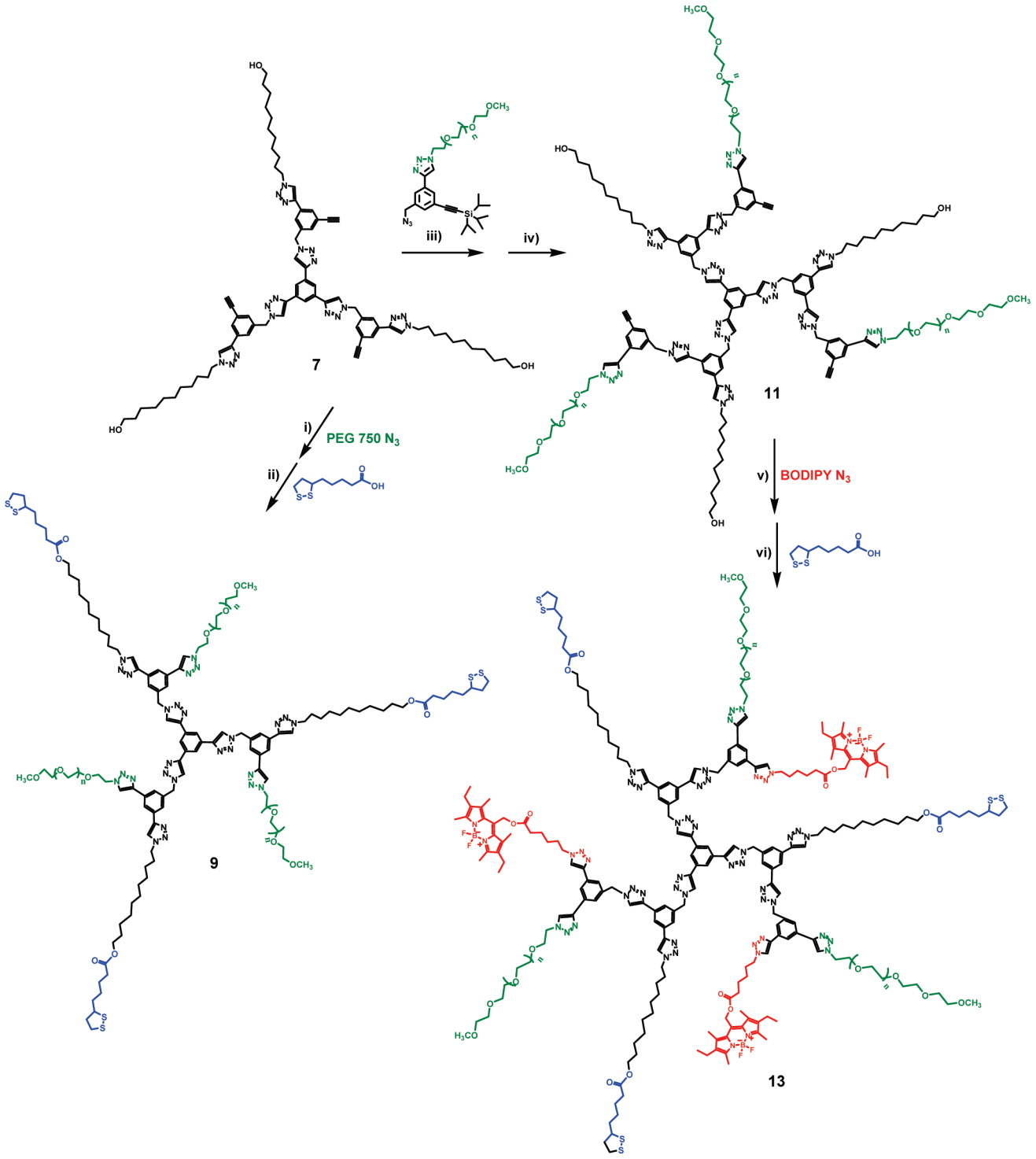


[a] Key: (i) $PEG_{750}N_3$, $CuSO_4 \cdot 5H_2O$/sodium ascorbate, H_2O/THF, room temperature, overnight (O/N), 73% yield; (ii) NaN_3, DMF, room temperature, 3 h, 79% yield; (iii) $CuSO_4 \cdot 5H_2O$/sodium ascorbate, H_2O/THF, room temperature, O/N, 90% yield; (iv) tetrabutylammonium fluoride (TBAF)/THF O/N, 65% yield; (v) $CuSO_4 \cdot 5H_2O$/sodium ascorbate, H_2O/THF, room temperature, O/N, 92% yield.

clicked with the azide-functionalized BODIPY dye to yield bifunctional dendrimer **6**. It should be noted that the PEG arm has to be attached first on **1**, and then the dye, since the azidation reaction in the presence of BODIPY on the molecule degrades the dye. It is essential to follow this particular sequence of reactions to avoid this degradation process.

The synthesis of another bifunctional dendrimer **9** with a combination of the drug α-lipoic acid and PEG_{750} was begun from **7**, which contains three terminal alcohols for the attachment of the drug and three free acetylenes available for the subsequent click reaction. Compound **7** was synthesized by clicking azido compound with long chain alcohol on triethynylbenzene core, followed by the deprotection of triisopropylsilyl-acetylene groups.[6e] PEG_{750}-azide was first clicked on **7** using the same procedure as described above, followed by the reaction of hydroxyl terminated arms with α-lipoic acid using a quantitative esterfication reaction, leading to the formation of the desired bifunctional dendrimer **9** (Scheme 2). To carry out the synthesis of this dendrimer, one must first attach long chain alcohols followed by PEG chains. We could not achieve this synthesis the other way by covalently linking three PEG chains on the dendrimer first, followed by long chain alcohols. This may be due to the steric hindrance caused by long PEG chains. Another important point is the attachment of α-lipoic acid, which should always be the last step as the sulfur of this drug interferes with click reaction leading to very poor yields. Thus, it is important to

Scheme 2. Synthesis of Bifunctional Dendrimer 9 (Containing α-Lipoic Acid and PEG_{750} Chains), and Trifunctional Dendrimer 13 (Containing α-lipoic acid, BODIPY Dye and PEG_{750} Chains)[a]

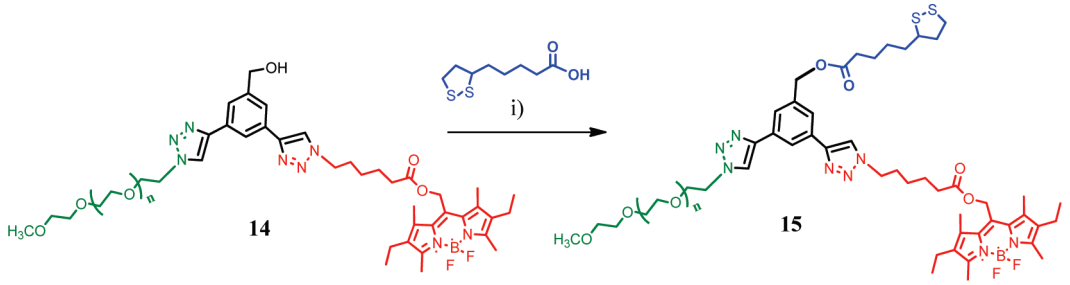


[a] Key: (i) $CuSO_4 \cdot 5H_2O$/sodium ascorbate, H_2O/THF, room temperature, O/N, 62% yield; (ii) *N*,*N*′-dicyclohexylcarbodiimide (DCC), 4-dimethylaminopyridine (DMAP), DCM, room temperature, 3 h, 78% yield; (iii) CuSO4·$5H_2O$/sodium ascorbate, H_2O/THF, room temperature, O/N, 43% yield; (iv) tetrabutylammonium fluoride (TBAF)/THF O/N, 70% yield; (v) $CuSO_4 \cdot 5H_2O$/sodium ascorbate, H_2O/THF, room temperature, O/N, 69% yield; (vi) 1-[3-(Dimethylamino)propyl]-3-ethylcarbodiimidemethiodide (EDC), DMAP, DCM, room temperature,O/N, 70% yield.

follow a particular sequence of reactions to synthesize bifunctional dendrimers with good yields.

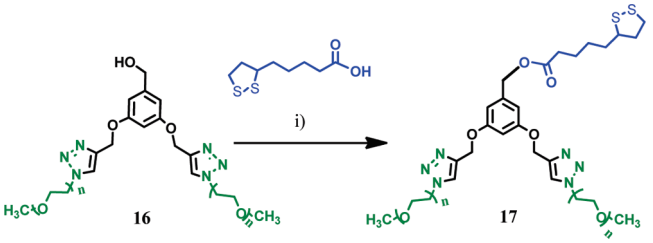
A similar synthetic approach was used to synthesize the trifunctional dendrimer **13**. Starting with compound **7**, we first clicked compound **3** containing PEG and a protected acetylene (Scheme 2). In this reaction, the product was isolated only in 43% yield. This is because the click reaction did not go efficiently, probably due to steric hindrance as the bulkier azide **3** is being clicked on to the compound **7,** which contains long chain alcohols. The triisopropylsilyl-acetylene groups were then deprotected followed by a second "click" reaction with the azide-functionalized BODIPY dye. The primary alcohols were then reacted with α-lipoic acid via an esterfication reaction to yield the desired trifunctional dendrimer **13**. Following this particular sequence of

Scheme 3. Synthesis of Miktoarm Unit 15 Having All Three Functionalities: PEG_{750}, BODIPY Dye, and α-Lipoic Acid[a]



[a] Key: (i) EDC, DMAP, DCM, room temperature, O/N, 66% yield.

Scheme 4. Synthesis of Miktoarm Unit 17 Having 2 PEG_{750} Chains and a Molecule of α-Lipoic Acid[a]



[a] Key: (i) EDC, DMAP, DCM, room temperature, O/N, 75% yield.

reactions is essential as there are now three functionalities which can interfere with each other. We attempted other sequences (e.g., PEG first followed by alcohols and dye), but the above-mentioned sequence gave the best results in terms of yields and purity.

Since the macromolecular structure may influence the overall behavior of the nanocarriers, we decided to construct two miktoarm structures: **15**, a trifunctional carrier containing PEG, BODIPY, and α-lipoic acid, and **17** with PEG and α-lipoic acid. To synthesize the miktoarm carrier **15** we started with compound **14** containing a PEG chain, a molecule of BODIPY dye, and benzylic alcohol. This compound was synthesized starting from a compound similar to **1** but having benzyl alcohol instead of benzyl bromide, a free acetylene and a protected acetylene.[19] PEG_{750} azide was clicked on the free acetylene followed by deprotection of triisopropylsilyl group of another acetylene which was then utilized to click BODIPY dye. The resulting compound was then reacted with α-lipoic acid to yield compound **15** (Scheme 3).

The miktoarm carrier **17** was synthesized starting with compound **16** containing two PEG chains and a benzylic alcohol (Scheme 4). Compound **16** was synthesized by carrying out o-alkylation at 3 and 5 positions of 3,5-dihydroxybenzyl alcohol using propargyl bromide. The two acetylenes were then used to "click" PEG_{750} chains.[20] The benzylic alcohol was then reacted with α-lipoic acid using simple esterification reaction to yield compound **17**.

The bi- and trifunctional dendrimer and miktoarm carriers were developed for the intracellular delivery of redox-regulating and antiapoptotic agents. α-Lipoic acid was used as a model drug for this purpose because it acts as a multimodal antioxidant. In addition to its direct function in the synthesis and/or regeneration of endogenous antioxidants, α-lipoic acid functions indirectly via transcriptional activation or inhibition of specific transcription factors (e.g., Nrf2 and NF-kappa B), leading to the expression or repression of a wide range of proteins. As such, the therapeutic potential of α-lipoic acid greatly exceeds the strict definition of an antioxidant.[21]

To track the uptake and cellular localization, dendrimer and miktoarm nanocarriers were conjugated with α-lipoic acid and BODIPY, a fluorescent probe with high affinity for lipid membranes. Fluorescent microscopy revealed that **6**, **13**, and **15** were rapidly internalized and diffusely distributed following 30 min

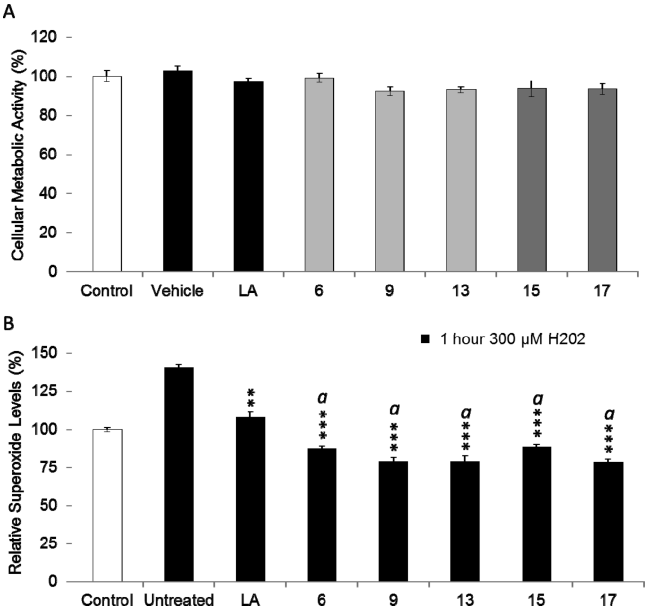


Figure 1. Measurement of cellular metabolic activity and inhibition of superoxide formation following exposure to α-lipoic acid conjugated dendrimer and miktoarm nanocarriers in PC12 cells. (A) Nanocarrier metabolic activity as assessed by Alamar Blue assay is indicative of cell viability. PC12 cells were treated for 24 h with equimolar concentrations of various dendrimer and miktoarm nanocarriers with respect to α-lipoic acid (200 μM). Cellular metabolic activity was determined and expressed as a percentage with respect to the untreated control. Data are presented as means ± SEM of three individual experiments of triplicates. No significant differences were detected. (B) Reactive oxygen species (ROS) generation following acute oxidative (1 h) insult was assessed using dihydroethidium (DHE), a fluorescent probe sensitive to super oxide radicals. PC12 cells were pretreated with dendrimers and miktoarm nanocarriers for 6 h prior to 1 h 300 μM H_2O_2 exposure. DHE fluorescent intensity was determined spectrofluorimetricly and expressed as a change (percentage) with respect to the untreated control cells. Data are presented as means ± SEM of three individual experiments of triplicates. Statistically significant differences from the H_2O_2 untreated control (first black bar) are shown (**, $p < 0.01$; ***, $p < 0.001$). Statistically significant differences from free α-lipoic acid are shown (*a*, $p < 0.001$).

exposure in PC12 cells (Supporting Information Figure 1). In some cases, conjugated nanocarriers appear to be localized in subcellular compartments, presumably lipid droplets.[22,6e]

Prior to the evaluation of the various macromolecule carriers as antioxidant agents and GSH inducers, nanocarrier cytotoxicity was assessed. Pheochromocytoma (PC12) cells were treated with equimolar concentrations of dendrimers and miktoarms with respect to α-lipoic acid (200 μM) and incubated for 24 h. There was no significant reduction in cellular metabolic activity following exposure to the nanocarriers (Figure 1A). Pretreatment with nontoxic concentrations of α-lipoic acid conjugated nanocarriers reduced

H_20_2 induced reactive oxygen species formation in PC12 cells, ranging from 37.8 ± 1.89% for free α-lipoic acid and 61.6 ± 3.08% for **17** with respect to untreated H_2O_2 control (Figure 1B). Interestingly, all the dendrimers and miktoarm nanocarriers tested reduced H_2O_2 induced formation of superoxide, irrespective of conjugated drug, and did so more effectively than free α-lipoic acid.

We subsequently investigated the capacity of α-lipoic acid conjugated nanocarriers to deliver the drug by measuring intracellular glutathione content. PC12 cells were treated with equimolar concentrations of α-lipoic acid conjugated dendrimer **9** and miktoarm **17** nanocarriers with respect to free α-lipoic acid (200 μM) for 24 h, and then incubated with mCBi, a fluorescent probe for GSH. Fluorescent micrographs suggested that free α-lipoic acid and **17** enhanced total intracellular glutathione concentrations were above those detected in untreated control cells (Figure 2A). Intracellular glutathione concentrations were quantified spectrofluormetrically following 24 h exposure to α-lipoic acid conjugated nanocarriers **9**, **13**, **15**, and **17** (Figure 2B). Only free α-lipoic acid and **17** significantly enhanced intracellular glutathione in PC12 cells with respect to control (204.3 ± 4.08% and 151.1 ± 3.78%, respectively). There was a significant difference in intracellular glutathione between free α-lipoic acid and **17** treated cells, with the former having a 53% increase over the latter (indicated by *a*). Even two or three day exposure to the α-lipoic acid conjugated nanocarriers did not increase intracellular glutathione concentrations above those measured in cells treated with unconjugated α-lipoic acid (Figure 2C). These findings suggest that the cleavage of α-lipoic acid from the drug nanocarrier is too slow to achieve effective intracellular concentrations of thiol residues necessary for enhanced synthesis of intracellular glutathione.

The results presented here suggest that dendrimer and miktoarm nanocarriers are readily internalized by PC12 cells. Both BODIPY and α-lipoic acid (lipophilic moiety) contribute to the rapid diffusion of conjugated nanocarriers through cellular membranes. Limited information is currently available concerning the mechanisms of transport and trafficking of dendrimers across biological barriers. In this regard, knock-down experiments employing specific siRNAs and specific pharmacological inhibitors of proteins participating in internalization processes, should be used to elucidate the modes of α-lipoic acid and BODIPY conjugated nanocarrier entry. Fluorescent microscopy in conjunction with specific pharmacological inhibitors of endocytosis has thus far revealed rapid, clathrin-dependent endocytosis of FITC labeled dendrimers.[23a] However, internalization by specific endocytic mechanisms appear to be highly dependent on nanocarrier size and charge.[23b]

Once taken up into the cell, dendrimers and miktoarms nanocarriers reduce reactive oxygen species formation more efficiently than free α-lipoic acid. Interestingly α-lipoic acid conjugated dendrimers and miktoarms do not enhance intracellular glutathione concentrations above that of equimolar free α-lipoic acid (200 μM). α-lipoic acid is not readily released from its carriers, likely due to the low concentration of enzymes required to cleave the covalent bond between the drug and the carriers in the cell culture system employed. Thus, an alternative approach that employs GSH sensitive bond cleavage and which should provide rapid delivery from the dendrimer-drug carriers, could be employed.[18a] This approach takes advantage of differences between intracellular and extracellular GSH concentrations (mM and μM respectively) allowing the drug to be released primarily upon entry into the cells.[18b]

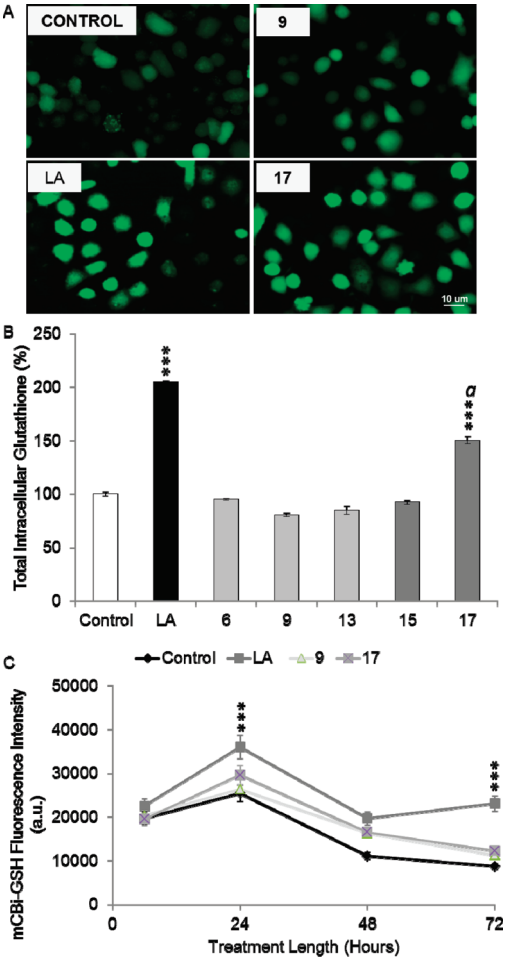


Figure 2. Assessment of total intracellular glutathione following exposure to α-lipoic acid conjugated dendrimer and miktoarm nanocarriers. (A) Total intracellular glutathione content was assessed using monochlorobimane (mCBI), a probe which binds specifically to reduced glutathione (GSH) forming the fluorescent mCBi-GSH adduct. Representative fluorescent micrographs of PC12 cells treated for 24 h with free α-lipoic acid (LA), **9** and **17** in equimolar concentrations with respect to α-lipoic acid (200 μM), were selected from at least three independent experiments of triplicates. The nucleus was stained with Hoechst and is visible in blue. Scale bar represents 10 um. (B) The fluorescent intensity of the mCBI-GSH adduct was measured using spectrofluorimetry in PC12 cells treated for 24 h with drug conjugated nanocarriers in equimolar concentrations with respect to α-lipoic acid (200 μM). Data is expressed as a percentage with respect to the untreated control. Data are presented as means ± SEM of three individual experiments of triplicates. Statistically significant differences from the untreated control are shown (***, $p < 0.001$). Statistically significant differences from free α-lipoic acid are shown (*a*, $p < 0.001$). (C) PC12 cells were treated for 6, 24, 48, and 72 h with drug conjugated nanocarriers. The fluorescent intensity of the mCBi-GSH adduct was measured spectrofluorimetrically and expressed as a mean fluorescent intensity in arbitrary units. Data are presented as means ± SEM of three individual experiments of triplicates. Statistically significant differences from the untreated control at each time point are shown (***, $p < 0.001$).

Conclusions

We have developed a general and simple methodology for the construction of multifunctional nanocarriers in which desired functionalities can be introduced using a combination of "click" reactions in sequence with esterification. Use of molecular building blocks with orthogonal functionalities facilitates the synthesis of noncytotoxic carriers with any combination of a therapeutic agent with an imaging dye and/or solubilizing polymeric chains. Our results show that the multifunctional dendrimer and miktoarm nanocarriers reduce H_2O_2-induced oxidative stress in PC12 cells. Interestingly, the reduction of superoxide did not depend on α-lipoic acid moiety, suggesting that nonconjugated or "naked" dendritic structures themselves could exert some antioxidant activity. Indeed, several dendrimers have shown an anti-inflammatory effect superior to that produced by anti-inflammatory agents attached to the dendrimers. These effects were ascribed to the

ability of dendrimers to inhibit cyclooxygenase-2 (COX-2).[24] Studies to reveal the mechanisms involved in the antioxidant and inflammatory effects of naked dendrimers and miktoarms presented in the current study are under investigation both in *in vitro* and *in vivo* systems in our laboratory.

Experimental Section

Materials and Methods. Copper(II) sulfate pentahydrate ($CuSO_4 \cdot 5H_2O$) (> 98.0%), sodium ascorbate (NaAsc) (crystalline) (98%), 6-bromohexanoic acid (97%), tetrabutylammonium fluoride (Bu4NF) (1.0 M in THF), 11-bromo-1-undecanol (98%), α-lipoic acid (> 99%), *N*,*N*′-dicyclohexylcarbodiimide (DCC) (99%), 1-[3-(dimethylamino)propyl]-3-ethylcarbodiimidemethiodide(EDC), and 4-(dimethylamino)pyridine (DMAP) (99%), and sodium azide (NaN_3) (> 99.5%) were purchased from Sigma-Aldrich Canada, and used as received. 8-Acetoxymethyl-2,6-diethyl-1,3,5,7-tetramethyl pyrromethene fluoroborate (PM605) was purchased from Exciton Inc., and used as received. All other solvents were used as received in their anhydrous forms. NMR spectra were recorded on a 400 or 500 MHz (as specified) spectrometer at ambient temperatures. The chemical shifts in ppm are reported relative to tetramethylsilane as an internal standard for ^1H and $^{13}C\{^1H\}$ NMR spectra. Gel permeation chromatography (GPC) analyses were performed in THF. A Waters 510 liquid chromatography pump, equipped with two (HR1 and HR4) Styragel columns connected in series, and a refractive index detector (Varian RI-4) were used at room temperature. Polystyrene standards (Scientific Polymer Products, Inc., Ontario, NY) with a narrow molecular weight distribution were used for calibration. The same instrument was used for all the compounds except **12**, **13**, and **15**, for which GPC analyses were carried out in DMF on a Viscogel G-MBLMW-3078 column equipped with a Waters 410 refractive index detector that was calibrated with poly(ethylene glycol) standards.

Synthesis. The following compounds were synthesized by adaptation of the previously published procedures: 1,3,5-triethynylbenzene,[25] 11-azido-undecan-1-ol,[6e] PEG_{750}-azide,[26] BODIPY-azide, miktoarm carrier containing PEG_{750}, BODIPY dye, and benzylic alcohol,[19] and another miktoarm carrier containing two PEG_{750} chains and a benzylic alcohol group[20] and the dendrimer containing the long chain alcohol arms and free acetylenic groups.[6e]

Compound **2**. Compound **1** (1 g, 2.59 mmol) and PEG_{750}-azide (2.01 g, 2.59 mmol) were dissolved in 3 mL of tetrahydrofuran (THF), followed by the addition of sodium ascorbate (0.051 g, 0.259 mmol). An aqueous solution (1 mL) of $CuSO_4 \cdot 5H_2O$ (0.032 g, 0.129 mmol) was added dropwise to the solution. The reaction mixture was left to stir overnight at room temperature. THF was then evaporated, and the remaining solution was extracted with ethyl acetate (3 × 30 mL), and then the organic layer was washed with brine (3 × 50 mL). It was dried over $MgSO_4$, and the solvent was evaporated. Silica-gel column chromatography was done, and the product was flushed through the column with 5% methanol in dichloromethane (DCM). The solvent was evaporated to yield the product as a transparent liquid (2.20 g, 73%). ^1H NMR (400 MHz, $CDCl_3$): δ (ppm) 1.13 (br s, 21H, $-Si(C_3\mathbf{H_7})$), 3.38 (s, 3H, $-OCH\mathbf{H}_3$), 3.54−3.64 (m, $(-OC\mathbf{H}_2C\mathbf{H}_2-)_n$), 3.91 (t, 2H, $-C\mathbf{H}_2OCH_3$), 4.48 (s, 2H, $-C\mathbf{H}_2Br$), 4.60 (t, 2H, $-OCHH_2C\mathbf{H}_2$triazole), 7.44 (s, 1H, Ar**H**), 7.86 (s, 2H, ArH), and 8.10 (s, 1H, triazole**H**). $^{13}C\{^1H\}$ NMR (125 MHz, $CDCl_3$): δ (ppm) 11.3, 18.7, 32.5, 50.5, 59.0, 69.4, 70.5, 71.9, 91.6, 105.97, 121.6, 124.6, 126.2, 129.0, 131.6, 131.8, 138.5, 146.2. GPC: M_n = 1820 g/mol. M_w/M_n = 1.09.

Compound **3**. To a solution of **2** (1.54 g, 1.33 mmol) in *N*,*N*-dimethylformamide (DMF), NaN_3 (0.431 g, 6.63 mmol) was added. The reaction mixture was left to stir at room temperature for 3 h. The solution was extracted with ethyl acetate (3 × 50 mL), and the organic phase was washed with brine (3 × 70 mL). It was dried over $MgSO_4$ and followed by removal of the solvent. The product was flushed through a short silica-gel column with 5% methanol in DCM to yield a transparent liquid (1.18 g, 79%). ^1H NMR (400 MHz, $CDCl_3$): δ (ppm) 1.13 (br s, 21H, $-Si(C_3\mathbf{H_7})$), 3.37 (s, 3H, $-OCH\mathbf{H}_3$), 3.54−3.64 (m, $(-OC\mathbf{H}_2C\mathbf{H}_2-)_n$), 3.92 (t, 2H, $-C\mathbf{H}_2OCH_3$), 4.39 (s, 2H, $-C\mathbf{H}_2N_3$), 4.60 (t, 2H, $-OCHH_2C\mathbf{H}_2$triazole), 7.37 (s, 1H, Ar**H**), 7.79 (s, 1H, Ar**H**), 7.88 (s, 1H, ArH), and 8.10 (s, 1H, triazole**H**). $^{13}C\{^1H\}$ NMR (125 MHz, $CDCl_3$): δ (ppm) 11.5, 18.9, 50.7, 57.4, 59.3, 69.7, 70.8, 72.1, 91.9, 105.9, 121.8, 124.9, 125.4, 129.1, 131.2, 131.8, 136.5, 146.2. GPC: M_n = 1900 g/mol. M_w/M_n = 1.13.

Compound **4**. 1,3,5-Triethynylbenzene (TEB) (0.050 g, 0.33 mmol) and compound **3** (1.12 g, 1.0 mmol) were dissolved in 2 mL of THF, followed by addition of sodium ascorbate (0.020 g, 0.10 mmol). An aqueous solution (1 mL) of $CuSO_4 \cdot 5H_2O$ (0.013 g, 0.05 mmol) was added dropwise to the solution. The reaction mixture was left to stir overnight at room temperature. THF was then evaporated, and the remaining solution was extracted with ethyl acetate (3 × 30 mL), and then the organic layer was extracted with brine (3 × 50 mL). It was dried over $MgSO_4$, and the solvent was evaporated. Silica-gel column chromatography was used to isolate the product with 5% methanol in DCM. The solvent was evaporated to yield the product as a thick viscous liquid (1.05 g, 90%). ^1H NMR (400 MHz, $CDCl_3$): δ (ppm) 1.11 (br s, 63H, $-Si(C_3\mathbf{H_7})$), 3.37 (s, 9H, $-OCH\mathbf{H}_3$), 3.54−3.64 (m, $(-OC\mathbf{H}_2C\mathbf{H}_2-)_n$), 3.91 (t, 6H, $-C\mathbf{H}_2OCH_3$), 4.59 (t, 6H, $-OCHH_2C\mathbf{H}_2$triazole), 5.59 (s, 6H, $-CH_2-$), 7.41 (s, 3H, Ar**H**), 7.79 (s, 3H, ArH), 7.97 (s, 6H, ArH), 8.09 (s, 3H, triazole**H**), and 8.26 (s, 3H, triazole**H**). $^{13}C\{^1H\}$ NMR (125 MHz, $CDCl_3$): δ (ppm) 11.3, 18.7, 50.4, 53.8, 59.0, 69.4, 70.5, 71.9, 92.3, 105.7, 120.5, 121.7, 122.4, 125.1, 124.4, 129.5, 131.1, 131.6, 132.1, 135.2, 145.9, and 147.6. GPC: M_n = 3500 g/mol. M_w/M_n = 1.11.

Compound **5**. To a solution of compound **4** (0.53 g, 0.15 mmol) in THF (3 mL) in a dry ice/acetone bath was added a solution of Bu_4NF 1 M solution in THF (0.75 mL, 0.75 mmol) in a dropwise fashion. The reaction mixture was allowed to warm to room temperature and left to stir overnight. The solvent was removed under vacuum, water (10 mL) was added, and the mixture was extracted with ethyl acetate (3 × 20 mL). The extract was then dried over $MgSO_4$, and solvent was evaporated. Silica-gel column chromatography was used to isolate the product with 5% methanol in DCM. The solvent was evaporated to yield the product as a transparent liquid (0.30 g, 65%). ^1H NMR (400 MHz, $CDCl_3$): δ (ppm) 3.14 (s, 3H, −CCH−), 3.36 (s, 9H, $-OCH\mathbf{H}_3$), 3.54−3.64 (m, $(-OC\mathbf{H}_2C\mathbf{H}_2-)_n$), 3.89 (t, 6H, $-C\mathbf{H}_2OCH_3$), 4.58 (t, 6H, $-OCHH_2C\mathbf{H}_2$triazole), 5.60 (s, 6H, $-CH_2-$), 7.36 (s, 3H, Ar**H**), 7.88 (s, 3H, ArH), 7.94 (s, 3H, ArH), 7.99 (s, 3H, ArH), 8.10 (s, 3H, triazole**H**), and 8.24 (s, 3H, triazole**H**). $^{13}C\{^1H\}$ NMR (125 MHz, $CDCl_3$): δ (ppm) 13.6, 19.7, 24.0, 50.4, 53.7, 58.9, 70.4, 70.6, 71.9, 78.7, 82.5, 120.7, 121.8, 122.4, 123.7, 125.7, 129.4, 130.9, 131.6, 132.2, 135.6, 145.8, 147.6. GPC: M_n = 3400 g/mol. M_w/M_n = 1.10.

Bifunctional Dendrimer **6**. Compound **5** (0.100 g, 0.03 mmol) and BODIPY-N_3 (0.062 g, 0.13 mmol) were dissolved in 2 mL of THF, followed by addition of sodium ascorbate (0.005 g, 0.03 mmol). An aqueous solution (1 mL) of $CuSO_4 \cdot 5H_2O$ (0.003 g, 0.01 mmol) was added dropwise to the solution. The reaction mixture was left to stir overnight at room temperature. THF was then evaporated, the remaining solution was extracted with DCM (3 × 20 mL), and then the organic layer was extracted with brine (3 × 50 mL). It was dried over $MgSO_4$, and the solvent was evaporated. Silica-gel column chromatography was used to isolate the product with 7% methanol in DCM. The solvent was evaporated to yield the product as a red liquid (0.135 g, 92%). ^1H NMR (400 MHz, $CDCl_3$): δ (ppm) 1.05 (t, 18H, $-ArCH_2C\mathbf{H_3}$), 1.40−1.42 (m, 6H, $-OOCCH_2C\mathbf{H_2}-$), 1.60−1.68 (m, 6H, $-C\mathbf{H_2}CH_2CH_2$traizole), 1.72−1.98 (m, 6H, $-C\mathbf{H_2}CH_2$triazole), 2.19 (s, 18H, $-ArC\mathbf{H_3}$), 2.30−2.45 (m, 18H, $-OOCC\mathbf{H_2}-$ and $-ArC\mathbf{H_2}CH_3$), 2.47 (s, 18H, $-ArC\mathbf{H_3}$), 3.36 (s, 9H, $-OCH\mathbf{H}_3$), 3.54−3.64 (m, $(-OC\mathbf{H}_2C\mathbf{H}_2-)_n$), 3.91 (t, 6H, $-C\mathbf{H}_2OCH_3$), 4.38 (t, 6H, $-CH_2CH_2C\mathbf{H_2}$triazole), 4.58 (t, 6H, $-OCHH_2C\mathbf{H}_2$triazole), 5.28 (s, 6H, $ArC\mathbf{H_2}OOCCH_2-$), 5.64 (s, 6H, $-CH_2-$), 7.80 (s, 3H, Ar**H**), 7.83 (s, 3H,

ArH), 7.94 (s, 3H, ArH), 8.04 (s, 3H, ArH), 8.14 (s, 3H, triazole**H**), 8.21 (s, 3H, triazole**H**), and 8.31 (s, 3H, triazole**H**). $^{13}C\{^1H\}$ NMR (125 MHz, $CDCl_3$): δ (ppm) 12.6, 13.8, 14.7, 17.1, 19.9, 24.2, 25.9, 29.7, 29.9, 33.7, 50.1, 50.5, 58.2, 59.0, 69.4, 70.5, 71.9, 120.9, 122.3, 125.1, 131.5, 132.2, 133.6, 135.9, 136.5, 146.4, 154.9, 172.9. GPC: M_n = 3300 g/mol. M_w/M_n = 1.10.

*Compound **8***. Compound **7** (0.150 g, 0.11 mmol) and $PEG_{750}-N_3$ (0.255 g, 0.33 mmol) were dissolved in 2 mL of THF, followed by addition of sodium ascorbate (0.008 g, 0.04 mmol). An aqueous solution (1 mL) of $CuSO_4 \cdot 5H_2O$ (0.005 g, 0.02 mmol) was added dropwise to the solution. The reaction mixture was left to stir overnight at room temperature. THF was then evaporated, and the remaining solution was extracted with DCM (3 × 20 mL), and then the organic layer was extracted with brine (3 × 50 mL). It was dried over $MgSO_4$, and the solvent was evaporated. Silica-gel column chromatography was used to isolate the product with 8% methanol in DCM. The solvent was evaporated to yield the product as a viscous liquid (0.250 g, 62%). ^1H NMR (400 MHz, $CDCl_3$): δ (ppm) 1.21−1.34 (m, 42H, $-CH_2-$), 1.49−1.51 (m, 6H, $-CH_2CH_2OH$), 1.87−1.91 (m, 6H, $-CH_2CH_2$-triazole), 3.36 (s, 9H, $-OCH_3$), 3.54−3.64 (m,$(-OCH_2CH_2-)_n$ and 6H,$-CH2OH$), 3.90 (t, 6H,$-CH_2OCH_3$), 4.37 (t, 6H, $-CH_2$-C**H2**triazole), 4.58 (t, 6H, $-OCHH_2CH_2$triazole), 5.62 (s, 6H,$-CH_2-$), 7.77 (s, 3H, Ar**H**), 7.83 (s, 3H, ArH), 7.94 (s, 3H, ArH), 8.07 (s, 3H, ArH), 8.14 (s, 3H, triazole**H**), 8.21 (s, 3H, triazole**H**), and 8.29 (s, 3H, triazole**H**). $^{13}C\{^1H\}$ NMR (125 MHz, $CDCl_3$): δ (ppm) 25.7, 26.4, 28.8, 29.1, 29.2, 29.4, 29.7, 30.2, 32.8, 50.5, 53.4, 59.0, 62.9, 69.4, 70.4, 70.5, 71.9, 108.7, 123.1, 124.8, 124.9, 131.7, 132.4, 132.5, 135.9, 172.6. GPC: M_n M_n = 3450 g/mol. M_w/M_n = 1.17.

*Bifunctional Dendrimer **9***. To a solution of compound **8** (0.080 g, 0.022 mmol), α-lipoic acid (0.015 g, 0.07 mmol), and DMAP (0.005 g. 0.04 mmol) in DCM (10 mL), DCC (0.023 g, 0.11 mmol) was added, and the solution was stirred at room temperature for 2 h. It was filtered, and the solid was washed with more DCM (10 mL). The filtrate was washed with a saturated solution of $NaHCO_3$ (3 × 30 mL) and dried over $MgSO_4$. The solvent was then evaporated, and the residue was flushed on a silica column using 5% methanol in DCM. The solvent was evaporated again to yield viscous liquid (0.065 g, 78%). ^1H NMR (400 MHz, $CDCl_3$): δ (ppm) 1.21−1.34 (m, 42H, $-CH_2-$), 1.38−1.50 (m, 6H, $-CH_2-$), 1.49−1.51 (m, 12H, $-CH_2-$), 1.87−1.91 (m, 12H, $-CH_2-$), 2.30 (t, 6H, $-CH_2COO-$), 2.39−2.50 (m, 6H, $-SCHCH_2-$), 3.05−3.22 (m, 9H, $-SSCH_2$ and $-SSCHCH_2-$), 3.37 (s, 9H, $-OCH_3$), 3.54−3.64 (m,-$(-OCH_2CH_2-)_n$), 3.91 (t, 6H, $-CH_2OCH_3$), 4.02 (t, 6H, $-CH_2$-OCO−), 4.39 (t, 6H, $-CH_2CH_2$triazole), 4.59 (t, 6H, $-OCHH_2CH_2$triazole), 5.65 (s, 6H,$-CH_2-$), 7.80 (s, 6H, Ar**H**), 7.91 (s, 3H, ArH), 7.99 (s, 3H, ArH), 8.12 (s, 3H, triazole**H**), 8.23 (s, 3H, triazole**H**), and 8.32 (s, 3H, triazole**H**). $^{13}C\{^1H\}$ NMR (125 MHz, $CDCl_3$): δ (ppm) 25.1, 25.9, 26.5, 28.6, 28.7, 29.4, 30.3, 34.1, 34.6, 38.5, 40.2, 50.4, 54.1, 56.3, 58.9, 64.5, 69.4, 70.5, 71.9, 120.3, 121.7, 122.4, 123.1, 124.8, 131.7, 132.4, 135.8, 146.4,146.5, 147.5, 173.5. GPC: M_n = 2715 g/mol. M_w/M_n = 1.14.

*Compound **10***. Compound **7** (0.150 g, 0.11 mmol) and compound **3** (0.442 g, 0.39 mmol) were dissolved in 3 mL of THF, followed by addition of sodium ascorbate (0.008 g, 0.04 mmol). An aqueous solution (1 mL) of $CuSO_4 \cdot 5H_2O$ (0.005 g, 0.02 mmol) was added dropwise to the solution. The reaction mixture was left to stir for 48 h at room temperature. THF was then evaporated, and the remaining solution was extracted with DCM (3 × 20 mL), and then the organic layer was extracted with brine (3 × 50 mL). It was dried over $MgSO_4$, and the solvent was evaporated. Silica-gel column chromatography was used to isolate the product with 8% methanol in DCM. The solvent was evaporated to yield the product as a viscous liquid (0.227 g, 43%). ^1H NMR (400 MHz, $CDCl_3$): δ (ppm) 1.09 (br s, 63H, $-Si(C_3H_7)$), 1.21−1.34 (m, 42H, $-CH_2-$), 1.49−1.51 (m, 6H, $-CH_2CH_2OH$), 1.97−2.01 (m, 6H, $-CH_2CH_2$-triazole), 3.36 (s, 9H, $-OCH_3$), 3.54−3.64 (m, $(-OCH_2CH_2-)_n$ and 6H, $-CH_2OH$), 3.88 (t, 6H, $-CH_2OCH_3$), 4.36 (t, 6H, $-CH_2CH_2$triazole), 4.56 (t, 6H, $-OCHH_2CH_2$triazole), 5.58 (s, 6H, $-CH_2-$), 5.62 (s, 6H, $-CH_2-$), 7.43 (s, 3H, Ar**H**), 7.76 (s, 3H, ArH), 7.79 (s, 3H, ArH), 7.83 (s, 3H, ArH),7.92 (s, 3H, ArH), 7.99 (s, 3H, ArH), 8.09 (s, 3H, ArH), 8.12 (s, 3H, triazole**H**), 8.18 (s, 3H, triazole**H**), 8.22 (s, 3H, triazole**H**), and 8.30 (s, 3H, triazole**H**). $^{13}C\{^1H\}$ NMR (125 MHz, $CDCl_3$): δ (ppm) 11.2, 18.6, 25.6, 26.3, 28.8, 29.1, 29.2, 29.3, 30.1, 32.7, 50.4, 53.7, 53.9, 58.9, 62.6, 69.3, 70.4, 71.8, 92.2,105.7, 120.6, 120.8, 120.9, 121.8, 122.9, 124.6, 124.7, 124.8, 124.9, 125.4, 129.3, 131.1, 131.4, 131.9, 132.0, 132.2, 135.4, 135.9, 154.9, 146.3, 146.4, 146.9, 147.2. GPC: M_n = 4300 g/mol. M_w/M_n = 1.17.

*Compound **11***. To a solution of compound **10** (0.227 g, 0.05 mmol) in THF (3 mL) in a dry ice/acetone bath was added a solution of Bu_4NF 1 M solution in THF (0.14 mL, 0.14 mmol) in a dropwise fashion. The reaction mixture was allowed to warm to room temperature and left to stir overnight. The solvent was removed under vacuum, and the residue was extracted with DCM. The extract was then dried over $MgSO_4$, and solvent was evaporated. Silica-gel column chromatography was used to isolate the product with 8% methanol in DCM. The solvent was evaporated to yield the product as a transparent liquid (0.142 g, 70%). ^1H NMR (400 MHz, $CDCl_3$): δ (ppm) 1.21−1.34 (m, 42H, $-CH_2-$), 1.49−1.53 (m, 6H, $-CH_2$-CH_2OH), 1.90−1.99 (m, 6H, $-CH_2CH_2$triazole), 3.15 (s, 3H, $-CCH-$) 3.37 (s, 9H, $-OCH_3$), 3.54−3.64 (m, $(-OCH_2$-$CH_2-)_n$ and 6H, $-CH_2OH$), 3.89 (t, 6H, $-CH_2OCH_3$), 4.36 (t, 6H, $-CH_2CH_2$triazole), 4.56 (t, 6H, $-OCHH_2CH_2$triazole), 5.60 (s, 6H,$-CH_2-$), 5.64 (s, 6H,$-CH_2-$), 7.37 (s, 3H, Ar**H**), 7.79 (s, 3H, Ar**H**), 7.83 (s, 3H, ArH), 7.93 (s, 3H, ArH), 7.94 (s, 3H, ArH), 8.03 (s, 3H, ArH), 8.12 (s, 3H, Ar**H**), 8.16 (s, 3H, triazole**H**), 8.20 (s, 3H, triazole**H**), 8.26 (s, 3H, triazole**H**), and 8.32 (s, 3H, triazole**H**). $^{13}C\{^1H\}$ NMR (125 MHz, $CDCl_3$): δ (ppm) 13.5, 19.6, 23.8, 25.7, 26.3, 28.9, 29.1, 29.2, 29.3, 30.1, 32.7, 50.4, 53.6, 53.9, 54.0, 58.9, 62.7, 69.3, 70.4, 70.5, 71.9, 78.7, 82.5, 120.5, 120.6, 120.8, 121.8, 122.9, 123.6, 124.8, 125.7, 128.8, 129.3, 130.9, 131.4, 131.5, 131.9, 132.3, 135.7, 135.9, 140.0, 145.8, 146.4, 147.0, 147.3. GPC: M_n = 3970 g/mol. M_w/M_n = 1.14.

*Compound **12***. Compound **11** (0.075 g, 0.018 mmol) and BODIPY-N_3 (0.034 g, 0.07 mmol) were dissolved in 2 mL of THF, followed by addition of sodium ascorbate (0.004 g, 0.02 mmol). An aqueous solution (1 mL) of $CuSO_4 \cdot 5H_2O$ (0.003 g, 0.01 mmol) was added dropwise to the solution. The reaction mixture was left to stir overnight at room temperature. THF was then evaporated, and the remaining solution was extracted with DCM (3 × 20 mL), and then the organic layer was extracted with brine (3 × 50 mL). It was dried over $MgSO_4$, and the solvent was evaporated. Silica-gel column chromatography was used to isolate the product with 7% methanol in DCM. The solvent was evaporated to yield the product as a red liquid (0.069 g, 69%). ^1H NMR (400 MHz, $CDCl_3$): δ (ppm) 0.99 (t, 18H, $-ArCH_2CH_3$), 1.19−1.34 (m, 42H, $-CH_2-$), 1.47−1.51 (m, 6H, $-CH_2CH_2OH$), 1.52−1.65 (m, 6H, $-OOCCH_2CH_2-$), 1.66−1.71 (m, 6H, $-CH_2$-CH_2CH_2traizole), 1.72−1.98 (m, 12H, $-CH_2CH_2$triazole), 2.19 (s, 18H, $-ArCH_3$), 2.30−2.45 (m, 18H, $-OOCCH_2-$ and $-ArC$-H_2CH_3), 2.47 (s, 18H, $-ArCH_3$), 3.37 (s, 9H, $-OCH_3$), 3.54−3.64 (m, $(-OCH_2CH_2-)_n$ and 6H, $-CH_2OH$), 3.89 (t, 6H,$-CH_2$-OCH_3), 4.16 (t, 6H, $-CH_2CH_2CH_2$triazole), 4.36 (t, 6H, $-CH_2$-CH_2triazole), 4.56 (t, 6H, $-OCHH_2CH_2$triazole), 5.27 (s, 6H, $ArCH_2OOCCH_2$-) 5.57 (s, 6H,$-CH_2-$), 5.62 (s, 6H,$-CH_2-$), 7.73 (s, 3H, Ar**H**), 7.76−7.82 (m, 6H, ArH), 7.89 (s, 3H, ArH), 7.83 (s, 3H, ArH), 7.92 (s, 6H, ArH), 7.99 (s, 6H, ArH), 8.09−8.14 (m, 7H, ArH), 8.20 (s, 2H, triazole**H**), and 8.22−8.29 (m, 3H, triazole**H**). $^{13}C\{^1H\}$ NMR (125 MHz, $CDCl_3$): δ (ppm) 12.6, 13.6, 14.7,17.1, 19.7, 23.9, 24.2, 24.9, 25.6, 25.7, 26.3, 28.2, 28.8, 29.4, 32.7, 33.6, 33.9, 34.1, 34.4, 34.9, 35.3, 49.7, 50.5, 59.0, 70.5, 70.6, 71.9, 104.9, 124.4, 124.9, 125.7, 125.9, 126.1, 131.1, 131.6, 131.9, 132.2, 133.3, 133.4, 133.6, 135.4, 136.3, 136.5, 136.9, 137.0, 146.4, 154.9, 172.9. GPC: M_n = 3266 g/mol. M_w/M_n = 1.02.

*Trifunctional Dendrimer **13***. To a solution of compound **12** (0.055 g, 0.01 mmol), α-lipoic acid (0.010 g, 0.05 mmol), and

DMAP (0.004 g, 0.03 mmol) in DCM (3 mL) was added 1-ethyl-3-(3-(dimethylamino)propyl)carbodiimide (EDC) (0.015 g, 0.05 mmol), and the solution was stirred at room temperature for 12 h. It was diluted with DCM (10 mL), and washed with water (2 × 20 mL), organic layer was dried over $MgSO_4$. The solvent was then evaporated, and the residue was purified on a silica column using 5% methanol in DCM. The solvent was evaporated again to yield viscous red liquid (42 mg, 70%). ^{1}H NMR (400 MHz, $CDCl_3$): δ (ppm) 0.94 (t, 18H, $-ArCH_2C\mathbf{H_3}$), 1.19−1.34 (m, 42H, $-C\mathbf{H_2}-$),1.34−1.40 (m, 6H, $-OOCCH_2C\mathbf{H_2}-$), 1.42−1.48 (m, 6H, $-C\mathbf{H_2}-$), 1.60−1.70 (m, 18H, $-C\mathbf{H_2}-$), 1.80−2.00 (m, 18H, $-C\mathbf{H_2}-$), 2.19 (s, 18H, $-ArC\mathbf{H_3}$), 2.30−2.45 (m, 18H, $-OOCC\mathbf{H_2}-$ and $-ArC\mathbf{H_2}CH_3$), 2.46 (s, 18H, $-ArC\mathbf{H_3}$), 3.05−3.22 (m, 9H, -SSC$\mathbf{H_2}$ and $-SSC\mathbf{H}CH_2-$), 3.22−3.27 (m, 6H, $-C\mathbf{H_2}OCO-$), 3.36 (s, 9H, $-OCH\mathbf{H_3}$), 3.54−3.64 (m,$(-OCH_2C\mathbf{H_2}-)_n$), 3.89 (t, 6H,$-C\mathbf{H_2}OCH_3$), 4.17 (t, 6H, $-CH_2$-$CH_2C\mathbf{H_2}$triazole), 4.36 (t, 6H, $-CH_2C\mathbf{H_2}$triazole), 4.56 (t, 6H, $-OCHH_2C\mathbf{H_2}$triazole), 5.27 (s, 6H, $ArC\mathbf{H_2}OOCCH_2-$), 5.58 (s, 6H,$-C\mathbf{H_2}-$), 5.64 (s, 6H,$-C\mathbf{H_2}-$), 7.80−7.86 (m, 12H, Ar**H**), 7.95−8.05 (m, 6H, Ar**H**), 8.10−8.18 (m, 8H, Ar**H**), 8.20−8.25 (m, 5H, Ar**H**), and 8.25−8.32 (m, 5H, triazole**H**). $^{13}C\{^1H\}$ NMR (125 MHz, $CDCl_3$): δ ppm 12.6, 13.6, 14.7, 17.1, 19.7, 24.1, 24.5, 24.7, 25.9, 26.5, 28.6, 28.7, 29.4, 29.7, 30.3, 34.1, 34.6, 38.5, 40.2, 50.1, 50.4, 50.5, 54.1, 56.3, 58.2, 58.9, 59.0, 64.5, 69.3, 70.4, 70.5, 71.9, 104.9, 121.9, 123.1, 123.2, 124.9, 125.0, 131.6, 132.1, 132.2, 132.3, 132.4, 133.5, 133.6, 135.9, 136.5, 146.4, 154.9, 172.9,173.6. GPC: M_n =2860 g/mol. M_w/M_n = 1.06.

*Miktoarm Carrier **15***. To a solution of compound **14** (0.035 g, 0.025 mmol) and DMAP (0.003 g, 0.025 mmol) in DCM (3 mL) was added α-lipoic acid (0.008 g, 0.04 mmol). Once the solution was fully dissolved, EDC (0.011 g, 0.04 mmol) was added, and the solution was stirred under nitrogen overnight at room temperature in the dark. The reaction mixture was then added directly into a column and purified by silica gel column chromatography in a mixture of 5% methanol in DCM. The solvent was then evaporated to yield a red liquid (0.026 g, 66%). ^{1}H NMR (400 MHz, $CDCl_3$): δ (ppm) 1.03 (t, 6H, $-ArCH_2C\mathbf{H_3}$), 1.40−1.52 (m, 4H, $-C\mathbf{H_2}-$), 1.60−1.80 (m, 4H, $-C\mathbf{H_2}-$), 1.80−1.88 (m, 2H, $-C\mathbf{H_2}-$),1.88−2.05 (m, 2H,$-C\mathbf{H_2}-$), 2.23 (s, 6H, $-ArC\mathbf{H_3}$), 2.35−2.45 (m, 10H, $-C\mathbf{H_2}-$), 2.49 (s, 6H, $-ArC\mathbf{H_3}$), 3.05−3.08 (m, 1H, $-SSC\mathbf{H}CH_2-$), 3.36 (s, 3H, $-OCH\mathbf{H_3}$), 3.51−3.54 (m, 2H, -SSC$\mathbf{H_2}$), 3.54−3.64 (m, $(-OCH_2C\mathbf{H_2}-)_n$), 3.93 (t, 2H,$-C\mathbf{H_2}OCH_3$), 4.40 (t, 2H, $-CH_2CH_2C\mathbf{H_2}$triazole), 4.61 (t, 2H, $-OCHH_2C\mathbf{H_2}$triazole), 5.19 (s, 2H, $ArC\mathbf{H_2}OOCCH_2-$), 5.32 (s, 2H,$-C\mathbf{H_2}-$), 7.82 (s, 1H, Ar**H**), 7.85 (s, 1H, ArH), 7.92 (s, 1H, ArH), 8.11(s, 1H, triazole**H**), and 8.26 (s, 1H, triazole**H**). $^{13}C\{^1H\}$ NMR (125 MHz, $CDCl_3$): δ (ppm) 12.6, 14.7, 17.1, 24.2, 24.7, 25.9, 28.7, 29.9, 33.7, 34.0, 34.5, 38.5, 40.2, 50.1, 50.5, 56.4, 58.3, 59.0, 64.2, 65.9, 69.5, 70.5, 70.6, 71.9, 120.1, 121.5, 122.7, 124.9, 125.1, 131.5, 131.7, 132.2, 133.6, 136.4, 137.4, 154.9, 172.9, 173.3. GPC: M_n = 840 g/mol. M_w/M_n = 1.13.

*Miktoarm Carrier **17***. The solution of compound **16** (300 mg, 0.16 mmol), α-lipoic acid (40 mg, 0.18 mmol), EDC (60 mg, 0.2 mmol), DMAP (20 mg, 0.16 mmol) in DCM (5 mL) in a flame-dried two neck round-bottom flask was stirred under nitrogen atmosphere for 12 h. The reaction mixture was diluted with water (10 mL) and extracted with dichloromethane (3 × 10 mL). The organic layer was separated and washed with brine (2 × 10 mL). It was then dried over anhydrous sodium sulfate and concentrated under reduced pressure. The compound was obtained as off white solid (250 mg, 75%). ^{1}H NMR (400 MHz, $CDCl_3$): δ (ppm) 1.38−1.48 (m, 2H, $-C\mathbf{H_2}-$), 1.60−1.75 (m, 2H, $-C\mathbf{H_2}-$), 1.85−1.98 (m, 2H, $-C\mathbf{H_2}-$), 2.38 (t, 2H, $-CH_2COO-$), 2.40−2.48 (m, 3H, $-SCHC\mathbf{H_2}-$), 3.05−3.22 (m, 3H, $-SSC\mathbf{H_2}-$ and $-SSC\mathbf{H}CH_2-$), 3.37 (s, 3H, $-OCH\mathbf{H_3}$), 3.54−3.64 (m,$(-OCH_2C\mathbf{H_2}-)_n$), 3.90 (t, 6H,$-C\mathbf{H_2}OCH_3$), 4.60 (t, 6H, $-OCHH_2C\mathbf{H_2}$triazole), 5.03 (s, 2H, $-C\mathbf{H_2}OCO-$), 5.15 (s, 4H, $-OCH\mathbf{H_2}-$), 6.59−6.63 (m, 3H, Ar**H**), 7.95 (s, 2H, triazole**H**). $^{13}C\{^1H\}$ NMR (100 MHz, $CDCl_3$): δ (ppm) 24.6, 28.7, 30.9, 34.0, 34.5, 38.4, 40.2, 50.2, 56.3, 59.0, 61.9, 65.8, 69.9, 101.4, 107.1, 124.3, 138.4, 143.4, 159.5, and 173.2. GPC: M_n = 1700 g/mol. M_w/M_n = 1.05.

Biological Studies. *Cell Culture and Media.* Undifferentiated rat pheochromocytoma cells (PC12) were cultured in RPMI 1640 media (Invitrogen) containing 5% fetal bovine serum (Gibco), 1% penicillin−streptomycin (Gibco) and free of phenol-red. Cells were maintained at 37 °C, 5% CO_2 in a humidified incubator. Cells were seeded at 25,000 cells/well in 96 back well, clear bottom plates (Costar) and at 50,000 cell/well in 24 well plates (Costar). All cell treatments were performed in serum free media for the times indicated.

Assessment of Cytotoxicity. To assess nanocarrier cytotoxicity, cells were incubated with Alamar Blue diluted in serum free media (10% vol/vol) for 1 h following 24 h exposure to dendritic nanocarriers. Mean fluorescent intensity was measured with a FLUROstar Optima fluorimeter (BGM, Labtech) with filters were set to Ex/Em = 544/590 nm and employed 3 × 3 matrix well scanning.

Assessment of Reactive Oxygen Species Formation (*ROS*). ROS formation was measured using dihydroethidium (DHE) (Molecular Probes), a fluorescent probe sensitive to super oxygen species. Following 6 h pretreatment with nanocarriers, oxidative stress was induced with 300 μM H_2O_2 for 1 h. Cells were then washed and incubated in the dark for 30 min with 10 μM DHE. The conversion of DHE into highly fluorescent ethidium bromide was measured spectrofluoremetrically with a FLUROstar Optima fluorimeter (BGM, Labtech) with filters set to Ex/Em = 544/612 nm and employed 3 × 3 matrix well scanning.

Spectrofluorometric Measurements of Total Intracellular Glutathione. GSH reacts specifically with nonfluorescent membrane permeable dye monochlorobimane (mCBi) to form a fluorescent adduct (mCBi-GSH). Following treatment, cells were washed and incubated at 37 °C with 50 μM mCBi for 1 h. mCBi containing media was aspirated, cells were washed with PBS and fresh serum free media was added. Fluorescence images were acquired with a Leica DFC350FX monochrome digital camera connected to a Leica DMI4000B inverted fluorescence microscope. Fluorescent intensity of the mCBi-GSH adduct was measured with a FLUROstar Optima fluorimeter (BGM, Labtech). Filters were set to Ex/Em = 380/460 nm and employed 3 × 3 matrix well scanning.

Cellular Internalization of BODIPY Labeled Dendrimers. To assess cellular internalization, cells were treated with equimolar concentrations (1 μM) of BODIPY conjugated dendritic compounds for 1 h. Following treatment, the nucleus was labeled with Hoechst 33258 (10 μM; 10 min) and lipid droplets were labeled with free BODIPY 493/503 (20 μM; 10 min). Fluorescence images were acquired with a Leica DFC350FX monochrome digital camera connected to a Leica DMI4000B inverted fluorescence microscope.

Acknowledgment. A.K. and D.M. thank the NSERC of Canada for financial assistance. We would also like to thank Dr. Tony Azzam for his assistance in performing GPC analyses of carriers.

Supporting Information Available: GPC profiles, mass spectral analyses of carriers, and assessment of cellular uptake of BODIPY and/or α-lipoic acid conjugated dendrimer and miktoarm nanocarriers, and their metabolic activity. This material is available free of charge via the Internet at http://pubs.acs.org.

Note Added after ASAP Publication. This article posted ASAP on January 12, 2011. Rami Hourani, a co-author of this paper, was omitted. The correct version posted on February 1, 2011.

References and Notes

(1) Tekade, R. K.; Kumar, P. V.; Jain, N. K. *Chem. Rev.* **2009**, *109*, 49–87.

(2) (a) Wolinsky, J. B.; Grinstaff, M. W. *Adv. Drug Delivery Rev.* **2008**, *60*, 1037–1055. (b) Menjoge, A. R.; Kannnan, R. M.; Tomalia, D. A. *Drug Discovery Today* **2010**, *15*, 171–185.
(3) Majoros, I. J.; Williams, C. R.; Baker, J. R. *Curr. Top. Med. Chem.* **2008**, *8*, 1165–1179.
(4) Hourani, R.; Kakkar, A. *Macromol. Rapid Commun.* **2010**, *31* (11), 947–974.
(5) (a) Tomalia, D. A.; Baker, H.; Dewald, J. R.; Hall, M.; Kallos, G.; Martin, S.; Roeck, J.; Ryder, J.; Smith, P. *Polym. J.* **1985**, *17*, 117–132. (b) Hawker, C. J.; Fréchet, J. M. J. *J. Am. Chem. Soc.* **1990**, *112*, 7638–7647. (c) Launay, N.; Caminade, A.-M.; Majoral, J.-P. *J. Am. Chem. Soc.* **1995**, *117*, 3282–3283. (d) Wu, P.; Feldman, A. K.; Nugent, A. K.; Hawker, C. J.; Scheel, A.; Voit, B.; Pyun, J.; Frechet, J. M. J.; Sharpless, K. B.; Fokin, V. V. *Angew. Chem., Int. Ed.* **2004**, *116*, 4018–4022. (e) Franc, G.; Kakkar, A. K. *Chem.—Eur. J.* **2009**, *15* (23), 5630–5639.
(6) (a) Wu, P.; Malkoch, M.; Hunt, J. N.; Vestberg, R.; Kaltgrad, E.; Finn, M. G.; Fokin, V. V.; Sharpless, K. B.; Hawker, C. J. *Chem. Commun.* **2005**, 5775–5777. (b) Goodwin, A. P.; Lam, S. S.; Fréchet, J. M. J. *J. Am. Chem. Soc.* **2007**, *129*, 6994–6995. (c) Franc, G.; Kakkar, A. *Chem. Commun.* **2008**, 5267–5276. (d) Antoni, P.; Hed, Y.; Nordber, A.; Nystrom, D.; von Holst, H.; Hult, A.; Malkoch, M. *Angew. Chem., Int. Ed.* **2009**, *48*, 2126–2130. (e) Hourani, R.; Jain, M.; Maysinger, D.; Kakkar, A. *Chem.—Eur. J.* **2010**, *16* (21), 6164–6168.
(7) (a) Steffensen, M. B.; Simanek, E. E. *Angew. Chem., Int. Ed. Engl.* **2004**, *43* (39), 5178–5180. (b) Sivanandan, K.; Vutukuri, D.; Thayumanavan, S. *J. Org. Chem.* **2004**, *69*, 2937–2944. Ornelas, C.; Weck, M. *Chem. Commun.* **2009**, *38*, 5710–5712.
(8) Franc, G.; Kakkar, A. K. *Chem. Soc. Rev.* **2010**, *39* (5), 1536–1544.
(9) Hourani, R.; Sharma, A.; Kakkar, A. *Tett. Lett.* **2010**, *51* (29), 3792–3795.
(10) Salinthone, S.; Yadav, V.; Bourdette, D. N.; Carr, D. Q. *Endocr. Metab. Immune Disord. Drug Targets* **2008**, *8*, 132–142.
(11) Ghibu, S.; Richard, C.; Vergely, C.; Zeller, M.; Cottin, Y.; Rochette, L. *J. Cardiovasc. Pharmacol.* **2009**, *54* (5), 391–398.
(12) Mijnhout, G. S.; Alkhalaf, A.; Kleefstra, N.; Bilo, H. J. *Biochim. Neth. J. Med.* **2010**, *68* (4), 158–162.
(13) Jain, M. P.; Choi, A. O.; Neibert, K. D.; Maysinger, D. *Nanomedicine* **2009**, *4* (3), 277–290.
(14) Shay, K. P.; Moreau, R. F.; Smith, E. J.; Smith, A. R.; Hagen, T. M. *Biochim. Biophys. Acta* **2009**, *1790* (10), 1149–1160.
(15) Suh, J. H.; Shenvi, S. V.; Dixon, D. M.; Liu, H.; Jaiswal, A. K.; Liu, R. M.; Hagen, T. M. *Proc. Natl. Acad. Sci. U.S.A.* **2004**, *101* (10), 3381–3386.
(16) Svenson, S. *Eur. J. Pharm. Biopharm.* **2009**, *71*, 445–462.
(17) (a) Chung, J. E.; Kurisawa, M.; Uyama, H.; Kobayashi, S. 1st International Conference on Polyphenols and Health, Vichy, France, November **2003**. (b) Lee, C. Y.; Sharma, A.; Uzarski, R. L.; Cheong, J. E.; Xu, H.; Held, R. A.; Upadhaya, S. K.; Nelson, J. L. *Free Radical Biol. Med.* **2010**, DOI:10.1016/j.freeradbiomed.2010.10.699.
(18) (a) Navath, R. S.; Kurtoglu, Y. E.; Wang, B.; Kannan, S.; Romero, R.; Kannan, R. M. *Bioconjugate Chem.* **2008**, *19*, 2446–2455. (b) Wang, B.; Navath, R. S.; Romero, R.; Kannan, S.; Kannan, R. *Int. J. Pharm.* **2009**, *337*, 159–168.
(19) Sharma, A.; Khatchadourian, A.; Khanna, K.; Sharma, R.; Kakkar, A.; Maysinger, D. *Biomaterials* **2011**, *32*, 1419–1429.
(20) Soliman, G. M.; Sharma, R.; Choi, A. O.; Varshney, S. K.; Winnik, F. M.; Kakkar, A. K.; Maysinger, D. *Biomaterials* **2010**, *31*, 8382–8392.
(21) Shay, K. P.; Moreau, R. F.; Smith, E. J.; Smith, A. R.; Hagen, T. M. *Biochim. Biophys. Acta* **2009**, *1790* (10), 1149–1160.
(22) Khatchadourian, A.; Maysinger, D. *Mol. Pharmaceutics* **2009**, *6* (4), 1125–1137.
(23) (a) Kitchens, K. M.; Forker, A. B.; Kolhatkar, R. B.; Swaan, P. W.; Ghandehari, H. *Pharm. Res.* **2007**, *24* (11), 2138–2145. (b) Shen, M.; Shi, X. *Nanoscale* **2010**, *2*, 1596–1610.
(24) Chauhan, A. S.; Diwan, P. V.; Jain, N. K.; Tomalia, D. A. *Biomacromolecules* **2009**, *10* (5), 1195–1202.
(25) Weber, E.; Hecker, M.; Koepp, E.; Orlia, W.; Czugler, M.; Csöregh, I. *J. Chem. Soc., Perkin Trans.* **1988**, *2*, 1251–1258.
(26) Khanna, K.; Varshney, S.; Kakkar, A. *Macromolecules* **2010**, *43*, 5688–5698.

530 *Macromolecules* **2011**, *44*, 530–539
DOI: 10.1021/ma102728z

Macromolecules
ARTICLE

Polythiophene-*block*-polyfluorene and Polythiophene-*block*-poly(fluorene-*co*-benzothiadiazole): Insights into the Self-Assembly of All-Conjugated Block Copolymers

Rafael Verduzco,*,† Ioan Botiz,‡ Deanna L. Pickel,∥ S. Michael Kilbey II,∥,⊥ Kunlun Hong,∥ Elaine Dimasi,§ and Seth B. Darling*,‡

†*Department of Chemical and Biomolecular Engineering, Rice University, 6100 Main Street, MS-362, Houston, Texas 77005, United States,* ‡*Center for Nanoscale Materials, Argonne National Laboratory, 9700 South Cass Avenue, Argonne, Illinois 60439, United States,* ∥*Center for Nanophase Materials Sciences, Oak Ridge National Laboratory, One Bethel Valley Road, Oak Ridge, Tennessee 37831, United States,* ⊥*Department of Chemistry, University of Tennessee, Knoxville, Tennessee 37996, United States, and* §*National Synchrotron Light Source, Brookhaven National Laboratory, Upton New York 11973, United States*

Received November 30, 2010; Revised Manuscript Received December 7, 2010

ABSTRACT: All-conjugated block copolymers have significant potential for solution-processed optoelectronic applications, in particular those relying on a p/n junction. Herein, we report the synthesis and structure of all-conjugated diblock copolymers poly(3-hexylthiophene)-*block*-poly(9,9-dioctylfluorene) and poly(3-hexylthiophene)-*block*-poly(9,9-dioctylfluorene-*co*-benzothiadiazole) in thin films and in the bulk. The diblock copolymers are prepared using a combination of Grignard metathesis polymerization and Suzuki polycondensation and characterized with NMR spectroscopy, size-exclusion chromatography, multiangle laser light scattering, and UV/vis spectroscopy. Structure in thin films and in the bulk is characterized using differential scanning calorimetry, X-ray diffraction, small-angle X-ray scattering, and atomic force microscopy. Diblock copolymer thin films self-assemble into a crystalline nanostructure with some long-range order after extended solvent annealing, and X-ray scattering measurements show that powder samples exhibit crystallinity throughout the bulk. By temperature dependent X-ray scattering measurements, we find that diblock copolymers self-assemble into crystalline nanowires with phase segregated block copolymer domains. These measurements show all-conjugated diblock copolymers may be useful for achieving solution-processed active layers in organic photovoltaics and light-emitting diodes with optimized structural and photophysical characteristics.

Introduction

Semiconducting polymers (also known as π-conjugated or simply conjugated polymers) combine the optical and electronic properties of semiconductors with the processing advantages of polymers. Because of the extended π-conjugated backbone (e.g., alternating double and single bonds), these polymers exhibit photophysical properties characteristic of inorganic semiconductors, including a finite energy bandgap and fluorescence. The rigid, π-conjugated backbone generally leads to decreased solubility in common organic and aqueous solvents, but incorporation of side chains into conjugated polymers improves their solubility and enables solution processing for thin-film, large-area device applications.[1] A number of potentially revolutionary technologies based on conjugated polymers have been proposed, including organic photovoltaics (OPVs),[1,2] thin-film transistors,[3] white organic light-emitting diodes,[4] and fluorescent chemical sensors.[5]

Many applications of organic semiconductors require two distinct semiconductors with different charge transport properties and energy bandgaps. OPVs and organic light-emitting diodes (OLEDs) in particular show improved performance when a p-type, or hole-transporting, component is combined with an n-type, or electron-transporting, component.[6] In OPVs, this can be achieved by solution blending a p-type conjugated polymer with an n-type fullerene derivative followed by solvent casting and annealing to create what is known as a bulk-heterojunction (BHJ) active layer.[7] The polymer and fullerene phase separate during the solvent casting and annealing process, resulting in an active layer with nanoscale p- and n-type domains with sizes that are correlated with relatively efficient exciton separation and charge transport. BHJ OPVs are currently the best performing polymer-based PVs, but efficiencies are still lower than expected for an optimized OPV device;[8,9] it is widely accepted that the nanoscale morphology of the active layer plays a critical role in determining the efficiency of the processes underlying photon-to-electricity conversion. Controlling the active layer morphology in BHJ OPVs is a major challenge because the final structure depends on processing conditions, including the choice of the casting solvent, annealing time and temperature, composition, and solution concentration.[10] New materials and/or processing methods that can reliably generate well-defined p- and n-type domains would facilitate investigation—and ultimately optimization—of the active layer structure for OPV devices or for multilayer constructs needed for polymer OLED devices.[4,11]

The use of block copolymers (BCPs) can potentially address these challenges because they can spontaneously self-assemble into regular nanostructures under a variety of processing conditions and environments.[12−14] As suggested in recent reviews,[15−18]

*Corresponding authors. E-mail: (R.V.) rafaelv@rice.edu; (S.B.D.) darling@anl.gov.

 Published on Web 01/10/2011 © 2011 American Chemical Society

self-assembly of all-conjugated BCPs may be particularly useful for achieving solution-processed active layers in OPVs and OLEDs with optimized structural and photophysical characteristics. Extensive work with BCPs has yet to produce an OPV or OLED that performs as well as polymer-fullerene devices, but the vast majority of this work has focused on BCPs where one or both polymer blocks is not conjugated. Conjugated polymers show the best performance in organic electronic applications, and all-conjugated BCPs can potentially act as both structure-directing agents as well as active components in a device. Furthermore, recent work suggests that all-conjugated BCPs can improve the performance of all-polymer OPV[19] and OLED[20] devices, and conjugated polymer blends have shown promising performance in OPVs.[21−30]

Conjugated polymers are typically synthesized by condensation and cross-coupling reactions, which give poor control over molecular weight, polydispersity (PDI), and end-group functionality. However, recent efforts have provided new methods for the synthesis of all-conjugated BCPs.[31] Grignard metathesis (GRIM) polymerization is a versatile method for making poly(3-alkylthiophenes) with targeted molecular weights, PDIs less than 1.2, and high regioregularity.[32] Several all-conjugated BCPs have also been synthesized by GRIM polymerization.[33−38] These polymers are based almost exclusively on a thiophene repeat unit and are typically p-type, but donor/acceptor block polymers can be made by functionalization of the polythiophene backbone with a variety of side-chains.[39,40] GRIM polymerization can also be used to prepare polyfluorene homopolymers and BCPs of polythiophene and polyfluorene.[41,42] Using a different approach that involves GRIM and Suzuki polymerization reactions, Scherf et al. reported the synthesis of polythiophene-*block*-polyfluorene copolymers that can self-assemble in thin films and at the air−water interface.[43,44] Currently, the only report of an OPV device based on an all-conjugated BCP is provided by Sun et al.[19] Other reports on all-conjugated BCPs have produced materials for white OLEDS[20] as well as other applications,[45] as detailed in recent reviews.[15−18,31]

While these studies have established novel synthetic routes to all-conjugated BCPs, much of the previous work has involved all-conjugated BCPs that contain two p-type polymers or wide-bandgap polymers not suitable for OPVs. Furthermore, the self-assembly of all-conjugated polymers is poorly understood and oftentimes characterized using only AFM imaging, which does not address the morphological structure throughout the bulk of polymer films. Also, all-conjugated BCPs are often not fully characterized with respect to the absolute molecular weight and the presence of homopolymer impurities. These factors underscore the considerable need for fundamental studies involving well-made, rigorously characterized all-conjugated BCPs and their self-assembly. Herein, we report the synthesis and characterization of two all conjugated diblock copolymers: poly(3-hexylthiophene)-*block*-poly(9,9-dioctylfluorene) and poly(3-hexylthiophene)-*block*-poly(9,9-dioctylfluorene-*co*-benzothiadiazole). These polymers are synthesized using a combination of GRIM and Suzuki polymerizations and characterized with a combination of NMR spectroscopy, size-exclusion chromatography (SEC), multiangle laser light scattering (MALLS), and UV/vis spectroscopy. We present a method for quantifying the amount of homopolymer impurities in all-conjugated block copolymer samples. The structure and thermal properties of thin film and polymer melt samples are investigated using differential scanning calorimetry (DSC), X-ray diffraction (XRD), atomic force microscopy (AFM), and small-angle X-ray scattering (SAXS). We find that all-conjugated diblock copolymers can self-assemble into periodic crystalline nanostructures in thin films and in bulk powder samples.

Experimental Section

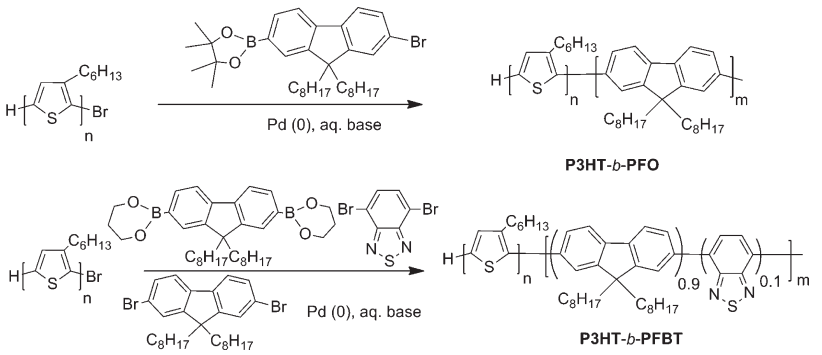
Materials. 9,9-Dioctyl-2,7-dibromofluorene, 4,7-dibromobenzo[1,2,5]thiadiazole, 9,9-dioctylfluorene-2,7-diboronic acid bis(1,3-propanediol) ester, Aliquat 336, tetrakis-(triphenylphosphine)palladium(0), and sodium carbonate (Na_2CO_3) were purchased from Aldrich and used as received. Anhydrous THF (Drisolve), chloroform, diethyl ether, methanol, hexanes, ethyl acetate, dichloromethane, and toluene were purchased from VWR and used as received. Bromo-terminated poly(3-hexylthiophene) (P3HT-Br)[34] and 7′-bromo-9′,9′-dioctylfluoren-2′-yl-4,4,5,5-tetramethyl[1,3,2]dioxaborolane[46] were synthesized as previously described.

Poly(3-hexylthiophene)-*b*-poly(9,9-dioctylfluorene) (P3HT-*b*-PFO). P3HT-Br (505 mg, 0.051 mmol), 7′-bromo-9′,9′-dioctylfluoren-2′-yl-4,4,5,5-tetramethyl[1,3,2]dioxaborolane (1.75 mg, 2.94 mmol), 1−2 drops of Aliquat 336, and tetrakis(triphenylphosphino)palladium(0) (123 mg, 0.108 mmol), 40 mL of toluene, and 20 mL of 2 M aqueous Na_2CO_3 were combined in a Schlenk tube, degassed by three freeze−pump−thaw cycles, and backfilled with nitrogen. The reaction was carried out at 85 °C for 72 h, after which the reaction was cooled to room temperature and precipitated into 200 mL of cold methanol. The product was recovered by filtration, loaded into a Soxhlet thimble, and washed with methanol (2 h), diethyl ether (2 h), and hexanes (7 h) to remove poly(9,9-dioctylfluorene) homopolymer and other small molecule impurities. The polymer was further purified by silica gel column chromatography to remove unreacted P3HT-Br using 90% toluene and 10% acetonitrile (v/v) as the eluent. ^{1}H NMR (500 MHz, $CDCl_3$): δ 7.5−8.0 (m, 1.5 H), 6.9−7.0 (s, 1.0 H), 2.7−2.9 (s, 2.0 H), 2.0−2.3 (m, 1.0 H), 0.7−1.7 (m). ^{13}C NMR (100 MHz, CDCl3): δ 150.8, 138.6, 132.7, 129.5, 127.8, 125.0, 122.0, 120.5, 119.0 54.3, 39.4, 30.8, 30.7, 29.5, 28.7, 22.9, 21.6, 13. SEC−RI/MALLS: dn/dc = 0.226, M_w = 16 700 g/mol, PDI = 1.31.

Poly(3-hexylthiophene)-*b*-poly[(9,9-dioctylfluorene)-*co*-(2,3,5-benzothiadiazole)] (P3HT-*b*-PFBT). P3HT-Br (386 mg, 0.039 mmol), 9,9-dioctyl-2,7-dibromofluorene (541 mg, 0.99 mmol), 4,7-dibromobenzo[1,2,5]thiadiazole (75 mg, 0.25 mmol), 9,9-dioctylfluorene-2,7-diboronic acid bis-(1,3-propanediol) ester (690 mg, 1.24 mmol), 1−2 drops of Aliquat 336, and tetrakis(triphenylphosphino)palladium-(0) (103 mg, 0.090 mmol), 30 mL of toluene, and 15 mL of 2 M aqueous Na_2CO_3 were combined in a Schlenk tube, degassed by three freeze−pump−thaw cycles, and backfilled with argon. As before, the reaction was carried out at 85 °C for 72 h, after which the reaction was cooled to room temperature and precipitated into 200 mL of cold methanol, recovered by filtration, and then loaded into a Soxhlet thimble and washed with methanol (2 h), diethyl ether (2 h), and hexanes (7 h) to remove PFO homopolymer and small molecule impurities. The polymer was further purified by silica gel column chromatography to remove unreacted P3HT-Br using 90% toluene and 10% acetonitrile as the eluent. While this synthesis can produce triblock copolymers in addition to the desired diblock copolymers, the proportion of triblock copolymers is insignificant due to the low molar content and relatively low reactivity of P3HT-Br. ^{1}H NMR (400 MHz, $CDCl_3$): δ 7.4−8.0 (m, 4.7 H), 6.95−7.0 (s, 1.0 H), 2.7−2.9 (t, 1.9 H), 1.9−2.3 (m, 2.6 H), 0.7−1.7 (m). ^{13}C NMR (100 MHz, CDCl3): δ 151.8, 139.9, 133.7, 130.5, 128.6, 126.2, 121.5, 120.0, 55.4, 40.4, 31.8, 30.5, 30.3, 30.0, 29.7, 29.3, 23.4, 22.7, 14.1. SEC−RI/MALLS: dn/dc = 0.242, M_w = 18 900 g/mol, PDI = 1.43.

Instrumentation. *Nuclear Magnetic Resonance Spectroscopy* (*NMR*). Solution ^{1}H NMR and ^{13}C NMR (d_1 = 5 s)

Scheme 1. Synthetic Scheme for the Preparation of All-Conjugated Rod−Rod Copolymers Poly(3-hexylthiophene)-*block*-poly(9,9-dioctylfluorene) (P3HT-*b*-PFO) and Poly(3-hexylthiophene)-*block*-poly(9,9-dioctylfluorene-*co*-benzothiadiazole) (P3HT-*b*-PFBT)



spectroscopy was performed on a Bruker 400 MHz multinuclear spectrometer. Samples were placed in 5 mm o.d. tubes with sample concentrations of 10 and 20% (w/v), respectively. Chloroform-*d* ($CDCl_3$, Cambridge Isotope) was used as the solvent with TMS (0.1%) as an internal standard.

Size-Exclusion Chromatography (*SEC*). Molecular weights and polydispersities were obtained by SEC using an Agilent 1200 module equipped with three PSS SDV columns in series (100, 1000, and 10 000 Å pore sizes), an Agilent variable wavelength UV/visible detector, a Wyatt Technology HELEOS II multiangle laser light scattering (MALLS) detector (λ = 658 nm), and a Wyatt Technology Optilab reX RI detector. This system enables SEC with simultaneous refractive index (SEC−RI), UV/vis (SEC−UV/vis), and MALLS detection. THF was used as the mobile phase at a flow rate of 1 mL/min at 40 °C. Absolute molecular weights are determined by light scattering with dn/dc values calculated using the RI detector and assuming 100% mass recovery of the injected sample (Astra Software Version 5.3.4).

Atomic Force Microscopy (*AFM*). Tapping-mode AFM imaging was performed using a Veeco MultiMode V scanning probe microscope equipped with acoustic and active vibration isolation. Etched silicon probes with force constants of ~40 N/m were used to acquire all images. Both phase-and height-modulated images were obtained. Height-modulated AFM measures changes in the amplitude of oscillation of the AFM cantilever while phase-modulated AFM measures the difference between the driven and the actual oscillations of the cantilever.[47]

X-ray Diffraction (XRD). X-ray diffraction data were obtained using a Bruker D8 Discover analytical X-ray system in a grazing incidence geometry (θ_i = 0.18).

Differential Scanning Calorimetry (*DSC*). Differential scanning calorimetry measurements were performed using a Mettler-Toledo DSC 823^e with a ramp rate of 10 °C/min.

Small-angle X-ray Scattering (*SAXS*). X-ray scattering experiments were performed at beamline X6B at the National Synchrotron Light Source at Brookhaven National Laboratory. Samples in powder form were loaded into 1.0 mm thick glass capillaries and inserted into aluminum cassettes which had a 1.5 mm hole with ±15 degrees of angular range for SAXS measurements. The cassettes fit into a standard hot stage (Instec model HCS402) with a temperature stability of approximately 0.1 °C. The hot stage containing the sample cassette was mounted in a vacuum chamber and centered in an evacuated flight path on the beamline. The incident beam energy was set to 16 keV (wavelength λ = 0.775 Å and energy resolution $\Delta E/E = 10^{-4}$) or 8 keV (wavelength λ = 1.55 Å and energy resolution $\Delta E/E = 10^{-4}$); the beam cross-section was reduced to 0.2 mm horizontal ×0.3 mm vertical by slits placed 1 m upstream of the sample. Two dimensional SAXS images were recorded by a Princeton Instruments CCD area detector (2084 × 2084 array with 116 mm wide active area) located approximately 1.2 m from the sample. The correspondence between CCD pixel position on the detector and scattering wavenumber q was determined by calibration using a standard silver behenate powder placed at the sample position. The effective q resolution of the apparatus was 0.0033 $Å^{-1}$. SAXS measurements were carried out on powder samples that were heated to 250 °C, which is above the crystallization temperature for all samples studied and therefore erases the thermal history of the samples. Samples were held at each temperature for 2 min for measurement, and SAXS patterns were acquired in 5 °C increments with a 5 min thermal equilibration at each temperature before measurement.

Results and Discussion

Synthesis of All-Conjugated Diblock Copolymers. The target BCPs chosen for this study are composed of poly(3-hexylthiophene) (P3HT) as the p-type block and a polyfluorene-based polymer as the n-type block (Scheme 1). P3HT is one of the most widely studied and best performing polymers in BHJ OPVs, serving as a benchmark material because it can be synthesized with controlled molecular weight, polydispersity less than 1.2, controlled end-group functionality, and high regioregularity.[32] Poly(9,9-dioctylfluorene) (PFO) is a wide bandgap polymer with good photoluminescence for OLEDs, and a variety of comonomers can be incorporated to reduce the bandgap for OPV applications. In particular, poly(9,9-dioctylfluorene-*co*-benzothiadiazole) (PFBT) has good electron mobility, a moderate energy bandgap, and HOMO and LUMO levels lower than those of P3HT.[48−50] Furthermore, PFBT and other fluorene-based copolymers have shown promising results in all-polymer OPVs,[28,29] including as an n-type material in combination with P3HT.[22,27,30] Here, we focus on PFBT with just 10% benzothiadiazole units which has been shown to have electronic properties comparable to the PFBT alternating copolymer[48] (i.e., 50% benzothiadiazole units) and which we expect will exhibit improved solubility due to increased 9,9-dioctylfluorene content.

As shown in Scheme 1, our overall synthetic strategy involves a Suzuki polymerization for the synthesis of a PFO or PFBT polymer block in the presence of a polythiophene macroreagent. The P3HT macroreagent was synthesized by GRIM polymerization,[34] and the same P3HT macroreagent was used to make two different diblock copolymers. This synthetic procedure is similar to that reported recently by Tu et al.,[44] but additional purification and analysis are carried out to remove homopolymer impurities and quantify the purity of the final diblock copolymer. Homopolymer

Table 1. Summary of Polymer Characteristics As Determined by SEC and NMR

polymer	MW[a]	PDI[b]	mole ratio[c] NMR	mass ratio[c] MALLS	mole ratio[c] MALLS
P3HT	9.9	1.1			
PFO	4.9	1.6			
PFBT	3.4	2.9			
P3HT-*b*-PFO	16.7	1.3	4.0	1.5	3.5
P3HT-*b*-PFBT	18.9	1.4	1.7	1.1	2.4

[a] kg/mol, as determined by MALLS. [b] Determined via SEC−RI calibration curve based on monodisperse polystyrene standards. [c] The mole and mass ratios correspond to P3HT relative to PFO or PFBT blocks in the diblock copolymers. Using ^{1}H NMR, the degree of polymerization (DP) and mass ratios are determined by comparing the integrated intensity of the aromatic P3HT peak (6.9 ppm) to the alkyl PFO or PFBT peaks at approximately 2.2 ppm. Using MALLS, the mass and mole ratios are determined by comparing the MW of the diblock copolymers to P3HT macroreagent.

impurities are removed by a combination of solvent extraction and column chromatography. PFO and PFBT homopolymers are soluble in refluxing hexanes, and extensive washing of the polymeric product with hexanes in a Soxhlet apparatus removed PFO and PFBT homopolymer without dissolving the diblocks. Silica gel column chromatography removes unreacted P3HT macroreagent. For comparison, PFO and PFBT homopolymers were synthesized using the same reaction conditions but without P3HT macroreagent (Table 1). Both were purified by washing with methanol and acetone in a Soxhlet apparatus to remove small molecule and then hexanes to recover the polymeric product. Similar materials can be synthesized using GRIM polymerization for both polymer blocks,[41,42] but the purity of the block copolymers produced using an all-GRIM method has not been quantified. Furthermore, an all-GRIM approach may not be applicable to the preparation of random and alternating copolymers such as PFBT using commercially available materials.

SEC−RI shows an increase in molecular weight for the BCPs compared with the starting P3HT macroreagent (Figure 1). A broadening of the molecular weight distribution was observed for the diblock copolymers, which is consistent with the behaviors observed for the PFO and PFBT homopolymers; Suzuki condensation polymerizations result in broader PDI materials. The absolute molecular weight of the polymers was determined using MALLS. The MALLS detector operates at a wavelength of 658 nm, which is beyond the range of solution absorbance for both polymer blocks. In both cases, chain-extension of the P3HT block to make P3HT-*b*-PFO and P3HT-*b*-PFBT resulted in an increase in molecular weight, as seen in Table 1 and in Figure 1. The shift in the peak molecular weight in SEC−RI traces indicates that diblocks are the major product, and the presence of polymeric byproducts can be quantified, as discussed in the following paragraphs.

^{1}H NMR was used to determine the composition of the diblock copolymers by integration of peaks characteristic of PFO, PFBT, and P3HT (Figure 2 and Supporting Information). In particular, the aromatic peaks corresponding to P3HT (6.9 ppm) as well as the aliphatic peaks corresponding to $-CH_2-$ in the alkyl side chains of PFO and PFBT (2.2 ppm) are clearly resolved. These integrated intensities can be used to estimate the mole ratio of each component in the diblock copolymers after purification, and the results are given in Table 1. Comparison to the results obtained from MALLS shows fairly good agreement. ^{1}H NMR also indicates that benzothiadiazole monomer is

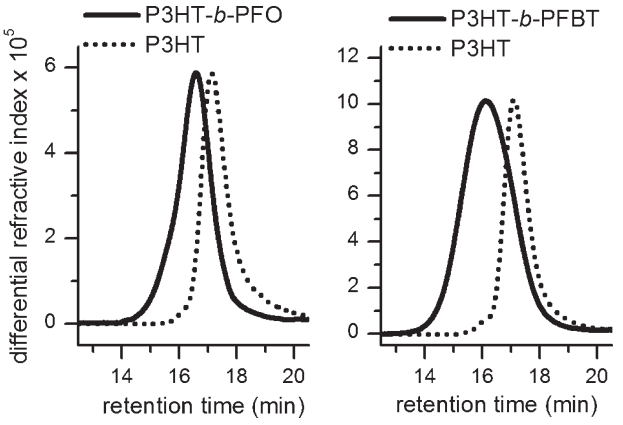


Figure 1. SEC−RI traces of P3HT-*b*-PFO (left) and P3HT-*b*-PFBT (right) block copolymers in comparison to P3HT macroreagent. Both copolymers show an increase in molecular weight relative to the P3HT macroreagent.

incorporated into P3HT-*b*-PFBT at the expected 10% molar content. First, PFBT aromatic peaks at 7.4−8.2 ppm are downshifted relative to the aromatic peaks for PFO, proving that benzothiadiazole is incorporated into PFBT and P3HT-*b*-PFBT (see Figure 2 and Supporting Information). Furthermore, the ratio of the peak intensity at 2.2 ppm to that at 7.4−8.2 ppm is 0.54 in P3HT-*b*-PFBT, close to the expected ratio of 0.59 for 10% benzothiadiazole incorporation, compared with 0.67 for P3HT-*b*-PFO. These ratios also match what is observed in the corresponding homopolymers (see Supporting Information).

To determine the amount of homopolymer impurity in the purified diblock copolymers, UV/vis spectroscopy was utilized. The absorbance of the diblock copolymers is treated as a superposition of the corresponding homopolymers, with P3HT showing maximum absorbance at 450 nm and PFO and PFBT at roughly 380 nm (Figure 3). PFO does not show any absorbance at 450 nm while PFBT shows some absorbance at 450 nm. On the basis of this, the traces at 450 and 380 nm from the UV/vis detector on the SEC system should appear qualitatively similar for diblock copolymer samples with little or no homopolymer impurity. As shown in Figure 4, the absorbance traces at 450 and 380 nm are similar in the case of P3HT-*b*-PFO but different in the case of P3HT-*b*-PFBT, suggesting a greater amount of P3HT impurity is present in the latter.

In order to quantify the amount of P3HT homopolymer impurity, solution UV/vis measurements are compared to SEC−UV/vis measurements. The ratio of the absorbance at 450 nm to that at 380 nm provides a measure of the amount of P3HT present in the mixture. It is assumed that absorbances corresponding to the peak in SEC−UV/vis elution traces reflect only diblock copolymers because absorbances due to homopolymer are observed at lower retention times relative to the diblock copolymer. On the other hand, the absorbance obtained from solution UV/vis measurements accounts for all species present in the mixture, including diblock and homopolymer. Therefore, the increase in the ratio of the absorbance at 450 and 380 nm in the solution UV/vis measurements compared with SEC−UV/vis measurements is due to the presence of P3HT homopolymer. The absorbance ratios can be related to the mass fractions of each polymer block and of P3HT homopolymers as follows: $R_{solution}/R_{sec} = (w_{P3HT}^{BCP} + w_{P3HT}^{homopolymer})/w_{P3HT}^{BCP}$, where $R_{solution}$ and R_{SEC} are the absorbance ratios in standard solution measurements and in the SEC−UV/vis measurement, respectively, w_{P3HT}^{BCP} is the mass fraction of P3HT in the diblock

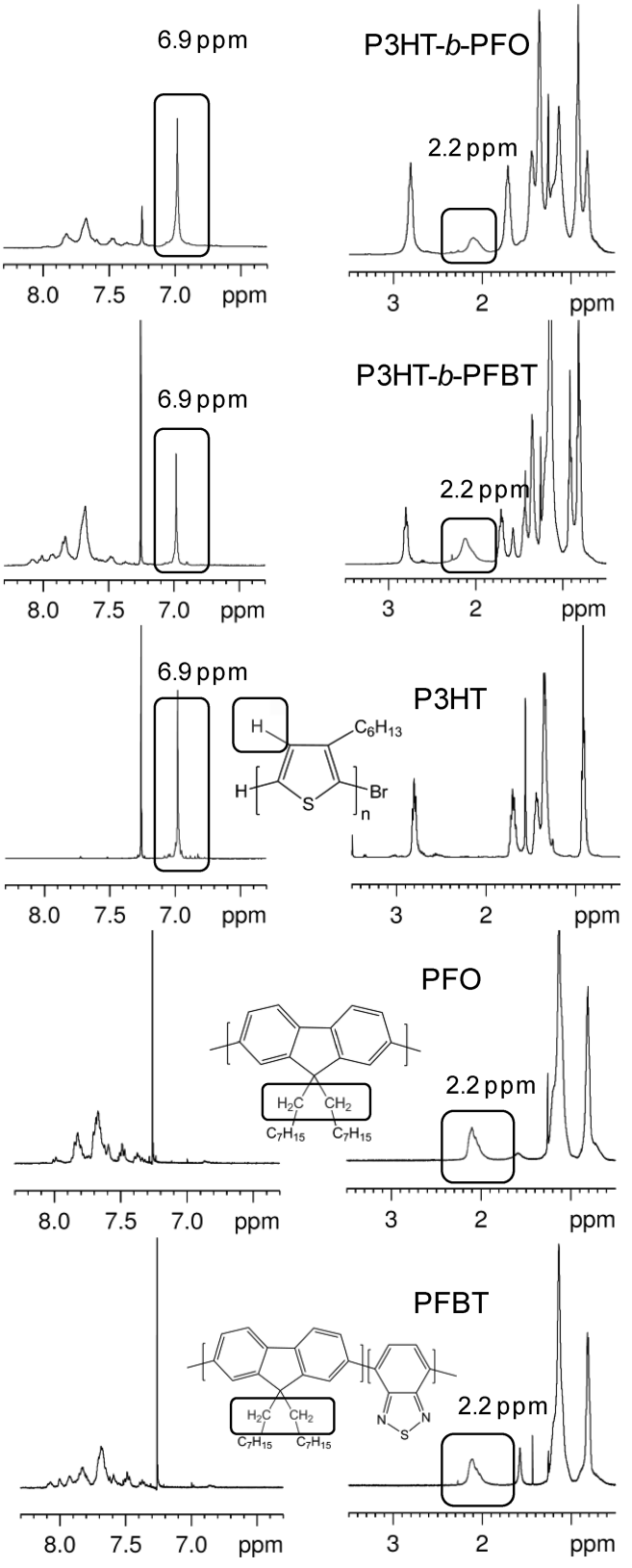


Figure 2. ^{1}H NMR spectra for conjugated block copolymers and homopolymers. The regions highlighted were used to determine the relative mole fractions of each polymer block.

copolymer, and $w_{P3HT}^{homopolymer}$ is the mass fraction of P3HT homopolymer relative to the total mass of diblock copolymer (see Supporting Information for a detailed derivation). SEC−UV/vis measurements give absorbance ratios of 0.81

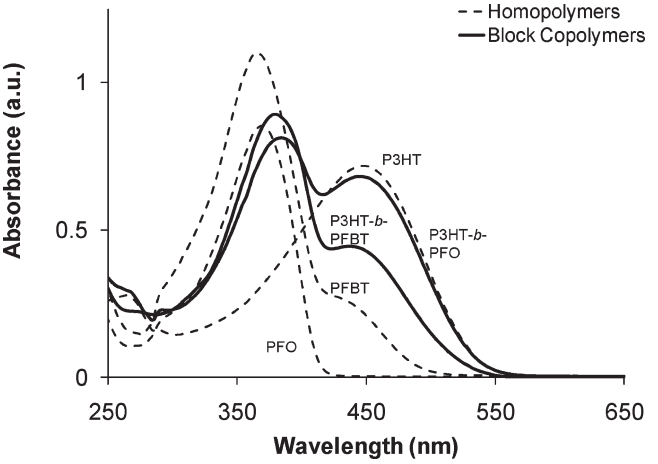


Figure 3. UV/vis absorbance measurements of block copolymers in THF. The absorbance data shows that P3HT absorbs more strongly at 450 nm compared with PFO and PFBT. On the other hand, absorbance at 380 nm is more significant in PFBT and PFO compared with P3HT.

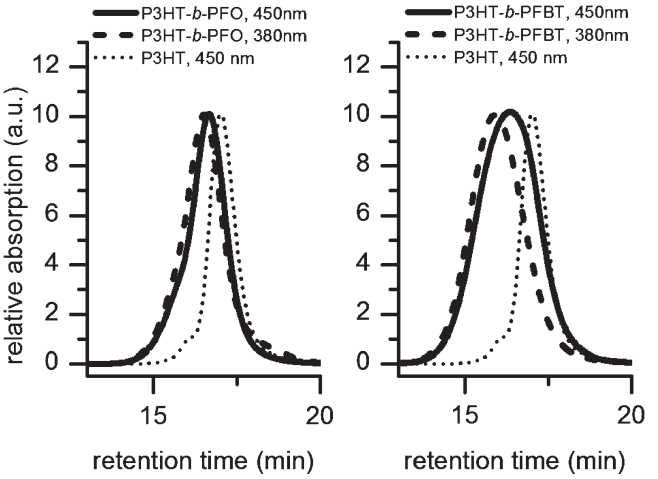


Figure 4. SEC−UV/vis traces for P3HT-*b*-PFO and P3HT-*b*-PFBT compared with P3HT macroreagent. The SEC−UV/vis traces are normalized for clarity.

and 0.38 for P3HT-*b*-PFO and P3HT-*b*-PFBT, respectively. By comparison, solution UV/vis measurements give ratios of 0.84 and 0.48 for P3HT-*b*-PFO and P3HT-*b*-PFBT, respectively. As expected, the ratios are larger in the standard solution measurements due to the presence P3HT homopolymer impurity. The relationship above and the compositions in Table 1 give an estimate of 2% and 17% P3HT homopolymer impurity ($w_{P3HT}^{homopolymer}$) in P3HT-*b*-PFO and P3HT-*b*-PFBT, respectively. Quantifying the amount of homopolymer impurity is important when interpreting physical behaviors, including the morphology of rod−rod copolymers. This has been neglected in many previous reports on all-conjugated block copolymers, and the method presented here can be applied to all-conjugated BCPs in which the conjugated polymer blocks have different absorbance properties.

As shown in Figure 5, DSC measurements of diblock copolymer samples show a thermal transition near 200 °C, where a crystal melting transition is observed for P3HT.[51] In the case of the diblocks, the peak is broad and contains multiple peaks, indicating that P3HT crystallization and other structural changes may be occurring near 200 °C. PFO shows a broad crystallization peak below 100 °C

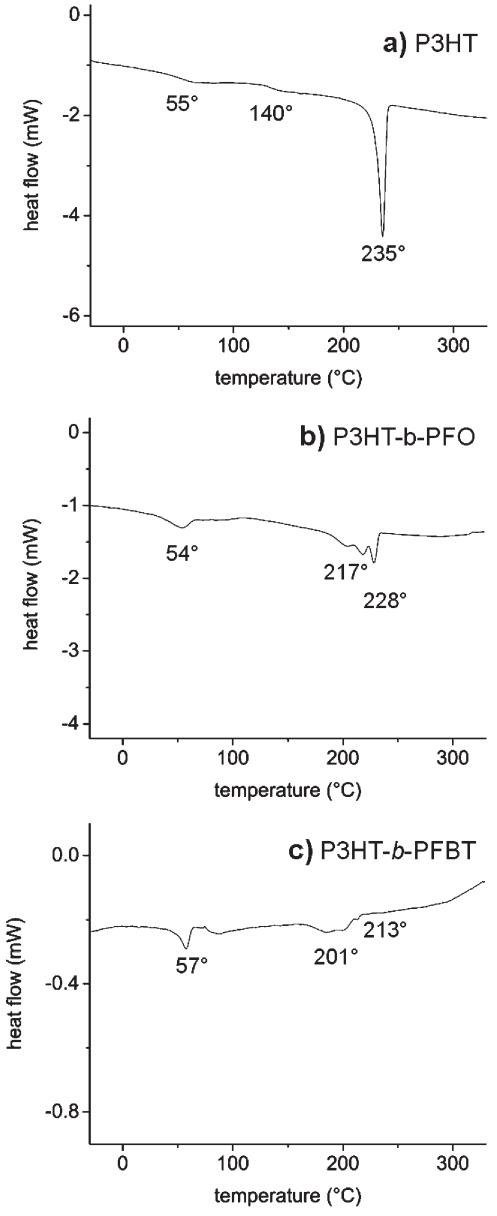


Figure 5. Differential scanning calorimetry data on second heating for (a) P3HT, (b) P3HT-*b*-PFO, and (c) P3HT-*b*-PFBT.

(see Supporting Information), but no comparable peaks are seen in the diblocks. All polymers also show a T_g near 50 °C.

Properties of All-Conjugated Diblock Copolymer Thin Films. In order to study the structure of these polymers in thin films, the polymers were spin-cast onto SiO_2 substrates, solvent annealed in dichlorobenzene at 150 °C, and characterized using XRD and AFM. The XRD data for the diblock copolymers and P3HT homopolymer presented in Figure 6 show peaks corresponding to a crystalline, lamellar morphology. The peak at $2\theta \approx 5.6°$ corresponds to an interlayer *d*-spacing of 16.36 Å, and the other two diffraction peaks at 2θ of approximately 11° and 15.8° represent second and third-order reflections of the lamellae. These values are close to those reported for P3HT thin films[52] and correspond to crystalline P3HT lamellae oriented parallel to the substrate. No diffraction peaks associated with PFO[53] are observed for the P3HT-*b*-PFO diblock copolymer thin films, which indicates that the crystallization of PFO block is suppressed in the diblock copolymer thin films. This may be due to the lower crystallization temperature of PFO or the lower degree

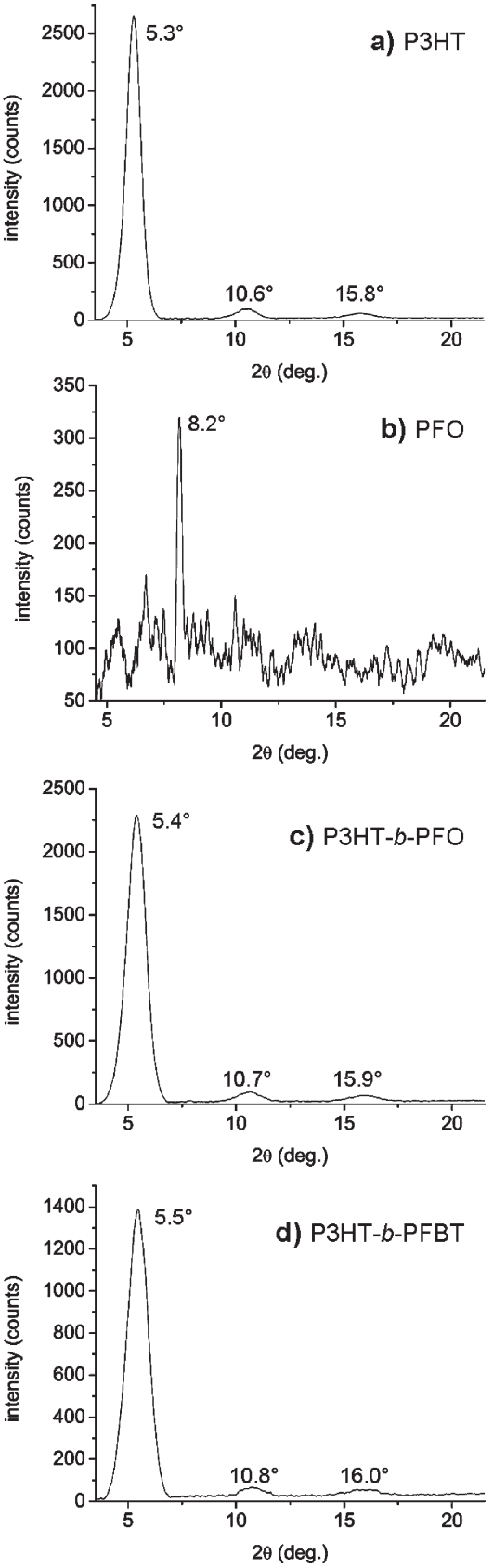


Figure 6. XRD traces for (a) P3HT, (b) PFO, (c) P3HT-*b*-PFO, and (d) P3HT-*b*-PFBT thin films spin-cast in chlorobenzene and annealed at 150 °C for 3 h.

of crystallinity of PFO, as indicated by the much weaker peak intensity observed for PFO thin films. These data suggest that

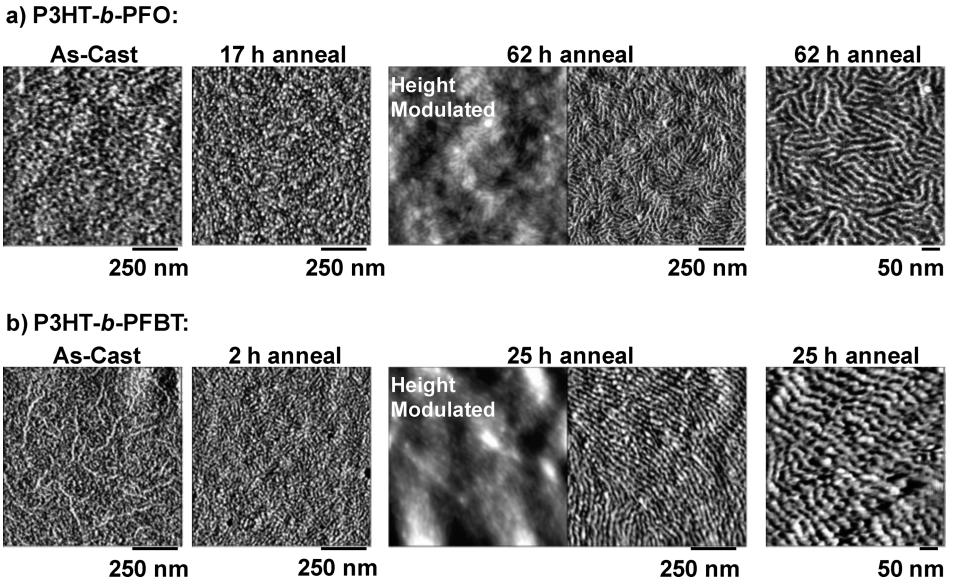


Figure 7. Atomic force microscopy images of all-conjugated block copolymer films on SiO_2. All images are obtained by phase modulation except where otherwise noted. Polymer films were solvent annealed with dichlorobenzene at 150 °C for the time shown.

the P3HT block in diblock copolymer films has a crystalline structure similar to that in P3HT homopolymer thin films. The covalent attachment of a crystalline PFO or amorphous PFBT polymer block has little or no impact on the crystallinity of the P3HT block in the diblocks. Furthermore, the suppression of PFO crystallinity may be due to limited mobility of the polymer chains after crystallization of the P3HT block. Similar behavior has been observed in related diblock copolymers with a P3HT polymer block, including both rod−coil[54,55] and rod−rod[36,56] diblocks.

AFM images show that diblock copolymer thin films develop a periodic nanostructure with some long-range order after extended solvent annealing (Figure 7). The periodic lateral nanostructure is evident in phase modulated AFM images, whereas height modulated AFM images exhibit significantly lower contrast for both P3HT-*b*-PFO and P3HT-*b*-PFBT. The formation of nanostructured domains requires long annealing times in the presence of a solvent, which may be due to the slow dynamics associated with the reorganization of a semicrystalline diblock copolymer. The width of the nanostructures is approximately 20 nm with some degree of long-range ordering, up to approximately 100 nm, and the morphology is similar to that of crystalline nanowires commonly observed in P3HT homopolymers[32] and P3HT rod−coil diblock copolymers.[57] Together with the XRD measurements, these AFM images show that diblock copolymers self-assemble into a crystalline nanostructure. Previous AFM studies of crystalline nanowires from P3HT of a similar molecular weight to the P3HT in the present diblocks revealed a significantly narrower nanowires,[58] less than 15 nm in width compared to domains of 20 nm observed in the diblocks. This suggests that the PFO and PFBT blocks assemble around the nanowires, increasing the average size and distance between the nanowires. Furthermore, thin films of P3HT homopolymer matching the molecular weight of the P3HT block in the BCP films and processed under similar conditions show crystallinity but not periodic nanoscale domains (Supporting Information). This discrepancy indicates that BCP phase separation may increase the kinetics for the formation of laterally periodic nanostructures.

Structure of Diblock Copolymers in the Melt State. In contrast to AFM, which is only useful for characterizing the surface structure of a film, SAXS measurements reveal structural details throughout the thickness of a sample. SAXS traces show peaks corresponding to P3HT crystallites and lamellar domains in the diblock copolymer samples (Figure 8). For P3HT-*b*-PFO, no peaks are observed at temperatures above 190 °C after cooling from 250 °C, but two peaks emerge below 190 °C. Both peaks are thermally reversible and appear within a 5 °C window during cooling, as seen in Figure 8. Similar peaks are present in the SAXS traces for P3HT-*b*-PFBT powder samples. Above 200 °C no peaks are observed, but on cooling to 180 °C a P3HT crystal peak emerges along with a low-angle peak. The low-angle peak is weaker than that for P3HT-*b*-PFO but can be clearly resolved, and the peak disappears and reappears as the temperature is cycled. The lower intensity in the low-angle peak observed for P3HT-*b*-PFBT relative to P3HT-*b*-PFO may be due to the higher content of P3HT homopolymer impurity in the former.

Thus, the diblock copolymer samples undergo a structural transition on cooling below the crystallization temperature that results in nanoscale, crystalline domains throughout the bulk samples, not just in thin films or at the surface. A domain size can be calculated from $d = 2\pi/q^*$, where d is the lamellar spacing and q^* the position of the peak low-angle peak (0.025 and 0.023 $Å^{-1}$ for P3HT-*b*-PFO and P3HT-*b*-PFBT, respectively) to give a spacing of approximately 25 and 27 nm for P3HT-*b*-PFO and P3HT-*b*-PFBT, respectively. These numbers are close to the values for the domain spacing observed in the AFM images of diblock copolymer thin films and significantly larger than previously reported for pure P3HT nanowires (13.5 and 15.0 nm for 10.5 and 11.7 kg/mol P3HT, respectively).[58]

Analysis of the temperature dependent SAXS data shows that nanostructure formation in the diblock copolymers is coincident with the crystallization of P3HT. The SAXS crystallization transition can be evaluated from a plot of the inverse primary peak intensity versus the inverse temperature (Figure 9). As shown in the cooling scans, two scattering peaks appear concurrently, within a 5 °C temperature range. The transitions are much sharper on cooling; on heating, both transitions occur gradually at first, possibly due to the preferential melting of smaller crystallites or the disappearance of domains at lower temperatures. Nevertheless, both occur within similar temperature ranges on

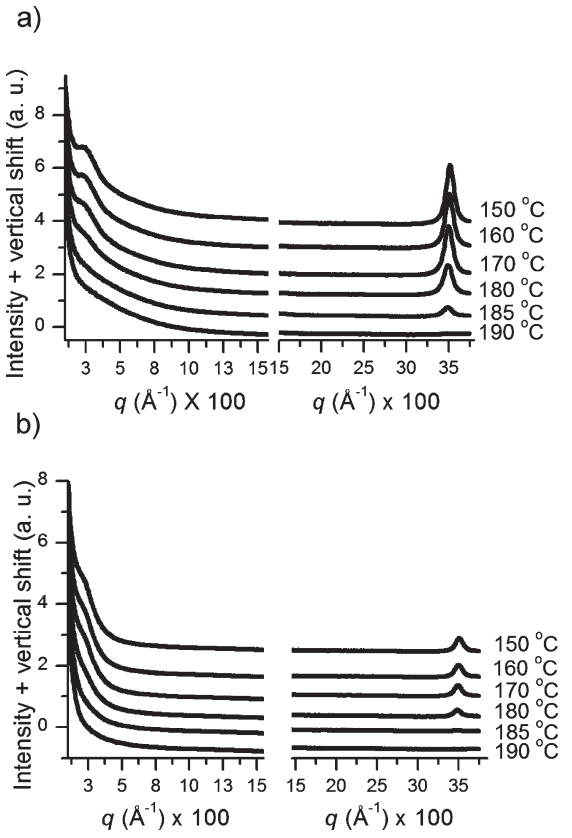


Figure 8. Small-angle X-ray scattering traces for (a) P3HT-*b*-PFO and (b) P3HT-*b*-PFBT measured at 8 keV (left axes) and 16 keV (right axes) on cooling from an annealing temperature of 250 °C.

cooling, and both transitions are shifted by approximately 20 °C on heating compared with cooling. The low-angle peak in diblock samples is only observed upon crystallization of P3HT, and no higher order peaks are present as is typical for self-assembled BCP nanostructures,[59] including some conjugated BCPs.[60] The polydispersity of the samples may preclude the formation of well-defined domains with long-range order, and the long-range ordering observed in polymer thin films could be indicative of nanostructuring influenced in part by interfacial effects that are less prominent in bulk samples. These interfacial effects may also account for the slower kinetics for self-assembly observed in polymer thin films compared with bulk polymer samples.

Previous reports on P3HT homopolymer films have found similar small-angle scattering traces, even in P3HT polymers with molecular weights as low as 2 kDa.[58,61] Therefore, both the SAXS and AFM data suggest that diblock copolymers self-assemble into crystalline nanofibrils or nanowires similar to those observed in P3HT. However, the presence of a PFO or PFBT block in the diblocks gives rise to BCP phase separation in addition to crystallization and nanowire formation. AFM and SAXS measurements indicate that the second polymer block increases the size and spacing between crystalline nanowires. In contrast to microphase segregation of coil−coil block copolymers,[59] phase separation accompanies nanowire formation and is driven by crystallization of the P3HT polymer block.

Conclusions

All-conjugated diblock copolymers can be synthesized using a two-step procedure that involves both GRIM and Suzuki polymerizations, followed by solvent extraction and column chromatography. The diblock copolymers produced in this study were

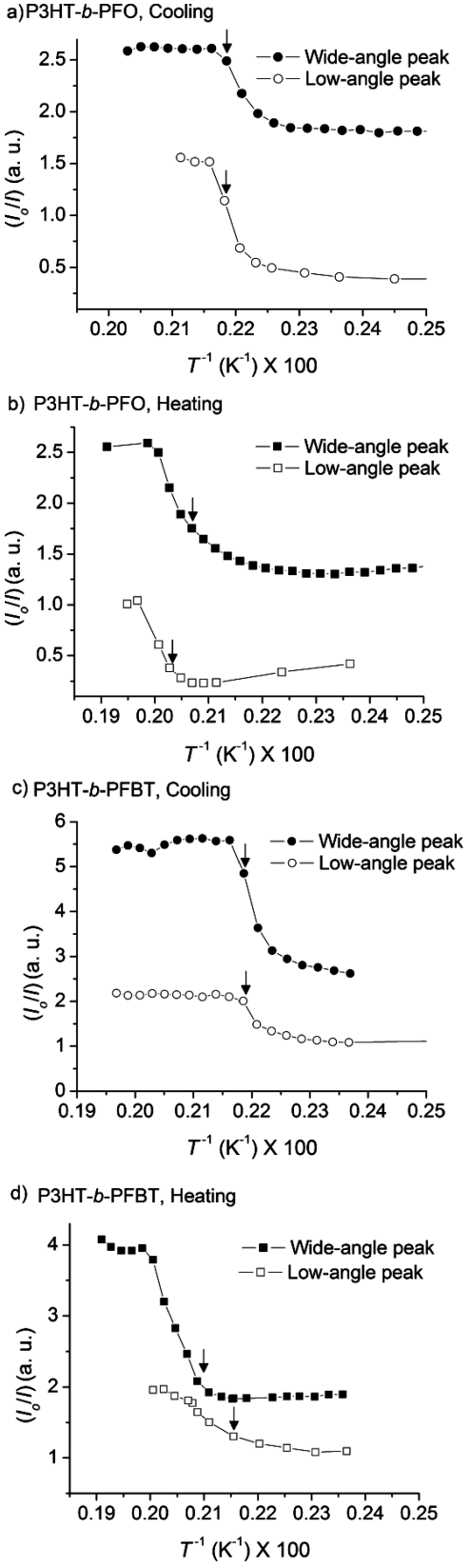


Figure 9. Inverse normalized intensity of peak heights in the vicinity of the order−disorder and crystallization transitions. Peak intensities are measured at 0.0252 and 0.348 Å^{-1} for P3HT-*b*-PFO and at 0.0232 and 0.351 Å^{-1} for P3HT-*b*-PFBT. The arrows mark the approximate positions for the start of a transition.

characterized using a combination of ^{1}H NMR, SEC−MALLS, and SEC−UV/vis to quantify the absolute molecular weight,

polymer compositions, and amount of homopolymer impurity. Our method for quantifying the amount of conjugated polymer impurities can be applied to conjugated BCPs in which the constituent polymer blocks have sufficiently different absorption spectra.

AFM measurements revealed the presence of periodic nanostructured domains in all-conjugated diblock copolymer thin films. These domains appeared only after extended solvent annealing and showed some long-range order. Analysis of temperature dependent SAXS data revealed simultaneous crystallization and nanostructure formation in powder diblock copolymer samples. This suggests that the diblock copolymers self-assemble into nanoscale domains due to crystallization of P3HT and incompatibility of the polymer blocks.

Crystallinity is a prerequisite for achieving organic materials with good mobilities for organic electronic applications, and the all-conjugated BCPs studied self-assemble into crystalline, nanoscale domains. The attachment of a second conjugated polymer block does not disrupt the crystallinity of P3HT, and periodic nanostructures can be formed both in thin films and in powder samples. All-conjugated diblock copolymers represent promising materials for controlling and tailoring the morphology of organic semiconductor systems, and the general approach presented here can be used to create tunable BCP organic active layers with nanoscale phase-separated p- and n-type regions.

Acknowledgment. R.V. acknowledges financial support from the Welch Foundation (Grant No. C-1750), the Louis Owen Foundation, and the Rice University School of Engineering start-up funds. Use of the Center for Nanoscale Materials was supported by the U.S. Department of Energy, Office of Science, Office of Basic Energy Sciences, under Contract DEAC02-06-CH11357. A portion of this research was conducted at the Center for Nanophase Materials Sciences, which is sponsored at Oak Ridge National Laboratory by the Division of Scientific User Facilities, U.S. Department of Energy. Use of the National Synchrotron Light Source, Brookhaven National Laboratory, was supported by the U.S. Department of Energy, Office of Science, Office of Basic Energy Sciences, under Contract No. DE-AC02-98CH10886.

Supporting Information Available: AFM images, small-angle X-ray scattering traces, DSC and TGA data, NMR spectra, and derivation of mathematical relationship between absorbance ratios and polymer composition and impurity.This material is available free of charge via the Internet at http://pubs.acs.org.

References and Notes

(1) Krebs, F. C.; Gevorgyan, S. A.; Alstrup, J. *J. Mater. Chem.* **2009**, *19* (30), 5442–5451.
(2) Zhan, X.; Zhu, D. *Polym. Chem.* **2010**, *1* (4), 409–419.
(3) Zaumseil, J.; Sirringhaus, H. *Chem. Rev.* **2007**, *107* (4), 1296–1323.
(4) D'Andrade, B. W.; Forrest, S. R. *Adv. Mater.* **2004**, *16* (18), 1585–1595.
(5) Thomas, S. W. I.; Joly, G. D.; Swager, T. M. *Chem. Rev.* **2007**, *107*, 1339–1386.
(6) Tang, C. W. *Appl. Phys. Lett.* **1986**, *48*, 183–185.
(7) Thompson, B. C.; Fréchet, J. M. J. *Angew. Chem., Int. Ed.* **2008**, *47* (1), 58–77.
(8) Dennler, G.; Scharber, M. C.; Brabec, C. J. *Adv. Mater.* **2009**, *21* (13), 1323–1338.
(9) Forrest, S. R. *MRS Bull.* **2005**, *30*, 28–32.
(10) Hoppe, H.; Sariciftci, N. S. *J. Mater. Chem.* **2006**, *16* (1), 45–61.
(11) Geffroy, B.; Roy, P. l.; Prat, C. *Polym. Int.* **2006**, *55* (6), 572–582.
(12) Bates, F. S.; Fredrickson, G. H. *Phys. Today* **1999**, *52*, 32–38.
(13) Park, C.; Yoon, J.; Thomas, E. L. *Polymer* **2003**, *44*, 6725–6760.
(14) Darling, S. B. *Prog. Polym. Sci.* **2007**, *32*, 1152–1204.
(15) Darling, S. B. *Energy Environm. Sci.* **2009**, *2*, 1266–1273.
(16) Segalman, R. A.; McCulloch, B.; Kirmayer, S.; Urban, J. J. *Macromolecules* **2009**, *42*, 9205–9216.
(17) Botiz, I.; Darling, S. B. *Mater. Today* **2010**, *13* (5), 42–51.
(18) Sommer, M.; Huettner, S.; Thelakkat, M. *J. Mater. Chem.* **2010**, *20* (48), 10788–10797.
(19) Sun, S. S.; Zhang, C.; Ledbetter, A.; Choi, S.; Seo, K.; Bonner, C. E.; Drees, M.; Sariciftci, N. S. *Appl. Phys. Lett.* **2007**, *90*, 043117.
(20) Xiao, X.; Fu, Y.; Sun, M.; Li, L.; Bo, Z. *J. Polym. Sci., Part A: Polym. Chem.* **2007**, *45* (12), 2410–2424.
(21) Veenstra, S. C.; Loos, J.; Kroon, J. M. *Prog. Photovolt.: Res. Appl.* **2007**, *15*, 727–740.
(22) McNeill, C. R.; Halls, J. J. M.; Wilson, R.; Whiting, G. L.; Berkebile, S.; Ramsey, M. G.; Friend, R. H.; Greenham, N. C. *Adv. Funct. Mater.* **2008**, *18* (16), 2309–2321.
(23) Kietzke, T.; Hörhold, H.-H.; Neher, D. *Chem. Mater.* **2005**, *17*, 6532–6537.
(24) Koetse, M. M.; Sweelssen, J.; Hoekerd, K. T.; Schoo, H. F. M.; Veenstra, S. C.; Kroon, J. M.; Yang, X.; Loos, J. *Appl. Phys. Lett.* **2006**, *88* (8), 083504.
(25) McNeill, C. R.; Greenham, N. C. *Adv. Mater.* **2009**, *21* (38−39), 3840–3850.
(26) Granstrom, M.; Petritsch, K.; Arias, A. C.; Lux, A.; Andersson, M. R.; Friend, R. H. *Nature* **1998**, *395* (6699), 257–260.
(27) McNeill, C. R.; Abrusci, A.; Zaumseil, J.; Wilson, R.; McKiernan, M. J.; Burroughes, J. H.; Halls, J. J. M.; Greenham, N. C.; Friend, R. H. *Appl. Phys. Lett.* **2007**, *90* (19), 193506–3.
(28) Arias, A. C.; MacKenzie, J. D.; Stevenson, R.; Halls, J. J. M.; Inbasekaran, M.; Woo, E. P.; Richards, D.; Friend, R. H. *Macromolecules* **2001**, *34* (17), 6005–6013.
(29) McNeill, C. R.; Watts, B.; Thomsen, L.; Ade, H.; Greenham, N. C.; Dastoor, P. C. *Macromolecules* **2007**, *40* (9), 3263–3270.
(30) Kim, Y.; Cook, S.; Choulis, S. A.; Nelson, J.; Durrant, J. R.; Bradley, D. D. C. *Chem. Mater.* **2004**, *16* (23), 4812–4818.
(31) Scherf, U.; Gutacker, A.; Koenen, N. *Acc. Chem. Res.* **2008**, *41* (9), 1086–1097.
(32) Osaka, I.; McCullough, R. D. *Acc. Chem. Res.* **2008**, *41* (9), 1202–1214.
(33) Wu, P.-T.; Ren, G.; Li, C.; Mezzenga, R.; Jenekhe, S. A. *Macromolecules* **2009**, *42*, 2317–2320.
(34) Iovu, M. C.; Sheina, E. E.; Gil, R. R.; McCullough, R. D. *Macromolecules* **2005**, *38*, 8649–8656.
(35) Yokozawa, T.; Adachi, I.; Miyakoshi, R.; Yokoyama, A. *High Perfom. Polym.* **2007**, *19*, 684–699.
(36) Zhang, Y.; Tajima, K.; Hirota, K.; Hashimoto, K. *J. Am. Chem. Soc.* **2008**, *130*, 7812–7813.
(37) Ouhib, F.; Khoukh, A.; Ledeuil, J.-B.; Martinez, H.; Desbrieres, J.-B.; Dagron-Lartigau, C. *Macromolecules* **2008**, *41*, 9736–9743.
(38) Zhang, Y.; Tajima, K.; Hashimoto, K. *Macromolecules* **2009**, *42*, 7008–7015.
(39) Ouhib, F.; Khoukh, A.; Ledeuil, J.-B.; Martinez, H.; Desbrieres, J.; Dagron-Lartigau, C. *Macromolecules* **2008**, *41* (24), 9736–9743.
(40) Miyanishi, S.; Zhang, Y.; Tajima, K.; Hashimoto, K. *Chem. Commun.* **2010**, *46* (36), 6723–6725.
(41) Javier, A. E.; Varshney, S. R.; McCullough, R. D. *Macromolecules* **2010**, *43* (7), 3233–3237.
(42) Huang, L.; Wu, S.; Qu, Y.; Geng, Y.; Wang, F. *Macromolecules* **2008**, *41* (22), 8944–8947.
(43) Park, J. Y.; Koenen, N.; Ponnapati, R.; Scherf, U.; Advincula, R. *Macromolecules* **2008**, *41* (16), 6169–6175.
(44) Tu, G.; Li, H.; Forster, M.; Heiderhoff, R.; Balk, L. J.; Sigel, R.; Scherf, U. *Small* **2007**, *3* (6), 1001–1006.
(45) Ohshimizu, K.; Shibasaki, Y.; Komura, M.; Nakajima, K.; Ueda, M. *Chem. Lett.* **2007**, *36* (6), 742–743.
(46) Zhang, X.; Tian, H.; Liu, Q.; Wang, L.; Geng, Y.; Wang, F. *J. Org. Chem.* **2006**, *71*, 4332–4335.
(47) Prillman, S.; Colvin, V., *TappminModeTM - Atomic Force Microscopy Manual*. In Colvin, V., Ed.; Rice University: Houston, TX, 1997; Vol. *1.1* (http://nanonet.rice.edu/manuals/afm.html).
(48) Herguth, P.; Jiang, X.; Liu, M. S.; Jen, A. K.-Y. *Macromolecules* **2002**, *35*, 6094–6100.
(49) Cheng, Y.-J.; Yang, S.-H.; Hsu, C.-S. *Chem. Rev.* **2009**, *109*, 5868–5923.
(50) Campbell, A. J.; Bradley, D. D. C.; Antoniadis, H. *Appl. Phys. Lett.* **2001**, *79* (14), 2133–2135.

(51) Malik, S.; Nandi, A. K. *J. Polym. Sci., Part B: Polym. Phys.* **2002**, *40* (18), 2073–2085.
(52) Chen, T.-A.; Wu, X.; Rieke, R. D. *J. Am. Chem. Soc.* **1995**, *117*, 233–244.
(53) Kawana, S.; Durrell, M.; Lu, J.; Macdonald, J. E.; Grell, M.; Bradley, D. D. C. *Polymer* **2002**, *43*, 1907–1913.
(54) Botiz, I.; Darling, S. B. *Macromolecules* **2009**, *42* (21), 8211–8217.
(55) Boudouris, B. W.; Frisbie, C. D.; Hillmyer, M. A. *Macromolecules* **2007**, *41* (1), 67–75.
(56) Zhang, Y.; Tajima, K.; Hashimoto, K. *Macromolecules* **2009**, *42* (18), 7008–7015.
(57) Iovu, M. C.; Jeffries-El, M.; Zhang, R.; Kowalewski, T.; McCullough, R. D. *J. Macromol. Sci.: Pure Appl. Chem.* **2006**, *43* (12), 1991–2000.
(58) Zhang, R.; Li, B.; Iovu, M. C.; Jeffries-El, M.; Sauvé, G.; Cooper, J.; Jia, S.; Tristram-Nagle, S.; Smilgies, D. M.; Lambeth, D. N.; McCullough, R. D.; Kowalewski, T. *J. Am. Chem. Soc.* **2006**, *128* (11), 3480–3481.
(59) Hamley, I. W., *The Physics of Block Copolymers*. Oxford University Press: Oxford, U.K., 1998.
(60) Olsen, B. D.; Segalman, R. A. *Macromolecules* **2006**, *39*, 7078–7083.
(61) Canetti, M.; Bertini, F.; Scavia, G.; Porzio, W. *Eur. Polym. J.* **2009**, *45* (9), 2572–2579.

540 *Macromolecules* **2011**, *44*, 540–549
DOI: 10.1021/ma102534f

Macromolecules
ARTICLE

Crystallization Behavior of Propylene−Butene Copolymers: The Trigonal Form of Isotactic Polypropylene and Form I of Isotactic Poly(1-butene)

Claudio De Rosa,*,† Finizia Auriemma,† Paolo Vollaro,† Luigi Resconi,‡,§ Simona Guidotti,‡ and Isabella Camurati‡

†*Dipartimento di Chimica "P. Corradini", Università di Napoli "Federico II", Complesso Monte S.Angelo, Via Cintia, 80126 Napoli, Italy, and* ‡*Basell Polyolefins, Centro Ricerche G. Natta, P.le G. Donegani 12, I-44100 Ferrara, Italy.* §*Present address: Borealis Polyolefine GmbH, St. Peter Str. 25, 4021 Linz, Austria*

Received November 7, 2010; Revised Manuscript Received December 12, 2010

ABSTRACT: A structural characterization of samples of isotactic propylene−butene copolymers (iPPBu), synthesized with a metallocene catalyst, is reported. The copolymers crystallize in the entire range of comonomer compositions, and α and γ forms of isotactic polypropylene (iPP) crystallize in propene-rich copolymers, whereas form I of isotactic polybutene (iPB) crystallizes in butene-rich samples. Butene and propene comonomeric units are included in crystals of iPP and iPB, respectively, as indicated by the change of the unit cell parameters of copolymer crystals with changing comonomer composition. The trigonal form of iPP, recently found in propylene−hexene and propylene−pentene copolymers, does not crystallize in as-prepared or melt-crystallized samples of iPPBu copolymers, but it has been obtained in oriented fibers of copolymers. In fact, in copolymers with butene concentrations lower than 10−15 mol %, crystals of α or γ forms present in the melt-crystallized compression-molded samples transform by stretching at high deformations into the mesomorphic form of iPP, whereas in samples with butene concentration of around 50%, crystals of α form of iPP transform into the trigonal form of iPP by stretching. This is the first evidence of the crystallization of the trigonal form of iPP in iPPBu copolymers.

Introduction

In recent papers the structure of the trigonal form of isotactic polypropylene (iPP) that crystallizes in propylene−hexene (iPPHe) and propylene−pentene (iPPPe) random copolymers has been described.[1−5] A comparison between the crystal structures of the α form,[6] γ form,[7] and trigonal form[3−5] of iPP is shown in Figure 1. We have suggested that the driving force that induces the crystallization of the trigonal form is the increase of density due to the inclusion of hexene or pentene units in the crystal.[3−5] The inclusion of hexene or pentene units in the crystals induces a suitable increase of density that allows crystallization of 3-fold helical chains in the trigonal form (space group $R\bar{3}c$),[3−5] where the helical symmetry of the chains is maintained in the crystal lattice, as predicted by principles of polymer crystallography,[8] giving a structure (Figure 1C) similar to that of form I of isotactic polybutene (iPB).[9] This trigonal structure represents the fulfillment of the principles of polymer crystallography and provides a clear example of the principle of *entropy-density driven phase formation in polymers* that suggests that the packing of polymer molecules is mainly driven by density.[3,4] This form does not crystallize and has never been observed so far for iPP homopolymer because in the absence of bulky side groups it would have too low value of density.[3,4]

For low concentrations of hexene or pentene comonomeric units, up to nearly 10 mol %, both iPPHe and iPPPe copolymers crystallize in the α form of iPP. The new trigonal form crystallizes when the hexene or pentene concentration achieves values higher than 9−10 mol %.[3−5] It has been demonstrated that hexene or pentene units are partially included in both crystals of α form and trigonal form, but the crystallization of the trigonal form at high comonomer concentrations (higher than 10 mol %) allows incorporation of high amounts of comonomeric units, higher than in the crystals of α form.[1−5]

A model of the crystal structure of the trigonal form has been proposed for both iPPHe and iPPPe copolymers.[3−5] Chains in 3-fold helical conformation are packed in a trigonal unit cell according to the space group $R3c$ or $R\bar{3}c$ (Figure 1C), as in the crystal structure of iPB.[9] The values of a and b axes of the unit cell depend on the comonomer concentration and increase with increasing hexene or pentene concentration.[3−5] For instance, values of $a = b = 17.5$ Å and $c = 6.5$ Å have been found for the iPPHe sample with 26 mol % of hexene,[3,4] whereas values of axes $a = b = 17.1$ Å and $c = 6.5$ Å have been found for iPPPe copolymers with 30 mol % of pentene.[5] In both cases, the crystallization of the trigonal form allows much higher incorporation of hexene or pentene units in the crystals, and a density of crystals as high as 0.91−0.92 g/cm^3 is achieved for the high comonomer concentration. The value of $a = b$ axes approaches the value of the unit cell of iPB ($a = b = 17.7$ Å)[9] for higher pentene concentrations (50−55 mol %) when the average composition of iPPPe copolymers approaches that of iPB.[5] Therefore, when propene and pentene or hexene units are randomly distributed along the same macromolecules and the average overall composition of the two comonomers approaches that of 1-butene (≈50% C_3H_6 + ≈50% C_5H_{10} = C_4H_8), copolymer chains behave as poly(butene) macromolecules and crystallize into the stable form I of iPB.[5] On the basis of these principles, it was predicted that the trigonal form is a stable form of iPP and can be easily obtained in copolymers of propene with other olefins, when the crystal density and the average composition of the copolymer approach those of iPB, provided that the distribution of the comonomer is random.[3−5] The latter condition is satisfied mainly by propylene-based copolymers prepared with single-center metallocene catalysts.

*To whom correspondence should be addressed: Tel ++39 081 674346; Fax ++39 081 674090; e-mail claudio.derosa@unina.it.

 Published on Web 01/10/2011 © 2011 American Chemical Society

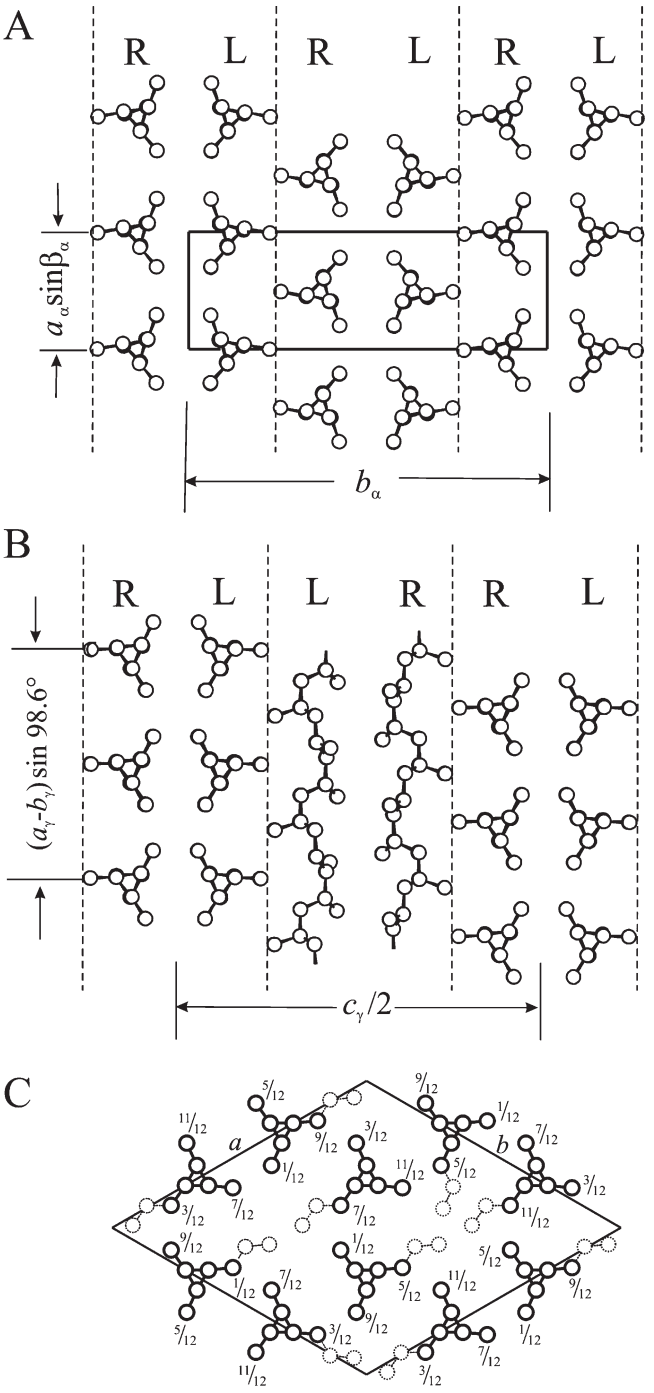
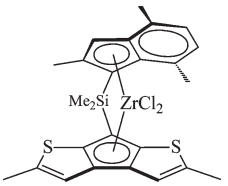


Figure 1. Models of the crystal structures of monoclinic α form (A),[6] orthorhombic γ form (B),[7] and trigonal form (C)[3−5] of iPP. R = right-handed helix, L = left-handed helix. In (C) the model for iPPPe copolymers[5] is shown, where the atoms of ethyl side groups of the pentene comonomeric units, randomly distributed along each iPP chain, are shown as thin lines. The heights of the propylene methyl groups are indicated in $c/12$ units (c = 6.5 Å).[5]

The structure and the crystallization behavior of isotactic propylene−butene copolymers (iPPBu) have been extensively studied.[10−16] As-prepared and melt-crystallized samples of iPPBu copolymers always crystallize as mixtures of α and γ forms; the fraction of γ form increases with increasing concentrations of comonomers, *rr* stereodefects, and crystallization temperature. The amount of γ form decreases for butene contents higher than 10 mol %, and samples with butene content higher than 25−30 mol % crystallize exclusively in the α form.[15] In any case the crystallization of the trigonal form has not been observed. These data have indicated that butene units favor crystallization of γ and α forms at low and high concentrations, respectively. This result has been explained on the basis of the favored inclusion of the butene units in the crystals of α form at high butene concentrations.[15] At low butene concentrations, up to nearly 10 mol %, the effect of shortening the length of regular propylene sequences ($\langle L_{iPP}\rangle$) prevails and induces crystallization of γ form. For higher butene concentrations, the effect of inclusion of butene units in crystals of α form prevails over that of the shortening of $\langle L_{iPP}\rangle$, producing a decrease in the amount of γ form and, then, a crystallization of the pure α form for butene content higher than 30 mol %.[15] However, the corresponding increase in density does not produce crystallization of the trigonal form up to 30−40 mol % of butene units.

Chart 1. Structure of the Metallocene Catalyst Used in This Study



In this paper we report a study of the crystallization properties of iPPBu copolymers prepared with metallocene catalysts in the entire range of comonomer compositions in bulk samples and in oriented fibers, aimed at finding the crystallization condition of the trigonal form of iPP in iPPBu copolymers.

Experimental Section

All samples of iPPBu copolymers have been prepared at temperatures between 60 and 70 °C in liquid monomers, with the C_1-symmetric metallocene catalyst shown in Chart 1, activated with methylalumoxane (MAO).[17] Samples of iPP and iPB homopolymers have been prepared with the same catalyst and in the same experimental conditions. The analyzed samples of iPPBu copolymers are reported in Table 1. The catalyst is fully regioselective but not perfectly isoselective.[18]

Analysis of the ^{13}C NMR spectra of the homopolymer iPP and iPB samples prepared with the catalyst of Chart 1 had shown that, indeed, both polymers are highly regioregular (no 2,1 and 4,1 regiodefects are detectable) but less stereoregular and, therefore, contain only stereo errors[18] due to the presence of *rr* triad defects. The concentrations of stereo errors *rr* in iPP and iPB are 3.5 and 0.8 mol %,[18] respectively (Table 1), and correspond to the percentage of primary stereo errors over all monomer units, [*rr*] = [*mrrm*] + [*mrrr*] + [*rrrr*]. The catalyst is more isospecific for iPB than for iPP.[18] Hence, the concentration of *rr* stereo errors is not constant with the comonomer concentration but decreases with increasing butene content (Table 1).[15]

The microstructural data of all samples have been obtained from ^{13}C NMR analysis. All spectra were obtained using a Bruker DPX-400 spectrometer operating in the Fourier transform mode at 120 °C and 100.61 MHz. The samples were dissolved with a 8% w/v concentration in 1,1,2,2-tetrachloroethane-d_2 at 120 °C. The carbon spectra were acquired with a 90° pulse and 15 s of delay between pulses and CPD (WALTZ 16) to remove ^{1}H−^{13}C coupling. About 1500−3000 transients were stored in 32K data points using a spectral window of 6000 Hz. For the iPP sample, the peak of the *mmmm* pentad in the ^{13}C spectra (21.8 ppm) was used as a reference. For the propylene−butene copolymers the assignments of the resonances and the 1-butene content were determined from the constitutional diad distribution using the resonances of the $S_{\alpha\alpha}$ methylene carbon atoms, according to Randall.[19] The peak of the propylene methine carbon atoms was used as internal reference at 28.83 ppm.

Table 1. Polymerization Temperatures (T_p), Concentration of Butene Comonomeric Units (mol %), Intrinsic Viscosity, Viscosity-Average Molecular Masses ($\bar{M}_v$), Weight-Average Molecular Masses ($\bar{M}_w$), Polydispersities ($\bar{M}_w/\bar{M}_n$), Melting Temperatures of As-Prepared Samples (T_{m1}), Melting Temperatures of Samples Crystallized from the Melt by Cooling to Room Temperature at 10 °C/min (T_{m2}), and Concentration of *rr* Triads Stereodefects (%) of the Isotactic Propylene−Butene Copolymers Prepared with the Catalyst of Chart 1

sample	T_p (°C)	mol % butene	[η] (dL/g)	$\overline{M}_v$[a]	$\overline{M}_w$[b]	$\overline{M}_w/\overline{M}_n$[b]	T_{m1} (°C)[c]	T_{m2} (°C)[c]	[*rr*] (%)
iPP	60	0	1.63	202 400	247 000	2.3	133.0	134.0	3.5
iPPBu1.4	60	1.4	1.29	148 000	214 000	2.0	126.3	127.7	3.4
iPPBu2.2	60	2.2	1.30	150 000	214 500	1.9	123.5	123.9	3.4
iPPBu6.4	60	6.4	1.40	168 000	214 400	1.8	113.0	114.0	2.5
iPPBu17.9	70	17.9	1.76	239 300	368 400	3.1	85.0	86.2	2.2
iPPBu36.4	70	36.4	1.42	204 000	284 000	2.7	67.0	62.5	2.2
iPPBu46.2	70	46.2	1.56	224 900	275 500	3.0	59.6	57.3	2
iPPBu58.4	70	58.4	1.65	253 900	322 600	2.1	57.9	55	1.1
iPPBu69.1	70	69.1	1.80	297 500	339 000	2.1	60.0 (I′)[d]	57.5 (I′)[e]	0.8
iPPBu83.2	70	83.2	1.98	357 500	407 600	2.1	86.1 (I′)[d]	76.0 (II),[f] 103.6 (I)[g]	0.8
iPPBu93.5	70	93.5	1.75	313 500	433 000	2.2	86.6 (I′)[d]	90.2 (II),[f] 113.6 (I)[g]	0.8
iPPBu95	70	95.0	2.03	387 000			87.8 (I′)[d]	94.3 (II),[f] 117.9 (I)[g]	0.8
iPB	70	100	2.21	443 400	506 000	2.1	94.4 (I′)[d]	106.3 (II),[f] 123 (I)[g]	0.8

[a] From the intrinsic viscosity values. [b] Weight-average molecular masses and polydispersities were obtained from the SEC curves. [c] Melting temperatures of as-prepared and melt-crystallized samples from DSC scans at heating rate of 10 °C/min. [d] Melting temperatures of as-prepared samples crystallized in form I′ of iPB. [e] Melting temperatures of samples crystallized from the melt in form I′ of iPB by cooling the melt to room temperature at 10 °C/min. [f] Melting temperatures of samples crystallized from the melt in form II of iPB by cooling the melt to room temperature at 10 °C/min. [g] Melting temperatures of samples crystallized in form I of iPB obtained by crystallization from the melt and aging at room temperature for long time, allowing the complete transformation of form II into form I of iPB.

The intrinsic viscosity [η] was measured in tetrahydronaphthalene at 135 °C using a standard Ubbelohde viscometer. The viscosity-average molecular masses M_v were determined from the intrinsic viscosity values according to the relationship $[\eta] = K(\bar{M}_v)^{\alpha}$, using values of K and α evaluated from the composition weighted average of the values determined for isotactic polypropylene ($K_{iPP} = 1.93 \times 10^{-4}$, $\alpha_{iPP} = 0.74$)[20] and polybutene ($K_{iPB} = 1.78 \times 10^{-4}$, $\alpha_{iPB} = 0.725$).[18b]

The mass-average molecular masses were evaluated from size-exclusion chromatography (SEC). The SEC curves of all samples show narrow molecular weight distributions, with M_w/M_n = 2−3, typical of single-center metallocene catalysts.

The calorimetric measurements were performed with a differential scanning calorimeter (DSC) Perkin-Elmer DSC-7 in a flowing N_2 atmosphere. The melting temperatures of the samples were taken as the peak temperature of the DSC curves recorder at 10 °C/min.

Oriented fibers of the copolymer samples have been obtained by stretching at room temperature specimens of compression-molded films of initial length L_0 = 1 mm at drawing rate of 10 mm/min at different degrees of deformation. Compression-molded films have been prepared by heating powder samples at temperatures higher than the melting temperatures under a press at low pressure and cooling to room temperature.

X-ray diffraction patterns were obtained with Ni filtered Cu Kα radiation. The powder diffraction profiles were obtained with a Philips diffractometer with continuous scans of the 2θ angle and a scanning rate of 0.02 deg/s The fiber diffraction patterns were recorded on a BAS-MS imaging plate (FUJIFILM) using a cylindrical camera and processed with a digital imaging reader (FUJIBAS 1800).

The indices of crystallinity (x_c) were evaluated from the X-ray powder diffraction profiles by the ratio between the crystalline diffraction area (A_c) and the total area of the diffraction profile (A_t), $x_c = A_c/A_t$. The crystalline diffraction area has been obtained from the total area of the diffraction profile by subtracting the amorphous halo. The amorphous halo of copolymer samples with butene contents lower that 35−40 mol %, which crystallize in the α form of iPP, has been obtained from the X-ray diffraction profile of atactic polypropylene, whereas for samples with butene contents higher than 69 mol % that crystallize in the form I of iPB, the amorphous halo has been obtained from the diffraction profile of atactic polybutene. The scattering of the amorphous phases of samples with butene concentrations in the range 45−65 mol %, which crystallize as mixtures of crystals of the α form of iPP and form I of iPB, has been obtained by the average of the amorphous haloes of atactic polypropylene and polybutene, weighted with respect to the composition. The amorphous haloes have then been scaled and subtracted to the X-ray diffraction profiles of the samples.

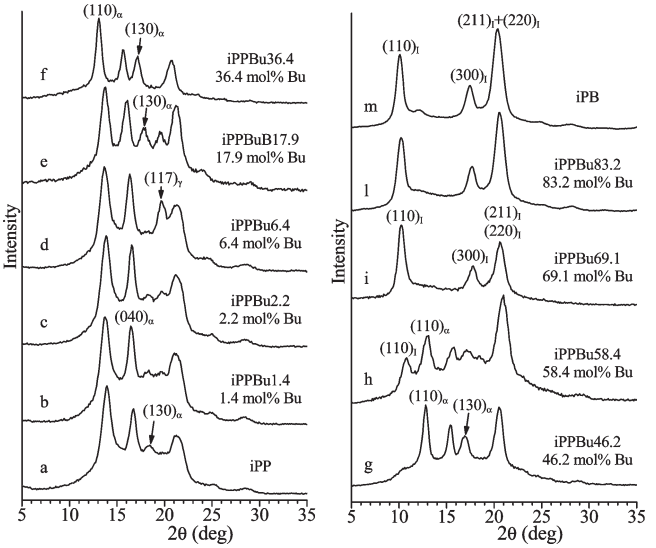


Figure 2. X-ray powder diffraction profiles of as-prepared samples iPPBu copolymers. The diffraction profiles of iPP and iPB homopolymer samples prepared with the same catalyst (profiles a and m) are also reported. The $(110)_\alpha$, $(040)_\alpha$, and $(130)_\alpha$ reflections at $2\theta \approx 12-14°$, 15−17°, and 16−18°, respectively, of α form of iPP,[6] the $(117)_\gamma$ reflection at $2\theta \approx 20°$ of γ form of iPP,[7] and the $(110)_I$, $(300)_I$, and $(220 + 211)_I$ reflections at $2\theta \approx 10°$, 17°, and 20°, respectively, of form I of iPB,[9] are indicated.

Results and Discussion

The X-ray powder diffraction profiles of as-prepared samples of iPPBu copolymers compared with those of the corresponding iPP and iPB homopolymer samples are reported in Figure 2. The iPP homopolymer sample is crystallized in the α form (Figure 1A), as indicated by the presence of the $(110)_\alpha$, $(040)_\alpha$, and $(130)_\alpha$ reflection at 2θ = 14°, 16.8°, and 18.6° of the α form,[6] and the absence of the $(117)_\gamma$ reflection at 2θ = 20.1° of the γ form,[7] in the X-ray powder diffraction profile a of Figure 2, whereas the iPB sample is crystallized in the form I, as indicated by the presence of

the $(110)_I$, $(300)_I$, and $(220)_I + (211)_I$ reflections at $2\theta = 9.9°$, 17.5°, and 20.5°, respectively, of the trigonal form I of iPB[9] in the diffraction profile m of Figure 2.

The data of Figure 2 indicate that iPPBu copolymers crystallize in the entire range of composition, up to 100% of butene content. Samples having concentrations of butene units up to 46−50 mol % crystallize in α and γ forms of iPP (Figure 1A,B) or as a mixture of both, as shown by the presence of typical $(110)_\alpha$, $(040)_\alpha$, and $(130)_\alpha$ reflections of α form at $2\theta \approx 12-14°$, 15−17°, and 16−18°, respectively, and of the $(117)_\gamma$ reflection at $2\theta \approx 20°$ of γ form, in the diffraction profiles b−g of Figure 2, the exact values of the Bragg angle 2θ depending on the butene concentration. Copolymers samples with butene content higher than 65−70 mol % are instead crystallized in the stable form I of iPB, as indicated by the presence of characteristic $(110)_I$, $(300)_I$, and $(220)_I + (211)_I$ reflections at $2\theta \approx 10°$, 17°, and 20°, respectively, of the trigonal form I of iPB[9] in the diffraction profiles i−l of Figure 2. Samples with similar concentrations of propylene and butene units (in the range 50−60 mol % of butene) crystallize as mixtures of the α form of iPP and form I of iPB, as shown by the diffraction profile h of Figure 2; this presents all reflections arising from α form of iPP and form I of iPB.

In samples that show crystallinity from iPP, the amount of crystals of γ form, with respect to that of α form, increases with increasing concentration of comonomeric units up to butene concentrations of 10−15 mol %, as indicated by the increase of the $(117)_\gamma$ reflection of the γ form with increasing content of butene units in the diffraction profiles of Figure 2b−d. The intensity of the $(117)_\gamma$ reflection of the γ form decreases for butene contents higher than 15 mol %, indicating a decrease in the amount of γ form, and is zero in the diffraction profiles of samples with 36.4 and 46.2 mol % of butene units, which are crystallized in the pure α form (profiles f and g of Figure 2).

We recall that the crystallization of α form, instead of γ form, for high concentrations of comonomeric units has been recently explained on the basis of favored inclusion of butene units in the crystals of α form at high butene concentrations.[15] At low butene concentrations, up to nearly 10 mol %, the effect of shortening the length of regular propylene sequences ($\langle L_{iPP} \rangle$) prevails and induces crystallization of the γ form. For higher butene concentrations, the effect of inclusion of butene units in crystals of α form prevails over that of the shortening of $\langle L_{iPP} \rangle$, producing a decrease in the amount of the γ form and, then, a crystallization of the pure α form for butene content higher than 30 mol %.[15]

It is worth noting that in the case of iPPPe and iPPHe copolymers a concentration of 9−10 mol % of pentene or hexene is enough to induce crystallization of the trigonal form of iPP.[3−5] The data of Figure 2 indicates that in the case of propene-rich iPPBu copolymers the trigonal form of iPP does not crystallize even for high butene concentrations up to 36−40 mol %. Moreover, even in samples isothermally crystallized from the melt at different temperatures, the trigonal form has never been observed and only the α and γ forms crystallize from the melt even at high temperatures.[12,15] These data suggest that for propene-rich iPPBu copolymers the α and γ forms of iPP are the most stable forms in all conditions of crystallization of bulk samples. For butene-rich copolymers at butene concentrations higher than 50−60 mol %, the copolymers show crystallinity from iPB and they crystallize into the trigonal form I of iPB.

The experimental evidence that iPPBu copolymers are crystalline in the entire range of compositions suggests a cocrystallization of propene and butene units in the crystals of iPP and iPB, as already observed in the past literature.[10,21,22] Moreover, for propylene-rich copolymers, the increase of the parameters of the unit cell of α form of iPP observed in the literature[13,21−24] also suggests that a significant proportion of butene can be incorporated into the crystal lattice of iPP. However, the fact that the trigonal form of iPP does not crystallize in propene-rich iPPBu copolymers indicates that this inclusion of butene units in crystals of iPP is not sufficient to produce the increase in density necessary to induce the crystallization of the trigonal form, as in the case of bulkier pentene or hexene comonomeric units.

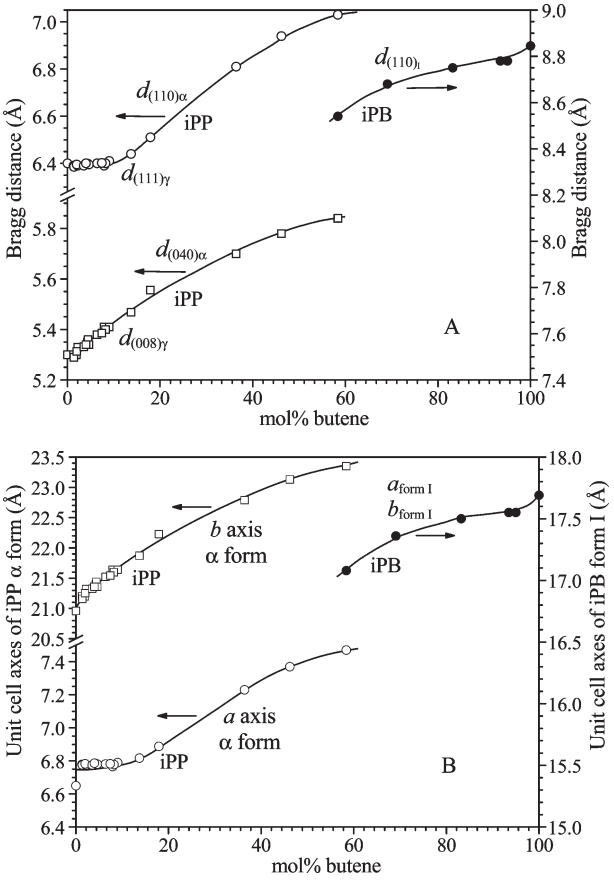


Figure 3. (A) Values of Bragg distances (d) of $(110)_\alpha$ ($(111)_\gamma$) (○) and $(040)_\alpha$ ($(008)_\gamma$) (□) reflections of α form (or γ form) of iPP and of the $(110)_I$ reflection of form I of iPB (●) observed in the X-ray powder diffraction profiles of as-prepared samples of iPPBu copolymers of Figure 2 as a function of butene content. (B) Values of a (○) and b (□) axes of the monoclinic unit cell of α form of iPP and of $a = b$ (●) axes of the trigonal unit cell of form I of iPB that crystallize in as-prepared samples of iPPBu copolymers as a function of butene concentration. The values of Bragg distances of the same reflections and of axes of unit cells of α form of iPP homopolymer and form I of iPB homopolymer are also reported at 0 and 100 mol % of butene, respectively.[6,9]

The values of Bragg distances of $(110)_\alpha$ and $(040)_\alpha$ reflections of α form, and $(111)_\gamma$ and $(008)_\gamma$ reflections of γ form, observed in the powder diffraction profiles of iPPBu samples of Figure 2, are reported in Figure 3A. These reflections occur at $2\theta = 14°$ and 16.7°, respectively, in the diffraction profile of α and γ forms of iPP homopolymer. As already shown in the ref 15, at low butene contents up to 10−14 mol %, the Bragg distances of $(110)_\alpha$ and $(111)_\gamma$ of α and γ forms, respectively, are nearly constant, whereas the Bragg distance of the $(040)_\alpha$ and $(008)_\gamma$ reflections of α and γ forms, respectively, show slight increase with increasing butene concentration (Figure 3A). This indicates an appreciable increase in the dimension of the b_α axis of the monoclinic unit cell of α form, and of the c_γ axis of the orthorhombic unit cell of γ form with increasing butene concentration, and the inclusion of butene comonomeric units in both crystals of α and γ forms of iPP. We recall that in the unit cell of the γ form the c_γ axis does not coincide with the chain axis direction (Figure 1B) but correspond to the b_α axis direction in the crystals of α form (the direction of stacking of bilayers of chains) (Figure 1A).[7]

In copolymers with butene concentrations higher than 15 mol % that crystallize only in the α form (Figure 2), a much larger increase of Bragg distances of $(110)_\alpha$ and $(040)_\alpha$ reflections and of dimensions of a_α and b_α axes of the unit cell of α form is observed (Figure 3). The values of a_α and b_α axes of the monoclinic unit cell for crystals of α form of iPPBu copolymers are reported in Figure 3B, compared to those of the iPP homopolymer (a_α = 6.65 Å, b_α = 20.96 Å).[6] The values of the chain axis c_α = 6.5 Å and of β_α = 99.3° of the monoclinic unit cell of the α form of iPP[6] have been assumed constant with the butene content.

For butene concentrations higher than 60 mol %, iPPBu copolymers crystallize into form I of iPB (profiles i−m of Figure 2). The Bragg distance of the $(110)_I$ reflection of form I of iPB, which occurs at 2θ = 9.9° for iPB homopolymer,[9] decreases with increasing concentration of propylene units (Figure 3A). This indicates that the axes of the trigonal unit cell of form I of iPB in crystals of iPPBu copolymers are smaller than those of form I of iPB homopolymer ($a = b$ = 17.7 Å)[9] and decrease with increasing propylene concentrations (Figure 3B). These data clearly show that iPPBu copolymers are crystalline in the entire range of composition, from 0 to 100% of butene, and propylene and butene comonomeric units cocrystallize at any compositions so that butene units are easily included in crystals of γ and α forms of iPP at low and high butene contents, respectively, and propylene units are included in crystals of form I of iPB.

The melting temperatures of as-prepared and melt-crystallized (by cooling the melt to room temperature at cooling rate of 10 °C/min) samples and the degree of crystallinity of as-prepared samples of iPPBu copolymers are reported in Figure 4 as a function of butene concentration. The melting temperatures of copolymers are intermediate between those of iPP (133 °C) and iPB (123 °C for form I) homopolymer samples prepared with the same catalyst.[18,25] For copolymers showing iPP crystallinity, the melting temperature decreases with increasing butene content down to a minimum of nearly 57 °C for butene concentrations of 55−60 mol % and then increases for higher butene contents due to the crystallization of iPB (Figure 4A).

It is worth noting that iPPBu samples with butene concentration higher than 80 mol % show a crystallization behavior similar to the iPB homopolymer sample.[25] They, indeed, crystallize from the melt into the kinetically favored form II of iPB that transforms by aging at room temperature into the more stable form I.[18b,25] As shown in Figure 2, as-prepared samples of copolymers with butene concentration higher than 69 mol % crystallize in the as-prepared samples directly in form I. The crystalline form I that is obtained directly by crystallization from melt or solution (as from the solution polymerization medium), and not from the transformation of crystals of form II, is generally defined form I′. Figure 4A shows that these crystals of form I′ of iPPBu copolymers present melting temperatures lower than those of form I obtained from transformation of form II and even lower than the melting temperatures of crystals of form II.[25] The plot of Figure 4A and the Table 1 report the melting temperatures of crystals of form I′ of as-prepared samples, of crystals of form II of samples crystallized from the melt by cooling to room temperature at 10 °C/min, and of crystals of form I of samples crystallized from the melt and aged at room temperature for long time, allowing the complete transformation of form II into form I of iPB.

All the iPPBu samples present high degrees of crystallinity, around 50%, that do not greatly change with the concentration of butene, up to nearly 14−15 mol % (Figure 4B). For higher butene contents, the crystallinity slightly decreases up to a minimum value of nearly 40% for butene content of 50−60 mol % and, then, increases with further increasing butene concentration when the samples crystallizes into form I of iPB (Figure 4B). The high values of crystallinity in the whole composition range

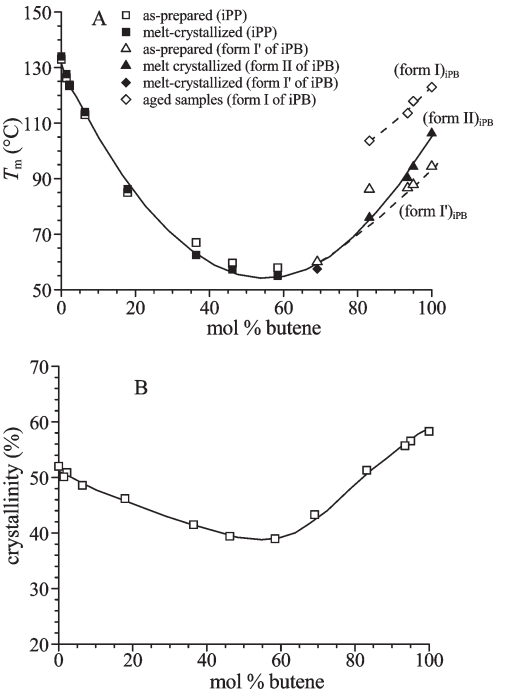


Figure 4. Melting temperatures obtained from DSC curves recorded at heating rate of 10 °C/min (A) and X-ray degree of crystallinity (B) of samples of iPPBu copolymers, as a function of butene concentration. The melting temperature of as-prepared samples (□, △), of samples crystallized from the melt by cooling the melt to room temperature at 10 °C/min (■, ▲, ◆), and of samples crystallized from the melt and aged at room temperature (◇) are reported (A). For samples with butene concentrations higher than 69 mol %, the melting temperatures of as-prepared samples crystallized in form I′ of iPB (△) and of samples crystallized from the melt in form II (▲) or in form I′ (◆) of iPB are shown. For samples with butene concentrations higher than 80 mol %, the melting temperatures of samples in form I of iPB crystallized from the melt in form II and aged at room temperature for long time, allowing the transformation of form II into form I, are also shown (◇). The degree of crystallinity (□) refers to the X-ray crystallinity of the as-prepared samples (B).

also confirms the cocrystallization of propene and butene in the crystals of iPP and iPB.

The X-ray powder diffraction profiles of samples of propene-rich iPPBu copolymers crystallized from the melt by compression molding are reported in Figure 5. The samples with low butene concentrations are crystallized in the γ form, as indicated by the presence of the $(117)_\gamma$ reflection at $2\theta \approx 20°$ of the γ form of iPP in the diffraction profiles b−d of Figure 5, whereas samples with butene concentrations higher than 10−15 mol % are crystallized mainly in the α form since the diffraction profiles present only the $(130)_\alpha$ reflection of α form at $2\theta \approx 16-18°$ (profiles e−g of Figure 5). The sample iPPBu58.4 with 58.4 mol % of butene units crystallize from the melt as mixtures of α form of iPP and form I of iPB, as shown by the diffraction profile h of Figure 5, which presents all reflections arising from α form of iPP and form I of iPB. Compared to the as-prepared sample (profile h of Figure 2), the melt-crystallized sample iPPBu58.4 shows higher concentrations of crystals of form I of iPB, as indicated by the higher intensity of the $(110)_I$ reflection at $2\theta \approx 10°$ of form I of iPB (profile h of Figure 5). These compression-molded films have been stretched at different deformations while recording the X-ray fiber diffraction.

The X-ray fiber diffraction patterns of fibers of some samples of the iPPBu copolymers stretched at various deformations while maintaining the fibers under tension are reported in Figure 6. For samples with low butene concentrations of up to 10−15 mol %, crystals of γ form present in the unstretched compression-molded

films (Figure 5b−d) transform by stretching into the disordered mesomorphic form of iPP. The X-ray fiber diffraction patterns of fibers of the sample iPPBu2.2, with 2.2 mol % of butene are reported in Figure 6A−C, as an example. It is apparent that crystals of the γ form transforms by stretching into the mesomorphic form

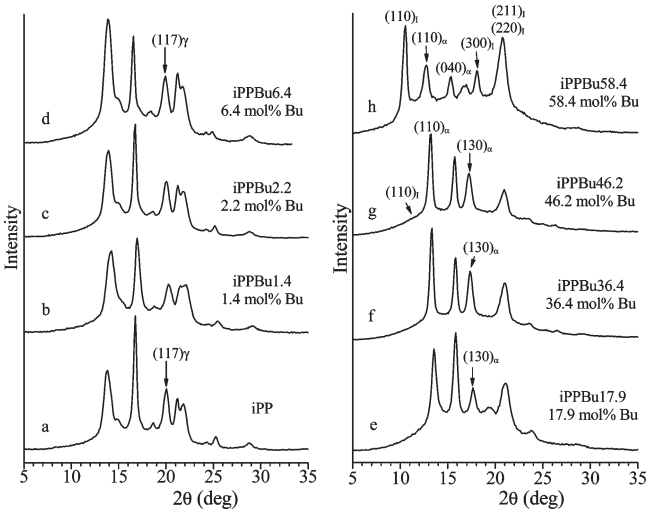


Figure 5. X-ray powder diffraction profiles of melt-crystallized compression-molded samples of propene-rich iPPBu copolymers. The $(110)_\alpha$, $(040)_\alpha$, and $(130)_\alpha$ reflections at $2\theta \approx 12-14°$, 15−17°, and 16−18°, respectively, of α form of iPP, the $(117)_\gamma$ reflection at $2\theta \approx 20°$ of γ form of iPP, and the $(110)_I$, $(300)_I$, and $(220 + 211)_I$ reflections at $2\theta \approx 10°$, 17°, and 20°, respectively, of form I of iPB, are indicated.

of iPP already at low values of deformation (100−200%), as indicated by the transformation of the three equatorial $(111)_\gamma$, $(008)_\gamma$, and $(117)_\gamma$ reflections of γ form (Figure 6A) into the broad halo in the range $2\theta = 13°-18°$ in the diffraction pattern of Figure 6B,B′. Fibers in the pure mesomorphic form are obtained at high degrees of deformation (Figure 6C,C′).

Similar behavior has been observed for iPPBu samples with butene content higher than 15−17 mol % that crystallize from the melt mainly in the α form (Figure 5e,f). Crystals of α form present in the unstretched compression-molded films also transform by stretching into the disordered mesomorphic form. The X-ray fiber diffraction patterns of fibers of the sample iPPBu17.9, with 17.9 mol % of butene are reported in Figure 6D−F, as an example. Also in this case defective crystals of the α form transform rapidly at low deformation into the mesomorphic form (Figure 6E) and fibers in the pure mesomorphic form are obtained at high deformations (Figure 6F,F′).

The transformation of the α or γ forms into the mesomorphic form by stretching has also been observed in iPP homopolymer samples prepared with Ziegler−Natta[26] as well as metallocene catalysts.[27] It has been argued that this transition occurs through the destruction of the lamellar crystals by pulling chains out from the original crystals and successive reorganization of chains in crystalline aggregates of the mesomorphic form,[26] which is characterized by bundles of parallel chains in 3/1 helical conformation and small order in the lateral packing.[28]

As discussed above, iPPBu copolymers with about 50 mol % of butene are crystallized in mixtures of crystals of the α form of iPP and form I of iPB, in both as-prepared (Figure 2) and melt-crystallized (Figure 5) samples. In these random copolymers, the

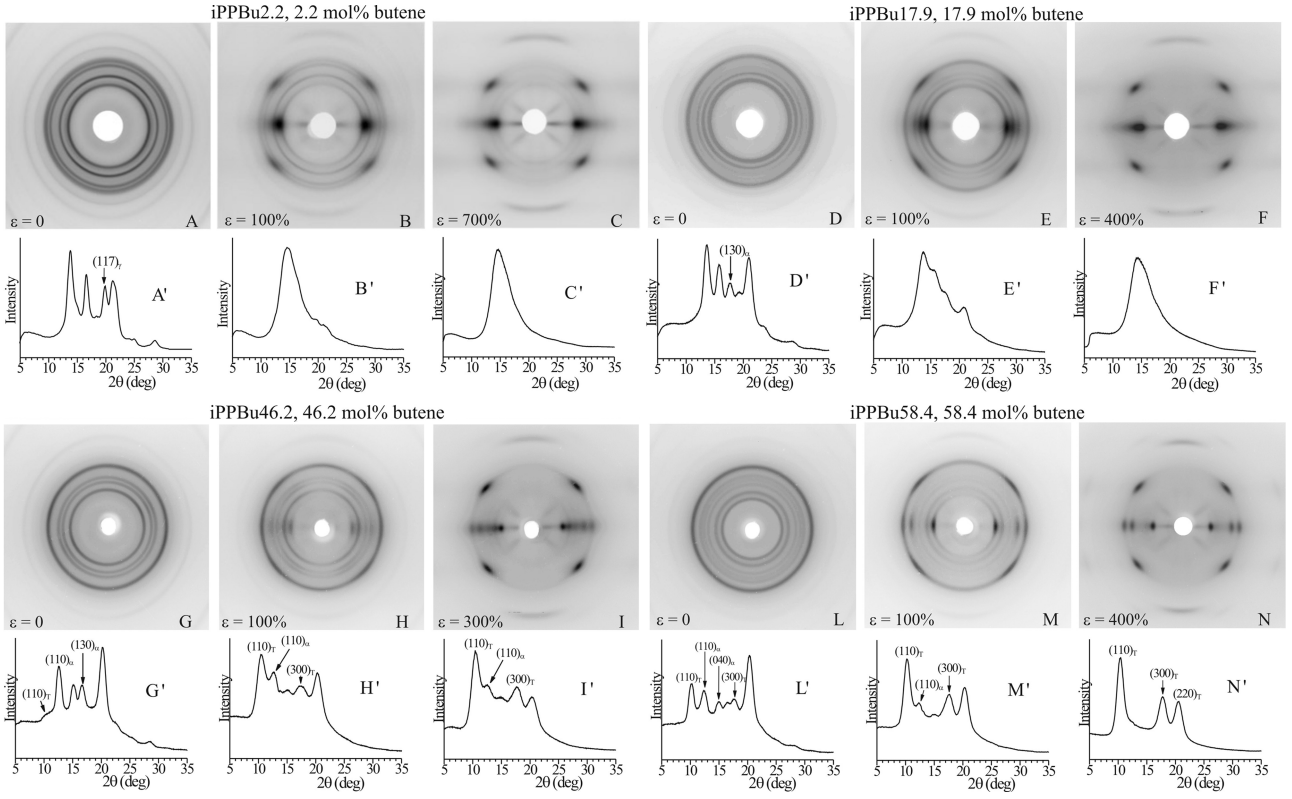


Figure 6. X-ray fiber diffraction patterns (A−N) and corresponding diffraction profiles read along the equator (A′−N′) of fibers of four iPPBu copolymer samples iPPBu2.2 (A−C), iPPBu17.9 (D−F), iPPBu46.2 (G−I), and iPPBu58.4 (L−N) with 2.2, 17.9, 46.2, and 58.4 mol % of butene, respectively, prepared by stretching compression-molded films at the indicated values of deformation ε. The $(110)_\alpha$, $(040)_\alpha$, and $(130)_\alpha$ reflections at $2\theta \approx 12-14°$, 15−17°, and 16−18°, respectively, of α form of iPP, the $(117)_\gamma$ reflection at $2\theta \approx 20°$ of γ form of iPP, and the $(110)_T$, $(300)_T$, and $(220)_T$ reflections at $2\theta \approx 10°$, 17°, and 20.5°, respectively, of the trigonal form of iPP, are indicated on the equatorial profiles. The diffraction profiles of samples before stretching ($\varepsilon = 0$) show intensities ratio slightly different with respect to that of the corresponding samples of Figure 5 due to the different geometry of the diffractometers (reflection geometry in the powder profiles of Figure 5 and transmission geometry in the fiber diffraction patterns).

simultaneous crystallization of iPP and iPB may be explained by the statistical presence of chains with long propylene sequences that crystallize as α form of iPP and of chains characterized by long butene sequences that crystallize as form I of iPB. In any case, the long propylene and butene sequences contain defects (butene and propene units, respectively) that are incorporated in the crystals of iPP and iPB, respectively, as demonstrated by the change of the unit cell parameters (Figure 3). An alternative explanation of the simultaneous crystallization of α form of iPP and form I of iPB may be envisaged in the fact that at equimolar concentrations of propene and butene units in the copolymers the trigonal form of iPP becomes stable because the inclusion of butene units in the crystals produces a suitable increase of density. In fact, as shown in Figure 3, for the sample iPPBu58.4, with 58.4 mol % of butene, the unit cell parameters of the trigonal form are $a = b =$ 17.08 Å, $c = 6.65$ Å. In the assumption of the full inclusion of propene and butene units in the unit cell, a crystal density of ≈0.9 g/cm^3 would be calculated, close to the density of 0.91−0.92 g/cm^3 of the crystals of the trigonal form in iPPHe and iPPPe copolymers and of 0.94 g/cm^3 of form I of iPB.[9] Therefore, the trigonal form that crystallizes in as-prepared and melt crystallized samples of iPPBu copolymers with equimolar composition of counits could be the density-driven trigonal form of iPP rather than the form I of iPB. The question is more than semantic, since the form I of iPB and the trigonal form of iPP are isomorphous. However, from our point of view this distinction may be useful to explain the stress-induced phase transitions occurring in iPPBu copolymers with butene content around 50 mol %, as shown in the following.

The compression-molded sample iPPBu46.2 with 46.2 mol % of butene is crystallized basically in the α form of iPP (profile g of Figure 5 and Figure 6G), with only a small amount of crystals of form I of iPB, as indicated by the very low intensity of the $(110)_I$ reflection of iPB at $2\theta \approx 10°$ in the diffraction profiles g of Figure 5 and Figure 6G′. By stretching compression-molded films of the sample iPPBu46.2, a neat decrease of the intensities of the $(110)_\alpha$, $(040)_\alpha$, and $(130)_\alpha$ reflections of α form of iPP at $2\theta = 12.6°$, 15.1°, and 16.6°, present in the unstretched film, is observed (Figure 6G−I). Contemporarily, a strong increase in the intensities of the $(110)_I$ and $(300)_I$ reflections at $2\theta = 10.4°$ and 17.8° of form I of iPB is observed with increasing deformation. At a high degree of deformation oriented fibers with a small amount of crystals of α form and, apparently, higher fraction of crystals of form I of iPB, are obtained (Figure 6I). These data seem to indicate a transformation of α form of iPP into form I of iPB during deformation, which is of course not reasonable. A more reasonable explanation of the data of Figure 6 is to assume that in the sample iPPBu46.2 crystals of α form of iPP transform by stretching into the trigonal form of iPP. Therefore, the reflections observed at $2\theta = 10.4°$, 17.8°, and 20.5° in the diffraction profiles of Figure 6H′−I′ correspond to the $(100)_T$, $(300)_T$, and $(220)_T$ reflections, respectively, of the trigonal form of iPP.

Similar behavior has been observed for the sample iPPBu58.4 with 58.4 mol % of butene that is initially crystallized in the compression-molded unstretched film as mixtures of α form of iPP and form I of iPB (Figure 6L). Also in this case, a neat decrease in the intensities of the $(110)_\alpha$, $(040)_\alpha$, and $(130)_\alpha$ reflections of α form of iPP at $2\theta = 12.4°$, 15°, and 16.4° and a strong increase of the intensities of the $(110)_I$, (or $(110)_T$) and $(300)_I$ (or $(300)_T$) reflections at $2\theta = 10.3°$ and 17.7° of form I of iPB (or the trigonal form of iPP) is observed with increasing deformation (Figure 6L′−N′). At high deformations the reflections of the α form of iPP disappear, and the diffraction pattern of fibers stretched at high deformations shows only the $(110)_I$, $(300)_I$, and $(220 + 211)_I$ reflections at $2\theta = 10.3°$, 17.7°, and 20.4°, respectively, of form I of iPB (or the trigonal form of iPP). Also these data seem to indicate that crystals of α form of iPP, initially present in the unstretched samples, disappear by stretching and fibers of the sample iPPBu58.4 stretched at high deformations contain only crystals of iPB. A more reasonable explanation is that in this sample crystals of α form transform completely into the trigonal form of iPP by stretching. The reflections observed at $2\theta = 10.3°$, 17.7°, and 20.4° in the diffraction profiles of Figure 6M′−N′ correspond, therefore, to the $(100)_T$, $(300)_T$, and $(220)_T$ reflections, respectively, of the trigonal form of iPP. In these stretched fibers, crystals of the trigonal form of iPP obtained by stretching from transformation of the α form are in mixture with crystals of form I of iPB present originally in the unstretched sample (Figure 6L). Of course, it is not possible to distinguish crystals of the trigonal form of iPP from the crystals of form I of iPB, the only difference being their origin and composition. In fact, as discussed above in the random iPPBu copolymers with nearly 50% composition, the contemporary crystallization of iPP and iPB in the bulk as-prepared or melt-crystallized samples is due to the cocrystallization of propene and butene in both crystals of α form of iPP and form I of iPB and by the statistical presence of chains with longer propylene sequences that crystallize as α form of iPP, containing butene units included in the crystals, and chains characterized by longer butene sequences that crystallize as form I of iPB containing propene units as defects. Crystals of α form crystallized from the chains with longer propylene sequences, including high concentrations of butene units as defects, transform by stretching in the trigonal form of iPP. Crystals of form I of iPB crystallized from the chains with longer butene sequences, including high concentrations of propene units as defects, do not transform by stretching, but only orient along the stretching direction. As already mentioned, the $(100)_T$, $(300)_T$, and $(220)_T$ reflections of the trigonal form of iPP are at $2\theta = 10.4°$ ($d = 8.51$ Å), 17.8° ($d = 4.98$ Å), and 20.5° ($d = 4.33$ Å) in the fiber diffraction pattern of the sample iPPBu46.2 of Figure 6I and at $2\theta = 10.3°$ ($d = 8.58$ Å), 17.7° ($d = 5.01$ Å), and 20.4° ($d = 4.35$ Å) in the fiber diffraction pattern of the sample iPPBu58.4 of Figure 6N. This indicates that also for the trigonal form of iPP obtained in the stretched fibers the Bragg distances and the unit cell dimensions depend on the butene concentration, as in the case of form I of iPB in powder samples (Figure 3), and a slight decrease of the Bragg distances and unit cell dimension is observed with increasing propene units ($a = 17.02$ Å for the sample iPPBu46.2 and $a =$ 17.16 Å for the sample iPPBu58.4).

The degrees of crystallinity of fibers of the samples iPPBu46.2 and iPPBu58.4 stretched at different deformations have been evaluated from the X-ray diffraction patterns of Figure 6G−I and Figure 6L−N. The values of crystallinity are nearly constant during deformation (45−50% for the sample iPPBu46.2 and 50−55% for the sample iPPBu58.4), indicating that no significant increase of crystallinity occurs during deformation.

The diffraction patterns of Figure 6G−M clearly arise from the contribution of the diffraction of crystals of α form, of the trigonal form, and of amorphous scattering. The equatorial diffraction profiles of Figure 6G′−I′ and Figure 6L′−N′ have been analyzed in the attempt to separate by deconvolution the different contributions and to find a possible contribution from the mesomorphic form of iPP. We found that the diffraction patterns of fibers of Figure 6G−N do not include the contribution of the mesomorphic form. The diffraction patterns of Figure 6G−M only include the contribution of the α and trigonal forms and of the amorphous scattering, whereas the fiber of Figure 6N is in the pure trigonal form. This indicates that in these samples the α form of iPP transforms by stretching only into the trigonal form of iPP and there is no partial transformation into the mesomorphic form, as it occurs for iPPBu samples with low butene concentration (Figure 6A−F). The transformation of the α form into the trigonal form probably occurs through mechanical melting of α form crystals by pulling chains out from the

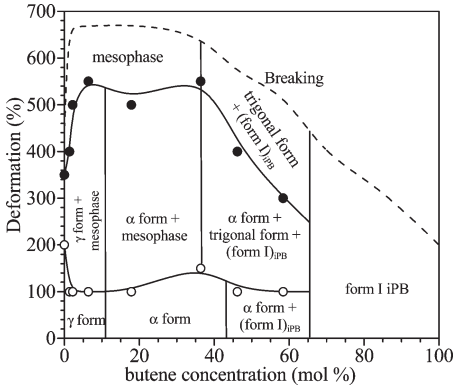


Figure 7. Phase diagram of iPPBu copolymers showing the regions of stability of the different polymorphic forms of iPP (α form, γ form, trigonal form, and mesomorphic form) and iPB (form I) as a function of tensile deformation and copolymer composition.

original crystals, and successive reorganization of chains and recrystallization in the fibrillar morphology of the trigonal form, as in the case of the transformation of α form into the mesophase.

It is worth recalling that also in iPPHe copolymers with hexene concentration lower than 9−10 mol % crystals of α form present in the melt-crystallized samples transform into the trigonal form by stretching.[29] In these samples with low hexene contents the trigonal form does not crystallize in the bulk as-prepared or melt-crystallized samples but is obtained by transformation of the α form during deformation. At higher hexene concentrations (higher than 10 mol %), the inclusion of hexene units in the crystals and the suitable increase of density produces direct crystallization of the trigonal form in the bulk samples.[3,4] In the case of iPPBu copolymers, even when the concentration of butene is about 50 mol %, the demonstrated inclusion of butene in the crystals of α form and the corresponding increase of density, are not sufficient to allow the crystallization of the trigonal form in the bulk samples (as in iPPHe at low hexene concentration). However, the trigonal form is obtained in these samples by transformation of the α form during deformation. As in the case of iPPHe and iPPPe copolymers,[3−5] this stress-induced transformation of α form into the trigonal form, rather than into the mesomorphic form, indicates that for butene concentration around 50% the trigonal form of iPP is more stable than the α form. This confirms the principle of *density-entropy driven phase formation in polymers*, which suggests that the packing of polymer molecules is mainly driven by density and the chain symmetry tends to be maintained in the crystal lattice.[3−5]

Fiber diffraction data of all samples of iPPBu copolymers of Table 1, similar to those of Figure 6, have allowed the building of a phase diagram of the iPPBu copolymers where the region of stability of the different polymorphic forms of iPP in oriented fibers are defined as a function of copolymer composition and degree of deformation (Figure 7). The boundary lines in the phase diagram define the transformations of the γ form and α form into the mesomorphic form of iPP and of the α form into the trigonal form of iPP during stretching. The boundary lines have been determined by the emergence during deformation of reflections typical of the polymorphic forms of iPP in the X-ray fiber diffraction patterns. From the phase diagram it is possible to read the stable forms in the unstretched melt-crystallized samples as a function of butene concentrations: the γ form for butene content lower than 10 mol %, the α form for butene concentration higher than 10−15 mol % up to 60 mol %, and the α form of iPP in mixture with the form I of iPB for butene concentrations in the range 45−65 mol %. For butene concentrations higher than 65 mol %, the form I of iPB is the most stable form. The γ and α forms transform at high deformations into the pure mesomorphic form for butene concentrations up to about 40 mol %. In the composition range 45−65 mol % of butene, the α form transforms instead into the trigonal form by stretching at high deformations (Figure 7). Finally, for butene contents higher than 65 mol %, the form I of iPB does not undergo any phase transformation during stretching, but only orientation of crystals is observed.

The X-ray fiber diffraction patterns of fibers of the iPPBu copolymers with butene contents higher than 17 mol % stretched at the highest deformation (Figure 6 F,I,N) and annealed at high temperatures, 10 °C lower than the melting temperature of each sample, and keeping the fibers under tension, are reported in Figure 8. It is apparent that for the samples iPPBu17.9 and iPPBu36.4 with 17.9 and 36.4 mol % of butene, respectively, the mesomorphic form obtained in the fibers stretched at the highest deformations (Figures 6F) transform by annealing into the α form and well-oriented fibers of α form with sharp reflections are obtained (Figure 8A,B). In the case of the samples iPPBu44.2 and iPPBu58.4 the trigonal form of iPP obtained in the fibers stretched at the highest deformations (Figures 6I,N) does not transform upon annealing (Figure 8C,D), and only improvement of crystallinity and crystal size after the thermal treatments is observed. This confirms that in these samples the trigonal form of iPP is the most stable form.

It is also worth noting that in the diffraction patterns of the annealed fibers of α form of Figure 8A,B the $(110)_\alpha$ reflection of the α form at $2\theta = 12-14°$ is polarized only on the equator, and no evidence of polarization of this reflection on the meridian is observed. This indicates that the crystals of α form obtained in annealed fibers of iPPBu copolymers with high butene concentrations are characterized by the absence of the typical cross-hatched morphology[30,31] generally observed in the α form crystals of the iPP homopolymer. The characteristic crystallization mechanism of homoepitaxy of α form crystals, involving the homoepitaxial α-branching of α form that leads to the typical cross-hatched morphology,[30,31] does not take place in these iPPBu copolymers. This crystallization mechanism involves the growth of transverse daughter lamellae of α form on mother lamellae of α form and nearly perpendicular orientation of chain axes, with *a* and *c* axes of daughter lamellae oriented parallel to the *c* and *a* axes of the parent one.[30,31] This mechanism of homoepitaxial crystallization and growth of α phase lamellar branching is possible, thanks to the dimensional equivalence of *a* and *c* axes of the crystals of α form of iPP homopolymer (a_α = 6.65 Å, c_α = 6.5 Å).[6] As shown in Figure 3, in iPPBu copolymers with butene concentrations higher than 15 mol %, up to 60 mol %, the inclusion of butene in the crystals of iPP produces a strong increase of both a_α and b_α axes dimensions of α form. Since the chain axis remains constant at 6.5−6.6 Å because the 3/1 helical chain conformation is not disturbed by the presence of butene;, the dimensional equivalence of a_α and c_α axes of α form is lost and the mechanism of homoepitaxy cannot take place. For the samples iPPBu17.9 and iPPBu36.4 the values of the unit cell parameters have been determined from the fiber diffraction patterns of the annealed fibers of Figure 8A,B. Values of a = 6.97 Å, b = 22.4 Å, c = 6.63 Å for the sample iPPBu17.9 and a = 7.25 Å, b = 23.3 Å, c = 6.64 Å for the sample iPPBu36.4, similar to those evaluated in the powder samples of Figure 3, have been obtained. These data confirm the loss of the dimensional equivalence between *a* and *c* axes with increasing butene concentration.

It is also worth mentioning that the data of unit cell parameters of Figure 3 and those evaluated from the fiber patterns also explain the experimental evidence that iPPBu copolymers tend to crystallize in the γ form at low butene content, up 10−15 mol % (Figures 2b−d and 7) and in the α form at higher concentrations (Figure 2e−g).[15] In fact, the dimensional equivalence of *a* and *c* axes of α form is the basis not only for the crystallization mechanism of homoepitaxial α-branching of α form but also

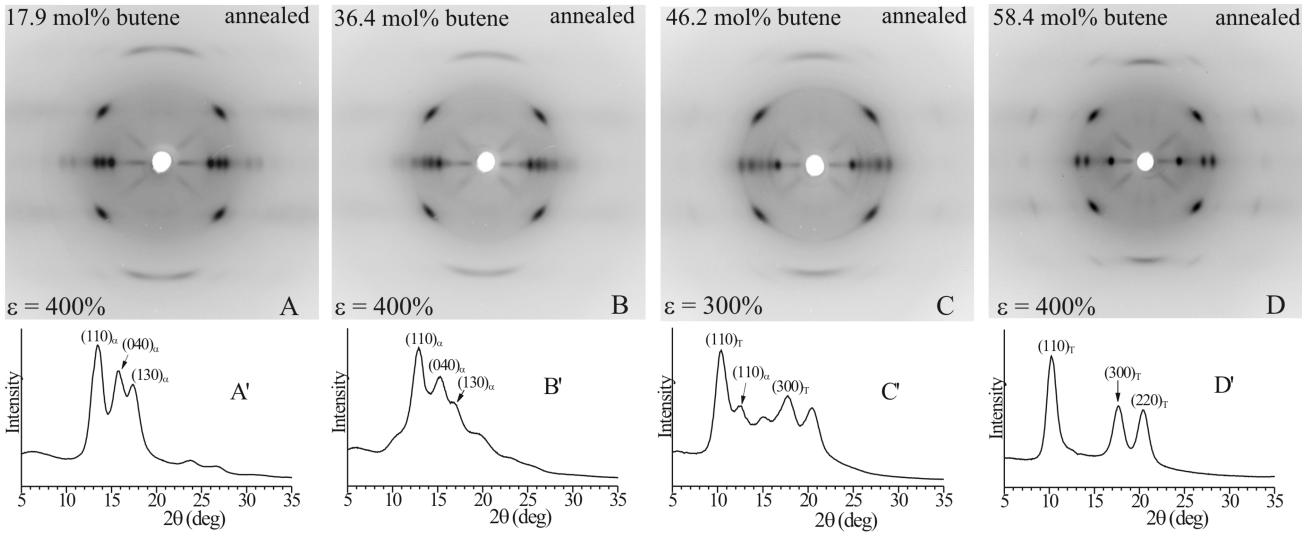


Figure 8. X-ray fiber diffraction patterns (A−D) and corresponding diffraction profiles read along the equator (A′−D′) of fibers of the copolymer samples iPPBu17.9 (A), iPPBu36.4 (B), iPPBu46.2 (C) and iPPBu58.4 (D) with 17.9, 36.4, 46.2, and 58.4 mol % of butene, respectively, stretched at the maximum deformation ε and annealed for 20 min at the temperatures of 86, 60, 50, and 48 °C, respectively. The $(110)_\alpha$, $(040)_\alpha$, and $(130)_\alpha$ reflections at $2\theta \approx 12-14°$, 15−17°, and 16−18°, respectively, of α form of iPP and the $(110)_T$, $(300)_T$, and $(220)_T$ reflections at $2\theta \approx 10°$, 17°, and 20°, respectively, of the trigonal form of iPP, are indicated on the equatorial profiles.

for the epitaxial deposition of γ phase on parent γ or α forms. The growth of transverse daughter lamellae on mother lamellae of α form with *a* and *c* axes of daughter lamellae oriented parallel to the *c* and *a* axes of the parent one involves a nearly perpendicular orientation of chain axes.[30,31] This packing scheme of isochiral layers occurs in the α form as a local accident, linked with a "stumble" in the alternation of helical hands. In the orthorhombic γ form this packing of isochiral layers becomes systematic and generates a bilayer structure with perpendicular orientation of chains at the molecular level.[7] Moreover, γ form can branch on the α phase through the same mechanism of homoepitaxy.[32] It has been, indeed, shown that when iPP crystallizes as mixtures of α and γ forms, crystals of γ form can epitaxially crystallize on the lateral (010) growth faces of the α form mother lamellae,[32] and even when a very high amount of γ form is evidenced by X-ray diffraction, crystals of γ form are probably nucleated over the preformed crystals of α form,[32,33] and the crystallization rates of α and γ forms become virtually identical.[12,34,35] In iPPBu copolymers with low butene content, up to 14−15 mol %, the inclusion of butene units in the crystals produces only expansions of b_α axis of α form (or c_γ axis of γ form), whereas the a_α and c_α axes of α crystals remain nearly constant (Figure 3). Therefore, at these butene concentrations the dimensional equivalence of a_α and c_α axes of α form is preserved and iPPBu copolymers probably crystallize as iPP homopolymer, giving α phase lamellar branching and/or epitaxial deposition of γ phase on parent γ or α forms. This mechanism allows and favors crystallization of γ form when the microstructure of the chains, as the presence of butene defects, tends to induce crystallization of γ form. In iPPBu copolymers with butene concentration higher than 15 mol %, the dimensional equivalence of a_α and c_α axes of α form is lost and the mechanism of homoepitaxy and epitaxial crystallization of γ form on crystals of α form becomes less probable. As a consequence, these iPPBu copolymers crystallize exclusively in the α form.

Conclusions

Samples of propylene−butene copolymers (iPPBu) have been synthesized with a metallocene catalyst that allow random placements of comonomers along the chains and high stereoregularity in the entire range of comonomer compositions. iPPBu copolymers crystallize for any comonomer concentration from 0 to 100% of butene, indicating a cocrystallization of propene and butene units in the crystals of iPP and iPB at any composition. The inclusions of butene units in the crystals of α form of iPP and that of propene units in the crystals of form I of iPB are demonstrated by the increase of the *a* and *b* axes of the monoclinic unit cell of α form of iPP in propene-rich iPPBu copolymers with increasing butene concentration and the decrease of the $a = b$ axes of the trigonal unit cell of form I of iPB in butene-rich iPPBu copolymers with increasing propylene content.

Samples of iPPBu having concentration of butene units up to nearly 50 mol % crystallize in α and γ forms of iPP, or as a mixture of both, whereas samples with butene contents higher than 65−70 mol % are crystallized in the stable form I of iPB. The trigonal form of iPP, recently found in propylene−hexene and propylene−pentene copolymers, has not been observed in bulk samples, in both as-prepared and melt-crystallized samples of propene-rich copolymers. The trigonal form has been instead obtained in stretched fibers of copolymers by stress-induced transformation of the α form. In fact, in iPPBu copolymers with low butene concentrations (lower than 10−15 mol %) crystals of α or γ forms present in the melt-crystallized compression-molded samples transform by stretching at high deformation into the mesomorphic form of iPP. In samples with butene concentrations of around 50%, that crystallize from the melt as mixtures of crystals of α form of iPP and form I of iPB, crystals of α form of iPP transforms into the trigonal form of iPP by stretching at high deformation. This is the first evidence of the crystallization of the trigonal form of iPP in iPPBu copolymers.

The crystals of α form obtained in annealed fibers of iPPBu copolymers with butene concentrations higher than 10−15 mol % are characterized by the absence of the typical cross-hatched morphology generally observed in the α form crystals of the iPP homopolymer. This is due to the fact that the dimensional equivalence of *a* and *c* axes of the crystals of α form of iPP homopolymer (a_α = 6.65 Å, c_α = 6.5 Å) is lost in iPPBu copolymers with high butene content because of the increase of the value of the *a* axis with increasing butene concentration, while the *c* axis of the 3/1 helix remains constant at 6.5−6.6 Å. The dimensional equivalence of *a* and *c* axes of α form is the basis for the crystallization mechanism of homoepitaxial α-branching of α form, which involves the growth of transverse daughter lamellae of α form on mother lamellae of α

form and nearly perpendicular orientation of chain axes, with *a* and *c* axes of daughter lamellae oriented parallel to the *c* and *a* axes of the parent one. The inclusion of butene units in the crystals of α form removes the equivalence of *a* and *c* axes, and the cross-hatched morphology is no longer observed at high butene concentrations.

Acknowledgment. Financial support from Basell Poliolefine Italia S.r.l., "a LyondellBasell company" (Ferrara), is gratefully acknowledged. We thank Davide Balboni of Basell for the synthesis of the catalyst and Alessandra Bonazza and Riccardo Frabetti of Basell for the polymerization experiments.

References and Notes

(1) Poon, B.; Rogunova, M.; Hiltner, A.; Baer, E.; Chum, S. P.; Galeski, A.; Piorkowska, E. *Macromolecules* **2005**, *38*, 1232.
(2) Lotz, B.; Ruan, J.; Thierry, A.; Alfonso, G. C.; Hiltner, A.; Baer, E.; Piorkowska, E.; Galeski, A. *Macromolecules* **2006**, *39*, 5777.
(3) De Rosa, C.; Auriemma, F.; Corradini, P.; Tarallo, O.; Dello Iacono, S.; Ciaccia, E.; Resconi, L. *J. Am. Chem. Soc.* **2006**, *128*, 80.
(4) De Rosa, C.; Dello Iacono, S.; Auriemma, F.; Ciaccia, E.; Resconi, L. *Macromolecules* **2006**, *39*, 6098.
(5) De Rosa, C.; Auriemma, F.; Talarico, G.; Ruiz de Ballesteros, O. *Macromolecules* **2007**, *40*, 8531.
(6) Natta, G.; Corradini, P. *Nuovo Cimento Suppl.* **1960**, *15*, 40.
(7) (a) Brückner, S.; Meille, S. V. *Nature* **1989**, *340*, 455. (b) Meille, S. V.; Brückner, S.; Porzio, W. *Macromolecules* **1990**, *23*, 4114.
(8) (a) Natta, G.; Corradini, P. *Nuovo Cimento, Suppl.* **1960**, *15*, 9. (b) Natta, G.; Corradini, P. *J. Polym. Sci., Polym. Phys. Ed.* **1959**, *29*, 29. (c) De Rosa, C. *Top. Stereochem.* **2003**, *24*, 71.
(9) Natta, G.; Corradini, P.; Bassi, I. W. *Nuovo Cimento, Suppl.* **1960**, *15*, 52.
(10) Arnold, M.; Henschke, O.; Knorr, J. *Macromol. Chem. Phys.* **1996**, *197*, 563.
(11) Arnold, M.; Bornemann, S.; Köller, F.; Menke, T. J.; Kressler, J. *Macromol. Chem. Phys.* **1998**, *199*, 2647.
(12) Hosier, I. L.; Alamo, R. G.; Esteso, P.; Isasi, G. R.; Mandelkern, L. *Macromolecules* **2003**, *36*, 5623.
(13) Hosoda, S.; Hori, H.; Yada, K.; Tsuji, M.; Nakahara, S. *Polymer* **2002**, *43*, 7451.
(14) Stagnaro, P.; Costa, G.; Trefiletti, V.; Canetti, M.; Forlini, F.; Alfonso, G. C. *Macromol. Chem. Phys.* **2006**, *207*, 2128.
(15) De Rosa, C.; Auriemma, F.; Ruiz de Ballesteros, O.; Resconi, L.; Camurati, I. *Macromolecules* **2007**, *40*, 6600.
(16) De Rosa, C.; Auriemma, F.; Ruiz de Ballesteros, O.; Resconi, L.; Camurati, I. *Chem. Mater.* **2007**, *19*, 5122.
(17) Resconi, L.; Guidotti, S.; Morhard, F.; Fait, A. Int. Appl. WO 2006/051035 to Basell Polyolefins.
(18) (a) Resconi, L.; Guidotti, S.; Camurati, I.; Frabetti, R.; Focante, F.; Nifant'ev, I. E.; Laishevtsev, I. P. *Macromol. Chem. Phys.* **2005**, *206*, 1405. (b) Resconi, L.; Camurati, I.; Malizia, F. *Macromol. Chem. Phys.* **2006**, *207*, 2257.
(19) Randall, J. C. *Macromolecules* **1978**, *11*, 592.
(20) Moraglio, G.; Gianotti, G.; Bonicelli, U. *Eur. Polym. J.* **1973**, *9*, 693.
(21) (a) Cimmino, S.; Martuscelli, E.; Nicolais, L.; Silvestre, C. *Polymer* **1978**, *19*, 1222. (b) Crispino, L.; Martuscelli, E.; Pracella, M. *Makromol. Chem.* **1980**, *181*, 1747. (c) Cavallo, P.; Martuscelli, E.; Pracella, M. *Polymer* **1997**, *18*, 891.
(22) Abiru, T.; Mizuno, A.; Weigand, F. *J. Appl. Polym. Sci.* **1998**, *68*, 1493.
(23) (a) Turner-Jones, A. *Polymer* **1966**, *7*, 23. (b) Turner-Jones, A. *Polymer* **1971**, *12*, 487.
(24) (a) Marega, C.; Marigo, A.; Saini, R.; Ferrari, P. *Polym. Int.* **2001**, *50*, 442. (b) Marigo, A.; Causin, V.; Marega, C.; Ferrari, P. *Polym. Int.* **2004**, *53*, 2001.
(25) (a) De Rosa, C.; Auriemma, F.; Resconi, L. *Angew. Chem., Int. Ed.* **2009**, *48*, 9875. (b) De Rosa, C.; Auriemma, F.; Ruiz de Ballesteros, O.; Esposito, F.; Laguzza, D.; Di Girolamo, R.; Resconi, L. *Macromolecules* **2009**, *42*, 8286.
(26) Ran, S.; Zong, X.; Fang, D.; Hsiao, B. S.; Chu, B.; Phillips, R. A. *Macromolecules* **2001**, *34*, 2569.
(27) De Rosa, C.; Auriemma, F.; Di Capua, A.; Resconi, L.; Guidotti, S.; Camurati, I.; Nifant'ev, I. E.; Laishevtsev, I. P. *J. Am. Chem. Soc.* **2004**, *126*, 17040.
(28) Corradini, P.; Petraccone, V.; De Rosa, C.; Guerra, G. *Macromolecules* **1986**, *19*, 2699.
(29) De Rosa, C.; Auriemma, F.; Ruiz de Ballesteros, O.; Dello Iacono, S.; De Luca, D.; Resconi, L. *Cryst. Growth Des.* **2009**, *9*, 165.
(30) (a) Khoury, F. *J. Res. Natl. Bur. Stand.* **1966**, *70A*, 29. (b) Khoury, F.; Passaglia, E. In *Treatise on Solid State Chemistry*; Hannay, N. B., Ed.; Plenum: New York, 1976, Vol. *3*, Chapter 6, p 335.
(31) Lotz, B.; Wittmann, J. C. *J. Polym. Sci., Polym. Phys. Ed.* **1986**, *24*, 1541.
(32) Lotz, B.; Graff, S.; Straupé, C.; Wittmann, J. C. *Polymer* **1991**, *32*, 2902.
(33) De Rosa, C.; Auriemma, F.; Resconi, L. *Macromolecules* **2005**, *38*, 10080.
(34) Hosier, I. L.; Alamo, R. G.; Lin, J. S. *Polymer* **2004**, *45*, 3441.
(35) Alamo, R. G.; Ghosal, A.; Chatterjee, J.; Thompson, K. L. *Polymer* **2005**, *46*, 8774.

DOI: 10.1021/ma101825j

Macromolecules
ARTICLE

Synthesis of *N*-Phenylaminomethyl POSS and Its Utilization in Polyurethane

Qiuhong Zhang,[†,‡,§] Hui He,[†,‡,§] Kai Xi,[†,‡,§] Xin Huang,[†,‡,§] Xuehai Yu, and Xudong Jia*[,†,‡,§]

[†]*State Key Laboratory of Coordination Chemistry,* [‡]*Department of Polymer Science and Engineering, and* [§]*Nanjing National Laboratory of Microstructures, Nanjing University, Nanjing 210093, P.R. China*

Received August 10, 2010; Revised Manuscript Received December 18, 2010

ABSTRACT: A new functional *N*-phenylaminomethyl POSS was synthesized by traditionally controlled hydrolytic condensation in one step reaction. The POSS structure was ascribed to a T_{10} and T_{12} derivative mixture as main component by varied characterization methods such as ^{1}H NMR, ^{13}C NMR, ^{29}Si NMR, gel permeation chromatography (GPC) and matrix assisted laser desorption ionization time of flight mass spectrometry (MALDI−TOF MS). Then based on this new POSS reacted with polyether diisocyanate, a series of POSS−PU composites with different POSS concentration was prepared and characterized. The POSS−PU composites showed no macrophase separation up to 52 wt % POSS concentration. The high resolution transmission electron microscopy (HRTEM) images of POSS−PU composites showed a well separated nanostructure of POSS with a typical phase size of 5−10 nm. A critical POSS concentration of 26 wt % was found by DMA, beyond which the POSS−PU showed a permanent network at high temperature. T_g and storage modulus of POSS−PU composites increased with increasing POSS concentration. Young's modulus largely enhanced with increasing POSS concentration at constant $T_{test} - T_g$. All the enhanced mechanical properties could be ascribed to the synergetic effect of POSS and PU, where POSS played a role as the nanoscale cross-linker in the PU system and formed a network, thus hindering the motion of the PU chain.

Introduction

In the past 2 decades, researchers have shown great interests in polyhedral oligosilsesquioxane (POSS), a family of nanoscale inorganic cage structures consisting of a silicon−oxygen based framework, because of its unique physical and chemical properties.[1−6] POSS plays an important role as building block for inorganic−organic hybrid materials containing the cage structure of POSS monomers. Interestingly, functional substitutions at POSS framework not only bring the diversity but also make POSS easily compatible and well dispersed in organic polymers. Through this approach, many inorganic−organic hybrid materials enhanced their macroscopic properties compared with their nonhybrid counterparts, such as increased thermo-oxidative, and ultraviolet stability,[7] enhanced abrasion resistance[8] and hardness,[9] reduced flammability,[10,11] and viscosity[12] during processing. However, due to the limited compatibilities of POSS in polymer, the research of polymer−POSS cooperation behavior at high concentration is still a challenge (beyond 50 wt %).

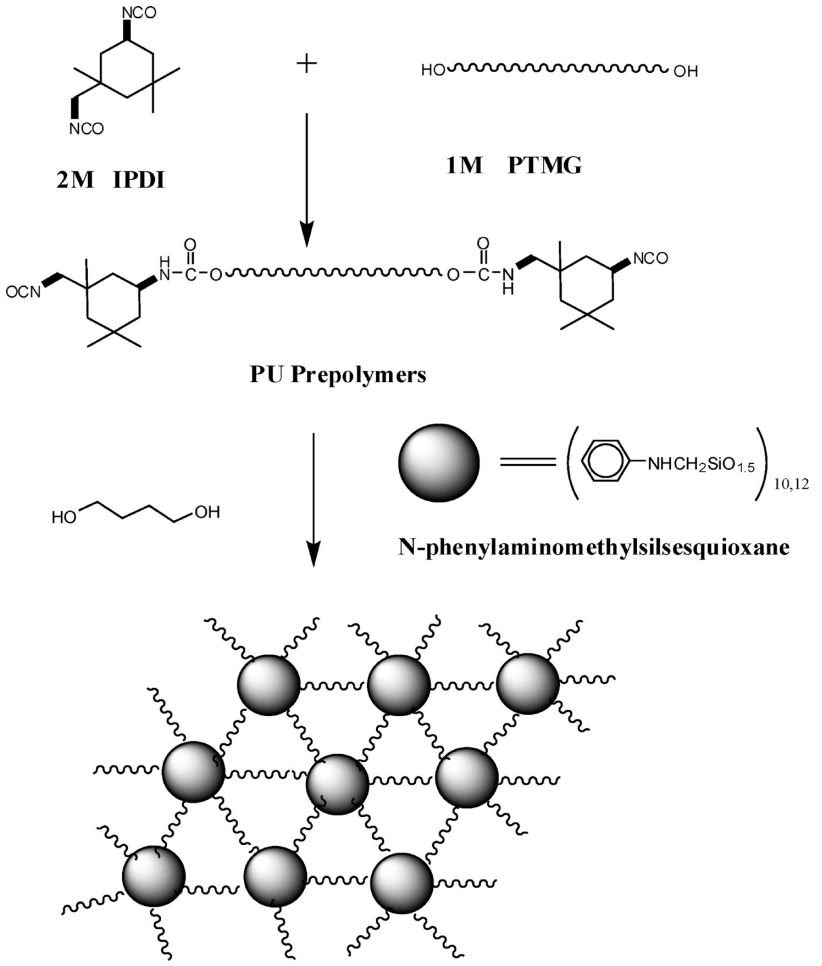
Typical POSS cages have the empirical formulas $(RSiO_{1.5})_{8,\,10,\,12}$, abbreviated as T_8, T_{10}, and T_{12} respectively.[13] Since the first discovery of the structures of T_8 cage in 1946,[14] many well-defined POSS structures with organic functional groups have been reported. In these frameworks, T_8 derivatives possess much more portions than T_{10} or T_{12} derivatives do. In most cases, the common structure of reaction product is T_8, while T_{10} and T_{12} cages are mostly obtained as side products with very low yields[15] or by cage arrangements from the corresponding T_8.[16] T_{12} cage of dodecaphenylsilsesquioxane was first synthesized as main product by Brown in 1964 through prepolymerization and rearrangement of prepolymer in tetrahydrofuran solution with alkali catalysis.[17] Laine and co-workers prepared dodecaaminophenylsilsesquioxane with reactive organic substituent groups from dodecaphenylsilsesquioxane by nitration in fuming HNO_3 and reduction with Pd/C catalysis.[18] However, to the best of our knowledge, few POSS with T_{10} or T_{12} cage structures, which also has organic functional groups, has been reported as main product from corresponding silane monomers up to the present. As part of an effort to obtain T_{10} or T_{12} frameworks with reactive functional groups, we hereby report an efficient synthetic route to prepare a novel POSS monomer of phenylaminomethylsilsesquioxane. Using traditionally controlled hydrolytic condensation with acid catalysis, it can be readily prepared from a commercially available organosilicon precursor (*N*-phenylaminomethyltriethoxysilane) in large scale with a high yield and mild reaction. The obtained POSS has been fully characterized and its structure has been confirmed as well.

PU is one of the most commercial elastomers that can be used as adhesives, flexible films, coatings, or hard plastics.[19] When PU cooperated with POSS, its properties would be greatly enhanced, such as mechanical properties,[20] thermo-oxidative stabilities,[21,22] biodegradable resistance,[23,24] and fire resistance.[10] Generally, POSS monomers preserved diols or diamines are more recipient to graft to PU chains as chain extenders because the functional groups can react with isocyanates. Turri and Levi obtained a series of stable aqueous dispersions using diol functionalized POSS,[25] Nanda et al. also got the diamino POSS grafted PU aqueous dispersions by using the "acetone process".[26,27] POSS was used as chain extenders instead of cross-linking agents in these works. Neumann first synthesized POSS possessing eight isocyanate substituents, which was used as a high cross-linker[28] to explore a new type of PU. Zheng and co-workers used octaaminophenyl-POSS and octa(propylglycidyl ether)-POSS as cross-linking agents to react with PU and enhanced the mechanical and thermal properties.[29,30]

*Corresponding author. E-mail: jiaxd@nju.edu.cn. Telephone: +86-25-83593041. Fax: +86-25-83621337.

 Published on Web 01/10/2011 © 2011 American Chemical Society

Scheme 1. Synthesis of PU−POSS Hybrids



These mechanical and thermal enhancements of POSS−PU hybrids were commonly caused by the restriction of the motion of PU chains. However, both sides could hardly be owned, the stress of PU increased while its elongation decreased and vice versa. So far as we know, there have been few reports about POSS−PU hybrids possessing both high stress and good elongation at the same time. Moreover, even though POSS can improve the thermal stability of PU, but it is not easy to obtain POSS−PU with high storage modulus over 473 K.

Here, we used hydrolytic condensation to synthesize a new kind of POSS with T_{10} and T_{12} structures as main product. It was then used as a cross-linking agent to react with PU. The POSS contents were controlled from 0 to 52 wt % in order to obtain a series of POSS−PU hybrids. The POSS−PU hybrids were all homogeneous and transparent. The degree of POSS dispersion was characterized by high resolution transmission electron microscopy (HRTEM). The enhanced mechanical properties of POSS−PU hybrids were confirmed by DMA and tensile test.

Experimental Section

Materials. *N*-phenylaminomethyltriethoxysilane (Mingtian Chemical Corporation, China, 95% purity) was further purified by distillation (bp 408 K/5 mm, 97% purity). Methanol, concentrated hydrochloric acid (12 N), dimethyl sulfoxide (DMSO) and stannous octoate were obtained from Shanghai Guoyao Corporation, China. Triethylamine (98%) was obtained from Nanjing Reagent Corporation, China. Polytetramethylene glycol (PTMG, $M_n = 1000$), isophorone diisocyanate (IPDI), and 1,4-butanediol (BD) were supplied by Sigma-Aldrich (USA) and dried under vacuum before use. *N*,*N*-Dimethylacetamide (DMAC, Shanghai Guoyao Corporation, China) was dried by CaH_2 and vacuum transferred.

Synthesis of Hydrochloride Salt of *N*-Phenylaminomethylsilsesquioxane (1). *N*-Phenylaminomethyltriethoxysilane (50 g) and methanol (1 L) were added into a 2 L flask equipped with a condenser under nitrogen atmosphere. The solution was cooled to 273 K, and concentrated hydrochloric acid (60 mL, 12 N) was carefully added with magnetic stirring over 2 h. After addition was completed, the reaction solution was stirred for 4 weeks at 293 K. The product was obtained as white solid by filtering the reaction mixture and washed three times with cold methanol (10 mL) and dried under vacuum at 313 K. The final yield was 75% (27.0 g). Solid state ^{29}Si NMR (400 MHz, 298 K): δ −83.1 ppm.

Synthesis of *N*-phenylaminomethylsilsesquioxane (2). Product **1** (6 g) was ground to fine powder and added to dry DMSO (24 mL) with stirring at room temperature under nitrogen atmosphere. Triethylamine (12 mL) was dropped to the solution, and the mixture was stirred for 30 min. The reactant was filtered and the filtrate was dropped into a saturated solution of sodium chloride (400 mL), and a white floccule was immediately produced. The precipitate was filtered, washed three times with water and cold methanol (15 mL) respectively, and dried under vacuum at 313 K. The product was obtained in 89% yield (4.14 g), and the total yield was 64%. The crude product was

Table 1. Compositions of Neat PU and PU−POSS Hybrids

sample	POSS, wt %	hard segments, wt %	IPDI, wt %	PTMG, wt %	BD, wt %
neat PU	0	34.8	28.9	65.2	5.9
PU11	11.4	40.2	26.6	59.8	2.2
PU18	18.0	43.2	25.2	56.8	0
PU22	22.0	46.0	24.0	54.0	0
PU26	26.0	48.8	22.8	51.2	0
PU30	30.0	51.5	21.5	48.5	0
PU40	40.0	58.5	18.5	41.5	0
PU52	52.3	67.0	14.7	33.0	0

dissolved in DMSO, and precipitated in brine again, filtered, and washed three times with water and cold methanol, respectively, and then dried. The refined product as white solid was finally obtained. ^{1}H NMR (500 MHz, DMSO-d_6, 25 °C): δ = 5.01−5.52 (t, NH, 8 H), 2.51, 2.88 (d, CH_2, 16 H), 7.06, 6.63, 6.58 (s, C_6H_5, 40 H). ^{13}C NMR (500 MHz, DMSO-d_6, 298 K): δ = 150.87, 129.63, 116.89, 113.13 (s, C_6H_5), 29.87 (s, CH_2). Solid state ^{29}Si NMR (400 MHz, 298 K): δ −71.6 ppm. GPC M_w = 1975.9, M_n = 1828.1, PDI = 1.08.

Synthesis of PU Prepolymer (3). The reference prepolymer was synthesized by dissolving PTMG (3.00 g, 0.003 mol) and IPDI (1.33 g, 0.006 mol) in a 100 mL three-necked flask equipped with mechanical stirrer under nitrogen atmosphere. Stannous octoate (0.1 wt %) was added as catalyst and the reactant was kept stirring at 358 K for 4 h to obtain prepolymer **3**. The prepolymer was dissolved in 10 mL of DMAC.

Synthesis of Neat PU (4). BD (0.27 g, 0.003 mol) dissolved in 10 mL of DMAC was added to prepolymer solution. With fully stirring for 10 min, the reactant was poured into a PTFE plate. After half of the solvent was evaporated off under vacuum at 333 K, the plate was put in an oven and the temperature kept at 368 K for 12 h to make the reaction completely execute. At last the neat PU film (**4**) was made.

Synthesis of POSS−PU Hybrids (5). Various amounts of product **2** were dissolved in DMAC (10 mL), the solutions were added into the prepolymer solution and kept stirring for 10 min at 368 K, and BD dissolved in 10 mL of DMAC was then dropped into the mixture. The amount of BD was accordingly adjusted in order to keep the NCO/(OH + NH) = 1 for PU11 and PU18, and it was not added for PU52 because NH/NCO exceed 1.With fully stirring for 5 min, the mixture was poured into a PTFE plate. After half amount of the solvent was evaporated off under vacuum at 333 K, the plates were put in an oven and kept the temperature at 368 K for 12 h to make the reaction completely execute. At last the POSS−PU hybrids films (**5**) were made. The procedure of the synthesis of PU−POSS hybrids is shown in Scheme 1. The compositions of neat PU and POSS−PU hybrids are listed in Table 1.

Molecular Structure Characterizations. The ^{1}H NMR and ^{13}C NMR were obtained on a Bruker AC 300 spectrometer at room temperature operating at 500 MHz. Dimethyl sulfoxide-d_6 was used as NMR solvent. Chemical shifts were reported in values relative to the residual solvent resonance of $(CD_3)_2SO$, (^{1}H, δ 2.5; ^{13}C, δ 40.5).

Solid state ^{29}Si NMR spectra were recorded on a Varian Infinityplus-400 wide-bore (89 mm) NMR spectrometer at a proton frequency of 399.7 MHz using a 7 mm T3 double resonance CPMAS probe and a zirconia PENCIL rotor. All of the NMR data were processed with Varian Spinsight software and the experiments were carried out at room temperature.

Gel permeation chromatography (GPC) was performed at room temperature on a Waters 515 equipped with a Wyatt Technology Optilab Rex refractive index detector. The columns were Styragel HR3, HR4, and HR5 (300 × 7.8 mm) from Waters. Tetrahydrofuran (THF, HPLC grade, Aldrich) was used as eluent at a flow rate of 1 mL/min. Sample solutions in THF were filtered over a filter with pore size of 0.45 μm (nylon, Millex-HN 13 mm Syringes Filters, Millipore). The columns were calibrated by using polystyrene standards with molecular weights in the range of 900 and 1.74 × 106 g/mol (with NMD for 1.02−1.11).

Matrix assisted laser desorption ionization time of flight mass spectrometry (MALDI−TOF MS) was performed using a Bruker Daltonics Autoflex TOF/TOF in linear and reflection modes. The matrix 2, 5-dihydroxybenzoic acid (DHB) was dissolved in THF (10 mg/mL), and mixed with the sample solution (1 mg/mL in THF) in 1:1 v/v ratio. Samples were spotted onto the target and dried in air.

The Fourier transform infrared spectra (FTIR) were recorded on a NICOLET NEXUS 870 spectrophotometer. The attenuated total reflection (ATR) accessories were used to measure the FTIR spectra of all the specimens on fresh surfaces. In all cases, 64 scans at a resolution of 2 cm^{-1} were used to record the spectra.

Morphological Characterizations. Morphological observations were done by HRTEM. The materials were frozen to 173 K, and ultrathin sections were made by using a Leica ULTRACUT UC6 with approximate thickness about 70 nm. The sections were collected onto copper grids. The grids were then imaged using a JEM-2100 transmission electron microscope at 200 kV.

Surface topographies were also characterized by atomic force microscopy (AFM) in tapping mode using silicon tips with Olympus OMCL-AC160TS and controller from Veeco Corporation. Samples were spin-coated on silicon wafer surfaces by DMAC solutions of polymer films (1 wt %) and cured in a vacuum oven at 368 K for 12 h.

Mechanical Measurements. The tensile tests were carried out on an Instron Series IX Automated Materials Testing System (Instron 4466, U.K.). The mechanical properties were measured according to ASTM D1708 standard method. Tests were performed in triplicate to give mean values reported in this paper. The dynamic mechanical tests were carried out on a dynamic mechanical analyzer (DMA) (METRAVIB DMA+450, France). The viscoelastic properties were measured under a nitrogen atmosphere, at a heating rate of 2 K/min from 153 to 473 K and a frequency of 10 Hz. The experiments were carried out until the samples became too soft to be tested.

Thermogravimetric Analysis. Thermal gravimetric analysis (TGA) was examined using a Perkin−Elmer TGA-7 thermogravimetric analyzer. Samples (5 mg) were loaded in alumina pans and ramping to 873 K at a heating rate of 20 K/min in nitrogen environment.

Results and Discussion

Synthesis of *N*-Phenylaminomethylsilsesquioxane and Its Hydrochloric Acid. Traditional polycondensation reaction, which was performed in acidic media, was kinetically controlled. The first step involved a sol−gel reaction of *N*-phenylaminomethyltriethoxysilane under a water-starved condition by using hydrochloric acid as water supply to give the calculated hydrochloric salt of *N*-phenylaminomethylsilsesquioxane. The controlled hydrolytic condensation for preparing POSS was originally developed by Laine et al.[31] The mechanism was considered to be hydrolytic polycondensation, which formed the basis for most sol−gel reactions. With the increasing of the weight ratio of *N*-phenylaminomethyltriethoxysilane,

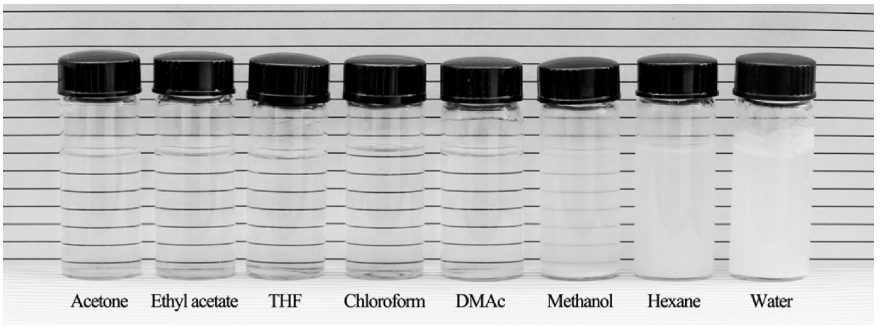


Figure 1. Solubility of POSS in different solvents (500 mg/10 mL solvent, 298 K).

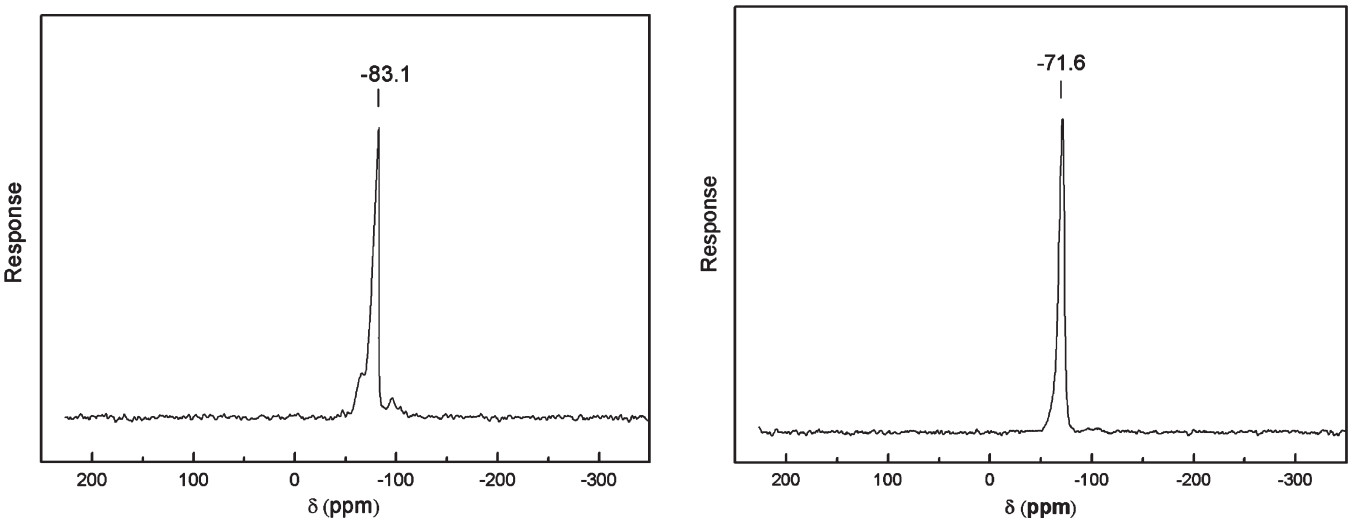


Figure 2. Solid State ^{29}Si NMR spectra of *N*-phenylaminomethylsilsesquioxane (right) and its hydrochloride salt (left).

the byproduct were increased, and the fit weight ratio of starting material in our system was under 5%. Hydrochloric salt of POSS could not dissolve in most organic solvents or mixture solvents for its special structure. However, after neutralized by triethylamine, the product showed good solubility in DMSO, DMAC, acetone, THF, et al., while poor solubility in water, methanol, ethanol, and hexane is observed (Figure 1).

The ^{1}H NMR and ^{13}C NMR results matched the reactive groups of the product well, indicating that the reaction did not happen at the *N*-phenylaminomethyl functional group. The solid state ^{29}Si NMR spectrum of hydrochloric salt of *N*-phenylaminomethyltriethoxysilane (Figure 2, left) exhibited a sharp and strong characteristic signal of $RSiO_3$ substructures (T^3) at δ −83.1 ppm and a broad weak intensity signal from δ −95 ppm to δ −110 ppm which could be assigned to the few cleavage of C−Si bonds or impure ingredient. With the neutralization of hydrochloric salt, the result of ^{29}Si NMR varied from δ −81.3 ppm to δ −71.6 ppm for the change of electromagnetic circumstance around Si atoms caused by the disappearance of chlorine atoms (Figure 2, right).

In most cases, the cube-octameric $R_8Si_8O_{12}$ framework forms spontaneously from hydrolysis/condensation reactions of many simple silanes, while in general, larger frameworks (e.g., $[HSiO_{3/2}]_n$ with $n = 10, 12, 14$) are more difficult to be obtained in one step reaction with a good yield.[6] The result of GPC showed that the production was a relative pure composition and there was no compound with high molecular weight in product (2). MALDI−TOF MS measurements showed that the major peaks of the products were

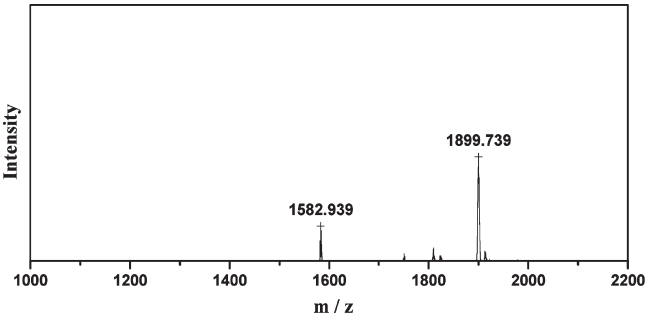


Figure 3. MALDI−TOF MS spectrum of POSS.

$[C_{70}H_{80}N_{10}Si_{10}O_{15} + H]^+$, calcd 1582.30, found 1582.94; $[C_{84}H_{96}N_{12}Si_{12}O_{24} + H]^+$, calcd 1899.77, found 1899.74 (Figure 3). Since the monomers are readily ionizable and have been successfully characterized by MALDI techniques, the peak heights in MALDI−TOF MS can be used as a relative qualitative measure of the amounts of each species in the sample.[32] It suggested that T_{10} and T_{12} derivatives were obtained as the major product. Although other low peaks showed that there were also a small portion of side products, considering the cost-effective synthesis and the difficulty to remove the side-products, we kept them down in the products.

All of the characterizations of product **2** showed that the POSS was mainly T_{10} and T_{12} structures. It is well-known that there are two different geometries of T_{12} structures: ideal D_{6h} and D_{2d} symmetry. The D_{6h} structure appears to be rare for molecular species.[6] In order to make sure the real

structure of T_{12}, models of D_{6h} and D_{2d} symmetry structure were performed by using Gaussian03 with HF/6-31G* basis sets. The total energy calculations showed that D_{2d} symmetry was much more stable than D_{6h} symmetry. The energy difference between them was 118.8 kca/mol per Si atom. Besides that, T_8 and T_{10} structures were also modeled and performed. The calculated results showed that both T_{10} and T_{12} (D_{2d}) structures were more stable than T_8 structure. These results suggested that the product was more inclined to form T_{10} and T_{12} (D_{2d}) structures instead of T_8 structure.

We provided a facile route to synthesize a new imino functionalized POSS: one step from triethoxysilane and then neutralized with organic alkali. What's more significant, it could be easily produced in a large scale with a high yield. The new type of POSS was well soluble in organic solvents such as DMAC and THF, and readily to cooperate with organic polymers such as PU.

Appearance of POSS−PU Hybrid Films. Various amounts of POSS were introduced into the PU networks. The appearance of the neat PU was colorless and transparent. When POSS content increased to 11 and 18 wt %, the films become yellow and still transparent. Even the POSS content reached 52 wt %, the POSS−PU film presented to be transparent. It exhibited the good compatibility of POSS in PU system. There were two factors that contributed the good compatibility: One is there existed the physical interactions between multiple organic groups of POSS and PU,[33,34] the other is that POSS was chemically bonded to the PU.

In order to confirm the reaction of POSS with isocyanates, FT-IR of neat PU and POSS−PU hybrids were carried out. Figure 4 represented a portion of amplificatory FT-IR spectra. From the figure, the following information could be obtained: (1) All of the isocyanates were reacted because there was no NCO absorption appeared at 2270 cm^{-1}. (2) POSS was introduced into the PU system. As we know, there was no phenyl in neat PU, hence, neat PU had no absorption at 1600 cm^{-1} (typical phenyl absorption), while phenyl absorption could be seen in POSS−PU hybrids, especially in PU52. (3) POSS was reacted with isocyanates. Usually, at 1530 cm^{-1}, there would be a sharp absorption derived from the resonance of N−H and C−N groups in PU. It was clearly seen that the absorption was blue-shifted when POSS was added into PU networks. This indicated that the formation of urea linkage which was different from the urethane linkage. Therefore, it was believed that POSS was introduced and chemically boned to PU. It was also evidenced by acetone-swelling ratio and loss weight ratio tests (see Supporting Information) and DMA measurements which would be discussed later.

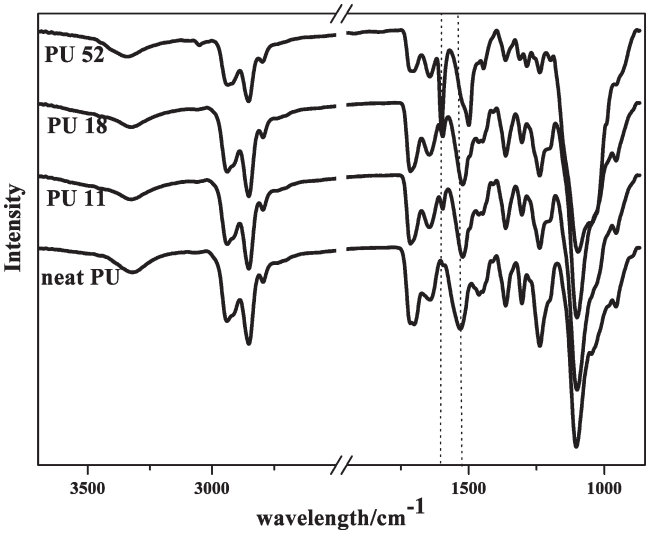


Figure 4. FTIR spectra of the neat PU and POSS−PU hybrids.

Morphological Characterization. HRTEM was carried out to analyze the microstructure of POSS−PU hybrids. As represented, PU18 was chosen to analyze the distributions of nanoparticles in POSS−PU networks. Parts A and B of Figure 5 represented the TEM micrographs of PU18, it could be seen that considerable amounts of dark spherical particles with a range of 5−10 nm uniformly dispersed in the POSS−PU networks. These dark particles could be attributed to POSS aggregates because of the high electron density of the POSS cages. In Figure 5B, lattice fringes were clearly shown in some dark spherical particles. They were ascribed to the formation of microcrystals derived from POSS clusters. Moreover, each cluster was consisted of several POSS cages. It revealed that POSS was nanophase separated in the matrix, which suggested excellent compatibility between polyurethane and POSS. The good compatibility was the basis of POSS cooperated with PU chain in high degree and more reactive groups of POSS which acted as a nanoscale cross-linker would take part in the reaction, thus formed network. Besides, as POSS content increased, the aggregates and the number densities of POSS in PU network were also increased. (See support information)

Morphology of POSS−PU was further characterized by AFM (Figure 6). The neat PU film presented a featureless surface in height image and showed microphase separation

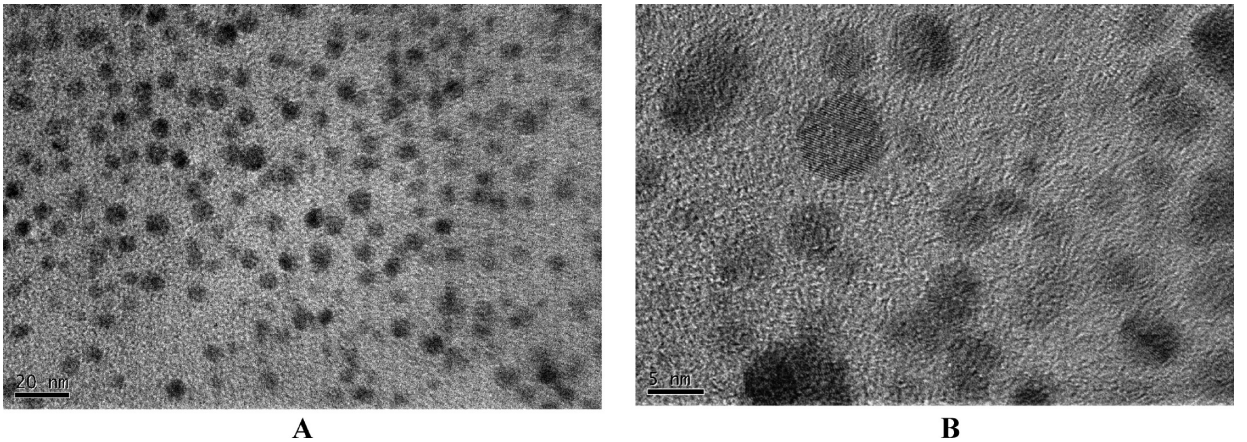


Figure 5. HRTEM micrographs for PU18 (A, scale bar = 20 nm; B, scale bar = 5 nm).

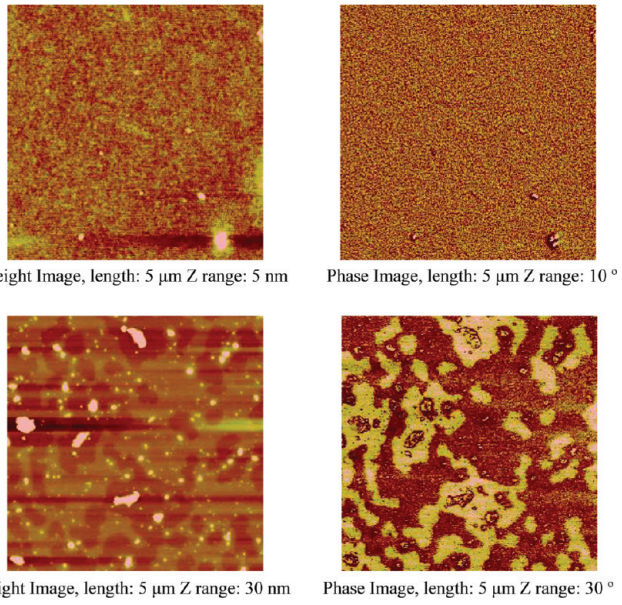


Figure 6. AFM height images and phase images of neat PU (up) and PU52 (down).

in phase image. On the contrary, the result was drastically different for PU52 which showed a distinct topology of phase separation of hard and soft segments. In PU52 height image, it exhibited rougher surface than neat PU did. Some of the parts were concave, and what's more interesting was that most of the caves were centered with bright, nubbly materials. Contrasted with the phase image of PU52, the caves along with centers were bright sight which belonged to the hard segments. Nanda and his co-workers have reported small amounts of POSS usually tend to combine with hard segments and affect the properties of the hard segments of PU.[26] The AFM images could be explained as follows. POSS aggregates reacted with IPDI and then formed island domain like hard segments. This usually companied with chemical reactions such as cross-link, so the segments shrunk as a result[35] and formed caves like those in PU52 film. Other POSS aggregates dispersed in soft segments and the sizes were smaller than those in hard segments and did not shrinkage. Therefore, in PU52, POSS aggregates both chemically bonded to hard segments and dispersed in soft segments greatly restricted the movements of PU molecular chains which resulted in the decrease of free volumes.

Mechanical Properties of POSS−PU Hybrids. The dynamic mechanical properties were tested on a Dynamic Mechanical Analyzer (DMA) (Figure 7).The storage modulus of neat PU started decreasing from glassy state to rubber state at about 225 K, the rubber plateau was kept from 275 to 350 K, then neat PU went into terminal region as the temperature was above 350 K. For POSS−PU hybrids, the glassy states were very similar to those of neat PU. The main effect of the incorporation of POSS was reflected in high temperature region. The storage modulus at high temperature increased with increasing POSS concentration. Interestingly, a critical concentration at 26 wt % was found. Below the critical concentration, PU22 showed a plateau from 333 to 393 K. When the temperature was higher than 393 K, the sample went into the terminal region. This suggested that the cross-link was not enough to form a 3-dimensional network at high temperature. Beyond the critical concentration, the storage modulus kept constant at high temperature meaned that a 3-dimensional permanent network at high temperature was formed. It should be pointed that the

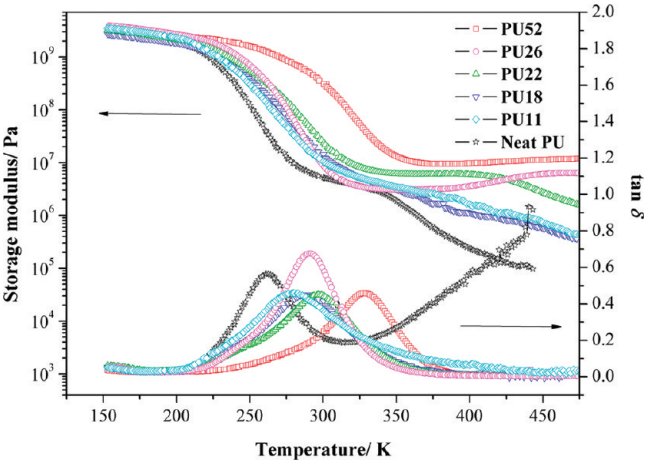


Figure 7. Dynamic mechanical analysis of neat PU and POSS−PU Hybrids.

activity of POSS was mild because its functional group was a secondary amine. When the POSS content was low, only a part of the functional groups of POSS participated in the reaction. Because of the excellent compatibility of POSS in PU, when the POSS content was overdue, all the NCO groups would react with POSS. Therefore, the hybrids showed obvious enhanced properties because more functional groups participated in the reaction would cause higher cross-linking density. The cross-linking density was increased with increasing POSS concentration, this could also be proved by equilibrium swelling test according to Flory−Rehner theory (See Supporting Information).

The glass transition temperature (T_g) could be evaluated by the peak of tan δ. All POSS−PU hybrids showed only one peak which belongs to the soft segments. T_gs increased regularly as POSS content increased. T_g of PU52 was ca. 60 K higher than that of neat PU. This observation suggested that the present of POSS, due to their nanophase dispersing and due to the chemical incorporation to the polyurethane chains, effectively hindered the motion of the network, thus the T_g of the network increased.[36] In addition, as POSS loadings increased, the cross-linking density of POSS−PU network increased and the free volumes of the network decreased rapidly, thus the T_g of the network increased.

The static mechanical properties of the neat PU and POSS−PU hybrids were evaluated by tensile tests at room temperature. Typical samples below and beyond critical concentration were chosen to make the figure as plain as possible. The stress−strain curves are shown in Figure 8. Neat PU and most of the POSS−PU films showed typical rubber elastic curves, while PU52 presented hard elastic properties. These could be attributed to the consolidation effects which could be interpreted on the following two factors. (1) The PU chain movement was restricted by the increasing cross-linking density of materials as POSS content increased. (2) When POSS content was low, POSS−PU films exhibited rubberlike properties because of the main part of the composite was soft segments (see Table 1). While in PU52, the hard segments of the hybrids were nearly 70 wt %, and the PU52 curve represented plastic properties. The increase of the hard segment content was another reason that caused the mechanical properties of hybrids to be enhanced.

It was important to note that PU18 and PU52 possessed high stress and good elongation which were not easily seen in common PU. As POSS content reached 52 wt %, POSS would aggregate and form rigid networks that forbid PU

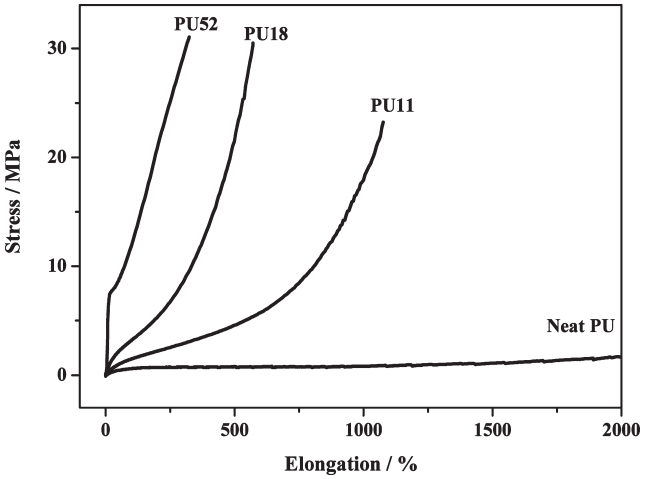


Figure 8. Tensile tests of neat PU and POSS−PU hybrids.

Table 2. T_g and T_{test} of the POSS−PU Hybrids

sample	T_g/K	T_{test}/K	$(T_{test} - T_g)$/K
neat PU	263	298	35
PU 11	280	315	35
PU 18	288	323	35
PU 52	328	363	35

chains to move freely. On the other hand, the nanofillers could provide more free volumes for the networks. Hence, PU52 showed toughened plastic properties caused by the competition factors of increasing cross-linking density and the nanofiller toughening effect.[37]

The PU chain motion was restricted when it interacted with POSS. This directly resulted in the enhancement of T_g of POSS−PU hybrids. The existence of hard and soft segment and their microphase separation led to the strong stress and good elongation of the POSS−PU hybrids. However, the tensile test was performed at the same temperature, which could be seriously influenced by the rheological status of the materials. So the tensile test at constant $T_{test} - T_g$ was performed to resurvey the POSS−PU hybrids. To further elucidate the cooperation behavior of POSS−PU, we performed tensile test at constant $T_{test} - T_g$. The constant $T_{test} - T_g$ was chosen as 35 K, because all the samples were in the rubber plateau at this condition (Table 2).

From Figure 9, we could see that the slope of the tensile curve at initial part was increased with increasing POSS content. This suggested that Young's modulus of the POSS−PU hybrids was increased. When the test temperature was 35 K above T_g, soft segments of the materials were mobile, thus the stress at break decreased. However, due to the existence of the cross-linker, the PU chain attached to the cross-link junctions were hardly influenced by the increasing temperature. Moreover as cross-linking density increased, the cross-link junctions were also increased, the molecular weight between cross-linking junctions was decreased as expected. So under the same $T_{test} - T_g$ conditions, the enhanced effect of the introduction of POSS was obvious without regard to T_g.

Thermal Stability. TGA exhibited the thermal stability of the PU−POSS hybrids. The addition of POSS usually did not alter the degradation of PU.[22,29] Within the experimental temperature range, the TGA curves of all samples displayed similar degradation steps. It could be found that the samples decomposed mainly in two steps (Figure 10). This indicated that the addition of POSS did not change the degradation mechanism of PU networks. The first step could be

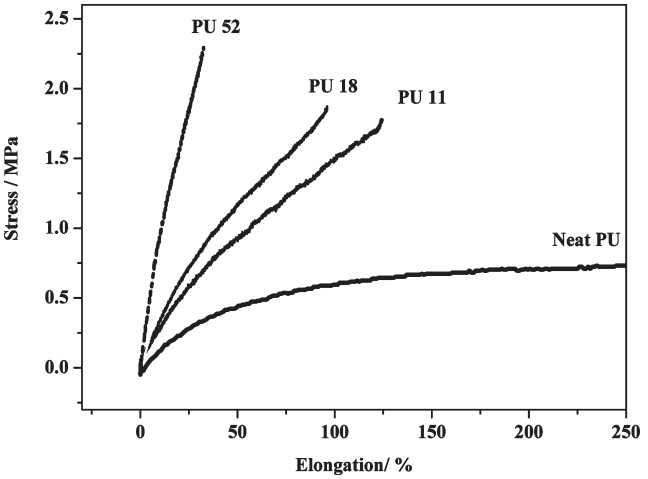


Figure 9. Tensile test at constant $T_{test} - T_g = 35$ K. For neat PU, the sample was tested at 263 K, 280 K for PU11, 288 K for PU18, and 328 K for PU52.

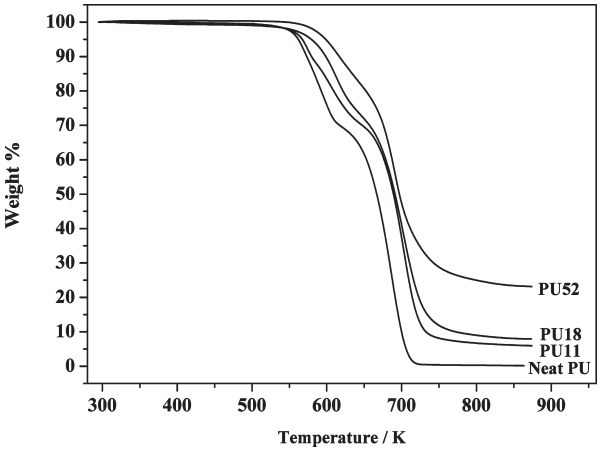


Figure 10. TGA curves of neat PU and POSS−PU hybrids.

Table 3. Thermo Decomposition Characterizations of POSS−PU Hybrids

	sample			
	neat PU	PU11	PU18	PU52
$T_{5\%}$, K	561	567	579	598
$T_{50\%}$, K	666	689	691	697
ΔW, % (873 K)	0	5.9	7.8	23

attributed to the degradation of the hard segments of the PU. The second step could be related to the degradation of the elastic segments.[22]

In general, $T_{5\%}$, $T_{50\%}$ and thermal residues (ΔW) could be obtained from the TGA curves, as summarized in Table 3. $T_{5\%}$ and $T_{50\%}$ were defined as the temperature at which the weight loss ratios were 5 and 50 wt % respectively. In Table 3, $T_{5\%}$, $T_{50\%}$ and ΔW increased with the increase of POSS content, which indicated the improvements of thermal stabilities of POSS−PU. $T_{5\%}$s of PU11, PU18 and PU52 were 6, 18, and 37 K, respectively, higher than that of neat PU. $T_{50\%}$s of PU11, PU18, and PU52 are also 23, 25, and 31 K, respectively, higher than that of neat PU. These two aspects revealed that the incorporation of POSS significantly enhanced the thermal stability of PU. The initial thermal decomposition temperatures increased when the POSS content of the hybrid polymers increased. This enhancement of POSS−PU hybrids could be explained by the restrictions of

molecular mobility of polymer chains caused by high cross-linking density, which had also been confirmed by measurements of tensile tests and DMA. Because the molecular mobility was the major factor that contributes to the transportation of reactive groups in the polymer, the POSS−PU hybrids were likely to have lower reactivity and, therefore, greater chemical and thermal stability than pristine PU.[22] In addition, the char residues of POSS−PU hybrids were higher than that of neat PU, and increased monotonously with the increase of POSS loadings. It was reasonable that POSS molecules had the silica-like Si−O−Si structure, which would lead to the higher inorganic components in the cured materials.

Conclusion

A new type of *N*-phenylaminomethyl-POSS was synthesized using a facile method in large scale with a high yield and mild reaction condition. NMR, GPC, and MALDI−TOF MS confirmed that the POSS was T_{10} and T_{12} cage structures possessed the main part of the product.

This new POSS had been used as a cross-linker to incorporate to conventional PU. The POSS−PU hybrids showed no macrophase separation even POSS concentration up to 52 wt %. HRTEM measurements showed the POSS was nanophase separated in PU networks. DMA revealed the storage modulus and T_g increased with increasing POSS concentration. POSS−PU formed a permanent network beyond the critical POSS concentration 26 wt %. Tensile test at constant $T_{test} - T_g$ temperature showed the increasing young's modulus of POSS−PU hybrids with increasing POSS concentration. TGA revealed the enhanced thermal properties of POSS−PU hybrids. From what had been mentioned above, the outstanding performance of PU52 was underlined: high storage modulus (10 MPa) at 473 K, high stress (31 MPa), and good elongation (300%) at room temperature (298 K).

The enhanced mechanical and thermal properties were ascribed to the synergetic effect of POSS and PU. Because of the good compatibility between POSS and PU, POSS which acted as a cross-linker could be dispersed into PU matrix in nanoscale. Therefore, PU chain would be restricted by the nanoscale cross-linker and resulted in the great enhancement of mechanical and thermal properties. Besides, as POSS concentration increased, the cross-linking density also increased, when POSS concentration reached 26 wt %, a permanent network formed.

Acknowledgment. The authors gratefully acknowledge support from the National Science Foundation of China (Grants 50373018 and 50533020). We also thank Prof. G Xue, Prof. Pingchuan Sun, Dr. Xiaoliang Wang (solid state ^{29}Si NMR), Prof. Zuanru Yuan (TGA), Dr. Jianglin Fang (FTIR), and Dr. Zexing Qu (Gaussian calculating).

Supporting Information Available: Detailed descriptions of sample recipes and preparation procedures. This material is available free of charge via the Internet at http://pubs.acs.org.

References and Notes

(1) Baney, R. H.; Itoh, M.; Sakakibara, A.; Suzuki, T. *Chem. Rev.* **1995**, *95*, 1409.
(2) Garces, J. M.; Moll, D. J.; Bicerano, J.; Fibiger, R.; McLeod, D. G. *Adv. Mater.* **2000**, *12*, 1835.
(3) Giannelis, E. P. *Adv. Mater.* **1996**, *8*, 29.
(4) LeBaron, P. C.; Wang, Z.; Pinnavaia, T. J. *Appl. Clay Sci.* **1999**, *15*, 11.
(5) Oriakhi, C. O. *J. Chem. Educ.* **2000**, *77*, 1138.
(6) Lickiss, P. D.; Rataboul, F. Fully condensed polyhedral oligosilsesquioxanes(POSS): From synthesis to application. *Adv. Organomet. Chem.*; **2008**; *57*, 1−116.
(7) Li, Q.; Zhou, Y.; Hang, X. D.; Deng, S. F.; Huang, F. R.; Du, L.; Li, Z. P. *Eur. Polym. J.* **2008**, *44*, 2538.
(8) Lichtenhan, J. D.; Fu, X.; Schwab, J. J.; Wheeler, P.; Abbenhuis, H. C. L. Metalized nanostructured chemicals alloyed into polymers. 2006-US32651 2008051190, 20060821, 2008.
(9) Schwab, J. J.; Lichtenhan, J. D.; Chaffee, K. P.; Mather, P. T.; Romo-Uribe, A. *Mater. Res. Soc. Symp. Proc.* **1998**, *519*, 21.
(10) Devaux, E.; Rochery, M.; Bourbigot, S. *Fire Mater.* **2002**, *26*, 149.
(11) Ni, Y.; Zheng, S. X. *Macromol. Chem. Phys.* **2005**, *206*, 2075.
(12) Wang, R. Y.; Wang, S. F.; Zhang, Y. *J. Appl. Polym. Sci.* **2009**, *113*, 3095.
(13) Haddad, T. S.; Lichtenhan, J. D. *Macromolecules* **1996**, *29*, 7302.
(14) Scott, D. W. *J. Am. Chem. Soc.* **1946**, *68*, 356.
(15) Feher, F. J.; Budzichowski, T. A. *J. Organomet. Chem.* **1989**, *379*, 33.
(16) Rikowski, E.; Marsmann, H. C. *Polyhedron* **1997**, *16*, 3357.
(17) Brown, J. F.; Vogt, L. H.; Prescott, P. I. *J. Am. Chem. Soc.* **1964**, *86*, 1120.
(18) Takahashi, K.; Sulaiman, S.; Katzenstein, J. M.; Snoblen, S.; Laine, R. M. *Aust. J. Chem.* **2006**, *59*, 564.
(19) Liaw, D. J.; Huang, C. C.; Liaw, B. Y. *Polymer* **1998**, *39*, 3529.
(20) Fu, B. X.; Hsiao, B. S.; Pagola, S.; Stephens, P.; White, H.; Rafailovich, M.; Sokolov, J.; Mather, P. T.; Jeon, H. G.; Phillips, S.; Lichtenhan, J.; Schwab, J. *Polymer* **2001**, *42*, 599.
(21) Takahashi, T.; Munstedt, H.; Modesti, M.; Colombo, P. *J. Eur. Ceram. Soc.* **2001**, *21*, 2821.
(22) Janowski, B.; Pielichowski, K. *Thermochim. Acta* **2008**, *478*, 51.
(23) Knight, P. T.; Lee, K. M.; Qin, H.; Mather, P. T. *Biomacromolecules* **2008**, *9*, 2458.
(24) Kannan Ruben, Y.; Salacinski Henryk, J.; Odlyha, M.; Butler Peter, E.; Seifalian Alexander, M. *Biomaterials* **2006**, *27*, 1971.
(25) Turri, S.; Levi, M. *Macromolecules* **2005**, *38*, 5569.
(26) Nanda, A. K.; Wicks, D. A.; Madbouly, S. A.; Otaigbe, J. U. *Macromolecules* **2006**, *39*, 7037.
(27) Madbouly, S. A.; Otaigbe, J. U.; Nanda, A. K.; Wicks, D. A. *Macromolecules* **2007**, *40*, 4982.
(28) Neumann, D.; Fisher, M.; Tran, L.; Matisons, J. G. *J. Am. Chem. Soc.* **2002**, *124*, 13998.
(29) Liu, H.; Zheng, S. *Macromol. Rapid Commun.* **2005**, *26*, 196.
(30) Liu, Y.; Ni, Y.; Zheng, S. *Macromol. Chem. Phys.* **2006**, *207*, 1842.
(31) Gravel, M. C.; Zhang, C.; Dinderman, M.; Laine, R. M. *Appl. Organomet. Chem.* **1999**, *13*, 329.
(32) Asuncion, M. Z.; Laine, R. M. *J. Am. Chem. Soc.* **2010**, *132*, 3723.
(33) Hao, N.; Boehning, M.; Schoenhals, A. *Macromolecules* **2007**, *40*, 9672.
(34) Hao, N.; Bohning, M.; Goering, H.; Schonhals, A. *Macromolecules* **2007**, *40*, 2955.
(35) Bliznyuk, V. N.; Tereshchenko, T. A.; Gumenna, M. A.; Gomza, Y. P.; Shevchuk, A. V.; Klimenko, N. S.; Shevchenko, V. V. *Polymer* **2008**, *49*, 2298.
(36) Lee, A.; Lichtenhan, J. D. *Macromolecules* **1998**, *31*, 4970.
(37) Kopesky, E. T.; McKinley, G. H.; Cohen, R. E. *Polymer* **2006**, *47*, 299.

558 *Macromolecules* **2011**, *44*, 558–565
DOI: 10.1021/ma102342c

Macromolecules
ARTICLE

Wide-Angle X-ray Scattering Study on Shear-Induced Crystallization of Propylene-1-Butylene Random Copolymer: Experiment and Diffraction Pattern Simulation

Yimin Mao, Christian Burger, Feng Zuo, and Benjamin S. Hsiao*

Department of Chemistry, Stony Brook University, Stony Brook, New York 11794-3400, United States

Aspy Mehta and Cynthia Mitchell

ExxonMobil Chemical Company 5200 Bayway Drive, Baytown, Texas 77520, United States

Andy H. Tsou

ExxonMobil Research and Engineering Company, Annandale, New Jersey 08801, United States

Received October 13, 2010; Revised Manuscript Received December 7, 2010

ABSTRACT: Shear-induced crystallization of a propylene-1-butylene random copolymer with low butylene content (5.7 mol %) was studied using time-resolved wide-angle X-ray scattering (WAXS) techniques. Polymorphism, preferred crystal orientation, crystallization kinetics, and disorder effect were investigated based on WAXS 2D whole pattern analysis. It was found that at 100 °C, the crystallite of P−B copolymer was a mixture of 80% γ-form and 20% α-form of isotactic polypropylene (iPP) crystals. The application of a step shear (shear rate = 100 s^{-1}, shear duration = 3s) induced γ-form crystals with *c*-axis oriented perpendicular to the shear direction. In contrast, the *c*-axis of α-form crystals was normally in parallel to the shear direction. Both crystallization kinetics and crystallinity were greatly enhanced by shear. The disorder effect was found to play an important role in the crystallization behavior of P−B copolymer. In the early stage crystallization, the chosen copolymer contained a large amount of structure defects, where crystals became more ordered upon annealing. The degree of crystal orientation was also found to decrease during crystallization due to the relaxation after shear.

Introduction

Isotactic polypropylene (iPP) is one of the most important thermoplastic polymers in the chemical industry. Its molecular structure is simple, but exhibits several polymorphic crystal forms. The relationship between polymorphism and property performance in iPP has long been an interesting subject to scientists. It is believed that its polymorphism can be controlled by tuning the microstructure of polymer chains through different routes, such as the use of different catalysts to control the stereoregularity and regioregularity of the chain,[1−7] and the process of copolymerization for making propylene-based random copolymers.[8−13] The latter is particularly interesting for practical reasons due to the easy accessibility and versatility of tuning chain structure by changing species of comonomers and their concentrations.

During the synthesis of propylene-based random copolymer, when concentration of comonomer is low, the comonomer unit serves as a chain defect and cannot be incorporated into the crystalline structure.[14] In this case, the resulting crystal forms are the same as those grown from an iPP homopolymer. In iPP, α-form and γ-form crystals are two of the most common polymorphs. The structure of α-form in iPP homopolymer was first determined by Natta and Corradini.[15] It has a monoclinic unit cell with parameters $a = 6.65$ Å, $b = 20.96$ Å, $c = 6.50$ Å and $\beta = 99.2°$. Polymer chains in the unit cell exhibit a *C2*/*c* space group (in reality, the resulting iPP crystal often possesses a symmetry between *C2*/*c* and *Cc* space groups because of the disorder) having chains configured in the 3_1 helix aligned parallel to the *c*-axis.[15] γ-form was the first observed crystal form showing nonparallel chain-packing in a unit cell. It has a large orthorhombic unit cell with parameters $a = 8.54$ Å, $b = 9.93$ Å, $c = 42.41$ Å. The diagonal of the *ab* plane is 13 Å, which is just enough to hold two chains of 3_1 helices. The *c*-axis of the unit cell is especially large because the chains are piled along this direction in a bilayered fashion (i.e., each layer contains two chains). There is an 80° angle between the layers, which means that each layer contains one of the diagonals of the *ab* plane in a cross-hatching style. The entire packing of polymer chains obeys the symmetry of *Fddd* space group.[16,17] The packing energy of α- and γ-form crystals are very close. Their X-ray diffraction patterns also resemble each other. The characteristics of the diffraction profile for α-form crystals consist of reflections from (110), (040), and (130) planes with *d*-spacings of 6.25 Å, 5.18 Å and 4.76 Å, respectively,[15] while for γ-phase they consist of reflections from (111), (008), and (117) planes with *d*-spacings of 6.40, 5.30, and 4.42 Å, respectively.[16,17] Because of various line broadening mechanisms, such as size effect and disorder, these peaks usually overlap with each other. Therefore, it is difficult to quantitatively separate peaks from different polymorphs based on 1D diffraction profiles alone.

In this work, we chose propylene-1-butylene (P−B) random copolymer with low butylene concentration (5.7 mol %) as a model polymer to investigate polymorphism and structure development in shear-induced crystallization. The experiments were

*To whom correspondence should be addressed. E-mail: bhsiao@notes.cc.sunysb.edu. Telephone: 631-632-7793. Fax: 631-632-6518.

 Published on Web 01/06/2011 © 2011 American Chemical Society

carried out using the *in situ* 2D synchrotron wide-angle X-ray scattering (WAXS) technique. As diffraction patterns in this study were anisotropic, data analysis was performed based on 2D whole pattern simulation. Although conventional 1D profile analysis can be used to determine the crystal modifications and their content, 2D whole pattern analysis is necessary to deal with the system with preferred orientation. The advantage of this approach is that scattering intensity dependence on absolute value of the scattering vector s (or d-spacing in real space) and polar angle can be retrieved simultaneously, which make it possible to discriminate diffraction peaks contributed from different crystal modifications. Crystallization kinetics, preferred orientation and influence of disorder for different polymorphs can therefore be quantitatively analyzed.

Experimental Section

Materials and Sample Preparation. The propylene-1-butylene (P−B) random copolymer was provided by ExxonMobil Chemical Company. The number-average molecular weight M_n of the sample was 56 000 g/mol and the polydispersity was 1.97. The mole fraction of the butylene component was 5.7%. A Linkam CSS-450 high-temperature shearing stage modified for *in situ* WAXS measurement was used to precisely control temperature and shear field. Detailed information on shear apparatus could be found in our previous publication.[18] As parallel plate geometry was used in this study, the applied shear rate varied along the radial direction of the sample. Since the X-ray illuminated only on one sample position, the reported shear rate represented the value at the measuring point.[18] The sample thickness was constrained at 1.0 mm, where the stress field had a gradient along the thickness direction. The chosen experimental procedure was as follows. First, the sample was melted and kept at 150 °C (i.e., 30 °C above the endothermic peak temperature in heating thermogram in differential scanning calorimetry) for 5 min. After that, it was cooled down to the crystallization temperature, 100 °C with a cooling rate of −30 °C/min. Immediately after the sample reached 100 °C, a step shear was applied. The shear rate was 100 s^{-1} and shear duration was 3s. The isothermal crystallization process of the sample at this temperature was recorded online. Since the chosen shear rate was relatively high, the sheared sample was further examined to check the integrity after each experiment. It was found that the sheared sample was able to maintain its original shape without fracture.

Time-Resolved WAXS Measurement. WAXS measurements were carried out at the Advanced Polymer Beamline (X27C) in the National Synchrotron Light Source (NSLS), Brookhaven National Laboratory (BNL). The wavelength of the X-ray beam was 1.371 Å. All scattering images were captured in real time by a 2D MAR CCD camera. The exposure time for each image collection was 30s. The sample-to-detector distance was 121 mm. The scattering angle was calibrated by Al_2O_3. Air and other background scattering were subtracted from the experimental data in all data analysis.

Diffraction Pattern Simulation Methodology. For the crystal system, the entire lattice in real space can be determined using three vectors $\boldsymbol{a}$, $\boldsymbol{b}$, and $\boldsymbol{c}$. It is convenient to choose these vectors in accordance with three coordinates of the unit cell. Correspondingly, a reciprocal space can be defined using another set of vectors $\boldsymbol{a}^*$, $\boldsymbol{b}^*$, and $\boldsymbol{c}^*$, so that each (hkl) reflection plane becomes a node in this space. Consequently, each moiety of crystal lattice in real space and each node representing a (hkl) plane in reciprocal space can be written as[19]

$$\begin{aligned} \mathbf{x}_j &= p_j\mathbf{a} + q_j\mathbf{b} + r_j\mathbf{c} \\ \mathbf{s}_{hkl} &= h\mathbf{a}^* + k\mathbf{b}^* + l\mathbf{c}^* \end{aligned} \tag{1}$$

In eq 1, $\boldsymbol{x_j}$ is the spatial position of the jth atomic group (hereafter, the atomic group will be used as the terminology referring to any type of repetitive unit in crystal lattice, be it ion, atom, or molecule, etc.). The symbols p_j, q_j, and r_j are its fractional coordinates in $\boldsymbol{a}$, $\boldsymbol{b}$, and $\boldsymbol{c}$ directions. Similarly, each (hkl) node is located in $\boldsymbol{s}_{hkl}$ with $s = (2/\lambda)[\sin(\theta/2)]$, where θ is the scattering angle. The structure factor of the (hkl) plane is

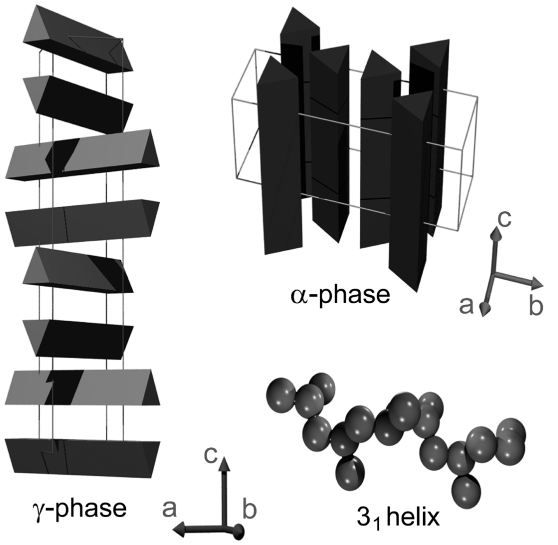


Figure 1. Illustration of γ-form, α-form unit cells in iPP. The building block of both unit cells is the propylene 3_1 helix.

$$\begin{aligned} F_{hkl} &= \sum_{j=1}^{n} f_j \exp(-i2\pi \boldsymbol{s}_{hkl}\cdot\mathbf{x}_j) \\ &= \sum_{j=1}^{n} f_j \exp[-i2\pi(p_j h + q_j k + r_j l)] \end{aligned} \tag{2}$$

where f_j is the atomic form factor. In our case, carbon atom is the repetitive unit of the crystal. Therefore, f_j is the same for all atomic groups, and it can be numerically expressed in exponential series.[20] All hydrogen atoms are neglected in our simulation, which will introduce error of about 2%. The fractional coordinates of α- and γ-form crystals were adopted from the original work of Natta and Corradini[15] as well as Brückner,[16,17] respectively. Since our objective system was a random copolymer, the cell parameters were adjusted slightly to fit our data. For the α-phase, a = 6.70 Å, b = 21.76 Å, c = 6.83 Å, and β = 99.3°. For the γ-phase, a = 8.54 Å, b = 9.93 Å, and c = 43.37 Å. An illustration of unit cells of α- and γ-form crystals are shown in Figure 1.

The scattering intensity is proportional to the square of structure factor's modulus. The powder intensity is the total intensity diluted over the spherical surface with radius of s_{hkl}

$$I_{hkl}(s) \propto |F_{hkl}(s)|^2 \tag{3}$$

$$\overline{I_{hkl}(s)} \propto \frac{1}{4\pi s_{hkl}^2}|F_{hkl}(s)|^2 \equiv \frac{1}{4\pi s_{hkl}^2} I_{hkl}(s) \tag{4}$$

$I_{hkl}(s)$ in eq 3 is the overall intensity from a given (hkl) plane; $\overline{I}_{hkl}(s)$ is its corresponding powder intensity. Line profiles of reflection peaks were computed using the Lorentzian distribution. The amorphous halo was fitted with three Gaussian distributions.

Considering crystal orientation, the scattering intensity distribution in 3D reciprocal space is not homogeneous. Intensity at any specific point in reciprocal space can be described in the spherical coordinate system, depending on three parameters: ϕ, ψ, and s, where ϕ and ψ are termed as polar angle and azimuthal angle, respectively; s is the absolute value of scattering vector. In

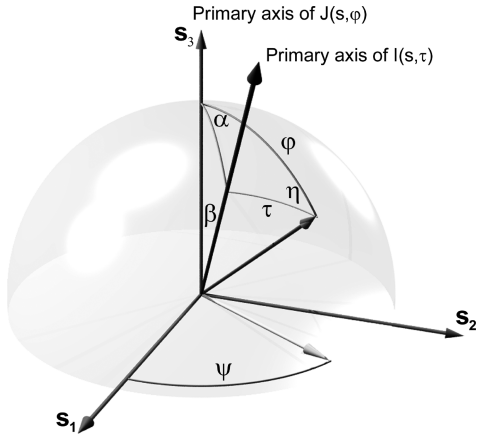


Figure 2. Illustration of spherical coordinate system and trigonometric relationship for fiber symmetry.

our simulation, the fiber symmetry was assumed to simplify the computation. That is, intensity remains unchanged over the azimuthal angle for given ϕ and s. This assumption is reasonable to a certain extent since shear flow was only applied uniaxially. The fiber axis is consistent with the c axis of the unit cell. It can be vertical or horizontal, depending on the external stress field. On the basis of this assumption, the fiber averaged intensity $\overline{J}(s,\phi)$ is now a function of s and ϕ, which can be written as[21−23]

$$\overline{J(s,\phi)} = \overline{I_{hkl}(s)} \cdot F(\phi, \phi_{hkl}) \tag{5}$$

where $\overline{I}_{hkl}(s)$ is the powder-averaged intensity as defined above. Function $F(\phi,\phi_{hkl})$ describes how intensity distributes over polar angle. ϕ_{hkl} is the polar angle of given (hkl) plane. A complete illustration of spherical coordinate system and trigonometric relationship for fiber symmetry is shown in Figure 2. The term $F(\phi,\phi_{hkl})$ is given by the following relation

$$F(\phi, \phi_{hkl}) = \frac{1}{\pi}\int_0^{\pi} g(\beta)\, \mathrm{d}\eta \tag{6}$$

where $g(\beta)$ describes the orientation distribution of scatterers. In this study, the Onsager distribution for $g(\beta)$ proposed by Burger[23] was adopted. It takes the following form

$$g(\beta) = p\cosh(p\cos\beta)/\sinh(p) \tag{7}$$

Advantages of using the Onsager distribution are that it has a reasonably good peak shape and can give analytic solution when substituting to eq 6. The final expression of $F(\phi,\phi_{hkl})$ now becomes

$$F(\phi, \phi_{hkl}) = \frac{p}{\sinh(p)}\cosh(p\cos\phi\cos\phi_{hkl})I_0(p\sin\phi\sin\phi_{hkl}) \tag{8}$$

where p determines the width of the Onsager distribution. I_0 is the modified Bessel function of the first kind of order zero. The fiber-averaged intensity $\overline{J}(s,\phi)$ satisfies the normalization condition

$$\int_0^{2\pi}\mathrm{d}\psi\int_0^{\pi}\sin\phi\,\mathrm{d}\phi\int_0^{\infty}\overline{J(s,\phi)}s^2\,\mathrm{d}s = I_{hkl} \tag{9}$$

This means that the integration of intensity from (hkl) plane over 3D reciprocal space should be equal to an invariant, the total intensity from this reflection plane, I_{hkl}.

Calculated patterns were compared with experimental ones to check peak positions as well as their intensity distributions (see Figures 3 and 4 for example). The main diffraction peaks from experimental and simulated results were examined with the

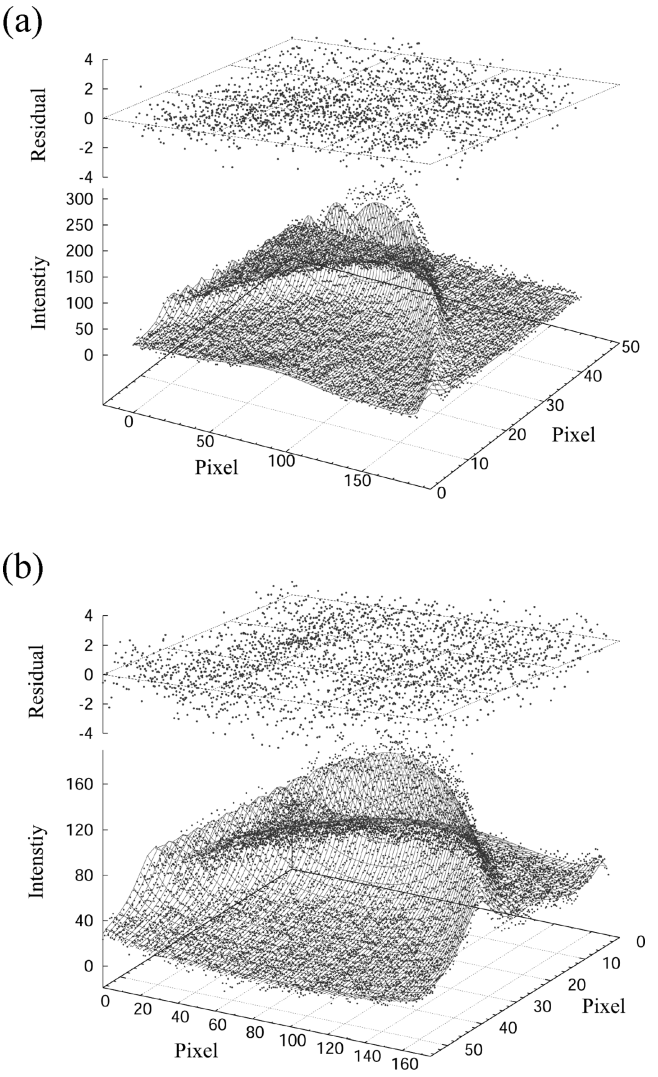


Figure 3. Examples of experimental (dot) and simulated intensity (mesh) of (111) (a) and (008) (b) reflection planes of γ-phase iPP. Residual was defined as $(X_{exp} - X_{sim})/\sigma$, with X_{exp} and X_{sim} being the intensities from the experimental data and simulation, respectively; and σ being the standard deviation obtained from the Poisson distribution according to photon counting statistics.

χ^2 analysis. Figure 3 shows the fitting of (008) and (111) peaks of the γ-phase iPP as an example. The fitting residual was defined as $(X_{exp} - X_{sim})/\sigma$, where X_{exp} and X_{sim} are the intensities from the experimental data and simulation, respectively; and σ is the standard deviation obtained from the Poisson distribution according to photon counting statistics. The parameter χ^2 per degree of freedom should be maintained to a value as close to one as possible.

Results and Discussion

The experimental 2D WAXD patterns were compared with simulated patterns of both α- and γ-phases. A typical comparison is shown in Figure 4 (the direction of the shear flow is vertical). In this figure, the upper-right corner represents the simulated WAXS pattern of γ-phase with fiber-axis perpendicular to the flow direction (i.e., along the horizontal direction). The simulated pattern of α-phase with fiber axis parallel to the flow direction is shown in the lower-left corner. Upper-left and lower-right corners of the figure are experimental results gathered at 960 s during isothermal crystallization (crystallization was accomplished at this time) after shear. It is clear that the simulated pattern of

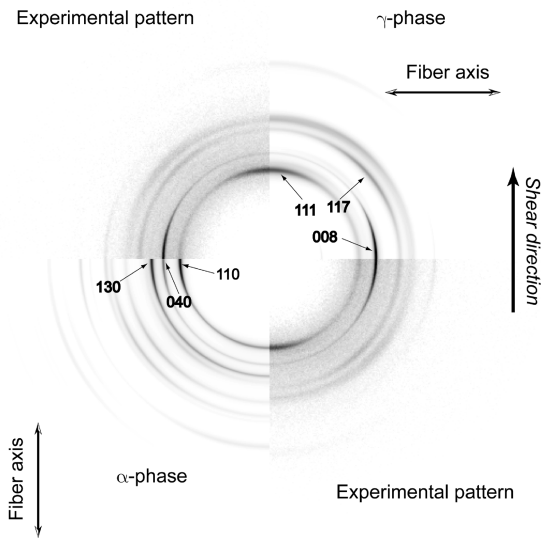


Figure 4. 2D WAXS patterns of experimental data (top-left and bottom-right corners), simulated γ-form (top-right corner) and simulated α-form (bottom-left corner) crystals. The experimental pattern was gathered after shear at 960 s during annealing when the crystallization process was complete. The flow direction was vertical; the fiber directions of γ-phase and α-phase were set to be horizontal and vertical, respectively.

γ-phase is much closer to experimental data, while that of α-phase is not. The simulated pattern of γ-phase with vertical fiber direction was also calculated, and it did not fit our data. Since polymer chains have a nonparallel packing style in the γ-phase unit cell, the *c*-axis has to be in a horizontal direction so that the reflection of (008) plane can appear in the WAXS pattern as arcs in horizontal direction, which is seen in Figure 4. It is interesting to note that the reflection of (111) plane in γ-phase appears in the vertical direction. In fact, this is not the case and can be explained as follows. The polar angle ϕ_{hkl} of the (111) plane is 81.5° (the horizontal direction is 0 deg), which is very close to the vertical direction. Because of its broad polar distribution, the (111) reflection plane appears to be one arc in this direction, although it actually consists of two arcs centered at 81.5° and 98.5°, respectively. The γ-phase with *c*-axis perpendicular to the strain direction has been reported for iPP, when processed by injection molding[24] as well as stretched uniaxially at very small strains[25] (at large strains, the *c*-axis tends to be in parallel to the stretching direction, forming so-called cross-β configuration; at even larger strains, the γ-phase will simply be stretched into α-phase with the parallel chain packing with respect to the *c*-axis[7]). There are two possibilities that might account for this unique orientation geometry. First, since in the γ-phase unit cell eight polymer chains go through diagonals of the *ab*-plane in a cross-hatching manner and pile along the *c*-axis, it is impossible to have all chains aligned along the strain direction. The perpendicular orientation of the *c*-axis with respect to the strain direction is formed due to a compromise, i.e., half of the eight chains are in parallel to the strain direction while the other half are in 80° with respect to it. Since the applied external field to P−B polymer is a shear flow, which is relatively weak compared to stretching (extensional flow), the nature of the shear flow should also be considered. For a shear flow, the deformation tensor can be decomposed into rate-of-strain tensor and vorticity tensor, denoted as $2D$ and $2W$, respectively.[26]

$$2D = \begin{vmatrix} 0 & \dot{\gamma} & 0 \\ \dot{\gamma} & 0 & 0 \\ 0 & 0 & 0 \end{vmatrix}; \quad 2W = \begin{vmatrix} 0 & \dot{\gamma} & 0 \\ -\dot{\gamma} & 0 & 0 \\ 0 & 0 & 0 \end{vmatrix} \qquad (10)$$

As seen from eq 10, in the rate-of-strain tensor, components $\dot{\gamma}_{12}$ and $\dot{\gamma}_{21}$ are equal ($\dot{\gamma}$ is the shear rate), which is responsible for the motion of uniaxial stretching. While the same components in the vorticity tensor are equal in magnitude but have opposite signs, indicating the rotational motion. The rotational flow might take an important role in formation of perpendicular orientation of the *c*-axis with respect to the flow direction. A similar result was also reported in the carbon nanotube-polymer composite under shear. For example, Ezquerra et, al.[27,28] tested the poly(butylene terephthalate) (PBT)/carbon nanotube nanocomposite with the rheo-SAXS measurement. A unique orientation of PBT lamellar crystals growing in parallel to shear direction was observed after applying a step shear at crystallization temperature. Shear was able to rotate carbon nanotube and small crystals grown at an early stage to 90° with respect to the flow direction, and therefore induced the growth of lamellar crystals in parallel to the flow direction.

Although the dominant polymorph in the chosen system is γ-form crystal, there is evidence indicating the existence of a small amount of α-form crystal, which can be analyzed according to Figure 5. Figure 5a shows the 1D integrated intensity profile comparing experimental data (cross data point) and simulated result (dashed line) which consists of 20 wt % of α-form and 80 wt % of γ-form crystals. The contribution of the α-form crystal was included because it was found that there was a small reflection peak appearing at $s = 0.205$ Å^{-1}. This peak was absent from calculated reflections of the γ-form crystal, which is shown below the overall scattering profile. Figure 5b illustrates the calculated diffraction impulses from pure α- and γ-form crystals. It is clear that this reflection peak at $s = 0.205$ Å^{-1} can be indexed as (130) plane in α-form crystal. Positions of other peaks from both crystal forms are very close to each other and cannot be easily used to separate α-form crystals from γ-form.

As described earlier, polymer chains in the α-form crystal are in parallel to the *c*-axis. When external force is applied, the *c*-axis is intended to align along the force field. Although our P−B copolymer is dominated by the γ-form crystal under shear, the orientation geometry of a small amount of α-form crystal can still be identified. Figure 6 shows the polar intensity scan of reflections from (*hkl*) planes at $s = 0.157$ Å^{-1}, i.e., (111) plane of γ-phase or (110) plane of α-phase. Since the arcs close to the vertical direction have been indexed as (111) plane of γ-phase, the intensity maxima in the horizontal direction (although very weak, it is still distinguishable) must be due to (110) plane of α-phase. This indicates that the α-form crystal adopted a different orientation mode when compared with the γ-form crystal; i.e., its *c*-axis must be in parallel to the shear direction.

The whole-pattern analysis also allowed us to distinguish scattered intensity from both portions of oriented crystals and unoriented crystals. Chains in bulk state cannot respond to an external field in a uniform manner. After the cessation of step shear, shorter chains tend to relax faster; and the orientation of later-grown crystals is less influenced by shear. Correspondingly, for a given (*hkl*) plane, both isotropic fraction (ring with uniform intensity distribution) and oriented fraction were observed in the diffraction pattern. In this case, eq 5 can be modified using an additional parameter P_0, which quantifies the portion of unoriented crystal as follows.

$$\overline{J(s,\phi)} = \overline{I_{hkl}(s)}[P_0 + (1 - P_0)F(\phi, \phi_{hkl})] \qquad (11)$$

where, P_0 varies from 0 to 1. For the powder pattern, $P_0 = 1$, since the second term in the bracket describing the polar distribution of intensity vanishes. More details of crystallization kinetics can thus be investigated, and results are shown in Figure 7. Overall crystallinity changes during shear-induced crystallization as well as quiescent crystallization are plotted together for

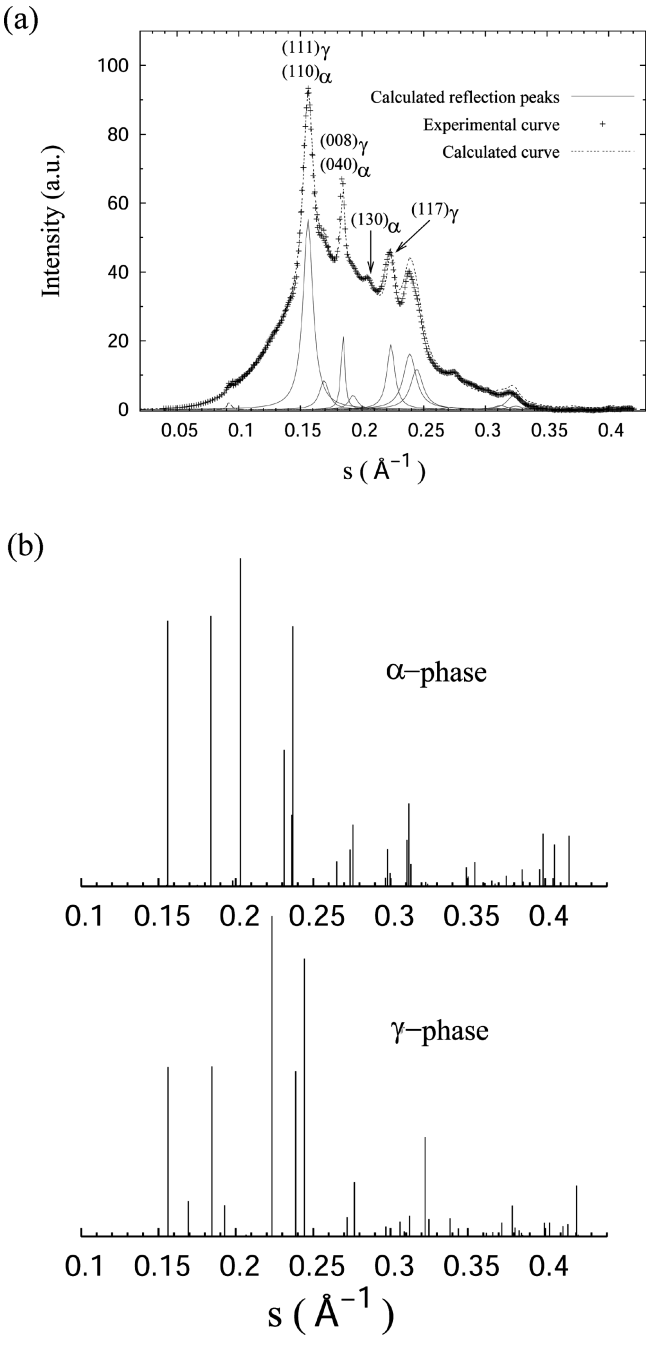


Figure 5. 1D integrated intensity profile (a) from experimental data (cross point) and simulation (dashed line), where 20% of α-phase was added in the simulation. Calculated reflection peaks from γ-phase iPP is shown below the overall profile. Simulated diffraction impulses from α- and γ-form crystals of iPP are shown in part b.

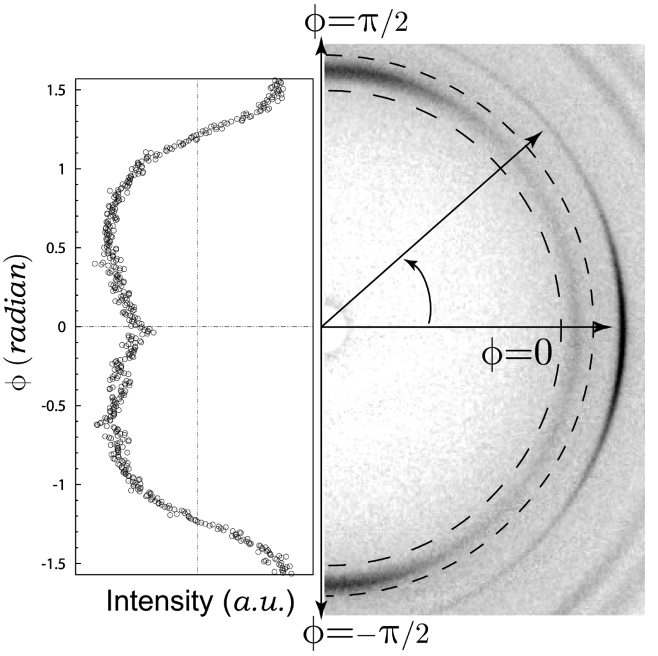


Figure 6. Polar intensity scan of reflections from (111) plane of γ-phase (close to the vertical direction) and (110) plane of α-phase (in the horizontal direction).

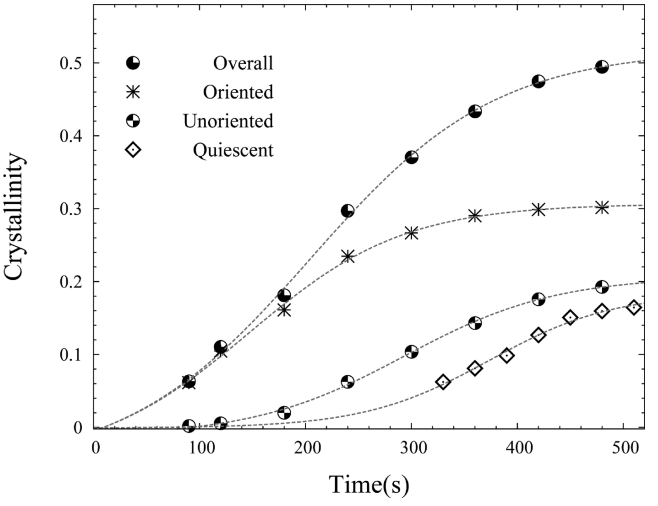


Figure 7. Crystallinity change as a function of time. Contributions from both oriented and unoriented crystals are shown. Result from quiescent crystallization is also shown for comparison purposes.

comparison purposes, where the first measurable value was about 5%. Below this value, the scattered intensity was too weak to give a confident result. In Figure 8, it is seen that the shear flow not only enhanced the crystallization kinetics but also the crystallinity of the P−B copolymer. In quiescent crystallization, the crystallization half-time was about 360 s and the final crystallinity was about 17%. With the application of a step shear, the crystallization half-time became 240 s and the final crystallinity became 49%. The enhancement of crystallization by external field (e.g., shear), in both the context of crystallization kinetics and the final crystallinity, has been reported by many authors before [refs 29 and 30, for example]. This phenomenon can be explained by the effect of shear on two aspects of the crystallization process, i.e., nucleation and growth. In nucleation, the shear field stretches and aligns polymer chains, lowering the nucleation barrier considerably[31−33] and greatly enhancing the nucleation density (through primary nucleation). On the other hand, flow-induced nuclei serve as good nucleating substrates to promote secondary nucleation and thus enhance the growth process. Such mechanisms have been experimentally observed, such as in the microscopic study of polypropylene after extrusion.[34] In these extruded samples, space filling by crystals in the skin layer was much higher than that in the core layer.[34,35] Furthermore, the large increase of crystallinity was mainly contributed by the oriented portion of the crystals. After subtraction of this portion, the remaining crystallinity (from the pure unoriented portion of the crystals) was found to be decreased to a level of about 20%. However, the unoriented crystal fraction was still slightly higher than that of quiescent crystallization; and the corresponding crystallization rate was also faster. This behavior might be due to the enhancement

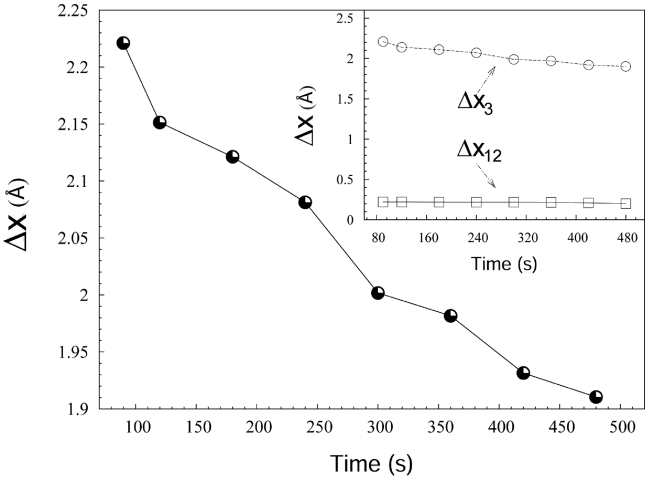


Figure 8. Change of deviation of atomic group from their ideal crystallographic positions, ΔX, as a function of crystallization time. Inset shows the deviations in the *ab*-plane (ΔX_{12}) and that along the *c*-axis (ΔX_3).

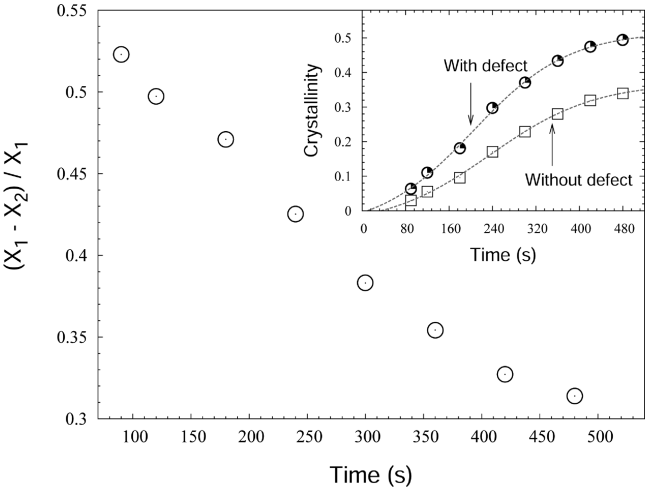


Figure 9. Ratio of crystallinity contributed by defect and overall crystallinity change as a function of time. Inset shows crystallization curves using crystallinity calculated with and without considering the influence of disorder.

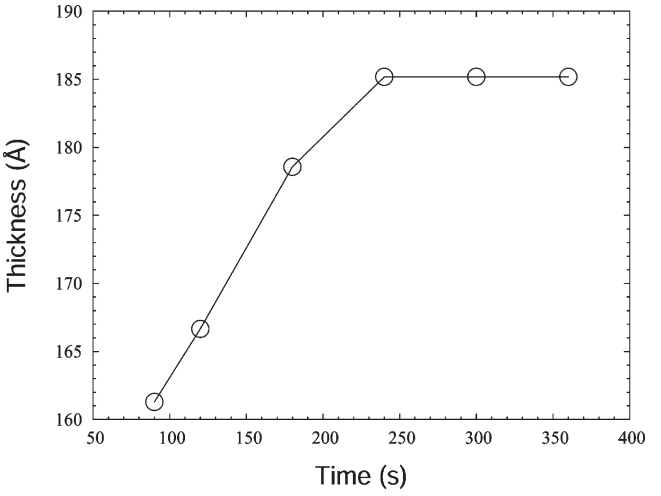


Figure 10. Change of crystal dimension of γ-phase along *c*-axis, derived from reciprocal integral peak width of the (008) peak.

of nucleation density induced by shear:[36] small nuclei may not induce the geometric orientation of crystals, but they can speed up the crystallization process. Figure 7 also indicates that even though the experimental data point below 5% was not accessible, the curve can be extrapolated to the very early stage of crystallization. In the early stage, the scattering was weak due to the low volume fraction of the nuclei and/or poor crystal ordering.

To investigate the change of crystal ordering, the model of disorder of the first kind was used to analyze the *in situ* WAXS results. In this analysis, each atomic group is allowed to deviate from its corresponding ideal crystallographic position independently, which is to say, the structure factors become different for the unit cell in different spatial positions. The averaged structure factor $\overline{F}_{hkl}$ can be written as follows, considering this random deviation[19]

$$\overline{F_{hkl}} = F_{hkl} \exp\left(-\frac{2\pi^2}{3} s^2 \Delta X^2\right)$$

$$= F_{hkl} \exp\left[-\frac{2\pi^2}{3}({s_{12}}^2 {\Delta X_{12}}^2 + {s_3}^2 {\Delta X_3}^2)\right] \qquad (12)$$

where ΔX represents the averaged deviation of atomic groups from their ideal crystallographic position. Since we assume the system consists of fiber symmetry, ΔX can be further decomposed to ΔX_{12} (deviation in the *ab*-plane) and ΔX_3 (deviation along the *c*-axis). This equation is equivalent to the formula of the Debye−Waller factor, which is often used to characterize the deviation due to thermal agitation. The change of ΔX as a function of time during crystallization is shown in Figure 8. It is seen that ΔX decreases continuously during crystallization, indicating crystals become more and more perfect. The continuous decrease of ΔX can give some insight into the crystallization structure formed at the early stage. If this trend is consistent, the deviation must be large at a very early stage, making it reasonable to speculate that during that period, small crystal blocks with a large degree of disorder have already been formed. These tiny crystal blocks eventually evolve into large crystalline lamellae.[37,38] The inset of Figure 8 shows the changes of ΔX_{12} and ΔX_3 with time. It is found that the overall deviation is mainly contributed by ΔX_3, i.e., along the horizontal direction. This is manifested in the scattering profile that reflection peaks near the horizontal direction suffer a systematic decrease in intensity. It further means that the stacking fault would be mainly due to the bilayer packing along the *c*-axis. This is reasonable since the *c*-axis direction has more spatial degree of freedom for γ-phase. Using eq 12, we can also compare the crystallinity with and without considering the disorder effect. The results are shown in Figure 9. In Figure 9, X_1 refers to the overall crystallinity, i.e., with consideration of disorder, where X_2 is crystallinity of "perfect" crystals without defect (their changes are shown in the inset). $(X_1 - X_2)/X_1$ naturally gives the content of defect in overall crystallinity. For our random copolymer system, this value is very high. It is about 50% in the early stage of crystallization. This is because the noncrystallizable comonomer segments hinder the chain arrangement in crystals. The ratio decreases with eclipse of time, indicating crystals become more and more ordered. These results are in agreement with Figure 8. In addition to the ordering process, crystals also grow simultaneously. The crystal size can be estimated by using the reciprocal integral width. In this study, the (008) plane was used because it is directly related to the crystal size along the *c*-axis of γ-form crystal. The result is plotted in Figure 10. The first measurable value was 16 nm at 90 s and increased to a plateau value of 18.5 nm at 150 s. After that, even though the ordering process continued to increase (as seen in Figures 8 and 9), the size of crystals did not change. This is reasonable since the ordering process and crystal

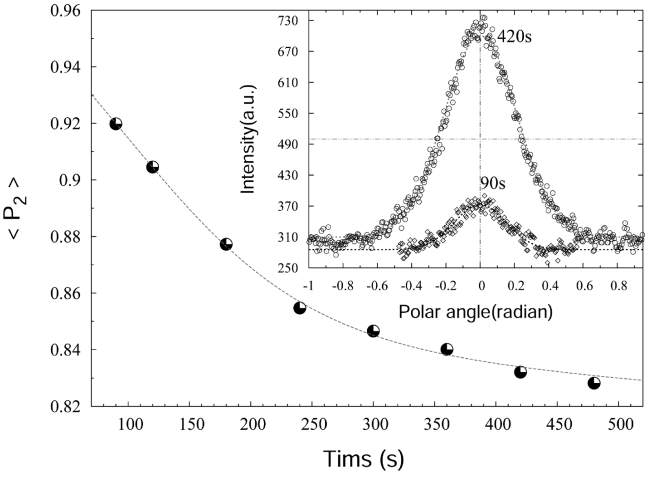


Figure 11. Change of $\langle P_2 \rangle$ as a function of time. Inset shows polar scans of intensity peaked at $s = 0.184$ Å^{-1} (i.e., the (008) plane for γ-phase and (040) plane for α-phase) from experimental data gathered at 90 and 420 s, respectively.

growth need not be dependent on each other as the crystal growth process can be affected by other factors such as crystal impingement, poisoning on the growth facet, and so on.

The degree of orientation can be quantified with the Hermans' orientation parameter $\langle P_2 \rangle$, which varies from -0.5 to 1. Using the Onsager distribution, $\langle P_2 \rangle$ can be analytically given by[23]

$$\langle P_2 \rangle = 1 - 3[\coth(p) - 1/p]/p \quad (13)$$

When the portion of unoriented crystals is subtracted, $\langle P_2 \rangle$ becomes the degree of orientation of pure oriented crystals. The results are shown in Figure 11, where the change of $\langle P_2 \rangle$ that is related to the breadth of polar distribution of intensity, is plotted as a function of crystallization time. In was seen that the value of $\langle P_2 \rangle$ exhibited a decrease trend during crystallization. This could be attributed to the chain relaxation after shear. The rate of decrease was significant in the early stage and was slowed down after that, due to the increase of viscosity during the solidification process.

Conclusions

The shear-induced crystallization behavior of the P−B random copolymer was investigated using the time-resolved WAXS technique. The experimental data was analyzed using the 2D whole-pattern simulation approach. Comprehensive consideration of scattered intensity dependence on both polar angle ϕ and scattering vector s made it possible to identify the polymorphism as well as preferred orientation of the polymer. The main conclusions can be summarized as follows:

1. When crystallized at 100 °C, the P−B copolymer was dominated by γ-form crystal of iPP, which was coexistent with about 20% of α-form crystal. The application of shear made the c-axis of γ-form crystal oriented perpendicular to the shear direction, while the α-form crystal showed a conventional orientation mode with the c-axis parallel to the shear direction.
2. The kinetics study indicated that the shear flow significantly accelerated the crystallization rate. The crystallinity was also greatly increased as compared with that in quiescent crystallization. These enhancements were mainly due to the increased fraction of oriented polymer chains.
3. The crystal perfection process was clearly revealed by the analysis using the model of first kind disorder. A very large amount of crystal defect was found in the P−B random copolymer, especially in the early stage.
4. The degree of crystal orientation was calculated, which indicated a continuous decrease in the early stage, which can be attributed to the relaxation behavior of polymer chains after step shear.

Acknowledgment. We wish to acknowledge the assistance of Drs. Lixia Rong and Jie Zhu for the synchrotron WAXS experimental setup. Financial support of this work was provided by the National Science Foundation (DMR-0906512) and ExxonMobil Chemical Company.

References and Notes

(1) Thomann, R.; Wang, C.; Kressler, J.; Mülhaupt, R. *Macromolecules* **1996**, *29*, 8425–8434.
(2) Alamo, R. G.; Kim, M.; Galante., M. J.; Isasi, J. R.; Mandelkern, L. *Macromolecules* **1999**, *32*, 4050–4064.
(3) Wiyatno, W.; Pople, J. A.; Gast, A. P.; Waymouth, R. M.; Fuller, G. G. *Macromolecules* **2002**, *35*, 8488–8497.
(4) Wiyatno, W.; Fuller, G. G.; Pople, J. A.; Gast, A. P.; Chen, Z.; Waymouth, R. M.; Myers, C. L. *Macromolecules* **2003**, *36*, 1178–1187.
(5) Wiyatno, W.; Chen, Z.; Liu, Y.; Waymouth, R. M.; Krukonis, V.; Brennan, K. *Macromolecules* **2004**, *37*, 701–708.
(6) Auriemma, F.; De Rosa, C. *Macromolecules* **2002**, *35*, 9057–9068.
(7) Auriemma, F.; De Rosa, C. *Macromolecules* **2006**, *39*, 7635–7647.
(8) Hosier, I. L.; Alamo, R. G.; Esteso, P.; Isasi, J. R.; Mandelkern, L. *Macromolecules* **2003**, *36*, 5623–5636.
(9) Alamo, R. G.; Ghosal, A.; Chatterjee, J.; Thompson, K. L. *Polymer* **2005**, *46*, 8774–8789.
(10) Jeona, K.; Palza, H.; Quijada, R.; Alamo, R. G. *Polymer* **2009**, *50*, 832–844.
(11) Poon, B.; Rogunova, M.; Hiltner, A.; Baer, E.; Chum, S. P.; Galeski, A.; Piorkowska, E. *Macromolecules* **2005**, *38*, 1232–1243.
(12) De Rosa, C.; Auriemma, F.; de Ballesteros, O. R.; Resconi, L.; Camurati, I. *Macromolecules* **2007**, *40*, 6600–6616.
(13) De Rosa, C.; Auriemma, F.; de Ballesteros, O. R.; De Luca, D.; Resconi, L. *Macromolecules* **2008**, *41*, 2172–2177.
(14) De Rosa, C.; Iacono, S. D.; Auriemma, F.; Ciaccia, E.; Resconi, L. *Macromolecules* **2006**, *39*, 6098–6109.
(15) Natta, G.; Corradini, P. *Nuovo Cimento Suppl.* **1960**, *15*, 40–51.
(16) Brückner, S.; Meille, S. V. *Nature* **1989**, *340*, 455–457.
(17) Meille, S. V.; Brückner, S.; Porzio, W. *Macromolecules* **1990**, *23*, 4114–4121.
(18) Somani, R. H.; Hsiao, B. S.; Nogales, A.; Srinivas, S.; Tsou, A. H.; Sics, I.; Balta-Calleja, F. J.; Ezquerra, T. A. *Macromolecules* **2000**, *33*, 9385–9394.
(19) Guinier, A. *X-Ray Diffraction: In Crystals, Imperfect Crystals, and Amorphous Bodies*; W. H. Freeman: San Francisco, CA, and London, 1963.
(20) Doyle, P. A.; Turner, P. S. *Acta Crystallogr.* **1968**, *A24*, 390–397.
(21) Ruland, W.; Tompa, H. *Acta Crystallogr.* **1968**, *A24*, 93–99.
(22) Ruland, W. *Colloid Polym. Sci.* **1977**, *255*, 833–836.
(23) Burger, C.; Zhou, H.; Sics, I.; Hsiao, B. S.; Chu, B.; Graham, L.; Glimcher, M. J. *J. Appl. Crystallogr.* **2008**, *41*, 252–261.
(24) Kalay, G.; Bevis, M. J. *J. Polym. Sci., Part B: Polym. Phys.* **1997**, *35*, 241–263.
(25) Auriemma, F.; De Rosa, C.; Boscato, T.; Corradini, P. *Macromolecules* **2001**, *34*, 4815–4826.
(26) Bird, R. B.; Armstrong, R. C.; Hassager, O. *Dynamics of Polymeric Liquids*; Wiley-Interscience: York, U.K., Chichester, U.K., Brisbane, Australia, Toronto, Canada, and Singapore, 1987; Vol. *1*, Chapter 3.
(27) Garcia-Gutierrez, M. C.; Hernandez, J. J.; Nogales, A.; Panine, P.; Rueda, D. R.; Ezquerra, T. A. *Macromolecules* **2008**, *41*, 844–851.
(28) Hernandez, J. J.; Garcia-Gutierrez, M. C.; Nogales, A.; Rueda, D. R.; Ezquerra, T. A. *Macromolecules* **2009**, *42*, 4374–4376.
(29) Kumaraswamy, G.; Verma, R. K.; Kornfield, J. A.; Yeh, F. J.; Hsiao, B. S. *Macromolecules* **2004**, *37*, 9005–9017.
(30) Balzano, L.; Rastogi, S.; Peters, G. W. M. *Macromolecules* **2009**, *42*, 2088–2092.
(31) Somani, R. H.; Yang, L.; Hsiao, B. S.; Agarwal, P. K.; Fruitwala, H. A.; Tsou, A. H. *Macromolecules* **2002**, *35*, 9096–9104.

(32) Somani, R. H.; Yang, L.; Hsiao, B. H.; Fruitwala, H. *J. Macromol. Sci., Phys.* **2003**, *B42*, 515–531.
(33) Kumaraswamy, G.; Kornfield, J. A.; Yeh, F.; Hsiao, B. S. *Macromolecules* **2002**, *35*, 1762–1769.
(34) Liedauer, S.; Eder, G.; Janeschitz-Kriegl, H. *Int. Polym. Process.* **1995**, *10*, 243–250.
(35) Kumaraswamy, G.; Verma, R. K.; Issaian, A. M.; Wang, P.; Kornfield, J. A.; Yeh, F.; Hsiao, B. S.; Olley, R. H. *Polymer* **2000**, *41*, 8931–8940.
(36) Janeschitz-Kriegl, H. *Colloid Polym. Sci.* **2003**, *281*, 1157–1171.
(37) Hugel, T.; Strobl, G.; Thomann, R. *Acta Polym.* **1999**, *50*, 214–217.
(38) Strobl, G. *Eur. Phys. J. E* **2000**, *3*, 165–183.

566 *Macromolecules* **2011**, *44*, 566–574
DOI: 10.1021/ma102047m

Macromolecules
ARTICLE

Nanostructured Organic−Inorganic Copolymer Networks Based on Polymethacrylate-Functionalized Octaphenylsilsesquioxane and Methyl Methacrylate: Synthesis and Characterization

Zhanbin Wang, Shiwei Leng, Zhonggang Wang,* Guiyang Li, and Hao Yu

Department of Polymer Science and Materials, State Key Laboratory of Fine Chemicals, School of Chemical Engineering, Dalian University of Technology, Dalian 116012, People's Republic of China

Received June 21, 2010; Revised Manuscript Received December 13, 2010

ABSTRACT: Novel polymethacrylate-functionalized octaphenylsilsesquioxanes (OPS) macromonomer was designed and synthesized, which was employed as nanofiller and cross-linker to copolymerize with MMA to produce OPS/PMMA hybrid nanocomposites with OPS contents ranging from 0 to 1.18 mol %. The synthesis route was that, OPS was brominated to yield polybromo-OPS, and polybromo-OPS was then reacted with BuLi and CO_2 to obtain polycarboxyl-OPS. After that, the carboxyls were converted to chlorocarbonyl groups, and the esterification reaction of polychlorocarbonyl-OPS with 2-hydroxyethyl methacrylate led to polymethacrylate-OPS. Their chemical structures were characterized by means of FTIR, ^{1}H NMR and ^{13}C NMR spectra. Moreover, after cleavage of C−Si bond by KF/H_2O_2, the position and number of functional groups on the benzene rings of OPS macromonomers and the molecular weight of PMMA in the nanocomposite were investigated in detail by LC−MS and GPC methods, respectively. The prepared OPS macromonomer can result into PMMA significantly improved thermal-chemical stability and apparently increased glass transition temperature. For example, the nanocomposites are insoluble in any common organic solvents due to the formation of three-dimensional networks. Compared to the pure PMMA, the OPS/PMMA nanocomposite with OPS content of only 0.94 mol % exhibits increased 5%-mass-loss temperature and glass transition temperature by 104 and 21 °C, respectively.

Introduction

Polyhedral oligomeric silsesquioxanes (POSS), in both nanoscience and nanomaterials, continue to receive considerable attention owing to their unique molecular characteristics such as the robust inorganic silica core surrounded by the identical or different organic groups, precisely controlled monodispersed nanometer size (ca. 1−2.5 nm in diameter), and diverse synthetic strategies for organic functionalization.[1−7] Of particular interest are chemically bonded POSS/polymer hybrid nanocomposites, wherein even very small amount of POSS particles uniformly distributed within the polymer matrix at the nanometer scale bring about significant improvement in heat-resistance, dimensional stability and mechanical properties of the materials.[8−17]

One of the most important aspects in POSS-chemistry is its functionalization with the aim to produce POSS macromonomers that can be used in linear, branching or cross-linking copolymerization reactions with other monomers. Depending on the number of pendant reactive groups, POSS can be classified as monofunctional,[18,19] bifunctional[20] and polyfunctional[21,22] compounds. Monofunctional cubic POSS are usually achieved through vertex-capping of incompletely condensed POSS trisilanols with $RSiCl_3$ (R is a functional group) and which, including vinyl-POSS, acrylate-POSS, methacrylate-POSS, and styryl-POSS,[18,19,23−25] have been copolymerized with methyl methacrylate (MMA) or styrene via free radical polymerization to obtain linear poly(methyl methacrylate), polystyrene or their copolymers bearing pendant POSS side groups, whereas epoxy-POSS, amino-POSS, and carboxyl-POSS are covalently incorporated into cured epoxy networks or used for the preparations of POSS/polyamide nanocomposites.[26−29] In addition, Leu et al synthesizes a bifunctional diamino-POSS macromonomer through the vertex-capping reaction, which together with 4,4′-oxidianiline, is polymerized with pyromellitic dianhydride to afford linear POSS/polyimide hybrid materials.[30]

Relative to mono- or bifunctional POSS, polyfunctional POSS are preferred since the formed branched, star-shape and cross-linked hybrid structures can more tightly tethered the polymer with POSS through multiple covalent conjunctions, and thereby significantly improve its physical properties compared to the linear one. In earlier work, polyfunctional POSS are often obtained through hydrosilylation of unsaturated compounds with $(HSiO_{1.5})_8$ or $(HMe_2SiO_{1.5})_8$ such as octavinyl-POSS,[21] octamethacryalte-POSS,[22,30] and octahydroxy-POSS.[31] However, the synthesis route utilizing hydrosilylation often gives rise to functional groups linked with POSS cores through aliphatic segments, which results into nanocomposite the low thermal and mechanical stability compared to the aromatic analogues, and consequently limits their application field to some extent.

Over the past decade, the study of completely condensed aromatic octaphenylsilsesquioxane (OPS) has become an active research area owing to its high thermal stability. Moreover, the presence of eight phenyls provides an opportunity for functionalization. However, a review of literature reveals that, up to now, only few types of polyfunctional OPS are reported except for the polybromo-OPS and octanitro- and octaamino-OPS (OAPS) synthesized by Laine et al.[32,33] OAPS has been employed as a building block to synthesize rigid cross-linked polyimides, as macromolecular curing agents to prepare thermosetting epoxy

*To whom all correspondence should be addressed. E-mail: zgwang@dlut.edu.cn.

 Published on Web 01/05/2011 © 2011 American Chemical Society

resins, or converted to octafunctionalized maleimide resins.[34−36] Thereafter, Zheng et al uses OAPS to prepare photocurable octacinnamamidophenyl silsesquioxane, which is then photo-cross-linked with polyvinylcinnamate (PVCIN) to yield the OPS/PVCIN nanocomposites.[37]

To further exploit the potential of OPS and extend the type of functionalized OPS macromonomers, herein we design and synthesize polycarboxyl-OPS and polychlorocarbonyl-OPS, which offer an access to a variety of novel polymer/inorganic nanocomposites. For example, polychlorocarbonyl-OPS can be applied for the preparations of hyperbranched or cross-linked polyesters or polyamides, whereas polycarboxyl-OPS may provide a possibility to construct micro/mesoporous rigid polybenzoxazoles, or as macromolecular curing agents to synthesize thermosetting epoxy resins. Besides, through the reaction of polychlorocarbonyl-OPS with 2-hydroxyethylmethacrylate, polymethacrylate-OPS has been readily obtained.

Poly(methyl methacrylate) is a transparent amorphous thermoplastic engineering material widely used in wide range of industrial fields. However, its chemical resistance and thermal stability have to be improved to meet the increasing demands of property for advanced electronic and optical applications. Cross-linking can be an effective way to enhance chemical and thermal stability by using diol dimethacrylate, divinylbenzene, aromatic phenolphthalein dimethacrylate, poly(2-acryloyloxyethyl methacrylate), and poly(2-methacryloyloxyethyl methacrylate) as cross-linking agents.[38−41] Recently, polyvinyl-POSS derived from hydrosilylation reaction is copolymerized with MMA, and thus formed POSS/PMMA networks show enhanced thermal/mechanical properties.[30,42,43]

The aim of the present work is to synthesize new polymethacrylate-OPS macromonomers, and then the mixtures of polymethacrylate-OPS and MMA with OPS contents from 0 to 1.18 mol % are copolymerized to produce OPS/PMMA nanocomposites with an expectation to significantly improve the chemical resistance and thermal property of PMMA material.

Experimental Section

Materials. Phenyltrichlorosilane was purchased from J&K-Chemical Co., Ltd. Octaphenylsilsesquioxane (OPS) was synthesized via hydrolysis and condensation of phenyltrichlorosilane according to the procedure in the literature[44] with 87% yield. 2-Hydroxyethylmethacrylate (HEMA) and MMA were purchased from Tianjin Chemical Reagent Co., and distilled under reduced pressure from hydroquinone and calcium hydride prior to use. Azobis(isobutyronitrile) (AIBN) was purchased from Shanghai Reagent. Benzene and THF were refluxed over sodium and distilled just before use. Pyridine was purified by distillation under reduced pressure from calcium hydride. The other solvents were of reagent grade and used as received.

Instrumentation. Fourier transform infrared (FTIR) spectra were recorded on a Nicolet-20DXB IR spectrometer at room temperature in the 400−4000 cm^{-1} region with a resolution of 2 cm^{-1}. Liquid samples were measured by casting film on KBr salt tablets, whereas solid samples were prepared by dispersing the sample in KBr and compressing the mixtures to tablets.

^1H NMR and ^{13}C NMR were carried out on a Varian INOVA400 spectrometer at room temperature. The NOE-suppressed ^{13}C NMR spectra were accumulated with the slowly changing homogeneity of the magnetic field. Typically pulse delay of 10 s, acquisition times of 0.5 s, and a 2500 Hz sweep width were utilized.

Gel permeation chromatography (GPC) analysis was conducted with a PL-GPC220 system using PS as standard and tetrahydrofuran (THF) as the eluent.

Elemental analyses were determined with an Elementar Vario EL III elemental analyzer.

High performance liquid chromatography (LC) analysis was conducted on HP1100LC/MSD instrument with a Zorbax Extend C18 (2.1 × 150 mm) column with mobile phase of mixed solution containing 89.9% of methanol, 10% of water and 0.1% of formic acid. Detection was at 254 nm, and a flow rate was constant at 0.2 mL/min. Mass selective detector (MS) analysis was conducted with an HP1100 Series MSD system.

Differential scanning calorimetry (DSC) was run on NETZSCH DSC204 at the temperature of 100−350 °C at a heating rate of 10 °C/min in nitrogen atmosphere. The glass transition temperatures (T_g) were read at the middle of the change in the heat capacity.

Wide angle X-ray diffraction (WAXD) study of the powder sample was performed using Rigku D/max-2400 X-ray diffractometer (40 kV, 200 mA) with a copper target at a scanning rate of 2°/min, scanned from 5 to 60°.

Thermal gravimetric analysis (TGA) was carried out on the NETZSCH TG209C under nitrogen atmosphere in the 50−600 °C region with a heating rate of 20 °C/min.

Synthesis of Polybromo-OPS. Polybromooctaphenylsilsesquioxane (polybromo-OPS) was prepared in reference to the procedure reported in the literature with some modifications:[32] 30 g of OPS (0.232 mol-phenyl), 2.85 g (0.051 mol) of iron powder, and 200 mL of dichloromethane were added into a 500 mL round-bottom flask equipped with magnetic stirring. Then, 13.4 mL of Br_2 (0.261 mol) was added dropwise over a period of 30 min at room temperature under the atmosphere of nitrogen. The mixture was stirred for 6 h. Then 50 mL of 10% aqueous $NaHSO_3$ was added to terminate the reaction. The organic layer was separated and washed with deionized water three times, and the solvent was removed by rotary evaporation. The crude product was dissolved in 60 mL of ethyl acetate and precipitated into 200 mL of methanol. The solution was filtered to afford 43 g white solid with the yield of 85%. Anal. Found: C, 34.42; H, 1.94; Br, 39.57. FTIR (cm^{-1}): 3069, 1578, 1102, 1067, 1010. ^1H NMR (DMSO-d_6, ppm): 6.9−8.0 ppm. ^{13}C NMR (DMSO-d_6, ppm): 6.9−8.0 ppm; 135.8, 133.4, 132.2, 131, 128.1, 126.2, 122.1, 120.6. GPC: M_n = 1457, M_w = 1493, M_w/M_n = 1.02.

Synthesis of Polycarboxyl-OPS. A dry four-neck flask, fitted with thermometer, nitrogen, and carbon dioxide inlet tubes and dropping funnel, was charged with 80 mL of anhydrous tetrahydrofuran and 12 g of polybromo-OPS. While maintaining the temperature at −78 °C, 60 mL of BuLi (2.5 M in hexane) was charged dropwise over a period of 2.5 h under the protection of nitrogen. It was observed that a white precipitate appeared because of the formed lithium compound. Then the CO_2, dried through a molecular sieve column, was flowed into reaction flask for another 14 h. The reaction was terminated by adding 10 mL methanol, 20 mL water and finally 5 mL 2N dilute aqueous HCl. The precipitate was filtered and dried to afford 7.6 g white powder with 77% yield. Anal. Found: C, 44.82; H, 2.97; Br, 2.71. FT-IR (cm^{-1}): 2800−3700, 3064, 1697, 1596, 1167; ^1H NMR (D_2O/NaOH, ppm): 6.9−8.0 (m, Ar−H). ^{13}C NMR (D_2O/NaOH, ppm): 182.6, 176.3, 172.1, 146.8, 142.9, 140.1, 137.1, 134.9, 134.1, 133.9, 132.1, 130.6, 131.1, 128.3, 126.8, 122.1, 120.5.

Synthesis of Polychlorocarbonyl-OPS. A 500 mL four-necked flask was equipped with a mechanical stirrer, nitrogen inlet and outlet and a condenser, using a bubbler trap containing aqueous NaOH attached to the end of condenser to absorb the released SO_2 gas. After 6 g of polycarboxyl-OPS, 250 mL of newly distilled thionyl chloride ($SOCl_2$) and 1.5 mL of pyridine were added, the system was heated gradually to refluxing temperature. It was observed that, with the reaction time, the polycarboxyl-OPS solid began to dissolve, and disappeared completely to become a homogeneous solution. Then the reaction was allowed to proceed at this temperature for 12 h. The excess $SOCl_2$ was distilled out under reduced pressure. The residual trace $SOCl_2$ was further removed by azeotropic distillation with

benzene three times. Thus 5.3 g of white solid was obtained in 73% yield, which was directly used for the preparation of polymethacylate-OPS.

Synthesis of Polymethacylate-OPS. At room temperature, to a 500-mL three-necked flask equipped with a mechanical stirrer, dry nitrogen inlet and outlet, a condenser, and a dropper was charged 150 mL of benzene, 5.3 g of polychlorocarbonyl-OPS, and 3.5 mL of pyridine. Then a solution of 2-hydroxyethylmethacrylate (HEMA) (34.2 g, 58.59 mmol in 30 mL of dried benzene) was added dropwise under stirring to the above mixture over a 1 h period. After reacting overnight, 0.1 g of hydroquinone was added and the solvent was distilled out under reduced pressure to give a pale yellow solid. The crude product was dissolved in ethanol and precipitated into the water. Repeating the above purification procedure three times gave 5.5 g of a white solid. Yield: 82%. FTIR (cm^{-1}): 3075, 2960, 2934, 1724, 1134, 1011. ^1H NMR (DMSO-d_6, ppm): 5.61−6.05 (=CH−), 3.62 and 4.09 ($-CH_2-O$), 1.88 ($-CH_3$), 7.32−7.91 (Ar−H).

Synthesis of Polymethacylate-OPS/MMA Copolymers. The bulk radical copolymerization of methyl methacrylate with 0.24 mol % of polymethacylate-OPS was described here as an example: 0.0189 g of $MMA_{6.5}OPS$ and 2 mL of MMA (1.89 g) were charged into a dry glass ampule. After polymethacylate-OPS dissolved completely in the MMA, 0.0142 g of AIBN was added, and the system was flushed with nitrogen and sealed. The solution was heated at 65 °C for 12 h and then 120 °C for another 2 h. In the similar procedures, the copolymers with polymethacylate-OPS contents of 0.47, 0.94, and 1.18 mol % were synthesized, respectively. In addition, the pure PMMA was prepared under the same polymerization conditions for comparison purpose.

Finely ground powder samples of thus synthesized copolymers were successively extracted with acetone using a Soxhlet apparatus for 12 h to remove any possible PMMA homopolymer or unreacted polymethacylate-OPS prior to the structure−property measurements.

For the sake of brevity, in this study, the nanocomposites synthesized with the polymethacylate-OPS content of 0.24, 0.47, 0.94, 1.18 mol % are referred to hereafter as $OPS_{0.24}$-PMMA, $OPS_{0.47}$-PMMA, $OPS_{0.94}$-PMMA and $OPS_{1.18}$-PMMA, respectively.

Cleavage of Si−C Bonds in OPS Macromonomers. The Si−C bonds of polybromo-OPS were cleaved according to the procedure of literature with some modifications:[32] 3.0 g of polybromo-OPS, 2.5 g of KF, 2.4 g of $NaHCO_3$, 25 mL of THF, and 25 mL of methanol were added to a 250 mL round-bottom flask equipped with a magnetic stirring, dry nitrogen inlet and outlet, a condenser, and a dropper. After stirring for 15 min, 20 mL of 30% H_2O_2 was added dropwise over a period of 30 min, and the system was allowed to reflux for another 4 h. The precipitated silica was filtered out, and the solution was concentrated by rotary evaporation to give a liquid brominated-phenol mixture, which composition was analyzed by LC−MS. Similarly, the carboxyl phenyls were cleaved from polycarboxyl-OPS, and were also analyzed by LC−MS method.

Cleavage of Si−C Bonds in PMMA/OPS Nanocomposites. Taking the PMMA/OPS nanocomposite containing 0.24 mol % of OPS as an example: to a 250 mL round-bottom flask equipped with a magnetic stirring, dry nitrogen inlet and outlet, a condenser and a dropper was added 0.5 g of finely ground composite sample, 1.3 g of KF, 1.2 g of $NaHCO_3$, 15 mL of THF, and 10 mL of methanol. After 15 mL of 30% H_2O_2 was added dropwise over a period of 20 min, the system was successively refluxed for 72 h. The solvent was removed to give the white solid, which was extracted with 5 mL of THF three times. The solutions were combined and concentrated, which was slowly poured into a stirred mixed solution of ethanol and deionized water (v/v, 4:1) to precipitate the white polymer. The obtained PMMA was dried under vacuum at 60 °C for 12 h to constant weight (0.4857 g) with a yield about 97%.

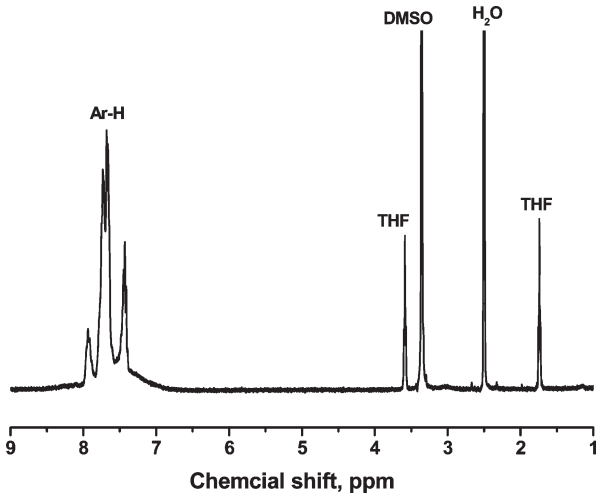


Figure 1. ^1H NMR spectrum of $Br_{8.5}OPS$ with THF as internal standard.

Results and Discussion

Synthesis of Polybromo-OPS. Polybromooctaphenylsilsesquioxane (Br_xOPS), where x is the average number of bromine per OPS molecule, was synthesized from OPS. According to the stoichiometric amount of bromine in the system, the expected x value of Br_xOPS is 9.0 if all the bromines charged are reacted onto the phenyl rings. The real bromine content is measured through ^1H NMR spectrum using tetrahydrofuran (THF) as an internal standard. As shown in Figure 1, the THF protons of $-CH_2-$ and $-O-CH_2-$ appear at 1.73 and 3.59 ppm, respectively, whereas the chemical shift at 7.2−8.1 ppm are attributed to phenyl protons (Ar−H). Accordingly, the average number of hydrogen atom of Ar−H replaced with bromine, i.e., the real x value, can be calculated from the relative peak area of Ar−H and THF−H as well as the amount of THF and Br_xOPS precisely added in the NMR-tube in term to the eq 1:

$$\frac{w(40-x)}{1034+79.9x}\times\frac{72.1}{0.889v\times 4}=\frac{A_{\mathrm{BrOPS}}}{A_{\mathrm{THF}}} \qquad (1)$$

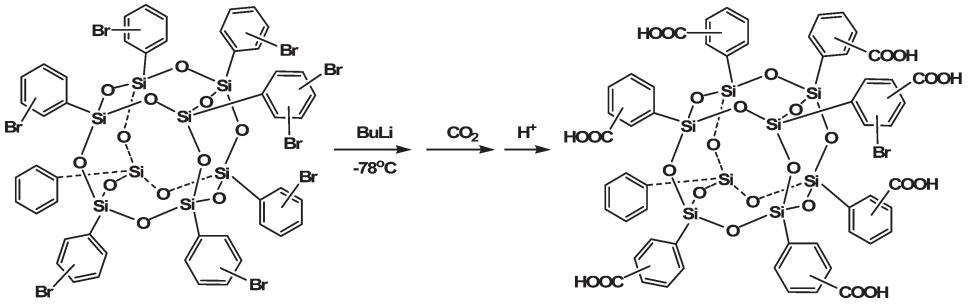
where w and v are the weight of Br_xOPS and volume of THF added, A_{BrOPS} and A_{THF} the integrated peak area of Ar−H and THF−H, respectively, whereas 1034 and 72.1 are molecular weight of OPS and THF, respectively. 79.9, 0.889, and 4 are atomic weight of bromine, density of THF and the proton number in each THF molecule, respectively.

As a result, the x value measured for the polybromo-OPS is 8.5. In order to determine the position of bromine in benzene ring, the Si−phenyl bonds were cleaved from $Br_{8.5}OPS$ by KF/H_2O_2 to produce various phenol compounds, which were collected and afforded for LC−MS analysis. On average, 58% of phenyls are monosubstituted, 24% of phenyls disubstituted, a very small amount of phenyls trisubstituted, and 17% of phenyls unsubsituted (Table 1S, Supporting Information).

Synthesis of Polycarboxyl-OPS ($COOH_yOPS$). Polycarboxyl-OPS was synthesized in two-steps: lithiation of the polybromo-OPS and subsequent carboxylation with carbon dioxide give $COOH_xOPS$ (Scheme 1).

As shown in Figure 2a, the wide peak at 3700−2800 cm^{-1} is attributed to OH stretching of the carboxyl group, whereas the sharp peak at 1699 cm^{-1} is due to the C=O absorption of hydrogen-bonded carboxyl group. A strong absorption at 1587 cm^{-1} is assigned to the benzene ring. In addition, the bands at 1134, 1108, and 491 cm^{-1} belong to the characteristic Si−O−Si vibrations of silsesquioxane cage skeleton.

Scheme 1. Synthesis Route of Polycarboxyl-OPS



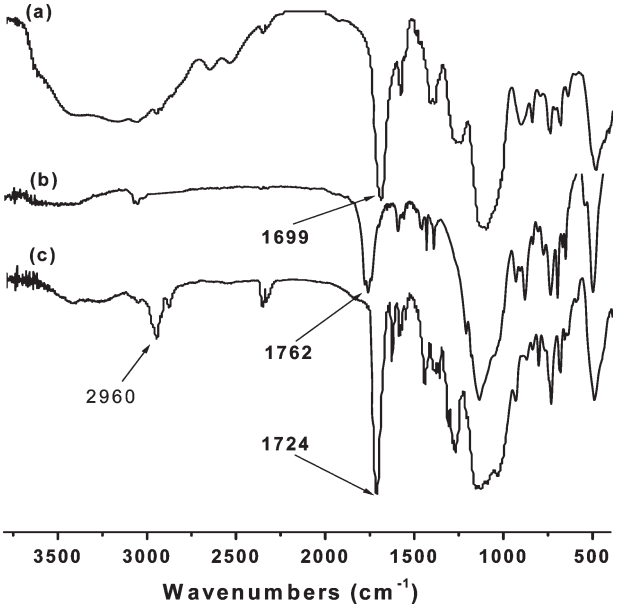


Figure 2. FTIR spectra of (a) $COOH_{6.5}OPS$, (b) $COCl_{6.5}OPS$, and (c) $MMA_{6.5}OPS$.

Similar to polybromo-OPS, $COOH_yOPS$ is also cleaved by KF/H_2O_2, and LC−MS technology is then utilized to analyze the composition of generated organic fragments. The data in Table 2S (Supporting Information) reveal that almost all the monosubstituted phenyls have been converted to carboxyl groups. However, for the di- or tribromo-substituted phenyls, only one bromine atom can be successfully carboxylated. The reason is that, similar to other polybromo-aromatic compounds,[45,46] after one bromine has been reacted with BuLi to form lithium compound, the reactivities of other bromines on the same phenyl are greatly inhibited due to the electropositive effect of lithium-cation so that the further lithiation reaction can not easily take place with BuLi at −78 °C.

NOE-suppressed ^{13}C NMR spectrum of $COOH_yOPS$ is illustrated in Figure 4S (Supporting Information), from which the average number of carboxyl groups in each OPS molecule (y) can be calculated from the integrated areas of corresponding peaks. As is shown, the peaks at 125−150 ppm are assigned to the aromatic carbon atoms, while the characteristic signals of carboxyl C═O are found at 170−180 ppm. Thus, the y value is calculated according to eq 2, and the result is 6.5.

$$y = \frac{48 \times A_1}{A_2} \quad (2)$$

where A_1 and A_2 are the integrated areas of carboxyl carbons and aryl carbons, respectively, and 48 is the whole aryl carbon number included in each OPS molecule.

Synthesis of Polymethacrylate-OPS ($MMA_{6.5}OPS$). The synthesis route of $MMA_{6.5}OPS$ is presented in Scheme 2. At first, the carboxyls in $COOH_{6.5}OPS$ are converted to chlorocarbonyl groups through the reaction with thionyl chloride to yield polychlorocarbonyl-OPS ($COCl_{6.5}OPS$). As shown in Figure 2b, the absorption peak at 1699 cm^{-1} corresponding to C═O stretching vibration of carboxyl group is absent in the spectrum of $COCl_{6.5}OPS$, whereas a new peak at 1762 cm^{-1} attributed to C═O stretching vibration of chlorocarbonyl group appears, indicating that carboxyls of $COOH_{6.5}OPS$ have been smoothly converted to chlorocarbonyl groups. Subsequently, using pyridine as the catalyst, the reaction of polychlorocarbonyl-OPS with 2-hydroxyethylmethacrylate leads to polymethacrylate-OPS macromonomer ($MMA_{6.5}OPS$).

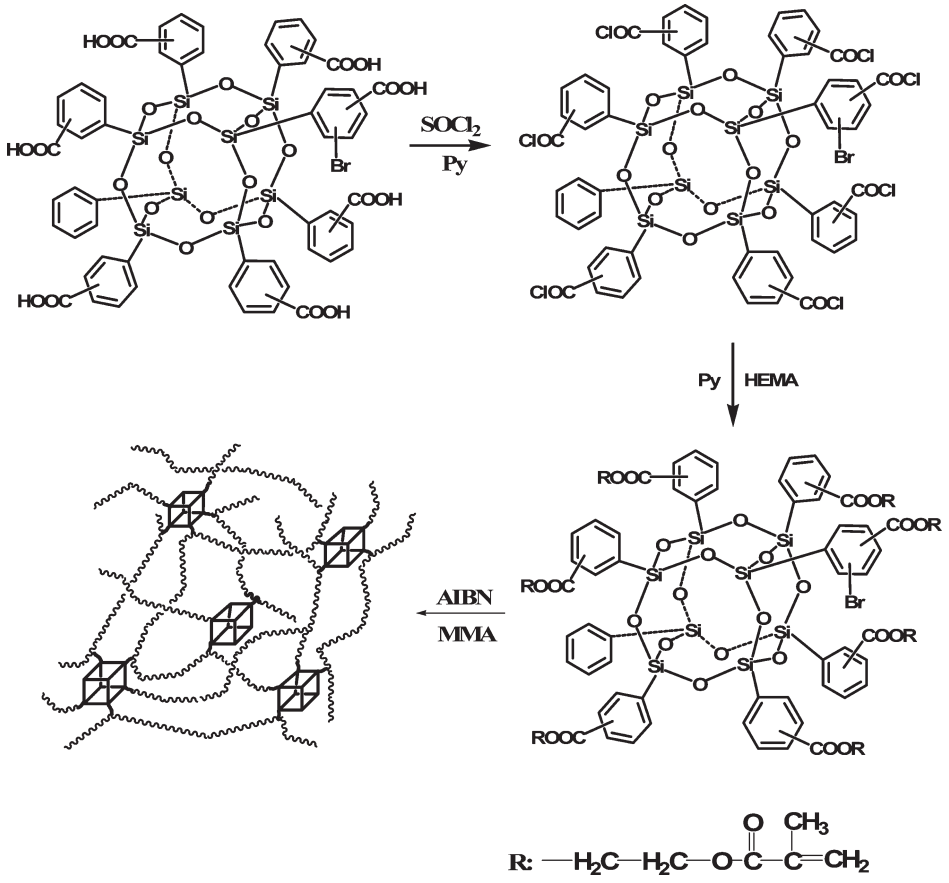
Figure 2c shows the FTIR spectrum of $MMA_{6.5}OPS$. The peaks at 2960 cm^{-1} are assigned to CH_3 and $-CH_2-CH_2-$ stretching vibrations, respectively. A peak at 1637 cm^{-1} is attributed to the C═C stretching of methacrylate group. The appearance of characteristic ester ν C═O at 1724 cm^{-1} and complete disappearance of chlorocarbonyl group at 1762 cm^{-1} suggest the successful synthesis of $MMA_{6.5}OPS$.

$MMA_{6.5}OPS$ is further identified by ^1H NMR method (Figure 3). The peaks at 7.32−7.91 ppm belong to the aromatic protons. The peaks at 3.62 and 4.09 ppm are assigned to the aliphatic $-O-CH_2-CH_2-O-$ protons, the two singlets at 5.65 and 6.05 ppm are attributed to the $C{=}CH_2$ protons, whereas the strong single peak at 1.88 ppm corresponds to the CH_3 of methacrylate group. From the integrated areas of protons from aromatic benzene ring and CH_3 of methacrylate group, on average, the calculated number of methacrylate group in each OPS molecule is 6.36, very close to the expected value of 6.5.

Synthesis and Characterization of OPS/MMA Copolymers. OPS/MMA copolymers were synthesized via bulk free radical polymerization with the $MMA_{6.5}OPS$ content in the nanocomposites of 0.24, 0.47, 0.94, and 1.18 mol %, respectively. The possible PMMA homopolymer and unreacted polymethacrylate-OPS had been removed by extraction with acetone. It is worth noting that after the extracts were concentrated, no any solid can be found, indicating that the formations of three-dimensional networks via cross-linking reactions between $MMA_{6.5}OPS$ and MMA are rapid and effective because of the multiple active methacrylate groups in OPS macromonomer.

Figure 4 shows the FTIR spectra of pure PMMA and OPS/PMMA nanocomposites. In the FTIR spectrum of PMMA, the absorptions at 2996−2850 cm^{-1} are associated to the methyl and methylene groups, while the strong peak at

Scheme 2. Synthesis Routes of $MMA_{6.5}OPS$ and the $MMA_{6.5}OPS$/MMA Copolymer Networks



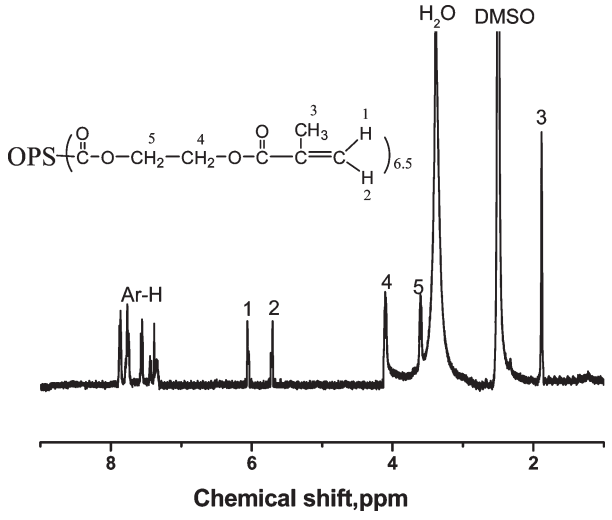


Figure 3. ^1H NMR spectrum of $MMA_{6.5}OPS$.

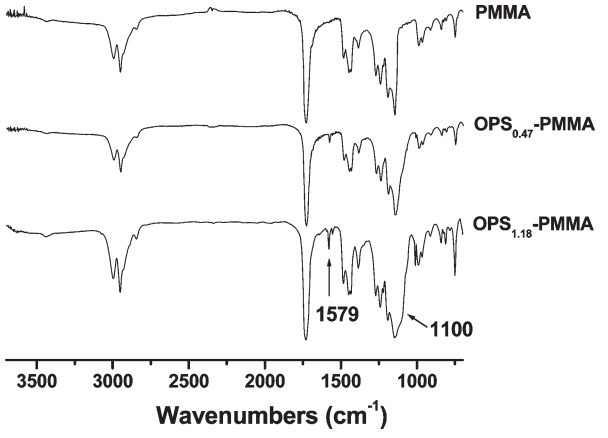


Figure 4. FTIR spectra of pure PMMA and OPS/PMMA nanocomposites.

$1732\ cm^{-1}$ corresponds to the carbonyl stretching vibration of PMMA. As a contrast, in the FTIR spectra of OPS/PMMA nanocomposites, besides the characteristic absorptions of PMMA, the peaks at 1579 and $1554\ cm^{-1}$ can be assigned to the OPS phenyls. Their intensities increase gradually with OPS content. The broadened peak from 1150 to $1100\ cm^{-1}$ is attributed to the characteristic Si−O−Si vibrations of the OPS cage. The above spectra data demonstrate that the OPS moieties are indeed incorporated covalently within PMMA matrix to form a copolymer network.

In this study, the methacrylate group is linked with OPS cage via a flexible $-O-CH_2-CH_2-O-$ spacer. The sufficient freedom offers the dangling methacrylate groups high radical polymerization reactivity. It is observed that the incorporation of only 0.24 mol % $MMA_{6.5}OPS$ gives a cross-linked copolymer that was only slightly swollen on heating in THF and $HCCl_3$, in which $MMA_{6.5}OPS$ and PMMA can dissolve. When the OPS content reaches 0.96 mol %, the product can not swell in the above solvents at all, suggesting that $MMA_{6.5}OPS$ acts as an effective cross-linker to form three-dimensional OPS/PMMA network. This phenomenon is much different from the previous report for polyvinyl-OPS/PMMA copolymer system, in which the

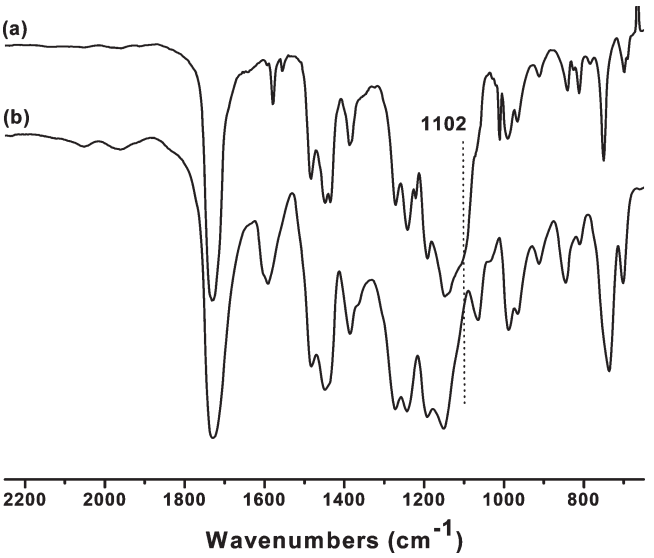


Figure 5. FT-IR spectra of $OPS_{1.18}$-PMMA nanocomposite: (a) untreated; (b) cleaved by KF/H_2O_2.

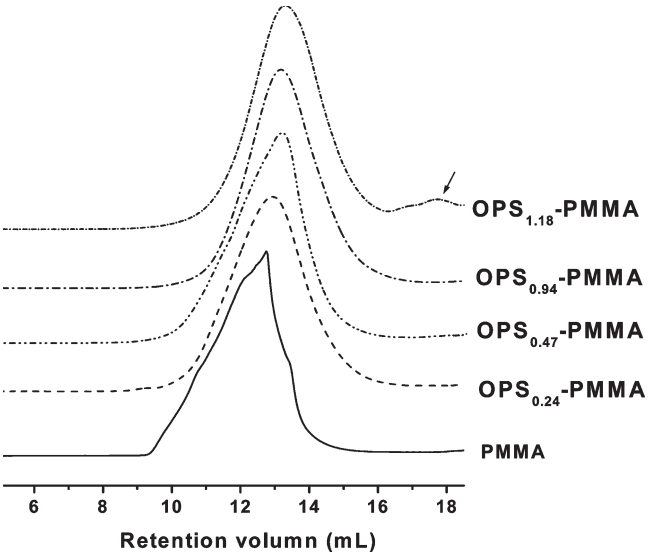


Figure 6. GPC traces of the cleaved products of OPS/PMMA nanocomposites by KF/H_2O_2.

Table 1. GPC Results of OPS/PMMA Nanocomposites Cleaved by KF/H_2O_2

samples	M_n ($\times 10^4$ g/mol)	M_w ($\times 10^4$ g/mol)	M_w/M_n
PMMA	7.52	14.9	1.99
$OPS_{0.24}$-PMMA	4.31	16.1	3.74
$OPS_{0.47}$-PMMA	2.67	7.68	2.88
$OPS_{0.94}$-PMMA	2.43	8.09	3.33
$OPS_{1.18}$-PMMA	2.23	7.89	3.54

vinyl groups are tightly tethered onto the bulky OPS core. Probably, the steric hindrance and restricted motility leads to vinyl group much decreased reactivity so that the polyvinyl-OPS/PMMA only creates branched rather than cross-linked copolymer network even at high contents of octavinyl-POSS over 3 mol %.[21]

In an effort to obtain the structural information about the OPS/PMMA nanocomposites, the finely ground powders were successively treated with KF/H_2O_2 in THF for 72 h to cleave Si−C bonds in OPS core. After removal of insoluble precipitate (SiO_2), the filtrate was poured into a mixed solution of ethanol and water and the white PMMA product is collected. The FTIR spectra demonstrate that the previous Si−O−Si bands at around 1102 cm^{-1} have completely disappeared (Figure 5). In addition, thus obtained PMMA samples were examined by GPC method in order to reveal the growth mechanism of PMMA chains in the $MMA_{6.5}$OPS/MMA polymerization system. As a comparison, the pure PMMA synthesized under the same polymerization conditions has a number average molecular weight (M_n) of 7.52×10^4 g/mol. Apparently, the incorporation of OPS leads to much reduced M_n of PMMA. For example, the M_n value of sample with $MMA_{6.5}$OPS content of 0.94 mol % is only 2.43×10^4 g/mol (Table 1). The high reactivity of attached methacrylate group on OPS makes it be easily initiated by a radical initiator or PMMA chain radical, and the newly generated OPS radical can initiate the polymerization of other MMA monomers. Repeating the above procedure leads to a PMMA cross-linking network. In this way, within this network, a number of OPS moieties can be linked onto one PMMA chain. Because $MMA_{6.5}$OPS is bulky polyfunctional macromonomer, in the initial polymerization stage, the copolymerization of $MMA_{6.5}$OPS with MMA should form branched polymer. The chain entanglement, viscosity increase and bulky OPS volume hinder the propagation ability of the PMMA chains to some extent. As a result, compared to pure PMMA, the PMMA chains in the nanocomposite network exhibit significantly lower molecular weight, and which values are found to continually decrease with the increased OPS content.

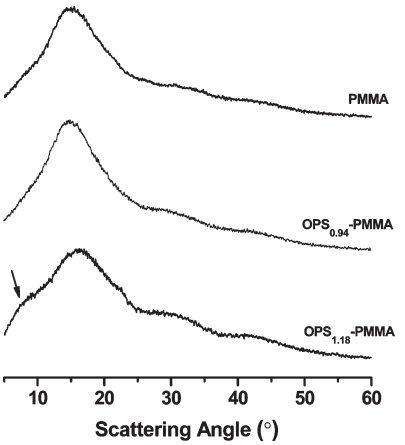


Figure 7. WAXD patterns of pure PMMA, $OPS_{0.94}$-PMMA, and $OPS_{1.18}$-PMMA nanocomposite.

On the other hand, Figure 6 shows that, for the copolymers with low $MMA_{6.5}$OPS contents, the GPC curves present only a single peak, implying that the chain propagation can proceed smoothly to form uniform PMMA network. However, when $MMA_{6.5}$OPS content is over 1.18 mol %, a weak peak corresponding to a short PMMA chain with M_n of 2054 g/mol appears because, in this case, the higher radical concentration in the system makes the viscosity rapidly increase even at the initial polymerization reaction stage, resulting into an increased termination probability of two short PMMA chain radicals.

The WAXD Study of OPS/MMA Nanocomposites. The WAXD diffractograms for PMMA and the PMMA/OPS nanocomposites are illustrated in Figure 7. PMMA obtained through radical polymerization is amorphous and displays a broad peak with 2θ angle at about 14°. The comparison of the diffraction patterns reveals that, for $OPS_{0.94}$-PMMA, its

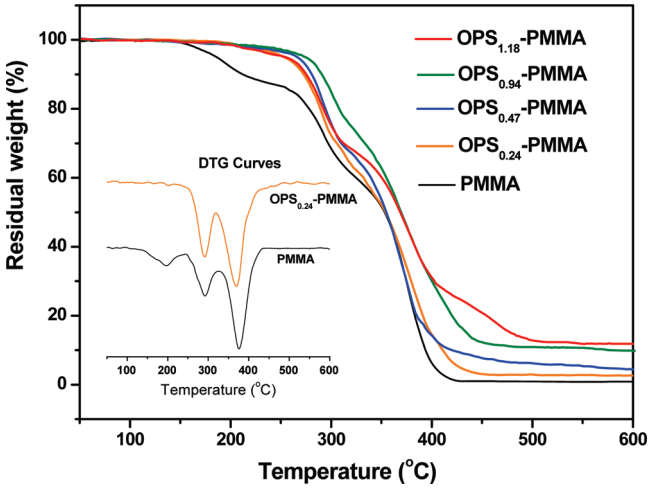


Figure 8. TGA and DTG curves of OPS/PMMA nanocomposites with various OPS content.

Table 2. Thermal Analysis Results of PMMA and OPS/PMMA Nanocomposites

samples	T_g (°C)	$T_{5\%}$ (°C)	$T_{step\text{-}1}$ (°C)	$T_{step\text{-}2}$ (°C)	$T_{step\text{-}3}$ (°C)	RW (wt %)
PMMA	114	183	191	293	367	0.7
$OPS_{0.24}$-PMMA	125	270		296	370	2.0
$OPS_{0.47}$-PMMA	133	271		302	372	4.3
$OPS_{0.94}$-PMMA	135	287		310	372	9.8
$OPS_{1.18}$-PMMA	115	275		304	378	10.3

curve shape is almost the same as that of PMMA, and no any hint of OPS can be observed, implying that OPS moieties are not only covalently cross-linked with PMMA chains but also homogeneously dispersed at the molecular level within the PMMA matrix, which is consistent well with the good transparency of PMMA/OPS nanocomposite samples at low OPS content. However, with the further increase of OPS content, e.g., for $OPS_{1.18}$-PMMA containing 1.18 mol % OPS, it becomes translucent, with some milky and hazy substance throughout the sample. Moreover, a weak peak with 2θ angle at about 8° appears in the curve, which can be assigned to the octaphenylsilsesquioxane core (1−1.1 nm),[47−49] indicating that the aggregation of OPS compound and microphase separation have occurred to some extent.

Thermal Properties of $MMA_{6.5}$OPS/PMMA Nanocomposites. The thermal stabilities of pure PMMA and various PMMA/OPS nanocomposites are compared and studied by TGA under nitrogen at a heating rate of 20 °C/min. Their thermogravimetric and DTG curves are presented in Figure 8 and the data are summarized in Table 2. The pure PMMA exhibits typical three thermal steps of degradation. The first stage at around 191 °C is associated with the cleavage of tertiary ester bond derived from coupling termination. The second one at 293 °C is attributed to the unsaturated vinyl ends caused by the disproportionation termination, and the third one at 367 °C is due to the random scission of main chains, respectively, which behavior is similar to the previously reported results except that the three decomposition steps occur respectively at the increased temperatures since the pure PMMA synthesized in this study has much higher molecular weight than that in the literature.[50,51] Of interest is the observation that, for all the OPS/PMMA nanocomposites, only two thermal decomposition steps appear in the degradation curves. Compared to the pure PMMA, the increase of 5% mass-loss temperature by 87 °C is achieved with only incorporation of 0.24 mol % OPS in the nanocomposite. As a matter of fact, the radical copolymerization of MMA and $MMA_{6.5}$OPS also undergo termination reaction of coupling and disproportionation. However, the high reactivity of polymethacrylate-OPS and its good miscibility with MMA make that the OPS are easily linked with PMMA chain through strong covalent bond and disperse uniformly in the cross-linked network. The low thermal conductivity of OPS because of its inorganic ceramic nature and intrinsic nanoporous structure can hinder the thermal transfer across the sample and effectively retard the degradation of weak bonds which are embedded within the network, leading to the composite materials greatly enhanced thermal stability. Moreover, the samples with high OPS content display obviously increased char yield. However, the increasing trend for the thermal decomposition temperature can not always continue. Relative to $OPS_{0.94}$-PMMA, the $OPS_{1.18}$-PMMA sample exhibits a decreased 5% mass-loss temperature by 12 °C. Just as indicated by the GPC results, relative to the nanocomposites with low OPS content, in the sample of $OPS_{1.18}$-PMMA, there are more number of short PMMA chains and thermally labile groups, such as the tertiary esters derived from coupling termination and the unsaturated vinyl end groups caused by the disproportionation termination, resulting into its decreased thermal stability.

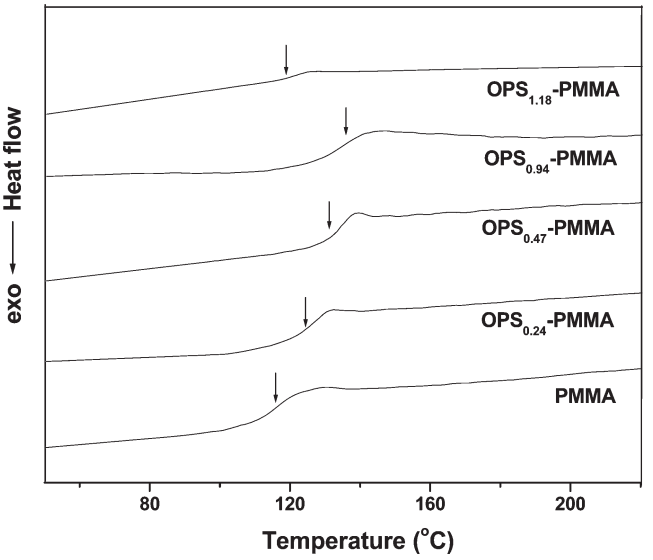


Figure 9. DSC curves of OPS/PMMA nanocomposites with various OPS content.

The previous studies show that the T_g variation of cross-linked PMMA is tightly related to the cross-linker employed. The cross-linking reaction caused by the flexible diol dimethacrylate cross-linker usually can not bring about significant T_g improvement, in some cases, even result in an obvious reduction in T_g. For example, the T_g value of PMMA network derived from the copolymerization between MMA and poly(ethylene glycol) dimethacrylate is only 66.8 °C.[52] On the contrary, the incorporation of rigid bridge between PMMA chains can effectively increase the T_g of PMMA network, depending on the content of cross-linker used in the system.[38,53,54] It was reported that the PMMA film thermally cured via epoxy group had an increased T_g value at 125 °C with 10 mol % cross-linkable component in the network.[53]

The glass transition temperatures (T_g) for the pure PMMA and OPS-modified PMMAs were measured and are presented in Figure 9. As is shown, the T_g values for the modified

PMMAs are obviously shifted from 114 °C of pure PMMA toward higher temperature. Relative to the pure PMMA, the T_g values for composites with OPS content of 0.24, 0.47, and 0.94 mol % increase by 11, 19, and 21 °C, respectively. At lower $MMA_{6.5}OPS$ content, the copolymerizations of $MMA_{6.5}OPS$ and MMA make the reactive methacrylate groups act as multiple claws to anchor PMMA chains onto the rigid OPS core, and thus formed network will restrict the mobility of PMMA segment and significantly increase the glass transition temperatures. For $OPS_{0.47}$-PMMA which incorporates OPS of only 0.47 mol %, its T_g value increases from 114 to 133 °C, exhibiting advantage over the other common cross-linkers reported in the literatures. Nevertheless, the T_g values do not monotonically increase with increased $MMA_{6.5}OPS$ content. It is found that the $OPS_{1.18}$-PMMA sample exhibits an obviously decreased glass transition temperature relative the other three samples. Similar phenomena have also been observed for other POSS/polymer nanocomposite systems, such as POSS−PEG−PMMA,[30] poly(vinyl cinnamate)-POSS,[37] epoxy-POSS,[55] poly(hydroxystyrene-*co*-vinylpyrolidone)-POSS hybrids,[56] which are explained as the increased free volume and chain separation because of bulkiness of POSS group although the real reason still remains a matter of debate.

In our study, the factors, that bulky OPS group opens up the polymer chains and the increased free volume are favorable for the segment motion, can also account for the reduced glass transition temperature of $OPS_{1.18}$-PMMA sample. In addition, the reason arisen from the copolymerization mechanism should be taken into account. The incorporation of high content of polyfunctional OPS cross-linker gives rise to the increased viscosity and rapid gel-formation, leading to the generation of more number of short PMMA chains and a relatively insufficient PMMA cross-linked network. As a result, compared to the OPS/PMMA nanocomposites with lower OPS contents, the glass transition of $OPS_{1.18}$-PMMA sample shifts toward the apparently lower temperature, and the transition range becomes broad.

Conclusions

In this paper, at first, polycarboxyl octaphenylsilsesquioxane with average carboxyl number of 6.5 ($COOH_{6.5}OPS$) was successfully synthesized by two-step reaction: bromination yields polybromo-OPS and subsequent carboxylation leads to the target product. Then, the $COOH_{6.5}OPS$ was further converted to $COCl_{6.5}OPS$ and $MMA_{6.5}OPS$. Their chemical structures were characterized by FTIR, NMR, LC−MS and GPC methods. The polymethacrylate-OPS macromonomers are miscible with methyl methacrylate (MMA), and the mixtures are readily copolymerized to obtain a series of OPS/PMMA copolymers with various OPS content. Thus synthesized nanocomposites are insoluble in any common solvents, demonstrating the formation of cross-linked networks. After being treated in KF/H_2O_2 agent, the PMMA chains were cleaved from the OPS core. For the copolymer systems with low $MMA_{6.5}OPS$ contents, the GPC curves of PMMA chains present only a single peak, implying that the $MMA_{6.5}OPS$ is miscible with MMA, and the chain propagation proceeds smoothly to form uniform PMMA networks, which are well consistent with the WAXD results. The TGA and DSC results reveal that, compared to pure PMMA, after incorporation of very few amount of OPS in PMMA matrix, e.g., 0.94 mol %, the composite exhibits greatly enhanced initial thermal decomposition temperature by 104 °C and apparently increased glass transition temperature by about 21 °C. The study of using polychlorocarbonyl-OPS to form cross-linked polyamides, polycarboxyl-OPS as macromonomer for micro/mesoporous polybenzoxazoles or as curing agent for cross-linked epoxy networks are being undertaken and will be reported subsequently.

Acknowledgment. We thank the National Science Foundation of China (Nos. 50673014 and 20874007) and the Program for New Century Excellent Talents in University of China (No. NCET-06-0280) for financial support of this research.

Supporting Information Available: GPC trace of polybromo-OPS, ^1H NMR spectra of polycarboxyl-OPS, NOE-suppressed ^{13}C NMR spectrum of polycarboxyl-OPS, LC spectra of cleaved products of polybromo-OPS and polycarboxyl-OPS, and their data. This material is available free of charge via the Internet at http://pubs.acs.org.

References and Notes

(1) Tuteja, A.; Choi, W.; Ma, M. L.; Mabry, J. M.; Mazzella, S. A.; Rutledge, G. C.; McKinley, G. H.; Cohen, R. E. *Science* **2007**, *318*, 1615–1622.
(2) Zhang, W. A; Muller, A. H. E. *Macromolecules* **2010**, *43*, 3148–3152.
(3) Escude, N. C.; Chen, E. Y. X. *Chem. Mater.* **2009**, *21*, 5743–5753.
(4) Sulaiman, S.; Bhaskar, A.; Zhang, J.; Guda, R.; Goodson, T., III; Laine, R. M. *Chem. Mater.* **2008**, *20*, 5563–5573.
(5) Cordes, D. B.; Lickiss, P. D.; Rataboul, F. *Chem. Rev.* **2010**, *110*, 2081–2173.
(6) Chen, Q.; Xu, R. W.; Zhang, J.; Yu, D. S. *Macromol. Rapid Commun.* **2005**, *26*, 1878–1882.
(7) Xiao, S.; Nguyen, M.; Gong, X.; Cao, Y.; Wu, H.; Moses, D.; Heeger, A. J. *Adv. Funct . Mater.* **2003**, *13*, 25–29.
(8) Crivello, J. V.; Malik, R. *J. Polym Sci., Part A: Polym. Chem.* **1997**, *35*, 407–425.
(9) Choi, J.; Yee, A. F.; Laine, R. M. *Macromolecules* **2003**, *36*, 5666–5682.
(10) Kickelbick, G. *Prog. Polym. Sci.* **2003**, *28*, 83–114.
(11) Pielichowski, K.; Njuguna, J.; Janowski, B.; Pielichowski, J. *Adv. Polym. Sci.* **2006**, *201*, 225–296.
(12) Phillips, S. H.; Haddad, T. S.; Tomczak, S. J. *Curr. Opin. Solid State Mater. Sci.* **2004**, *8*, 21–29.
(13) Madbouly, S. A.; Otaigbe, J. U. *Prog. Polym. Sci.* **2009**, *34*, 1283–1332.
(14) Brus, J.; Urbanova, M.; Strachota, A. *Macromolecules* **2008**, *41*, 372–386.
(15) Lee, A.; Lichtenhan, J. D. *Macromolecules* **1998**, *31*, 4970–4974.
(16) Mather, P. T.; Jeon, H. G.; Romo, A.; Haddad, T. S.; Lichtenhan, J. D. *Macromolecules* **1999**, *32*, 1194–1203.
(17) Lichtenhan, J. D.; Otonari, Y. A.; Carr, M. J. *Macromolecules* **1995**, *28*, 8435–8437.
(18) Schiavo, S. L.; Mineo, P.; Cardiano, P.; Piraino, P. *Eur. Polym. J.* **2007**, *43*, 4898–4904.
(19) Shockey, E. G.; Bolf, A. G.; Jones, P. F.; Schwab, J. J.; Chaffee, K. P.; Haddad, T. S.; Lichtenhan, J. D. *Appl. Organomet. Chem.* **1999**, *13*, 311–327.
(20) Leu, C. M.; Chang, Y. T.; Wei, K. H. *Macromolecules* **2003**, *36*, 9122–9127.
(21) Xu, H. Y.; Yang, B. H.; Wang, J. F.; Guang, S. Y.; Li, C. *J. Polym Sci., Part A: Polym. Chem.* **2007**, *45*, 5308–5317.
(22) Sellinger, A.; Laine, R. M. *Macromolecules* **1996**, *29*, 2327–2330.
(23) Lichtenhan, J. D.; Otonari, Y. A.; Carr, M. J. *Macromolecules* **1995**, *28*, 8435–8437.
(24) Tsuchida, A.; Bolln, C.; Sernetz, F. G.; Frey, H.; Mulhaupt, R. *Macromolecules* **1997**, *30*, 2818–2824.
(25) Haddad, T. S.; Lichtenhan, J. D. *Macromolecules* **1996**, *29*, 7302–7304.
(26) Lee, A.; Lichtenhan, J. D. *Macromolecules* **1998**, *31*, 4970–4974.
(27) Lee, A.; Lichtenhan, J. D.; Reinerth, W. A. *Polym. Mater. Sci. Eng.* **2000**, *82*, 235–241.
(28) Liu, Y. L.; Lee, H. C. *J. Polym Sci., Part A: Polym. Chem.* **2006**, *44*, 4632–4623.
(29) Baldi, F.; Bignotti, F.; Ricco, L.; Monticelli, O.; Ricco, T. *J. Appl. Polym. Sci.* **2006**, *100*, 3409–3414.
(30) Markovic, E.; Clarke, S.; Matisons, J.; Simon, G. *Macromolecules* **2008**, *41*, 1685–1692.

(31) Zhang, C.; Laine, R. M. *J. Am. Chem. Soc.* **2000**, *122*, 6979–6988.
(32) Brick, C. M.; Tamaki, R.; Kim, S. G.; Asuncion, M. Z.; Roll, M.; Nemoto, T.; Ouchi, Y.; Chujo, Y.; Laine, R. M. *Macromolecules* **2005**, *38*, 4655–4660.
(33) Tamaki, R.; Tanaka, Y.; Asuncion, M. Z.; Choi, J.; Laine, R. M. *J. Am. Chem. Soc.* **2001**, *123*, 12416–12417.
(34) Kim, S. G.; Choi, J.; Tamaki, R.; Laine, R. M. *Polymer* **2005**, *46*, 4514–4524.
(35) Choi, J.; Kim, S. G.; Laine, R. M. *Macromolecules* **2004**, *37*, 99–109.
(36) Won, J.; Tamaki, R.; Kim, S. G.; Laine, R. M. *Chem. Mater.* **2003**, *15*, 3365–3375.
(37) Ni, Y.; Zheng, S. *Chem. Mater.* **2004**, *16*, 5141–5148.
(38) Jantas, R.; Szocik, H.; Stawski, D. *Polym. Bull.* **2005**, *53*, 277–284.
(39) Okaya, O.; Naghash, H. J.; Capaek, I. *Polymer* **1995**, *36*, 2413–2419.
(40) Kelch, S.; Choi, N. Y.; Wang, Z. G.; Lendlein, A. *Adv. Eng. Mater.* **2008**, *10*, 494–502.
(41) Allen, P. E. M.; Bennet, D. J.; Williams, D. R. G. *Eur. Polym. J.* **1992**, *28*, 347–353.
(42) Toepfer, O.; Neumann, D.; Choudhury, N. R.; Whittaker, A.; Matisons, J. *Chem. Mater.* **2005**, *17*, 1027–1035.
(43) Soh, M. S.; Yap, A. U. J.; Sellinger, A. *Eur. Polym. J.* **2007**, *43*, 315–327.
(44) Brown, J. F.; Vogt, L. H.; Prescott, P. I. *J. Am. Chem. Soc.* **1964**, *86*, 1120–1125.
(45) Fournier, J. H.; Wang, X.; Wuest, J. *Can. J. Chem.* **2003**, *81*, 376–379.
(46) Zhang, B. F.; Wang, Z. G. *Chem. Commun.* **2009**, *33*, 5027–5029.
(47) Kopesky, E. T.; Haddad, T. S.; McKinley, G. H.; Cohen, R. E. *Polymer* **2005**, *46*, 4743–4752.
(48) Tamaki, R.; Choi, J.; Laine, R. M. *Chem. Mater.* **2003**, *15*, 793–797.
(49) Choi, J.; Tamaki, R.; Kim, S. G.; Laine, R. M. *Chem. Mater.* **2003**, *15*, 3365–3375.
(50) Kashiwagi, T.; Inaba, A.; Brown, J. E.; Hatada, K.; Kitayama, T.; Masuda, E. *Macromolecules* **1986**, *19*, 2160–2168.
(51) Peterson, J. D.; Vyazovkin, S.; Wight, A. *J. Phys. Chem. B* **1999**, *103*, 8087–8092.
(52) Smith, K. E.; Temenoff, J. S.; Gall, K. *J. Appl. Polym. Sci.* **2009**, *114*, 2711–2722.
(53) Fei, X.; Fu, N.; Wang, Y.; Hu, J.; Cui, Z.; Zhang, D.; Ma, C.; Liu, S.; Yang, B. *Chem. J. Chinese Univ.* **2006**, *27*, 571–574.
(54) Wu, S.; Jorgensen, J. D.; Soucek, M. D. *Polymer* **2000**, *41*, 81–92.
(55) Liu, H. Z.; Zheng, S. X.; Nie, K. M. *Macromolecules* **2005**, *38*, 5088–5097.
(56) Xu, H. Y.; Kuo, S. W.; Lee, J. S.; Chang, F. C. *Polymer* **2002**, *43*, 5117–5124.

Macromolecules
ARTICLE

Macromolecules **2011**, *44*, 575–582 **575**
DOI: 10.1021/ma1016314

Perforated Lamellae Morphology in Novel P2VP(PDMS-*b*-PI-*b*-PS)$_2$ 3-Miktoarm Star Quarterpolymer

Jacob Judas Kain Kirkensgaard,*,† Panagiota Fragouli,‡ Nikos Hadjichristidis,‡ and Kell Mortensen†

†*Department of Basic Sciences and Environment, Faculty of Life Sciences, University of Copenhagen, Copenhagen, Denmark, and* ‡*Department of Chemistry, University of Athens, Panepistimiopolis-Zografou, Athens, Greece*

Received August 29, 2010; Revised Manuscript Received November 22, 2010

ABSTRACT: The melt morphology of a novel P2VP(PDMS-*b*-PI-*b*-PS)$_2$ 3-miktoarm star quarterpolymer is investigated. The melt morphology is determined using rheology and small-angle neutron and X-ray scattering data in conjunction with dissipative particle dynamics simulations of a model molecule matching the volume fractions of the experimental system. The simulations are used to interpret the scattering data and identify the melt morphology as a new perforated lamellae structure. In this structure the P2VP forms hexagonally perforated lamellae containing close-packed protrusions of PS connecting adjacent lamellae layers of PS. The PI part forms a lining between the P2VP and PS domains constrained by the molecular architecture.

Introduction

The study of molecular self-assembly remains a topic of great attention in material science as well as in biology and biotechnology. Special interests concern self-assembly properties of the variety of novel complex block copolymer architectures that modern chemistry allows, ABC 3-miktoarm star terpolymers being one example. Here three different polymer chains are attached to a common junction,[1,2] and the constraints imposed by the molecular star architecture have already been shown to induce a range of interesting morphologies and properties, among these various cylindrical structures whose cross-sectional organization follow Archimedean tiling patterns[3−13] or even show quasi-crystalline features.[14,15] Further, it has recently been speculated that these new block copolymer architectures will lead to other novel ordered structures with attractive characteristics, for example, being cholesteric,[16] forming complex network phases,[17] or resulting in various hierarchically structured morphologies.[18]

In this study we investigate a new miktoarm block copolymer, the 3-armed star quarterpolymer P2VP(PDMS-*b*-PI-*b*-PS)$_2$ illustrated schematically in Figure 1. Here the complexity of the 3-miktoarm star topology is raised even further as two arms consist of equivalent (PDMS-*b*-PI-*b*-PS)-triblocks and the third arm of a single P2VP polymer species. We investigate the melt morphology of this miktoarm star using combined dissipative particle dynamics simulations (DPD) and experimental structural analysis using simultaneous small-angle neutron scattering and rheology (rheo-SANS) as well as small-angle X-ray scattering (SAXS).

DPD is a mesoscopic simulation technique where a "particle" represents a small volume of fluid which interacts with other particles through a soft potential. In its most common implementation[19] the DPD method has become a standard tool in soft matter research and has been applied successfully to a number of polymeric systems with varying structural complexity.[20−25]

*Corresponding author. E-mail: kirkensgaard@life.ku.dk.

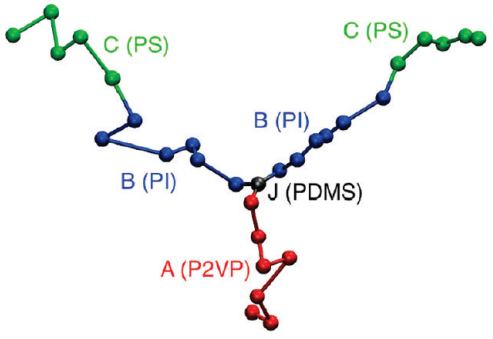


Figure 1. Rendering of the model 3-miktoarm star molecule as represented in the DPD simulations. The volume fractions of the different blocks are reflected in the relative arm lengths set to 1:5:6:7 for PDMS (gray junction J), PS (green C), PI (blue B), and P2VP (red A), respectively (see Table 2).

The experimental determination of the melt morphology is done using small-angle neutron scattering (SANS) and *in situ* rheology with a modified rheometer allowing simultaneous determination of structural and dynamic mechanical properties as well as the response to large-amplitude oscillatory shear (LAOS). As has been frequently shown, LAOS has the ability to dramatically change the texture of ordered soft matter materials and in some cases produce close to single-domain crystallographic structures (see for example refs 26 and 27). The shear-aligned samples are subsequently also investigated with SAXS.

This paper is organized as follows: First, the polymer synthesis and characteristics are described. Second, we briefly outline the model used in the simulations and describe the details of the experimental procedures. We then present the structures predicted by the DPD simulations followed by rheological and structural data where the latter is shown to be consistent with only one of two possible structures predicted by the simulations.

© 2011 American Chemical Society
Published on Web 01/04/2011

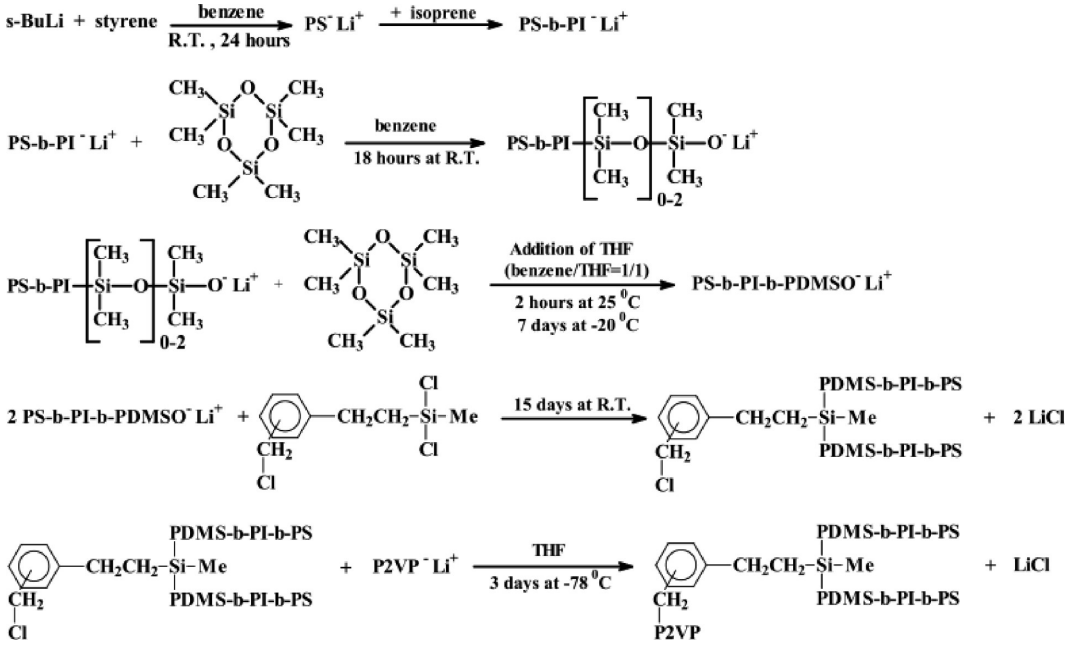


Figure 2. Synthesis of 3-miktoarm star quarterpolymer P2VP(PDMS-*b*-PI-*b*-PS)$_2$.

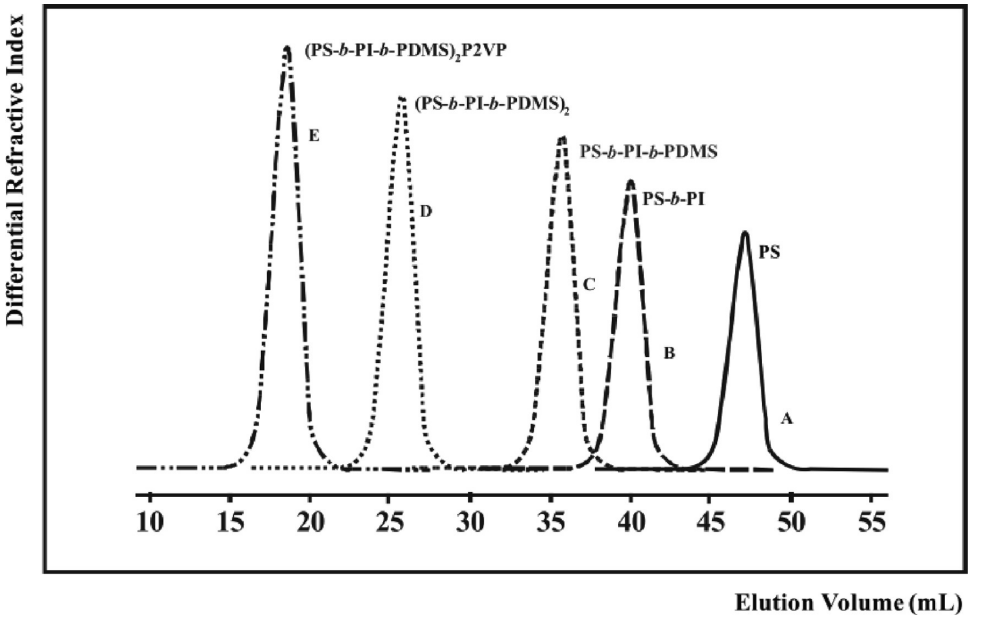


Figure 3. Monitoring the steps of the synthesis of the 3-miktoarm star quarterpolymer by size exclusion chromatography (SEC): (A) PS block, (B) PI-*b*-PS diblock, (C) PDMS-*b*-PI-*b*-PS precursor, (D) (PDMS-*b*-PI-*b*-PS)$_2$ precursor, and (E) final P2VP(PDMS-*b*-PI-*b*-PS)$_2$ star quarterpolymer.

Polymer Synthesis and Molecular Characterization

The synthesis of the 3-miktoarm star quarterpolymer P2VP-(PDMS-*b*-PI-*b*-PS)$_2$ was based, on one hand, on recent advances in the controlled high-vacuum anionic polymerization of hexamethylcyclotrisiloxane (D_3)[28] and, on the other hand, on the selective linking of PDMSOLi or PDMSOLi-terminated chains with the chlorosilane groups of the heterofunctional linking agent chloromethylphenylethenyldichloromethylsilane (CMPMDS).[29] The synthetic approach involves the replacement of the two chlorines ($SiMeCl_2$) of CMPMDS by PDMS-*b*-PI-*b*-PS triblock terpolymer chains and of the remaining chlorine (CH_2Cl) by P2VP.[30]

The basic reactions for the synthesis are given in the scheme in Figure 2, and the molecular characteristics of the precursors and final miktoarm star based on the SEC runs presented in Figure 3 are summarized in Table 1. All polymerizations were carried out in evacuated, *n*-BuLi-washed, and solvent-rinsed glass reactors, equipped with break-seals for the addition of reagents and constrictions, for the removal of intermediate products. Full details

Table 1. Molecular Characteristics of Precursors and Final 3-Miktoarm Star Quarterpolymer

polymer	M_n [kg/mol]	M_w/M_n
PS	13.6[a]	1.02[a]
PI-*b*-PS	26.8[b]	1.03[a]
PDMS-*b*-PI-*b*-PS	29.5[b]	1.04[a]
(PDMS-*b*-PI-*b*-PS)$_2$	57.8[b]	1.04[a]
P2VP(PDMS-*b*-PI-*b*-PS)$_2$	77.8[b]	1.04[a]

[a] SEC in THF at 40 °C calibrated with PS standards. [b] Membrane osmometry in toluene at 35 °C.

Table 2. Molar Mass M_n [kg/mol] of Each Polymer Component, Densities ρ [g/cm^3], Volume Fractions in the Experiments (ϕ), Ratios Relative to Volume Fraction of PDMS, and Volume Fractions in the Simulations (ϕ_{DPD})

polymer	M_n	ρ	ϕ	ϕ/ϕ_D	ϕ_{DPD}
PDMS	2.7	0.965	0.05	1.0	1
PS	13.6	0.969	0.26	5.0	5
PI	13.2	0.830	0.3	5.7	6
P2VP	20	0.97	0.39	7.4	7

regarding apparatuses and techniques used have been reported elsewhere.[31]

Simulation Model

On the basis of the molecular weights of the P2VP(PDMS-*b*-PI-*b*-PS)$_2$ 3-miktoarm quarterpolymer shown in Table 2, we set up the coarse-grained model illustrated in Figure 1 where the number of beads of each color directly reflects the volume fractions of the different blocks relative to the minority component PDMS. Although a detailed mapping of the interactions between different polymer species in principle is possible via a link with Flory−Huggins theory,[32] we will employ a purely qualitative approach and present only two scenarios that give results of relevance to the scattering data presented below. One scenario is assuming symmetric interactions between all unlike polymer components, and the other is assuming that the interaction parameter between the red A and the blue B component is higher. This reflects the fact that the interaction parameter between P2VP and PI is usually found to be higher than the other cross interaction terms which are roughly equal.[5,24,33,34] In terms of the DPD interaction parameter a_{ij}, we set this to 36 between all different species i and j in the first scenario and then raise a_{AB} to 45 in the second scenario. Other numbers have also been used yielding the same structures. For complete details of the simulations presented here we refer to ref 35 where a comprehensive simulation study of this star architecture is presented. Simulations were run using the ESPResSo package[36] within the framework developed earlier to simulate the equilibrium structure of branched molecules in general.[16]

Rheo-SANS and SAXS

SANS experiments and rheology measurements were performed using a modified Rheometrics RSA II rheometer at the SANS-II instrument at the Swiss Spallation Neutron Source (SINQ) located at the Paul Scherrer Institute, Switzerland. The setup allows simultaneous determination of dynamic mechanical and structural properties as well as structural response to LAOS. The employed neutron wavelength was 6 Å with a 9% wavelength spread. The sample−detector distance and the collimation length were both 4 m. The polymer samples were mounted in a sandwich shear cell of 0.1 mm thickness as illustrated in Figure 4 and subjected to various rheological measurements as well as LAOS.

Referring to Figure 4, we acquire two-dimensional SANS patterns in the (q_e, q_v) scattering-plane, where the indexes e refer to the neutral vorticity direction and v to the shear-velocity direction. After shear alignment the sample was quenched with liquid nitrogen to ambient temperature. The shear cell was mechanically fixed and remounted to perform crystallographic measurements using a custom-designed goniometer. The shear alignment and subsequent crystallographic measurements were performed with slight modifications on three independent sample outtakes, and the results obtained were identical within experimental error. The quenched and shear-aligned samples were saved and used for SAXS measurements done at room temperature. The SAXS measurements were done at the new SAXSLab facility at Copenhagen University employing a 1.54 Å wavelength.

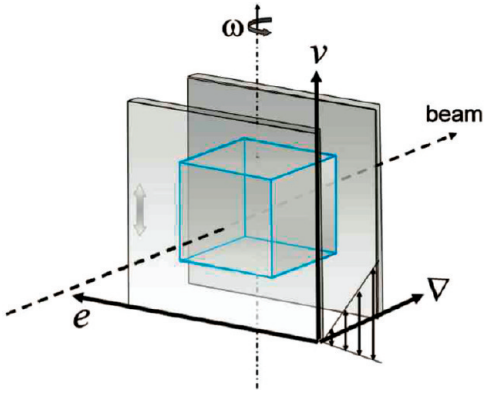


Figure 4. Schematics of the experimental *in situ* rheo-SANS setup defining the principal axes: flow direction v, gradient direction ∇, and neutral direction e. Chrystallographic measurements are done rotating angles ω around the flow axis v.

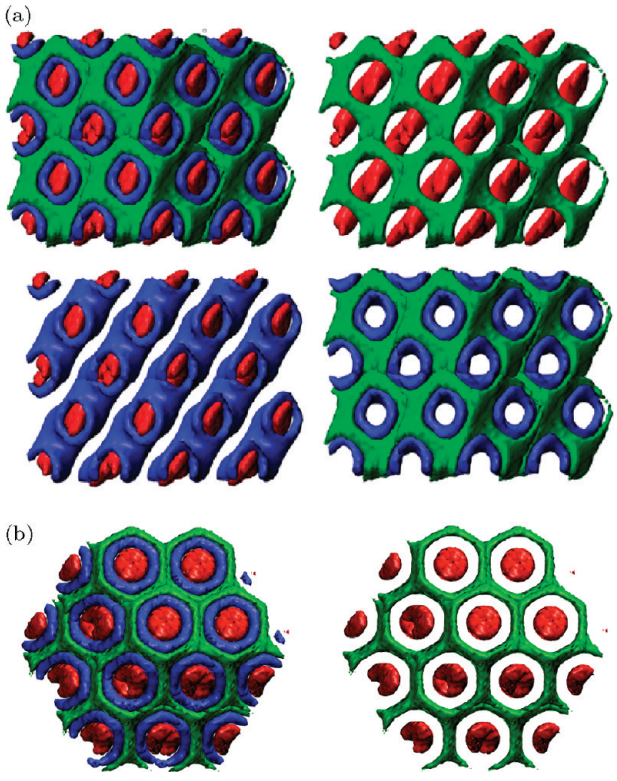


Figure 5. DPD simulation result split into pairs of colors. (a) For symmetric interactions, the red A (P2VP) component forms perforated lamellae (seen here edge on) with protrusions of green C (PS) connecting adjacent layers of green C (PS). The blue B (PI) component forms a lining between the red A (P2VP) and green C (PS) constrained by the molecular topology. (b) When raising the interaction parameter between the red A and blue B component, the simulation predicts a cylindrical core−shell structure. Images are based on 8 ($2 \times 2 \times 2$) simulation boxes.

Results and Discussion

Simulations. The self-assembled structures from the 3-miktoarm star predicted by the DPD simulations are shown in Figure 5 where the colors correspond to the ones used in Figure 1. In this particular system the volume fraction of the PDMS is small compared to the other components so for

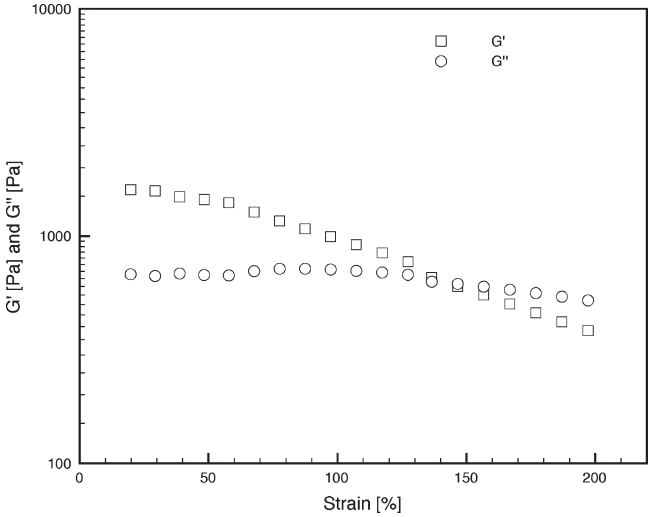


Figure 6. Rheological data showing the strain dependence of the elastic modulus G' and loss modulus G'' at $T = 200$ °C and shear frequency $\omega = 1$ Hz.

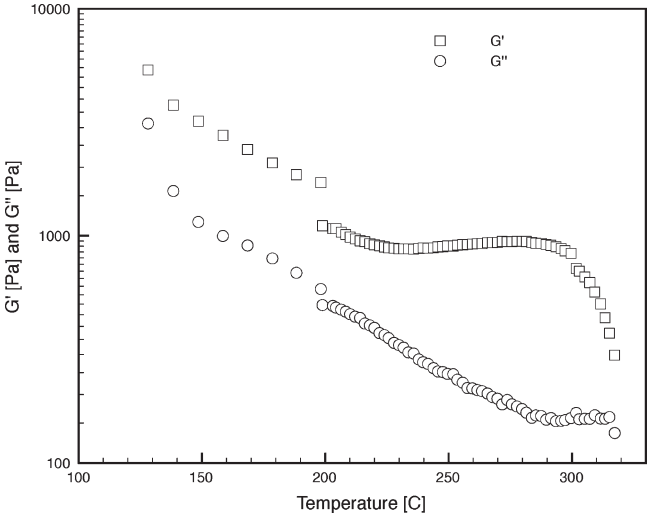


Figure 7. Temperature dependence of the elastic modulus G' and loss modulus G'' from measurements with frequency $\omega = 1$ Hz and shear amplitude $\gamma = 2\%$.

visual clarity we omit this component in the structural images shown in Figure 5. The PDMS part simply forms a thin lining between the red and blue domains. Assuming symmetric interactions, the resulting morphology is shown in Figure 5a. This structure has perforated lamellae of the red A (P2VP) component with the perforations arranged hexagonally in each plane and the overall packing of the perforations being fcc. Through the perforations protrusions of green C (PS) connects adjacent lamellae of green C (PS). The blue B (PI) component forms a lining between red A (P2VP) and green C (PS) constrained by the molecular architecture. As is shown in ref 35, this structure is robust in terms of modest variations of both (symmetric) interactions and relative arm lengths in this star architecture. Thus, there is good reason to assume this structure to be a candidate equilibrium morphology of the system studied experimentally, even though the detailed interaction parameters are not exact. On the other hand, as mentioned above, the interaction parameter between P2VP and PI is usually considered to be higher than that between PI−PS and PS−P2VP. Increasing the simulation interaction parameter between red A and blue B, the resulting morphology is a core−shell cylindrical structure shown in Figure 5b. With the employed volume fractions no other structures are predicted from the simulations. Further, given the scattering data shown below, these two structures are clearly feasible candidates for the melt morphology of the experimental system so we will focus on these.

Rheology and Scattering from Nonaligned Samples. Figures 6 and 7 shows rheological data from the P2VP(PDMS-*b*-PI-*b*-PS)$_2$ 3-miktoarm star quarterpolymer, as obtained at $T = 200$ °C, well above any of the components glass-transition temperature. The strain sweep shows a crossover from dominating elastic character to dominating dissipative character for strain amplitudes of the order of 100−150%, which is a typical value also observed for simple linear block copolymers.The temperature dependent moduli in Figure 7 shows a significant softening between 100 and 200 °C and a leveling off in the elastic value between 200 and 300 °C (the jump around 200 °C is due to the data being obtained on two different sample outtakes). There is no signature of any marked phase transition, which is also verified by the structural characteristics presented in Figure 8.

The azimuthally averaged scattering function is shown in Figure 8a. The intensity is dominated by three peaks at q^*, $2q^*$, and $3q^*$ with $q^* \sim 0.023$ Å^{-1} indicating dominating lamellar structure with a characteristic repeat distance around 275 Å. With good will there could be indications of hexagonal $(3)^{1/2}$ and $(7)^{1/2}$ peaks, but the limited resolution does not allow a definite answer to this. The scattering peak intensity (Figure 8b) decreases gradually to ∼65% by raising the temperature from $T = 100$ °C to $T = 318$ °C, while the peak position, q, and peak width remain basically unchanged. At $T \approx 300$ °C, the shear modulus seems to vanish, which may indicate the proximity of an order-to-disorder phase transition (see Figure 7), although the scattering function does not show indications of any transition up to $T = 318$ °C. However, at $T \approx 300$ °C the sample is chemically unstable, and any conclusion on phase changes is therefore doubtful at these temperatures.

Scattering from Shear-Aligned Samples. The structural determination relies on rotation studies of the shear-aligned samples, and both the neutron and X-ray scattering from one of these are shown in Figure 10. Chronologically the SAXS measurements were done almost a year after the SANS measurements in order to gain additional information from the altered contrast conditions. The SAXS data are seen to be in accordance with the SANS data and so illustrate that the morphology of the quenched samples are stable at room temperature for many months. Since the initial alignment was done using the *in situ* rheo-SANS setup, we will start with looking at the SANS data and also discuss how these rule out the cylindrical structure predicted from the DPD simulations. Following this we look at the full set of data and describe crystallographic model calculations based on the perforated lamellae structure predicted from the DPD simulations and show that these agree with both the SANS and SAXS data, thus lending strong support for this structure as the morphology of the P2VP(PDMS-*b*-PI-*b*-PS)$_2$ 3-miktoarm quarterpolymer.

Starting with the cylindrical structure, let us assume this is the correct structure. It is clear that the dominating feature of all the SANS data is the first-order peak lying along the *e*-direction. This would then indicate that the cylinders are preferentially aligned along the flow axis. This leaves two possibilities for the behavior of the scattering patterns when rotating the sample around the flow axis. First, the cylinders

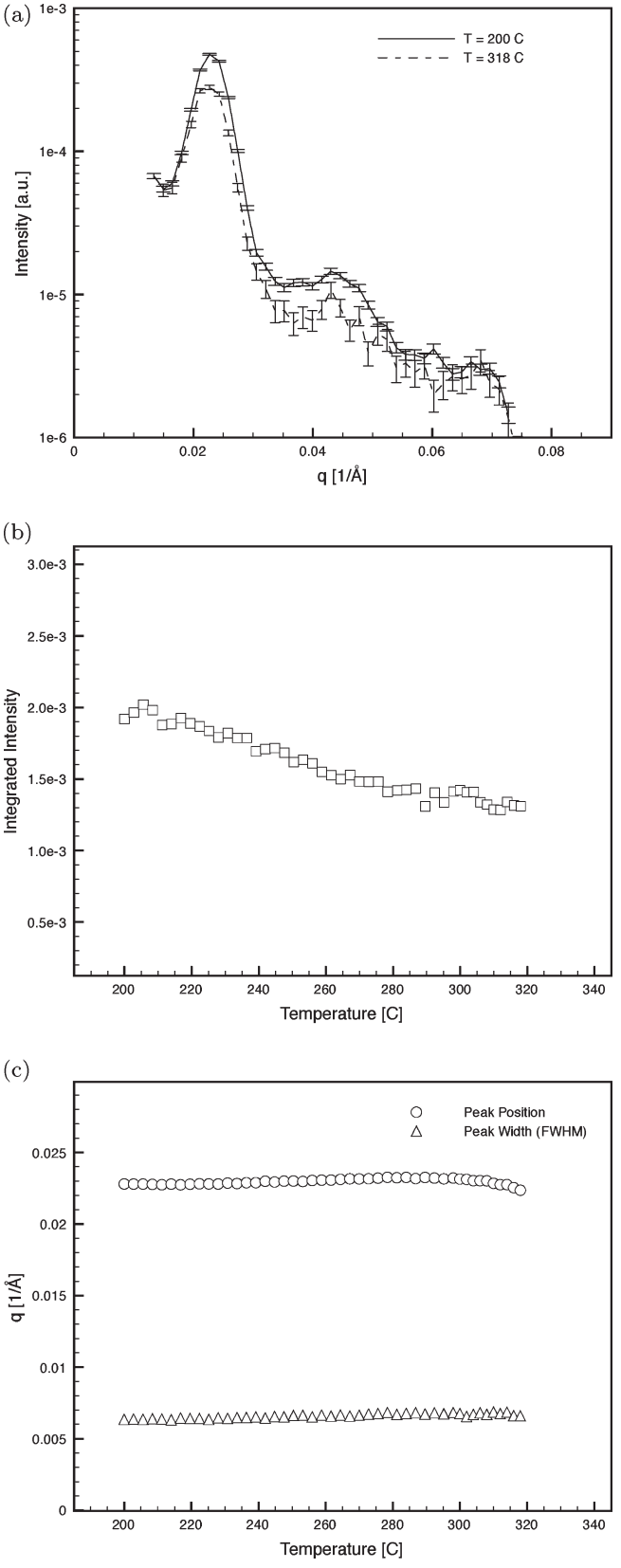


Figure 8. Temperature dependence of structural parameters. (a) Azimuthally averaged scattering function before shear alignment. (b) Integrated intensity for $q \in [0.015, 0.03]$ Å^{-1}. (c) Peak position and peak width (full width half-maximum).

could all be positioned randomly in the $e-\nabla$ plane, but then all rotations should give equivalent scattering patterns, which is clearly not the case. The other option is that the 90° data

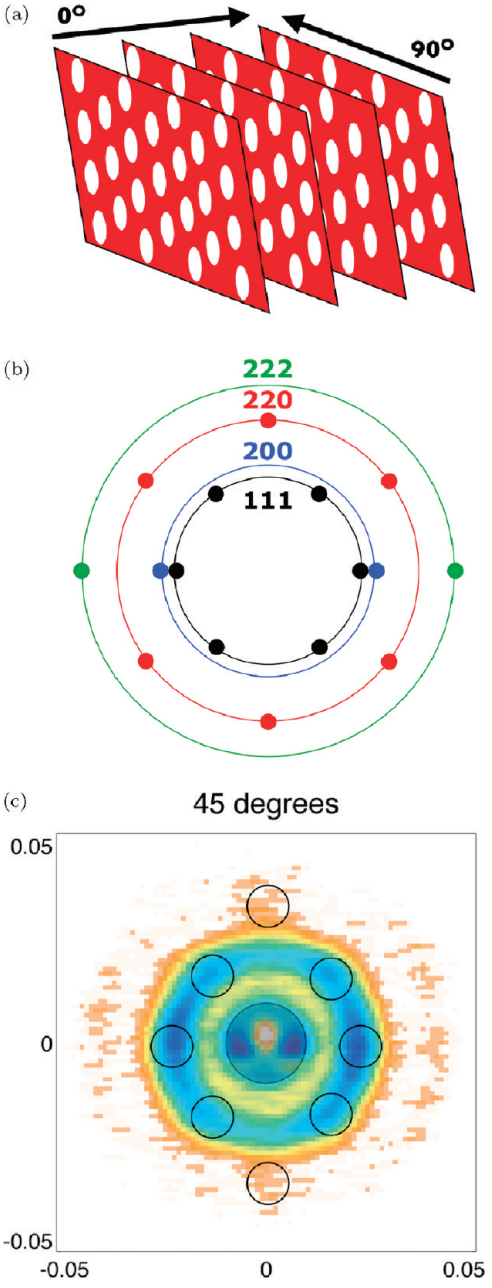


Figure 9. (a) Illustration of the fcc packing of the perforated lamellae of the DPD structure and how this is related to the scattering beam directions. (b) Illustration of all relevant crystallographic reflections from the rotation of a fcc crystal corresponding to (a). (c) Indications of (111) and (220) peaks in the 45° SANS data discussed in more detail below (axis units are Å^{-1}).

result from shooting parallel to the cylinder planes, but then the scattering pattern should be the same when rotating 60°; i.e., the 30° and 90° data should be equivalent, which again is not the case. Further, if the cylinders are preferentially aligned along ν, then we would expect a different scattering pattern to emerge if shooting neutrons along the flow axis ν but this is not the case—these data (not shown) are indistinguishable from the 90° data shown in Figure 10. Thus, it seems clear to conclude that the data are not consistent with the cylindrical structure or in fact with any type of modulated cylindrical structure[37,38] where the same arguments would apply. Also, the same line of reasoning could be practiced with the SAXS data.

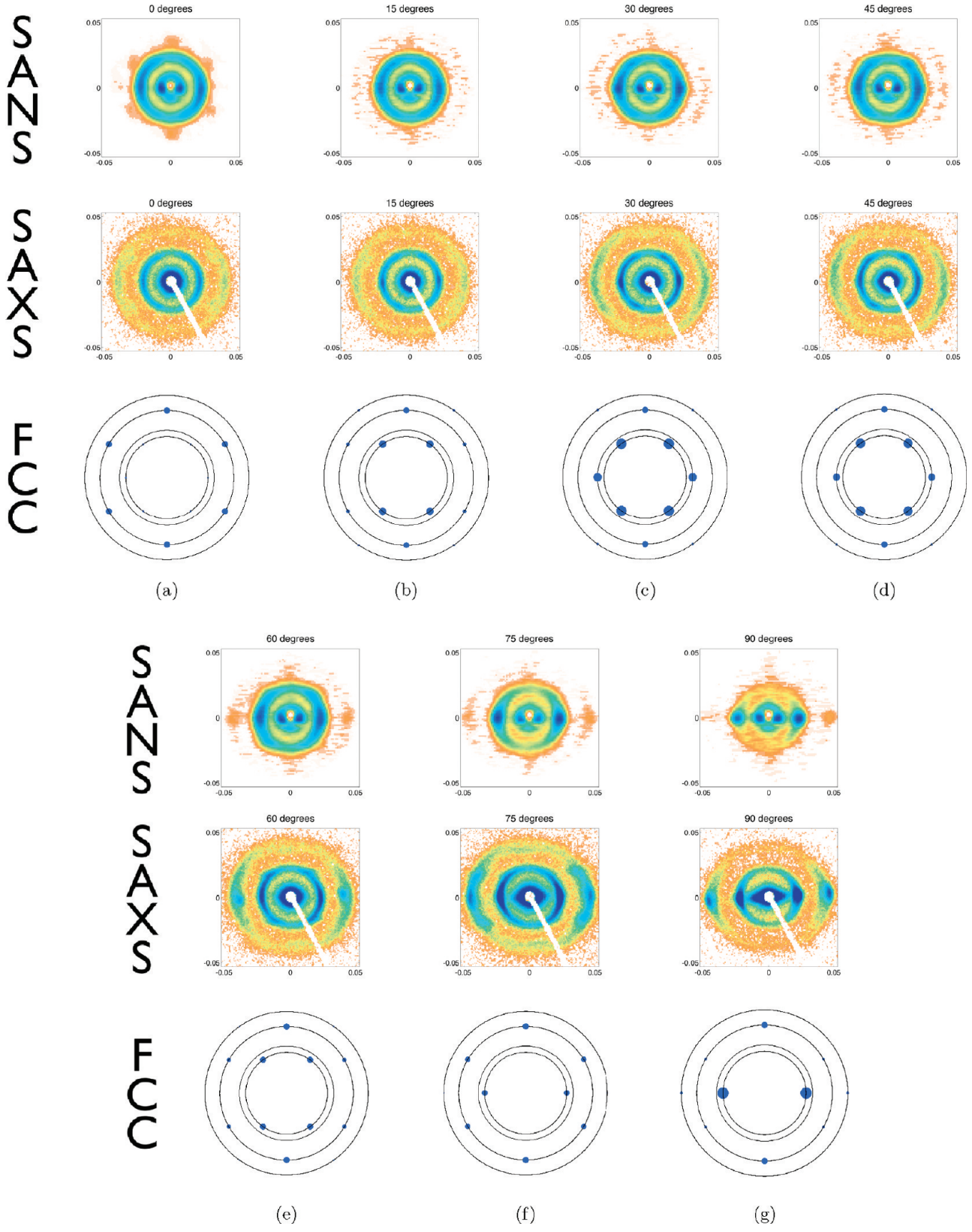


Figure 10. SANS and SAXS data from shear-aligned P2VP(PDMS-*b*-PI-*b*-PS)$_2$ 3-miktoarm quarterpolymers at different rotations and crystallographic model calculations from a fcc structure. Rotation 0° corresponds to the (v,e)-scattering plane, while rotation 90° corresponds to the (v, ∇)-scattering plane. Intensity is shown on a logarithmic scale with values ranging from 0 to 5, and axis units are Å^{-1} (note that the inner peaks in the SANS data are the forward scattering around the beamstop).

In contrast, the data are quite similar to measurements on diblock copolymers previously published in ref 27 where the structure is assigned as a perforated lamellar structure. There the experimental observations were compared with the calculated scattering patterns from one or more crystalline domains of fcc symmetry. Here we perform corresponding

calculations adopting the symmetry of the perforated lamellae structure predicted from the DPD simulations. In Figure 8a we illustrate the relation between the DPD structure, the scattering directions and the crystallographic calculations. To accommodate the 90° data, the perforated lamellae have to be aligned parallel with the shearing planes and thus perpendicular to the beam direction at 0° rotation. As mentioned, the DPD simulations predicts that the perforations are packed as fcc, so in the model calculations we assume fcc symmetry with the [111] direction coinciding with the 0° beam direction, i.e., along the ∇ axis. We then rotate the structure 90° around the $[\bar{1}10]$ directions in steps of 15° matching the experimental procedure. The calculations are done assuming a crystal mosaicity of 10°, and the size of the calculated reflections in Figure 10 scales with the distance between the reflection and the ideal Bragg condition. In Figure 8b we illustrate the relevant reflection families found in the calculations, and below that in Figure 8c a marked version of the 45° SANS data is shown, indicating these reflections as they appear in the data. Also, in Figure 8c the central part of the data has been masked out, illustrating that the inner peaks here are to be ignored since this stems from forward scattering around the beamstop.

Referring now to Figure 10, the figure is structured so that each of the panels a−g contain three images with the SANS pattern, SAXS pattern, and crystallographic model calculation arranged from top to bottom, respectively, and corresponding to the rotation in question. Each line is labeled clearly in the figure. The different patterns correspond to various rotations around the shear-velocity direction. The pattern indexed 0° corresponds to the (e, v)-plane while the pattern indexed 90° corresponds to the (∇, v)-plane (see Figure 4). Because of the highly asymmetric planar sample geometry during the SANS experiments, with the sample situated inside the shear fixture, we were not able to resolve the relative intensities, only the three-dimensional position in q-space. Different routes were tried to obtain optimal texture for unique determination of the ordered phase. These include studies at different temperatures between 120 and 318 °C as well as varying shear amplitudes and frequencies. All attempts resulted in the same structure and only minor variation in texture. In no case did we get perfect single-domain or corresponding simple texture, but the two-dimensional scattering pattern showed marked texture overlaid with a more or less significant contribution from non-oriented domains. The pattern obtained in the perpendicular (q_v,q_∇)-scattering plane (see 90° SANS data in Figure 10g) gives the best measure of the degree of aligned texture (there is a small asymmetry in the data from the edge-on 90° data due to scattering from the shear cell edges). These patterns shows very well resolved reflections, including higher order scattering peaks, which strongly indicate a dominating lamellar structure. Thus, this configuration gives a very good indication of the degree of shear-induced alignment as there is a clear underlying isotropic Debye−Scherrer scattering ring, but this is still an order of magnitude below the intensity of the 3D-resolved Bragg peak. The apparent dominance of the first-order lamellar peak is not only a matter of limited aligned texture. It is highly dominated by the effect of the form factor which reduces the intensity dramatically at high q-values.

Starting at 0° or in the (q_v, q_e)-scattering plane, which is the natural plane of *in situ* investigations with our instrument, the powder contribution dominates, but a distinct hexagonal pattern appears in the SANS data at large q-values corresponding to the (220) type of fcc reflections. In this configuration these (220) reflections are the only ones to be expected from the shear-aligned domain as shown in the theoretical calculations. This is in fact strong evidence of the fcc symmetry from the ABCABC-type stacking of the perforations since for example a hexagonally close-packed ABABAB stacking would predict the (111) peaks to be dominating (tested, not shown). These reflections are also visible in the SAXS data although weaker since here the powder contribution is even stronger, clearly displaying both first- and second-order lamellar peaks.

When we start to rotate the sample several things are worth noting. For various rotations the calculations predict 4-fold (111) reflections to appear at ~55° over the horizontal axis. These can both be seen in the SANS and SAXS data, weakly in the SANS data at rotation angles of 15°, 30°, 45°, and 60° and more clearly in the SAXS data. This is in total agreement with the model calculations, also the increasing intensity of the reflections in the 30° and 45° data compared to the 15° and to some extent 60° data. These reflections disappear at 75° and 90° as also predicted by the fcc model calculations. Further, for all rotations the (220) peaks along the v axis are predicted to be seen which we also have indications of in all SANS rotations. These are not seen in the SAXS data though which we ascribe to either or both the different contrast conditions and increased dominance of the powder part of the scattering. On the contrary, the SAXS data remarkably capture the off-meridional (220) reflections predicted for particularly the 75° rotation. Also, as we approach the 90° rotation, the horizontal (111) reflections increasingly dominate until finally these are the only peaks to be expected also in agreement with both SANS and SAXS data. In the model calculations the (222) reflections are probably represented too weakly which is in part due to the chosen peak size scaling. Overall, the observed scattering patterns are in very good agreement with the calculated pattern from a perforated lamellar phase where the perforations are ordered in a fcc structure, as also previously observed in linear diblock copolymers,[27,39−41] and thereby in agreement with the perforated lamellae structure predicted on the basis of the DPD simulations discussed above.

Conclusions

In conclusion, we have shown that by combining DPD simulations, rheo-SANS, and SAXS, the determination of the melt morphology of a newly synthesized 3-miktoarm star quarterpolymer, the P2VP(PDMS-*b*-PI-*b*-PS)$_2$, has been possible. The resulting morphology is shown to be a novel perforated lamellae structure with hexagonally perforated lamellae of P2VP containing close-packed protrusions of PS connecting adjacent lamellae layers of PS. The PI part forms a lining between the P2VP and PS domains constrained by the molecular architecture. We believe this is the first experimental report of this morphology in the literature.

Further, it is interesting to speculate if the increased molecular complexity represented by this new polymer system has helped increase the stability of the perforated lamellae phase. The question of the stability of perforated lamellae phases has been the subject of some interest in diblock copolymer systems.[39−55] Also, due to its topology, these structures have interesting perspectives as functional soft materials since one might selectively remove one component and thus for example generate continuous structures with well-defined nanopores.[27]

Finally, we have shown that results from DPD simulations on complex architectured copolymers are in good agreement with experimental results and can thereby be used effectively as a guidance for design of novel structured polymer materials. This concerns for example exciting new morphologies predicted in

ref 35 such as a potentially chiral gyroidal single network structure and a combined network and sphere packing structure.

Acknowledgment. Thanks to Liliana de Campo for valuable comments to the manuscript. This study was financially supported by the Danish Natural Science Research Council through the support of Instrument Centre for Synchrotron X-ray and Neutron Scattering (DANSCATT). Thanks to the Paul Scherrer Institute, Switzerland, for providing access to the SANS-II facility. Finally, thanks to Karsten Joensen, JJ-Xray, for valuable assistance with the SAXSLab facility.

References and Notes

(1) Hadjichristidis, N.; Iatrou, H.; Pitsikalis, M.; Pispas, S.; Avgeropoulos, A. *Prog. Polym. Sci.* **2005**, *30*, 725–782.
(2) Hadjichristidis, N.; Pispas, S.; Floudas, G. *Block Copolymers: Synthetic Strategies, Physical Properties and Applications*; Wiley: New York, 2003.
(3) Sioula, S.; Hadjichristidis, N.; Thomas, E. *Macromolecules* **1998**, *31* (23), 8429–8432.
(4) Sioula, S.; Hadjichristidis, N.; Thomas, E. *Macromolecules* **1998**, *31* (16), 5272–5277.
(5) Zioga, A.; Sioula, S.; Hadjichristidis, N. *Macromol. Symp.* **2000**, *157*, 239–249.
(6) Gemma, T.; Hatano, A.; Dotera, T. *Macromolecules* **2002**, *35*, 3225–3227.
(7) Yamauchi, K.; Takahashi, K.; Hasegawa, H.; Iatrou, H.; Hadjichristidis, N.; Kaneko, T.; Nishikawa, Y.; Jinnai, H.; Matsui, T.; Nishioka, H.; Shimizu, M.; Fukukawa, H. *Macromolecules* **2003**, *36* (19), 6962–6966.
(8) Takano, A.; Wada, S.; Sato, S.; Araki, T.; Hirahara, K.; Kazama, T.; Kawahara, S.; Isono, Y.; Ohno, A.; Tanaka, N.; Matsushita, Y. *Macromolecules* **2004**, *37* (26), 9941–9946.
(9) Yamauchi, K.; Akasaka, S.; Hasegawa, H.; Iatrou, H.; Hadjichristidis, N. *Macromolecules* **2005**, *38* (19), 8022–8027.
(10) Takano, A.; Kawashima, W.; Noro, A.; Isono, Y.; Tanaka, N.; Dotera, T.; Matsushita, Y. *J. Polym. Sci., Part B: Polym. Phys.* **2005**, *43* (18), 2427–2432.
(11) Hayashida, K.; Takano, A.; Arai, S.; Shinohara, Y.; Amemiya, Y.; Matsushita, Y. *Macromolecules* **2006**, *39* (26), 9402–9408.
(12) Hayashida, K.; Kawashima, W.; Takano, A.; Shinohara, Y.; Amemiya, Y.; Nozue, Y.; Matsushita, Y. *Macromolecules* **2006**, *39* (14), 4869–4872.
(13) Takano, A.; Kawashima, W.; Wada, S.; Hayashida, K.; Sato, S.; Kawahara, S.; Isono, Y.; Makihara, M.; Tanaka, N.; Kawaguchi, D.; Matsushita, Y. *J. Polym. Sci., Part B* **2007**, *45* (16), 2277–2283.
(14) Dotera, T.; Gemma, T. *Philos. Mag.* **2006**, *86*, 1085–109.
(15) Hayashida, K.; Dotera, T.; Takano, A.; Matsushita, Y. *Phys. Rev. Lett.* **2007**, *98* (19).
(16) Kirkensgaard, J. J. K.; Hyde, S. *Phys. Chem. Chem. Phys.* **2009**, *11*, 2016–2022.
(17) Hyde, S. T.; de Campo, L.; Oguey, C. *Soft Matter* **2009**, *5*.
(18) Hayashida, K.; Saito, N.; Arai, S.; Takano, A.; Tanaka, N.; Matsushita, Y. *Macromolecules* **2007**, *40* (10), 3695–3699.
(19) Espanol, P.; Warren, P. *Europhys. Lett.* **1995**, *30* (4), 191.
(20) Groot, R.; Madden, T. *J. Chem. Phys.* **1998**, *108* (20), 8713.
(21) Ortiz, V.; Nielsen, S.; Discher, D.; Klein, M.; Lipowsky, R.; Shillcock, J. *J. Phys. Chem. B* **2005**, *109*, 17708–17714.
(22) Abu-Sharkh, B.; AlSunaidi, A. *Macromol. Theory Simul.* **2006**, *15*, 507–515.
(23) Huang, C.; Yu, H. *Polymer* **2007**, *48*, 4537–4546.
(24) Huang, C.; Fang, H.; Lin, C. *Phys. Rev. E* **2008**, *77*, 031804.
(25) Klymko, T.; Markov, V.; Subbotin, A.; ten Brinke, G. *Soft Matter* **2009**, *5*, 98–103.
(26) Mortensen, K.; Theunissen, E.; Kleppinger, R.; Almdal, K.; Reynaers, H. *Macromolecules* **2002**, *35*, 7773–7781.
(27) Mortensen, K.; Vigild, M. E. *Macromolecules* **2009**, *42*, 1685–1690.
(28) Bellas, V.; Iatrou, H.; Hadjichristidis, N. *Macromolecules* **2000**, *33*, 6993.
(29) Bellas, V.; Iatrou, H.; Pitsinos, N. E.; Hadjichristidis, N. *Macromolecules* **2001**, *34*, 5376.
(30) Fragouli, P.; Iatrou, H.; Hadjichristidis, N.; Sakurai, T.; Matsunaga, Y.; Hirao, A. *J. Polym. Sci., Part A* **2006**, *44*, 6587–6599.
(31) Hadjichristidis, N.; Iatrou, H.; Pispas, S.; Pitsikalis, M. *J. Polym. Sci., Part A* **2000**, *38*, 3211.
(32) Groot, R.; Warren, P. *J. Chem. Phys.* **1997**, *107* (11), 4423.
(33) Huckstadt, H.; Göpfert, A.; Abetz, V. *Polymer* **2000**, *41* (26), 9089–9094.
(34) James, M. E. *Physical Properties of Polymers Handbook*, 2nd ed.; Springer: Berlin, 2007.
(35) Kirkensgaard, J. J. K. *Soft Matter* **2010**, DOI: 10.1039/c0sm00358a.
(36) Limbach, H. J.; Arnold, A.; Mann, B. A.; Holm, C. *Comput. Phys. Commun.* **2006**, *174* (9), 704–727.
(37) Hamley, I. *Phys. Rev. E* **1994**, *50* (4), 2872–2880.
(38) Koppi, K.; Tirrell, M.; Bates, F.; Almdal, K.; Mortensen, K. *J. Rheol.* **1994**, *38* (4), 999–1027.
(39) Hamley, I. W.; Koppi, K. A.; Rosedale, J. H.; Bates, F. S.; Almdal, K.; Mortensen, K. *Macromolecules* **1993**, *26*, 5959–5970.
(40) Zhu, L.; Huang, P.; Chen, W. Y.; Weng, X.; Cheng, S. Z. D.; Ge, Q.; Quirk, R. P.; Senador, T.; Shaw, M. T.; Thomas, E. L.; Lotz, B.; Hsiao, B. S.; Yeh, F.; Liu, L. *Macromolecules* **2003**, *36*, 3180–3188.
(41) Hamley, I. W.; Castelletto, V.; Mykhaylyk, O. O.; Gleeson, A. J. *J. Appl. Crystallogr.* **2004**, *37*, 341–344.
(42) Almdal, K.; Koppi, K.; Bates, F.; Mortensen, K. *Macromolecules* **1992**, *25*, 1743–1751.
(43) Hashimoto, T.; Koizumi, S.; Hasegawa, H.; Izumitani, T.; Hyde, S. *Macromolecules* **1992**, *25*, 1433–1439.
(44) Spontak, R. J.; Smith, S. D.; Ashraf, A. *Macromolecules* **1993**, *26*, 956–962.
(45) Disko, M.; Liang, K. S.; Behal, S. K.; Roe, R. J.; Jeon, K. J. *Macromolecules* **1993**, *26*, 2983–2986.
(46) Hamley, I. W.; Gehlsen, M. D.; Khandpur, A. K.; Koppi, K. A.; Rosedale, J. H.; Schulz, M. F.; Bates, F. S.; Almdal, K.; Mortensen, K. *J. Phys. II* **1994**, *4*, 2161–2186.
(47) Matsen, M. W.; Schick, M. *Phys. Rev. Lett.* **1994**, *72*, 2660–2663.
(48) Qi, S.; Wang, Z. G. *Phys. Rev. Lett.* **1996**, *76*, 1679–1782.
(49) Qi, S.; Wang, Z. G. *Phys. Rev. E* **1997**, *55*, 1682–1697.
(50) Matsen, M. W.; Bates, F. S. *J. Chem. Phys.* **1997**, *106*, 2436–2448.
(51) Vigild, M. E.; Almdal, K.; Mortensen, K.; Hamley, I. W.; Fairclough, J. P. A.; Ryan, A. J. *Macromolecules* **1998**, *31*, 5702–5716.
(52) Hajduk, D. A.; Ho, R. H.; Hillmyer, M. A.; Bates, F. S.; Almdal, K. *J. Phys. Chem. B* **1998**, *102*, 1356–1363.
(53) Wang, C. Y.; Lodge, T. P. *Macromolecules* **2002**, *35*, 6997–7006.
(54) Eskimergen, R.; Mortensen, K.; Vigild, M. E. *Macromolecules* **2005**, *38*, 1286–1291.
(55) Mareau, V. H.; Akasaka, S.; Osaka, T.; Hasegawa, H. *Macromolecules* **2007**, *40*, 9032–9039.

Macromolecules
ARTICLE

Macromolecules **2011**, *44*, 583–593 **583**
DOI: 10.1021/ma102232z

Synthesis and Self-Organization of Poly(propylene oxide)-Based Amphiphilic and Triphilic Block Copolymers

Samuel O. Kyerematen,[†] Karsten Busse,[†] Joachim Kohlbrecher,[‡] and Jörg Kressler*,[†]

[†]*Department of Chemistry, Martin Luther University, von-Danckelmann-Platz 4, D-06120 Halle (Saale), Germany, and* [‡]*Paul Scherrer Institut, CH-5232 Villigen PSI, Switzerland*

Received September 28, 2010; Revised Manuscript Received December 15, 2010

ABSTRACT: A series of amphiphilic diblock copolymers and triphilic triblock copolymer analogues of the architectures BA, CAB, and CBA have been synthesized and characterized with respect to their aggregation behavior in water. The A, B, and C components of the block copolymers are formed by hydrophilic poly(glycerol monomethacrylate) (PGMA), lipophilic poly(propylene oxide) (PPO), and a fluorophilic perfluoroalkyl segment, respectively. Their critical micelle concentrations in water are determined from surface tension measurements. The aggregation behavior of the copolymers, as investigated by DLS, SANS, AFM, and TEM, is found to be governed by the strong immiscibility between the lipophilic PPO blocks and the fluorophilic perfluorocarbon segments as well as the blocks sequence. It is found that the BA and CBA copolymers form clear micellar solutions in contrast to the CAB copolymer solutions which exhibit phase-separation above the LCST of the PPO block.

1. Introduction

The combination of three mutually incompatible hydrophilic (A), lipophilic (B), and fluorophilic (C) blocks (i.e., triphilic) in polymer synthesis has generated much interest because of the intriguing structures formed in bulk and in solution.[1−14] In aqueous media, the micelle structures formed by these copolymers have mostly a phase-separated core due to the immiscibility between the hydrophobic components (fluorophilic and lipophilic), thus forming multicompartment micelles.[1] One such recent report involves the combination of thermoresponsive-lipophilic PPO, hydrophilic poly(glycerol monomethacrylate) (PGMA), and fluorophilic perfluoroalkyl segments to form CABAC pentablock copolymer analogues.[15] The micelle core of this triphilic system, if the A-block is long enough for looping, is composed of immiscible perfluoroalkyl segments and PPO blocks.

This study investigates the difference in the aqueous solution behavior of the triphilic CAB copolymer analogue compared to the triphilic CBA counterpart, and the amphiphilic BA diblock copolymer. Similarly, the hydrophilic, lipophilic, and fluorophilic components of these systems are PGMA, PPO, and a perfluoroalkyl segment, respectively. Because of the sequence of the hydrophobic components (C and B), it is obvious that for the CBA architecture both the fluorophilic and lipophilic components should form the core structure when aggregation occurs because they are covalently linked to each other.[2] However, in the case of the CAB architecture, where the hydrophilic A block is sandwiched between the fluorophilic and lipophilic components, two possibilities exist during aggregation as illustrated in Figure 1. One possibility involves the looping of the hydrophilic middle to incorporate both the fluorophilic and lipophilic components in to block the same core, thus, forming a compartmentalized flower-like micelle.[5,9,14,16] The other possibility is the adaptation of a two-compartment network with spatially distinct fluorophilic and lipophilic core domains as illustrated in Figure 1.[17]

*Corresponding author. E-mail: joerg.kressler@chemie.uni-halle.de.

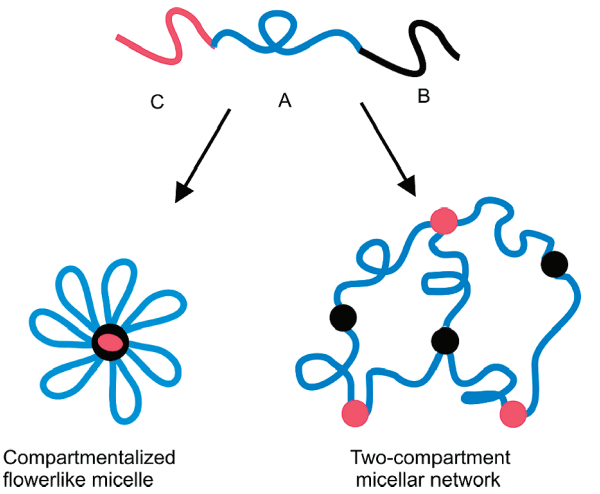


Figure 1. Possible aggregation structures formed by triphilic CAB triblock copolymer analogue in water.

Weberkirch et al.[4] using the triphilic CAB triblock copolymer analogue of the structure, α-fluorocarbon-ω-hydrocarbon end-capped poly(*N*-acylethylenimine), found that at high concentration the copolymer forms a two-compartment network with hydrophilic poly(*N*-acylethylenimine) bridges. However, using a larger length of the hydrophilic poly(*N*-acylethylenimine) block, Kubowicz et al.[5] found that the middle block in this case loops to form cylindrical micelles with a compartmentalized core. Shunmugam et al.[18] prepared polymethacrylate-based triphilic CAB triblock copolymers, investigated their behavior in water, and showed that these copolymers formed hydrogels ostensibly due to two-compartment network formation. More recently, Taribagil et al.[19,20] investigated the morphology of hydrogels formed by triphilic CAB block copolymer based on poly(perfluoropropylene oxide) (PFPO), poly(ethylene oxide) (PEO), and poly(1,2-butadiene) (PB), respectively. They established through SANS and cryogenic scanning electron microscopy (cryo-SEM) measurements

© 2011 American Chemical Society
Published on Web 01/10/2011

that the PFPO−PEO−PB copolymer self-assembles into a compartmentalized network in which the PFPO blocks form disk-shaped assemblies which are embedded in thin bicontinuous PB sheets with both faces of the sheets covered by looped PEO brushes. The authors reasoned that the disk-shaped adaptation over spherical-shaped by the assembled PFPO blocks is due to the strong hydrophobicity, large interfacial tension, and rodlike behavior exhibited by fluorocarbon molecules in aqueous environment. They further argued that in order to circumvent the enthalpic penalty associated with formation of disk edges in aqueous solution, the PFPO−PEO−PB system associates the fluorocarbon disk domains with the less hydrophobic PB chains to form PB sheets.

Thus, while exclusive bridging of the middle blocks might be naively expected for any triphilic CAB network, the interplay of the interactions among the three components and water can offset the significance of the incompatibility between the lipophilic and the fluorophilic end-components and give rise to a different nanostructure.[20] Particularly, we demonstrate this with thermoresponsive PPO block as the lipophilic component in our case. The PPO homopolymer with molar mass ~2000 g/mol has a lower critical solution temperature (LCST) at around 15 °C in water.[21] Thus, below the LCST the PPO chains are hydrated and behave as hydrophilic entities. Conversely, at temperatures above the LCST they become dehydrated (insoluble) and as such behave as hydrophobic entities.[22] It implies that, at temperatures below the LCST of the PPO block, the copolymer will behave as an amphiphile because it has the perfluoroalkyl segment as the only hydrophobic component, while the hydrophilic component consists of PGMA and PPO. Meaning, the copolymer can form micelles composed of a fluorocarbon core stabilized by the PGMA and PPO as the hydrophilic corona. The question then is what happens when the PPO component becomes hydrophobic as temperature is raised above its LCST. Will the middle PGMA block loop to incorporate the hydrophobic PPO chains into the micelle core or will the PPO chains form hydrophobic junctions leading to the formation of a two-compartment network?

In this article, the synthetic route to the CAB block copolymer is described and the characterization is carried out by size exclusion chromatography (SEC), ^{1}H and ^{19}F NMR spectroscopy, and FTIR spectroscopy. The route involves a combination of atom transfer radical polymerization, ATRP, and the copper(I)-catalyzed alkyne−azide cycloaddition (CuAAC) reaction often referred to as "click" chemistry.[23,24] The block copolymer CAB is investigated for aggregation behavior in aqueous solution. Furthermore, the CBA triblock copolymer analogue, and the amphiphilic BA diblock copolymer are also investigated for comparative purposes. The investigative techniques used include surface tension measurement, temperature-dependent ^{1}H NMR spectroscopy, dynamic light scattering (DLS), small angle neutron scattering (SANS), atomic force microscopy (AFM), and transmission electron microscopy (TEM).

2. Experimental Part

2.1. Materials. All chemicals were purchased from Sigma-Aldrich unless otherwise stated. Toluene (99%) and pyridine (99%) were dried over calcium hydride overnight, distilled under atmospheric condition and stored over molecular sieve. Dimethylformamide (DMF) (99.8%) and anisole (Alf-Aesar, 99%) were dried over calcium hydride overnight, distilled under reduced pressure and kept over molecular sieve. Anhydrous dichloromethane (CH_2Cl_2) (99.8%), anhydrous α,α,α-trifluorotoluene (99%), *n*-hexane (97%), diethyl ether (98%), 1,4-dioxane (99%), ethanol (99.8%), methanol (99.8%) and monohydroxy terminated poly(propylene oxide) (PPO_{34}−OH) [M_n(SEC) ~ 2500 g/mol, M_n(^{1}H NMR) ~ 2000 g/mol] were used as received. Tetrahydrofuran (THF) (99.5%) was distilled from potassium hydroxide and stored over molecular sieve. Copper bromide (CuBr) (99%) was purified by stirring in glacial acetic acid under nitrogen for 24 h to dissolve the Cu(II) species, filtered, washed several times with ethanol and dried under vacuum. Copper chloride (CuCl) (99%), *N*-ethyldiisopropylamine (DIPEA) (98%), tris(benzyltriazolylmethyl)amine (TBTA) (97%), sodium azide (NaN_3) (99.5%), hex-5-ynoic acid (97%), 2-bromoisobutyryl bromide (BIB) (98%), heneicosafluoro-1-undecanol ($C_{10}F_{21}CH_2OH$) (95%), *N*,*N*′-(dicyclohexyl)carbodiimide (DCC) (99%), 2,2′-bipyridine (Bipy) (Merck, 99.5%), α,α,α-trifluorotoluene (TFT) (99%), and 4-(dimethylamino) pyridine (DMAP) (99%) were used without further purification.

2.2. Characterization. *NMR Spectroscopy*. ^{1}H and ^{19}F NMR spectra were recorded using a Varian Gemini 2000 spectrometer operating at 400 MHz (^{1}H) and 200 MHz (^{19}F) at 25 °C in $CDCl_3$ or DMSO-d_6. Temperature-dependent ^{1}H NMR spectra were recorded in D_2O from 7 to 40 °C on a BRUKER Avance III NMR spectrometer operating at frequency of 600 MHz.

Size Exclusion Chromatography (*SEC*). SEC measurements were performed in THF at room temperature on Viscotek VE 2001 column equipped with RI detector Viscotek 3580. Polystyrene was used as the calibration standard.

Surface Tension Measurement (*STM*). The surface tension γ of the aqueous solutions of the polymer samples at different concentrations was measured by the Wilhelmy plate method using the automated DCAT11 tensiometer (DataPhysics Instruments GmbH, Filderstadt, Germany). Stock solutions of 2.5 g/L were prepared by dissolution of the polymer in bidistilled water, stirred overnight at room temperature and filtered through 0.45 μm pore-size PTFE before usage. The tensiometer works by automatically injecting predetermined volumes of the stock solution into a thermostated glass vessel containing initially only bistilled water. Following each injection, the surface tension is then measured after 10 min of stirring and a 3 h waiting period. Measurements were carried out at 25 °C by circulating thermostated water accurate to ±0.1 °C. For samples which showed phase separation at room temperature, solutions of different concentrations were prepared at 5 °C and measurements were carried out at 8 °C.

Dynamic Light Scattering (*DLS*). DLS measurements of aqueous solutions of the block copolymers were performed using an ALV-NIBS/HPPS automatic goniometer from ALV-Laser (Langen, Germany), in the scattering angle θ range of 30° to 130°. The light source was a neodymium:YAG DPSS-200 laser (λ = 532 nm) with a power output of 200 mW. Intensity time correlation functions were measured with an ALV-5000E multiple-τ digital correlator. The CONTIN algorithm was applied to obtain distribution functions from the obtained autocorrelation function. The diffusion constant, D_{app}, is related to the reciprocal of the characteristic decay time, Γ and the scattering vector, q as $D_{app} = \Gamma/q^2$ [where $q = (4\pi n_o/\lambda)\sin(\theta/2)$, with n_0 = refractive index of the medium]. The corresponding apparent hydrodynamic radii R_h were obtained via Stokes−Einstein equation $R_h = kT/(6\pi\eta D_{app})$, where k is the Boltzmann constant and η is the viscosity of the solvent, water in this case, corrected at the absolute temperature T. Polymer solutions of different concentrations were prepared by dissolution in bidistilled water at room temperature and stirring overnight. The solutions were filtered directly into the dust-free light scattering cells through a 0.45 μm pore size filter. For samples which showed phase separation at room temperature, solution preparation and filtration were carried out at 5 °C.

Small Angle Neutron Scattering (*SANS*). Appropriate amounts of polymer samples were dissolved in D_2O at room temperature and stirred overnight to give 0.6 wt % solution. The homogeneous transparent solutions were filtered through a 0.45 μm pore size filter and transferred into 1 or 2 mm thick quartz containers. The use of D_2O as solvent instead of H_2O provides better contrast in neutron scattering experiments. Experiments were carried out using SANS II diffractometer at the Swiss Spallation Neutron Source SINQ, Paul Scherrer Institute. The wavelength of the neutrons was 0.53 nm and the experiments were performed at

two different samples to detector distances of 2 and 6 m to cover a q range of 0.1 to 2.5 nm^{-1}. The scattered neutrons were detected using a two-dimensional 128 × 128 pixel detector (64 cm diameter). In all the measurements the temperature was kept constant at 15, 20, and 40 °C. The measured SANS data have been corrected and normalized to a cross-sectional unit, using standard procedures.

Transmission Electron Microscopy (*TEM*). The TEM images were obtained from a JEOL 100CX microscope, operating at an acceleration voltage of 100 kV. Samples were prepared by drop coating 0.014 g/L aqueous solution of polymer on carbon coated copper grids and allowed to dry under ambient conditions.

Atomic Force Microscopy (*AFM*). The block copolymer morphology was analyzed using an atomic force microscope Nano-Wizard (JPK Instruments AG, Germany) working in tapping-mode. For the experiments, silicon cantilevers of type Arrow (NanoWorld AG, Switzerland) with a resonance frequency of about 285 kHz and a force constant of about 42 $N \cdot m^{-1}$ were used.

2.3. Syntheses. *Initiators Synthesis*. The ATRP initiators were synthesized by reaction of the terminal hydroxyl groups of heneicosafluoro-1-undecanol ($C_{10}F_{21}CH_2OH$), and PPO_{34}−OH with excess BIB for 48 h at room temperature. This afforded heneicosafluoro-1-undecyl 2-bromoisobutanoate (perfluoroalkyl-initiator) (F_{10}−Br) and 2-bromoisobutanoate poly(propylene oxide) (PPO_{34}−Br), respectively. Details of the experimental procedures are provided in the Supporting Information

F_{10}−Br: ^{1}H NMR (400 MHz, $CDCl_3$): δ (ppm) = 4.65 [t, $-CF_2-CH_2-$], 1.95 [s, $-C(Br)-(CH_3)_2$]. ^{19}F NMR (200 MHz, $CDCl_3$): δ (ppm) = −126.51 [s, $-(CF_2)_7-CF_2-CF_3$], −123.71−122.21 [m, $-(CF_2)_7-CF_2-CF_3$], −119.78 [s, $-CH_2-CF_2-(CF_2)_7-$], −81.18 [s, $-(CF_2)_7-CF_2-CF_3$]. PPO_{34}−Br: ^{1}H NMR (400 MHz, $CDCl_3$): δ (ppm) = 1.0−1.28 [m, $-CH-(CH_3)-CH_2-$], 1.9 [s, $-C(Br)-(CH_3)_2$], 3.27−3.41 [m, $-CH-(CH_3)-CH_2-$], 3.44−3.73 [m, $-CH(CH_3)-CH_2-$].

α-*Alkyne-Terminated Poly*(*propylene oxide*) (*PPO_{34}−C≡CH*). The alkyne functionality was introduced at the end of the poly(propylene oxide) chain by esterifying PPO_{34}−OH with excess hex-5-ynoic anhydride for 48 h at room temperature. Details of the experimental procedure are provided in the Supporting Information.

^{1}H NMR (400 MHz, $CDCl_3$): δ (ppm) = 1.0−1.28 [m, $-CH-(CH_3)-CH_2-$], 1.9 [s, $-C(Br)-(CH_3)_2$], 3.27−3.41 [m, $-CH-(CH_3)-CH_2-$], 3.44−3.73 [m, $-CH(CH_3)-CH_2-$], 2.42 [t, $-C(O)-CH_2-CH_2-$], 2.24 [t, $-C(O)-CH_2-CH_2-$], 1.96 [s, $-CH_2-C\equiv CH$], 1.84 [m, $-CH_2-C\equiv CH$].

α-*Perfluoroalkyl-ω-azido Poly*(*solketal methacrylate*) (*F_{10}−$PSMA_z$−N_3*). As an example for the general ATRP synthesis, 28 mg (0.29 mmol) of CuCl, 90 mg (0.57 mmol) of Bipy and 200 mg (0.287 mmol) of the perfluoro-initiator were placed in a dry Schlenk flask equipped with a stir bar. The flask was evacuated under high vacuum and backfilled with nitrogen three times before leaving it under nitrogen. Two mL of previously degassed TFT was introduced into the flask via a nitrogen-purged syringe. The solution was stirred for 30 min to enable homogenization and formation of the catalyst-ligand complex. This was followed by adding 1.72 g (8.6 mmol) of degassed solketal methacrylate (SMA) via a nitrogen-purged syringe.

Further degassing was carried out for 15 min after which polymerization was carried out at 50 °C. Monomer conversion during polymerization was monitored by ^{1}H NMR spectroscopy. After 40 min the flask was opened to air, allowed to cool and excess THF was added. The polymer was purified by column chromatography, precipitated into excess hexane and dried under high vacuum for 48 h at room temperature.[25]

Afterward, the terminal halogen group of the polymer was replaced with N_3 through azidation reaction with excess NaN_3 in DMF according to a reported method.[26] Scheme 1 (step 1) illustrates the synthetic route to F_{10}−PSMA−N_3. ^{1}H NMR (400 MHz, DMSO-d_6): δ (ppm) = 0.60−0.99 (d, $-C-CH_3$), 1.17−1.39 [d, $-C-(CH_3)_2$], 1.52−2.09 (s, $-CH_2-C-CH_3$), 3.76−4.11 (m, $-CH_2-CH(O)-CH_2-$), 4.14−4.32 (s, $-CH_2-CH(O)-CH_2-$). ^{19}F NMR (200 MHz, DMSO-d_6): δ (ppm) = −131.20 [s, $-(CF_2)_7-CF_2-CF_3$], −128.35−126.87 [m, $-(CF_2)_7-CF_2-CF_3$], −124.46 [s, $-CH_2-CF_2-(CF_2)_7-$], −85.88 [s, $-(CF_2)_7-CF_2-CF_3$].

Coupling of PPO_{34}−C≡CH and F_{10}−$PSMA$−N_3 via CuAAC. The α-alkyne-terminated poly(propylene oxide) was coupled to the F_{10}−PSMA−N_3 through the copper(I)-catalyzed alkyne−azide cycloaddition as shown in Scheme 1 (step 2). CuBr was used as the catalyst, DIPEA as the main ligand, and TBTA as a coligand. A yield of 95% was obtained after complete reaction and purification of the product. The general experimental procedure for the reaction is provided in the Supporting Information.

Poly(*propylene oxide*)-*block*-*poly*(*solketal methacrylate*) (*PPO_{34}−$PSMA_y$*). The same ATRP experimental procedure as above was followed for the polymerization of SMA with the PPO_{34}−Br initiator except that CuCl and TFT were replaced with CuBr and anisole, respectively.

^{1}H NMR (400 MHz, DMSO-d_6): δ (ppm) = 0.60−0.99 (d, $-C-CH_3$), 1.02−1.06 (d $-CH-CH_3$, PPO), 1.17−1.39 [d $-C-(CH_3)_2$], 1.86 [s $-C(Br)CH_3$], 1.52−2.09 (s, $-CH_2-C-CH_3$), 3.14−3.56 (m, $-O-CH_2-CH-CH_3$, PPO), 3.76−4.11 (m, $-CH_2-CH(O)-CH_2-$), 4.14−4.32 (s, $-CH_2-CH(O)-CH_2-$).

Removal of the Acetonide Groups of the Block Copolymers. The acetonide groups of the PSMA block of the copolymers were removed through acidic hydrolysis as indicated in Scheme 1 (step 3). In a typical procedure 200 mg of PPO_{34}−$PSMA_y$ or F_{10}−$PSMA_z$−PPO_{34} was dissolved in 10 mL of 1,4-dioxane in an open single neck round-bottom flask. One mL of 1 N HCl solution was added dropwise and slowly via a syringe. The transparent solution was left to stir for 48 h at room temperature after which it was dialyzed against water for 48 h, and then freeze-dried.[27]

3. Results and Discussion

3.1. Block Copolymers. The monomer, solketal methacrylate, used in the polymerization reactions is synthesized according to a literature procedure.[27] Two block copolymers were synthesized using PPO_{34}−Br as initiator and are given in Table 1 as entries 3 and 4. SEC traces and ^{1}H NMR spectra confirmed the formation of block copolymers (see Supporting Information). Likewise, the perfluoroalkyl-initiator, F_{10}−Br, can also initiate the polymerization of SMA to give polymers with narrow polydispersity (M_w/M_n) as given in Table 1 (entries 1 and 2).

In order to guarantee high degree of the halogen end-group functionality of the formed polymers, the polymerization reactions are conducted at moderate conversions of about 70%.[28] However compared to the theoretical molar mass expected based on monomer conversion $M_{n(theo)}$, a low initiation efficiency, f, value of about 0.18 is obtained [$f = M_{n(theo)}/M_{n(NMR)}$]. The low f value can be attributed to the low solubility of the perfluoro-initiator in SMA. Nevertheless, the F_{10}−$PSMA_z$−N_3 polymers obtained show low polydispersities.

The degree of polymerization (DP) of the PSMA blocks of the PPO_{34}−$PSMA_y$ copolymers is determined from the ^{1}H NMR spectra using the relation $I_e/I_c \times 34$, where I_e/I_c corresponds to the ratio of the integral of the PSMA backbone CH_3 signal to that of the PPO CH_3 signal The DP of the PSMA blocks of the F_{10}−$PSMA_z$−N_3 polymers is estimated from the ^{19}F NMR spectra recorded in DMSO-d_6 solutions which contained 0.2 vol % TFT as an internal reference standard, using the relation $5I_p/3I_{TFT} \times A$, where A corresponds the ratio of the integral of the CF_3 signal from TFT to that of the polymer in the ^{19}F NMR spectrum. I_p and I_{TFT} denote the integral values of the backbone methyl protons of the polymer and the phenyl protons of TFT, respectively, in the ^{1}H NMR

Scheme 1. Synthetic Route to Triphilic $F_{10}-PGMA_z-PPO_{34}$ block copolymers

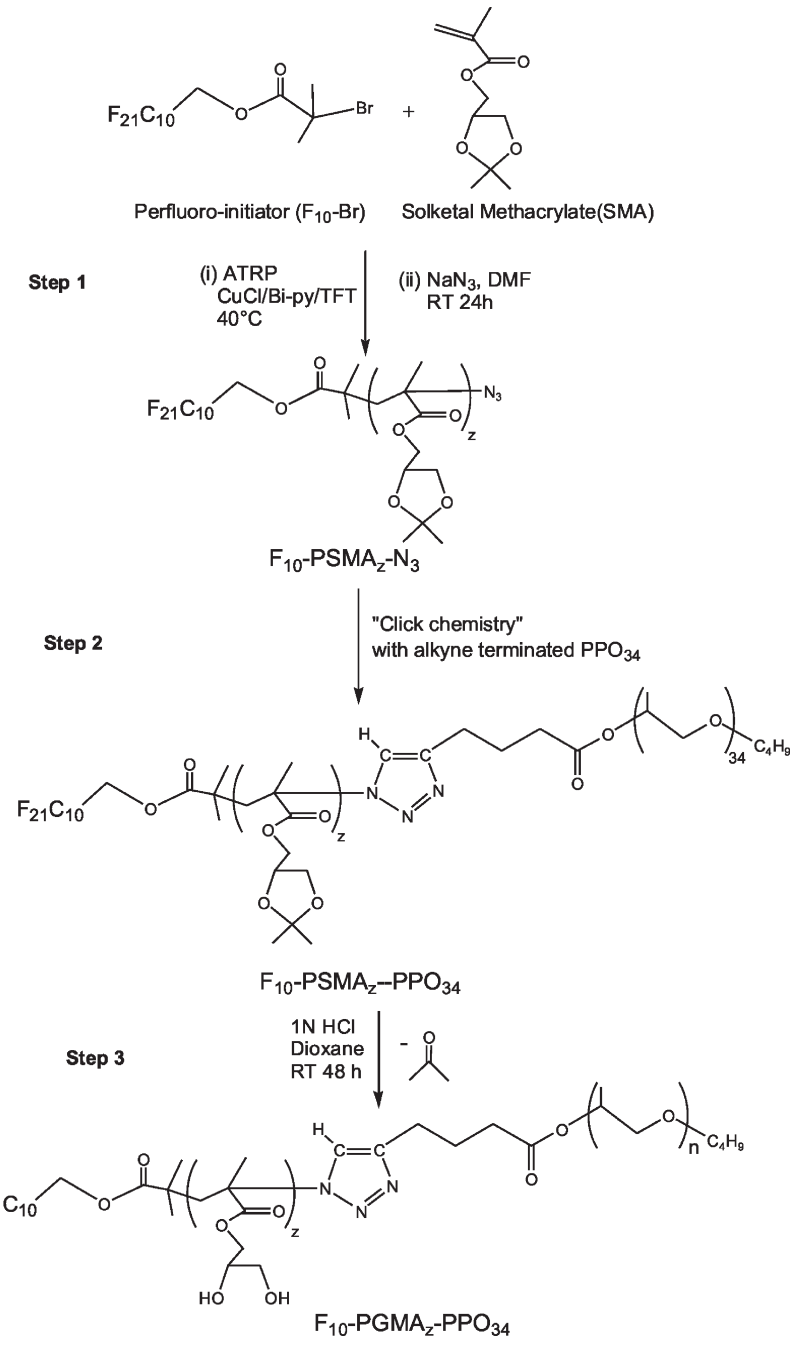


Table 1. Degree of Polymerization (DP), Molar Mass (M_n), and Polydispersity (M_w/M_n) of Polymers Synthesized (Prior to Cleaving PSMA)

	DP PSMA		SEC	
polymer	^{1}H NMR (y)	^{19}F NMR (z)	M_n (g/mol)	M_w/M_n
$F_{10}-PSMA_z-N_3$ (**1**)		85	7300	1.2
$F_{10}-PSMA_z-N_3$ (**2**)		66	6500	1.4
$PPO_{34}-PSMA_y$ (**3**)	66		12 000	1.4
$PPO_{34}-PSMA_y$ (**4**)	37		10 000	1.3
$F_{10}-PSMA_z-PPO_{34}$ (**5**)	93	85	8500	1.3
$F_{10}-PSMA_z-PPO_{34}$ (**6**)	84	66	7500	1.4

spectrum. Although the DP values of the perfluoro end-capped polymers determined from ^{19}F NMR spectroscopy are high, their corresponding SEC based M_n values are comparatively low as given in Table 1. This discrepancy is presumably due to the presence of the high fluorine containing moiety at the polymer chain end which can reduce the hydrodynamic volume of polymer chains or cause specific interaction with the column. Similar observations have been made for fluorine containing polymers by other authors.[29,30]

The efficiency afforded by CuAAC has influenced the field of macromolecular engineering in many ways.[24] Many CuAAC reactions have proven capable of coupling preexisting homopolymers to prepare block copolymers in a modular and highly efficient manner.[31−34] Benefits that arise from employing a modular method of this type is that each block can be individually characterized prior to coupling, and block copolymers can be prepared from monomers that cannot be polymerized by the same polymerization technique. Opsteen and van Hest first demonstrated the possibility

Table 2. Molar Mass, Polydispersity, and Critical Micellization Concentration (cmc) of the Synthesized Amphiphilic and Triphilic Block Copolymers

block copolymer	analogous block architecture	philicity	NMR M_n (g/mol)	SEC[c] M_w/M_n	cmc (μM)
$F_{10}-PGMA_{85}-PPO_{34}$	CAB	triphilic	16300[a]	1.4	0.85[d]
$F_{10}-PGMA_{66}-PPO_{34}$	CAB	triphilic	13300[a]	1.3	0.80[d]
$PPO_{34}-PGMA_{66}$	BA	amphiphilic	12600[b]	1.4	12.0[e]
$PPO_{34}-PGMA_{37}$	BA	amphiphilic	7900[b]	1.3	10.0[e]
[f]$PPO_{27}-PGMA_{44}$	BA	amphiphilic	8800[b]	1.2	12.4[e]
[f]$F_9-PPO_{27}-PGMA_{94}$	CBA	triphilic	17400[b]	1.4	1.3[e]

[a] Calculated from ^{19}F NMR spectroscopy. [b] Calculated from ^{1}H NMR spectroscopy. [c] Obtained from measurements of unhydrolyzed polymers in THF with polystyrene calibration standards. cmc (critical micellization concentration). [d] Determined at 8 °C. [e] Determined at 25 °C. [f] Synthesis is described in ref 25.

to prepare a library of AB[35] or ABC[34] block copolymers by coupling various combinations of azido- or alkyne-terminated polymers by CuAAC.

The postpolymerization halogen end-group modification of the $F_{10}-PSMA_z$ polymers with NaN_3 in DMF to give ω-azido-terminated polymers ($F_{10}-PSMA_z-N_3$) is confirmed by the appearance of the azide absorption band at 2112 cm^{-1} in the FTIR spectrum of the polymers after purification. Coupling the ω-azido-terminated polymers with $PPO_{34}-C\equiv CH$ via CuAAC in the presence of CuBr, DIPEA and TBTA afforded $F_{10}-PSMA_z-PPO_{34}$ block copolymers. Investigations have shown that the presence of small quantities of the polytriazole ligand, TBTA, stabilizes the Cu(I) species and help drive the reaction to completion.[36] The completion of the reaction is confirmed by the disappearance of the azide band in the FTIR spectrum of the product as shown in Figure S4. Accordingly, there is an increase in the intensities of the CH_3 symmetric and asymmetric stretching vibration bands at 2887 and 2988 cm^{-1}, respectively, due to the contributions from the coupled PPO block. Furthermore, the CH_2 stretching vibration at 2947 cm^{-1} and the band at 1085 cm^{-1} corresponding to the ether linkage also increased in intensities due to the contributions from the PPO block. Analysis of the ^{1}H NMR spectrum of the product showed the usual resonance signals attributable to the PPO protons. The increase in M_n after the coupling reactions is reflected in the SEC results given in Table 1 for entries 5 and 6.

Assuming all the polymer chains of $F_{10}-PSMA_z-N_3$ are 100% N_3 terminated, then, the DP of the PSMA block can be estimated from the ^{1}H NMR spectrum after coupling with the PPO block using the usual relation $I_e/I_c \times 34$ (the notations are explained above). Table 1 lists the DP values of the PSMA blocks of the $F_{10}-PSMA_z-PPO_{34}$ block copolymers obtained from ^{1}H NMR spectroscopy by this method. It can be realized that there is an apparent difference between these DP values and those obtained from ^{19}F NMR spectroscopy. This may be due to the fact that for polymers prepared by ATRP, the percentage of chains capped by halogen atoms (which are eventually substituted with N_3 in the azidation reaction) is less than 100% because of radical termination and other side reactions which occur during the polymerization.[37,38] However, traces of the $F_{10}-PSMA_z-N_3$ precursor polymer either as a shoulder peak or a tailing, are not observed in the SEC trace after the coupling reaction (Figure S5, Supporting Information). Thus, the apparent DP values difference may also be due to the different determination techniques, i.e., ^{1}H and ^{19}F NMR spectroscopy.

Water-soluble block copolymers are obtained upon complete acidic hydrolysis of the acetonide rings of the hydrophobic PSMA blocks in 1,4-dioxane to give hydrophilic poly(glycerol monomethacrylate) (PGMA). Thus, the ^{1}H NMR spectra after full hydrolysis of the copolymers showed the complete disappearance of the pendant methyl groups on the SMA units and appearance of the hydroxyl groups as shown in Figure S6. The hydrolyzed block copolymers are designated as $PPO_{34}-PGMA_y$ and $F_{10}-PGMA_z-PPO_{34}$, where the subscripts y and z represent the degree of polymerization as determined from ^{1}H and ^{19}F NMR spectroscopy, respectively. The water-soluble block polymers synthesized can be categorized into amphiphilic and triphilic block copolymers as listed in Table 2.

In addition, the amphiphilic block copolymer, $PPO_{27}-PGMA_{44}$ and the triphilic block copolymer, $F_9-PPO_{27}-PGMA_{94}$, are included in Table 2. The detailed synthesis and characterization of $PPO_{27}-PGMA_{44}$ and $F_9-PPO_{27}-PGMA_{94}$ have been reported previously.[25]

3.2. Aqueous Solution Properties of Block Copolymers. The block copolymers are anticipated to be thermoresponsive in aqueous solution since the PGMA block is permanently hydrophilic, whereas the PPO block becomes increasingly hydrophobic with temperature increase. To further investigate, characterize, and understand the effect of temperature on the aqueous solution behavior of the block copolymers, surface tension, ^{1}H NMR, DLS, and SANS techniques have been employed.

Surface Tension Measurement. For low-molar mass surfactants or amphiphilic block copolymers that self-assemble in solution, the critical micelle concentration (cmc) is an important physical parameter that characterizes such systems. Therefore, surface tension measurements are carried out on aqueous solutions of the block copolymers in order to obtain information on micelle formation. The surface tensions γ are measured as a function of polymer concentrations at 25 °C for the amphiphilic block copolymers and the triphilic $F_9-PPO_{27}-PGMA_{94}$ block copolymer. Plotting γ versus the polymer concentration yields the cmc, indicated by intersection of the extrapolations of the two linear regimes where the curve show abrupt change in slope as illustrated in Figure 2 for $F_9-PPO_{27}-PGMA_{94}$ and $PPO_{34}-PGMA_{66}$. The surface tension data are summarized in Table 2. The cmc values of the amphiphilic block copolymers are about 2 orders of magnitude less than those obtained for the micellization of PPO−PEO and PEO−PPO−PEO block copolymers of comparable composition at similar temperature.[39,40]

This suggests that substitution of the PEO blocks with hydroxyl-bearing PGMA blocks facilitates formation of micelles. A similar trend is also observed when the PEO block is replaced by a hydroxyl-bearing poly(glycidol)(PG) as in PG−PPO−PG triblock copolymers.[41] Intuitively, one will expect a higher hydrophilic character for the PGMA and PG blocks compared to the PEO block, due the presence of the hydroxyl groups on the former. This expected higher hydrophilic character should in turn be reflected in higher cmc values since cmc is known to increase with hydrophilicity.[42] However, the contrary is observed because of the self-association through strong hydrogen bonding in these hydroxyl-bearing blocks.[15,43] The self-association leads to fewer interactions with water molecules,[44] i.e., lower hydrophilicity compared to PEO. Thus, the hydrogen bonding effect in the PGMA- and

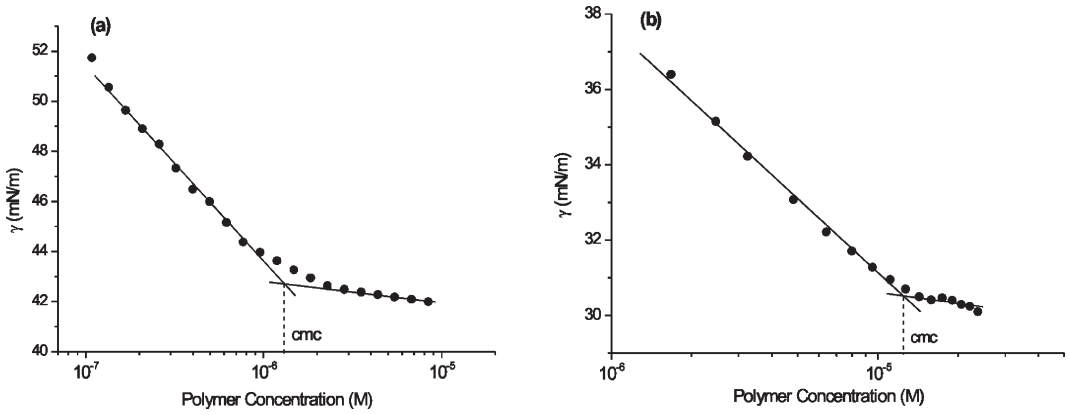


Figure 2. Critical micelle concentration (cmc) determination of (a) $F_9-PPO_{27}-PGMA_{94}$ and (b) $PPO_{34}-PGMA_{66}$ from surface tension measurements as a function of concentration at 25 °C.

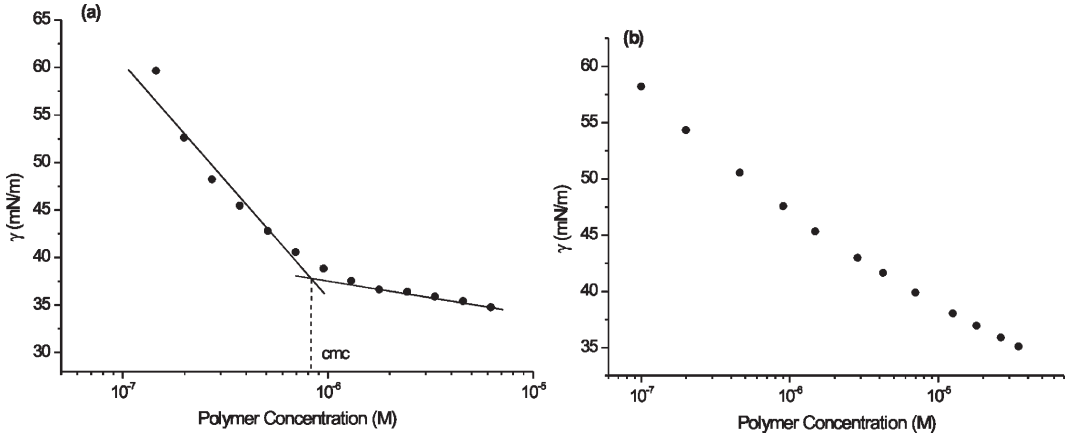


Figure 3. Surface tension measurements as a function of concentration at 8 °C for (a) $F_{10}-PGMA_{66}-PPO_{34}$ aqueous solution and (b) $PPO_{34}-PGMA_{66}$ aqueous solution.

PG-based block copolymers gives them the unexpected lesser hydrophilic character; hence, lower cmc values than their PEO-based counterparts.[41,45]

Interestingly, the aqueous solutions of the triphilic block copolymers $F_{10}-PGMA_{85}-PPO_{34}$ and $F_{10}-PGMA_{66}-PPO_{34}$ show phase separation behavior at room temperature (see DLS discussion). Therefore, the γ measurements are carried out at 8 °C to ascertain whether micelles are formed at temperature below the LCST of the PPO block. The γ measurement curve shown in Figure 3a for $F_{10}-PGMA_{66}-PPO_{34}$ exhibits an abrupt slope change at 0.85 μM, indicating that micelles are indeed formed at this temperature.

This suggests that, at temperatures below the LCST of PPO (around 15 °C for the given molar mass),[21] the highly hydrophobic F_{10} segments at the ends of the PGMA blocks are able to aggregate to form micelle cores.[5,46] Similarly, γ measurements on the aqueous solution of $F_{10}-PGMA_{85}-PPO_{34}$ at 8 °C also show cmc at 0.8 μM. It should be emphasized that γ measurements carried out on $PPO_{34}-PGMA_{66}$ aqueous solution at 8 °C, shown in Figure 3b, reveal a continuous decrease of γ without any abrupt change in slope, thus, indicating lack of micelle formation at this temperature.

DLS Measurements. In order to investigate and understand the influence of the thermoresponsiveness of the PPO block on the aggregation behavior and size of aggregates formed, temperature-dependent DLS measurements are performed on aqueous solutions of the block copolymers. The chosen concentration is about ten times above their cmc as determined from surface tension measurements. Figure 4a shows the evolution of the R_h distribution with temperature for 1.4 g/L aqueous solution of $PPO_{34}-PGMA_{66}$.

At 5 °C a multimodal R_h peak distribution is obtained. The peak with R_h at 3.4 nm corresponds to unimer species while the broad bimodal peak distribution at 186 nm is a result of aggregates formed by unimer-clustering through hydrogen bonding of the hydroxyl groups of the PGMA block.[15] On increasing temperature to 15 °C, the unimer peak diminishes and the aggregate peak transforms into a monodal peak with R_h = 80 nm. These changes signify the transition of the block copolymer chains into micelles as the PPO blocks become hydrophobic. At 25 °C, only a single narrow peak distribution with R_h of 18 nm is obtained in solution. This distribution corresponds to micelles which are composed of hydrophobic PPO core stabilized by hydrophilic PGMA chains which serve as corona. Similarly, micelles with R_h of 14 and 21 nm are obtained for aqueous solutions of $PPO_{27}-PGMA_{44}$ and $F_9-PPO_{27}-PGMA_{94}$, respectively.

On the contrary, at 5 °C, $F_{10}-PGMA_{66}-PPO_{34}$ aqueous solution (1.4 g/L) showed a monomodal peak distribution with R_h of ~50 nm as shown in Figure 4b. This suggests that while the PPO block is still hydrophilic at 5 °C, the highly hydrophobic perfluoro F_{10} segments at the ends of the PGMA blocks are able to aggregate to form micelles. The observation is in agreement with the above discussions on the surface tension behavior of $F_{10}-PGMA_{66}-PPO_{34}$ at temperature below the LCST of the PPO block. Increasing the temperature to 15 °C (around the LCST of the PPO component) leads to the appearance of a new peak at R_h = 460 nm. The new peak

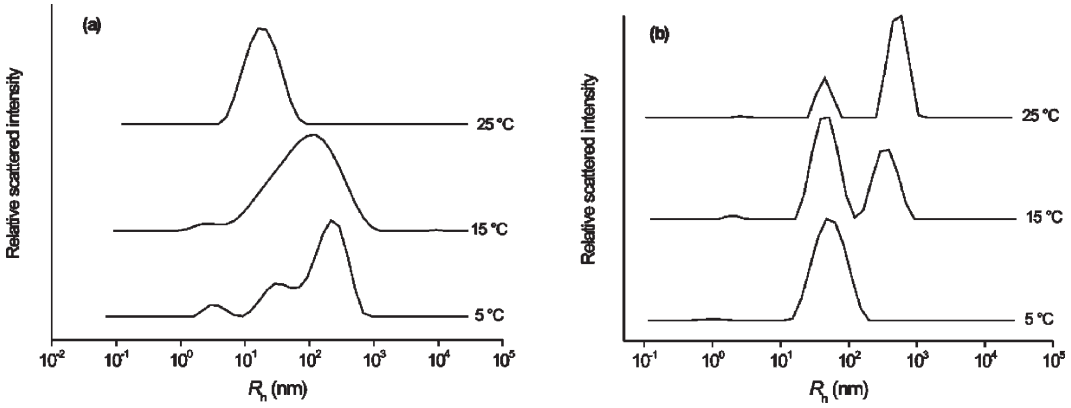


Figure 4. DLS data obtained at $\theta = 90°$ for hydrodynamic radii R_h distributions as a function of temperature for 1.4 g/L aqueous solution of (a) $PPO_{34}-PGMA_{66}$ and (b) $F_{10}-PGMA_{66}-PPO_{34}$.

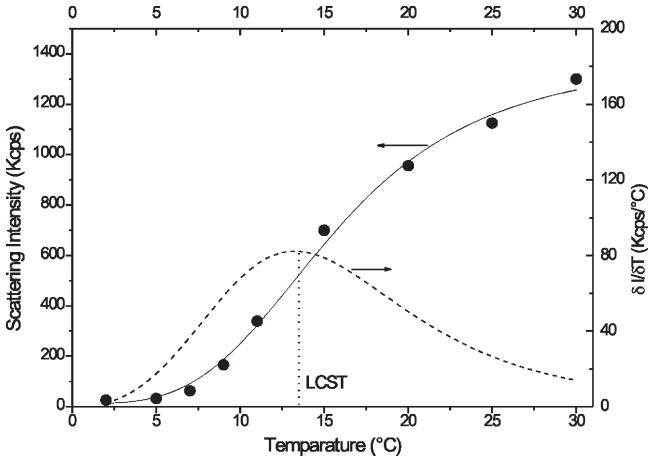


Figure 5. Temperature dependence of scattered light intensity data obtained at $\theta = 90°$ for 5 g/L aqueous solution of $F_{10}-PGMA_{66}-PPO_{34}$ (●). The solid line is obtained from the data fitting while the dash line curve is the corresponding derivative from which the LCST is taken as the maximum.

increases in intensity and size ($R_h = 546$ nm) at the expense of the micelle peak on increasing temperature to 25 °C. Visual inspection of the polymer solution at this point confirmed a macroscopically phase-separated (cloud) solution. The increase of scattered light intensity as a function of temperature is used to determine the LCST for 5 g/L aqueous solution of $F_{10}-PGMA_{66}-PPO_{34}$. The LCST value is determined as the maximum point of the first derivative curve ($\delta I/\delta T$) as shown in Figure 5. A value of 13 °C is estimated for the $F_{10}-PGMA_{66}-PPO_{34}$ solution by this method.

As schematically illustrated in Figure 6, at temperatures where the PPO block is hydrophilic alongside the PGMA block, the presence of the highly hydrophobic perfluoro segments at the ends of the PGMA blocks causes micellization of $F_{10}-PGMA_{66}-PPO_{34}$ block copolymer in aqueous solution. Thus, the PGMA−PPO blocks serve as coronae of the formed fluorocarbon core micelles. However, as temperature is increased, the PPO blocks become increasingly hydrophobic. Eventually, at around 13 °C, the PPO component of the micelle coronae collapses and aggregates leading to clustering of the micelles which is macroscopically manifested as LCST behavior.

As pointed out recently, for both the PPO block and the perfluoro segment to fully coexist in the same core, the PPO blocks must be rendered hydrophobic through dehydration at temperatures well above its lower critical solution temperature (LCST).[15] Given this condition, it means when the PPO blocks become insoluble at temperatures just above its LCST, they will still be forced to stay outside the fluorocarbon core micelles even though the middle PGMA block is long enough to loop.[15] Preferentially, the insoluble PPO blocks of the micelles start to interact with each other, which in principle, should lead to formation of a two-compartment micellar network. However, it seems that the hydrophilic PGMA blocks are ineffective in stabilizing this micellar network at this temperature, thus, resulting in phase-separation. Two reasons could possibly account for the inability of the hydrophilic PGMA to stabilize the two-compartment micellar network in this case.

(i) It has been shown, that hydroxyl bearing hydrophilic polymers such as PGMA and PG interact less effectively with water at 25 °C, behaving as polymer coils in poor solvent.[44,47] This can be attributed to the effect of self-association through H-bonding that occurs among the hydroxyl groups, thus, limiting the number of hydroxyl sites available for effective interaction with water.[44]

(ii) Fluorocarbon-based micelles in water adopt flat disklike interface due to strong interfacial tension that exist between the fluorocarbon core and water.[48,49] It has been argued that hydrophobic disk edges are enthalpically unfavorable in aqueous environment. To circumvent the enthalpic penalty of fluorocarbon core/water interface, the fluorocarbon core may crowd its surface with PGMA chains; thereby expelling water from the interface.[20] This will also lessen the effective interaction of the PGMA chains with water.

Temperature-Dependent ^1H NMR Measurements. The thermoresponsive behavior of $PPO_{34}-PGMA_{66}$ and $F_{10}-PGMA_{66}-PPO_{34}$ is further studied by temperature-dependent ^1H NMR spectroscopy in D_2O. Generally, the effect of temperature on the mobility and collapse of polymer chains in solution can be followed by monitoring the variations in the relative peak width and intensity in the spectra.[50] Figure 7 shows the ^1H NMR spectra of the methyl protons of the PPO ($PPO-CH_3$) and the PGMA ($PGMA-CH_3$) blocks of $PPO_{34}-PGMA_{66}$ and $F_{10}-PGMA_{66}-PPO_{34}$ at 7, 15, 25, and 40 °C in D_2O. At 7 °C, the resonance signals at 0.63 and 0.76 ppm correspond to the syndiotactic rr and heterotactic rm triads of the $PGMA-CH_3$, respectively, while the signal at 0.84 ppm correspond to the $PPO-CH_3$.[15]

Clearly, at 7 °C the $PGMA-CH_3$ signals are more prominent for $F_{10}-PGMA_{66}-PPO_{34}$ (Figure 7b) than $PPO_{34}-PGMA_{66}$ (Figure 7a). This is indicative for a higher solubility

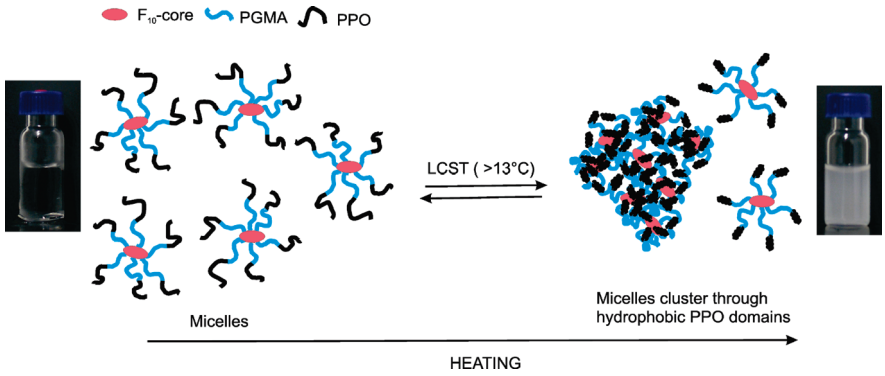


Figure 6. Schematic representation of micelle structures and aggregates obtained as a result of increasing temperature of 5 g/L aqueous solution of $F_{10}-PGMA_{66}-PPO_{34}$.

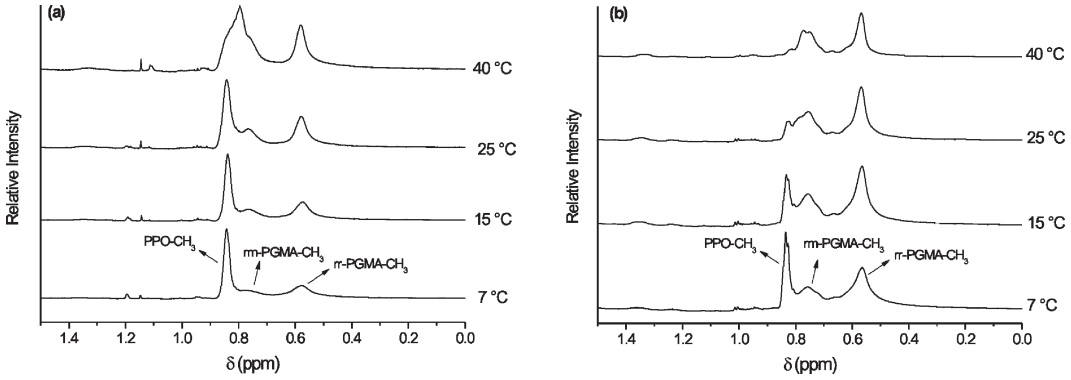


Figure 7. ^{1}H NMR spectra at 600 MHz of 10 g/L: (a) $PPO_{34}-PGMA_{66}$ and (b) $F_{10}-PGMA_{66}-PPO_{34}$ in D_2O at different temperatures, showing the $PGMA-CH_3$ and $PPO-CH_3$ resonance signals.

and mobility of the PGMA blocks in aqueous environment of $F_{10}-PGMA_{66}-PPO_{34}$ compared to $PPO_{34}-PGMA_{66}$. This solubility difference can be attributed to the fact that below the micellization temperature a significant amount of the PGMA chains of $PPO_{34}-PGMA_{66}$ exist as unimer-clusters through H-bonding as observed in the DLS measurements (see Figure 4a). On increasing temperature to 15 °C, the $PPO-CH_3$ signal intensity for $F_{10}-PGMA_{66}-PPO_{34}$ is strongly reduced and continues to do so as temperature is further increased to 25 °C. At 40 °C, the signal completely disappears. The strong reduction and eventual disappearance of the $PPO-CH_3$ signal is due to the collapse of the PPO component of $F_{10}-PGMA_{66}-PPO_{34}$ as temperature is raised to 15 °C and above.

On the contrary, for $PPO_{34}-PGMA_{66}$, the $PPO-CH_3$ signal reduces in intensity and broadens as temperature is raised to 15 °C and above. In addition, the $PPO-CH_3$ signal also shifts upfield as temperature is raised and eventually overlaps with the heterotactic rm signal of $PGMA-CH_3$ at 40 °C. The reduction and broadening of the $PPO-CH_3$ signal of $PPO_{34}-PGMA_{66}$ is due to the reduced mobility the PPO blocks. These significant changes in the $PPO-CH_3$ signal are indicative of the PPO blocks being in the microenvironment of a micelle core.[50,51] The upfield shift of the $PPO-CH_3$ signal with temperature, and its eventual overlap with the heterotactic rm signal of $PGMA-CH_3$ at 40 °C, is due to the dehydration of the PPO blocks within the liquid-like micelle core as temperature is increased.[15]

Also, the $PGMA-CH_3$ signals of $PPO_{34}-PGMA_{66}$ increase in intensity and narrow with increasing temperature. This behavior can be attributed to H-bonding weakening between the partially self-associated PGMA blocks resulting in increasing solubility and mobility of the PGMA blocks in the aqueous medium.[15]

Thus, the temperature-dependent behavior of the ^{1}H NMR spectra of $PPO_{34}-PGMA_{66}$ and $F_{10}-PGMA_{66}-PPO_{34}$ in aqueous medium supports their aggregation behavior as observed by DLS.

SANS Measurements. To obtain further information about the structural features of the micelles formed by $PPO_{34}-PGMA_{66}$, $PPO_{27}-PGMA_{44}$ and $F_9-PPO_{27}-PGMA_{94}$, SANS measurements at 15, 20, and 40 °C, for 0.6 wt % D_2O solutions of the copolymers are carried out. As with the chosen concentration micelle−micelle interactions should be negligible and the obtained SANS profiles reflect mainly the micelle form factor.[52] It is observed that the scattering profiles of $PPO_{27}-PGMA_{66}$ and $PPO_{34}-PGMA_{66}$ are dominated by contribution from the PPO core. The outer hydrated PGMA shell gives a small contribution at low q-values but due to the limited q-range of our measurement and the low scattering intensity from this part, it is treated as background and not discussed within this investigation. A hard sphere model is not able to describe the PPO core due to a dehydration gradient from outer to inner part of the core.[53] Therefore, the fitting model consists of a radially decreasing PPO density, following a $r^{-\alpha}$ power law, with a maximum outer core radius r_0. Typical values for the exponent are $\alpha = 2$ in case of stretched chains or $\alpha = {}^4/_3$ for star like micelles. To prevent the unphysical infinite density in the limit $r \rightarrow 0$, the center of the core was set to neat PPO scattering length density of 0.347×10^{-14} cm Å^{-3}.[54] The radial size of this center part, r_i is slightly varied (approximately 10%, log-normal distribution) to remove sharp fringes and is typically in the range of 1−2 nm for all fitted curves. The r_0 and α values are also varied during the fitting procedure.

Figure 8 shows the SANS profiles of $PPO_{27}-PGMA_{66}$ and $PPO_{34}-PGMA_{44}$ obtained at various temperatures together with their corresponding fitting curves. The curves

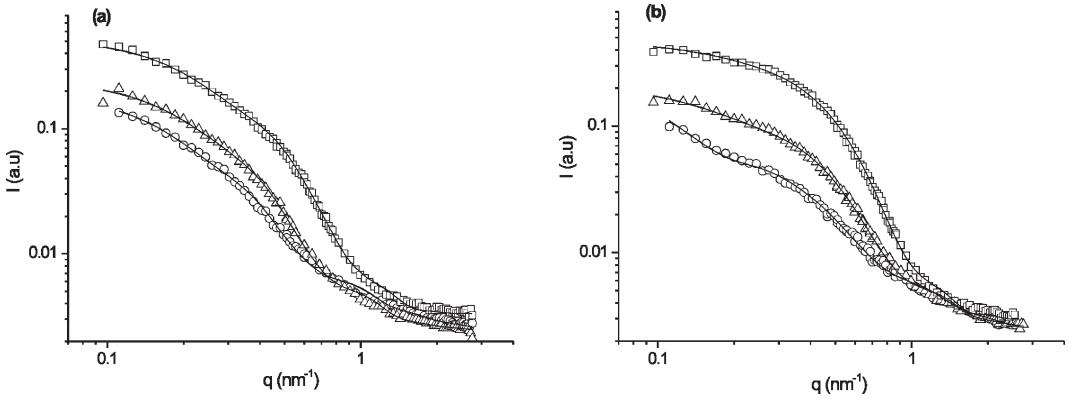


Figure 8. SANS profiles of 0.6 wt % D_2O solution of (a) $PPO_{27}-PGMA_{44}$ and (b) $PPO_{34}-PGMA_{66}$ at 15 (○), 20 (Δ), and 40 °C (□).The solid curves represent the fits using the $R^{-\alpha}$ model and the fitted parameters are given in Table 3.

Table 3. Fitting Parameters Obtained from Model for 0.6 wt % D_2O Solution of $PPO_{34}-PGMA_{66}$, and $PPO_{27}-PGMA_{44}$ at 15, 20, and 40 °C

sample	temperature (°C)	α	core radius r_0 (nm)
$PPO_{34}-PGMA_{66}$	15	2.1	8.5
	20	2.1	7.4
	40	2.3	5.8
$PPO_{27}-PGMA_{44}$	15	2.2	7.2
	20	2.0	6.0
	40	2.2	5.3

show the typical scattering profile of a particle with spherical density profile. Table 3 lists the obtained r_0 and α values after the fitting process. The increase in total scattering intensity at low q values might originate from a change in the aggregation number, but also a contribution of the structure factor cannot be omitted.

As seen in Table 3 the PPO core radius decreases with increasing temperature for both block copolymers reaching about 70% of their initial values at 40 °C. This decrease in core radius on increasing temperature can be attributed dehydration of the PPO core.[55]

At any given temperature, the core radius of $PPO_{34}-PGMA_{66}$ is approximately 10−20% larger than $PPO_{27}-PGMA_{44}$, which can be attributed to the larger molar mass of the PPO block of $PPO_{34}-PGMA_{66}$. It can be seen from Table 3 that the exponent α remains at approximately 2, indicating that the PPO chains at the core/shell interface are in stretched-chain conformation directed toward the attached PGMA chains.

In contrast, the SANS profile of the triphilic $F_9-PPO_{27}-PGMA_{94}$ sample is remarkably different from the amphiphilic counterparts at all temperatures under investigation. In Figure 9 the Holtzer plot (Iq vs q, here with logarithmic q axis for better resolution in the small q regime) of the scattering data for the samples $F_9-PPO_{27}-PGMA_{94}$ and $PPO_{27}-PGMA_{44}$ measured at 15 °C are depicted together with the SANS profiles (inset, a constant background contribution is subtracted for more clarity). In this plot, horizontal tangents indicate a stiff or rodlike behavior of the scatterers.[56] It is obvious that the prominent spherical shape (the step in the curve) observed for $PPO_{27}-PGMA_{44}$ is almost absent in case of the fluorinated species. The transition between spherical and rod like shape is indicated by q^{*1}. In case of single molecules, a persistence length of $l_k = 1.9/q^{*1} = 2$ nm can be calculated from this behavior.[57] This value is in agreement with typical values of PGMA[15] or could indicate the PPO stretching, as PPO has in relaxed morphology a typical persistence length of ~0.5 nm.[58]

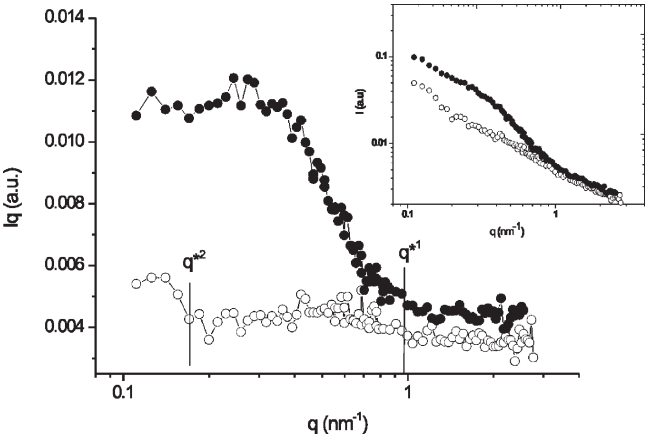


Figure 9. Holtzer plot of the SANS profiles of 0.6 wt % D_2O solutions of $PPO_{27}-PGMA_{44}$ (●) and $F_9-PPO_{27}-PGMA_{94}$ (○) at 15 °C. The inset shows the corresponding SANS profiles.

The $F_9-PPO_{27}-PGMA_{94}$ sample shows also a similar transition region, although, the change in intensity is much less. Furthermore, a second rod like structure with a typical persistence length of 11 nm is calculated from q^{*2}. We assume that the high orientation of the perfluorocarbon domains when the F_9 segments aggregate (as observed in the TEM image discussed in the next section) coupled with the strong segregation between the perfluorocabon and PPO domains within the core is responsible for the remarkably different scattering profile of $F_9-PPO_{27}-PGMA_{94}$ micelles. Similar observations are discussed by Zhou et al.[2] on the SANS profile of the aqueous micellar solution obtained after fluorination of the butadiene component of poly(butadiene)-*b*-poly(styrene)-*b*-poly(ethylene oxide). The authors note that the spherical-core micelle SANS profile of the hitherto amphiphilic block copolymer was dramatically changed to ellipsoidal profile after rendering the block copolymer "triphilic". They attributed the change to the strong segregation between the perfluorocarbon and hydrocarbon components within the core of the micelle.

3.3. AFM and TEM Investigations on Polymer Aggregates. Additional information about the shape and size of the self-assembled structures formed by $F_{10}-PGMA_{66}-PPO_{34}$ and $PPO_{34}-PGMA_{66}$ are obtained from AFM measurements at room temperature. Figure 10a shows the height image of $PPO_{34}-PGMA_{66}$ aggregates obtained after coating a silicon substrate with 1.4 g/L aqueous polymer solution, drying for 2 min, followed by washing with bidistilled water and drying overnight at room temperature.[59] Fortuitously, the image reveals spherical structures with diameter of 28−32 nm

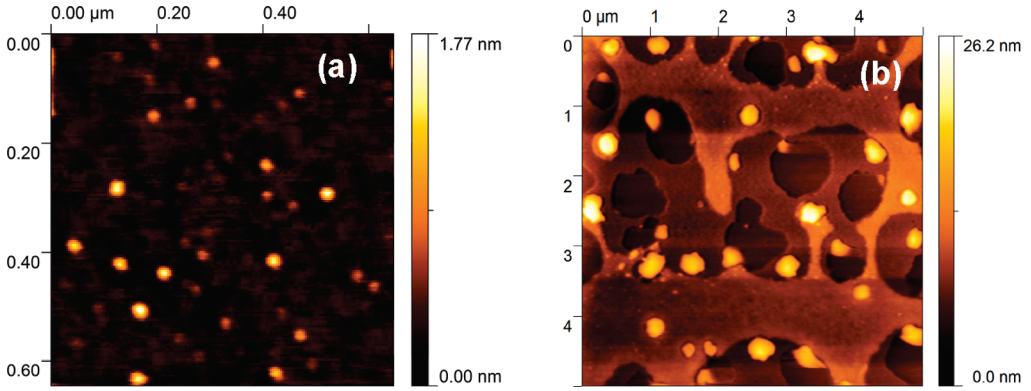


Figure 10. Height image obtained after coating a silicon substrate with 1.4 g/L aqueous polymer solution of (a) $PPO_{34}-PGMA_{66}$, and (b) $F_{10}-PGMA_{66}-PPO_{34}$ (for preparation details see text).

which is slightly smaller than the micellar diameter of 36 nm (R_h = 18 nm) observed for aqueous $PPO_{34}-PGMA_{66}$ solution at 25 °C.

Figure 10b shows the height image of aggregated structures formed by $F_{10}-PGMA_{66}-PPO_{34}$. The sample is prepared under conditions similar to $PPO_{34}-PGMA_{66}$, except that coating is done at 5 °C before drying overnight at room temperature. Large irregular aggregates with size ranging from 200 to 400 nm can be seen embedded in double layered sheets with thickness of ~2.5 nm each. The observed sheets can be attributed to formation of a two-compartment micellar network.[20] As opposed to what is observed in bulk aqueous solution, it seems that the presence of the solid support helps stabilize the initially formed micelle network structure to form the sheets. Nevertheless, some regions of the network remain unstable and thus aggregate into the large irregular structures observed in the image.

Because of the linking sequence and the incompatibility between the perfluoro segment and PPO, $F_9-PPO_{27}-PGMA_{94}$ is expected to segregate into fluorocarbon- and PPO-rich domains when it self-assembles. Therefore, TEM imaging is carried out on the $F_9-PPO_{27}-PGMA_{94}$ copolymer. Figure 11 shows the TEM image obtained on a carbon coated copper grid after coating with 0.014 g/L aqueous polymer solution followed by evaporation of water at room temperature.

Although, the concentration of the solution used is slightly below the cmc, it should be realized that as water slowly evaporates from the surface the cmc threshold will be passed and micelles or well-defined aggregates will be formed during this process. This preparative method is adopted because initial attempts using solution with concentration much higher than cmc resulted in TEM images showing only polymer films. The image shows large supramolecular structures with lengths in the range of 300−900 nm. The driving forces responsibly for the supramolecular self-organization of $F_9-PPO_{27}-PGMA_{94}$ into such structures are, multiple intra- and interchain hydrogen bonds in the hydrophilic PGMA blocks,[43] lipophilic association of the PPO blocks, and fluorophilic association of the perfluoro segment. During the self-organization because the PPO and perfluoro segments are hydrophobic, they self-assemble inside the structure formed to minimize contact with water. However, due to the incompatibility between PPO and perfluoro segments, they segregate nanoscopically to give ~30 nm thick fluorocarbon-rich domains which appear as dark stripes in the TEM image as observed for different block copolymers.[13] The PPO and PGMA components of the aggregates appear as white and gray contrast, respectively, in the image.

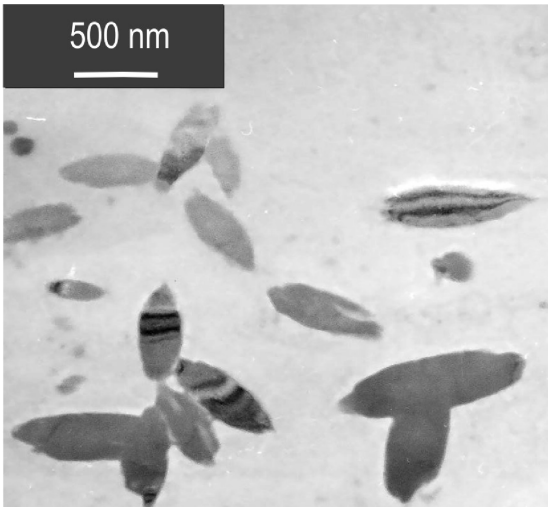


Figure 11. Transmission electron microscopy (TEM) image of $F_9-PPO_{27}-PGMA_{94}$ obtained after coating the grid with 0.014 g/L aqueous polymer solution and evaporation of water at room temperature.

In fact, the behavior of the perfluoroalkyl segments is in agreement with theoretical predictions by Semenov, Khokhlov, and co-workers who identified a new regime of phase behavior that they dubbed "superstrong segregation".[60,61] In this regime, the repulsive interactions between two adjoining blocks become so strong that the interfacial energy overwhelms the conformational entropy or coronal crowding, as such, the minor block becomes nearly stretched out completely.[60]

4. Conclusions

Water-soluble amphiphilic BA diblock copolymers and triphilic CAB triblock copolymer analogues have been synthesized by ATRP and "click" chemistry. The aggregation behavior of the triphilic CAB triblock copolymer analogues, $F_{10}-PGMA_{66}-PPO_{34}$ and $F_{10}-PGMA_{85}-PPO_{34}$, in water has been investigated and compared with the amphiphilic diblock counterparts, $PPO_{34}-PGMA_{66}$ and $PPO_{27}-PGMA_{44}$, and the triphilic CBA counterpart, $F_9-PPO_{27}-PGMA_{94}$. It is found that while the amphiphilic block copolymers and the triphilic $F_9-PPO_{27}-PGMA_{94}$ form clear micellar solutions, $F_{10}-PGMA_{66}-PPO_{34}$ and $F_{10}-PGMA_{85}-PPO_{34}$ solutions exhibit phase-separation above 13 °C. However, at temperatures below the LCST of the PPO block component, $F_{10}-PGMA_{66}-PPO_{34}$ and $F_{10}-PGMA_{85}-PPO_{34}$ form clear solutions containing fluorocarbon core micelles. As observed by DLS measurement and also confirmed by AFM

measurement, the phase separation is due to formation of large micellar clusters with $R_h \sim 500$ nm as temperature is raised above the LCST of the PPO component. It seems the clustering effect is due to the inability of the hydrophilic PGMA blocks to stabilize the resulting two-compartment micellar network formed through hydrophobic PPO junctions between the fluorocarbon core micelles.

Comparatively, the $F_9-PPO_{27}-PGMA_{94}$ architecture cannot form such two-compartment micellar network because the perfluoroalkyl segment and the PPO block are covalently linked. However, they segregate into fluorocarbon and PPO-rich domains when they self-assemble as observed in the TEM image. Furthermore, the segregation between the perfluoroalkyl segments and PPO is reflected in the nonspherical shape of $F_9-PPO_{27}-PGMA_{94}$ micelle cores in comparison to the spherical shape of $PPO_{34}-PGMA_{66}$ and $PPO_{27}-PGMA_{44}$ micelle cores as observed by SANS measurements.

Acknowledgment. We thank the Deutsche Forschungsgemeinschaft (DFG), FOR 1145 for the financial support, Robert Sachsenhofer (Chemistry Department) and Thomas Thurn-Albrecht (Physics Department) of Martin Luther University for their assistance with the TEM and AFM images, respectively. We thank J. Balbach and S. Gröger for NMR support (Net-T3 (BMBF)). Significant investments into the NMR infrastructure from the European Regional Development Fund (ERDF) by the European Union are also gratefully acknowledged.

Supporting Information Available: Experimental details for synthesis of the ATRP initiators, synthesis of polymers, ^{1}H NMR spectra of polymers, SEC traces, and FTIR spectra of the polymers. This material is available free of charge via the Internet at http://pubs.acs.org.

References and Notes

(1) Li, Z.; Hillmyer, M. A.; Lodge, T. P. *Langmuir* **2006**, *22*, 9409–9417.
(2) Zhou, Z.; Li, Z.; Ren, Y.; Hillmyer, M. A.; Lodge, T. P. *J. Am. Chem. Soc.* **2003**, *125*, 10182–10183.
(3) Thünemann, A. F.; Kubowicz, S.; Berlepsch, H. v.; Möhwald, H. *Langmuir* **2006**, *22*, 2506–2510.
(4) Weberskirch, R.; Preuschen, J.; Spiess, H. W.; Nuyken, O. *Macromol. Chem. Phys.* **2000**, *201*, 995–1007.
(5) Kubowicz, S.; Thünemann, A. F.; Weberskirch, R.; Möhwald, H. *Langmuir* **2005**, *21*, 7214–7219.
(6) Mao, J.; Ni, P.; Mai, Y.; Yan, D. *Langmuir* **2007**, *23*, 5127–5134.
(7) Lodge, T. P.; Hillmyer, M. A.; Zhou, Z. *Macromolecules* **2004**, *37*, 6680–6682.
(8) Zhao, Y.; Liu, Y.-T.; Lu, Z.-Y.; Sun, C.-C. *Polymer* **2008**, *49*, 4899–4909.
(9) Zhang, H.; Ni, P.; He, J.; Liu, C. *Langmuir* **2008**, *24*, 4647–4654.
(10) Lodge, T. P.; Rasdal, A.; Li, Z.; Hillmyer, M. A. *J. Am. Chem. Soc.* **2005**, *127*, 17608–17609.
(11) Ott, C.; Hoogenboom, R.; Hoeppener, S.; Wouters, D.; Gohy, J.-F.; Schubert, U. S. *Soft Matter* **2009**, *5*, 84–91.
(12) Kubowicz, S.; Baussard, J.-F.; Lutz, J.-F.; Thünemann, A. F.; Berlesch, H.; Laschewsky, A. *Angew. Chem., Int. Ed.* **2005**, *44*, 5262–5265.
(13) Skrabania, K.; Laschewsky, A.; Berlepsch, H.v.; Böttcher, C. *Langmuir* **2009**, *25*, 7594–7601.
(14) (a) Berlepsch, H.v.; Böttcher, C.; Skrabania, K.; Laschewsky, A. *Chem. Commun.* **2009**, 2290–2292. (b) Fang, B.; Walther, A.; Wolf, A.; Xu, Y.; Yuan, J.; Müller, A. H. E. *Angew Chem. Int. Ed.* **2009**, *48*, 2877–2880.
(15) Kyerematen, S. O.; Henze, T.; Busse, K.; Kressler, J. *Macromolecules* **2010**, *43*, 2502–2511.
(16) Skrabania, K.; Berlepsch, H. V.; Boöttcher, C.; Laschewsky, A. *Macromolecules* **2010**, *43*, 271–281.
(17) Hillmyer, M. A.; Lodge, T. P. *J. Polym. Sci., A: Polym. Chem.* **2002**, *40*, 1–8.
(18) Shunmugam, R.; Simth, C. E.; Tew, G. N. *J. Polym. Sci., A: Polym. Chem.* **2007**, *45*, 2601–2608.
(19) Taribagil, R. R.; Hillmyer, M.; Lodge, T. P. *Macromolecules* **2009**, *42*, 1796–1800.
(20) Taribagil, R. R.; Hillmyer, M.; Lodge, T. P. *Macromolecules* **2010**, *43*, 5396–5404.
(21) Save, M.; Weaver, J. V. M.; Armes, S. P.; McKenna, P. *Macromolecules* **2002**, *35*, 1152–1159.
(22) Xu, J.; Ge, Z.; Zhu, Z.; Luo, S.; Liu, H.; Liu, S. *Macromolecules* **2006**, *39*, 8178–8185.
(23) Tsarevsky, N. V.; Sumerlin, B. S.; Matyjaszewki, K. *Macromolecules* **2005**, *38*, 3558–3561.
(24) Sumerlin, B. S.; Vogt, A. P. *Macromolecules* **2010**, *43*, 1–13.
(25) Kyerematen, S. O.; Amado, E.; Blume, A.; Kressler, J. *Macromol. Rapid Commun.* **2008**, *29*, 1140–1146.
(26) Coessens, V.; Nakagawa, Y.; Matyjaszewski, K. *Polym. Bull.* **1998**, *40*, 135–142.
(27) Kyerematen, S. O.; Amado, E.; Kressler, J. *Eur. Polym. J.* **2007**, *43*, 3380–3391.
(28) Lutz, J.-F.; Matyjaszewki, K. *J. Polym. Sci., Part A: Polym. Chem.* **2005**, *43*, 897–910.
(29) Hussain, H.; Budde, H.; Höring, S.; Busse, K.; Kressler, J. *Macromol. Chem. Phys.* **2002**, *203*, 2103–2112.
(30) Radhakrishnan, K.; Switek, K. A.; Hillmyer, M. A. *J. Polym. Sci., Part A: Polym. Chem.* **2004**, *42*, 853–861.
(31) Binder, W. H.; Sachsenhofer, R. *Macromol. Rapid Commun.* **2007**, *29*, 1097–1103.
(32) Durmaz, H.; Dag, A.; Altintas, O.; Erdogan, T.; Hizal, G.; Tunca, U. *Macromolecules* **2007**, *40*, 191–198.
(33) Agut, W.; Taton, D.; Lecommandoux, S. *Macromolecules* **2007**, *40*, 5653–5661.
(34) Opsteen, J. A.; van Hest, J. C. M. *J. Polym. Sci., Part A: Polym. Chem.* **2007**, *45*, 2913–2924.
(35) Opsteen, J. A.; van Hest, J. C. M. *Chem. Commun.* **2005**, 57–59.
(36) Chan, T. R.; Hilgraf, R.; Sharpless, K. B.; Fokin, V. V. *Org. Lett.* **2004**, *6*, 2853–2855.
(37) J.-F Lutz, K.; Matyjaszewski *J. Polym. Sci., Part A: Polym. Chem.* **2005**, *43*, 897–910.
(38) Matyjaszewski, K.; Xia, J. *Chem. Rev.* **2001**, *101*, 2921–2990.
(39) Altinok, H.; Nixon, S. K.; Gorry, P. A.; Attwood, D.; Booth, C.; Kelarakis, A.; Havredaki, V. *Colloids Surf., B* **1999**, *16*, 73–91.
(40) Lopes, J. R.; Loh, W. *Langmuir* **1998**, *14*, 750–756.
(41) Halacheva, S.; Rangelov, S.; Tsvetanov, C. *Macromolecules* **2006**, *39*, 6845–6852.
(42) Alexandridis, P.; Holzwarth, J. F.; Hatton, T. A. *Macromolecules* **1994**, *27*, 2414–2425.
(43) Rangelov, S.; Almgren, M.; Halacheva, S.; Tsvetanov, C. *J. Phys. Chem. C* **2007**, *111*, 13185–13191.
(44) Wang, C.; Yu, B.; Knudsen, B.; Harmon, J.; Moussy, F.; Moussy, Y. *Biomacromolecules* **2008**, *9*, 561–567.
(45) Mao, J.; Gan, Z. *Macromol. Biosci.* **2009**, *9*, 1080–1089.
(46) Li, Z.; Kyerematen, S. O.; Fuchise, K.; Kakuchi, R.; Sakai, R.; Kakuchi, T.; Kressler, J. *Macromol. Chem. Phys.* **2009**, *210*, 2138–2147.
(47) Rangelov, S.; Trzebicka, B.; Jamroz-Piegza, M.; Dworak, A. *J. Phys. Chem. B* **2007**, *111*, 11127–11133.
(48) Rogers, S. E.; Eastoe, J.; Hudson, L.; Gold, S.; Heenan, R. K.; Grillo, I. *J. Colloid Interface Sci.* **2009**, *330*, 437–442.
(49) Eastoe, J.; Rogers, S. E.; Martin, L. J.; Paul, A.; Guittard, F.; Guittard, E.; Heenan, R. K.; Webster, J. R. *Langmuir* **2006**, *22*, 2034–2038.
(50) Ma, J.; Guo, C.; Tang, Y.; Liu, H. *Langmuir* **2007**, *23*, 9596–9605.
(51) Cau, F.; Lacelle, S. *Macromolecules* **1996**, *29*, 170–178.
(52) Alexandridis, P.; Yang, L. *Macromolecules* **2000**, *33*, 5574–5587.
(53) Bedrov, D.; Smith, G. D.; Yoon, J. *Langmuir* **2007**, *23*, 12032–12041.
(54) Mortensen, K.; Pedersen, J. S. *Macromolecules* **1993**, *26*, 805–812.
(55) Goldmints, I.; Yu, G.-E.; Booth, C.; Smith, K. A.; Hatton, T. A. *Langmuir* **1999**, *15*, 1651–1656.
(56) Denkinger, P.; Burchard, W. *J. Polym. Sci., Part B: Polym. Phys.* **1991**, *29*, 589–600.
(57) Alexander, L. E. *X-ray Diffraction Methods in Polymer Science*; Reprint; R.E. Krieger Publishing Company: New York, 1979.
(58) Mortensen, K. *J. Phys.: Condens. Matter* **1996**, *8*, 103–124.
(59) Rakhmatullina, E.; Braun, T.; Chami, M.; Malinova, V.; Meier, W. *Langmuir* **2007**, *23*, 12371–12379.
(60) Semenov, A. N.; Nyrkova, I. A.; Khokhlov, A. R. *Macromolecules* **1995**, *28*, 7491–7500.
(61) Nyrkova, I. A.; Khokhlov, A. R.; Doi, M. *Macromolecules* **1993**, *26*, 3601–3610.

594 *Macromolecules* **2011**, *44*, 594–603
DOI: 10.1021/ma102284y

Macromolecules
ARTICLE

Core Cross-Linking of Dynamic Diblock Copolymer Micelles: Quantitative Study of Photopolymerization Efficiency and Micelle Structure.

Sandie Piogé,[†,‡] Alla Nesterenko,[†,‡] Guillaume Brotons,[§] Sagrario Pascual,[‡] Laurent Fontaine,[‡] Cédric Gaillard,[⊥] and Erwan Nicol*[,†]

[†]*Polymères, Colloïdes, Interfaces, UMR CNRS 6120, Université du Maine, Le Mans, France,* [‡]*Unité de Chimie Organique Moléculaire et Macromoléculaire, UCO2M, UMR CNRS 6011, Université du Maine, Le Mans, France,* [§]*Laboratoire de Physique de l'Etat Condensé, UMR CNRS 6087, Université du Maine, Le Mans, France, and* [⊥]*Laboratoire de Microscopie, plate-forme RIO BIBS, U.R. BIA, INRA, Nantes, France*

Received October 5, 2010; Revised Manuscript Received December 10, 2010

ABSTRACT: Asymmetric poly(ethylene oxide)-*b*-poly(ethyl acrylate) block copolymers bearing polymerizable (meth)acrylate groups at the end of the hydrophobic block were synthesized and self-assembled in water. The micellar structures were studied by static light scattering (SLS), dynamic light scattering (DLS) and small angle neutrons scattering (SANS). The micelles were checked to be dynamical and in a thermodynamic equilibrium. In order to stabilize the micelles, a photoinitiator was added and UV light was applied to initiate the cross-linking of micelles cores. Light scattering and SANS showed a very weak influence of the addition of the photoinitiator on the size and aggregation number of micelles. The photopolymerization takes place within a few seconds and the cross-linking process barely modifies the structural properties of the micelles. The efficiency of the core cross-linking was estimated in terms of (meth)acrylate double bonds conversion and rate of incorporation of unimers into the cross-linked structures. ^{1}H NMR showed a complete conversion of double bonds. Transmission electron microscopy (TEM), light and neutron scattering studies showed almost no modification of the structures, indicating that the exchange dynamics of unimers barely affects the structure during the cross-linking process. Size exclusion chromatography (SEC) analyses in DMF revealed a non-negligible amount of nonstabilized unimers. The cross-linked stars can be easily isolated from the remaining unimers by flash chromatography using hydrophobically modified silica gel.

Introduction

Amphiphilic block copolymers self-associate to give micellar structures in selective solvents. Many of these self-assembled systems are potentially interesting in the field of biotechnology, surface modification, removal of pollutants, catalysis, ...[1] However, when dynamical micelles are used, the sensitivity to the environment (solvent, concentration, temperature, ionic strength, pH, ...) can be a problem, leading to a lack of stability. In order to improve the stability of such self-assembled systems, various strategies were developed to cross-link the micellar architectures.[2] This cross-linking can be an organic reaction or a polymerization reaction (mainly free radical polymerization), and it can concern the core or the corona of the core−shell structures.

Several research teams used the quaternization reaction in order to cross-link either the core or the shell of micelles after self-assembly.[3−8] Wooley et al. used the reaction of a diamine on PAA-based copolymers to stabilize the shell of micellar structures.[3,4] After selective degradation of the core, nanocages, that could be used for controlled release, are obtained. The amidation reaction was also used by Fuji et al. to cross-link the shell of aggregates made of ABC triblock copolymer and used as pH responsive emulsifiers.[5] Other organic chemical reactions such as thiol oxidation,[6] Michael reaction,[7,8] formation of urethane links,[9,10] reaction of double bonds with disulfur dichloride (S_2Cl_2),[11−15] and "click" reactions[16,17] were also reported to stabilize block copolymer self-assemblies.

*Corresponding author. E-mail: erwan.nicol@univ-lemans.fr.

The stabilization by organic reaction necessitates the incorporation of a reactive moiety in one block together with a cross-linking agent. Also, these organic chemistry processes usually need thermal activation. To avoid these drawbacks and to work at room temperature, photochemical process can be an alternative. The most commonly used reactions are the photocycloaddition and the photopolymerization. For instance, the [2 + 2] cycloaddition of cinnamate derivatives was employed to cross-link poly(cinnamoylethyl methacrylate) based copolymers micelles.[18−27] The same chemical reaction occurs when coumarin derivatives are used.[28,29] In that case, the cross-linking occurs at wavelengths above 310 nm and the process is partially reversible if wavelengths below 260 nm are used. These copolymers lead to stimuli-responsive nanostructures.

The last strategy used to cross-link nanostructures consists in polymerizing vinylic or acrylic moieties grafted onto one of the block of the copolymer. In many instances, this strategy is applied to cross-link the micelles cores but Thurmond et al. also applied it to shell cross-linking.[30,31] Thermal initiated conventional free radical polymerizations together with redox initiated ones,[32−38] Atom transfer radical polymerization (ATRP)[39,40] or γ-irradiation[41,42] have been used to synthesize core cross-linked nanoparticles. These reactions usually take a long time to be completed or require unusual equipment (in the case of γ-irradiation). In order to improve the reaction time, photoinitiated polymerization was used by different teams. Indeed, photopolymerization using efficient photoinitiators is known to be completed in a few seconds in thin films,[43,44] and short reaction times are expected in confined

 Published on Web 01/12/2011 © 2011 American Chemical Society

medium such as nanoaggregates. Micelles cores were cross-linked either by introducing a photoinitiator and applying UV light[45−48] or simply by UV irradiation of the polymerizable groups in the self-assembled systems.[49,50]

Comparing the results published in literature on the core cross-linked micelles, differences appear concerning the evolution of the aggregates structure before and after the cross-linking process. Some authors reported the retaining of the structures during the cross-linking of the assemblies, mainly, by measuring the hydrodynamic radii by DLS[6,21,25,35,48,51] or by measuring also the aggregation numbers by SLS.[50,52] Other groups also observed by TEM that the aggregates size remained unchanged.[41,46,53] However, some articles reported more or less important changes in the aggregates structures after the cross-linking step.[38,49,54−60] The reasons why some systems retain their structures while others do not are not yet fully established. A track that would be worth examining is the dynamical aspect of the self-assembled systems. Indeed, it is well-known in the literature that the cross-linking of polymerizable surfactants lead to modifications of the micelles structures.[61−65] Cochin et al. explained this phenomenon by the very fast exchange of unimers that empty noninitiated micelles on behalf of initiated ones that grow by polymerizing.[66] In the case of block copolymers in selective solvents, Nicolai et al. recently highlighted that the dynamic or frozen character of the aggregates has a crucial influence on their physical-chemical properties.[67] Thus, to our knowledge, a question remains that has not been yet answered in the literature: Do dynamic block copolymer micelles behave as surfactant ones during a core cross-linking process?

We recently synthesized poly(ethylene oxide) (PEO) -*b*-poly-(ethyl acrylate) (PEA) block copolymers.[68] Various PEA block lengths were grown by ATRP from a PEO macroinitiator. The self-assembling properties of these copolymers were studied by pyrene fluorescence measurements, static and dynamic light scattering and transmission electron microscopy. Micelles exhibiting aggregation numbers up to 110 were formed in water and were shown to be in a thermodynamic equilibrium. The lifetime of a unimer into the micelle could not be precisely determined but various experiments led to the conclusion that the micelles were dynamic and not frozen at a time scale of a few seconds. These copolymers were functionalized by introducing polymerizable methacrylate moieties at the PEA chain-end.[69] Various ways were tried to functionalize the bromide chain-end after the ATRP of ethyl acrylate and the substitution by the 6-mercaptohexanol followed by the reaction of methacryloyl chloride was shown to give quantitative functionalization rates. In the present study, we report the synthesis of two new cross-linkable triblock copolymers (PEO-*b*-PEA-*b*-poly(2-methacryloyloxyethyl acrylate) (PMEA) and PEO-*b*-PEA-*b*-poly(2-acryloyloxyethyl acrylate) (PAEA) and the stabilization of the dynamic micelles formed by the self-assembly of these (meth)acrylate functionalized PEO-*b*-PEA copolymers in water. The influence and efficiency of the micelles core cross-linking are quantitatively studied by combining ^{1}H NMR, static and dynamic light scattering, size exclusion chromatography, and small angle neutron scattering measurements.

Experimental Section

Materials. The PEO_{108}-*b*-PEA_{11}-Br diblock copolymer (DP_{EO} = 108, DP_{EA} = 11, $M_{n,NMR}$ = 6050 g·mol^{-1}, $M_{n,SEC}$ = 5700 g·mol^{-1}, PDI = 1.04) was synthesized by ATRP of ethyl acrylate and initiated by bromo-functionalized PEO, as detailed elsewhere.[68] The methacrylate functionalized diblock copolymer (PEO_{108}-*b*-PEA_{11}−$S(CH_2)_6$−OCO−$C(CH_3)$=CH_2) called **S1**, was obtained through two successive reactions according to a reported procedure.[69] 2-Hydroxyethyl acrylate (HEA, 96%), acryloyl chloride (97%) and methacryloyl chloride (97%) from Aldrich were distilled under reduced pressure and were stored at −18 °C after purification. Triethylamine (TEA, 99.5%) was distilled and stored over KOH prior to use. CuBr (99.999%), *N*,*N*,*N*′,*N*″,*N*″-pentamethyldiethylenetriamine (PMDETA, 99%), neutral alumina, diethyl ether, dichloromethane, anhydrous toluene (99.8%), acetonitrile (99%), tetrahydrofuran (99.5%), butanediol dimethacrylate (BDDM, 98%) and 2,2-dimethoxy-2-phenylacetophenone (DMPA, 99%) were purchased from Aldrich and were used without further purification. 4-(Dimethylamino)pyridine (DMAP, 99%), was used as received from Acros. The dialysis tubing was purchased from Spectrum Laboratories (MWCO = 3500 Da).

Size Exclusion Chromatography (SEC). Molecular weights and molecular weight distributions were measured using size exclusion chromatography (SEC). In DMF, analyses were done on a system equipped with a Waters 510 pump, with a Guard column (Polymer Laboratories, PL gel 5 μm Guard column, 50 × 7.5 mm) followed by two columns (Polymer Laboratories (PL)), 2 PL gel 5 μm MIXED-D columns, 2 × 300 × 7.5), with a Waters 410 RI detector. The flow rate of DMF was 1 mL.min^{-1} at 30 °C. Polystyrene standards (580−4.83 × 10^5 g·mol^{-1}) were used to calibrate the SEC.

SEC in THF on a system equipped with a SpectraSYSTEM AS100 autosampler, a column (JORDI gel 500 Å, 5 μm, 50 cm) followed by a Spectra Physics RI-71 refractive index detector and a Spectra Physics UV1000 detector (λ = 254 nm). The flow rate was 1 mL·min^{-1} at room temperature. The column was calibrated with the narrow molecular weight PEO standards (630−25000 g·mol^{-1}).

NMR Spectroscopy. NMR spectra were recorded on a Bruker AC-400 spectrometer for ^{1}H NMR (400 MHz) and $CDCl_3$ or D_2O as solvent. Chemical shifts are reported in ppm relative to the deuterated solvent resonances.

Light Scattering (LS). Static and dynamic light scattering were performed with a ALV-5000 multibit, multitau, full digital correlator in combination with a Spectra-Physics laser (emitting vertically polarized light at λ = 532 nm) and a thermostat bath controller. The autocorrelation functions were analyzed in terms of relaxation time (t) distribution. Measurements were made at the angle 40, 50, 70, 90, 110 and 130° at concentrations ranging from 1 to 20 g·L^{-1}, and at 20 °C. Prior to measurement, the polymer solutions were filtered using inorganic membrane filter to 0.2−0.45 μm and were placed in a 5 mL flask previously cleaned.

A more detailed description of the data treatment was given previously.[68]

Small Angle Neutron Scattering (SANS): Experiments and Analysis. SANS experiments were performed at the Laboratoire Léon Brillouin (LLB, Saclay, France) on the PACE spectrometer using two configurations for the sample to detector distances (5 and 1 m) with a wavelength of 0.6 nm, a wavelength spread of 10% and a neutron collimation distance tuned to the sample−detector distance. The data are shown in Figure 5 after following the standard instrument procedures to reach the absolute scale intensity, i.e. the scattering cross-section per unit volume in cm^{-1}. Data were corrected for electronic background, empty cell signal and incoherent scattering background (mainly due to the samples protons) and they were normalized with H_2O as calibration standard.

The analysis of the SANS curves was obtained assuming a model representation of the diblock copolymer spherical micelles with a PEA core and highly hydrated PEO chains attached to it. The core with radius R_C contains N_{agg} PEA chains and a non negligible amount of water for **S1**. It is surrounded by N_{agg} PEO chains exhibiting a noninteracting Gaussian conformation with a radius of gyration R_g^S so that the shell thickness is $2R_g^S$ and only contains PEO or water molecules. The SANS calculations that were compared to the data within a homemade fitting program are based on the Pedersen and Gerstenberg micelle form factor.[70] The fitting program algorithm and detailed SANS

calculation are beyond the scope of this paper and will be given in a dedicated paper. For diluted samples (S1 at 1% w/w in water), the fits to the data are conducted by optimizing a reduce set of parameters, namely the micelle aggregation number (N_{agg}), the volume fraction of PEA in the core ($\phi_{PEA}{}^{C}$), the volume fraction of PEO in the shell ($\phi_{PEO}{}^{S}$) and the width (ΔR_m) of the micelles size distribution Gauss function (polydispersity parameter). All parameters needed for the SANS calculation were obtained from this reduced set of adjustable parameters (see Table 3). In this model, the core is a mixture of PEA, water and added hydrophobic molecules such as DMPA and BDDM for some samples. The PEA block represents 23.51% of the copolymer chain volume assuming a PEA density of 1.121 $g\cdot cm^{-3}$ and a PEO density of 1.202 $g\cdot cm^{-3}$ for all samples composition. The neutron scattering length densities (NSLD in $Å^{-2}$ units) that are used in the SANS expressions were calculated assuming that: a PEA chain counts 11 EA monomers plus a terminal group ($H_{17}C_{10}O_2S_1$) and a bridge ($H_6C_4O_1$) to a PEO chain that counts 108 EO monomers plus a terminal group ($H_3C_1O_1$). In this way we obtained for pure materials: $\rho b_{PEA} = 0.942 \times 10^{-6}$ $Å^{-2}$ and $\rho b_{PEO} = 0.678 \times 10^{-6}$ $Å^{-2}$, both exhibiting a high scattering contrast with the heavy water ($\rho b_{D_2O} = 6.3634 \times 10^{-6}$ $Å^{-2}$ at 20 °C). To calculate the NSLD of the DMPA photoinitiator we considered a density of 1.21 $g\cdot cm^{-3}$ giving $\rho b_{DMPA} = 1.8185 \times 10^{-6}$ $Å^{-2}$ and we used a density of 1.023 $g\cdot cm^{-3}$ for the BDDM cross-linker giving $\rho b_{BDDM} = 0.97153 \times 10^{-6}$ $Å^{-2}$. We assumed that both hydrophobic molecules enter in the core and we calculated the core NSLD from: $\rho b_C = \phi_{PEA}{}^{C}\rho b_{PEA} + \phi_{D_2O}{}^{C}\rho b_{D_2O} + \phi_{\mathrm{DMPA}}{}^{C}\rho b_{\mathrm{DMPA}} + \phi_{\mathrm{BDDM}}{}^{C}\rho b_{\mathrm{BDDM}}$, were the only fitting parameter is $\phi_{PEA}{}^{C}$ that imposes the value of $\phi_{D_2O}{}^{C}$. For higher copolymer concentrations (**S1** at 5% w/w), a strong structure peak appeared due to position correlations between micelles (inset of Figure 5b). The micelle−micelle interactions peak was very well reproduced using the Percus−Yevick approximation for hard-spheres and Pedersen expressions including the micelles polydispersity that affects also the structure peak calculation.[71] In this case, two more fitting parameters were introduced, namely the hard sphere radius of micelles R_{HS} and the volume fraction of interacting spheres ϕ_{HS} (Table 3).

Microscopy. *TEM*. A drop of each sample previously dispersed in dried toluene (at 0.15 $g\cdot L^{-1}$) was first placed on a carbon-coated TEM copper grid (Quantifoil, Germany) and permitted a brief air-drying. The sample was then negatively stained with uranyl acetate (Merck, Germany). For that, the sample-coated TEM grid was successively placed on a drop of a solution of uranyl acetate in anhydrous butanol (2% w/w). The grid was then air-dried before introducing it in the electron microscope.

The samples were observed using a JEM 1230 microscope (Jeol, Japan) operated at 80 kV and equipped with a LaB_6 filament. The micrographs were recorded on a Gatan 1.35 K × 1.04 K × 12 bit ES500W CCD camera.

Image analysis. The software ImageJ (Research Services Branch NIMH & NINDS) has been used to determine particle size distributions and apply a contrast enhancement of the TEM images. The mean values of the diameters and the corresponding square-roots were calculated from a total number of particles of 486 and 512 for, respectively, **S1** and **S2a** samples.

Typical ATRP of 2-Hydroxyethyl Acrylate Initiated by PEO_{108}-*b*-PEA_{11}-Br. In a Schlenk tube, a solution of 5.2 mL (0.05 mol) of 2-hydroxyethyl acrylate, 10 g (1.65 mmol) of PEO_{108}-*b*-PEA_{11}Br diblock copolymer and 37 mL (80% v/v) of toluene previously degassed by three freeze−pump−thaw cycles was added to another Schlenk tube containing 234 mg (1.65 mmol) of CuBr, under argon, with a cannula. The reaction mixture was degassed by three freeze−pump−thaw cycles and backfilled with argon. It was then placed in an oil bath thermostated at 50 °C. 0.34 mL (1.65 mmol) of PMDETA was added under argon. When 10% of HEA conversion was reached as determined by ^{1}H NMR spectroscopy, the sample was dissolved in dichloromethane and filtered through a neutral alumina column to remove copper complex. The solution was then concentrated under vacuum and precipitated in a large excess of cold diethyl ether. The resulting triblock copolymer recovered by filtration, was dried under vacuum at room temperature prior to analysis. ^{1}H NMR (DMSO-d_6) δ (ppm): in addition to the characteristic peaks of PEO and PEA (see ref 51), the PHEA characteristic signals are observed at 1.2−2.4 (m, 3H, **main chain protons**) ; 3.6 (m, 2H, HO−**CH_2**−CH_2−O−) ; 4.12 (m, 2H, HO−CH_2−**CH_2**−O−) and 4.75 (s, 1H, **HO**−CH_2−CH_2−O−). Note that, except the hydroxyl proton, all the PHEA peaks merge with the PEO and PEA signals. SEC in THF using poly(ethylene oxide) standards: $M_{n,SEC}$ = 6100 $g\cdot mol^{-1}$, PDI = 1.12.

Esterification of the PEO-*b*-PEA-*b*-PHEA Triblock Copolymer. A freeze-dried hydroxy-functionalized PEO-*b*-PEA-*b*-PHEA block copolymer (4 g, 0.6 mmol) and 22 mg (0.018 mmol) of DMAP were dissolved in 40 mL of dry toluene. The solution was purged with argon for 30 min and was cooled to 0 °C. TEA (0.42 mL, 3 mmol) and methacryloyl chloride (0.29 mL, 3 mmol) were added dropwise to the reaction mixture under continuous stirring. Then, the reaction was stirred for 72 h at 30 °C. The solution was filtered in order to remove salts and the solvent was removed under vacuum. After evaporation, the resulting solid was dissolved in deionized water and the solution was dialyzed for 1 day. After dialysis, the solution was freeze-dried in order to recover quantitatively the PEO-*b*-PEA-*b*-PMEA (**S2a** copolymer).

The same procedure was applied to obtain the acrylate functionality instead of the methacrylate one. In that case, acryloyl chloride was used instead of methacryloyl chloride. The PEO-*b*-PEA-*b*-PAEA (**S2b** copolymer) was also recovered quantitatively. Because of the high reactivity of the acrylate groups, this copolymer was stored at −18 °C in order to avoid uncontrolled cross-linking of the material even in the solid state. ^{1}H NMR spectra (in $CDCl_3$) of **S2a** and **S2b** are shown in Figure 4.

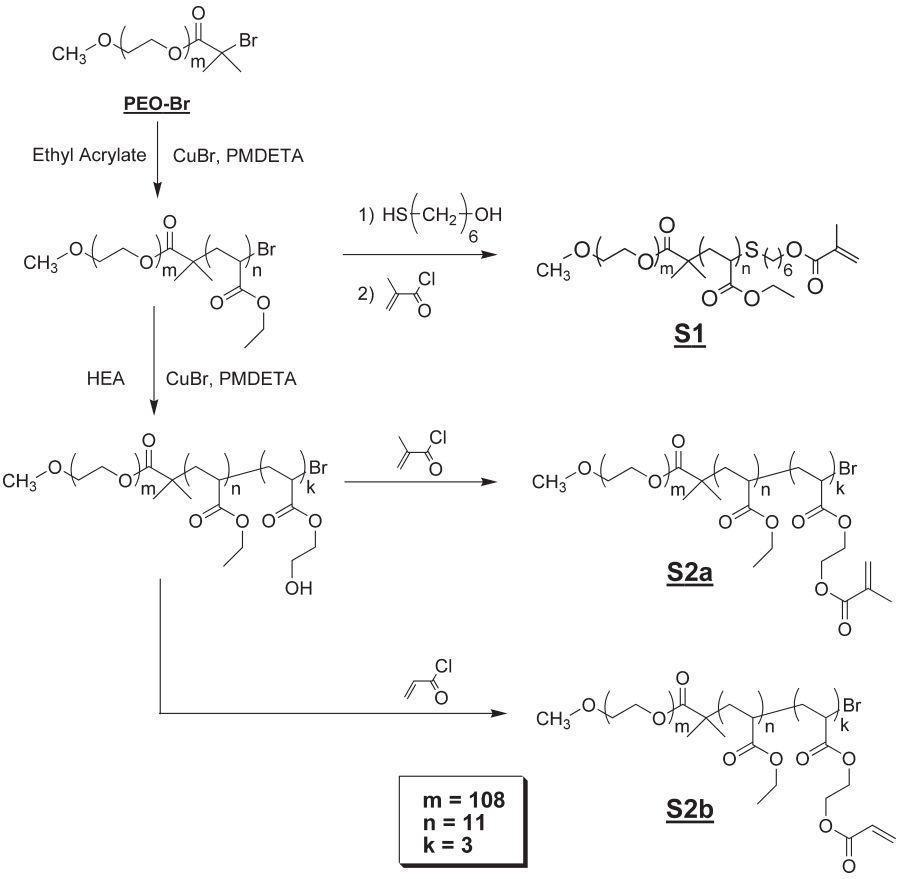
Determination of the Critical Micelle Concentration (CMC). The CMC values were determined using pyrene fluorescence measurements. The detailed procedure was described elsewhere.[68] The CMC values were estimated as the first inflection point of the evolution of the ratio $I_{337\ nm}/I_{334\ nm}$ vs concentration obtained from pyrene excitation spectra.

Typical Photo-Cross-Linking of (Meth)acrylate Functionalized Block Copolymers. A 5 μL sample of a solution of photoinitiator (DMPA, 4.13×10^{-4} $mol\cdot L^{-1}$) in THF and 5 μL of a solution of cross-linker (BDDM, 6.8×10^{-4} $mol\cdot L^{-1}$) in the THF were mixed in a flask. Then the THF was evaporated in order to obtain a film of photoinitiator and cross-linker. An aqueous solution of copolymer at 10 $g\cdot L^{-1}$ was added in the flask containing the film. The solution was stirred during 1 h and was purged with argon. Then 5 mL of the final solution were cross-linked by applying UV light (Dymax BlueWave 200 UV lamp, λ_{max} = 365 nm). The solutions were studied in aqueous medium or freeze-dried to recover the copolymer and to study the system in organic medium.

Results and Discussion

Synthesis of the (Meth)acrylate Functionalized PEO-*b*-PEA Block Copolymers. Two copolymers, PEO-*b*-PEA-*b*-PMEA (**S2a**) and PEO-*b*-PEA-*b*-PAEA (**S2b**), bearing polymerizable groups as pendant chains at the end of the hydrophobic block were prepared by esterification of PEO-*b*-PEA-*b*-PHEA using methacryloyl chloride and acryloyl chloride, respectively. The PEO-*b*-PEA-*b*-PHEA triblock copolymer was synthesized by ATRP of HEA in toluene (80% v/v) at 50 °C in the presence of PEO_{108}-*b*-PEA_{11}-Br and CuBr/PMDETA employed as a macroinitiator and as the catalytic system respectively using the following ratios: $[HEA]_0/[PEO_{108}$-*b*-PEA_{11}-$Br]_0/[CuBr]_0/[PMDETA]_0 = 30/1/1/1$ (Scheme 1).

Scheme 1. Synthesis Route of the ω-Methacryloyl-PEO-*b*-PEA (S1), PEO-*b*-PEA-*b*-PMEA (S2a) and PEO-*b*-PEA-*b*-PAEA (S2b) Copolymers



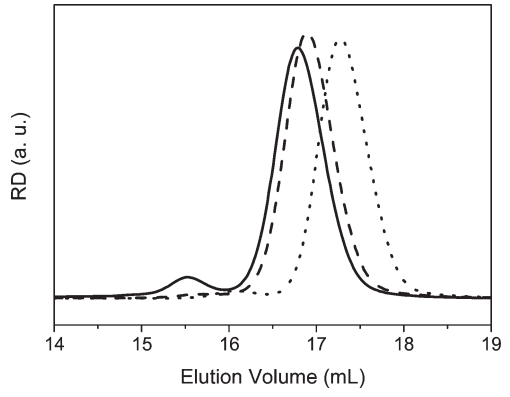


Figure 1. SEC traces of the PEO macroinitiator (dotted line), PEO-*b*-PEA copolymer (dashed line) and PEO-*b*-PEA-*b*-PMEA copolymer (straight line).

When the HEA conversion reaches 10%, the polymerization is stopped and the resulting PEO-*b*-PEA-*b*-PHEA triblock copolymer was isolated and purified by precipitation. A number-average molecular weight of 6100 $g \cdot mol^{-1}$ and a polydispersity index of 1.12 were obtained for the triblock. The molar composition of the triblock copolymer can be determined by ^1H NMR from the relative intensity at 3.4 ppm, which is attributed to the CH_3O- protons of the PEO block, and the relative intensity at 4.0−4.2 ppm, corresponding to the $-COOCH_2-$ protons of the EA and HEA units. By comparing the relative intensities before and after polymerization, a mean degree of polymerization of HEA equal to 3 was obtained. Figure 1 shows the SEC traces of the polymers after each step of ATRP. As previously described,[68] the polymerization of ethyl acrylate is well controlled and no remaining macroinitiator was observed. After the addition of the PHEA block, the SEC trace showed a small increase of the molar mass in agreement with what expected. The polydispersity of the peak at 16.8 mL remained low (1.12) but a second peak at 15.5 mL was observed. This population has exactly twice the molar mass of the block copolymer and is probably due to polymer chains coupling during the polymerization. At the beginning of the polymerization reaction, the concentration of radicals is high leading to a very fast consumption of the monomer and to a small amount of termination reactions by chain coupling.

In the last step, the PEO-*b*-PEA-*b*-PHEA was either esterified with methacryloyl chloride or acryloyl chloride in the presence of triethylamine (TEA) and 4-(dimethylamino)-pyridine (DMAP) in dry toluene at 30 °C. The resulting macromonomers **S2a** and **S2b** were characterized by ^1H NMR spectroscopy (Figure 2). The signal (a) at 3.4 ppm is assigned to the methyl groups of poly(ethylene oxide) chain ends. For **S2a**, the signals (g and g′) at 5.60 and 6.09 ppm respectively, can be attributed to the methacrylate group, indicating a successful esterification. A quantitative functionalization was calculated by comparing the integrations of vinyl protons (g, g′) and methyl protons (a). For **S2b**, the acrylic protons (f, g and g′) have chemical shifts of 6.15, 5.88 and 6.43 ppm, respectively. The comparison of integrations of vinyl protons and chain-end signal (a) allowed us to conclude to a quantitative esterification of the hydroxyl groups. In both cases, SEC traces of the functionalized block copolymers did not show significant changes in the molecular weights and in the PDI. The characteristics of the final copolymers are reported in Table 1.

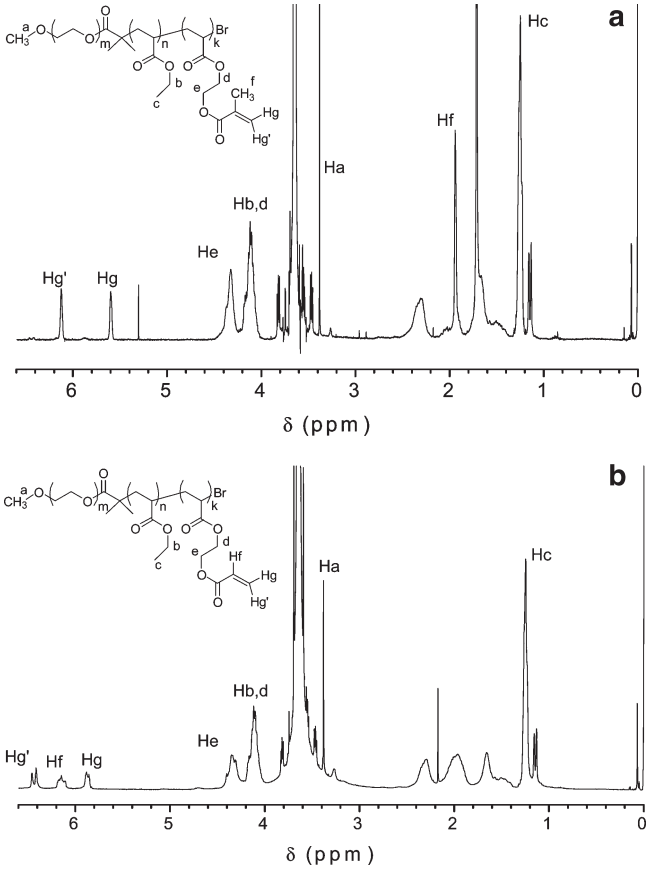


Figure 2. ^{1}H NMR spectra of **S2a** (top) and **S2b** (bottom) copolymers.

Photo-Cross-Linking of Block Copolymer Micelles. Both block copolymers (**S1** and **S2**) were self-assembled in water (selective solvent of the PEO block). As previously described,[68] it was checked that different ways of preparing the samples gave the same structures. Furthermore, the copolymers dissolve rapidly in water to give transparent solutions. These observations indicate that the micelles formed are not frozen. The determination of the mean residence time (τ_R) of the hydrophobic block into the micelle core is very complex in the case of diblock copolymers. This time has not been determined for the present systems. However, we recently studied the rheological properties of $PMEA_6$-*b*-PEO_{200}-*b*-$PMEA_6$ triblock copolymer aqueous solutions.[72] This copolymer exhibits self-assembling properties close to **S1** ones (CMC = 6×10^{-2} g·L^{-1} and $N_{agg} \sim 30$). The characteristic relaxation time of the transient network formed at high concentration is usually related to the mean residence time of the hydrophobic block into the micelle core.[73] This characteristic time has been estimated to around 10^{-2} s. for the $PMEA_6$-*b*-PEO_{200}-*b*-$PMEA_6$ triblock copolymer. Thus, the present diblock copolymers being slightly more hydrophobic, slightly higher mean residence time are expected. The aggregation numbers (N_{agg}) and hydrodynamic radii (R_h) were determined by SLS and DLS respectively and results are gathered in Table 2.

In order to stabilize the micellar structures by cross-linking the cores, a hydrophobic photoinitiator (DMPA) was introduced into the micelles cores. For the copolymer **S1** bearing only one polymerizable group per chain, a cross-linker, butanediol dimethacrylate (BDDM), was added to improve the efficiency of the core cross-linking. Contrarily to what has been observed on polymerizable surfactant systems,[62] the introduction of these small hydrophobic molecules, up to 40 molecules per micelle core, did not modify significantly the aggregation properties of the block copolymers, all the micelles having nearly the same characteristics from light scattering (aggregation number and hydrodynamic radius) (Figure 3). The introduction of DMPA and BDDM molecules and their influence on the core structure have been studied by small angle neutron scattering and results are presented in next section.

Polymerization of the methacrylate (**S1** and **S2a**) or acrylate (**S2b**) groups was initiated by applying a UV irradiation at 365 nm under argon atmosphere. Kinetics of the polymerization process was determined by ^{1}H NMR by following the decrease of ethylenic protons located at 5.60 and 6.09 ppm in the case of methacrylate moieties and 5.88, 6.15, and 6.43 ppm in the case of acrylate moieties. The conversions of double bond as a function of the exposure time are shown in Figure 4.

Two light intensities (0.4 W·cm^{-2} and 2 W·cm^{-2}) were studied. All the samples exhibit a very fast polymerization process, the fastest one being the acrylate groups irradiated with a light intensity of 2 W·cm^{-2}. In that case, a conversion higher than 85% is reached after 5 s. of UV irradiation. As expected, methacrylate double bonds polymerize slower that the acrylate ones and the polymerization rate increases with the light intensity. A disappearance of around 10% of the double bonds was also observed even in the absence of photoinitiator. However, SEC traces of these samples showed no evolution in the molar mass. Nor ^{1}H or ^{13}C NMR allowed us to understand what reaction is involved in this photochemical process. It was also observed, in the case of **S2b** polymerized at 2 W·cm^{-2}, that the conversion reached a maximum value of 95%. This could be explained by a trapping of some acrylate groups in the cross-linked network; these groups becoming inaccessible to the propagating radicals. As shown in Figure 4, the acrylate moieties polymerize very fast. Their reactivity is so high that they are difficult to handle and to store. For this reason, the following studies were done on methacrylate functionalized copolymers.

Influence of the Photo-Cross-Linking Process on the Micellar Structure. As shown from light scattering, the micelle loading with a small amount of hydrophobic organic molecules barely modifies the self-assembled structure. Aqueous solutions of cross-linkable micelles were studied by SLS and DLS before and after irradiation at 365 nm. Figure 3 shows the evolution of the apparent molar mass and hydrodynamic radius of **S1** micelles at 10 g·L^{-1} loaded with DMPA and different amount of cross-linker (BDDM) after 90 s. under UV light at 0.4 W·cm^{-2}. Light scattering measurements showed that big aggregates did not appear during the process and that micelles sizes remained almost unchanged. Under the same conditions, the triblock copolymer **S2a** exhibited a small increase of its aggregation number of about 10% and a small decrease of the micelles radius was observed (see Table 2). In order to reach a higher resolution for the micelles structure and composition determination, SANS experiments were carried out on **S1** solutions at 1% and 5% w/w in D_2O (see Figure 5). The influence of DMPA and BDDM addition and UV irradiation was also studied. Solutions were kept in sample holder with 1 mm thickness and UV-transparent quartz walls and irradiated at 365 nm and 0.4 W·cm^{-2} for 90 s.

The fits to the SANS data are very good, assuming a spherical micelle with an hydrated PEA core surrounded by PEO chains adopting a noninteracting Gaussian chain configuration responsible for the intensity decrease as a function of Q^{-2} at large Q values. At smaller angles (low Q region), the

Table 1. Characteristics of Block Copolymers S1, S2a and S2b Determined by SEC in THF Using Poly(ethylene oxide) Standards

sample	$\overline{M}_n$ (g·mol^{-1})	$\overline{M}_w$ (g·mol^{-1})	PDI
S1 (PEO_{108}-*b*-PEA_{11}-MA)	5700	5900	1.04
S2a (PEO_{108}-*b*-PEA_{11}-*b*-$PMEA_3$) or **S2b** (PEO_{108}-*b*-PEA_{11}-*b*-$PAEA_3$)	6100	6800	1.12

Table 2. Characteristics of the Un-Cross-Linked and Cross-Linked Self-Assembled Systems

	in water			in water after cross-linking[a]		in organic medium after cross-linking[b]	
sample	CMC (g·L^{-1})	N_{agg}	R_h (nm)	N_{agg}	R_h (nm)	N_{agg}	R_h (nm)
S1	2.5×10^{-2}	39 ± 3	10.4 ± 0.3	41 ± 3	10.6 ± 0.3	40 ± 3	12.1 ± 0.3
S2a	6×10^{-3}	83 ± 5	14.1 ± 0.3	92 ± 5	12.5 ± 0.3	110 ± 7	11.1 ± 0.3

[a] **S1** contained 3 DMPA per micelle and **S2a** contained 4 DMPA per micelle. [b] Acetonitrile was used for **S1** and THF for **S2a**.

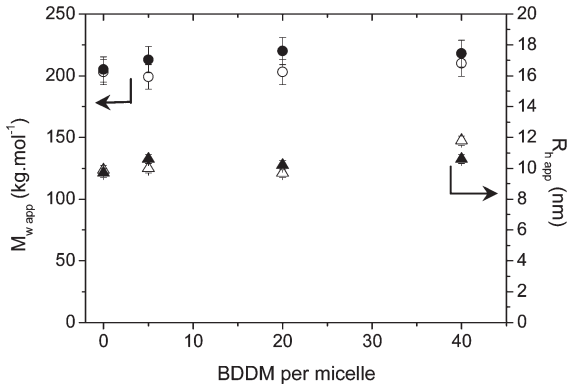


Figure 3. Apparent molar masses (circles) and hydrodynamic radii (triangles) of **S1** copolymer micelles measured at 10 g·L^{-1} in water as a function of the number of cross-linking (BDDM) molecules introduced per micelle. All the micelles are also loaded with three DMPA molecules per micelle (open symbols, before UV irradiation; closed symbols, after UV irradiation).

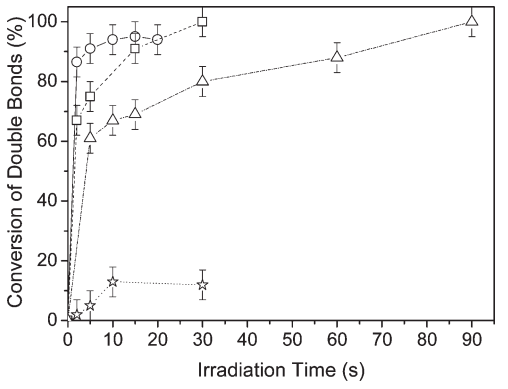


Figure 4. Double bond conversion as a function of irradiation time of acrylate groups at 2 W·cm^{-2} (circles), methacrylate groups at 2 W·cm^{-2} (squares), methacrylate groups at 0.4 W·cm^{-2} (triangles) and methacrylate groups at 2 W·cm^{-2} without photoinitiator (stars). The error bars are estimated from the errors made on the ^{1}H NMR integrations.

SANS intensity saturates to a plateau indicating that diluted solutions are made of isolated micelles with well-defined volumes (polydispersity below 10%). Since our fits were conducted while imposing that the copolymer and added molecules concentrations match the values known from preparation, the plateau intensity could only be matched when allowing a non-negligible amount of water to enter in the core. All fitting parameters and deduced quantities, given in Table 3, were in full agreement with the solution composition. The structure deduced from SANS was in excellent agreement with the light scattering results showing a micelle radius (R_m) of ~10 nm and aggregation numbers (N_{agg}) between 30 and 40 copolymer molecules per micelle. The SANS data pointed out that the core volume contains about 40% of water molecules with a 3 nm core radius (R_C), corresponding roughly to 4 solvent molecules per monomer of the PEA_{11} chains. The PEO shell is highly swollen and contains more than 90% of water in volume. It forms a corona with a thickness of 6.6 nm ($2R_g^S$) that is in good agreement with the radius of gyration (R_g^S) expected for Gaussian PEO_{108} chains.[74,75] We noticed from SANS that the insertion of 5 or 13 DMPA plus BDDM molecules dehydrated slightly the core but increased its volume proportionally to the volume of added hydrophobic molecules. The UV-polymerization was found to be accompanied by a slight increase of the core volume (+ 0.1 to 0.2 nm of radius) that explains the increase of SANS intensities with UV exposure assuming constant densities of mixed materials over the process (insets of Figure 5). This is more visible for more concentrated solutions (5% w/w of copolymer) since the structure peak is slightly shifted toward small Q values, indicating slightly larger micelles after DMPA plus BDDM addition and after UV cross-linking. For concentrated samples, the micellar volume represented 50% of the total solution but same conclusions were obtained. It is clear from light and neutron scattering experiments that the micelles are almost not affected in size and composition by the core cross-linking.

In order to check whether the micellar structures were efficiently cross-linked, irradiated samples were freeze-dried then dissolved in THF (good solvent of both blocks). A molecular weight higher than expected was measured by SLS (see Table 2), however a second population of larger aggregates was observed leading to a more complicated treatment of the DLS and SLS data. As these aggregates are not due to the photocross-linking process (they are not present in water), they may be due to a poor dispersion of the polymer in THF after freeze-drying. The hydrodynamic radius of the micelles was smaller in THF than in water indicating a lesser solvatation of the PEO chains in this solvent.

Transmission electron microscopy (TEM) was used to visualize the micelles structure after photocross-linking. In order to control the stability of self-assembled architectures after cross-linking, TEM samples were prepared from dry toluene solutions (a good solvent of both blocks) and negatively stained using a solution of uranyl acetate dissolved in dried butanol. Micrographs of cross-linked micelles of **S1** and **S2a** copolymers are shown in Figure 6. TEM micrographs taken from dilute toluene solutions (0.15 g·L^{-1}) show spherical nanosized objects with a low dispersion of the diameters. The mean diameters of **S1** and **S2a** particles were, respectively, 11.0 and 12.9 nm. These sizes are in very good agreement with those measured previously on PEO_{108}-*b*-PEA_{10} copolymer self-assembled in water[68] and with

Table 3. Fits Results of the SANS Experiments

fitted parameters	N_{agg}		$\phi_{PEA}{}^{C}$				$\phi_{PEO}{}^{S}$		ΔR_m	R_{HS}	ϕ_{HS}		
calculated parameters		R_C		$\phi_{D_2O}{}^{C}$	$\phi_{rest}{}^{C}$	$R_g{}^{S}$		R_m				$N_{DMPA}{}^{C}$	$N_{BDDM}{}^{C}$
error bars (±)	3	0.1	0.05	0.05	-	0.2	0.02	0.3	0.2	0.5	0.05	-	-
units	-	nm	-	-	-	nm	-	nm	nm	nm	-	-	-
S1; $C_{\mathbf{S1}} = 10.713\ g\cdot L^{-1}$													
	28	2.9	0.59	0.41	-	3.2	0.06	9.4	0.7	-	-	-	-
S1 + DMPA + BDDM; $C_{\mathbf{S1}} = 10.713\ g\cdot L^{-1}$; $C_{DMPA} = 0.0653\ g\cdot L^{-1}$ and $C_{BDDM} = 0.0577\ g\cdot L^{-1}$													
	31	2.9	0.60	0.37	0.03	3.3	0.06	9.5	0.7	-	-	5	5
+ UV													
	41	3.1	0.64	0.33	0.03	3.4	0.07	10.0	0.6	-	-	6	6
S1 + DMPA + BDDM; $C_{\mathbf{S1}} = 10.713\ g\cdot L^{-1}$; $C_{DMPA} = 0.1306\ g\cdot L^{-1}$ and $C_{BDDM} = 0.1154\ g\cdot L^{-1}$													
	34	3.1	0.61	0.33	0.06	3.2	0.07	9.5	0.6	-	-	10	10
+ UV													
	43	3.2	0.63	0.30	0.07	3.3	0.07	9.9	0.6	-	-	12	12
S1; $C_{\mathbf{S1}} = 48.217\ g\cdot L^{-1}$													
	37	3.1	0.60	0.40	-	3.4	0.06	9.9	0.7	9.6	0.30	-	-
S1 + DMPA + BDDM; $C_{\mathbf{S1}} = 48.217\ g\cdot L^{-1}$; $C_{DMPA} = 0.294\ g\cdot L^{-1}$ and $C_{BDDM} = 0.26\ g\cdot L^{-1}$													
	35	3.1	0.59	0.38	0.03	3.4	0.06	9.9	0.7	9.7	0.28	5	5
S1 + DMPA + BDDM; $C_{\mathbf{S1}} = 48.217\ g\cdot L^{-1}$; $C_{DMPA} = 0.588\ g\cdot L^{-1}$ and $C_{BDDM} = 0.519\ g\cdot L^{-1}$													
	43	3.2	0.64	0.29	0.07	3.7	0.06	10.5	0.8	10.3	0.29	13	13
+ UV													
	40	3.2	0.57	0.37	0.06	3.4	0.06	10.0	0.7	10.7	0.28	12	12

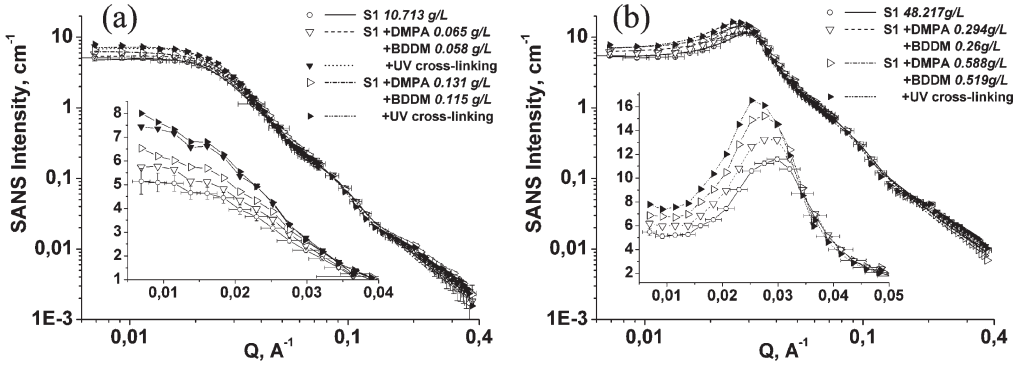


Figure 5. SANS curves of **S1** solutions prepared at (a) 10.713 $g\cdot L^{-1}$ and (b) 48.217 $g\cdot L^{-1}$ in D_2O, with or without addition of DMPA−BDDM molecules and before and after UV polymerization. A zoom to the raw data is plotted as an inset with linear scales. The best fits to the data obtained with the SANS model described in the text are plotted with lines in the log−log representation and coincide to the data over the full Q range measured in absolute scale of the intensity (cm^{-1}). The solutions composition and corresponding fitting parameters are given in Table 3. Note that error bars were only plotted for the two pure polymer samples.

scattering experiments presented here, confirming the low impact of the photocross-linking process and of the cryo-TEM sample preparation on the micelles size.

Size Exclusion Chromatography in *N*,*N*-dimethylformamide (DMF) as eluent was used to estimate the rate of incorporation of unimers in the stabilized cross-linked structures derived from **S1** and from **S2a** (see Figure 7). Un-cross-linked unimers are eluted at high volume (14.7 mL) while cross-linked micelles are eluted at 11.5 mL. The population eluted at low volume (below 10 mL) in Figure 7a can be attributed to aggregates of micelles in pure DMF. These aggregates are not due to intermolecular covalent cross-linking as they are not observed by light scattering in water. Addition of 0.01 M of LiBr in DMF avoided the formation of aggregates in the case of **S2a** analysis (Figure 7b). Notwithstanding the fact that all scattering and TEM experiments indicated that the micelles are effectively stabilized after cross-linking, SEC traces showed a remaining population of un-cross-linked chains. Similar observations were done by various groups on self-assemblies cross-linked in water[56,76] or in organic solvents.[21,48]

In the case of copolymer **S2a**, the percentage of remaining unimers (around 17%) is independent of the photoinitiator amount and of the concentration at which the micelles were photopolymerized (see Table 4). This could be partially explained by the fact that, due to the synthesis conditions of the PHEA block, **S2a** sample may contain polymer chains that are not functionalized by polymerizable moieties. For **S1** copolymer, the amount of dimethacrylate agent (BDDM) added to the micelles has an influence on the efficiency of the core cross-linking. The rate of nonincorporated macromolecules in the star-like structure increases with the quantity of cross-linker. The first hypothesis involves termination reactions that occur during this free radical polymerization

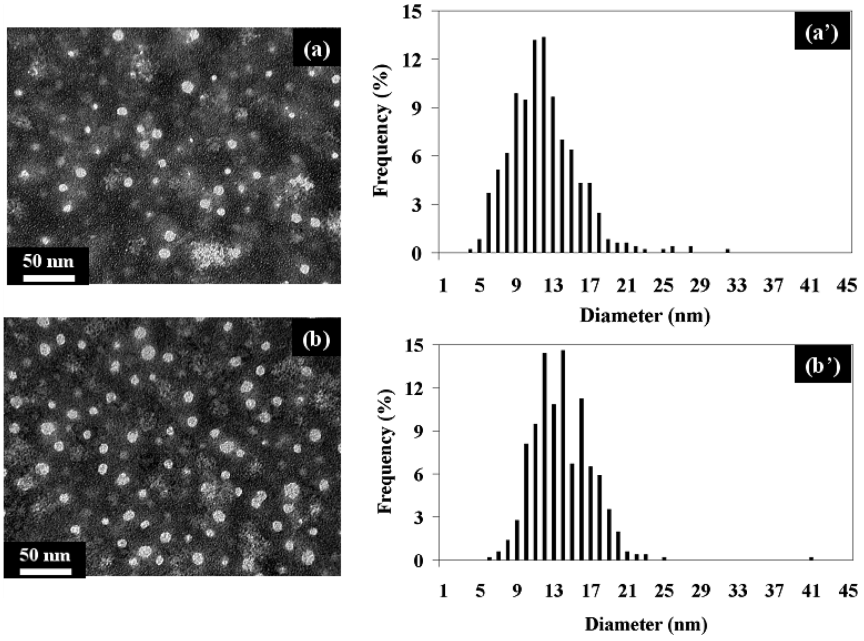


Figure 6. Negatively stained TEM images of (a) **S1** and (b) **S2a** samples with a concentration of 0.15 g·L^{-1}. the histograms (a′) and (b′) correspond respectively to **S1** and **S2a** diameter distributions. The mean diameter and the mean square deviation are equal to 11.0 and 3.7 nm, and to 12.9 and 3.2 nm, for **S1** and **S2a**, respectively.

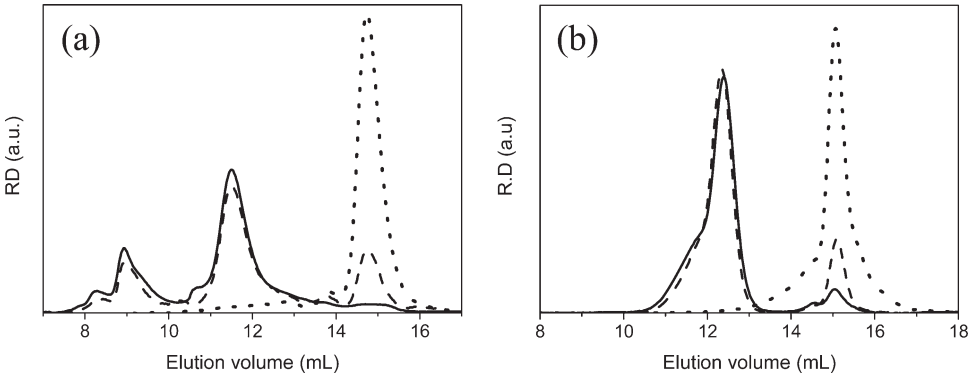


Figure 7. SEC traces of (a) copolymer **S1** in DMF before UV irradiation (dot line), after UV irradiation with 3 DMPA and 5 BDDM per micelle (dashed line) and after UV and purification through a hydrophobically modified silica column (straight line) and (b) copolymer **S2a** in DMF + 0.01 M LiBr before UV irradiation (dot line), after UV irradiation with 4 DMPA per micelle (dashed line) and after UV and purification through a hydrophobically modified silica column (straight line).

Table 4. Evolution of Remaining Un-Cross-Linked Unimers in the Photo-Polymerized Systems

copolymer	DMPA per micelle	BDDM per micelle	concentration (g·L^{-1})	% un-cross-linked unimers[a]
S1	3	0	10	10
S1	3	5	10	14
S1	3	20	10	18
S1	3	40	10	26
S2a	4		10	16
S2a	4		190	18
S2a	10		10	17

[a] Determined by SEC (see text).

process. The probability of incorporating a unimer instead of a BDDM molecule decreases as the amount of BDDM added to the core increases. Assuming that the rate of termination reactions remains the same whatever the amount of methacrylate groups in the micelle core, it can be concluded that an increase of the fraction of cross-linker will be unfavorable to a high rate of incorporation of unimers. However, we expected that the excess of DMPA could reinitiate a radical propagation and complete the stabilization of unimers in the micelles but it does not seem to be the case. The second hypothesis lies in the difficulties encountered by a macromonomer to diffuse to the active radical in the cross-linked core at high conversion rate. Indeed, the radical can be trapped into the cross-linked network and becomes inaccessible to the (meth)acrylate moieties.

However, the cross-linked micelles can be separated from the un-cross-linked unimers using flash chromatography. The mixture can be easily passed through a column filled with octyl-grafted silica gel and eluted with pure water. The PEA block of the remaining amphiphilic copolymers

interacts with the hydrophobically modified silica and adsorbs on the column while the star cores are protected by their PEO shell leading to a fast elution of the desired structure. The efficiency of this separation method is illustrated in Figure 7. The percentage of un-cross-linked diblock copolymer molecules remaining in the purified samples was thus lowered down to 3% for **S1** and to 7% for **S2a**. The recovery ratio was around 60% of purified star-polymer.

Conclusion

Diblock PEO-*b*-PEA copolymers bearing polymerizable acrylate or methacrylate end-groups were synthesized using ATRP technique. These copolymers self-assemble in dynamic micellar structures in water. The transient micelles can be stabilized by introducing a photoinitiator into the micellar cores and irradiating with UV light. Neutron and light scattering experiments showed a very small dehydration and increase in size and aggregation number of the micelles, when hydrophobic molecules such as DMPA photoinitiator and BDDM cross-linkers were added in small quantity. The rate of photopolymerization was estimated by ^{1}H NMR. A complete reaction of the double bonds has been reached within a few seconds. The photocross-linking process induced a very weak increase of the micelles aggregation number but one can consider that, despite of a polymerization rate probably slower than the mean residence time (τ_R) of a unimer in the core, the micelles sizes are practically unchanged. This observation could seem surprising and one could have expected rearrangements of the micelles structure. However, as highlighted by Cochin et al.[66] for polymerizable surfactants, the mean lifetime of the initial micelle (τ_M) should be considered, rather than τ_R, to compare the polymerization rate to the dynamics of the micelles. It has been shown that τ_M can be much larger than τ_R. Thus, it is probable, for **S1** and **S2a**, as the micelles structure is barely affected, that the cross-linking process is faster than the mean lifetime of the micelles. A precise determination of both τ_M and the polymerization rate would be helpful to support this hypothesis.

SEC in DMF can be used to separate the cross-linked star-polymers from remaining un-cross-linked unimers. Even if all the meth(acrylic) double bonds have reacted, the efficiency of the cross-linking reaction reached a maximum rate of 90%. This could be explained by the termination reaction occurring during the photopolymerization process or by the difficulty for a macromonomer to find an active radical at high conversion. Anyway, this self-assembly/cross-linking strategy is a promising way for elaborating complex macromolecular architectures. By mixing diblock and triblock copolymers at various ratio and various concentrations, original architectures such as pom-pom, flower-like, or garland-like polymers could be synthesized.

Acknowledgment. The authors thank the Région des Pays de la Loire and the National Research Agency (ANR − program HYPARC) for their financial support. Jacques Jestin from the LLB is greatly thanked for his help during the SANS experiment and for fruitful discussions. Martin Levere, Hien The Ho, and Olivier Boyron are acknowledged for SEC analyses in DMF.

References and Notes

(1) Riess, G. *Prog. Polym. Sci.* **2003**, *28*, 1107–1170.
(2) Rodríguez-Hernández, J.; Chécot, F.; Gnanou, Y.; Lecommandoux, S. *Prog. Polym. Sci.* **2005**, *30*, 691–724.
(3) Huang, H.; Kowalewski, T.; Remsen, E. E.; Gertzmann, R.; Wooley, K. L. *J. Am. Chem. Soc.* **1997**, *119*, 11653–11659.
(4) Zhang, Q.; Remsen, E. E.; Wooley, K. L. *J. Am. Chem. Soc.* **2000**, *122*, 3642–3651.
(5) Fujii, S.; Cai, Y.; Weaver, J. V. M.; Armes, S. P. *J. Am. Chem. Soc.* **2005**, *127*, 7304–7305.
(6) Kakizawa, Y.; Harada, A.; Kataoka, K. *J. Am. Chem. Soc.* **1999**, *121*, 11247–11248.
(7) Gao, H.; Jones, M.-C.; Chen, J.; Prud'homme, R. E.; Leroux, J.-C. *Chem. Mater.* **2008**, *20*, 3063–3067.
(8) Liu, S.; Weaver, J. V. M.; Save, M.; Armes, S. P. *Langmuir* **2002**, *18*, 8350–8357.
(9) Saito, R.; Akiyama, Y.; Ishizu, K. *Polymer* **1999**, *40*, 655–660.
(10) Saito, R.; Yoshida, S.; Ishizu, K. *J. Appl. Polym. Sci.* **1997**, *63*, 849–854.
(11) Erhardt, R.; Böker, A.; Zettl, H.; Kaya, H.; Pyckhout-Hintzen, W.; Krausch, G.; Abetz, V.; Müller, A. H. E. *Macromolecules* **2001**, *34*, 1069–1075.
(12) Erhardt, R.; Zhang, M.; Böker, A.; Zettl, H.; Abetz, C.; Frederik, P.; Krausch, G.; Abetz, V.; Müller, A. H. E. *J. Am. Chem. Soc.* **2003**, *125*, 3260–3267.
(13) Liu, G.; Yan, X.; Duncan, S. *Macromolecules* **2002**, *35*, 9788–9793.
(14) Park, S.-Y.; Park, M.-Y. *Langmuir* **2007**, *23*, 6788–6795.
(15) Walther, A.; André, X.; Drechsler, M.; Abetz, W.; Müller, A. H. E. *J. Am. Chem. Soc.* **2007**, *129*, 6187–6198.
(16) Jiang, X.; Zhang, G.; Narain, R.; Liu, S. *Langmuir* **2009**, *25*, 2046–2054.
(17) Joralemon, M. J.; O'Reilly, R. K.; Hawker, C. J.; Wooley, K. *J. Am. Chem. Soc.* **2005**, *127*, 16892–16899.
(18) Ding, J.; Liu, G. *J. Phys. Chem. B* **1998**, *102*, 6107–6113.
(19) Ding, J.; Liu, G. *Chem. Mater.* **1998**, *10*, 537–542.
(20) Ding, J.; Liu, G. *Macromolecules* **1998**, *31*, 6554–6558.
(21) Guo, A.; Liu, G.; Tao, J. *Macromolecules* **1996**, *29*, 2487–2493.
(22) Henselwood, F.; Liu, G. *Macromolecules* **1997**, *30*, 488–493.
(23) Liu, G.; Zhou, J. *Macromolecules* **2002**, *35*, 8167–8172.
(24) Liu, G.; Zhou, J. *Macromolecules* **2003**, *36*, 5279–5284.
(25) Stewart, S.; Liu, G. *Chem. Mater.* **1999**, *11*, 1048–1054.
(26) Tao, J.; Stewart, S.; Liu, G.; Yang, M. *Macromolecules* **1997**, *30*, 2738–2745.
(27) Yan, X.; Liu, G.; Li, Z. *J. Am. Chem. Soc.* **2004**, *126*, 10059–10066.
(28) Babin, J.; Lepage, M.; Zhao, Y. *Macromolecules* **2008**, *41*, 1246–1253.
(29) Jiang, J.; Qi, B.; M., L.; Zhao, Y. *Macromolecules* **2007**, *40*, 790–792.
(30) Thurmond, K. B., II; Kowalewski, T.; Wooley, K. L. *J. Am. Chem. Soc.* **1996**, *118*, 7239–7240.
(31) Thurmond, K. B., II; Kowalewski, T.; Wooley, K. L. *J. Am. Chem. Soc.* **1997**, *119*, 6656–6665.
(32) Chiang, W.-H.; Hsu, Y.-H.; Lou, T.-W.; Chern, C.-S.; Chiu, H.-C. *Macromolecules* **2009**, *42*, 3611–3619.
(33) Discher, B. M.; Bermudez, H.; Hammer, D. A.; Discher, D. E.; Won, Y.-Y.; Bates, F. S. *J. Phys. Chem. B* **2002**, *106*, 2848–2854.
(34) Emoto, K.; Nagasaki, Y.; Kataoka, K. *Langmuir* **1999**, *15*, 5212–5218.
(35) Iijima, M.; Nagasaki, Y.; Okada, T.; Kato, M.; Kataoka, K. *Macromolecules* **1999**, *32*, 1140–1146.
(36) Ishizu, K.; Kitano, H. *Macromol. Rapid Commun.* **2000**, *21*, 979–982.
(37) Meier, W. *Macromolecules* **1998**, *31*, 2212–2217.
(38) Shuai, X.; Merdan, T.; Schaper, A. K.; Xi, F.; Kissel, T. *Bioconjugate Chem.* **2004**, *15*, 441–448.
(39) Goh, T. K.; Coventry, K. D.; Blencowe, A.; Qiao, G. G. *Polymer* **2008**, *49*, 5095–5104.
(40) Wiltshire, J. T.; Qiao, G. G. *Macromolecules* **2008**, *41*, 623–631.
(41) Maskos, M. *Polymer* **2006**, *47*, 1172–1178.
(42) Maskos, M.; Harris, J. R. *Macromol. Rapid Commun.* **2001**, *22*, 271–273.
(43) Osborn, C. L. *J. Rad. Curing* **1976**, *3*, 2–11.
(44) Osborn, C. L.; Sandner, M. R. *Coating Plast. Prepr.* **1974**, *34*, 660–663.
(45) Nicol, E.; Niepceron, F.; Bonnans-Plaisance, C.; Durand, D. *Polymer* **2005**, *46*, 2020–2028.
(46) Rheingans, O.; Hugenberg, N.; Harris, J. R.; Fischer, K.; Maskos, M. *Macromolecules* **2000**, *33*, 4780–4790.
(47) Walther, A.; Goldmann, A. S.; Yelamanchili, R. S.; Drechsler, M.; Schmalz, H.; Eisenberg, A.; Müller, A. H. E. *Macromolecules* **2008**, *41*, 3254–3260.
(48) Wilson, D. J.; Riess, G. *Eur. Polym. J.* **1988**, *24*, 617–621.
(49) Huang, H.; Hoogenboom, R.; Leenen, M. A.; Guillet, P.; M., J, A.; Shubert, U. S.; Gohy, J.-F. *J. Am. Chem. Soc.* **2006**, *128*, 3784–3788.
(50) Nardin, C.; Hirt, T.; Leukel, J.; Meier, W. *Langmuir* **2000**, *16*, 1035–1041.
(51) Li, W. W.; Matyjaszewski, K. *J. Am. Chem. Soc.* **2009**, *131*, 10378–10379.
(52) Yusa, S.-I.; Sugahara, M.; Endo, T.; Morishima, Y. *Langmuir* **2009**, *25*, 5258–5265.

(53) Chen, Y.; Tavakley, A. E.; Mathiason, T. M.; Taton, A. T. *J. Polym. Sci., Part A: Polym. Chem.* **2006**, *44*, 2604–2614.
(54) Chan, Y.; Wong, T.; Byrne, F.; Kavallaris, M.; Bulmus, V. *Biomacromolecules* **2008**, *9*, 1826–1836.
(55) Duong, H. T. T.; Huynh, V. T.; de Souza, P.; Stenzel, M. H. *Biomacromolecules* **2010**, *11*, 2290–2299.
(56) Jamroz-Piegza, M.; Walach, W.; Dworak, A.; Trzebicka, B. *J. Colloid Interface Sci.* **2008**, *325*, 141–148.
(57) Kim, B. J.; Chang, J. Y. *Macromolecules* **2006**, *39*, 90–94.
(58) Kim, J. S.; Youk, J. H. *Polymer* **2009**, *50*, 2204–2208.
(59) Mendrek, S.; Mendrek, A.; Adler, H. J.; Dworak, A.; Kuckling, D. *Macromolecules* **2009**, *42*, 9161–9169.
(60) Sakellariou, G.; Avgeropoulos, A.; Hadjichristidis, N.; Mays, J. W.; Baskaran, D. *Polymer* **2009**, *50*, 6202–6211.
(61) Cochin, D.; Candau, F.; Zana, R. *Macromolecules* **1993**, *26*, 5755–5764.
(62) Francova, D.; Kickelbick, G. *Macromol. Chem. Phys.* **2009**, *210*, 2037–2045.
(63) Liu, S. Y.; Gonzalez, Y. I.; Danino, D.; Kaler, E. W. *Macromolecules* **2005**, *38*, 2482–2491.
(64) Tomatsu, I.; Hashidzume, A.; Harada, A. *Macromol. Chem. Phys.* **2009**, *210*, 1640–1646.
(65) Zhu, Z.; Gonzalez, Y. I.; Xu, H.; Kaler, E.; Liu, S. *Langmuir* **2006**, *22*, 949–955.
(66) Cochin, D.; Zana, R.; Candau, F. *Macromolecules* **1993**, *26*, 5765–5771.
(67) Nicolai, T.; Colombani, O.; Chassenieux, C. *Soft Matter* **2010**, *6*, 3111–3118.
(68) Piogé, S.; Fontaine, L.; Gaillard, C.; Nicol, E.; Pascual, S. *Macromolecules* **2009**, *42*, 4262–4272.
(69) Piogé, S.; Fontaine, L.; Soutif, J.-C.; Nicol, E.; Pascual, S. *J. Polym. Sci., Part A: Polym. Chem.* **2010**, *48*, 1526–1537.
(70) Pedersen, J. S.; Gerstenberg, M. C. *Macromolecules* **1996**, *29*, 1363–1365.
(71) Pedersen, J. S. *J. Chem. Phys.* **2001**, *114*, 2839–2846.
(72) Kadam, V. S.; Benyahia, L.; Nicolai, T.; Nicol, E. Manuscript in preparation.
(73) Winnik, M. A.; Yekta, A. *Curr. Opin. Colloid Interface Sci.* **1997**, *2*, 424–436.
(74) Abbott, N. L.; Blankschtein, D.; Hatton, T. A. *Macromolecules* **1992**, *25*, 3917–3931.
(75) Devanand, K.; Selser, J. C. *Macromolecules* **1991**, *24*, 5943–5949.
(76) Liu, Y. Q.; Pollock, K. L.; Cavicchi, K. A. *Polymer* **2009**, *50*, 6212–6217.

604 *Macromolecules* **2011**, *44*, 604–611
DOI: 10.1021/ma1024544

Macromolecules
ARTICLE

Photoresponse of Complexes between Surfactants and Azobenzene-Modified Polymers Accounting for the Random Distribution of Hydrophobic Side Groups

Juliette Ruchmann,[†] Sarra C. Sebai,*[,‡] and Christophe Tribet[‡]

[†]*UPMC & CNRS UMR 7615, Laboratoire de Physico-chimie des polymères et des milieux dispersés, ESPCI, 10 rue Vauquelin, 75005 Paris, France, and* [‡]*Ecole Normale Supérieure & CNRS UMR 8640, Pôle Chimie Biophysique, 24 rue Lhomond, 75005 Paris, France*

Received October 28, 2010; Revised Manuscript Received December 15, 2010

ABSTRACT: The design of photoresponsive macromolecules has opened the route to many applications, in particular to trigger macroscopic responses induced by light irradiation in complex fluids and polymer−surfactant formulations. In this report, we studied the association of three sets of azobenzene modified polymer (AMPs) derived from poly(acrylic)acid with varying integration levels of azobenzene and various azobenzene hydrophobic moieties, with the neutral surfactant Triton X 100 (TX 100). Binding isotherms in dilute aqueous solutions were determined by spectrophotometry (to measure the fraction of bound azobenzene) and capillary electrophoresis (to measure the amount of bound TX 100). The degree of binding of TX 100 to AMPs increases markedly with increasing azobenzene hydrophobicity and density in AMPs. A noticeable and reversible photoresponse of the associates was observed upon exposure to UV/visible lights, although the magnitude of the UV-triggered photodissociation and blue-triggered association depends on the chemical structure of both the azobenzene and AMPs. We introduce a critical distance l_c that accounts as single parameter for the balance between energy gain of hydrophobic binding and energy loss due to chain conformational constraints. Only segments of chains flanked with two azobenzene groups at their ends and shorter than l_c are assumed to bind tightly. l_c is used to fit both the maximum fraction of azobenzene transferred into TX 100 micelles (with saturation well below 100% despite the presence of excess free TX 100) and the amount of bound TX 100 as a function of the density of azobenzene in the chains. The model includes the effect of random distribution of azobenzene moieties along the chains. From this analysis, we find criterions for optimization of the photoresponse as a function of the azobenzene hydrophobicity and density in the chain, and the chain length.

Introduction

Light-responsive polymers and surfactants are attractive command-molecules for remote control of complex fluids. Such systems have been tailored for many applications, in particular in reversible photoswitching properties including phase transition,[1] gelation[2−4] and controlled release,[5] motion or relief on surfaces,[6] and surface properties including surface tension[7,8] and wettability.[9] The macroscopic responses often rely on phototriggered interactions and assemblies between polymers,[10,11] or polymer and surfactant molecules (either conventional surfactants[12,13] or photoresponsive ones[14−16]). At the molecular scale, the interactions are controlled by photoisomerisation of chromophore groups such as azobenzene. For instance, the trans-azobenzene group (apolar isomer) undergoes a reversible transconvertion into its cis-polar isomer under exposure to UV light. Because of their chemical stability and the versatility of their chemistry, azobenzene derivatives have been tailored for application in all fields cited above, as reviewed in refs 17 and 18.

Here with focus on light-responsiveness of assemblies between azobenzene-modified polymers (AMPs) and surfactants in aqueous solutions. These assemblies transduce the photoresponse achieved at the molecular level and amplify it up to the macroscopic scale. The magnitude of responses shows however a complex relationship between AMPs and surfactants, with composition and structural parameters variation (polymer length and hydrophobicity, density and distribution of side groups, etc.) involved. Because of their large field of applications, polymer/surfactants systems (without sensitivity to light) have been extensively studied (for reviews:[19,20]). The trends and properties achieved upon varying the chemical structures of polymers (e.g., increasing the amount or the length of hydrophobic side groups in chains) are generally well described, though hardly in quantitative terms. Hence, prediction on the magnitude of responses that can be achieved in these systems is difficult. In particular, we wonder whether the photoswitch of azobenzene side groups provides a sufficient drive to trigger macroscopic photoresponses. Therefore, we studied a set of AMPs/surfactant systems as models of choice for a better understanding of the stability of these complexes, and eventually to uncover a matrix of optimized parameters, which are more relevant for the formulation of (highly) light-responsive complex fluids.

We present data on the association between the neutral surfactant Triton X 100 (TX 100) and a homologous set of post-modified poly(acrylic)acid with varying amount of azobenzene side groups, to compare polymers with varying hydrophobicities but with the same parent chain. The hydrophobicity of the azobenzene side groups was also varied by using three different precursor molecules and substituents of various hydrocarbon contents (Scheme 1). In addition, those three groups display various spacer lengths between the azobenzene and the polymer backbone. We accordingly evaluated the effects on binding isotherms and photoresponse of (i) the amount of azobenzene per chain and (ii) the chemical structure of the azobenzene side group.

Binding isotherms of TX 100 on AMPs were characterized by capillary electrophoresis to measure the equilibrium amount of

*Corresponding author.

 Published on Web 01/12/2011 © 2011 American Chemical Society

bound surfactants per polymer chain. Binding of azobenzene moieties was studied by spectrophotometry to evaluate the amount of micelle-bound azobenzene, i.e., the intrachain equilibrium between micelle-bound and unbound azobenzene side groups. Data were analyzed with a binding model accounting for the random distribution of azobenzene in the polymer chain and a graphical representation of the model was shown to fit reasonably well to the data.

This binding model is therefore proposed to predict the combined impact of the following experimental parameters: chain length, hydrophobicity of azobenzene side groups, and degree of modification of the chain. Conditions for an optimal response to light are hence discussed on quantitative basis.

Materials and Methods

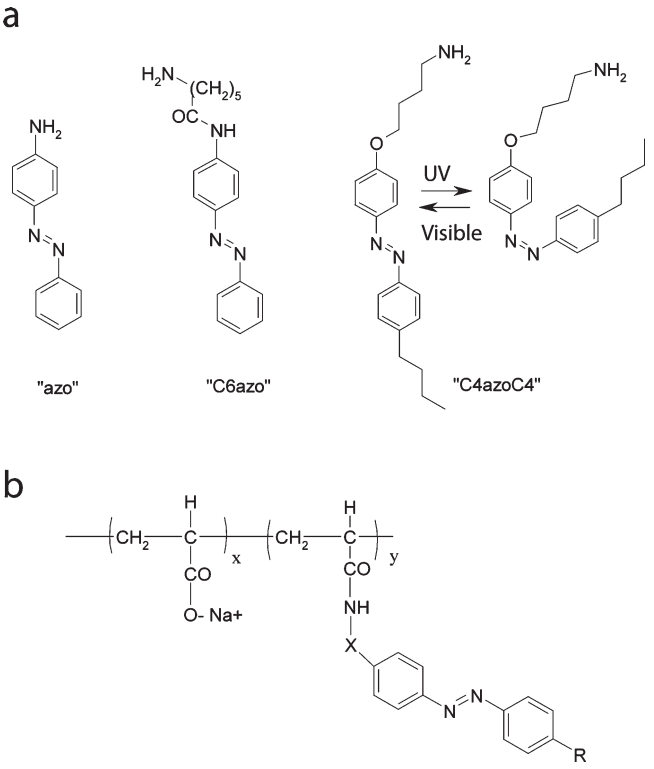
Materials. Nonionic poly(ethylene glycol) tert-octylphenyl ether surfactant (TX 100) was purchased from Fluka. Except if specified, reagents and solvents for the synthesis of polymers were from Aldrich. Synthesis of amino derivatives of azobenzene, C6azo-NH2[21] and C4azoC4-NH2, is detailed in the Supporting Information. The synthesis and characterization of AMPs (structure shown in Scheme 1) is described in refs 2 and 21. Briefly, random copolymers were obtained by coupling poly(acrylic) acid chains (PAA) with either 4-phenylazoanilin, C6azo-NH2, or C4azoC4-NH2 in *N*-methyl-pyrrolidone in presence of 1.2 equiv of dicyclohexylcarbodiimide. A first PAA (Polysciences, Inc., Warrington) had a number-average molecular weight of 42 000 g/mol and polydispersity index of 2.5. Another parent PAA, with M_n 60 000 g/mol and polydispersity 6, was also used. The integration level of azobenzene (Table 1) was determined by ^{1}H NMR: integration ratios were obtained from peaks at 2.0 ppm (for CH in the main chain), 3 ppm (α-amido CH_2 in the grafted moieties), or 0.5 ppm (end CH_3 in one azobenzene moieties, C4azoC4, cf. Scheme 1), and in the range 7−8 ppm for aromatic protons of the azobenzenes. An additional determination was obtained by UV−visible spectrophotometry. The absorbance of an azobenzene polymer solution can be expressed as a function of its azobenzene integration level, τ, the average molar mass of a monomer, $M = (1-\tau)M_0 + \tau M_{azo}$ (with M_0 the molar mass of sodium acrylate, and M_{azo} the molar mass of the azobenzene-containing monomer), the polymer concentration by weight, c, and the extinction coefficient of the azobenzene moiety ε as

$$A = \frac{\varepsilon l c \tau}{M}$$

where l is the optical path in the cuvette. The extinction coefficient used was 2.32×10^4 L·mol^{-1}·cm^{-1} at 350 nm for the phenylazoanilin and C6azo-NH2 dyes,[21,12] or 2.45×10^4 L·mol^{-1}·cm^{-1} for the C4azoC4 group. Possible residual amount of water (< 10 wt %) in the lyophilized powder of the polymers may introduce a slight bias in the latter estimate, which leads to a possible overestimation of its value in Table 1. AMPs are denoted "*m*_τazo", "*m*_τC6azo" or "*m*_τC4azoC4" depending on the nature of the azobenzene side chain (see Scheme 1), with *m* being the number-average molecular weight of the parent PAA (in kg/mol) and τ the mol % degree of modification. Stock solutions of AMPs and surfactant in NaOH-boric acid buffer (20 mM, pH = 9.1) and 150 mM NaCl were stirred for 24 h in the dark prior to measurements (dark-adapted samples).

Dynamic (DLS) and Static Light Scattering (SLS). Simultaneous dynamic and static laser light scattering were carried out on a Brookhaven system, equipped with goniometer, multiple τ digital correlator, and laser with an output power of 30 mW, at a wavelength of 637 nm. The data were collected at 25 °C and 90° angle. Temperature control within 0.1 °C was achieved using a Julabo F25 refrigerated bath circulator. Sample solutions were prepared by mixing equal volumes of a 2 g/L TX 100 stock solution in buffer, with a 2 g/L polymer stock solution in 20 mM boric acid-NaOH buffer pH 9.2, with 150 mM NaCl, and filtered on 0.2 μm pore size Millex filters (Millipores). Exposure to UV (365 nm) or blue light (470 nm) was performed in situ

Scheme 1. Structures of Amino Derivatives of Azobenzenes "azo", "C6azo", "C4azoC4" (a) and Randomly Modified Polyacrylic acids (AMPs) (b), with y Typically < 6 mol %, x = (100 - y), X = ∅, −$(CH_2)_5$CONH−, or −$(CH_2)_4$−O−[a]



[a] Illustrated with C4azoC4, the apolar isomer (trans) is reversibly converted to the polar cis isomer by exposure to UV light. The photostationary cis/trans ratio depends on the wavelength (~5:1 at 365 nm; ~1:5 at 436 nm).

Table 1. Composition of the Azobenzene-Modified Polyacrylic Acids (AMPs)

		degree of modification (mol %) (τ)		
		from ^{1}H NMR		
	molecular weight (g/mol)[a]	based on protons at 3 ppm	based on aromatic protons	from UV absorbance at 350 nm
42_1C6azo	42 000	1.1 ± 0.1	0.7 ± 0.1	0.9 ± 0.1
60_2.5C6azo	60 000	2.6 ± 0.2	2.1 ± 0.2	2.5 ± 0.2
42_3.5C6azo	42 000	3.4 ± 0.3	3.6 ± 0.3	3.2 ± 0.2
42_5C6azo	42 000	6.1 ± 0.5	4.6 ± 0.4	4.9 ± 0.3
42_1C4azoC4	42 000	0.9 ± 0.1	0.8 ± 0.1	0.7 ± 0.1
42_4.5C4azoC4	42 000	5.0 ± 0.5	3.9 ± 0.2	4.5 ± 0.5
60_1azo	60 000	n.a.	1.4 ± 0.1	0.9 ± 0.1
60_6azo	60 000	n.a.	6.3 ± 0.5	6.1 ± 0.2

[a] Number-average M_n of the parent poly(acrylic acid) under its sodium form.

from a fiber optic placed on the top of the cell (photodiode system CoolLED PE-2, Roper Scientific, France)

Frontal Analysis Continuous Capillary Electrophoresis. Experiments were carried out with a Beckman P/ACE system MDQ instrument equipped with a diode array multiwavelength UV visible detector (Beckman Instruments Fullerton, CA) operating at 25 °C and fitted with bare silica capillaries of 75 μm × 31 cm; effective length: 21 cm (Chromoptic, France). The capillary was flushed daily with 0.1 M NaOH, followed by a water rinse, and finally was allowed to equilibrate with the buffer (20 mM boric acid-NaOH, pH 9.1, 150 mM NaCl). Sample solutions were prepared by mixing aliquots of a 2 g/L TX 100 stock solution in buffer, with 2 g/L polymer stock solution in buffer. The final TX 100 concentration range was 0.05 g/L −1.2 g/L, and the final polymer concentration was 0.2 g/L. Frontal analysis electrophoresis (see ref 21), was carried out using the continuous electrokinetic injection mode against the running buffer, with a positive voltage (3.5 kV) and constant pressure (0.1 psi) applied to the inlet. A first separation was run on the dark-adapted sample, which was thereafter exposed to 365 nm UV light for 20 min (1 mW/cm^2) before being reanalyzed immediately after irradiation. The concentration of free TX 100 was determined from its UV absorbance, using a calibration curve constructed with samples of known concentrations of TX 100 and no polymer.

UV−Visible Spectrophotometry. Absorbance measurements were carried out with a diode array UV−visible spectrophotometer (Evolution Array, Thermo Scientific). A 3 mL sample solution of 0.2 g/L AMPs (in 20 mM boric acid−NaOH buffer, pH 9.1 and 150 mM NaCl) was gradually supplemented by aliquots (typically 15 μL) of the surfactant stock solution at 5 g/L. In order to maintain a stationary fraction of 80% of trans isomer of azobenzene during the experiments, the samples were vertically exposed to visible light (436 ± 10 nm, from a 250 W mercury arc lamp (Oriel) equipped with interference filter). The differential absorption spectra of the samples were obtained by subtracting the spectrum of polymer with no surfactant to the spectrum in the presence of surfactant, after normalization to the dilution factor due to the addition of surfactant. (A UV−vis spectrum is given in the Supporting Information, Figure S1.)

Results and Discussion

Light-Responsive Complexes. Light scattering measurements were carried out to assess the formation of complexes between AMPs and TX 100 (Figure 1). Mixtures of 1 g/L TX 100 and 1 g/L of AMPs (under its dark adapted form) scattered significantly more light than a solution of 1 g/L AMPs and 1 g/L TX 100 separately. In the dilute conditions used here, the scattered intensity was mainly affected by variation of average molar masses of complexes, arising from the binding of TX 100 to the polymer. The association with TX 100 was hence detected by a significant increase in scattering intensities in TX 100/AMPs mixtures (Figure 1), irrespective of side group of the polymers (either azo, C4azoC4, or C6azo). A noticeable feature in Figure 1 is the marked decrease in the scattering intensity after exposure to UV light (365 nm) of the TX 100/AMP mixture, followed by significant recovery of scattering after exposure to blue light (470 nm) in solutions containing azo-modified, C4azoC4-modified, and C6azo-modified chains. These variations illustrate the photodissociation of complexes under UV light and reassociation under blue light. In contrast, the intensity scattered by mixtures of TX 100 and 42_4.5C4azoC4 is less affected by light, suggesting that the nature of the azobenzene chromophore side group plays an important role in the magnitude of the photoresponse. Also light scattering analysis showed that the apparent hydrodynamic radii of the complexes does not change upon exposure to either UV or blue light irradiations and are similar to that of the radius of the polymer with no TX 100

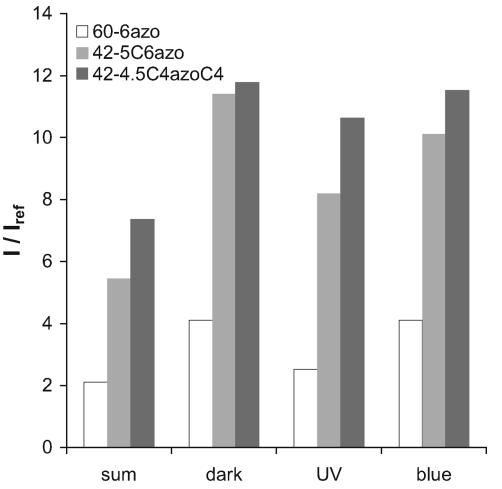


Figure 1. Intensity scattered at 90° angle by solutions of 1 g/L TX 100 and 1 g/L AMPs in 150 mM NaCl, 20 mM boric acid−NaOH buffer pH 9.2, with polymers 60_6azo, 42_5C6azo, and 42_4.5C4azoC4. Key: "sum" represents the sum of intensities scattered by independent solutions of TX 100 and polymer at 1 g/L each; "dark", dark-adapted mixture; "UV", same sample after 2 min exposure under UV light (365 nm); "blue", UV-sample after 2 min exposure to visible light (436 nm). Intensities are normalized by the intensity I_{ref} scattered by toluene.

(ref 22 for examples on C6azo polymers). Here radii in the range 20−30 nm were measured by dynamic light scattering irrespective of the composition of polymer and presence or absence of TX 100 (See Supporting Information, Figure S2). Micelles of TX 100 in absence of polymers have a radius of ca. 4−5 nm, and complexation is accordingly assumed to proceed by "decoration" of long AMPs chains with one or several micelles of TX 100.

Binding of Azobenzene Moiety to Micelles. To evaluate the fraction F_{exp} of bound azobenzene moieties to micelles, we measured by spectrophotometry their spectral shift in solutions of polymers supplemented with TX 100. Results are shown in Figure 2. The transfer of an azobenzene from water to the apolar core of micelles red-shifts its UV−visible absorbance spectrum, resulting in a differential absorbance of the azobenzene in presence and absence of TX 100. The spectral distortion combines the effect of transfer from polar to less polar solvent, which typically induces blue-shifts,[23] and red-shifts due to, e.g., self-assemblies of azobenzenes.[24] In our case, the differential absorbance varies in proportion with the fraction of bound azobenzene chromophore.[12] The differential extinction coefficient of C6azo has been established in[12] and used in eq 1 to estimate F_{exp},. For the sake of simplicity, we used the same equation for C4azoC4 polymers and azo-modified polymers. In practice, UV−vis spectra of C4azoaC4-modified polymers and azo-modifed polymers displayed the same absorption peak in absence of TX 100, although extinction coefficients of the C4azoC4 moieties differ slightly: $\varepsilon_{347\,nm} = 2.32 \times 10^4\ L \cdot mol^{-1} \cdot cm^{-1}$ and $2.45 \times 10^4\ L \cdot mol^{-1} \cdot cm^{-1}$ for C6azo and C4azoC4, respectively.

Therefore, the experimental fraction of bound azobenzene F_{exp} is defined as

$$F_{\exp} = \frac{\mathrm{Abs(TX100)} - \mathrm{Abs(no\ TX100)}}{h\Delta\varepsilon[\mathrm{azobenzene}]} \qquad (1)$$

with $\Delta\varepsilon = 5.1 \times 10^3\ L \cdot mol^{-1} \cdot cm^{-1}$, h the thickness of the cell, [azobenzene] the molar concentrations of azobenzene, Abs() the absorbance at 370 ± 1 nm in presence and absence of TX 100. Figure 2 shows a rapid increase in F_{exp} with increasing concentration of TX 100 occurring above a threshold concentration of TX 100 that is close to its critical

micellar concentration (cmc = 0.1 g/L). At incipient binding, the composition of the surfactant/azobenzene assemblies is however likely to contain a dominant fraction of azobenzene and to vary rapidly with concentrations in samples.[22] The implicit assumption of Beer's law in eq 1 may not be valid if azobenzene moieties form clusters and the value of F_{exp} close to cmc is thus only indicative of the formation of complexes. In contrast, in presence of excess of surfactant (i.e., beyond 0.3 g/L of TX 100 in Figure 2), F_{exp} levels down and slowly reaches a plateau. In this range of composition, the ratio of bound azobenzene per surfactant is low and azobenzene groups are diluted in excess bound TX 100, hence eq 1 should be valid (cf below, the ratio of bound TX 100/polymer reaches up to ~1.6 g/g in presence of excess TX 100, which corresponds to less than two azobenzene groups every 100 molecules of bound TX 100). In order to analyze the binding of AMPs of different compositions, we considered accordingly F_{exp} in the presence of excess TX 100. The parameter quoted F_{max} in Table 2, equals the value of F_{exp} reached at TX 100 of 0.8 g/L, an abscissa somewhat arbitrarily fixed in the plateau region of the data. F_{max} depends markedly on the composition of polymer. The obvious jump of F_{max} upon increasing τ from 1 mol % to 2.5 mol % in C6azo-modified polymers is indicative of a sharp transition between weak binding and tight binding regimes upon increasing the degree of modification of AMPs. The full (100%) binding is however gradually approached with increasing τ. Also in Table 2, comparisons of

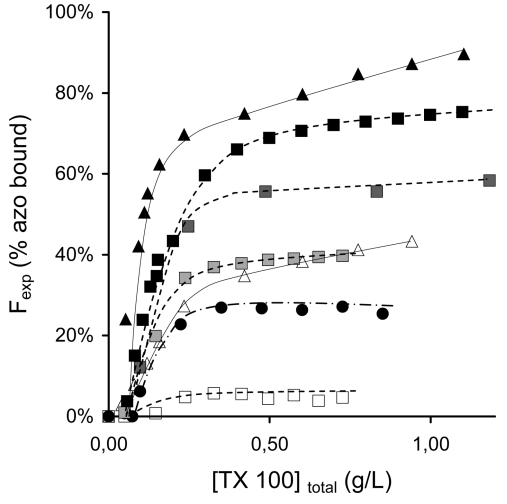


Figure 2. Fraction of micelle-bound azobenzene, F_{exp}, as a function of total TX 100 concentration, as obtained from the variation of absorbance at 370 ± 1 nm and eq 1. Samples were maintained under blue light (436 nm). (●) 60_6azo, (□) 42_1C6azo, (light gray box) 60_2.5C6azo, (dark gray box) 42_3.5C6azo, (■) 42_5C6azo, (△) 42_1C4azoC4, (▲) 42_4.5C4azoC4. All solutions were in 20 mM boric acid-NaOH pH 9.2, 150 mM NaCl. Lines are guide for the eye.

polymers with similar degree of modification show that the degree of association increases with increasing hydrophobicity of the azobenzene in the following order: azo < C6azo < C4azoC4 (N.B. F_{exp} for 60_1azo was too low to be determined). All these features are characteristic properties of hydrophobic associations between surfactants and amphiphilic polymers.

Binding Isotherms of Surfactant into AMPs. Capillary electrophoresis was used to evaluate the binding isotherms, i.e. the amount of polymer-bound TX 100 as a function of concentration of unbound surfactant. Figure 3 shows an abrupt onset of binding at $[TX\ 100]_{free}$ of ca. 0.1 g/L, which is consistent with the above measurements by spectrophotometry. These isotherms also confirm the enhancement of binding upon either increasing the hydrophobicity of the azobenzene side group, or increasing the density of side group of the polymer chains. At concentrations of free TX 100 between 0.1 and 0.2 g/L, we observe on all isotherms a regime of high affinity. In this regime, our measurements show that the amount of bound TX 100 is not markedly dependent on exposure to light. In contrast, in the presence of excess free micelles, which in practice was reached above $[TX\ 100]_{free}$ = 0.2 g/L, the composition of complexes varies markedly less with increasing TX 100 (quasi-saturation) and the association becomes light-responsive. The lack of association below the cmc of the surfactant points out that the binding of AMPs does not markedly perturb micellization of TX 100. Accordingly, in the presence of excess TX 100, the association can be schematically described as a complex of AMP with one or a few micelles of TX 100. The molar mass of TX 100 micelles are of the order of 66 000 g/mol.[25] Association of one micelle on average per chain of AMP thus corresponds to a calculated TX 100/polymer weight ratio of 1 g/g to 1.6 g/g. Table 2 reports the measured amount of bound TX 100 per AMP, in the quasi-saturation conditions, that typically range in the window of 1 g/g to 1.8 g/g in the case of AMPs having the highest hydrophobicities (42_4.5C4azoC4, 42_3.5C6azo, and 42_5C6azo). Some isotherms display a drift in the plateauing regime. The uncertainty of measurement becomes however larger in presence of increasing excess of surfactant, because the amplitude of the signal of bound TX 100 relative to the free ones decreases below 10%. To compare AMPs, irrespective of drifts in the measurements, we determined the binding ratio at the end of the high affinity regime, i.e. at the cross over between the rapid increase in association and the quasi-plateau (cf. lines in Figure 3 A, B).

Model for Critical Segment Hydrophobicity vs Experimental Binding Ratios. The cartoon model conventionally proposed for the binding of surfactant to amphiphilic polymers in dilute solutions is the so-called necklace of micelle-like pearls. Hydrophobic side groups of an isolated macromolecule penetrate the core of surfactant aggregates whose size and properties are similar to those of unbound micelles

Table 2. Characteristic Parameters of Association and Photoresponse

polymer	F_{max} (%)	TX_{bound}:AMP (dark) (g/g)	TX_{bound}:AMP (UV) (g/g)	$l_c\tau$ (spectro)	$\langle L\rangle l_c\tau^2$ (dark)	$\langle L\rangle l_c\tau^2$ (UV)
42_1C6azo	5	0.25	0.08	0.09	0.16	0.03
60_2.5C6azo	38	1.1	0.4	0.28	1.22	0.25
42_3.5C6azo	56	1.3	0.62	0.44	2.25	0.46
42_5C6azo	75	1.4	0.85	0.7	4.87	1.0
42_1C4azoC4	42	0.5	0.2	0.31	0.36	0.12
42_4.5C4azoC4	90	1.8	1.6	15	9.1	3.0
60_1azo	n.d.	0.13	0.08	n.d.	0.06	0.02
60_6azo	27	0.95	0.4	0.16	1.62	0.54

F_{max} is the maximum values of F_{exp} determined from Figure 2, in presence of excess TX 100, as detailed in text ; rows 2 and 3 provide experimental weight ratios of bound TX 100 per (total) AMPs at the cross over regimes shown in Figure 3 ; $l_c\tau$ is determined from Figure 4 and $\langle L\rangle l_c\tau^2$ from Figure 5; n.d., too low to be determined.

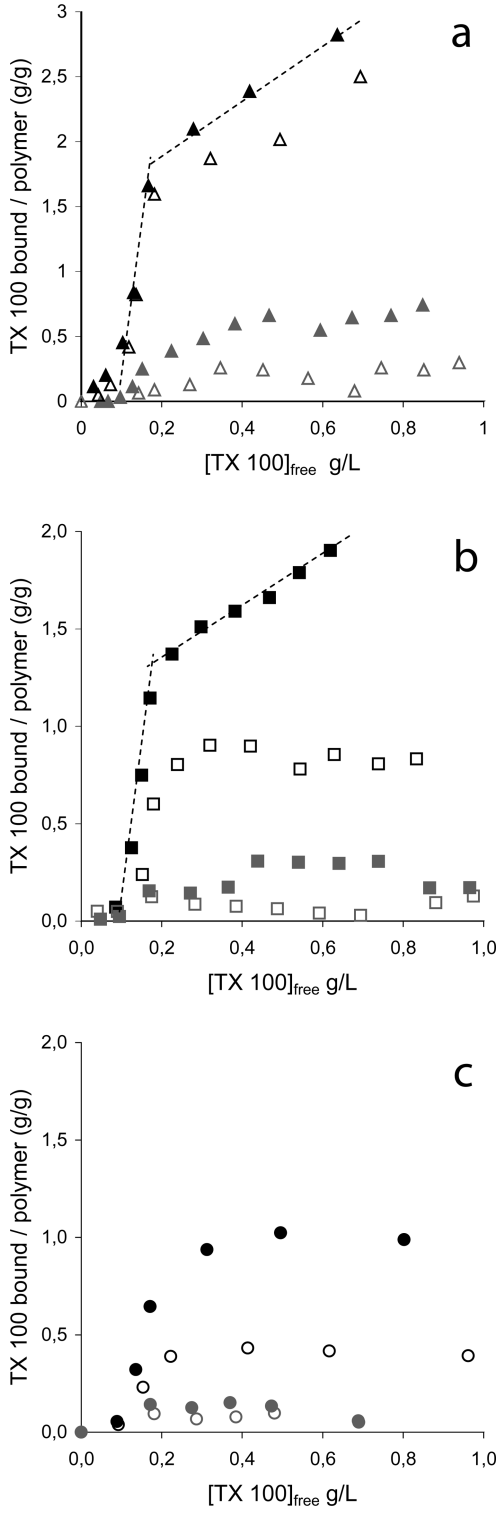
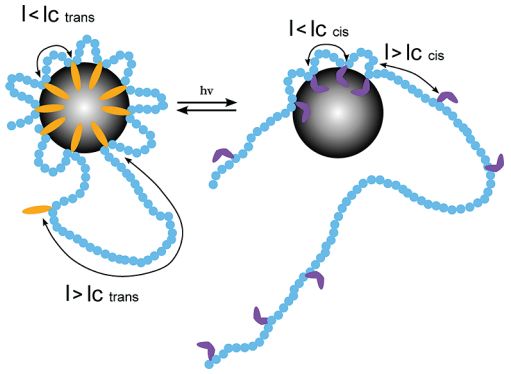


Figure 3. Binding isotherms of TX 100 on AMPs at 0.2 g/L in 20 mM NaOH−boric acid buffer pH 9.2 and 150 mM NaCl. Black and gray symbols are meant for dark-adapted samples, open symbols are for UV-exposed ones: (A) (gray triangle) 42_1C4azoC4, (▲) 42_4.5C4azoC4; (B) (gray square) 42_1C6azo, (■) 42_5C6azo; (C) (gray dot) 60_1azo, (●) 60_6azo.

(Scheme 2). On the basis of this scheme, we propose to identify relevant parameter(s) for optimization of the response to light. In the generally accepted view, association of one (hydrophobic) monomer in a micelle-like cluster competes with steric and entropic loss due to conformational constraints in the backbone. Considering flexible chains and

Scheme 2. Illustration of AMP Multiple Association onto a Hydrophobic Cluster As Controlled by the Balance between the Loop Free Energy and the Free Energy of Transfer of Azobenzene between Water and the Apolar Core upon Light Irradiation



only hydrophobic association (no other significant energy gain due to ionic or hydrogen bond formation) the competition mentioned above comes down to balancing the energy gain from transfer of a hydrophobic monomer from water into the apolar core of a micelle, with the free energy cost of transition from coil to loop conformation of the backbone. Additional loop−loop repulsions may be important in the case of micelles with a dense corona of polymer(s), especially when the polymer hydrophobic grafts dominate the composition of the micelles (e.g., in absence of surfactant or close to critical micellar concentration of the surfactant). The corresponding theory accounting for interloop effect has been developed by Borisov et al.[26,27] Here we will restrain the present purpose to conditions where the energy term arising from interloop interactions can be neglected. In practice, excess micelles and surfactant concentrations well above the critical micellar concentration fulfill these conditions because the number of loops per micelle is low. In this case, Lairez et al.[28] have shown that conformational penalty of a loop is balanced by the energy of transfer (into the micelle core) of the hydrophobes located at both ends of the loop. In the case of flexible neutral chains studied by Lairez, the free energy of loop formation increases monotonously with the length of the loop, which in turn defines a maximal length compatible with the hydrophobes binding. In the same spirit, we define a critical length, l_c, at which the free energy required to fold the loop (i.e., including all the complex coulombic and steric contributions in our case) equals the free energy gain of transfer of the azobenzene end group from water to the micelle-like cluster. Thus, the parameter l_c only depends on the hydrophobicity of an isolated chromophore as measured by its energy of transfer from water to an apolar solvant.

From the remarks above, it is expected that copolymers whose grafting density is over the threshold density of 1 azobenzene every l_c monomers should bind tightly to micelles. The distance between hydrophobic monomers is however polydisperse in synthetic copolymers. We have to account for this practical feature, and include the impact of statistic distributions of hydrophobes on the chains in the model. Random distribution matches with most practical cases of amphiphilic copolymers, in particular with polymers used in the present study.[29] First, we calculate the fraction of azobenzene in an isolated (bound) chain that undergoes association. According to the model above, all segments of the chain shorter than l_c and with azobenzenes at both ends must attach to the micelle and form a loop. Consequently, the fraction F_{azoth} of micelle-bound azobenzene corresponds to the fraction of azobenzene groups that are separated from

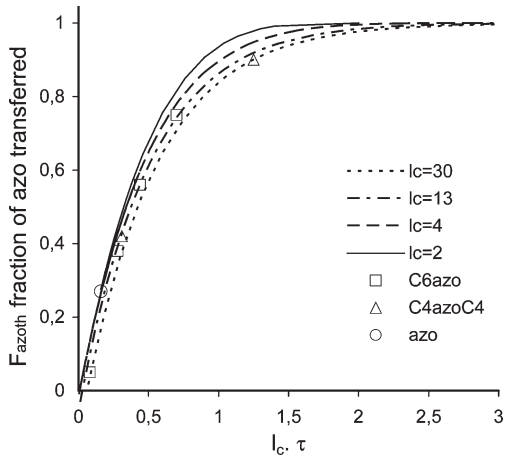


Figure 4. Variation of F_{azoth} with parameters l_c and τ from eq 2 and graphic determination of the product $l_c\tau$ from matching F_{azoth} with F_{max} as given in Table 2. Here $\langle L\rangle = 450$.

another azobenzene by a length smaller than l_c monomers. In a chain of number-average length of $\langle L\rangle$ with an integration level of τ hydrophobes every 100 monomers, F_{azoth} reads as:

$$F_{azoth} = 1 - \frac{\langle L\rangle\tau - 2}{\langle L\rangle\tau}(1-\tau)^{2l_c} - \frac{2}{\langle L\rangle\tau}(1-\tau)^{l_c} \qquad (2)$$

The product $\langle L\rangle\tau$ is the number of hydrophobes (azobenzene) per chain. The first term in eq 2 accounts for the $(\langle L\rangle\tau - 2)$ azobenzene groups located in the middle of the chain and flanked by two azobenzene neighbors distant from each other by a distance bigger than l_c units. Therefore, both segments on their left and right side must display a sequence of l_c successive hydrophilic monomers, which gives the probability of occurrence $(1-\tau)^{2l_c}$. Last term in eq 2 accounts for the two azobenzene groups close to both ends of the chain. They are flanked by one azobenzene group only on one side distant by a segment of minimal length l_c, leaving the other side devoid from hydrophobes (end of the chain). Additional details on eq 2 are provided in the Supporting Information. Finally, F_{azoth} increases rapidly with τ and with l_c, and is weakly sensitive to $\langle L\rangle$ in the window of experimental interest ($\langle L\rangle \sim 450$). Variation of F_{azoth} are plotted in Figure 4 as a function of $l_c\tau$ which enabled us to represent in the same graph the curves representative of experimental range of the parameters l_c, and τ. $\langle L\rangle$ was somewhat arbitrarily fixed to 450 (450 monomers correspond to M_n of 42000 g/mol of the parent poly(acrylic)acid under its sodium form). Except in the window of $l_c\tau$ values between 0.5 and 1.5, differences between the curves in Figure 4 appears of similar magnitude as the uncertainty of measurement of F_{max} obtained from Figure 2. The coordinates ($l_c\tau$, F_{max}), with F_{max} given in Table 2 for each of the various AMPs, were accordingly graphically determined in Figure 4. Self-consistence was achieved by matching the values of τ experimentally determined (as the mean of the values in Table 1) with the position of data points in Figure 4 on the theoretical curve corresponding to the same τ, within uncertainty. Eventually, we evaluated $l_c = 30 \pm 5$ for the C4azoC4 polymers, $l_c = 12 \pm 2$ for the C6azo polymers, and $l_c = 3 \pm 1$ for the azo polymers under their predominantly trans form.

Finally, the gradual increase in association of C6azo polymers with increasing τ is thus fairly compatible with a model assuming 100% binding of the segments of polymer chain whose density is above the critical threshold of two azobenzene every 12 monomers, together with a random distribution of the monomers. The threshold density of binding is found

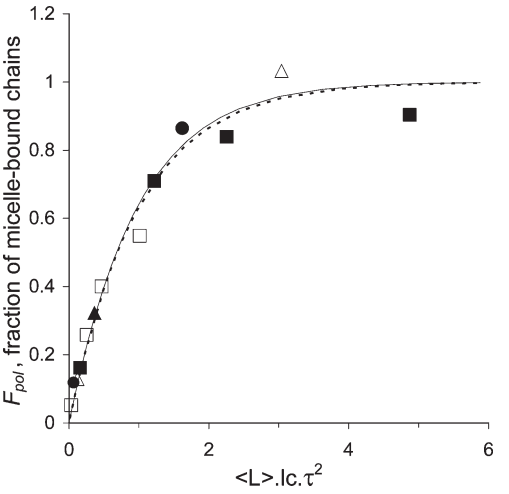


Figure 5. Variation of F_{pol}, the fraction of bound AMP chains in micelles as given by eq 4. Two examples covering the range of experimental parameters are given: dashed line: $\langle L\rangle = 450$, $l_c = 30$; full line $\langle L\rangle = 150$ and $l_c = 2$ and varying τ. Determination of the coordinates of experimental data points obtained from binding isotherms are explained in the text; AMPs modified with (▲, △) C4azoC4, (■, □) C6azo, (●, ○) azo; closed symbols, in the dark; open symbols, exposed to UV.

to decrease with increasing azobenzene side group hydrophobicity.

Variation of l_c upon Trans−Cis Transconversion. Within the same framework, we calculate now the effect of parameters l_c, $\langle L\rangle$, and τ on the amount of bound surfactant in order to evaluate the variation of l_c upon cis−trans isomerization, which may help the optimization of photoresponses. To keep the number of parameters as low as possible, we made several assumptions. First, we restrained the model to conditions of surfactant concentration above cmc and excess micelles equilibrated with bound or free polymer chains. Experimental results shown on Figure 3 showed that the response to light was maximal in this regime, with micelles containing a predominant fraction of TX 100. Then we assumed that when a polymer chain contains at least one segment with a hydrophobicity above the critical threshold value (i.e., a segment shorter than l_c with at least two azobenzene in it), conditions for tight binding are fulfilled with this chain binding to a micelle. The latter assumption simplifies the presumably more gradual transition from weak association to tight association regimes with increasing the number of upper-critical segments in one chain. Finally we did not account here for chain polydispersity in length. Under these assumptions, a chain of total length $\langle L\rangle$ can be decomposed into $\langle L\rangle\tau$ segments of length l_c, each of those beginning with an azobenzene. According to the first hypothesis, a chain composed solely by $\langle L\rangle\tau$ subcritical segments will not bind to a micelle. It is possible to write the probability, P, for a segment of l_c monomers to feature subcritical hydrophobicity as:

$$P = (1-\tau)^{l_c} \qquad (3)$$

Thus, the fraction of micelle-bound chains F_{pol} can be expressed as the complement to 1 of the fraction of chains containing only subcritical segments:

$$F_{pol} = 1 - P^{\langle L\rangle\tau} = 1 - (1-\tau)^{\langle L\rangle l_c\tau} \qquad (4)$$

The influence of parameters l_c and τ on binding is shown in Figure 5. The range of experimentally relevant parameters corresponds to $l_c \sim 1$ to 30, $\tau \sim 1\%$ to 6%, and $L \sim 100-1000$.

The exponent term in eq 4, $\langle L\rangle l_c\tau$, is accordingly well above 1, with τ being significantly smaller than 1. At first approximation, F_{pol} could thus be developed as a polynomial function of $\langle L\rangle l_c\tau^2$. Plotting F_{pol} as a function of the reduced parameter $\langle L\rangle l_c\tau^2$ validates in Figure 5 that a quasi master curve is obtained in the range of experimentally reasonable values of the parameters l_c, τ, and $\langle L\rangle$. This curve enables the comparison between the experimental values of the amount of bound surfactant and calculated ones. Namely, the model assumes the binding of a chain onto an isolated micelle whose properties should be close to micelles of pure TX 100. Hence, the experimental weight ratio, TX $_{\text{bound}}$/polymer, is relied to F_{pol} by:

$$\frac{M_{pol}}{M_{mic}}\frac{\text{TX}_{\text{bound}}}{\text{polymer}} = F_{pol} \qquad (5)$$

with M_{mic} and M_{pol} the molar masses of micelle and AMP of ca. 66 000 and 42 000 g/mol respectively). In the case of dark-adapted samples, experimental ratios were used to place data points in Figure 5 using the values of l_c obtained from spectrophotometry (Table 2, τ given in Table 1, and floating $\langle L\rangle$). Data matched fairly with calculated F_{pol}, irrespective of τ and of the nature of the azobenzene, with a value of $\langle L\rangle$ of 150 $\pm$ 10 (closed symbols in Figure 5, corresponding abscissa in Table 2). We believe that it would be rather delicate to comment on the difference between this value of $\langle L\rangle$ and the number-average $\langle L\rangle$ of ca. 450, especially since the polydispersity of the AMPs is not included in the model. Of more importance to rank the AMPs as a function of binding strength, however, is the amount of bound TX 100 at saturation with various AMPs that matched the theoretical curves in Figure 5 using the parameters τ and l_c measured independently by spectrophotometry.

A value of the reduced parameter $\langle L\rangle l_c\tau^2$ can thus be ascribed to each polymer, either in dark-adapted or UV-exposed conditions. The value of $\langle L\rangle l_c\tau^2$ determined for dark adapted conditions can be divided by $\langle L\rangle l_c\tau^2$ determined in UV conditions to provide the ratio l_c (dark)/l_c (UV) which gives a clear quantification of the photoresponse irrespective of the structural parameters $\langle L\rangle$ and τ. To get an accurate estimation of $\langle L\rangle l_c\tau^2$, for UV-exposed samples, we restricted the analysis to the cases of $F_{pol} < 0.8$ and $\langle L\rangle l_c\tau^2 < 2$, avoiding the plateau region in the theoretical curve. Using $\langle L\rangle = 150$ and the mean values of τ given in Table 1, l_c was floated to fit the data corresponding to UV-adapted sample, and values of the abscissa are reported in Table 2. In the case of C6azo polymers, the same l_c can be used for all the degree of modification (open squares in Figure 5). This analysis finally brings the following ratios of l_c (UV)/l_c (dark): 0.33 for both "azo" and "C4azoC4" AMPs, and 0.21 for C6azo AMPs. These values are of the same order of magnitude. Upon exposure to UV light, the threshold density for binding is typically increased by a factor of 3 to 4, irrespective of the nature of the azobenzene and the degree of modification of AMPs.

Discussion

Altogether, our results bring a consistent picture of conditions of tight hydrophobic association of random amphiphilic copolymers with TX 100 in dilute conditions. Namely, tight surfactant/polymer association is assumed to proceed, without marked change in micellar properties, from the attachment of segments of the chain whose density of azobenzene is above a critical threshold. The assumption of weak or no perturbation of micellar properties is valid in absence of marked stabilization of the micelle upon attachment of the polymer. This may be more frequently occurring with neutral surfactants, in absence of strong interaction between the head groups of the surfactant and the polymer.[30−33] Strong stabilization of surfactant assemblies and comicellization well below the cmc of the surfactant are, for instance, occurring with polymer and surfactant of different charges[34,35] Here, the weak perturbation of surfactant assembling in presence of AMPs is reflected by their lack of effect on the cmc of TX 100. An advantage of our simple binding model is that the composition of complexes can be predicted as a function of molecular and structural parameters such as the polymer length, the average density of modification with hydrophobes, and the threshold density defined by a maximal number of l_c monomers between two hydrophobes undergoing tight associations. Finally, the control of associations between a given pair of AMPs and surfactant partners comes down to the magnitude of variation achieved upon varying l_c.

We now discuss the consequences of the above remarks on the response to stimuli, i.e., on small stimulus-triggered variations of l_c. Stimuli-responsive hydrophobic association is associated here with the effect of light irradiation on azobenzene-modified chains, but it may more generally encompass any variation of the energy of transfer of hydrophobic side groups into micelles under the control of other external conditions that affect l_c (e.g., change in the solvent condition, effect of temperature on water-solubility of polymers, modulation of the ionic charge by pH variation, etc.). In practice, large response to a trans−cis conversion of azobenzene side groups is not easy to achieve and requires tedious synthesis and studies of homologous sets of polymers. The first conclusion drawn from the above analysis is that the polymer architecture is important: sequential distribution of hydrophobes is preferable since a random distribution leads to a broader transition from conditions of no association ($\tau < 1/l_c$) and tight association ($\tau > 1/l_c$). As a second consequence, we note that the amplitude of stimuli-triggered release strongly depends on τ. At high τ a plateau regime is reached (Figures 4 and 5), and no change in the degree of association can be expected upon small stimuli-triggered variation of l_c.

The optimum photoresponse is thus obtained at low τs, when the amount of binding (F_{pol} and F_{azoth}) varies almost linearly with l_c (cf. Figures 4 and 5), which is achieved typically when both $l_c\tau < 1$ and $\langle L\rangle l_c\tau^2 < 2$. In practice, the chemical nature of azobenzene, that affects l_c, is not as easy to modulate as chain length, $\langle L\rangle$, or degree of integration of azobenzene, τ. A procedure for optimizing the photoresponse consists accordingly to screen in a set of AMPs modified with the same azobenzene side group, either decreasing τ, or $\langle L\rangle$, until the above two conditions are reached. The optimal range of τ will depend on the azobenzene side group hydrophobicity, but finally similar degree of sensitivity to the reduced parameters ($l_c\tau$ and $\langle L\rangle l_c\tau^2$) is expected to be reached if τ, or $\langle L\rangle$, is low enough. From this approach, the effect of changing the nature of the azobenzene side group can always be balanced by adjusting the chain length or the density of azobenzene. In addition, we found experimentally that the magnitude of photovariation of l_c does not markedly differ for azobenzene with no spacer ("azo"-modified AMPs), C6azo and C4azoC4 AMPs. This point is reflected by the fact that in each set of AMPs, one example at least showed a photorelease of ca. 50%-60% of bound TX 100 upon exposure to UV (Figure 3A−C). In order to achieve such a high response to UV, one just needs a higher density of azobenzene side groups while decreasing their hydrophobicity; 60−6azo, 42−2.5 C6azo, and 42−1C4azoC4 display accordingly similar magnitude of response. Increasing chain length is expected to produce similar effect as increasing l_c (this is translated in the abscissa of Figures 4 and 5 by the product $\langle L\rangle l_c$), but this point is not validated yet and deserves future investigations. Making longer chains is however likely to favor associations, since the probability to have at least one segment of high local density of azobenzene increases with the chain length in random copolymers.

It may be desirable to lower the degree of modification of the chains and to use low concentrations of azobenzene. For instance, the absorbance of samples must be low enough to permit penetration of light deep into the materials. For millimeter-thick systems, a concentration of azobenzene below one millimolar should hence be preferred (accounting for extinction coefficient of azobenzene of the order of 10^4 $L \cdot mol^{-1} \cdot cm^{-1}$). Conventional application of surfactant/polymer mixtures as emulsifiers, or in gelation and viscosity control, typically requires a few weight percent polymers in solutions, and the upper limit of millimolar concentration of azobenzene are thus corresponded to degree of modification typically lower than 1 mol %. In this case, our analysis pleads in favor of azobenzenes imparted with high hydrophobicity (e.g., by alkyl substituents like in C4azoC4) grafted on long chains at low density of modification.

Conclusion

We have studied the association of three sets of azobenzene-modified copolymers (AMP), bearing photochromes with different hydrophobicities, with TX 100. Our results show that the degrees of binding of both TX 100 (amount of bound surfactant per AMP) and azobenzenes (maximal fraction of bound azobenzene) increase with increasing hydrophobicity and density of azobenzene in AMPs. A marked and reversible response to trans−cis isomerization can be achieved under exposure to UV/visible lights, with up to 50−60% of the dark-bound TX 100 being released under UV light. However the magnitude of photoresponse of AMP:TX 100 complexes and the composition of complexes markedly depends on the chemical structure of both the azobenzene and AMPs. A simple model of binding that takes into account the varying hydrophobicity of the diverse azobenzene and their random distributions in AMPs is proposed. On the basis of the assumption that tight association takes place on polymer segments whose density of azobenzene is above a threshold value, the degrees of (tight) binding are written as a function of three molecular and structural parameters: the average polymer length $\langle L \rangle$, the average density of modification of AMP, τ, and the threshold density as defined by l_c, the maximal number of monomers between two hydrophobes undergoing tight association. Experimental results on the fraction of bound azobenzene and the amount of bound TX 100 are fitting with this model. On this basis, it is shown that isomerization under UV exposure to the cis azobenzene increases the threshold density (decrease in l_c). Optimization of the amount of association/release and of the photoresponse can accordingly be predicted from our model. Interestingly, the magnitude of decrease in l_c that was experimentally achieved points out that photovariation of l_c does not differ significantly among the azobenzene bearing different substituents (i.e., having different hydrophobicities). We conclude that τ can always be adjusted depending on l_c (i.e., here on the hydrohobicity of the azobenzene derivative) in order to get similar responses to light irrespective of the chemical nature of the azobenzene. A more hydrophobic azobenzene requires lower τ, which has the important consequence to lower the concentration of azobenzene used in practice and therefore help the design of photoactive material imparted with low absorbance.

Acknowledgment. This work was supported by the Agence National de la Recherche France for the award of Grant No ANR BLAN 0278-01 and the European Network of Excellence (FP6 NOE "SoftComp" Soft Matter Composite) for financial support. The authors would like to thank I. Iliopoulos and L. Leibler for helpful suggestions.

Supporting Information Available: UV−visible absorption spectra, distribution of AMPs hydrodynamic radii, synthesis and characterization of amino derivatives of azobenzenes, ^{1}H NMR spectra, and calculation of the fraction of tightly bound hydrophobes. This material is available free of charge via the Internet at http://pubs.acs.org.

References and Notes

(1) Irie, M. *Adv. Polym. Sci.* **1993**, *110*, 49–65.
(2) Pouliquen, G.; Tribet, C. *Macromolecules* **2006**, *39*, 373–383.
(3) Tomatsu, I.; Hashidzume, A.; Harada, A. *Macromolecules* **2005**, *38*, 5223–5227.
(4) Sugiura, S.; Szilagyi, A.; Sumaru, K.; Hattori, K.; Takagi, T.; Filipcsei, G.; Zrinyi, M.; Kanamori, T. *Lab Chip* **2009**, *9*, 196–198.
(5) Alvarez-Lorenzo, C.; Bromberg, L.; Concheiro, A. *Photochem. Photobiol.* **2009**, *85*, 848–860.
(6) Katsonis, N.; Lubomska, M.; Pollard, M. M.; Feringa, B. L.; Rudolf, P. *Prog. Surf. Sci.* **2007**, *82*, 407–434.
(7) Eastoe, J.; Dominguez, M. S.; Wyatt, P.; Beeby, A.; Heenan, R. K. *Langmuir* **2002**, *18*, 7837–7844.
(8) Shang, T. G.; Smith, K. A.; Hatton, T. A. *Langmuir* **2003**, *19*, 10764–10773.
(9) Lim, H. S.; Han, J. T.; Kwak, D.; Jin, M.; Cho, K. *J. Am. Chem. Soc.* **2006**, *128*, 14458–14459.
(10) Jochum, F. D.; Theato, P. *Chem. Commun.* **2010**, *46*, 6717–6719.
(11) Tong, X.; Wang, G.; Soldera, A.; Zhao, Y. *J. Phys. Chem. B* **2005**, *109*, 20281–20287.
(12) Khoukh, S.; Oda, R.; Labrot, T.; Perrin, P.; Tribet, C. *Langmuir* **2007**, *23*, 94–104.
(13) Howley, C.; Marangoni, D. G.; Kwak, J. C. T. *Colloid Polym. Sci.* **1997**, *275*, 760–768.
(14) Lee, C. T.; Smith, K. A.; Hatton, T. A. *Macromolecules* **2004**, *37*, 5397–5405.
(15) Ma, N.; Wang, Y. P.; Wang, B. Y.; Wang, Z. Q.; Zhang, X.; Wang, G.; Zhao, Y. *Langmuir* **2007**, *23*, 2874–2878.
(16) Bradley, M.; Vincent, B.; Warren, N.; Eastoe, J.; Vesperinas, A. *Langmuir* **2006**, *22*, 101–105.
(17) Ercole, F.; Davis, T. P.; Evans, R. A. *Polym. Chem.* **2010**, *1*, 37–54.
(18) Zhao, Y.; Ikeda, T. *Smart Light-Responsive Materials: Azobenzene-Containing Polymers and Liquid Crystals*; Wiley: New York, 2009.
(19) Goddard, E. D. In *Principles of Polymer Science and Technology in Cosmetics and Personal Care*; Goddard, E. D., Gruber, J. W., Eds.; Marcel Dekker: New York, 1999; pp 113−180.
(20) La Mesa, C. *J. Colloid Interface Sci.* **2005**, *286*, 148–157.
(21) Pouliquen, G.; Amiel, C.; Tribet, C. *J. Phys. Chem. B* **2007**, *111*, 5587–5595.
(22) Ruchmann, J.; Fouilloux, S.; Tribet, C. *Soft Matter* **2008**, *4*, 2098–2108.
(23) Hutchings, M. G.; Gregory, P.; Campbell, J. S.; Strong, A.; Zamy, J. P.; Lepre, A.; Mills, A. *Chem.—Eur. J.* **1997**, *3*, 1719–1727.
(24) Labarthet, F. L.; Freiberg, S.; Pellerin, C.; Pezolet, M.; Natansohn, A.; Rochon, P. *Macromolecules* **2000**, *33*, 6815–6823.
(25) Molina-Bolivar, J. A.; Aguiar, J.; Ruiz, C. C. *J. Phys. Chem. B* **2002**, *106*, 870–877.
(26) Borisov, O. V.; Halperin, A. *Curr. Opin. Colloid Interface Sci.* **1998**, *3*, 415–421.
(27) Borisov, O. V.; Zhulina, E. B. *Macromolecules* **2005**, *38*, 2506–2514.
(28) Lairez, D.; Adam, M.; Carton, J. P.; Raspaud, E. *Macromolecules* **1997**, *30*, 6798–6809.
(29) Magny, B.; Lafuma, F.; Iliopoulos, I. *Polymer* **1992**, *33*, 3151–3154.
(30) Diab, C.; Winnik, F. M.; Tribet, C. *Langmuir* **2007**, *23*, 3025–2035.
(31) Miyazawa, K.; Winnik, F. M. *J. Phys. Chem. B* **2003**, *107*, 10677–10682.
(32) Johnson, K. M.; Fevola, M. J.; Lochhead, R. Y.; McCormick, C. L. *J. Appl. Polym. Sci.* **2004**, *92*, 658–671.
(33) Sarrazincartalas, A.; Iliopoulos, I.; Audebert, R.; Olsson, U. *Langmuir* **1994**, *10*, 1421–1426.
(34) Magny, B.; Iliopoulos, I.; Zana, R.; Audebert, R. *Langmuir* **1994**, *10*, 3180–3187.
(35) Piculell, L.; Guillemet, F.; Thuresson, K.; Shubin, V.; Ericsson, O. *Adv. Colloid Interface Sci.* **1996**, *63*, 1–21.

612 *Macromolecules* **2011**, *44*, 612–621
DOI: 10.1021/ma1025016

Macromolecules
ARTICLE

Tannic Acid Mediated Suppression of PNIPAAm Microgels Thermoresponsive Behavior

Eunice Costa,[†,§] Margarida Coelho,[†] Laura M. Ilharco,[‡] Ana Aguiar-Ricardo,*[,†] and Paula T. Hammond*[,§]

[†]*REQUIMTE, Departamento de Química, Faculdade de Ciências e Tecnologia, Universidade Nova de Lisboa, 2829-516 Caparica, Portugal,* [‡]*Centro de Química-Física Molecular and IN-Institute of Nanoscience and Nanotechnology, Instituto Superior Técnico, Av. Rovisco Pais, 1, 1049-001 Lisboa, Portugal, and* [§]*Department of Chemical Engineering, Massachusetts Institute of Technology, Cambridge, Massachusetts 02139, United States*

Received November 3, 2010; Revised Manuscript Received December 10, 2010

ABSTRACT: Tannic acid (TA) complexation with poly(*N*-isopropylacrylamide) (PNIPAAm) microgels changed their morphology and temperature responsiveness, depending on TA concentration and pH (below the TA pK_a). Complexes prepared with a low TA content had higher low critical solution temperature than pure PNIPAAm microgels as a consequence of the hydrophilic character of TA; however, above a concentration threshold, TA physically cross-links the polymeric network, altering their morphology and suppressing the thermodynamically driven PNIPAAm coil-to-globule transition. DRIFT spectral analysis indicated that within PNIPAAm−TA complexes hydrogen bonds were established between PNIPAAm amide and TA phenolic (C═O···H-O and N−H···O−H) and ester (N−H···O−C) groups. At pH 4, H-bonding was more diverse and extensive than at pH 7; hence the complexes thermoresponsive behavior was altered at lower TA contents for the acidic pH. Above the TA pK_a, H-bonding is destabilized and the complexes recovered their spherical morphology and the ability to respond to temperature stimulus, thus demonstrating a reversible process with pH.

Introduction

Intelligent polymers which have the ability to respond to small external stimuli, namely changes in temperature and pH, have attracted great interest for several biomedical and bioengineering applications such as protein−ligand recognition,[1] on−off switches for modulated drug delivery,[2−4] development of artificial organs,[5] enzyme immobilization[6] and cell-sheet technology.[7] Poly(*N*-isopropylacrylamide) (PNIPAAm) is a well-characterized thermosensitive polymer, containing a hydrophilic amide and a hydrophobic isopropyl group.[8] It is soluble in water up to its lower critical solution temperature (LCST), around 31−32 °C,[9] due to hydrogen H-bonding interactions between the amide group and surrounding water molecules.[10−12] At temperatures above the LCST, intramolecular H-bonding between amide groups and increasing hydrophobic interactions among isopropyl groups prevail, leading to a compact conformation and consequent precipitation of PNIPAAm from aqueous solutions.[10,12] PNIPAAm polymer (Figure 1A) can be cross-linked, forming hydrogels in which the thermoresponsive behavior translates into swelling of the polymeric network below the transition temperature and the release of water above it.[13]

Tannic acid (TA) is a water-soluble high molecular weight polyphenolic compound containing a central carbohydrate (glucose) core, which is esterified by phenols (gallic acid) (Figure 1B). TA is a natural hydrolyzable tannin, mostly extracted from plants and microorganisms, and hence, it is fully biodegradable. The high biological activity of TA as an antimutagenic, anticarcinogenic, antimicrobial, antioxidant, and antibacterial agent prompted researchers to further investigate its potential especially in the biomedical field.[14,15] In fact, several studies have been performed on the association of TA with biopolymers such as collagen, gelatin, albumin and some polysaccharides through noncovalent interactions.[16−19] Polyphenols such as tannic acid appear to associate with macromolecules by H-bonding through donating and accepting groups,[20] and by hydrophobic interactions with the aromatic rings on its galloyl phenols.[21] Ionic interactions with positively charged aminoacids and polyelectrolytes have also been reported.[22] A previous study confirmed the presence of specific intermolecular H-bonding interactions between the carbonyl groups of polyesters and the phenolic hydroxyl groups of TA.[23] Recently, there has been increasing interest in H-bonded assembly of tannic acid with several neutral polymers such as poly(*N*-vinylcaprolactam), poly(*N*-vinylpyrrolidone), poly(ethylene oxide) and PNIPAAm for the development of physiologically stable thin films[24] and hollow capsules[25] for controlled drug release[26] and other biotechnology applications.[27] Specifically, Sukhisvili and Erel-Unal have demonstrated the formation of TA and PNIPAAm multilayers through H-bonding that remained stable up to the critical dissolution pH of about 8.[24]

Despite the development of devices combining TA and PNIPAAm little is known about the impact of TA association on PNIPAAm properties. It has been shown that the presence of macromolecules such as polyelectrolytes within the hydrogel network can change the PNIPAAm microgel phase transition behavior.[28,29] Therefore, it is essential to fully understand the interactions and dynamics between PNIPAAm and complexed

*Corresponding authors. E-mail: (A.A.-R.) aar@dq.fct.unl.pt; (P.T.H.) hammond@mit.edu.

 Published on Web 01/10/2011 © 2011 American Chemical Society

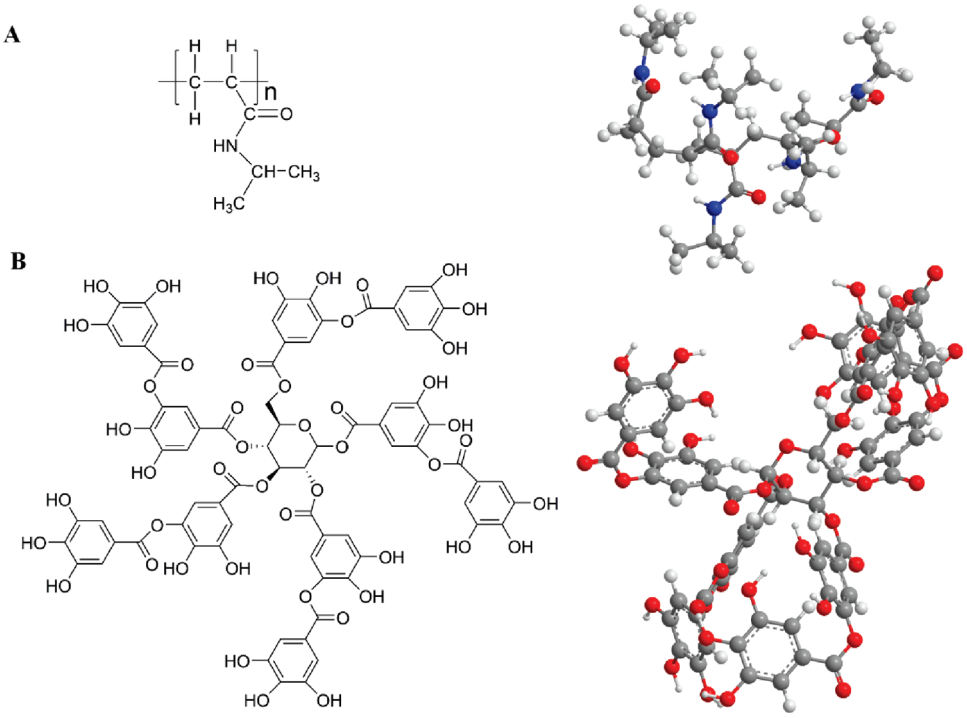


Figure 1. Chemical structure and ball and stick models of PNIPAAm with $n = 5$ (A) and tannic acid (B), in the minimum energy conformation optimized by the MM2 module of Chem 3D Ultra 10.0.

molecules, and its relation with environmental conditions such as pH, for the rational design and application of these responsive systems. Studies concerning the effect of phenols on the PNIPAAm phase transition in aqueous solutions have shown that the LCST decreases in the presence of phenols by reducing thermodynamic interactions between the polymer and water. Furthermore, at a constant temperature, the PNIPAAm phase transition can also be induced when the concentration of phenols is above a certain threshold. The threshold concentration decreases with increasing hydroxyl substitution in the aromatic molecules.[30] On the other hand this trend cannot be generalized for complex polyphenolic compounds as shown in a recent study on the phase transition behavior of PNIPAAm cross-linked microgels in TA solutions. For TA concentrations in solution lower than 10^{-5} M, the LCST of PNIPAAm microgels with mean diameters of ~233 μm shifts slightly to higher temperatures and, above that critical TA concentration, the thermoresponsive behavior of PNIPAAm microgels is inhibited.[31]

In the present work, the effect of tannic acid complexation on PNIPAAm microgels morphology and thermoresponsive behavior was evaluated as a function of initial TA concentration and solution pH. Monodisperse and well-defined PNIPAAm microgels with a dry mean diameter below 4 μm were prepared by free-radical dispersion polymerization in supercritical carbon dioxide. This green synthesis approach renders highly pure PNIPAAm microgels suitable for future applications in biomedical devices or as biosensors. The specific interactions between TA and PNIPAAm in the microgels were thoroughly assessed by analysis of their diffuse reflectance infrared Fourier transform (DRIFT) spectra.

Experimental Section

Materials and Sample Preparation. *N*-Isopropylacrylamide (NIPAAm; 97% purity), di(ethylene glycol) dimethacrylate (DEGDMA, 95% purity), 2,2′-azobis(isobutyronitrile) (AIBN; 98% purity), tannic acid (TA; M_W 1701.2) hydrochloric acid (HCl, 37% purity) and potassium bromide (KBr; FTIR grade) were purchased from Sigma-Aldrich. Krytox 157 FSL was purchased from DuPont. Carbon dioxide was obtained from Air Liquide with 99.998% purity. Sodium phosphate dibasic dihydrate (99.5% purity), sodium phosphate monobasic dihydrate (>98% purity) and sodium hydroxide (NaOH) were obtained from Riedel-de Haën. All the materials were used without any further purification. Deionized water was purified through a Milli-Q system and had a resistivity greater than 18 MΩ·cm.

Synthesis of cross-linked PNIPAAm microgels (0.74 mol % DEGDMA relative to monomer amount) was carried out by free-radical dispersion polymerization in supercritical carbon dioxide at 27.0 MPa for 24 h, using a NIPAAm concentration of 4.8 wt % relative to CO_2 and Krytox at 10 wt % relative to NIPAAm amount. Monodisperse and well-defined dry particles with an average diameter of 3.6 ± 0.7 μm were obtained. The cross-linked microgels were fully insoluble. More details on the synthesis and polymer characterization may be found in a previous report.[32]

Complexation experiments between TA and PNIPAAm microgels were performed in 10 mM phosphate buffer at pH 4 and pH 7 at increasing TA to PNIPAAm weight ratios: 1, 5, 50, 100, and 500 wt %. Dispersions of PNIPAAm microgels were added dropwise to TA solutions to a final PNIPAAm concentration of 1 mg/mL, and were stirred for 20 min. All solutions were freshly prepared beforehand. Afterward the obtained microgels were collected by centrifuging the dispersions for 10 min at 7800*g*. Microgels were further rinsed in the respective buffer by at least three centrifugation and resuspension cycles to remove all noncomplexed TA (as monitored by absorption measurements in a UV/vis spectrometer). All supernatants were collected for further analysis. A similar experiment was conducted between GA (tannic acid structural unit) and PNIPAAm microgels at pH 7 using an initial concentration of 46 wt % in GA, in order to have the same amount of hydroxyl groups as those found in TA at 50 wt %. At pH 7 the contributions from GA carboxylic acid for H-bonding may be neglected as it is mostly ionized (GA −COOH pK_a ~ 4.3 and −OH pK_a ~ 8.7).[33] PNIPAAm microgels complexed with

TA (PNIPAAm−TA) and GA were lyophilized for 3 h before further analysis. Lyophilization did not compromise microgel structure.

Determination of the Amount of Complexed TA. The UV/vis absorption spectrum of TA depends on the degree of ionization of the molecule.[24] The absorbance spectra of the TA solutions in 10 mM phosphate buffer at pH 4 and pH 7 were determined using a UV/vis spectrometer PerkinElmer Lambda 35 (PerkinElmer Inc., USA). TA solutions at pH 4 exhibited two absorption peaks at 213 and 275 nm, while at pH 7 the peaks shift to 211 and 276 nm. Therefore, the amount of TA present in the collected supernatants ($m_{TA,supernatant}$) was calculated by comparison with calibration curves established for each pH. The amount of complexed TA (q) was determined as in eq 1:

$$q(wt\%) = \frac{m_{TA,initial} - \sum m_{TA,supernatant}}{m_{PNIPAAm}} \times 100 \qquad (1)$$

where $m_{TA,initial}$ and $m_{PNIPAAm}$ refer to the initial amount of TA and PNIPAAm in solution, respectively.

TA complexation on PNIPAAm was described using Langmuir isotherms. The model can be represented by the following linear form shown in eq 2:[34]

$$\frac{C}{q} = \frac{1}{Q_{\max}K_d} + \frac{C}{Q_{\max}} \qquad (2)$$

Here C is the equilibrium concentration (mg/mL) of tannic acid in solution in the preparation of the PNIPAAm−TA complexes, $Q_{\max}$ is the Langmuir constant describing the maximum attainable amount of TA complexed with PNIPAAm (wt %), and K_d is the Langmuir affinity constant (mL/mg). The essential characteristics of the Langmuir isotherm can be expressed as a dimensionless separation factor or equilibrium parameter, R_L, defined by eq 3:

$$R_L = \frac{1}{1 + K_d C_0} \qquad (3)$$

where C_0 is the initial tannic acid concentration (mg/mL).

Turbidimetric Analysis for the Assessment of Thermoresponsive Behavior. Turbidity of PNIPAAm and PNIPAAm−TA aqueous buffered microgels dispersions at a concentration of 0.2 mg/mL was measured using a UV/vis spectrometer PerkinElmer Lambda 35 (PerkinElmer Inc., USA), equipped with a water-jacketed cell holder coupled to a temperature-controlled circulating bath. Measurements were performed at 600 nm where both individual PNIPAAm and TA or PNIPAAm−TA microgels have no absorption bands. Turbidity was recorded upon heating from 24 °C up to a temperature at which an absorbance plateau was clearly defined (after 5 min of equilibration for each temperature step) and cooling back to 24 °C. The temperature of the sample dispersion was continuously monitored by a thermocouple inside the cuvette. The increase in turbidity with increasing temperature is a result of the volume phase transition, both in individual PNIPAAm and PNIPAAm−TA complexes. The LCST for the thermoresponsive samples was calculated as the inflection point of the normalized absorbance to temperature curve using OriginPro 8.04 software.

Microgels Morphology and Thermoresponsive Behavior. Optical micrographs of prepared PNIPAAm and PNIPAAm−TA microgels were obtained with an automatic Malvern Morphologi G3 optical microscope (Malvern Inc., UK) kept inside a temperature-controlled chamber with an infrared lamp coupled to a PID temperature controller. PNIPAAm−TA complexes were dispersed in phosphate buffer (according to the pH at which they were initially prepared) and observed at 24, 32, and 37 °C upon heating and cooling the samples. Furthermore, samples were titrated up to pH 9 and down to the initial complexation pH using 1 M NaOH and HCl solutions to assess TA complexation and decomplexation reversibility and its effects on PNIPAAm microgels morphology and thermoresponsive behavior. Particle morphology of PNIPAAm microgels and lyophilized PNIPAAm−TA complexes was assessed using scanning electron microscopy (SEM) in a Hitachi S-2400, with an accelerating voltage set to 15 kV. All samples were gold coated before analysis.

DRIFT Spectra Analysis. PNIPAAm, TA, and lyophilized PNIPAAm−TA complexes were analyzed by diffuse reflectance infrared Fourier transform spectroscopy (DRIFT). Sample preparation consisted in grinding a mixture of KBr and each sample in appropriate weight proportions in order to obtain spectral absorbance in the range of applicability of the Kubelka−Munk transformation.[35] The amount of sample was sufficient to be considered of infinite thickness. The DRIFT spectra were measured in a Mattson Research Series 1 FTIR spectrometer, equipped with a wide-band MCT detector (4000−400 cm^{-1}) and a Graseby/Specac Selector (with specular reflection blocker). A total of 500 scans were performed with 4 cm^{-1} resolution. No baseline corrections were made. The diffuse reflectance spectra were transformed to Kubelka−Munk units using the FIRST software.

The specific interactions between TA molecules and PNIPAAm chains were not always inferred directly from the infrared spectra of the PNIPAAm−TA complexes, because of partial band overlaps. In order to clarify those interactions, and when necessary, a detailed spectral analysis was made by deconvolution to identify the constituent components of relevant bands, using OriginPro 8.04 software. A nonlinear least-squares fitting method was used, assuming Gaussian and Lorentzian band profiles for the components. No baseline corrections were made, and no restrictions were imposed on the band positions and widths. The best fits were obtained with reduced $\chi^2 \approx 10^{-6}$ and a correlation coefficient of ≈0.999. Upon deconvolution the intensity of the methyl vibrations of PNIPAAm isopropyl group ($\nu_s CH_3$ and $\nu_{as} CH_3$ at 2878 and 2972 cm^{-1}, respectively) relative to the methylene groups ($\nu_{as} CH_2$ at 2933 cm^{-1}) on the polymer backbone (I_{rel}) in both the pure component and prepared PNIPAAm−TA complexes was determined using eq 4:

$$I_{rel} = 100 \times \left[\frac{\text{area}(\nu_{as}CH_3 + \nu_s CH_3)}{\text{area}(\nu_{as}CH_2)}\right] \qquad (4)$$

Results and Discussion

PNIPAAm−TA Complexes. The influence of tannic acid concentration and of solution pH on TA complexation with PNIPAAm lightly cross-linked microgels was assessed. Tannic acid assembly on PNIPAAm microgels was performed at pH 4 and pH 7 (below the TA pK_a of about 8.5)[24] in increasing TA to PNIPAAm weight ratios. The amounts of tannic acid effectively complexed with PNIPAAm microgels are shown in Table 1. PNIPAAm−TA complexes content in TA increased with increasing initial concentration of TA, as expected. Nevertheless, the increase in TA content from the experiments performed at initial TA weight ratio of 100 to 500 wt % (relative to PNIPAAm amount at a concentration of 1 mg/mL in PNIPAAm) was much less than five times, indicating that all available interactive PNIPAAm moieties may have reached saturation in between these concentrations. Overall, a higher amount of TA was present on PNIPAAm microgels at pH 4 than at pH 7, indicating that TA complexation is dependent on its protonation.

The complexation of TA with PNIPAAm can be described through a Langmuir isotherm as shown by the correlation factor values in Table 1. Overall, the obtained R_L values were between 0 and 1, indicating that the complexation of tannic

Table 1. Langmuir Isotherm Parameters for Tannic Acid Complexation with PNIPAAm Microgels and LCST of Obtained PNIPAAm−TA Complexes

	Langmuir isotherm						
pH	C_0, wt %[a]	q, wt %[b]	R_L	Q_{max}, wt %	K_d, mL/mg	R^2	LCST, °C
4	0			68	9.2	0.998	31.5 ± 0.07
	1	0.7 ± 0.2	0.92				34.6 ± 0.18
	5	4.2 ± 0.2	0.68				
	50	42 ± 1	0.18				
	100	62 ± 1	0.10				
	500	66 ± 5	0.021				
7	0			66	6.2	0.997	31.7 ± 0.12
	1	0.4 ± 0.1	0.94				31.4 ± 0.06
	5	3.4 ± 0.1	0.76				34.4 ± 0.60
	50	43 ± 0.2	0.24				
	100	56 ± 0.4	0.14				
	500	63 ± 1	0.031				

[a] Initial TA concentration in solution in wt % relative to PNIPAAm. [b] q is the amount of complexed TA in wt % relative to PNIPAAm (± standard deviation for a 95% confidence interval; assembly performed in solution to a final PNIPAAm concentration of 1 mg/mL).

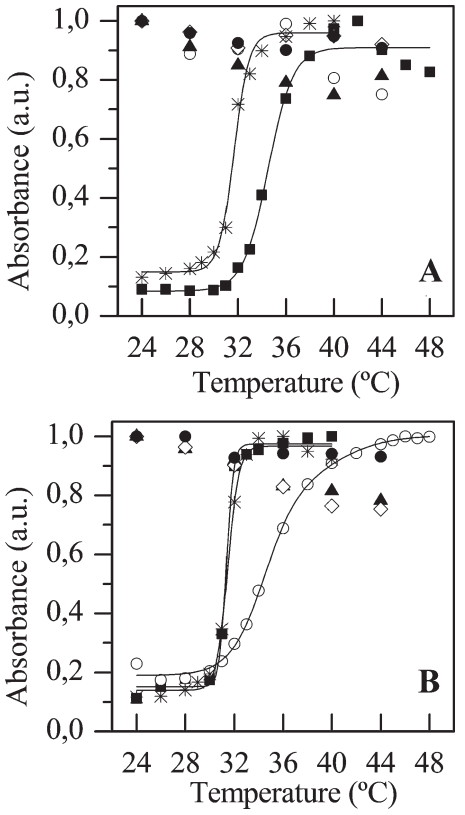


Figure 2. Turbidimetry analysis of PNIPAAm−TA complexes assembled in 10 mM phosphate buffer at pH 4 (A) and pH 7 (B). Key: (■) TA 1 wt %; (○) TA 5 wt %; (▲) TA 50 wt %; (◇) TA 100 wt %; (●) TA 500 wt % (relative to PNIPAAm amount at 1 mg/mL final concentration); (∗) PNIPAAm. The data shown were obtained upon heating from 24 °C up to a temperature at which an absorbance plateau was clearly defined. A similar profile was obtained upon cooling with no significant hysteresis.

acid with PNIPAAm is a thermodynamically favorable process at both pH. However at pH 4, the binding capacity of PNIPAAm, Q_{max}, was higher and the affinity constant K_d was lower, clearly emphasizing that the complexation process was more favorable when TA was more protonated at acidic pH.

The lower critical solution temperature (LCST) behavior of the synthesized PNIPAAm microgels and PNIPAAm−TA complexes was investigated in aqueous dispersions by turbidity measurements, as shown in Figure 2. For that purpose, turbidity measurements were performed at 600 nm on particles dispersed in 10 mM phosphate buffer at the initial assembly pH. Absorbance was recorded upon heating from 24 °C up to a temperature at which an absorbance plateau was clearly defined and cooling back to 24 °C. Microgel thermoresponsive behavior was dependent on the initial assembly conditions in terms of TA concentration and pH. When heating PNIPAAm microgel dispersions, turbidity increased with temperature, exhibiting a sharp slope at the LCST. The derived values for the LCST are in agreement with previous reports on PNIPAAm (see Table 1).[9] The observed thermoresponsive behavior is totally reversible upon cooling, as no hysteresis was observed (data not shown). In general, no cloud points were observed for PNIPAAm−TA microgels complexed at pH 4 and a TA weight ratio above 5 wt % (relative to PNIPAAm amount at a concentration of 1 mg/mL in PNIPAAm); and at pH 7 above 50 wt % - Table 1 and Figure 2. For lower TA concentrations, the complexes prepared with an initial ratio of 1 wt % at pH 4 and of 1 and 5 wt % at pH 7 exhibited a volume phase transition with temperature. However, the LCST increased about 3 °C for PNIPAAm−TA 1 wt % pH 4 and 5 wt % pH 7, in comparison with pure PNIPAAm, and the transition was not as sharp. A similar trend was described recently in a paper by Chen et al. for the behavior of PNIPAAm microgels dispersed in solutions of tannic acid. The PNIPAAm volume phase transition was suppressed in solutions with concentrations above 0.02 mg/mL.[31] Below that critical concentration, the LCST of PNIPAAm microgels also exhibited a slight shift to higher values. Nevertheless, it is not possible to directly compare this report with the results described above, as they refer to distinct systems. Herein, the behavior of PNIPAAm microgels effectively complexed with a defined amount of TA is analyzed, while Chen et al. refers to the behavior of PNIPAAm microgels dispersed in solutions of tannic acid. Furthermore, the effect of TA protonation on the interactions with PNIPAAm is not analyzed in the latter.

Optical micrographs of the PNIPAAm−TA complexes dispersed in 10 mM phosphate buffer solutions at pH 4 and pH 7 are shown in Figure 3 at increasing temperature. Volume phase transition was clearly observed for microgels prepared with TA to PNIPAAm ratios of 1 wt % when complexed at pH 4 and 1 and 5 wt % at pH 7; while no thermoresponsive behavior was obtained for higher TA ratios, further emphasizing the results obtained from the turbidimetric analysis. The assembly of tannic acid on the prepared PNIPAAm microparticles had a dramatic impact on the microgel morphology. For low TA to PNIPAAm ratios, the microgels maintain a spherical morphology. As the amount of TA is increased the particles become more deformed. The effect of TA on

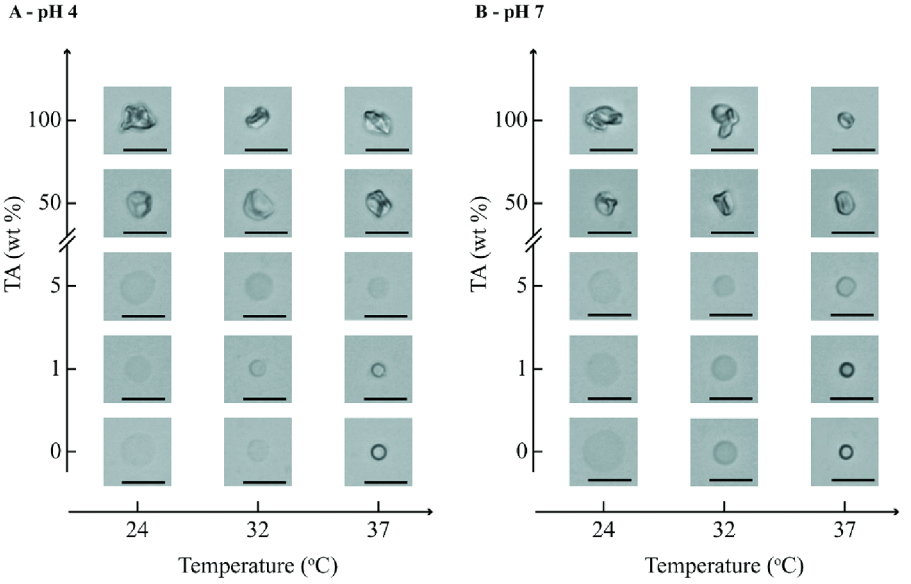


Figure 3. Optical micrograms showing the response to solution temperature of PNIPAAm−TA complexes dispersed in 10 mM phosphate buffer at pH 4 (A) and pH 7 (B). Data shown refers to observed behavior upon heating since similar response is observed when cooling. Scale bar: 10 μm.

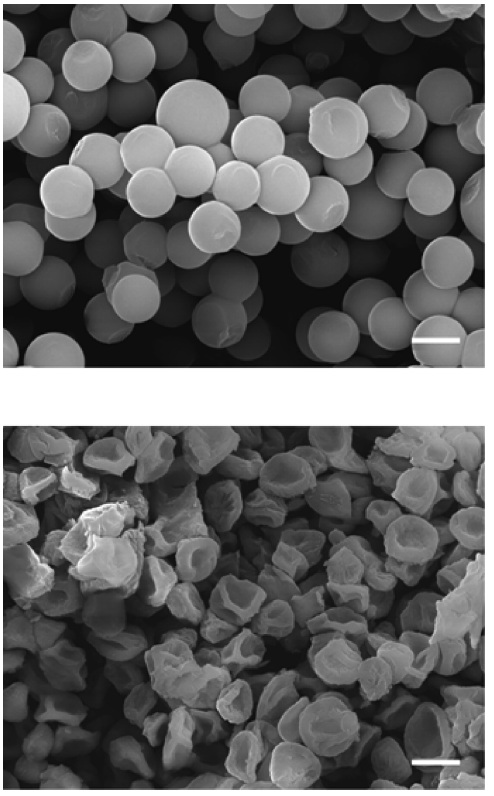


Figure 4. SEM micrographs of PNIPAAm microparticles (A) and PNIPAAm−TA complexes after complexation with TA at an initial concentration of 50 wt % (relative to PNIPAAm amount at 1 mg/mL final concentration) in 10 mM phosphate buffer at pH 4 (B). Scale bar: 2 μm.

PNIPAAm microparticles morphology can also be clearly observed in the SEM micrographs depicting PNIPAAm microgels before and after TA complexation at an initial concentration of 50 wt % at pH 4, Figure 4. In fact, it seems that the increasing interactions between TA and lightly cross-linked PNIPAAm microparticles lead to physical cross-linking of the polymeric network and therefore to microparticle collapse.

pH Reversibility of PNIPAAm−TA Thermoresponsive Behavior. PNIPAAm−TA complexes prepared at an initial TA ratio of 1 wt % were dispersed in 10 mM phosphate buffer pH 4 or 7, according to the complexation pH. These dispersions were titrated up to pH 9, above the tannic acid pK_a, equilibrated for 10 min, and then titrated down to the initial pH; the microgels were observed under an optical microscope at 24, 32 and 37 °C in each titration step, as shown in Figure 5. For particles prepared at both of these TA complexation pH, it can be observed that they regain their spherical shape at pH 9 regardless of temperature. Furthermore, as temperature was increased, it was clear that at pH 9 PNIPAAm microgels recovered their thermoresponsive behavior, as shown by a deswelling of the microgels above the LCST temperature at 37 °C. As the pH was titrated back down to the original complexation pH, the particle swells a small amount at 37 °C rather than retaining the more compact size of the microgel that is anticipated at this temperature. On the other hand, at 32 and 24 °C, the microgels actually contract and release water rather than exhibiting the highly swollen state characteristic of PNIPAAm at these temperatures. At all three temperatures, it appears that the condition anticipated for the thermoresponsive polymer has been suppressed, and the microgel particles are all very close to the same size. This on−off suppression of the thermoresponsive behavior in response to pH for the PNIPAAm−TA complexes is probably due to the reversible complexation and decomplexation of TA on PNIPAAm at pH values below and above the TA pK_a. Indeed, infrared spectra analysis confirmed that TA was partly retained in PNIPAAm−TA microgels after successive rinses using 10 mM phosphate buffer at pH 9 (data not shown), further supporting the quasi-reversible nature of this process.

The mechanisms underlining PNIPAAm and TA complexation and the modification or suppression of the complexes thermoresponsive behavior at different pH and TA concentration were elucidated through the analysis of the infrared spectra of the different complexes, as described in the next section.

DRIFT Spectroscopy Analysis of PNIPAAm−TA Complexes. In order to avoid the overlapping of water characteristic bands, the vibrational study was executed with dry

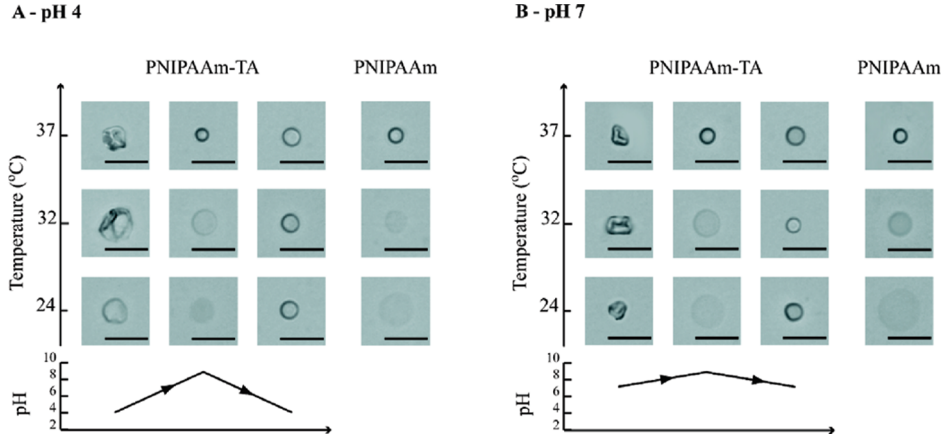


Figure 5. Optical micrographs showing PNIPAAm−TA complexes response to temperature when titrated up to pH 9 and down to original assembly pH. Complexes were initially prepared with 100 wt % TA (relative to PNIPAAm amount at 1 mg/mL final concentration) in (A) 10 mM phosphate buffer pH 4 and (B) in 10 mM phosphate buffer at pH 7. Micrographs shown were obtained upon heating from 24 to 37 °C; micrographs obtained upon cooling demonstrated a similar behavior (data not shown). Scale bar: 10 μm.

microgels, in diffuse reflectance infrared Fourier transform mode (DRIFT). For the purpose of this study, the DRIFT spectra will be discussed in the wavenumber regions of interest for describing the interactions between tannic acid and PNIPAAm within the complexes. A more detailed spectral analysis is described in the Supporting Information. The deconvoluted DRIFT spectra of pure PNIPAAm, TA, and dry PNIPAAm−TA complexes with increasing TA contents, prepared at pH 4 and pH 7, are shown in Figure 6 and 7 for the spectral regions 900−1400 and 1400−1800 cm^{-1}, respectively. The spectral region 2400−3800 cm^{-1} is depicted in Supporting Information (Figure S3). A summary of the proposed band assignment and deconvolution results as well as the relative contributions of each component to the bands of the pure PNIPAAm and TA and microgel complexes are shown in Table 2 and Supporting Information (Tables S1 and S2).

(*i*). *DRIFT Analysis of the 900−1400 cm^{-1} Spectral Region*. The analysis of the complexes DRIFT spectra required a previous assignment of the pure components bands. The spectrum of tannic acid was in good agreement with those collected by Cowen et al. above 1000 cm^{-1} in diffuse reflectance mode,[36] and by Jastrzebska et al.[37] in transmission (Figure S1). Their partial analysis and, in some cases, comparison with gallic acid allowed band assignments.[33,36,38,39] In the low wavenumber region, several bands from C−O stretching modes in different TA functional groups are observed, namely the carbohydrate νC−OCH mode at 1089 cm^{-1} and the phenolic νC−OH mode at 1027 cm^{-1}. The DRIFT spectra of the PNIPAAm−TA complexes (Figure 6) prepared with the lowest TA concentration, 1 wt %, were very similar to those of PNIPAAm in the 900−1400 cm^{-1} region for both pH values. However, for the microgels prepared with 5 wt % in TA at pH 7, the main bands of TA can already be observed as shoulders, with the phenolic νC−OH shifted to 1038 cm^{-1}. For the same TA initial content at pH 4, the phenolic νC−OH shoulder is better defined and shifted to higher wavenumbers (~1040 cm^{-1}) and the νC−OCH mode of the carbohydrate moiety has higher relative intensity and shifts to 1099 cm^{-1}. Similar shifts to higher energy states in the νC−O modes were observed for TA-hydrates and other carbohydrates.[36] Therefore, it is proposed that at both pH PNIPAAm and TA interactions involved TA phenolic groups and that at pH 4 the carbohydrate oxygen of TA was additionally engaged in H-bonding (which can act as charge donors in H-bonding with the NH groups of PNIPAAm). When increasing TA initial amount to 50 wt % at both pH values, TA bands became dominant and the phenolic νC−OH mode remained shifted to 1040 cm^{-1}. In the 1150−1250 cm^{-1} region, the two PNIPAAm bands (isopropyl νN−C at 1173 cm^{-1} and amide III at 1242 cm^{-1}) appeared as shoulders of the strong νC−O (ester) of TA at 1201 cm^{-1}. Surprisingly, this band became much narrower than in pure TA, suggesting that TA ester moieties were involved in more specific interactions when complexed with PNIPAAm, or that a more isotropic microenvironment was observed.

(*ii*). *DRIFT Analysis of the 1400−1800 cm^{-1} Spectral Region*. The near and mid infrared spectra of PNIPAAm have received considerable attention due to efforts to understand the changes in conformation, interactions and microenvironment of the individual chemical groups that occur upon its coil-to-globule transition (Figure S1, Supporting Information).[40,41] In the 1400−1800 cm^{-1} spectral region, the dominant bands in the PNIPAAm spectrum, at 1646 and 1540 cm^{-1}, are assigned to amide I and amide II vibrations, respectively. The main contribution to the amide I band is the carbonyl stretching mode, whereas the amide II is mainly due to the in-plane N−H bending.[42] The spectral deconvolution in the amide I band revealed the presence of three components at 1607, 1644, and 1669 cm^{-1} that were assigned to intermolecular, intramolecular H bonded and free or freer C═O groups, respectively, with the majority involved in intramolecular interactions (Figure 7 and Table 2).[43] Similarly, in the amide II band, hydrogen bonded N−H groups originated the components at 1529 and 1548 cm^{-1} (intra- and intermolecularly, respectively),[11] with similar relative intensities, plus a minority of free or freer N−H groups appearing at 1509 cm^{-1}. In the DRIFT spectra of PNIPAAm−TA complexes prepared with 1 and 5 wt % of TA, the component related with the intramolecularly H bonded NH groups in the amide II band was absent and the fractions of the freer ones and of those involved in intermolecular bonds increased significantly for both pH. For pH 7, the amide I band is similar to pure PNIPAAm. On the other hand, at pH 4, all the carbonyl components in the amide I band shift to higher wavenumbers, indicating that all the intermolecular H-bonds have been replaced by less strong ones with TA molecules (in spite of the overlapping with the TA band at 1608 cm^{-1}). Upon increasing the initial TA concentration to 50 wt %, a

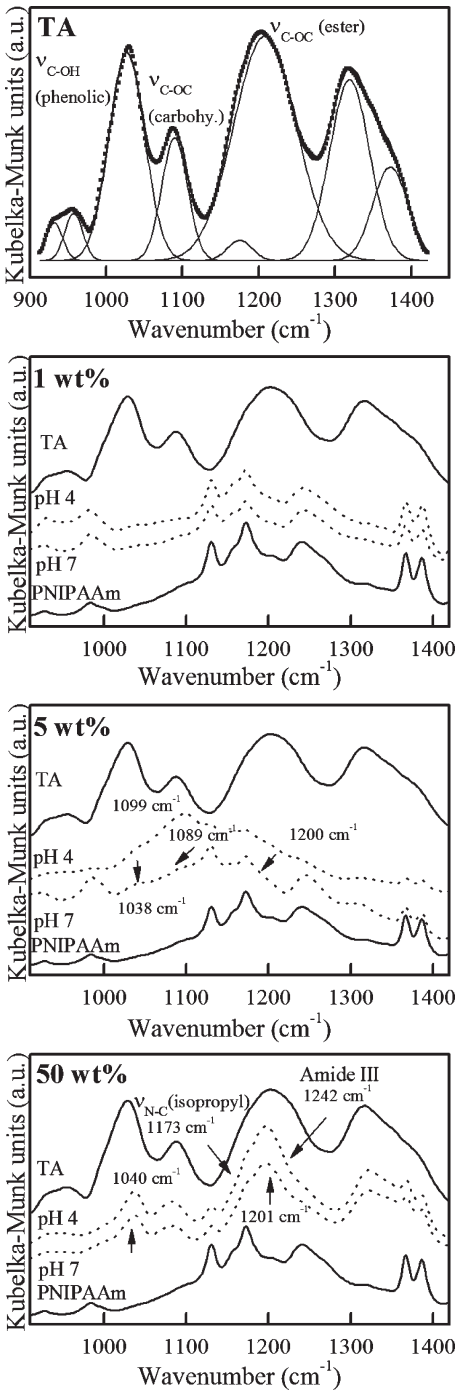


Figure 6. DRIFT spectra from 900 to 1420 cm^{-1} of TA, PNIPAAm−TA complexes and PNIPAAm: deconvoluted TA spectra (TA); PNIPAAm−TA complexes prepared with 1 wt % TA at pH 4 and pH 7 (1 wt %), 5 wt % at pH 4 and pH 7 (5 wt %), and 50 wt % at pH 4 and pH 7 (50 wt %).

component attributed to intramolecular H-bonded NH appeared at ~1530 cm^{-1} (Table 2). The latter is due to the overlap of TA νC−C modes of aromatic rings that became more significant with increasing TA content in the complexes. Therefore, the relative contribution of the constituent components of the δNH band cannot be evaluated in complexes prepared with 50 wt % TA initial concentration and above.

(*iii*). *DRIFT analysis of the 2400−3800 cm^{-1} spectral region*. For all the PNIPAAm−TA complexes (Figure S3, Supporting Information), there were neither observable changes nor shifts in the C−H stretching modes ($\nu_{as}CH_3$ at 2972 cm^{-1} and ν_sCH_3 at 2878 cm^{-1}), when compared with pure PNIPAAm (Figure S2D, Supporting Information), suggesting that there are no hydrophobic interactions between TA and PNIPAAm, as proposed in previous studies.[31] A deconvolution in this region allowed estimating the relative intensities of the νCH_3 using $\nu_{as}CH_2$ modes (2933 cm^{-1}) as a reference (I_{rel}), since it can be assumed that the methylene groups on the polymer backbone are not affected by TA complexation. The I_{rel} of the PNIPAAm−TA complexes prepared with the lowest TA concentration at pH 7 was similar to that of pure PNIPAAm (~110), increasing for the complexes prepared with higher TA amount and protonation. These observations suggest that not only PNIPAAm and TA show no hydrophobic interactions but also that PNIPAAm isopropyl groups are freer in the complexes than in the pure polymer. The 2400−3800 cm^{-1} spectral region of PNIPAAm also included the strong N−H stretching modes (as a broad band with maximum at 3294 cm^{-1} and shoulders at higher wavenumbers in Figure S1, Supporting Information). In the PNIPAAm−TA complexes, the νNH band broadened with increasing TA concentration due to the superposition of the νOH band of TA (Figure S3, Supporting Information). Nevertheless, it did not reach the full width at half-height of this band for pure TA. This means that the diversity of hydrogen bonds in which the hydroxyl groups of TA are involved was much reduced, as H-bonding preferentially occurred with PNIPAAm moieties.

The information derived from the DRIFT spectra was consistent across the analyzed spectral regions and clearly indicated that TA complexation on PNIPAAm microgels was a consequence of preferential hydrogen bonding between polymer and TA molecules: both C=O···H−O (phenolic), NH···O−H and N−H···O−C (ester), at the expense of intra- and intermolecular interactions between identical species. At pH 4, TA is more protonated and H-bonding with PNIPAAm is more favorable than pH 7, as demonstrated by the higher diversity of TA and PNIPAAm functional groups involved in the interactions. As a consequence, a higher TA amount was effectively complexed at pH 4 than at pH 7 and a smaller amount of TA is necessary for increasing the LCST or for suppressing PNIPAAm−TA complexes thermosensitivity. Specifically, for the complexes prepared at 1 wt % TA, more TA was complexed at pH 4 because PNIPAAm carbonyl groups were additional engaged in H-bonding (besides the NH groups at both pHs). The thermodynamically driven coil−globule transition of PNIPAAm was shifted to higher temperatures in the complexes at pH 4 (Table 1; Figures 2A and 3A), possibly due to the presence of free TA hydrophilic hydroxyl groups. However, the phase transition was not as sharp as in pure PNIPAAm, since interactions with TA may have displaced water from their adsorption sites on PNIPAAm. The increasing amount of TA in the complexes prepared with 5 wt % lead to an upper shift on the LCST at pH 7 and to the inhibition of the thermoresponsive behavior at pH 4. At these concentrations the involvement of TA phenolic moieties in the TA interaction with PNIPAAm became visible on the DRIFT spectra. Furthermore, TA complexation on the microgels at pH 4 additionally included the carbohydrate oxygen of TA. As the amount of TA increases in the complexes, extensive H-bonding also involving TA ester moieties lead to physical cross-linking and a nonspherical morphology of the microgels. Above an initial TA concentration of 100 wt % there were no significant changes in the complexes DRIFT spectra at both pH (data not shown), which confirms that a saturation occurred between 100 and 500 wt %.

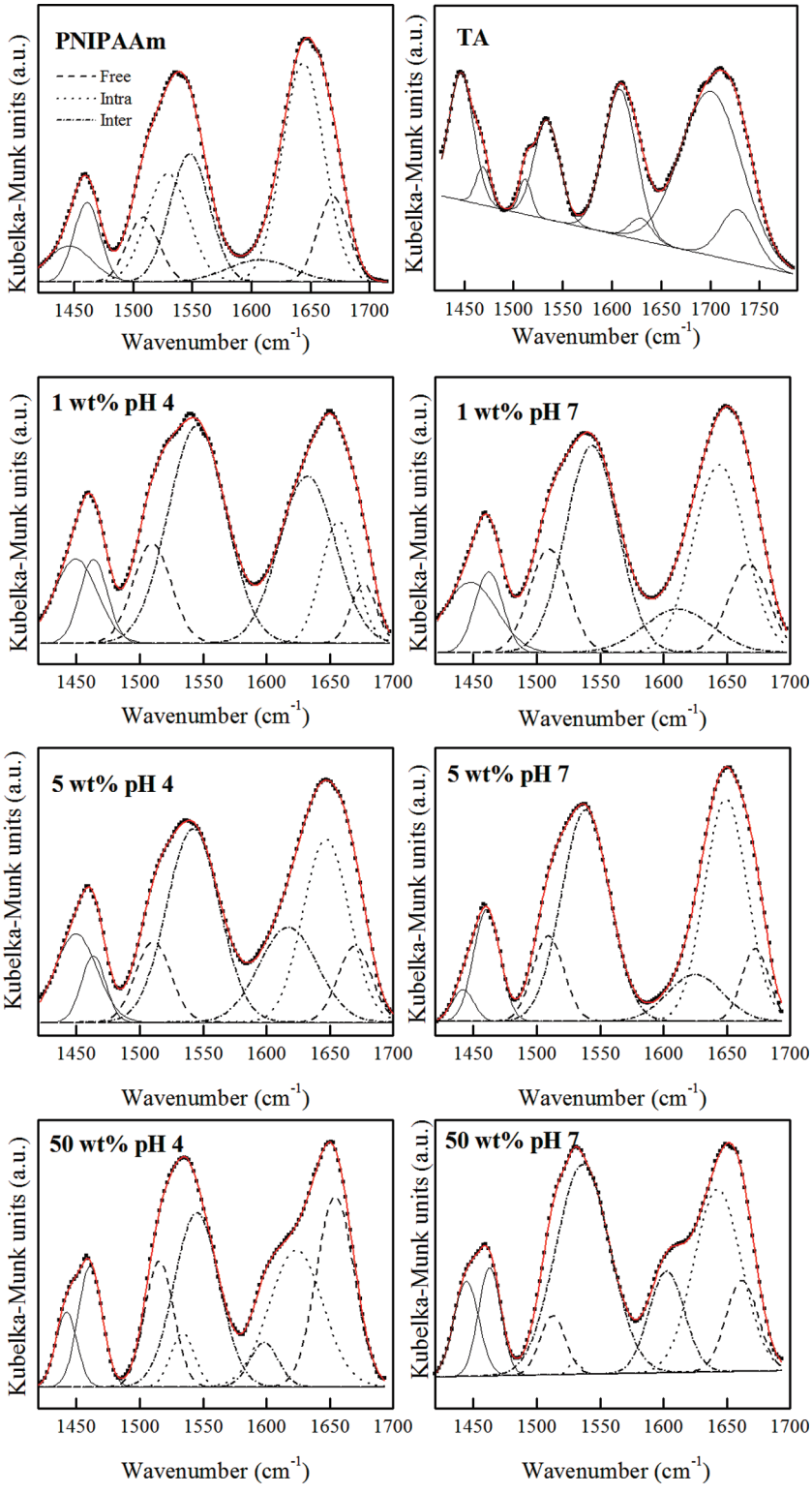


Figure 7. Deconvoluted DRIFT spectra from 1400 to 1800 cm^{-1} of PNIPAAm, TA and PNIPAAm−TA complexes prepared with: 1 wt % TA at pH 4 (1 wt % pH 4) and pH 7 (1 wt % pH 7); 5 wt % TA at pH 4 (5 wt % pH 4) and pH 7 (5 wt % pH 7); and 50 wt % TA at pH 4 (50 wt % pH 4) and pH 7 (50 wt % pH 7).

The 3D molecular structure of TA (Figure 1B) is responsible for the extension and diversity of interactions that enabled the preparation of PNIPAAm−TA complexes. Indeed, a similar complexation experiment with gallic acid (tannic acid structural unit) at equivalent conditions as those used for TA at a initial concentration of 50 wt % in pH 7 was performed and no gallic acid remained complexed, as confirmed from absorbance measurements and DRIFT spectra (data not shown). The different complexation behaviors should be related to the different entropic terms contributions. While the gallic acid complexation on PNIPAAm involves an enormous entropy drop, the much larger and constrained TA molecule has a smaller entropy variation when changes

Table 2. Summary of the Deconvolution Results (Positions and Relative Areas of the Components) Obtained for Relevant Regions of the DRIFT Spectra of Pure TA, Pure PNIPAAm, and Dry PNIPAAm−TA Complexes Prepared at pH 4 and pH 7

	wavenumber, cm^{-1} (area %)							
	Tannic Acid							
assignments	932 (1.7)	957 (2.3)	1027 (19.9)	1090 (8.6)	1175 (1.4)	1208 (37.7)	1319 (19.5)	1373 (8.9)
	νC−OH (phenolic)			νC−OCH (carbohy)	νC−OCH (ester)		δCH	νC−O/δCOH
	1447 (12.7)	1469 (2.3)	1512 (1.9)	1534 (10.8)	1608 (20.2)	1629 (2.0)	1701 (42.4)	1728 (7.7)
	νC−C, aromatic						νC=O, HB[a]	νC=O, free
	PNIPAAm							
assigments, I_{rel} = 110	1446 (5.7)	1461 (7.3)	1509 (7.2)	1529 (16.0)	1548 (17.7)	1607 (5.0)	1644 (32.0)	1669 (9.1)
	δCH_2 *gauche*	$\delta_{as}CH_3$	δNH free	δNH intra HB	δNH inter HB	νC=O inter HB	νC=O intra HB	νC=O "freer"
	PNIPAAm−TA Complexes							
1 wt %, pH 4 I_{rel} = 115	1446 (5.6)	1463 (7.9)	1513 (14.3)		1549 (28.2)	1640 (36.0)	1654 (3.6)	1674 (4.1)
1 wt %, pH 7 I_{rel} = 110	1448 (10)	1462 (6.1)	1510 (10.9)		1544 (29.1)	1611 (8.0)	1644 (26.4)	1667 (9.6)
5 wt %, pH 4 I_{rel} = 130	1450 (10.6)	1463 (4.6)	1511 (8.2)		1542 (29.2)	1617 (15.9)	1647 (24.2)	1670 (7.3)
5 wt %, pH 7 I_{rel} = 115	1443 (3.2)	1461 (8.8)	1509 (8.3)		1539 (32.5)	1605 (4.2)	1649 (37.8)	1674 (5.2)
50 wt %, pH 4 I_{rel} = 140	1442 (4.8)	1461 (8.8)	1515 (11.0)	1534 (3.9)[b]	1545 (23.7)	1598 (3.9)	1624 (22.2)	1654 (21.7)
50 wt %, pH 7 I_{rel} = 130	1444 (7.2)	1463 (7.4)	1513 (4.6)	1530 (0.5)[b]	1536 (34.4)	1603 (10.9)	1643 (26.2)	1662 (8.8)

[a] HB: hydrogen bonded. [b] Overlapping of TA νC−C modes of aromatic rings.

from the initial hydrated state to the PNIPAAm−TA complex.

Conclusions

This study demonstrates that tannic acid complexation with cross-linked poly(*N*-isopropylacrylamide) microgels is a thermodynamically favorable process that can be explored for tuning the PNIPAAm thermoresponsive behavior, depending on the initial amount of TA and complex pH. PNIPAAm−TA complexes with a low content on TA exhibited a LCST shifted to higher temperatures due to the hydrophilic character of the complexed tannic acid. However, above a critical concentration, TA physically cross-links the polymer chains due to extensive H-bonding between PNIPAAm and TA and displaces water from the polymeric network, inhibiting the temperature driven coil-to-globule transition of PNIPAAm. PNIPAAm−TA thermoresponsive behavior depends also on the assembly pH: for complexes assembled at pH 7, closer to TA pK_a, a larger amount of TA is required for altering or suppressing response to temperature stimuli than at pH 4. Furthermore, upon titration of PNIPAAm−TA aqueous dispersions to a pH above tannic acid pK_a (pH 9), interactions between PNIPAAm and TA within the microgels were destabilized and the microgels totally recover the ability to respond to temperature stimuli. Nevertheless, tannic acid is still partly retained within the polymeric network assuring the quasi-reversibility of the process. The mechanism of pH-dependent PNIPAAm−TA microgels temperature response was elucidated using a DRIFT analysis approach. It has been shown that PNIPAAm and TA interact through hydrogen bonding between PNIPAAm amide groups and hydroxyl and ester groups of TA. At acidic pH, H-bonding is more diverse, as the carbohydrate oxygen of TA is also clearly engaged, leading to stronger interactions between the species. Moreover, the PNIPAAm isopropyl groups are not involved in any hydrophobic interactions with TA aromatic rings.

This study clearly underlines that the performance of controlled release formulations, or other intelligent devices, exploring tannic acid as a bioactive H-donor/acceptor for including neutrally charged responsive polymer such as PNIPAAm, can depend on the assembly conditions. Herein, the prepared PNIPAAm−TA complexes may potentially be used for different applications, such as pH on−off switches in microfluidic devices or pH and temperature-driven drug delivery platforms. Furthermore, since TA can successfully complex a diversity of macromolecules, these PNIPAAm−TA microgels could be further functionalized with other guest molecules of interest.

Acknowledgment. This project was funded in part by the MIT-Portugal Program. The authors thank the financial support from Fundação para a Ciência e Tecnologia through the doctoral grant SFRH/BD/35382/2007 (E.C.), projects MIT-Pt/BS-CTRM/0051/2008, POCTI/QUI/73939/2006, and POCTI/CTM/70513/2006, FEDER, FSE, and POCTI. We thank T. Casimiro for valuable suggestions.

Supporting Information Available: DRIFT spectra and detailed spectral analysis of pure tannic acid and poly(*N*-isopropylacrylamide) as well as the DRIFT spectra of PNIPAAm−TA complexes in the high wavenumber region (2400−3800 cm^{-1}). This material is available free of charge via the Internet at http://pubs.acs.org.

References and Notes

(1) Stayton, P. S.; Shimoboji, T.; Long, C.; Chilkoti, A.; Chen, G. H.; Harris, J. M.; Hoffman, A. S. *Nature* **1995**, *378*, 472–474.
(2) Ramkissoon-Ganorkar, C.; Liu, F.; Baudys, M.; Kim, S. W. *J. Controlled Release* **1999**, *59*, 287–298.
(3) Gutowska, A.; Bae, Y. H.; Jacobs, H.; Mohammad, F.; Mix, D.; Feijen, J.; Kim, S. W. *J. Biomed. Mater. Res.* **1995**, *29*, 811–821.
(4) Vakkalanka, S. K.; Brazel, C. S.; Peppas, N. A. *J. Biomater. Sci.-Polym. E.* **1996**, *8*, 119–129.
(5) Osada, Y.; Okuzaki, H.; Hori, H. *Nature* **1992**, *355*, 242–244.
(6) Liu, F.; Tao, G. L.; Zhuo, R. X. *Polym. J.* **1993**, *25*, 561–567.
(7) Okano, T.; Yamada, N.; Sakai, H.; Sakurai, Y. *J. Biomed. Mater. Res.* **1993**, *27*, 1243–1251.

(8) Yoshida, R.; Uchida, K.; Kaneko, Y.; Sakai, K.; Kikuchi, A.; Sakurai, Y.; Okano, T. *Nature* **1995**, *374*, 240–242.
(9) Heskins, M.; Guillet, J. E. *J. Macromol. Sci. Chem. A* **1968**, *2*, 1441.
(10) Fernandez, V. V. A.; Tepale, N.; Sanchez-Diaz, J. C.; Mendizabal, E.; Puig, J. E.; Soltero, J. F. A. *Colloid Polym. Sci.* **2006**, *284*, 387–395.
(11) Lin, S. Y.; Chen, K. S.; Liang, R. C. *Polymer* **1999**, *40*, 2619–2624.
(12) Tanaka, N.; Matsukawa, S.; Kurosu, H.; Ando, I. *Polymer* **1998**, *39*, 4703–4706.
(13) Pelton, R. H.; Chibante, P. *Colloids Surf.* **1986**, *20*, 247–256.
(14) Akagawa, M.; Suyama, K. *Eur. J. Biochem.* **2001**, *268*, 1953–1963.
(15) Chung, K. T.; Lu, Z.; Chou, M. W. *Food Chem. Toxicol.* **1998**, *36*, 1053–1060.
(16) Haslam, E. *J. Nat. Prod.* **1996**, *59*, 205–215.
(17) Edelmann, A.; Lendl, B. *J. Am. Chem. Soc.* **2002**, *124*, 14741–14747.
(18) Frazier, R. A.; Papadopoulou, A.; Mueller-Harvey, I.; Kissoon, D.; Green, R. J. *J. Agr. Food Chem.* **2003**, *51*, 5189–5195.
(19) Baxter, N. J.; Lilley, T. H.; Haslam, E.; Williamson, M. P. *Biochemistry* **1997**, *36*, 5566–5577.
(20) Haslam, E.; Lilley, T. H.; Cai, Y.; Martin, R.; Magnolato, D. *Planta Med.* **1989**, 1–8.
(21) Oh, H. I.; Hoff, J. E.; Armstrong, G. S.; Haff, L. A. *J. Agr. Food Chem.* **1980**, *28*, 394–398.
(22) Shutava, T.; Prouty, M.; Kommireddy, D.; Lvov, Y. *Macromolecules* **2005**, *38*, 2850–2858.
(23) Yen, K. C.; Mandal, T. K.; Woo, E. M. *J. Biomed. Mater. Res. A* **2008**, *86A*, 701–712.
(24) Erel-Unal, I.; Sukhishvili, S. A. *Macromolecules* **2008**, *41*, 3962–3970.
(25) Kozlovskaya, V.; Kharlampieva, E.; Drachuk, I.; Cheng, D.; Tsukruk, V. V. *Soft Matter* **2010**, *6*, 3596–3608.
(26) Kim, B. S.; Lee, H.; Min, Y. H.; Poon, Z.; Hammond, P. T. *Chem. Commun.* **2009**, 4194–4196.
(27) Schmidt, D. J.; Hammond, P. T. *Chem. Commun.* **2010**, *46*, 7358–7360.
(28) Wong, J. E.; Richtering, W. *Prog. Colloid Polym. Sci.* **2006**, *133*, 45–51.
(29) Keerl, M.; Smirnovas, V.; Winter, R.; Richtering, W. *Macromolecules* **2008**, *41*, 6830–6836.
(30) Kosik, K.; Wilk, E.; Geissler, E.; Laszlo, K. *Macromolecules* **2007**, *40*, 2141–2147.
(31) Chen, G.; Niu, C. H.; Zhou, M. Y.; Ju, X. J.; Xie, R.; Chu, L. Y. *J. Colloid Interface Sci.* **2010**, *343*, 168–175.
(32) Costa, E.; de-Carvalho, J.; Casimiro, T.; Lobato da Silva, C.; Cidade, M. T.; Aguiar-Ricardo, A. *J. Supercrit. Fluid.* **2010**, DOI:10.1016/j.supflu.2010.10.039.
(33) Araujo, P. Z.; Morando, P. J.; Blesa, M. A. *Langmuir* **2005**, *21*, 3470–3474.
(34) Langmuir, I. *J. Am. Chem. Soc.* **1918**, *40*, 1361–1403.
(35) Kubelka, P.; Munk, F. *Z. Tech. Phys.* **1931**, *12*, 593–601.
(36) Cowen, S.; Al-Abadleh, H. A. *Phys. Chem. Chem. Phys.* **2009**, *11*, 7838–7847.
(37) Jastrzebska, M.; Zalewska-Rejdak, J.; Wrzalik, R.; Kocot, A.; Mroz, I.; Barwinski, B.; Turek, A.; Cwalina, B. *J. Biomed. Mater. Res. Part A* **2006**, *78A*, 148–156.
(38) Mohammed-Ziegler, I.; Billes, F. *J. Mol. Struct.−Theochem.* **2002**, *618*, 259–265.
(39) Jankovic, I. A.; Saponjic, Z. V.; Dzunuzovic, E. S.; Nedeljkovic, J. M. *Nanoscale Res. Lett.* **2010**, *5*, 81–88.
(40) Maeda, Y.; Higuchi, T.; Ikeda, I. *Langmuir* **2000**, *16*, 7503–7509.
(41) Sun, B. J.; Lin, Y. A.; Wu, P. Y. *Appl. Spectrosc.* **2007**, *61*, 765–771.
(42) Haris, P. I.; Chapman, D. *Trends Biochem. Sci.* **1992**, *17*, 328–333.
(43) Skrovanek, D. J.; Painter, P. C.; Coleman, M. M. *Macromolecules* **1986**, *19*, 699–705.

622 *Macromolecules* **2011**, *44*, 622–631
DOI: 10.1021/ma102510u

Macromolecules
ARTICLE

Tailoring Micelle Formation and Gelation in (PEG−P(MA-POSS)) Amphiphilic Hybrid Block Copolymers

B. H. Tan,[†] H. Hussain,*[,†] and C. B. He*[,†,‡]

[†]*Institute of Materials Research and Engineering (IMRE), A*STAR (Agency for Science, Technology and Research), 3 Research Link, Singapore 117602, and* [‡]*Department of Materials Science and Engineering, National University of Singapore, Singapore 117576, Singapore*

Received November 5, 2010; Revised Manuscript Received December 12, 2010

ABSTRACT: We demonstrate that hydrophobic POSS (polyhedral oligomeric-silsesquioxane) nanoparticles, added to block copolymer solutions of poly(ethylene glycol) (PEG) and poly(methacrylisobutyl polyhedral oligomericsilsesquioxane) P(MA-POSS) as the hydrophilic and hydrophobic blocks respectively, could be employed to tailor their micelle formation, gelation, and rheological performance. For example, the hydrodynamic size of the micelles, formed by PEG_{5k}-*b*-$P(MA\text{-}POSS)_{3.6}$, increased from 13.6 ± 1.0 to 56.9 ± 3.7, an increase of more than four times, with 0.1 wt % (with respect to block copolymer) POSS nanoparticles in solution. However, the micelles retain their spherical morphology with core−shell structure as evidenced by calculating the values of dimensionless ratios, R_g/R_h for micelles as a function of added POSS nanoparticles content. For P(MA-POSS)-*b*-PEG_{10k}-*b*-P(MA-POSS) triblock copolymers, which is associative in nature, addition of POSS nanoparticles resulted in formation of more robust and stronger hydrogels with a significantly higher storage modulus, G', yield strengths, σ_y, and lower critical gelation concentration, c_g, as compared with those for the pristine triblock copolymer. The presence of eight vinyl groups, attached to the POSS nanoparticles under investigations, is also exploited for further enhancement of rheological properties of the hydrogels with UV treatment. Finally, gel formation is induced in aqueous solutions of PEG_{5k}-*b*-$P(MA\text{-}POSS)_{3.6}$ diblock copolymer by introducing P(MA-POSS)-*b*-PEG_{10k}-*b*-P(MA-POSS) triblock copolymer chains, and the rheological performance of the produced hydrogels, with certain compositions, is even superior to that of pure triblock copolymer gel.

Introduction

Polyhedral oligomeric silsesquioxanes (POSS), considered as the smallest possible silica particles, are unique three-dimensional nanobuilding blocks with a well-defined cage-like structure made of silicon and oxygen atoms linked together in a cubic form.[1−6] They can be easily functionalized with organic substituents at corners to facilitate their solubility in organic solvents, miscibility and/or covalent incorporation into polymer matrices.[7−14] Recently, Gnanasekaran et al.[15] and Cordes et al.[16] have published excellent reviews on various aspects of polyhedral oligosilsesquioxanes (POSS) and nanocomposites. Numerous strategies, including both chemical and physical, have been explored to disperse POSS into polymer matrices to achieve hybrid materials with novel properties such as enhanced thermal[17−20] and mechanical performance,[21−23] low dielectric constant,[24−26] surface properties, such as improved hydrophobicity,[27] etc.[28−38]

The latest advances in organic and polymer syntheses have made it possible to integrate POSS into well-defined (co)polymers of various topologies, that could potentially expand POSS based materials in to new areas.[39−49] Particular focus is also directed to the self-assembly of these newly developed well-defined hybrids.[50−52] For example, Matyjaszewski et al.[53] reported the synthesis of p(MA-POSS)-*b*-poly(*n*-butyl acrylate)-*b*-p(MA-POSS) triblock copolymers via ATRP, and the self-assembly structure formed in thin films. Jianjun et al.[54] investigated the self-assembly and chain-folding in well-defined co-oligomeric polyethylene-*b*-poly(ethylene oxide)-*b*-POSS. Hiari et al.[55,56] reported the synthesis by anionic polymerization and the formation of hierarchical nanostructures of PMMA-*b*-P(MA-POSS) and PS-*b*-P(MA-POSS) diblock copolymers in thin films. Escude et. al[57] synthesized stereoregular PMMA-*co*-P(MA-POSS) copolymers and investigated their self-assembly in various organic solvents. Amphiphilic hybrid macromolecules with POSS as the hydrophobic segment, however, have received significantly less attention. Notable examples include, the synthesis, characterization, and solution behavior of amphiphilic telechelic polymers with POSS as the end groups,[58−62] and amphiphilic star-like polymers having POSS as the core and PEG as arms.[63−65] Also, Zhang et al.[66,67] reported the synthesis by reversible addition−fragmentation transfer (RAFT), using POSS-containing RAFT agent, and self-assembly in aqueous solution of amphiphilic tadpole-shaped hybrid POSS−poly(*N*-isopropylacrylamide) (PNIPAAm) and POSS−poly(acrylic acid). The POSS−PNIPAAm were found to self-assemble into core−shell micelles with uniform diameter, while the POSS−poly(acrylic acid) self-assembled into larger aggregates in aqueous solutions, but no typical core−shell structure was observed. The literature survey reveals that most of the investigations on POSS containing amphiphilic hybrid macromolecules are focused on hydrophilic polymers with a single POSS nanocage either at one end (tadpole shaped and star-like) or at both ends (telechelic). Surprisingly, no attention has been paid to amphiphilic block copolymers having more than one POSS nanocages in hydrophobic segment of the block copolymers, let alone their self-assembly. The variation in length of the POSS containing hydrophobic block in amphiphilic block copolymers would offer an extra degree of freedom, i.e., changing composition, to tune their self-assembly behavior in solution as well as hydrogel formation

*Corresponding authors. E-mail: (H.H.) h-hussain@imre.a-star.edu.sg; (C.B.H.) cb-he@imre.a-star.edu.sg.

 Published on Web 01/10/2011 © 2011 American Chemical Society

that could result novel properties and offer new insights into the behavior of block copolymers. Recently, we published our first results on the micelle formation and preliminary observations on gelation in aqueous solutions, of a new series of well-defined amphiphilic PEG_{5k}-*b*-$P(MA\text{-}POSS)_x$ diblock and $P(MA\text{-}POSS)_x$-*b*-PEG_{10k}-*b*-$P(MA\text{-}POSS)_x$ triblock copolymers, having poly(ethylene glycol) (PEG) and poly(methacrylisobutyl polyhedral oligomeric silsesquioxane) P(MA-POSS) as the hydrophilic and hydrophobic blocks respectively.[68] The current work presents detailed account of tuning micelle formation, hydrogelation, and rheological properties of (PEG-P(MA-POSS)) block copolymers by adding POSS nanoparticles to block copolymer aqueous solutions. Furthermore, it is also demonstrated that aqueous solution of diblock copolymer; PEG_{5k}-*b*-P(MA-POSS), could be transformed into hydrogel by introducing associative-triblock copolymer chains; P(MA-POSS)-*b*-PEG_{10k}-*b*-P(MA-POSS). Rheological performance of the obtained hydrogels was investigated as function of triblock copolymer content.

Experimental Section

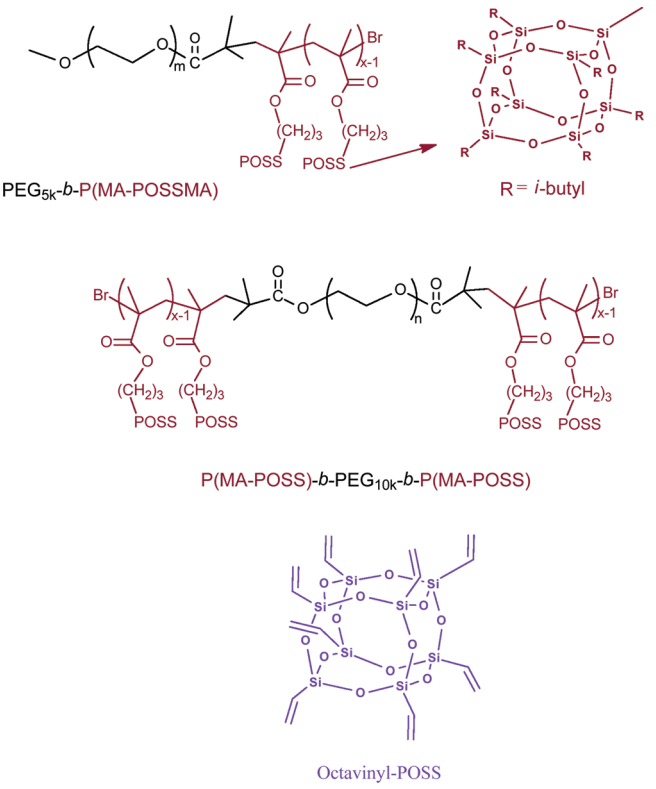
Materials. The amphiphilic block copolymers under investigations; PEG_{5k}-*b*-$P(MA\text{-}POSS)_{3.6}$, $P(MA\text{-}POSS)_{3.4}$-*b*-PEG_{10k}-*b*- $P(MA\text{-}POSS)_{3.4}$, and $P(MA\text{-}POSS)_{4.7}$-*b*-PEG_{10k}-*b*-$P(MA\text{-}POSS)_{4.7}$, were synthesized by ATRP as detailed elswhere,[68] where, the subscript to PEG and P(MA-POSS), represents, respectively, the molar mass of PEG and the average degree of polymerization (DP) of the (P(MA-POSS) segment, in respective block copolymer. For example, for PEG_{5k}-*b*-$P(MA\text{-}POSS)_{3.6}$, the molar mass of PEG is 5000 g/mol and the average DP of P(MA-POSS) is 3.6. OctaVinyl POSS (POSS nanoparticles) (product no.: OL1160) was purchased from Hybrid Plastics and used as received. The chemical structures of the investigated block copolymers and POSS nanoparticles are given in Scheme 1. Benzoyl peroxide (BP) as photoinitiator, was purchased from Aldrich and used as received. Deionized water was taken from a Millipore Alpha-Q purification system equipped with a 0.22 μm filter.

Dynamic Light Scattering (DLS). Room-temperature light scattering measurements were made with a Brookhaven BI-200SM multiangle goniometer equipped with a BI-APD detector. The light source was a 35 mW He−Ne laser emitting vertically polarized light of 632.8 nm wavelength. In DLS measurements, the intensity correlation function was measured at 25 °C (unless otherwise stated) with a maximum number of 256-channels using a BI-9000AT digital autocorrelator. Non-negative least-squares (NNLS) algorithm, developed by Lawson and Hansen,[69] was applied to obtain best-fit values of the parameters from DLS measurements. DLS measures the intensity autocorrelation function, $g^{(2)}(\tau)$ which is related to the electric field autocorrelation function, $g^{(1)}(\tau)$ by means of the Siegert relation.[70] From the expression $\Gamma = D_{app}q^2$, the apparent translational diffusion coefficients, D_{app}, were determined. Γ is the decay rate, which is the inverse of the relaxation time, τ; q is the scattering vector defined as $q = (4\pi n \sin(\theta/2)/\lambda)$ (where n is the refractive index of the solution, θ is the scattering angle, and λ is the wavelength of the incident laser light in vacuum).[70,71] The apparent hydrodynamic radius (R_h) can be determined by the Stokes−Einstein relationship:[70,71]

$$R_h = \frac{kT}{6\pi\eta D_{app}} \quad (1)$$

where k_B, η, and T are the Boltzmann constant, viscosity of solvent, and the absolute temperature, respectively. The hydrodynamic sizes of the micelles in aqueous solution formed by block copolymers were measured using DLS for copolymer concentrations ranging from 0.1 to 2.5 mg/mL, well above the cmc, to ensure the micelle formation.

Scheme 1. Chemical Structures of the Investigated Block Copolymers and POSS Nanoparticles



Static Light Scattering (SLS). Static light scattering was used to measure and analyze the time-average scattered intensities where the weight-average molecular weight ($\overline{M}_w$) and the second virial coefficient (A_2) of the block copolymer unimers and micelles can be determined.[72,73] The refractive index increment of the copolymer solution, (dn/dc) was measured using a BI-DNDC differential refractometer at a wavelength of 620 nm to determine the refractive index increment (dn/dc) of each solution. The instrument was calibrated primarily with potassium chloride (KCl) in aqueous solution.

Rheology Measurement. Dynamic rheological measurements were performed on a Thermo Haake RS600 rheometer at 25 ± 0.1 °C with parallel plate geometry (35 mm diameter) at a gap of 1 to 2 mm. The polymer sample that had been equilibrated for 24 h prior to measurements was carefully loaded onto the measuring geometry. Precautions, which include gradual gap closing and careful sample trimming, were taken to minimize disruption to the gel network and ensure optimal filling within the measuring geometry. Water was added around the measuring geometry to minimize the effect of water evaporation on the rheology data. Each measurement of the same sample was repeated at least twice in order to ensure that the rheological data were reproducible. Oscillatory stress sweeps were performed by applying increasing shear stress logarithmically from 0.50 Pa at a fix angular frequency of 1 rad/s to determine a suitable shear stress value, where the material exhibits linear viscoelastic behavior. This shear stress value was later used in the oscillatory frequency sweeps experiments where the measurements were performed from 100 to 0.10 rad/s to determine the frequency dependence of storage and loss modulus, G' and G'' respectively. This procedure ensured that the dynamic property measurements were carried out within the linear viscoelastic regime of each sample. The rheometer is calibrated once a month using silicon calibration oils at three different rotational speeds to verify the accuracy and response of the rheometers when sensing low, medium, and high torque values.

Preparation of Aqueous Solutions of Block Copolymers. As an example, to prepare 2.0 mg/mL aqueous solution of PEG_{5k}-*b*-$P(MA\text{-}POSS)_{3.6}$, 4.0 mg of block copolymer was dissolved in 0.5 mL of THF, and this solution was added dropwise to 2 mL deionized water with continuous stirring. THF was allowed to evaporate off at room temperature for 24 h that allowed the formation of block copolymer micelles in aqueous solution.[68] For the preparation of aqueous solutions, containing mixtures of diblock and triblock, for example, 60 wt % diblock and 40 wt % triblock, 2.4 mg of diblock copolymer was dissolved in 0.5 mL of THF and this solution was added dropwise to 2 mL of deionized water with continuous stirring. After allowing THF to evaporate for 24 h, solution of triblock copolymer (1.6 mg/0.5 mL) in THF was added dropwise with continuous stirring and allowed THF evaporation for another 24 h. The composition was varied in mixtures, but the overall concentration of block copolymer (diblock + triblock) was fixed at 2.0 mg/mL. A slightly different protocol was adopted for the preparation of aqueous solutions containing diblock and POSS nanoparticles. As an example, for the preparation of 2.0 mg/mL diblock copolymer solution having 0.1 wt % POSS nanoparticles, 4.0 mg of block copolymer and 0.004 mg (*the stated amount of POSS nanoparticles in solution was achieved by diluting a concentrated solution of POSS in THF*) of POSS nanoparticles were dissolved in 0.5 mL of THF, and this solution was added dropwise into 2 mL of deionized water with continuous stirring followed by THF evaporation at room temperature for 24 h. The detailed method to investigate the evaporation of THF from the copolymer solution has been described elsewhere.[68] Note that the weight percent of POSS nanoparticles in solution was calculated with reference to the mass of block copolymer in solution as:

$$\text{content of POSS nanoparticles (wt \%)} = \frac{\text{mass of POSS nanoparticles}}{\text{mass of block copolymer}} \times 100\% \qquad (2)$$

Preparation of Hydrogels. A similar respective protocols (*vide supra*) were followed for the preparation of block copolymer hydrogels but at much higher copolymer concentrations (in the range of 10 wt %). In sample for UV treatment, 1.0 wt % benzoyl Peroxide (BP) (mass of BP/mass of POSS nanoparticles) was dissolved in THF along with $P(MA\text{-}POSS)_{4.7}$-*b*-PEG_{10k}-*b*-$P(MA\text{-}POSS)_{4.7}$ and 0.1 wt % POSS nanoparticles (calculated according to eq 2). The obtained hydrogel was subsequently exposed to UV light at wavelength of 365 nm for 10 min.

Results and Discussion

Influence of POSS Nanoparticles on the Micelle Formation by PEG_{5k}-*b*-P(MA-POSS) in Aqueous Solutions. The micelle formation of the PEG_{5k}-*b*-P(MA-POSS) block copolymers in aqueous solution is driven by hydrophobic interactions among the P(MA-POSS) segments, resulting into micelles, where, the PEG block would constitute the shell and P(MA-POSS) the core of the micelle. Various parameters, such as changing the block chemistry, block lengths, composition, architecture, external environment, for example, solvent, temperature, pH, and etc are generally reported to tailor the micelle formation by amphiphilic block copolymers.[74−78] Here, we investigated the influence of hydrophobic POSS nanoparticles, added to the block copolymer solutions, as a new parameter, to tune the micellization of (PEG−P(MA-POSS)) amphiphilic block copolymers in aqueous solution. For this purpose, a series of aqueous solutions, having a fixed concentration of PEG_{5k}-*b*-$P(MA\text{-}POSS)_{3.6}$ diblock copolymer and varying amounts (wt %) of POSS nanoparticles (with respect to block copolymer−calculated using eq 2), ranging from 1×10^{-5} to 5.0 wt % were prepared as described in the Experimental Section. The solutions were visually examined, looking for qualitative changes in transparency and external appearance. Samples containing up to 0.1 wt % of POSS nanoparticles were similar in appearance to that of pure PEG_{5k}-*b*-$P(MA\text{-}POSS)_{3.6}$ diblock copolymer solutions, however, as the concentration of POSS nanoparticles increased, the transparency lost progressively and

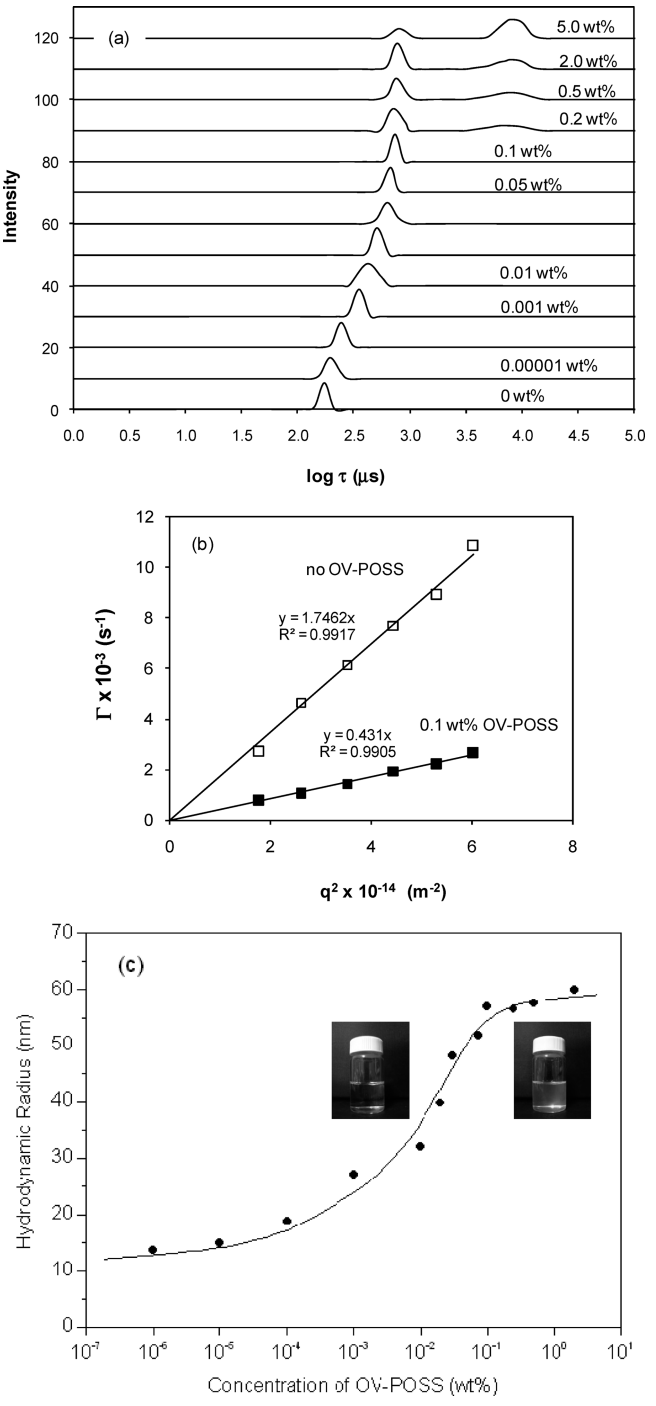


Figure 1. (a) Relaxation time, τ distribution functions of PEG_{5k}-*b*-$P(MA\text{-}POSS)_{3.6}$ in aqueous solutions with varying content (wt %) of added POSS nanoparticles (wt % of POSS nanoparticles were calculated using eq 2), measured at scattering angle 90° and maintaining total copolymer concentration at 2 mg/mL. (b) Dependence of decay rate Γ on q^2 of PEG_{5k}-*b*-$P(MA\text{-}POSS)_{3.6}$ without POSS nanoparticles (open symbol) and 0.1 wt % POSS nanoparticles (closed symbol). (c) Hydrodynamic radius, R_h of micelles as a function of concentrations (wt %) of POSS nanoparticles at fixed copolymer concentration (2 mg/mL) in aqueous solution. Digital photographs are from copolymer solutions with 0.1 wt % (left side) and 5 wt % (right side) of POSS nanoparticles.

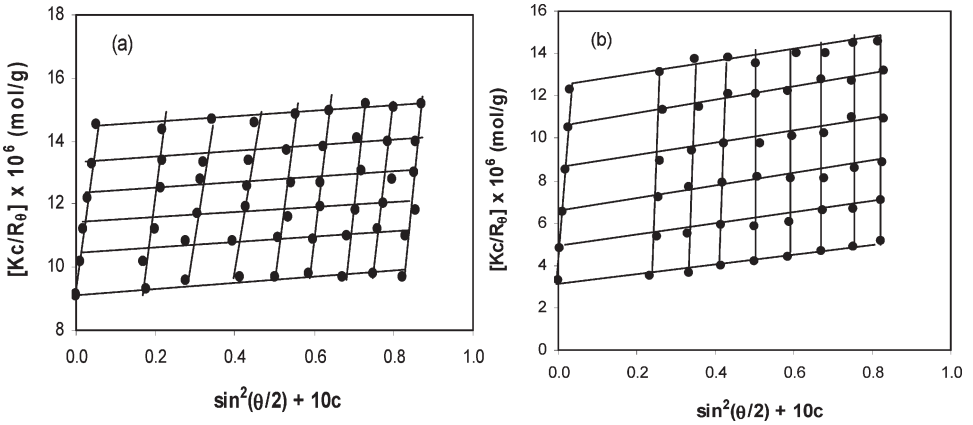


Figure 2. Zimm plots of PEG_{5k}-*b*-$(MA\text{-}POSS)_{3.6}$ diblock copolymers in aqueous solution with (a) 0 wt % and (b) 0.1 wt % POSS nanoparticles. The measurements were carried out at room temperature and the copolymer concentration range was from 0.1 to 2.5 mg/mL, with the scattering angle ranging from 50 to 130°.

Table 1. Characteristic Parameters of Micelles Formed by PEG_{5k}-*b*-$P(MA\text{-}POSS)_{3.6}$ as a Function of POSS Nanoparticles Content in Aqueous Solutions at 25 °C

content of POSS nanoparticles (wt %)[a]	R_h[b] (nm)	R_g (nm)	R_g/R_h	$M_{w,\ micelle} \times 10^{-3}$ (g/mol)	N_{agg}	$A_2 \times 10^5$ (cm^3 mol/g^2)
0	13.6 ± 1.0	8.7 ± 0.8	0.64	109.7 ± 7.2	14.8	11.8 ± 0.90
0.0001	15.1 ± 1.3	9.7 ± 0.8	0.64	122.4 ± 10.6	16.6	11.0 ± 0.75
0.01	32.0 ± 2.2	20.8 ± 1.3	0.65	205.4 ± 15.8	27.8	8.6 ± 0.60
0.05	50.4 ± 2.9	35.2 ± 2.1	0.70	275.8 ± 21.4	37.3	6.2 ± 0.29
0.1	56.9 ± 3.7	41.0 ± 2.7	0.72	303.6 ± 19.0	41.1	4.5 ± 0.10

[a] wt % of POSS nanoparticles calculated using eq 2. [b] Measured at fixed PEG_{5k}-*b*-$P(MA\text{-}POSS)_{3.6}$ concentration of 2.0 mg/mL.

the solution changed from slightly translucent to hazy at 5 wt % POSS nanoparticles, as depicted in the digital photographs inserted in Figure 1c. The dynamic light scattering (DLS) data, (relaxation time distribution functions, measured at scattering angle 90°) shown in Figure 1a, reveals a unimodal τ distribution function for solutions up to 0.1 wt % POSS nanoparticles, suggesting the formation of one kind of micellar aggregates. Also the linear dependence of decay rate, Γ on q^2, shown in Figure 1b, verifies that the observed peaks in Figure 1a originated from the translational diffusion of the copolymer micelles and not from internal diffusions. Surprisingly, the hydrodynamic size, R_h of micelles, calculated using the Stokes−Einstein equation (eq 1), increased almost twice with the introduction of a negligibly small amount (0.001 wt %) of POSS nanoparticles into the block copolymer solution, i.e., from $R_h \sim 13.6 \pm 1.0$ nm to $R_h \sim 27.2 \pm 1.9$ nm. As shown in Figure 1c, the maximum $R_h \sim 56.9 \pm 3.7$ was achieved with ~0.1 wt % of POSS nanoparticles in solution, above which a plateau could be seen, with no significant change in the micelle size up to the investigated concentration of POSS nanoparticles = 5 wt %. To mention that for concentrations >0.1 wt % of POSS nanoparticles, the R_h plotted in Figure 1c is based on the fast mode.

As seen in Figure 1a, at POSS nanoparticles >0.1 wt %, an additional broad secondary peak appeared at larger relaxation time; corresponding to larger aggregates of equivalent hydrodynamic radius, R_h~650 nm, which, with increasing POSS nanoparticles in solution, becomes more distinct with increased area under the curve, concurrently, area under the fast mode reduced; much more obvious at 5.0 wt %. This suggests that the larger aggregates resulted from the coalescence of micelles at higher hydrophobic POSS nanoparticles concentration in solution. It can be concluded that the micelles of PEG-*b*-P(MA-POSS) reach their maximum solubilization/loading capacity for POSS nanoparticles at 0.1 wt % POSS nanoparticles in solution, above which the micelles could not retain their integrity due to imbalance in hydrophobic/hydrophilic interactions, leading to coalescence and finally complete phase separation above 5 wt %.

Taking into consideration, the small size ~1.2−1.4 nm of individual POSS nanoparticles,[6] the observed increase in hydrodynamic size, R_h; more than four times with 0.1 wt % POSS nanoparticles (*vide supra*), was unexpected. To get insight, static light scattering (SLS) experiments were conducted to evaluate the weight-average molecular weight of the micelles ($M_{w,\ micelle}$), the *z*-average radius of gyration (R_g) and the second virial coefficient (A_2) of micelles as a function of POSS nanoparticles concentration. Representative Zimm plots, for PEG_{5K}-*b*-$P(MA\text{-}POSS)_{3.6}$ pure and with added 0.1 wt % POSS nanoparticles are depicted in Figure 2.

The extracted data, summarized in Table 1, shows a significant increase in molecular weight ($M_{w,\ micelle}$) and aggregation number (N_{agg}) of the micelles with increasing POSS concentration in solution. Thus, the $M_{w,\ micelle}$ for PEG_{5k}-*b*-$P(MA\text{-}POSS)_{3.6}$ increased from ~110 000 g/mol to ~302 000 g/mol with 0.1 wt % POSS nanoparticles in solution, while the corresponding apparent aggregation number, $N_{agg,}$ calculated from $N_{agg} = M_{w,micelle}/M_{w,single}$, (where, $M_{w,micelle}$ and $M_{w,single}$ represents the molecular weight of micelles obtained from SLS and single block copolymer chain obtained from GPC, respectively), varied from ~15 to ~42. Because of the minimal amounts of the added POSS nanoparticles, the molecular weight contribution from POSS nanoparticles will be negligible when calculating the N_{agg} of micelles. The solutions with POSS nanoparticles >0.1 wt % were not investigated by SLS due to bimodal particle size distributions (see Figure 1a). These observations clearly suggest that the added POSS nanoparticles in block copolymer solution enhance the hydrophobic interactions, which consequently leads to the formation of bigger micelles due to higher aggregation numbers (N_{agg}). The enhanced hydrophobicity with increasing POSS nanoparticles in solution could be verified by the decreasing value of second virial

coefficient, A_2 (which represents the polymer−solvent interactions) from $\sim 11.8 \times 10^{-5}$ to $\sim 4.5 \times 10^{-5}$ cm^3 mol/g^2 with increasing POSS nanoparticles from 0 to 0.1 wt % (see Table 1).

Furthermore, the influence of POSS nanoparticles on the morphology of micelles was evaluated by calculating the dimensionless ratio, R_g/R_h; a characteristic parameter providing information on the morphology of particles in solution, as a function of POSS nanoparticles concentration in solution. The data given in Table 1 reveals an increase in R_g/R_h from 0.64 at 0.0 wt % to 0.72 at 0.1 wt % POSS nanoparticles. In literature, the values of R_g/R_h for hard-sphere, random coil, and rod-like morphology are reported as 0.78, 1.78, and ≥2, respectively,[79,80] suggesting that in current study, the micelles remains spherical in morphology, having a higher density at the center ($R_g/R_h <$ 0.78 was interpreted by Tu et al.[81] as particles having higher density at the center, thus representing the formation of a core−shell structure).

Hydrogel Formation and Rheology of P(MA-POSS)-*b*-PEG$_{10k}$-*b*-P(MA-POSS) Triblock Copolymers. The P(MA-POSS)-*b*-PEG$_{10k}$-*b*-P(MA-POSS) type triblock copolymers, i.e., having terminal hydrophobic segments and middle hydrophilic block, are associative in nature and are expected to form hydrogels with increasing block copolymer concentration in aqueous solution due to the formation of a transient intermicellar network structure.[68] Figure 3a depicts the oscillatory stress sweep curves of P(MA-POSS)$_{4.7}$-*b*-PEG$_{10k}$-*b*-P(MA-POSS)$_{4.7}$ at 11.0 wt % copolymer concentration, revealing that the gel, within its linear viscoelastic range up to ∼1000 Pa in terms of shear stress, has a storage modulus, G' (the amount of stress required to shear the elastic component of the gel by a unit strain) dominating over its loss modulus, G'' (the amount of stress required to shear the viscous component of the gel by a unit strain) with a magnitude in the order of 10^4 Pa. A shear stress of approximately 3.2 kPa (see Figure 3a) is required to destroy the network structure of the triblock copolymer gel into a liquid-like phase and is manifested by a G'/G'' crossover in Figure 3a and is termed as yield point, σ_y.[82] Figure 3b demonstrates the effect of concentration of P(MA-POSS)$_{4.7}$-*b*-PEG$_{10k}$-*b*-P(MA-POSS)$_{4.7}$ on the oscillatory frequency sweep, where the *X*-axis was shifted to higher frequency range by a factor "*a*" ranging from 1 to 10^4 to obtain a valid comparison. The data in Figure 3b reveal different behaviors, depending on the copolymer concentration, i.e., at copolymer concentrations ≤6.5 wt %, the magnitudes of G' are much lower than those of G'' and are shear frequency dependent, at 7.8 wt % copolymer concentration, the value of G' becomes slightly higher than G'' at the higher frequency range, indicating that this copolymer concentration is located near the gel boundary and at ≥8.5 wt %, the values of G' and G'' are no longer frequency dependent and G' is almost 1 order of magnitude higher than G'', showing the attainment of equilibrium modulus, G_{eq}, which is a typical criterion for the formation of an elastic gel. Generally, the gelation behavior is based on the formation of fractal aggregates or gel, grown to an extent to occupy the total volume of the dispersion, leading to optimal packing. The P(MA-POSS)-*b*-PEG$_{10k}$-*b*-P(MA-POSS) type associative triblock copolymers develop this fractal network via the formation of intermicellar network-like structure in solution which expands with concentration leading to gel formation (see Scheme 2).[68] In case of diblock copolymers, though, the viscosity, observed visually, does increase with increasing concentration of copolymer, yet due to inability of the star-like micelles to develop intermicellar network-like structure, gel formation by PEG$_{5k}$-*b*-P(MA-POSS)$_{3.6}$ could not be observed up to 11.0 wt % copolymer concentration. The increase in viscosity of the diblock system at higher concentration is mainly due to the increasing hydrodynamic interactions between the particles when the interparticle distance reduces.

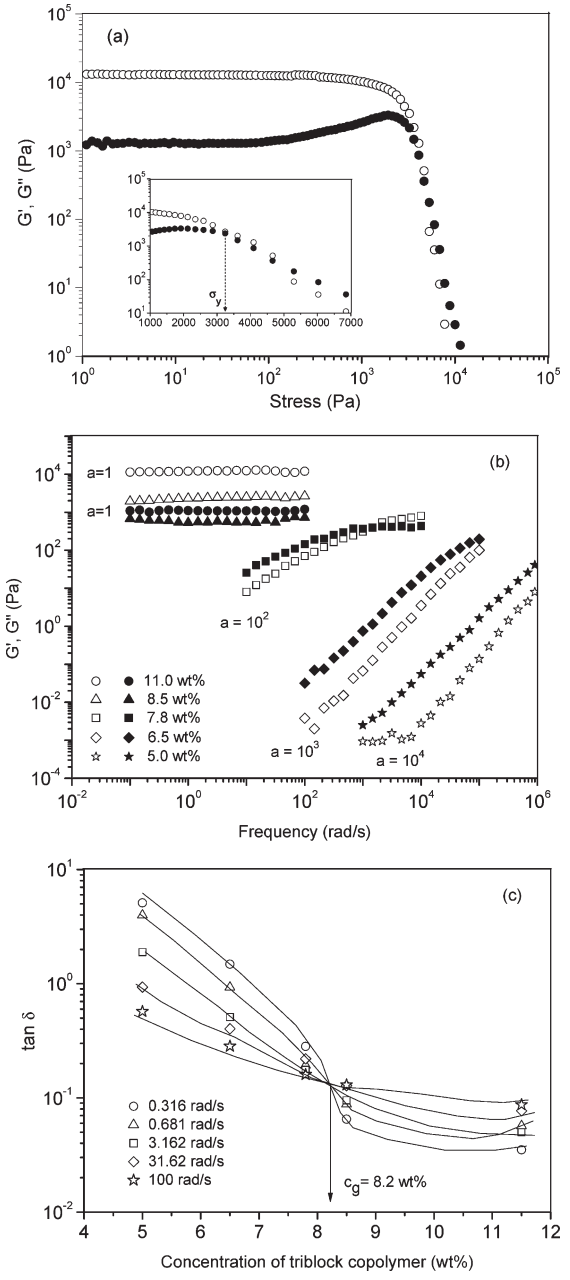
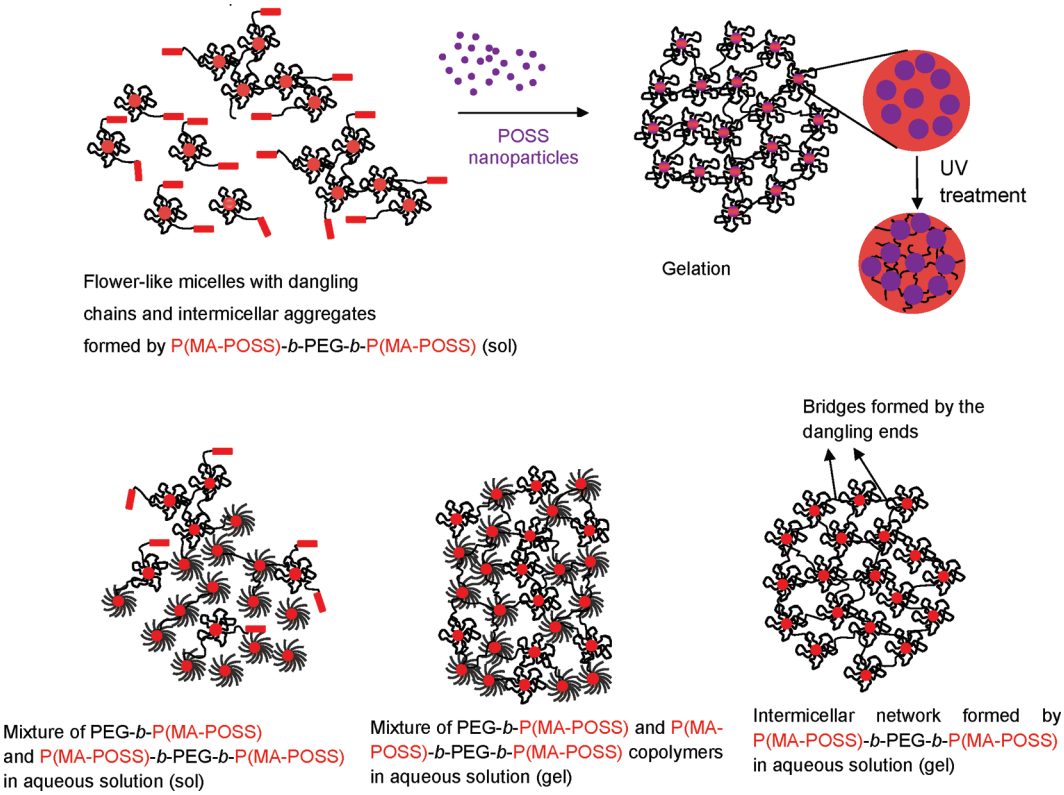


Figure 3. (a) Oscillatory stress sweep measurements of P(MA-POSS)$_{4.7}$-*b*-PEG$_{10k}$-*b*-P(MA-POSS)$_{4.7}$ at constant ω = 1 rad/s and copolymer concentration of 11.0 wt %. Inset is an expansion of the region where G'/G'' crossover occurred and the applied shear stress at this point is defined as yield stress, σ_y. (b) Oscillatory frequency sweep measurements of P(MA-POSS)$_{4.7}$-*b*-PEG$_{10k}$-*b*-P(MA-POSS)$_{4.7}$ in aqueous solution at various copolymer concentrations (wt %). The storage modulus, G' and loss modulus, G'' are represented by the open and closed symbols, respectively. The *X*-axis is shifted by a factor $a = 1-10^4$ to obtain a valid comparison. (c) Loss tangent, tan δ as a function of copolymer concentration of P(MA-POSS)$_{4.7}$-*b*-PEG$_{10k}$-*b*-P(MA-POSS)$_{4.7}$ at various angular frequencies, ω to obtain the critical gelation concentration, c_g.

The degree of polymerization (DP) of P(MA-POSS) segment in P(MA-POSS)-*b*-PEG$_{10k}$-*b*-P(MA-POSS) block copolymer also affected the rheological behavior of the obtained gel. Thus, at 11.0 wt % block copolymer concentration, the G' and σ_y reduced by almost half, i.e., from

Scheme 2. Schematic Presentations of Proposed Intermicellar Aggregates in Solutions and Gels



~11.5 to ~6.8 kPa and from ~3.2 to ~1.5 kPa, respectively, when the DP of P(MA-POSS) was slightly reduced from 4.7 to 3.4.

The critical gelation concentration, c_g for both P(MA-POSS)$_{3.4}$-*b*-PEG$_{10k}$-*b*-P(MA-POSS)$_{3.4}$ and P(MA-POSS)$_{4.7}$-*b*-PEG$_{10k}$-*b*-P(MA-POSS)$_{4.7}$ was determined by plotting the tan δ as a function of copolymer concentrations at different angular frequencies, ω. As shown in Figure 3c for P(MA-POSS)$_{4.7}$-*b*-PEG$_{10k}$-*b*-P(MA-POSS)$_{4.7}$, all the curves intersect at a characteristic concentration, defined as c_g, which is found to be ~8.2 wt %. The c_g of P(MA-POSS)$_{3.4}$-*b*-PEG$_{10k}$-*b*-P(MA-POSS)$_{3.4}$ triblock copolymer was calculated slightly higher (~8.9 wt %) because of the lower hydrophobic MA-POSS content, thus requiring a higher copolymer concentration to form the critical fractal network for gelation. It is to be mentioned here, that not only the hydrophobic-*b*-hydrophilic-*b*-hydrophobic type associative block copolymers form hydrogels in aqueous solution, but also the hydrophilic-*b*-hydrophobic-*b*-hydrophilic type could form hydrogels, via a different mechanism though, under appropriate conditions. For example, it has been reported that an aqueous solution (high concentration) of biodegradable poly(ethylene glycol-*b*-(DL-lactic acid-*co*-glycolic acid)-*b*-ethylene glycol) PEG-*b*-(PL-*co*-GA)-*b*-PEG, and poly(ethylene glycol-*b*-DL-lactic acid-*b*-ethylene glycol, PEG-*b*-PL-*b*-PEG, with a specific composition, transforms into a *gel* at ~37 °C.[83,84]

Influence of POSS Nanoparticles on the Rheological Behavior of P(MA-POSS)-*b*-PEG$_{10k}$-*b*-P(MA-POSS) Triblock Copolymers. As demonstrated earlier that POSS nanoparticles, added to block copolymer solutions, exert a significant influence on the micellization behavior of PEG-*b*-P(MA-POSS) in aqueous solutions by enhancing hydrophobic interactions. It would also be interesting to investigate the influence of POSS nanoparticles on gelation and rheological properties of the P(MA-POSS)-*b*-PEG$_{10k}$-*b*-P(MA-POSS). The gel formation, by aqueous solutions having a fixed concentration of P(MA-POSS)$_{4.7}$-*b*-PEG$_{10k}$-*b*-P(MA-POSS)$_{4.7}$ and various amounts of POSS nanoparticles; ranging from 0 to 2 wt %, was achieved. Figure 4a depicts that the storage modulus, G' is larger than the loss modulus, G'' and independent of frequency over the entire frequency range, confirming their gel states. The data in Figure 4b reveal a superior rheological performance of the gels with increasing POSS nanoparticles content with a maximum reached at 0.1 wt %, where, the storage modulus, G' and yield strength, σ_y reached, respectively to ~43.7 kPa and ~12.1 kPa, i.e., an increase of almost four times compared with the gel of pristine P(MA-POSS)$_{4.7}$-*b*-PEG$_{10k}$-*b*-P(MA-POSS)$_{4.7}$. The superior rheological properties are a consequence of the finely dispersed POSS nanoparticles into hydrophobic domains of the gel, enhancing hydrophobic interactions, thus providing extra strength to the gel. The enhanced hydrophobic interaction could also be judged by the fact that the gel point concentration, c_g decreased with increasing POSS nanoparticles content in the mixture, e.g., the c_g ~ 7.3 wt % was calculated for P(MA-POSS)$_{4.7}$-*b*-PEG$_{10k}$-*b*-P(MA-POSS)$_{4.7}$ having 0.1 wt % POSS nanoparticles as compared to 8.2 wt % for pure P(MA-POSS)$_{4.7}$-*b*-PEG$_{10k}$-*b*-P(MA-POSS)$_{4.7}$ (see Table 2). However, as shown in Figure 4b, POSS nanoparticles above 0.1 wt %, results into deterioration of the rheological properties, e.g., G' and σ_y reduces to ~31.0 and 8.4 kPa respectively, with 2 wt % POSS nanoparticles content. This could be attributed to the fact that the hydrophobic domains formed by the triblock copolymer chains are no longer stable due to the incorporation of exceeding amounts of hydrophobic POSS nanoparticles, and hence, the uniform fine distribution of the added POSS nanoparticles, which is responsible for enhancing rheological properties of the gel, could no longer be maintained in the gel. Interestingly, as discussed earlier, a similar influence of POSS nanoparticles on the micellization behavior of the PEG$_{5k}$-*b*-P(MA-POSS)$_{3.6}$ diblock copolymer was observed.

The POSS nanoparticles under investigations are equipped with eight vinyl groups and therefore could be exploited for further improving rheological properties of the hydrogels, via

chemical cross-linking inside the hydrophobic domains. To investigate, a hydrogel sample was prepared from calculated amounts of benzoyl peroxide (BP), as photoinitiator, P(MA-POSS)$_{4.7}$-*b*-PEG$_{10k}$-*b*-P(MA-POSS)$_{4.7}$ and POSS nanoparticles. Being hydrophobic in nature, BP is expected to be encapsulated into the hydrophobic domains of the hydrogel. The obtained hydrogel was subjected to UV irradiation to induce free radical cross-linking inside the hydrophobic domains of the gel via vinyl groups of the POSS nanoparticles. Preliminary data, shown in Table 2, reveals a significant enhancement in rheological performance of the gel (sample 3) after the UV-treatment, where, the storage modulus, G' and yield stress, σ_y increased almost two times to ~76.0 kPa and ~18.2 kPa, respectively as compared with un-cross-linked hydrogel (Sample 2) having the same POSS nanoparticles content (0.1 wt %). It is worth noting, that because the chemical cross-linking involves only POSS nanoparticles inside the hydrophobic domains of the gel, the UV treatment does not produce a permanent gel that could have resulted if both the hydrophobic segment of the copolymer and POSS nanoparticles, were chemically intercorsslinked. To verify the chemical cross-linking, FTIR analysis was carried out; however, no conclusion could be drawn from the data, probably due to the very small content of POSS nanoparticles in the sample and overlap of peaks in the IR regions, where signals, due to −C═C−, could be identified. One could argue that the enhanced rheological performance of the UV treated nanocomposite hydrogel could be contributed by the increased concentration as a result of water evaporation during UV treatment. This argument, however, could be overruled by the fact that UV treatment (Sample 4, Table 2), in absence of the photoinitiator, did not result any noticeable change in storage modulus, G' and yield strength, σ_y as compared with the untreated sample of the same composition (sample 2). This further confirmed the role of chemical cross-linking on the enhancement of the gel stiffness and strength.

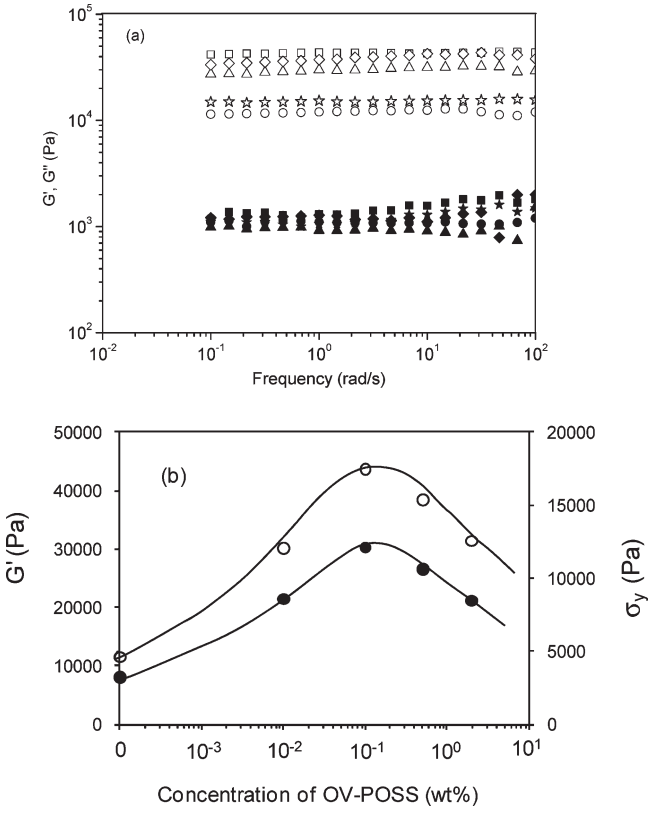


Figure 4. (a) Oscillatory frequency sweep measurements of P(MA-POSS)$_{4.7}$-*b*-PEG$_{10k}$-*b*-P(MA-POSS)$_{4.7}$ triblock copolymer in aqueous solution blended with various amounts of POSS nanoparticles (wt %) (wt % of POSS nanoparticles was calculated using eq 2), i.e.: 0 (circle symbol), 0.01 (triangle symbol), 0.1 (square symbol), 0.5 (diamond symbol), and 2.0 (star symbol). The total copolymer concentration was kept at 11.0 wt %. The storage modulus, G' and loss modulus, G'' are represented by the open and closed symbols, respectively. (b) Storage modulus, G' (open symbol) and yield strength, σ_y (closed symbol) of P(MA-POSS)$_{4.7}$-*b*-PEG$_{10k}$-*b*-P(MA-POSS)$_{4.7}$ as a function of POSS nanoparticles content (wt %) in aqueous solution at fixed copolymer concentration of 11.0 wt %.

Inducing Gelation in PEG$_{5k}$-*b*-P(MA-POSS) Diblock Copolymer Micelle Solutions With the Addition of P(MA-POSS)-*b*-PEG$_{10k}$-*b*-P(MA-POSS) Triblock Copolymer Chains and Rheology. There are various strategies to control gel formation in amphiphilic diblock copolymers, for example, adding hydrophilic homopolymer,[85] block copolymer of a different composition,[86] by inducing attractive interactions between the micelles coronas,[87] and etc.[88] Herein, we investigated the induction of gel formation in PEG$_{5k}$-*b*-P(MA-POSS) micelle solution by adding P(MA-POSS)$_{4.7}$-*b*-PEG$_{10k}$-*b*-P(MA-POSS)$_{4.7}$ triblock copolymer chains, via the formation of intermicellar network-with triblock copolymer chains forming the bridges connecting different micelles. To explore the formation of intermicellar network, DLS experiments were carried out on the mixtures at lower copolymer concentrations, containing various amounts of P(MA-POSS)$_{4.7}$-*b*-PEG$_{10k}$-*b*-P(MA-POSS)$_{4.7}$ and PEG-*b*-P(MA-POSS)$_{3.6}$ and the data are summarized in Figure 5 (relaxation time distribution functions, extracted by analysis of the dynamic correlation functions, $g^{(1)}(\tau)$ using NNLS,[69] at a scattering angle 90°) for a fixed copolymer concentration of 2.0 mg/mL and various compositions. As anticipated, for pure PEG$_{5k}$-*b*-P(MA-POSS)$_{3.6}$, the data depicts a unimodal distribution function, represented by a single peak in Figure 5; corresponding to micellar aggregates of equivalent hydrodynamic radius, $R_h \sim 13.6 \pm 1.0$ nm. However, in the mixture, having 20 wt % of P(MA-POSS)$_{4.7}$-*b*-PEG$_{10k}$-*b*-P(MA-POSS)$_{4.7}$, a broad secondary peak appeared at higher relaxation times. The secondary peak (slow mode) becomes more prominent and well-defined and concurrently the primary peak (fast mode) diminished with increasing triblock copolymer content in solution up to 40 wt %. The decrease in area under the fast mode peak, with increasing triblock copolymer content, is a clear indication that the population of micelles formed by the diblock copolymer chains decreases and the simultaneous increase in area under the slow mode suggests that the micelles have merged

Table 2. Influence of UV Treatment on the Rheological Behavior of P(MA-POSS)$_{4.7}$-*b*-PEG$_{10k}$-*b*-P(MA-POSS)$_{4.7}$ Triblock Copolymer

gel[a]	POSS nanoparticles (wt %)[b]	BP (wt %)	UV irradiation	G' (kPa)[c]	G'' (kPa)[d]	σ_y (kPa)[e]	c_g (wt %)[f]
sample 1	0	0	no	11.5	1.1	3.2	8.2
sample 2	0.1	0	no	43.7	1.3	12.1	7.3
sample 3	0.1	0.1	yes	76.0	5.2	18.2	6.8
sample 4	0.1	0	yes	45.1	1.5	12.5	

[a] Sample 1 is a gel of pure triblock copolymer, while samples 2−4 also have POSS nanoparticles; the concentration of triblock copolymer was 11.0 wt %. [b] Calculated using eq 2. [c] Storage modulus in the linear viscoelastic region. [d] Loss modulus in the linear viscoelastic region. [e] Yield stress, defined as the applied shear stress value at G'/G'' crossover. [f] Gel point determined by plotting the tan δ as a function of triblock polymer concentrations for different angular frequencies.

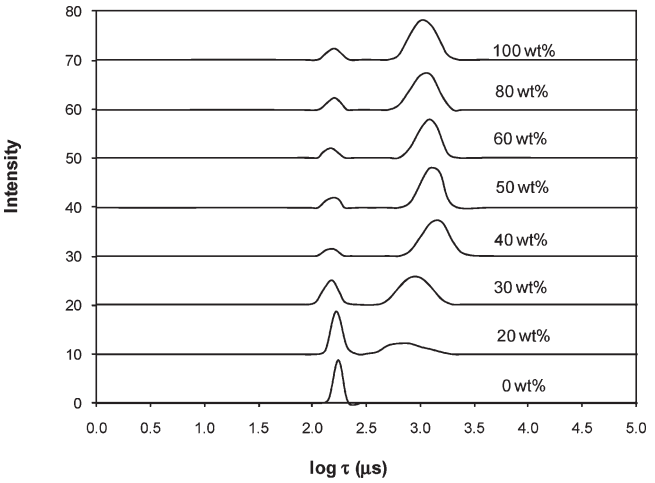


Figure 5. Relaxation time, τ distribution function of the mixture of PEG_{5k}-*b*-P(MA-POSS)$_{3.6}$ and (MA-POSS)$_{4.7}$-*b*-PEG_{10k}-*b*-P(MA-POSS)$_{4.7}$ in aqueous solutions at scattering angle 90° and varying triblock copolymer content (wt %). Total copolymer concentration was maintained at 2 mg/mL. To note that 0 wt % means pure diblock copolymer and 100 wt % represents pure triblock copolymer.

with the larger aggregates (slow mode), wherein, they are interconnected via bridges formed by the triblock copolymer chains. It can be concluded that the introduction of P(MA-POSS)$_{4.7}$-*b*-PEG_{10k}-*b*-P(MA-POSS)$_{4.7}$ does promote the formation of intermicellar networks (slow mode) as a result of bridging via the triblock copolymer chains (Scheme 2). The area under both the peaks, beyond 40 wt % triblock copolymer content in the mixtures, remains constant, where the fast mode could be ascribed to the flower-like micelles, formed by P(MA-POSS)-*b*-PEG_{10k}-*b*-P(MA-POSS) as reported previously.[68] It is worth mentionening here, that the formation of self-assembled structures by ABA type triblock copolymers dissolved in a solvent selective for the B block depends upon two competing forces: the entropy loss due to loop formation of the central block in the micelle corona and the interfacial energy penalty that accompanies the transfer of insoluble block from the micelle corona to solution.[89] It is suggested that in order to compensate for the entropy loss due to the loop formation by the middle A block (PEG block in current systems) in micelle corona, some A/PEG chains may assume an extended conformation having one end dangling in solution, leading to the formation of larger aggregates as a result of intermicellar interactions via the dangling chains ends (see Scheme 2).[68] Therefore, we assume that the slow mode in Figure 5 could be due to complex intermicellar network structures, constituting diblock copolymer micelles interconnected by individual triblock copolymer chains and interconnected flower-like micelles of triblock copolymer and star-like micelles of diblock copolymer via dangling chain ends of the triblock copolymer (see Scheme 2).

The formation of complex intermicellar network could transform the mixture into gel with increasing copolymer concentration. Figure 6 depicts rheological behavior of the obtained hydrogels, where, G' is greater than G'' for the mixtures having P(MA-POSS)$_{4.7}$-*b*-PEG-*b*-P(MA-POSS)$_{4.7}$ content ≥30 wt % over the entire frequency range (see Figure 6a), verifying their gel states. The mixture with 20 wt % triblock copolymer content behaves liquid-like as confirmed by the frequency dependence of both the storage modulus, G' and loss modulus, G'' (Figure 6a). Figure 6b shows storage modulus, G' and yield strength, σ_y of the mixtures as a function of triblock content, revealing an increase in values of both G' and σ_y with increasing triblock copolymer content in the mixture, with a maximum reached at approximately 40 wt %, above which the values

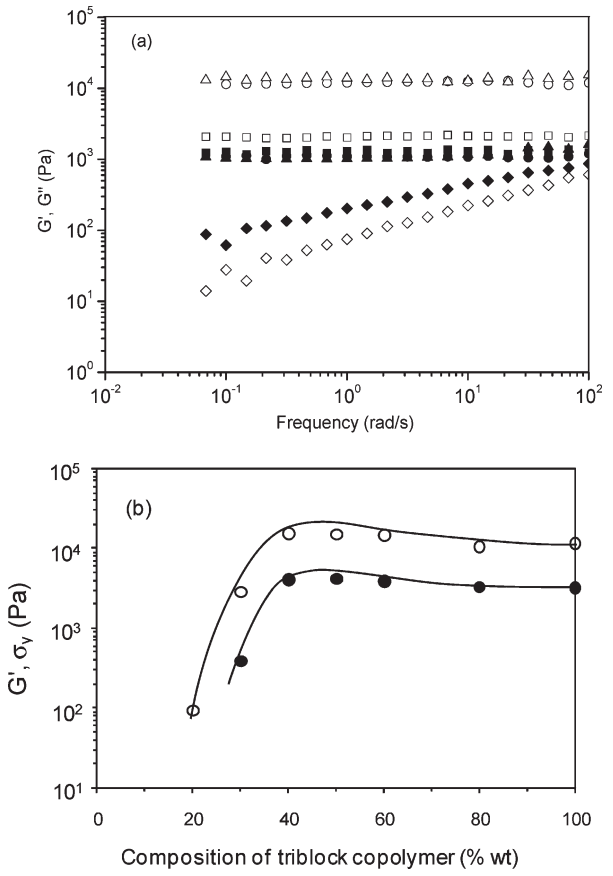


Figure 6. (a) Oscillatory frequency sweep measurements of mixtures of PEG_{5k}-*b*-P(MA-POSS)$_{3.6}$ and P(MA-POSS)$_{4.7}$-*b*-PEG_{10k}-*b*-P(MA-POSS)$_{4.7}$ in aqueous solution of various compositions (wt % of triblock), i.e.; 20 (diamond symbol), 30 (square symbol), 40 (triangle symbol), and 100 (circle symbol). The total copolymer concentration was kept at 11.0 wt %. The storage modulus, G' and loss modulus, G'' are represented by the open and closed symbols, respectively. (b) Storage modulus, G' (open symbol) and yield strength, σ_y (closed symbol) as a function of triblock copolymer content (wt %) in mixture, with total copolymer concentration of 11.0 wt %.

decrease slightly. Quantitatively, the G' (gel stiffness) increases almost 2 orders of magnitude, i.e. from ∼0.1 to ∼15.3 kPa, with increasing triblock copolymer content from 20 to 40 wt %. The data in Figure 6b also show a significant increase in yield strength (gel strength), σ_y from ∼380 to ∼4000 Pa with increasing triblock copolymer content from 30 to 40 wt %, (the solution at 20 wt % triblock copolymer content is liquid-like and the measurement of σ_y is not relevant). Interestingly, the calculated (determined by plotting tan δ as a function of concentrations for different angular frequencies, plots not shown) critical gelation concentration, c_g (∼7.9 wt %) for the mixture with 40 wt % triblock copolymer content, was lower as compared with that of the pure triblock copolymer; c_g ∼ 8.2 wt %. The observed pattern in rheological properties as a function of triblock copolymer content could be correlated to the DLS observations described earlier, where the maximum hydrodynamic size (R_h ∼ 130 nm) of the intermicellar aggregates (slow mode, Figure 5) was calculated at 40 wt % triblock copolymer content in the mixture and shrank slightly at >40 wt %. Thus, the rheological behaviors of the mixtures could be attributed to the size of the formed intermicellar network as a result of bridging of micelles (flower-like and star-like) via the triblock copolymer chains. A schematic presentation of intermicellar network formation in mixture of di- and triblock and pure triblock copolymer is shown in Scheme 2.

Summary

New ways of tailoring micelle formation, gelation, and rheological performance of (PEG-P(MA-POSS) hybrid block copolymers were explored. The addition of hydrophobic POSS nanoparticles to PEG_{5k}-*b*-P(MA-POSS) diblock copolymer solutions was found to have a significant influence on their self-assembly behavior in aqueous solutions and resulted the formation of micelles of larger hydrodynamic sizes and higher aggregation numbers (N_{agg}) with increasing POSS nanoparticles content up to 0.1 wt %. Addition of POSS nanoparticles to P(MA-POSS)-*b*-PEG_{10k}-*b*-P(MA-POSS) triblock copolymer solutions also enhanced rheological performance of the hydrogels with higher storage modulus, G', yield strengths, σ_y, and lower critical gelation concentration, c_g, as compared with the pure triblock copolymers. The presence of eight vinyl groups attached to POSS nanoparticles under investigation lead to further enhancement in rheological properties of the gels with UV treatment. Finally, gelation was induced in micelle solution of PEG_{5k}-*b*-P(MA-POSS) diblock copolymer by introducing P(MA-POSS)-*b*-PEG_{10k}-*b*-P(MA-POSS) triblock copolymer chains. The rheological performance, even superior to that of pure triblock copolymer gel, was achieved with 40 wt % content of (MA-POSS)-*b*-PEG_{10k}-*b*-P(MA-POSS) in the mixture. The reported results could provide new tool to custom design systems with desired rheological behavior by controlling the composition of gel with the choice of di-triblock copolymers and POSS nanoparticles. Furthermore, the research illustrates strong hydrophobicity of POSS block and its ability to self-assemble into micelles and of gel formation at relatively lower block copolymer concentrations. This could open up new avenues for functional POSS polymers in cosmetic and drug delivery applications.

Acknowledgment. The authors gratefully acknowledge financial support from the Institute of Materials Research and Engineering (IMRE) under the Agency for Science, Technology, and Research (A*STAR).

References and Notes

(1) Cassagneau, T.; Caruso, F. *J. Am. Chem. Soc.* **2002**, *124*, 8172–8180.
(2) Choi, J. W.; Tamaki, R.; Kim, S. G.; Laine, R. M. *Chem. Mater.* **2003**, *15*, 3365–3375.
(3) Roll, M. F.; Asuncion, M. Z.; Kampf, J.; Laine, R. M. *ACS Nano* **2008**, *2*, 320–326.
(4) Sulaiman, S.; Bhaskar, A.; Zhang, J.; Guda, R.; Goodson, T.; Laine, R. M. *Chem. Mater.* **2008**, *20*, 5563–5573.
(5) Zhang, L.; Abbenhuis, H. C. L.; Yang, Q. H.; Wang, Y. M.; Magusin, P. C. M. M.; Mezari, B.; van Santen, R. A.; Li, C. *Angew. Chem., Int. Ed.* **2007**, *46*, 5003–5006.
(6) Laine, R. M. *J. Mater. Chem.* **2005**, *15*, 3725–3744.
(7) Xu, H. Y.; Yang, B. H.; Wang, J. F.; Guang, S. Y.; Li, C. *J. Polym. Sci., Part A: Polym. Chem.* **2007**, *45*, 5308–5317.
(8) Yang, B. H.; Xu, H. Y.; Wang, J. F.; Gang, S. Y.; Li, C. *J. Appl. Polym. Sci.* **2007**, *106*, 320–326.
(9) Liu, Y. L.; Tseng, M. C.; Fangchiang, M. H. *J. Polym. Sci., Part A: Polym. Chem.* **2008**, *46*, 5157–5166.
(10) Leu, C. M.; Chang, Y. T.; Wei, K. H. *Chem. Mater.* **2003**, *15*, 3721–3727.
(11) Chen, Y. W.; Kang, E. T. *Mater. Lett.* **2004**, *58*, 3716–3719.
(12) Mya, K. Y.; Wang, Y. X.; Shen, L.; Xu, J. W.; Wu, Y. L.; Lu, X. H.; He, C. B. *J. Polym. Sci., Part A: Polym. Chem.* **2009**, *47*, 4602–4616.
(13) Choi, J.; Harcup, J.; Yee, A. F.; Zhu, Q.; Laine, R. M. *J. Am. Chem. Soc.* **2001**, *123*, 11420–11430.
(14) Wu, F. M.; Xie, T. X.; Yang, G. S. *J. Polym. Sci., Part B: Polym. Phys.* **2010**, *48*, 1853–1859.
(15) Gnanasekaran, D.; Madhavan, K.; Reddy, B. S. R. *J. Sci. Ind. Res.* **2009**, *68*, 437–464.
(16) Cordes, D. B.; Lickiss, P. D.; Rataboul, F. *Chem. Rev.* **2010**, *110*, 2081–2173.
(17) Lewicki, J. P.; Pielichowski, K.; De la Croix, P. T.; Janowski, B.; Todd, D.; Liggat, J. J. *Polym. Degrad. Stab.* **2010**, *95*, 1099–1105.
(18) Strachota, A.; Kroutilova, I.; Kovarova, J.; Matejka, L. *Macromolecules* **2004**, *37*, 9457–9464.
(19) Xu, H. Y.; Yang, B. H.; Wang, J. F.; Guang, S. Y.; Li, C. *J. Polym. Sci., Part A: Polym. Chem.* **2007**, *45*, 5308–5317.
(20) Liang, K. W.; Li, G. Z.; Toghiani, H.; Koo, J. H.; Pittman, C. U. *Chem. Mater.* **2006**, *18*, 301–312.
(21) Liu, Y.; Shi, Z.; Xu, H.; Fang, J.; Ma, X.; Yin, J. *Macromolecules* **2010**, *43*, 6731–6738.
(22) Constable, G. S.; Lesser, A. J.; Coughlin, E. B. *Macromolecules* **2004**, *37*, 1276–1282.
(23) Liu, H.; Zheng, S.; Nie, K. *Macromolecules* **2005**, *38*, 5088–5097.
(24) Liu, Y. L.; Tseng, M. C.; Fangchiang, M. H. *J. Polym. Sci., Part A: Polym. Chem.* **2008**, *46*, 5157–5166.
(25) Xi, K.; He, H.; Xu, D.; Ge, R. J.; Meng, Z.; Jia, X. D.; Yu, X. H. *Thin Solid Films* **2010**, *518*, 4768–4772.
(26) Wahab, M. A.; Mya, K. Y.; He, C. B. *J. Polym. Sci., Part A: Polym. Chem.* **2008**, *46*, 5887–5896.
(27) Zeng, K.; Wang, L.; Zheng, S. X.; Qian, X. F. *Polymer* **2009**, *50*, 685–695.
(28) Su, X.; Guang, S.; Li, C.; Xu, H.; Liu, X.; Wang, X.; Song, Y. *Macromolecules* **2010**, *43*, 2840–2845.
(29) Monticelli, O.; Fina, A.; Ullah, A.; Waghmare, P. *Macromolecules* **2009**, *42*, 6614–6623.
(30) Chou, C. H.; Hsu, S. L.; Dinakaran, K.; Chiu, M. Y.; Wei, K. H. *Macromolecules* **2005**, *38*, 745–751.
(31) Kang, J. M.; Cho, H. J.; Lee, J.; Lee, J. I.; Lee, S. K.; Cho, N. S.; Hwang, D. H.; Shim, H. K. *Macromolecules* **2006**, *39*, 4999–5008.
(32) Lee, A.; Xiao, J.; Feher, F. J. *Macromolecules* **2004**, *38*, 438–444.
(33) Hottle, J. R.; Deng, J.; Kim, H. J.; Farmer-Creely, C. E.; Viers, B. D.; Esker, A. R. *Langmuir* **2005**, *21*, 2250–2259.
(34) Knight, P. T.; Lee, K. M.; Qin, H.; Mather, P. T. *Biomacromolecules* **2008**, *9*, 2458–2467.
(35) Kotal, A.; Si, S.; Paira, T. K.; Mandal, T. K. *J. Polym. Sci., Part A: Polym. Chem.* **2008**, *46*, 1111–1123.
(36) Amir, N.; Levina, A.; Silverstein, M. S. *J. Polym. Sci., Part A: Polym. Chem.* **2007**, *45*, 4264–4275.
(37) Nie, W. Y.; Li, G.; Li, Y.; Xu, H. Y. *Chin. Chem. Lett.* **2009**, *20*, 738–742.
(38) Zhou, Z.; Cui, L. M.; Zhang, Y.; Zhang, Y. X.; Yin, N. A. W. *Eur. Polym. J.* **2008**, *44*, 3057–3066.
(39) Liu, L.; Wang, W. P. *Polym. Bull.* **2009**, *62*, 315–325.
(40) Zhang, W. A.; Zhuang, X. D.; Li, X. H.; Lin, Y.; Bai, J. R.; Chen, Y. *React. Funct. Polym.* **2009**, *69*, 124–129.
(41) Pyun, J.; Xia, J. H.; Matyjaszewski, K. *Organic-inorganic hybrid materials from polysiloxanes and polysilsesquioxanes using controlled/living radical polymerization*; Clarson, S. J.; Fitzgerald, J. J.; Owen, M. J.; Smith, D.; Van Dyke, M. E., Eds.; ACS Symposium Series 838; American Chemical Society: Washington, DC, 2003.
(42) Mya, K. Y.; Lin, E. M. J.; Gudipati, C. S.; Shen, L.; He, C. *J. Phys. Chem. B* **2010**, *114*, 9119–9127.
(43) Zhang, W. A.; Muller, A. H. E. *Polymer* **2010**, *51*, 2133–2139.
(44) Ge, Z.; Wang, D.; Zhou, Y.; Liu, H.; Liu, S. *Macromolecules* **2009**, *42*, 2903–2910.
(45) Zhang, W.; Muêller, A. H. E. *Macromolecules* **2010**, *43*, 3148–3152.
(46) Hussain, H.; Mya, K. Y.; Xiao, Y.; He, C. B. *J. Polym. Sci., Part A: Polym. Chem.* **2008**, *46*, 766–776.
(47) Hussain, H.; Tan, B. H.; Gudipati, C. S.; Xaio, Y.; Liu, Y.; Davis, T. P.; He, C. B. *J. Polym. Sci., Part A: Polym. Chem.* **2008**, *46*, 7287–7298.
(48) Lu, C. H.; Wang, J. H.; Chang, F. C.; Kuo, S. W. *Macromol. Chem. Phys.* **2010**, *211*, 1339–1347.
(49) Ohno, K.; Sugiyama, S.; Koh, K.; Tsujii, Y.; Fukuda, T.; Yamahiro, M.; Oikawa, H.; Yamamoto, Y.; Ootake, N.; Watanabe, K. *Macromolecules* **2004**, *37*, 8517–8522.
(50) Ni, C.; Wu, G.; Zhu, C.; Yao, B. *J. Phys. Chem. C* **2010**, *114*, 13471–13476.
(51) Jin, S.; Hirai, T.; Ahn, B.; Rho, Y.; Kim, K. W.; Kakimoto, M. a.; Gopalan, P.; Hayakawa, T.; Ree, M. *J. Phys. Chem. B* **2010**, *114*, 8033–8042.
(52) Hussain, H.; Tan, B. H.; Mya, K. Y.; Liu, Y.; He, C. B.; Davis, T. P. *J. Polym. Sci., Part A: Polym. Chem.* **2010**, *48*, 152–163.
(53) Pyun, J.; Matyjaszewski, K.; Wu, J.; Kim, G. M.; Chun, S. B.; Mather, P. T. *Polymer* **2003**, *44*, 2739–2750.
(54) Miao, J.; Cui, L.; Lau, H. P.; Mather, P. T.; Zhu, L. *Macromolecules* **2007**, *40*, 5460–5470.

(55) Hirai, T.; Leolukman, M.; Jin, S.; Goseki, R.; Ishida, Y.; Kakimoto, M. A.; Hayakawa, T.; Ree, M.; Gopalan, P. *Macromolecules* **2009**, *42*, 8835–8843.
(56) Hirai, T.; Leolukman, M.; Hayakawa, T.; Kakimoto, M.; Gopalan, P. *Macromolecules* **2008**, *41*, 4558–4560.
(57) Escude, N. C.; Chen, E. Y. X. *Chem. Mater.* **2009**, *21*, 5743–5753.
(58) Kim, B. S.; Mather, P. T. *Macromolecules* **2002**, *35*, 8378–8384.
(59) Kim, B. S.; Mather, P. T. *Polymer* **2006**, *47*, 6202–6207.
(60) Kim, B. S.; Mather, P. T. *Macromolecules* **2006**, *39*, 9253–9260.
(61) Lee, W.; Ni, S. L.; Deng, J. J.; Kim, B. S.; Satija, S. K.; Mather, P. T.; Esker, A. R. *Macromolecules* **2007**, *40*, 682–688.
(62) Zeng, K.; Wang, L.; Zheng, S. *J. Phys. Chem. B* **2009**, *113*, 11831–11840.
(63) Markovic, E.; Ginic-Markovic, M.; Clarke, S.; Matisons, J.; Hussain, M.; Simon, G. P. *Macromolecules* **2007**, *40*, 2694–2701.
(64) Markovic, E.; Matisons, J.; Hussain, M.; Simon, G. P. *Macromolecules* **2007**, *40*, 4530–4534.
(65) Mya, K. Y.; Li, X.; Chen, L.; Ni, X.; Li, J.; He, C. *J. Phys. Chem. B* **2005**, *109*, 9455–9462.
(66) Zhang, W. A.; Liu, L.; Zhuang, X. D.; Li, X. H.; Bai, J. R.; Chen, Y. *J. Polym. Sci., Part A: Polym. Chem.* **2008**, *46*, 7049–7061.
(67) Zhang, W.; Fang, B.; Walther, A.; Muêller, A. H. E. *Macromolecules* **2009**, *42*, 2563–2569.
(68) Hussain, H.; Tan, B. H.; Seah, G. L.; Liu, Y.; He, C. B.; Davis, T. P. *Langmuir* **2010**, *26*, 11763–11773.
(69) Lawson, C. L.; Hanson, R. J. *Solving Least Squares Problems*; Prentice-Hall: Englewood Cliffs, NJ, 1974.
(70) Štìpánek, P. Data analysis in dynamic light scattering. In *Dynamic Light Scattering-The Method and Some Applications*; Brown, D., Ed.; Clarendon Press: Oxford, U.K., 1993; pp 177−241.
(71) Chu, B. *Laser Light Scattering: Basic Principles and Practice*, 2nd ed.; Academic Press: New York. 1991.
(72) Zimm, B. H. *J. Chem. Phys.* **1948**, *16*, 1099–1116.
(73) Zimm, B. H. *J. Chem. Phys.* **1948**, *16*, 1093–1099.
(74) Hussain, H.; Tan, B. H.; Gudipati, C. S.; He, C. B.; Liu, Y.; Davis, T. P. *Langmuir* **2009**, *25*, 5557–5564.
(75) Tan, B. H.; Gudipati, C. S.; Hussain, H.; He, C. B.; Liu, Y.; Davis, T. P. *Macromol. Rapid Commun.* **2009**, *30*, 1002–1008.
(76) Booth, C.; Attwood, D. *Macromol. Rapid Commun.* **2000**, *21*, 501–527.
(77) Riess, G. *Prog. Polym. Sci.* **2003**, *28*, 1107–1170.
(78) Zamurovic, M.; Christodoulou, S.; Vazaios, A.; Iatrou, E.; Pitsikalis, M.; Hadjichristidis, N. *Macromolecules* **2007**, *40*, 5835–5849.
(79) Burchard, W. Combined static and dynamic light scattering. In *Light Scatttering-Principles and Development*; Brown, W., Ed.; Clarendon Press: Oxford, U.K., 1996; pp 439−476.
(80) Wu, P. Q.; Siddiq, M.; Chen, H. Y.; Di, Q.; Wu, C. *Macromolecules* **1996**, *29*, 277–281.
(81) Tu, Y. F.; Wan, X. H.; Zhang, D.; Zhou, Q. F.; Wu, C. *J. Am. Chem. Soc.* **2000**, *122*, 10201–10205.
(82) Pek, Y. S.; Wan, A. C. A.; Shekaran, A.; Zhuo, L.; Ying, J. Y. *Nature Nanotechnol.* **2008**, *3*, 671–675.
(83) Jeong, B.; Bae, Y. H.; Lee, D. S.; Kim, S. W. *Nature* **1997**, *388*, 860–862.
(84) Jeong, B.; Bae, Y. H.; Kim, S. W. *J. Controlled Release* **2000**, *63*, 155–163.
(85) Renou, F.; Benyahia, L.; Nicolai, T. *Macromolecules* **2007**, *40*, 4626–4634.
(86) Renou, F.; Nicolai, T.; Nicol, E.; Benyahia, L. *Langmuir* **2008**, *25*, 515–521.
(87) Tang, T.; Castelletto, V.; Parras, P.; Hamley, I. W.; King, S. M.; Roy, D.; Perrier, S.; Hoogenboom, R.; Schubert, U. S. *Macromol. Chem. Phys.* **2006**, *207*, 1718–1726.
(88) Chassenieux, C.; Nicolai, T.; Benyahia, L. *Curr. Opin. Colloid Interface Sci.* **2010**, DOI org/10.1016/j.cocis.2010.07.007.
(89) Chu, B.; Zhou, Z. Physical Chemistry of Polyoxyalkylene Block Copolymer Surfactants. In *Nonionic Surfactants*; Nace, V. M., Ed.; Marcel Dekker Inc.: New York, 1996; Volume *60*, pp 67−144.

632 *Macromolecules* **2011**, *44*, 632–639
DOI: 10.1021/ma102337c

Macromolecules
ARTICLE

Synthesis of Magnetic Spherical Polyelectrolyte Brushes

Kaimin Chen,[†] Yan Zhu,[†] Yifei Zhang,[†] Li Li,[†] Yan Lu,[‡] and Xuhong Guo*,[†]

[†]*State Key Laboratory of Chemical Engineering, School of Chemical Engineering, East China University of Science and Technology, Shanghai 200237, China, and* [‡]*German Soft Matter and Functional Materials, Helmholtz-Zentrum Berlin für Materialien und Energie GmbH, Berlin 14109, Germany*

Received October 13, 2010; Revised Manuscript Received December 27, 2010

ABSTRACT: Magnetic spherical polyelectrolyte brushes (MSPB) with embedded magnetite nanoparticles in core were successfully synthesized and characterized by dynamic light scattering (DLS), a scanning electron microscope (SEM), a high resolution transmission electron microscope (HRTEM), thermal gravimetric analysis (TGA), X-ray diffraction (XRD), and a vibrating sample magnetometer (VSM). At first, oleic acid modified magnetite nanoparticles (MNP) were synthesized by the coprecipitation method and then embedded into the polystyrene core by miniemulsion polymerization to obtain magnetic polystyrene latices (MPL). Finally, magnetic spherical poly(acrylic acid) (PAA) brushes were synthesized by photoemulsion polymerization. Effects of MNP and acrylic acid (AA) content on the brush structure were studied in detail. The obtained MSPB are narrowly dispersed, pH sensitive, superparamagnetic, and redispersible after aggregating by external magnetic field. Magnetic control is thus introduced into nanosized spherical polyelectrolyte brushes to achieve the recovery and controllable delivery. This approach opens a new way for the recoverable and cost-effective applications of spherical polyelectrolyte brushes.

Introduction

The area of polyelectrolyte brushes is one of the most active research fields in polymer science.[1] Spherical polyelectrolyte brushes (SPB), serving as a simple model between star polyelectrolyte[2] and planar polyelectrolyte brushes,[3,4] are extremely useful in both fundamental science and industrial applications.[5] As smart nanoparticles, SPB have been used for adsorption of proteins,[6,7] ideal carrier for high-efficiency catalyst,[8,9] and synthesis of metal nanoparticles.[10,11] The nanosized SPB are very stable in water due to the steric protection and the electrostatic repulsion of polyelectrolyte brush layer, while their recycle after application becomes quite difficult. Therefore, it is highly desirable for the applications of SPB to possess a tunable stability and mobility that can be conveniently controlled by external stimuli such as magnetic field.

Recently, magnetic nanoparticles (MNP), especially magnetite nanoparticles, attract a growing interest.[12−18] Compared with their bulk counterparts, the main advantages of MNP lie in high specific surface areas, low sedimentation rate, reduced magnetic dipole−dipole interactions, which pronounce a promising future in drug or gene delivery,[19] magnetic resonance imaging[20] and hyperthermia.[21] To avoid the aggregation of MNP, their surfaces are normally modified by polymers[22−31] or inorganic materials[32−34] to obtain necessary stability for applications.

Among methods to modify MNP surface, polymers can be covered onto a single MNP by physical absorption[35] or in situ polymerizations such as surface-initiated atom transfer radical polymerization (ATRP).[36−39] MNP also can be embedded into polymer matrices by in situ polymerization[40−43] or encapsulated by polyorganosiloxane by polycondensation reaction[44,45] to form magnetic composite particles with controllable size and magnetite content. However, to the best of our knowledge, it is still a challenge to control the surface structure of polymers and the size distribution of particles.

*To whom correspondence should be addressed. Telephone: +86 21 6425 3491. Fax: +86 21 6425 3491. E-mail: guoxuhong@ecust.edu.cn.

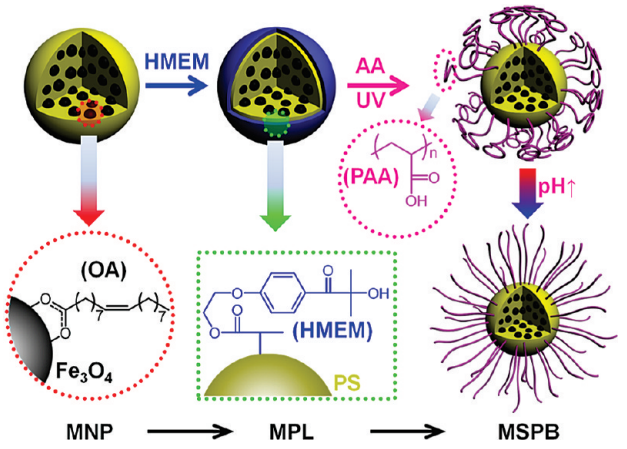
In this work, we demonstrate a novel approach to prepare narrowly dispersed polymer/magnetite nanocomposite particles with well-controlled surface and particle size. These magnetic spherical polyelectrolyte brushes (MSPB) consist of a polystyrene (PS) core around 100 nm in diameter embedded with magnetite nanoparticles and a well-defined shell of poly(acrylic acid) (PAA) brush (Scheme 1). The magnetic properties, the brush thickness and the grafting density of PAA chains on the core surface are tunable by controlling the dose of MNP, acrylic acid (AA) and the photoinitiator 2[*p*-(2-hydroxy-2-methylpropiophenone)]−ethylene glycol−methacrylate (HMEM), respectively (Scheme 1). Magnetic polystyrene latices (MPL) are synthesized via miniemulsion polymerization and MSPB by photoemulsion polymerization. The introduction of surface modified MNP into SPB core makes it possible to recycle SPB magnetically and redisperse after removing external magnetic field.

Experimental Section

1. Materials. Ferric chloride hexahydrate ($FeCl_3 \cdot 6H_2O$), ferrous sulfate heptahydrate ($FeSO_4 \cdot 7H_2O$) and anhydrous ethyl alcohol were purchased from Sinopharm Chemical Reagent Co., Ltd. Oleic acid (OA), sodium dodecyl sulfate (SDS), *n*-octane, acetone, ammonium hydroxide (25 wt %), hydrochloride acid (36 wt %), potassium persulfate (KPS) and pyridine were bought from Lingfeng Chemical Reagent Co., Ltd. Hexadecane (99%) was purchased from Acros Organics and methacryloyl chloride (MC) from Technical Choices, Inc. The 2-hydroxy-4′-hydroxyethoxy-2-methylpropiophenone (HMP) (Irgacure 2959) was kindly donated by Ciba Specialty Chemicals Inc. All these chemicals were used without further purification. The 2,2′-azo-bis-iso-butyronitrile (AIBN) (from Shanghai No.4 Reagent & H.V. Chemical Company) was recrystallized in methanol before use. Styrene and acrylic acid (AA) (from Shanghai Lingfeng Chemical Regent Co., Ltd.) were distilled under reduced pressure and stored in refrigerator at 4 °C before use. The water used in all experiments was purified by reverse osmosis (Shanghai RO Micro Q).

 Published on Web 01/12/2011 © 2011 American Chemical Society

Scheme 1. Schematic Illustration of the Synthesis of MSPB



2. Preparation of Magnetite Nanoparticles (MNP). Magnetic nanoparticles were synthesized by coprecipitation method in the presence of oleic acid (OA). In a typical run, 48.60 g of $FeCl_3 \cdot 6H_2O$ and 33.36 g of $FeSO_4 \cdot 7H_2O$ with a molar ratio of 3:2 were dissolved in water and heated to 90 °C under vigorous stirring. 23.2 g of OA was dissolved in 25 mL of acetone and added to the reaction system followed by 120 mL of ammonia solution. After 2 h, the sediment was neutralized by 1 N hydrochloride acid. Then anhydrous ethyl alcohol was introduced to get rid of the residual OA. Finally the byproduct ammonium chloride was eluted by water from the black sediment. A black product was collected with the help of a magnet and dried in lyophilizer for 24 h. Dried MNP were stored at room temperature or dispersed in *n*-octane with a concentration of 62.5 wt % to form a magnetic fluid for further use.

3. Synthesis of Magnetic Polystyrene Latices (MPL). Magnetic polystyrene latices were synthesized by miniemulsion polymerization. In the case of using AIBN as initiator, 0.10 g of hexadecane, 0.075 g of AIBN and 2.50 g of styrene were mixed with a certain amount of MNP followed by ultrasonication for 15 min in an ice bath. The ultrasonication device is Model SK7210LHC from KUDOS Co. with the highest frequency of 53 kHz and power of 350 W. The obtained oil phase was added into 200 mL of SDS solution (0.1 wt %) followed by miniemulsification for 60 min in an ice bath. Miniemulsion polymerization was then started at 65 °C and performed for 20 h under stirring of 300 rpm. At the end of the miniemulsion polymerization, 4.5 g of acetone solution with 0.5 g of photoinitiator HMEM synthesized in our laboratory[46] was added in 30 min under "starved condition". MPL with a thin layer of HMEM were thus obtained after further 2.5 h reaction.

In the case of using KPS as initiator, the required amount of MNP magnetic fluid was added to SDS solution and mixed by ultrasonication for 60 min in an ice bath to form MNP clusters. Then, 2.50 g of styrene and 0.10 g of hexadecane (as costabilizer) was added followed by another 60 min ultrasonication. Miniemulsion polymerization was then performed after adding 0.05 g of KPS at 80 °C for 20 h under stirring of 300 rpm. HMEM was introduced with the same procedure as described above.

4. Synthesis of Magnetic Spherical Polyelectrolyte Brushes (MSPB). MPL were charged into a homemade UV-reactor (range of wavelengths: 200−600 nm, power: 150 W), and diluted to 0.5 wt % with water until the total weight reached 500 g. A defined amount of acrylic acid (AA) was added. The whole reactor was degassed by repeated evacuation and subsequent addition of nitrogen at least three times. Photoemulsion polymerization was accomplished with UV radiation at room temperature with vigorous stirring in 2.5 h. The obtained MSPB emulsion was purified exhaustively by dialysis against water until the conductance of the eluate did not change anymore.

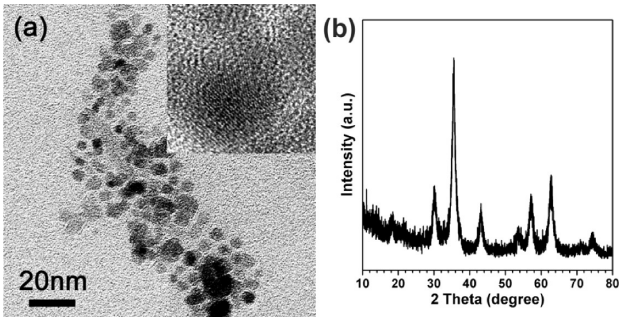


Figure 1. Characterization of MNP: (a) TEM image, where the inset shows the HRTEM image of a single MNP; (b) XRD spectrum of MNP.

5. Characterization. Dynamic light scattering (DLS) was used to determine the apparent hydrodynamic size of particles and performed by a particle sizing system of NICOMP 380 ZLS at a fixed scattering angle of 90°. Without extrapolation to zero scattering angle, the apparent hydrodynamic radius obtained by DLS at 90° should be smaller than the true one. X-ray diffraction (XRD) were carried out on a Bruker D8 Advance X-ray diffractometer with a scan rate of 6° /min. Thermal gravimetric analysis (TGA) WRT-2P was employed to determine the magnetite content in particles. The high resolution transmission electron microscopy (HRTEM) was performed using a JEOL-2100F electron microscope operating at 200 kV. Samples were magnetically separated before TEM observation. The magnetic properties of samples were characterized by vibrating sample magnetometer (VSM) of Lakeshore 7407 at room temperature. Turbidity was monitored with a Brinkman PC 950 colorimeter equipped with a 2 cm path length optical probe.

Results and Discussion

1. Magnetic Property. *1.1. Magnetite Nanoparticles.* Magnetite nanoparticles modified by OA (MNP) were synthesized by coprecipitation route.[15,47−54] As shown in Figure 1a, the obtained MNP are around 10 nm. The crystal lattice can be clearly seen in the HRTEM image of a single MNP while the surface becomes fuzzy due to the small-size effect of nanoparticles.[55] The crystal structure of MNP was also confirmed by XRD (Figure 1b). The six characteristic peaks of magnetite at 30.2° (220), 35.5° (311), 43.2° (400), 53.6° (422), 57.2° (511), and 62.8° (440) can be determined, and the calculated diameter from XRD patterns by Scherrer's formula[56] is 9.5 nm, which is consistent with the size observed in TEM image. OA was adsorbed on MNP surface via coordination interaction between carboxylate group in oleic acid and iron atom.[54] OA content was ca. 25 wt % as determined by TGA.

1.2. MNP in MSPB. In the first instance, we used the conventional emulsion polymerization to embed MNP into polystyrene core. However, the magnetite content in obtained yellowish MPL was below 2 wt % as determined by TGA, which was not sufficient for magnetic separation. The similar results were reported in literatures.[57,58] Therefore, we turned to employ miniemulsion polymerization method[22,24,26,28,59,60] to introduce more MNP into polystyrene core. Followed this strategy, MPL with narrow size distribution were synthesized. Poly(acrylic acid) (PAA) brushes were then grown from the surface of MPL via photoemulsion polymerization technique.

Figure 2 shows the HRTEM images of prepared MSPB encapsulating MNP in PS core. Obviously, MNP are successfully embedded in MSPB and mainly locate inside the core. The MSPB show narrow size distribution and well-defined

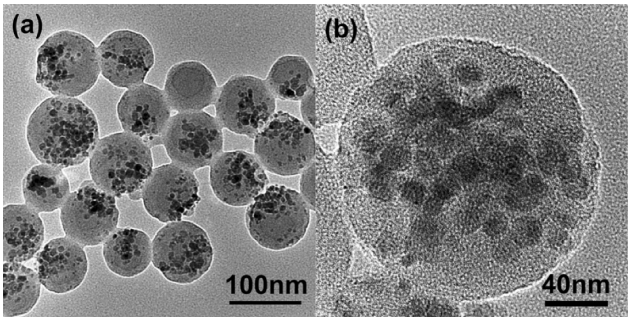


Figure 2. TEM images of as-synthesized MSPB. Their magnetite content is 10.9 wt % determined by TGA.

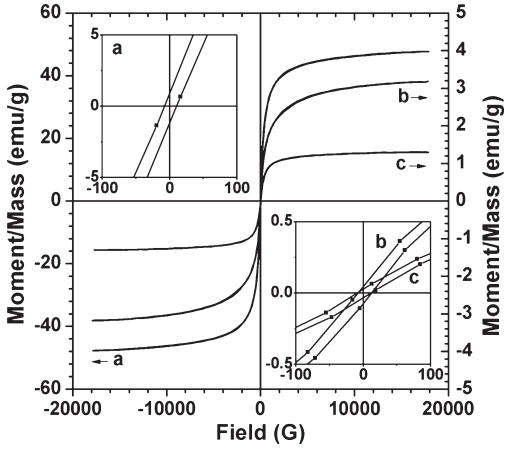


Figure 3. Magnetization curves at room temperature of MNP (a), MPL (b), and MSPB (c). The sample has a magnetite content of 5 wt %. Insets are corresponding magnetization curves at low magnetic field to show residual magnetization and coercive force.

structure although the PAA brush shell can hardly be observed in dry state.

1.3. Hysteresis Loops. Vibrating sample magnetometer (VSM) was employed to compare the magnetic property of synthesized MNP, MPL, and MSPB. As shown in Figure 3, the saturation magnetization value of MNP was 47.7 emu/g at room temperature. Their remanence and coercive force were very small and could be at the range of superparamagnetism.[16,61] The small remanence may come from few relatively large magnetite nanoparticles prepared by coprecipitation method, which should bring limited effect on the overall magnetic properties of MPL and MSPB. After embedding MNP into PS core, the saturation magnetizations of MPL and MSPB reduced to 3.18 and 1.30 emu/g, respectively. Their remanences, calculated from residual magnetization divided by saturation magnetization, were as small as MNP (around 0.02, see Figure 3). The coercive forces of MPL and MSPB were 10.0 and 10.7 Oe, respectively, which should be also within the superparamagnetism range.[62] The saturation magnetization of MNP encapsulated in MSPB is reduced to 26 emu/g of magnetite. The loss of magnetization is probably due to the polymer encapsulation[63] or partial oxidation forming nonmagnetic iron oxide such as α-Fe_2O_3 during the ultrasonication.[23] Therefore, the synthesized MPL and MSPB were still superparamagnetic although their saturation magnetizations were much lower than that of MNP.

2. Brush Structure and Property. *2.1. Ultrasonication and Core Size.* The droplet size before miniemulsion polymerization has strong impact on brush core size. Long time of

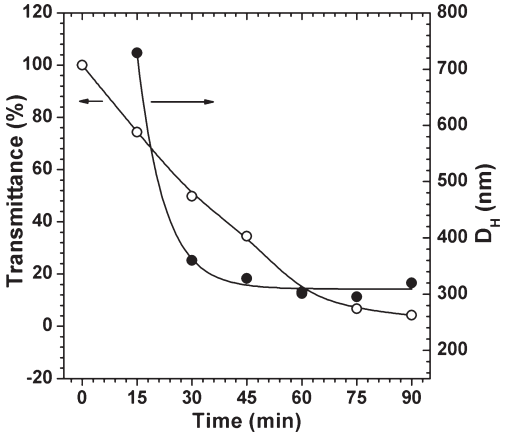


Figure 4. Transmittance (○) and D_H (●) as a function of ultrasonication time during miniemulsification.

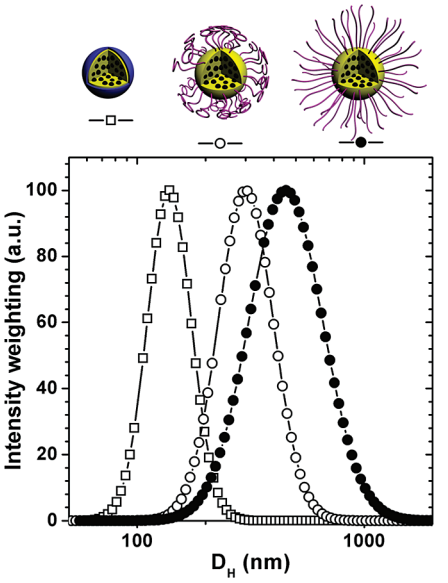


Figure 5. Size and size distribution of MPL (□), MSPB at pH 4 (○) and pH 9 (●) as determined by DLS. The magnetite content of MSPB is 3.9 wt %.

ultrasonication with high power and frequency is favorable to form homogeneous emulsion with small size.[23,64] In our experiments, 53 kHz and 350 W were chosen as the ultrasonication parameters by employing an ultrasonicator SK7210LHC from KUDOS Co. Both the transmittance and apparent hydrodynamic diameter (D_H) of droplets during miniemulsification were monitored by colorimeter and DLS, respectively (Figure 4).

Upon increasing the ultrasonication time, the transmittance decreased gradually and reached a plateau after ca. 60 min, while D_H of droplets decreased dramatically in 30 min followed by a plateau (Figure 4). These results implied that large droplets were broken early and fast in the first 30 min since they had more contribution to the scattering intensity during DLS measurements while the average size of droplets reduced gradually. During ultrasonication, an ice bath was applied to control the temperature in order to obtain MPL with narrow size distribution. The optimal ultrasonication time was 60 min (Figure 4).

2.2. Growing of PAA Brush. The growing of PAA brushes can be monitored from the size change by DLS. The size and size distribution of MSPB with PAA shell are shown in

Table 1. Brush Thickness and Magnetite Content

MSPB	AA[a] (wt %)	L[b] (nm)	PDI[c]	MC[d] (wt %)
A-0	0	0	0.040	6.8
A-1	25	8	0.044	5.0
A-2	50	37	0.010	4.9
A-3	75	110	0.112	4.7
A-4	100	155	0.140	3.9

[a] AA: Content of AA compared with MPL by weight. [b] L: Brush layer thickness of MSPB determined by DLS at pH 9.0. [c] PDI: Polydispersity index of MSPB determined by DLS. [d] MC: Magnetite content in MSPB determined by TGA.

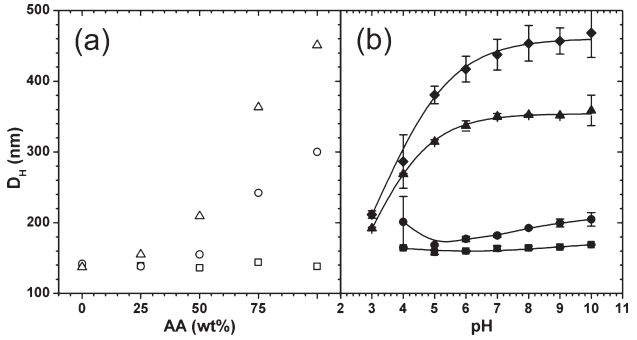


Figure 6. (a) Effect of AA content on size of MSPB. Key: (□) MPL, (○) MSPB at pH 4; (△) MSPB at pH 9. (b) Size of MSPB as a function of pH. Key: (■) 25 wt % AA; (●) 50 wt % AA; (▲) 75 wt % AA; (♦) 100 wt % AA. Lines are to guide the eye.

Figure 5. The D_H of MPL was around 140 nm which was much smaller than droplets before miniemulsion polymerization (Figure 4). This observation is consistent with that of other authors[65] whose explanation is that DLS gave a "wrong size" to nonsolid styrene droplets containing MNP. After grafting of PAA through photoemulsion polymerization, D_H of MSPB increased to 300 nm at pH 4.0 and 450 nm at pH 9.0. PAA grafted MSPB expanded at high pH due to the dissociation of carboxyl groups in PAA and thus the electrostatic repulsion between adjacent PAA chains. The size distribution of MSPB fitted by Gaussian distribution is of a polydispersity index of 0.14 as determined by DLS which is higher than that of MPL. The increase in polydispersity of MSPB may come from the possible agglomerates, especially at high pH when all the PAA are fully extended.

2.3. Brush Thickness and pH Sensitivity. The thickness of SPB brush is tunable by the dose of monomer AA.[46] When MNP were introduced inside SPB, the effect of AA dose on MSPB thickness is shown in Table 1. The size of MPL core is around 140 nm with a polydispersity index of 0.04. Upon increasing the AA dose, the thickness of MSPB increased monotonically while the relative content of magnetite decreased (Table 1). If AA amount is over 100 wt %, MSPB become unstable with a broad size distribution due to the possible cross-linking among them.[46]

Figure 6 displayed the effect of AA content and pH value on the diameter (D_H) of MSPB. Like other PAA SPB without MNP inside the core, MSPB are sensitive to both pH value and ionic strength.[46,66,67] 1 mL of 0.5 wt % MSPB was diluted 100 times by adding into 99 mL of 10 mM NaCl solution. For all the samples, pH decreased from 10.0 by adding 10 mM HCl while the ionic strength kept 10 mM adjusted by NaCl. The size increase of MSPB with pH is due to the increase of the electrostatic repulsion among PAA chains in MSPB. As shown in Figure 6, MSPB with low AA dose are unstable at low pH (pH ≤ 4) because of the inadequate steric protection and reduced electrostatic repulsion.

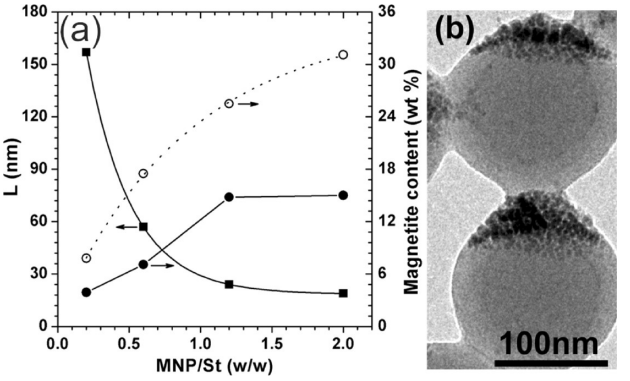


Figure 7. (a) Effect of MNP dose ratio on the thickness of MSPB and magnetite content. Key: (■) brush thickness L; magnetite amount in MSPB as determined (●) by TGA and (○) in theory. (b) TEM image of a sample with magnetite content of 14.8 wt % by TGA.

Table 2. Brush Thickness and Magnetite Content Using AIBN as Initiator

MSPB	MNP/St[a]	AA (wt %)	MPL[b] (nm)	L (nm)	MC (wt %)
A-4	0.2	100	140	157	3.9
A-5	0.6	100	181	57	7.1
A-6	1.2	100	184	24	14.8
A-7	2.0	100	177	19	15.0

[a] MNP/St: Feed ratio of MNP to styrene. [b] MPL: Diameter of polystyrene particles containing magnetite nanoparticles.

3. Morphology Control. The morphology of MPL and the grafting of PAA chains on MPL surface will be affected by the encapsulation of MNP.[68] In our experiments, the employment of different initiators during the miniemulsion polymerization for MPL synthesis was found to have significant impact on the morphology of MSPB.

3.1. Using AIBN. AIBN was selected as the initiator since its oil solubility can effectively reduce secondary nucleation.[69] According to the miniemulsion mechanism, droplets are the main reaction site.[65,70−72] The secondary nucleation and further growing will form much more nonmagnetic SPB in MSPB emulsions, which has negative effects on the encapsulation of MNP particles and size distribution of MPL.

In order to respond quickly to magnetic field for MSPB, more embedded MNP are favorable. If the magnetite content reaches ca. 15 wt %, the magnetic separation time can be reduced to a reasonable value.[73] However, upon increasing the dose of MNP, the thickness of MSPB reduced significantly and reached a plateau of ca. 20 nm when the weight ratio of MNP to styrene approached 1.2 (Figure 7a). The increased amount of MNP is unfavorable to the covalent attachment of photoinitiator on the core surface and thus the growth of PAA brushes.

The magnetite content in MSPB determined by TGA was much lower than that calculated theoretically (Figure 7a). For example, sample A-6 and A-7 had the similar magnetite content in the final MSPB while the dose of MNP for A-6 was only 60% of A-7 (Table 2). We tried even higher dose of MNP than A-7, but the highest magnetite content in MSPB was around 15 wt %. This result accords with the report in literatures where 15 wt % seems to be the upper limit magnetite content if MNP were mixed with styrene without other treatment.[24,26,28] The possible reason is the limited compatibility between PS matrix and hydrophobic OA backbone on the surface of MNP. Therefore, some MNP are easy to lose during the polymerization. This hypothesis has been confirmed in our experiments where black sediments always

can be found at the bottom of flasks at high dose of magnetite content.

Figure 7b showed the typical TEM image of MSPB based on AIBN initiator. Janus particles were observed where the MNP located far away from the particle center. Instead of PS core, we also tried to use poly(methyl methacrylate) (PMMA) core which has improved compatibility with OA modified magnetite nanoparticles.[29] But the obtained particles were irregular in shape.

The acentric phenomenum for MNP in MSPB (Figure 7b) can also be explained by the mechanism of miniemulsion polymerization. The polymerization is initiated and performed inside the magnetic droplets where oil soluble initiator AIBN dissolved (Scheme 2a). As a result, the MNP tend to be pushed aside of the droplet during the polymerization due to the relatively poor compatibility between PS matrix and OA surfactant on the surface of magnetite nanoparticles.

3.2. Using KPS. KPS was an alternative initiator for miniemulsion polymerization.[22,28,29] Although it may bring the secondary nucleation problem, KPS dissolves in water and initiates the polymerization from out to center pushing the MNP to the center of core (Scheme 2b). By choosing the type and optimizing the amount of surfactant, the secondary nucleation problem for KPS can be minimized.[74] Even though the secondary nucleation happens, the formed SPB without MNP can be removed by applying an external magnetic field. Therefore, KPS should be a good choice to improve the encapsulation of MNP.

Additionally, in order to encapsulate more than 15 wt % magnetite in MSPB, which cannot reach by simply using KPS as initiator,[26] MNP clusters were prepared prior to the miniemulsion polymerization. Several methods were reported to prepare MNP clusters.[34,75] We used SDS as surfactant to prepare MNP clusters with the help of ultrasonication.[30,31] As observed by TEM (Figure 8c), the obtained MNP clusters are spherical with an average diameter of 150 nm.

Magnetite content in MSPB determined by TGA is listed in Table 3 and compared with theoretical data (Figure 8a). During the experiment, no black sediments can be found even at high feed ratio of MNP/styrene, which implied that almost all of the MNP were encapsulated into PS core. Compared with MSPB prepared using AIBN as initiator with the same feed ratio of MNP/styrene (Table 2), the MNP content in MSPB (Table 3) enhanced significantly. The highest MNP content in MSPB by using KPS as initiator can reach 52.3 wt %. However, the brush thickness of MSPB also reduced dramatically upon increasing the dose of MNP due to the similar reason as discussed above. Interestingly, the magnetite content of MSPB was higher than theoretical value by following this route (Figure 8a), which was mainly attributed to the reduced polymerization of styrene by deactivation of radicals decomposited by KPS in water and the removal of nonmagnetic SPB from secondary nucleation during magnetic separation.

TEM image in Figure 8b indicated that most MNP locate in the center even at very high dose (Figure 8d). It seems that the MNP content in MSPB can be even higher than 52.3 wt % by using MNP cluster technique.[23] However, the thickness of PAA brush did not increase any more when MNP content reached 52.3 wt % even though we increased the amount of AA monomer and photoinitiator content.

4. Dispersibility. *4.1. Apparent Dispersibility.* As shown in Figure 9, MPL after dialyze against water is unstable and will totally precipitate after standing at room temperature for several minutes, while MSPB are very stable even after several months without sediments. Higher stability of MSPB

Scheme 2. Morphology Change during Miniemulsion Polymerization Using Different Initiators

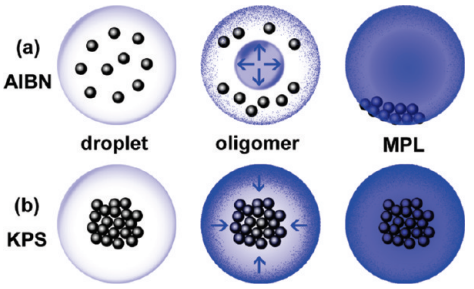


Table 3. Brush Thickness and Magnetite Content Using KPS as Initiator

MSPB	MNP/St	AA (wt %)	MPL (nm)	*L* (nm)	MC (wt %)
K-1	0.015	100	97	107	5.2
K-2	0.08	100	111	60	10.9
K-3	0.17	100	112	26	13.7
K-4	0.2	100	88	14	17.4
K-5	0.4	100	98	17	24.0
K-6	1.2	100	125	25	52.3

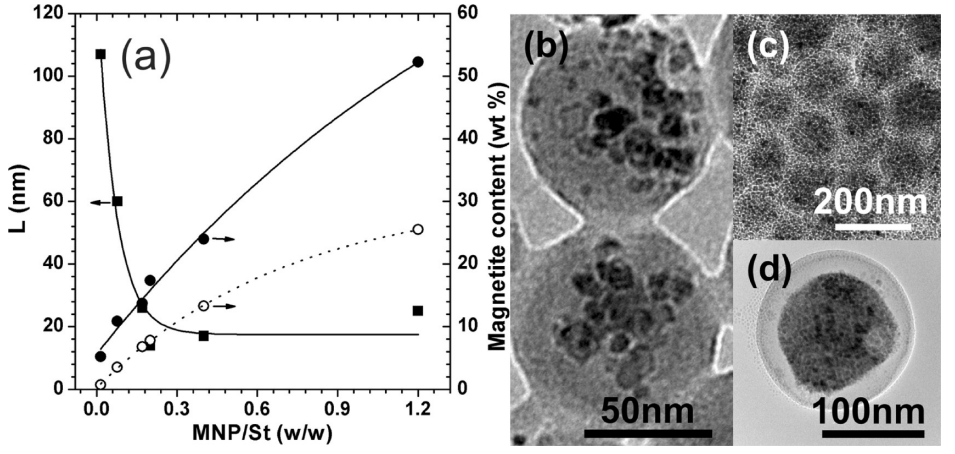


Figure 8. (a) Effect of MNP dose ratio on the thickness of MSPB. Key: (■) brush thickness *L*; magnetite amount in MSPB as determined (●) by TGA and (○) in theory. (b) MSPB with magnetite content 10.9 wt %. (c) TEM image of a MNP clusters and (d) MSPB with a high magnetite content of 52.3 wt %.

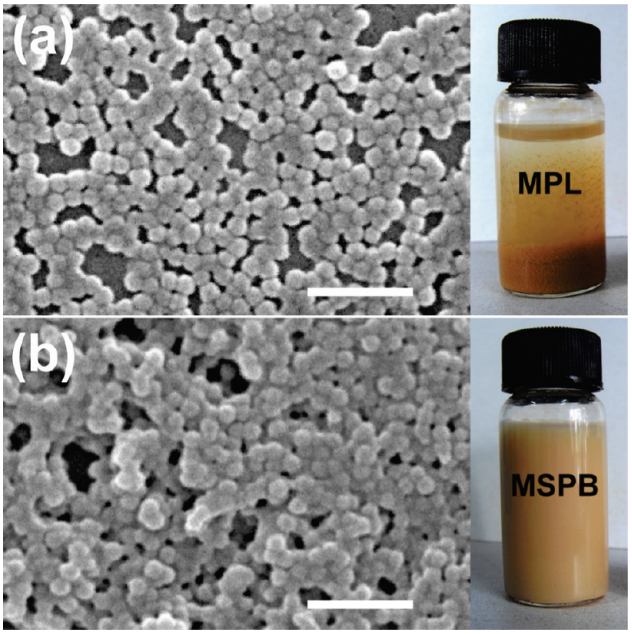


Figure 9. SEM image and optical photo of (a) MPL and (b) MSPB (sample A5, Table 2) after dialysis. The scale bar in SEM images represents 1 μm.

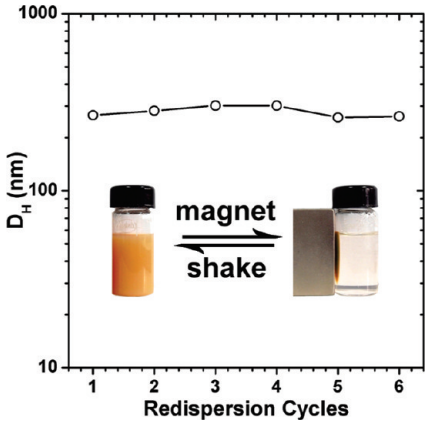


Figure 10. Size of the MSPB after several cycles of aggregation by magnet (NdFeB, 0.5 T) and redispersion as determined by dynamic light scattering (DLS), inset photos show the aggregation and redispersion of MSPB.

is attributed to the spherical PAA brushes on the core surface which provide, especially at high pH, both steric hindrance and electrostatic repulsion.

Both MPL and MSPB were collected by a strong permanent magnet (NdFeB, 0.5T). SEM images (Figure 9) showed that both sediments have a narrow size distribution. Although the MSPB particles seem sticky and adherent each other at dry state, it is still able to redisperse in water by slight shaking.

4.2. Redispersibility. In order to study the redispersibility, MSPB were repeatedly aggregated by a 0.5T magnetic field, and then redispersed for 5 min by untrasonication after removal of the external magnetic field. The average particle size is hardly changed within the experimental error after six cycles of aggregation and redispersion as determined by dynamic light scattering (Figure 10), which reflects the excellent redispersibility of MSPB.

Two factors may affect the redispersibility of MSPB. First, the electrostatic repulsions provided by carboxyl groups

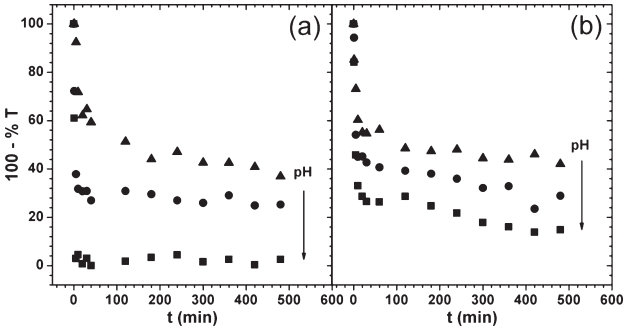


Figure 11. Turbidity as a function of separation time with external magnetic field (NdFeB, 0.5 T) for MSPB with magnetite content (a) 52.3 wt % and (b) 24.0 wt %. Key: (▲) pH = 9.0, ionic strength of 10 mM; (●) pH = 5.0, ionic strength of 10 mM; (■) pH = 3.0, ionic strength of 10 mM.

hinder the entanglement of PAAs among MSPB after collecting by magnet which should enhance the redispersibility of MSPB. Second, superparamagnetism of MSPB ensures the redispersibility. Although the magnetization of MNP decreased after encapsulation into PS core, the MPL and MSPB were still superparamagnetic. Therefore, when magnet was removed after collection, their magnetism lost would be helpful for dispersion of MSPB into water again.

4.3. Control of Separation. The separation of MSPB by external magnetic field was observed by colorimetry (Figure 11). The original turbidity of MSPB solution at pH = 9.0 without external magnetic field was set as 100 (%T) and that of water as zero.

As shown in Figure 11a, MSPB with magnetite content of 52.3 wt % at pH 3.0 were separated most fast and completely. Their suspension became totally transparent after 20 min. At pH 3.0 carboxyl groups in PAA of MSPB did not dissociate to form effective electrostatic repulsion between PAAs and MSPB (Figure 6b). As a result, MSPB shrank and became easy to separate. Upon increasing pH, both the swelling of MSPB and the increased electrostatic repulsion hindered their separating.

When magnetite content decreased to 24.0 wt % (Figure 11b), the separating of MSPB at different pH values became more slowly and incompletely compared to those with high magnetite content. Obviously, high magnetite content and low pH value are favorable for the magnetic separation of MSPB. Therefore, the separation of MSPB can be well controlled by modulating the magnetite content or adjusting pH value.

Nanosized MSPB open the way of many potential applications for SPB, such as catalysis,[9,11] protein immobilization[76,77] and magnetic field-guided drug delivery.[78] Quick magnetic response and good redispersibility guarantee the easy recycling of MSPB for industrial applications.

Conclusions

A novel approach has been developed to introduce magnetic control into spherical polyelectrolyte brushes to achieve the recovery and controllable delivery. Magnetic spherical polyelectrolyte brushes (MSPB) were prepared by photoemulsion polymerization using magnetic polystyrene latices (MPL) as core where the magnetite nanoparticles modified by oleic acid (MNP) were embedded. The MNP were synthesized via coprecipitation method and MPL by miniemulsion polymerization. The fabricated MSPB are narrowly dispersed, superparamagnetic and redispersible after aggregating by external magnetic field. The thickness of MSPB can be controlled by the dose of monomer AA.

Upon increasing the MNP content the brush thickness on MSPB decreases significantly due to the possible inhibition of MNP to the grafting of photoinitiator. Optimal MSPB with high content of MNP were prepared by turning MNP to clusters and using KPS as initiator. Separation process can be well controlled by adjusting magnetite content and pH.

This approach opens the way for the cost-effective applications of SPB in catalysis, wastewater treatment, protein separation, magnetic field-guided drug delivery, disease diagnosis/treatment, and magnetic resonance imaging.

Acknowledgment. We gratefully acknowledge the National Natural Science Foundation of China (No. 20644003, 20774028), the National Special Fund for State Key Laboratory of Bioreactor Engineering (2060204), the Fundamental Research Funds for the Central Universities, the Key Basic Research Project of Shanghai Science and Technology Commission (10JC1403800), and the China Scholarship Council for support of this work.

References and Notes

(1) Rühe, J.; Ballauff, M.; Biesalski, M.; Dziezok, P.; Gröhn, F.; Johannsmann, D.; Houbenov, N.; Hugenberg, N.; Konradi, R.; Minko, S.; Motornov, M.; Netz, R. R.; Schmidt, M.; Seidel, C.; Stamm, M.; Stephan, T.; Usov, D.; Zhang, H. *Adv. Polym. Sci.* **2004**, *165*, 79–150.
(2) Moinard, D.; Borsali, R.; Taton, D.; Gnanou, Y. *Macromolecules* **2005**, *38*, 7105–7120.
(3) Biesalski, M.; Ruhe, J. *Macromolecules* **1999**, *32*, 2309–2316.
(4) Wynveen, A.; Likos, C. N. *Soft Matter* **2010**, *6*, 163–171.
(5) Ballauff, M. *Prog. Polym. Sci.* **2007**, *32*, 1135–1151.
(6) Czeslik, C.; Jackler, G.; Hazlett, T.; Gratton, E.; Steitz, R.; Wittemann, A.; Ballauff, M. *Phys. Chem. Chem. Phys.* **2004**, *6*, 5557–5563.
(7) Wittemann, A.; Haupt, B.; Ballauff, M. *Phys. Chem. Chem. Phys.* **2003**, *5*, 1671–1677.
(8) Lu, Y.; Wittemann, A.; Ballauff, M. *Macromol. Rapid Commun.* **2009**, *30*, 806–815.
(9) Schrinner, M.; Ballauff, M.; Talmon, Y.; Kauffmann, Y.; Thun, J.; Moller, M.; Breu, J. *Science* **2009**, *323*, 617–620.
(10) Lu, Y.; Mei, Y.; Schrinner, M.; Ballauff, M.; Moller, M. W. *J. Phys. Chem. C.* **2007**, *111*, 7676–7681.
(11) Schrinner, M.; Proch, S.; Mei, Y.; Kempe, R.; Miyajima, N.; Ballauff, M. *Adv. Mater.* **2008**, *20*, 1928–1933.
(12) De, M.; Ghosh, P. S.; Rotello, V. M. *Adv. Mater.* **2008**, *20*, 4225–4241.
(13) Kang, Y. S.; Risbud, S.; Rabolt, J. F.; Stroeve, P. *Chem. Mater.* **1996**, *8*, 2209–2211.
(14) Landfester, K. *Adv. Mater.* **2001**, *13*, 765–768.
(15) Laurent, S.; Forge, D.; Port, M.; Roch, A.; Robic, C.; Elst, L. V.; Muller, R. N. *Chem. Rev.* **2008**, *108*, 2064–2110.
(16) Tartaj, P.; Morales, M. D. P.; Veintemillas-Verdaguer, S.; Gonzalez-Carreno, T.; Serna, C. J. *J. Phys. D Appl. Phys.* **2003**, *36*, R182–R197.
(17) Tartaj, P.; Morales, M. P.; Gonzalez-Carreqo, T.; Veintemillas-Verdaguer, S.; Serna, C. J. *J. Magn. Magn. Mater.* **2005**, *290*−*291*, 28–34.
(18) Teja, A. S.; Koh, P. *Prog. Cryst. Growth Charact.* **2009**, *55*, 22–45.
(19) Kim, J.; Lee, J. E.; Lee, S. H.; Yu, J. H.; Lee, J. H.; Park, T. G.; Hyeon, T. *Adv. Mater.* **2008**, *20*, 478–483.
(20) Sun, C.; Lee, J.; Zhang, M. Q. *Adv. Drug Deliver. Rev.* **2008**, *60*, 1252–1265.
(21) Shi, D.; Cho, H. S.; Chen, Y.; Xu, H.; Gu, H.; Lian, J.; Wang, W.; Liu, G.; Huth, C.; Wang, L.; Ewing, R. C.; Budko, S.; Pauletti, G. M.; Dong, Z. *Adv. Mater.* **2009**, *21*, 2170–2173.
(22) Cui, L. L.; Xu, H.; He, P.; Sumitomo, K. K.; Yamaguchi, Y.; Gu, H. C. *J. Polym. Sci., Part A: Polym. Chem.* **2007**, *45*, 5285–5295.
(23) Gong, T.; Yang, D.; Hu, J. H.; Yang, W. L.; Wang, C. C.; Lu, J. Q. *Colloid. Surface. A.* **2009**, *339*, 232–239.
(24) Hoffmann, H.; Landfester, K.; Antonietti, M. *Magnetohydrodynamics* **2001**, *37*, 217–221.
(25) Hong, R. Y.; Feng, B.; Cai, X.; Liu, G.; Li, H. Z.; Ding, J.; Zheng, Y.; Wei, D. G. *J. Appl. Polym. Sci.* **2009**, *112*, 89–98.
(26) Landfester, K.; Ramirez, L. P. *J. Phys: Condens. Matter* **2003**, *15*, S1345–S1361.
(27) Lu, S. H.; Forcada, J. *J. Polym. Sci., Part A: Polym. Chem.* **2006**, *44*, 4187–4203.
(28) Ramirez, L. P.; Landfester, K. *Macromol. Chem. Phys.* **2003**, *204*, 22–31.
(29) Xia, A.; Hu, J.; Wang, C.; Jiang, D. *Small* **2007**, *3*, 1811–1817.
(30) Xu, H.; Cui, L. L.; Tong, N. H.; Gu, H. C. *J. Am. Chem. Soc.* **2006**, *128*, 15582–15583.
(31) Zheng, W. M.; Gao, F.; Gu, H. C. *J. Magn. Magn. Mater.* **2005**, *288*, 403–410.
(32) Jaeyun Kim, H. K. N. L. *Angew. Chem., Int. Ed.* **2008**, *47*, 8438–8441.
(33) Shamim, N.; Hong, L.; Hidajat, K.; Uddin, M. S. *Colloids Surf. B: Biointerfaces* **2007**, *55*, 51–58.
(34) Xu, H.; Tong, N. H.; Cui, L. L.; Lu, Y.; Gu, H. C. *J. Magn. Magn. Mater.* **2007**, *311*, 125–130.
(35) Bakandritsos, A.; Bouropoulos, N.; Zboril, R.; Iliopoulos, K.; Boukos, N.; Chatzikyriakos, G.; Couris, S. *Adv. Funct. Mater.* **2008**, *18*, 1694–1706.
(36) Garcia, I.; Tercjak, A.; Rueda, L.; Mondragon, I. *Macromolecules* **2008**, *41*, 9295–9298.
(37) Gelbrich, T.; Feyen, M.; Schmidt, A. M. *Macromolecules* **2006**, *39*, 3469–3472.
(38) Huang, J. S.; Han, B. Z.; Yue, W.; Yan, H. *J. Mater. Chem.* **2007**, *17*, 3812–3818.
(39) Huang, J. S.; Li, X. T.; Zheng, Y. H.; Zhang, Y.; Zhao, R. Y.; Gao, X. C.; Yan, H. S. *Macromol. Biosci.* **2008**, *8*, 508–515.
(40) Deng, Y. H.; Yang, W. L.; Wang, C. C.; Fu, S. K. *Adv. Mater.* **2003**, *15*, 1729–1732.
(41) Ge, J. P.; Hu, Y. X.; Yin, Y. D. *Angew. Chem., Int. Ed.* **2007**, *46*, 7428–7431.
(42) Mefford, O. T.; Carroll, M.; Vadala, M. L.; Goff, J. D.; Mejia-Ariza, R.; Saunders, M.; Woodward, R. C.; St Pierre, T. G.; Davis, R. M.; Riffle, J. S. *Chem. Mater.* **2008**, *20*, 2184–2191.
(43) Miles, W. C.; Goff, J. D.; Huffstetler, P. P.; Reinholz, C. M.; Pothayee, N.; Caba, B. L.; Boyd, J. S.; Davis, R. A.; Riffle, J. S. *Langmuir* **2009**, *25*, 803–813.
(44) Utech, S.; Scherer, C.; Maskos, M. *J. Magn. Magn. Mater.* **2009**, *321*, 1386–1388.
(45) Utech, S.; Scherer, C.; Krohne, K.; Carrella, L.; Rentschler, E.; Gasi, T.; Ksenofontov, V.; Felser, C.; Maskos, M. *J. Magn. Magn. Mater.* **2010**, *322*, 3519–3526.
(46) Guo, X.; Weiss, A.; Ballauff, M. *Macromolecules* **1999**, *32*, 6043–6046.
(47) Gnanaprakash, G.; Philip, J.; Jayakumar, T.; Raj, B. *J. Phys. Chem. B* **2007**, *111*, 7978–7986.
(48) Lee, S. Y.; Harris, M. T. *J. Colloid Interface Sci.* **2006**, *293*, 401–408.
(49) Qiao, R.; Yang, C.; Gao, M. *J. Mater. Chem.* **2009**, *19*, 6274–6293.
(50) Soler, M.; Alcantara, G. B.; Soares, F. Q.; Viali, W. R.; Sartoratto, P. C.; Fernandez, J.; Da Silva, S. W.; Garg, V. K.; Oliveira, A. C.; Morais, P. C. *Surf. Sci.* **2007**, *601*, 3921–3925.
(51) Vereda, F.; de Vicente, J.; Hidalgo-Alvarez, R. *Langmuir* **2007**, *23*, 3581–3589.
(52) Wang, J.; Chen, Q. W.; Zeng, C.; Hou, B. Y. *Adv. Mater.* **2004**, *16*, 137–140.
(53) Wang, X. M.; Zhang, C. N.; Wang, X. L.; Gu, H. C. *Appl. Surf. Sci.* **2007**, *253*, 7516–7521.
(54) Zhang, L.; He, R.; Gu, H. C. *Appl. Surf. Sci.* **2006**, *253*, 2611–2617.
(55) Goesmann, H.; Feldmann, C. *Angew. Chem., Int. Ed.* **2010**, *49*, 1362–1395.
(56) Wan, M.; Zhou, W.; Li, J. *Synth. Met.* **1996**, *78*, 27–31.
(57) Xu, X. L.; Friedman, G.; Humfeld, K. D.; Majetich, S. A.; Asher, S. A. *Adv. Mater.* **2001**, *13*, 1681–1684.
(58) Xu, X. L.; Friedman, G.; Humfeld, K. D.; Majetich, S. A.; Asher, S. A. *Chem. Mater.* **2002**, *14*, 1249–1256.
(59) Schreiber, E.; Ziener, U.; Manzke, A.; Plettl, A.; Ziemann, P.; Landfester, K. *Chem. Mater.* **2009**, *21*, 1750–1760.
(60) Tiarks, F.; Landfester, K.; Anonietti, M. *Macromol. Chem. Phys.* **2001**, *202*, 51–60.
(61) Liu, X. Q.; Guan, Y. P.; Ma, Z. Y.; Liu, H. Z. *Langmuir* **2004**, *20*, 10278–10282.
(62) Li, L.; Yang, Y.; Ding, J.; Xue, J. *Chem. Mater.* **2010**, *22*, 3183–3191.
(63) Hong, R. Y.; Feng, B.; Liu, G.; Wang, S.; Li, H. Z.; Ding, J. M.; Zheng, Y.; Wei, D. G. *J. Alloy. Compd* **2009**, *476*, 612–618.
(64) Landfester, K.; Bechthold, N.; Tiarks, F.; Antonietti, M. *Macromolecules* **1999**, *32*, 5222–5228.

(65) Asua, J. M. *Prog. Polym. Sci.* **2002**, *27*, 1283–1346.
(66) Guo, X.; Ballauff, M. *Langmuir* **2000**, *16*, 8719–8726.
(67) Guo, X.; Ballauff, M. *Phys. Rev. E* **2001**, *64*, 051406.
(68) Chen, K.; Zhu, Y.; Li, L.; Lu, Y.; Guo, X. *Macromol. Rapid Commun.* **2010**, *31*, 1440–1443.
(69) Luo, Y.; Dai, C.; Chiu, W. *J. Polym. Sci., Part A: Polym. Chem.* **2008**, *46*, 1014–1024.
(70) Antonietti, M.; Landfester, K. *Prog. Polym. Sci.* **2002**, *27*, 689–757.
(71) Landfester, K. *Angew. Chem., Int. Ed.* **2009**, *48*, 4488–4507.
(72) Schork, F. J.; Luo, Y.; Smulders, W.; Russum, J. P.; Butté, A.; Fontenot, K. *Adv. Polym. Sci.* **2005**, 129–255.
(73) Elaissari, A. *Macromol. Symp.* **2009**, *281*, 14–19.
(74) Mori, Y.; Kawaguchi, H. *Colloids Surf. B: Biointerfaces* **2007**, *56*, 246–254.
(75) Sondjaja, R.; Alan Hatton, T.; Tam, M. K. C. *J. Magn. Magn. Mater.* **2009**, *321*, 2393–2397.
(76) Majhi, P. R.; Ganta, R. R.; Vanam, R. P.; Seyrek, E.; Giger, K.; Dubin, P. L. *Langmuir* **2006**, *22*, 9150–9159.
(77) Wittemann, A.; Haupt, B.; Merkle, R.; Ballauff, M. *Macromol. Symp.* **2003**, *191*, 81–88.
(78) Lu, Y.; Hoffmann, M.; Yelamanchili, R. S.; Terrenoire, A.; Schrinner, M.; Drechsler, M.; Moller, M. W.; Breu, J.; Ballauff, M. *Macromol. Chem. Phys.* **2009**, *210*, 377–386.

640 *Macromolecules* **2011**, *44*, 640–646
DOI: 10.1021/ma101813q

Macromolecules
ARTICLE

On Maxwell's Relations of Thermodynamics for Polymeric Liquids away from Equilibrium

Chunggi Baig,*,† Vlasis G. Mavrantzas,*,† and Hans Christian Öttinger‡

†*Department of Chemical Engineering, University of Patras & FORTH-ICE/HT, Patras, GR 26504, Greece, and* ‡*Department of Materials, Polymer Physics, ETH Zürich, HCI H 543, CH-8093 Zürich, Switzerland*

Received August 9, 2010; Revised Manuscript Received December 9, 2010

ABSTRACT: To describe complex systems deeply in the nonlinear regime, advanced formulations of nonequilibrium thermodynamics such as the extended irreversible thermodynamics (EIT), the matrix model, the generalized bracket formalism, and the GENERIC (= general equation for the nonequilibrium reversible−irreversible coupling) formalism consider generalized versions of thermodynamic potentials in terms of a few, well-defined position-dependent state variables (defining the system at a *coarse-grained* level). Straightforward statistical mechanics considerations then imply a set of equalities for its second derivatives with respect to the corresponding state variables, typically known as Maxwell's relations. We provide here direct numerical estimates of these relations from detailed atomistic Monte Carlo (MC) simulations of an unentangled polymeric melt coarse-grained to the level of the chain conformation tensor, under both weak and strong flows. We also report results for the nonequilbrium (i.e., relative to the quiescent fluid) internal energy, entropy, and free energy functions of the simulated melt, which indicate a strong coupling of the second derivatives of the corresponding thermodynamic potential at high flow fields.

1. Introduction

Since Onsager's pioneering work[1] on irreversible phenomena back in 1931, thermodynamics began to describe a wide variety of dissipative processes (e.g., diffusion, heat and electric conduction, viscous relaxation, chemical reactions, dielectric relaxation) and their coupling (leading, e.g., to electrokinetic, thermoelectric, thermokinetic, and other effects) by assuming a linear relationship between the generalized thermodynamic (or driving) forces and the resulting fluxes. Onsager's reciprocal relations, which were later generalized by Casimir,[2] were derived based on the classical principle of microscopic reversibility at equilibrium and the so-called regression hypothesis (namely that the dissipation mechanism accompanying natural fluctuations is the same both at equilibrium and under nonequilibrium conditions). Following Onsager's and Casimir's seminal contributions, intense research work in the ensuing years led to a number of elegant thermodynamic and statistical theories on the fundamental nature of irreversible processes,[3−9] which eventually culminated to what is known today as the theory of linear irreversible thermodynamics (LIT) for dissipative systems.[10] Founded on the local equilibrium assumption (which allows one to take full advantage of the rigor of the known fundamental laws of equilibrium thermodynamics), LIT has offered a unified description of many nonequilibrium processes (associated with the transport of conserved quantities such as mass, momentum and energy) in a systematic and compact way.[10,11]

Modern nonequilibrium thermodynamic formulations, on the other hand, such as the extended irreversible thermodynamics,[12] the generalized bracket formalism,[13−17] the matrix model,[18,19] and the GENERIC (general equation for the nonequilibrium reversible-irreversible coupling) approach[20−22] recover LIT as a special case. The starting point in these formalisms is to choose the set $\mathbf{x}$ of the proper state variables, a step of paramount importance requiring deep physical insight and experience. This happens because thermodynamics is generally concerned with the description of a system at a coarse-grained level where, by eliminating an enormous number of microscopic degrees of freedom associated with fast dynamics (*fast degrees of freedom*), the emphasis is placed on the evolution of a limited set of slowly evolving variables (*slow degrees of freedom*). This in turn implies the existence of an intermediate time scale τ separating fast and slow variables;[23] coarse-graining then means that it is only the latter that are kept in the list of state variables.[24] The next step is to identify generalizations of thermodynamic potentials as the primary source of complete thermodynamic information. In the generalized bracket formalism, this is the dissipative Hamiltonian H. In the GENERIC framework, it is the generators E (the energy) and S (the entropy) describing reversible and irreversible contributions, respectively. The third and final step is to obtain the transport equations by *postulating* a fundamental equation for the time evolution of the set $\mathbf{x}$ of nonequilibrium variables. In GENERIC, for example, such an equation reads:

$$\frac{\mathrm{d}\mathbf{x}}{\mathrm{d}t} = \mathbf{L}(\mathbf{x})\frac{\delta E(\mathbf{x})}{\delta \mathbf{x}} + \mathbf{M}(\mathbf{x})\frac{\delta S(\mathbf{x})}{\delta \mathbf{x}} \tag{1}$$

and comes together with a number of important properties for the generators E and S and the matrices $\mathbf{L}$ and $\mathbf{M}$. For example, $\mathbf{L}$ is always antisymmetric while $\mathbf{M}$ is symmetric (expressing the Onsager−Casimir symmetry of LIT) and positive-semidefinite (this can be considered as a strong nonequilibrium generalization of the second law of thermodynamics). In fact, a strict separation of reversible and irreversible contributions in GENERIC is provided by the mutual degeneracy requirements

$$\mathbf{M}(\mathbf{x})\frac{\delta E(\mathbf{x})}{\delta \mathbf{x}} = 0, \quad \mathbf{L}(\mathbf{x})\frac{\delta S(\mathbf{x})}{\delta \mathbf{x}} = 0 \tag{2}$$

*Authors to whom correspondence should be addressed. E-mail: cbaig@iceht.forth.gr (C.B.); vlasis@chemeng.upatras.gr (V.M.). Telephone: +30-2610-997398. Fax: +30-2610-965223.

 Published on Web 01/06/2011 © 2011 American Chemical Society

expressing the conservation of energy even in the presence of dissipation and the conservation of entropy for any reversible dynamics (entropy can only be produced by irreversible dynamics), respectively. As explained by Öttinger,[24] E and $\mathbf{L}$ can be obtained by straightforwardly averaging the microscopic energy and Poisson bracket of classical mechanics. S and $\mathbf{M}$, on the other hand, should account correctly for the increase in entropy and dissipation (or friction) associated with the elimination of fast degrees of freedom or the grouping of microstates to coarser states. To see this, let $\rho_{\mathbf{x}}(\mathbf{z})$ be the probability density to find a microstate $\mathbf{z}$ (in classical mechanics, this is defined by the positions and momenta of the atomistic units) for given values of the set of coarse-grained variables $\mathbf{x}$, and $\Pi(\mathbf{z})$ a mapping that assigns a coarse-grained state to any microstate $\mathbf{z}$. In any ensemble, the variables $\mathbf{x}$ are the averages of $\Pi(\mathbf{z})$ evaluated with the probability density $\rho_{\mathbf{x}}(\mathbf{z})$, i.e., $\mathbf{x} = \langle \Pi(\mathbf{z}) \rangle_{\mathbf{x}}$. Then, one can show using projection operation techniques[25,26] that the friction matrix $\mathbf{M}$ can be obtained by the following Green−Kubo equation:[27]

$$\mathbf{M}(\mathbf{x}) = \frac{1}{k_{\mathrm{B}}} \int_0^{\tau} \langle \dot{\Pi}^f(\mathbf{z}(t)) \dot{\Pi}^f(\mathbf{z}(0)) \rangle_{\mathrm{x}} \, \mathrm{d}t \tag{3}$$

Here, k_B is the Boltzmann constant and $\dot{\Pi}^f$ denotes the (fast) time derivative of Π. How to apply eq 3 in order to compute $\mathbf{M}$ from dynamic simulations (executed, however, only for a small fraction of the longest system time scale, as dictated by the upper limit of integration in eq 3, namely the intermediate time τ) has been discussed by Ilg et al.[28]

Each of the new nonequilibrium thermodynamics formulations has its advantages and disadvantages; however, all of them are very useful in our effort to *consistently* understand or describe irreversible processes far away from equilibrium. Furthermore, and despite key differences in their fundamental structure or starting point, they bear striking similarities to a degree that one can even prove equivalence of any such two formalisms in certain cases.[29−31] Regarding, in particular, the issue of the existence of thermodynamic potentials, we recall that from a statistical mechanics point of view these are well-defined at equilibrium. And they can be calculated via partition functions in terms of statistical weighting by sampling equilibrium configurations in a predefined statistical ensemble. All the information about a particular system at equilibrium is thus contained in a single thermodynamic potential whose form is limited only by convexity conditions. For example, for a system specified by the variables T, V, and N, namely temperature, volume and number of molecules, the Helmholtz free energy $A = A(T,V,N)$ is the proper thermodynamic potential to consider, from which (e.g.) all equations of state can be obtained by simple partial differentiations. Furthermore, the function $A = A(T,V,N)$ is obtainable from molecular simulations in the NVT ensemble through the canonical partition function. Beyond equilibrium, however, even the choice of variables can be bad. But one can still check (based on the corresponding Green−Kubo equation for the $\mathbf{M}$ matrix, eq 3 above) whether a separating time scale does exist in which case the choice of the variables should be a reasonable one. On the other hand, the consideration of additional structural variables in the set $\mathbf{x}$ implies that we should resort to an expanded ensemble, wherein the coarse-grained variables appear explicitly. Then, despite the elegance and rigor (expressed through a set of consistency conditions) of the nonequilibrium thermodynamics approach adopted, one is still faced with the question whether or not "well-defined thermodynamic potentials (such as the entropy and energy functions postulated in GENERIC or the extended Helmholtz free energy function assumed in the generalized bracket) really exist far beyond equilibrium"[32−34] and how these can be computed. We demonstrate here how, given a set of nonequilibrium variables for a model system (an unentangled polymer melt), one can actually carry out accurate calculations of such a nonequilibrium potential (in particular of the entropy) and of a few other thermodynamic functions in terms of the chosen coarse-grained variable(s) through detailed atomistic MC simulations in an expanded statistical ensemble.[35−38] We also provide a consistency check of our numerical method by directly demonstrating the validity of Maxwell's relations relating certain pairs of the second derivatives of the generalized potential with respect to the nonequilibrium variables.

2. Nonequilibrium System Studied and Simulation Methodology

As a test case, let us consider a polymeric melt containing short polyethylene (PE) chains under an arbitrary flow field with shear rates covering both the linear and the nonlinear regime. For such a system, Mavrantzas and Theodorou already back in 1998[35] showed how one can compute the Helmholtz free energy function in terms of its density ρ, temperature T, and a tensorial structural variable, namely the conformation tensor $\mathbf{c}$ defined as $3\langle \mathbf{RR} \rangle / \langle R^2 \rangle_{eq}$ where $\mathbf{R}$ is the chain end-to-end vector, by making use of the conjugate thermodynamic variables to ρ and $\mathbf{c}$: The first is a scalar quantity, the "pressure" P, and the second a tensorial quantity, the "orienting field" $\boldsymbol{\alpha}$ which is intimately related to the strain rate in a flow situation.[36] Building on these very first considerations, Baig and Mavrantzas[37,38] proposed recently a powerful MC methodology capable of sampling nonequilibrium states for short polymers with an overall conformation identical to that obtained from a direct nonequilibrium molecular dynamics simulation. The method was termed GENERIC MC, because it was founded on the GENERIC formalism of nonequilibrium thermodynamics. However, it is more general, since it makes no a priori assumption about the relationship between thermodynamic field(s) employed in the simulation and the corresponding state variable(s). It can be routinely reformulated in any other nonequilibrium thermodynamics framework, in which the complete coarse-grained information is assumed to be contained in the generalized thermodynamic potential. But we should keep in mind that any MC method, being intrinsically nondynamic in nature, provides results that strictly apply only to stationary systems (systems for which the free energy A is time-independent). Thus, although thermodynamic potentials exist regardless of time and the same happens with the Maxwell equations (they hold independently of whether the system undergoes a stationary or a time-dependent process), our GENERIC MC methodology can provide numerical evaluation for them for a given system only when this system undergoes a stationary process. To confirm Maxwell's equations under general time-dependent process, one should devise a different methodology (see, e.g., ref 28).

The generalized fundamental Gibbs equation for the system under consideration is written as

$$\mathrm{d}E = \sum_k \lambda_k dx_k \tag{4}$$

where λ_k represents the thermodynamic force field conjugate to the extensive state variable x_k. Considering points in the nonequilibrium phase space as well-defined thermodynamic states, the energy function E plays the role of a generalized thermodynamic potential [and, of course, other thermodynamic potentials can be obtained via appropriate Legendre transforms[39]] for the nonequilibrium system considered. In this case, one comes up also with a set of equalities of the form

$$\left(\frac{\partial \lambda_i}{\partial x_j}\right)_{\forall x_{k \neq j}} = \left(\frac{\partial \lambda_j}{\partial x_i}\right)_{\forall x_{k \neq i}} \tag{5}$$

which are the analogues of the well-known Maxwell relations of equilibrium thermodynamics for nonequilibrium systems. In eq 5, the subscript $\forall x_{k\neq j}$ denotes all state variables x_k except x_j. Alternatively (see, e.g., eq 6.17 or the solution to exercise 139 in ref 22), eq 5 can be derived starting from the probability density function $\rho \sim \exp(\Sigma_j \lambda_j \Pi_j)$ computing the average of Π_i and differentiating with respect to λ_j. Then one obtains that $(\partial\langle\Pi_i\rangle)/(\partial\lambda_j) = (\partial\langle\Pi_j\rangle)/(\partial\lambda_i) = \langle\Pi_i\Pi_j\rangle - \langle\Pi_i\rangle\langle\Pi_j\rangle$, physically representing the degree of mutual correlation of the different thermodynamic variables or the degree of fluctuations for the same variable. Clearly, if one works with a different thermodynamic potential, a different set of Maxwell relations will be derived. It is also understood that for a given system the λ_k's have a different meaning under equilibrium and nonequilibrium conditions, since under nonequilibrium conditions they are affected by the extra structural variables considered to account for deviations from equilibrium.

For the system at hand, an unentangled polymer melt whose internal microstructure is described by the conformation tensor **c**, the fundamental thermodynamic representation in terms of the energy E dictates that

$$\mathrm{d}E = T\,\mathrm{d}S - P\,\mathrm{d}V + \mu\,\mathrm{d}N_{ch} + k_\mathrm{B}T\boldsymbol{\alpha} : \mathrm{d}(N_{ch}\mathbf{c}) \tag{6}$$

where N_{ch} denotes the number of chains, P the pressure, T the temperature, V the volume, S the entropy, and $\boldsymbol{\alpha}$ the conjugate thermodynamic field to tensor **c** accounting for flow effects. Given that E is a first-order homogeneous thermodynamic function with respect to S, V, and $N_{ch}\mathbf{c}$, eq 6 implies the following Euler equation

$$E = TS - PV + \mu N_{ch} + N_{ch}k_\mathrm{B}T\boldsymbol{\alpha} : \mathbf{c} \tag{7}$$

and thus, also the following generalized Gibbs−Duhem relationship:

$$-S\,\mathrm{d}T + V\,\mathrm{d}P - N_{ch}\,\mathrm{d}\mu - N_{ch}\mathbf{c} : \mathrm{d}(k_\mathrm{B}T\boldsymbol{\alpha}) = 0 \tag{8}$$

Other thermodynamic functions can be derived from these expressions through appropriate Legendre transforms, such as the extended (generalized) Helmholtz free energy A and the extended (generalized) Gibbs free energy G:[36,38]

$$dA(T, V, N_{ch}, N_{ch}\tilde{c}) = -S\,\mathrm{d}T - P\,\mathrm{d}V + \mu\,\mathrm{d}N_{ch} + k_\mathrm{B}T\boldsymbol{\alpha} : \mathrm{d}(N_{ch}\mathbf{c}) \tag{9}$$

and

$$\mathrm{d}G(T, P, N_{ch}, \boldsymbol{\alpha}) = -S\,\mathrm{d}T + V\,\mathrm{d}P + \mu\,\mathrm{d}N_{ch} - N_{ch}\mathbf{c} : \mathrm{d}(k_\mathrm{B}T\boldsymbol{\alpha}) \tag{10}$$

respectively. For the purpose of confirming Maxwell's relations, it is more convenient to work with the thermodynamic potential $A' = A'(T,V,N_{ch},\boldsymbol{\alpha})$ defined as $A' = A' - N_{ch}k_B T\boldsymbol{\alpha}:\mathbf{c}$ so that:

$$\mathrm{d}A'(T, V, N_{ch}, \boldsymbol{\alpha}) = -S\,\mathrm{d}T - P\,\mathrm{d}V + \mu\,\mathrm{d}N_{ch} - N_{ch}\mathbf{c} : \mathrm{d}(k_\mathrm{B}T\boldsymbol{\alpha}) \tag{11}$$

Equation 11 is the starting point for executing MC simulations in the expanded ensemble $\{N_{ch}NVT\boldsymbol{\mu}^*\boldsymbol{\alpha}\}$, in which the following variables are specified: The number of chains N_{ch}, the average number of atoms per chain N, the volume V, the temperature T, the spectrum of chain relative chemical potentials $\boldsymbol{\mu}^*$controlling the distribution of chain lengths in the system,[40] and the tensorial field $\boldsymbol{\alpha}$ accounting indirectly for flow effects. The spectrum $\boldsymbol{\mu}^*$ enters the analysis when one converts from a description in terms of a Helmholtz free energy representation to a representation in terms of the variables $\{N_{ch}NVT\boldsymbol{\mu}^*\boldsymbol{\alpha}\}$ for an m-component system,[40−42] in which case if k ($k = 1, 21...m$) denotes the kth component in the mixture (characterized by chain length N_k) and (i,j) is a selected arbitrary pair of reference species (of lengths N_i and N_j, respectively) for which $\mu_i^* = \mu_i^* = 0$ to maintain the total number of atoms and the total number of chains constant, then each of the μ_k^*,$k = 1, 2, ..., m$ denotes the relative chemical potential of chains of species k (and thus of length N_k). The spectrum $\boldsymbol{\mu}^*$ should reproduce the desired distribution of chain lengths (e.g., Gaussian, uniform, most probable, Flory, etc.) in the course of the simulations and should be an input to the MC algorithm[40−42] (see ref 40 for the mathematical specification of $\boldsymbol{\mu}^*$ that generates the most widely employed chain length distributions). The field $\boldsymbol{\alpha}$, on the other hand, couples with the tensor **c** in the thermodynamic function and drives the system away from equilibrium, based on the following probability density function:

$$\rho^{N_{ch}NVT\boldsymbol{\mu}^*\boldsymbol{\alpha}}(\mathbf{r}_1, \mathbf{r}_2, ..., \mathbf{r}_n, V) \sim \exp[-\beta(U(\mathbf{r}_1, \mathbf{r}_2, ..., \mathbf{r}_n, V) - \sum_{k=1}^{N_{ch}} \mu_k^* N_k - k_\mathrm{B}T\boldsymbol{\alpha} : \sum_{k=1}^{N_{ch}} \mathbf{c}_k)] \tag{12}$$

Consequently, in the proposed GENERIC MC simulations, system configurations are sampled according to the following modified Metropolis criterion:

$$p_{acc}^{N_{ch}NVT\boldsymbol{\mu}^*\boldsymbol{\alpha}} \sim \exp[-\beta(\Delta U - \sum_{k=1}^{N_{ch}} \mu_k^* \Delta N_k - k_\mathrm{B}T\boldsymbol{\alpha} : \sum_{k=1}^{N_{ch}} \Delta\mathbf{c}_k)] \tag{13}$$

where $\beta \equiv 1/k_B T$, n ($= N_{ch} \times N$) denotes the total number of atoms in the system, $\{\mathbf{r}\} = \{\mathbf{r}_1, \mathbf{r}_2, ..., \mathbf{r}_n\}$ the space of their position vectors, U the potential energy of the system, μ_k^* the relative chemical potential of the k-mer long chain and $\mathbf{c}_k$ the conformation tensor of this chain. With appropriate input data for the set $\{N_{ch}NVT\boldsymbol{\mu}^*\boldsymbol{\alpha}\}$, eq 13 allows one to sample nonequilbrium steady states by assigning nonzero values to $\boldsymbol{\alpha}$.

All simulation results presented here have been obtained with a model linear PE melt containing 160 $C_{78}H_{158}$ chains in a rectangular box [enlarged in the stretching, x, direction to avoid undesirable system-size effects, especially at high flow fields] with dimensions x, y, and z equal to 130.5, 54, and 54 Å, respectively. The simulations were executed at temperature $T = 450$ K and density $\rho = 0.7638$ g/cm^3 starting from a fully pre-equilibrated initial configuration of the $C_{78}H_{158}$ melt, using the following form of $\boldsymbol{\alpha}$:

$$\boldsymbol{\alpha} = \begin{pmatrix} \alpha_{xx} & \alpha_{xy} & 0 \\ \alpha_{xy} & 0 & 0 \\ 0 & 0 & 0 \end{pmatrix} \tag{14}$$

How $\boldsymbol{\alpha}$ is related to the velocity gradient tensor $\dot{\gamma}$ in a real flow has been analyzed in detail in ref 38 where it is also explained that the above form, eq 14, represents a mixed flow comprising both pure stretching and rotational components. We chose it because it gives rise to more intriguing set of Maxwell's relations than that corresponding either to pure shear or to pure elongation. The tensor $\boldsymbol{\alpha}$ is also intimately related to the stress tensor $\boldsymbol{\sigma}$ developing in the system. In fact, if the stress is only elastic in nature, then the tensor $\boldsymbol{\alpha}$ imposed directly in the MC simulations and the tensor **c** that results from the simulations should satisfy a consistency relation which reflects the inherent symmetric nature of the stress tensor $\boldsymbol{\sigma}$. We refer the interested reader to ref 38 for more details.

The phase space explored in the present simulations corresponded to α_{xx} and α_{xy} values in the interval [0, 0.35] with a spacing equal to 0.05. As also explained in ref 38, for the $C_{78}H_{158}$

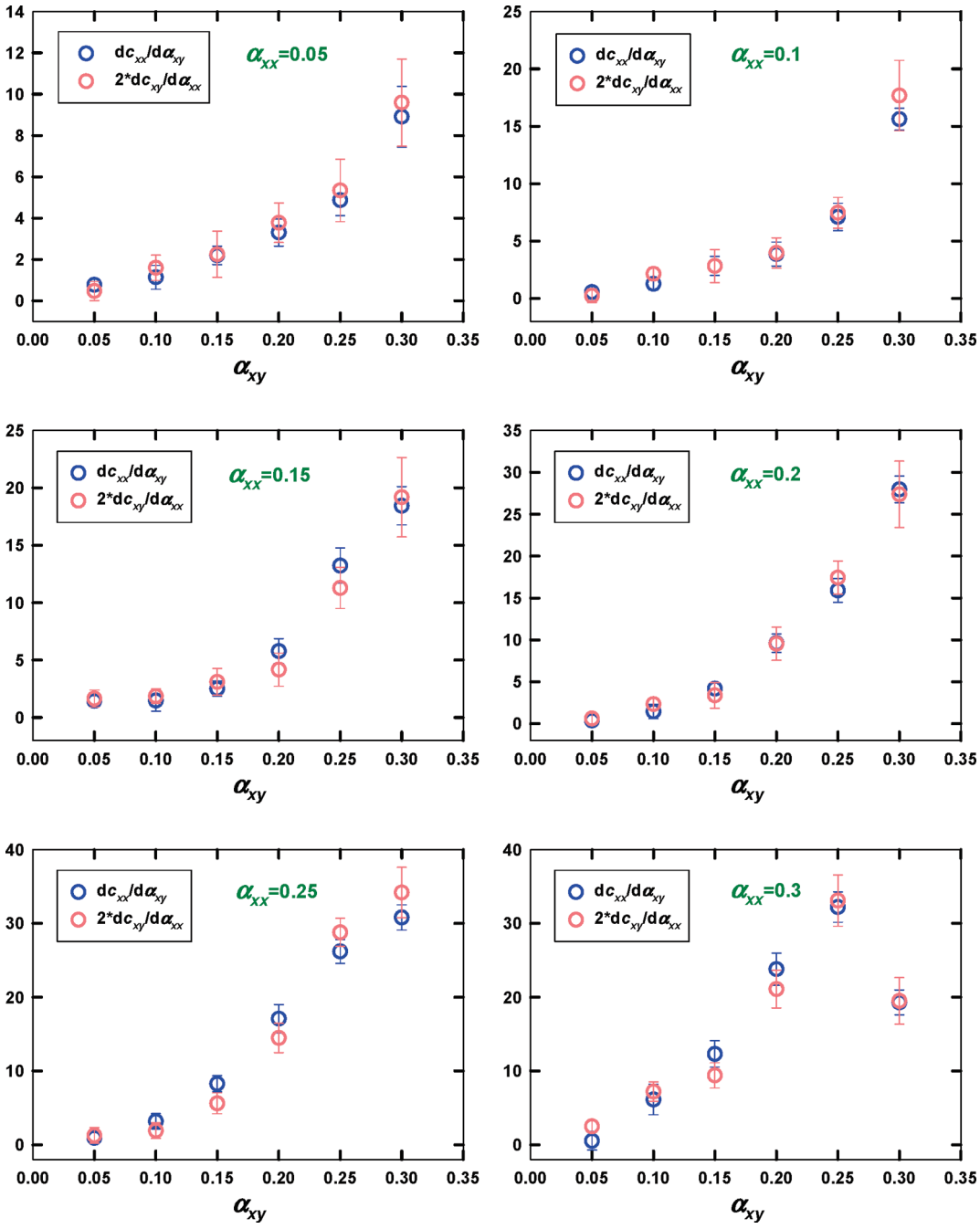


Figure 1. Comparison of the two thermodynamic derivatives ($\partial c_{xx}/\partial\alpha_{xy}$ and $\partial c_{xy}/\partial\alpha_{xx}$) in the entire range of values of the applied flow field $\boldsymbol{\alpha}$ investigated here.

PE melt considered here, this corresponds to Deborah numbers from 0.3 up to 1000, implying that our simulations spanned both the linear and the nonlinear regime. Of course, Deborah numbers equal to 1000 might be too large for a model based on a single mode (the chain end-to-end conformation tensor $\mathbf{c}$ here) to accurately describe its response to the applied flow but we included them in our study only in order to test the proposed numerical method in the highly nonlinear regime.

Substituting eq 14 for $\boldsymbol{\alpha}$ into eq 11 implies then the following Maxwell relation

$$\left(\frac{\partial c_{xx}}{\partial \alpha_{xy}}\right)_{T,V,N_{ch},\alpha_{xx}} = 2\left(\frac{\partial c_{xy}}{\partial \alpha_{xx}}\right)_{T,V,N_{ch},\alpha_{xy}} \quad (15)$$

for the system at hand.

In the simulations, the well-known end-bridging MC algorithm[40−42] was employed, the most efficient MC method available today for the equilibration of the long-length scale characteristics of linear polymers irrespective of their length. The method is capable of generating disparate and practically uncorrelated polymer conformations with a probability prescribed by the acceptance criterion of eq 13. A small polydispersity was allowed in the simulations (in conjunction with the use of the end-bridging move) corresponding to a polydispersity index $I \approx 1.083$. In the simulations the following mix of MC moves was used: end-bridgings, 50%; reptations, 10%; end-mer rotations, 2%; flips, 6%; concerted rotations, 32%. A total of about 2 billion MC steps were seen to be enough for the full equilibration of the structural, volumetric and conformational properties of the simulated liquid at each state point.

3. Nonequilibrium Simulation Results

The simulation results for the two partial derivatives appearing in eq 15 are presented in Figure 1. We see that (a) the two derivatives are always positive and that (b) they increase monotonically and rather rapidly as the flow components are increased except for the very last (and highly nonlinear) point corresponding to $\alpha_{xx} = \alpha_{xy} = 0.3$. It is also surprising that $\partial c_{xx}/\partial\alpha_{xy}$ increases steeply with α_{xy} (at a fixed value of α_{xx}): given that α_{xy} is an off-diagonal component, it cannot cause any preferential deformation of the chain dimensions along the x- or y-directions by itself; clearly, this reflects the strong, highly nonlinear coupling of the α_{xx} and α_{xy} components. Regarding the maximum exhibited by the two derivatives for $\alpha_{xx} = 0.3$ (bottom right in Figure 1), this should be attributed to two effects: (a) the finite extensibility of the relatively short chains simulated here and (b) the nonzero value of the shear component α_{xy} which precludes chains from assuming fully stretched configurations along the x-direction. By far, however, the most important result of the simulations is that the two thermodynamic derivatives are practically identical to each other over the entire range of field values investigated. This can be seen more clearly in the 3-dimensional graphs reported in Figure 2; Maxwell's relations (eq 15) for the simulated system are numerically confirmed by our GENERIC MC simulations not only in the linear but also deeply in the nonlinear flow regime. The shapes of the resulting surfaces are convex upward and rather steep (except from the very last state point, corresponding to $\alpha_{xx} = \alpha_{xy} = 0.3$), also indicative of nonlinear effects.

In addition to directly evaluating the Maxwell equations, our GENERIC MC simulations have allowed us to calculate the nonequilibrium thermodynamic functions (energy, entropy and Helmholtz free energy; see eq 11) as a function of the imposed nonequilibrium field. Typical results for the system addressed here are reported in Figure 3 as 3-d plots and reveal that for small up to intermediate field values, the internal energy either remains unchanged or shows a small decrease but beyond a value of α_{xx} approximately equal to 0.15 and a value of α_{xy} approximately equal to 0.2 decreases abruptly (Figure 3A). A qualitatively similar behavior is observed for the entropy function S (Figure 3B), except for the highest fields where S is seen to drop rapidly (actually more rapidly than the energy). The decrease of S manifests the significant reduction in the number of allowed system configurations due to large chain stretching and orientation (accompanying the application of the flow). Finally, the sum of energy and entropy which defines the Helmholtz free energy of the system is seen to increase as the strength of the applied field is increased (Figure 3C), but rather smoothly, i.e., not as abruptly as is separately observed for the (decrease in) energy and entropy.

A few additional points are in order here:

(a) We evaluated numerically the Helmholtz free energy function at the various state points following different thermodynamic paths and we always obtained the same result.

(b) One can show analytically that expressions for the Helmholtz free energy function underlying the most widely used conformation-tensor viscoelastic models (e.g., the upper-convected Maxwell, the Giesekus, the finite-extensible nonlinear elastic, the Leonov, etc.) satisfy the Maxwell relations. In fact, the proof covers all models whose Helmholtz free energy is expressible in terms of the three invariants of the conformation tensor (i.e., tr(**c**), tr(**c** · **c**), and det(**c**), where "tr" and "det" denotes the trace and determinant, respectively). No such assumption was made in the present work: we addressed the problem to its full generality and showed that the Maxwell relations are a more general property. As a result, one can use Maxwell's relations in order to admit or not new rheological models built on the concept of the conformation tensor.

(c) Although only the xx and yy components of the tensor $\boldsymbol{\alpha}$ were taken to be nonzero (for simplicity), the general conclusions drawn from our computations are valid for any other type of flow.

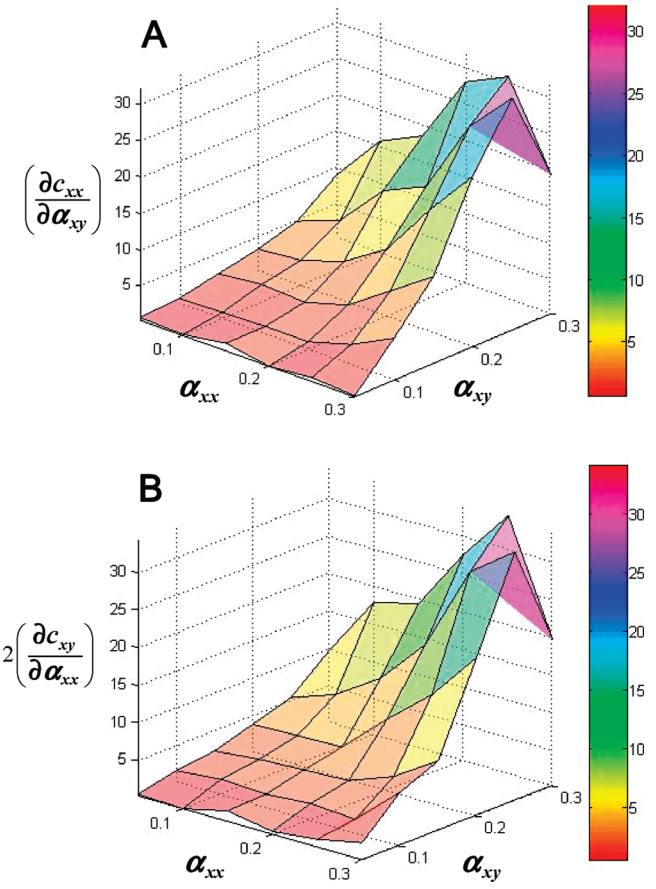


Figure 2. Three-dimensional representations of the thermodynamic derivatives (A) $\partial c_{xx}/\partial\alpha_{xy}$ and (B) $\partial c_{xy}/\partial\alpha_{xx}$), as a function of field strength.

By nature, polymer molecules possess an enormous number of configurational degrees of freedom at the atomistic level. Thus, entropic contributions should dominate their response to an externally applied flow field relative to energetic ones, especially for truly long molecules. We can therefore assume that the entropy function is separable into an equilibrium part S_0 (corresponding to $\boldsymbol{\alpha} = \mathbf{0}$ or, equivalently, to $\mathbf{c} = \mathbf{I}$) and a configurational part S_{config} accounting for flow effects; and thus to rewrite eq 6 as

$$dE = T\,dS_0 + T\,dS_{config} - P\,dV + \mu\,dN_{ch} + k_B T\boldsymbol{\alpha} : d(N_{ch}\mathbf{c}) \tag{16}$$

We can even go one step further and completely neglect the energy change during deformation; i.e., we can set $E = E_0$ in eq 16 or, equivalently, $E_{config} = 0$ (this is what is customarily assumed in typical viscoelastic models) at fixed values of temperature and density. Then eq 16 leads to

$$T\,dS_{config} = -k_B T\boldsymbol{\alpha} : d(N_{ch}\mathbf{c}) \tag{17}$$

implying that

$$S_{config} = -N_{ch}k_B\boldsymbol{\alpha} : \mathbf{c} \tag{18}$$

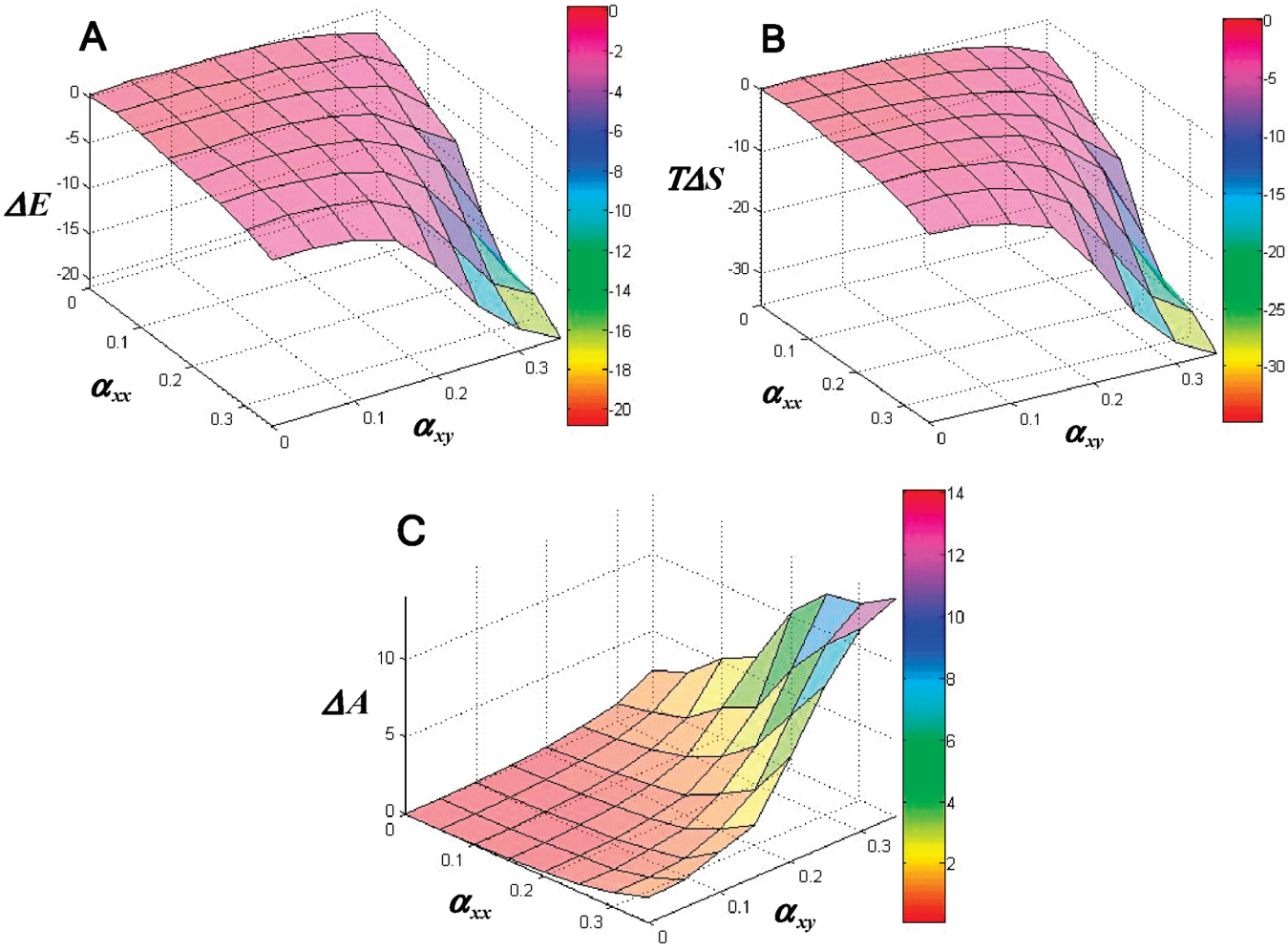


Figure 3. Three-dimensional plots of the fundamental nonequilibrium thermodynamic functions (relative to equilibrium) vs field strength: (A) the internal energy U, (B) the entropy multiplied by temperature TS, and (C) the Helmholtz free energy A.

This expression sheds some extra light on the principles underlying eqs 6 and 7, since it makes the connection with models (e.g., transient network models) based on the theory of purely entropic polymer elasticity. Conversely, one can arrive at eqs 6 and 7 starting from a proposition for the configuational entropy of the form of eq 18. In fact, GENERIC MC simulations of the type presented here can be used[35,43] to quantify the relative magnitude of enthalpic and entropic contributions to the Helmholtz free energy of deformation for short PE melts. For the system addressed here, a $C_{78}H_{158}$ PE melt, the results are shown in Figure 3 clearly demonstrating that energetic contributions to the free energy of deformation are as significant as entropic ones. In fact, by computing the changes in the different components of the total potential energy due to flow,[43] one can see that for the simulated system the ones that are mostly responsible for its decrease are the nonbonded intermolecular Lennard-Jones interactions (a direct consequence of the tendency of chains to orient with the flow, which enhances attractive lateral interactions) and the interactions associated with torsional angles (due to enhancement of *trans* conformational states, as chains tend to unravel and assume rather elongated shapes at high deformations).

4. Discussion and Outlook

We have shown how one can employ detailed atomistic MC simulations in an expanded ensemble to accurately calculate important thermodynamic functions (such as the entropy and its derivatives) for systems away from equilibrium and deeply in the nonlinear regime. We have also demonstrated the internal consistency of these calculations through a computation of the corresponding Maxwell equations for the nonequilibrium variables. In fact, in extended irreversible thermodynamics[12,30] where the thermodynamic fluxes are also taken as independent state variables in the extended Gibbs equation (eqs 4 and 5), the corresponding conjugate fields are usually assumed to be proportional to the thermodynamic fluxes (in order for the formalism to automatically satisfy the second law of thermodynamics); in this case, the Maxwell relations are automatically satisfied. In the present GENERIC MC methodology, however, based on the extended thermodynamic formulation prescribed by eqs 6−11, we have not made any such assumption about the relationship between forces and fluxes as a function of the field strength. This further indicates that thermodynamic integration works quite well in practice even in the highly nonlinear regime thereby allowing one to calculate the entropy and other thermodynamic functions for a nonequilibrium system. We also note that our GENERIC MC-based approach of estimating the entropy change accompanying the deformation of polymeric liquids, which relies on the judicious choice of a few state variables describing the conformation of polymer chains beyond equilibrium in an overall sense, is more advantageous over direct statistical methods[44,45] because of its simplicity and computational efficiency.

Our methodology for confirming Maxwell's equations and the results obtained here refer to the family of systems known as unentangled polymer melts. But the general principles carry on to other polymeric fluids as well. For example, our work is of relevance to entangled polymers where one can resort to a

description either in terms of the conformation tensor for the entanglement strands in the topological network underlying their atomistic structure or in terms of the orientational distribution function $f(\mathbf{u},s)$ representing the probability that the tangent vector $\mathbf{u}$ at segment s along the reduced primitive path of a given chain is $\mathbf{u}$ within d$\mathbf{u}$ (inspired by Doi−Edwards' perspective). It is also applicable to block copolymers and self-assembled systems, as long as the selected structural variables are capable of describing morphology (e.g., lamellae, perforated layers, etc.) at the nanoscale. Guided by experimental observations and field theoretical approaches to the problem,[46] proper candidate variables here could be the volume fraction for each block component and a set of (scalar or tensorial) parameters capturing ordering (pattern formation) at long length scales.

In general, we could say that our results for the generalized Gibbs equation (eqs 4 and 5) *are of relevance to any system* (and not just to polymeric fluids) as long as a proper set of state variables has been chosen. In contrast, if an improper choice of structural variable(s) is made, the obtained numerical results may either be not useful or bear no meaning. To appreciate the value of the proper choice of state variables, we can consider an interesting problem often encountered in viscoelastic constitutive modeling when one attempts a jump in the system description from the level of the distribution function to the level of the tensor $\mathbf{c}$: closed-form nonequilibrium equations cannot be derived without additional "closure" approximations for polymers under nonequilibrium conditions.[47] Rigorously, the evolution equation for $\mathbf{c}$ in the case of nonlinear elastic models is obtained from the diffusion equation for the distribution function through some preaveraging procedure. The same (or a very similar) equation can practically be obtained by working directly at the level of $\mathbf{c}$ by assuming a particular functional form for the free energy in terms of this variable. The choice is dictated by the available closed-form evolution equation from kinetic theory. The present work justifies our search for a nonequilibrium thermodynamic potential function that can match the evolution equations as derived from the two descriptions. That is, it justifies the strategy to adopt certain closure approximations either at the beginning (nonequilibrium thermodynamics approach) or at the end (kinetic theory approach). Of course, one can even go one step further and ask if, based solely on principles of nonequilibrium thermodynamics, one could guess (somewhat) the exact form of this potential. Unfortunately, the answer is "no": although thermodynamics (especially the second law) puts certain restrictions on the allowed form of this potential, the admissible solutions are too many. The interested reader is referred to a recent work (ref 38) on this issue.

Acknowledgment. Support provided by the European Commission through the NANODIRECT (FP7-NMP-2007-SMALL-1, Code 213948) and MODIFY (FP7-NMP-2008-SMALL-2, Code 228320) research projects and the National Science Foundation (USA) under Grant No. CBET-0742679 through the resources of the PolyHub Virtual Organization is greatly acknowledged.

References and Notes

(1) Onsager, L. *Phys. Rev.* **1931**, *37*, 405. *38*, 2265.
(2) Casimir, H. B. G. *Rev. Mod. Phys.* **1945**, *17*, 343.
(3) Callen, H. B.; Greene, R. F. *Phys. Rev.* **1952**, *86*, 702.
(4) Kirkwood, J. G. *J. Chem. Phys.* **1946**, *14*, 180.
(5) Irving, J. H.; Kirkwood, J. G. *J. Chem. Phys.* **1950**, *18*, 817.
(6) Green, M. S. *J. Chem. Phys.* **1954**, *22*, 398.
(7) Kubo, R. *J. Phys. Soc.* (*Jpn.*) **1957**, *12*, 570.
(8) Mori, H. *Phys. Rev.* **1958**, *112*, 1829.
(9) Zwanzig, R. *Annu. Rev. Phys. Chem.* **1965**, *16*, 67.
(10) de Groot, S. R.; Mazur, P. *Non-equilibrium Thermodynamics*; North-Holland: Amsterdam, 1962.
(11) Bird, R. B.; Stewart, W. E.; Lightfoot, E. N. *Transport Phenomena*, 2nd ed.; John Wiley & Sons: New York, 2002.
(12) Jou, D.; Casas-Vázquez, J.; Lebon, G. *Rep. Prog. Phys.* **1988**, *51*, 1105.
(13) Kaufman, A. N. *Phys. Lett. A* **1984**, *100*, 419.
(14) Morrison, P. J. *Phys. Lett. A* **1984**, *100*, 423.
(15) Grmela, M. *Phys. Lett. A* **1984**, *102*, 355.
(16) Edwards, B. J.; Beris, A. N. *Ind. Eng. Chem. Res.* **1991**, *30*, 873.
(17) Beris, A. N.; Edwards, B. J. *Thermodynamics of Flowing Systems*; Oxford University Press: New York, 1994.
(18) Jongschaap, R. J. J. *Rep. Prog. Phys.* **1990**, *53*, 1.
(19) Jongschaap, R. J. J. *J. Non-Newtonian Fluid Mech.* **2001**, *96*, 63.
(20) Grmela, M.; Öttinger, H. C. *Phys. Rev. E* **1997**, *56*, 6620.
(21) Öttinger, H. C.; Grmela, M. *Phys. Rev. E* **1997**, *56*, 6633.
(22) Öttinger, H. C. *Beyond Equilibrium Thermodynamics*; John Wiley & Sons: NJ, 2005.
(23) Woods, L. C. *The Thermodynamics of Fluid Systems*; Oxford University Press: Oxford, U.K., 1975.
(24) Öttinger, H. C. *MRS Bull.* **2007**, *32*, 936.
(25) Öttinger, H. C. *Phys. Rev. E* **1998**, *57*, 1416.
(26) Grabert, H. *Projection Operator Techniques in Nonequilibrium Statistical Mechanics*; Springer: Berlin, 1982.
(27) Kubo, R.; Toda, M.; Hashitsume, N. *Statistical Physics, Nonequilibrium Statistical Mechanics*, 2nd ed.; Springer: Berlin, 1991; Vol. *II*.
(28) Ilg, P.; Öttinger, H. C.; Kröger, M. *Phys. Rev. E* **2009**, *79*, 011802.
(29) Edwards, B. J.; Öttinger, H. C.; Jongschaap, R. J. J. *J. Non-Equilib. Thermodyn.* **1997**, *22*, 356.
(30) Jou, D.; Casas-Vázquez, J. *J. Non-Newtonian Fluid Mech.* **2001**, *96*, 77.
(31) Pasquali, M.; Scriven, L. E. *J. Non-Newtonian Fluid Mech.* **2004**, *120*, 101.
(32) Holian, B. L.; Hoover, W. G.; Posch, H. A. *Phys. Rev. Lett.* **1987**, *59*, 10.
(33) Chernov, N. I.; Eyink, G. L.; Lebowitz, J. L.; Sinai, Y. G. *Phys. Rev. Lett.* **1993**, *70*, 2209.
(34) Tuckerman, M. E.; Mundy, C. J.; Klein, M. L. *Phys. Rev. Lett.* **1997**, *78*, 2042.
(35) Mavrantzas, V. G.; Theodorou, D. N. *Macromolecules* **1998**, *31*, 6310.
(36) Mavrantzas, V. G.; Öttinger, H. C. *Macromolecules* **2002**, *35*, 960.
(37) Baig, C.; Mavrantzas, V. G. *Phys. Rev. Lett.* **2007**, *99*, 257801.
(38) Baig, C.; Mavrantzas, V. G. *Phys. Rev. B* **2009**, *79*, 144302.
(39) Callen, H. B. *Thermodynamics and an Introduction to Thermostatistics*, 2nd ed.; John Wiley & Sons: New York, 1985.
(40) Pant, P. V. K.; Theodorou, D. N. *Macromolecules* **1995**, *28*, 7224.
(41) Daoulas, K.; Terzis, A. F.; Mavrantzas, V. G. *Macromolecules* **2003**, *36*, 6674.
(42) Mavrantzas, V. G.; Boone, T. D.; Zervopoulou, E.; Theodorou, D. N. *Macromolecules* **1999**, *32*, 5072.
(43) Ionescu, T. C.; Edwards, B. J.; Keffer, D. J.; Mavrantzas, V. G. *J. Rheol.* **2008**, *52*, 567.
(44) Wu, D.; Kofke, D. A. *J. Chem. Phys.* **2005**, *122*, 204104.
(45) Athènes, M.; Adjanor, G. *J. Chem. Phys.* **2008**, *129*, 024116.
(46) Larson, R. G. *The Structure and Rheology of Complex Fluids*; Oxford University Press: New York, 1999.
(47) Öttinger, H. C. *J. Rheol.* **2009**, *53*, 1285.

Macromolecules
ARTICLE

Macromolecules **2011**, *44*, 647–659 **647**
DOI: 10.1021/ma102041h

Time Marching Algorithm for Predicting the Linear Rheology of Monodisperse Comb Polymer Melts

Mostafa Ahmadi,[†,§] Christian Bailly,[†] Roland Keunings,[‡] Mehdi Nekoomanesh,[§] Hassan Arabi,[§] and Evelyne van Ruymbeke*[,†]

[†]*Bio and Soft Matter, Institute of Condensed Matter and Nano-science, Université Catholique de Louvain, Louvain-la-Neuve, Belgium,* [‡]*Louvain School of Engineering, ICTEAM Institute, Université Catholique de Louvain, Louvain-la-Neuve, Belgium, and* [§]*Polymerization Group, Engineering Department, Iran Polymer and Petrochemical Institute, Tehran, Iran*

Received September 2, 2010; Revised Manuscript Received December 10, 2010

ABSTRACT: We extend van Ruymbeke et al.'s time marching algorithm (TMA) (*Macromolecules* **2006**, *39*, 6248) in order to predict the linear viscoelastic properties of comb polymer melts. While former tube models have shown limitations for predicting the relaxation of comb polymer with short side branches, we observe here a good agreement between predictions and the experimental data for both combs with long and short side branches. In order to determine the origin of this improvement, we study the influence of the different elements present in the TMA model. In particular, we show the importance of taking into account the monomeric friction coming from the backbone itself in the total drag of the molecule, considering the modification of early time fluctuations and introducing the tube dilation process as a continuous function evolving through time. Then, based on a wide range of experimental data on different comb structures, we explore the limits of the relaxation behavior that comb polymers can show. If the friction from the relaxed side branches is significant, the backbone segments seem to fluctuate with respect to the closest branching point, just like a Cayley-tree molecule. On the other hand if the extra friction is negligible in comparison to the potential barrier of retraction along the backbone, the segments fluctuate with respect to the middle of the molecule, just like a linear chain.

I. Introduction

One of the important objectives of polymer rheology is to relate the microstructure of macromolecules to their macroscopic flow behavior. The original picture of stress relaxation in a tube defined by topological constraints from neighboring chains has yielded fundamental results in this direction.[1,2] In the framework of tube models, linear chains mainly relax their orientation by curvilinear diffusion along the confining tube. This is called reptation. However, reptation is unlikely for stars due to anchoring effect of the branching point. Stars have to relax their orientation by entropically unfavorable retraction along the tube toward the branching point,[3−5] which is called fluctuations. When relaxation by fluctuations spans a wide time scale, relaxed segments can be considered as solvent for oriented ones. They accelerate relaxation by reducing entanglement density, which is called dynamic tube dilation (DTD).[6,7] Combining the processes mentioned above enables quantitative predictions of experimental linear viscoelastic (LVE) properties for simple and even complex architectures.[8,9]

Tube-based models have now become mature enough to yield excellent LVE predictions for model architectures such as asymmetric star,[10,11] H-shaped,[12] pom-pom,[13,14] Cayley-tree,[15,16] "branch on branch"[17−19] macromolecules, and even supra-molecular structures.[20] The key concept is that complex molecules relax hierarchically in the framework of DTD.[17−22] In other words, stress relaxation starts from the outer parts such as the free ends of dangling branches and ends up at the most constrained inner parts of the molecule. The relaxed outer parts yield more friction for relaxation of inner segments while they make the tube dilated by acting as solvent according to the DTD picture.

*Corresponding author. E-mail: evelyne.vanruymbeke@uclouvain.be.

On the basis of the success of the hierarchical relaxation concept for predicting the relaxation of H-shaped and pom-pom polymers, application of this idea to comb structures has been the subject of several publications.[23−29] A model comb chain consists of a linear backbone with randomly distributed branches of equal length. Stress relaxation starts by retraction of the branches and backbone free ends, generating a star-like signature at high frequencies. This is followed by slow fluctuations of the oriented backbone along a dilated tube, subject to the extra friction from relaxed branches. As the final relaxation process, reptation of the backbone can occur.[21] This model has been applied to different classes of lightly and heavily branched combs by Daniels et al.[23] The input parameters of their model belong to three categories: (i) the chemistry dependent parameters, i.e. the entanglement molecular weight, M_e, the plateau modulus, G_N^0, and characteristic Rouse time of an entanglement, τ_e; (ii) the tube model parameters, i.e., the dilution exponent, α and the branch point hopping fraction, p^2; (iii) the structural parameters, i.e., the backbone length, the length and the number of branches. In order to obtain good predictions when keeping the fundamental tube parameters α and p^2 constant, Daniels et al. had to make minor adjustments of the chemistry dependent parameters and to fit the structural parameters. Inkson et al. have used a modified version of this model to describe rheology of monodisperse polybutadiene combs and managed to explain the complexity of experimentally determined zero-shear rate viscosity of various polyethylene combs.[24]

The model developed by Kapnistos et al. by minor modification of the previous models can successfully predict the LVE behavior of combs with long branches but shows shortcomings in the case of combs with short, i.e., unentangled or barely entangled, branches.[25] The same model was recently used by Kirkwood et al., who confirmed that it cannot correctly predict the behavior of

© 2011 American Chemical Society
Published on Web 01/10/2011

combs with short branches, yielding the suggestion that such branches cause more drag than expected from tube models.[28] This idea is further supported by two additional findings: (i) the unreasonably low branch hopping fraction parameter p^2 that must be used for asymmetric stars with a short third arm, as found by Frischknecht et al.[11] and (ii) coarse-grained simulations of branch point motion in asymmetric stars by Zhou and Larson.[30] Recent neutron spin echo spectroscopy measurements of branch point motion of similar asymmetric stars published by Zamponi et al. also show that the branch point is immobile on the time scale of the experiment while the traditional tube models predict unentangled short arms should be able to move along the tube made by the two long arms at that time scale.[31]

Recently, the time marching algorithm (TMA) developed by van Ruymbeke et al. has been successfully applied to a wide range of macromolecular architectures, namely, asymmetric stars, H-shaped, pom-pom, Cayley-tree and has been extended to supra-molecular structures.[13−17,32] The TMA model is based on the same mesoscopic description of relaxation mechanisms as traditional tube-based models. However, as opposed to the latter, it follows the relaxation of molecules on a discretized time axis and can thus handle all interrelated events simultaneously, such as reptation, fluctuations, constraint release Rouse motion, and dynamic tube dilation, without the need for an artificial separation of time scales. DTD can be considered conveniently using an extended Graessley criterion. Moreover, there is no need to fit an additional branch point hopping fraction parameter p^2. Since the value of p^2 is uncertain, we prefer fixing it as equal to 1 in the TMA model. This simple approach has been shown already to give excellent results for a wide variety of architectures. The idea of removing time-scale separation between fluctuations and reptation mechanisms by use of product of these relaxation probabilities has been also successfully used by Pattamaprom et al. in the dual-constraint model.[33−35]

The objective of this paper is to extend the TMA model, including recent modifications,[36] to comb structures and confront the results to three published sets of rheological data on polystyrene (PS), polybutadiene (PBd) and polyisoperene (PI) combs.[25,28,29,37] The success of this comparison confirms the universal validity of the TMA model for complex architectures and its applicability to molecules with short dangling branches. One of our goals is to find out the origin of discrepancies between the predictions of former models and experimental LVE data on such systems.

Thus, the paper is organized as follows. Section II describes in detail the modifications of the TMA model needed to describe comb structures. Section III presents the results of the comparison between the model predictions and experimental data for three sets of polymers. Section IV provides some conclusions and perspectives.

II. Theory

Following a careful definition of the chosen segmental coordinate system for the comb architectures, we first describe the general structure of the model. Next, we detail all the relevant relaxation mechanisms for combs, i.e. branch fluctuations, backbone fluctuations and backbone reptation. The treatment of high frequency Rouse motions and early fluctuations is further described.

II.1. Definition of Coordinate System. As the segmental fluctuation times are exponentially dependent on the square of their depth and the unrelaxed fraction, the final predictions strongly depend on the detailed definition of branch and effective backbone segments. Here, we assume that q branches with the same mass M_a (see Figure 1.a, the bright lines) are uniformly distributed along the *real* backbone (i.e., as defined from the synthesis), which has a mass M_b (Figure 1a). Thus, we assume that each segment between two branching points or between a backbone extremity and the nearest branching point has a molecular weight $M_{segment}$ equal to $M_b/(q+1)$. However, in order to simplify the modeling, an *effective* backbone (*eb*) is used, as highlighted in Figure 1b, and which is defined as the longest end-to-end path of the molecule. Thus, it contains the inner part of the *real* backbone plus the longer branches fixed to the first and the last branching points (and with a mass $= \max(M_a, M_{segment})$). Using this backbone definition, two kinds of side branches (i.e., fixed on the effective backbone) must be defined (see Figure 1.b): $(q-2)$ branches with a molecular weight equal to M_a, and the two outer branches, fixed to the first and the last branching points, and which can be shorter than the other side-branches. Indeed, their molecular weight is equal to $M_{sb} = \min(M_a, M_{segment})$. Note that for comb polymers with only few short branches along the backbone, i.e with $M_a < M_{segment}$, these two outer short branches have the same length than the other side-branches ($M_a = M_{sb}$), which represents a particular case of the general definition proposed here. In addition to these two kinds of side-branches, the free ends of the *effective* backbone can also be seen as branches. Having a molecular weight equal to $\max(M_a, M_{segment})$, they are always longer or equal to the side-branches., and therefore, can be called "long branches". Using an effective backbone is motivated by the fact that the extra friction coming from the relaxed side branches is exponentially dependent on the branch length, so it is faster for the backbone to relax along the longer path in order to experience less extra friction coming from relaxed side branches.[25] The corresponding volumetric fractions of the effective backbone, the (normal) branches and the short branches are defined as

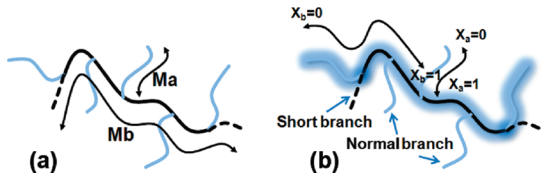


Figure 1. Definition of the coordinate system; (a) backbone's inner part (dark bold line), short branches, sb (dark dashed lines) and normal branches (bright lines) and (b) definition of the effective backbone, eb (highlighted), with $M_{eb} = (q-1)M_{segement} + 2\max(M_a, M_{segment})$.

$$\varphi_{eb} = ((q-1)M_{segment} + 2\max(M_a, M_{segment}))/(M_b + qM_a) \quad (1)$$

$$\varphi_a = (q-2)M_a/(M_b + qM_a) \quad (2)$$

$$\varphi_{sb} = 2M_{sb}/(M_b + qM_a) \quad (3)$$

where $M_{segment} = M_b/(q+1)$ is the molecular weight of the segment between two following branching points along the backbone.

In contrast with the traditional coordinate systems for the combs where the dimensionless position along the effective backbone, x_b, is zero at the first branching point,[23−25] here we specify the origin, $x_b = 0$, at the effective backbone's free ends and $x_b = 1$ at the middle of the molecule (Figure 1b). In the traditional approaches, reptation is only considered for the part of the backbone that is not relaxed by fluctuations. Therefore, the outer segments of the backbone, relaxed by fluctuations before reptation time, have no role in the final

reptation process.[23−25] In the TMA model instead, reptation and fluctuations are independent probabilities that are determined for all segments along the backbone and reptation is considered to occur in a tube of effective backbone length.[13,32] Note however that fluctuations will speed up the reptation process through Dynamic Tube Dilution concept (see eq 21), and that the terminal relaxation time of the molecules is determined from the combination of both processes (see eqs 4,5).[36] The dimensionless positions along short and long branches change from zero at the free end of the branches to one at the branching points as depicted in Figure 1.b.

II.2. TMA Model Overview. At times shorter than the characteristic Rouse time of an entanglement, chain dynamics are not affected by topological constraints and are instead governed by fast Rouse modes. At longer times, segments are prevented from lateral motions and the concept of tube becomes relevant. The outermost segments of the backbone and branches start relaxing their orientation by fluctuations, like the arms of a star, while the frozen branching points hold the inner backbone segments oriented. For segments with a potential barrier less than thermal energy ($U < kT$), fluctuations follow the unconstrained Rouse mechanism while deeper segments are slowed down and become activated by the entropic barrier. Since the fluctuation times of deeper segments are exponentially separated, contour length fluctuations can instantaneously take the advantage of extra solvent corresponding to relaxed segments, according to DTD. After complete relaxation of the side branches, the backbone is free to fluctuate in a dilated tube as a linear chain with extra friction blobs at branching points. Finally the effective backbone can reptate in a tube dilated according to the extended Graessley criterion[13] with friction coming from both the relaxed side branches and the monomeric friction of backbone segments.

The relaxation modulus of a monodisperse polymer melt is generally described by three terms representing the relaxation of the polymer from its equilibrium state by reptation or fluctuations ($\mathbf{\Phi}(t)$), constraint release ($\mathbf{\Phi}_{CRR}(t)$), longitudinal Rouse modes and finally the unconstrained fast Rouse motions inside the tube:

$$G(t)/G_N^0 = \Phi(t)\Phi_{CRR}^{\alpha}(t) + F_{Rouse,\,longitudinal}(t) + F_{Rouse,\,fast}(t) \quad (4)$$

where $\Phi(t)$ is the global survival probability from reptation and fluctuations and represents the unrelaxed fraction of the initial tube segments, while $\Phi_{CRR}(t)$ determines the effective tube diameter by taking into account the constraint release Rouse motion (CRR). The survival probability $\Phi(t)$ can be calculated by summing up the contributions from all segments along the chain path that have survived by both reptation and fluctuations relaxation mechanisms:

$$\Phi(t) = \sum_i \varphi_i \int_0^1 (p_{rept}(x_i,t)p_{fluc}(x_i,t))\,\mathrm{d}x_i \quad i\text{: } eb, a, sb \quad (5)$$

where $p_{\mathrm{rept}}(x_i,t)$ and $p_{\mathrm{fluc}}(x_i,t)$ are the probabilities that segment x_i survives from relaxation by reptation and fluctuations, respectively, at time t, and φ_i is the volumetric fraction of part i of the molecule, either the effective backbone (*eb*), branches (*a*) or short branches (*sb*).

According to the TMA model, the characteristic times corresponding to the different relaxation mechanisms are determined based on the unrelaxed polymer fraction at each time step, and the survival probabilities of the segments have to be updated in consequence. In this way the relaxation modulus, $G(t)$, is determined at each time step without using an explicit analytical function. The dynamic storage and loss moduli (G' and G''), can be derived from the relaxation modulus using Schwarzl approximation.[38] In the following sections, different elements of the TMA model used in this overview are explained in detail.

II.3. Branch Fluctuations. Contour length fluctuations are the only possible way for the dangling short and long branches of a comb to relax completely, following the same rules as fluctuations of the arms of a star:[8]

$$p_{fluc}(x,t) = \exp\left(\frac{-t}{\tau_{fluc}(x)}\right) \quad (6)$$

The early fluctuation times for segments with potential barrier less than thermal energy ($U < kT$) follow unconstrained Rouse motions:

$$\tau_{early}(x) = \frac{9\pi^3}{16}\tau_e x^4 Z^4 \quad (7)$$

where $Z = M/M_e$ is the number of entanglements of the branch. For deeper segments, retraction needs to overcome the potential penalty:

$$U(x) = \frac{3kT}{2Nb^2}(L_{eq}x)^2 + \mathrm{const} \quad (8)$$

$$\tau_{late}(x) = \tau_0 \exp\left(\frac{U(x)}{kT}\right) \quad (9)$$

where L_{eq} is the equilibrium length of the branch. Since characteristic fluctuation times of segments along a branch are well separated, we can consider the outer relaxed segments as solvent for the relaxation of inner segments. The first difference with the calculation of fluctuation times of the arms of a star is the presence of the frozen part of the backbone, which is considered in eq 10-2:

$$\frac{\partial[\ln \tau_{late}(x)]}{\partial x} = 3Zx\Phi(x)^{\alpha} \quad (10\text{-}1)$$

$$\Phi(x) = \varphi_{eb}(1-x_b) + \varphi_a(1-x_a) + \varphi_{sb}(1-x_{sb}) \quad (10\text{-}2)$$

The dimensionless positions x_{b}, x_{a}, and x_{sb} correspond to segments of the effective backbone, branches and short branches are related by potential equivalency as described by Milner, McLeish,[40] and Blottiere et al.:[41]

$$x_2 = x_1\sqrt{M_1/M_2} \quad (11)$$

where x_1 and x_2 are the corresponding transition segments on subchains with molecular weight of M_1 and M_2, respectively.

The transition between two fluctuations processes happens at a transition segment x_{trans}, for which the potential is equal to the thermal energy ($U(x_{trans}) = kT$). The TMA model uses a unique expression that guarantees the continuity of the fluctuation times curve at the transition segment:

$$\tau_{fluc}(x) = \tau_{early}(x) \quad \text{for } x < x_trans \quad (12\text{-}1)$$

$$\tau_{fluc}(x) = \tau_{early}(x_{trans})\exp\left(\frac{\Delta U(x_{trans} \rightarrow x)}{kT}\right) \quad \text{for } x > x_{trans} \quad (12\text{-}2)$$

II.4. Backbone Fluctuations. The free ends of the effective backbone fluctuate similarly as the branches of a star molecule as described in section II.3. Before complete relaxation of the short branch, the first branching point is frozen and

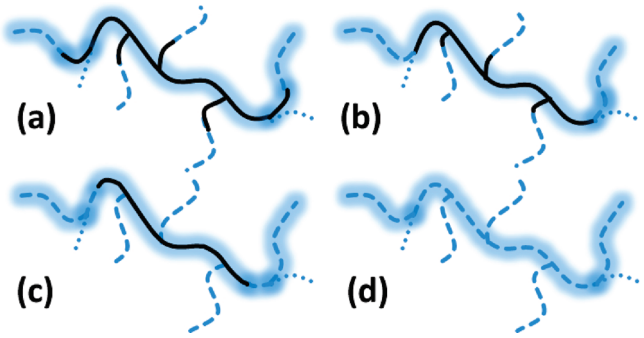


Figure 2. Schematic representation of fluctuations of a comb by triple fluctuations modes (TFM). The effective backbone is highlighted, short branches are represented by dotted curves, relaxed and unrelaxed segments are illustrated by dark bold and bright broken curves, respectively: (a) until the complete relaxation of the short branches, the outer segments of the backbone relax according to the first branching point (mode 1); (b and c) after relaxation of short branches but before long branches are fully relaxed, the outer segments of the backbone can fluctuate (b) first, according to mode 1 or mode 2 (i.e., the second branching point) and (c) then only according to mode 2; (d) after relaxation of long branches, the backbone fluctuates according to mode 3.

the inner segments of the backbone cannot fluctuate. The outermost segments of the free ends can only fluctuate with respect to the first branching point, i.e., they can only fluctuate in "first mode". After complete relaxation of the short branches (see Figure 2a), the remaining oriented segments of the free backbone's ends can also fluctuate with respect to the second branching point, i.e., according to the "second mode". Fluctuations by the first mode (i.e., according to the first branching point) suffer from more potential penalty since the free end has reach deeper fluctuations levels, i.e. to squeeze its length more toward the branching point, but only experience monomeric friction. On the other hand, fluctuations by the second mode suffer from more friction coming from the relaxed short branch but only need shallower fluctuations. So, after relaxation of the short branches, the segments between the relaxed part of the backbone and the first branching point are allowed to fluctuate by either first or second fluctuations modes and we expect that the segments will relax by the faster option. This mechanism corresponds to the transition from Figure 2a to Figure 2b.

Going toward deeper segments along the backbone, there comes a point when relaxation has reached the first branching point but not yet the second branching point. At this stage, the effective backbone can only relax by fluctuations with respect to the second branching point (since the first mode is exhausted and, due to the immobility of branching points of the side- branches, fluctuations with respect to the inner branching points are still impossible). This corresponds to the transition from Figure 2b to Figure 2c. (Note that in the specific case of a comb polymer with few short side-branches (and thus with $M_a = M_{sb}$), this step does not exist, since the short and "normal" side-branches are relaxed simultaneously.)

Later still, after complete relaxation of all the side-branches, all branching points become mobile at once and the backbone can fluctuate in a dilated tube. In most of the former tube models proposed for comb architecture, fluctuations of the backbone exclusively happen with respect to the middle of the molecule.[23−25] In our new model, backbone segments are free to fluctuate with respect to all branching points. Note that a similar idea has been proposed in ref 17 for branch-on-branch structures, without, however, looking at the influence of this statement on the relaxation of the comb polymer. Fluctuations with respect to closer branching points have the advantage of carrying less extra friction from relaxed side branches. On the other hand, fluctuations with respect to the middle of the molecule have the advantage of suffering from less potential penalty. This effect has not been tested yet on comb polymers and we think it could be very important. As will be shown later, fluctuations with respect to the middle of the molecule are favored when the extra friction coming from the side branches is negligible, but fluctuations with respect to the closest branching point are more likely when the relaxed branches provide a drag that outweighs the monomeric friction along the fluctuating part of the backbone. The difference between the predictions with and without considering this effect becomes very significant when stepwise fluctuations are favored due to significant friction of relaxed long side branches. We call this new relaxation possibility the multifluctuations-modes (MFM) relaxation. In this approach, the probabilities of fluctuating with respect to all branching points have to be calculated and the segment is considered relaxing according to the fastest mode. Keeping in mind that the extra friction affects the early time fluctuations through τ_e, we have to adjust the total friction for each fluctuations mode:[13]

$$\xi_{tot} = N_i\xi_0 + \frac{2kT}{a^2}\left(\tau_{fluc,sb}(1) + (i-2)\tau_{fluc,a}(1)\right) \qquad (13)$$

where ξ_0 is the monomeric friction coefficient, the first term on the right side accounts for the drag due to the monomeric friction of the effective backbone segments involved in mode i, and the second term is the contribution from the branches that have to be carried in that mode.

It is more convenient to divide the effective backbone into mobile (*meb*) and immobile (*imeb*) parts as follows:

$$\varphi_{eb}(1-x_b) = \varphi_{imeb} + \varphi_{meb}(1-x_{mb}) \qquad (14)$$

where x_{mb}, the dimensionless position along the mobile part of the effective backbone, changes from zero at the free end of the backbone to one at the frozen branch point at each fluctuation mode. The corresponding volume fractions correspond to the first fluctuation mode are defined as:

$$\varphi_{meb} = 2\max(M_a, M_{segment})/(M_b + qM_a) \qquad (15\text{-}1)$$

$$\varphi_{imeb} = (q-1)M_{segment}/(M_b + qM_a) \qquad (16\text{-}1)$$

Before complete relaxation of the short branch, the first branching point is frozen and the mobile part of the backbone is limited to the free ends of the effective backbone. Therefore, the dimensionless position x_{mb} changes from zero at the free end of the effective backbone to one at the first branching point. After relaxation of the short branch, the first branching point is no longer frozen and the mobile part of the backbone, which corresponds to the next fluctuations mode, will increase by $M_{segment}$ (Figure 2, parts a and b). The dimensionless position x_{mb} now changes from 0 at the free end of the effective backbone to 1 at the second branching point. The remaining oriented part of the outermost backbone segments can therefore feel a new environment where the potential equivalency (eq 11) should now be updated by taking into account the longer mobile part of the effective backbone. As a consequence, when the side-branches are relaxed up to the branching points, the relaxed part of the backbone can be longer than $\max(M_a, M_{segment})$ (Figure 2.c), according to eq 11.

If the backbone can relax by reptation, it will be the final step of the relaxation process. Hence we can neglect the effect of the solvent coming from relaxation by reptation on fluctuation times and late fluctuation times can be calculated according to eqs 7−14, except for the volume fraction of

mobile and immobile parts of the effective backbone that should be updated at each fluctuations mode. It should also be noted that the dimensionless position for fluctuations mode i varies between zero at the free end of the effective backbone to one at the ith branching point:

$$\varphi_{meb} = (2 \quad \max(M_a, M_{segment}) + 2(i-1)M_{segment})/(M_b + qM_a) \tag{15-2}$$

$$\varphi_{imeb} = (q + 1 - 2i)M_{segment}/(M_b + qM_a) \tag{16-2}$$

As a simpler approach to describe fluctuations of the effective backbone after relaxation of all side branches, we can consider that all inner backbone segments only fluctuate with respect to the middle of the molecule. This approach, which involves just three fluctuations modes (with respect to first branching point, second branching point and middle of the molecule), is a simplified MFM approach where all inner backbone segments fluctuate in the last mode. Figure 2d shows the last step of fluctuations according to this triple-fluctuations-modes (TFM) approach.

As discussed by van Ruymbeke et al.[13] for the case of a pom-pom molecule, the transition between two successive fluctuations modes may lead to discontinuity of fluctuation times at the branching points. Indeed, in reality, fluctuation of the backbone chain ends is a superposition of several relaxation modes, from the fast relaxation modes at the chain extremities (which have low friction) to the slower relaxation modes toward the backbone center (which have higher friction). The fast fluctuations of the outer modes are still active when the internal modes become important, and these faster modes contribute to the relaxation of internal tube segments (speeding up their relaxation). Thus, a one-dimensional approximation to the relaxation based on a single internal mode (with friction summed over all side arms, and fluctuation coordinate x set to zero at the chain end) will overestimate the relaxation time. In order to account for this, we rescale the relaxation coordinate x so that the point $x = 0$ from which the retraction potential is calculated no longer corresponds to the chain end (but, rather, is a point internal to the backbone chain). For each mode, we fix the point $x = 0$ by requiring continuity of relaxation times across the branching points, rescaling the outer part of the effective backbone, between the free end and the last branching point at $\max(M_a, M_{segment})+(i-2)M_{segment}$. In such a way, the fluctuation time of the segment right before the $(i-1)$th branching point in mode $i-1$, is equal to the fluctuation time of the segment right after that branching point, in mode i:[13]

$$\tau^{i}_{fluc}(x_{br.point}) = \tau^{i-1}_{fluc}(1) \tag{17}$$

$$x_{br.point} = \frac{M_n}{M_n + M_{segment}} \tag{18}$$

where M_n is the rescaled length of the outer part of the backbone in mode i. In other words, the length of the mobile part of the equivalent backbone would be $M_n+M_{segment}$. Therefore, it takes a time equal to $\tau_{fluc}{}^{i-1}(1)$ for the free end of the effective backbone of the equivalent comb molecule to diffuse up to the last branching point in mode i, while feeling the total friction according to eq 13, as explained in details in ref 13. In this new coordinate system, the dimensionless position $x_{b,rescaled}$ varies from zero at the free end of the rescaled effective backbone to one at ith branching point.

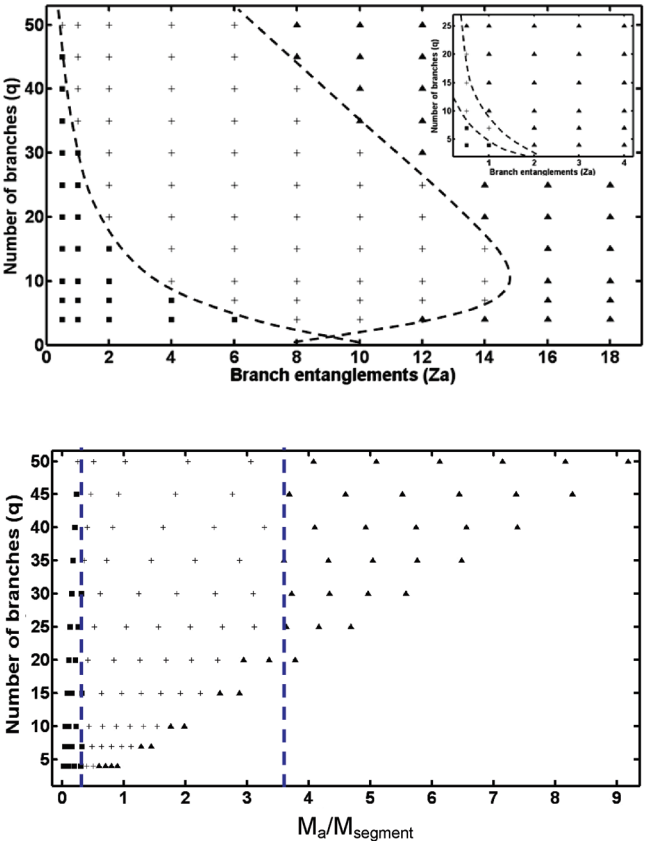


Figure 3. Contour plot of fluctuations behavior of combs with 100 and 20 (inset) numbers of backbone entanglements as a function of (a) the number of branch entanglements or (b) the ratio between M_a and $M_{segment}$: linear-like fluctuations, where there is no rescaling (squares), intermediate zone, where the number of rescaling is less than the number of modes (crosses), and fully hierarchical fluctuations, where the number of rescaling is equal to the number of modes (triangles). Lines are for guiding the eye.

For calculating the corresponding fluctuation times in the rescaled coordinate, x_b should be replaced by $x_{b,rescaled}$:

$$x_{b,rescaled} = [x_b(\max(M_a, M_{segment}) + (i-1)M_{segment}) - (i-2)M_{segment} + M_n - \max(M_a, M_{segment})]/[M_n + M_{segment}] \tag{19}$$

In this way, a continuous fluctuation times curve can be obtained for both the MFM and TFM approaches.

Superiority of the stepwise hierarchical fluctuations idea, as considered in MFM approach, versus the simple picture of fluctuations with respect to the middle of the molecule, as assumed in former tube models for combs, depends on the detailed structure of the comb. There are a lot of structural variations possible for combs, leading to numerous classes of relaxation behavior and it is therefore a complex task to carry out a systematic sensitivity analysis for the dynamic behavior of combs as a function of structural variables. Here, we consider a limited set, corresponding to the range covered by the experimental data tested in this paper. Thus, we analyze the fluctuations of two series of combs, with 100 and 20 backbone entanglements, respectively. Figure 3 presents a contour plot of the regions characterized by linear-like, intermediate, and hierarchical behavior, as a function of number and length of branches, or as a function of the ratio between M_a and $M_{segment}$. There is a zone where combs fluctuate with respect to the middle of the molecule, at low

branch entanglement levels and low number of branches. Opposite, there is a zone where comb segments fluctuate with respect to the closest branching point, at high number of branches and high level of branch entanglements. In between, there is an intermediate region where outer backbone segments fluctuate with respect to the closest branching points and inner segments fluctuate with respect to the middle of the molecule. When plotted as a function of the ratio $M_a/M_{segment}$ (see Figure 3b), we observe an almost vertical transition between linear like fluctuations and the intermediate zone (around $M_a/M_{segment} = 0.4$). For combs with a large amount a branches ($q > 25$), a second transition appears around $M_a/M_{segment} = 3.5$, separating the intermediate region and the fully hierarchical fluctuations.

Figure 3 highlights the finding that the linear like behavior is limited to a narrow range of comb structures and for most combs, partial to fully hierarchical fluctuations are the rule. In this case, a MFM approach is superior. Note that the BoB model[17] also considers different fluctuation modes, but in a different way than the one proposed here. In this model,[17] the contributions from the different branching points to the final fluctuation times of the backbone segments are considered separately rather than summing up their contributions as proposed in eq 13.

II.5. Backbone Reptation. The probability of relaxation by reptation at time t, for a segment of the effective backbone at position x, is calculated by the classical Doi−Edwards equation:[2]

$$p_{rept}(x,t) = \sum_{i,\,odd} \frac{4}{i\pi} \sin\left(\frac{i\pi x}{2}\right) \exp\left(\frac{-i^2 t}{\tau_{rept}}\right) \qquad (20)$$

The characteristic reptation time of a comb molecule is calculated by taking into account the contribution of the monomeric friction of the backbone segments and the extra friction coming from relaxed side branches, to the total drag:[11,13]

$$\tau_{rept} = 3\tau_e Z^3 \Phi^{\alpha}_{active}(t) + \frac{2}{\pi^2} Z^2 (2\tau_{fluc,\,sb}(1) + (q-2)\tau_{fluc,\,a}(1)) \Phi^{2\alpha}_{active}(t) \qquad (21)$$

where the first term represents the contribution of monomeric friction of the effective backbone segments and the second term corresponds to the contribution of relaxed short and long branches. If the characteristic times of fluctuations and reptation mechanisms were well separated, the reptation process can take the advantage of the fluctuations solvent and the backbone reptates in a fully dilated tube. Although, as the global effect of constraint release, the tube can dilate gradually by CRR motions, it also takes a while for the linear backbone to fill the dilated tube by lateral Rouse motions. In other words, the fast relaxing parts can be considered as solvent for relaxation of slow relaxing parts only if the oriented fraction has enough time to explore the dilated tube, which itself dilates at rate controlled by CRR process. Since fluctuation times of successive segments are exponentially separated, the relaxed parts have enough time to act as solvent for the fluctuations of oriented segments, and therefore DTD works. The problem arises when one has a system with different relaxation times that might be not well separated. This can be the case for complex architecture (including combs) or blends of different structures.[42−46] In the TMA model the rate at which the linear chain can take the advantage of the solvent is determined by the so-called extended Graessley criterion:[13]

$$\Phi_{active}(t) = \Phi(t/Z^2) \qquad (22)$$

In a classical case of binary blends of two monodisperse linear chains with widely separated molecular weights, after reptation of the short chains, it takes a time equal to $\tau_{dS} Z_L^2$ for the long chain to occupy the effective tube diameter. So if a solvent appears at time τ_{dS}, it takes $\tau_{dS} Z_L^2$ to be felt.[5] Conversely, for a chain to benefit from new solvent at time t, that solvent has to appear at time t/Z^2. The TMA model allows looking back through time space and updating the active solvent at each time step. The lag time between global survival probability and the "active solvents", i.e. the solvent truly effective in dilating the tube, guarantees the time required for the chain to fill the dilated tube by Rouse like lateral movements. Therefore, the reptation time is not a constant value and it evolves through time, parallel to the unrelaxed polymer fraction. The global effect of CRR process is to limit the maximum rate at which the entanglement density can decrease:

$$\Phi_{CRR}(t_i) \geq \Phi(t_{i-1}) \left(\frac{t_{i-1}}{t_i}\right)^{0.5} \qquad (23)$$

II.6. High Frequency Rouse Relaxation. The second and third terms of eq 4 are the longitudinal relaxation modes and fast Rouse motions inside the tube, which can be calculated as:

$$F_{Rouse,\,longitudinal}(t) = \sum_i \frac{\varphi_i}{4Z_i} \sum_{j=1}^{Z_i - 1} \exp\left(\frac{-j^2 t}{\tau_{Rouse,\,i}}\right) \quad i: eb, a, sb \qquad (24)$$

$$F_{Rouse,\,fast}(t) = \sum_i \frac{5\varphi_i}{4Z_i} \sum_{j=Z_i}^{N} \exp\left(\frac{-2j^2 t}{\tau_{Rouse,\,i}}\right) \quad i: eb, a, sb \qquad (25)$$

where N is the number of Kuhn segments and $\tau_{Rouse,i} = \tau_e Z_i^2$ is the Rouse time for different parts of the comb including the effective backbone and normal and short side branches.

II.7. Modification of Early Time Fluctuations. Recently, van Ruymbeke et al. have investigated the origin of discrepancies between measured values of plateau modulus and predictions from traditional tube models.[36] For poorly entangled chains, tube models predict that the storage modulus at a frequency equal to the inverse of Rouse time of an entanglement, $1/\tau_e$, is strongly molecular weight dependent.[47−50] Since at this time the entanglement obstacles cannot be felt, the equilibrium values should not depend on molecular weight. By investigating the fluctuation times of a moderately entangled linear polymer, they have noticed that a significant portion of the chains is predicted to relax before τ_e, which is inconsistent; i.e., a considerable fraction of polymer has relaxed from its equilibrium state, before even reaching to this state by longitudinal and fast Rouse motions. The problem arises because tube models usually consider relaxation by reptation or fluctuations to start immediately after deformation. In reality, the chain needs the characteristic Rouse time of an entanglement, in order to restore the equilibrium in the tube. Missing this point leads to underestimation of early fluctuation times of the chain. To overcome this problem van Ruymbeke et al. have proposed a rescaled segmental coordinate system, so that the predicted

fluctuation time at $x = 0$ is equal to τ_e:

$$\tau_{fluc}(x = 0) = \tau_{fluc}\left(x_{rescaled} = \frac{M^+}{M + M^+}\right) = \tau_e \quad (26)$$

where M^+ is the molecular weight of the segment added to the chain ends (close to half M_e), and M is half the molecular weight of a linear chain or the molecular weight of a branch.

For using the calculations in this new coordinate system, the dimensionless position along the actual chain, x, should be rescaled as follows:

$$x_{rescaled} = \frac{xM + M^+}{M + M^+} \quad (27)$$

The improvement for long chains will be negligible, but this correction becomes very important for weakly entangled chains. In particular, in the case of combs with a large number of small side branches, this modification is expected to play a significant role.

III. Results and Discussion

III.1. Materials and Parameters. In order to evaluate the capability of the TMA model to predict LVE properties of different classes of comb architectures, independent from their chemistry, the model was applied to experimentally available data from three references.[25,28,29] Molecular characteristics of all low polydispersity anionic samples used in this work are described in Table 1. The first samples consist of two series of PS combs named c6 and c7, comprising linear backbones of 275 and 860 kg/mol, respectively, and approximately $q = 25-30$ side branches of molecular weight increasing from 6.5 to 98 kg/mol, i.e., from almost half an entanglement up to six entanglements. The chemistry dependent parameters τ_e, M_e, and G_N^0 were respectively fixed to 0.6 to 1×10^{-3} s, 14 kg/mol, and 0.24 MPa at the reference temperature of 170 °C. Note that τ_e slightly depends on the samples architecture. This is not unreasonable as τ_e reflects the local dynamics, through monomeric friction and hence depends on the chemical structure (and of course temperature) as explained by Liu et al.[46] Such a structure dependence of τ_e has been previously reported in literature.[25] The next samples are three PBd combs consisting of 50 kg/mol linear backbone and including $q = 17-18$ side branches of various molecular weights between 7 and 23.2 kg/mol, which implies both backbone and branches are well-entangled. The corresponding material parameters are $\tau_e = 1$ to 1.5×10^{-6} s, $M_e = 1.65$ kg/mol, and $G_N^0 = 1.1$ MPa at reference temperature of 27.5 °C. These samples were synthesized by Roovers[37,39] and recently remeasured by Kapnistos et al.[25]

The next set of data consists of two series of PI combs, synthesized by Hadjichristidis and used by Kirkwood et al.[28] and Lee et al.[29] respectively. Altogether, those samples consist of linear backbones with molecular weights varying from 85 to 370 kg/mol and approximately $q = 4-18$ branches with molecular weights between 2.7 to 17.9 g/mol, i.e. from almost half an entanglement to about four entanglements. The corresponding material parameters used in this work are $\tau_e = 6 \times 10^{-6}$ s, $M_e = 3.9$ kg/mol, and $G_N^0 = 0.55$ MPa at reference temperature of 25 °C.

For all three polymers, the M_e vs G_N^0 relationship almost perfectly follows the "G" definition according to ref 51 and is in good agreement with previously reported values by Kapnistos et al.,[25] Liu et al.,[52] and Fetters et al.[53]

We use the value $\alpha = 1$ for the dilution exponent, consistently with our previous works.[13−17,46] Kapnistos et al. have found better predictions for combs with linear and star backbones in linear and nonlinear regimes using this value.[25,26,54] They have also shown that despite of using $\alpha = 1$, their model predictions for the ratio between the plateau modulus before and after relaxation of branches has the correct scaling with respect to the backbone volume fraction (approximate power 7/3).[25] As mentioned before, we have avoided the use of an adjustable branch point hopping fraction parameter p^2 by fixing its value to 1.

Table 1. Molecular Characteristics of the Combs Used

sample	$M_{backbone}$ (kg/mol)	M_a (kg/mol)	q (branches/backbone)	ref
PS-c712	860	6.5	31	25
PS-c722	860	11.7	30	25
PS-c732	860	25.7	25	25
PS-c742	860	47	29	25
PS-c752	860	98	29	25
PS-c612	275	6.5	30	25
PS-c622	275	11.7	28	25
PS-c632	275	25.7	26	25
PS-c642	275	47	29	25
PS-c652	275	98	28	25
PBd-lc1	50	11.3	18	25
PBd-lc2	50	23.2	17.8	25
PBd-lc3	50	7	17	25
PI-132k	85.1	10.2	4.6	28
PI-159k	137	2.7	8.2	28
PI-211k	157	6.3	8.6	28
PI-472k	370	5.8	17.6	28
PI−C14	151	17.9	5	29
PI−C15	90	9.2	4	29

III.2. General Relaxation Behavior of Comb Structures. Figure 4 compares the experimental dynamic moduli of some PS comb samples with longer backbone and various branch lengths, with the corresponding TMA model predictions. The depth of valley in the loss modulus at high frequencies corresponding to the dissipation due to fluctuations of the branches increases with increasing branch length, which is relatively well captured by the model predictions, taken into account the fact that the samples are considered monodisperse both in molecular weight and in architecture (which leads to a too strong and too narrow relaxation peak).[15] In particular, TMA works well for both combs with long and short side branches. Note that there are different elements that might be responsible for this improvement. The most straightforward explanation is that, as the length of side branches decreases (at the same total number of branches) the contribution to the total drag on the backbone from the relaxed branches becomes comparable with the monomeric friction from the backbone segments. Ignoring contribution of monomeric friction in such case would cause the prediction to diverge from the experimental behavior. Predictions made by ignoring monomeric friction of backbone segments are shown by dashed lines in Figure 4. This oversimplification leads to underestimation of the moduli, especially at low frequencies which correspond to the backbone terminal relaxation. However, it leaves intermediate frequencies, corresponding to the relaxation of branches, totally unchanged. Influence of monomeric friction of backbone segments becomes more pronounced as the length of branches decreases (also consider Figure 4b for sample PS-c712 with the shortest branches for this set of combs). Note that the predicted backbone reptation peaks are narrower and higher than the experimental features. This discrepancy is believed to be due to ignorance of samples polydispersity.[13,25] As explained by van Ruymbeke et al.[13] polydispersity smears out the relaxation peak. Because of the large influence of branch length on the motion of branching points and reptation of the backbone, dispersity of branch length

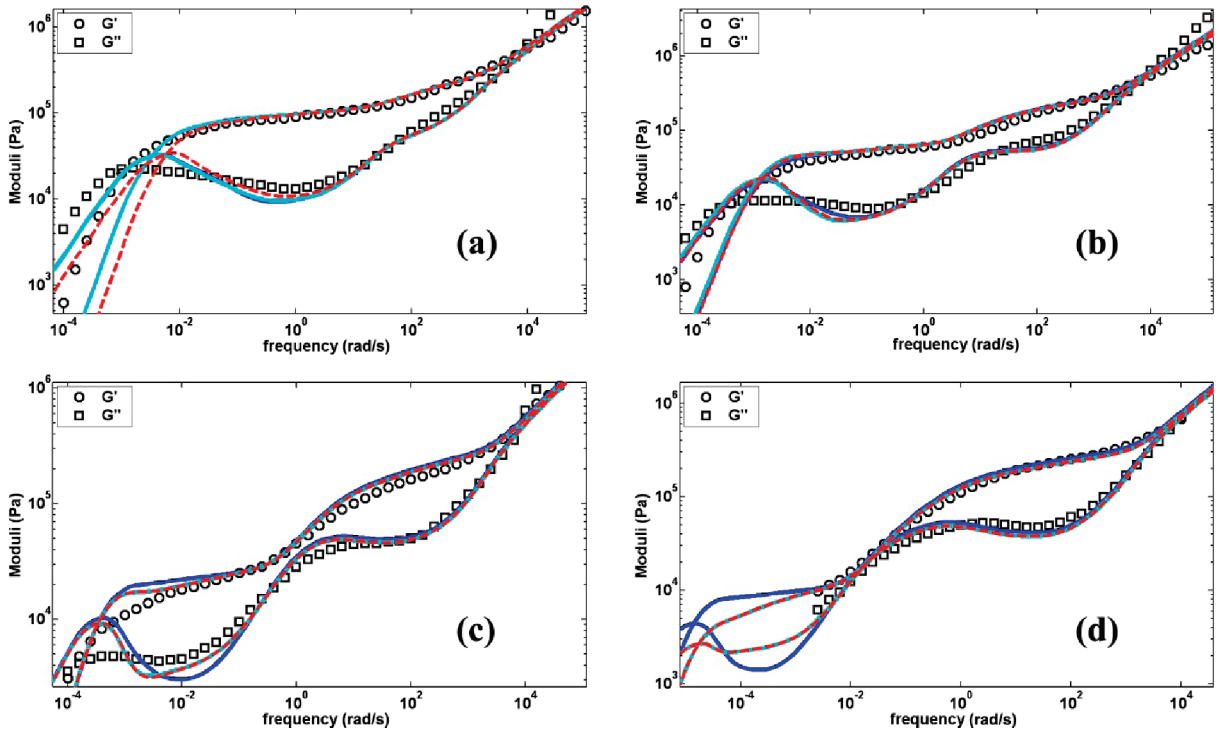


Figure 4. Experimental dynamic moduli (points) and TMA model predictions; MFM approach (bright lines), TFM approach (dark lines) or MFM approach without accounting for the monomeric friction of backbone segments (dashed lines), for PS-c7 comb samples: (a) PS-c722, (b) PS-c732, (c) PS-c742, and (d) PS-c752. Note that in part a, results obtained by considering the TFM approach or the MFM approach superimpose.

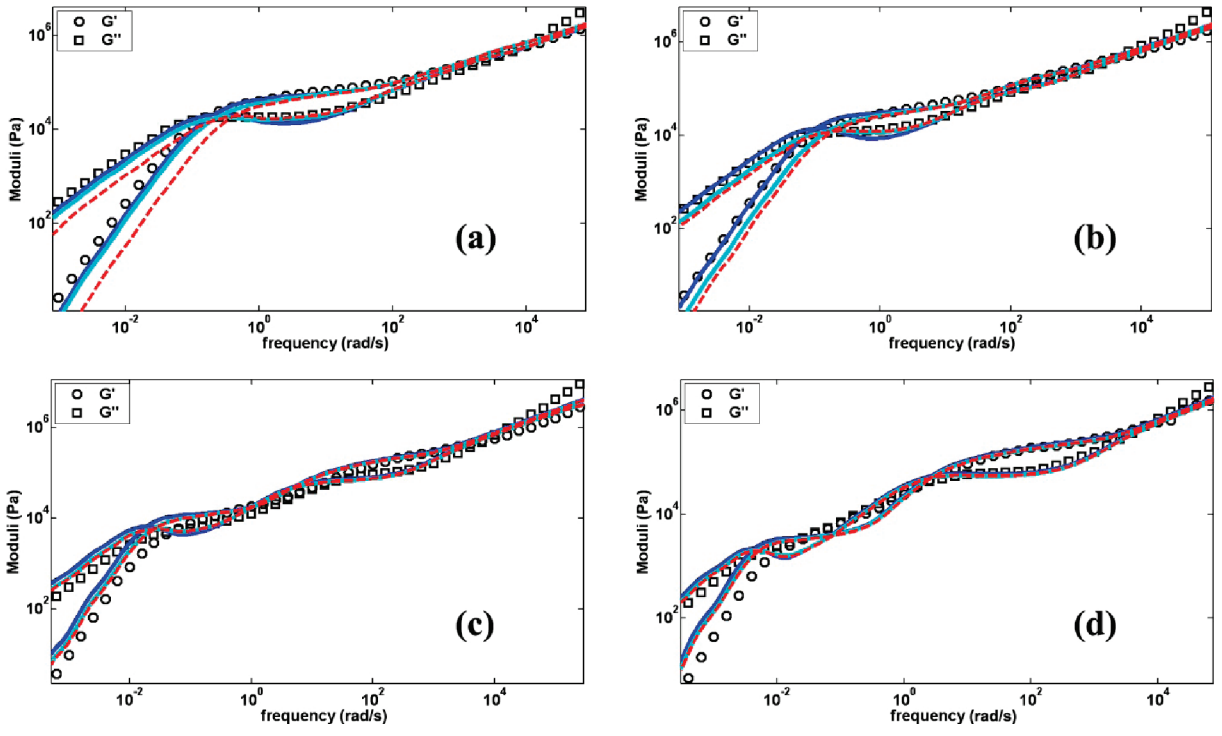


Figure 5. Experimental dynamic moduli (points) and TMA model predictions; MFM approach (bright lines), TFM approach (dark lines), or MFM approach without accounting for the monomeric friction of backbone segments (dashed lines) for PS-c6 comb samples: (a) PS-c612, (b) PS-c622, (c) PS-c632, and (d) PS-c642.

has a very significant effect. The effects of polydispersity will be discussed later in section III.4.

Figure 5 compares the experimental behavior of some selected PS comb samples with shorter backbone and various branch lengths, with the corresponding TMA model predictions. Again the model predictions properly capture the behavior of both combs with short and long branches. As the friction barrier due to the relaxed branches increases (due to increase of the branch lengths) the MFM predictions become superior as can also be seen in Figure 6d for sample PS-c652 having

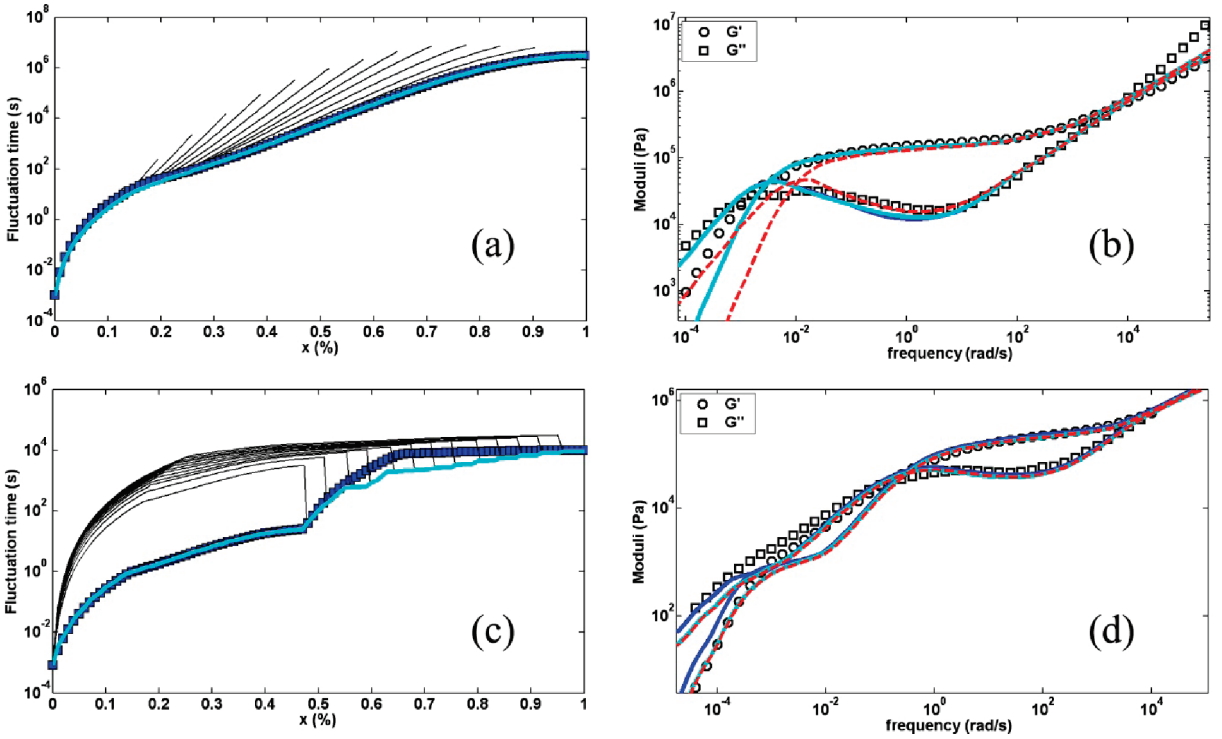


Figure 6. Fluctuation times of the effective backbone; different fluctuations modes (thin lines), MFM approach (bright lines), TFM approach (squares) [(a) PS-c712, (c) PS-c652] and corresponding LVE predictions [(b) PS-c712, (d) PS-c652], by considering the MFM approach (bright lines), the TFM approach (dark lines), or the MFM approach without considering the monomeric friction of backbone segments (dashed lines). Note that in part b, results obtained by MFM and TFM superimpose.

longest branches for this set. This is due to the fact that, when the backbone segment between two following branches becomes shorter and the length of side branches increases, the friction from relaxed branches outweighs the potential barrier and the segment prefers to retract toward closer branching points instead retracting with respect to ones farther, thus avoiding the price of carrying the friction of the relaxed branches. In other words, in the extreme case when the extra friction from side branches is very high, fluctuations take place step by step, just as in a Cayley-tree molecule where inner generations wait for the relaxation of outer generations. In the long-branch comb case, the inner backbone segments wait for full relaxation of outer segments of the backbone to start their fluctuations.[15,16] Considering a Cayley-tree-like behavior, the MFM approach provides the most precise predictions. On the other hand, when the side branches are so short that their contribution to the total friction becomes imperceptible, the backbone prefers to carry all the relaxed branches and take the advantage of a smaller potential barrier by fluctuating with respect to the middle of the molecule. In this extreme case where the comb simulates a linear chain behavior, the more simple TFM approach provides the same precise predictions as MFM, and due to lower calculation costs, it will be preferred. This ensures consistency of the model, which stays valid for extreme structures. Predictions obtained by ignoring the contribution of monomeric friction of backbone segments are again shown by dashed lines in Figure 5. In comparison to Figure 4, it is clear that the significance of monomeric friction is reduced for combs with shorter backbones.

Figure 6 shows model predictions and the corresponding backbone fluctuation times for two extreme cases of PS combs, already mentioned above. In sample PS-c712, the side branches are half an entanglement long and the length of backbone segments between branches is considerable. Hence, the potential barrier for retraction along the backbone is high and dominates the extra friction from short side branches. Figure 6a shows the corresponding relaxation times for all possible fluctuations modes as well as selected fluctuation times according to TFM and MFM approaches. In this specific case, the backbone segments relax faster with respect to the middle of the molecule than with respect to the next branching point. Therefore, the result of the MFM approach, which always considers the faster mode, is identical to the TFM approach, and no switch from one mode to another one is observed. Thus, for these short branches, segments prefer to fluctuate like a linear chain, with respect to the middle of the molecule, as this corresponds to the lowest potential barrier. Fluctuation times according to MFM merge with the predictions of TFM as extra friction from relaxed branches become negligible. Conversely, in sample PS-c652, side branches are longer than six entanglements and the backbone is shorter which implies exponentially higher extra friction and lower potential barrier at each mode. Figure 6c shows the corresponding backbone fluctuation times. Now, segments relax by fluctuations with respect to the closest branching point, which requires a rescaling of the outer part of the backbone in order to keep the continuity of the fluctuation times curve (see section II.4). In this case, fluctuations according to MFM are faster than according to TFM and the corresponding predictions of dynamic moduli are in better agreement. All PS combs of the c6 series with shorter backbones behave like Cayley-tree molecules and the importance of using MFM increases in relation to branch length. While sample PS-c712 thoroughly fluctuates like a linear chain, sample PS-C752 exhibits a pure Cayley-tree-like behavior. Some polymers like combs of the c7 series relax according to both mechanisms i.e. like a Cayley-tree molecule at the outer segments and like a linear chain at the inner parts of the backbone. Predictions of the model, ignoring contribution of

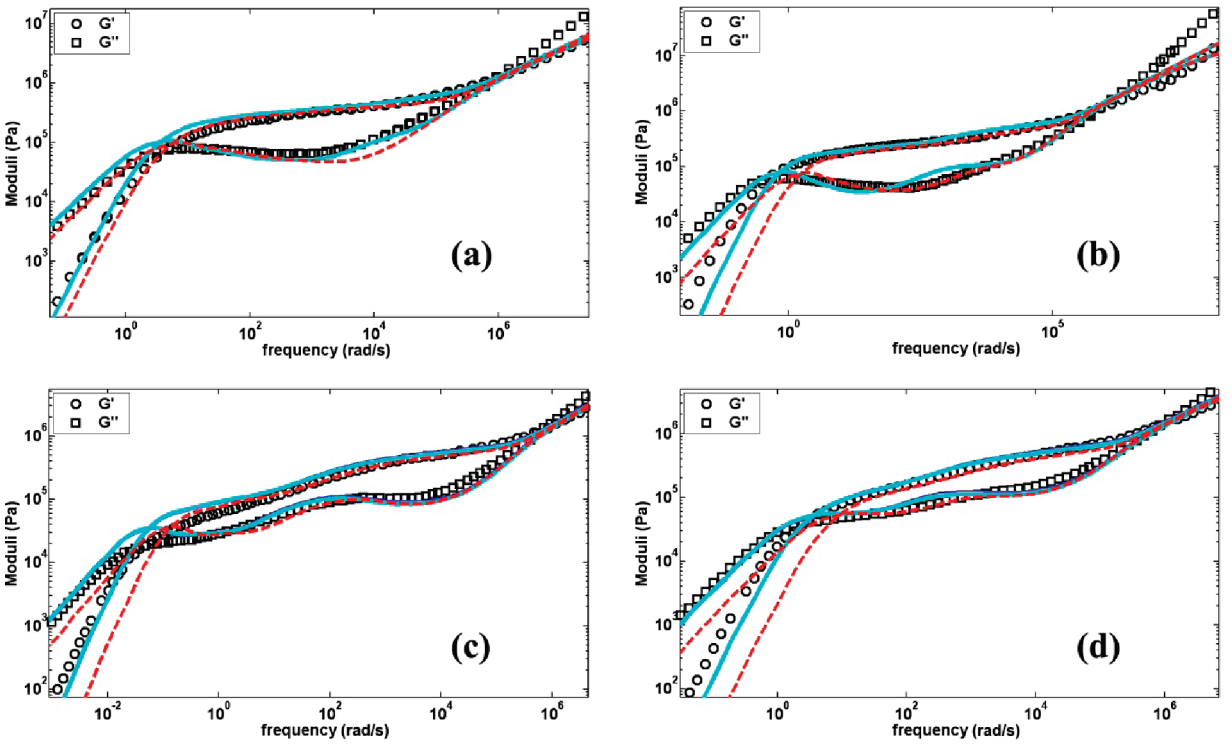


Figure 7. Experimental dynamic moduli (points) and TMA model predictions (lines); TFM approach (dark lines), MFM approach (bright lines), and without modification of early fluctuations (dashed lines), for PI comb samples: (a) PI-159, (b) PI-211, (c) PI-c14, and (d) PI-c15.

monomeric friction are shown by dashed lines, as well. It is apparent that while for combs with long branches, the contribution of monomeric friction to the total drag is negligible, it plays an important role for combs with short branches.

III.3. TMA Model and Extra Drag of Short Side Branches. Recently Kirkwood et al.[28] have used the tube model for combs from the work of Kapnistos et al.[25] in order to see whether it can predict the relaxation of PI combs with unentangled to marginally entangled branches. They found that the model considerably underpredicts the relaxation behavior of combs with shorter branches, leading to the idea that short branches cause more drag than what is expected from tube theories. A recent atomistic simulation by Zhou and Larson on asymmetric stars also suggests a stronger friction from short arms than anticipated.[30] The authors have suggested that the entanglement molecular weight on the time scale of τ_e is roughly half of M_e calculated from the plateau modulus, and this is why the short branches appear to be more effectively entangled. Starting from this proposal, Kirkwood et al. have amplified the corresponding friction by increasing the number of entanglements of side branches so that the model provides correct predictions. However, it can be argued that ignoring the contribution of monomeric friction to the total drag is one of the main missing points in existing models for combs and that it can cause such an underestimation. Nonetheless, neglect of monomeric friction cannot be the full origin of the anomalous drag from short branches, as the problem is still observed in systems that do not suffer from this oversimplification. Frischknecht et al.[11] have extended the original tube model of Milner and McLeish[8] to the case of asymmetric stars by considering the short arm causing extra drag that decreases the curvilinear diffusion rate of the linear backbone formed by the two long arms. The total drag on the reptating backbone is correctly obtained by adding the effective drag caused by the short arm to the drag from monomeric friction along the backbone. Nevertheless, the authors also find that progressively smaller values of p^2 are needed to capture the terminal relaxation behavior of asymmetric stars with lightly entangled branches, confirming that the short arm imposes a larger drag than expected. Recently, Zamponi et al. have used neutron spin echo spectroscopy to compare the motion of labeled branch points of two symmetric and asymmetric polyethylene stars, at the molecular scale.[31] They found that, although the applied tube model predicts that the branching point of the asymmetric star should be able to move along the tube formed by two long arms in the time frame of the observation, a short arm of only one entanglement length is sufficient to localize the branching point, similar to the case of a much longer arm in a symmetric star. This discrepancy between tube models and observed behavior of asymmetric stars should be even more pronounced in the case of combs with short branches. With this question in mind, we have applied the TMA model to available PI combs with unentangled to well entangled branches from different sources.[28,29]

Figure 7 shows the TMA model predictions for some selected PI combs from recent works of Kirkwood et al.[28] and Lee et al.[29] It is interesting that the model can capture the behavior of combs from different sources with the same chemistry dependent parameters. For combs with branches having more than two entanglements, the general behavior is Cayley-tree-like while for the other samples with unentangled to marginally entangled side branches the behavior varies from Cayley tree-like at the outer parts to linear chain-like at the most inner parts. There is no indication of anomalously high friction for the sample with the shortest branches of 2.7 kg/mol molecular weight (Figure 7a). The correct prediction by the TMA model for short branch combs with a standard value for side branch friction is partially due to inclusion of the monomeric friction of backbone segments in the model, but presumably also to the modification of early time fluctuations presented in section II.7. Rescaling of the coordinate system by addition of molecular weight of M^+ to the branches free ends, in order to have fluctuation time τ_e at the branch ends, definitely increases the

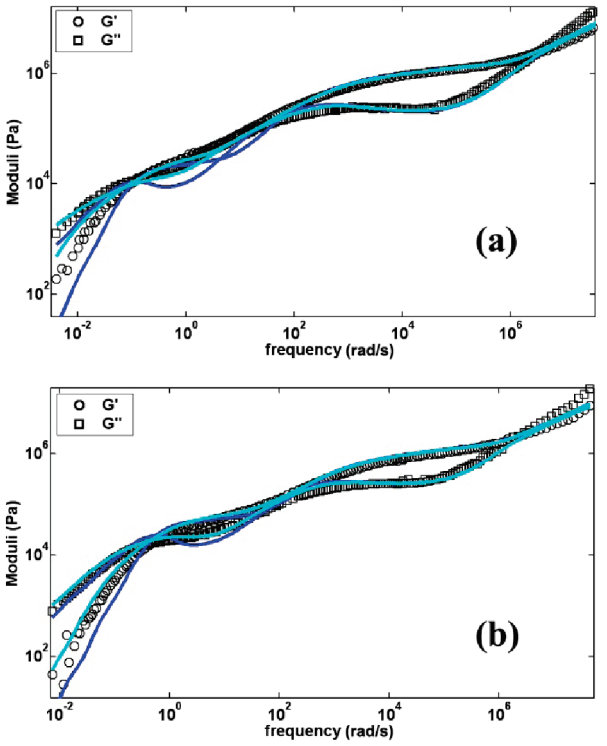


Figure 8. Experimental dynamic moduli (points) and TMA model predictions; MFM approach with (bright lines) and without (dark lines) incorporation of polydispersity effects; for PBd comb samples: (a) PBd-lc1; (b) PBd-lc3.

corresponding friction from relaxed side branches. The behavior of samples in absence of this modification was determined and the corresponding predictions are shown in Figure 7 by dashed lines. In contrast to the contribution of monomeric friction, it can be noticed that the early fluctuation time modification also affects the intermediate zone corresponding to the relaxation of side branches. It seems that this modification yields a remarkable improvement and is necessary for capturing the general behavior of all samples. As a consequence we can say that ignoring the required time to restore equilibrium in the tube before the start of relaxation mechanisms, as is the case in traditional tube models, can lead to the underestimation of the relaxation time of short branches and impose an artificial extra drag correction.

III.4. Effect of Polydispersity. Figure 8 shows the LVE properties of two of PBd combs with well-entangled branches and corresponding predictions. All samples studied here were anionically synthesized but although polydispersity is low, it can have a large influence on the relaxation spectrum, especially the distribution in length and number of side branches.[25] Moreover, most of commercial polymers are polydisperse and it is very important to incorporate this effect in the study of real polymers.[46] In order to handle polydispersity effect, an approach was introduced by Larson[18] for general branched structures and developed by Das et al.[17] to branch on branch polymers, where at each time step the relaxing segments of all model chains involved are determined.[17−19,21] Besides this method, two indirect ways of incorporating polydispersity have been utilized in literature. Kapnistos et al.[25] have used a simple weighted summation for incorporating different comb structures with each being treated independently. This method has the drawback of ignoring the mutual interaction of chains, which is very important for calculating dynamic dilution. Frischknecht et al. have adjusted the average arm relaxation time with respect to a Gaussian distribution of arm lengths.[11] Daniels et al.[23] and Inkson et al.[24] have also followed the same approach and used modified versions of this treatment. We believe both methods oversimplify the cooperative effect of chain dilution. However, in order to show the influence of polydispersity on the delay of the terminal zone and the broadening of the reptation hump, as a rough estimate, we follow the Kapnistos et al.'s approach. Three backbone lengths, M_b, three branch lengths, M_a, and three number of branches, q, are considered, so that each one is the representative of one-third of a Gaussian distribution.[13] The polydispersity indices of 1.1, 1.1, and 1.05 (as a reasonable "guesstimate" in the absence of experimental values) are used for the backbone length, branch length, and the number of branches, respectively. The overall behavior is calculated by averaging over 27 chains of different structural parameters and the results are shown as bright lines in Figure 8. Polydispersity broadens the spectrum of relaxation times with a shift of the mean value to higher times, which results in "smoothing out" terminal relaxation. The assumptions of random distribution of arms and of a fixed number of arms per comb have been already studied by Chambon et al. and it was shown that this simple analytical approach based on constant number of arms is valid.[27]

Note that, besides the polydispersity in molecular weight, architectural polydispersity (such as small variations in the number of branches per backbone, or in the branches distribution along the backbone) can also influence the linear viscoelastic of comb polymers, which is not discussed in this work.

III.5. Limitation of the Dynamic Tube Dilution concept. It is worth noting that the predictions of the TMA model for the polydisperse sample are very satisfactory and are obtained using $p^2 = 1$ and without manual determination of the extent of tube dilation. In fact there is a strong debate on applicability of DTD in cases where there is a second relaxation process that can take the advantage of solvent coming from the first process.[45,47] There is clear evidence in literature of DTD failure in the case of star and linear chain blends.[42−44] In the case of complex architectures where there might not be enough time separation between relaxation processes that follow each other in the framework of hierarchical relaxation, the same breakdown is suspected. Frischknecht et al. have analyzed the situation for the case of asymmetric stars.[11] They could capture the relaxation behavior by assuming that backbone reptation takes place in the dilated tube and branch point hopping in the "skinny" one (as the undilated tube is sometimes called). By the use of progressively lower p^2 parameter, they could also make good predictions assuming reptation and hopping both happening in the dilated tube. Former models for comb architectures have also proposed the relaxation of backbone to happen in the dilated tube.[23−25] However, since there is no independent evidence for the validity of this assumption and it is not clear whether reptation and fluctuations of the backbone happen in the same dilated tube, we prefer considering here the time evolving solvent described in ref 13, which is based on an extended Graessley condition for determining the tube dilation level. The latter evolves through time from a skinny to a dilated tube. In the model, this is implemented through Φ_{active}, the oriented part of the polymer while $(1 - \Phi_{active})$ is responsible for tube dilation as a function of time. Its evolution is shown in Figure 9, for samples PS-c612 and PS-c652. As it can be seen there is a time lag between creation and effectiveness of the solvent, which guarantees the necessary time for the chain to fill the dilated tube by lateral movements, while the tube itself dilates by CRR process as shown by the dashed lines. Note that for the sample with long branches (see Figure 9b), there is also a lag time for the tube to take the advantage of the disoriented

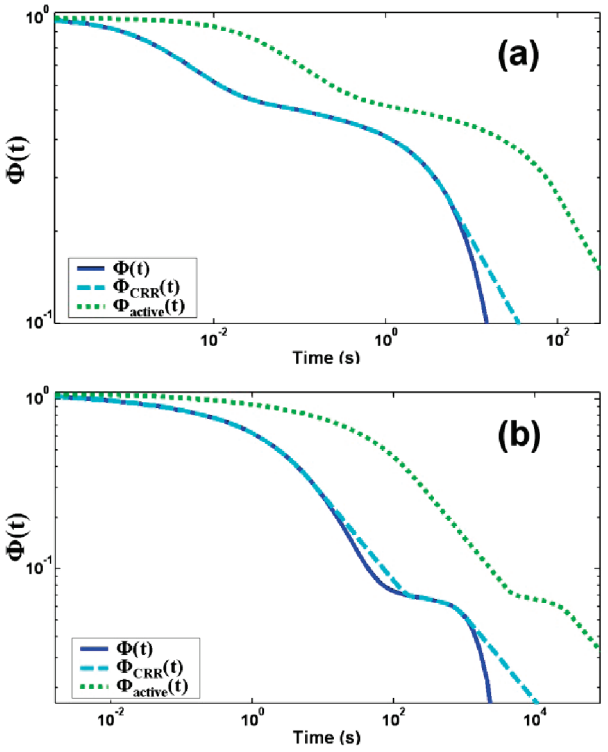


Figure 9. Survival probability (dark lines), contribution of CRR process (dashed lines), and Φ_{active} (dotted lines) for samples (a) PS-c612 and (b) PS-c652.

fraction of the sample and to dilate according to CRR, after relaxation of the side branches.

IV. Conclusions

Although the TMA model is based on the same mesoscopic physics as other tube-based models, the algorithmic implementation of the relevant physical processes is specific. In particular, the expressions for reptation time (eq 21), modified early fluctuation times (eq 26), tube dilation (eq 22), and the method for calculating the overall oriented fraction of polymer (eq 5) are different from former models for comb architectures. In the TMA model, there is neither time scale separation between different relaxation processes nor the flexibility for ad hoc determination of tube dilation effectiveness since it derives from the modified Graessley criterion (eq 22). These features make the TMA model very flexible and highly suited to explore the dynamics of comb structures with widely different characteristics. We have first extended the model to make it suitable for comb architectures. In particular we have introduced the concepts of "Multiple Fluctuations Modes" (MFM) and the simplified version "Triple Fluctuations Modes" (TFM) to cover the wide dynamic range exhibited by combs depending on their branch length. We have also included the early fluctuation times correction recently proposed for linear chains. Next, the extended model was tested on comb samples from several sources and different chemistries, encompassing a broad range of backbone and branch lengths. In all cases, the predictions are found in good agreement with experimental data. In particular, while other tube models require an ad hoc increase of the equivalent friction coming from relaxed branches in order to correctly describe the linear viscoelastic response of short side branch combs,[25,28,30,31] no adjustment of the friction is needed here. This is mainly due to two reasons: the importance of considering the contribution of the monomeric friction from the backbone itself to the total drag, and the importance of considering the time required to equilibrate an entanglement segment before the molecule can start relaxing.[36] Finally, we have studied the extreme limits of relaxation behavior by comb structures with the help of the MFM and TFM approaches. In particular, if the extra friction from the relaxed side branches is significant, comb molecules fluctuate in the same way as a Cayley-tree molecule, i.e., allowing gradually deeper backbone segments to move with respect to the next branching point, from the outer one to the middle one. On the other hand, if the extra friction from the relaxed side branches becomes negligible in comparison with the potential barrier of retraction along the backbone, the whole backbone segments fluctuate just as a linear chain, i.e., with respect to the middle of the molecule.

Acknowledgment. The authors thank Michalis Kapnistos, Keith M. Kirkwood, and Dimitris Vlassopoulos for providing parts of the experimental data and for their useful comments. Financial support by EU under the framework of the DYNACOP project and the SOFTCOMP network is gratefully acknowledged. E.V.R. thanks the Belgian National Fund for Scientific Research (FNRS) for financial support (as Chargé de Recherches). The authors would also like to thank the reviewers for their constructive comments.

References and Notes

(1) de Gennes, P. G. *J. Chem. Phys.* **1971**, *55*, 572–579.
(2) Doi, M.; Edwards, S. F. *The Theory of Polymer Dynamics*; Oxford University Press: New York, 1986.
(3) Watanabe, H. *Prog. Polym. Sci.* **1999**, *24*, 1253–1403.
(4) McLeish, T. C. B. *Adv. Phys.* **2002**, *51*, 1379–1527.
(5) Dealy, J. M.; Larson, R. G. *Structure and Rheology of Molten Polymers*; Hanser Verlag: Munich, Germany, 2006.
(6) Ball, R. C.; McLeish, T. C. B. *Macromolecules* **1989**, *22*, 1911–1913.
(7) Marrucci, G. *J. Polym. Sci., Polym. Phys. Ed.* **1985**, *23*, 159–177.
(8) Milner, S. T.; McLeish, T. C. B. *Macromolecules* **1997**, *30*, 2159–2166.
(9) Milner, S. T.; McLeish, T. C. B. *Macromolecules* **1998**, *31*, 7479–7482.
(10) Frischknecht, A. L.; Milner, S. T. *Macromolecules* **2000**, *33*, 9764–9768.
(11) Frischknecht, A. L.; Milner, S. T.; Pryke, A.; Young, R. N.; Hawkins, R.; McLeish, T. C. B. *Macromolecules* **2002**, *35*, 4801–4820.
(12) McLeish, T. C. B.; Allgaier, J.; Bick, D. K.; Bishko, G.; Biswas, P.; Blackwell, R.; Blottiere, B.; Clarke, N.; Gibbs, B.; Groves, D. J.; Hakiki, A.; Heenan, R. K.; Johnson, J. M.; Kant, R.; Read, D. J.; Young, R. N. *Macromolecules* **1999**, *32*, 6734–6758.
(13) van Ruymbeke, E.; Bailly, C.; Keunings, R.; Vlassopoulos, D. *Macromolecules* **2006**, *39*, 6248–6259.
(14) van Ruymbeke, E.; Kapnistos, M.; Knauss, D. M.; Vlassopoulos, D. *Macromolecules* **2007**, *40*, 1713–1719.
(15) van Ruymbeke, E.; Orfanou, K.; Kapnistos, M.; Iatrou, H.; Pitsikalis, M.; Hadjichristidis, N.; Lohse, D. J.; Vlassopoulos, D. *Macromolecules* **2007**, *40*, 594159–52. Watanabe, H.; Matsumiya, Y.; van Ruymbeke, E.; Vlassopoulos, D.; Hadjichristidis, N. *Macromolecules* **2008**, *41*, 6110–6124.
(16) van Ruymbeke, E.; Muliawan, E. B.; Hatzikiriakos, S. G.; Watanabe, H.; Hirao, A.; Vlassopoulos, D. *J. Rheol.* **2010**, *54*, 643–662.
(17) Das, C.; Inkson, N. J.; Read, D. J.; Kelmanson, M. A.; McLeish, T. C. B. *J. Rheol.* **2006**, *50*, 207–234.
(18) Larson, R. G. *Macromolecules* **2001**, *34*, 4556–4571.
(19) Park, S. J.; Shanbhag, S.; Larson, R. G. *Rheol. Acta* **2005**, *44*, 319–330.
(20) van Ruymbeke, E.; Vlassopoulos, D.; Mierzwa, M.; Pakula, T.; Charalabidis, D.; Pitsikalis, M.; Hadjichristidis, N. *Macromolecules* **2010**, *43*, 4401–4411.
(21) Wang, Z.; Chen, X.; Larson, R. G. *J. Rheol.* **2010**, *54*, 223–260.
(22) Blackwell, R. J.; Harlen, O. G.; McLeish, T. C. B. *Macromolecules* **2001**, *34*, 2579–2596.
(23) Daniels, D. R.; McLeish, T. C. B.; Crosby, B. J.; Young, R. N.; Fernyhough, C. M. *Macromolecules* **2001**, *34*, 7025–7033.
(24) Inkson, N. J.; Graham, R. S.; McLeish, T. C. B.; Groves, D. J.; Fernyhough, C. M. *Macromolecules* **2006**, *39*, 4217–4227.
(25) Kapnistos, M.; Vlassopoulos, D.; Roovers, J.; Leal, L. G. *Macromolecules* **2005**, *38*, 7852–7862.

(26) Kapnistos, M.; Koutalas, G.; Hadjichristidis, N.; Roovers, J.; Lohse, D. J.; Vlassopoulos, D. *Rheol. Acta* **2006**, *46*, 273–286.
(27) Chambon, P.; Fernyhough, C. M.; Im, K.; Chang, T.; Das, C.; Embery, J.; McLeish, T. C. B.; Read, D. J. *Macromolecules* **2008**, *41*, 5869–5875.
(28) Kirkwood, K. M.; Leal, L. G.; Vlassopoulos, D.; Driva, P.; Hadjichristidis, N. *Macromolecules* **2009**, *42*, 9592–9608.
(29) Lee, J. H.; Driva, P.; Hadjichristidis, N.; Wright, P. J.; Rucker, S. P.; Lohse, D. J. *Macromolecules* **2009**, *42*, 1392–1399.
(30) Zhou, Q.; Larson, R. G. *Macromolecules* **2007**, *40*, 3443–3449.
(31) Zamponi, M.; Pyckhout-Hintzen, W.; Wischnewski, A.; Monkenbusch, M.; Willner, L.; Kali, G.; Richter, D. *Macromolecules* **2010**, *43*, 518–524.
(32) van Ruymbeke, E.; Keunings, R.; Bailly, C. *J. Non-Newtonian Fluid Mech.* **2005**, *128*, 7–22.
(33) Pattamaprom, C.; Larson, R. G. *Rheol. Acta* **2000**, *39*, 517–531.
(34) Pattamaprom, C.; Larson, R. G. *Rheol. Acta* **2001**, *40*, 516–532.
(35) Pattamaprom, C.; Larson, R. G.; Sirivant, A. *Rheol. Acta* **2008**, *47*, 689–700.
(36) van Ruymbeke, E.; Vlassopoulos, D.; Kapnistos, M.; Liu, C. Y.; Bailly, C. *Macromolecules* **2010**, *43*, 525–531.
(37) Roovers, J.; Graessley, W. W. *Macromolecules* **1981**, *14*, 766–773.
(38) Schwarzl, F. R. *Rheol. Acta* **1971**, *10*, 166–173.
(39) Roovers, J.; Toporowski, P. *Macromolecules* **1987**, *20*, 2300–2306.
(40) Milner, S. T.; McLeish, T. C. B.; Young, R. N.; Johnson, J.; Hakiki, A. *Macromolecules* **1998**, *31*, 9345–9353.
(41) Blottiere, B.; McLeish, T. C. B.; Hakiki, A.; Young, R. N.; Milner, S. T. *Macromolecules* **1998**, *31*, 9295–9304.
(42) Watanabe, H.; Ishida, S.; Matsumiya, Y.; Inoue, T. *Macromolecules* **2004**, *37*, 6619–6631.
(43) Watanabe, H.; Ishida, S.; Matsumiya, Y.; Inoue, T. *Macromolecules* **2004**, *37*, 1937–1951.
(44) Watanabe, H.; Matsumiya, Y.; Inoue, T. *Macromolecules* **2002**, *35*, 2339–2357.
(45) McLeish, T. C. B. *J. Rheol.* **2003**, *47*, 177–198.
(46) van Ruymbeke, E.; Balacca, L.; Coppola, S.; Righi, S.; Vlassopoulos, D. *J. Rheol.* **2010**, *54*, 507–538.
(47) Park, S. J.; Larson, R. G. *Macromolecules* **2004**, *37*, 597–604.
(48) Likhtman, A. E.; McLeish, T. *Macromolecules* **2002**, *35*, 6332–6343.
(49) Liu, C. Y.; He, J. S.; Keunings, R.; Bailly, C. *Macromolecules* **2006**, *39*, 3093–3097.
(50) Liu, C. Y.; Halasa, A. F.; Keunings, R.; Bailly, C. *Macromolecules* **2006**, *39*, 7415–7424.
(51) Larson, R. G.; Sridhar, T.; Leal, L. G.; McKinley, G. H.; Likhtman, A. E.; McLeish, T. C. B. *J. Rheol.* **2003**, *47*, 809–818.
(52) Liu, C. Y.; He, J. S.; van Ruymbeke, E.; Keunings, R.; Bailly, C. *Polymer* **2006**, *47*, 4461–4479.
(53) Fetters, L. J.; Lohse, D. J.; Colby, R. H. Chain Dimensions and Entanglement Spacing. In *Physical Properties of Polymers Handbook*, 2nd ed., Mark, J. E., Ed.; Springer: Berlin, 2007.
(54) Kapnistos, M.; Kirkwood, K. M.; Ramirez, J.; Vlassopoulos, D.; Leal, L. G. *J. Rheol.* **2009**, *53*, 1133–1153.

660 *Macromolecules* **2011**, *44*, 660–670
DOI: 10.1021/ma102094f

Macromolecules
ARTICLE

Universal Behavior of Dendrimer Solutions

Jaroslaw T. Bosko

Department of Chemical Engineering, Monash University, Melbourne, Victoria 3800, Australia

J. Ravi Prakash*

Department of Chemical Engineering, Monash University, Melbourne, Victoria 3800, Australia

Received September 10, 2010; Revised Manuscript Received December 17, 2010

ABSTRACT: The effect of molecular topology on the structural and dynamic properties of dendrimers with different generation numbers and molecular weights is studied in solvents of varying solvent quality and compared with the behavior of linear polymer chains of similar molecular weights. Brownian dynamics simulations are used, with a coarse-grained bead−spring chain model for the dendrimer, and both intramolecular hydrodynamic and excluded volume interactions are incorporated. The successive fine graining technique is applied to obtain parameter free predictions of properties as a function of solvent quality. In particular, it is shown that with a suitable definition of the solvent quality parameter, the swelling of dendrimers with increasing solvent quality can be collapsed on to a single master curve for molecules with the same topology. The swelling of dendrimers is found to cause a decrease in the translational diffusivity, and a shift in the characteristic maximum in intrinsic viscosity with molecular mass to higher generation numbers. Ratios of the radius of gyration to the hydrodynamic and viscometric radii converge to constant universal values for dendrimers with a fixed degree of branching.

1. Introduction

Dendrimers represent a special class of macromolecules, whose hyperbranched and well-defined architecture leads to some unusual structural and transport properties, which find many potential applications.[1−5] For instance, dendrimers are promising candidates as additives, viscosity modifiers, or nanoscale building blocks, since their solubility, viscosity, and diffusivity differ significantly from that of linear polymers of a similar molecular weight. Another group of potential applications of dendrimers are as drug delivery vehicles, stimuli sensitive molecules or chemical catalysts. These applications require an understanding of the response of dendrimer molecules to changes in the environment, such as the temperature or pH, since these parameters determine both the structure of dendrimers as well as their transport properties. Many experimental,[6−22] theoretical,[23−40] and computational[41−67] studies have appeared in recent years attempting to determine the factors that control the static and dynamic properties of dendrimers in solution. For neutral dendrimers, it has been shown that a critical factor determining molecular configurations is the quality of the solvent, which describes the nature of thermodynamic interactions between monomers in the dendrimer and solvent molecules.[3,18] In this paper, we develop a framework for studying the influence of solvent quality on the static and dynamic properties of dendrimers in solution. In addition, we show that such a framework enables the systematic examination of the universal behavior of dendrimer solutions.

The role of solvent quality in determining the properties of dilute solutions of linear polymers has been very well understood both experimentally and theoretically.[68,69] Extensive experimental investigations of static polymer solutions has established that both the temperature of the solution and the molecular weight of the dissolved polymer control the strength of monomer−solvent interactions. Indeed their influence can be combined together in terms of a single scaling variable, the so-called solvent quality parameter, $z = v_0(1 - T_\theta/T)(M)^{1/2}$, where, v_0 is a polymer−solvent system dependent constant, T is the temperature of the solution, T_θ is the θ-temperature, and M is the molecular weight. The limit $z \to 0$ corresponds to a θ-solution, while $z \to \infty$ is usually termed the *excluded volume limit*. As is well-known, various properties of linear polymer solutions obey power law scalings with molecular weight in these two limits. Interestingly, however, away from these limits, at intermediate values of z, (the *crossover* regime) a type of scaling still persists, and the behavior of a host of different polymer−solvent systems has been found to be collapsible onto universal master plots with a suitable choice of the constant v_0.[70−73] This universal behavior stems from the fact that these properties are entirely determined by the large scale features of the polymer molecule and not by the local details of the chemistry of the individual molecules.

The entire range of experimentally observed behavior for linear polymers has been successfully modeled, theoretically and computationally, by mimicking the influence of the solvent molecules on the conformations of a polymer coil with the help of a potential that acts pairwise between the various parts of the chain. Typically, by representing the linear polymer molecule by a bead−spring chain consisting of N beads connected together by $N_s = (N - 1)$ springs, more or less repulsion by the solvent molecules is accommodated by varying the magnitude of the pairwise *excluded volume* interaction parameter (denoted here by $\tilde{z}^*$), between the beads.[68,69,74−76] In particular, by noting that

$$\tilde{z}^* \sim (1 - T_\theta/T)$$

and $N \sim M$, a quantitative prediction of both the excluded volume limit and the crossover regime behavior of a number of static and dynamic properties has been achieved with the help of

*Corresponding author. E-mail: ravi.jagadeeshan@monash.edu.

 Published on Web 01/12/2011 © 2011 American Chemical Society

the mapping[68,77−80]

$$z = \tilde{z}^*\sqrt{N}$$

It is widely accepted that the single most important reason for the successful prediction of experimental observations of properties of solutions of linear polymers with the help of crude models like bead−spring chains to represent polymer molecules, is because of the universal behavior exhibited by these solutions. The aspect of molecular theories that corresponds to the physically observed universality is the fact that theoretical predictions become independent of the coarse-grained model used to represent the polymer molecule, when a sufficiently large number of degrees of freedom are considered. In particular, in the case of bead−spring chain models, it has been shown that when chains with a large number of beads and, consequently, a large number of length and time scales, are examined, the results become independent of model parameters.[77,78,80]

A similar framework, to our knowledge, has so far not been adopted to describe the influence of solvent quality on dendrimer solution properties. Nor has there been an attempt to systematically examine the universal behavior of dendrimer solutions. Instead, solvent quality effects have typically been understood within the context of Flory theory (where entropic elasticity is balanced with monomer interactions), and simulations have been carried out to validate the predictions of Flory theory.[25,39,54,56,58,66] This approach is briefly summarized in the subsequent section. In contrast, there is a wealth of literature on the universal behavior of solutions of branched polymers such as stars, combs, and brushes,[81−87] and there have also been experimental attempts to describe the influence of solvent quality on solutions of star polymers in terms of the parameter z.[88−91] These studies indicate that there are subtle aspects to the issue of similarity and differences in the scaling behavior of branched and linear polymers.

Essentially, while some properties are unaffected by the existence of branching architecture, other properties are significantly affected. For instance, while the Flory exponent ν is identical for linear and star polymers, the power-law exponent γ, which describes the scaling of the number of configurations of a branched polymer on a lattice with the number of monomers in the polymer, is significantly different, and is a strong function of the number of arms. This has led to the observation that stars with different numbers of arms belong to different universality classes.[87,92] Interestingly, the swelling of branched molecules in good solvents appears to be largely unaffected by branching.[84,87,90,91] On the other hand, the universal Flory constant displays an intriguing dependence on the branching architecture. While the value is a universal constant (independent of molecular weight) for a fixed number of arms, it varies a great deal with an increase in the number of arms.[88,90]

The aim of the present work is to verify if a framework similar to that used to describe the influence of solvent quality on the behavior of linear and star polymers can be fruitfully applied to the case of dendrimers. In particular, we wish to examine if there is a scaling variable z, analogous to that for linear and star chains, which uniquely defines the solvent quality of a dendrimer solution, and with the help of which the crossover data for different dendrimer-solvent systems can be collapsed onto master plots. Such a framework would also enable us to address the question of the existence of universal behavior in dendrimer solutions. We anticipate that the influence of branching on dendrimer solution behavior will display many similarities with that already observed for star polymer solutions.

Our approach is to use Brownian dynamics simulations of a coarse-grained bead−spring chain model for dendrimers, with pairwise excluded volume interactions between the beads taken into account with a narrow Gaussian potential,[93] and with hydrodynamic interactions incorporated with the help of the Rotne−Prager−Yamakawa tensor,[94,95] We assume that the reference state is a phantom dendrimer, with all repulsive interactions between monomers switched off. The influence of solvent quality for good solvents is then examined by varying the strength of the pairwise repulsion between monomers. For linear chains this approach has been shown previously to lead to correct predictions of scaling laws at the θ-temperature, and to a quantitative prediction of the influence of solvent quality on equilibrium static and dynamic properties.[77,78,80]

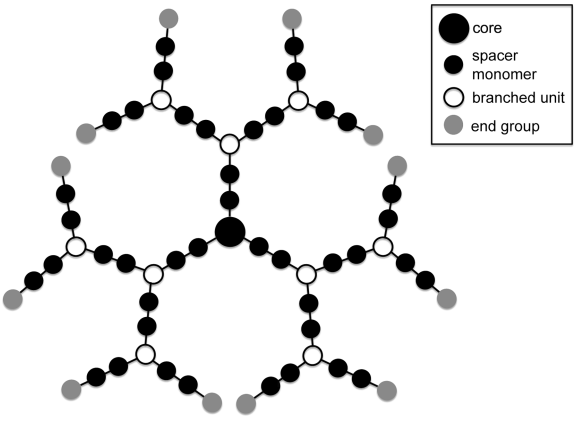


Figure 1. Schematic diagram representing the architecture of a dendrimer of generation 2 with a 3-functional core.

The plan of the paper is as follows. In section 2, we discuss earlier treatments of solvent quality effects, and the approach adopted here. Section 3 introduces the simulation algorithm, while our principle results are discussed in section 4. Section 5 summarizes our conclusions.

2. Scaling Theory and θ Conditions

It is appropriate at first to introduce some notation commonly used to describe the structure of dendrimers. As is well-known, dendrimers are monodisperse macromolecules with a regular and highly branched topology.[96−98] They are composed of linear segments with multifunctional groups at both ends built around the central core with one layer added per generation (see Figure 1). Their structure is characterized by the number of generations (g), functionality of the central core (f), the number of monomers in the chain units called spacers (b), and the order of dendra (m), which defines the number of arms that linear segments split into at branching points. Generation 0 dendrimers correspond to the limiting case of a simple star polymer with a central core and f linear arms. Dendrimers of higher generations are constructed by adding consecutive layers of linear units to the terminal groups of the previous generation. All dendrimers addressed in this study are characterized by three-functional core and branching groups, i.e., $f = 3$ and $m = 2$. The mass of molecules is varied by extending the spacers between the branching points or increasing the number of generations for molecules with fixed spacer length.

The necessity to incorporate three body interactions into a Flory theory for dendrimers, was first recognized by Sheng et al.,[54] who argued that unlike in the case of linear polymer chains, three-body interactions become important in dendrimers due to their densely packed nature. Within such a theory, the radius of gyration R_g was shown to obey the following scaling law, in terms of the parameters characterizing dendrimer architecture

$$R_g \sim N^{1/5}(g+1)^{2/5}b^{2/5} \quad (1)$$

where, in this context, N is the total number of monomers in the dendrimer. Each of the power-law exponents for N, g and b were

shown by Sheng et al. to be valid by carrying out off-lattice Monte Carlo simulations. Even though Sheng et al. did not study the crossover region between the θ-state and the excluded volume limit, they defined the θ-point analogously with linear chains as the temperature at which attractive and excluded volume interactions effectively cancel each other, leading to each of the linear branches of a dendrimer, with $(g+1)b$ segments, behaving ideally.

While Giupponi and Buzza[56] also use Flory theory to describe the effects of solvent quality, in contrast to Sheng et al.,[54] they define the θ-point as the temperature at which two-body interactions vanish, but three-body terms remain significant. The θ-point for dendrimers is therefore assumed, as in the case of linear chains, to coincide with the zero of the second virial coefficient, but to differ from linear chains with regard to the importance of three-body interactions. This leads to the radius of gyration obeying the following scaling law at the θ-temperature,

$$R_g^\theta \sim N^{1/4}(g+1)^{1/4}b^{1/4} \tag{2}$$

suggesting that the nonvanishing of the three body terms implies nonideality in dendrimer behavior at the θ-temperature. By carrying out lattice Monte Carlo simulations, with the Flory interaction parameter χ used to characterize solvent quality, Giupponi and Buzza[56] have verified the various predictions of their Flory theory for poor, θ and good solvents.

It is interesting to note that since $N = 3b\,(2^{g+1}-1)+1$ for the dendrimers studied in ref 56 (with trifunctional core and trifunctional branch points), even within this definition of the θ-point, R_g^θ still scales with molecular mass as $N^{1/2}$ for dendrimers with fixed generation number g. Further, due to the linear relationship between N and b, the contribution to the dendrimer free energy from three-body interactions at the θ-temperature[56]

$$\frac{F_3}{k_B T} = w\,\frac{N^2}{[(g+1)b]^2} \tag{3}$$

is a *constant* independent of molecular mass for a dendrimer with fixed g. Here, k_B is Boltzmann's constant, and w is the three-body interaction parameter. As a result, even with only the second virial coefficient term set equal to zero, and a nonzero third virial coefficient, the dendrimers behave ideally if g is fixed.

The effect of solvent quality on dendrimer solution properties has also been considered within the framework of Flory theory by Lyulin et al.[58] However, unlike in the Flory theory of refs 54 and 56, where both repulsive and attractive interactions are clubbed together within the two-body interaction term, Lyulin et al. include an additional term that specifically accounts for attractive interactions between monomers, with the extent of attraction controlled by the magnitude of a parameter $\varepsilon > 0$. In this framework, the θ-point is defined by Lyulin et al. to be the value of ε at which the swelling $\alpha_G = 1$, where,

$$\alpha_G \equiv \frac{R_g}{R_{g0}} \tag{4}$$

is the ratio of the radius of gyration in a good solvent to the radius of gyration of an ideal Gaussian dendrimer. The dendrimer is consequently assumed to behave ideally at the θ-temperature, as assumed earlier by Sheng et al.[54] However, with this definition of the θ-state, it turns out that for certain values of spacer length b and high generation numbers g, the θ-temperature is not always attainable with physically meaningful values of ε, since α_G is always greater than unity.

Klos and Sommer[66] have examined the static properties of dendrimers in athermal solvents, using lattice Monte Carlo simulations based on the bond fluctuation model. Their results concur with the scaling results obtained earlier by Sheng et al.[54] More recently, Kröger et al.[39] have reformulated Flory theory to obtain a unified description of dendrimers, dendronized polymers and forests, and have derived scaling laws in terms of parameters characterizing these different architectures. Interestingly, they distinguish two subregimes at the θ-temperature: one in line with the earlier definition in ref 56 (with the second virial coefficient set to zero), which they term the swollen θ regime, and another regime they term the Gaussian θ regime, where the chains are Gaussian, in line with the definition in refs 54 and 58.

The recognition that characterizing the θ-point uniquely in dendrimer systems is a subtle problem is also echoed in discussions of this issue in the literature on star polymers. The questions of whether the arms of a star polymer obey Gaussian statistics at the temperature where the second virial coefficient is zero, and whether branching causes a shift in the θ-temperature from linear chains, have been addressed both theoretically and experimentally.[84,85,87,88,90,91] The difference in the θ-temperature between linear chains and star polymers observed in Monte Carlo simulations and in experiments has been attributed to the more prominent existence of ternary interactions at the θ-temperature.[85,87] However, Batoulis and Kremer[85] have shown with high precision Monte Carlo simulations that the θ-temperature is identical for linear and star polymers in the limit of long arms. The experiments of Okumoto et al.[88,90] for four arm and six arm star polystyrene in cyclohexane indicate that the θ-temperature for these systems is indistinguishable from that for linear polystyrene in cyclohexane. These authors suggest that the shift seen in earlier experimental observations is due to the molecular weights of the star polymers that were studied not being large enough.

Typically, the examination of the influence of solvent quality for linear polymer−solvent systems involves a choice of reference state, and the study of static and dynamic property changes that occur as a result of chain swelling relative to this state. Both experimentally and theoretically, the reference state is chosen to be the θ state.[68] In molecular simulations, a representation of the θ state is typically captured in one of two ways; either by selecting parameter values in the pairwise excluded volume interaction potential such that attractive forces exactly balance repulsive interactions, or by simply not including any excluded volume effects in the model (i.e., with phantom chains). Both approaches have been shown to accurately predict scaling relations at the θ state, and to lead to similar quantitative descriptions of solvent quality effects.[77−80,99] In the case of dendrimers, even though there does not currently exist a commonly accepted definition of the θ state, a systematic study of the influence of solvent quality can be carried out by choosing a reference state, and examining changes in behavior relative to the reference state as a function of changing solvent quality. Here, we adopt the approach previously followed in Brownian dynamics simulations studies of linear chains, i.e, we use phantom chains with no excluded volume effects as the reference state, and examine changes relative to this state when repulsive excluded volume interactions are turned on.

3. Brownian Dynamics Simulations

A dilute solution of dendrimers is modeled as an ensemble of noninteracting coarse-grained molecules composed of beads and springs. Each molecule contains N beads, which represent parts of the molecule, and act as centers of hydrodynamic resistance. Molecular topology determines the connectivity between the beads. The attractive spring force between connected beads, which models the resistance of the underlying linear segment to stretching, is approximated by the finitely extensible nonlinear elastic (FENE) spring force law of the form[100,101]

$$\boldsymbol{F}_i^c = H\left(\frac{1}{1-Q_i^2/Q_0^2}\right)\boldsymbol{Q}_i \tag{5}$$

where, H is the spring constant, $\boldsymbol{Q}_i$ is the spring extension, and Q_0 is the contour length of the molecular segment represented by a single spring, i.e., the maximum spring extension. If b_k represents the length of a single Kuhn step, then $Q_0 = b_k N_{k,s}$, where $N_{k,s} = N_k/N_s$ is the number of Kuhn steps per spring, N_k is the number of Kuhn steps in the whole molecule, and N_s is the number of springs used in the coarse-grained dendrimer model. The value of the spring constant, H, is assigned to reproduce the equilibrium mean squared end-to-end distance of the underlying segments of the phantom dendrimer. For segments composed of $N_{k,s} \geq 10$, the mean squared end-to-end distance approaches ${b_k}^2 N_{k,s}$. On the other hand, for FENE springs:[78]

$$\langle {R_e}^2 \rangle = \frac{3k_B T}{H} \chi^2 \tag{6}$$

where

$$\chi^2 = \frac{{Q_0}^2 H/k_B T}{({Q_0}^2 H/k_B T) + 5} \tag{7}$$

This yields the formula relating the spring constant to the parameters describing the underlying molecular segments (b_k, $N_{k,s}$):

$$H = \frac{k_B T}{{b_k}^2} \frac{3N_{k,s} - 5}{{N_{k,s}}^2} \tag{8}$$

The equations and results in the reminder of this paper are nondimensionalised using the length scale $l_s = \chi(k_B T/H)^{1/2}$ and the time scale $\lambda_s = \zeta {l_s}^2/4k_B T$, where $\zeta = 6\pi\eta_s a$ is the Stokes drag for a spherical bead of radius a in a solvent with viscosity η_s. Expressed in these units, the equilibrium extension of a single FENE spring is $\langle {R_e}^2 \rangle = 3{l_s}^2$.

In the context of Brownian dynamics simulations, interactions of the beads with the surrounding solvent are treated implicitly. These include the drag experienced by beads when they move relative to the solvent, and hydrodynamic interactions, which lead to pairwise dynamic correlations between beads. The dimensionless diffusion tensor representing pairwise hydrodynamic interaction between a bead μ and another bead ν, is given by the equation:

$$\boldsymbol{\Gamma}_{\mu\nu} = \delta_{\mu\nu}\boldsymbol{\delta} + \zeta\boldsymbol{\Omega}_{\mu\nu} \tag{9}$$

where, $\boldsymbol{\Omega}_{\mu\nu}$, for $\mu \neq \nu$, represents the hydrodynamic interaction matrix, and $\boldsymbol{\delta}$ and $\delta_{\mu\nu}$ represent a unit tensor and a Kronecker delta, respectively. The first term describes the drag on beads in homogeneous flow and corresponds to the free draining limit, whereas the second term describes pairwise hydrodynamic interactions between beads. The tensor $\boldsymbol{\Omega}_{\mu\nu}$ is a function of the bead separation, $\boldsymbol{\Omega}_{\mu\nu} = \boldsymbol{\Omega}(\boldsymbol{r}_{\mu\nu})$ and is described by the Rotne–Prager–Yamakawa interaction tensor:[94,95]

$$\boldsymbol{\Omega}(\boldsymbol{r}_{\mu\nu}) = \left[\Omega_1 \delta + \Omega_2 \frac{\boldsymbol{r}_{\mu\nu}\boldsymbol{r}_{\mu\nu}}{{r_{\mu\nu}}^2}\right] \tag{10}$$

where, for $r_{\mu\nu} \geq 2\pi^{1/2}\,\tilde{h}^*$,

$$\Omega_1 = \frac{3\sqrt{\pi}}{4}\frac{\tilde{h}^*}{r_{\mu\nu}}\left(1 + \frac{2\pi}{3}\frac{\tilde{h}^{*2}}{{r_{\mu\nu}}^2}\right) \tag{11}$$

$$\Omega_2 = \frac{3\sqrt{\pi}}{4}\frac{\tilde{h}^*}{r_{\mu\nu}}\left(1 - 2\pi\frac{\tilde{h}^{*2}}{{r_{\mu\nu}}^2}\right) \tag{12}$$

and for $0 < r_{\mu\nu} < 2\pi\tilde{h}^*$,

$$\Omega_1 = 1 - \frac{9}{32}\frac{r_{\mu\nu}}{\tilde{h}^*\sqrt{\pi}} \tag{13}$$

$$\Omega_2 = \frac{3}{32}\frac{r_{\mu\nu}}{\tilde{h}^*\sqrt{\pi}} \tag{14}$$

The hydrodynamic interaction parameter, $\tilde{h}^*$, is related to the hydrodynamic bead radius a through:

$$\tilde{h}^* \equiv \frac{a}{\sqrt{\pi} l_s} \tag{15}$$

In all simulations the hydrodynamic interaction parameter was assigned a value of $\tilde{h}^* = 0.26$.[78]

The influence of solvent quality on dendrimer solution properties is captured by incorporating pairwise repulsive excluded volume interactions (EV) between beads. Specifically, a repulsive narrow Gaussian potential has been used, which has been successfully applied previously to study the structure of linear polymers in good solvents.[77−80,93,102] For bead−spring chain models with finitely extensible springs, it is given by:

$$E_{\mu\nu} = \frac{\tilde{z}^*}{\tilde{d}^{*3}} \exp\left(-\frac{{r_{\mu\nu}}^2}{\tilde{d}^{*2}}\right) \tag{16}$$

where $\tilde{d}^*$ is a nondimensional parameter measuring the range of the excluded volume interaction and $\tilde{z}^*$ is its nondimensional strength. The narrow Gaussian potential is a means of regularizing the Dirac delta potential since it reduces to a δ-function potential in the limit of $\tilde{d}^*$ tending to zero. In this study, the absence of EV interactions ($\tilde{z}^* = 0$) corresponds to a phantom dendrimer, which is used as the reference state.

The Brownian dynamics technique used in this study consists in the numerical solution of the stochastic equations of motion for each bead:

$$\mathrm{d}\boldsymbol{r}_\mu = \frac{1}{4}\sum_{\nu=1}^{N} \boldsymbol{\Gamma}_{\mu\nu} \cdot (\boldsymbol{F}_\nu^s + \boldsymbol{F}_\nu^{EV})\,\mathrm{d}t + \sum_{\nu=1}^{N} \frac{1}{\sqrt{2}}\boldsymbol{B}_{\mu\nu} \cdot \mathrm{d}\boldsymbol{W}_\nu \tag{17}$$

where, $\boldsymbol{F}_\nu^s$ and $\boldsymbol{F}_\nu^{EV}$ are the total forces acting on a bead due to the springs and EV forces, $\mathrm{d}\boldsymbol{W}_\nu$ is an increment of the Wiener process, and $\boldsymbol{B}_{\mu\nu}$ is the square root of the diffusion tensor, $\sum_\sigma \boldsymbol{B}_{\mu\sigma}\boldsymbol{B}_{\nu\sigma}^T = \boldsymbol{\Gamma}_{\mu\nu}$.[103] Note that $\boldsymbol{F}_\nu^s = \sum_i \boldsymbol{F}_i^c$, where the counter i runs over all springs connecting bead ν with its neighbors, and

$$\boldsymbol{F}_\nu^{EV} = -\sum_{\substack{\mu=1 \\ \mu\neq\nu}} \frac{\partial E_{\mu\nu}}{\partial \mathbf{r}_\nu} \tag{18}$$

In the present work, the spatial configuration of the chain, $\boldsymbol{r}_\mu$ at any time t is obtained by integrating eq 17 using a semi-implicit predictor−corrector scheme proposed by Prabhakar and Prakash.[104] The problem of the computational intensity of calculating the Brownian term has been attenuated by the use of a Chebyshev polynomial representation for the Brownian term.[105] The macroscopic properties of the solutions are obtained by simulating a large ensemble of independent trajectories.

4. Results and Discussion

4.1. Dendrimer Size in Good Solvents. The radius of gyration of long linear polymers in solution scales as $R_g \propto N^\nu$, where the Flory exponent ν is independent of the polymer−solvent system. At the θ temperature $\nu = 0.5$, whereas in the good solvent limit $\nu = 0.592$.[69,74] As discussed in section 2, the radius of gyration of dendrimers does not follow a single power law but is a function of the topological parameters defining molecular architecture.[26,54] For fixed

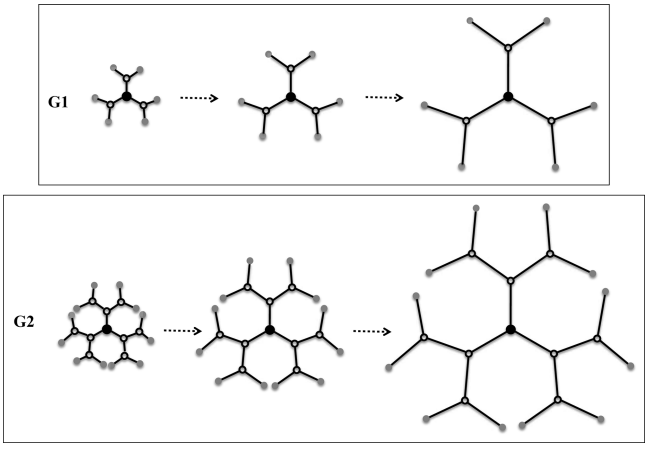


Figure 2. Schematic diagram illustrating the effect of increasing spacer length on the shape of dendrimers with fixed generation numbers 1 and 2. Since the spacer length is increased uniformly across the entire dendrimer, the dendritic structure remains *self-similar* with repeated transformation of the spacer length.

generation number, however, a dendrimer can be seen as a collection of interconnected linear segments---the spacers. Keeping generation number constant allows one to investigate how the size of a dendrimer scales with molecular mass as the length of the spacers is increased. Figure 2 is a schematic diagram illustrating the geometric consequence of uniformly increasing the spacer length while keeping the generation number fixed for generation 1 and generation 2 dendrimers. Essentially, the dendrimer shape remains identical with each transformation of the spacer length.

Dendrimers of generation 2 and 3 with varied spacer length have been simulated at the reference phantom state (corresponding to $\tilde{z}^* = 0$) and at a temperature corresponding to $\tilde{z}^* = 0.21$. The spacers are increased by adding additional springs between the branching points with each spring representing a segment of 20 Kuhn steps. Figure 3 shows the radius of gyration as a function of the number of beads for these systems. For each generation, the size scales with Flory exponent $\nu \sim 0.5$ at the reference state, whereas for $\tilde{z}^* = 0.21$, $\nu \sim 0.58$. The latter results indicates that the temperature corresponding to $\tilde{z}^* = 0.21$ is close to the good solvent limit. These results are in line with the scaling exponents obtained earlier with a variety of different computational techniques, both for ideal dendrimers, and dendrimers in good solvents, when g is kept fixed.[54,56,66] The agreement with the scaling of linear polymers is also identical to the behavior seen in earlier studies of star polymer systems, where the exponent ν was shown to be independent of the number of arms.[81,84,86,87]

An alternative means of investigating the molecular mass dependence of dendrimers is to keep the spacer length fixed, and to increase the number of generations. In this case, the size of the dendrimer has a complex functional dependence on f, m, b, and g. In the excluded volume limit, Flory theory suggests that the scaling law is given by eq 1 for dendrimers with fixed number of arms f and order of dendra m. For the special case of *phantom* dendrimers, an analytical expression for R_g has been derived by La Ferla.[26] In our previous paper,[64] we have shown that results of Brownian dynamics simulations for phantom dendrimers agree exactly with La Ferla's expression. Here, we have examined the dependence of R_g^2 on N, at fixed values of the solvent quality z, for dendrimers of generations 0 to 5. In this crossover regime, there are no scaling theories or analytical predictions for the radius of gyration of dendrimers. Note that in order to keep z

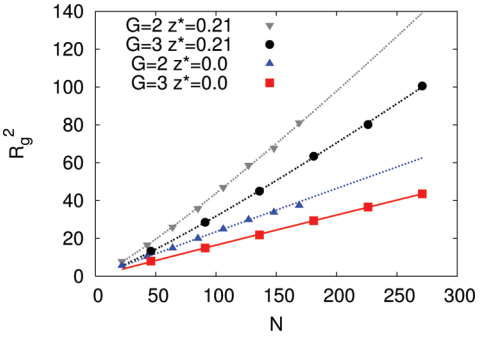


Figure 3. Molecular mass dependence of the squared radius of gyration for dendrimers of generation 2 and 3, at the reference state (corresponding to $\tilde{z}^* = 0$) and at a temperature corresponding to $\tilde{z}^* = 0.21$. Lines are fitted power-laws with exponents $\nu = 0.5$ and $\nu = 0.58$ for $\tilde{z}^* = 0$ and $\tilde{z}^* = 0.21$, respectively. $N_{k,s} = 20$.

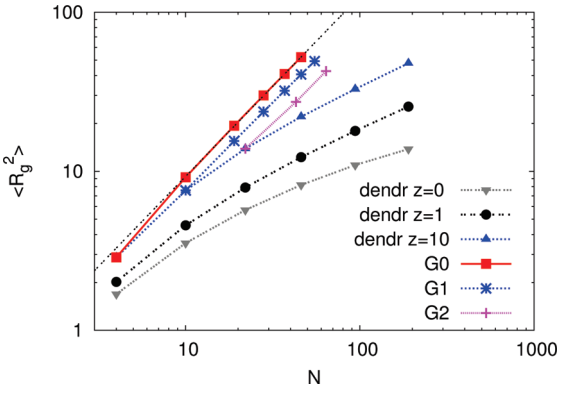


Figure 4. The molecular mass dependence of the squared radius of gyration at fixed values of the solvent quality z. The curves denote values for increasing generation numbers, at the reference state (corresponding to $z = 0$), and at $z = 1$ and $z = 10$. The straight lines represent dendrimers of fixed generation number (0, 1, and 2) at $z = 10$.

constant, $\tilde{z}^*$ must be reduced as N is increased such that the product $\tilde{z}^* N^{1/2}$ is constant. The level of coarse-graining has been kept fixed, with single springs corresponding to spacers of length 20 Kuhn steps. Figure 4 displays the squared radius of gyration for all the systems addressed. For the purpose of comparison, the result for phantom dendrimers obtained earlier,[64] is reproduced here as the curve corresponding to $z = 0$. Clearly, when the generation numbers are varied, the dependence of the size on the molecular structure is a nontrivial function. Notably, the curves corresponding to $z = 1$ and $z = 10$ have a shape similar to that for phantom dendrimers, but in line with expectation, the size of the molecules increases with increasing solvent quality

Figure 4 also displays the molecular mass dependence of the squared radius of gyration at fixed generation numbers 0, 1, and 2. In this case, linear-chain-like power law behavior is observed. Unlike in Figure 3, however, where the temperature was held constant with increasing molecular mass, in this case the solvent quality is kept fixed at $z = 10$. Since the slope of the line through the generation 0 data (square symbols) is 1.13, this indicates a value of the effective power law exponent $\nu = 0.565$. The solvent quality at $z = 10$ is consequently approaching the good solvent limit.

4.2. Universal Swelling in Good Solvents. To exclude effects due to the level of coarse-graining used to represent a molecule, we have applied the successive fine-graining technique[78,106,107] to our simulations of dendrimers in good solvents. As shown by Pham et al.,[107] the successive fine graining technique enables the determination of properties

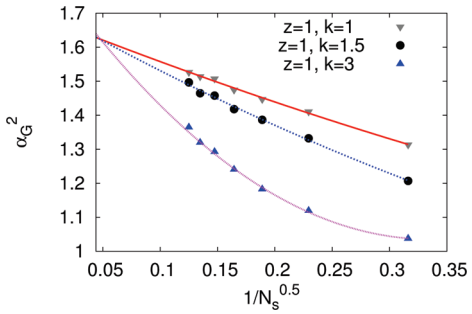


Figure 5. Swelling of a generation 1 dendrimer as a function of the number of beads N_s, for three values of k, at a constant value of solvent quality, $z = 1$. The x-axis starts at the value corresponding to the molecular mass $N_k = 500$.

of bead-rod models by suitably extrapolating the results of a bead−spring chain model. Basically, in the successive fine graining technique, the molecular mass N_k is kept constant while the number of springs N_s is systematically increased. Results accumulated for several values of N_s are then extrapolated to the limit N_k. In the process of fine graining, the number of Kuhn steps per spring decreases and consequently, the parameters of the narrow Gaussian potential capturing molecule-solvent interactions, $\tilde{d}^*$ and $\tilde{z}^*$, also have to be modified appropriately. Further details of the technique can be found in ref 78. At different levels of coarse-graining, the product $z = \tilde{z}^* N^{1/2}$ is kept constant, ensuring that the solvent quality is constant. It has been shown that for linear chains with a sufficiently large number of Kuhn steps N_k, results are independent of the choice of the parameter $d^* = \chi\tilde{d}^*$, in the limit of $N_s \rightarrow N_k$.[78,107] As in ref 78, for any choice of $\tilde{z}^*$ and N, the range of the EV interactions is determined by $d^* = k[\tilde{z}^*\chi^3]^{0.2}$, where k is an arbitrary constant. Our study is limited to dendrimers of generation 0, 1, and 2 because of the rapid increase in the number of beads required to model molecules at successive levels of fine-graining. Spacers in the most coarse-grained model are represented by a single spring.

The swelling $\alpha_G^2 = R_g^2/R_{g0}^2$, of an $N_k = 500$ generation 1 dendrimer, as a function of $1/(N_s)^{1/2}$, is shown in Figure 5 for three values of k. Here, R_{g0} is the radius of gyration of a dendrimer in the reference state (i.e., a phantom dendrimer). Second order polynomials were found to be sufficient to fit the data. The swelling corresponding to a bead-rod model dendrimer with $N_k = 500$ segments can be estimated by extrapolating the data accumulated for various values of N_s to the limit $N_s \rightarrow N_k = 500$. As is evident from Figure 5, while the swelling depends on the choice of parameters at intermediate levels of coarse-graining, in the limit $N_s \rightarrow N_k$ these parameters become irrelevant, since all the curves extrapolate to a unique limit. The extrapolated value is consequently the *parameter free* value of α_G^2 at $z = 1$ for a bead-rod dendrimer with $N_k = 500$.

In all the remaining simulations only one value of $k = 1$ has been used. This choice of k leads to almost linear dependence of the swelling α_G^2 on $1/(N_s)^{1/2}$ in the whole range of N_s selected. A series of simulations at various values of z have been performed for dendrimers of various generations and masses. The results for dendrimers of generation 1 and 2 with $N_k = 500$ are presented in Figure 6, parts a and b. The extrapolated values in the limit $N_s \rightarrow N_k = 500$ are consequently the parameters-free predictions of α_G^2 as a function of z, with $z = \tilde{z}^* N_k^{1/2}$.

As is well-known, the function $\alpha_G^2(z)$ is independent of molecular mass and temperature for long linear chain polymers.[68−70,72] In the case of star polymers, z has been

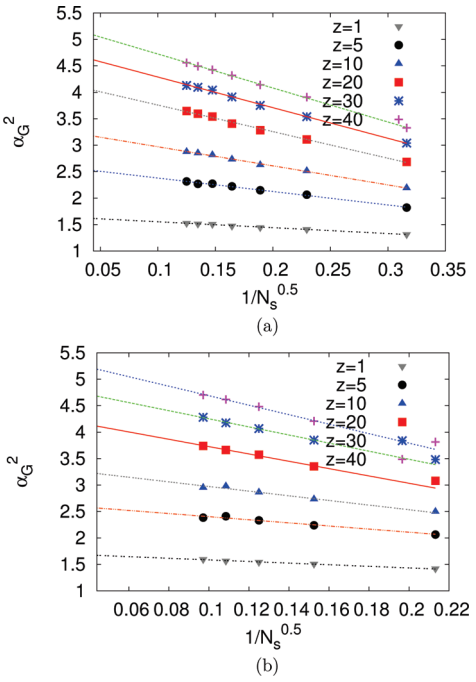


Figure 6. Swelling of dendrimers versus number of springs at various values of solvent quality z: (a) generation 1 and (b) generation 2. $N_k = 500$ and $k = 1$. Fitted lines are second order polynomials. The x-axis starts at the value corresponding to the molecular mass $N_k = 500$.

shown to be the appropriate scaling variable to describe swelling in the crossover regime, both by numerical simulations,[85] and by experimental observations.[88−91] To test whether a similar universal behavior exists for dendrimers, simulations of dendrimers with masses $N_k = 900$ and $N_k = 2100$ were carried out. The results are displayed in Figure 7, parts a−c. Clearly, the swelling is unaffected by changes in the molecular mass, suggesting that the masses are large enough to observe universal behavior. As a result, the master plots in Figures 7 can be used to predict the swelling for a dendrimer of known generation number, once the solvent quality of the solution is known, regardless of the chemical details of the dendrimer-solvent system.

Figure 8a compares the dependence on solvent quality of the swelling of molecules with different architectures—from linear chains through star molecules (generation 0 dendrimers) to generation 1 and 2 dendrimers. Each of the curves is obtained for molecules with mass $N_k = 2100$ using the successive fine graining procedure described earlier in the context of Figures 5−7. There are several aspects to the results displayed in Figure 8a, which we discuss in turn:

(a) We have verified that the curve for linear chains agrees excellently with a similar curve obtained earlier by Kumar and Prakash[77] by extrapolating finite chain data for Hookean bead−spring chains to the infinite chain length limit. This supports our earlier conclusion that the successive fine graining procedure is able to predict universal behavior for molecules with sufficiently large N_k. Further, in the case of linear chains, Kumar and Prakash[77] have shown that the Brownian dynamics simulations data is in excellent agreement with experimental observations of swelling.

(b) The swelling of the 3 arm star polymer (generation 0) is nearly identical to the swelling for linear chains when represented in terms of the scaling variable z. This prediction agrees with the experimental observations of Okumoto et al. for 4 arm and 6 arm

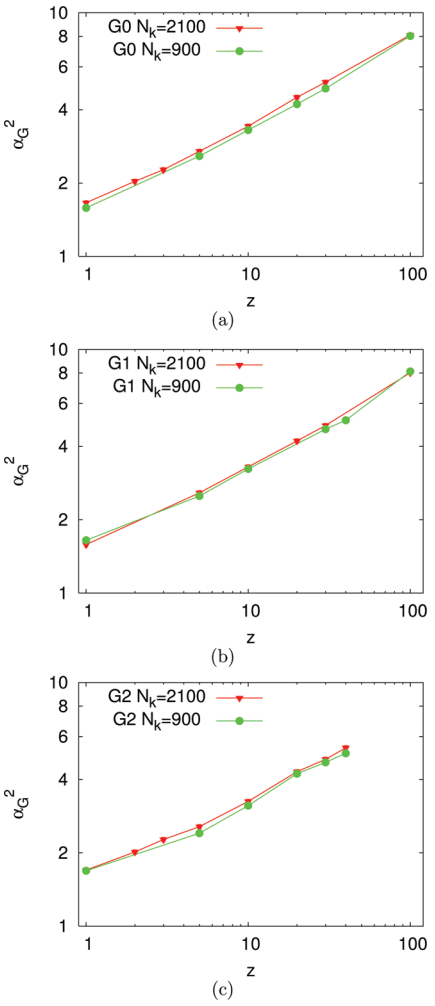


Figure 7. Universal swelling as a function of solvent quality for dendrimers of generations 0, 1, and 2.

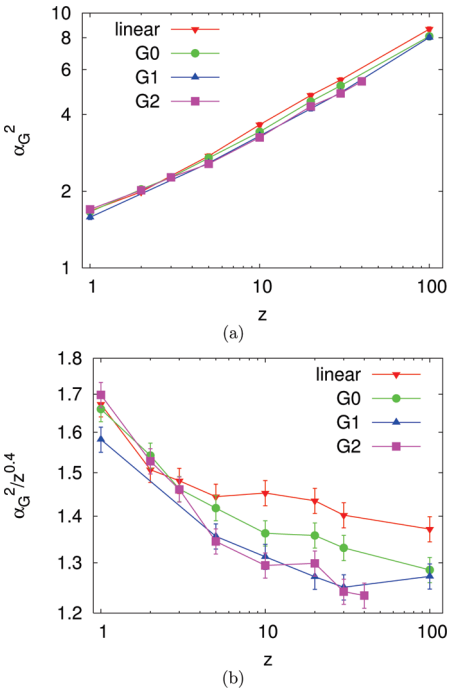


Figure 8. Parameter free swelling of molecules with different architectures as a function of solvent quality. The degree of branching increases from linear chain through star molecule (generation 0 dendrimer) to generation 1 and 2 dendrimers.

star polystyrene in benzene and cyclohexane.[88−90] The origin of the insensitivity of the swelling of branched polymers in good solvents to branching architecture has been explained in the context of renormalization group theory by Douglas et al.[87] Indeed in the excluded volume limit, Douglas and Freed[81] estimate that α_G varies between 1.0 and 1.10 for stars and combs with various numbers of arms.

(c) Figure 8a indicates that for dendrimers as well, the effect of branching is marginal. To examine the difference more closely, Figure 8b displays the data in a manner that highlights the behavior for large z. Since $\alpha_G^2 \sim N^{2\nu-1}$ for large z, and $z \sim N^{1/2}$, this implies that for these values of z, $\alpha_G^2 \sim z^{0.4}$. As a result, we expect $\ln(\alpha_G^2/z^{0.4})$ to become constant as $z \to \infty$. Figure 8b does show a leveling off of the data for all architectures for $z \gg 1$. Further, in this limit, the variation in the swelling across architectures is of the same order of magnitude (within error bars) as that predicted earlier by Douglas and Freed.[81]

4.3. Transport Properties in Good Solvents. To investigate the dynamic properties of dendrimers at fixed values of the solvent quality, dendrimers of generations 0 to 5 have been simulated at a fixed level of coarse-graining, with single springs corresponding to spacers of length 20 Kuhn steps. In our previous paper,[64] results for phantom dendrimers were presented. Here the same molecules are studied in solvents characterized by solvent quality $z = 1$ and $z = 10$. Some of the results for phantom dendrimers are also repeated for comparison. To analyze the dynamic scaling behavior of molecules with fixed topology, molecules of generations 0, 1, and 2, with varying spacer lengths, are also studied.

The long-time diffusivity is evaluated here directly from the mean square displacement of the molecule's center-of-mass $\boldsymbol{r}_c$ using Einstein's formula:

$$D_{COM} = \frac{k_B T}{\zeta} \lim_{t \to \infty} \left\langle \frac{|\boldsymbol{r}_c(t) - \boldsymbol{r}_c(0)|^2}{6t} \right\rangle \qquad (19)$$

For linear chains the diffusion coefficient scales as $D_{COM} \sim N^{-\nu}$.[69,74] It is clear from Figure 9 that in the case of dendrimers, like for the dependence of R_g on molecular mass, no simple power law scaling is observed with increasing generation number. Similar behavior was observed earlier in our simulations of phantom dendrimers[64] (reproduced here as the curve corresponding to $z = 0$) and in Brownian dynamics simulations of dendrimers using a bead-rod model.[57] With increasing degree of branching, the rate at which the diffusion coefficient decreases with molecular weight is smaller than that for linear chains. This observation is in agreement with experimental findings for poly(propyleneimine) dendrimers,[14,20] where a strong dependence on temperature and solvent was observed. In all cases, increasing solvent quality leads to a decrease in the diffusivity, which is expected due to the more swollen state of the dendrimers.

In the case of R_g, we have seen earlier (Figure 4) that for molecules with fixed architecture, on the other hand, power law scaling with molecular mass, similar to that for linear chains, is observed. Not surprisingly, Figure 9 indicates that, for $z = 10$, independent of dendrimer architecture, the center-of-mass diffusivity also obeys power law scaling with molecular mass, with exponent $\nu = 0.6$. This is identical to the

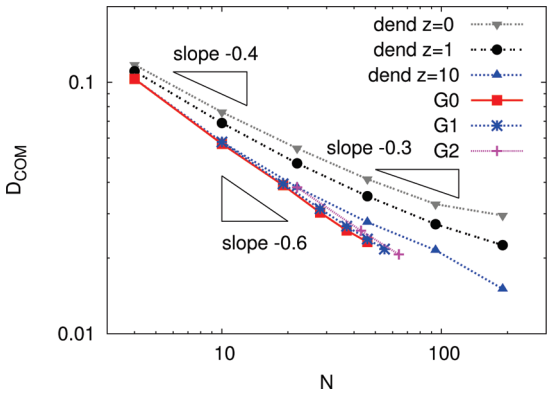


Figure 9. Molecular mass dependence of the center-of-mass diffusivity at fixed values of the solvent quality z. The curves denote values for increasing generation numbers, at the reference state (corresponding to $z = 0$), and at $z = 1$ and $z = 10$. The straight lines represent dendrimers of fixed generation number (0, 1, and 2) at $z = 10$.

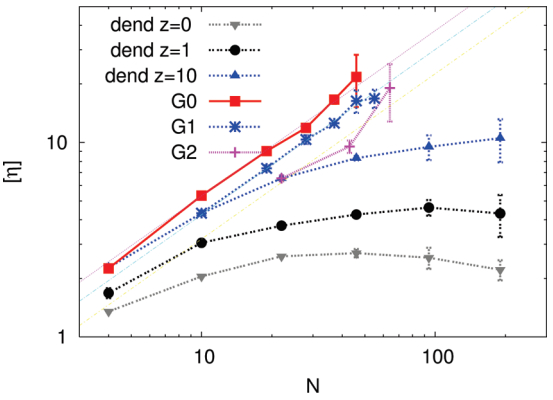


Figure 10. Molecular mass dependence of the intrinsic viscosity at fixed values of the solvent quality z. The curves denote values for increasing generation numbers, at the reference state (corresponding to $z = 0$), and at $z = 1$ and $z = 10$. The straight lines represent dendrimers of fixed generation number (0, 1 and 2) at $z = 10$.

scaling observed for linear chains in good solvents in the good solvent limit.[69,74]

The zero-shear-rate polymer contribution to viscosity $\eta_{p,0}$, for the various systems studied here, was obtained from a Green-Kubo formula based on the stress autocorrelation function:[74,108]

$$\eta_{p,0} = \int_0^\infty \mathrm{d}t\, \tau_{xy}(t)\tau_{xy}(0) \qquad (20)$$

Here τ_{xy} is the polymer contribution to the shear stress component of the stress tensor.

In Figure 10, we plot the molecular mass dependence of the nondimensional intrinsic viscosity, defined here as $[\eta] = \eta_{p,0}/N_k$. Since the level of coarse-graining is kept fixed at $N_{k,s} = 20$, the number of Kuhn steps N_k increases proportionately with N. For linear chains, $\eta_{p,0}$ scales with molecular mass as $N^{3\nu}$, which implies $[\eta] \sim N^{3\nu-1}$. It is clear from Figure 10 that for dendrimers, the intrinsic viscosity does not obey power law scaling with N with increasing generation number. On the contrary, the intrinsic viscosity clearly exhibits a maximum for $z = 0$ at around generation 3. The existence of a maximum in the intrinsic viscosity has been observed experimentally,[6] and its occurrence has been predicted previously with Brownian dynamics simulations of a bead-rod model which includes excluded volume and hydrodynamic interactions.[50] Bosko and Prakash[64] have shown, by simulating phantom dendrimers, that in order to predict the maximum it is sufficient to have fluctuating hydrodynamic interactions alone. The curve corresponding to $z = 0$ is a reproduction of their earlier results.

The existence of a maximum has often been explained with the help of the following reasoning.[41,50,56] From the definition of the viscometric radius

$$R_\eta^{\,3} = \frac{3}{10\pi}\frac{\eta_{p,0}}{n_p \eta_s} \qquad (21)$$

where n_p is the number of molecules per unit volume and η_s is the solvent viscosity, it can be seen that the intrinsic viscosity scales as, $[\eta] = \eta_{p,0}/N_k \sim R_\eta^{\,3}/N$. As a result, $[\eta]$ has units of volume divided by mass. Because of the densely packed nature of dendrimers, the volume grows more slowly with N in comparison to linear chains, thus giving rise to a maximum with increasing generation number. In earlier Monte Carlo literature, $R_g^{\,3}$ has frequently been used to study the scaling of $[\eta]$ in place of $R_\eta^{\,3}$, because it is not possible to find $\eta_{p,0}$ using Monte Carlo simulations. Giupponi and Buzza[56] have used eqs 1 and 2 for R_g and the above scaling argument to show that the intrinsic viscosity is expected to demonstrate a maximum both in good and in θ solvents (see Figures (5) and (6) in ref 56). As mentioned earlier, Lyulin et al. have shown with the help of Brownian dynamics simulations, that a maximum exists in good solvents, both for dendrimers and for hyperbranched polymers.[50,109] However, there has not been a prediction so far of the dependence of intrinsic viscosity on generation number as a function of solvent quality in the crossover regime.

Figure 10 displays the dependence of $[\eta]$ on N for $z = 1$ and $z = 10$. The shape of the curve for $z = 1$ suggests a maximum at generation number 4 or 5, while the existence of a maximum for $z = 10$ cannot be ascertained with certainty since simulations have only been performed until generation number 5. The maximum which clearly occurs at around generation 3 for $z = 0$ appears to be postponed to higher generation numbers with increasing solvent quality. This behavior can be understood to arise from the fact that the viscometric volume increases with g faster for dendrimers in good solvents than it does for phantom dendrimers, and as a result, there is a shift in the maximum to the right. The significant influence of solvent quality on the viscometric volume of dendrimers has been observed experimentally.[3,18] The present approach provides a systematic framework within which the influence of solvent quality can be quantified.

For molecules with fixed architecture, Figure 10 indicates that for $z = 10$, the intrinsic viscosity increases following a power law. A straight line fit to the generation 0 data (square symbols) gives $[\eta] \sim N^{0.85}$, which implies, $\nu = 0.62$—a value close to that observed for linear chain molecules in the good solvent limit.[69] It must be noted that for an identical number of simulation trajectories, the error bars for the viscosity, obtained from a Green−Kubo formula, are typically greater than those for the center of mass diffusivity. This is responsible for the larger degree of uncertainty at higher generation numbers in Figure 10 relative to Figure 9.

For sufficiently long linear chains, it is well-known that certain ratios of dynamic to static properties are universal constants. Here we consider two such ratios, U_{RD} and $U_{\eta R}$, which are widely measured in the experimental literature on dendrimers, since they are believed to lead to some insight into the internal packing of dendrimers.[8,9,12−15,18] For linear chains, a large number of experimental observations and computational predictions of these ratios have been compiled by Kröger et al. and reported in ref 110, where the following definitions have been used,

$$U_{RD} = \frac{R_g}{R_h} \qquad (22)$$

with $R_h = k_B T/(6\pi\eta_s D_{COM})$, and

$$U_{\eta R} = \frac{\eta_{p,0}}{n_p \eta_s (4\pi/3) {R_g}^3} \quad (23)$$

Experiments suggest that in θ-solvents, $U^{\theta}_{RD} = 1.27 \pm 0.06$, and $U^{\theta}_{\eta R} = 1.49 \pm 0.06$. Brownian dynamics simulations of Gaussian chains with fluctuating hydrodynamic interactions yield the values $U^{\theta}_{RD} = 1.38 \pm 0.01$[80] and $U^{\theta}_{\eta R} = 1.55 \pm 0.06$.[110] For four arm and six arm star polystyrene in cyclohexane, Okumoto et al.[88,89] have shown that the Flory viscosity factor Φ, which is related to $U^{\theta}_{\eta R}$, is a universal constant independent of molecular weight for each architecture, but varies with the number of arms.

For dendrimers, in general, both these ratios are found to be significantly different from those for linear chains, with values closer to those for a uniformly dense sphere, rather than the values observed for randomly coiled polymers.[3] Furthermore, both the number of generations, and the quality of the solvent are seen to significantly influence the measured value. Tande et al.[18] have compiled experimental observations on a number of different dendrimer-solvent systems, ranging in solvent quality all the way from poor solvents to very good solvents. They report that U_{RD} varies between 0.89 to 0.68 for generation 3 to generation 10 dendrimers, and $U_{\eta R}$ varies between 1.16 to 7.29 for generation 3 to generation 6 monodendrons and dendrimers. Unlike in the case of linear and star polymer chains, universal constants have not been reported.

Figures 11 and 12 report the results of our simulations. Note that in terms of nondimensional quantities,

$$U_{RD} = \frac{4}{\sqrt{\pi}\tilde{h}^*} D_{COM} R_g \quad \text{and} \quad U_{\eta R} = \frac{9\sqrt{\pi}}{8} \tilde{h}^* \frac{\eta_{p,0}}{{R_g}^3}$$

Both U_{RD} and $U_{\eta R}$ are seen to depend significantly on generation number and solvent quality, as observed in experiments, with no indication of universal behavior. While the simulated values of U_{RD} seem to approach experimental values only for generation numbers greater than 4, the simulated values of $U_{\eta R}$ lie within the range of experimentally observed values. It is difficult to directly compare predictions with experiments since a quantitative value for the quality of solvents used in the experiments is not known. Notably, measurements conducted for a fixed solvent at constant temperature, for dendrimers of varying molecular weight, correspond to different values of z according to the definition of solvent quality. In the simulations, we ensure that z is maintained constant as the generation number is increased, by suitably decreasing $\tilde{z}^*$.

We have seen so far that while the radius of gyration, the center-of-mass diffusivity, and the intrinsic viscosity do not obey power law scaling with molecular mass when viewed in terms of increasing generation numbers, they do obey power law scaling identical to those for linear and star polymers when viewed from the perspective of a fixed molecular topology. In line with these observations, and with the observations of Okumoto et al. for the Flory viscosity ratio for star polymers, Figures 11 and 12 suggest that for molecules of fixed generation, the ratios U_{RD} and $U_{\eta R}$ remain constant, independent of molecular mass. In order to observe this universal behavior, it has been necessary to carry out simulations for molecules having a fixed topology, and in solutions of constant solvent quality. It would be worthwhile to validate these predictions experimentally.

The observation for star polymer solutions that while the Flory exponent ν is independent of the number of arms f, the exponent γ depends on f, has led to the suggestion that stars with different numbers of arms belong to different

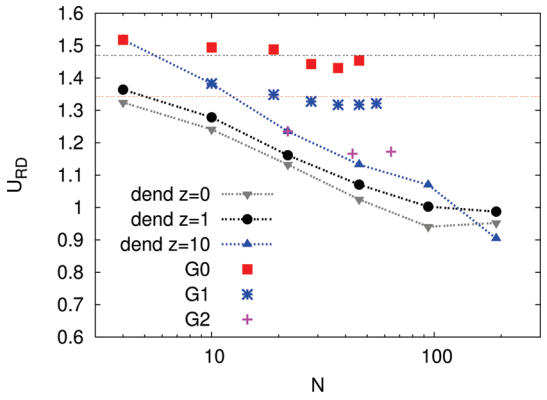


Figure 11. Molecular mass dependence of the ratio U_{RD} at fixed values of the solvent quality z. The curves denote values for increasing generation numbers, at the reference state (corresponding to $z = 0$), and at $z = 1$ and $z = 10$. The square, asterisk, and plus symbols represent dendrimers of fixed generation number (0, 1, and 2) at $z = 10$. The horizontal best fit line through the square symbols corresponds to $U_{RD} = 1.47$, while that through asterisk symbols corresponds to $U_{RD} = 1.343$.

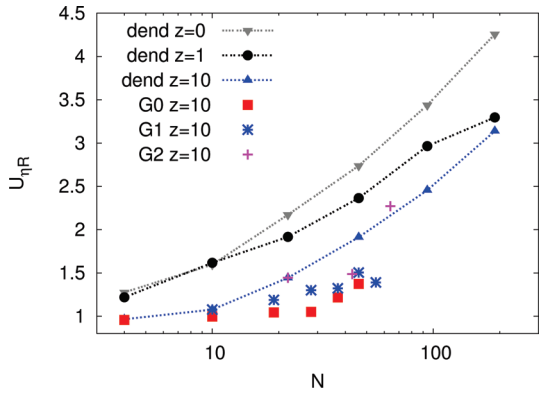


Figure 12. Molecular mass dependence of the ratio $U_{\eta R}$ at fixed values of the solvent quality z. The curves denote values for increasing generation numbers, at the reference state (corresponding to $z = 0$), and at $z = 1$ and $z = 10$. The square, asterisk, and plus symbols represent dendrimers of fixed generation number (0, 1, and 2) at $z = 10$.

universality classes.[87,92] We have observed a similar behavior in the case of dendrimers in the sense that while ν is unaffected by branching, the ratios U_{RD} and $U_{\eta R}$ are constant for a fixed generation number, but vary with varying architecture. This leads us to conjecture that each generation dendrimer constitutes a separate universality class. Experimental validation of this conjecture would establish the strong similarity between the behavior of star polymers and dendrimers.

5. Conclusions

Brownian dynamics simulations have been carried out to systematically examine the influence of solvent quality on the static and dynamic properties of a coarse-grained bead−spring chain model for dendrimers, with both intramolecular hydrodynamic and excluded volume interactions incorporated. The reference state is assumed to be a phantom dendrimer, with all repulsive interactions between monomers switched off. A scaling variable z, analogous to that for linear and star polymer systems, is shown to exist which uniquely defines the solvent quality of a dendrimer solution. Changes relative to the phantom reference state due to changes in solvent quality have been computed.

The radius of gyration of dendrimers exhibits a complex dependence on functionality, spacer length and generation number, increasing monotonically with increasing solvent quality.

For dendrimers with fixed generation number, however, power law scaling with increasing molecular mass is observed, identical to the behavior for linear and star polymer systems (see Figures 3 and 4).

The swelling of dendrimers with different architectures, relative to the reference state, is shown to collapse onto master plots in terms of z. As seen earlier for star polymers, the universal swelling of dendrimers appears to be nearly independent of molecular topology (see Figure 8).

The dependence of the translational diffusivity of dendrimers on generation number does not obey a power law, rather it decreases with increasing molecular mass less rapidly than is the case for linear chains. However, for dendrimers with a fixed topology, a power law scaling with molecular mass is observed. The swelling of dendrimers leads to a uniform decrease in the translational diffusivity (see Figure 9).

The experimentally observed characteristic maximum in intrinsic viscosity with increasing generation number is reproduced in our simulations, with increasing solvent quality leading to a shift in the maximum to higher generation numbers. The intrinsic viscosity of fixed generation dendrimers obeys a scaling law with increasing molecular mass, similar to that observed for linear chains (see Figure 10).

The ratios U_{RD} and $U_{\eta R}$ depend significantly on generation number and solvent quality, and do not assume constant values when the molecular mass is increased by increasing generation number. However, for fixed generation numbers, both ratios appear to approach constant values with increasing molecular mass. This behavior is similar to that observed for linear and star polymer systems. The dependence of the universal value on the dendrimer architecture suggests that each generation constitutes a separate universality class (see Figures 11 and 12).

The majority of the results discussed above are parameter free, and consequently very amenable to experimental validation. In particular, in the light of earlier results on star polymers, our results suggest that the following questions should be answered for dendritic systems through careful experiments:

(i) Is the θ temperature identical for dendritic and linear systems? How do ternary interactions affect the θ temperature?
(ii) Can the swelling of dendrimers be represented in terms of the scaling variable z, and how does the architecture influence swelling?
(iii) How does the solvent quality z affect the dependence of intrinsic viscosity on generation number?
(iv) Are the ratios U_{RD} and $U_{\eta R}$ universal constants for dendrimers with constant generation number?

Previous experimental observations on linear and star polymer systems suggest that though theoretical predictions of universal behavior require the existence of large numbers of length and time scales, in practice, universality is realized at surprisingly low values of molecular weight. It would not be surprising, therefore, if experimental observations reveal that this is indeed also the case for actual dendritic systems.

Acknowledgment. This work is supported by the Monash-CSIRO Collaborative Research Support Scheme, and a grant from the Australian Research Council, under the Discovery-Projects program. The simulations were performed on the Australian Partnership for Advanced Computing (APAC) cluster and on the Monash Sun Grid and generous allocation of the CPU time is kindly acknowledged. The authors are grateful for very helpful discussions with Burkhard Dünweg.

References and Notes

(1) Bosman, A. W.; Janssen, H. M.; Meijer, E. W. *Chem. Rev.* **1999**, *99*, 1665–1688.
(2) Frechèt, J. M. J., Tomalia, D., Eds. *Dendrimers and Other Dendritic Polymers*; John Wiley & Sons: Chichester, U.K., and New York, 2001.
(3) Mackay, M. *C. R. Chim.* **2003**, *6*, 747–754.
(4) Lee, C. C.; MacKay, J. A.; Frèchet, J. M. J.; Szoka, F. C. *Nat. Biotechnol.* **2005**, *23*, 1517–1526.
(5) Astruc, D.; Boisselier, E.; Ornelas, C. *Chem. Rev.* **2010**, *110*, 1857–1959.
(6) Mourey, T. H.; Turner, S. R.; Rubinstein, M.; Frèchet, J. M. J.; Hawker, C. J.; Wooley, K. L. *Macromolecules* **1992**, *25*, 2401.
(7) Mansfield, M. L.; Klushin, L. I. *J. Phys. Chem.* **1992**, *96*, 3994.
(8) Prosa, T. J.; Bauer, B. J.; Amis, E. J.; Tomalia, D. A.; Scherrenberg, R. *J. Polym. Sci.: Part B: Polym. Phys.* **1997**, *35*, 2913.
(9) Stechemesser, S.; Eimer, W. *Macromolecules* **1997**, *30*, 2204–2206.
(10) Wooley, K. L.; King, C. A.; Tasaki, K.; Schaefer, J. *J. Am. Chem. Soc.* **1997**, *119*, 53.
(11) De Backer, S.; Prinzie, Y.; Verheijen, W.; Smet, M.; Desmedt, K.; Dehaen, W.; De Schryver, F. C. *J. Phys. Chem. A* **1998**, *102*, 5451–5455.
(12) Scherrenberg, R.; Coussens, B.; van Vliet, P.; Edouard, G.; Brackman, J.; de Brabander, E.; Mortensen, K. *Macromolecules* **1998**, *31*, 456–461.
(13) Rietveld, I. B.; Smit, J. A. M. *Macromolecules* **1999**, *32*, 4608.
(14) Rietveld, I. B.; Bedeaux, D. *Macromolecules* **2000**, *33*, 7912–7917.
(15) Bodnar, I.; Silva, A. S.; Deitcher, R. W.; Weisman, N. E.; Kim, Y. H.; Wagner, N. J. *J. Polym. Sci. B Polym. Phys.* **2000**, *38*, 857–873.
(16) Hay, G.; Mackay, M. E.; Hawker, C. J. *J. Polym. Sci., B: Polym. Phys.* **2001**, *39*, 1766–1777.
(17) Jeong, M.; Mackay, M. E.; Vestberg, R.; Hawker, C. J. *Macromolecules* **2001**, *34*, 4927–4936.
(18) Tande, B. M.; Wagner, N. J.; Mackay, M. E.; Hawker, C. J.; Jeong, M. *Macromolecules* **2001**, *34*, 8580–8585.
(19) Sagidullin, A. I.; Muzafarov, A. M.; Krykin, M. A.; Ozerin, A. N.; Skirda, V. D.; Ignat'eva, G. M. *Macromolecules* **2002**, *35*, 9472.
(20) Baille, W. E.; Malveau, C.; Zhu, X. X.; Kim, Y. H.; Ford, W. T. *Macromolecules* **2003**, *36*, 839.
(21) Asteriadi, A.; Sigel, R.; Vlassopoulos, D.; Meier, G.; Dorgan, J. R.; Knauss, D. M. *Macromolecules* **2004**, *37*, 1016.
(22) Jana, C.; Jayamurugan, G.; Ganapathy, R.; Maiti, P. K.; Jayaraman, N.; Sood, A. K. *J. Chem. Phys.* **2006**, *124*, 204719.
(23) de Gennes, P.; Hervet, H. *J. Phys., Lett.* **1983**, *44*, 351–360.
(24) Biswas, P.; Cherayil, B. J. *J. Chem. Phys.* **1994**, *100*, 3201.
(25) Boris, D.; Rubinstein, M. *Macromolecules* **1996**, *29*, 7251–7260.
(26) La Ferla, R. *J. Chem. Phys.* **1997**, *106*, 688.
(27) Cai, C.; Chen, Z. Y. *Macromolecules* **1997**, *30*, 5104.
(28) Chen, Z. Y.; Cai, C. *Macromolecules* **1999**, *32*, 5423.
(29) Burchard, W. *Adv. Polym. Sci.* **1999**, *143*, 113.
(30) Ganazzoli, F.; La Ferla, R. *J. Chem. Phys.* **2000**, *113*, 9288.
(31) Mallamace, F.; Canetta, E.; Lombardo, D.; Mazzaglia, A.; Romeo, A.; Scolaro, L. M.; Maino, G. *Physica A* **2002**, *304*, 235.
(32) von Ferber, C.; Blumen, A. *J. Chem. Phys.* **2002**, *116*, 8616.
(33) Timoshenko, E. G.; Kuznetsov, Y. A.; Connolly, R. *J. Chem. Phys.* **2002**, *117*, 9050–9062.
(34) Timoshenko, E. G.; Kuznetsov, Y. A.; Ronan, C. *J. Chem. Phys.* **2002**, *117*, 9050.
(35) Zook, T. C.; Pickett, G. T. *Phys. Rev. Lett.* **2003**, *90*, 015502.
(36) Ballauff, M.; Likos, C. N. *Angew. Chem., Int. Ed.* **2004**, *43*, 2998–3020.
(37) Likos, C. N. *Soft Matter* **2006**, *2*, 478–498.
(38) Konkolewicz, D.; Gilbert, R. G.; Gray-Weale, A. *Phys. Rev. Lett.* **2007**, *98*, 238301.
(39) Kröger, M.; Peleg, O.; Halperin, A. *Macromolecules* **2010**, *43*, 6213–6224.
(40) Lu, Y.; Shi, T.; An, L.; Jin, L.; Wang, Z.-G. *Soft Matter* **2010**, *6*, 2619–2622.
(41) Lescanec, R. L.; Muthukumar, M. *Macromolecules* **1990**, *23*, 2280–2288.
(42) Murat, M.; Grest, G. S. *Macromolecules* **1996**, *29*, 1278–1285.
(43) Chen, Z. Y.; Cui, S.-M. *Macromolecules* **1996**, *29*, 7943.
(44) Cai, C.; Chen, Z. Y. *Macromolecules* **1998**, *31*, 6393.
(45) Welch, P.; Muthukumar, M. *Macromolecules* **1998**, *31*, 5892–5897.
(46) Freire, J. J. *Adv. Polym. Sci.* **1999**, *143*, 35.
(47) Cagin, T.; Wang, G.; Martin, R.; Breen, N.; Goddard, W. A., III. *Nanotechnology* **2000**, *11*, 77.
(48) Lyulin, A. V.; Davies, G. R.; Adolf, D. B. *Macromolecules* **2000**, *33*, 6899.

(49) Mansfield, M. L. *Macromolecules* **2000**, *33*, 8043.
(50) Lyulin, A. V.; Davies, G. R.; Adolf, D. B. *Macromolecules* **2000**, *33*, 3294–3304.
(51) Lee, A. T.; McHugh, A. J. *Macromol. Theory Simul.* **2001**, *10*, 244–254.
(52) Lee, A. T.; McHugh, A. J. *Macromol. Theory Simul.* **2001**, *10*, 430–433.
(53) Lee, I.; Athey, B. D.; Wetzel, A. W.; Meixner, W.; Baker, J. R., Jr. *Macromolecules* **2002**, *35*, 4510.
(54) Sheng, Y.-J.; Jing, S.; Tsao, H.-K. *Macromolecules* **2002**, *35*, 7865.
(55) Sheridan, P. F.; Adolf, D. B.; Lyulin, A. V.; Neelov, I.; Daivies, G. R. *J. Chem. Phys.* **2002**, *117*, 7802.
(56) Giupponi, G.; Buzza, M. A. *J. Chem. Phys.* **2004**, *120*, 10290.
(57) Lyulin, S. V.; Darinskii, A. A.; Lyulin, A. V.; Michels, M. A. J. *Macromolecules* **2004**, *37*, 4676.
(58) Lyulin, S. V.; Evers, L. J.; van der Schoot, P.; Darinskii, A. A.; Lyulin, A. V.; Michels, M. A. J. *Macromolecules* **2004**, *37*, 3049–3063.
(59) Freire, J. J.; Rodriguez, E.; Rubio, A. M. *J. Chem. Phys.* **2005**, *123*, 154901–14.
(60) Drew, P. M.; Adolf, D. B. *Soft Matter* **2005**, *1*, 146–151.
(61) Karatasos, K.; Lyulin, A. V. *J. Chem. Phys.* **2006**, *125*, 184907.
(62) Lee, Y. M.; Joo, Y. L. *J. Non-Newtonian Fluid Mech.* **2006**, *140*, 71.
(63) Rathgeber, S.; Monokenbush, M.; Hedrick, J. L.; Trollsas, M.; Gast, A. P. *J. Chem. Phys.* **2006**, *125*, 204908.
(64) Bosko, J. T.; Prakash, J. R. *J. Chem. Phys.* **2008**, *128*, 034902.
(65) Freire, J. J. *Soft Matter* **2008**, *4*, 2139–2143.
(66) Klos, J. S.; Sommer, J.-U. *Macromolecules* **2009**, *42*, 4878–4886.
(67) Welch, P. M.; Welch, C. F. *Macromolecules* **2009**, *42*, 7571–7578.
(68) Schäfer, L. *Excluded Volume Effects in Polymer Solutions*; Springer-Verlag: Berlin, 1999.
(69) Rubinstein, M.; Colby, R. H. *Polymer Physics*; Oxford University Press: London, 2003.
(70) Miyaki, Y.; Fujita, H. *Macromolecules* **1981**, *14*, 742–746.
(71) Vidakovic, P.; Rondelez, F. *Macromolecules* **1985**, *18*, 700–708.
(72) Hayward, R. C.; Graessley, W. W. *Macromolecules* **1999**, *32*, 3502–3509.
(73) Bercea, M.; Ioan, C.; Ioan, S.; Simionescu, B. C.; Simionescu, C. I. *Prog. Polym. Sci.* **1999**, *24*, 379–424.
(74) Doi, M.; Edwards, S. F. *The Theory of Polymer Dynamics*; Clarendon Press: Oxford, 1986.
(75) Freed, K. F. *Renormalization Group Theory of Macromolecules*; Wiley: New York, 1987.
(76) Des Cloizeaux, J.; Jannink, G. *Polymers in Solution, Their Modeling and Structure*; Oxford Science Publishers: New York, 1990.
(77) Kumar, K. S.; Prakash, J. R. *Macromolecules* **2003**, *36*, 7842–7856.
(78) Sunthar, P.; Prakash, J. R. *Macromolecules* **2005**, *38*, 617–640.
(79) Sunthar, P.; Nguyen, D. A.; Dubbelboer, R.; Prakash, J. R.; Sridhar, T. *Macromolecules* **2005**, *38*, 10200–10209.
(80) Sunthar, P.; Prakash, J. R. *Europhys. Lett.* **2006**, *75*, 77–83.
(81) Douglas, J.; Freed, K. F. *Macromolecules* **1984**, *17*, 2344–2354.
(82) Freire, J. J.; Prats, R.; Pla, J.; Garcia de la Torre, J. *Macromolecules* **1984**, *17*, 1815–1821.
(83) Wilkinson, M. K.; Gaunt, D. S.; Lipson, J. E. G.; Whittington, S. G. *J. Phys. A: Math. Gen.* **1986**, *19*, 789.
(84) Lipson, J. E. G.; Gaunt, D. S.; Wilkinson, M. K.; Whittington, S. G. *Macromolecules* **1987**, *20*, 186–190.
(85) Batoulis, J.; Kremer, K. *EPL* (*Europhys. Lett.*) **1988**, *7*, 683–688.
(86) Batoulis, J.; Kremer, K. *Macromolecules* **1989**, *22*, 4277–4285.
(87) Douglas, J. F.; Roovers, J.; Freed, K. F. *Macromolecules* **1990**, *23*, 4168–4180.
(88) Okumoto, M.; Terao, K.; Nakamura, Y.; Norisuye, T.; Teramoto, A. *Macromolecules* **1997**, *30*, 7493–7499.
(89) Okumoto, M.; Nakamura, Y.; Norisuye, T.; Teramoto, A. *Macromolecules* **1998**, *31*, 1615–1620.
(90) Okumoto, M.; Tasaka, Y.; Nakamura, Y.; Norisuye, T. *Macromolecules* **1999**, *32*, 7430–7436.
(91) Striolo, A.; Prausnitz, J. M.; Bertucco, A. *Macromolecules* **2000**, *33*, 9583–9586.
(92) Ohno, K.; Binder, K. *J. Phys.* (*Paris*) **1988**, *49*, 1329–1351.
(93) Prakash, J. R.; Öttinger, H. C. *Macromolecules* **1999**, *32*, 2028–2043.
(94) Rotne, J.; Prager, S. *J. Chem. Phys.* **1969**, *50*, 4831.
(95) Yamakawa, H. *J. Chem. Phys.* **1970**, *53*, 436.
(96) Tomalia, D. A.; Baker, H.; Dewald, J.; Hall, M.; Kallos, G.; Martin, S.; Roeck, J.; Ryder, J.; Smith, P. *Polym. J.* **1985**, *17*, 117–132.
(97) Tomalia, D. A.; Baker, H.; Dewald, J.; Hall, M.; Kallos, G.; Martin, S.; Roeck, J.; Ryder, J.; Smith, P. *Macromolecules* **1986**, *19*, 2466–2468.
(98) Tomalia, D. A.; Frechet, J. M. J. *J. Polym. Sci., A: Polym. Chem.* **2002**, *40*, 2719–2728.
(99) Graessley, W. W.; Hayward, R. C.; Grest, G. S. *Macromolecules* **1999**, *32*, 3510–3517.
(100) Warner, H. R. *Ind. Eng. Chem. Fundam.* **1972**, *11*, 379.
(101) Bird, R. B.; Curtiss, C. F.; Armstrong, R. C.; Hassager, O. *Dynamics of Polymeric Liquids—Vol. 2: Kinetic Theory*, 2nd ed.; John Wiley: New York, 1987.
(102) Kumar, K. S.; Prakash, J. R. *J. Chem. Phys.* **2004**, *121*, 3886.
(103) Öttinger, H. C. *Stochastic Processes in Polymeric Fluids*; Springer-Verlag: Berlin, 1996.
(104) Prabhakar, R.; Prakash, J. R. *J. Non-Newtonian Fluid Mech.* **2004**, *116*, 163–182.
(105) Jendrejack, R. M.; Graham, M. D.; de Pablo, J. J. *J. Chem. Phys.* **2000**, *113*, 2894–2900.
(106) Prabhakar, R.; Prakash, J. R.; Sridhar, T. *J. Rheol.* **2004**, *48*, 1251–1278.
(107) Pham, T. T.; Sunthar, P.; Prakash, J. R. *J. Non-Newtonian Fluid Mech.* **2008**, *149*, 9–19.
(108) Prabhakar, R.; Prakash, J. R. *J. Rheol.* **2002**, *46*, 1191–1220.
(109) Lyulin, A. V.; Adolf, D. B.; Daivies, G. R. *Macromolecules* **2001**, *34*, 3783.
(110) Kröger, M.; Alba-Perez, A.; Laso, M.; Öttinger, H. *J. Chem. Phys.* **2000**, *113*, 4767–4773.

Macromolecules
ARTICLE

Macromolecules **2011**, *44*, 671–682 **671**
DOI: 10.1021/ma102349k

Mesoscopic Simulations of Morphological Transitions of Stimuli-Responsive Diblock Copolymer Brushes

O. A. Guskova* and C. Seidel*

Max Planck Institute of Colloids and Interfaces, Science Park Golm, D-14424 Potsdam, Germany

Received October 14, 2010; Revised Manuscript Received December 17, 2010

ABSTRACT: Using coarse-grained DPD simulations, we study the morphology of AB diblock copolymer brushes in selective solvents which are good for the anchored A blocks but poor (of varying degrees measured by the distance from the Θ-point, τ_B) for B blocks. Choosing appropriate polymer compositions given by the fraction of B blocks, f_B, we find transitions between spherical and cylindrical micelles as well as inverted morphologies (perforated layer). We discuss the phase diagram in the $f_B-\tau_B$ parameter space and analyze characteristic quantities of the structures obtained such as domain size, periodic spacing and brush height. The internal structure of the uniform (lamellar) structure is investigated in detail. The simulation results are compared with theoretical predictions and experimental observations.

1. Introduction

Polymer brushes, i.e., polymers densely end-anchored to an interface are interesting because of their scientific and technological importance including, for example, colloid stability, biomimetic materials, and drug delivery.[1−3] If polymers are tethered densely enough, i.e., basically if the area per chain $A = 1/\rho_a$ (with ρ_a being the grafting density) becomes smaller than the free coil size squared R_0^2, chains are enforced to stretch away from the surface to avoid overlapping. Brushes consisting of two or more incompatible components are of special interest because they exhibit phase separation on nanometer length scales. Both mixed brushed of different homopolymers grafted to the same substrate[4−6] and brushes of diblock copolymers (DCBs)[7−12] were studied. Structure transitions and microphase separation are driven by immiscibility and/or the contrast in solvent affinity. Because of the end-tethering there occur two different types of phase separation: (i) perpendicular to the grafting plane on length scales set by block lengths or the length of the collapsing chain in mixed brushes, and (ii) at the brush surface laterally on length scales of the polymer correlation length or governed by the particular grafting procedure. Lateral segregation can result in stable surface nanopatterns and enables surface tuning or "smart" surfaces that respond to some extent to external stimuli.[13−15] Because of their unique structure and novel properties, DCBs have attracted increasing attention. Varying grafting density ρ_a, chain length N, relative block lengths $f_{A,B}$ as well as composition and sequence of the blocks, the interaction strength between blocks and with surrounding media, a variety of well-ordered structures have been predicted by theory[10,11,16,17] and confirmed experimentally,[9,18−23] as well as by means of computer simulations.[12,24−26]

Beside the interest of fundamental research DCBs come up also with a strong potential of new and innovative applications in particular as stimuli responsive material in sensors, biomimetics, and microfluidics. That is why extensive research was focused on the design of new diblock copolymer brushes. Because of a strong contrast between different polymer blocks with respect to certain molecular parameters such as hydrophobicity and flexibility, DCBs can undergo structural transitions and drastic changes in specific properties under the influence of external stimuli. Exposing DCBs, for example, alternately to selective and nonselective solvents a self-reorganization of the brushes was demonstrated[21] and the mechanism is used to implement surfaces of dual functionality.[27] Using thin block copolymer films as template, it was shown that ordered metal clusters, chains and even nanowires can be produced because of the different affinity of nanoparticles to core and shell domains of copolymer brushes.[28,29] While macroscopic surface properties such as wettability and adhesion only depend on the average composition of the top layer on large length scales, the interaction of brushes on nanoscales is governed by the details of its morphology. Recently, it was shown that the main parameter that governs the ordering of nanoparticles at the polymer brush surface is the size ratio of nanoparticles and brush patterns. Depending on its value nanoparticles can be accommodated either inside preferred domains or on the top of them. Multiblock copolymer brushes are used for the specific adsorption of proteins and nanoparticles from solution.[30−32] However, to establish an effectively selective mechanism the hydrophobic patches on the top of the brush have to have lateral dimensions that are comparable to the size of the solute. To make substantial progress with applications based on polymer pattern on nanoscales doubtless a detailed understanding of the microphase separation in multiblock brushes is of fundamental importance.

Using self-consistent field (SCF) approaches, scaling arguments and computer simulations, theoretical studies of block copolymer brushes have predicted a highly complex behavior that depends on (i) molecular parameters such as overall molecular weight, partial fraction of the blocks, miscibility, surface free energy, chain flexibility, and on (ii) preparation conditions and external parameters such as grafting density, solvent selectivity, temperature.[11,24,33−36] Already in the 1990s it was shown that linear AB diblock copolymer brushes exposed to a poor solvent form patterned films if the polymer−solvent interaction differs for the two blocks.[33] Similar structures of such brushes were demonstrated in selective solvents which are Θ-like or marginally good, respectively, for one block but poor for the other one.

*Corresponding authors. E-mail: (O.A.G.) olga.guskova@mpikg.mpg.de; (C.S.) seidel@mpikg.mpg.de.

© 2011 American Chemical Society

Published on Web 01/06/2011

Similarly to free chains in solution, tethered chains are found to self-assemble into micelles, the core of which consists of the less soluble blocks while the better soluble ones form the outer shell. On large length scales, ordered arrays of such micelles appear as patterned films. Segregation phenomena both perpendicular to the substrate surface and in lateral directions were investigated by SCF studies.[17,24,26,34] For AB copolymers of two immiscible blocks ($\chi_{AB} > 0$) in a nonselective solvent the quality of which is not too good, a perpendicular demixing transition was found likewise that in the uniform lamella morphology obtained for DCBs in selective solvents.[10] In summary, a rich phase behavior of DCBs was predicted where the equilibrium morphology is governed by the total chain length, the volume fraction of the two blocks and the Flory−Huggins parameters χ_{PS} and χ_{AB} of the interactions between polymers and solvent and between the two polymer blocks, respectively.

Although the theory developed during the last one and a half decades convincingly captures the general features of the self-assembly of block copolymers in selective solvents, there are still important points to elucidate such as the subtle interplay between the immiscibility of polymer blocks and solvent selectivity, the particular composition of the brush surface, and correlations between morphologies and memory effects. Numerical simulations offer an efficient means of improving the understanding and some progress has been achieved in recent years.[25,26,36] Nevertheless, more studies on block copolymer brushes are necessary to understand not only their microphase-separated structures but also their response to external stimuli such as solvents of different quality. The knowledge of the behavior of particular structure parameters (domain size, periodic spacing, inhomogeneity) is essential to succeed in the specific design of smart surfaces produced by coating with a thin polymer film.

In this article, we study the microphase separation of diblock copolymer brushes in selective solvents by means of dissipative particle dynamics (DPD) simulations. Each polymer consists of two blocks of length N_A and N_B, respectively. The composition of polymers is measured by the parameter $f_B = N_B/N$ with N being the constant total length $N = N_A + N_B$. The selective solvent is assumed to be good for A blocks and poor for B blocks. The selectivity is varied by tuning the solvent quality with respect to the B blocks which is measured by the dimensionless distance from the Θ-point, τ_B. To form a brush the polymers are tethered by their A end to a solid interface. The DPD method developed by Hoogerbrugge and Koelman[37] is a mesoscopic simulation technique that works with coarse-grained soft particles (representing either a fluid element containing hundreds of solvent molecules or a chain section of a few monomers) and enables to reach length and time scales not accessible by molecular dynamics or Monte Carlo simulations. This approach allows one to study microphase separation and structure formation in sufficiently large systems and the morphology diagram of diblock copolymer brushes can be constructed as a function of block composition f_B and the solvent quality τ_B.

The outline of the article is as follows: in the next section we give a short summary of the coarse-grained model and the simulation technique used in the study. The morphology diagram of DCBs in selective solvents obtained by DPD simulations is presented in subsection 3.1. Before comparing simulation results for various geometrical parameters such as domain size and periodic spacing with theoretical predictions in subsection 3.2, we report briefly the scaling theory of spherically micellar phases and suggest an extension to the stripe-like phase of cylindrical micelles. Section 3 is completed with a discussion of the interfacial width of lamellar phases both in selective and nonselective solvents. Finally we conclude with a brief summary outlook.

2. Simulation Model and Method

We study microphase separation of A-*b*-B diblock copolymer brushes in selective solvents using DPD simulations within a coarse-grained model. This mesoscopic approach was successfully applied to simulate homopolymer brushes.[38,39] In our case we have four different types of beads: solvent (S), polymer A block (A), polymer B block (B), and wall (W). Wall beads being fixed in space are used (i) to mimic the grafting plane at $z = 0$ and (ii) to close the simulation box on the opposite side in order to ensure 2D + 1 slab geometry. The beads interact via effective forces chosen to reproduce the hydrodynamic behavior of the fluid. In our model all the beads have the same mass m_0 and the same size (radius) r_c, but they may differ in their interaction strength a_{ij}. Forces are pairwise additive, are short ranged, and do not have a hard-core part.[40] Time and length scales are set by these parameters and should be extracted from the simulations. The DPD method solves the Newtonian equations of motion for particles subject to interparticle conservative, dissipative and random forces. Thus, we have

$$\frac{d\mathbf{r}_i}{dt} = \mathbf{v}_i \quad m_i \frac{d\mathbf{v}_i}{dt} = \mathbf{f}_i \tag{1}$$

where $\mathbf{f}_i$ is the pairwise additive force

$$\mathbf{f}_i = \sum_{j \neq i} (\mathbf{F}_{ij}^C + \mathbf{F}_{ij}^D + \mathbf{F}_{ij}^R) \tag{2}$$

At $r_{ij} < r_c$, the slowly varying conservative force is given by $\mathbf{F}_{ij}^C = a_{ij}(1 - r_{ij}/r_c)\hat{\mathbf{r}}_{ij}$, while it is zero at distances larger than r_c. $\hat{\mathbf{r}}_{ij} = \mathbf{r}_{ij}/\mathbf{r}_{ij}$ gives the direction of the force. The strength of the repulsion is set by the interaction parameter a_{ij}. The dissipative force is linear and expressed as $\mathbf{F}_{ij}^D = -\gamma_{ij}\omega^D(r_{ij})(\hat{\mathbf{r}}_{ij} \cdot \mathbf{v}_{ij})\hat{\mathbf{r}}_{ij}$, where γ_{ij} is the strength of the dissipation (friction coefficient) and v_{ij} is the relative velocity of beads i, j. The random force reads $\mathbf{F}_{ij}^R = (\sigma_{ij}\omega^R(r_{ij})\zeta_{ij}\hat{\mathbf{r}}_{ij})/(\Delta t)^{1/2}$. $\omega^D(r_{ij})$ and $\omega^R(r_{ij})$ are weight functions which become zero at $r_{ij} > r_c$, and ζ_{ij} is a Gaussian random variable. According to the fluctuation−dissipation theorem friction coefficient γ_{ij} and noise amplitude σ_{ij} are coupled by $\sigma_{ij}^2 = 2k_BT\gamma_{ij}$[40] which gives the relation to temperature. In this study γ_{ij} and σ_{ij} are set as $\gamma_{ij} = 4.5\ k_BTt_0/r_c^2$ and $\sigma_{ij} = 3.0\ k_BTt_0^{1/2}/r_c$, where the DPD unit of time is given by $t_0 = (m_0r_c^2/k_BT)^{1/2}$. Neighboring beads along polymer chains are connected by harmonic springs giving an additional force $\mathbf{F}_{ij}^S = k_s\mathbf{r}_{ij}$. We use a spring constant $k_s = 4\ k_BT/r_c^2$ while end-grafting to the wall is modeled by springs of strength $k_s = 10\ k_BT/r_c^2$. If rescaled quantities are used in the following, for simplicity, they are measured in units of $k_BT = r_c = m_0 = 1$. The simulations are performed in a tetragonal box of constant volume $V = L_x L_y L_z$ which is considered to be periodic in the x and y directions. Walls consisting of two dense layers of fixed beads at $z = 0$ and $z = L_z$, respectively, make sure that no particles cross the grafting plane as well as the top boundary of the simulation box. In our standard system, we simulate brushes of $M = 362$ chains randomly grafted by one end to the interface at $z = 0$ each of which has $N = 30$ nonanchored beads. Counting from the grafted chain end, the first $N_A = f_AN$ beads are of type A while the last $N_B = (1 - f_A)N = f_BN$ beads are of type B. As mentioned above, in the simulations reported in the paper the total length of each polymer chain is constant but their composition is changed by varying f_B as the corresponding control parameter. Choosing $L_x = L_y = 25r_c$ and $L_z = 40r_c$ the grafting density becomes $\rho_a = M/(L_xL_y) = 0.58r_c^{-2}$. To check for possible finite-size effects, the simulation of a few points in the a_{BS}−f_B parameter space was repeated in a large system of $M = 2090$ chains with $L_x = L_y = 60$. The total number of beads (polymers and solvent) in the simulation box is chosen to fix the overall reduced density at $\rho r_c^3 = 3.0$ The complete set of

interaction parameters a_{ij} used are given in Table 1. Let us remember the following points: (i) Conservative DPD interactions are purely repulsive, i.e., the larger the value of a_{ij} the stronger the repulsion between the corresponding beads. (ii) The parameters chosen in the simulations are similar to those suggested by Groot and Warren[41] to ensure correct hydrodynamic behavior on large length scales. (iii) The parameter a_{AB} sets the incompatibility between the two polymer blocks. Although its exact value is arbitrary to same extent, $a_{AB} = 40$ is an intermediate value that guarantees a rich phase diagram. (iv) The interaction parameters a_{ij} are related to the Flory−Huggins parameters χ_{ij} and phenomenological relations can be used to map the model system to real polymers.[41,42] The equation of motion eq 1 is integrated by means of a modified velocity-Verlet algorithm[41] with time step $\Delta t = 0.04t_0$. The first 2×10^5 configurations are discarded, and production runs were done for 1×10^6 to 2×10^6 configurations.

3. Simulation Results and Discussion

First we determine the Θ-point of the model system under consideration. Simulating free, isolated homopolymer chains (P) with $a_{PP} = a_{SS} = 25$ and analyzing the chain length dependence of coil size at varying strength of polymer−solvent interaction a_{PS}, Gaussian behavior $R \sim R_0 \sim aN^{1/2}$ was found to occur at $a_{PS} = a_{PS}^{(\Theta)} \approx 27.3$, which is in agreement with the data recently obtained by Nardai and Zifferer.[43] Thus, for $a_{BS} \geq 30$ according to the parameter set given in Table 1, we are considering tethered

Table 1. DPD Interaction Parameters Used in the Present Simulations[a]

a_{ij}	A	B	S	W
A	25	40	25	25
B	40	25	a_{BS}	25
S	25	a_{BS}	25	25
W	25	25	25	0

[a] S, A, B, and W represent solvent, A and B polymer beads, and wall beads, respectively (in units of k_BT/r_c). The values are chosen to reproduce the compressibility of water. The strength of the repulsion between B polymer beads and solvent is varied.

diblock copolymers in selective solvents where polymers are anchored by the end of the soluble A block while the solvent is poor for the B block. Under such conditions, at sufficiently large grafting densities the A blocks are expected to form brushes whereas the insoluble B blocks can exhibit several distinct morphologies the realization of which depends on chain composition $f_B = N_B/(N_A + N_B)$ and solvent quality $\tau_B = a_{BS}/a_{BS}^{(\Theta)} - 1 > 0$. The B block rich phase can be either on the top of the brush or partly inside the A rich phase. Varying f_B as well as a_{BS}, in the following we discuss the influence of both factors on morphology as well as on different quantitative parameters of the various structures. For spherically micellar structures, a scaling theory was suggested by Zhulina et al.[35] Below we give an extension of the scaling approach to tethered cylindrical micelles. The behavior obtained by simulations is compared with the predictions supplied by scaling theory. Si/SiO_2//PS-*b*-PMMA brushes immersed in cyclohexane are a typical real example of the system under consideration.[21]

3.1. Morphology Diagram. The morphology diagram (indicated by equilibrium snapshots represented as top view of equidensity plots) obtained by simulations in the parameter range $25 \leq a_{BS} \leq 50$, $0.17 \leq f_B \leq 0.67$ is given in Figure 1. For moderately selective solvent, $\tau_B \approx 0.5$ ($a_{BS} = 40$), the four typical morphologies appearing with growing length of the nonsoluble B block, i.e., (hexagonally ordered) spherical micelles, stripe-like cylindrical micelles, perforated layer, and two-layer lamella, are shown as three-dimensional snapshots in Figure 2. In Figure 3, we plot equilibrium morphologies theoretically predicted by Matsen and Griffiths.[11] Although the theoretical study was done for melt brushes of diblock copolymers the qualitative agreement with the simulation results is almost perfect. Obviously the corresponding quantitative copolymer compositions are different because the selective solvent causes an additional segregation tendency not present in melt systems. Recently Wang and Müller[12] studied the microphase separation of DCBs in selective solvents modeled by effective monomer−monomer interactions by means of single-chain-in-mean-field Monte Carlo (MC) simulations. The morphology diagram in the

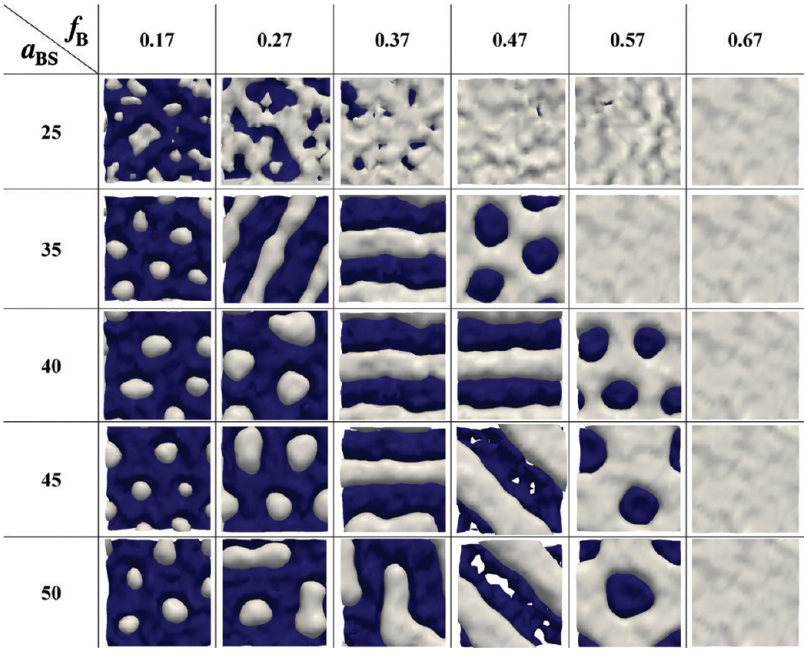


Figure 1. Morphology diagram of a diblock copolymer brush exposed to a selective solvent in terms of the interaction strength between B beads and solvent (a_{BS}) and polymer composition (f_B). Shown is the top view of equidensity plots where A and B regions are colored dark and light gray, respectively.

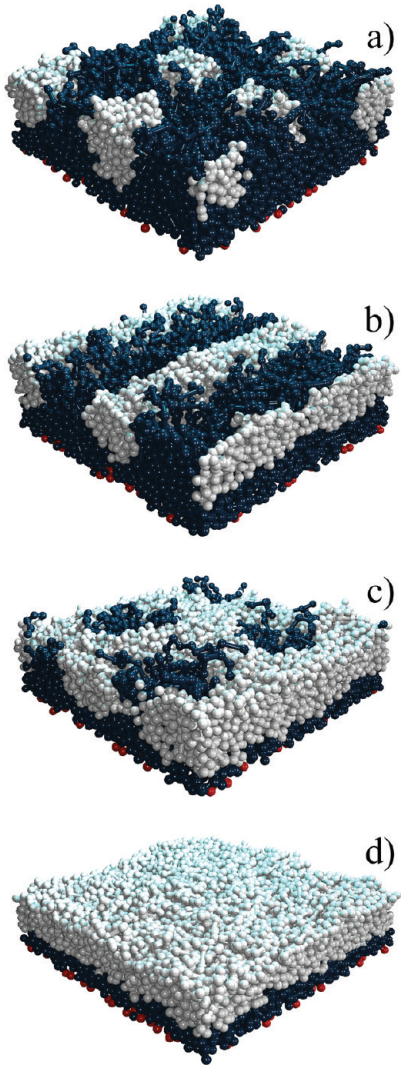


Figure 2. Simulation snapshots of typical morphologies obtained at $a_{AS} = 25$, $a_{AB} = 40$, $a_{BS} = 40$ and varying polymer composition: (a) $f_B = 0.17$ hexagonal phase of B micelles, (b) $f_B = 0.37$ stripes of B rich regions, (c) $f_B = 0.57$ hexagonal phase of A spots (perforated layer), and (d) $f_B = 0.67$ lamella (B layer on the top of A layer). The coloring of A and B beads is chosen in the same way as in Figure 1; anchors are red.

$\rho_a - f$ parameter space exhibits similar phases labeled as dimple (spherical micelles), ripple (nearly bicontinuous), perforated layer, and sandwich (lamella). Although it is not given at which τ_B their morphology diagram is determined in the case of a highly selective solvent, the corresponding phase boundaries roughly extrapolated for $\rho_a R_{e0}^2 \approx 17.7$, with R_{e0} being the mean-square end-to-end distance of a free chain in good solvents which is in our case about $5.5r_c$, are not in disagreement with those obtained in our study. In contrast to both our results and the SCF theory predictions by Matsen and Griffiths, the MC results do not show any clear order of the laterally structured phases. The authors note, however, that at small f_B the B micelles tend to arrange in a locally hexagonal pattern. Unlike ref 12 in the present study the grafting density is fixed and we address the effect of a varying quality of the selective solvent measured by the distance from the Θ-point $\tau_B(a_{BS})$. Most likely, the particular case called in ref 12 weakly selective solvent, where the perforated layer phase is missing, corresponds in our model to weak excess repulsion $a_{BS} < 35$, i.e., $\tau_B < 0.28$. Note that in contrast to previous simulations the model used in the present study includes explicit solvent. Therefore, monomer−monomer

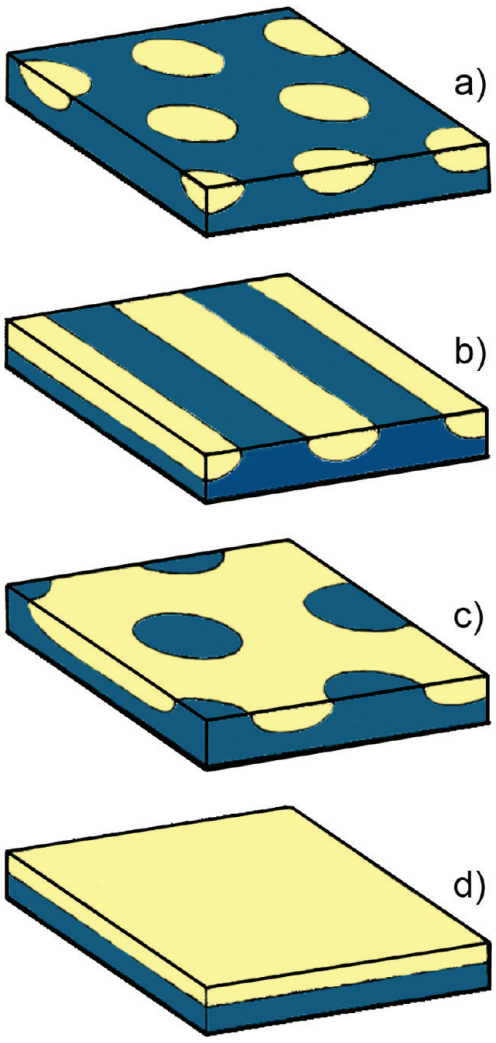


Figure 3. Equilibrium morphologies predicted by SCF theory at different diblock compositions f_B: (a) 0.15 (hexagonal), (b) 0.25 (stripe), (c) 0.35 (inverted hexagonal), and (d) 0.45 (uniform) (adapted from Matsen and Griffiths[11]).

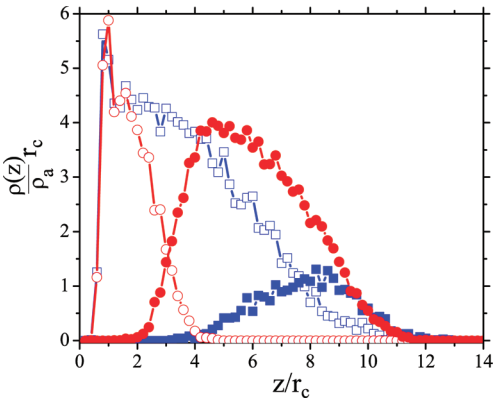


Figure 4. Partial density profiles of diblock copolymers with incompatible A (open symbols) and B (filled symbols) blocks ($a_{AB} = 40$) in a nonselective (good) solvent ($a_{AS} = a_{BS} = 25$) at two different polymer compositions: $f_B = 0.17$ (blue squares) and 0.67 (red circles).

interactions and monomer−solvent interactions are treated independently. Below we will show that this particular extension of the model gives rise to new features in the behavior of DCBs. For $a_{BS} = 25$, the solvent is nonselective

Table 2. Domain Sizes and Periodic Spacing for Observed Morphologies[a]

	f_B				
a_{BS}	0.17	0.27	0.37	0.47	0.57
35	hexagonally ordered spherical domains of B blocks $R = 2.94$, $D = 9.95$	stripes of B blocks $W = 4.11$, $D = 9.76$	stripes of B blocks $W = 6.00$, $D = 12.11$	hexagonally ordered "spot"-domains of A blocks $R = 7.72$, $D = 13.90$	uniform (lamella)
40	hexagonally ordered spherical domains of B blocks $R = 2.95$, $D = 10.89$	deformed spherical domains of B blocks	stripes of B blocks $W = 5.37$, $D = 12.78$	stripes of B blocks $W = 6.88$, $D = 12.50$	hexagonally ordered "spot"-domains of A blocks) $R = 7.60$, $D = 13.45$
45	hexagonally ordered spherical domains of B blocks $R = 2.95$, $D = 11.42$	deformed spherical domains of B blocks	stripes of B blocks $W = 5.36$, $D = 13.46$	stripes of B blocks	perforated layer
50	nonregular domains of B blocks	wormlike domains of B blocks	wormlike domains of B blocks	stripes of B blocks	perforated layer

[a] Key: R, radius of spherical aggregates; D, periodicity; W, stripe width.

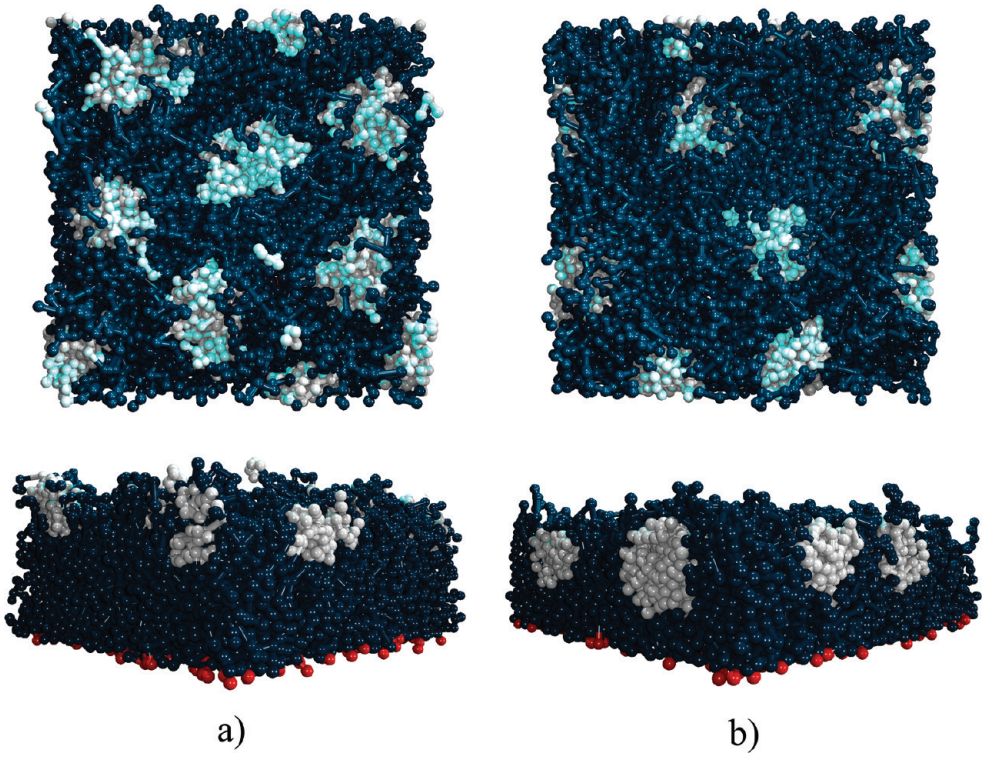


Figure 5. Simulation snapshots of spherical-micelle morphologies obtained at $f_B = 0.17$ and $a_{BS} = 35$ (a) and 47.5 (b). Top and side view have color coding as in Figure 2.

but both A and B blocks are soluble. The only driving force for segregation effects is the incompatibility between the two polymer blocks set by $a_{AB} = 40$. In this case, the snapshot analysis (not shown in the paper) indicates vertical (perpendicular to the grafting plane) segregated structures in which the number of unfavorable A/B contacts is minimized. A layer preferentially consisting of tethered A blocks occurs close to the grafting plane while the B blocks are located on the top of the A matrix. At low and moderate length of the B block ($0.17 < f_B < 0.37$), we see some lateral segregation as well. However, the B aggregates exhibit neither specific shapes nor long-range order. In Figure 4, we plot the partial monomer number densities per chain for A and B blocks $\rho_{A,B}$, respectively, as a function of the distance from the grafting plane. $\rho_{A,B}$ is normalized such that $\int dz\ \rho_{A,B}/\rho_a = N_{A,B}$. These profiles give specific information about vertical segregation. For rather short B blocks ($f_B = 0.17$, i.e., $N_B = 5$), the density profiles indicate that B aggregates are embedded at the rim of the A region. Increasing the length of B blocks, first for $f_B = 0.47$ we obtain a complete lamella structure which is more or less uniform in lateral directions (see Figure 1). For $f_B = 0.67$, the density profiles show a well-defined A/B interface region with a width of about $2r_c$. Details of the interface of lamellar structures are discussed in section 3.3.

Note that there is experimental evidence for both structures obtained in the simulations with a nonselective, good solvent. On the one hand smooth, featureless surfaces without lateral segregation were reported for DCBs of moderate grafting density in nonselective solvents.[19,20] On the other hand, for sufficiently large grafting density and/or high A/B incompatibility, lateral pattern were obtained also in

nonselective good solvents such as for PS-*b*-PMA brushes in dichloromethane.[19] Actually the grafting density $\rho_a r_c^2$ of our model system is about 0.6 which is a rather high value that can indeed favor the formation of disordered lateral structures. For short A blocks and long, nontethered B blocks, weak lateral segregation is smeared out and we obtain a smooth lamellar phase.

The situation is drastically changed as soon as the solvent becomes selective with growing $a_{BS} > a_{BS}^{(\Theta)}$. Obviously in all cases simulated with a selective solvent $a_{BS} > 25$ (see Figure 1) B blocks are insoluble while the solvent is a good one for tethered A blocks. For $f_B = 5/30 \approx 0.17$, $a_{BS} > 25$ and $f_B = 8/30 \approx 0.27$, $a_{BS} = 40$, the B blocks form small, roughly spherical aggregates hexagonally placed on the A matrix. Both average radii and distances are given in Table 2. With increasing interaction strength a_{BS}, i.e., decreasing solvent quality for the B blocks, the average number of chains per micelle is expected to grow in order to reduce the total surface of B regions. Note that for $a_{BS} = 50$, the restricted size of the system simulated does not enable a reliable study of any long-range order. In the parameter range under consideration the structure of B regions resembles to surface attracted spherical micelles usually formed by nongrafted amphiphiles in selective solvents. Looking closely (see Figure 5) one realizes that the solvophobic B blocks are partially embedded in the layer of solvophilic A blocks. To wrap the B rich domains and to shield them from poor solvent the grafted A blocks are stretched and bent. The effect increases with growing a_{BS}: The micelle cores are pushed deep into the A layer and the shielding at the brush rim is improved. This particular feature is well-known from the so-called onion-like structure predicted by Zhulina et al.[16] for spherical micelles. Actually it is not restricted to spherical micelles but a more general behavior obtained for various morphologies. In Figures 6 and 7 we plot snapshots of stripe-like structures that illustrate the shielding tendency discussed. The snapshots demonstrate also the growing lateral tension within A blocks with growing f_B and a_{AB}. For $f_B \approx 0.27$, stripe-like structures are found at intermediate solvent selectivity $a_{BS} = 35$, where the solvophobic B blocks form cylindrical micelles. In general, the stripes are not full cylinders but can be flattened or composed of two half-lenses. For a detailed discussion of both spherically micellar and stripe morphologies we refer to the next subsection. For polymer composition $f_B \approx 0.27$, with increasing solvent selectivity $a_{BS} > 40$, the spherical B domains become deformed and are merging to form wormlike aggregates at $a_{BS} = 50$.

Replacing more solvophilic A beads by solvophobic B beads, at $f_B = 0.37$ spherical B micelles disappear, and basically we find stripes. For $f_B = 0.37$ and very strong selectivity ($a_{BS} = 50$), there remain wormlike aggregates. If the B block length is further increased the formation of an inverted hexagonal phase (or perforated lamella) is observed where A spots are distributed in the B matrix. Finally at $f_B > 0.57$, $a_{BS} < 40$ and at $f_B = 0.67$ for the complete a_{BS} parameter range simulated, lateral segregation disappears but we find a perpendicularly segregated phase consisting of two lamellae of A and B blocks, respectively. Figure 8 shows the brush density profile in a selective solvent ($a_{BS} = 40$) at three different chain compositions. For short B blocks ($f_B = 0.17$), the B micelles are pushed deeply into the A rich region compared to the structure in nonselective good solvents shown in Figure 4 . Hence, the partial monomer densities confirm the onion structure mentioned above in which the solvophobic B domains are partially covered by solvophilic A chains. At a copolymer composition of almost 50:50 ($f_B = 0.47$) the B stripes are located at the rim of the A brush and finally at $f_B = 0.67$ there appear two clearly separated distributions which indicates a two-layer structure with a well-defined interface (see subsection 3.3). However, the bottom A region exhibits a long tail into the B rich top layer. Note that because of the particular setting $a_{AB} = a_{BS} = 40$, the B density profile appears almost perfectly symmetric. The corresponding total polymer density profiles are plotted in Figure 9. For $f_B = 0.17$, where the B micelles are embedded in the A brush, the total density profile shows no fingerprint of the complex morphology but it looks like

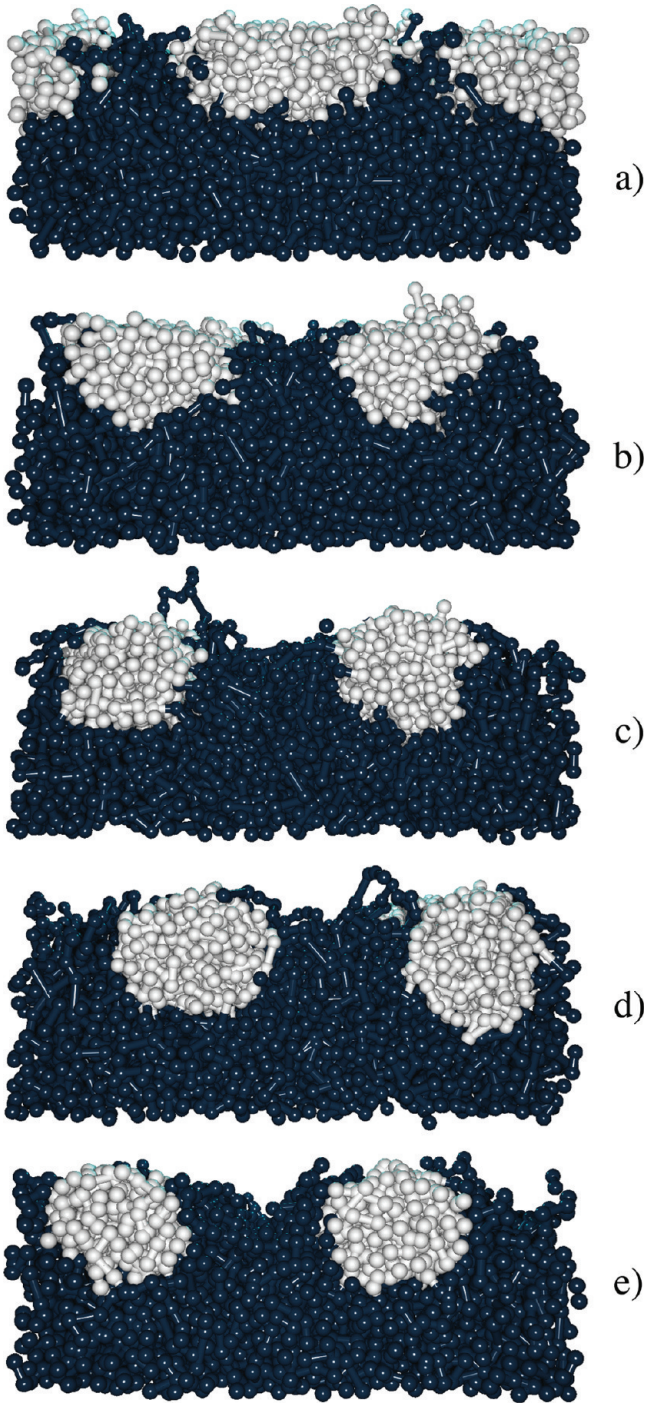


Figure 6. Simulation snapshots of stripe morphologies obtained at $f_B = 0.37$ and different a_{BS}: (a) 32.5, (b) 36, (c) 40, (d) 45, and (e) 47.5. Shown are cross sections perpendicular to the stripes with color coding as in Figure 2.

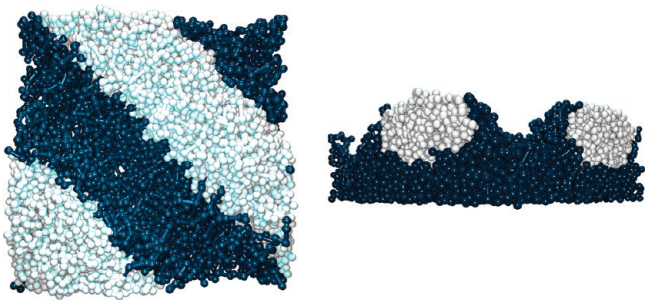


Figure 7. Simulation snapshots of the stripe-like phase obtained at $f_B = 0.47$, $a_{BS} = 50$. Top and side view, respectively.

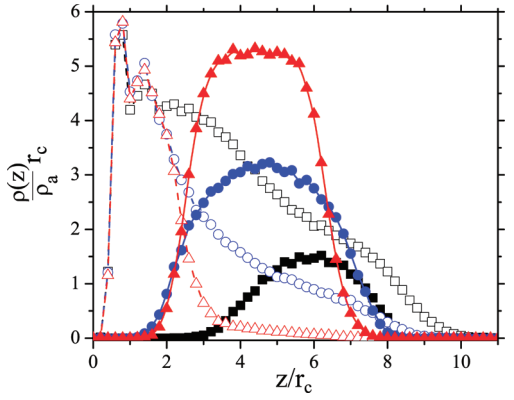


Figure 8. Partial brush density profiles of tethered A blocks (open symbols) and free-end B blocks (filled symbols), respectively, perpendicular to grafting plane at $a_{BS} = 40$ and varying chain composition f_B: 0.17 (squares), 0.47 (circles), and 0.67 (triangles).

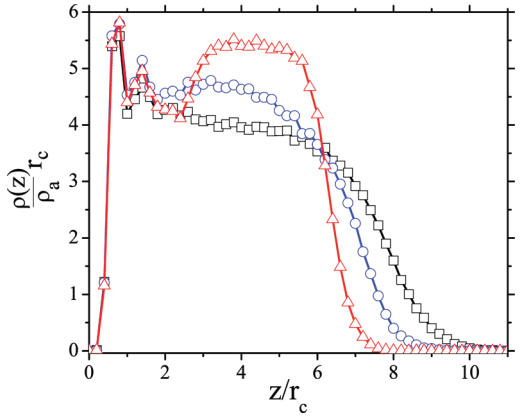


Figure 9. Total brush density profiles perpendicular to grafting plane at $a_{BS} = 40$ and varying chain composition f_B: 0.17 (squares), 0.47 (circles), and 0.67 (triangles).

typical profiles seen in simulations of homopolymer brushes.[39] On the other hand, for simple homopolymer brushes, the profiles obtained at large f_B would clearly indicate nonequilibrated structures which are now stabilized by both the incompatibility between A and B beads and the selective solvent. In Figure 10, we plot the dependence of brush height on polymer composition at varying quality of the selective solvent. For simplicity, the brush height is assumed to be determined by the inflection point of the total polymer density profile at large z. The figure illustrates the shrinking of the brush with increasing length of the solvophobic block. Note that we consider systems of constant total chain length, i.e., an increase in f_B implicates a

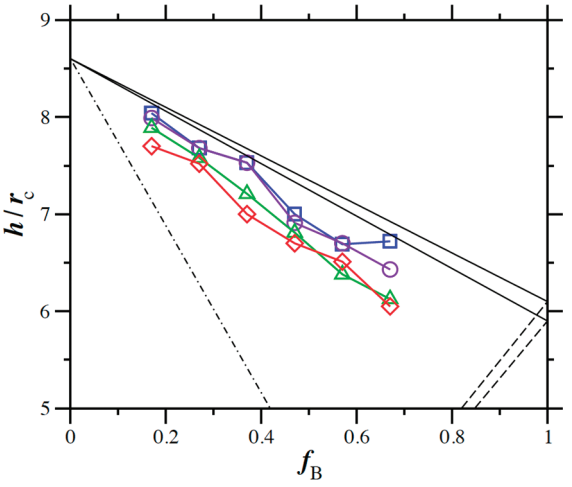


Figure 10. Polymer brush height vs chain composition for different selective solvent: $a_{BS} = 35$ (squares), 40 (circles), 45 (triangles up), and 50 (triangles down). In addition the brush heights extrapolated for uniblock brushes of corresponding partial chain lengths are shown: purely A (dash-dotted), purely B at $a_{BS} = 35$ and 50, respectively (dashed). The heights of hypothetical two-layer systems of A and B brushes are plotted as solid lines.

decreasing length of solvophilic A blocks. The height of corresponding homopolymer brushes with chain length $N_{tot} = 30$ are $h_A^{(0)} \approx 8.6r_c$, $h_B^{(0)} \approx 6.1r_c$ ($a_{BS} = 35$) and $h_B^{(0)} \approx 5.9r_c$ ($a_{BS} = 50$), respectively. Assuming linear scaling with chain length, in Figure 10 the heights of homopolymer brushes are plotted as $h_A(f_B) \sim (1 - f_B)h_A^{(0)}$ and $h_B(f_B) \sim f_B h_B^{(0)}$. Additionally, the height of a hypothetical two-layer system is given as $h_A(f_B) + h_B(f_B)$. For all the brush realizations studied, the obtained heights lie below the extrapolated homopolymer values $h_A(f_B) + h_B(f_B)$. This behavior is reasonable but it does not give additional insight into the properties of block copolymer brushes. To understand the behavior of the brush height over the whole f_B range, one would have to consider the various morphologies in detail. Within the framework of scaling theories, however, this is only possible for lamellar structures. Note the conceptual problems to define the brush height of highly structured surfaces like that shown in Figure 7.

The simulation results discussed above can be compared with recent experiments by Santer et al.[20,44] and O'Driscoll et al.[45] Like in our model system, in these experiments, the solvent was selective to the grafted blocks and poor to the top blocks. For all brushes, regardless of different chemical nature transitions from ripple-like (stripe-like) via wormlike to spherical-like patterns were obtained with increasing length of tethered blocks, i.e., with decreasing f_B. Although long-range order could not be experimentally detected, the morphological transitions observed are very similar to those obtained in our simulations at sufficiently selective solvent (see Figure 1).

3.2. Hexagonally Ordered Spherical Micelles and Stripe-Like Cylindrical Micelles. *Theory*. A scaling theory of grafted diblock copolymers in selective solvents that describes the formation of spherical micelles was developed by Zhulina and co-workers in the mid-1990s.[35] Following de Gennes,[46] the dimensionless monomer number density inside a globule obeys $\phi \sim \tau$. Hence, the core density of a spherical micelle reads

$$\phi \sim m_3 N_B a^3 / {R_B}^3 \sim \tau_B \qquad (3)$$

where m_3 is the number of copolymers included in one micelle. Henceforth we use the common notation m_d where $d = 1, 2, 3$ for planar, cylindrical, and spherical aggregates.

Note, however, that only m_3 is a dimensionless number while, e.g., m_2 is the line density of polymers. Equation 3 yields the core radius

$$R_B \sim a(m_3 N_B/\tau_B)^{1/3} \quad (4)$$

The total size D of the micelle (B core plus A corona) is determined by the grafting area per m_3 chains

$$D \sim (m_3/\rho_a)^{1/2} \quad (5)$$

For micellar morphologies, the free energy per polymer can be written as the sum of three contributions

$$F = F_{int} + F_A + F_B \quad (6)$$

where F_{int} is the free energy of the interface between the corona of dissolved A blocks and the core of collapsed B blocks, and F_A and F_B are the free energies of an A block and B block, respectively. According to Zhulina et al.[35] the term F_B that accounts for the stretching of B blocks can be neglected at $\tau_B{}^2 N_B \gg 1$. Thus, the equilibrium structure is determined by the balance of the interface free energy and the corona contribution. The interfacial term reads (free energy is measured in units of $k_B T$)

$$F_{int} \sim \gamma \sigma_d \quad (7)$$

where the interfacial tension is given by $\gamma \sim 1/\xi_T{}^2 \sim \tau^2/a^2$ with $\xi_T \sim a/\tau$ being the thermal correlation length. For spherical micelles, the interface area per chain σ_d is given by $\sigma_3 \sim R_B{}^2/m_3$. Hence, eq 7 yields

$$F_{int} \sim \frac{\tau_B{}^2}{m_3}\left(\frac{R_B}{a}\right)^2 \quad (8)$$

In the case of F_A, one has to distinguish between two different situations.[35] For long A blocks with $H \gg D$, the system can be considered as a planar brush of thickness $H \sim N_A \rho_a{}^{1/3}$ covered by spherical micelles of size D. In this case the free energy of the A block is governed by the loss of entropy due to its grafting at the core surface and F_A becomes (neglecting logarithmic prefactors)[47]

$$F_A \sim m_3{}^{1/2} \quad (9)$$

Collecting all the terms together and minimizing eq 6 with respect to m_3, finally one obtains

$$m_3 \sim (\tau_B{}^2 N_B)^{4/5}, \quad R_B \sim a\tau_B{}^{1/5} N_B{}^{3/5},$$
$$D \sim a\tau_B{}^{4/5} N_B{}^{2/5}/(\rho_a a^2)^{1/2} \quad (10)$$

With decreasing N_A, however, the elastic energy of the A blocks becomes significant. Though the layer around the core remains spherical, the A blocks become considerably stretched in lateral direction. Hence for short A blocks with $H \ll D$, their leading contribution to the free energy becomes

$$F_A \sim \frac{D^2}{N_A a^2} \quad (11)$$

Now the equilibrium structure of the micelle is governed by the balance of the core surface free energy and the elastic energy of A blocks which gives the following scaling relations

$$m_3 \sim \tau_B N_B{}^{1/2} N_A{}^{3/4} (\rho_a a^2)^{3/4}, \quad R_B \sim a N_B{}^{1/2} N_A{}^{1/4} (\rho_a a^2)^{1/4},$$
$$D \sim a\tau_B{}^{1/2} N_B{}^{1/4} N_A{}^{3/8}/(\rho_a a^2)^{1/8} \quad (12)$$

Henceforth the two regimes of long and short A blocks are called covered brush or deformed micelle, respectively. In the subsequent theoretical discussion the scaling approach first suggested by Zhulina et al.[35] will be extended to treat not only tethered spherical micelles but also cylindrical ones ($d = 2$). Although we assume theta solvent conditions for A blocks for the sake of simplicity, the approach can easily be generalized for good solvents. For cylindrical micelles, the core density reads

$$\phi \sim m_2 N_B a^3/R_B{}^2 \sim \tau_B \quad (13)$$

which yields a core radius

$$R_B \sim a(\tilde{m}_2 N_B/\tau_B)^{1/2} \quad (14)$$

where m_2 is the number of polymers per unit length with the corresponding dimensionless quantity $\tilde{m}_2 = m_2 a$. The total size of a tethered cylindrical micelle in transverse direction becomes

$$D \sim \frac{\tilde{m}_2}{a\rho_a} \quad (15)$$

Because of the changed geometry the area per chain at the core surface reads now $\sigma_2 \sim R_B a/\tilde{m}_2$ which results in an interfacial free energy

$$F_{int} \sim \frac{\tau_B{}^2}{\tilde{m}_2}\frac{R_B}{a} \quad (16)$$

In the deformed micelle regime, the leading free energy contribution of A blocks is still the stretching energy given in eq 11. However, the free energy of a chain in the corona of a cylindrical micelle is different from that of a spherical one given in eq 9 and for long A blocks the corresponding term becomes[47]

$$F_A \sim N_A{}^{1/3} \tilde{m}_2^{2/3} \quad (17)$$

Minimizing eq 6 with respect to $\tilde{m}_2$, finally one obtains the following scaling relations of tethered cylindrical micelles (i) in the covered brush regime

$$\tilde{m}_2 \sim \tau_B{}^{9/7} N_B{}^{3/7} N_A{}^{-2/7}, \quad R_B \sim a\tau_B{}^{1/7} N_B{}^{5/7} N_A{}^{-1/7},$$
$$D \sim a\tau_B{}^{9/7} N_B{}^{3/7} N_A{}^{-2/7}/(\rho_a a^2) \quad (18)$$

and (ii) in the deformed micelle regime

$$\tilde{m}_2 \sim \tau_B{}^{3/5} N_B{}^{1/5} N_A{}^{2/5} (\rho_a a^2)^{4/5},$$
$$R_B \sim a\tau_B{}^{-1/5} N_B{}^{3/5} N_A{}^{1/5} (\rho_a a^2)^{2/5},$$
$$D \sim a\tau_B{}^{3/5} N_B{}^{1/5} N_A{}^{2/5}/(\rho_a a^2)^{1/5} \quad (19)$$

Note that the dependences of $\tilde{m}_2$ and R_B on block lengths N_B, N_A agree with those previously found for cylindrical micelles in solution.[47]

Simulation Results. A rough analysis of both Figure 2a and Figure 4 shows that we are far from the limit $H \gg D$. In the simulations we obtain a total layer thickness of about $8r_c$ (for details see below) whereas the core size is about $6r_c$ and the lateral micelle about $10...11r_c$ (see Table 2). Thus, the structure of the A layer is significantly different from that of a planar brush but lateral stretching plays an important role and at small f_B diblock copolymer brushes are expected to obey the deformed micelle regime. Because $N_A = (1 - f_B)N_{tot}$ and $N_B = f_B N_{tot}$ are not independent in

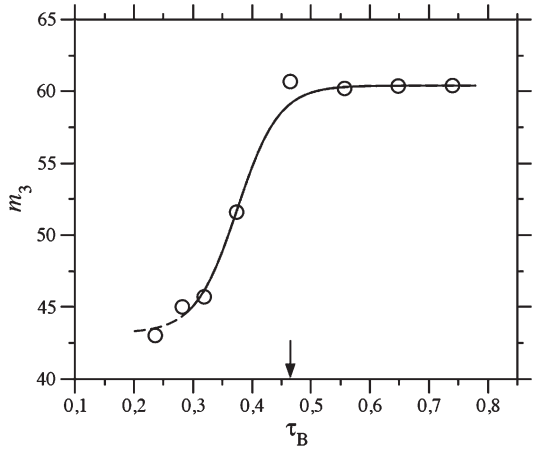


Figure 11. Spherical micelles at $f_B = 0.17$. Average number of chains per micelle m_3 versus solvent quality τ_B. The line gives the fit by a hyperbolic tangent and the arrow indicates τ_B^* where a_{BS} equals a_{AB}.

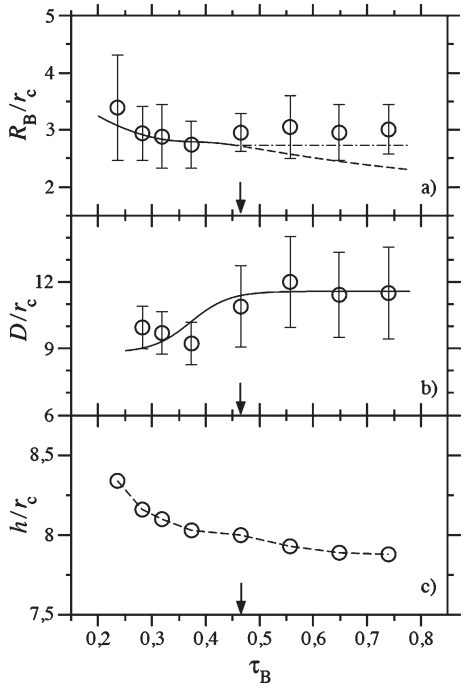


Figure 12. Spherical micelles at $f_B = 0.17$ and varying solvent quality τ_B: (a) core size R_B, (b) separation D (micelle size), and (c) total layer thickness h. In parts a and b, solid and dashed lines give the results of eqs 4 and 5, respectively, with $m_3(\tau_B)$ taken from the hyperbolic tangent fit shown in Figure 11 whereas the dash-dotted line in a) shows the behavior if in eq 4 additionally the effective τ is fixed at $a_{BS} > a_{AB}$ (see text). The dashed line in part c is a guide for the eyes. Similarly to Figure 11 arrows indicate τ_B^* where a_{BS} equals a_{AB}.

our model, eqs 12 yield a nonmonotonic behavior of both R_B and D versus f_B. In the relevant region $f_B < 0.4$, however, R_B as well as D grow monotonously with increasing f_B. The lateral tension within the A blocks D/N_A is monotonously growing over the whole f_B-range. As previously pointed out by Zhulina at al.,[35] this particular behavior is responsible for the merging of micellar cores and the formation of a continuous B structure with decreasing N_A.

Following eqs 12, the scaling predictions are $m_3 \sim \tau_B$, $D \sim \tau_B^{1/2}$ whereas R_B is expected to be independent of the solvent quality. In Figures 11 and 12, we plot the corresponding simulation results. Surprisingly, the average number of chains per micelle shows saturation at intermediate solvent quality. Obviously m_3 becomes constant at $a_{BS} > a_{AB}$. Remembering the structural changes with growing a_{BS} discussed above, i.e., the dipping of B cores deeply into the A layer or the covering by A legs, respectively, it seems reasonable that B blocks interact then first of all with A blocks while their interaction with the solvent becomes weak. Hence, in our simple model the effective solvent quality is given by τ_B only at $a_{BS} < a_{AB}$ while it becomes constant with $\tau_B^* = a_{AB}/a_{BS}^{(\theta)} - 1$ at larger a_{BS}. Note (i) that this effect could not be obtained in previous one-parameter models used in theory and simulations where both unmiscibility and selectivity are projected either to an effective polymer−solvent interaction[35] or to an effective polymer block−block interaction,[12] and (ii) that the effect is suppressed with growing f_B because of the decreasing number of available A monomers. Although in Figure 11, we fit the simulation results by a hyperbolic tangent, it should be noted that the behavior in the limit of small τ_B (dashed line) is not well determined. For $\tau_B < 0.2$ ($a_{BS} < 32.5$) we do not observe stable micelles. To check possible finite size effects, at $a_{BS} = 40$ simulations were performed not only within our standard system (I) of 362 chains ($L_x = L_y = 25\ r_c$) but also in an enlarged one (II) of 2090 chains ($L_x = L_y = 60\ r_c$). The results obtained in the two systems are: (I) $m_3 = 60.7 \pm 6.1$, $R_B = (3.0 \pm 0.3)\ r_c$, $D = (10.9 \pm 1.8)\ r_c$ and (II) $m_3 = 58.6 \pm 6.6$, $R_B = (2.9 \pm 0.6)\ r_c$, $D = (10.7 \pm 1.3)\ r_c$. Hence, possible finite size errors are within the order of 2−3%, i.e., smaller than the width of error bars shown in Figure 12.

Because the number of chains per micelle governs both R and D (see eqs 4, 5) the particular behavior shown in 11 is expected to have substantial consequences. Although the core radius R plotted in Figure 12a could be considered to be constant within the (large) error bars in agreement with theory, below we will show that the reason for the behavior obtained is different from that assumed in the theoretical model. For the micelle size D shown in Figure 12b) the situation is obvious: There is no chance to fit the simulation data with a square root function predicted by theory. The lines plotted in Figure 12, parts a and b, were obtained by using eqs 4 and 5 as fit functions after replacing $m_3(\tau_B)$ by the hyperbolic tangent received above. For D, we find reasonable agreement, i.e., a transition from smaller values at small τ_B to a constant value at large τ_B, although the transition point seems to be shifted a bit. At small τ_B, probably the simulation data on D are unreliable because of the polydispersity of the micelles. In general, no regime is known in which the micelle size decreases with growing τ_B. Because of the explicit dependence of R on τ_B (see eq 4) the correct fitting procedure is tricky in that case. After fitting the small-τ_B data with eq 4 (solid and dashed lines in Figure 12a), the solvent quality is set $\tau = \text{const} = \tau_B^*$ at $\tau_B > \tau_B^*$ (dash-dotted line). Hence, the data obtained for the spherical-micelle morphology can be consistently described by assuming a constant "solvent" quality at $\tau_B > \tau_B^*$. Note that in the deformed-micelle regime of the scaling theory the core size becomes independent of τ_B because in the particular case the explicit dependence on τ_B in eq 4 cancels with that of m_3. Figure 12c shows the total brush height in the parameter range under consideration. Note that this global quantity varies much less in the τ_B range considered than the local micelle parameters R and D (by about 5% compared to about 20% or 25%, respectively).

As discussed in detail in subsection 3.1, for growing B block length f_B, we obtain a stripe-like morphology that is of particular interest because it can be used as structure-guiding matrix scaffold to control the spatial distribution of nanoobjects into ordered nanochains.[28,29] Both stripe width

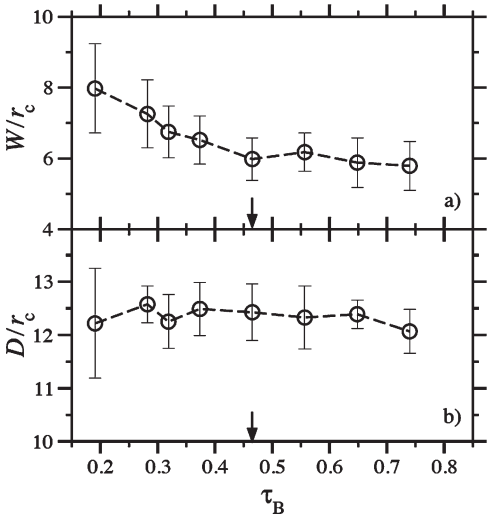


Figure 13. Stripe morphology obtained at constant polymer composition $f_B = 0.37$: Width W (a) and periodicity D (b) versus solvent quality $\tau_B(a_{BS})$. Similarly to Figure 11 arrows indicate τ_B^* where a_{BS} equals a_{AB}.

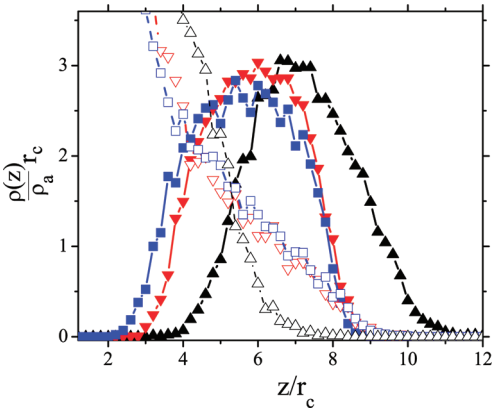


Figure 14. B block density profiles (filled symbols) at $f_B = 0.37$ and varying interaction parameter a_{BS} [25 (triangles up), 35 (triangles down), 45 (squares)] exhibiting disordered or stripe-like morphologies, respectively (see Figure 1). To complete the picture the tails of corresponding A profiles tails are shown with open symbols.

W (width of B domains) and the periodicity D of the stripes are plotted in Figure 13 as a function of solvent quality τ_B. With decreasing solvent quality the globular B domains undergo a shape transformation from half-cylinders over baquet-like aggregates to cylindrical ones (see Figure 6). That is why the theoretical predictions for grafted cylindrical micelles given in eq 19 are to be treated with caution. For $\tau_B < \tau_B^*$, from simulation data, we estimate a scaling behavior of about $W \sim {\tau_B}^{-1/3}$, i.e., a stronger decay than predicted for the core size $R_B \sim \tau^{-1/5}$. The enhanced dependence on τ_B is likely to occur due to the shape transformation that enforces the shrinkage of the effective width of B domains at the brush surface (see Figure 6). However for $\tau_B > \tau_B^*$, similarly to the behavior of spherical micelles the size of globular domains becomes independent of τ_B. The density profiles plotted in Figure 14 confirm the general picture illustrated by the series of snapshots shown in Figure 6. Reducing the solvent quality of B blocks from good to poor, at polymer composition $f_B = 0.37$ we observe a transition from a disordered phase to a stripe-like one (see Figure 1). On the other hand solvophobic B blocks are increasingly pushed into the solvophilic A matrix that exhibits simultaneously pronounced tails in order to cover partially the solvophobic domains.

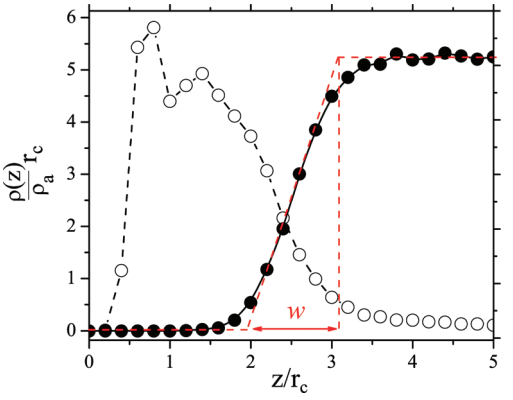


Figure 15. Density profiles of A and B blocks (open and filled symbols, respectively) in the neighborhood of the A/B interface ($f_B = 0.67$, $a_{AB} = 40$, selective solvent with $a_{BS} = 40$). The interfacial width w is determined by a tangent construction.

In contrast to the theoretical prediction given in eq 19 the periodicity (total micelle size) D is constant within the error bars not only at $\tau_B > \tau_B^*$ but over the whole τ_B range. Unfortunately our model system is too small to extract reliable date on the linear chain density m_2. In fact we obtain only two different numbers: $m_2 r_c \approx 7.1$ at $a_{BS} \leq 35$ and 7.2 at $a_{BS} \geq 36$. Therefore, it is not possible to check the validity of the two basic equations of grafted cylindrical micelles, eqs 14 and 15, with a fit function of m_2 as it has been discussed above for grafted spherical micelles. However, in contrast to the successful description of spherically micellar structures by scaling theory, a similar scaling model used for grafted cylindrical micelles seems to be too simple to yield a convincing description of stripe-like morphologies of DCBs. Shape transformations obtained in simulations are clearly beyond the scope of scaling approaches.

3.3. Internal Structure of Lamellar Phases. For selective solvents, lamellar phases occur at $f_B > 0.57$. This particular morphology consisting of two sublayers each of which being rich in one polymer block is the simplest structure one can imagine for DCBs which consist of two nonmiscible blocks. The particular surface pattern was already addressed in first studies on the structure of diblock copolymer brushes.[19] For ideal DCBs, it was assumed that the interface between the two sublayers is sharp. A first theoretical understanding of A/B copolymer brushes in good solvents was established by Fereira and Leibler[10] by means of a SCF approach. In particular they found that the width of the A/B interfacial region decreases with growing Flory−Huggins parameter χ_{AB}. In the limit of very strong interaction strength, the tethered blocks form a step-like A brush near the grafting plane. However, with increasing solvent quality the A/B demixing transition is suppressed. This behavior indicates the importance of selective solvents to facilitate demixing.

In the remaining part of the subsection, we consider the interfacial width of two-layer lamellar structures obtained at $f_B = 0.67$ with varying incompatibility of the two polymer blocks $30 < a_{AB} < 57$. Two different systems are studied: (i) brushes in a good solvent for both blocks ($a_{AS} = a_{BS} = 25$) and (ii) brushes in a selective solvent for the A blocks ($a_{AS} = 25$, $a_{BS} = 40$). In Figure 15, we plot a typical density profile that shows clearly a two-layer structure and the finite interfacial area where A and B rich layers overlap, i.e., where A and B blocks coexist. The interfacial width is estimated by a tangent construction in analogy to Helfand's convention.[48] According to the conventional Helfand-Tagami regime of free block copolymers the interfacial width scales as $W \sim a/{\chi_{AB}}^{1/2}$.[49]

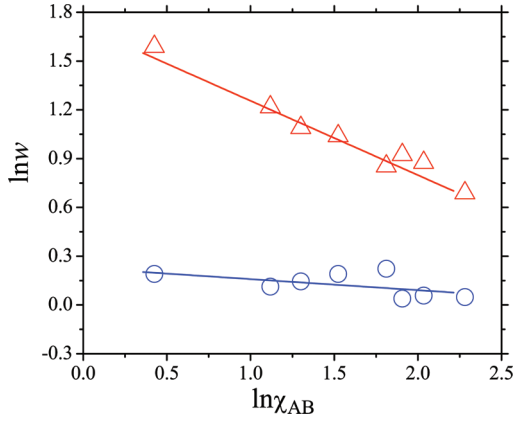


Figure 16. Scaling of interfacial width w vs Flory−Huggins parameter χ_{AB} for nonselective (triangles) and selective solvent (circles). The lines are best power-law fits to the two data sets.

For strongly stretched brushes with $(h/R_g^{(0)})^2 > N_{tot}\chi_{AB}$ where $R_g^{(0)}$ is the radius of gyration of a corresponding free chain, Akgun et al.[9] predicted a stretched interface regime that obeys $W \sim a(\rho_a a^2)^{1/3}/\chi_{AB}$. Note that in this regime not only the scaling exponent of the Flory−Huggins parameter is changed but the width becomes also dependent on grafting density. In Figure 16, the results for both systems defined above are shown. Note that the Flory−Huggins parameter is calculated by using the phenomenological relation $\chi_{AB} \approx 0.306\ (a_{AB} - a_{AA})$.[41] For both nonselective and selective solvents, we obtain reasonable power-law scaling. In the nonselective case the exponent is about −0.45 which is indeed very close to the value expected in the Helfand-Tagami regime. Rough estimates for the chains considered yield $\chi_{AB} N \approx 60...300$, $(h/R_g)^2 \approx 10...60$. Thus, the stretching of the chains is too weak to see the stretched interface regime. On the other hand for selective solvents in which the B blocks are collapsed and form a dense layer, we obtain a rather sharp interface with a width which depends only very weakly on the A/B interaction parameter, i.e., $W \sim 1/\chi_{AB}^{0.007}$. Hence, the structure of lamellar phases of block copolymer brushes in nonselective solvents agrees with the established model of dry brushes while the behavior in selective solvents obviously requires a deeper theoretical understanding.

4. Conclusions

To our knowledge for the first time DPD simulations are used to investigate morphological transitions of diblock copolymer brushes in selective solvents and to elucidate the internal structure of particular morphologies in detail. In our model, the immiscibility of different polymer blocks and solvent selectivity are treated on an equal footing by means of three independent interactions (excess repulsions) the strength of which is set by the DPD parameters a_{AB}, a_{AS}, and a_{BS}. Note that these a_{ij}'s are related to the corresponding Flory−Huggins parameters χ_{AB}, χ_{AS}, and χ_{BS}. The solvent is a good one for anchored A blocks but poor for B blocks. The variable solvent quality τ_B is considered as external stimulus and equilibrium morphologies are studied at different copolymer compositions determined by the fraction of B monomers f_B. Grafted diblock copolymers exhibit a rich phase diagram in the f_B−τ_B parameter space. With growing f_B, we obtain hexagonally ordered spherical micelles, stripe-like morphologies consisting of cylindrical micelles, perforated layer, or inverted hexagonal structures and finally a laterally uniform two-layer lamella. Choosing appropriate polymer compositions, we have shown that variations in τ_B can stimulate transitions between spherical and cylindrical micelles as well as between cylindrical micelles and a perforated layer structure.

Beside the morphology of copolymer brushes we address their surface properties. The composition of top layer as well as any pattering are of high interest. Partial density profiles of A and B blocks in the z direction reflect perpendicular segregation effects. In particular, they indicate the location of solvophobic B aggregates. Depending on polymer composition and solvent quality, they can be either embedded in the solvophilic A brush or pushed out to its rim. One has to bear in mind, however, that density profiles do not adequately reflect a monolayer-like coverage of B domains by, e.g., A legs. The inspection of simulation snapshots can be a useful tool to detect such particular structures. To analyze lateral surface patterns, we consider domain sizes such as the core radius of micelles as well as possible periodic spacing of micellar aggregates. For spherically and cylindrically micellar morphologies, we compare the simulation results with previously obtained or newly established scaling predictions. We obtain an interesting feature that could not be found in previous one-parameter models where all the differences between A and B blocks were projected either onto inherent incompatibility (block immiscibility) or solvent selectivity. Decreasing the solvent quality, i.e., enlarging the distance τ_B to the θ-point, we see the fingerprint of a cutoff $\tau_B^* = a_{AB}/a_{BS}^{(\theta)} - 1$. For $\tau_B > \tau_B^*$, i.e., $a_{BS} > a_{AB}$, the system does not respond to the external stimulus given by a changing solvent quality: Both core size and separation of spherical micelles become constant as well as the width of cylindrical aggregates. The effect can be understood by assuming that an embedded solvophobic B aggregate interacts first of all with surrounding solvophilic A blocks while the unfavorable interaction with the solvent becomes weak. Obviously the effect is suppressed for growing f_B because of the decreasing number of available A monomers.

While completing the manuscript we learned about a recent paper by O'Driscoll et al.[50] The authors report new preliminary SCF calculations similarly to that previously published[11] but within an extended model of film-solvent systems where the interactions between each of the polymer blocks and the solvent, $\chi_{AS}N$ and $\chi_{BS}N$ are included in addition to the usual incompatibility parameter $\chi_{AB}N$. The phase boundaries of hexagonal, stripe, inverse hexagonal, and lamella phases obtained within this many-parameter model are much more consistent with experimental results observed for PS−PMMA diblock copolymer brushes. Hence, the independent treatment of block immiscibility and solvent selectivity seems to be a quite natural and necessary extension of the standard model of DCBs not only for wet but also for dry films because of remaining solvent.

For the uniform two-layer lamella obtained at $f_B > 0.57$, we analyze the dependence of interfacial thickness w on Flory−Huggins parameter χ_{AB}. With increasing χ_{AB}, the width of the interface region where both types of monomers coexist is shrinking. For selective and nonselective solvents, however, we observe quite different behavior. In the case of good solvents for both blocks, the scaling behavior obtained is in good agreement with the conventional Helfand−Tagami theory of free block copolymers.[49] We find no fingerprint of the so-called stretched interface regime recently proposed.[9] A rough estimate indicates that the stretching of chains is too weak to reach that regime. For selective solvents where the B blocks are collapsed into a dense layer, the interfacial width is smaller by a factor of at least 2 and almost independent of χ_{AB}. This behavior desires a deeper theoretical understanding.

To use patterned copolymer brush surfaces as templates for a specific deposition of nanoparticles it is necessary to understand the self-organization of the brush in detail. We hope that the simulation study presented in the paper can give new impact for further experimental and theoretical work. A simulation study

that addresses the organization of nanoparticles at the copolymer surface is under progress.

References and Notes

(1) Milner, S. T. *Science* **1991**, *251*, 905–914.
(2) Halperin, A.; Tirrell, M.; Lodge, T. P. *Adv. Polym. Sci.* **1992**, *100*, 31–71.
(3) *Polymer Brushes*; Advincula, R. C., Britain, W. J., Caster, K. C., Rühe, J., Eds.; Wiley- VCH: Weinheim, Germany, 2004.
(4) Minko, S.; Müller, M.; Usov, D.; Scholl, A.; Froeck, C.; Stamm, M. *Phys. Rev. Lett.* **2002**, *88*, 035502(1)−035502(4).
(5) Santer, S.; Kopyshev, A.; Donges, J.; Rühe, J.; Jiang, X.; Zhao, B.; Müller, M. *Langmuir* **2007**, *23*, 279–285.
(6) Merlitz, H.; He, G.-L.; Sommer., J.-U.; Wu, C.-X. *Macromolecules* **2009**, *42*, 445–451.
(7) Zhao, B.; Brittain, W. J. *Prog. Polym. Sci.* **2000**, *25*, 677–710.
(8) Boyes, S. G.; Granville, A. M.; Baum, M.; Akgun, B.; Mirous, B. K.; Brittain, W. J. *Surf. Sci.* **2004**, *570*, 1–12.
(9) Akgun, B.; Uğur, G.; Brittain, W. J.; Majkrzak, C. F.; Li, X.; Wang, J.; Li, H.; Wu, D. T.; Wang, Q.; Foster, M. D. *Macromolecules* **2009**, *42*, 8411–8422.
(10) Ferreira, P. G.; Leibler, L. *J. Chem. Phys.* **1996**, *105*, 9362–9370.
(11) Matsen, M. W.; Griffiths, G. H. *Eur. Phys. J. E* **2009**, *29*, 219–227.
(12) Wang, J.; Müller, M. *Macromolecules* **2009**, *42*, 2251–2264.
(13) Minko, S. *Polym. Rev.* **2006**, *46*, 397–420.
(14) Zhou, F.; Huck, W. T. S. *Phys. Chem. Chem. Phys.* **2006**, *8*, 3815–3823.
(15) Uhlmann, P.; Merlitz, H.; Sommer, J.-U.; Stamm, M. *Macromol. Rapid Commun.* **2009**, *30*, 732–740.
(16) Zhulina, E. B.; Singh, C.; Balazs, A. C. *Macromolecules* **1996**, *29*, 6338–6348.
(17) Meng, D.; Wang, Q. *J. Chem. Phys.* **2009**, *130*, 134904(1−9)
(18) Zhao, B.; Haasch, R. T.; MacLaren, S. *J. Am. Chem. Soc.* **2000**, *122*, 2407–2408.
(19) Zhao, B.; Brittain, W. J.; Zhou, W. S.; Cheng, S. Z. D. *Macromolecules* **2000**, *33*, 8821–8827.
(20) Santer, S.; Rühe, J. *Polymer* **2004**, *45*, 8279–8297.
(21) Brittain, W. J.; Boyes, S. G.; Granville, A. M.; Baum, M.; Mirous, B. K.; Akgun, B.; Zhao, B.; Blickle, C.; Foster, M. D. *Adv. Polym. Sci.* **2006**, *198*, 125–147.
(22) Xu, C.; Wu, T.; Drain, C. M.; Batteas, J. D.; Fasolka, M. J.; Beers, K. L. *Macromolecules* **2006**, *39*, 3359–3364.
(23) Kong, B.; Lee, J. K.; Choi, I. S. *Langmuir* **2007**, *23*, 6761–6765.
(24) Gersappe, D.; Fasolka, M.; Israels, R.; Balazs, A. C. *Macromolecules* **1995**, *28*, 4753–4755.
(25) Romiszowski, P.; Sikorski, A. *J. Phys.: Condens. Matter* **2007**, *19*, 205137(1−6)
(26) Yin, Y.; Sun, P.; Li, B.; Chen, T.; Jin, Q.; Ding, D.; Shi, A.-C. *Macromolecules* **2007**, *40*, 5161–5170.
(27) Rahane, S. B.; Floyd, J. A.; Metters, A. T.; Kilbey, S. M. *Adv. Func. Mater.* **2008**, *18*, 1232–1240.
(28) Niu, S.; Saraf, R. F. *Nanotechnolgy* **2007**, *18*, 12607(1−4)
(29) Li, Q.; He, J.; Glogowski, E.; Li, X.; Wang, J.; Emrik, T.; Russel, T. P. *Adv. Mater.* **2008**, *20*, 1462–1466.
(30) Yu, K.; Wang, H.; Han, Y. *Langmuir* **2007**, *23*, 8957–8964.
(31) Wang, D.-Y.; Teng, T.-S.; Wu, Y.-C.; Lee, Y.-C.; Chen, K.-H.; Chen, C.-H.; Chang, Y.-C.; Chen, C.-C. *J. Phys. Chem. C* **2009**, *113*, 13498–13504.
(32) Oren, R.; Liang, Z.; Barnard, J. S.; Warren, S. C.; Wiesner, U.; Huck, W. T. S. *J. Am. Chem. Soc.* **2009**, *131*, 1670–1671.
(33) Brown, G.; Chakrabarti, A.; Marko, J. F. *Macromolecules* **1995**, *28*, 7817–7821.
(34) Zhulina, E. B.; Balazs, A. C. *Macromolecules* **1996**, *29*, 2667–2673.
(35) Zhulina, E. B.; Singh, C.; Balazs, A. C. *Macromolecules* **1996**, *29*, 8254–8259.
(36) Wang, J.; Müller, M. *Langmuir* **2010**, *26*, 1291–1303.
(37) Hoogerbrugge, P. J.; Koelman, J. M. V. A. *Europhys. Lett.* **1992**, *19*, 155–160.
(38) Malfreyt, P.; Tildesley, D. J. *Langmuir* **2000**, *16*, 4732–4740.
(39) Pal, S.; Seidel, C. *Macromol. Theory Simul.* **2006**, *15*, 668–673.
(40) Español, P.; Warren, P. *Europhys. Lett.* **1995**, *30*, 191–196.
(41) Groot, R. D.; Warren, P. B. *J. Chem. Phys.* **1997**, *107*, 4423–4435.
(42) Maly, M.; Posocco, P.; Pricl, S.; Fermeglia, M. *Ind. Eng. Chem. Res.* **2008**, *47*, 5023–5038.
(43) Nardei, M. M.; Zifferer, G. *J. Chem. Phys.* **2009**, *131*, 124903(1−8)
(44) Prokhorova, S. A.; Kopyshev, A.; Ramakrishnan, A.; Zhang, H.; Rühe, J. *Nanotechnology* **2003**, *14*, 1098–1108.
(45) O'Driscoll, B. M. D.; Oren, R.; Hamley, I. W. *Polym. Adv. Technol.* **2009**, DOI 10.1002/pat.1597, published online
(46) de Gennes, P. G. *J. Phys.-Lett.* **1975**, *36*, L-55–L-57.
(47) Birshtein, T. M.; Zhulina, E. B. *Polymer* **1989**, *30*, 170–177.
(48) Helfand, E.; Wasserman, Y. R. *Macromolecules* **1976**, *9*, 879–888.
(49) Helfand, E.; Tagami, Y. *J. Chem. Phys.* **1971**, *56*, 3592–3601.
(50) O'Driscoll, B. M. D.; Griffiths, G. H.; Matsen, M. W.; Perrier, S.; Ladmiral, V.; Hamley, I. W. *Macromolecules* **2010**, *43*, 8177–8184.